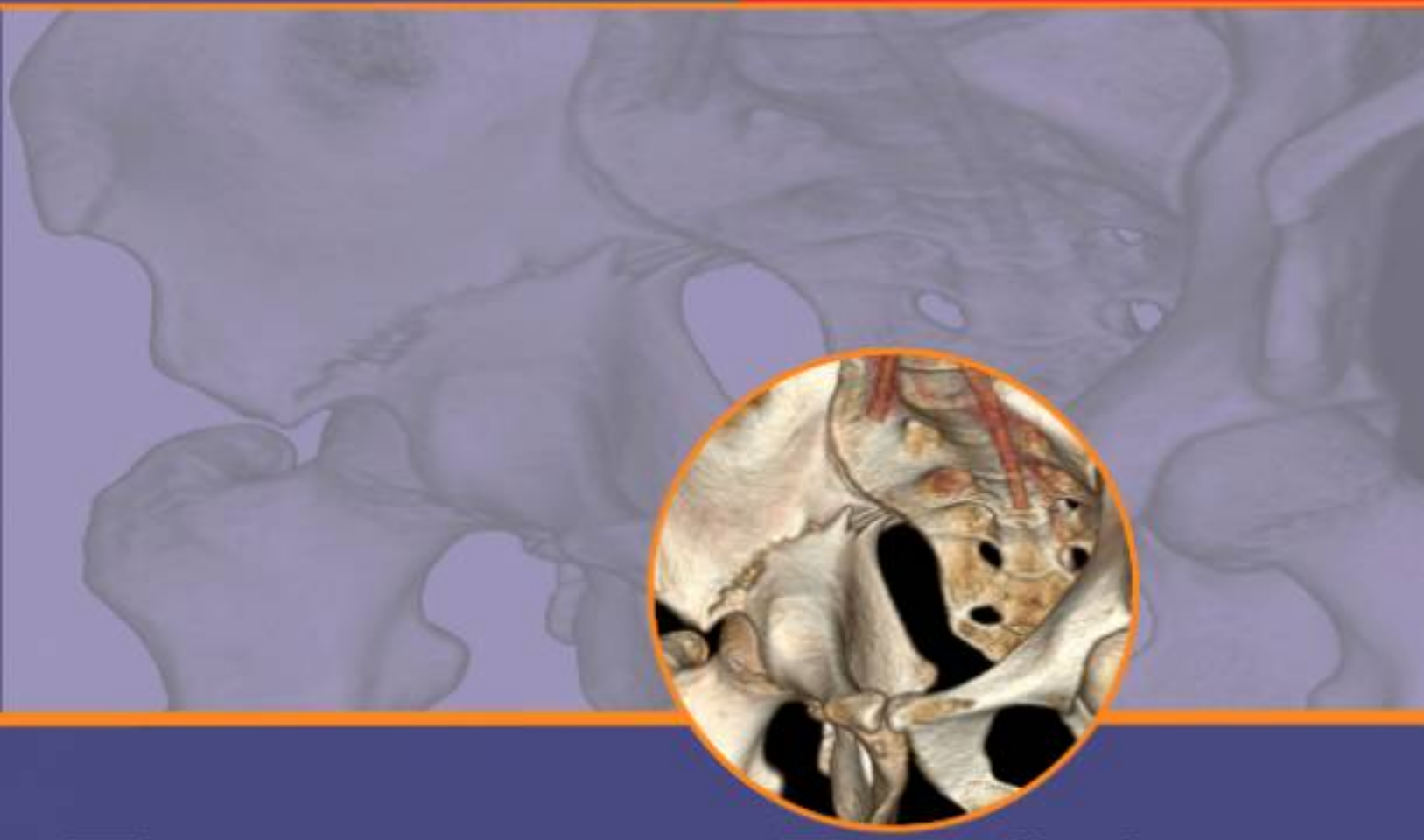
THE REQUISITES



Emergency Radiology

Jorge A. Soto and Brian C. Lucey

MOSBY
ELSEVIER

MOSBY
ELSEVIER

1600 John F. Kennedy Boulevard
Suite 1800
Philadelphia, PA 19103-2899

EMERGENCY RADIOLOGY: THE REQUISITES ISBN: 978-0-323-05407-2
Copyright © 2009 by Mosby, Inc., an affiliate of Elsevier, Inc.

All rights reserved. No part of this publication may be reproduced or transmitted in any form or by any means, electronic or mechanical, including photocopying, recording, or any information storage and retrieval system, without permission in writing from the publisher. Permissions may be sought directly from Elsevier's Rights Department: phone: (+1) 215 239 3804 (U.S.) or (+44)1865 843830 (UK); fax: (+44)1865 853333; e-mail: healthpermissions@elsevier.com. You may also complete your request online via the Elsevier (US) website at http://www.elsevier.com/permissions.

Notice

Knowledge and best practice in this field are constantly changing. As new research and experience broaden our knowledge, changes in practice, treatment and drug therapy may become necessary or appropriate. Readers are advised to check the most current information provided (i) on procedures featured or (ii) by the manufacturer of each product to be administered, to verify the recommended dose or formula, the method and duration of administration, and contraindications. It is the responsibility of the practitioner, relying on their own experience and knowledge of the patient, to make diagnoses, to determine dosages and the best treatment for each individual patient, and to take all appropriate safety precautions. To the fullest extent of the law, neither the Publisher nor the Editors assume any liability for any injury and/or damage to persons or property arising out or related to any use of the material contained in this book

The Publisher

Library of Congress Cataloging-in-Publication Data
Soto, Jorge A.
Emergency radiology : the requisites / Jorge A. Soto, Brian C. Lucey.—1st ed.
p. ; cm.—(Requisites series)
Includes bibliographical references.
ISBN 978-0-323-05407-2
1. Medical emergencies—Imaging. I. Lucey, Brian C. II. Title. III. Series.
[DNLM: 1. Diagnostic Imaging. 2. Emergency Medical Services. WN 180 S718e 2009]

RC86.7.S685 2009
616.07'54--dc22 2008037239

Acquisitions Editor: Rebecca Gaertner
Developmental Editor: Martha Limbach
Project Manager: Bryan Hayward
Design Direction: Steven Stave

Printed in the United States of America

Last digit is the print number: 9 8 7 6 5 4 3 2 1

Working together to grow libraries in developing countries
www.elsevier.com | www.bookaid.org | www.sabre.org
ELSEVIER BOOK AID International Sabre Foundation

Dedication

I dedicate this book to my parents, Jorge Sr. and Socorro, for their example and guidance, and to my wife, Ana, and children, Andrea and Alejandro, for their sustained support and patience as I devote time to academic radiology.

JAS

To my parents, James and Anne; sister, Suzanne; wife, Ciara; and son, James. Thanks for the unconditional support.

BCL

Contributors

Carlos A. Anaya, MD

Program Director
UCLA Interventional Radiology Fellowship
West Los Angeles VA Medical Center
University of California—Los Angeles
Interventional Radiologist
Department of Radiology
West Los Angeles VA Medical Center
Los Angeles, California
Vascular Emergencies

Stephan W. Anderson, MD

Assistant Professor, Director of Computed Tomography
Department of Radiology
Boston University Medical Center
Boston, Massachusetts
Nontrauma Abdomen

Laura Avery

Instructor in Radiology
Diagnostic Radiology
Massachusetts General Hospital and Harvard Medical School
Assistant Radiologist
Diagnostic Radiology
Massachusetts General Hospital
Boston, Massachusetts
Chest Trauma

Glenn D. Barest, MD

Assistant Professor
Department of Radiology
Boston University School of Medicine
Section Head, Neuroradiology
Department of Radiology
Boston Medical Center
Boston, Massachusetts
Traumatic and Nontraumatic Emergencies of the Brain, Head, and Neck; Traumatic and Nontraumatic Spine Emergencies

Sarah D. Bixby, MD

Instructor of Radiology
Department of Radiology
Harvard Medical School
Pediatric Radiologist
Department of Radiology
Children's Hospital Boston
Boston, Massachusetts
Imaging Evaluation of Common Pediatric Emergencies

Anna K. Chacko, MD

Professor
Department of Radiology
Boston University
Boston, Massachusetts
Chair
Department of Radiology
VA Pittsburgh Health System
Pittsburgh, Pennsylvania
Professor
Anatomy Department
John A. Burns School of Medicine
University of Hawaii
Honolulu, Hawaii
Emergency Nuclear Radiology

J. Andrew Chacko, MSEng

Emergency Nuclear Radiology

Luis E. Diaz, MD

Associate Professor
Department of Radiology
Boston University
Associate Chief of Radiology
Department of Radiology
Boston VA Health Care System
Staff Physician
Department of Radiology
Boston Medical Center
Boston, Massachusetts
Extremities: Nontrauma

Alejandra Duran-Mendicuti, MD

Instructor in Radiology
Department of Radiology
Harvard Medical School
Radiologist
Department of Radiology, Emergency Radiology
Brigham and Women's Hospital
Boston, Massachusetts
Nontraumatic Emergency Radiology of the Thorax

Ana Maria Gomez, MD

Radiology Resident
Department of Radiology
Ronald Reagan Medical Center
David Geffen School of Medicine
University of California—Los Angeles
Los Angeles, California
Vascular Emergencies

Rathachai Kaewlai, MD

Instructor
Department of Radiology
Harvard Medical School
Clinical Fellow
Department of Radiology
Massachusetts General Hospital
Boston, Massachusetts
Extremity Trauma

M. Stephen Ledbetter, MD

Assistant Professor of Radiology
Department of Radiology
Harvard Medical School
Director of Emergency Radiology
Department of Radiology, Emergency Radiology
Brigham and Women's Hospital
Boston, Massachusetts
Nontraumatic Emergency Radiology of the Thorax

Brian C. Lucey, MB, Bch, BAO, MRCPI, FFR(RCSI)

Associate Professor
Department of Radiology
Boston University School of Medicine
Boston, Massachusetts
Clinical Director
Department of Radiology
The Galway Clinic
Doughiska, County Galway, Ireland
Nontrauma Abdomen; Pelvic Emergencies

Asim Z. Mian, MD

Assistant Professor
Department of Radiology
Boston University School of Medicine
Attending Neuroradiologist
Department of Radiology
Boston Medical Center
Boston, Massachusetts
Traumatic and Nontraumatic Emergencies of the Brain, Head, and Neck

Sarah Sarvis Milla, MD

Assistant Professor of Radiology
Department of Radiology
New York University Medical Center
New York, New York
Imaging Evaluation of Common Pediatric Emergencies

Felipe Munera, MD

Associate Professor, Clinical Radiology
Department of Radiology
Miller School of Medicine
University of Miami
Jackson Memorial Hospital
University of Miami Health System
Miami, Florida
Vascular Emergencies

Rohini N. Nadgir, MD

Assistant Professor
Department of Radiology
Boston University School of Medicine
Attending Neuroradiologist
Department of Radiology
Boston Medical Center
Boston, Massachusetts
Traumatic and Nontraumatic Emergencies of the Brain, Head, and Neck

Robert A. Novelline, MD

Professor of Radiology
Harvard Medical School
Director of Emergency Radiology
Department of Radiology
Massachusetts General Hospital
Boston, Massachusetts
Chest Trauma

Osamu Sakai, MD, PhD

Associate Professor
Department of Radiology
Boston University School of Medicine
Attending Neuroradiologist
Director of Head and Neck Imaging
Department of Radiology
Boston Medical Center
Boston, Massachusetts
Traumatic and Nontraumatic Emergencies of the Brain, Head, and Neck

Rashmikant B. Shah, MD, ABR–ABNM, ABPath

Staff, Radiology and Nuclear Medicine
Radiology
VA Hospital, University Drive Division
Pittsburgh, PA
Emergency Nuclear Radiology

Ajay K. Singh, MD

Assistant Professor
Department of Radiology
Massachusetts General Hospital
Boston, Massachusetts
Extremity Trauma

Aaron Sodickson, MD

Instructor in Radiology
Department of Radiology
Harvard Medical School
Radiologist
Department of Radiology, Emergency Radiology
Brigham and Women's Hospital
Boston, Massachusetts
Nontraumatic Emergency Radiology of the Thorax

Jorge A. Soto, MD

Professor of Radiology
Department of Radiology
Boston University School of Medicine
Vice Chairman
Department of Radiology
Boston Medical Center
Boston, Massachusetts
Abdomen Trauma; Nontrauma Abdomen

Michael Stella, MD

Instructor in Radiology
Department of Radiology
Harvard Medical School
Radiologist
Department of Radiology, Emergency Radiology
Brigham and Women's Hospital
Boston, Massachusetts
Nontraumatic Emergency Radiology of the Thorax

Joshua W. Stuhlfaut, MD

Director of Computed Tomography
Department of Radiology
Jordan Hospital
Plymouth, Massachusetts
Abdomen Trauma

Salvatore Viscomi, MD

Instructor in Radiology
Department of Radiology
Harvard Medical School
Radiologist
Department of Radiology, Emergency Radiology
Brigham and Women's Hospital
Boston, Massachusetts
Nontraumatic Emergency Radiology of the Thorax

Scott White, MD

Instructor in Radiology
Department of Radiology
Harvard Medical School
Radiologist
Department of Radiology, Emergency Radiology
Brigham and Women's Hospital
Boston, Massachusetts
Nontraumatic Emergency Radiology of the Thorax

Foreword

THE REQUISITES is a series of textbooks encompassing the fundamental building blocks of radiology practice. The series is approaching its third decade and continues to flourish due to the diligence and success of its authors in producing very high quality work. Publication of *Emergency Radiology: THE REQUISITES* brings a new addition to THE REQUISITES series and reflects the growing importance of imaging in the management of patients presenting to emergency rooms for care. Drs. Soto and Lucey are to be congratulated for their outstanding new book that captures the philosophy of the series.

Imaging has played an important role in emergency medicine ever since the discovery of the x-ray. In the past two decades, the development of new applications, most importantly with CT, ultrasound, and MRI, has revolutionized the use of imaging in the emergency setting. Cross-sectional methods offer more anatomic and functional information and have displaced conventional radiography in many diagnostic scenarios while also greatly extending non–trauma-related applications of emergency imaging. Drs. Soto and Lucey and their team of authors have captured this transformation and have produced a book that addresses both trauma related and non–trauma-related emergencies.

To help them capture the full scope of contemporary applications of emergency imaging, Drs. Soto and Lucey have assembled a stellar team of co-authors for their book including Drs. Glenn D. Barest, Asim Z. Mian, Osamu Sakai, Rohini N. Nadgir, Laura Avery, Robert A. Novelline, Joshua W. Stuhlfaut, Ajay K. Singh, Rathachai Kaewlai, Luis E. Diaz, Sarah Bixby, Sarah Sarvis Milla, Scott White, Alejandra Duran-Mendicuti, Aaron Sodickson, Salvatore Viscomi, Michael Stella, M. Stephen Ledbetter, Stephan W. Anderson, Felipe Munera, Carlos A. Anaya, Ana Maria Gomez, Anna K. Chacko, Rashmikant B. Shah, and J. Andrew Chacko. The book is logically structured by organ systems and body regions.

One of the features of THE REQUISITES series most noted and appreciated in reader feedback is the use of tables and boxes to restate and summarize essential information in concise form. This reinforces the narrative discussion and the liberal use of this approach highlights *Emergency Radiology: THE REQUISITES*.

THE REQUISTES have now become old friends to two or three generations of medical imagers. We have tried to remain true to the original intent of the series, which was to provide the resident, fellow, or practicing physician with a text that might be reasonably read within several days. In practice, we see residents and fellows doing exactly that at the beginning of each subspecialty rotation. The concise presentation and reasonable length of THE REQUISITES books allows them to be read and reread several times during subsequent rotations and during preparation for board examinations.

THE REQUISITES are not intended to be exhaustive but to provide basic conceptional, factual, and interpretative material required for clinical practice. Each book is written by nationally recognized authorities in the respective subspecialty areas. Each author is challenged to present material in the context of today's practice of radiology rather than grafting information about new imaging methods onto old, out-of-date material.

Drs. Soto and Lucey and their coauthors have done an outstanding job in sustaining the philosophy of THE REQUISITES in radiology series. They have produced a truly contemporary text for emergency imaging. I believe that *Emergency Radiology: THE REQUISITES* will serve radiologists, emergency medicine specialists and other physicians who deal with emergency cases as a concise and useful introduction to the subject and will also serve as a very manageable text for review by fellows and practicing radiologists and cardiologists.

James H. Thrall, MD
Radiologist-in-Chief
Massachusetts General Hospital
Juan M. Taveras Professor of Radiology
Harvard Medical School
Boston, Massachusetts

Preface

Emergency Radiology is the newest addition to THE REQUISITES series. Although both the organ system–based and modality-based division of radiology have existed for some considerable time, this is the first of THE REQUISITES series to embrace a multimodality, multisystem approach to radiology. There has been a paradigm shift in medical management over the past 20 years or so, away from inpatient-oriented healthcare toward an increasingly outpatient-based system. Nowhere is this more apparent than in the emergency rooms around the country and around the world. The reliance on imaging for diagnosis and guiding management throughout medicine has been increasing, and this is exemplified in the emergency room. Current practice means that all imaging modalities are available to the emergency room physician. More than any other modality, it is the massive increase in the use of CT that has led to the development of the specialty of emergency radiology. The value of CT in the setting of trauma, investigation of severe headache, abdominal pain, and the evaluation of patients suspected of pulmonary embolus form the bedrock of emergency imaging, although there is an increasing role for MR imaging in the emergency room setting, particularly for the rapid evaluation of musculoskeletal injury and emergent neurological evaluation. Against this background of the emerging subspecialty of emergency radiology, and being on the "front line," as it were at Boston University Medical Center, it seemed only logical to both of us to add this title to THE REQUISITES series. The book is an attempt to collate all the radiology information required in order to provide comprehensive coverage to an emergency room into one text that can be used by both residents-in-training and also general radiologists in practice, as well as emergency room physicians and trauma surgeons.

The goal of this first edition is to provide a framework for people with an interest in emergency imaging. It is expected that revision will be required regularly to keep up with the rapid changes in imaging requirements from the emergency room. Given the new direction taken by this book, stepping away from the organ- and modality-based divisions, we acknowledge that there is potential for overlap between this text and many of the other texts in THE REQUISITES series; however, to avoid this, we have endeavored to confine the text to medical and surgical conditions that commonly present through the emergency room rather than to include every imaging possibility that may present. We apologize in advance if any overlap is identified—it was included for completeness—or for any deficiencies—some rare entities may have been omitted for sake of brevity. The fundamental division of the book is in two parts, one dealing with acute trauma and the other with nontraumatic acute processes, and the division of the chapters reflects this. This makes it possible to easily select the chapters relevant to an individual radiology practice. Some departments, especially large academic departments with residency programs, will have trauma units, whereas some community practices may run an emergency room without dealing with acute trauma.

We are pleased with how this first edition has developed from an abstract concept into reality. It has taken substantial effort, and we fully appreciate the contributions from all authors, all of whom have considerable experience in emergency imaging. We hope that the text will be well received and will act as an integral resource for all radiology departments and training programs

Acknowledgments

We would like to thank many people who helped transform the concept of this book into a reality. First, we owe thanks to innumerable individuals (staff, residents, fellows, technologists, and nurses) at the Boston University Medical Center in Boston, MA, who helped us and our colleagues build multidisciplinary groups for the care of the acutely ill patient. This was the principal driving force behind our growing interest in the field of emergency radiology. We would also like to thank Dr. James Thrall for insisting on the timeliness and necessity for this text to add to THE REQUISITES series. We would also like to extend a sincere thank you to the contributing authors, all of whom are experienced radiologists with extensive knowledge in various aspects of emergency radiology. Each author has added his or her own subspecialty expertise to the chapter, and this has resulted in the final product, a textbook that we believe they should all be proud of. Finally, thanks to all the staff at Elsevier, especially to Martha Limbach, who waited patiently for us to deliver the various parts of the book, sometimes at a slower-than-hoped-for pace.

JAS
BCL

CHAPTER 1

Traumatic and Nontraumatic Emergencies of the Brain, Head, and Neck

Glenn D. Barest, Asim Z. Mian, Rohini N. Nadgir, and Osamu Sakai

Create a list of the disorders of the brain, head, and neck that might commonly be expected to present to an emergency department (ED) and describe the typical imaging features. At first, this challenge seems straightforward enough. However, when put to the task, it soon becomes clear that almost every disorder within the realm of neuroradiology/head and neck radiology might at one time or another present as an acute emergency. Certain diagnoses like stroke, fractures, and epiglottitis are musts. Others such as oligodendroglioma, perhaps a slowly growing lesion, might seem less clear-cut. But realize that a wide variety of processes will result in an alteration in mental status leading to an ED visit with imaging playing a key role in diagnosis and appropriate management. On admission, inpatient workups now occur on a 24/7 basis with many complex exams completed during the night shift. On-call radiologists (often residents or fellows) are expected to provide wet readings or complete interpretations for complex cases covering the full spectrum of medicine, pediatrics, surgery, and related subspecialties. It was not that many years ago that the radiologist was faced with a seemingly never-ending stack of plain films from the ED, inpatient wards, and intensive care units in need of rapid interpretations. This work was interrupted by an occasional computed tomography (CT) scan. In this new millennium, the radiologist must maintain a rapid pace to review thousands of cross-sectional CT and magnetic resonance (MR) images with two-dimensional (2D) and three-dimensional (3D) reformats during a typical shift. For this reason, the majority of the discussion and examples in this chapter are based on these modalities and latest techniques. The last realization for authors is that the most daunting part of the task is to boil down all of the disorders and details to a set of requisites. Division of this chapter into sections is not quite as neat as one might think. It is not possible to separate the vascular system from discussion of the brain, head and neck, or spine. The imaging methods applied to the extracranial vessels in the setting of stroke are similar to those for blunt or penetrating trauma to the neck. One may, therefore, notice mention of similar techniques and findings in several places with examples appropriate to the context. All would do well to study the other volumes in the Requisites series (especially Neuroradiology, Musculoskeletal Imaging, and Pediatric Radiology), which cover this material in great detail. In this first attempt at condensing so much material into one useful volume, important topics have inevitably been neglected. It is hoped that this section can serve as a starting point for further study and become a valuable reference to on-call radiologists, emergency room physicians, and residents of both specialties.

INTRACRANIAL HEMORRHAGE AND TRAUMATIC BRAIN INJURY

Whether in the setting of head trauma or spontaneous development of headache or alteration of mental status, the ability to diagnose intracranial hemorrhage is of primary importance for all practitioners. These are some of the most common indications for brain imaging in the emergency setting. Almost invariably, the requisition will read, "Rule out bleed." An understanding of traumatic and nontraumatic causes of intracranial hemorrhage, the usual workup, and their recognition is, therefore, important and seems like a natural starting point. Discussion of the important types of mass effect resulting from intracranial hemorrhages and traumatic brain injury is also included in this section. An understanding of hemorrhage and herniation syndromes is central to the discussion of other topics that follow, such as stroke and neoplasms.

The word *hemorrhage* has Greek origins: the prefix *haima-*, meaning "blood," and the suffix *rrhage*, meaning "to gush or burst forth." Intracranial hemorrhage (ICH) affects 15 per 100,000 individuals, with 350 hypertensive hemorrhages per 100,000 elderly patients. ICH is typically more common in the African American and Asian populations. Bleeding may take place within the substance of the brain (intra-axial) or along the surface of the brain (extra-axial). Intra-axial hemorrhage implies parenchymal hemorrhage located in the cerebrum, cerebellum, or brainstem. Extra-axial hemorrhages include epidural, subdural, and subarachnoid hemorrhages, and intraventricular hemorrhage can be considered in this group as well. Hemorrhages can lead to different types of brain herniation, from direct mass effect and associated edema to development of hydrocephalus, causing significant morbidity and mortality.

General Imaging Characteristics of Hemorrhage

The appearance of ICH by CT can vary depending on the age of the hemorrhage and the hemoglobin level. The attenuation of blood is typically based on the protein content of which hemoglobin contributes a major portion. Therefore, the appearance of hyperacute/acute blood is easily detected on CT in patients with normal hemoglobin levels (approximately 15 g/dL) and typically appears as a hyperattenuating mass. This is because, immediately following extravasation, clot formation occurs with a progressive increase in attenuation over 72 hours due to increased hemoglobin concentration and separation of low-density serum. On the other hand, in anemic patients with hemoglobin less than 10 g/dL, acute hemorrhage can appear isoattenuating to the brain and can make detection difficult. Subsequently, following breakdown and hemolysis, the attenuation of the clot decreases until it becomes nearly isoattenuating to cerebrospinal fluid (CSF) by approximately 2 months. In the emergency setting, one should be aware of the "swirl" sign with unretracted clot appearing hypoattenuating and resembling a whirlpool; this may indicate active bleeding and typically occurs in a post-traumatic setting. It is important to recognize this sign, as prompt surgical evacuation may be required. The amount of mass effect on nearby tissues will depend on the size and location of the hemorrhage as well as the amount of secondary vasogenic edema that develops.

Administration of intravenous contrast material is usually not necessary for CT evaluation of ICH. If contrast is given, intra-axial hemorrhage can demonstrate an enhancing ring that is usually due to reactive changes and formation of a vascularized capsule, which typically occurs 5 to 7 days after the event and can last up to 6 months. Subacute and chronic extra-axial hematomas can also demonstrate peripheral enhancement usually due to reactive changes and granulation tissue formation. Unexpected areas of enhancement should raise concern, as active bleeding can appear as contrast pooling.

MR imaging has greatly revolutionized the evaluation of intracranial hemorrhage. The evolution of hemorrhage from the hyperacute to the chronic stage will have corresponding signal changes on T1-weighted images (T1WI), T2-weighted images (T2WI), fluid attenuated inversion recovery (FLAIR) images, and gradient-echo sequences. These properties can assist in detection and understanding of the time course of the injury. While beyond the scope of this chapter, description of the physics of the signal characteristics of blood products on MR is generally based on the paramagnetic effects of iron and the diamagnetic effects of protein in the hemoglobin molecule. The usual signal characteristics of hemorrhage and the general time course over which they evolve is summarized in Table 1-1.

EXTRA-AXIAL HEMORRHAGE

Extra-axial hemorrhage occurs within the cranial vault but outside of brain tissue. Hemorrhage can collect in the epidural, subdural, or subarachnoid spaces and may be traumatic or spontaneous. It is important to recognize these entities because of their potential for significant morbidity and mortality. Poor clinical outcomes are usually the result of mass effect from the hemorrhage, which can lead to herniation, increased intracranial pressure, and ischemia. Intraventricular hemorrhage will be considered with these other types of extracerebral hemorrhage.

Epidural Hemorrhage

Epidural hematoma is the term generally applied to hemorrhage that forms between the inner table of the calvarium and the outer layer of the dura due to its masslike behavior. More than 90% are associated with fractures in the temporoparietal, frontal, and parieto-occipital regions. CT is usually the most efficient method for evaluation of this type of hemorrhage. Epidural hematoma typically has a hyperdense, biconvex, or lens-shaped appearance. It may cross the midline but does not cross sutures (since the dura has its attachment at the sutures). This might not hold true if a fracture disrupts the suture. There is usually an arterial source, commonly due to tear of the middle meningeal artery and much less commonly (less than 10%) due to tear of the middle meningeal vein, diploic vein, or venous sinus (Figs. 1-1 and 1-2). The classic clinical presentation describes a patient with a "lucid" interval, although the incidence of this finding varies from 5% to 50% in the literature. Prompt identification of an epidural hematoma is critical, as evacuation or early reevaluation may be required. Management is based on clinical status, and therefore alert and oriented patients with small hematomas may be safely observed. The timing of follow-up CT depends on patient condition, but, generally, the first CT scan may be obtained in 6 to 8 hours and, if the patient is stable, follow-up may be extended to 24 hours or more afterward.

Subdural Collections

Subdural hematoma (SDH) is the term generally applied to hemorrhage that collects in the potential space between the inner layer of the dura and the arachnoid membrane. It is typically the result of trauma (motor vehicle

Table 1-1 Usual MR Signal Characteristics of Hemorrhage

Stage	Time	Component	T1	T2
Hyperacute	(0–12 hr)	Oxyhemoglobin	Isointense	Hyperintense
Acute	(12 hr–3 days)	Deoxyhemoglobin	Isointense	Hypointense
Early subacute	(3–7 days)	Methemoglobin (intracellular)	Hyperintense	Hypointense
Late subacute	(1 wk–1 mo)	Methemoglobin (extracellular)	Hyperintense	Hyperintense
Chronic	(>1 mo)	Hemosiderin	Hypointense	Hypointense

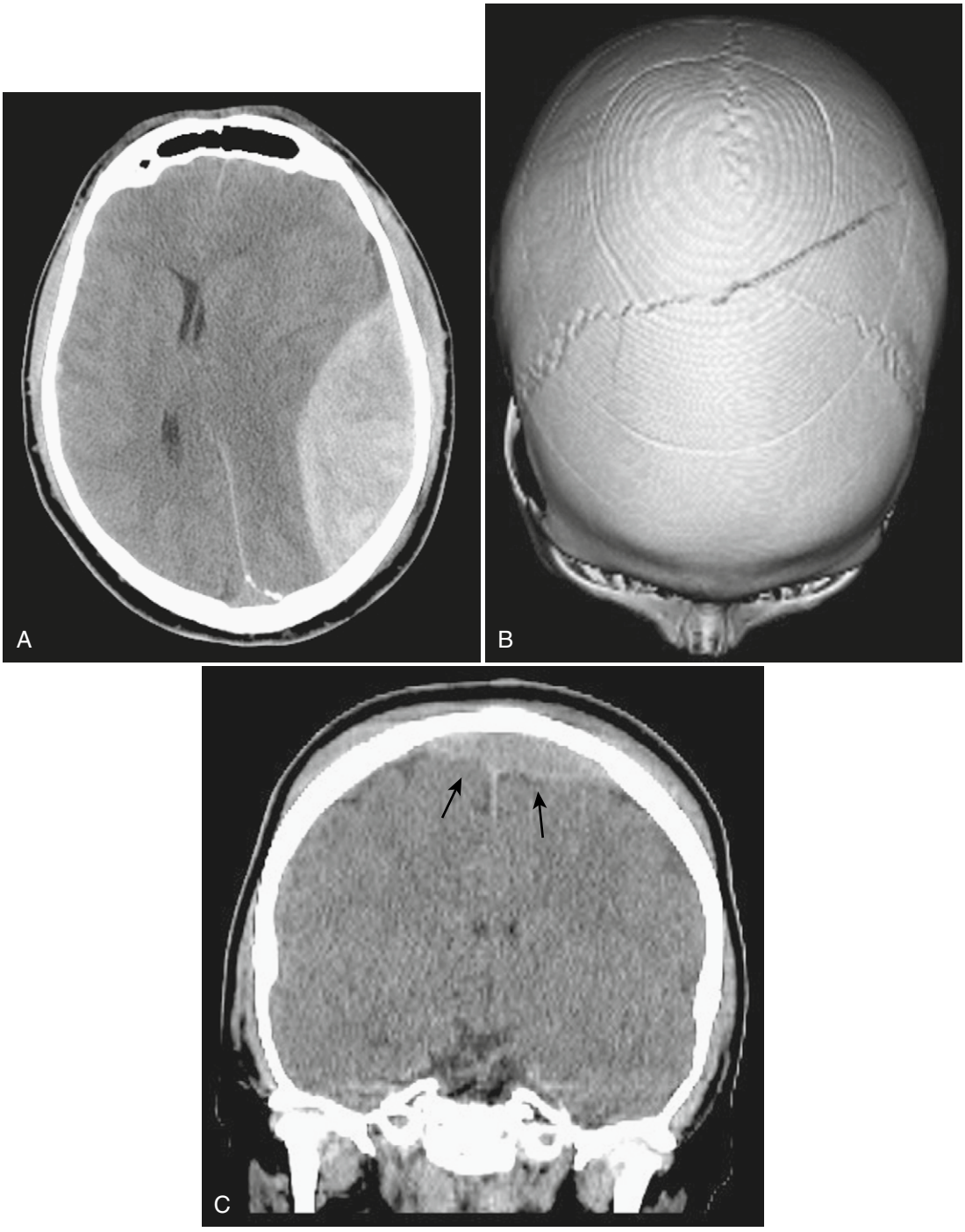


FIGURE 1-1. Epidural hematoma. **A,** CT shows usual biconvex, hyperdense acute epidural hematoma causing effacement of sulci and lateral ventricles and shift of midline structures. **B,** CT volume-rendered image shows nondisplaced fracture at vertex involving coronal suture. **C,** Coronal multiplanar reconstruction shows biconvex epidural hematoma crossing midline over the superior sagittal sinus.

collision, assaults, and falls, the latter especially in the elderly population), causing tear of the bridging vein(s), and has a hyperattenuating, crescentic appearance overlying the cerebral hemisphere (Fig. 1-3). These hemorrhages can cross sutures and may track along the falx and tentorium but do not cross the midline. Inward displacement of the cortical vessels may be noted on a contrast-enhanced scan. There is a high association with subarachnoid hemorrhage. Acute SDHs thicker than 2 cm, seen with other parenchymal injuries, are associated with greater than 50% mortality. As the SDH evolves to the subacute (5 days to 3 weeks) and then chronic (more than 3 weeks) stage, it decreases in attenuation, becoming isodense to the brain and finally to CSF. Subacute SDH can have a layered appearance due to separation of formed elements from serum. Subacute hemorrhages may be relatively inconspicuous when isodense, and therefore it is especially important to recognize signs of mass effect, such as sulcal

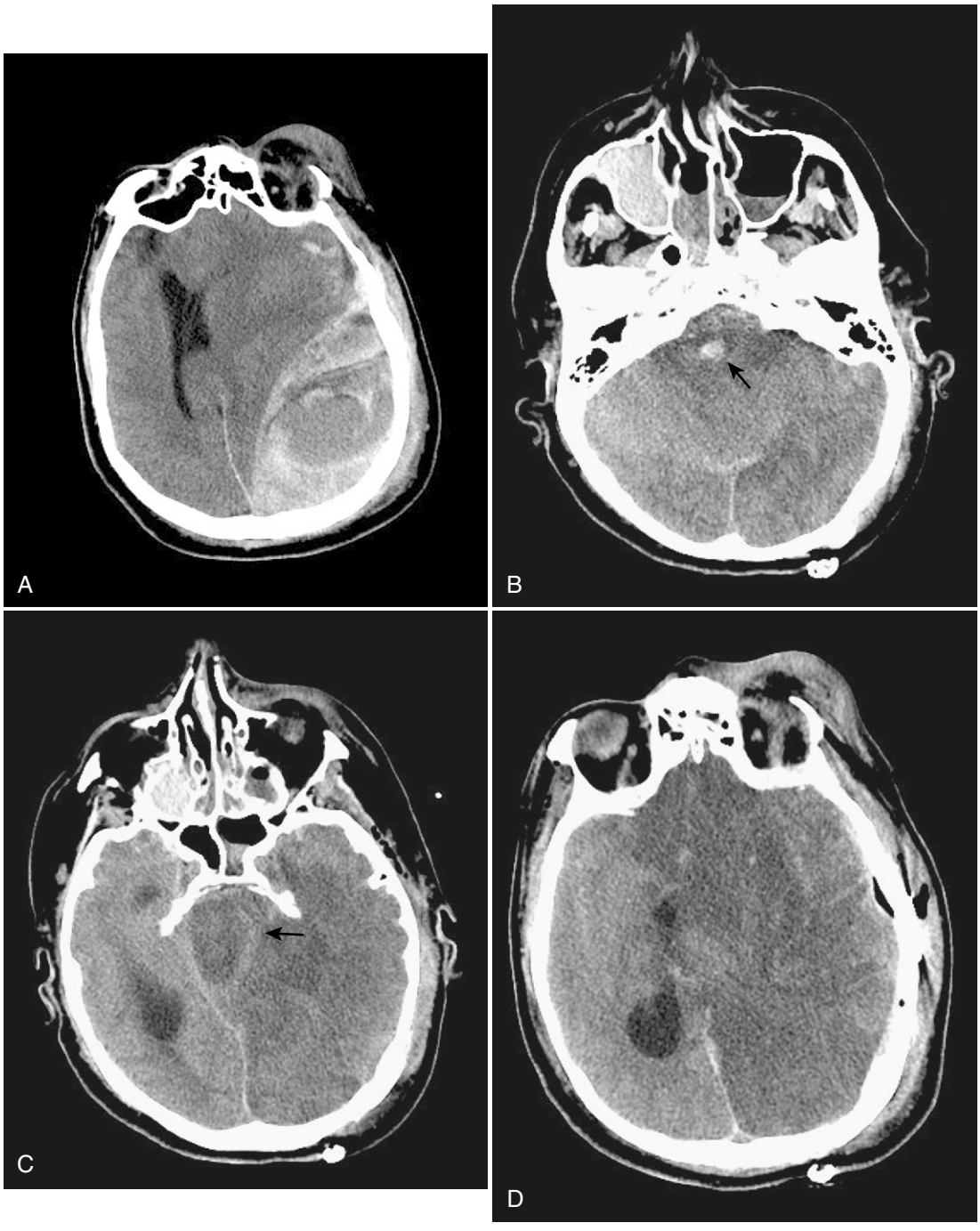


Figure 1-2. Epidural hematoma and complications. **A,** "Swirl" sign in this large epidural hematoma suggests continued bleeding. **B,** Pontine (Duret) hemorrhage *(arrow)* and effacement of basal cisterns as a result of downward herniation. **C,** Uncal herniation (*arrow* shows margin of left temporal lobe) and resultant left posterior cerebral artery territory infarct. The brainstem is distorted left and also abnormally hypodense. **D,** Infarcts in bilateral anterior, left middle, and left posterior cerebral artery territories as a result of herniations.

effacement, asymmetry of lateral ventricles, and shift of midline structures, as well as sulci that do not extend to the skull (Fig. 1-4). Bilateral isoattenuating SDHs can be especially challenging since findings are symmetric. Beware of this, particularly in the elderly patient who does not have generous sulci and ventricles. At this stage, the SDH should be conspicuous on MR imaging, especially on FLAIR sequences. A subacute SDH may also be very conspicuous on T1-weighted images due to the hyperintensity of methemoglobin.

Chronic subdural hematomas are collections that have been present for more than 3 weeks. Even a chronic hematoma may present in the emergency setting; for example, in a patient prone to repeated falls, brought in because of a change in mental status. On both CT and MR, these collections typically have a crescentic shape and may demonstrate enhancing septations and membranes surrounding the collection after contrast administration. Calcification of chronic SDH can occur and be quite extensive (Fig. 1-5). Areas of hyperdensity within a larger hypodense SDH may



FIGURE 1-3. Subdural hematoma. Mixed density layered pattern due to recurrent hemorrhages. Image *(arrow)* shows one method of measuring midline shift.

indicate an acute component due to recurrent bleeding, an "acute on chronic subdural hemorrhage." Mixed density collections may also be acute, due to active bleeding or CSF accumulation due to tear of the arachnoid membrane. Chronic SDH is usually isointense to CSF on both T1WI and T2WI, but the appearance can be variable depending on any recurrent bleeding within the collection. The FLAIR sequence is typically very sensitive for detection of chronic SDH due to hyperintensity based on protein content. Hemosiderin within the hematoma will cause a signal void due to susceptibility effect, and "blooming" (appears to be larger than its true size) will be noted on gradient-echo sequence.

Subdural hygroma is another type of collection and is commonly thought to be synonymous with chronic subdural hemorrhage. The actual definition of a hygroma is an accumulation of fluid due to a tear in the arachnoid membrane, usually by some type of trauma or from rapid ventricular decompression with associated accumulation of CSF within the subdural space. Many still use this term interchangeably with chronic subdural hematoma. CT demonstrates a fluid collection isodense to CSF in the subdural space. MR can be useful in differentiating CSF from chronic hematoma based on the imaging characteristics of the fluid on all sequences. Occasionally hygromas are difficult to differentiate from the prominence of the extra-axial CSF space associated with cerebral atrophy. Position of the cortical veins can be a helpful clue. In atrophy, the cortical veins are visible traversing the subarachnoid space, whereas with a hygroma they are displaced inward along with the arachnoid membrane by the fluid in the subdural space.

Subarachnoid Hemorrhage

Subarachnoid hemorrhage (SAH) fills the space between the pia and the arachnoid membrane, outlining the sulci and basilar cisterns. This can be due to a variety of causes, including trauma, ruptured aneurysm,

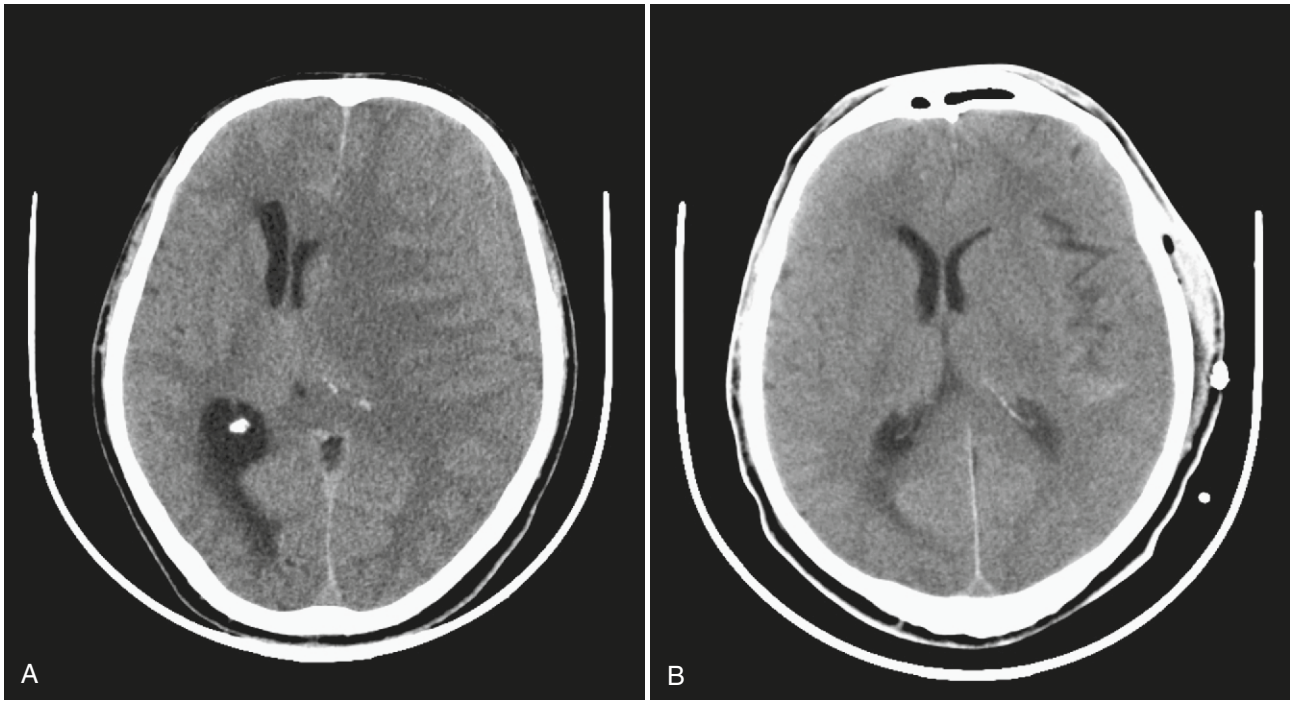


FIGURE 1-4. Isodense subdural hematoma. **A,** Sulcal effacement and midline shift to the right are clues to the presence of a left-sided subdural hematoma. **B,** Re-expansion of left Sylvian fissure and reduction in midline shift following evacuation.

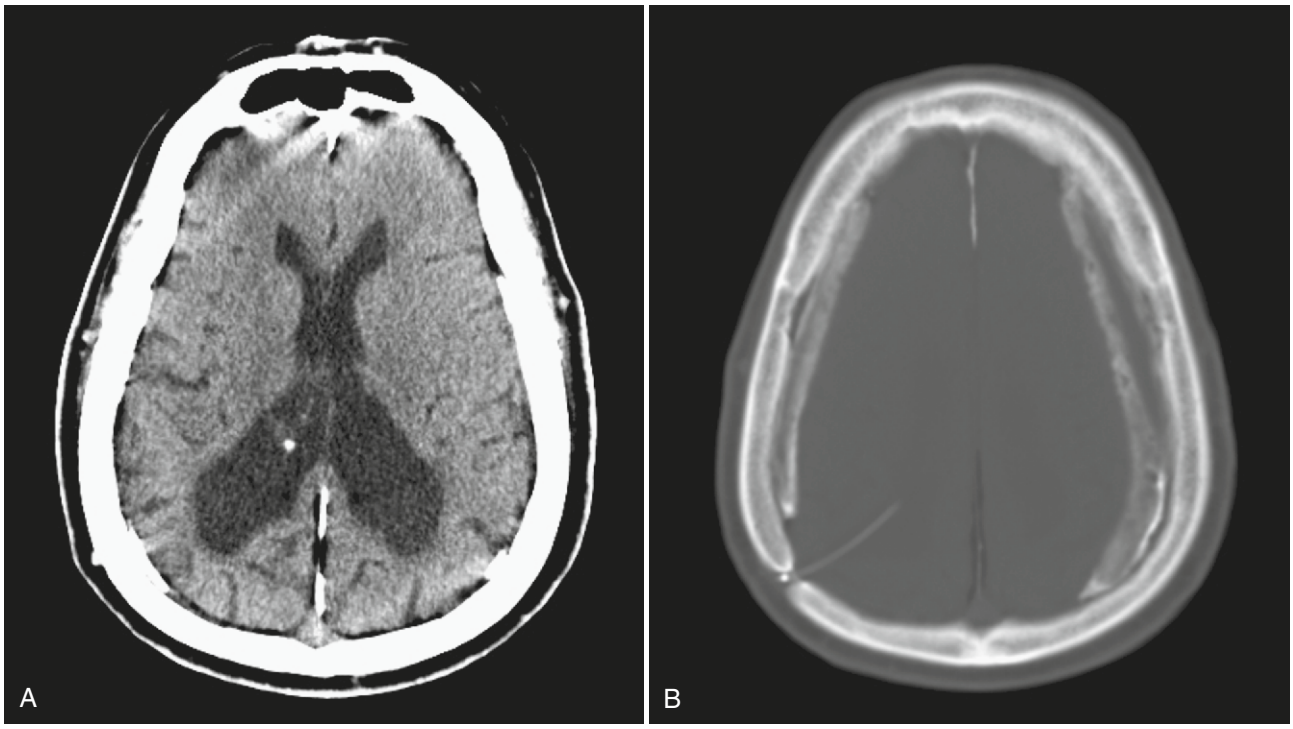


Figure 1-5. Calcified subdural hematomas. **A,** Colpocephaly configuration of lateral ventricles. **B,** Bone window/level settings more clearly show the calcified subdurals in this adult patient shunted as a child for congenital hydrocephalus.

hypertension, arteriovenous malformation, occult spinal vascular malformation, and hemorrhagic transformation of ischemic infarction. SAH is often associated with overlying traumatic subdural hematoma. Subarachnoid hemorrhages generally do not cause mass effect or edema. On CT, hyperdensity is seen within the sulci and/or basilar cisterns (Figs. 1-6 and 1-7).

Although MR imaging may be as sensitive for the detection of acute intraparenchymal and subarachnoid hemorrhage, CT generally remains the modality of choice (and imaging gold standard). Sensitivity of CT for detection of SAH compared with CSF analysis can vary from up to 98% to 100% within 12 hours to approximately 85% to 90% after 24 hours of symptom onset. Other factors affecting sensitivity are hemoglobin concentration, size, and location of the hemorrhage. CT is widely available, rapid, and relatively inexpensive. In several small studies, MR has demonstrated sensitivity equivalent to CT for detection of acute parenchymal hemorrhage and SAH. In some cases of "CT-negative" (subacute) hemorrhage, MR has shown greater sensitivity. However, results may be confounded by artifacts from CSF pulsations, elevated protein (meningitis), or oxygen concentration (high fraction of inspired oxygen) in CSF on FLAIR images and presence of blood products from previous microhemorrhages on gradient-echo images.

Intraventricular Hemorrhage

Intraventricular hemorrhage (IVH) is typically caused by trauma in the adult population. It can result from extension of parenchymal hemorrhage into the ventricles or redistribution of subarachnoid hemorrhage. Primary intraventricular hemorrhage is uncommon and usually caused by a ruptured aneurysm, intraventricular tumor, vascular malformation, or coagulopathy (Fig. 1-8). Large IVHs are quite conspicuous on CT or MR. They may occupy a majority of the ventricle(s) and may result in hydrocephalus and increased intracranial pressure. Small amounts of IVH may be difficult to detect; one must check carefully for layering hemorrhage within the atria and occipital horns of the lateral ventricles. Normal choroid plexus calcifications in the atria of lateral ventricles, the fourth ventricle, and extending through the foramina of Luschka should not be mistaken for acute IVH.

Another less common type of extracerebral intracranial hemorrhage that may present acutely is pituitary hemorrhage. It is usually associated with pituitary apoplexy due to pituitary necrosis that may become hemorrhagic. Presenting symptoms may include headache, visual loss, ophthalmoplegia, nausea, and vomiting. Other causes of pituitary hemorrhage include tumors (macroadenoma, germinoma) and, less commonly, trauma.

INTRA-AXIAL HEMORRHAGE

The cause of intra-axial (parenchymal) hemorrhages can generally be categorized as spontaneous or traumatic. Traumatic causes include blunt injury from motor vehicle collision (MVC) assault, and penetrating injuries such as gunshot wounds. There are many spontaneous causes, and these are discussed in the section on hemorrhagic stroke.

Contusion

Parenchymal contusions result from blunt trauma and can occur in the cortex or white matter. Their locations are typically at the site of greatest impact of brain on bone,

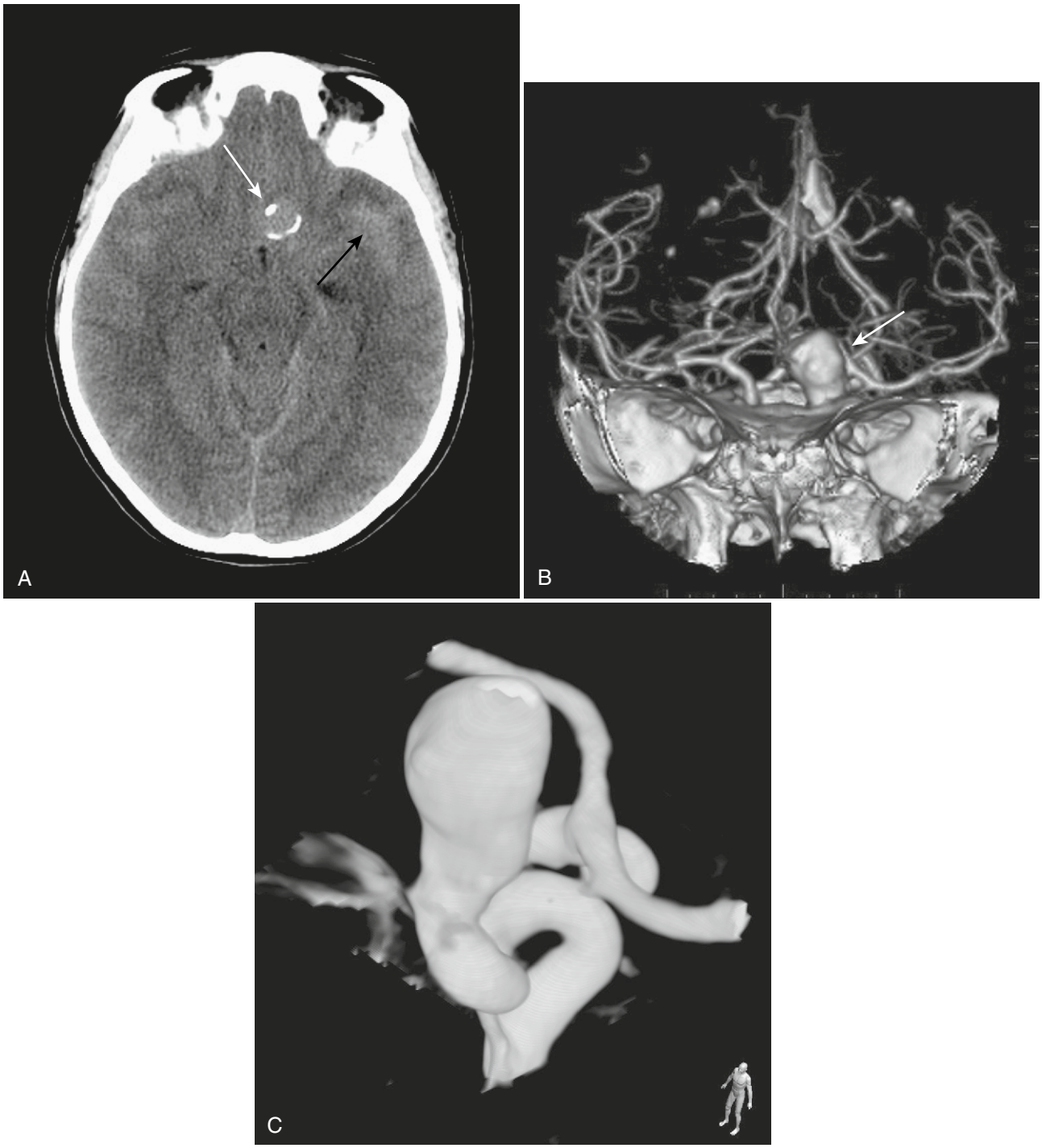
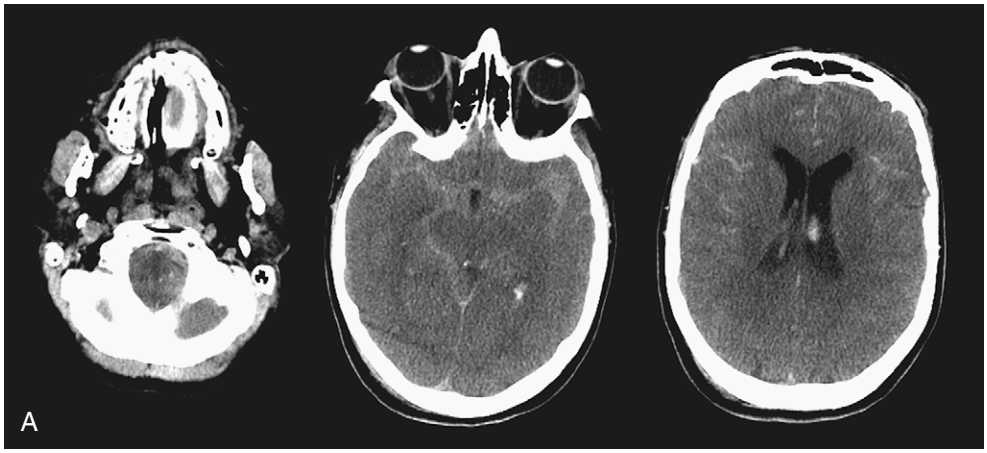


Figure 1-6. Subarachnoid hemorrhage from ruptured aneurysm. **A,** Noncontrast CT shows ill-defined hyperdense subarachnoid hemorrhage in left Sylvian cistern *(black arrow)* and rim calcification in the wall of the aneurysm *(white arrow)*. **B,** Volume-rendered image from CT angiography shows large aneurysm projecting above lesser sphenoid wing. **C,** Reconstruction from 3D rotational digital subtraction angiogram shows carotid-ophthalmic aneurysm to best advantage.

including the anterior/inferior frontal lobes and the temporal lobes. They can be considered coup (occurring at the site of impact) or contrecoup (opposite the site of impact) types. On CT, a contusion typically appears as an area of hyperdensity with a surrounding rim of hypodense edema. It can initially appear as a focal area of subtle hypodensity and may blossom on follow-up exam at 12 to 24 hours with development of an obvious central area of hyperdensity and a larger surrounding zone of hypodense edema (Fig. 1-9). On MR, signal characteristics reflect the hemorrhagic and edematous components. Over time, the density and signal characteristics of the hemorrhage will evolve in a fashion similar to a spontaneous hemorrhage. Parenchymal hemorrhage due to penetrating trauma, such as from gunshot wound or impalement, will follow the same general pattern of evolution.



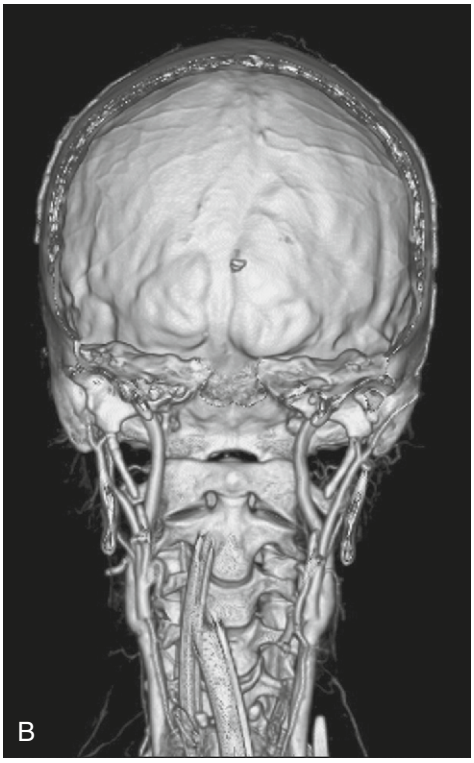


Figure 1-7. Subarachnoid hemorrhage and complications. **A,** Three CT images show diffuse hyperdense subarachnoid hemorrhage filling basal cisterns and cerebral sulci bilaterally. Diffuse loss of gray–white differentiation and effacement of sulci and cisterns probably preclude the need for further workup. **B,** Volume-rendered image from CT angiography demonstrates lack of intracranial flow consistent with expected elevation of intracranial pressure.

Diffuse Axonal Injury

Diffuse axonal injury (DAI) is another type of traumatic brain injury that may present with parenchymal hemorrhages and is distinct from parenchymal contusion. DAI is an injury to the axons caused by acceleration/deceleration injury with a rotational component (usually from motor vehicle collision or other blunt trauma to the head). There may be complete transection of axons with injury to the associated capillaries, or partial disruption of the axons. The lesions of DAI typically occur at the interfaces of gray and white matter in the cerebral hemispheres, the body and splenium of the corpus callosum, midbrain, and upper pons. Lesions may also be seen in the basal ganglia. Patients sustaining DAI typically lose consciousness at the moment of impact. DAI may be suspected when the clinical exam is worse than expected based on the findings on initial CT scan. Usually, the greater the number of lesions, the worse the prognosis. Individuals who recover usually demonstrate lingering effects such as headaches and cognitive deficits. Initial CT scans in more than half of patients with DAI may be negative. CT findings include hypodense foci due to edema in areas of incomplete axonal disruption and hyperdense foci due to petechial hemorrhage where there is complete transection of the axons and associated capillaries (Fig. 1-10). MR is more sensitive than CT for detection of DAI. Approximately 30% of those negative by CT will demonstrate abnormal findings on MR. These findings include FLAIR and T2 hyperintensities (edema) and gradient-echo hypointensities (hemorrhages) (Fig. 1-11). Lesions may appear hyperintense on diffusion-weighted images. It is estimated that more than 80% of the lesions of DAI are nonhemorrhagic. Generally, if imaging is repeated within 3 to 5 days, more lesions will become apparent as the process evolves.

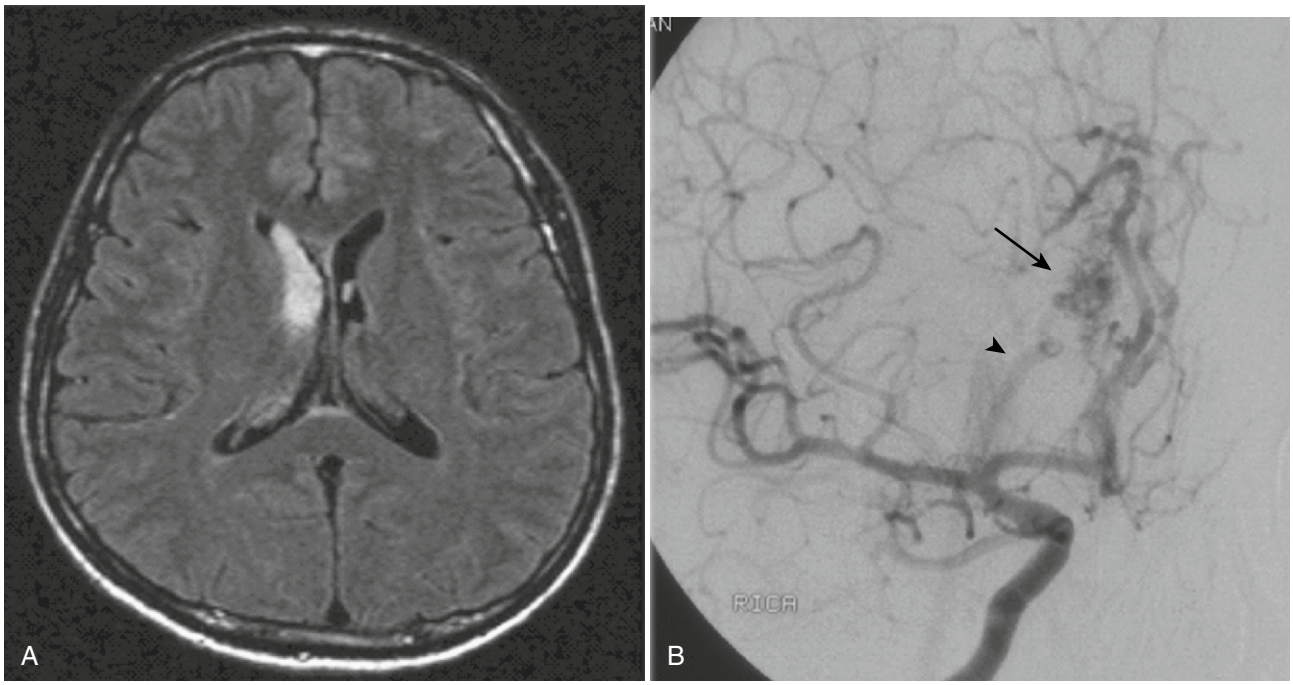


FIGURE 1-8. Intraventricular hemorrhage. **A,** FLAIR MR image shows hyperintense hemorrhage isolated to frontal horn of right lateral ventricle. **B,** Image from right internal carotid artery digital subtraction angiogram in late arterial phase shows nidus (*arrow*) and early draining vein *(arrowhead)* diagnostic of an arteriovenous malformation.

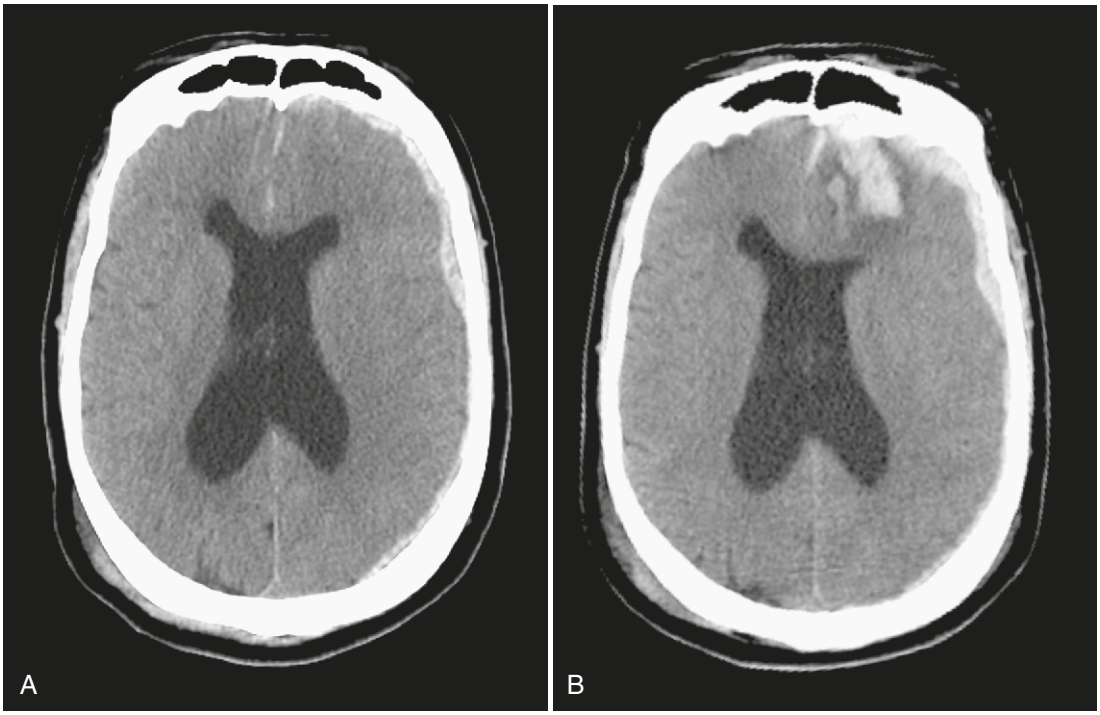


FIGURE 1-9. Blossoming contusion. **A,** CT shows thin left frontoparietal subdural hematoma tracking along anterior falx and mild sulcal effacement. **B,** Follow-up CT after 24 hours shows hyperdense parenchymal hemorrhage and surrounding edema in left frontal lobe and stable subdural hematoma. Notice mass effect on left lateral ventricle.

A staging system for DAI based on locations of lesions on histopathology may be applied to MR findings. Stage 1 is based on subcortical lesions in the frontal and temporal lobes. Stage 2 will also show lesions in the corpus callosum and lobar white matter, and stage 3 will have lesions in the midbrain and pons. Diffusion tensor imaging, particularly helpful in evaluation of white matter tracts, has been shown to be more sensitive than conventional MR for detection of diffuse axonal injury and correlates more closely with clinical outcomes.

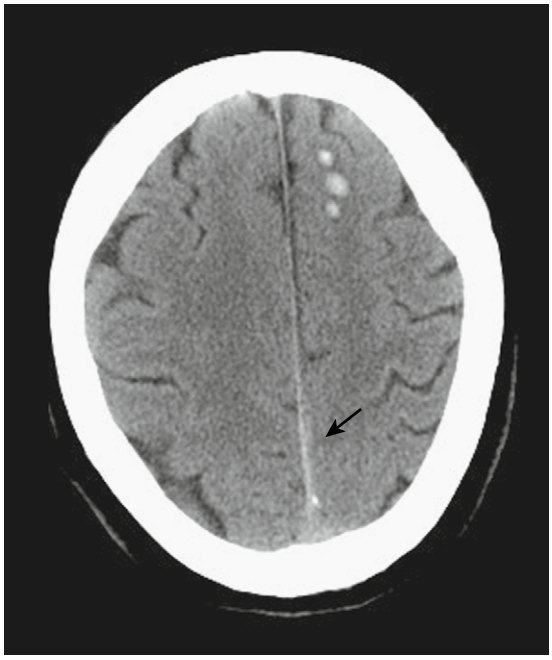


Figure 1-10. Shear hemorrhages of diffuse axonal injury. Noncontrast CT shows three small hemorrhages in the left superior frontal gyrus following blunt head trauma.

BRAIN HERNIATIONS

Brain herniation is a potentially devastating complication of increased intracranial pressure. The most common causes include intracranial hemorrhages, brain tumors, and cerebral edema from stroke or anoxic injury. To explain this concept, a common example from the literature describes the brain as being separated into multiple compartments within a rigid container. Any shift of the brain from one compartment to another is considered herniation. With shift of the brain, there can be mass effect on adjacent and contralateral parenchyma, the brainstem, major intracranial vessels, and cranial nerves. As a result, the feared complications of herniations include ischemic infarcts due to compression of the major intracranial vessels (commonly, the anterior and posterior cerebral arteries), cranial nerve palsies, and "brain death" due to compression and ischemia of the brainstem. The major types of intracranial herniations include subfalcine, transtentorial, tonsillar herniation through the foramen magnum, extracranial (through a defect in the skull), and, less commonly, transalar herniation. Once the complications of herniation have developed, it is often too late to intervene. Therefore, it is best to recognize the signs of impending herniation, when prompt neurosurgical intervention may avert disaster.

Subfalcine Herniation

Subfalcine herniation is due to displacement and impingement of the cingulate gyrus underneath the falx. It is usually caused by mass effect on the frontal lobe and is associated with ipsilateral lateral ventricle compression and obstruction of the foramen of Monro with dilatation of the contralateral ventricle ("trapped ventricle"). The degree of midline shift (not synonymous with subfalcine herniation) can be estimated by drawing a line between the anterior and posterior attachments of the falx and measuring the shift of the septum pellucidum relative to this line (see Fig. 1-3). Anterior cerebral artery territory infarct(s) may result from this type of herniation.

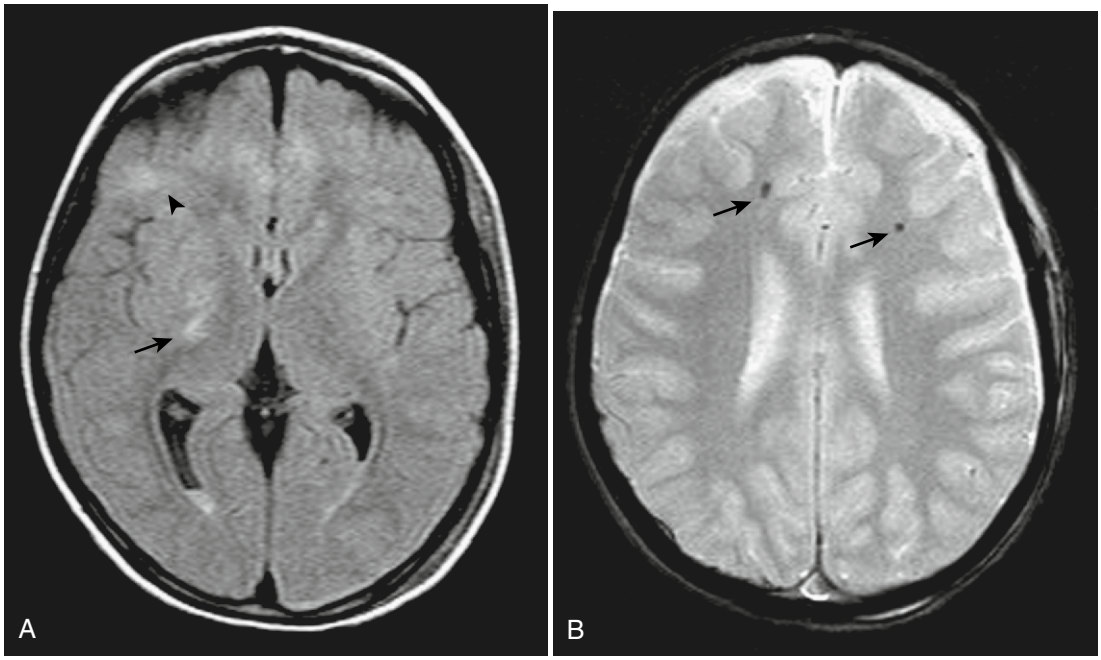


Figure 1-11. Diffuse axonal injury. **A,** FLAIR hyperintensities in posterior limb of internal capsule *(arrow)* and subcortical white matter *(arrowhead)*. **B,** Gradient-echo hypointensities in subcortical white matter indicative of hemorrhages *(arrows)* were not evident on other sequences. Note IVH in occipital horns of lateral ventricles.

Transtentorial Herniation

Transtentorial herniations include two major types, which are the descending transtentorial herniation (DTH) and the ascending transtentorial herniation (ATH). An early DTH is known as uncal herniation, in which the uncus is displaced medially and occupies the ipsilateral suprasellar cistern. A later-stage DTH is caused by continued mass effect with displacement of the medial temporal lobe through the incisura, which completely occupies the suprasellar cistern (along with the uncus) and causes enlargement of the ipsilateral and effacement of the contralateral ambient cisterns. This phenomenon occurs because, as there is marked shifting of brain in the supratentorial compartment, there is also shift of the brainstem in the same direction. There is also compression of the ipsilateral cerebral peduncle. Occasionally, when there is marked mass effect, there can be compression of the contralateral cerebral peduncle against the tentorium, or "Kernohan's notch," which leads to ipsilateral motor weakness (this phenomenon may be a false localizing sign). Other imaging findings include a "trapped" temporal horn of the lateral ventricle contralateral to the side of the mass and Duret hemorrhages—hemorrhages of the midbrain and pons caused by stretching and tearing of the arterial perforators. In cases of bilateral mass effect, there can be displacement of both temporal lobes and midbrain through the incisura leading to effacement of the basilar cisterns bilaterally. Complications of this type of herniation include compression of the posterior cerebral artery and penetrating basal arteries with associated infarcts in these vascular distributions (see Fig. 1-2). In addition, there can be compression of the oculomotor nerve (CN III) with an associated palsy. ATH is less common and is caused by superior displacement of the cerebellum and brainstem through the incisura. It is usually due to mass effect in the posterior fossa (as from hemorrhage, tumor, or infarct), and on imaging there is compression on the posterolateral midbrain bilaterally with associated effacement of the ambient and quadrigeminal plate cisterns. There is usually hydrocephalus due to obstruction at the level of the cerebral aqueduct of Sylvius.

Tonsillar Herniation

Tonsillar herniation is caused by downward displacement of the cerebellar tonsils through the foramen magnum into the spinal canal (generally by more than 5 mm). On imaging, there is a peglike configuration to the tonsils with obliteration of the CSF space in the foramen magnum (Fig. 1-12). Complications include obstructive hydrocephalus from compression of the fourth ventricle. Mild tonsillar ectopia, Chiari I malformations, and sagging tonsils due to intracranial hypotension should not be mistaken for acute tonsillar herniation, but should be considered seriously when downward mass effect is expected based on brain edema, mass, or hemorrhage.

Extracranial Herniation

An extracranial herniation is the displacement of brain parenchyma through a cranial and dural defect that is usually caused by trauma or craniectomy (usually performed to prevent downward herniation from acute cerebral edema). Complications may include infarct of the herniated brain tissue.

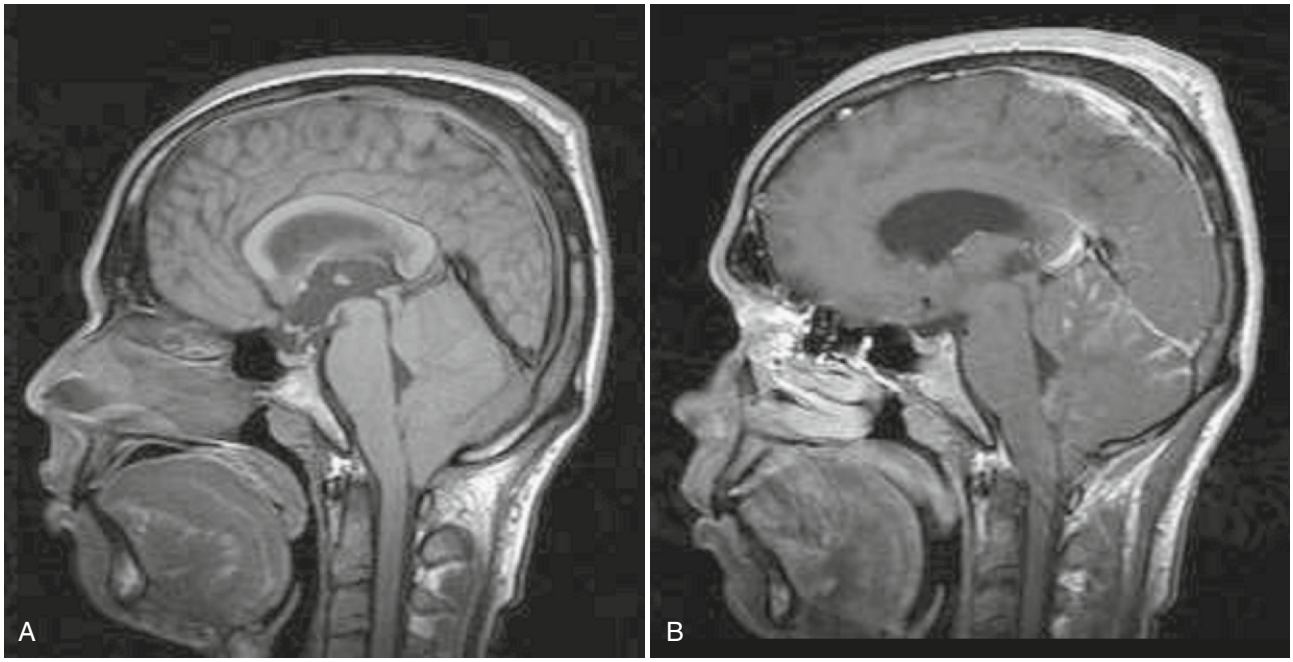


Figure 1-12. Tonsillar herniation. **A,** Sagittal T1 image shows pegged appearance of the cerebellar tonsils extending through the foramen magnum, simulating a Chiari I malformation. (This was a dramatic change from a previous exam.) **B,** Postgadolinium T1 image shows cerebellar leptomeningeal enhancement due to cryptococcal meningoencephalitis in this patient with AIDS.

Transalar Herniation

Transalar herniation is uncommon and, by itself, does not cause symptoms. It is usually associated with subfalcine and transtentorial herniations. This type of herniation is caused by displacement of the temporal lobe anteriorly or frontal lobe posteriorly across the sphenoid wing. Look for anterior or posterior displacement of the middle cerebral artery to identify this type of herniation.

In the setting of severe head trauma, many of these different types of injuries may coexist. The mechanism of injury should correspond with the degree of injury. In cases when the reported mechanism is mild, nonaccidental trauma ("Trauma X," "shaken-baby syndrome") should be considered. Infants, children, those with mental or physical disabilities, and the elderly are particularly at risk. Skull fractures, SAH, SDH, contusions, shear injuries, infarcts, vertebral compression fractures, and retinal hemorrhages constitute the usual neuroradiologic spectrum of abnormalities. Injuries of different ages, metaphyseal and rib fractures, and visceral injuries are other common findings in child abuse.

ACUTE CEREBROVASCULAR DISORDERS

Although usually not due to trauma, acute cerebrovascular disorders are treated with the same urgency as traumatic injuries or spontaneous intracranial hemorrhage. In the United States approximately 700,000 strokes occur each year. Almost 30% are recurrent, and 75% occur in patients over the age of 65. The 20% mortality rate is surpassed only by cardiac disease and cancer. Stroke is the leading cause of severe, long-term disability and long-term care. Estimates of annual cost exceed $50 billion. One clinical definition of stroke is a neurologic deficit caused by inadequate supply of oxygen to a region of the brain. Stroke can be due to a low flow state or rupture of a vessel and therefore may be divided into ischemic and hemorrhagic varieties. The definition of stroke used for current clinical trials requires symptoms lasting more than 24 hours or imaging of an acute clinically relevant brain lesion in a patient with rapidly vanishing symptoms. A transient ischemic attack (TIA) used to imply resolution of the deficit within a 24-hour time period. The proposed new definition of TIA is a brief episode of neurologic dysfunction caused by a focal disturbance of brain or retinal ischemia, with clinical symptoms typically lasting less than 1 hour, and without evidence of infarction. Estimates of the annual incidence of TIA in the United States vary from 200,000 to 500,000. Evidence of acute infarction may be identified by MR imaging in up to 50% of patients who meet the clinical criteria for a TIA. Semantics can be unclear when an abnormality is detected on imaging in the absence of symptoms.

Hemorrhagic Stroke: Spontaneous Parenchymal Hemorrhage

Approximately 10% to 15% of strokes present with an acute parenchymal hemorrhage. The most common cause is hypertension (Fig. 1-13). Coagulopathies, hematologic disorders including hypercoagulable states, amyloid angiopathy, drugs, vascular malformations and aneurysms, vasculitides, and tumors round out the usual list of etiologies. Hemorrhages resulting from illicit drug use and vascular malformations are commonly found in young adults (Fig. 1-14). Sickle cell disease and venous infarcts may also present with parenchymal hemorrhage. A ruptured intracranial aneurysm may occasionally cause a parenchymal hemorrhage in association with subarachnoid hemorrhage. Hypertensive hemorrhages most commonly occur in the basal ganglia and thalami but may also primarily arise within the cerebral hemispheres, brainstem, or cerebellum. Cerebral amyloid angiopathy (CAA) is another common cause of intracranial hemorrhages in patients over 65 years of age. CAA can be found in patients with mild cognitive impairment, dementia of Alzheimer type, and Down syndrome with extracellular deposition of beta amyloid occurring in the cortex and subcortical white matter. CAA can be hereditary (autosomal dominant, Dutch type), sporadic (presence of Apoε4 allele), or acquired (as from hemodialysis). The lobar hemorrhages of CAA typically occur in the frontal and parietal regions. MR is sensitive for the detection of hemosiderin deposition resulting from multiple microhemorrhages over the course of time appearing as small hypointense foci on gradient-echo sequences.



Figure 1-13. Spontaneous parenchymal hemorrhage secondary to uncontrolled hypertension. Noncontrast CT in a patient with uncontrolled hypertension shows a large hyperdense parenchymal hemorrhage arising in the basal ganglia with intraventricular extension. Note the ventriculostomy catheter in the right lateral ventricle.

Imaging of Acute Ischemic Stroke

Computed Tomography

The role of imaging in acute stroke diagnosis and management continues to evolve. Since the mid-1970s, unenhanced CT has been the first-line modality to determine the etiology of acute neurologic deficits. CT can offer the chance to detect an ischemic infarct, generally in the

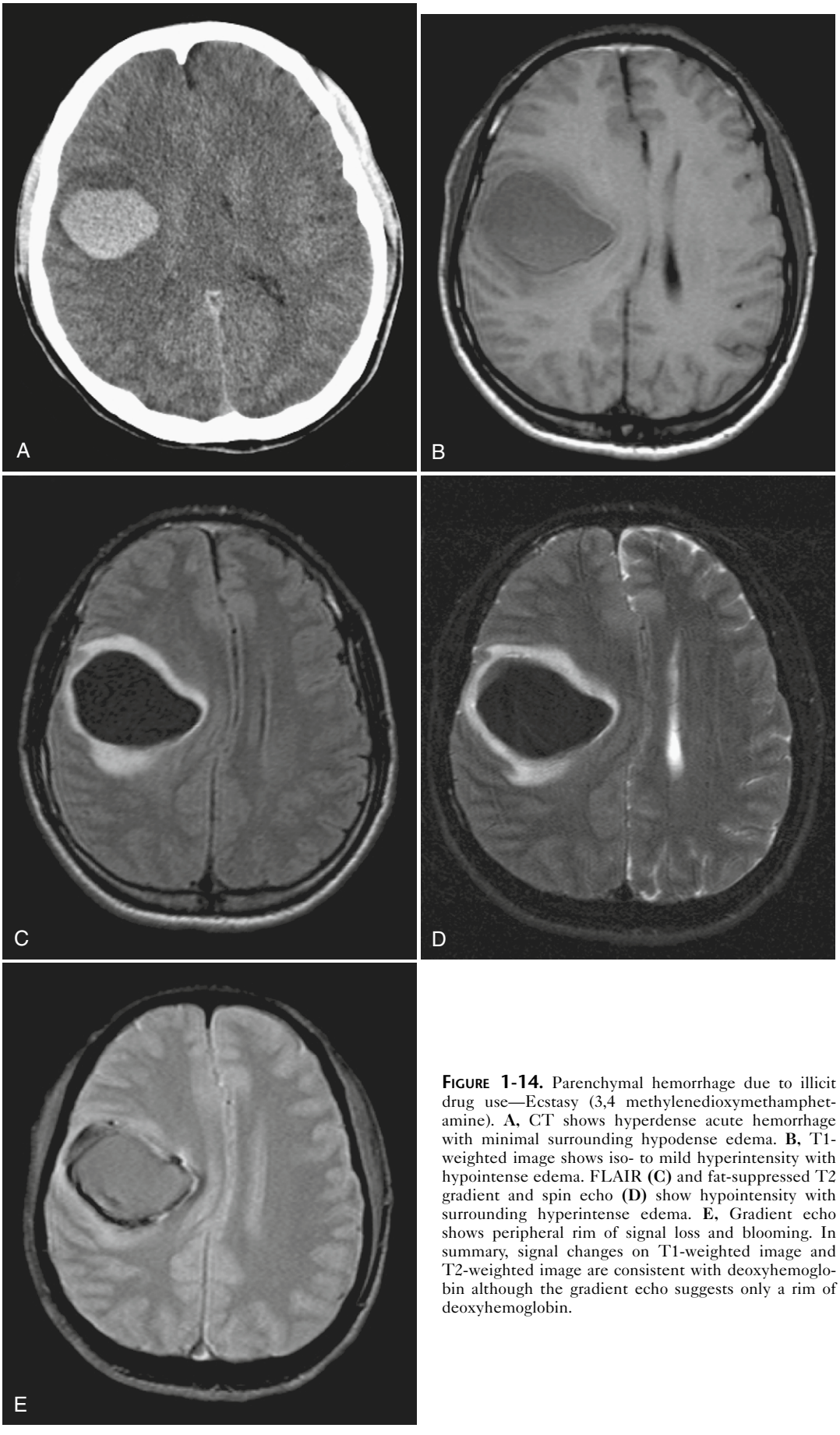


FIGURE 1-14. Parenchymal hemorrhage due to illicit drug use—Ecstasy (3,4 methylenedioxymethamphetamine). **A,** CT shows hyperdense acute hemorrhage with minimal surrounding hypodense edema. **B,** T1-weighted image shows iso- to mild hyperintensity with hypointense edema. FLAIR **(C)** and fat-suppressed T2 gradient and spin echo **(D)** show hypointensity with surrounding hyperintense edema. **E,** Gradient echo shows peripheral rim of signal loss and blooming. In summary, signal changes on T1-weighted image and T2-weighted image are consistent with deoxyhemoglobin although the gradient echo suggests only a rim of deoxyhemoglobin.

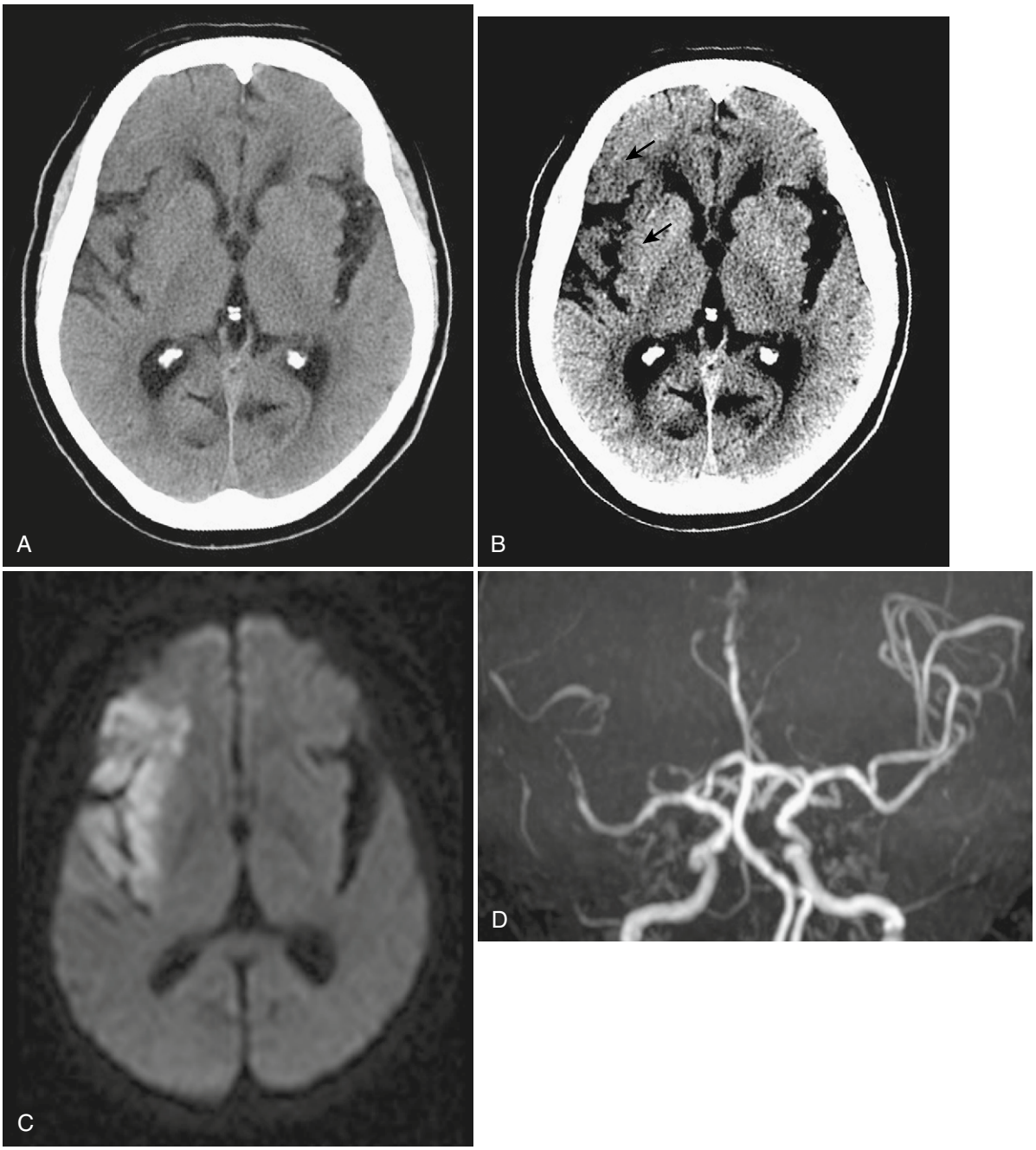


Figure 1-15. Hyperacute infarct. **A,** Noncontrast CT with window/level of 80/40 shows subtle decrease in density of the right insular cortex. **B,** Insular "ribbon" sign is more conspicuous with stroke window/level of 40/40 *(arrows).* **C,** Infarct is much more conspicuous on diffusion-weighted image. **D,** Time-of-flight MR angiography shows attenuation of right middle cerebral artery distal branches.

middle cerebral artery territory, within 3 hours in up to one third of cases based on findings of subtle parenchymal hypodensity, loss of gray–white matter differentiation (including loss of the insular ribbon or margins of basal ganglia; Fig. 1-15), and effacement of sulci. A hyperdense vessel sign may indicate the presence of an acute thrombus and support the diagnosis. The sensitivity for detection of acute stroke has been shown to increase with the use of an "acute stroke" window and level settings (see Fig. 1-15). A very narrow window width of 8 Hounsfield units (HU) and a level of 32 HU (compared with 80 and 20 HU, respectively) may increase the sensitivity of CT to approximately 70% without a loss of specificity. CT is currently used to screen patients who may be considered for treatment with intravenous recombinant tissue plasminogen activator (rt-PA) within 3 hours of onset based on guidelines from the National Institute of Neurologic Disorders and Stroke (NINDS) rt-PA trial. Beyond 3 hours, the risk of intracranial hemorrhage due to intravenous thrombolysis was shown to outweigh potential benefits. An association between larger stroke volumes (greater than one third of the middle cerebral artery territory) and reperfusion hemorrhage was initially reported. This criterion for the use of 100 mL estimated infarct volume has been commonly

applied in stroke trials. The Alberta Stroke Program early CT score (ASPECTS), a 10-point topographic scoring system, was later developed to try to more easily quantify initial stroke volumes. This score has been shown to correlate with the initial National Institutes of Health stroke score (NIHSS).

Magnetic Resonance: Diffusion-weighted Imaging

MR, with diffusion-weighted imaging (DWI), which became widely available in routine clinical practice in the late 1990s, offers significantly greater sensitivity and specificity for the detection of acute stroke (greater than 90% compared with approximately 60% for CT). To put it very simply, energy depletion will trigger a cascade that will alter the internal cellular milieu and result in development of cytotoxic edema. The restriction of water molecule diffusion appears as hyperintensity on diffusion-weighted images. The diffusion "experiment" can be performed with a variety of rapid imaging techniques, such as echo planar imaging, and can acquire images of the entire brain in half a minute. This minimizes the effects of patient motion, especially important when the clinical presentation includes alteration of mental status. The apparent diffusion coefficient value is a quantitative measure that may be calculated from the diffusion-weighted images. Since diffusion-weighted images rely on both diffusion and T2 effects, it is wise to confirm that the apparent diffusion coefficient values are indeed reduced before diagnosing an acute infarct. This will reduce the number of false positives due to "T2 shine-through" effect from old infarcts (gliosis) or other T2 hyperintense processes such as vasogenic edema.

Acute ischemic infarcts may appear as hyperintense regions on DWI (see Fig. 1-15), and this can occur as quickly as 30 minutes after onset. Up to 100% sensitivity has been demonstrated in clinical studies. However, in routine practice, small lesions in the brainstem may not be perceived initially, only to be detected on a follow-up exam prompted by persistent symptoms. It is also possible that a region of ischemia (prior to completed infarction) may go undetected on an initial imaging study, resulting in a false negative result. False positives on DWI can be due to processes that mimic stroke and also cause diffusion restriction, such as certain neoplasms, multifocal metastatic disease, and abscesses. Presence or absence of associated findings on conventional MR sequences—such as loss of gray–white matter differentiation on T1WI, and hyperintense edema on FLAIR and T2WI—may help with diagnosis, although these signs may be inconspicuous for 6 to 12 hours after stroke onset. Blooming on gradient-echo sequences due to intravascular thrombus and loss of expected vascular flow voids are other useful clues.

Lacunar infarcts are generally less than 1 cm in diameter and presumed to be due to occlusion of small perforating branches due to embolic, atheromatous, or thrombotic lesions. They occur most commonly in the basal ganglia, internal and external capsules, immediate periventricular white matter (corona radiata), and, less frequently, the centrum semiovale. Occlusion of basilar artery perforators will result in lacunes in the brainstem. Diffusion imaging offers the ability to identify very small, acute infarcts even in the background of chronic white matter disease and remote lacunes (Fig. 1-16). While MR is still considered a relatively expensive technique, it has the potential to reduce the number of unnecessary hospital admissions for recurrent small vessel infarcts in many patients. It may also help to select the most appropriate pathway for patients with central embolic sources of infarcts based on detection of infarcts in different vascular territories.

MR is also valuable in the setting of neonatal hypoxic ischemic encephalopathy. Cranial ultrasonography and CT may be used to evaluate germinal matrix hemorrhages, periventricular leukomalacia, and hydrocephalus. Diffusion-weighted MR is most sensitive for evaluating the different patterns of injury. In preterm infants subjected to mild hypotension, the periventricular regions are most often affected. With more severe hypotension, the basal ganglia, brainstem, and cerebellum may be involved. In full-term infants with mild hypotension, infarcts in the border zones between anterior and middle cerebral arteries or between middle and posterior cerebral arteries may result. Severe hypotension may result in infarcts of basal ganglia, hippocampi, corticospinal tracts, and sensorimotor cortex.

Diffusion-weighted hyperintensity generally begins to decline after a few days, with the process of apparent diffusion coefficient (ADC) pseudonormalization usually taking place over the next few weeks. Final ADC values will vary based on degree of gliosis or cavitation of the infarct. It should be noted that infarction development depends on the magnitude and duration of ischemia and the metabolic demands of the affected tissue. While diffusion restriction due to ischemia almost always results in infarction, rare cases of spontaneous reversible diffusion abnormalities have been reported, as well as those occurring in the setting of thrombolytic therapy.

Magnetic Resonance Angiography

Noninvasive imaging of the vessels of the head and neck with MR angiography (MRA) based upon time-of-flight or phase-contrast MRA techniques can be used to locate stenoses and occlusions in the extracranial and intracranial arterial systems (see Fig. 1-15). Gadolinium-enhanced MRA has become the standard of care at some institutions; this requires consideration of renal function. Complete brain MR and head and neck MRA examinations can be acquired in less than 30 minutes and have become the routine standard of care, often performed immediately or soon after completion of CT. It must be stressed that patient safety is a primary concern and therefore careful attention to screening for potential contraindications prior to MR scanning is a requisite at all times.

Magnetic Resonance: Perfusion Imaging

It became clear from imaging-based stroke trials that final infarct volumes were often larger than those identified by imaging at the time of admission. Advances in rapid scanning techniques soon led to the ability to obtain functional images of brain perfusion. By demonstrating an ischemic zone at the periphery of an acute infarct, salvageable tissue (the so-called penumbra) could be targeted with novel therapies. Dynamic gadolinium-enhanced T2* perfusion-weighted imaging (PWI) is a commercially available technique that is based on the decrease in tissue

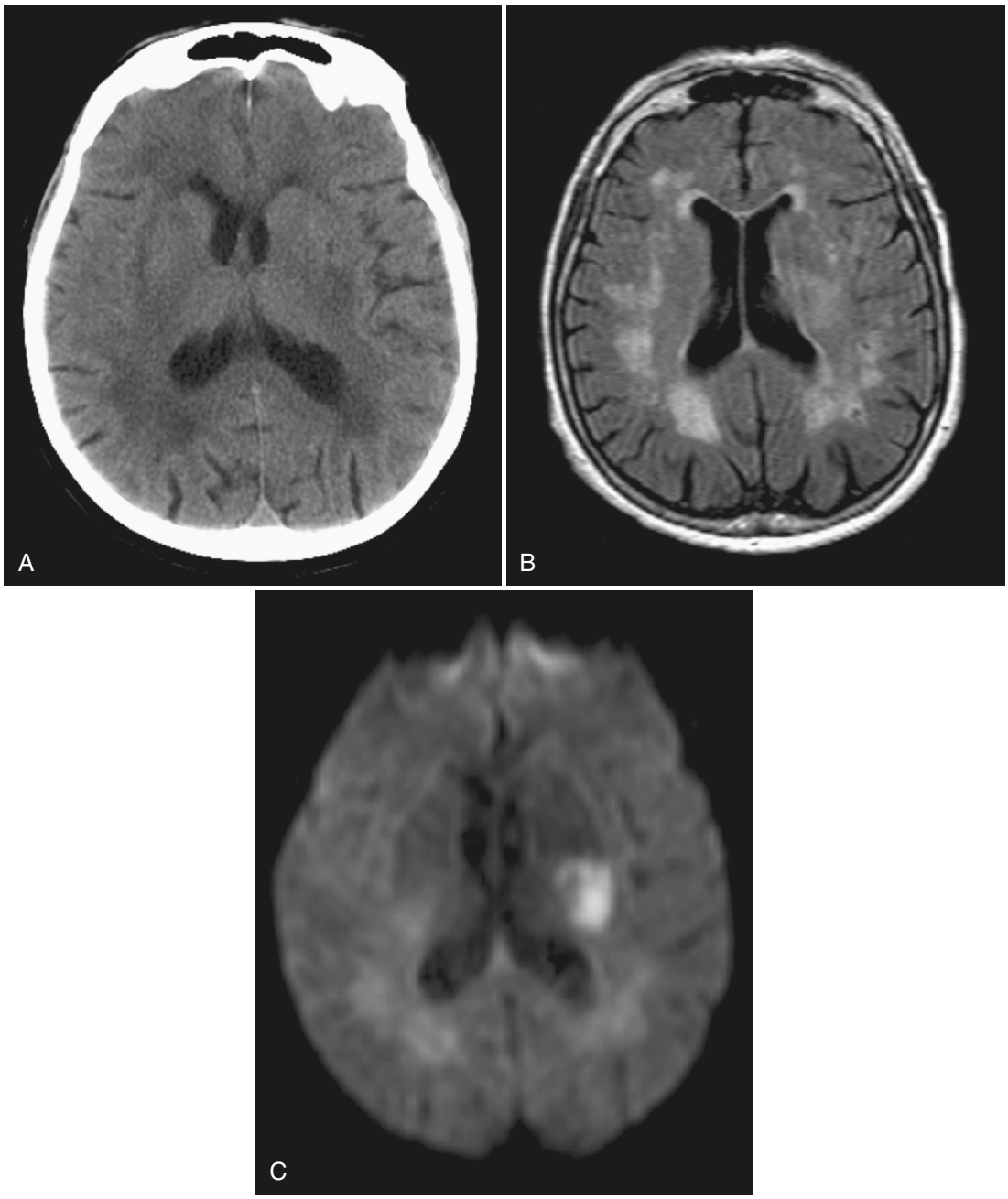


Figure 1-16. Acute lacunar infarct. **A,** CT shows multifocal hypodensities. **B,** FLAIR image shows corresponding hyperintensities due to chronic small vessel disease. **C,** Diffusion-weighted image shows the acute infarct in the left lentiform nucleus/posterior limb of internal capsule in a patient with acute onset of right-sided weakness. Apparent diffusion coefficient map (not shown) confirmed restricted diffusion. Other periventricular white matter mild hyperintensities are the result of "T2 shine-through."

signal intensity as a function of time during passage of a bolus of contrast. Functional "maps" of different perfusion parameters in the entire brain may be calculated from the time-signal intensity curves obtained during a minute-long acquisition. Cerebral blood volume (CBV) and tissue mean transit time (MTT) can be estimated using different methods, most commonly with deconvolution analysis. One limitation of MR-based techniques is that the blood volume estimate is a relative value. Cerebral blood flow (CBF) can be estimated by dividing CBV by MTT. A penumbra will be identified when a region of decreased CBF or prolonged MTT is larger than the infarct detected by DWI—a perfusion mismatch. Based on the extent of the mismatch, aggressive therapies may be pursued in order to limit the final infarct volume.

In some cases, the perfusion abnormality may exactly match the diffusion abnormality, and thus there is no penumbra. The final infarct volume is not expected to increase further. In other cases, where prompt reperfusion has occurred, such as from early vessel recanalization, the

perfusion abnormality may be smaller than the diffusion abnormality. In both of these situations, the risk of aggressive treatment is probably not warranted. The potential of improved clinical outcomes from therapeutic strategies based on perfusion imaging may result from either salvage of tissue at risk or reduction of complications.

Thus, the paradigm of acute stroke imaging is shifting based on therapeutic trials such as Desmoteplase in Acute Ischemic Stoke (DIAS) and Dose Escalation of Desmoteplase for Acute Ischemic Stroke (DEDAS). These were imaging-based trials of a novel drug derived from bat saliva that catalyzes the conversion of plasminogen to plasmin, which breaks down fibrin to dissolve intravascular blood clots. Eligibility was based on clinical symptoms and demonstration of a perfusion mismatch within 3 to 9 hours of onset. Results were promising and demonstrated the value of advanced imaging compared with unenhanced CT and a strict time limit alone.

Computed Tomography: Perfusion Imaging

The advent and wide availability of helical and, more recently, of multidetector CT (MDCT) scanners has led to the use of CT angiography (CTA) and CT perfusion (CTP) imaging in the workup of suspected acute ischemic stroke. The ability to acquire a large 3D volume of data rapidly during bolus contrast administration combined with submillimeter spatial resolution results in CT angiographic images that in many instances approach the diagnostic quality of more invasive digital subtraction angiograms. Large detector arrays and cine or shuttle modes of scanner operation allow for generous coverage of the brain during perfusion studies. Detector arrays from 4 to 64 rows wide are available now and newer models with 256 and more are in development. Analogous to PWI, CT perfusion is based on measurement of tissue density as a function of time during a first pass of intravenous contrast and commonly uses deconvolution analysis. In contrast to PWI, as a result of the proportionate increase in tissue attenuation due to iodine concentration, quantitative (rather than relative) estimation of CBV (and therefore CBF) can be obtained by CTP.

CTP applied in the setting of acute stroke has been validated with clinical outcomes and follow-up imaging and also by comparison with diffusion-weighted imaging. Wintermark and colleagues have proposed that regions with CBV less than 2.5 mL/100 g be considered the "core infarct" and regions with CBF reduction of more than 34% be defined as the penumbra. These values are based on correspondence with initial DWI abnormality and final infarct size. Schaefer and colleagues have proposed other absolute values and the use of normalized CBV and CBF ratios to help distinguish ischemic tissue likely to infarct from that likely to survive following intra-arterial recanalization therapy. Perfusion maps can be visually compared to determine if a penumbra is present but may underestimate or overestimate the extent of tissue at risk (Fig. 1-17). Software packages are available that can automatically segment the processed perfusion maps into core infarct, penumbra, and normal regions based on thresholding techniques.

The ongoing MR RESCUE (MR and recanalization of stroke clots using embolectomy) trial is employing a similar, automated analysis of PWI data to determine eligibility for inclusion. Patients presenting with intracranial arterial occlusions within 8 hours of symptom onset and having a suitable penumbra are randomized to embolectomy with the Merci Retriever device (Fig. 1-18).

Data from the recently completed DIAS 2 trial, a phase III study that used either DWI/PWI/MRA or CT/CTP/CTA as eligibility criteria, are still being analyzed. However, initial reports suggest that the results were not as favorable as those of previous trials. It is hoped that analysis of outcomes with respect to imaging features may help to identify a subset of patients who might achieve therapeutic benefits with a reduced risk of symptomatic hemorrhage.

Hemorrhagic Transformation

Hemorrhagic transformation of an ischemic infarct, thought to result from reperfusion injury, can be a dreaded complication of therapy or may happen spontaneously within hours or after a period of several weeks (Fig. 1-19). If a large hematoma is present at the time of initial imaging, it may not be possible to distinguish a primary parenchymal hemorrhage from hemorrhagic transformation. The blood products generally cause substantial artifacts on DWI. However, if the hemorrhage is confined within a larger zone of restricted diffusion, the etiology may be clear. Petechial hemorrhage occurs very commonly within an ischemic infarct, is best detected by gradient-echo imaging, and does not usually lead to increased morbidity.

Cortical Laminar Necrosis

A pattern of gyriform T1 hyperintensity developing a week or two after an ischemic infarct may be attributed to cortical laminar necrosis (Fig. 1-20). It seems that gray matter is more vulnerable to ischemic necrosis than white matter (especially the third layer of the six cortical layers), and, although the signal changes may lead one to diagnose hemorrhage or calcification, in one histologic study neither was detected. The exact cause of the T1 shortening is uncertain, but it may be due to high concentrations of proteins and macromolecules.

Cerebral Venous Infarction and Sinus Thrombosis

An uncommon (annual incidence estimates of less than 1 case per 100,000 population) but important cause of hemorrhage is cerebral venous thrombosis (Fig. 1-21). This may affect cortical veins and other portions of the superficial and deep venous drainage systems. Hypercoagulable states due to pregnancy and the postpartum period, or from oral contraceptive use, dehydration, regional infections, and trauma, are relatively common causes. Common presenting symptoms include headache, seizure, and focal neurologic deficits. Fluctuating symptoms and intracranial hypertension are common as well. Bilateral parenchymal hemorrhages or infarcts that do not obey usual arterial territorial borders can be clues to diagnosis. A working knowledge of the normal anatomy of the major venous structures and the common variants is necessary to avoid diagnostic pitfalls, especially false positives. On unenhanced CT, normal

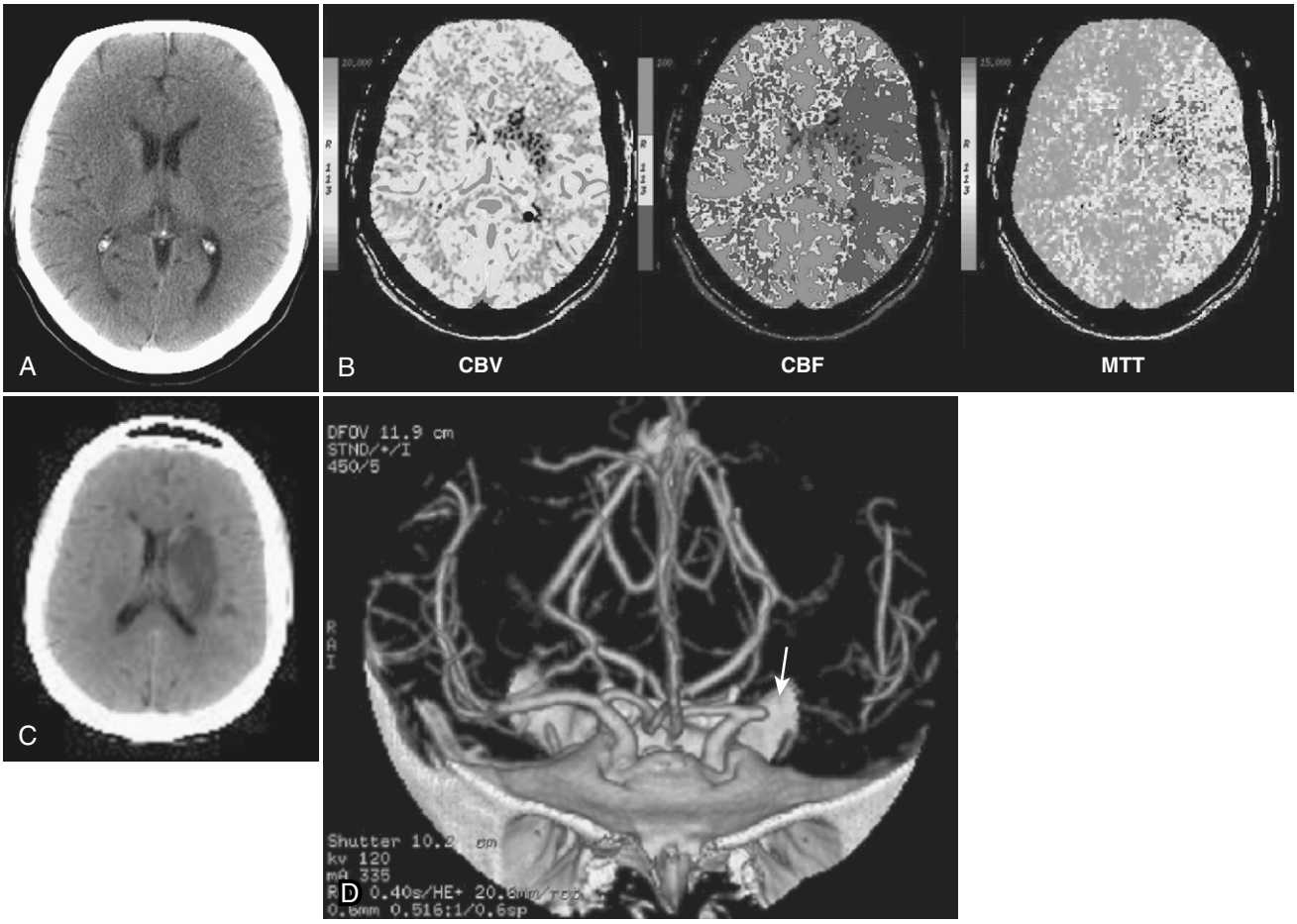


Figure 1-17. Perfusion CT—large mismatch. **A,** Noncontrast CT shows decreased density of left caudate head and putamen. **B,** CBF and mean transit time abnormalities are much larger than core infarct (CBV abnormality). (Color functional maps are more easily interpreted on a color monitor.) **C,** CT follow-up 1 week after conservative management shows that the final infarct volume closely matches the initial CBV abnormality. **D,** Initial CT angiogram showed abrupt occlusion of left middle cerebral artery stem (*arrow*) but with filling of distal branches due to robust leptomeningeal collateral circulation.

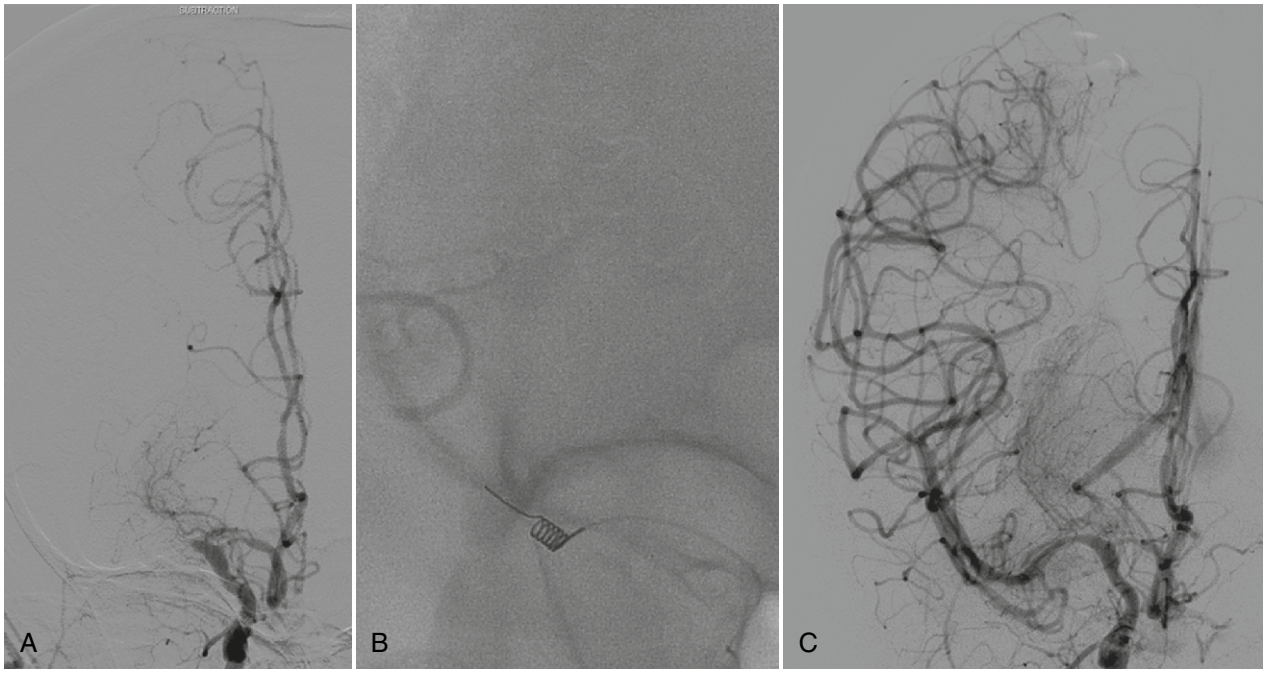


Figure 1-18. Mechanical thrombectomy. **A,** Acute right middle cerebral artery occlusion. **B,** Merci retriever deployed distal to thrombus. **C,** Recanalization of right middle cerebral artery following clot retrieval.



FIGURE 1-19. Hemorrhagic transformation of ischemic infarct. Noncontrast CT 24 hours postictus shows hyperdense hemorrhage within a large left middle cerebral artery territory infarct.

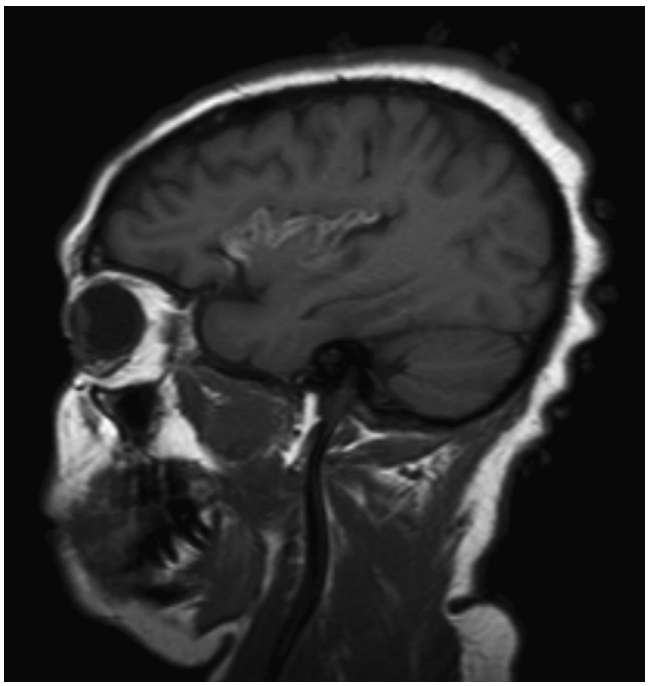


FIGURE 1-20. Cortical laminar necrosis. T1-weighted image shows gyriform hyperintensity in a perisylvian distribution 1 week after middle cerebral artery infarct.

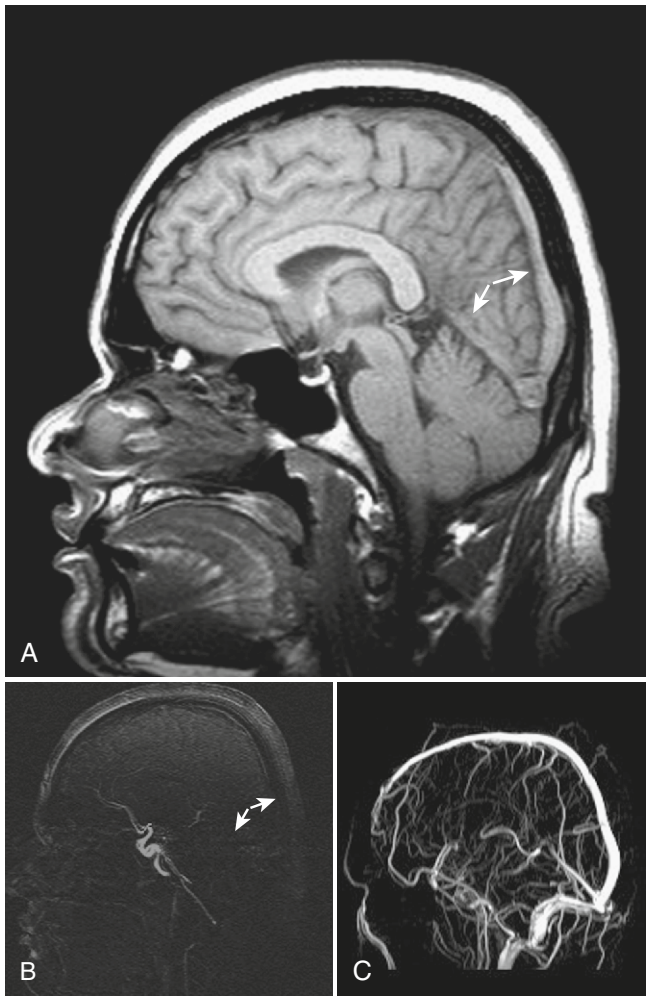


FIGURE 1-21. Venous sinus thrombosis. **A,** T1-weighted image shows loss of usual flow voids in superior sagittal and straight sinuses *(arrows)*. **B,** Two-dimensional phase contrast MR venography shows corresponding lack of flow-related signal. **C,** Three-dimensional phase contrast MR venography 1 week after systemic anticoagulation shows recanalization.

venous structures may appear denser than usual due to dehydration or elevated hematocrit, whereas thrombosis should appear hyperdense relative to arteries. A filling defect or occlusion may be detected on contrast-enhanced CT. CT venography can be performed with thin-section, volumetric technique allowing for creation of 2D and 3D reconstructions. Normal and thrombosed venous sinuses take on many different appearances on MR depending on scan parameters, flow velocity, and turbulence. Unexpected hyperintensity, loss of usual flow voids, and blooming on gradient-echo sequence are clues that flow-sensitive MR venography (MRV) should be performed. Time-of-flight MRV may be less sensitive than phase contrast technique due to shine-through of methemoglobin in a thrombosed sinus simulating flow in the vessel. Contrast-enhanced MRV may be more sensitive, although enhancement of chronic thrombus can be misleading. Associated findings of edema, hemorrhage, or ischemic infarct may help toward arriving at the correct diagnosis, but brain swelling without signal changes has been reported in up to approximately 40% of patients. Cavernous sinus thrombosis is discussed in relation to complex sinus and orbit infections in the section on head and neck imaging. Prompt diagnosis of cerebral thrombosis is critical, as many of the parenchymal changes may be reversible. Systemic anticoagulation and local catheter-based thrombolytic, mechanical, or rheolytic

clot dissolution are treatment considerations. Intracranial hypertension and collateral formation leading to dural arteriovenous malformations are possible long-term sequelae.

ANEURYSMS, VASCULAR MALFORMATIONS, AND VASCULAR INJURIES

Aneurysms and cerebral vascular malformations present in various ways in the emergency setting. Subarachnoid hemorrhage resulting from a ruptured aneurysm and parenchymal hemorrhage related to an arteriovenous malformation are dramatic examples of problems that may present with headache as the chief complaint. Presenting symptoms of nausea and vomiting are common with hemorrhages arising in the posterior fossa. On routine noncontrast CT, large unruptured aneurysms may simulate other mass lesions and displace or compress adjacent structures. Arteriovenous malformations may also be conspicuous on routine CT based on abnormally enlarged feeding arteries and draining veins or internal calcifications (Fig. 1-22).

The traditional gold standard for diagnostic evaluation of vascular lesions, both spontaneous and traumatic, is digital subtraction angiography (DSA). The risk of major complication from this invasive procedure is low in experienced hands and treatment (complete or partial) with endovascular techniques is possible for many types of aneurysms and other vascular lesions. That being said, the constantly improving technology and clinical experience with CT angiography have led to a substantial decrease in the number of diagnostic angiograms (at some institutions). CTA is commonly applied in the setting of spine, facial, and skull base fractures. One study of CTA in 2004 in the setting of acute SAH reported a sensitivity of 89% and specificity of 100% for detection of aneurysms. Many centers have adopted immediate CTA in their protocol for the workup of spontaneous SAH (Fig. 1-23). If a ruptured aneurysm is detected by this method, detail may be adequate for treatment planning in certain situations. However, others have offered the opinion that the gold standard of DSA (with the recent enhancement of 3D rotational angiography) provides greater sensitivity and should not yet be replaced by CTA. This is based on recent reports of a 10% false negative rate of CTA for aneurysm detection and the belief that the greater spatial resolution of DSA is necessary for accurately determining proper triage to surgery versus endovascular coiling. Both of these reasons support the use of DSA regardless of a negative or positive result from CTA. Given its availability and lack of invasive risks, CTA will probably continue to be used as a diagnostic tool in this setting. In the setting of SAH, a negative CTA or DSA exam often requires a repeat examination, depending on the pattern of hemorrhage. DSA offers evaluation of cerebral hemodynamics, important for the diagnosis of brain and dural vascular malformations. This type of detail is not available from most current CTA techniques. On occasion, arteriovenous shunting may be inferred from the presence of dilated draining veins, or from asymmetric opacification of the cavernous sinuses, although this might just as well be due to normal physiologic variation. Evaluation of the smallest arteries is necessary for the evaluation of cerebral vasculitis, still not quite within the realm of CTA. Improvements in spatial and temporal resolution and reconstruction techniques will certainly reduce the number of false negative aneurysm hunts and increase the clinical utility of CTA for evaluation of arteriovenous malformations and vasculitis. Use of CTA in the setting of spontaneous parenchymal hemorrhage is gaining favor. One



Figure 1-22. Arteriovenous malformation. Noncontrast CT shows hyperdense lesion extending from third ventricle to right occipital lobe and associated hydrocephalus.

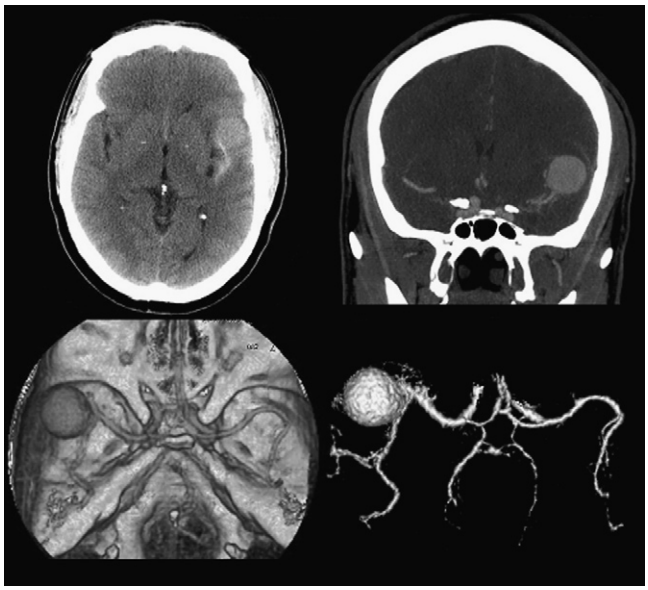


Figure 1-23. Subarachnoid hemorrhage—ruptured aneurysm. Noncontrast CT *(upper left)* shows subarachnoid hemorrhage in left Sylvian fissure and a round hyperdense mass. Images from CT angiogram (coronal multiplanar reconstruction, volume-rendered volume of interest, and volume created from a seed point) confirm a large left middle cerebral artery bifurcation aneurysm.

recent prospective study of CT angiography in the setting of acute intracerebral hemorrhage demonstrated that tiny enhancing foci within the hematoma are an independent predictor of hematoma expansion. Lack of a "spot" sign had a very high negative predictive value for worsening of hemorrhage. These findings may have important clinical value in future therapeutic trials.

CERVICOCEREBRAL ARTERIAL INJURIES

Spontaneous Cervical Dissection

Spontaneous cervical arterial dissection used to be considered a rarity, but since the 1980s, largely due to improvements in imaging, there has been an increase in awareness of this cause of stroke. It is now estimated that up to 25% of strokes in young and middle-aged adults occur on this basis. Community-based studies have found annual incidence of internal carotid artery dissection at 3 per 100,000 per year and of vertebral artery dissection at 1.5 per 100,000 per year. History of a trivial precipitating event, such as minor movement of the neck, is commonly reported. Chiropractic manipulation of the cervical spine has become recognized as a potential cause of dissection, but estimates of the rate of occurrence vary widely. Many different kinds of triggering events associated with hyperextension or rotation of the neck—including sport and recreational activities, ceiling painting, coughing, sneezing, and vomiting—have been reported. A higher incidence in the autumn suggests inflammation or an excess amount of sneezing and coughing related to upper respiratory tract infections as predisposing factors. The effect of genetics has not yet been completely determined, but approximately half of patients show mild ultrastructural connective tissue alterations similar to Ehlers-Danlos syndrome. Traditional vascular risk factors have not been systematically studied, but atherosclerosis is generally not found in patients with spontaneous dissections. Migraine has been suggested as an independent risk factor.

Traumatic Cervicocerebral Injuries

The evaluation of vascular injuries of the neck and head has undergone a dramatic transformation due to the capabilities of helical and now multidetector CT angiography. Since 2000, favorable results from the use of CTA in the setting of penetrating trauma have supported its clinical application on a routine basis. High sensitivity and specificity for the detection of vascular injuries has been reported in a number of studies. It has essentially replaced DSA, still the gold standard, as the initial screening modality of choice for penetrating neck injuries at many institutions. In many cases it has been used as a complementary technique to surgical exploration of the neck, but, more recently, a normal CTA may avert the need for exploration. CTA has been applied to the setting of blunt trauma with similar results and has resulted in a decrease in the number of DSA exams performed. Abnormalities that may be detected include stenosis, occlusion, dissection, pseudoaneurysm formation, and contrast extravasation from vessel rupture. Vascular evaluation is generally limited to the common carotid, internal carotid, and vertebral and proximal branches of the external carotid arteries. With currently available equipment, submillimeter, subsecond imaging is possible, and even minor abnormalities of the distal external carotid branches are now being diagnosed prospectively. Nondiagnostic exams may occur as a result of technical deficiencies such as extravascular contrast infiltration from intravenous catheter problems, patient motion, and so on. Using a contrast test bolus or bolus tracking techniques helps to reduce the number of poor-quality scans due to arrhythmias or compromised cardiac output. Since intravenous contrast bolus may be impeded by transient compression of the left brachiocephalic vein due to pulsations of the great vessels, a right-sided antecubital injection site is preferred. Streak artifacts from dental fillings and hardware and beam-hardening effects also take their toll on image quality. Positive findings on CTA help guide therapeutic decisions toward medical, surgical, or endovascular intervention; however, well-defined pathways do not yet exist for most vascular injuries. It is the clinical expectation that by prompt diagnosis and implementation of antithrombotic or other vascular treatments, the incidence of stroke will be reduced. As more subtle injuries will be detected with advances in CT technology, outcomes research will be necessary to help determine the most appropriate therapy. It is well known that a certain (small) percentage of patients will present with delayed formation and rupture of a post-traumatic pseudoaneurysm, yet recommendations for and timing of follow-up examination remain rather dubious (Fig. 1-24).

Dissection of the internal carotid and vertebral arteries may be the direct result of blunt trauma with a reported incidence of less than 1% in some series. As might be expected, the risk of vascular injury in the setting of spine fracture is substantially higher. Another mechanism of carotid injury is intraoral trauma, such as from a fall with a pencil in the mouth or from iatrogenic causes. Basilar skull fracture, especially involving the carotid canal, is also included in this category in most studies of traumatic dissection. The indications for CTA continue to broaden. Due to the potential for devastating neurologic consequences of cerebrovascular injuries, some have suggested a liberalized screening approach—including not only patients with symptoms referable to vascular injury, but also asymptomatic patients undergoing CT for head and cervical spine trauma. In such a study reported by Biffl and colleagues in 2006, 5.4% of patients had blunt cerebrovascular injuries. In a recent 2-year retrospective review of patients at our center (unpublished data), 8% of 106 patients with fractures of the cervical spine and skull base (involving foramen transversarium or near the carotid canal) had vascular injuries detected by CTA. Of 161 trauma patients without fractures who also underwent CTA, 2% had vascular injuries detected. Therefore, presence of a fracture yielded an odds ratio for vascular injury of approximately 4 to 1 in this population. False positive and false negative results are generally considered few in number, with the expectation that they will continue to decline as technology advances and experience with the technique increases.

Some authors propose mandatory imaging for the following reasons: (1) arterial bleeding from the mouth, nose, ears, or wound; (2) expanding cervical hematoma; (3) bruit in patients over 50 years of age; (4) acute infarct; (5) unexplained neurologic defect or TIA; (6) Horner syndrome,

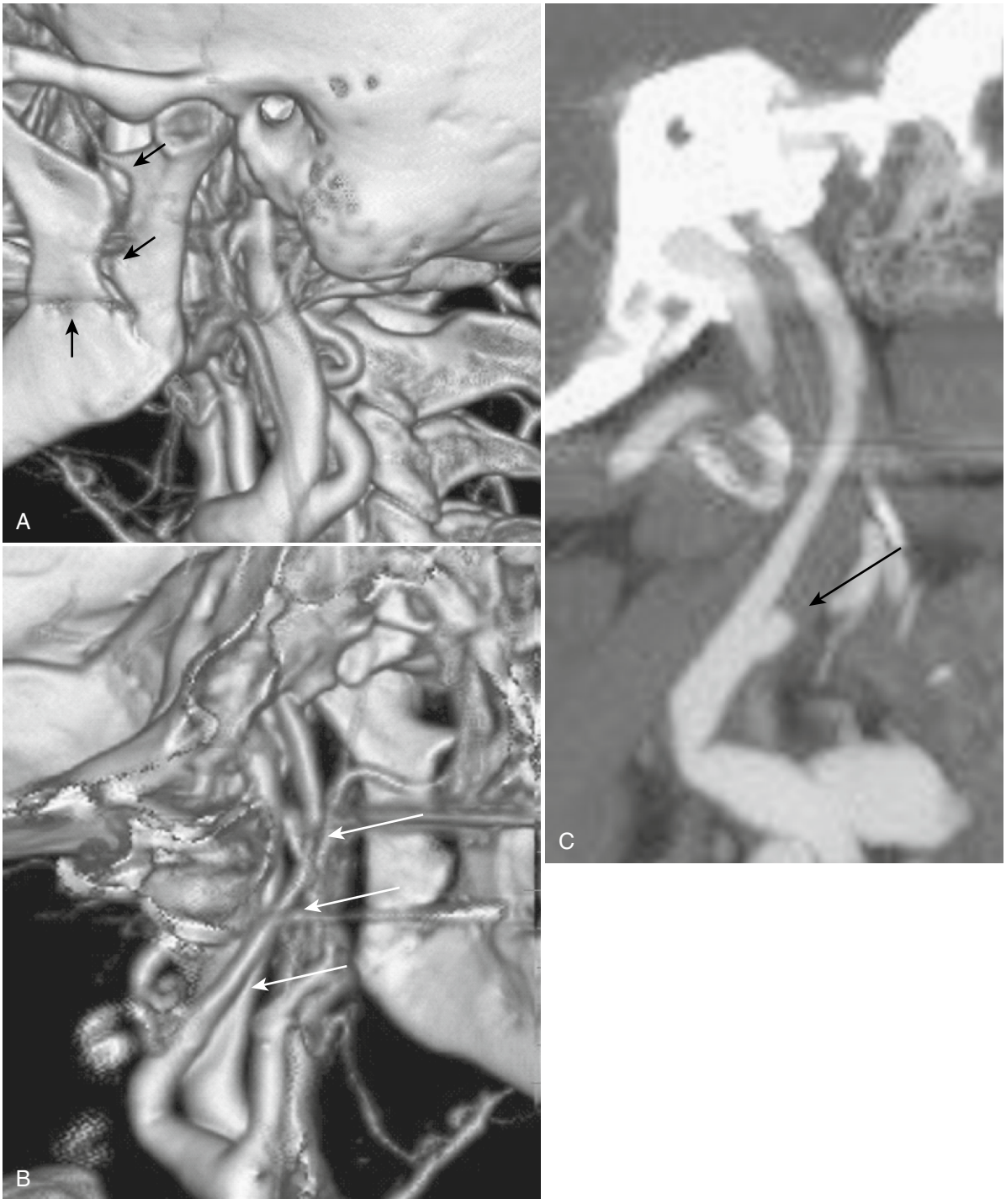


Figure 1-24. Arterial dissection secondary to blunt trauma. **A,** Volume-rendered image from CT angiogram shows comminuted mandibular fracture *(arrows)*. Internal jugular vein obscures internal carotid artery. **B,** 180-degree rotation and application of an anterior cutting plane reveal tapered contour of the internal carotid artery *(arrows)* due to dissection. **C,** Multiplanar reconstruction from follow-up CT angiogram 1 week later shows development of a small pseudoaneurysm *(arrow)* with residual, mild, distal stenosis.

neck or head pain. In one angiographic study of asymptomatic patients with skull base fractures, up to 60% had abnormal angiograms. Other studies have reported significantly lower rates of serious injury. One recent series found a 4% incidence of traumatic carotid-cavernous fistula in patients with skull base fractures. While prompt diagnosis and treatment of carotid-cavernous fistula are desirable, diagnosis at the time of admission is not as critical as it is for dissection with its inherent risk of stroke.

Whether performed for screening or based on symptoms, the workup and treatment of dissection continue to evolve. As with other vascular disorders, catheter angiography was once the only method available and is still used for confirmation if other studies are equivocal. The most common finding is a smoothly or mildly irregular tapered mid-cervical narrowing. Dissections that result in occlusion may show a "rat tail" or "flame-shaped" lumen; this may help distinguish other causes such as thromboembolism or atherosclerotic disease from dissection (Fig. 1-25). Saccular or fusiform aneurysmal dilatation (pseudoaneurysm) may also be identified. Presence of an intimal flap or a false or double lumen is unusual in the cervicocerebral vessels. In the internal carotid, the dissection is typically found a few centimeters beyond the carotid bifurcation or a few centimeters below the skull base. The most common sites of vertebral artery dissection are at the entry into the C6 foramen transversarium and at the C1-C2 level.

Ultrasound assessment of cervical internal carotid and vertebral artery dissections is possible, but there are many pitfalls. In addition to the findings that may be demonstrated by angiography, a thickened, hyperechoic vessel wall may be detected. This technique may be better for exclusion of dissection based on high negative predictive value.

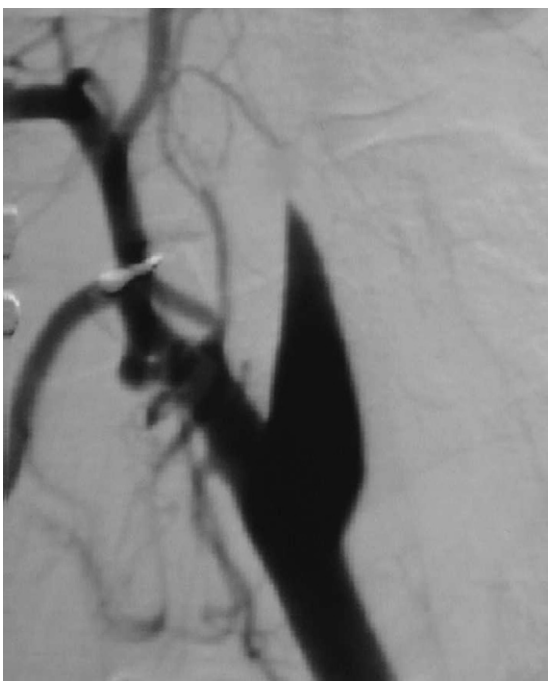


Figure 1-25. Acute dissection. Digital subtraction angiogram shows sharply tapered occlusion of the internal carotid artery due to spontaneous dissection.

The combination of MR and MRA is considered by many to be the preferred technique. MRA should be able to demonstrate the morphologic features of the vessel in a fashion similar to DSA. In addition, MR images may demonstrate an eccentrically located narrowed lumen, a crescentic or circumferential intramural hematoma, and an increase in the external artery diameter. Fat-suppressed T1-weighted images are recommended to improve sensitivity for detection of the intramural hematoma (Fig. 1-26). However, in the acute setting, the clot should not be expected to appear hyperintense, as it may take a few days for conversion to methemoglobin to take place. The reported sensitivity and specificity for detection of carotid dissection are very high, approximately 95% and 99%, respectively. Sensitivity is lower for vertebral dissection (approximately 60%) due to the smaller size of the native vessel and relatively high incidence of hypoplasia. One must remember that lack of flow-related signal due to slow flow in a vessel may simulate occlusion. These noninvasive techniques are very useful for follow-up of dissection due to the lack of ionizing radiation or need for contrast injection.

CT angiography shares many of the advantages of MRA and provides higher spatial resolution. Another specific sign reported by CTA is the "target" sign, composed of a thickened wall and a narrowed eccentric lumen surrounded by a thin rim of contrast enhancement. CTA is certainly the fastest way to screen patients in the emergency setting, often done immediately after imaging of the head and cervical spine.

CT angiography has also become the initial method for evaluation of stable patients with penetrating trauma to the neck, face, and head based on availability, efficiency, and similar profiles of sensitivity and specificity as in blunt trauma. The high sensitivity of CT for the detection of small amounts of contrast extravasation or air in the soft tissues helps to localize subtle injuries to major vessels that might otherwise go unnoticed. An understanding of the expected trajectory of bullets or knives based on skin entry and exit wounds may increase the likelihood of injury detection. Detection of dissection, transection, pseudoaneurysm, and arteriovenous fistula formation can help guide treatment—medical versus open surgical versus endovascular. Post-traumatic vasospasm may lead to a false positive diagnosis of dissection or transection, appearing normal on immediate follow-up angiography. Retained bullets and shrapnel often cause substantial artifacts that limit the diagnostic value of CTA. Digital subtraction angiography can usually overcome this limitation through the use of multiple oblique projections.

Spontaneous Intracranial Dissection

Intracranial arteries lack an external elastic lamina and have thinner media and adventitia compared with extracranial vessels. Therefore, intracranial dissections may behave differently. If the dissection occurs between the intima and media, then luminal stenosis or occlusion may lead to ischemia or infarct similar to the extracranial setting. If the dissection plane is between the media and adventitia, then (dissecting) pseudoaneurysm formation is likely. Due to the thin media and adventitia, rupture and subarachnoid hemorrhage may occur. SAH is reported in approximately

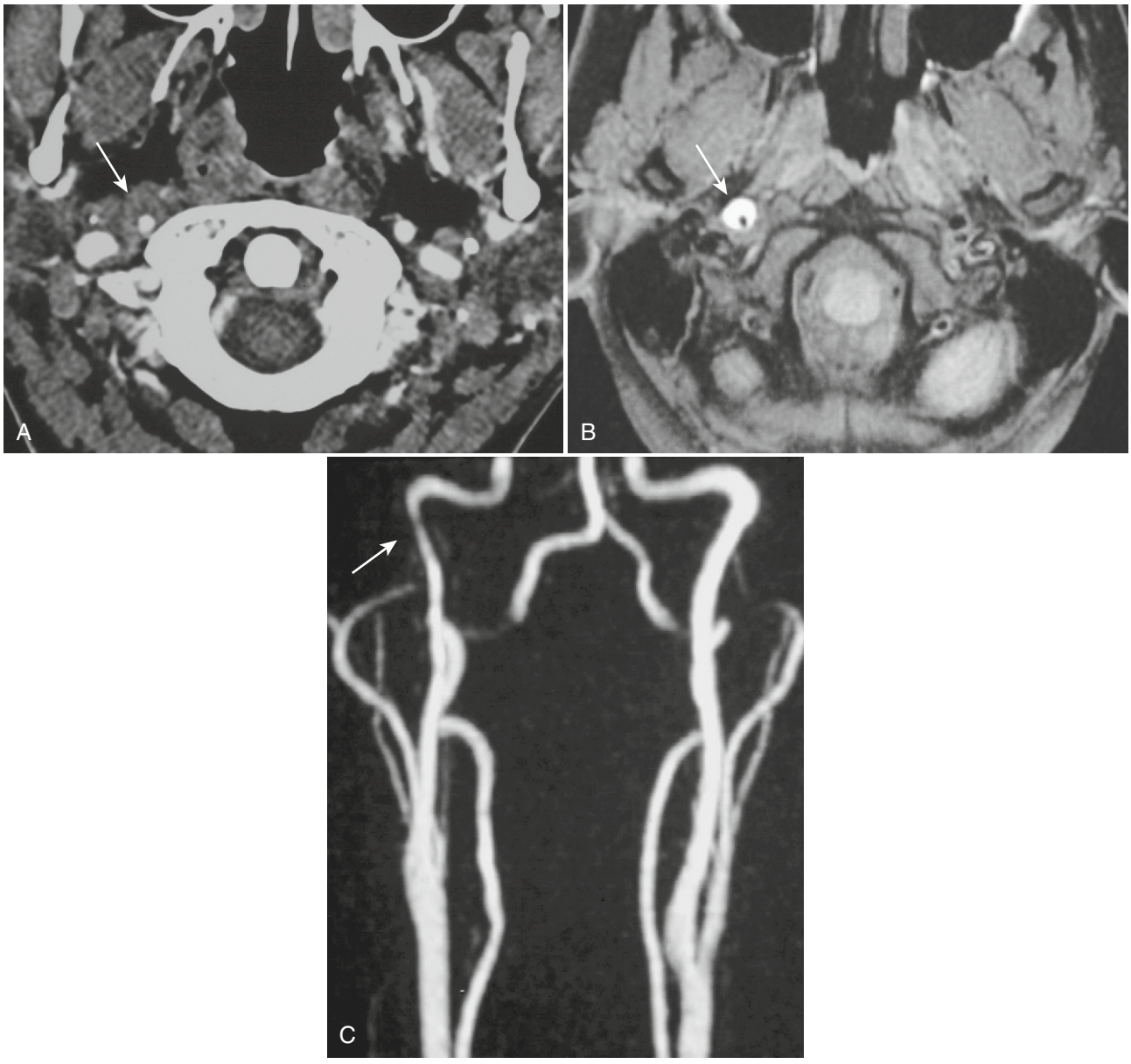


Figure 1-26. Internal carotid artery dissection—CT and MR angiograms. **A,** CT angiogram source image shows narrowed upper cervical right internal carotid artery lumen with increase in external caliber of vessel *(arrow)*. **B,** Fat-suppressed T1WI shows corresponding narrowed flow void with hyperintense eccentric intramural hematoma *(arrow)*. **C,** Time-of-flight MR angiogram shows narrowed segment of right internal carotid artery *(arrow)*.

20% of intracranial internal carotid dissections and more than 50% of intracranial vertebral dissections. The supraclinoid segment of the internal carotid and the segment of the vertebral near the posterior inferior cerebellar artery (V4) are the most common sites of intracranial dissection. The cause of intracranial dissection remains unknown, with some related to trauma or underlying connective tissue disorders (such as fibromuscular dysplasia, Marfan's, and Ehlers-Danlos types). It may not be possible to differentiate traumatic stenosis or occlusion from atherosclerosis or thromboembolism by any imaging technique. The only truly diagnostic findings of dissection are presence of a dissecting pseudoaneurysm and a double lumen.

Treatment options vary depending on stenosis versus pseudoaneurysm configuration and presence of infarct or subarachnoid hemorrhage. Endovascular intervention with stent placement may be considered when medical therapy for stenosis has failed. Aneurysm coiling, proximal occlusion, and trapping of an abnormal segment are other possible techniques.

OTHER NONTRAUMATIC INTRACRANIAL EMERGENCIES

As with ischemic stroke and spontaneous hemorrhage, the indication for workup of other non-traumatic emergencies affecting the brain will be based on an acute change in mental status or onset of headache, seizure, or a focal neurologic deficit. Delirium, or acute confusional state, is a common indication for brain imaging in concert with

a search for other causes such as hypoxia, cerebral hypoperfusion, systemic or regional infection, intoxication, and other metabolic causes. Noncontrast head CT offers rapid noninvasive detection of lesions producing mass effect or brain edema. Spontaneous and subacute hemorrhages have been addressed in previous sections. Other causes run the gamut of infection, inflammation, tumors, and other causes of encephalopathy. The following sections illustrate a few of the more commonly seen entities from these categories.

Hydrocephalus

Disturbance of the usual pattern of CSF flow or production/absorption may result in dilatation of the ventricular system. Hydrocephalus may occur acutely or may be of chronic duration, and the distinction between the two forms may not be entirely clear based on imaging alone. Hypodensities/T2 hyperintensities in the periventricular white matter of the frontal and periatrial regions may be a sign of transependymal flow of CSF and may be seen with acute hydrocephalus. Chronically compensated hydrocephalus is less likely to demonstrate this finding. Terminology can be confusing: obstruction at the level of foramen of Monro, cerebral aqueduct of Sylvius, or foramina of Magendie and Luschka is considered noncommunicating hydrocephalus, whereas obstruction at the level of the arachnoid granulations is considered communicating hydrocephalus. One should always remember the value of prior exams, since long-standing, compensated hydrocephalus is generally not a cause for alarm even if encountered in the emergency setting. Ventricular obstruction may develop as a result of SAH, IVH, intraventricular mass, aqueductal stenosis, and any lesion that may cause extrinsic mass effect. Analysis should include evaluation of basal cisterns and search for possible complications that may result from herniation. Ideally, treatment of hydrocephalus will prevent such complications. Recurrence of symptoms due to ventricular shunt malfunction is a common problem that may result from catheter/tubing obstruction (intrinsic or in the peritoneal cavity), disconnection, or migration (Fig. 1-27).

Classification is complicated further by normal pressure hydrocephalus; the etiology of this disorder in which intracranial pressure is not elevated is unknown. In the setting of ventriculomegaly out of proportion to sulcal prominence, the presence of the classic triad of dementia, abnormal gait, and urinary incontinence can help to make this diagnosis. However, by the time the classic symptoms are evident, treatment may be ineffective. The fourth ventricle may be relatively spared and signs of transependymal flow of CSF may be present in normal pressure hydrocephalus.

A related disorder is pseudotumor cerebri (idiopathic intracranial hypertension), which may be due to poor CSF absorption such as from venous sinus thrombosis. Incidence is highest in obese females of child-bearing age and may present with headache and visual loss due to papilledema. Although intracranial pressure may be severely elevated in this disorder, the ventricular system is generally small. Progressive visual loss may be an indication for emergent, fluoroscopic-guided, therapeutic lumbar puncture.



FIGURE 1-27. Hydrocephalus—shunt malfunction. Severe hydrocephalus. Portions of bilateral ventriculoperitoneal shunts are visible. Abdominal CT (not shown) demonstrated a pseudocyst as a cause for malfunction.

Colpocephaly is the term applied to enlarged occipital horns of lateral ventricles that are due to a developmental structural abnormality of the brain and that may sometimes be mistaken for acute hydrocephalus. Other congenital abnormalities such as agenesis of corpus callosum will also present with abnormal ventricular configuration and should be recognized as an expected part of the constellation of findings. Benign external hydrocephalus is the term applied to the pattern of mild ventriculomegaly and generous subarachnoid spaces in neonates and infants. It is associated with macrocephaly and usually resolves spontaneously by 1 to 2 years of age.

Infections

Meningitis

Suspected meningitis is a very common cause for imaging, not necessarily for diagnosis, but as a precaution prior to performance of a lumbar puncture. In adults with suspected meningitis, clinical features can be used to identify those who are unlikely to have abnormal findings on CT of the head. However, many practitioners still rely on CT prior to lumbar puncture in order to exclude unsuspected mass effect and lesions that might result in rapid increases in intracranial pressure; this is especially true for patients who are immunocompromised or older than 60 years. The majority of exams are normal, but detection of findings such as brain edema possibly leading to herniation, hydrocephalus, or other complication will alter management. On FLAIR images, sulci may appear hyperintense due to proteinaceous exudates; however, SAH or high concentration of inspired oxygen may also cause the same appearance. In

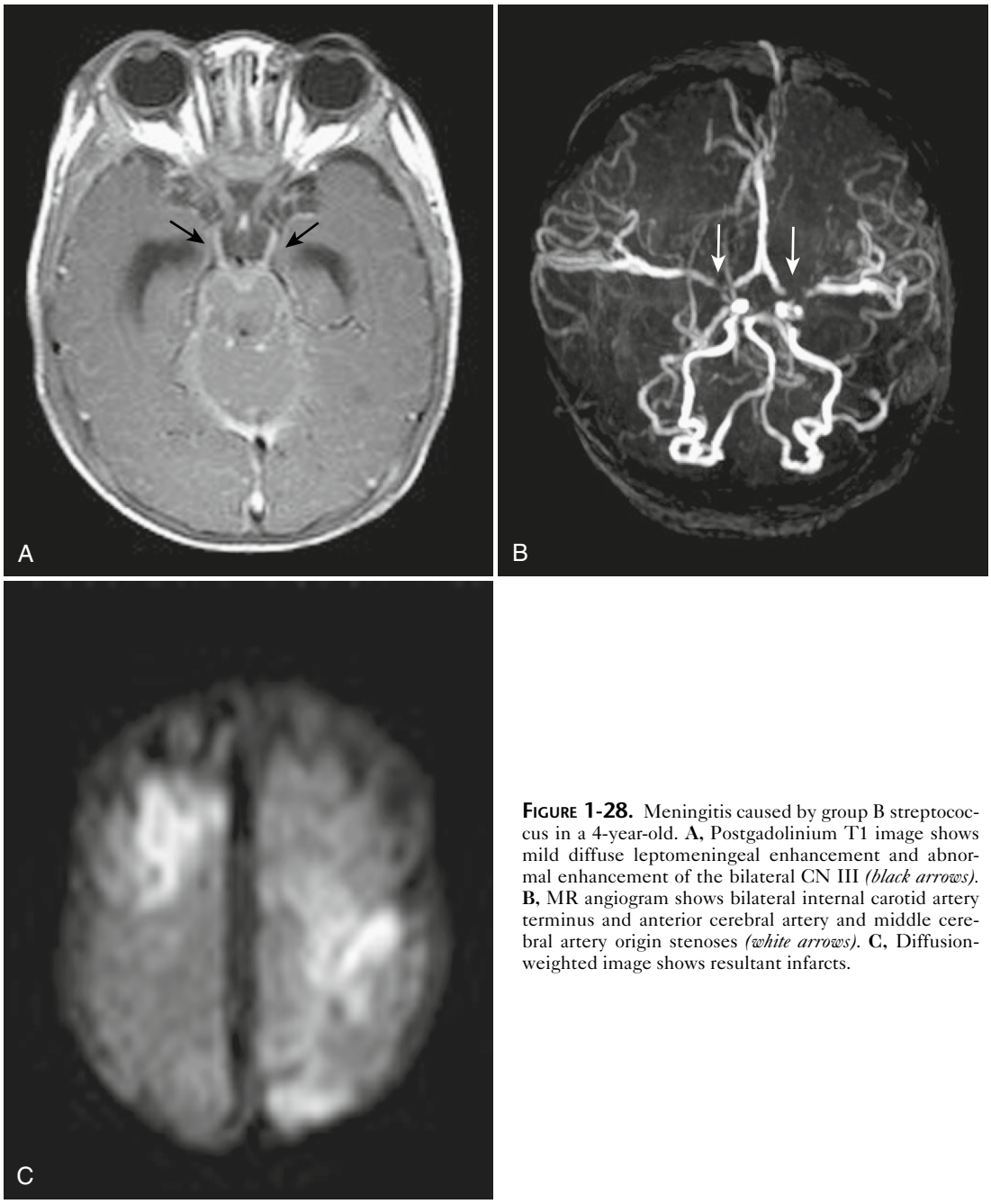


Figure 1-28. Meningitis caused by group B streptococcus in a 4-year-old. **A,** Postgadolinium T1 image shows mild diffuse leptomeningeal enhancement and abnormal enhancement of the bilateral CN III *(black arrows).* **B,** MR angiogram shows bilateral internal carotid artery terminus and anterior cerebral artery and middle cerebral artery origin stenoses *(white arrows).* **C,** Diffusion-weighted image shows resultant infarcts.

the vast majority of cases, meningitis is aseptic (generally of viral origin, commonly enteroviruses) and is self-limited. Bacterial meningitis is more likely to result in severe disease, and in some cases the source of meningitis may be evident on imaging, such as a sinus or ear infection. On intravenous contrast-enhanced CT and MR exams, diffuse enhancement within the sulci (leptomeningeal) may be detected. Imaging is also indicated for those patients who do not respond to antibiotic treatment in hope of detecting a drainable source such as subdural empyema or parenchymal abscess. Gadolinium-enhanced MR is generally preferred to CT due to its relatively higher soft tissue contrast. Neonatal meningitis due to *Citrobacter* species is another indication for imaging since brain abscess develops in 80% to 90% of cases. Meningoencephalitis (encephalomeningitis) is the term applied to brain parenchymal infection in association with meningitis. Other complications of meningitis include infarcts, venous thrombosis, subdural empyema or hygroma, and obstructive or communicating hydrocephalus (Fig. 1-28). Subdural empyema and epidural abscess are illustrated in the section on head and neck imaging.

Many other infectious agents may cause meningitis, including Lyme disease (*Borrelia*) and, especially in

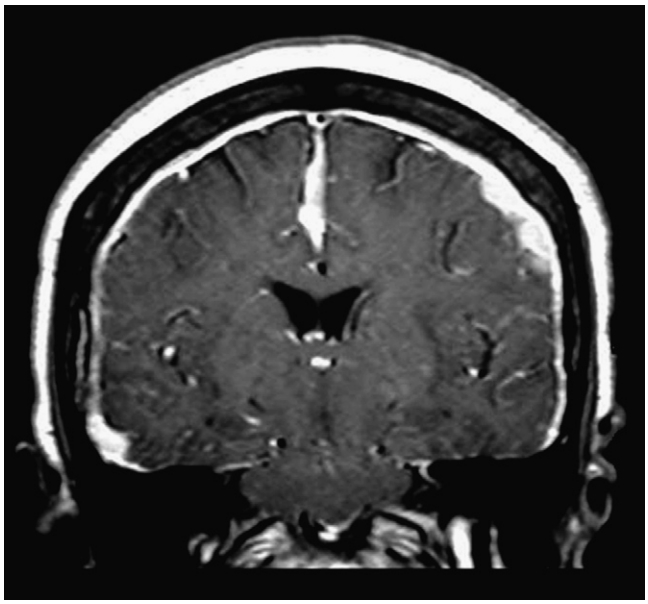


FIGURE 1-29. Pachymeningitis. Postgadolinium T1-weighted image shows diffuse, pachymeningeal, thickened enhancement due to neurosarcoidosis.

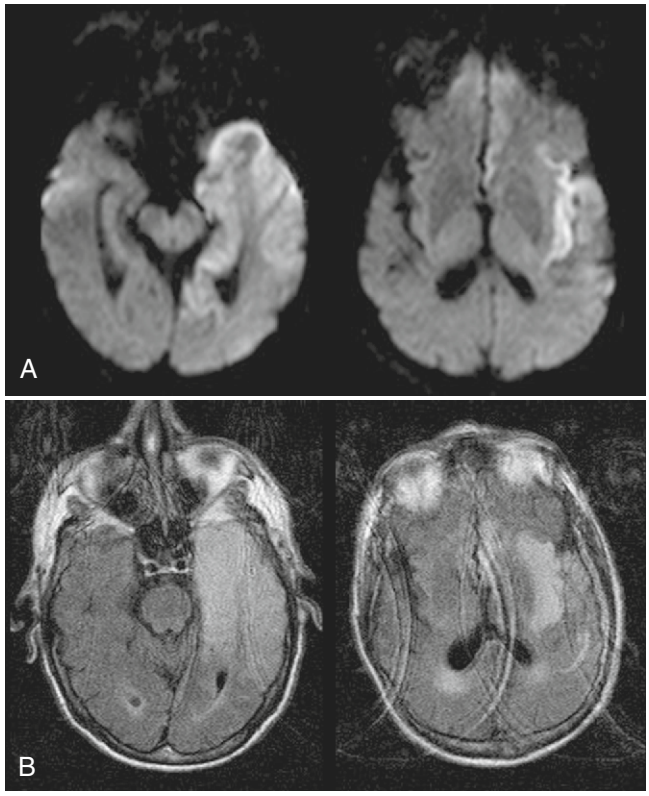


FIGURE 1-30. Herpes encephalitis. Diffusion-weighted **(A)** and FLAIR **(B)** images show corresponding hyperintensities in left temporal lobe and insula as a result of herpes simplex virus type I infection. Note the motion artifact so commonly encountered in patients evaluated for a change in mental status.

the immunocompromised setting, HIV, toxoplasmosis, cryptococcosis, tuberculosis, syphilis, cytomegalovirus, and a variety of fungi (see Fig. 1-12).

Diffuse thickened enhancement of the dura is a sign of pachymeningitis. This can be due to carcinomatous, granulomatous, and noninfectious causes including idiopathic intracranial hypotension (Fig. 1-29). Tuberculosis has a predilection for causing basal meningitis with resultant stroke due to involvement of arteries at the base of the brain.

Brain Parenchymal Infection

The term *encephalitis* refers to inflammation of the brain and is usually applied in the setting of viral infection. Cerebritis is often used interchangeably; however, it should be reserved for the cerebrum with cerebellitis added when necessary. Usually the findings are nonspecific, with simultaneous involvement of various structures. A certain pattern may suggest a particular organism, such as the classic findings of T2 hyperintensity, restricted diffusion, and minimal enhancement within the temporal lobe(s) and limbic system due to herpes simplex type 1 infection (Fig. 1-30). Nonspecific patchy T2 hyperintensities, variable diffusion, and enhancement characteristics may lead to a differential diagnosis including ischemia, infiltrating neoplasm, status epilepticus, and toxic/metabolic causes. Rather than identify the exact agent, imaging findings may be able to suggest infection and exclude other possibilities.

Abscess

Abscess is a focal parenchymal infection due to bacteria, fungi, or parasites. The imaging characteristics reflect the phase of the infection as it evolves from early cerebritis to late cerebritis, then to early and finally late encapsulated stages. If diagnosed early, it often appears as a low-density (on CT), T2 hyperintense region with faint enhancement and a mild amount of surrounding edema. Once in the capsule stage, a typical fluid collection with a thin rim of enhancement and larger amount of edema becomes evident (Fig. 1-31). Over time (with treatment), the lesion may decrease in size and develop a thicker rim of enhancement and surrounding edema will wane. The rim is typically T2 hypointense and thinner along the deep margin. This may predispose cerebral lesions to rupture into the ventricular system, leading to ventriculitis and a dramatic clinical decline. A bacterial abscess typically shows diffusion-weighted hyperintensity; this may help to distinguish a bacterial abscess from a necrotic tumor. Lesions in the differential diagnosis other than neoplasm might include demyelination, subacute infarct, and subacute hematoma. In the setting of immune suppression, fungal abscess should be considered. In the setting of AIDS, the differential for single or multiple ring-enhancing lesions includes toxoplasmosis versus lymphoma (Fig. 1-32). Also prevalent in the AIDS population is *M. tuberculosis* and *Cryptococcus*, which can present as either meningitis or focal parenchymal lesions. To further complicate matters, another classic presentation of cryptococcosis is that of nonenhancing, gelatinous pseudocysts that distend the perivascular spaces.

Single or multiple abscesses may develop from septic emboli due to endocarditis. Initially, these appear similar to other cardioembolic infarcts but in time develop relatively more surrounding edema and enhancement due to the inflammatory response (Fig. 1-33). If cardiac valve

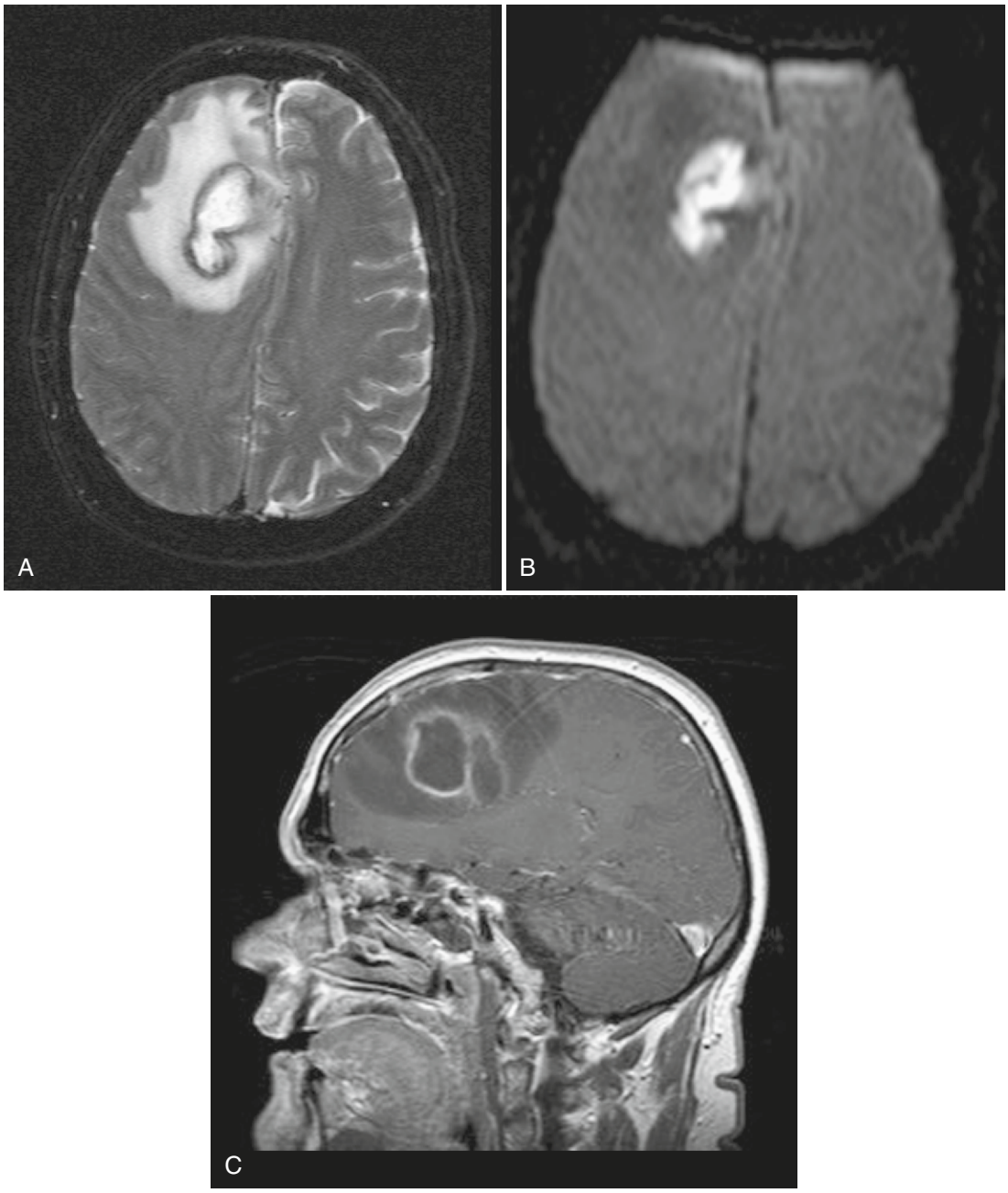


Figure 1-31. Pyogenic abscess. **A,** T2 image shows hyperintense fluid collection in the right frontal lobe with a hypointense rim and extensive surrounding edema. **B,** Corresponding hyperintensity on diffusion-weighted image. **C,** Postgadolinium T1-weighted image shows a relatively thin rim along the deeper portion of the abscess adjacent to the lateral ventricle.

replacement is considered, screening for mycotic aneurysms may be requested prior to surgery.

Neurocysticercosis is the intracranial infection by the pork tapeworm, *Taenia solium*, which is endemic in many parts of the world. It is the leading cause of seizures worldwide and has a unique life cycle and imaging characteristics. After ingestion of contaminated food or water, larvae migrate from the gastrointestinal tract to the brain and skeletal muscle. Once intracranial, the larvae develop into cysticerci, and these cysts may be located in the subarachnoid spaces, brain parenchyma, or ventricular system. The cysts then progress through four stages with distinct imaging features based on the lesion and the host response. In the vesicular stage, the lesions appear as thin-walled, fluid-filled cysts, possibly with mild rim enhancement, but without surrounding edema. Lesions are generally small (less than 1 cm), and often an eccentric scolex of a few millimeters can be detected. In the colloidal vesicular stage, in which the larva starts degenerating, a thicker rim of enhancement and surrounding edema develops. It is in this stage that the appearance is similar to any other brain abscess. Next is the granular nodular stage in which the cyst involutes, the wall thickens, the lesion begins to calcify, and edema decreases. In the final

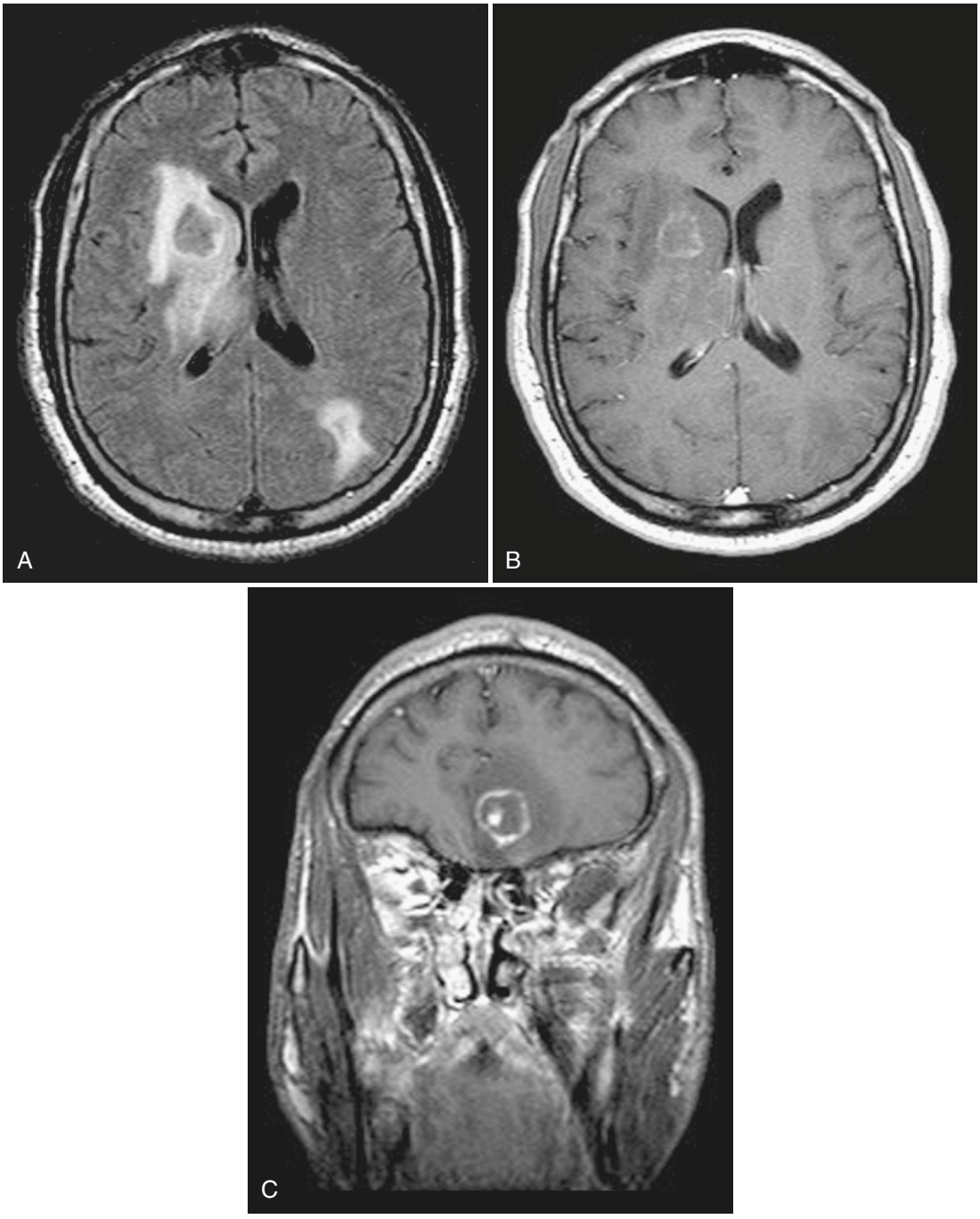


FIGURE 1-32. Toxoplasmosis. **A,** FLAIR image shows isointense lesions in right basal ganglia and left parietal lobe with surrounding edema. **B,** Postgadolinium T1-weighted image shows faint rim enhancement of right basal ganglia lesion. **C,** Postgadolinium T1-weighted image shows typical "target" sign in left frontal lobe lesion.

nodular calcified stage, only a small calcification persists and edema resolves completely. Since lesions may progress at different rates, it is not uncommon to find more than one type of lesion. Identification of cysts in different compartments, presence of a scolex, variable amounts of edema, and small calcifications in the same patient offer great sensitivity and specificity. It is not often that the radiologist can show such confidence in diagnosis, and therefore neurocysticercosis deserves special recognition (Fig. 1-34). One might not expect this to be common in the United States; however, due to travel and immigration, it presents fairly commonly in patients presenting to our ED with new or recurrent seizures.

Tumors

As with infection, it is not possible to review all of the myriad entities in this category. Within the scope of this chapter it is possible to provide only a limited framework and describe some of the more common lesions.

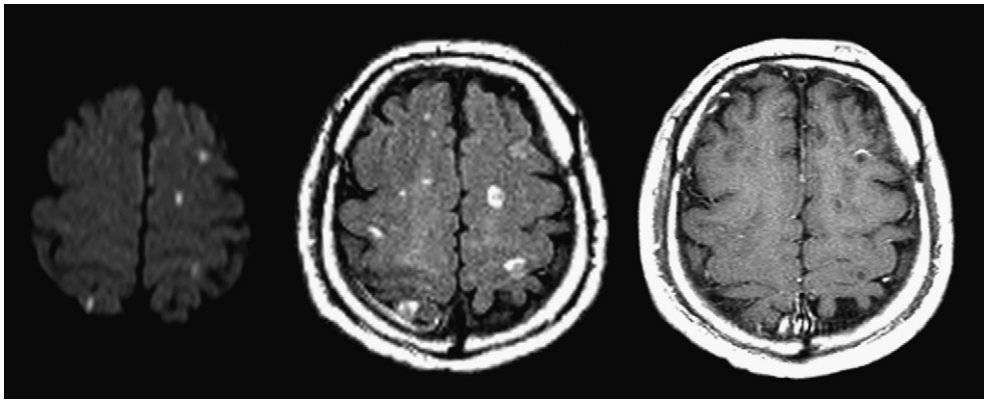
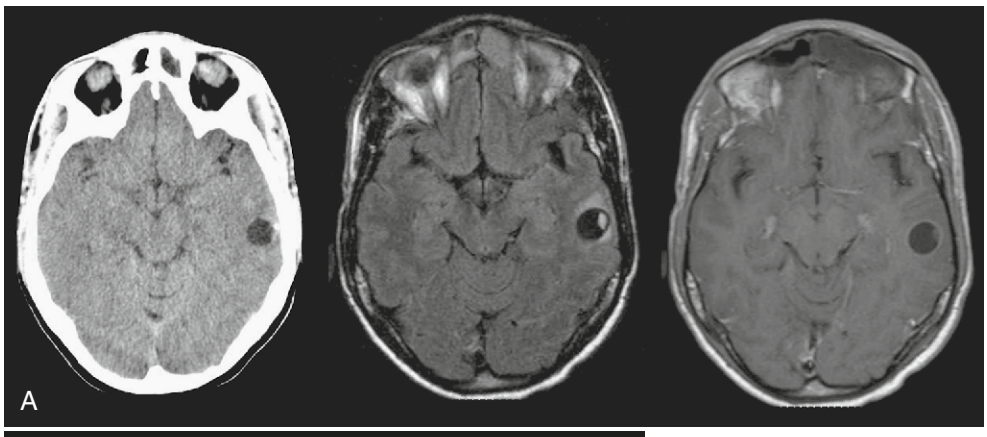


Figure 1-33. Septic emboli. Diffusion *(left)*, FLAIR *(middle)*, and postgadolinium T1-weighted image *(right)* show multiple small lesions with edema and faint rim enhancement.

Metastases account for approximately half of all intracranial neoplasms in adults. They may present as multiple small enhancing lesions at the gray–white junction or as a single large lesion with extensive surrounding edema. Lesions are usually found in the cerebral hemispheres, and may be solid, cystic, calcified, or hemorrhagic, and approximately 50% will present as a solitary lesion. The most common primary tumors are lung, breast, and melanoma. Calcification may imply a tumor of mucinous origin (gastrointestinal tract), and hemorrhage may indicate hypervascular primaries such as choriocarcinoma or renal or thyroid primaries in addition to the other most common culprits. The World Health Organization classification of primary central nervous system neoplasms is generally based on either cell type of origin or other location (e.g., sellar). Knowledge of this classification system is important for accurate communication among clinicians from different subspecialties, especially pathology, neuro-oncology, and neurosurgery. In addition, the radiologist should be familiar with the typical imaging characteristics, locations, and demographics of the common lesions in each category. As in any field, expertise requires effort and experience. Although it may be very satisfying to correctly identify the tumor histology (or at least narrow the differential diagnosis to a select few), the major goal in the emergency setting is to recognize subtle lesions, bring attention to those that may soon result in significant complications, and provide reassurance when intervention is not indicated. Perhaps the first step in this process should be to try to determine whether a mass is intra-axial or extra-axial. While not always clear, this distinction helps to guide the differential diagnosis toward the proper category. Location of the



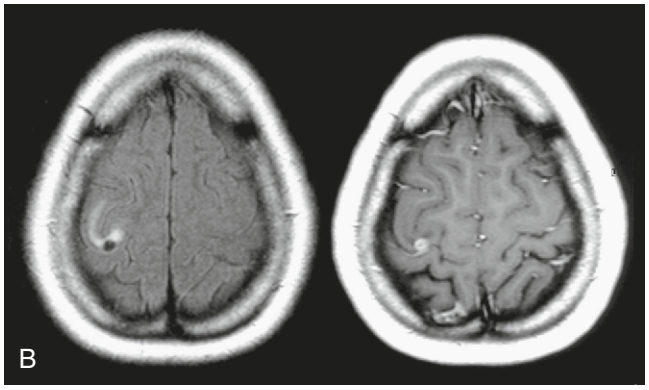


Figure 1-34. Neurocysticercosis. **A,** CT *(left)*, FLAIR *(middle)*, and postgadolinium T1-weighted image *(right)* demonstrate cyst with scolex, thin rim of enhancement, and surrounding edema in the vesicular stage. **B,** FLAIR *(left)* and postgadolinium T1-weighted image *(right)* showing signal loss related to calcification, small amount of edema, and rim enhancement in the granular nodular stage.

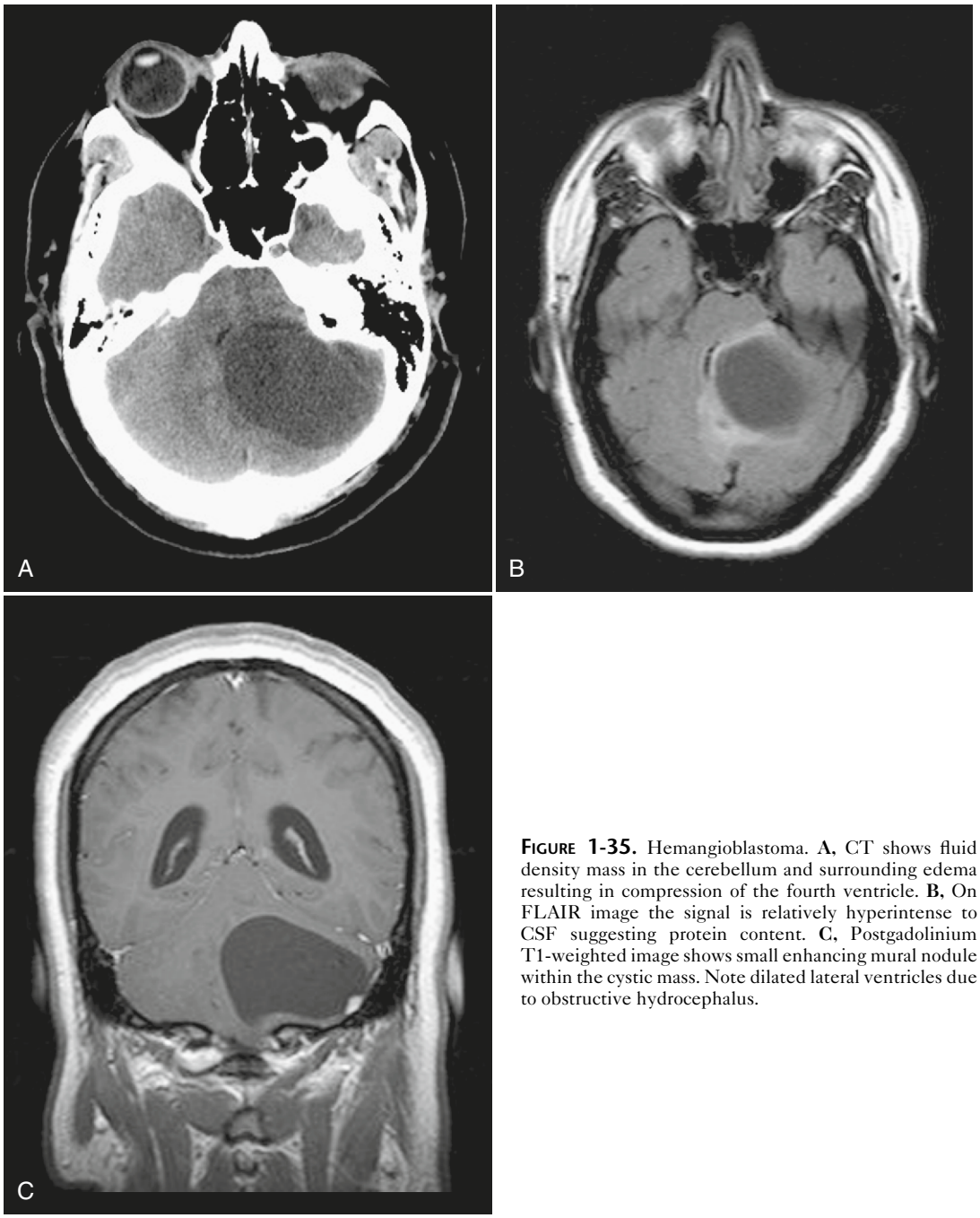


FIGURE 1-35. Hemangioblastoma. **A,** CT shows fluid density mass in the cerebellum and surrounding edema resulting in compression of the fourth ventricle. **B,** On FLAIR image the signal is relatively hyperintense to CSF suggesting protein content. **C,** Postgadolinium T1-weighted image shows small enhancing mural nodule within the cystic mass. Note dilated lateral ventricles due to obstructive hydrocephalus.

lesion, supratentorial versus infratentorial; relation to the skull base and cisterns (anterior or middle fossa, sellar/parasellar, pineal region, cerebellopontine angle cistern, intraventricular, etc.); and multiplicity are also important details. Demographics and clinical presentation may be equally important. One must also be aware that the differential for many primary neoplasms includes metastasis, as well as infection, infarct, demyelination, inflammatory conditions, and congenital/developmental anomalies. Although space limitations preclude even the most basic description of each of the intracranial tumors, a few examples are presented to illustrate common imaging features to be recognized during workup of patients in the emergency setting (Figs. 1-35 to 1-39).

Disorders of White Matter

No review of nontraumatic emergencies could be complete without mention of the following set of loosely related disorders. The common bond may be that they do not fall into the infectious or neoplastic categories. Some are quite common and the others are becoming more frequently diagnosed due to the relatively classic imaging features and recognized clinical associations.

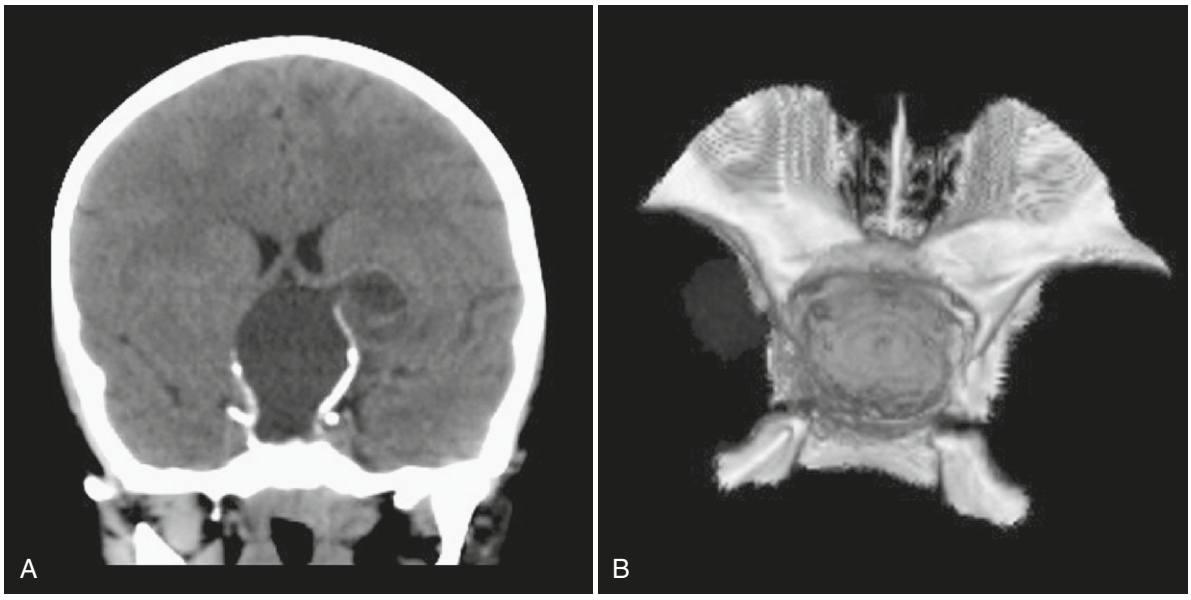
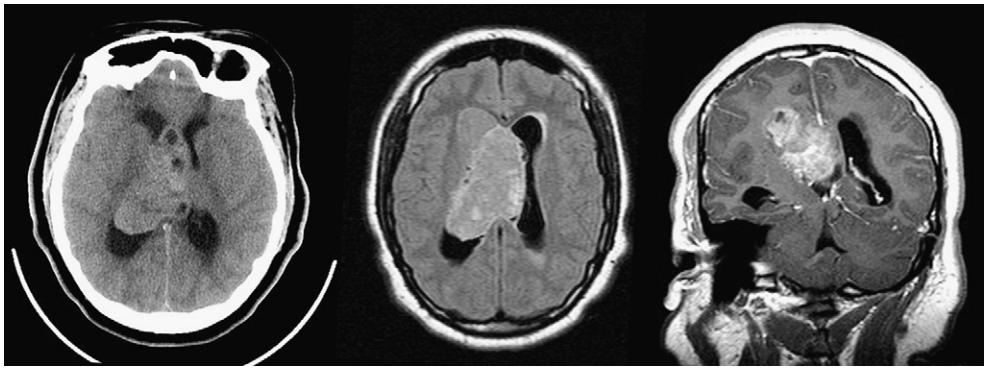


Figure 1-36. Craniopharyngioma. **A,** Coronal reformat of noncontrast CT shows a large cystic sellar/suprasellar mass with peripheral calcifications. **B,** Volume-rendered image shows the cystic components of the lesion as a semitransparent surface. It is more easily appreciated on a color monitor. By varying the transparency of the mass, the remodeled sella is easily demonstrated. This 5-year-old girl was sent by her ophthalmologist for urgent CT due to worsening visual acuity.

Figure 1-37. Central neurocytoma. Noncontrast CT *(left)*, FLAIR *(middle)*, and postgadolinium T1-weighted image *(right)* show a large, enhancing intraventricular mass related to the septum pellucidum causing hydrocephalus. This 22-year-old female presented to the emergency department with worsening headaches.



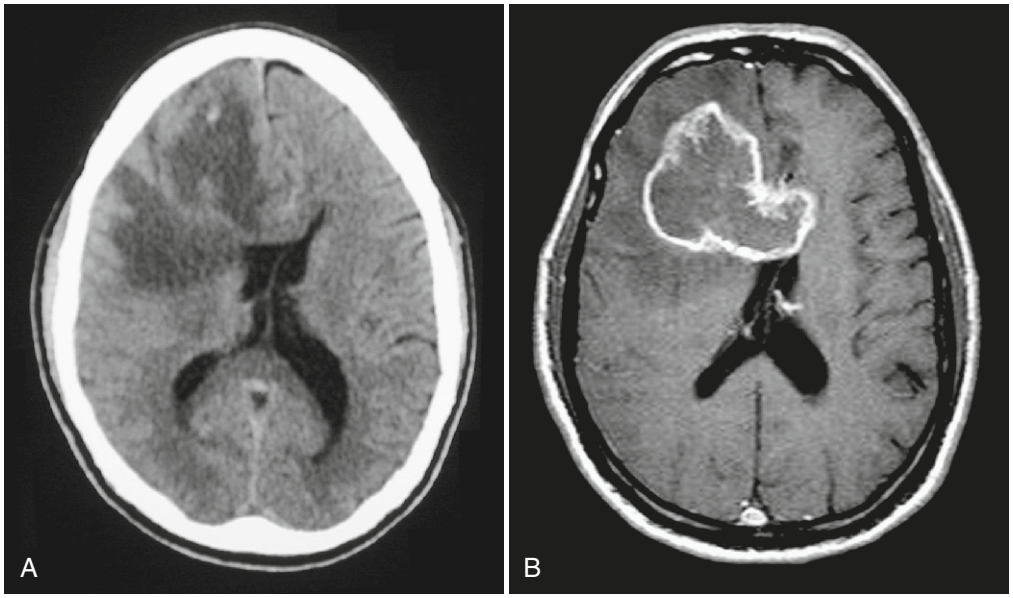


Figure 1-38. Glioblastoma multiforme (astrocytoma WHO Grade IV/IV). **A,** On noncontrast CT the mass cannot be clearly separated from the edema. **B,** Postgadolinium T1-weighted image shows an irregular rim of enhancement of this mass that crosses the midline via the corpus callosum. This 50-year-old male presented with altered mental status.

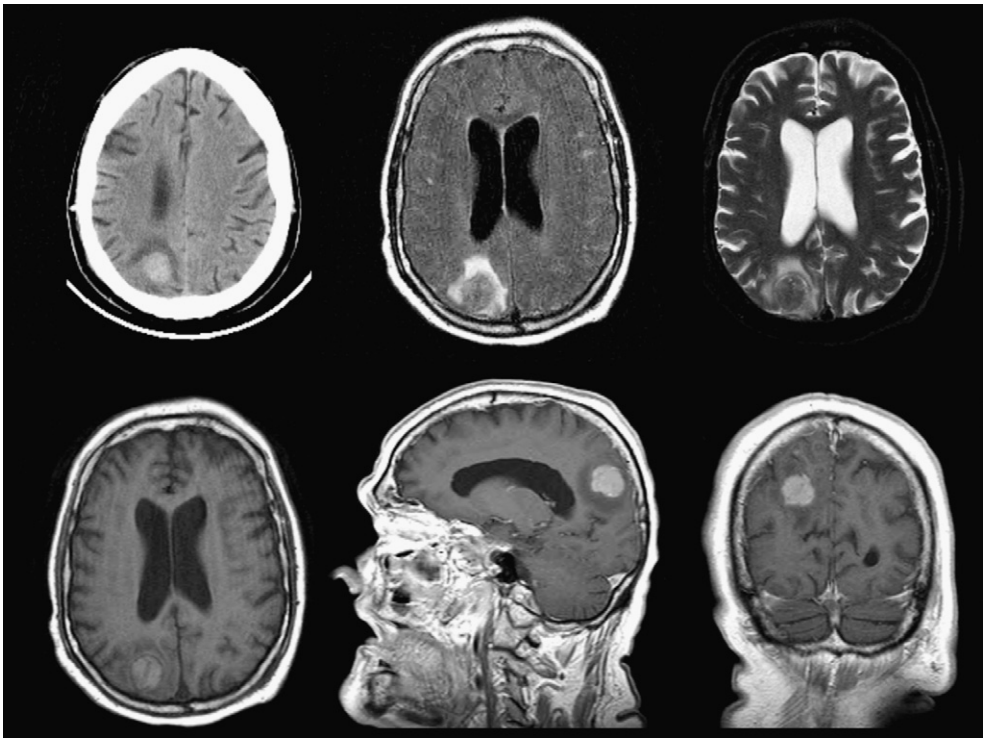


FIGURE 1-39. Metastatic lung carcinoma. Noncontrast axial CT, FLAIR, T2, T1, and sagittal and coronal postgadolinium T1-weighted images. This single lesion is hyperdense, FLAIR/T2 isointense, T1 mildly hyperintense, and homogeneously enhancing. There is a moderate amount of edema relative to the size of the lesion.

Multiple Sclerosis

Patients presenting with a clinically isolated syndrome (first episode of neurologic dysfunction) often undergo imaging in the emergency setting mainly to exclude infarction or other process. White matter lesions detected by CT or MR may raise the suspicion of a demyelinating disorder. The diagnosis of multiple sclerosis (MS) can be complex, requiring dissemination of lesions in time and space and exclusion of other causes such as Lyme disease, vasculitis, neurosarcoidosis, lupus, and others. The 2005 Revisions to the McDonald Diagnostic Criteria for MS imaging are a standardized set of diagnostic guidelines that are applied clinically and to clinical trials; these are based on number, location, and enhancement of lesions. Classically, hypodense/T2 hyperintense lesions are located in a periventricular distribution, in the corpus callosum (callosal-septal interface), and also the brainstem, cerebellum, and spinal cord. Transient disruption of the blood-brain barrier will lead to solid or rim enhancement of active plaques (Fig. 1-40). Active demyelination may appear hyperintense on DWI. Magnetization transfer and MR spectroscopy techniques may demonstrate abnormalities even in normal-appearing white matter. Genetic and environmental factors and female to male ratios of almost 2 to 1 (adults) and greater than 5 to 1 (children) have been found. As the name implies, the unusual tumefactive variety simulates a neoplasm, often leading to biopsy. Another autoimmune-mediated disorder that is generally monophasic is acute disseminated encephalomyelitis (ADEM) and may be indistinguishable from MS on initial imaging (Fig. 1-41). Another presumably autoimmune disorder that mimics MS and ADEM is Susac syndrome. This rare syndrome has a clinical triad of encephalopathy, branch retinal artery occlusions, and hearing loss.

Progressive Multifocal Leukoencephalopathy

In the immunocompromised host (especially due to AIDS), nonenhancing T2 hyperintensities (often confluent) in the parietal and occipital lobes should raise suspicion of progressive multifocal leukoencephalopathy (Fig. 1-42). This demyelinating process due to infection with the JC virus was originally thought to affect only white matter, but cases with both gray and white matter lesions and variable enhancement have been reported. The progressive nature of the disorder is also less certain due to current, highly active, antiretroviral regimens.

Posterior Reversible Encephalopathy Syndrome

Posterior reversible encephalopathy (and seizure) syndrome (PRES) has a number of common causes such as (pre)eclampsia, hypertensive crisis, lupus and other causes of nephropathy, and drug toxicity (including immunosuppressants and erythropoietin). In the workup of new seizures, the classic features of T2 hyperintensity in a rather symmetric distribution within the occipital, parietal, and posterior frontal lobes should bring this diagnosis to mind (Fig. 1-43). Although white matter is primarily affected, gray matter structures in the basal ganglia, brainstem, and cerebellum may also be involved. Diffusion imaging is most helpful to differentiate this process from acute

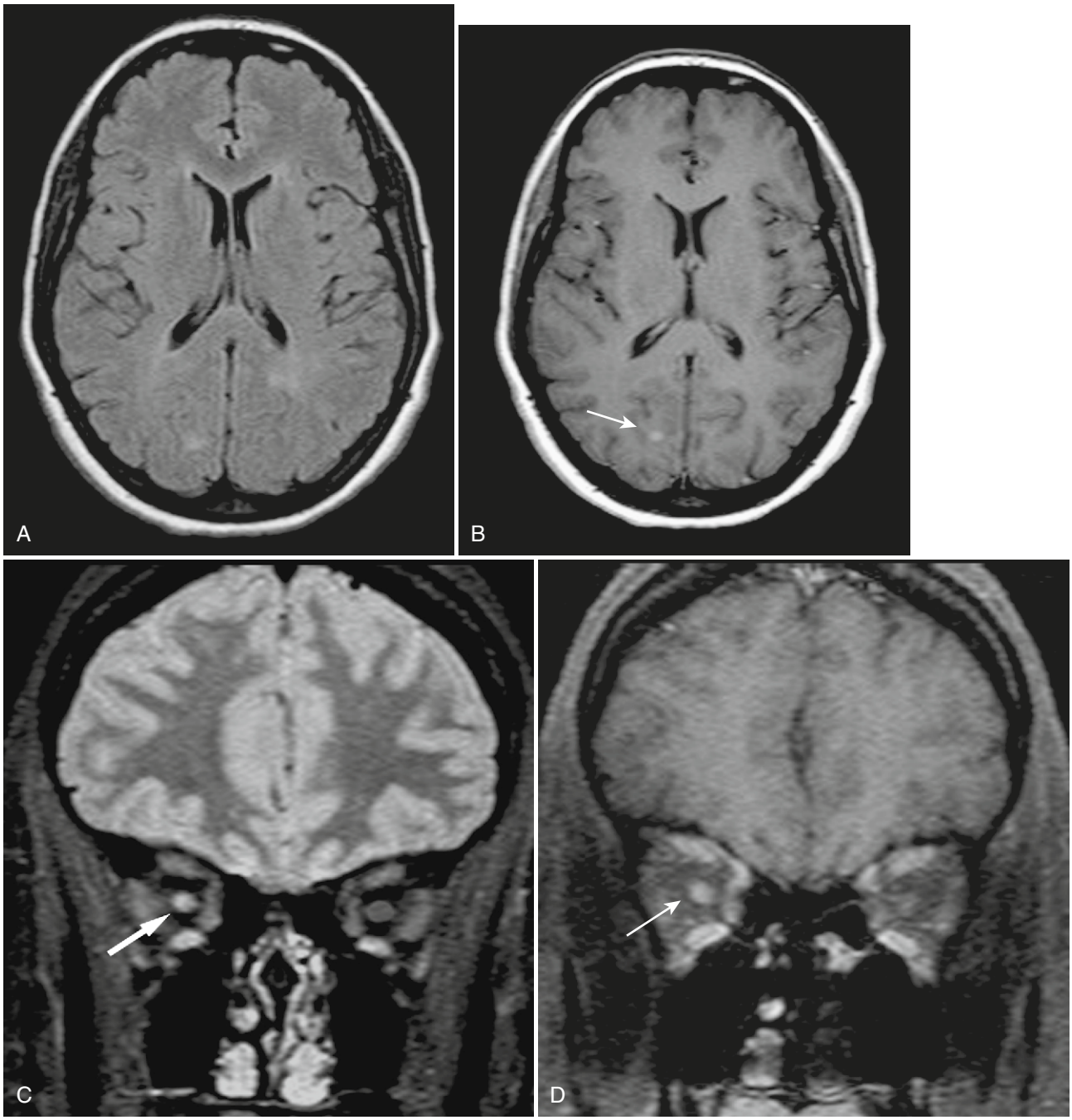


Figure 1-40. Multiple sclerosis—optic neuritis. **A,** FLAIR image shows a few white matter hyperintensities. **B,** One enhancing lesion *(arrow)* is detected on postgadolinium T1-weighted image. **C,** Coronal STIR image shows asymmetric hyperintensity of the right optic nerve *(arrow)*. **D,** Asymmetric enhancement of the right optic nerve *(arrow)* is shown on postgadolinium, fat-suppressed T1-weighted image.

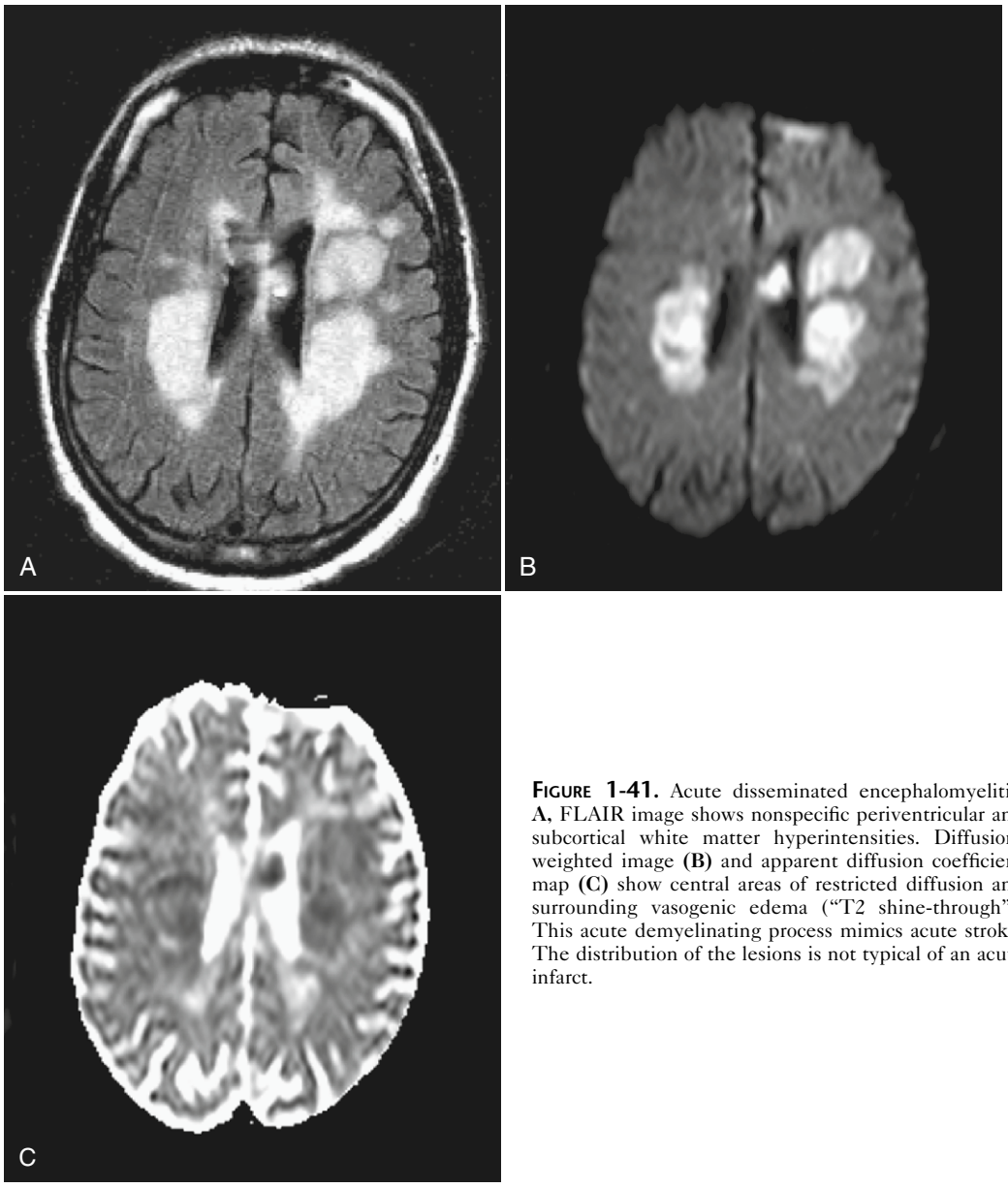


FIGURE 1-41. Acute disseminated encephalomyelitis. **A,** FLAIR image shows nonspecific periventricular and subcortical white matter hyperintensities. Diffusion-weighted image **(B)** and apparent diffusion coefficient map **(C)** show central areas of restricted diffusion and surrounding vasogenic edema ("T2 shine-through"). This acute demyelinating process mimics acute stroke. The distribution of the lesions is not typical of an acute infarct.

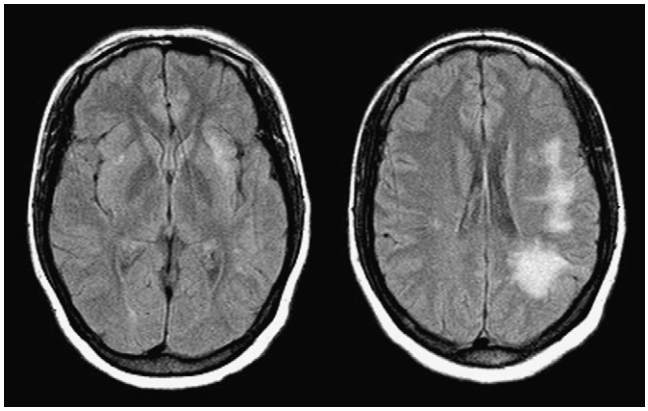


FIGURE 1-42. Progressive multifocal leukoencephalopathy. FLAIR images show asymmetric white matter hyperintensities involving predominantly the left external capsule and periventricular and subcortical white matter. No enhancement or mass effect was present. This patient with AIDS presented with a rapid decline in mental status.

infarction. Small amounts of hemorrhage (and infarcts) may occur within the background of vasogenic edema resulting from abnormal vascular autoregulation. Differentiation from acute or subacute stroke is important in directing the search toward an offending agent rather than initiating the stroke clinical pathway.

Toxic Encephalopathy

Whether due to accidental or intentional exposure/ingestion, a variety of well-known toxins may cause encephalopathy. Symmetric bilateral hypodensities/T2 hyperintensities in the globus pallidus are the hallmark of hypoxic damage due to carbon monoxide poisoning; hemispheric white matter may also be involved. Methanol toxicity typically affects the putamen and can be hemorrhagic. In addition to cerebellar degeneration, chronic alcoholism may lead to the development of Wernicke encephalopathy. It can also be

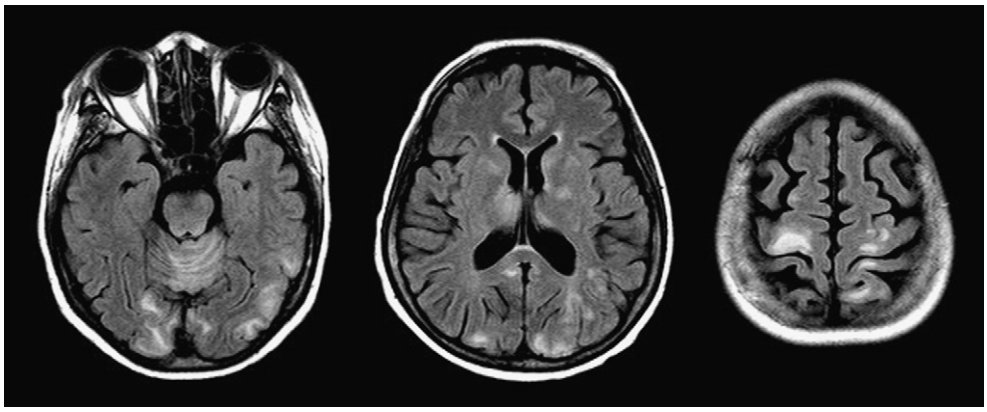


Figure 1-43. Posterior reversible encephalopathy syndrome. FLAIR images demonstrate slightly asymmetric hyperintensities primarily involving the cerebellum, thalami, and posterior frontal, parietal, and occipital lobes. Note involvement of both gray and white matter structures. This patient presented with new-onset seizures. Signal abnormalities resolved completely within 1 month.

the result of thiamine deficiency and a variety of other, less common, systemic conditions, presenting with lesions of the hypothalamus, mammillary bodies, dorsal medial thalamus, and periaqueductal gray matter. Ischemic and hemorrhagic complications related to illicit drug use have already been discussed. Toxic encephalopathy may also result from drug abuse. The pattern of white matter abnormality that results from inhalation of heroin vapor (known as "chasing the dragon") can be quite dramatic (Fig. 1-44). Encephalopathy may also be iatrogenic and related to chemotherapy (e.g., methotrexate) or radiation therapy, and generally affets the periventricular white matter in a diffuse fashion.

Another potentially iatrogenic disorder may result from the rapid correction of hyponatremia, leading to the classic central pontine or extrapontine varieties of demyelination (myelinolysis).

HEAD AND NECK TRAUMA

According to statistics from the 2006 American College of Surgeons National Trauma Data Bank survey (based on more than 1 million reports from 2001 to 2005), injuries resulting from motor vehicle collisions accounted for 41% of all cases. The others were due to falls (22%), being struck (6%), and gunshot wounds (6%). A large percentage of the injuries involve the head and neck. Diagnostic imaging plays an important role in decision making for immediate patient management as well as surveillance for potential long-term complications. Osseous injuries including facial, skull, and skull base fractures, and soft tissue injuries to orbits, vessels, airway, and pharynx, should be considered in the routine workup performed in the settings of blunt and penetrating trauma.

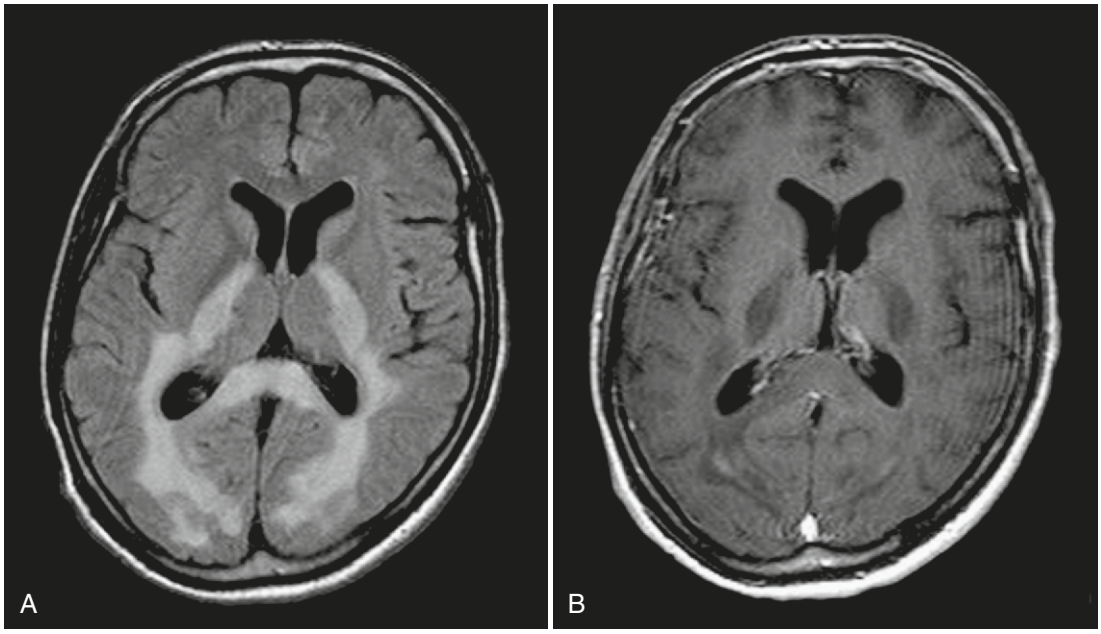


Figure 1-44. Toxic encephalopathy. **A,** FLAIR image shows symmetric, confluent, primarily white matter hyperintensities. **B,** Postgadolinium T1-weighted image shows minimal enhancement. The key to the diagnosis is the association with inhalation of heroin vapor—"chasing the dragon."

Acute traumatic injuries in the head and neck region are best evaluated by CT. At our institution, we use a 64-row detector helical scanner with 0.625-mm detector size. Depending on the protocol, images may be prospectively processed as contiguous 5-mm sections for review of the brain, 1.25-mm sections for the facial bones, calvarium, and neck, or 0.625-mm sections of the skull base. Images are processed using both soft tissue and bone algorithms, and coronal and sagittal reformats are routinely created. Images through any region can be retrospectively processed at 0.625-mm section thickness if finer detail is necessary. Three-dimensional volume-rendered reconstructions are often created to present an overview for referring physicians and for surgical planning. CT angiography technique has been discussed in detail elsewhere in this chapter.

Skull Fractures

The workup of head trauma used to include skull radiographs, but those days are gone. The use of CT has become the standard of care for rapid assessment of the skull and intracranial contents. In the early days of CT, it was estimated that more than half of skull fractures were not detected, since they were oriented almost parallel to the imaging plane and therefore volume averaged with adjacent normal bone. With recent decreases in section thickness and multidetector-row technique, this limitation has effectively been overcome (Fig. 1-45). Careful review of millimeter or submillimeter thickness sections and 3D volume-rendered images and familiarity with normal sutural anatomy and variants may be necessary to accurately detect fractures. The radiologic evaluation should start with the scalp, as soft tissue swelling and scalp hematoma are very helpful indicators of possible underlying fracture. Skull fractures may be linear or comminuted and either type may be depressed. Diastasis is the term applied to separation of linear fracture fragments or sutures. Diastatic fractures occur more commonly in children. If the arachnoid membrane gets trapped within a diastatic fracture, a "growing fracture" (leptomeningeal cyst) may develop over time. Bullet wounds may leave behind a wake of comminuted bone and metallic fragments and burst fractures at the point of exit. Identification of a fracture should lead to the dedicated search for other important findings, such as intracranial hemorrhage. Fractures through the skull base may lead to other complications such as vascular or cranial nerve injuries or CSF leak. Intracranial air should prompt the search for fracture through an aerated paranasal sinus or pneumatized portion of the temporal bone, as antibiotic therapy may be indicated for prophylaxis against meningitis. One should not be alarmed by all bubbles of air, since reflux into the cavernous and other dural sinuses often occurs following insertion of intravenous catheters and injections of saline, medications, or contrast material with lax technique. The presence of fluid within the sphenoid sinuses, middle ear cavities, or mastoid air cells should also prompt a search for fractures through these regions. Temporal bone fractures may result in damage to the facial nerve, ossicles, and otic capsule. Screening for potential vascular injury in the setting of fracture of the central skull base may be accomplished with CTA. This was discussed in the section on cerebrovascular emergencies. (see also Fig. 1-54).

Maxillofacial Fractures

MDCT has also revolutionized the workup of facial fractures. Once within the realm of plain film radiography, now these injuries are almost exclusively evaluated with CT. The general principles of fracture detection are often taken for granted but deserve quick mention. An

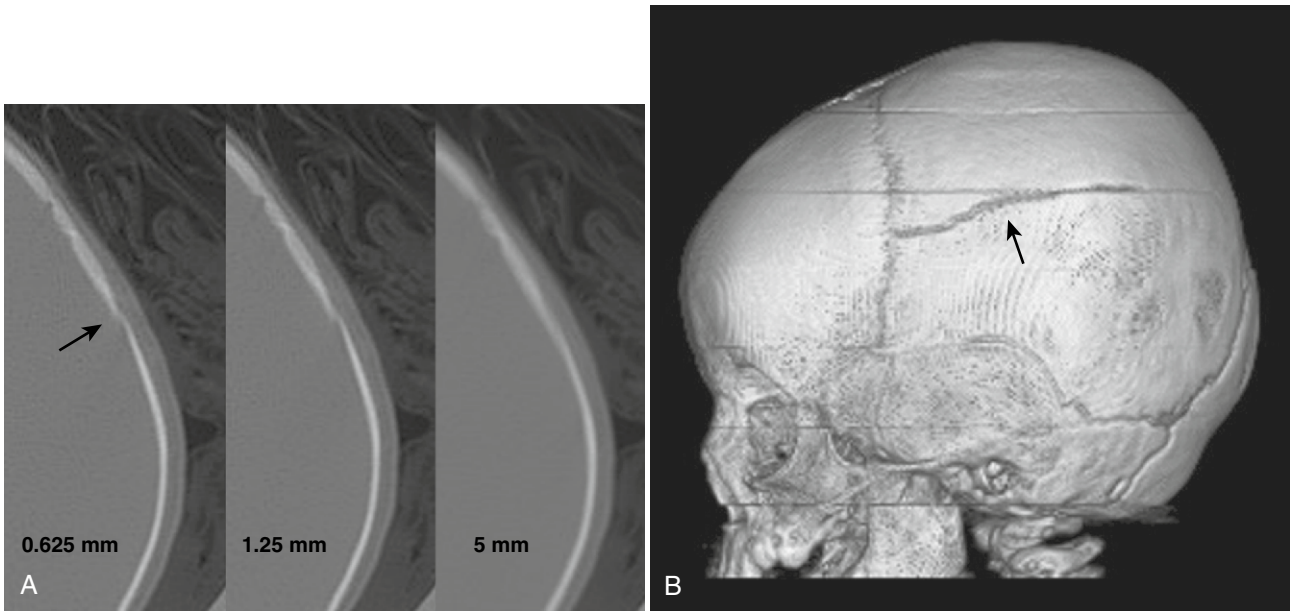


FIGURE 1-45. Skull fracture. **A,** Nondisplaced skull fracture is occult on routine 5-mm-thick section due to volume averaging. Fracture is most conspicuous on 0.625-mm section although with an increase in noise. **B,** Volume-rendered image shows fracture is nearly parallel to axial imaging plane.

unexpected linear lucency, disappearance or displacement of a normal structure, and a double density from abnormal overlap of adjacent structures are classic radiographic findings of facial fractures. A cortical defect, separation of a suture, and presence of subcutaneous, orbital, or periorbital air are findings that apply equally to radiographic and CT examinations. Likewise, soft tissue swelling and fluid levels in the paranasal sinuses are equally important clues to recognize, although these are less specific and may occur without fractures. Whereas several CT scans used to be necessary to evaluate the brain and face (including both thin-section axial and direct coronal scans), now complete evaluation of the head and facial skeleton can be performed with a single exposure. As an example, our 64-detector scanner offers the prospective creation of routine 5-mm-thick contiguous sections processed with a soft tissue algorithm to evaluate the brain and 0.625- or 1.25-mm-thick contiguous sections processed with a bone algorithm for evaluation of the face and skull. The thinner sections are routinely reformatted in coronal and sagittal planes, and, if desired, 3D volume-rendered images may be created at the CT console or other workstation. Depending on clinical exam findings, imaging of the head may begin at the level of the dental occlusal plane or include the chin and continue to the vertex. This method improves detection and characterization of facial fractures and reduces the amount of additional radiation exposure and scan time. Comprehension of the fracture may be improved by illustrating its relationship to normal anatomic landmarks. This helps the radiologist to apply the most appropriate terminology or classification and the surgeon to determine the need for operative reduction and fixation, usually with titanium plates and screws. Sometimes an implant is necessary to repair a large defect, as for the orbital floor. The reader is encouraged to consult review articles or texts (see Suggested Readings) for descriptions of commonly used medical devices.

The facial skeleton can be considered as composed of several vertical and horizontal buttresses of thickened bone that support the functions of the face, eyes, mouth, and airway. The buttresses are linked to each other and act as attachments of the face to the calvarium and skull base. The individual components of this system and the sutures are important anatomical landmarks for the radiologist and the surgeon but are beyond the scope and space limitations of this chapter. A brief overview of common facial fractures and associated injuries follows.

Orbital Blow-out Fractures

Isolated trauma to the orbit, a common cause of ED visits, plays a role in many cases of head trauma. Nontraumatic orbital emergencies are discussed later in this chapter. Fractures and injuries to the orbital soft tissues come in many different varieties. A blow to the eye causes an increase in intraorbital pressure, which is transmitted to the thin walls of the orbit. Blow-out fractures may involve the orbital floor, the medial wall, or both; the orbital rim should not be involved (Fig. 1-46). Even though the medial wall (lamina papyracea) is thinner, the network of ethmoid sinus septations acts as a support, and therefore isolated orbital floor fractures are more common. In up to about half of floor fractures, medial wall fractures will also occur. Orbital emphysema and herniation of orbital contents are possible associated findings. Coronal images are very useful to assess the degree of displacement of fracture fragments. Sagittal reformatted images help to define the anteroposterior extent of orbital floor fractures. Fragment size and displacement help to determine conservative versus operative management. Numbness of the upper cheek due to injury to the infraorbital nerve and diplopia may be presenting symptoms. Persistent diplopia and enophthalmos are possible long-term complications. Fractures that affect the orbital apex may be surgical emergencies. A bone fragment or hematoma can compress the optic nerve leading to acute decrease in visual acuity. An afferent papillary defect should also prompt careful review of this region with bone and soft tissue algorithms and display settings. While extraocular muscle entrapment is a clinical

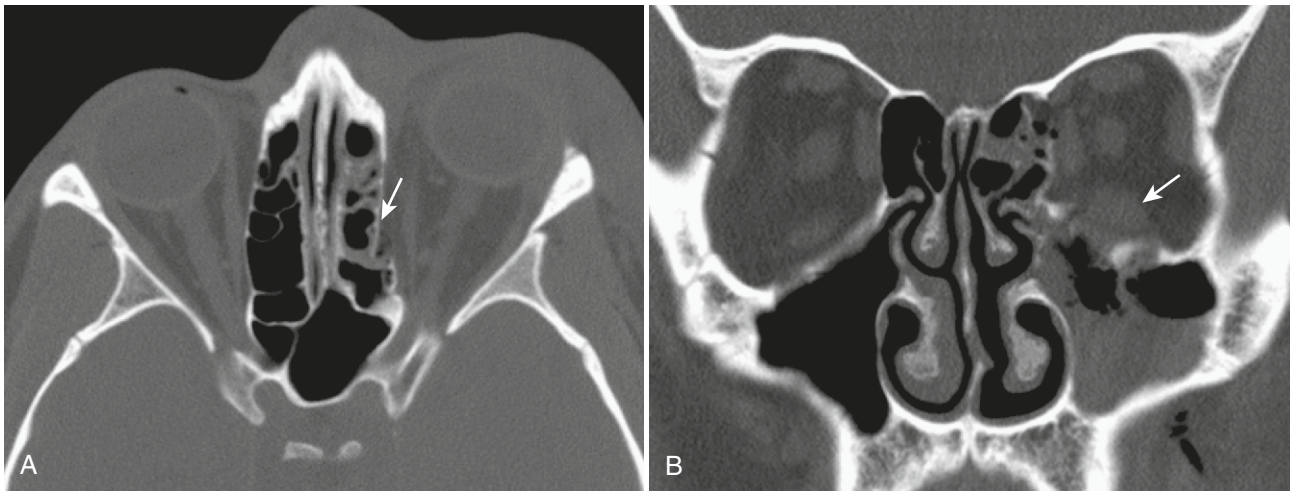


Figure 1-46. Orbital blow-out fractures. **A,** Axial CT shows displaced fracture of medial wall of the left orbit (lamina papyracea). **B,** Direct coronal CT image shows displaced left orbital floor fracture with an air–fluid level in the maxillary sinus. (This is of historical value, as most coronal images are now obtained by reformation.) Inferior rectus muscle is swollen *(arrow)*. This patient was hit in the eye with a baseball.

diagnosis, certain imaging features may offer guidance to the surgeon. If the inferior rectus muscle is displaced and does not retain its normal flattened shape on coronal images, then the fascial sling of the globe may be disrupted. Herniation of the muscle into the maxillary sinus can occur in the absence of a visible defect in the floor, implying that a "trap-door" fragment has sprung back into place, and prompt repair will clearly be necessary. Hematomas within the orbital soft tissues may occur in association with fractures, including retrobulbar and subperiosteal locations.

Although orbital decompression results from the blow-out mechanism, up to 25% have an associated ocular injury. Imaging findings can signal the need for ophthalmologic exam that may be overlooked in the setting of multitrauma. A ruptured globe, caused by either blunt or penetrating trauma, is small, often with a flattened contour. Hemorrhage within the eye appears relatively hyperdense and can occur in several different compartments, including subretinal, subchoroidal, and subhyaloid. The distinction between these can often be made based on shape and limits of the hemorrhage but is best made by physical exam. Dislocation of the lens, whether partial or complete, is not usually a subtle finding but can be easily overlooked if not included in the usual search pattern. Rupture of the capsule of the lens results in lens edema, appearing as a decrease in attenuation of this usually high density (proteinaceous) structure. Intraorbital and intraocular foreign bodies may be detected by CT; however, certain materials, such as wood, are better detected by ultrasound or MR. Calcifications of the trochlear apparatus, the sclera, and optic drusen are common and should not be misinterpreted as foreign bodies. The shrunken, calcified globe (phthisis bulbi) resulting from past trauma or infection should not be mistaken for an acute injury. Likewise, intraocular silicone oil or gas, and scleral buckles (both high- and low-density silicone) for treatment of retinal detachments and other devices, should also be properly recognized and not become causes of concern.

Orbital roof fracture is an uncommon injury that may extend to the frontal or ethmoid sinuses. It is best appreciated with coronal and sagittal reformatted images. With a "blow-in" type of fracture, as from pressure phenomenon due to a gunshot wound to the head, progressive herniation of the frontal lobe into the orbit may result from cerebral edema. Blow-out fracture of the orbital roof is rarely seen.

Nasal Fractures

Nasal fractures commonly occur in isolation but are often associated with other fractures of the midface. They account for approximately half of all facial fractures. Radiographs may occasionally be requested for isolated nasal trauma, and therefore one should be aware that fractures are usually oriented perpendicular to the nasal bridge and will cross the normal nasomaxillary suture and groove for the nasociliary nerve. These can be of cosmetic importance or may result in airway obstruction. Attention must be paid to the nasal septum since treatment of a septal hematoma might be necessary to avoid possible complications of ischemic necrosis, saddle deformity, and abscess formation.

As the name implies, naso-orbitoethmoid fractures are more complex and involve the nasal bones as well as the central upper midface. Impaction of the nose and disruption of the medial canthal regions, medial orbital walls, and ethmoid sinuses will result in widening of the intercanthal distance and the need for repair. Involvement of the nasofrontal duct or nasolacrimal canal may lead to significant morbidity and may also require surgical attention in order to reduce the chance of frontal sinus mucocele development.

Zygomaticomaxillary Complex Fractures

The zygoma has four sutural attachments, two to the skull and two to the maxilla. The zygoma is the second most commonly fractured facial bone. Isolated arch fractures account for a minority of zygomatic fractures and can be easily demonstrated with the traditional submentovertex view ("bucket handle") radiograph. More commonly, 3D volume-rendered images from an MDCT dataset are used to arrive at the same impression. This injury may require repair for cosmetic reasons, or because impaction of fracture fragments against the coronoid process of the mandible or temporalis muscle may result in trismus.

The more common injury to the zygoma involves the three major attachments (zygomaticomaxillary, zygomaticofrontal, and zygomaticosphenoid) and therefore has acquired the term *tripod fracture*. The preferred term may be zygomaticomaxillary complex (ZMC) fracture as it is more aptly considered a quadripod fracture due to involvement of the posteriorly located zygomaticotemporal attachment. Specific components include the infraorbital rim, orbital floor, and lateral wall, as well as the attachments to the skull base (sphenoid and temporal bones). Impaction and rotation of a large fracture fragment will result in significant deformity of the cheek and orbit (Fig. 1-47). Fractures of the pterygoid plates or greater wing of the sphenoid may sometimes be seen with severe ZMC fractures.

Le Fort Fractures

The Le Fort classification of midface fractures applies to separations of the maxilla from the skull base. The three-tier classification was developed by Le Fort in 1901 based on cadaveric experiments. These fractures rarely occur in their pure forms and while originally described as being bilateral, common usage allows for unilateral and combined bilateral types. The Le Fort I type is a fracture involving the maxillary antra, crossing midline above the hard palate. If unilateral, a sagittally oriented fracture of the palate will be present. Fractures of the pterygoid plates may occur, although some consider this a requirement by definition. With this injury, the hard palate will be allowed to separate from the rest of the face, and this will often be diagnosed by physical exam. In Le Fort II type, fractures involve both maxillary antra and inferior orbital rims crossing at the nasion (either at the nasofrontal junction or frontal process of the maxilla). The maxilla will be separated from the rest of the face. In Le Fort III type, also termed craniofacial dissociation, the inferior orbital rims are intact but the lateral orbital walls and zygomatic arches are fractured. This allows separation of the face from the rest of the skull. Variations and combinations of Le Fort and ZMC fractures are common (Fig. 1-48).

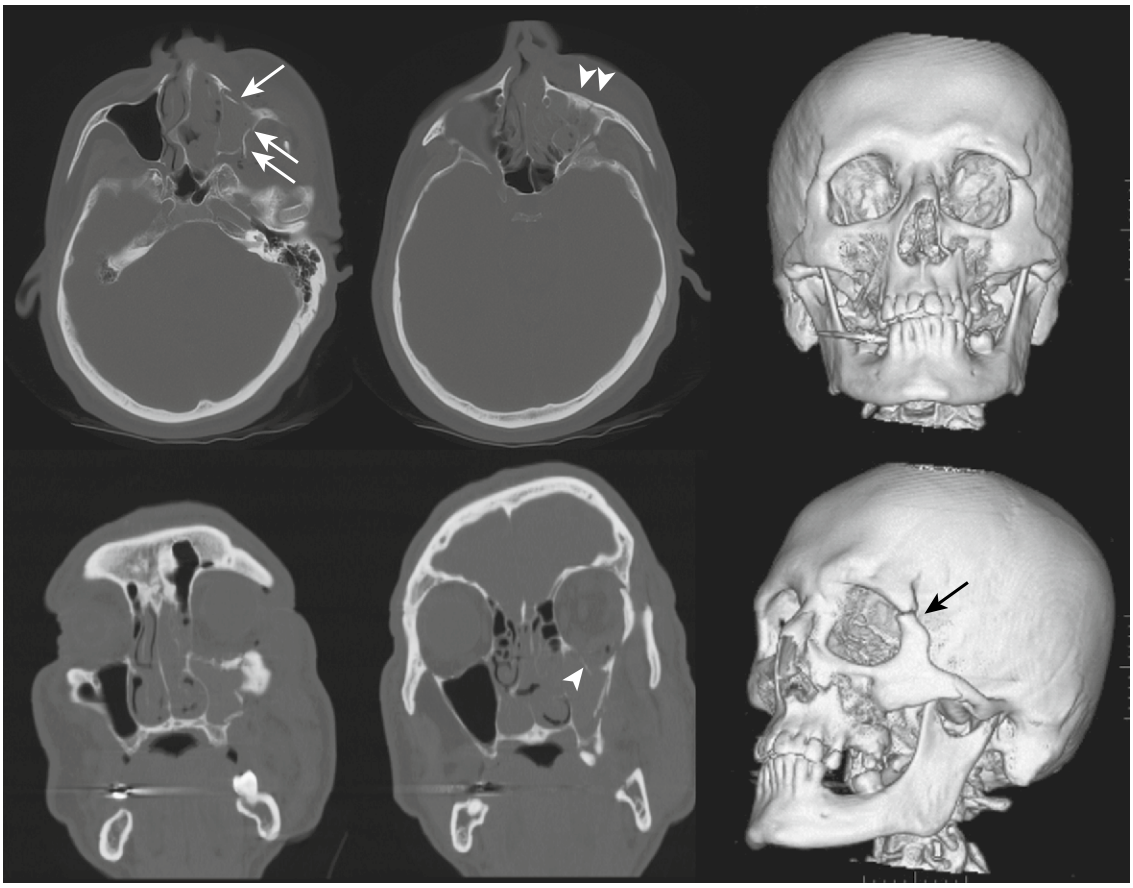


Figure 1-47. Zygomaticomaxillary complex fracture. Composite images show fractures of the left maxillary sinus anterior wall *(white arrow)* and posterolateral wall (*double arrows*), orbital floor *(arrowhead)*, and infraorbital rim *(double arrowheads)*. Volume-rendered images demonstrate diastasis of zygomaticofrontal suture *(black arrow)* and degree of impaction of the malar eminence.

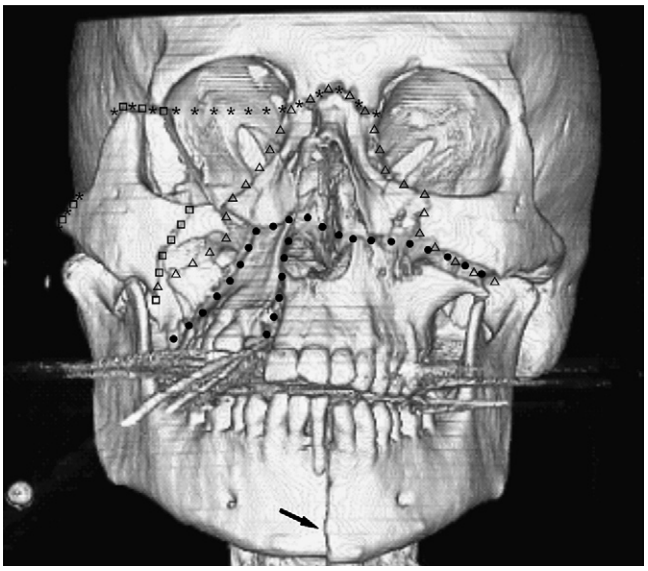


Figure 1-48. Le Fort fractures. Volume-rendered image from an unrestrained driver involved in a rollover motor vehicle collision shows multiple displaced fractures. Components: dots, Le Fort I; triangles, unilateral Le Fort II; asterisks, unilateral Le Fort III; squares may be considered the zygomaticomaxillary complex. *Arrow*, fracture of mandibular symphysis.

Smash Fractures

The term facial smash is a general term applied to severely comminuted fractures of the facial bones that generally occur in association with fractures of the calvarium. Intracranial hemorrhage and traumatic brain injury occur commonly with these types of fractures. The frontal type commonly involves the anterior and posterior walls of the frontal sinus (Fig. 1-49). The naso-orbitoethmoid complex can be considered in this category. Central skull base types include fractures of the sphenoid bone. Vascular injuries related to skull base fractures are discussed in the sections on temporal bone fractures and cerebrovascular emergencies.

Mandibular Trauma

Fractures of the mandible are common and are classified by location—alveolar, symphyseal, parasymphyseal, body, angle, ramus, subcondylar (neck), or condylar. The mandible may be considered a ring structure, but with some flexibility due to the temporomandibular joints. Therefore, one, two, or more fractures may occur depending on the magnitude and direction of the applied force.

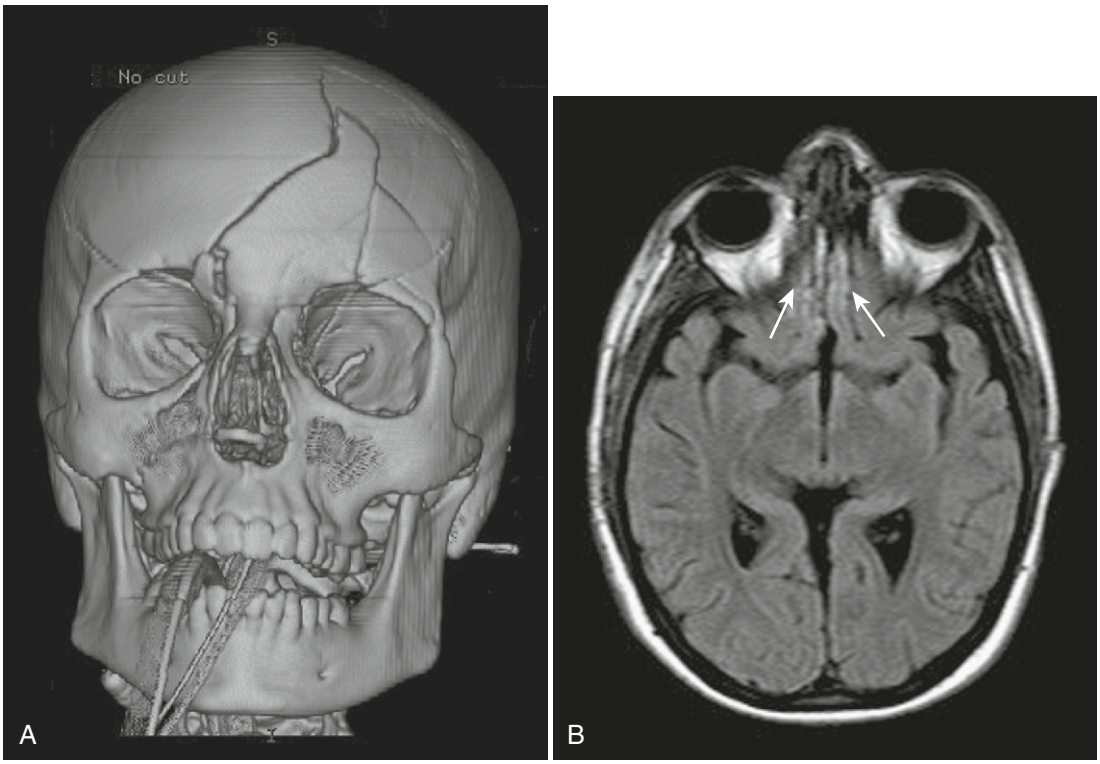


FIGURE 1-49. Smash fracture. **A,** Volume-rendered image shows complexity of comminuted frontal smash fracture that involves frontal sinuses and both orbits. **B,** FLAIR image months later shows residual signal abnormality involving gyrus rectus of both frontal lobes due to prior contusions.

Bilateral temporomandibular joint dislocation without fracture is an uncommon injury resulting from a blow to the symphysis. The mandibular condyles should normally be seated symmetrically in the glenoid fossae. On occasion, the condyles may be anteriorly displaced, simply a reflection of normal open mouth position at the time of image acquisition. However, in a true dislocation, the glenoid fossae are empty, with condyles positioned anterior to the glenoid tubercles, and the jaw locked in the open position.

If the styloid process is disrupted in the setting of mandibular fracture, air may be seen in the infratemporal fossa, possibly related to oral or Eustachian tube laceration. Mandibular fractures may be associated with hematomas within the masticator space.

Airway compromise may result from bilateral parasymphyseal fractures since the symphysis becomes a free fragment, allowing the tongue to obstruct the oral cavity. Fractures across the mandibular canal may cause injury to the inferior alveolar nerve (branch of mandibular division of the trigeminal nerve) and result in paresthesia of the chin. Fractures affecting the teeth are considered open and require antibiotic prophylaxis. Fractured or avulsed teeth can pose a risk for aspiration, particularly in the unresponsive patient. A dedicated search for radiopaque foreign bodies in the airway on all other imaging studies is therefore necessary. Muscular forces may act favorably or unfavorably, resulting in nondisplaced or displaced fractures, respectively. Displacement may occur in either the vertical or horizontal direction. Reduction with maxillomandibular fixation or open reduction and internal fixation may be required to restore occlusion and allow proper masticatory function, speech, and facial contour. As with other facial fractures, multiplanar reconstruction and 3D volume-rendered images are helpful in comprehending the injury, especially the orientation of fracture fragments and relationships to the coronoid processes and condyles, as well as aid in surgical planning (Figs. 1-50 and 1-51).

Temporal Bone Fractures

Temporal bone fracture should always be suspected when opacification of the mastoid air cells and/or middle ear compartments is present in the trauma setting. Slice thickness of 1 mm or less may be necessary to clearly identify and fully characterize the fracture. Temporal bone fracture usually occurs secondary to blunt head injury and is classically characterized as either longitudinally or transversely oriented relative to the long axis of the petrous bone. The other components of the temporal bone, namely, the mastoid, styloid, squamous, and tympanic, can be involved as well. Temporomandibular joint dislocation and styloid process fracture are discussed with mandibular fractures in the section on facial trauma. In practice, however, fractures through this region tend to be complex, and more typically than not demonstrate both longitudinal and transverse fracture characteristics (Fig. 1-52). In these cases, it is more important to characterize whether or not the otic capsule (the bony housing of the inner ear structures including cochlea and semicircular canals) and internal auditory canal are involved.

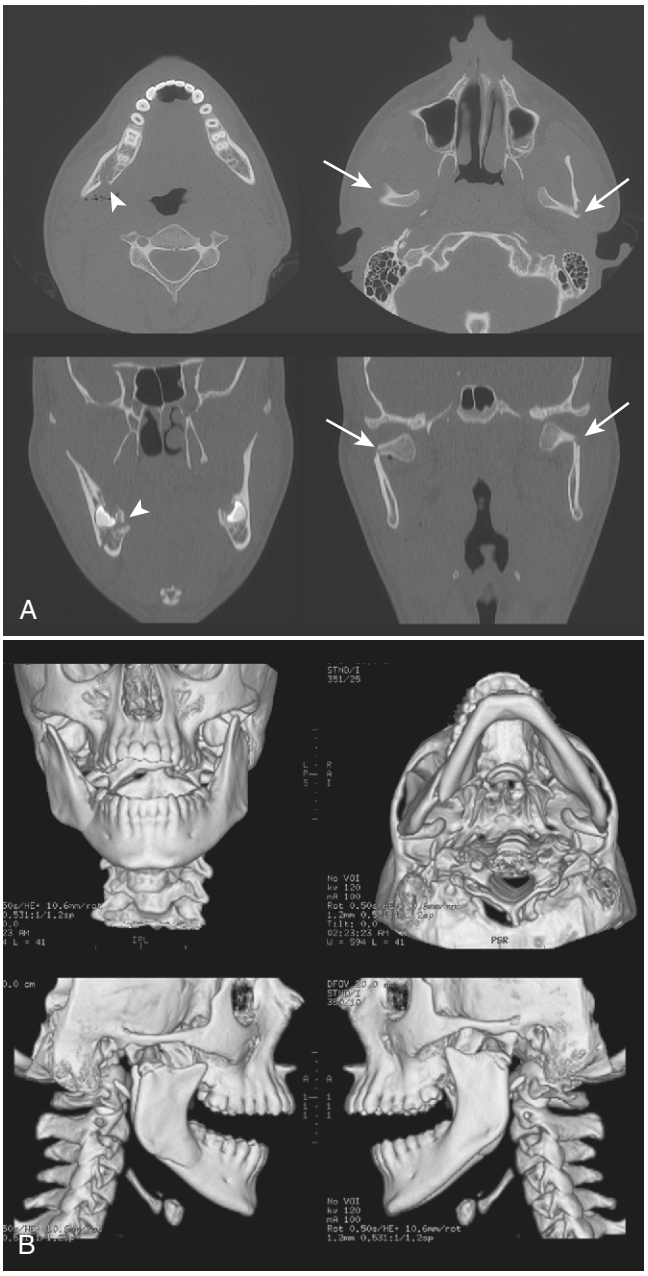


FIGURE 1-50. Mandibular fractures. **A,** Axial and reformatted coronal CT images show bilateral mandibular subcondylar fractures *(arrows)* and fracture of right ramus *(arrowheads)*. **B,** Volume-rendered images provide a clear overview of the fractures.

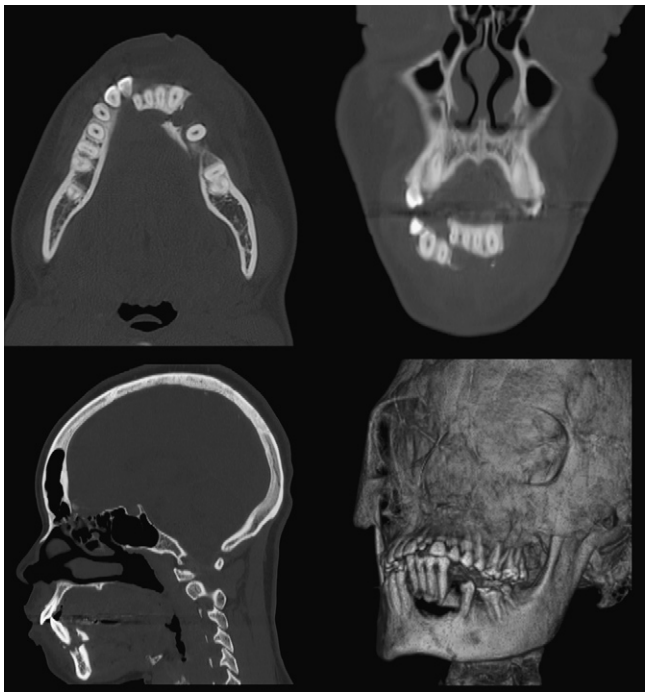


FIGURE 1-51. Mandible fracture. Axial, reformatted coronal and sagittal images show a comminuted displaced fracture of the mandible with involvement of the alveolar ridge. Volume-rendered image clearly demonstrates the relationship of the mobile teeth. (Volume-rendered image with dental shading is more realistic on a color monitor.)

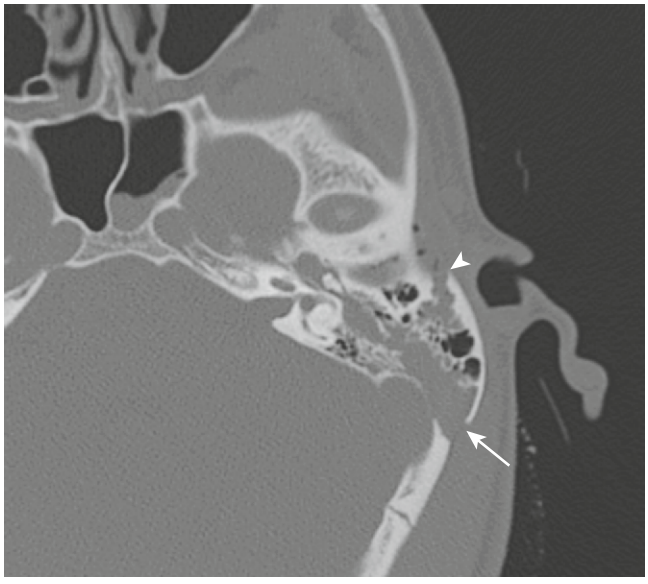


FIGURE 1-52. Complex temporal bone fracture. Longitudinal *(arrow)* and transverse *(arrowhead)* components are shown. Ossicles and otic capsule were not disrupted in this case.

Longitudinal fractures parallel the long axis of the petrous bone and are more common than transverse temporal bone fractures (Fig. 1-53). Fracture components can secondarily involve the external auditory canal, tympanic cavity, and squamosal portions of the temporal bone. Blood and fracture fragments in the external auditory canal and tympanic cavity and ossicular disruption can account for the common clinical presentation of conductive hearing loss. Longitudinally oriented fracture planes tend to extend anteriorly toward the Eustachian tube and middle cranial fossa avoiding the bony labyrinth (anterior subtype). The glenoid fossa can be involved, and disruption of the middle meningeal artery can result in concomitant epidural hematoma. Less often the fracture plane may extend posteriorly behind the bony labyrinth to involve the jugular foramen and posterior fossa (posterior subtype). In these instances, careful attention should be paid to evaluate for involvement of the foramen lacerum and the sphenoid bone, which puts the traversing internal carotid artery at risk for traumatic injury. If the fracture

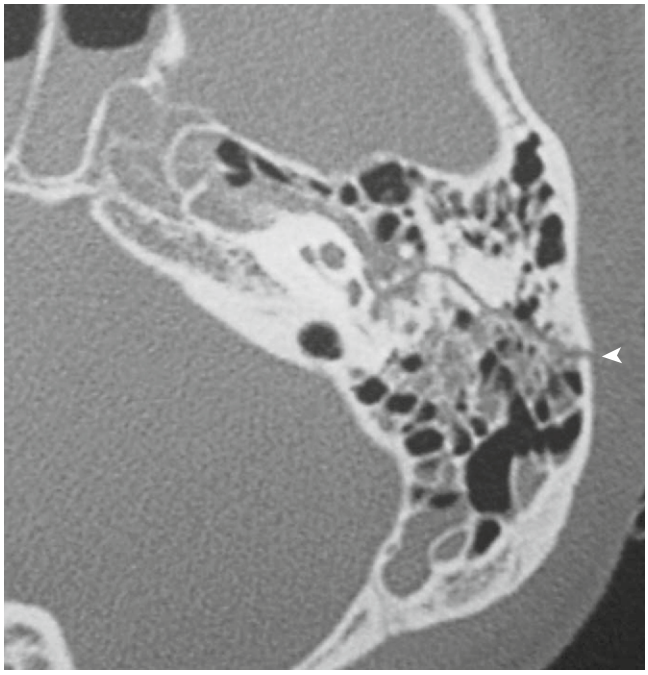


FIGURE 1-53. Longitudinal temporal bone fracture. Fracture *(arrowhead)* extends along orientation of petrous bone. Note partial opacification of mastoid air cells.

plane is demonstrated to approximate the carotid canal, or if fractures extend into the carotid canal, CT angiography or conventional angiography can be performed to evaluate for possible internal carotid artery injury at the skull base (Fig. 1-54).

Injury to the facial nerve is not uncommon in the setting of longitudinal fracture, although most literature emphasizes facial nerve injury with transverse fractures. Careful search for fractures along the entire course of the facial nerve from the internal auditory canal to the stylomastoid foramen is necessary. Focal swelling or hematoma developing within an otherwise intact facial nerve may manifest clinically as partial facial weakness in a delayed rather than immediate fashion. This is associated with better long-term prognosis for facial nerve function since the nerve is not disrupted.

Transversely oriented fractures are perpendicular to the long axis of the petrous bone and can be further classified into medial and lateral subtypes, depending on the position of the fracture plane relative to the arcuate eminence. The medial subtype transgresses at or medial to the lateral-most aspect of the internal auditory canal, while the lateral subtype transgresses the bony labyrinth. As with longitudinal fractures, careful attention must be paid to the relationship of the fracture plane with the carotid canal, as injury to the internal carotid artery can be seen in this setting. Both transverse subtypes can be associated with acute and permanent sensorineural hearing loss, secondary to acute transection of the vestibulocochlear nerve. Facial nerve paralysis, if present, is also immediate and complete, due to transection of the facial nerve.

Given the complex anatomy of the temporal bone, normal sutures and channels can often be mistaken for fracture planes. Normal petro-occipital, temporo-occipital, and occipitomastoid sutures can demonstrate irregular, coarse margins, raising concern for possible fracture (Fig. 1-55). Diastasis of sutures (equivalent to a fracture) can be seen without apparent fracture. Intrinsic sutures to the temporal bone itself, including tympanosquamous, tympanomastoid, and petrotympanic sutures, also can be confused with acute fractures (Fig. 1-56). Small channels in the middle and inner ear such as the cochlear and vestibular aqueducts, singular canal, and subarcuate fossa can also convey an appearance similar to fracture planes. An understanding of normal temporal bone anatomy is essential to avoid these errors. Symmetry, lack of opacification of mastoid air cells and middle ear compartments, absence of overlying soft tissue swelling, and the clinical context can also provide reassurance that no fracture is present.

In addition to varied severity of facial weakness and conductive and sensorineural hearing loss, complex temporal bone fractures can have long-term complications. Squamous epithelial proliferation along fracture planes can result in cholesteatoma without concurrent mastoid disease. CSF leak can result from disruption of the epitympanic roof; this frank communication of the intracranial CSF space and middle ear can present as otorrhea if the tympanic membrane is disrupted or rhinorrhea if the tympanic membrane is intact. While otorrhea and rhinorrhea may resolve in the early posttraumatic setting, persistent leakage needs to be surgically managed due to increased risk of meningitis. Cephalocele is also possible, if the bony defect is large enough. Posttraumatic perilymphatic fistula between the inner and middle ear can occur with disruption of the oval or round windows, or fractures through the otic capsule, and may present with hearing loss and vertiginous symptoms. Perilymphatic fistulas are difficult to demonstrate radiographically, but can be suspected based on clinical manifestations.

Airway and Pharyngeal Injuries

Acute trauma to the airway and pharynx occurs typically in the setting of penetrating trauma (stab wounds and gunshot wounds) or can be iatrogenic (traumatic intubation). Injury to the aerodigestive tract should be suspected in the setting of unexplained gas in the soft tissues adjacent to the airway or pharynx. It is important to keep in mind that lack of associated soft tissue gas does not exclude injury to these structures. Soft tissue gas adjacent to the aerodigestive tract could be secondary to superior tracking of pneumomediastinum and pneumothorax from a penetrating chest wound or could be related to the tract of the penetrating object itself. Tracheal diverticula are often seen at the thoracic inlet level on the right; this is a common normal variant. Presence of air along the aerodigestive tract can be idiopathic or related to asthmatic pneumomediastinum. Correlation with clinical presentation is necessary to avoid unnecessary imaging studies.

If injury is suspected, endoscopic evaluation with direct visual inspection is essential. A single contrast radiographic swallow study with water-soluble contrast may be helpful in the initial evaluation of hypopharyngeal injury; however, in a patient with potential concomitant airway injury or poor airway control, it may not be safe to do such an examination given the risk of aspiration and possible complication of chemical pneumonitis.

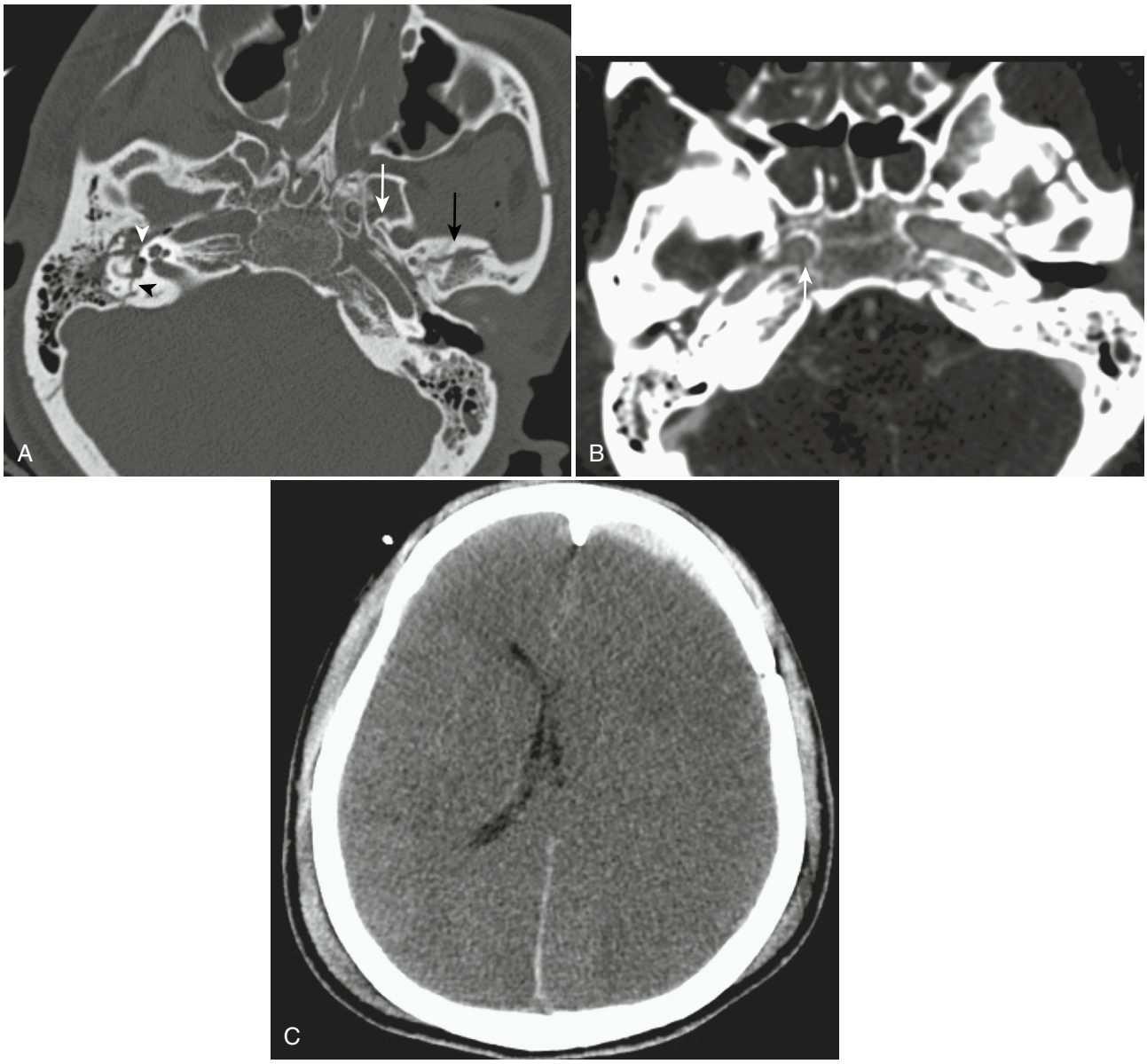


Figure 1-54. Skull base fractures—vascular injury. **A,** This patient sustained bilateral temporal bone fractures after a motor vehicle collision. On the right, nondisplaced transverse temporal bone fracture, lateral subtype *(black arrowhead)*, and associated air in the vestibule of the semicircular canals *(white arrowhead)* were identified. Nondisplaced fracture through the left temporal bone perpendicular to the carotid canal *(black arrow)* was also identified. Incidental note made of foramen of Vesalius *(white arrow)*, normal anatomy seen in up to 80% of patients. **B,** Given concern of fracture plane extending to carotid canal, CT angiogram was performed, and demonstrated intimal flap within the petrous portion of the right internal carotid artery *(arrow)*. There was also suspicion of left petrous internal carotid artery dissection on multiple contiguous images. **C,** Noncontrast head CT 6 days post-trauma demonstrates diffuse loss of the gray–white differentiation and sulcal and ventricular effacement consistent with bilateral hemispheric infarcts.

Injuries to the airway may be accompanied by injury to the larynx and vocal cords. Presence of laryngeal hematoma and vocal cord injury should be suspected if there is asymmetry in these regions when comparing right and left (Fig. 1-57). Patients with such injury typically present with hoarseness soon after the acute event. Again, if such injury is suspected, direct visualization by endoscopy is indicated. It should be remembered that patient phonation or phase of respiration can result in apposition of the vocal cords, creating an appearance of airway obstruction. Lack of associated soft tissue swelling and clinical correlation can help in minimizing the false positive diagnosis of laryngeal injury in these cases.

INFECTIONS

Infections in the head and neck region are commonly seen in the emergency room setting. Most often, the diagnosis is clear by physical examination and history. The role of imaging is to define the extent of infection and to provide information critical to immediate patient management.

Peritonsillar Abscess

Pharyngitis is typically a clinical diagnosis, but imaging may be performed if there is clinical suspicion of complications. Imaging findings of tonsillar or peritonsillar soft

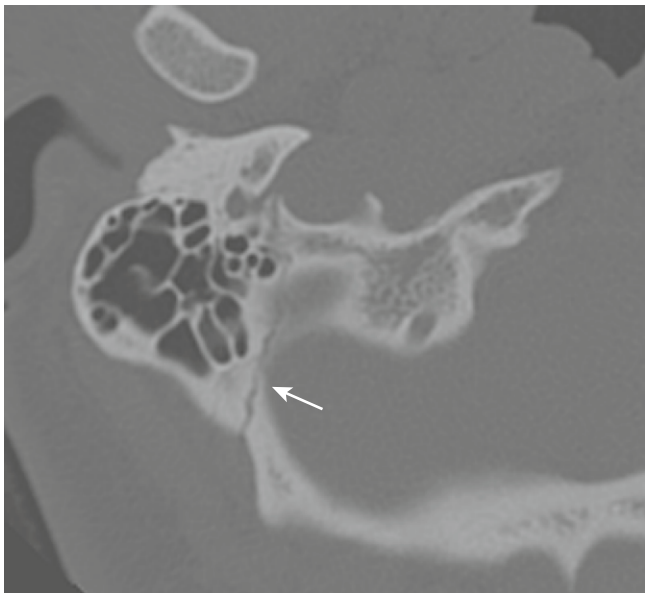


FIGURE 1-55. Normal occipitomastoid suture. Note jagged but well-corticated margins along suture plane.

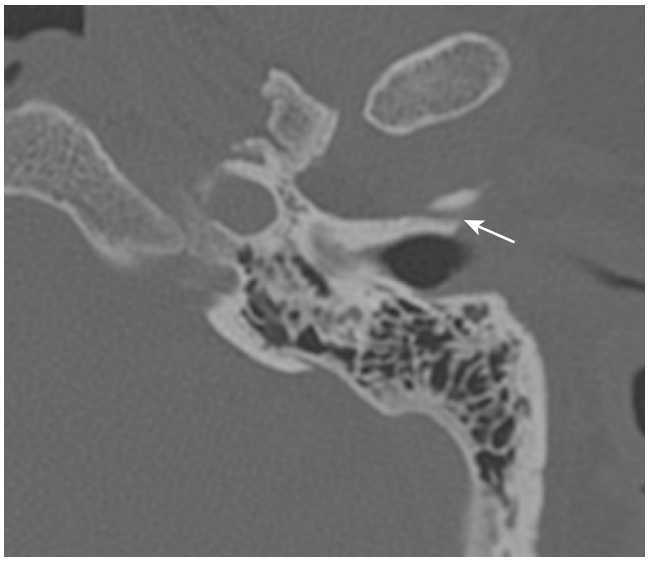


FIGURE 1-56. Normal tympanosquamous suture. Suture is present at the anterior bony wall of the external auditory canal.

tissue asymmetric enlargement with adjacent fat stranding may signal inflammation. Peritonsillar abscess is often seen in pediatric and immunocompromised patients. It is a peripherally enhancing fluid collection formed in the potential space between the fibrous capsule of the tonsil and pharyngeal constrictor muscles. The patient typically presents with dysphagia, odynophagia, ear pain, and trismus after improvement of acute symptoms of tonsillitis. Infection extending beyond the pharyngeal constrictor muscles into the parapharyngeal space may cause mycotic aneurysms and thrombophlebitis. A discrete abscess identified by imaging may require immediate incision and drainage. Associated reactive lymphadenopathy is usually present.

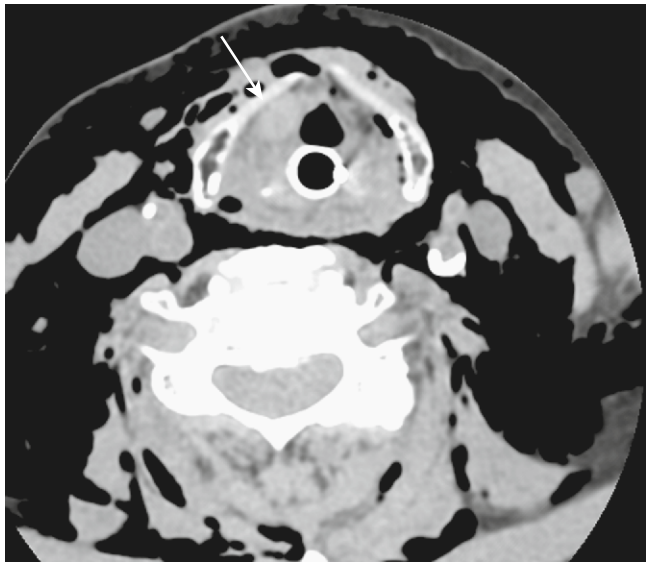


FIGURE 1-57. Laryngeal fracture. Extensive subcutaneous and deep space emphysema was due to extension of pneumothoraces in this patient after a motor vehicle collision. However, due to soft tissue density in the right supraglottic larynx, laryngeal hematoma was suspected. This was confirmed on endoscopy.

Retropharyngeal Infection

Spread of pharyngeal infection to the medial or lateral (Rouvière) retropharyngeal nodes may lead to cellulitis or development of suppurative adenitis (enlarged, rim-enhancing node). Associated edema of the retropharyngeal soft tissues is quite common, noted by expansion and diffusely increased density of the retropharyngeal fat. Extracapsular spread of nodal infection may result in a true retropharyngeal abscess typically identified as a rim-enhancing bow-tie-shaped fluid collection. Retropharyngeal space infections may quickly spread into the mediastinum (Fig. 1-58), which is a serious complication with high mortality and morbidity. Immediate surgical drainage of a retropharyngeal abscess may be indicated. Imaging plays an important role in determining the indication and access route for surgical drainage. Vascular complications of infection include spasm, arteritis and mycotic aneurysm of the internal carotid artery, and thrombophlebitis of the internal jugular vein (Lemierre syndrome). The latter condition was more common in the preantibiotic era, with rare cases still encountered in the present day. On postcontrast CT or MR imaging, a filling defect in the internal jugular vein with enhancement of the vessel wall can be demonstrated. Early diagnosis is critical, as the untreated thrombus can propagate systemically, resulting in septicemia and pulmonary emboli/infarcts.

In the setting of peritonsillar and retropharyngeal infections, careful examination of the airway is vital. Prophylactic intubation should be considered if the airway is significantly compromised.

Prevertebral Infection/Inflammation

Prevertebral collections in the neck typically occur in the setting of discitis and osteomyelitis of the cervical spine (Fig. 1-59). An associated prevertebral abscess can progress

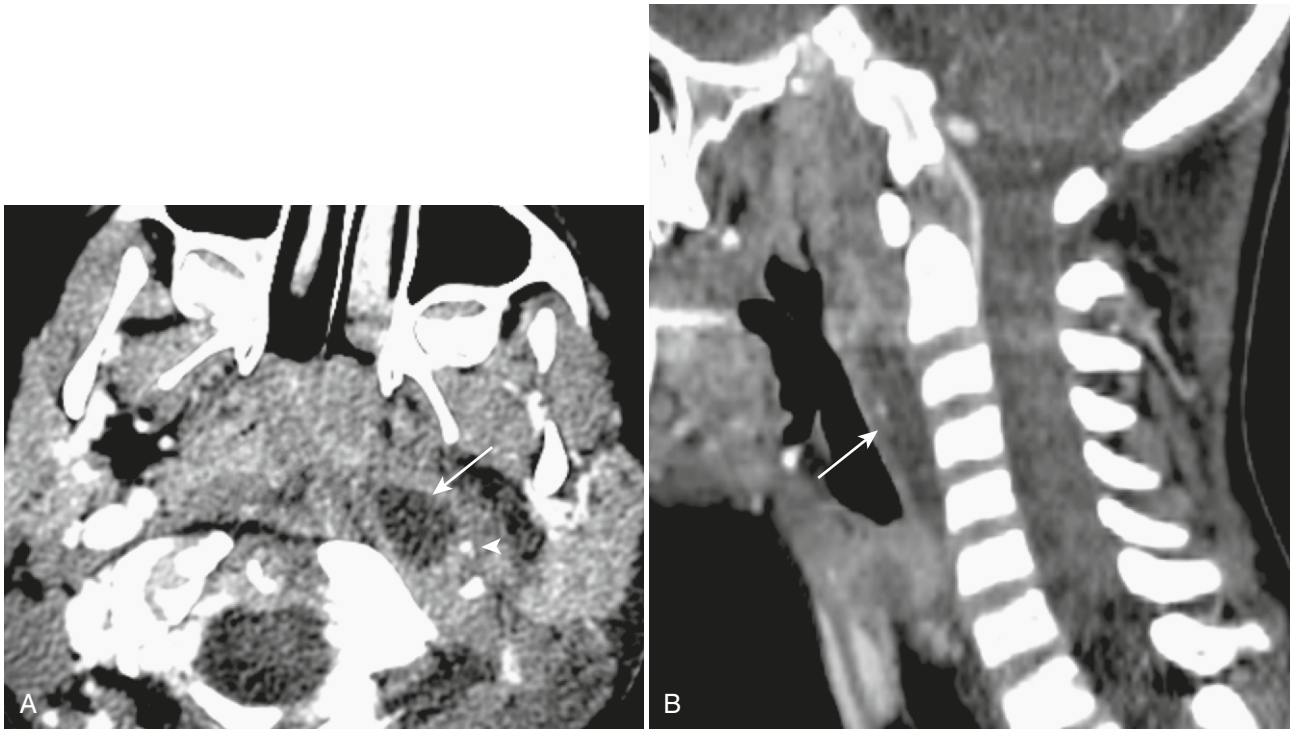


FIGURE 1-58. Retropharyngeal abscess. **A,** Abscess *(arrow)* is demonstrated within the lateral retropharyngeal node (of Rouvière) in a young patient presenting with painful swallowing. Note associated smaller caliber of the cervical left internal carotid artery secondary to vasospasm *(arrowhead)*, common in pediatric patients with intranodal abscess. **B,** Sagittal reformat demonstrates associated retropharyngeal fluid extending to the C5 level. Lack of peripheral enhancement suggested that this fluid was reactive, rather than a discrete abscess. Because the patient's condition did not improve with intravenous antibiotics, incision and drainage was required.

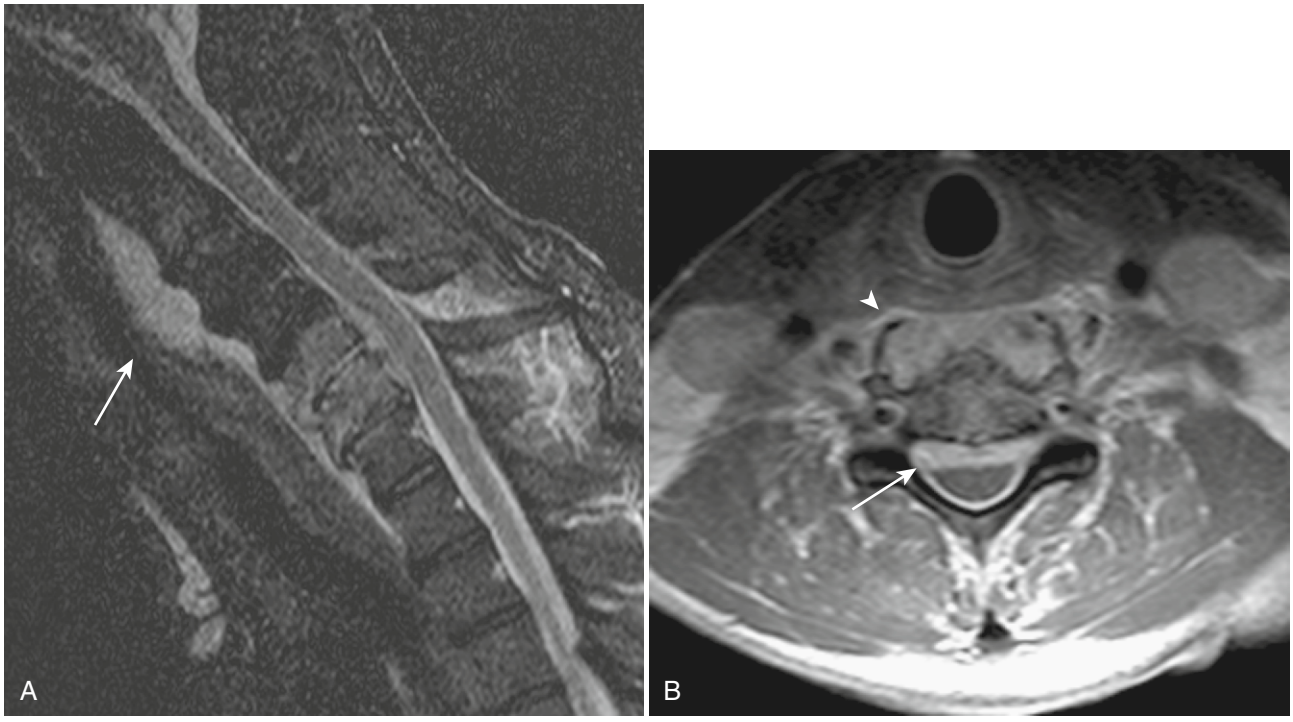


FIGURE 1-59. Discitis/osteomyelitis secondary to intravenous drug use. **A,** Sagittal fat-suppressed T2-weighted image shows abnormally hyperintense signal in the C5-C6 disc and adjacent vertebral bodies and a large associated prevertebral process *(arrow)*. **B,** Postgadolinium axial T1-weighted image shows enhancement of prevertebral phlegmon *(arrowhead)* and circumferential epidural extension *(arrow)* resulting in spinal cord compression.

in size to potentially compromise the airway. In these cases, urgent intubation and surgical drainage may have to be considered. Retropharyngeal inflammation is often seen secondary to prevertebral space infection. Diagnosing the primary site of infection is important for appropriate patient management.

Salivary Gland Disorders

Inflammation of the submandibular or parotid glands demonstrated by glandular enlargement and associated surrounding fat stranding could be related to distal obstruction in Wharton's or Stensen's ducts, respectively, often due to obstructing calculus. Of the salivary glands, the submandibular gland is most prone to sialolithiasis, due in part to stasis from the descending then ascending course of its duct and the relatively more alkaline nature of its glandular secretions. Bacterial and viral infections can also result in salivary gland inflammation. Bacterial inflammation is most commonly seen in debilitated patients or neonates, caused by localized *Staphylococcus aureus* infection, and is typically unilateral. Viral inflammation occurs in children, tends to be related to systemic infection, most commonly mumps, and is usually bilateral. The inflamed gland is enlarged, hyperenhancing, with stranding of adjacent fat reflecting cellulitis, or may contain a discrete abscess (Fig. 1-60). Enlarged heterogeneous parotid glands with solid and cystic changes may reflect lymphoepithelial lesions seen in the setting of HIV disease. Similar lesions can be seen in Sjögren syndrome and other autoimmune disorders. In the chronic phase of this condition, atrophy of the parotid gland with parenchymal calcifications can be seen.

Thyroid-related Disorders

When inflamed, the thyroid gland can appear diffusely enlarged, or relatively hypoenhancing, and may demonstrate an associated fluid collection. Suppurative thyroiditis is rare due to its iodine content. In such cases, pyriform sinus fistula, or third or fourth branchial pouch anomaly, should be considered as an underlying etiology. Most involve the left lobe of the thyroid. Such patients require a barium swallow after completion of antibiotic therapy to identify the fistulous tract.

Thyroglossal duct cyst is a remnant of the thyroglossal duct and can be found in a midline or paramidline location between the foramen cecum at the base of the tongue and the thyroid bed. The cyst is classically embedded within the strap muscles, which helps distinguish this lesion from other midline neck masses such as dermoid and epidermoid. While these cysts are found most commonly at the level of the hyoid bone, they can also be suprahyoid or infrahyoid in location. If the cystic lesion exhibits peripheral rim enhancement, superinfection should be suspected in the appropriate clinical setting. The cyst is usually lined by respiratory or squamous epithelium and may occasionally contain thyroid tissue; this carries the potential for development of malignancy, most commonly papillary carcinoma. For this reason, any enhancing soft tissue within

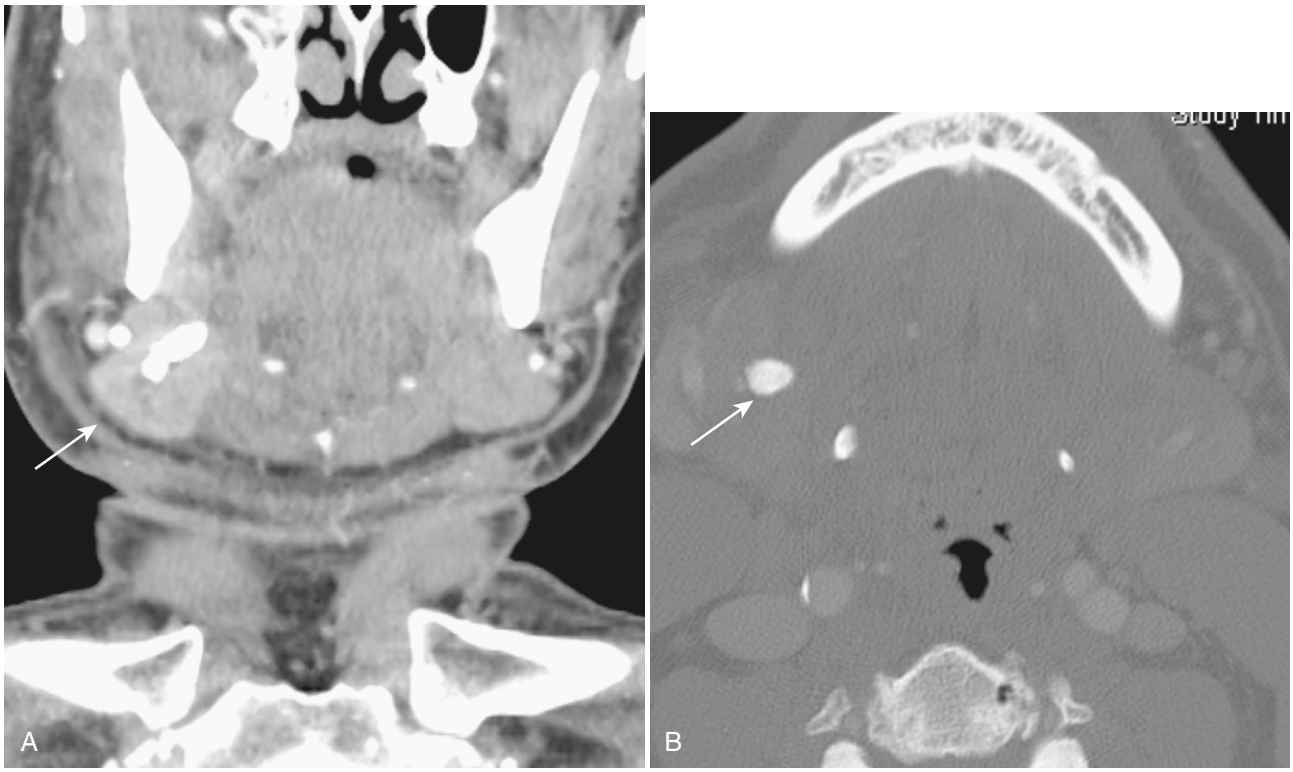


FIGURE 1-60. Salivary gland inflammation. **A,** In this patient with acute right facial swelling, computed tomography coronal reformat demonstrates an enlarged, hyperenhancing right parotid gland *(arrow)* with stranding of the subcutaneous fat. **B,** Axial image with bone window/level settings confirms a sialolith *(arrow)* within the gland.

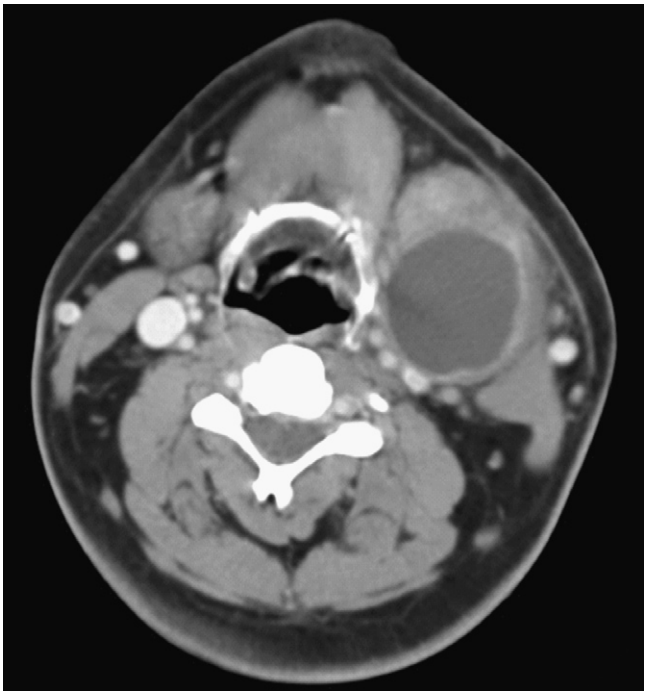


Figure 1-61. Second branchial cleft cyst. This second branchial cleft cyst is in the classic location, that is, the submandibular region, anteromedial to the sternocleidomastoid muscle and anterolateral to the carotid vessels.

a thyroglossal duct cyst should be reported, and surgical excision should be strongly considered.

Branchial Cleft Cysts

Branchial cleft cysts are congenital epithelial-lined cystic lesions in the neck originating anywhere from the level of the mandible (first branchial cleft) to the supraclavicular region (fourth branchial cleft). These can become superinfected and present as an acutely enlarging neck mass. The second branchial cleft cyst is most common, present in the submandibular region, anteromedial to the sternocleidomastoid muscle and anterolateral to the carotid vessels (Fig. 1-61). An infected branchial cleft cyst will demonstrate peripheral rim enhancement. Necrotic infectious and metastatic lymphadenopathy may present similarly and should be considered in the differential diagnosis, particularly in adult patients.

Superficial Abscesses

Multiple bilateral superficial neck abscesses can be seen in intravenous drug abusers or "skin poppers." Broken needles may occasionally be found. Following routine operations on the neck, fluid collections may develop in the superficial or deep soft tissues. In these cases, careful evaluation of adjacent vascular structures is warranted to assess for potential injury (pseudoaneurysm, dissection, thrombosis, or occlusion) or extension of inflammation (Fig. 1-62).

Lymphadenopathy

Cervical lymphadenopathy can present clinically as diffuse neck swelling, and may be related to an inflammatory process or underlying neoplasm. The presence of necrosis within normal-sized or enlarged cervical lymph nodes can be due to intranodal abscess formation but should raise suspicion for metastatic disease, especially from squamous cell carcinoma. If metastatic, the primary tumor typically arises from the base of the tongue, tonsils, nasopharynx, and pyriform sinus, or from papillary thyroid cancer. This form of thyroid cancer often affects relatively young women. Certainly, necrotic adenopathy can be seen in the setting of infection such as tuberculosis and atypical mycobacterial infections such as *Mycobacterium avium-intracellulare* complex, particularly in immunocompromised patients. Large conglomerations of necrotic lymph nodes can be seen in these settings. Careful evaluation of the lung apices for an inflammatory process is necessary, as this can support the diagnosis of tuberculous adenitis. Imaging can play an important role in raising the possibility of tuberculosis in unsuspected patients. In such a case, the referring service should be notified immediately, since isolation may be required. Interestingly, calcifications related to tuberculosis are not typically found in the cervical lymph nodes.

Croup

In the pediatric patient population, laryngotracheobronchitis, or "croup," presents clinically with a characteristic cough. The condition usually occurs in children younger than 3 years of age, and is thought to be most often caused by parainfluenza virus, although other respiratory viruses and *Mycoplasma* have also been implicated. Croup is the most common pediatric infection causing stridor, accounting for approximately 15% of clinic and ED visits for pediatric respiratory infections. The cough is a consequence of subglottic edema and manifests classically on plain radiographs with symmetric, subglottic narrowing, the so-called "steeple" sign (Fig. 1-63). Coronal CT reformats can now replicate this appearance, although cross-sectional imaging is typically not necessary for this particular indication.

Epiglottitis

Epiglottitis is now less commonly seen in the pediatric emergency room setting, due to childhood immunization against the offending agent, *H. influenzae*. However, epiglottitis can occur at any age, and there has been a recent increase in incidence in the adult population, which is often underappreciated. Patients who have not been immunized can present with acute airway compromise and may require urgent intubation. On lateral radiograph, the classic "thumb" (or "thumbprint") sign is produced by the thickened, inflamed epiglottis (Fig. 1-64). The clinical picture and radiographic imaging are usually so characteristic that cross-sectional imaging is generally unnecessary. CT imaging can provide greater diagnostic detail and can demonstrate the inflamed epiglottis along with symmetrically thickened and inflamed aryepiglottic and pharyngoepiglottic folds. However, management should be based on clinical and radiographic findings,



FIGURE 1-62. Neck abscess. **A,** In this patient who developed an infected graft soon after carotid endarterectomy, post-contrast axial CT image demonstrates organized fluid collection *(arrowhead)* adjacent to abnormal enhancing inflammatory tissue surrounding the carotid bifurcation on the right *(arrow)*. **B,** Slightly inferiorly, a fistulous tract between the collection and the inflammatory tissue is identified *(arrow)*. **C,** Coronal reformat demonstrates that the inflammatory tissue encasing the carotid bifurcation extends superiorly along the internal carotid artery, causing focal critical stenosis.

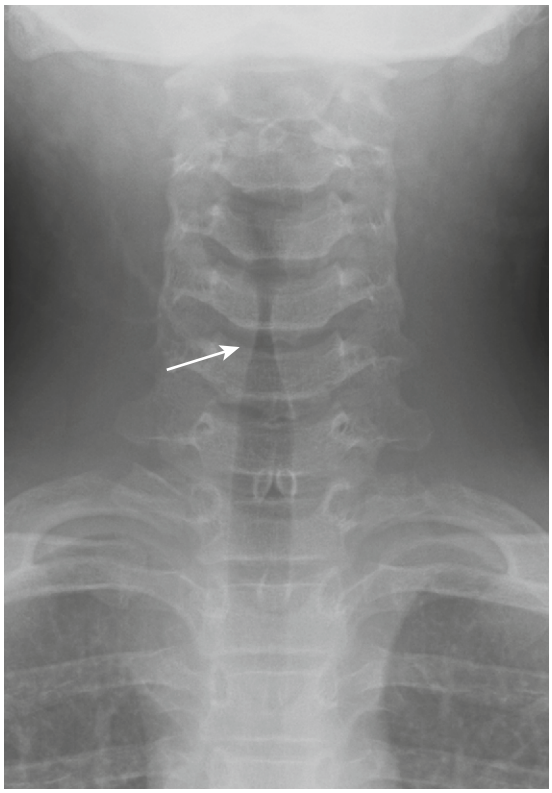


Figure 1-63. Croup. In this patient who presented acutely with barking cough, frontal radiograph of the neck demonstrates the classic "steeple" sign *(arrow)* representing concentric subglottic edema.

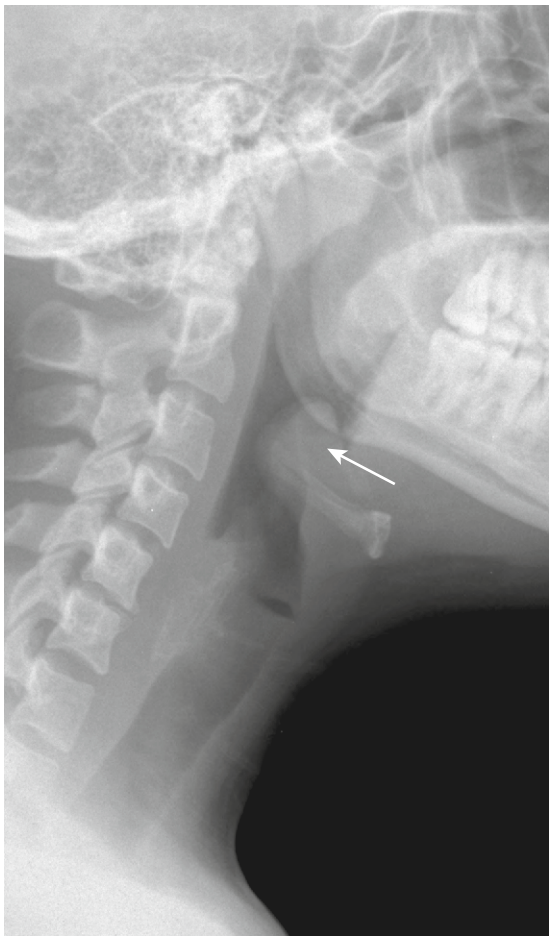


Figure 1-64. Epiglottitis. In this young child who presented with difficulty breathing, lateral neck radiograph demonstrates classic "thumb(print)" sign *(arrow)* of the inflamed epiglottis.

and obtaining a CT examination might delay proper treatment.

Angioedema

Although not due to infection, angioedema is included in this section on airway disorders. It can be hereditary or acquired and may be idiopathic, manifesting as acute narrowing of the airway, possibly resulting in airway compromise. Angioedema due to allergic reactions is often associated with urticaria. While clinical diagnosis should be straightforward, CT imaging can be useful for further evaluation. Imaging can show diffuse mucosal and submucosal swelling involving the hypopharynx and larynx, with infiltration of the subcutaneous fat and deep tissue planes of the neck.

Sinus and Orbital Infections

Uncomplicated acute sinusitis is typically clinically diagnosed and managed. On imaging, findings of acute sinusitis are not very specific. An air–fluid level within a sinus can suggest acute sinusitis; however, lack of this finding does not mean a patient does not have acute sinusitis. Occasionally, hyperdense opacification in the paranasal sinuses can be seen; the hyperdensity can reflect hemorrhage related to trauma, trapped proteinaceous debris, or fungal infection. Fungal infection is an important diagnostic consideration, since steroids probably should be incorporated into the treatment regimen if the cause is related to allergic disease (Fig. 1-65).

When more advanced sinus disease is of concern, imaging plays a more definitive role. Complicated sinus disease should be clinically suspected if the patient presents with visual changes, altered mental status, or seizures. Initial imaging for workup of complicated sinusitis can begin with CT. At our institution, axial images through the facial bones are routinely acquired at 1.25-mm intervals with coronal and sagittal reformats using bone and soft tissue algorithms. If there is concern for intracranial or orbital extension of infection, contrast-enhanced CT using similar imaging parameters can provide additional critical information. If there is clinical concern for intracranial extension, the entire brain should be imaged. Since complicated sinus infection usually warrants close follow-up imaging, MR is the preferred imaging modality to minimize radiation exposure, especially in the pediatric setting. Typical brain MR protocol includes sagittal T1, axial FLAIR, fat-suppressed T2, gradient echo, and diffusion-weighted images, followed by multiplanar postcontrast T1 images of the brain. If orbital extension is of clinical concern, high spatial resolution T2 images with and without fat suppression through the orbits, and axial and coronal pre- and postcontrast T1-weighted images, can provide excellent diagnostic detail.

CT is particularly useful in establishing the integrity of paranasal sinus walls and can effectively demonstrate areas

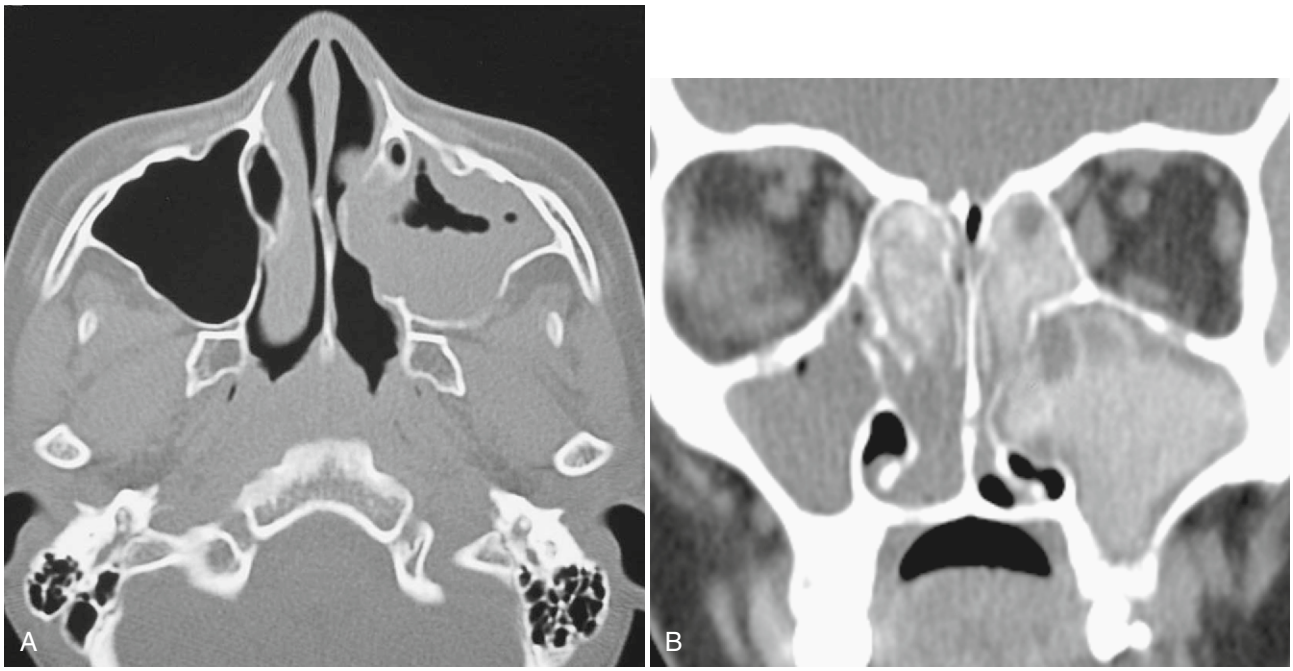


FIGURE 1-65. Sinusitis. **A,** Mucosal thickening in the left maxillary sinus is accompanied by an air–fluid level due to acute sinusitis in this patient presenting with sinus pressure, pain, and headache. **B,** In a different patient, coronal reformat in soft tissue window/level settings demonstrates hyperdense material in most of the paranasal sinuses due to allergic fungal sinusitis.

of bony dehiscence. Intracranial or orbital spread of infection can occur directly through areas of bony dehiscence or indirectly by perivascular extension, most commonly secondary to frontal or ethmoid sinus disease. Perivascular spread more commonly occurs in the pediatric setting. Intracranial extension is usually seen in the setting of frontal sinus infection, with involvement of the anterior cranial fossa and frontal lobes (Fig. 1-66). Imaging can demonstrate associated dural enhancement, epidural or subdural collections, and meningoencephalitis with abscess formation. There may be concomitant swelling of the overlying soft tissues of the forehead, known as Pott's puffy tumor (Fig. 1-67). This does not imply neoplastic involvement, but rather describes osteomyelitis with extracranial soft

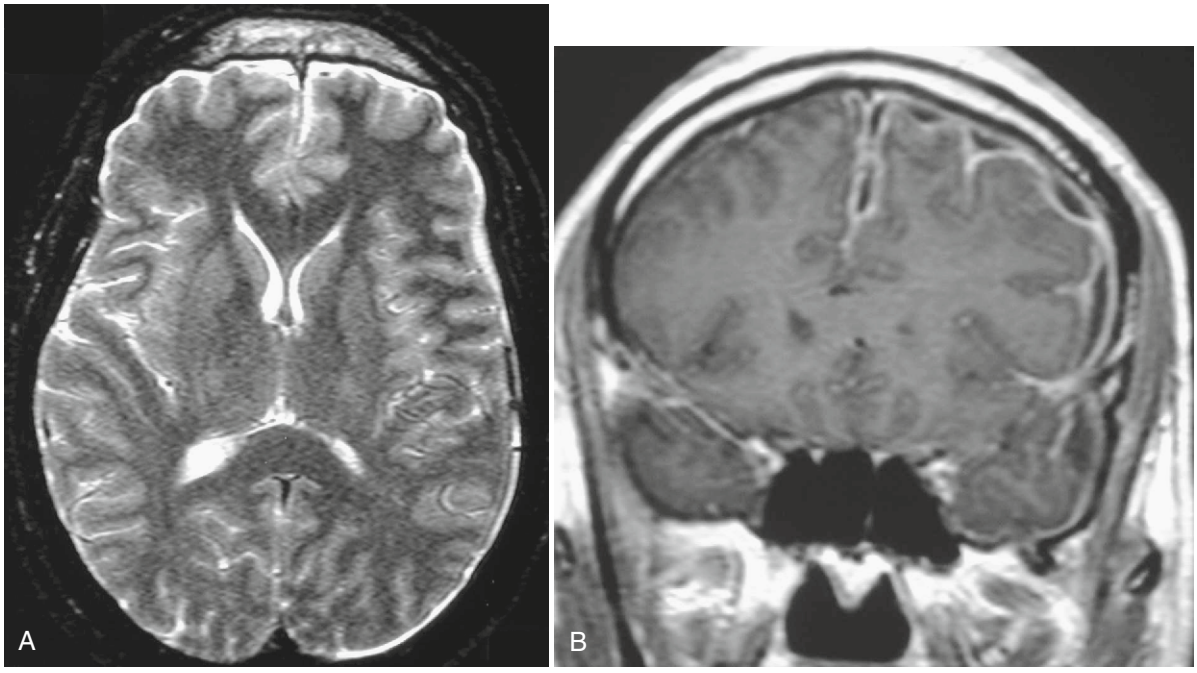


FIGURE 1-66. Sinusitis—subdural empyema and infarct. **A,** Axial T2-weighted image shows proteinaceous material within the frontal sinuses. **B,** Post-gadolinium coronal T1-weighted image demonstrates associated subdural abscess and leptomeningeal enhancement.

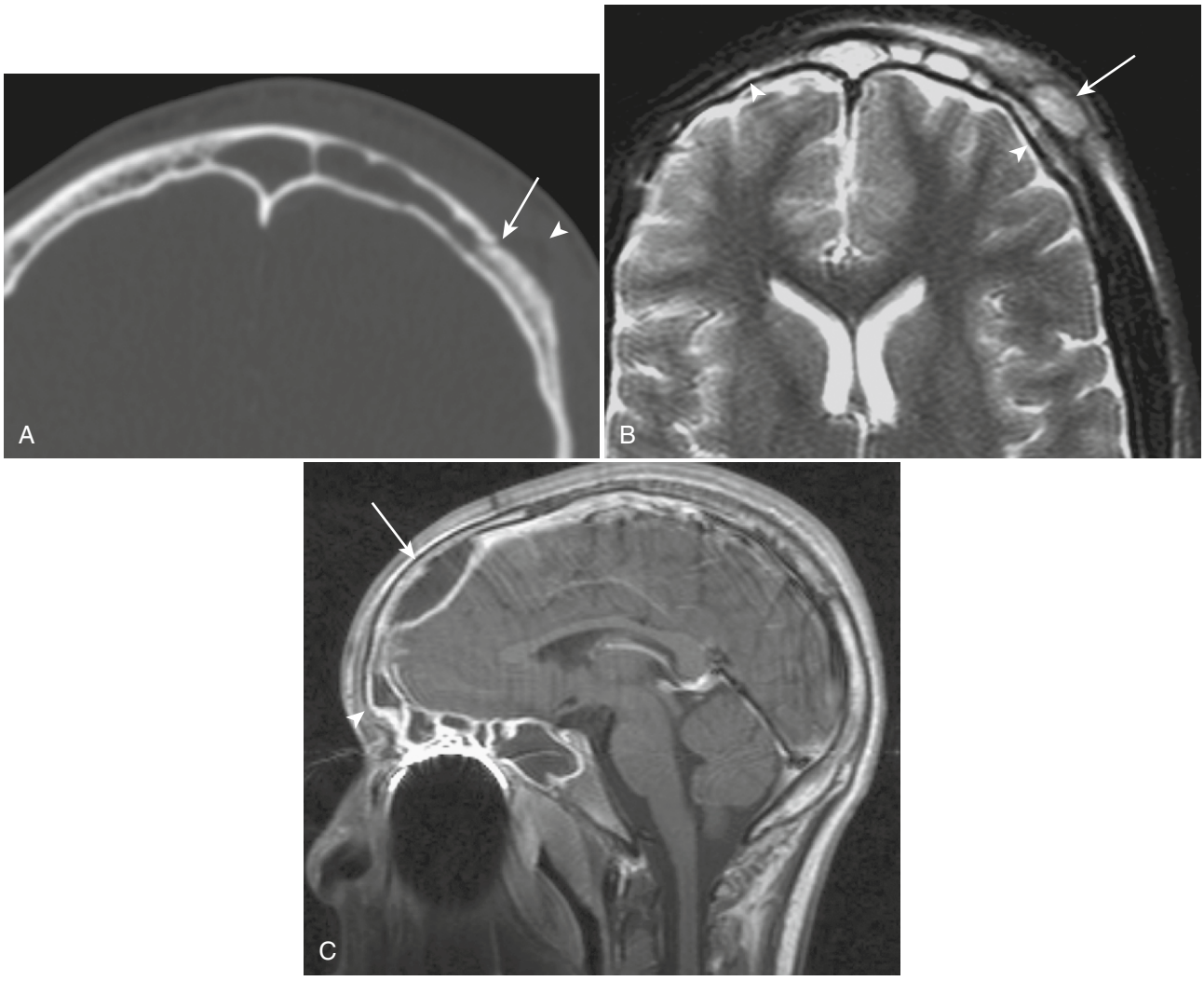


Figure 1-67. Sinusitis—Pott's puffy tumor and epidural abscess. **A,** Axial CT image shows opacification of the frontal sinuses and overlying soft tissue swelling. A tract from the anterior table of the frontal sinus *(arrow)* and adjacent fluid collection *(arrowhead)* are shown. **B,** Axial T2-weighted image demonstrates abnormal hyperintensity of marrow in the frontal bone *(arrowheads)* and overlying soft tissue swelling, including small scalp fluid collection *(arrow)*. **C,** Postgadolinium sagittal T1-weighted image shows epidural abscess *(arrow)* and fluid-filled paranasal sinuses with inflamed mucosa *(arrowhead)*.

tissue abscess formation. The presence of pachymeningeal enhancement does not necessarily imply that brain parenchyma is involved, and may only reflect dural reaction. Epidural and subdural collections can be demonstrated on either CT or MR as extra-axial fluid, possibly compressing the subjacent brain parenchyma. Subdural collections can cross sutures and generally maintain a crescentic shape, whereas epidural collections are restricted by sutures and may have a lentiform (biconvex) shape. While a reactive subdural effusion may be associated with smooth pachymeningeal enhancement, an infected subdural or epidural collection can demonstrate restricted diffusion and thickened, more irregular dural enhancement on MR. Leptomeningeal involvement is demonstrated as curvilinear enhancement extending into sulci. This may be accompanied by FLAIR hyperintensity in a corresponding distribution, which is a sensitive but nonspecific finding. Parenchymal involvement can be demonstrated by FLAIR hyperintensity and enhancement. Frank abscess formation can be demonstrated by CT or MR as a peripherally enhancing fluid collection. Restricted diffusion in the collection can support this impression.

While posterior ethmoid disease can also lead to intracranial involvement, more commonly, untreated ethmoid sinusitis can extend into the medial aspect of the orbit (Fig. 1-68). Infection can spread in a subperiosteal fashion along the medial wall of the orbit, appearing as an elliptical shaped phlegmon or fluid collection. This may cause displacement of extraocular muscles. Without treatment, the phlegmon or abscess can then break through the periosteum and extend directly into the orbit and into the extraocular muscles. Depending on the size of the inflammatory process, there can be displacement of extraocular muscles and the globe, along with distortion, stretching, and compression of the optic nerve. Such findings constitute an ophthalmologic emergency, as prolonged mass effect on the optic nerve can result in permanent blindness.



FIGURE 1-68. Sinusitis—complications. **A,** Axial CT in a young patient with mild acute proptosis demonstrates opacification of the right ethmoid air cells with abnormal soft tissue in the medial aspect of the right orbit *(arrowhead)*, displacing the medial rectus muscle. Normally, this space should contain orbital fat, but in this case, there has been perivascular extension of inflammation into the orbit; note that the lamina papyracea is intact. **B,** Coronal T1-weighted image demonstrates extensive collection extending from the sinuses *(arrowhead)* into the orbit *(arrow)*, displacing extraocular muscles and optic nerve inferiorly. **C,** Postgadolinium coronal T1-weighted image shows that much of the abnormal soft tissue in the orbit *(arrow)* is due to subperiosteal abscess *(arrowhead)*.

Other possible critical complications of orbital infection include extension of infection and involvement of contents of the orbital apex (cranial nerve II), superior orbital fissure (cranial nerves III, IV, V1, VI, and superior orbital vein), and inferior orbital fissure (V2, infraorbital nerve). Idiopathic inflammation involving the cavernous sinus, known as Tolosa-Hunt syndrome, can manifest clinically as palsies of the cranial nerves that traverse the cavernous sinus, namely, III, IV, V1, V2, and VI.

Venous sinus thrombosis can result from ethmoid or sphenoid sinus or orbital infection, and careful attention to the cavernous sinuses on postcontrast images is necessary. Facial soft tissue, dental, and ear infections are other possible causes. Direct signs of septic cavernous sinus thrombosis, also termed cavernous sinus thrombophlebitis (CST), include an enlarged sinus with a convex border, and a single large or multiple irregular filling defect(s). Normal neural structures and intracavernous fat deposits should not be mistaken as true filling defects. Indirect signs include dilation of the superior ophthalmic vein, exophthalmos, soft tissue edema, thrombi in the superior ophthalmic vein, superior and inferior petrosal, or sigmoid sinuses, and decrease in caliber of the internal carotid artery. Thin-section, contrast-enhanced CT with coronal reformats may be equivalent

to MR for the detection of these findings. However, once venous sinus thrombosis is suspected, MR imaging of the brain may confirm the diagnosis and evaluate for possible complications of meningitis, subdural empyema, cerebritis, and even pituitary necrosis. Postcontrast T1 coronal and axial images are generally sufficient to make the diagnosis. Contrast-enhanced MR venography may also offer support in diagnosis. (Phase contrast MR venography is generally limited for this evaluation. Contrast-enhanced CT [CT venography] and MR with thin slices are generally more helpful to diagnose CST.) Prior to the antibiotic era, CST was almost always fatal. In the modern era, mortality in the range of 20% to 30% may still be expected. In addition to antibiotics, early institution of anticoagulant therapy may reduce mortality. Morbidity may result from cranial nerve dysfunction including blindness, pituitary insufficiency, and hemiparesis.

Ear Infections

Much like uncomplicated paranasal sinus disease, external and middle ear infections can be diagnosed and followed clinically. Acute and chronic otomastoiditis can occasionally be picked up on imaging and should be reported since these conditions may be clinically unsuspected (Fig. 1-69). If there is clinical concern for a more complicated infectious process, CT and MR can be very useful adjuncts in diagnosis. CT imaging of the temporal bone includes the entire auditory system. At our institution it is performed with overlapping 0.625-mm-thick sections with coronal and sagittal reformats in bone and soft tissue algorithms. If there is clinical concern for intracranial involvement, contrast-enhanced CT using the same imaging parameters can provide additional diagnostic detail. MR imaging can be particularly useful in the setting of cranial nerve involvement. Our technique includes high spatial resolution T2, and pre- and postcontrast axial and coronal images from the level of the orbits to the base of the brain, in addition to routine brain imaging.

Malignant otitis externa is typically seen in diabetic and immunocompromised patients, and is a rare but serious complication of external ear infection. The inflammation can quickly progress to involve the entire ear, external auditory canal, and middle and inner ear structures. Evaluation of the stylomastoid foramen for extension of inflammation with fat stranding is important, particularly in patients with facial nerve symptoms. Associated osteomyelitis is seen as a locally aggressive destructive process of the temporal bone. Urgent treatment is indicated usually with surgical débridement, as intracranial extension of infection can develop rapidly. Cranial nerve involvement from untreated middle ear infection can occur secondarily by spread of inflammation into the cavernous sinus, typically involving cranial nerve V within Meckel's cave and cranial nerve VI within the cavernous sinus (Gradenigo syndrome) (Fig. 1-70). Additional cranial nerve involvement can quickly ensue. Intracranial extension can result from dehiscence of the temporal bone, with direct spread into the middle cranial fossa. As with complicated paranasal sinus infection, extension into the middle cranial fossa can result in epidural abscess, subdural empyema, meningoencephalitis, or brain abscess. Transverse sinus, sigmoid sinus, and jugular vein thrombosis are other possible complications (Fig. 1-71).

Complicated Dental Disease

Periapical lucencies around individually infected teeth are often incidentally detected on routine CT images of the mandible and maxilla performed for other reasons.

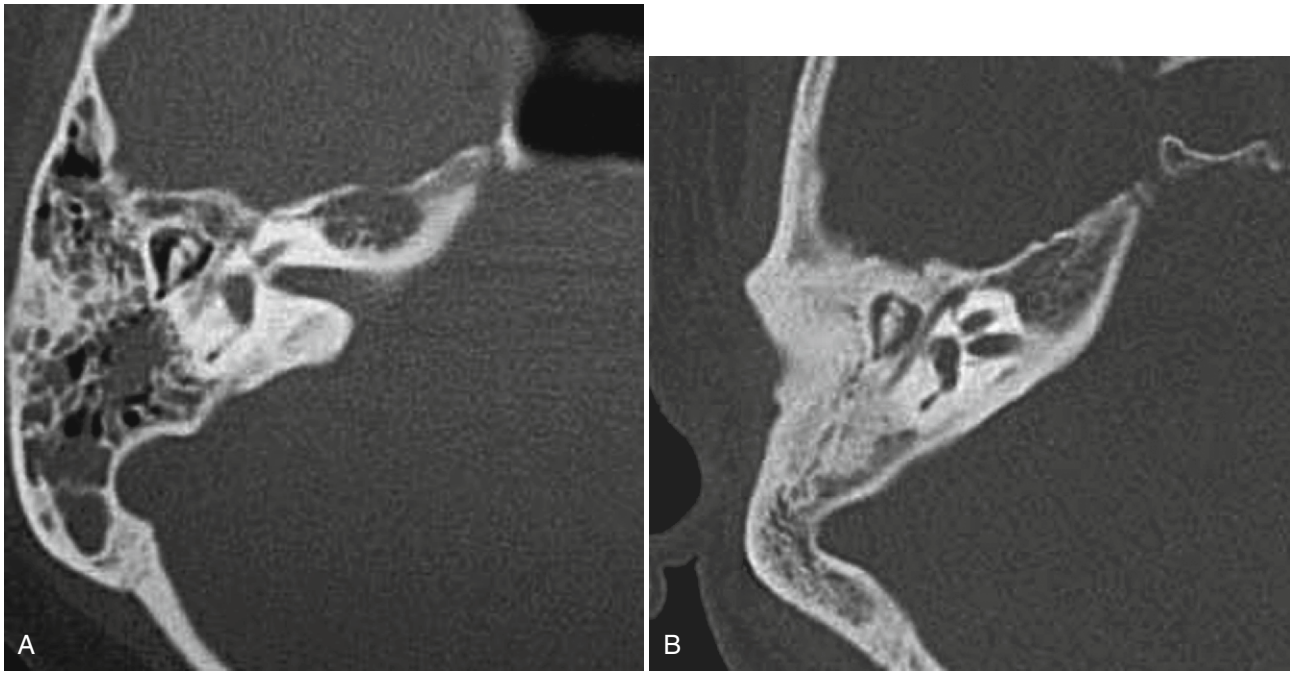


Figure 1-69. Mastoiditis. **A,** Opacification of mastoid air cells without bony changes in a patient with symptoms of acute mastoiditis. **B,** Opacification of the middle ear with sclerotic changes of the mastoid bone in a patient with a history of chronic otomastoiditis.

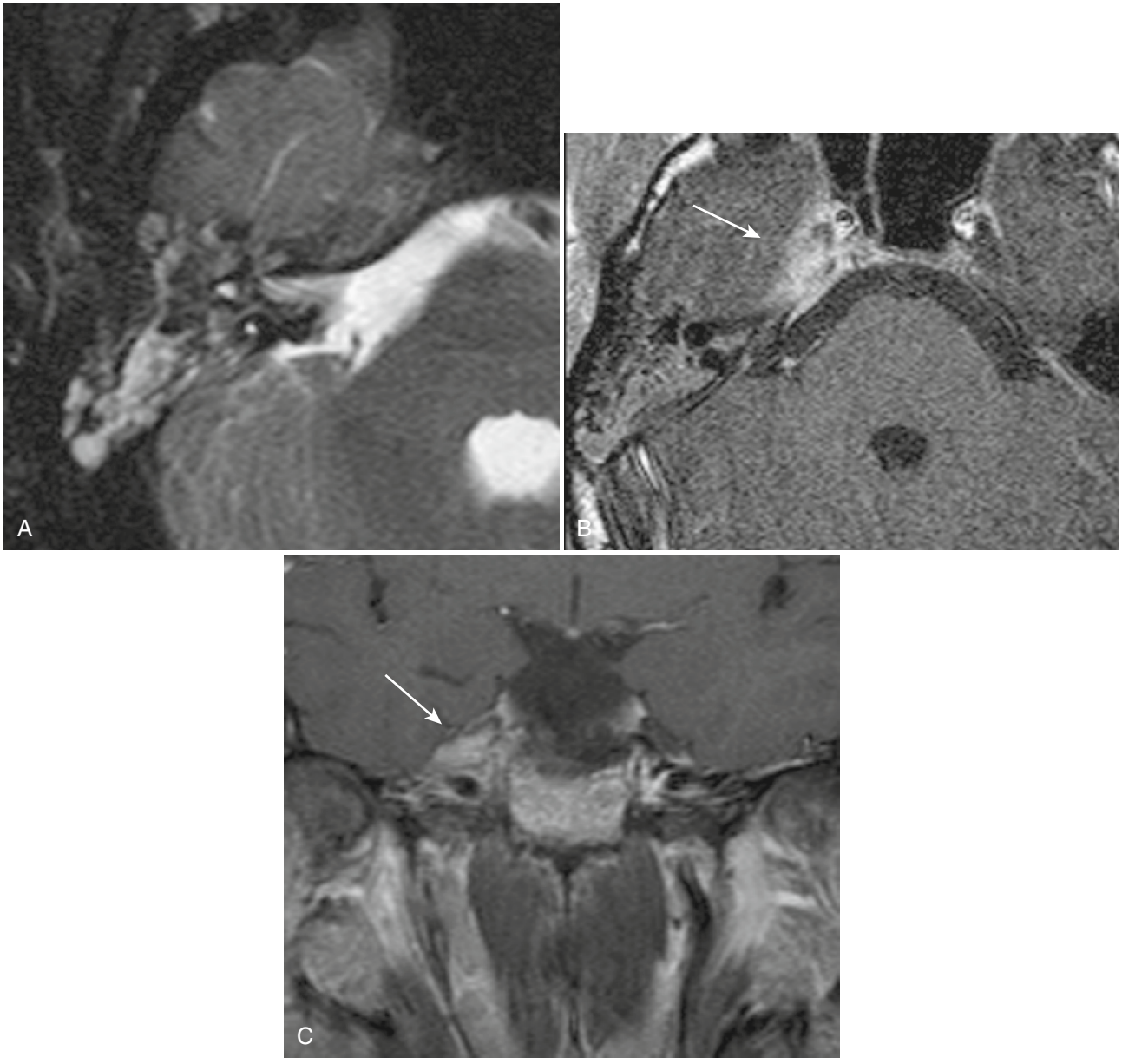


FIGURE 1-70. Gradenigo syndrome. **A,** In this patient with mastoiditis and facial pain, axial fat-suppressed T2-weighted image demonstrates bright signal in the right mastoid air cells. Axial **(B)** and coronal **(C)** postgadolinium T1-weighted images demonstrate abnormal enhancement within Meckel's cave on the right side. This patient complained of new facial pain in the setting of chronic mastoid disease.

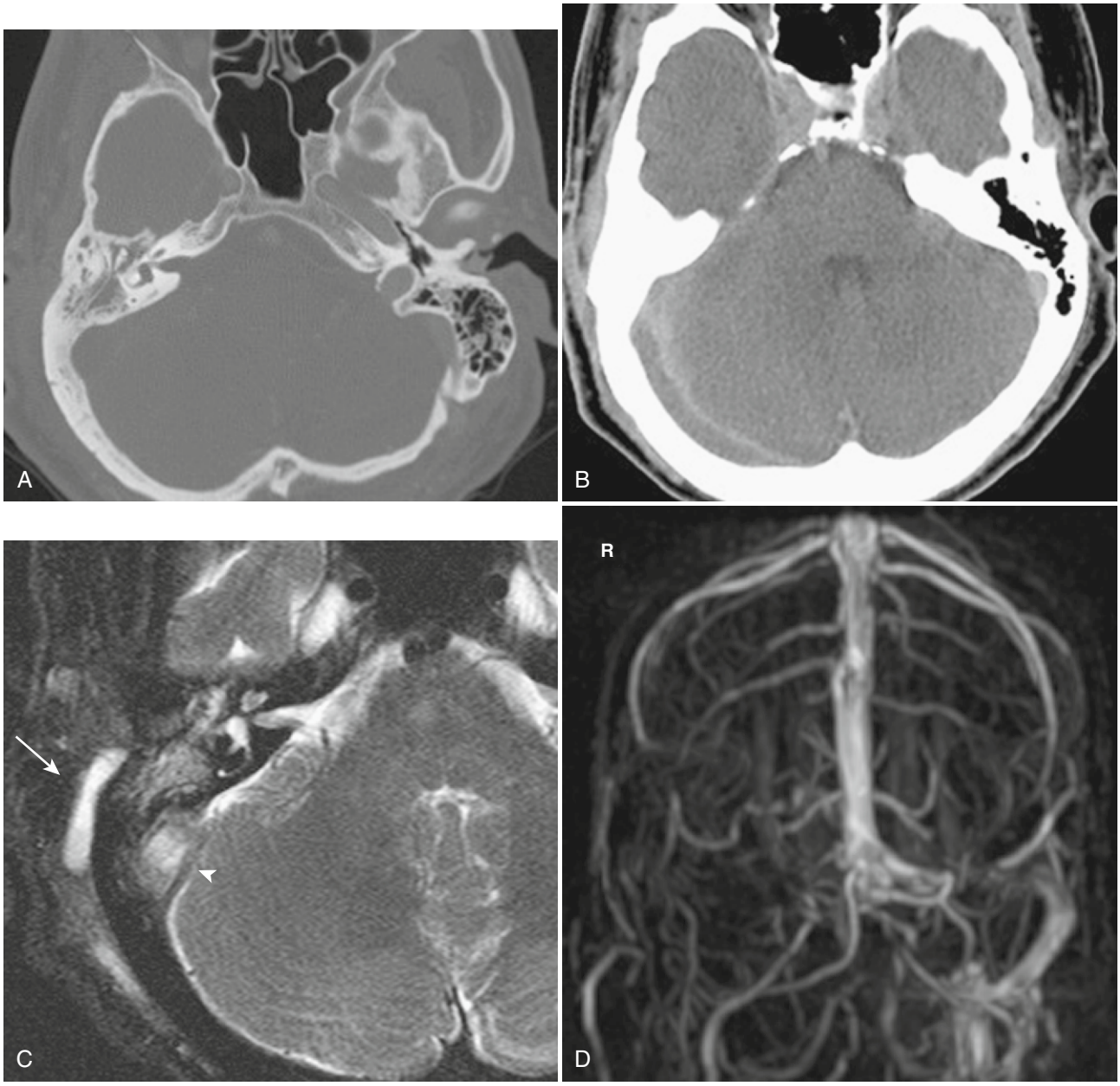


Figure 1-71. Mastoiditis—septic thrombophlebitis. **A,** Initial noncontrast CT in patient with headache demonstrates chronic right otomastoiditis. **B,** Based on suspicious findings on the noncontrast exam, a contrast-enhanced CT study was performed, demonstrating filling defect within the right transverse sinus. **C,** T2-weighted image shows hyperintense subperiosteal abscess *(arrow)*. There is also T2 hyperintense signal in the expanded sigmoid sinus *(arrowhead)* rather than the expected flow void. **D,** Maximal intensity projection reformat from three-dimensional phase contrast MR venography demonstrates lack of flow-related signal in the right transverse and sigmoid sinuses and right internal jugular vein, consistent with venous sinus thrombosis.

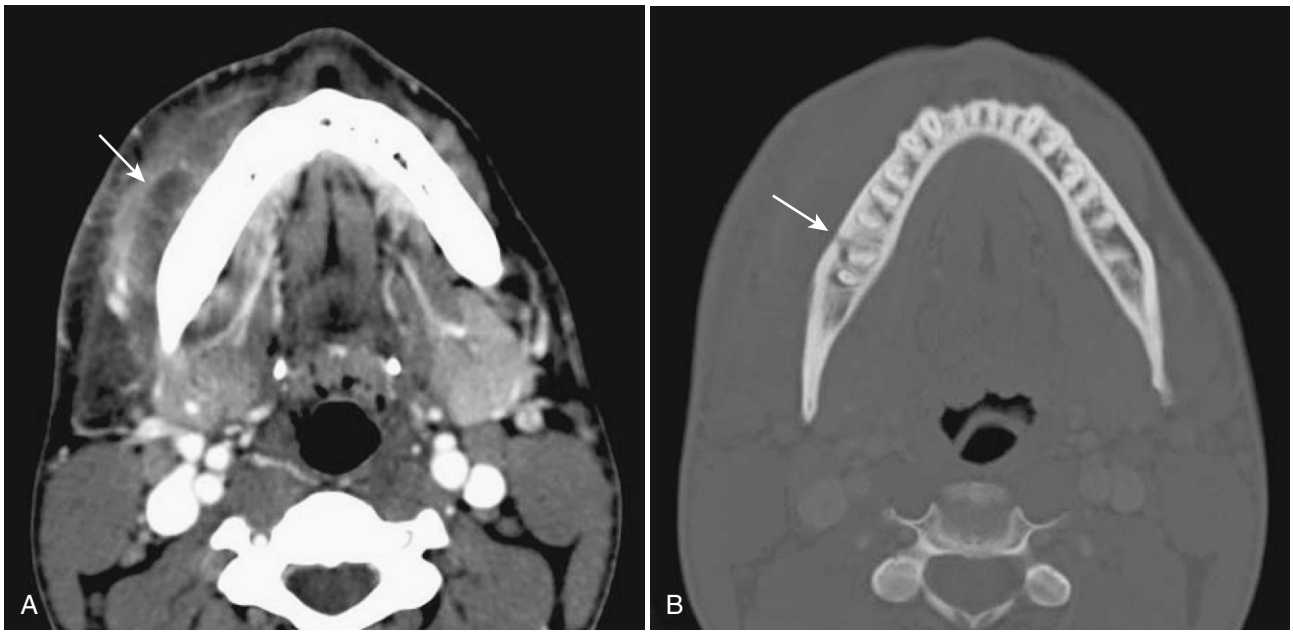


FIGURE 1-72. Perimandibular abscess. **A,** In this patient with right facial pain and swelling, contrast-enhanced CT demonstrates a fluid collection *(arrow)* and subcutaneous stranding along the buccal surface of the right mandible. **B,** Within the mandible at the same level is a periapical lucency related to a molar tooth with a defect consistent with a sinus tract.

Occasionally, the infection can progress to the medullary bone, eventually breaking through the overlying buccal or lingual cortex. In these cases, this sinus tract acts as a conduit for spread of infection into the adjacent soft tissues (Fig. 1-72). With time, an abscess can develop, and the patient may present to the emergency room with pain, swelling, and elevated white blood cell count. Fluid collections in the face should therefore be carefully evaluated for a possible dental source, since the soft tissue infection will not be cured by drainage alone. Rapid progression of infection into other spaces, including the orbit and intracranial compartment, is a serious and potentially life-threatening complication. Ludwig's angina is characterized by extensive facial swelling and hardened cellulitis centered in the submandibular space, classically bilaterally, related to periodontal disease (Fig. 1-73).

In the case of a suspected dental-related facial abscess, maxillofacial CT with thin (1.25 mm) axial sections and coronal and sagittal reformats in bone and soft tissue algorithms should be performed. Intravenous contrast-enhanced exam increases the sensitivity for detection of abscess based on peripheral rim enhancement. CT is particularly useful in identifying areas of cortical disruption of the mandible or maxilla, whereas MR may identify the fluid collection but could easily miss the source of the infection, namely, the affected tooth, due to artifacts inherent to MR imaging.

Summary: Head and Neck

There is a wide variety of pathology that may present as emergencies in the head and neck region. While many conditions can be diagnosed and managed clinically, imaging plays an important role in the diagnosis and management when more complicated disease and acute traumatic injuries are encountered. A clear understanding of the history and physical findings based on communication between radiologist and referring clinician will guide selection of the most appropriate imaging modality and protocol.

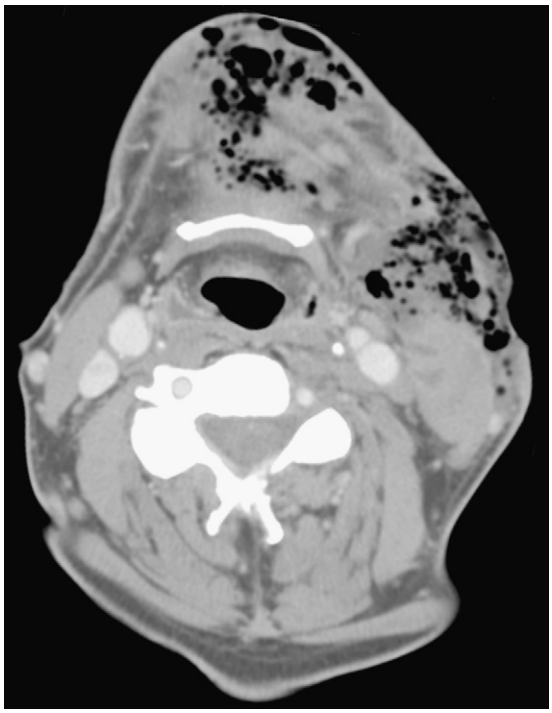


FIGURE 1-73. Ludwig's angina. This patient presented with massive neck swelling and on imaging the inflammation extended from the upper face to the axilla. Extensive emphysema throughout the neck was of concern for necrotizing fasciitis. On surgical exploration, the source of inflammation was suspected to be dental disease, but the dentition was so poor and inflammation so extensive that the causative tooth could not be determined. Cultures from the neck grew mixed flora, including fusobacterium, commonly found in oral flora.

As with all other parts of the body, a working knowledge of the anatomy and variants as well as the disorders specific to the region is necessary to provide excellent patient care.

ACKNOWLEDGMENTS

The authors would like to acknowledge Keith Begelman, MD, for assistance with the section on facial trauma.

Suggested Readings: Brain

Adams JH, Doyle D, Ford I, et al: Diffuse axonal injury in head injury: Definitions, diagnosis and grading. Histopathology 15:49–59, 1989.
Al-Nakshabandi NA: The swirl sign. Radiology 218:433, 2001.
Arfanakis K, Haughton VM, Carew JD, et al: Diffusion tensor MR imaging in diffuse axonal injury. AJNR Am J Neuroradiol 23:794–802, 2002.
Biffl WL, Egglin T, Benedetto B, et al: Sixteen-slice computed tomographic angiography is a reliable noninvasive screening test for clinically significant blunt cerebrovascular injuries. J Trauma 60:745–752, 2006.
Blackmore CC, Avey GD: Imaging of the spine in victims of trauma. In Medina LS, Blackmore CC (eds): Evidence-based Imaging. Optimizing Imaging in Patient Care. New York, Springer Science+Business Media, 2006, pp 319–333.
Casey SO, Sampaio RC, Michel E, et al: Posterior reversible encephalopathy syndrome: Utility of fluid-attenuated inversion recovery MR imaging in the detection of cortical and subcortical lesions. AJNR Am J Neuroradiol 21: 1199–1206, 2000.
Chao CP, Zaleski CG, Patton AC: Neonatal hypoxic-ischemic encephalopathy: Multimodality imaging findings. Radiographics 26(Suppl):S159–S172, 2006.
Chen M, Caplan L: Intracranial dissections. In Baumgartner RW (ed): Handbook on Cerebral Artery Dissection. Basel (Switzerland), Karger, 2005, pp 160–173.
Copen WA, Schwamm LH, Gonzalez RG, et al: Ischemic stroke: Effects of etiology and patient age on the time course of the core apparent diffusion coefficient. Radiology 221:27–34, 2001.
Davis PC for the Expert Panel on Neurologic Imaging. Head trauma. AJNR Am J Neuroradiol 28:1619–1621, 2007.
Eastwood JD, Lev MH, Azhari T, et al: CT perfusion scanning with deconvolution analysis: Pilot study in patients with acute middle cerebral artery stroke. Radiology 222:227–236, 2002.
Filley CM, Kleinschmidt-DeMasters BK: Toxic leukoencephalopathy. N Engl J Med 345:425–432, 2001.
Given CA, Burdette JH, Elster AD, et al: Pseudo-subarachnoid hemorrhage: A potential imaging pitfall associated with diffuse cerebral edema. AJNR Am J Neuroradiol 24:254–256, 2003.
Grossman RI, Yousem DM: Neuroradiology: The Requisites, 2nd ed. Philadelphia, Elsevier, 2003.
Gupta RK, Nath K, Prasad A, et al: In vivo demonstration of neuroinflammatory molecule expression in brain abscess with diffusion tensor imaging. AJNR Am J Neuroradiol 29:326–332, 2008.
Hennerici M, Daffertshofer M, Jakobs L: Failure to identify cerebral infarct mechanisms from topography of vascular territory lesions. AJNR Am J Neuroradiol 19:1067–1074, 1998.
Huisman TA, Schwamm LH, Schaefer PW, et al: Diffusion tensor imaging as potential biomarker of white matter injury in diffuse axonal injury. AJNR Am J Neuroradiol 25:370–376, 2004.
Johnston SC: Clinical Practice. Transient ischemic attack. N Engl J Med 347:1687–1692, 2002.
Jones KM, Seeger JF, Yoshino MT: Ipsilateral motor deficit resulting from a subdural hematoma and a Kernohan notch. AJNR Am J Neuroradiol 12: 1238–1239, 1991.
Keogh CF, Andrews GT, Spacey SD, et al: Neuroimaging features of heroin inhalation toxicity: "Chasing the dragon." AJR Am J Roentgenol 180:847–850, 2003.
Laine FJ, Shedden AI, Dunn MM, et al: Acquired intracranial herniations: MR imaging findings. AJR Am J Roentgenol 165:967–973, 1995.
Leach JL, Fortuna RB, Jones BV, et al: Imaging of cerebral venous thrombosis: Current techniques, spectrum of findings, and diagnostic pitfalls. Radiographics 26(Suppl):S19–S43, 2006.
Lev MH, Segal AZ, Farkas J, et al: Utility of perfusion-weighted CT imaging in acute middle cerebral artery stroke treated with intra-arterial thrombolysis. Prediction of final infarct volume and clinical outcome. Stroke 32:2021–2028, 2001.
Liang L, Korogi Y, Sugahara T, et al: Detection of intracranial hemorrhage with susceptibility-weighted MR sequences. AJNR Am J Neuroradiol 20:1527–1534, 1999.
Lonergan GJ, Baker AM, Morey MK, et al: From the archives of the AFIP: Child abuse: Radiologic-pathologic correlation. Radiographics 23:811–845, 2003.
Louis DN, Ohgaki H, Wiestler OD, Cavenee WK: WHO Classification of Tumours of the Central Nervous System, 4th ed. Geneva, WHO, 2007.
Nadgir RN, Loevner LA, Ahmed T, et al: Simultaneous bilateral internal carotid and vertebral artery dissection following chiropractic manipulation: Case report and review of the literature. Neuroradiology 45:311–314, 2003.
Noguchi K, Seto H, Kamisaki Y, et al: Comparison of fluid-attenuated inversion-recovery MR imaging with CT in a simulated model of acute subarachnoid hemorrhage. AJNR Am J Neuroradiol 21:923–927, 2000.
Nunez DB, Torres-Leon M, Munera F: Vascular injuries of the neck and thoracic inlet: Helical CT-angiographic correlation. Radiographics 24:1087–1100, 2004.
Osborn AG, Blaser S, Salzman K: Diagnostic Imaging. Brain. Salt Lake City, UT, Amirsys, 2004.
Packard AS, Kase CS, Aly AS, et al: "Computed tomography-negative" intracerebral hemorrhage. Arch Neurol 60:1156–1159, 2003.
Pelkonen O, Tikkakakoski T, Pyhtinen J, et al: Cerebral CT and MRI findings in cervicocephalic artery dissection. Acta Radiol 45:259–265, 2004.
Polman CH, Reingold SC, Edan G, et al: Diagnostic criteria for multiple sclerosis: 2005 revisions to the "McDonald criteria." Ann Neurol 58:840–846, 2005.
Rodallec MH, Krainik A, Feydy A, et al: Cerebral venous thrombosis and multi-detector CT angiography: Tips and tricks. Radiographics 26(Suppl):S5–S18, 2006.
Schaefer PW, Roccatagliata L, Ledzema C, et al: First-pass quantitative CT perfusion identifies thresholds for salvageable penunbra in a acute stroke patients treated with intra-arterial therapy. AJNR Am J Neuroradiol 27:20–25, 2006.
Siskas N, Lefkopoulos A, Ioannidis I, et al: Cortical laminar necrosis in brain infarcts: Serial MRI. Neuroradiology 45:283–288, 2003.
Srinivasan A, Goyal M, Al Azri F: State-of-the-art imaging of acute stroke. Radiographics 26(Suppl):S75–S95, 2006.
Stuhlfaut JW, Barest G, Sakai O, et al: Impact of MDCT angiography on the use of catheter angiography for the assessment of cervical arterial injury after blunt or penetrating trauma. AJR Am J Roentgenol 185:1063–1068, 2005.
Susac JO, Murtagh FR, Egan RA, et al: MRI findings in Susac's syndrome. Neurology 61:1783–1787, 2003.
Tomandl BF, Kostner NC, Schempershofe M, et al: CT angiography of intracranial aneurysms: A focus on postprocessing. Radiographics 24:637–655, 2004.
van der Vorp HB, van Gijn J: Acute ischemic stroke. N Engl J Med 357:572–579, 2007.
Vo KD, Lin W, Lee J-M: Neuroimaging in acute ischemic stroke. In Medina LS, Blackmore CC (eds): Evidence-based Imaging. Optimizing Imaging in Patient Care. New York, Springer Science+Business Media, 2006, pp 160–179.
Wada R, Aviv RI, Fox AJ, et al: CT angiography "spot sign" predicts hematoma expansion in acute intracerebral hemorrhage. Stroke 38:1257–1262, 2007.
Wintermark M, Reichhart M, Cuisenaire O, et al: Comparison of admission perfusion computed tomography and qualitative diffusion- and perfusion-weighted magnetic resonance imaging in acute stroke patients. Stroke 33:2025–2031, 2002.
Woo K, Magner DP, Wilson MT, et al: CT angiography in penetrating neck trauma reduces the need for operative neck exploration. Am Surg 71:754–758, 2005.

Suggested Readings: Head and Neck

Al-Dajani N, Wootton SH: Cervical lymphadenitis, suppurative parotitis, thyroiditis, and infected cysts. Infect Dis Clin North Am 21:523–541, 2007.
Alvi A, Bereliani A 4th: Trauma to the temporal bone: Diagnosis and management of complications. J Craniomaxillofac Trauma 2:36–48, 1996.
Battista RA, Baredes S, Krieger A, et al: Prevertebral space infections associated with cervical osteomyelitis. Otolaryngol Head Neck Surg 108:160–166, 1993.
Bentsianov BL, Parhiscar A, Azer M, et al: The role of fiberoptic nasopharyngoscopy in the management of the acute airway in angioneurotic edema. Laryngoscope 110:2016–2019, 2000.
Caruso PA, Watkins LM, Suwansaard P, et al: Odontogenic orbital inflammation: Clinical and CT findings—initial observations. Radiology 239:187–194, 2006.
Clary RA, Cunningham MJ, Eavey RD: Orbital complications of acute sinusitis: Comparison of computed tomography scan and surgical findings. Ann Otol Rhinol Laryngol 101:598–600, 1992.
Dolan KD, Jacoby CG, Smoker WR: Facial fractures. Radiographics 4:577–663, 1984.
Freeman J: Temporal bone fractures and cholesteatoma. Ann Otol Rhinol Laryngol 92:558–560, 1983.
Ginsberg LE, Pruett SW, Chen MY, et al: Skull-base foramina of the middle cranial fossa: Reassessment of normal variation with high-resolution CT. AJNR Am J Neuroradiol 15:283–291, 1994.
Harris JH, Harris WH: The Radiology of Emergency Medicine. 4th ed. Philadelphia, Lippincott Williams and Wilkins, 2000, pp 1–30, 49–134.
Hopper RA, Salemy S, Sze RW: Diagnosis of midface fractures with CT: What the surgeon needs to know. Radiographics 26:783–793, 2006.
Ishman SL, Friedland DR: Temporal bone fractures: Traditional classification and clinical relevance. Laryngoscope 114:1734–1741, 2004.
Kinoshita T, Ishii K, Naganuma H, et al: Acute suppurative thyroiditis arising from a piriform sinus fistula: CT diagnosis. Radiat Med 16:217–219, 1998.
Koesling S, Kunkel P, Schul T: Vascular anomalies, sutures and small canals of the temporal bone on axial CT. Eur J Radiol 54:335–343, 2005.

LeBedis CA, Sakai O: Nontraumatic orbital conditions: Diagnosis with CT and MR imaging in the emergent setting. Radiographics 28:1741–1753, 2008.
Little SC, Kesser BW: Radiographic classification of temporal bone fractures: Clinical predictability using a new system. Arch Otolaryngol Head Neck Surg 132:1300–1304, 2006.
Lyos AT, Marsh MA, Jenkins HA, et al: Progressive hearing loss after transverse temporal bone fracture. Arch Otolaryngol Head Neck Surg 121:795–799, 1995.
McKennan KX, Chole RA: Post-traumatic cholesteatoma. Laryngoscope 99:779–782, 1989.
Peralta R, Hurford WE: Airway trauma. Int Anesthesiol Clin 38:111–127, 2000.
Rafferty MA, McConn Walsh R, Walsh MA: A comparison of temporal bone fracture classification systems. Clin Otolaryngol 31:287–291, 2006.
Reynolds SC, Chow AW: Life-threatening infections of the peripharyngeal and deep fascial spaces of the head and neck. Infect Dis Clin North Am 21:557–576, 2007.
Rhea JT, Rao PM, Novelline RA: Helical CT and three-dimensional CT of facial and orbital injury. Radiol Clin North Am 37:489–513, 1999.
Rodt T, Bartling SO, Zajaczek JE, et al: Evaluation of surface and volume rendering in 3D-CT of facial fractures. Dentomaxillofac Radiol 35:227–231, 2006.
Saigal K, Winokur RS, Finden S, et al: Use of three-dimensional computerized tomography reconstruction in complex facial trauma. Facial Plast Surg 21:214–220, 2005.
Schuknecht B, Graetz K: Radiologic assessment of maxillofacial, mandibular, and skull base trauma. Eur Radiol 15:560–568. Epub 2005 Jan 21.
Shah S, Sharieff GQ: Pediatric respiratory infections. Emerg Med Clin North Am 25:961–979, 2007.
Sherman SC, Buchanan A: Gradenigo syndrome: A case report and review of a rare complication of otitis media. J Emerg Med 27:253–256, 2004.
Simons JP, Branstetter BF 4th, Mandell DL: Bilateral peritonsillar abscesses: Case report and literature review. Am J Otolaryngol 27:443–445, 2006.
Smith JA, Danner CJ: Complications of chronic otitis media and cholesteatoma. Otolaryngol Clin North Am 39:1237–1255, 2006.
Snow JB Jr: Diagnosis and therapy for acute laryngeal and tracheal trauma. Otolaryngol Clin North Am 17:101–106, 1984.
Stassen NA, Hoth JJ, Scott MJ, et al: Laryngotracheal injuries: Does injury mechanism matter? Am Surg 70:522–525, 2004.
Takao M, Ido M, Hamaguchi K, et al: Descending necrotizing mediastinitis secondary to a retropharyngeal abscess. Eur Respir J 7:1716–1718, 1994.

CHAPTER 2

Chest Trauma

Laura Avery and Robert A. Novelline

Thoracic injuries account for about 25% of trauma deaths, second in number only to head trauma. In the United States each year, more than 300,000 patients are hospitalized and more than 25,000 die as a result of sustaining chest trauma. Blunt trauma accounts for 90% of chest trauma, and the most common cases of blunt trauma are motor vehicle collisions and falls.

The imaging protocol of patients with suspected thoracic injuries usually begins with a supine portable anteroposterior chest radiograph. Many obvious thoracic injuries such as displaced rib fractures, large pneumothoraces, and hemothoraces may be quickly detected with this exam. The chest radiograph is also useful in confirming the correct positioning of an endotracheal tube or nasogastric tube. Other traumatic conditions, such as small pneumothorax, small hemothorax, parenchymal lung laceration, aortic trauma, tracheobronchial injury, cardiac injury, diaphragm rupture, and thoracic spine injury, usually require further imaging with computed tomography (CT). Multidetector CT (MDCT) scanners can quickly and accurately diagnose and display a wide variety of thoracic injuries. The use of multiplanar and volumetric images derived from the acquired axial images may not only aid in diagnostic evaluation but also better display the extent of injuries, and this may assist optimal treatment planning.

MDCT PROTOCOL FOR SUSPECTED THORACIC INJURY

Chest CT scans for suspected thoracic trauma should be performed with intravenous contrast material in order to demonstrate any sites of active bleeding and to opacify the heart, aorta, and thoracic blood vessels. CT scanning of the chest following trauma is best performed in the arterial phase after a 25- to 30-second delay. Scans should be acquired at thin detector configurations so that high-quality multiplanar volumetric reformations and a CT arteriogram can be produced from the thin axial images. Routine coronal and sagittal reformations of the chest are recommended on all chest trauma patients in order to better demonstrate injuries, particularly injuries to the major vessels, diaphragm, or spine, which are best shown on these planes. A detector configuration of 16 • 1.25 mm is preferable for 16-slice scanners, while 64-slice scanners would utilize axial slices having less than 1-mm thickness. The thin slices may be reformatted to 2.5 mm for viewing axial slices and transmitted to the Picture Archival Computer System (PACS) along with the coronal and sagittal reformations for formal examination interpretation. All axial and multiplanar images should be reviewed on soft tissue, lung, and bone windows.

INJURIES OF THE PLEURAL SPACE

A hemothorax, blood in the pleural space, may result from injury to the chest wall, diaphragm, lung, or mediastinal structures. CT may confirm a hemothorax when a pleural fluid collection in a trauma patient seen on CT measures blood density over 35 to 40 Hounsfield units (HU) (Fig. 2-1). A pneumothorax, air in the pleural space, may result from a lung injury, tracheobronchial injury, or esophageal rupture. The most common cause is lung injury associated with a rib fracture. A pneumothorax occurs in about 15% to 40% of patients with acute chest trauma. Many small and even moderate-sized pneumothoraces that are not visible on the supine chest film may be identified on CT. A pneumothorax seen on CT that cannot be identified on a supine chest film is referred to as an "occult" pneumothorax. Studies estimate that 10% to 50% of pneumothoraces seen on CT are not evident on the supine anteroposterior film. Radiographic signs of pneumothorax may be subtle. In the supine patient air collects in nondependent locations such as the anterior costophrenic sulcus. This region extends from the seventh costal cartilage to the eleventh rib in the midaxillary line. The air collection appears as an abnormal lucency in the lower chest or upper abdomen, frequently referred to as the "deep sulcus" sign. Additional signs of pneumothorax in a supine patient include a sharply outlined cardiac or diaphragmatic border and depression of the hemidiaphragm (Fig. 2-2). Detection of even a small pneumothorax is important as it may enlarge during positive-pressure ventilation or general anesthesia. A tension pneumothorax is an emergency condition resulting from a lung or airway injury associated with a one-way accumulation of air within the pleural space. As intrapleural pressure rises the mediastinal structures are compressed, decreasing venous return to the heart, leading to hemodynamic instability. Radiography and CT will show mediastinal shift to the contralateral hemithorax, hyperexpansion of the ipsilateral thorax, and depression of the ipsilateral hemidiaphragm.

ESOPHAGEAL INJURIES

Blunt trauma to the esophagus is extremely rare since this structure is well protected in the posterior mediastinum. Most esophageal injuries occur from penetrating or iatrogenic trauma. Blunt trauma may result in rupture or intramural hematoma. These injuries normally involve the upper thoracic esophagus or the lower esophagus just above the gastroesophageal junction. The most commonly accepted theory regarding the pathophysiology of rupture is similar to the mechanism in Boerhaave syndrome in that an increase in intraluminal pressure against a closed glottis results in a tear at the weakest point of the esophageal wall, usually the distal third of the esophagus on the left

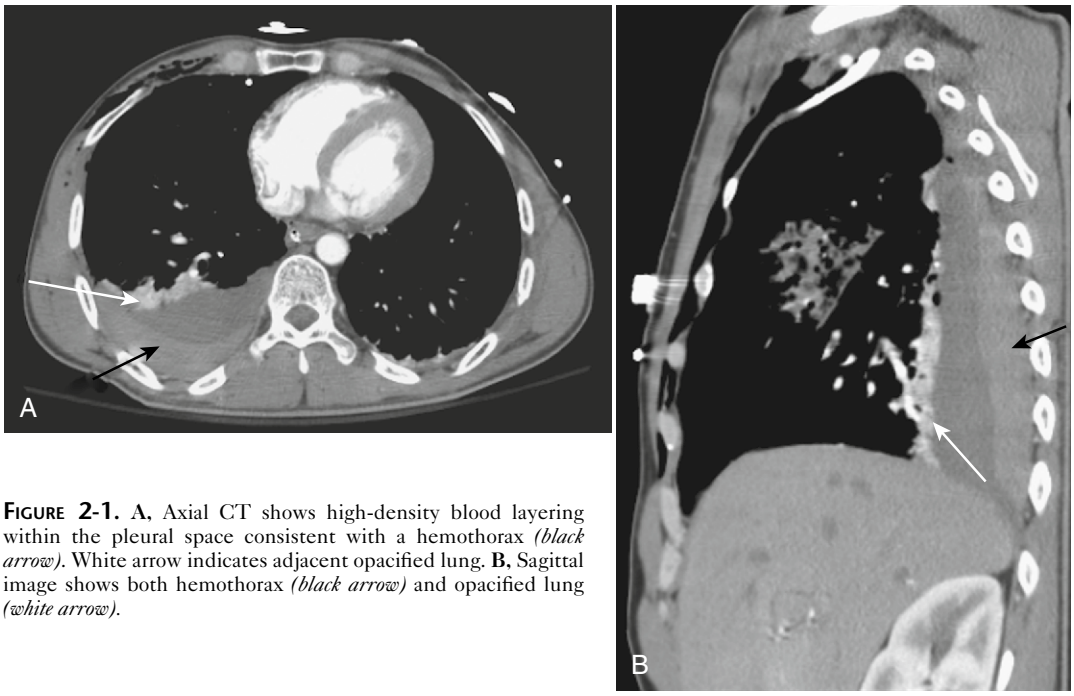


FIGURE 2-1. **A,** Axial CT shows high-density blood layering within the pleural space consistent with a hemothorax *(black arrow)*. White arrow indicates adjacent opacified lung. **B,** Sagittal image shows both hemothorax *(black arrow)* and opacified lung *(white arrow)*.

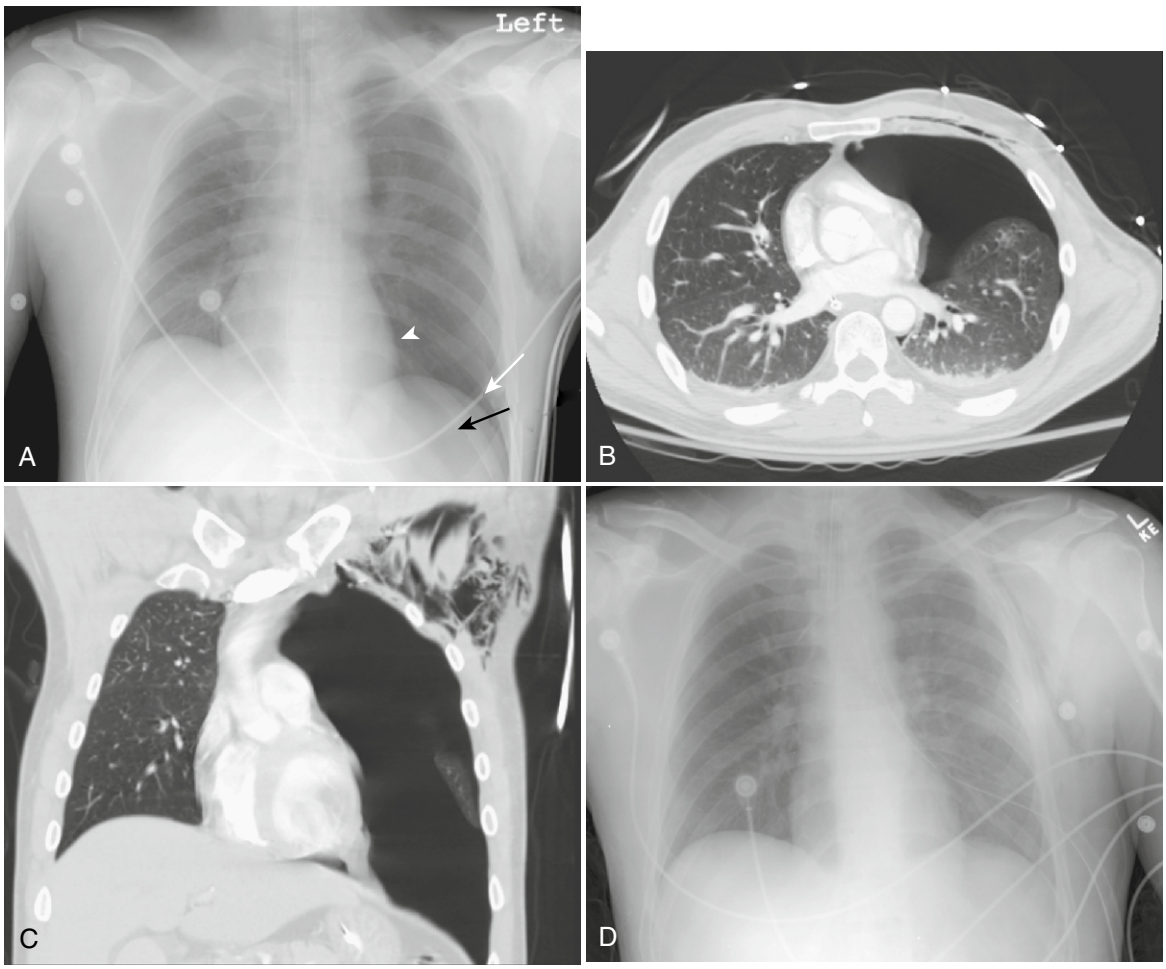


FIGURE 2-2. **A,** Anteroposterior chest radiograph findings of tension pneumothorax including the "deep sulcus" sign *(black arrow)*, sharply outlined cardiac and diaphragmatic border *(arrowhead)*, and depression of the hemidiaphragm *(white arrow)*. Note rightward deviation of the mediastinum consistent with tension. **B,** Axial image from MDCT demonstrates air collecting nondependently in the anterior costophrenic sulcus. Note rightward deviation of the heart indicating developing tension. **C,** Coronal image demonstrates depression of the hemidiaphragm and rightward deviation of the mediastinum. **D,** Chest tube placement results in normal positioning of the hemidiaphragm and mediastinum.

where there is less protection from the pleural lining and the heart. Other etiologies for injury include disruption of the esophageal blood supply, resulting in ischemia and late perforation, and a blast effect caused by a concomitant tracheal injury. Direct injury may also result from adjacent thoracic spine fractures or compression between the sternum and thoracic spine, as observed in high-speed road traffic accidents. Esophageal injuries are often associated with clinical symptoms, including blood in the esophagus or pain on swallowing. CT may suggest the diagnosis of traumatic esophageal perforation with the presence of pneumomediastinum, mediastinitis, hydropneumothorax, or leakage of oral contrast medium into the mediastinum or the pleural space. Water-soluble contrast esophagography, followed by flexible esophagoscopy, may be required to fully evaluate the site of injury.

CARDIAC INJURIES

Cardiac and pericardial injuries are uncommon with blunt thoracic trauma but do occur with severe blows to the anterior chest. The diagnosis of blunt cardiac injury relies on a high clinical suspicion. Cardiac injuries often occur in conjunction with sternal fractures. The anterior aspect of the heart that abuts the sternum is most vulnerable to injury. Patients with cardiac injuries may have an abnormal electrocardiogram and elevated cardiac enzymes. Cardiac injuries include cardiac contusion, cardiac rupture, pneumopericardium, hemopericardium, cardiac tamponade, and cardiac valve injury. Hemopericardium from a cardiac injury or cardiac rupture may quickly produce cardiac tamponade with hemodynamic compromise (Fig. 2-3). Cardiomegaly may be seen on the plain chest radiograph, while CT or cardiac sonography may confirm hemopericardium.

AORTIC AND GREAT VESSEL INJURIES

Injuries of the aorta account for a significant number of fatalities following blunt trauma. Seventy percent of all thoracic aortic injuries are fatal at the scene of trauma. Of patients who are transported to the hospital, 90% of aortic rupture occurs at the aortic isthmus, located at the junction of the posterior aortic arch and descending aorta, just distal to the origin of the left subclavian artery. The proposed

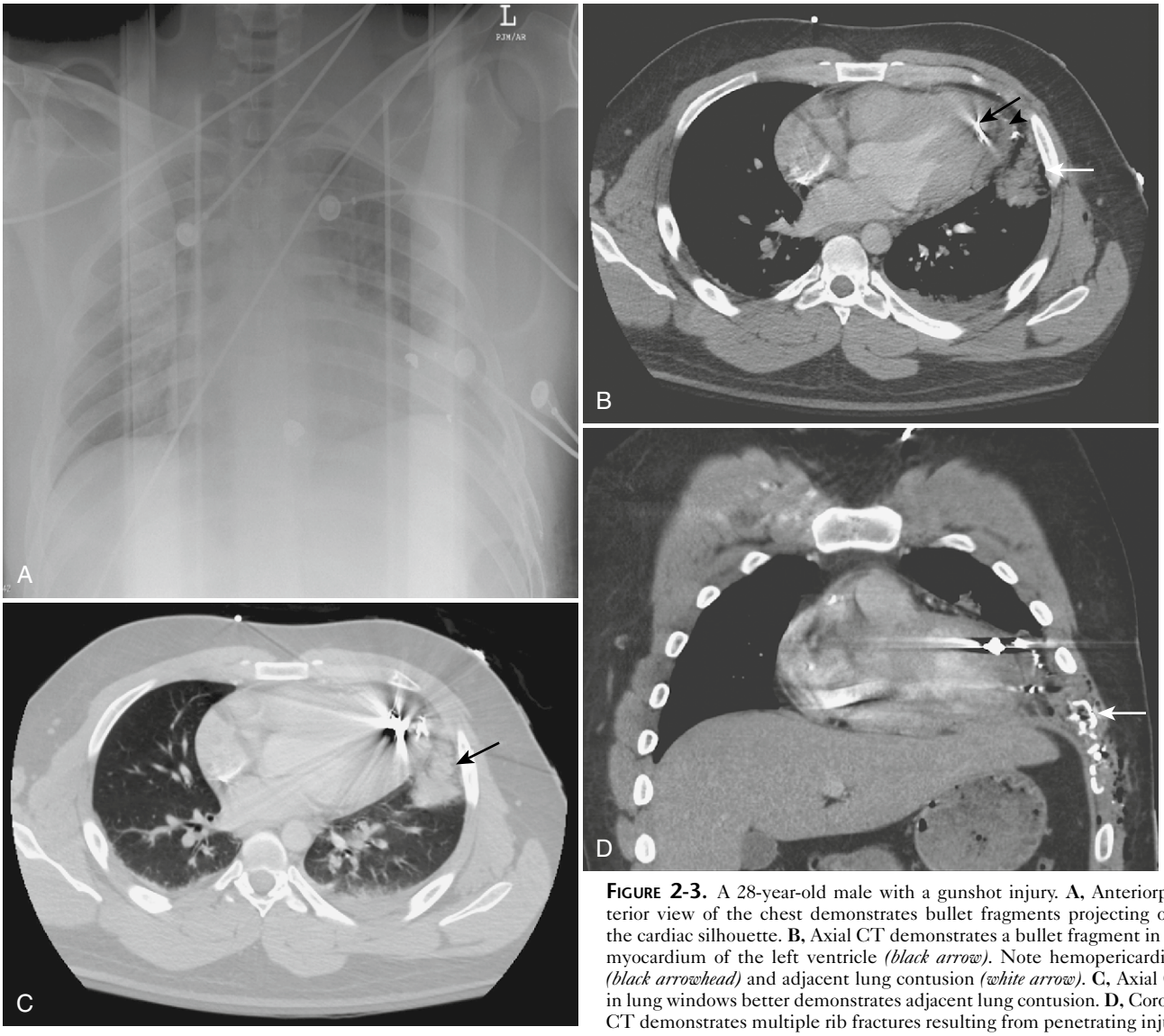


Figure 2-3. A 28-year-old male with a gunshot injury. **A,** Anteriorposterior view of the chest demonstrates bullet fragments projecting over the cardiac silhouette. **B,** Axial CT demonstrates a bullet fragment in the myocardium of the left ventricle *(black arrow)*. Note hemopericardium *(black arrowhead)* and adjacent lung contusion *(white arrow)*. **C,** Axial CT in lung windows better demonstrates adjacent lung contusion. **D,** Coronal CT demonstrates multiple rib fractures resulting from penetrating injury.

mechanism of injury is rapid deceleration producing shear injury at the site where the rate of deceleration of the mobile aortic arch differs from that of the relatively fixed descending aorta. In addition, bending stress occurs because the aorta is flexed over the left pulmonary artery and left mainstem bronchus. Only 5% of aortic injuries in clinical series involve the ascending aorta, and these injuries may be associated with life-threatening cardiac and pericardial injuries. Rarely, aortic injuries may involve the descending aorta at the level of the diaphragmatic hiatus.

A normal chest radiograph has a high negative predictive value (98%) but a low positive predictive value for aortic injury. The chest film findings suggestive of aortic injury include mediastinal widening greater than 8 cm, loss of the normal aortic arch contour, a left apical pleural cap, displacement of the nasogastric tube to the right, widened paraspinal lines, and loss of the descending aortic line. Most of the plain film findings of aortic injury are nonspecific. The gold standard for the diagnosis of aortic injury has traditionally been aortography; however, at most trauma centers today, aortography has been replaced with MDCT.

The sensitivity of CT has been reported to be 92% to 100% and specificity 62% to 100% for the detection of aortic injury. The accuracy of aortic trauma detection with CT has been improving in parallel with technological improvements in CT scanning. Current fast MDCT scanners decrease motion artifact and provide higher-quality two- and three-dimensional reformations for diagnosis and treatment planning.

The CT findings of aortic trauma include indirect signs, such as mediastinal hematoma surrounding the posterior aortic arch and proximal descending aorta, as well as the direct signs of intimal tear/flap, aortic contour abnormality, thrombus protruding into the aortic lumen, false aneurysm formation, pseudocoarctation, and extravasation of intravenous contrast material. If only direct signs are utilized, the sensitive and negative predictive value remains at 100% but the specificity increases to 96% (Fig. 2-4).

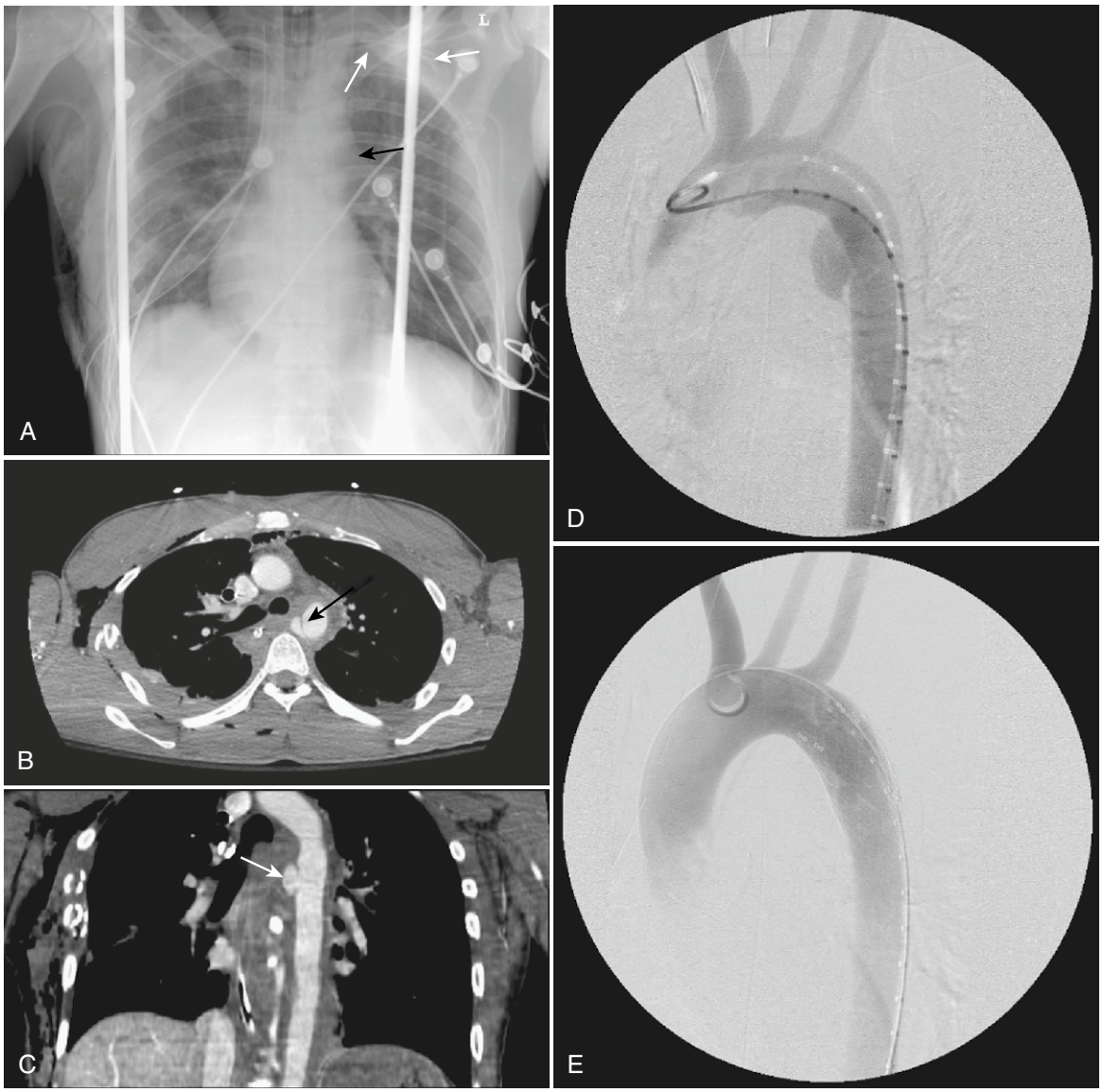


FIGURE 2-4. **A,** Portable chest radiograph shows an enlarged indistinct aortic arch *(black arrow)*, a left apical pleural cap, and upper rib fractures *(white arrows)*. **B,** Axial CT demonstrates mediastinal hematoma, intimal flap, and pseudoaneurysm *(arrow)*. **C,** Oblique coronal reformation shows the extent of pseudoaneurysm *(arrow)*. **D** and **E,** Thoracic aortography before and after treatment with an aortic stent.

A common aortic injury is a traumatic false aneurysm resulting from disruption of the vessel intima and media while the adventitia remains intact. The intravascular blood confined by only the adventitia bulges outward forming a pseudoaneurysm. In many cases, the aortic injury may be limited to a partial circumferential tear. CT findings typically consist of a saccular out-pouching demarcated from the aortic lumen by torn intima. It frequently results in hemomediastinum. Treatment of a pseudoaneurysm may today be performed with intravascular stent grafting. False positive examinations may be related to a prominent ductus diverticulum or an ulcerated atheromatous plaque. A traumatic pseudoaneurysm is usually surrounded by mediastinal blood whereas a ductus diverticulum and an ulcerated atheromatous plaque are not (Figs. 2-5 to 2-7).

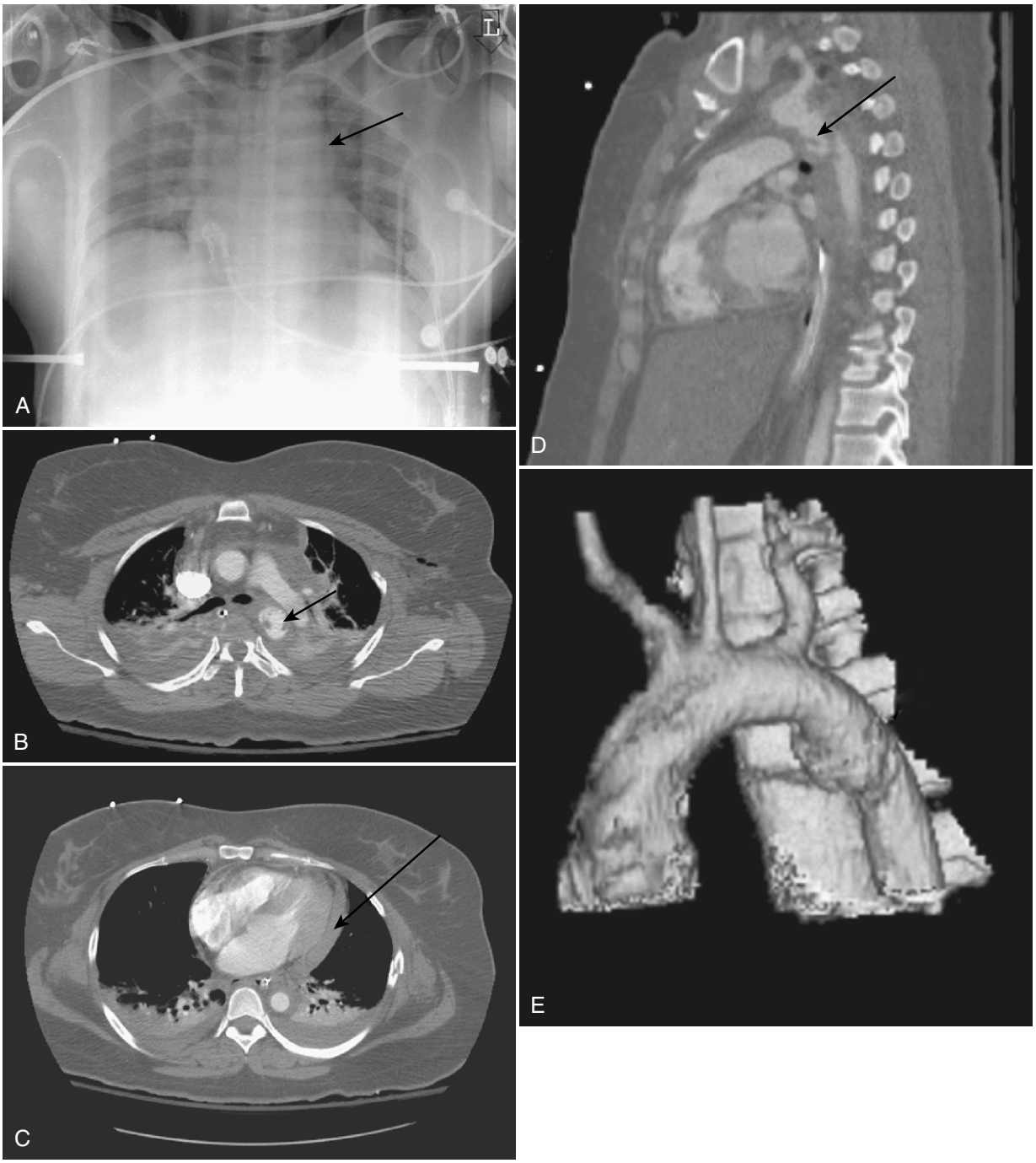


Figure 2-5. A 39-year-old female involved in a rollover motor vehicle accident. **A,** Portable chest radiograph demonstrates widened superior mediastinum *(arrow)*. **B,** Axial CT section shows intimal flap and pseudoaneurysm formation with extraluminal extension of contrast *(arrow)*. **C,** Lower axial section shows hemopericardium; the patient had cardiac enzyme elevation consistent with cardiac contusion *(arrow)*. **D,** Sagittal volume-rendered image shows pseudoaneurysm more clearly *(arrow)*. **E,** Three-dimensional images demonstrate pseudoaneurysm formation.

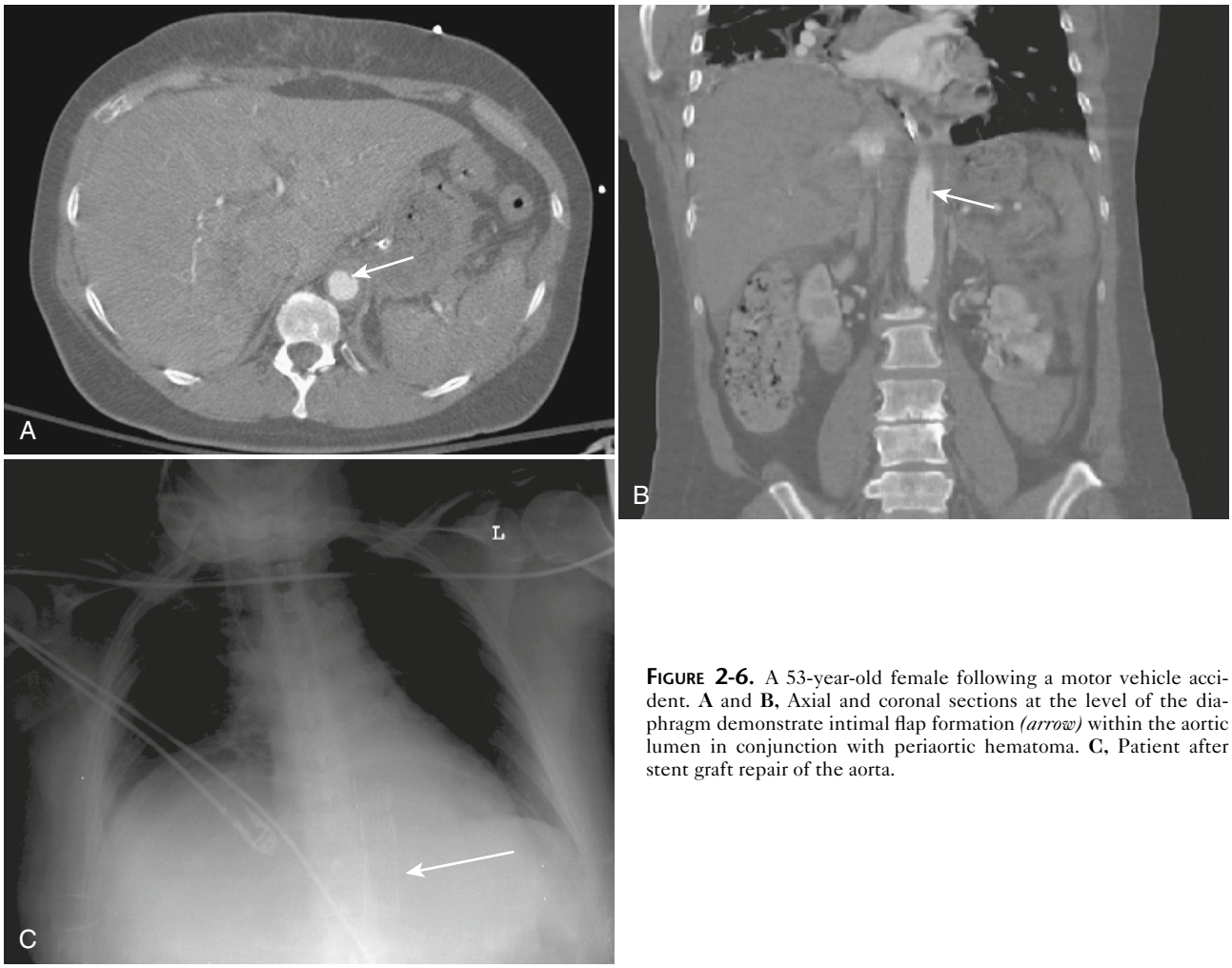


FIGURE 2-6. A 53-year-old female following a motor vehicle accident. **A** and **B,** Axial and coronal sections at the level of the diaphragm demonstrate intimal flap formation *(arrow)* within the aortic lumen in conjunction with periaortic hematoma. **C,** Patient after stent graft repair of the aorta.

LUNG INJURIES AND LUNG CONTUSION

Lung contusion results from traumatic extravasation of blood and edema fluid into the pulmonary interstitium and air spaces of the lung as a result of disruption of alveolar-capillary integrity without significant disruption of the pulmonary parenchyma. The injury is caused by energy transmitted directly to the lung from an impact to the overlying chest wall. On radiographs, contusion appears as patchy areas of consolidation (Fig. 2-8). When extensive, radiographs may show diffuse dense homogeneous lung consolidation. These opacities resulting from lung contusion are said to differ from those of bronchopneumonia and aspiration in that they are not confined to the anatomic limits of various segments or lobes. This may be difficult to definitively ascertain on an initial anteroposterior chest radiograph. Contusion may be absent on the initial chest film but usually becomes evident within 6 hours of injury. CT can usually detect pulmonary contusion immediately after injury. Contusions usually resolve rapidly and disappear in a few days.

CT may show areas of consolidation often directly beneath the site of injury in a nonsegmental distribution and often sparing 1 to 2 mm of the subpleural lung parenchyma. The opacities may be single or multiple and both coup and contracoup contusions may be identified. Contusion is often seen surrounding pulmonary lacerations.

LUNG LACERATION

Pulmonary lacerations are tears of the lung parenchyma that fill with air, blood, or both. If the laceration fills with air the injury is termed a traumatic pneumatocele. If it fills with blood a spherical hematoma or hematocele forms. If both air and fluid are present, an air–fluid level may be identified. The spherical shape of intraparenchymal lacerations has been attributed to normal elastic recoil of the lung parenchyma pulling centrifugally in all directions on the disrupted region (Fig. 2-9).

On chest radiograph, lacerations may initially be obscured by surrounding lung contusion; however, they become visible once the contusion clears. In contrast, acute lung lacerations are nearly always detected on CT imaging. Four types have been described with blunt trauma (Fig. 2-10): type 1, compression rupture laceration, resulting from sudden compression of a pliable chest wall wherein the air-containing lung is ruptured; type 2, compression shear laceration, which occurs in a para-vertebral lower lobe of the lung (the mechanism occurs when the more pliable lower

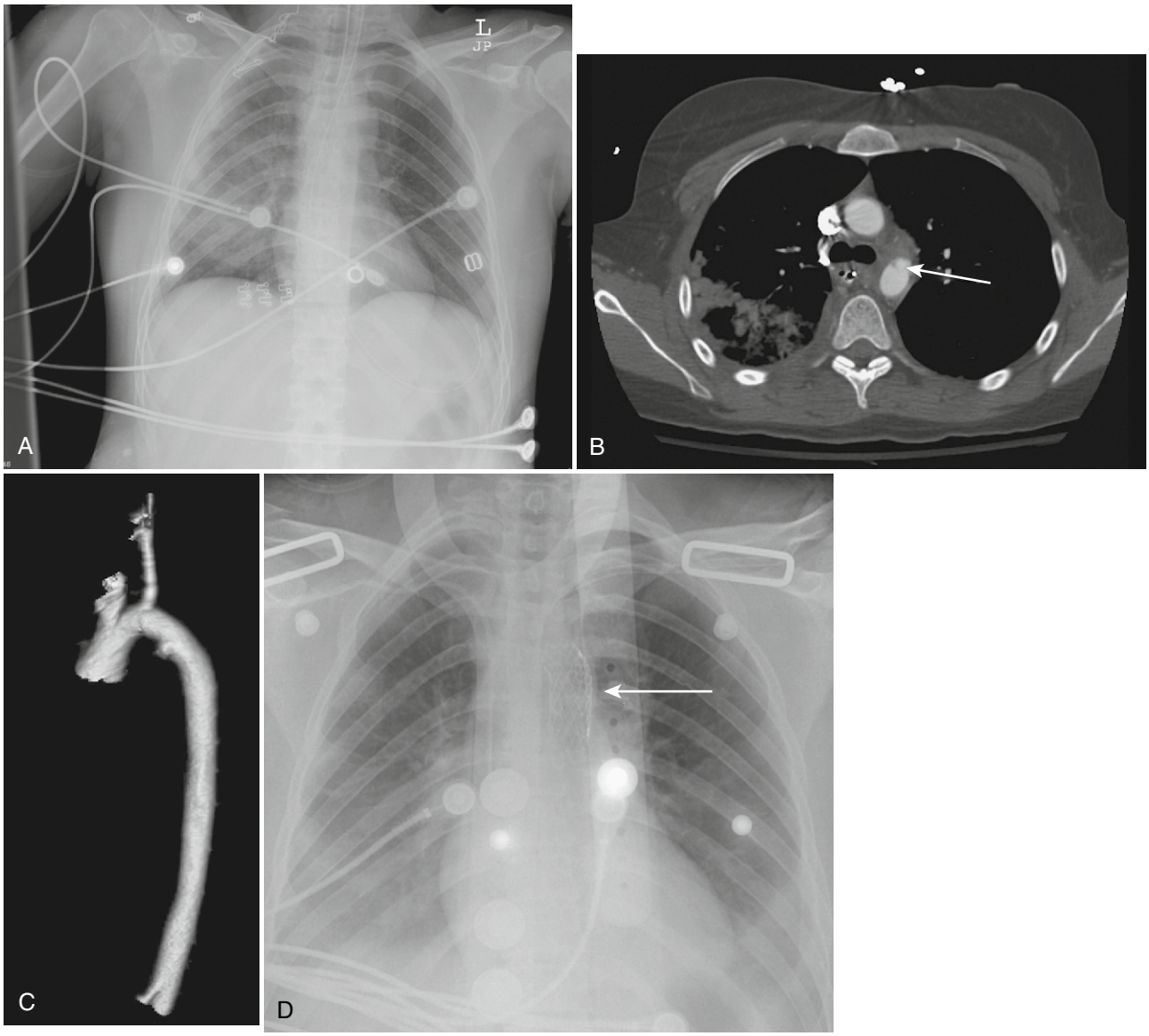


Figure 2-7. A 21-year-old patient after a high-speed motor vehicle accident. The patient was an unrestrained driver. **A,** Portable anteroposterior chest radiograph showing patchy opacity in the right lung representing pulmonary contusion. **B,** Axial CT section demonstrates mediastinal hematoma with intimal flap formation *(arrow)* and contour irregularity of the aortic lumen. **C,** Three-dimensional reformation demonstrates a small pseudoaneurysm. **D,** Note stent graft placement for treatment of pseudoaneurysm.

chest wall is acutely compressed causing the lower lobe to shift suddenly across the vertebral body in a shearing-type injury, Fig. 2-11); type 3, rib penetration tear, causing a peripheral injury adjacent to a rib fracture (a pneumothorax is generally associated with this type of injury as it represents a penetrating injury); type 4, adhesion tear, which results from tear of prior pleural-pulmonary adhesions causing the lung to tear when the overlying chest wall is violently moved inward or fractured. Lung lacerations may also result from penetrating trauma, most frequently from stab wounds and gunshot wounds. Pulmonary lacerations are better shown and more extensively evaluated with CT than with plain films. Unlike pulmonary contusion, lung lacerations may take weeks or months to heal and may result in residual lung scarring. Frequently, as lacerations resolve they appear as lung nodules (Fig. 2-12).

TRACHEOBRONCHIAL INJURIES

Injuries to the airways are uncommon, occurring in approximately 1.5% of blunt trauma cases. Tears and fractures of the tracheobronchial tree are frequently not recognized on initial imaging, and delayed diagnosis is common. Eighty percent of tracheobroncheal injuries occur within 2 cm of the carina. Rupture of the left and right mainstem bronchi occur with equal frequency. Chest radiograph findings most commonly include pneumomediastinum and subcutaneous emphysema (Fig. 2-13). Air continuously leaks through the rupture and flows into the surrounding mediastinal soft tissues with dissection up into the neck. Pneumomediastinum is an anticipated accompaniment of tracheobronchial injury. Large volumes of pneumomediastinum are easy to identify on plain radiographs, but volumes may

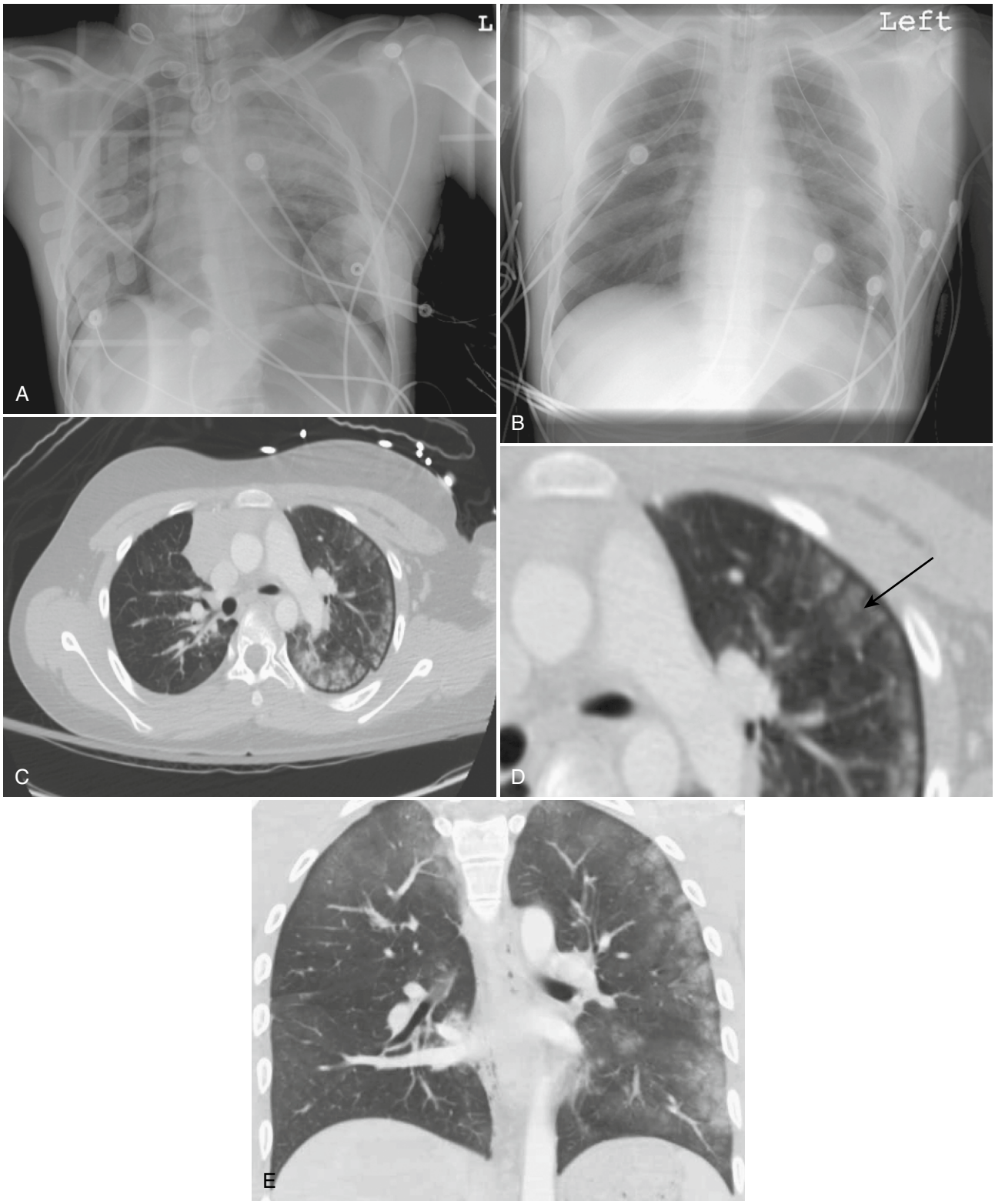


FIGURE 2-8. A 19-year-old male patient following a motor vehicle accident. **A,** Initial chest radiograph demonstrates left upper lung patchy consolidation consistent with contusion. **B,** Chest radiograph 3 days later demonstrates rapid resolution of pulmonary contusion. **C,** Axial section through a CT scan demonstrates left-sided contusion affecting both the upper and lower lobes, not confined to a single lobe. **D,** There is sparing of 1 to 2 mm of subpleural space *(arrow)*. **E,** Coronal image demonstrates extent of lung contusion.

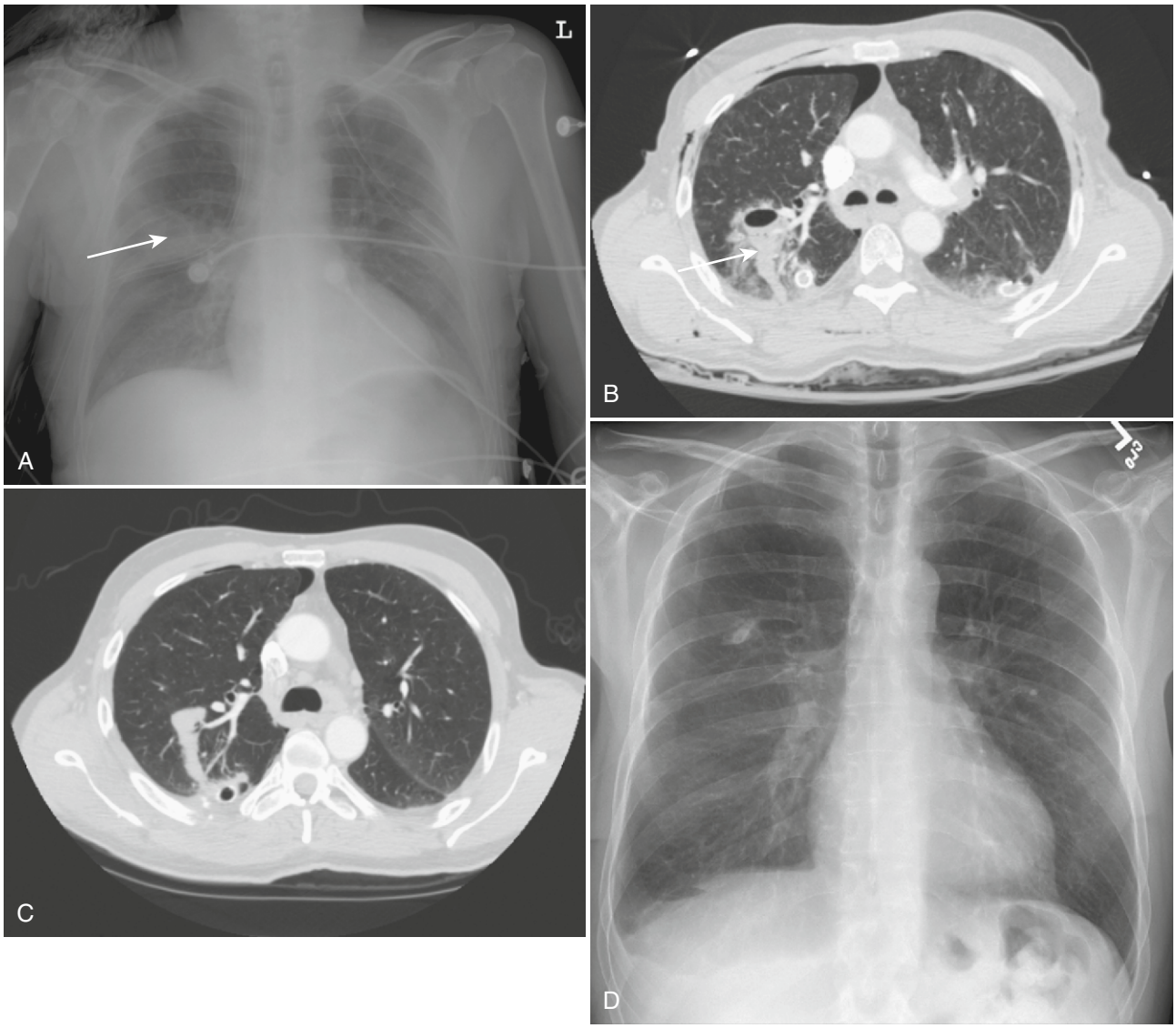


Figure 2-9. A 55-year-old patient stabbed in the chest. **A,** Anteroposterior chest radiograph demonstrates patchy opacities surrounding a lucent cavity lesion consistent with pulmonary pneumatocele with surrounding contusion resulting from penetrating stab injury. **B,** Axial CT image demonstrates lung laceration with track to the skin surface. **C,** Follow-up chest CT 6 days after injury demonstrates resolution of contusion with involution of hematocele. **D,** Remote follow-up chest radiograph demonstrates scarring related to laceration.

not be visible on the initial portable chest radiograph. Pneumomediastinal air should initiate a search for possible tracheobronchial injury; however, there are other causes of pneumomediastinum, including complications of dyspnea, aggressive mechanical ventilation, and esophageal rupture. In the presence of a tracheobronchial laceration, air dissects into fascial planes as a consequence of the continuous air leak. Hence, on sequential radiographs, the subcutaneous emphysema is expected to persist or increase (Fig. 2-14).

Tracheal lacerations are usually longitudinal and located at the junction of the cartilaginous and membranous parts of the trachea. Tears of the trachea or proximal left main bronchus normally cause central dissection of air with mediastinal and cervical emphysema without pneumothorax. In bronchial injuries the majority of cases also have an associated pneumothorax. Pneumothorax in patients with tracheobronchial transection is the result of rupture of the mediastinal pleura, or injury to the right mainstem bronchus or distal left bronchus. Air is allowed to enter the pleural space on the ipsilateral side. The classic clinical feature of this condition is a pneumothorax that does not resolve despite chest tube suction secondary to a continuous leakage of air through the airway rupture. However, resolution of a pneumothorax after chest tube placement does not exclude the diagnosis. Another pathognomonic finding is that of a "fallen lung," which is a sign of complete bronchial transection. This occurs when the lung collapses toward the lateral chest wall or diaphragm, rather than toward the pulmonary hilum, which is the usual situation.

Other signs of tracheobronchial injury include a sharply angulated bronchus, bronchial discontinuity, and bronchial "cut-off." Abnormalities of an endotracheal tube

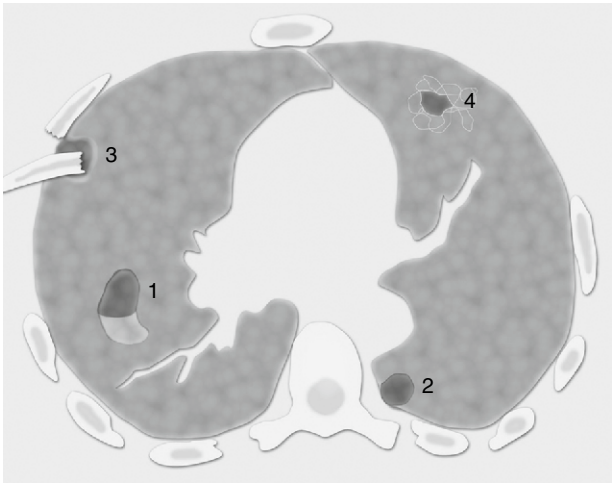


FIGURE 2-10. Four types of pulmonary lacerations. (1) Compression rupture injury, (2) compression shear injury, (3) rib penetration injury, and (4) adhesion tear injury.

balloon may also be noted with tracheal laceration. The balloon may appear overinflated or more spherical as it actually herniates through a vertical laceration of the trachea. An extratracheal location of the endotracheal tube might be seen, but it is rare. All of these findings are better depicted on CT than on plain radiography. CT can reveal the exact site of tracheal injury by directly showing focal defects or the circumferential absence of the tracheal wall, a contour deformity, or abnormal communication with other mediastinal structures. CT can show more subtle secondary signs, such as smaller volumes of pneumomediastinum, than can the chest radiograph.

The diagnosis of tracheobronchial injury should be confirmed by flexible bronchoscopy. Late complications of untreated tracheobronchial injury include bronchial stenosis, recurrent pneumonia, and bronchiectasis. Prompt diagnosis and treatment generally lead to good functional recovery.

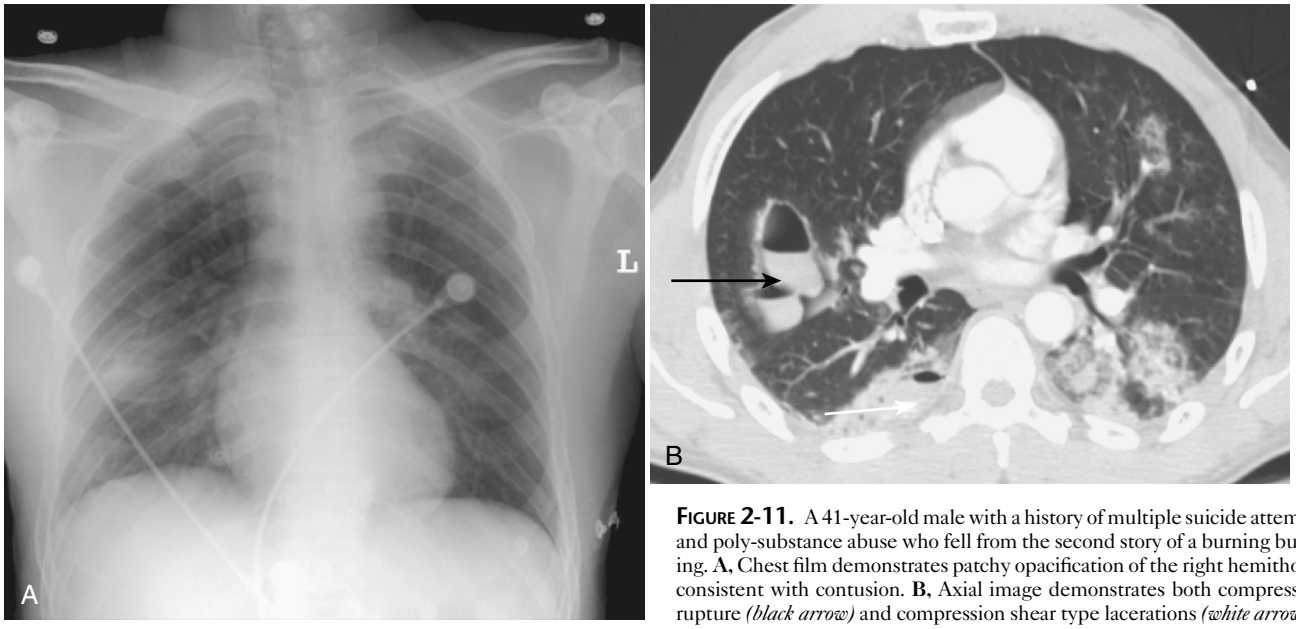


FIGURE 2-11. A 41-year-old male with a history of multiple suicide attempts and poly-substance abuse who fell from the second story of a burning building. **A,** Chest film demonstrates patchy opacification of the right hemithorax consistent with contusion. **B,** Axial image demonstrates both compression rupture *(black arrow)* and compression shear type lacerations *(white arrow)*.

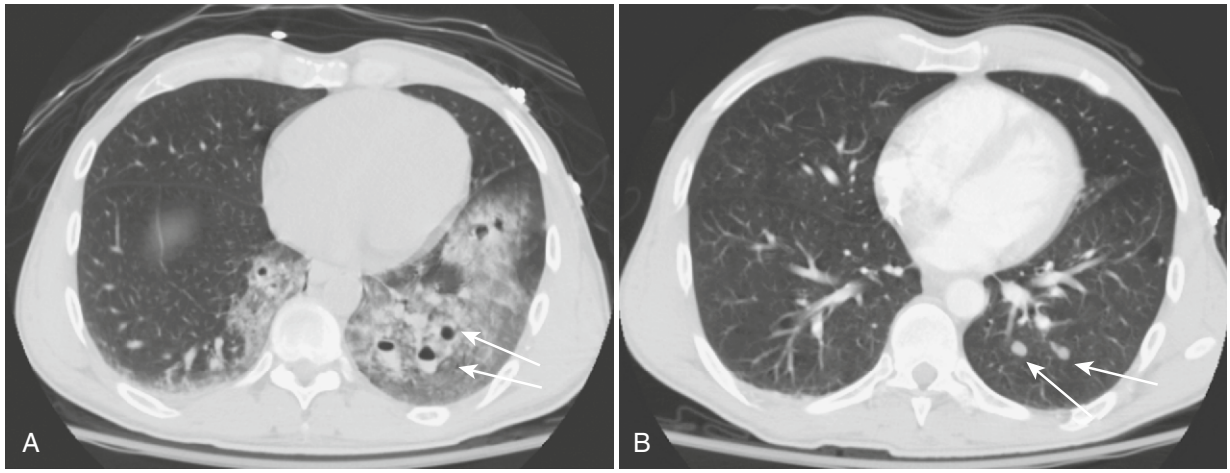


FIGURE 2-12. A 40-year-old male after a fall from a third floor window. **A,** Initial axial CT image demonstrates multiple lung lacerations *(arrows)* with surrounding contusion. **B,** Follow-up CT 3 weeks after initial event demonstrates involution of hematoceles, which now have the appearance of pulmonary nodules.

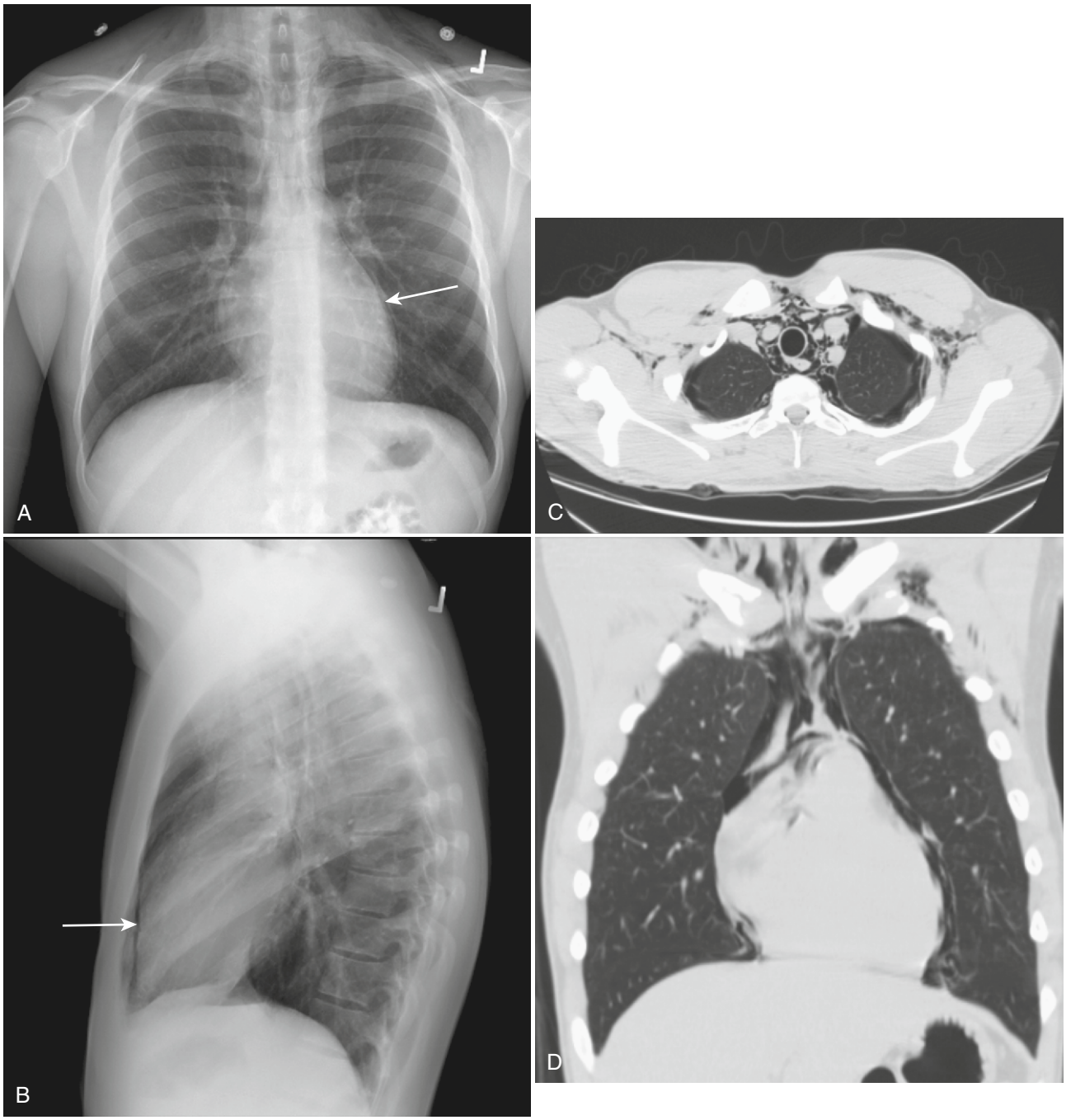


Figure 2-13. A 22-year-old male after a motor vehicle accident. **A** and **B,** Posteroanterior and lateral view of the chest demonstrate both pneumomediastinum *(arrow)* and subcutaneous emphysema. **C** and **D,** Axial and coronal CT images demonstrating extensive pneumomediastinum.

DIAPHRAGMATIC INJURIES

Diaphragmatic rupture is an uncommon injury seen in about 5% of patients undergoing laparotomy or thoracotomy for trauma. The postulated mechanism for blunt diaphragmatic injuries is a lateral blow causing shearing of the diaphragm and disruption of the attachments to the chest wall with concomitant increase in intra-abdominal pressure resulting from a frontal impact. Hence, diaphragm rupture is more common with lateral impact motor vehicle collisions. Early diagnosis of diaphragmatic rupture is clinically important, as complications related to visceral herniation through the lacerated diaphragm may result in respiratory compromise due to impairment of lung inflation. As well, visceral incarceration may lead to strangulation and possible perforation.

Left-sided injuries are more common, having a reported left-to-right ratio of 3:1. Bilateral and central tendon ruptures are uncommon. The increased frequency of left-sided injury has been attributed to an area of congenital weakness in the posterolateral diaphragm with central radiation of the tear. Right-sided injuries are thought to be less frequent because of the inherent increased strength of the right hemidiaphragm and the protective effect of the liver (Fig. 2-15).

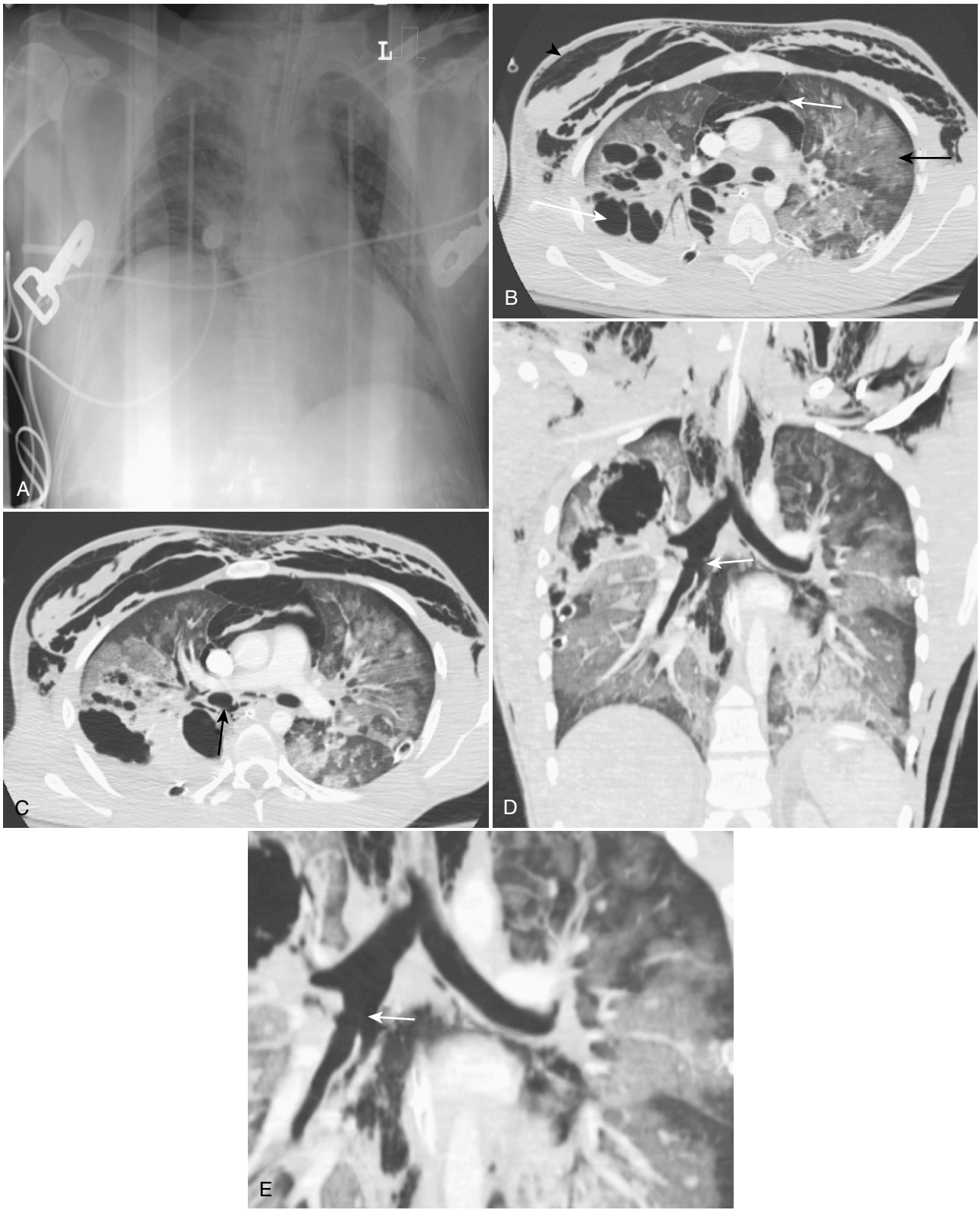


FIGURE 2-14. An 18-year-old patient after a motor vehicle crash involving a manhole cover, which blew from the street and acted as a projectile into a front window of a moving truck. The patient was an unrestrained passenger and was struck by the manhole cover, sustaining maxillofacial, right humerus, right clavicle, and upper thoracic injuries, among others. **A,** Portable anteroposterior image of the chest demonstrates extensive subcutaneous emphysema and patchy opacification of the lungs consistent with contusion. **B,** Axial image demonstrates lung contusion and lacerations. There is extensive subcutaneous emphysema *(arrowhead)* and pneumomediastinum. **C,** Axial image demonstrates a laceration in the posterior aspect of the right bronchus intermedius *(arrow)*. **D,** Coronal image demonstrates bronchial laceration in the bronchus intermedius. **E,** Thick-section maximal intensity projection improves visualization of the laceration.

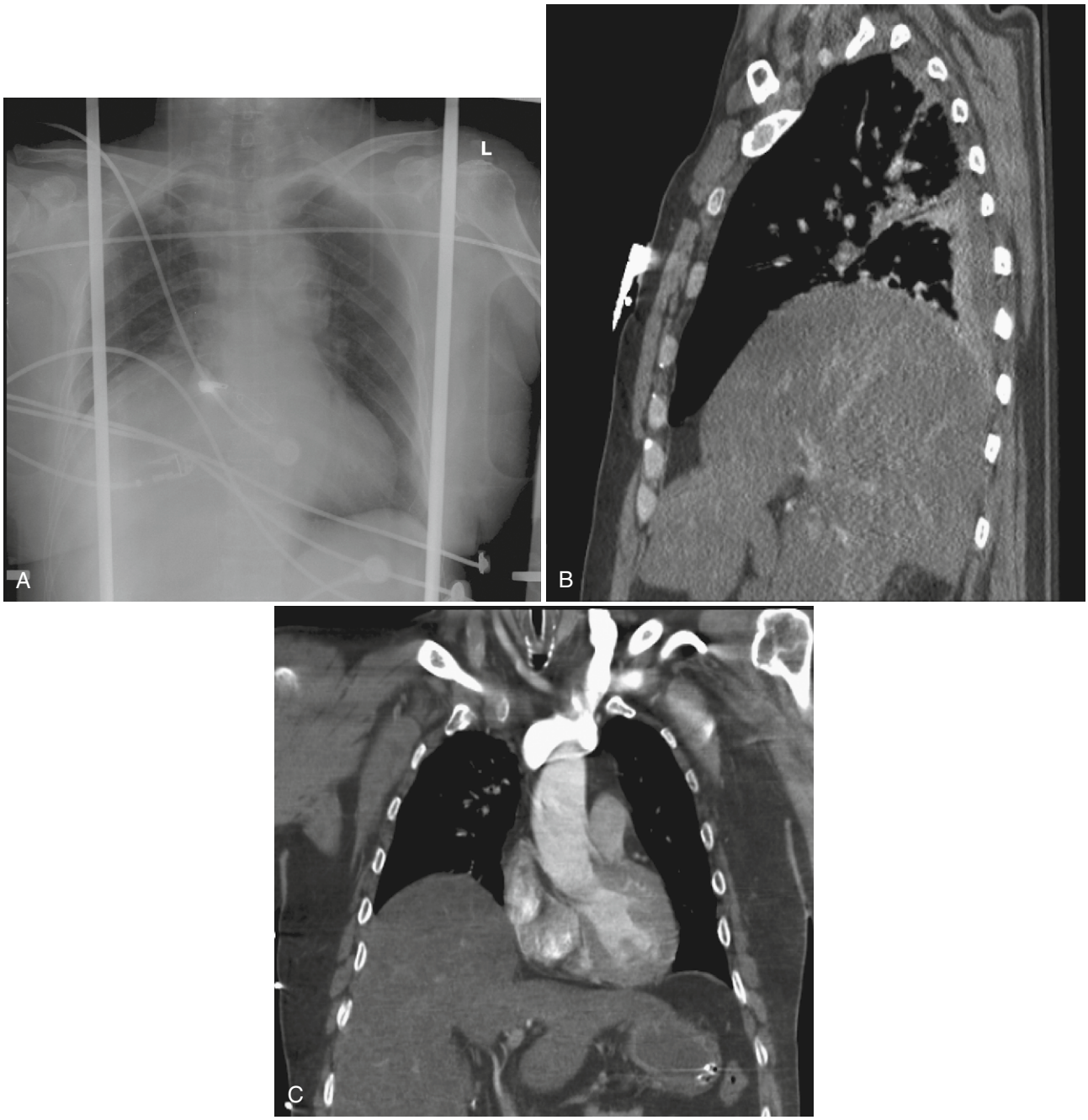


Figure 2-15. A 19-year-old male after a fall. **A,** Anteroposterior view of the chest demonstrates elevation of the right hemidiaphragm. **B,** Sagittal CT image demonstrates that a portion of the upper third of the liver abuts the posterior chest wall, consistent with the "dependent viscera" sign. **C,** Coronal CT image shows elevation of the liver through a diaphragmatic defect.

Imaging of diaphragmatic rupture may be difficult owing to the great variation in the normal diaphragm. These normal variants include incidental posterolateral diaphragmatic defects (Bochdalek hernia), localized diaphragmatic thinning (i.e., eventration), and areas of diaphragmatic discontinuity. These defects of the diaphragm advance with age and are uncommon in younger age groups.

The chest radiograph is usually the initial imaging examination of trauma patients. The supine positioning and portable technique may limit the ability to evaluate for diaphragmatic integrity. The chest radiograph may show an intrathoracic location of abdominal viscera with possible focal constriction known as the "collar" sign (Fig. 2-16). A nasogastric tube tip may be visible above the left hemidiaphragm. Significant elevation of the hemidiaphragm without associated atelectasis may be a sign of diaphragm rupture (Fig. 2-17).

Today, MDCT axial scans combined with high-quality coronal and sagittal reformations may show both large and small ruptures of the diaphragm, in addition to showing any abdominal organs herniated across the rupture. CT signs of diaphragm injury include the direct visualization of injury, intrathoracic herniation of viscera with a "collar" sign, the "dependent viscera" sign, and peridiaphragmatic

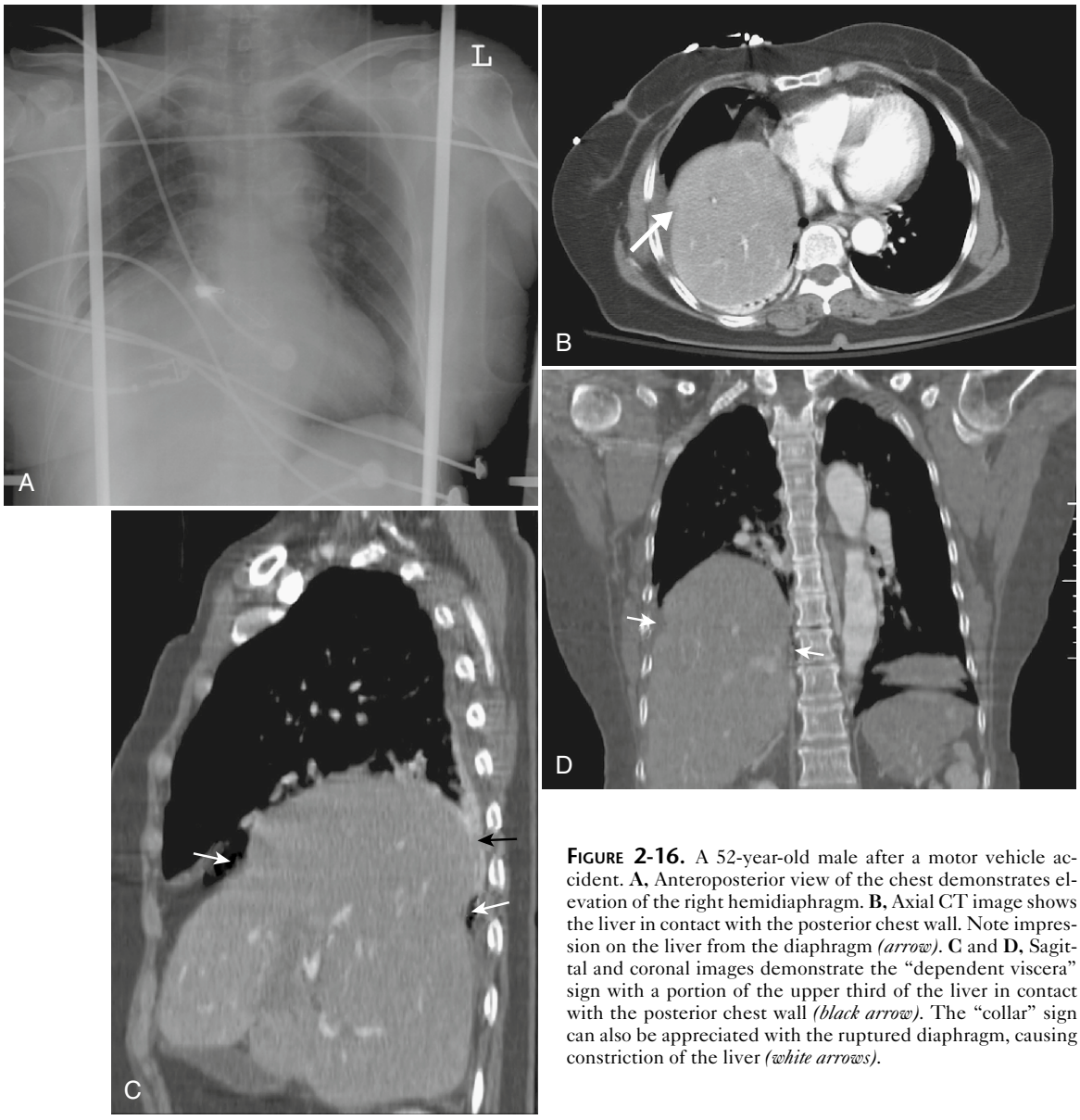


FIGURE 2-16. A 52-year-old male after a motor vehicle accident. **A,** Anteroposterior view of the chest demonstrates elevation of the right hemidiaphragm. **B,** Axial CT image shows the liver in contact with the posterior chest wall. Note impression on the liver from the diaphragm *(arrow)*. **C** and **D,** Sagittal and coronal images demonstrate the "dependent viscera" sign with a portion of the upper third of the liver in contact with the posterior chest wall *(black arrow)*. The "collar" sign can also be appreciated with the ruptured diaphragm, causing constriction of the liver *(white arrows)*.

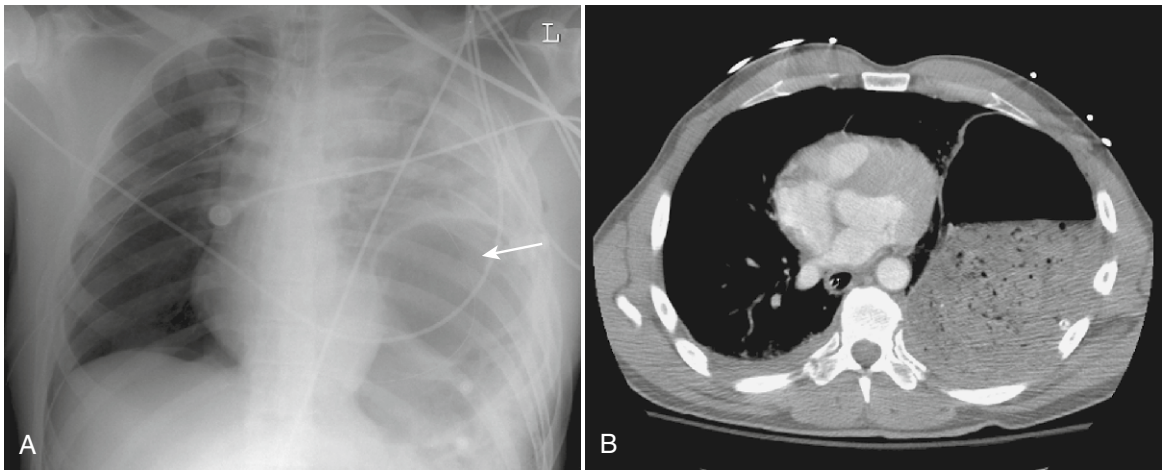


FIGURE 2-17. A 25-year-old male patient ejected from a motor vehicle following a crash. **A,** Anteroposterior view of the chest demonstrates a nasogastric tube within the lumen of the stomach, which is located in the left chest *(arrow)*. **B,** Axial CT image shows the stomach abutting the posterior chest wall. Note the shift of the mediastinum to the right.

active contrast extravasation. Additional findings of hemothorax, hemoperitoneum, and adjacent visceral injury may increase the suspicion of diaphragm injury. Of particular note, intrathoracic herniation of viscera is highly sensitive (up to 90.9%) when limited to left-sided injury. When abdominal viscera herniate through a diaphragm tear, the edges of the diaphragm may constrict the herniated organ, resulting in the "collar." The "dependent viscera" sign is diagnostic of diaphragm rupture (Fig. 2-18). An intact diaphragm prevents the upper abdominal viscera from directly contacting the posterior chest wall in the supine patient. Conversely, when the diaphragm is torn, the viscera may lie dependently against the posterior chest wall.

INJURIES OF THE THORACIC SKELETON

Skeletal injuries of the thorax may be apparent on initial portable chest radiograph imaging. Therefore, a careful evaluation for rib fractures should be performed. Knowledge of the presence of rib fractures may result in a CT scan for further evaluation given that the fractures may be a harbinger of more extensive underlying injury. Fractured ribs may lacerate the pleura or lung. Upper rib fractures indicate "high-energy" trauma, as these ribs are relatively well protected by the shoulder girdle and adjacent musculature. Upper rib fractures may be associated with injuries of the aorta, great vessels, or brachial plexus. Lower rib fractures may be associated with injuries to the liver, spleen, or kidneys. Flail chest occurs when five contiguous simple or three contiguous segmental rib fractures occur and result in paradoxical movement of the chest wall (Fig. 2-19). Flail chest may lead to altered chest wall mechanics and interfere with ventilation, and may lead to respiratory failure. There is a much greater incidence of rib fractures in older patients, whose ribs are fairly inelastic, as compared with children where the incidence of fracture is low secondary to more pliable and resilient ribs. Chest radiographs are limited, as they may show only 40% to 50% of rib fractures. Nearly all skeletal injuries are better shown with CT.

Rarely, a segment of lung may herniate through a defect in the chest wall created by rib or costochondral fracture (Figs. 2-20 and 2-21). The incidence of transthoracic

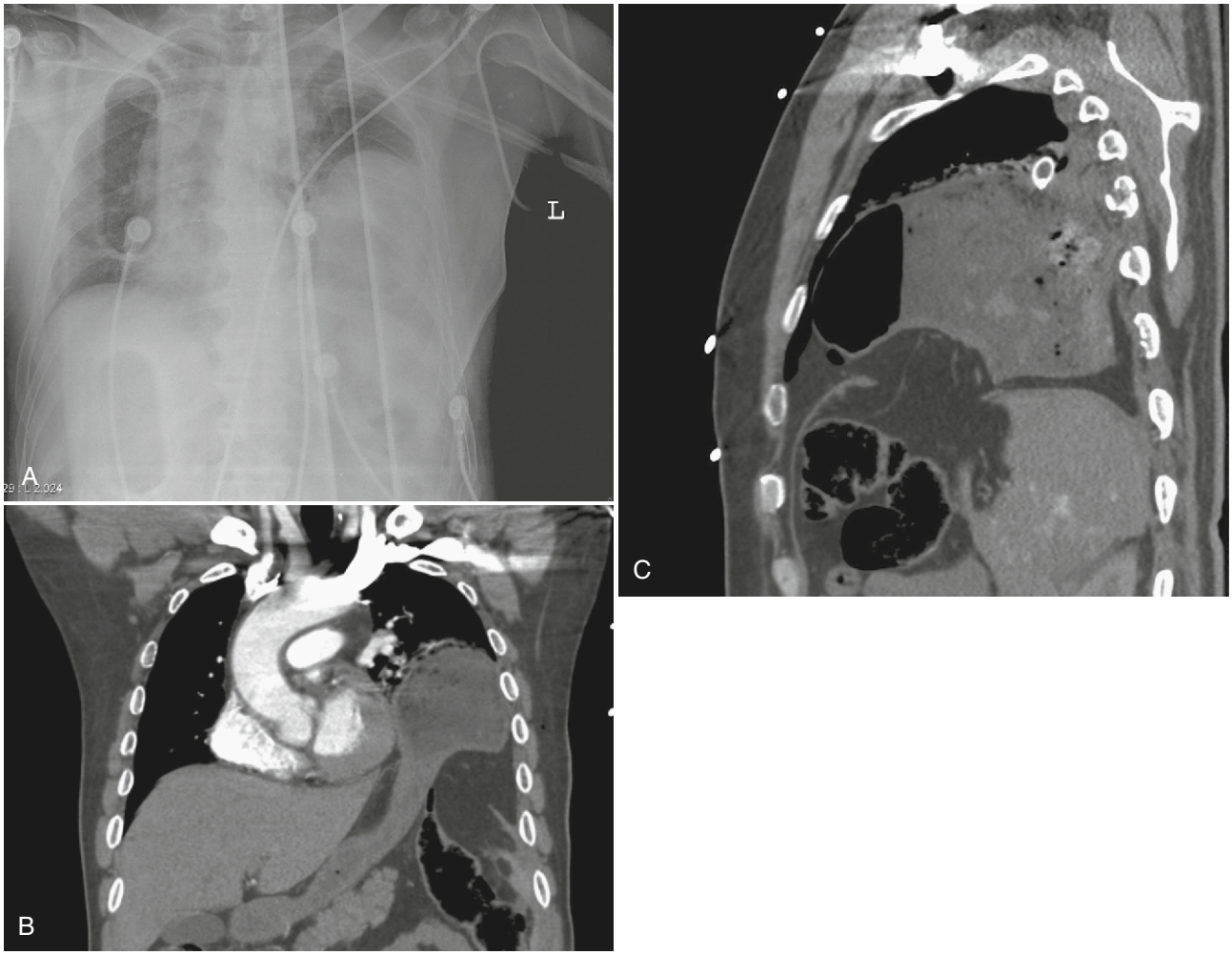


Figure 2-18. A 42-year-old male after a motor vehicle collision. **A,** Anteroposterior view of the chest demonstrates elevation of the left hemidiaphragm. **B** and **C,** Coronal and sagittal CT images demonstrate herniation of the stomach through a defect in the diaphragm. Again, note that the "dependent viscera" and "collar" signs are present.

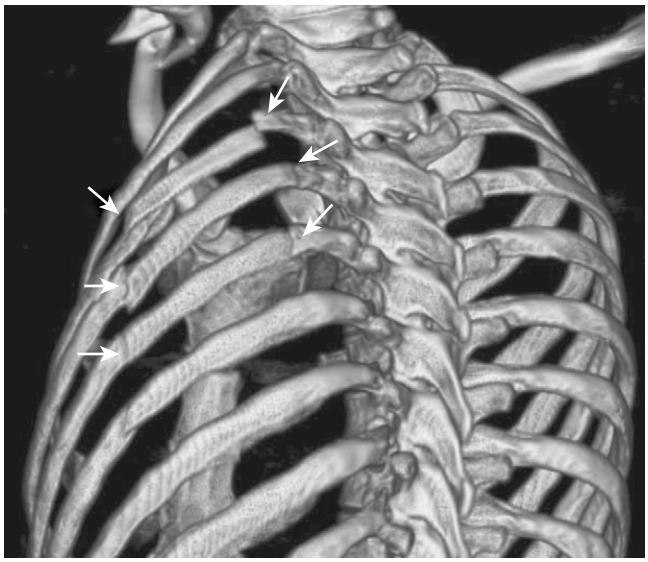


FIGURE 2-19. Three-dimensional reformation from a chest CT demonstrates segmental fractures of three posterior ribs *(arrows)*. This results in a flail chest.

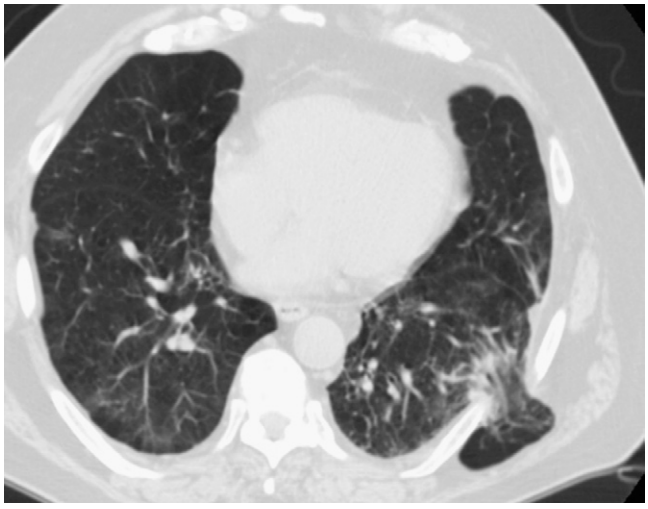


FIGURE 2-20. Axial CT image demonstrates herniation of lung parenchyma through the chest wall following ejection from a motor vehicle.

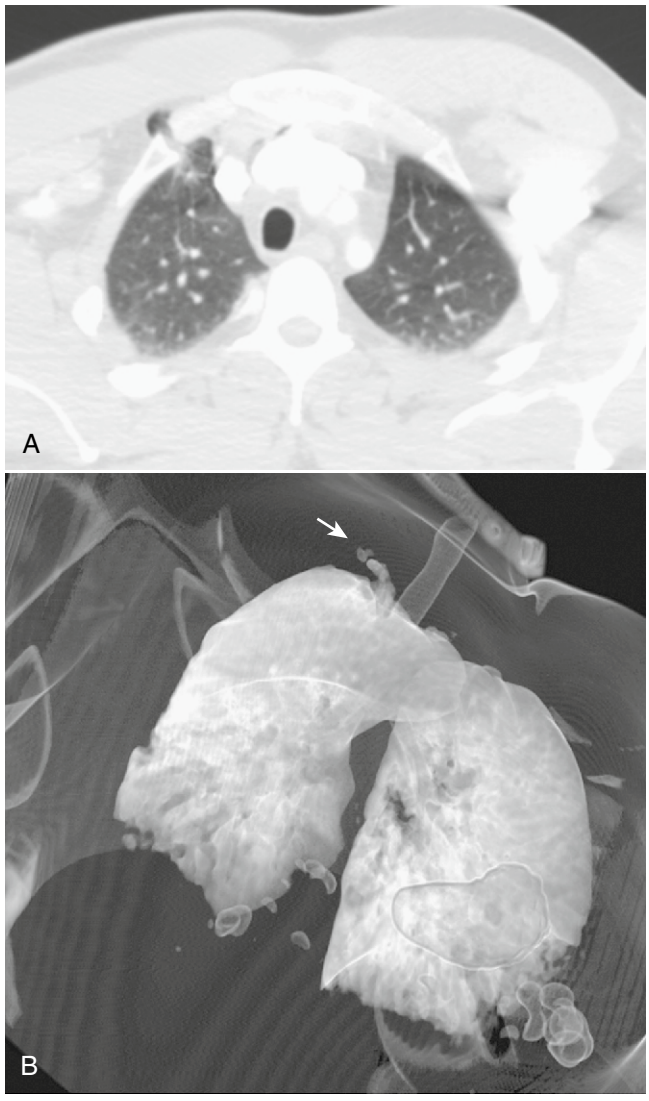


FIGURE 2-21. **A,** Axial CT image demonstrates herniation of the lung through a fracture at the costochondral junction. **B,** Three-dimensional reformation shows the herniated portion of the lung *(arrow)*.

lung herniation increases with the use of positive-pressure ventilation. Lung herniation may occur as a result of blunt chest trauma or iatrogenic surgical trauma. The herniated lung may become entrapped or strangulated. Since lung herniation may increase with positive-pressure ventilation, it may require treatment before mechanical ventilation and general anesthesia.

Other common injuries of the thoracic skeleton include scapular fractures, sternal fractures, sternoclavicular dislocation, and thoracic spine injuries. Posterior sternoclavicular dislocation typically results from a posterior blow to the shoulder or a blow to the medial clavicle; the latter results in a posteriorly displaced clavicular head relative to the manubrium (Fig. 2-22). Serious morbidity and even death have been associated with posterior dislocation of the clavicle at the sternoclavicular joint, as the displaced clavicle head may impinge on or injure the trachea, esophagus, great vessels, or major nerves in the superior mediastinum. Anterior sternoclavicular dislocations usually result from an anterior blow to the shoulder. Anterior dislocations are more common than posterior dislocations, and typically are less dangerous as there is no significant risk of great vessel injury. Sternoclavicular dislocation is generally well shown by CT.

Sternal fractures are usually not seen on the anteroposterior portable chest radiograph and may be difficult to see on the lateral chest radiograph. However, nearly all sternal fractures are visible on CT, especially on sagittal reformations (Fig. 2-23). As well, CT frequently shows any associated retrosternal hematoma. Sternal fractures have a high association with both aortic and cardiac injuries. Most patients with sternal fractures are monitored for myocardial contusion with serial enzyme analysis and telemetry monitoring (Fig. 2-24).

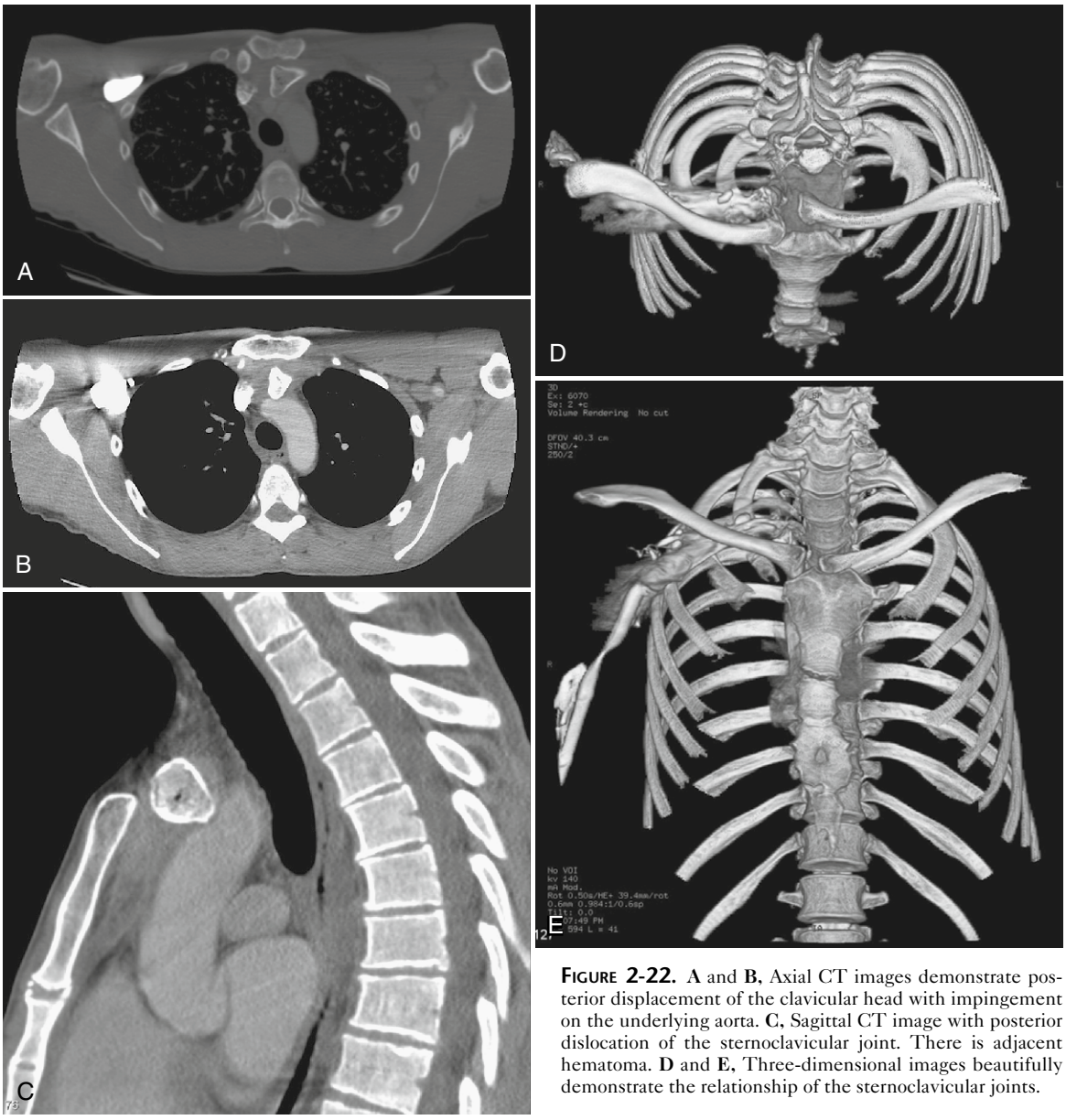


FIGURE 2-22. **A** and **B,** Axial CT images demonstrate posterior displacement of the clavicular head with impingement on the underlying aorta. **C,** Sagittal CT image with posterior dislocation of the sternoclavicular joint. There is adjacent hematoma. **D** and **E,** Three-dimensional images beautifully demonstrate the relationship of the sternoclavicular joints.

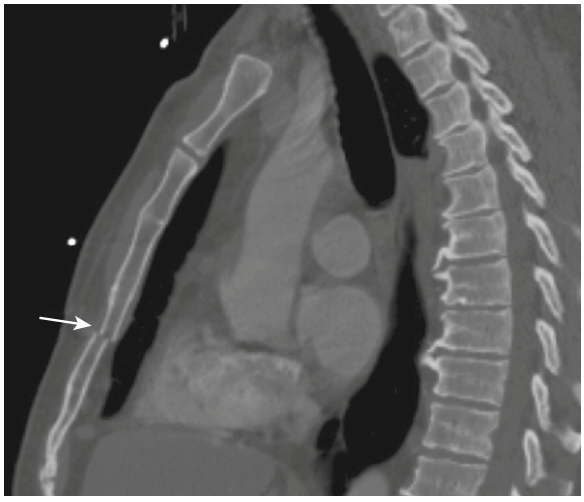


FIGURE 2-23. Sagittal CT image demonstrates fracture of the sternum *(arrow).*

Fractures of the thoracic spine account for 15% to 30% of all spine fractures. These fractures often result from hyperflexion or axial loading forces. The most vulnerable segment of the thoracic spine is at the thoracoabdominal junction from T9 to T12. The most common fractures are anterior wedge compression and burst fractures. Multiple fractures, often present, are frequently at noncontiguous levels, which highlights the need to evaluate the entire spine. The thoracic spinal cord is very susceptible to injury because the thoracic cord is tightly packed into the central canal and is easily injured by displaced bone fragments or disc material. Moreover, the blood supply of the mid-thoracic spinal cord is tenuous. Only 12% of patients with fracture-dislocation of the thoracic spine are neurologically intact; 62% of patients with thoracic spine fracture-dislocation have complete neurologic deficits.

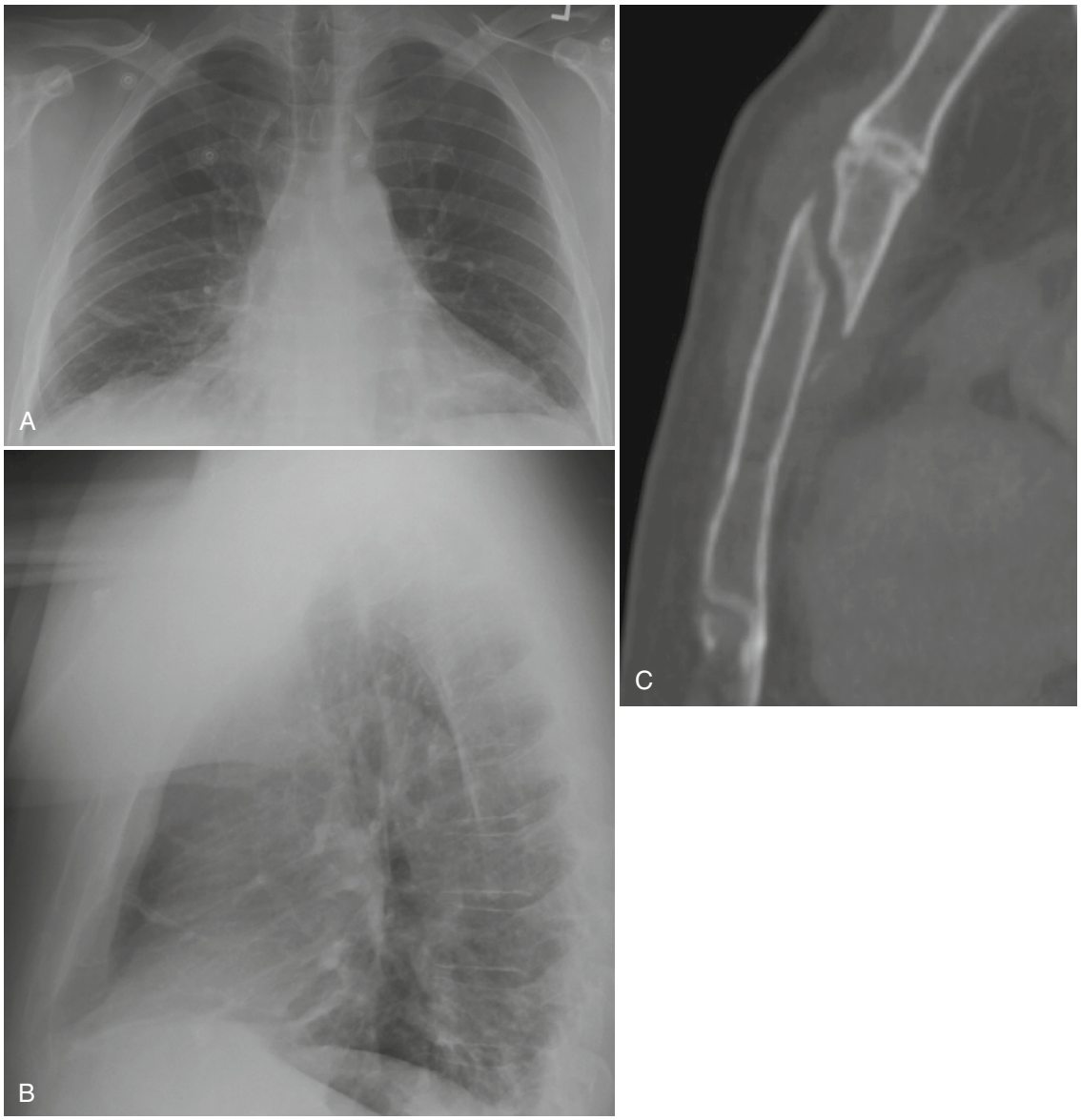


FIGURE 2-24. Anteroposterior (**A**) and lateral (**B**) radiographs of a 32-year-old male patient after a motor vehicle collision. No sternal injury can be appreciated on these images. **C,** Sagittal reconstructed images through the sternum clearly show the minimally displaced sternal fracture that was not seen on plain radiographs.

Thoracic spine fractures are occasionally detected on a portable chest radiograph. The radiographic signs might include flattened vertebral body, increased intrapedicular distance, and loss of vertebral body height. A possible sign on plain radiograph of thoracic spine fracture is widening of the right or left paravertebral stripe, which results from a paraspinal hematoma. Between 10% and 30% of thoracic spine fractures are not visible on portable radiograph. CT scan with coronal and sagittal reformations can both diagnose fractures with greater accuracy and better define the relationship of osseous fragments to the spinal cord. Magnetic resonance imaging is better for defining spinal cord or nerve root injury.

SUGGESTED READINGS

Bergin D, Ennis R, Keogh C, et al: The "dependent viscera" sign in CT diagnosis of blunt traumatic diaphragmatic rupture. AJR Am J Roentgenol 177:1137–1140, 2001.

Blaisdell F, Trunkey D: Trauma Management III: Cervicothoracic Trauma, 2nd ed. New York, Thieme, 1994.

Caskey CI, Zerhouni EA, Fishman EK, et al: Aging of the diaphragm: A CT study. Radiology 171:385–389, 1989.

Collins J, Primack SL: CT of non-penetrating chest trauma. Applied Radiology Online 30:1–10, 2001.

Dyer DS, Moore EE, Mestek MF, et al: Can chest CT be used to exclude aortic injury? Radiology 213:195–202, 1999.

Gavant ML, Menke PG, Fabian T, et al: Blunt traumatic aortic rupture: Detection with helical CT of the chest. Radiology 197:125–133, 1995.

Gelman R, Mirvis SE, Gens E: Diaphragmatic rupture due to blunt trauma: Sensitivity of plain chest radiographs. AJR Am J Roentgenol 156:51–57, 1991.

Groskin SA: Selected topics in chest trauma. Semin Ultrasound CT MR 17: 119–141, 1996.

Iochum S, Ludig T, Walter F, et al: Imaging of diaphragmatic injury: A diagnostic challenge? Radiographics 22(Suppl):S103–S118, 2002.

Kearney PA, Rouhana SW, Burney RE: Blunt rupture of the diaphragm: Mechanism, diagnosis, and treatment. Ann Emerg Med 18:1326–1330, 1989.

Mazurek A: Pediatric injury patterns. Int Anesthesiol Clin 32:11–25, 1994.

Mirvis SE, Bidwell JK, Buddemeyer EU, et al: Value of chest radiography in excluding traumatic aortic rupture. Radiology 163:487–493, 1987.

Mirvis SE, Shanmuganathan K, Miller BH, et al: Traumatic aortic injury: Diagnosis with contrast-enhanced thoracic CT—Five-year experience at a major trauma center. Radiology 200:413–422, 1996.

Mueller CF, Pendarvis RW: Traumatic injury of the diaphragm: Report of seven cases and extensive literature review. Emerg Radiol 1:118–132, 1994.
Rhea JT, Sheridan RL, Mullins ME, Novelline RA: Can chest and abdominal CT eliminate the need for plain films of the spine? Emerg Radiol 8:99–104, 2001.
Sevitt S: The mechanisms of traumatic rupture of the thoracic aorta. Br J Surg 64:166–173, 1977.
Shah R, Sabanathan S, Mearns AJ, et al: Traumatic rupture of diaphragm. Ann Thorac Surg 60:1444–1449, 1995.
Shettry VR, Bolman RM: Chest trauma. Assessment, diagnosis, and management. Clin Chest Med 15:137–146, 1994.
Spencer JA, Rogers CE, Westaby S: Clinico-radiological correlates in rupture of the major airways. Clin Radiol 43:371–376, 1991.
Wegner R, Crawford W, Schimpf P: Classification of parenchymal injuries of the lung. Radiology 167:77–82, 1988.
Williams JS, Graff JA, Uku JM, et al: Aortic injury in vehicular trauma. Ann Thorac Surg 57:726–730, 1994.
Wintermark M, Wicky S, Schnyder P: Imaging of acute traumatic injuries of the thoracic aorta. Eur Radiology 12:431–442, 2002.
Wiot JF: The radiologic manifestations of blunt chest trauma. JAMA 231:500–503, 1975.

CHAPTER 3

Abdomen Trauma

Joshua W. Stuhlfaut and Jorge A. Soto

Blunt and penetrating abdominal trauma are two of the more common indications for radiologic investigation in the emergency room setting and are common causes of morbidity and mortality among patients admitted to trauma centers. Many of these patients have multisystem injuries resulting from high-velocity mechanisms, and the full extent of these injuries is often difficult to detect clinically. A variety of imaging and nonimaging methods have been used to aid the clinician in the evaluation of abdominal trauma patients, but in recent years ultrasonography (US) and computed tomography (CT) have become the cornerstones of diagnosis and management. The almost universal use of CT, and of US in specific settings or circumstances, has modified the diagnostic approach of the poly-trauma patient and has relegated diagnostic peritoneal lavage to almost a historical procedure. This state-of-the-art imaging allows rapid detection of potentially life-threatening injuries that can be difficult or impossible to detect clinically, especially when the presence of associated injuries may mask overt clinical manifestations or divert the attention of the admitting physician away from major intra-abdominal bleeding.

BLUNT TRAUMA

Blunt trauma mechanisms leading to significant intra-abdominal injuries often include compression and deceleration forces. Motor vehicle collisions are the leading cause of injury, both in the United States and throughout the world. Other common mechanisms include falls from high altitudes, assaults, projectile injuries, and sports-related trauma. Although the likelihood of injuring an individual organ depends on the specific mechanism of trauma and the vulnerability of the patient at the time of the event, the data in the trauma literature have repeatedly demonstrated that the liver and spleen are the most frequently injured organs. Other potentially injured organs include the kidneys, bowel and mesentery, pancreas, adrenals, diaphragm, intra-abdominal vessels, and bladder.

Over the past 2 decades, improvements in imaging technology have considerably improved our ability to detect intra-abdominal injuries from blunt trauma. Of the available imaging modalities, CT and US are the two most commonly used imaging techniques when evaluating for acute traumatic abdominal injury. Other modalities, such as plain film radiography, magnetic resonance imaging (MRI), nuclear scintigraphy, and catheter angiography, are typically employed in specific circumstances for further characterization of injuries, for detection of complications from the initial injury, and for the treatment of such injuries.

Focused Abdominal Sonography for Trauma

Typically, US is used during the initial assessment of the poly-trauma patient, while CT images are obtained once the patient has been stabilized. Rapid assessment of the trauma patient can be performed at the bedside by experienced sonographers as part of the focused abdominal sonogram for trauma (FAST). Such scans can readily identify free fluid within the abdomen or pelvis and can help triage patients at the time of initial assessment. FAST evaluation consists of visualization of five spaces:

1. Pericardium (subxiphoid view)
2. Splenorenal and hepatorenal (i.e., Morrison's pouch)
3. Right paracolic gutter (Fig. 3-1)
4. Left paracolic gutter (see Fig. 3-1)
5. Pouch of Douglas

Multiple studies have demonstrated the benefit of a FAST study in the emergent decision-making process of the acutely traumatized patient. The main use of FAST is in the detection of free fluid (acute hemorrhage in this setting) in the peritoneal, pericardial, or pleural spaces to direct immediate therapeutic interventions by the trauma surgeons in the unstable or marginally stable patient. More recently, the development of contrast-enhanced US has improved detection of solid organ injuries and active bleeding. This technique, although not commonly used in the United States, does have potential as a means of evaluating the trauma patient without the use of ionizing radiation.



FIGURE 3-1. Intraperitoneal hemorrhage due to blunt abdominal trauma. FAST scan of the abdomen shows complex free fluid in the left lower quadrant in this patient following motor vehicle collision.

Computed Tomography Technique

Once stabilized, the abdominal trauma patient can be more completely imaged by a CT examination. With multidetector CT (MDCT) scanners, imaging of the head, cervical spine, chest, abdomen, and pelvis is performed as a single examination ("panscan"). Although adequate evaluation is possible with 4- and 8-row detector scanners, most large trauma centers now use 16- or 64-row detector scanners for trauma and other emergency room applications. Specific protocols regarding slice thickness, volume of intravenous contrast administered, timing of image acquisition, and use of oral contrast are continually reconfigured and vary between institutions.

In general, optimal evaluation of the abdomen and pelvis is performed by acquiring the axial dataset of CT images following intravenous injection of iodinated contrast material during the portal venous phase of hepatic enhancement. Intravenous contrast, 100 to 150 mL injected at a rate of 3 to 5 mL per second, is routinely employed for CT imaging of the trauma patient. If a dual syringe power injector is used (and this is the preferred system), the contrast bolus is followed by a 30- to 50-mL bolus of normal saline solution, typically injected at the same rate as the contrast material. This saline "chaser" ensures delivery of the complete contrast bolus into the circulation, rather than it remaining in the tubing or wasted in the veins of the upper extremities or mediastinum.

Regardless of the scanning protocol employed, modern 16- and 64-row detector scanners share several definite advantages over earlier-generation scanners. The most important of these is their markedly improved temporal resolution. With the development of these multidetector-row scanners, thin images (1 to 2 mm) can be easily acquired while still keeping scan time at 8 seconds or less per body part. In order to facilitate review at the interpretation workstations, it is advisable to reconstruct a separate set of thicker axial images by "fusing" the thin sections. For example, images acquired with 0.625- or 1.25-mm thickness can be reconstructed at 3.75- or 5-mm thickness. In addition, sagittal and coronal reformations are now generated almost routinely, taking advantage of the rapid scan times that nearly eliminate motion artifact. These sagittal and coronal reformations are ideal for adequate evaluation of the diaphragm, long vascular territories, and thoracic and lumbosacral spine, and reduce the need for lumbosacral and thoracic spine radiographs in the vast majority of patients. All series are sent to the Picture Archival Computer System (PACS) and are available at the time of interpretation and for further postprocessing (if necessary). Other benefits include the ability to combine routine protocols with CT angiograms of multiple body parts while still using a single bolus of contrast. This is possible due to the increased scanner table length (2 m) available with many of the 64 MDCT scanners. Using the scout images of the whole body, multiple complex CT examinations (including CT angiograms of the neck or extremities) are planned and combined in succession into one scan using a single contrast injection (Fig. 3-2).

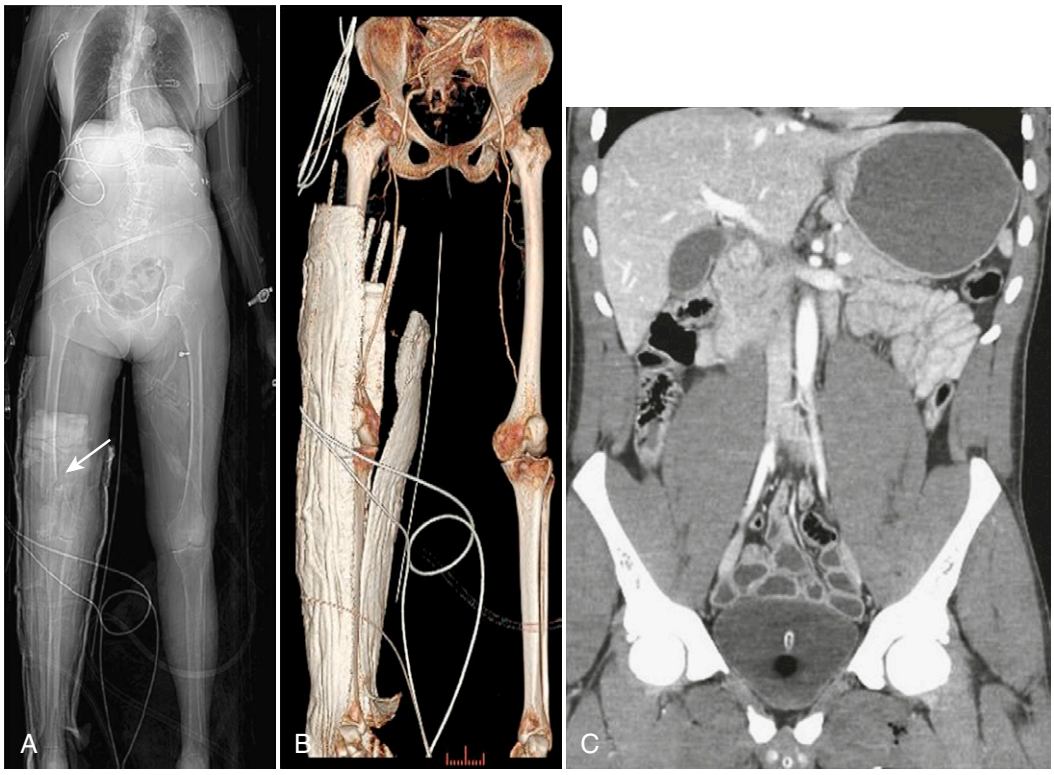


Figure 3-2. Multitrauma CT in a patient with injury following blunt trauma. **A,** Scout image obtained on a 64 detector CT scanner. Using the single scout image, multiple CT studies can be planned, including dedicated CT angiographic studies of focal areas of injury. Note the presence of a distal right femur fracture *(arrow)* in this patient who suffered significant trauma after being struck by a car. **B,** In this case, CT angiography of the extremities was requested to evaluate the peripheral arteries of the lower extremity. No injury was detected. **C,** Abdominal-pelvic CT was also obtained at the same time as the CT angiography. This coronal image was reconstructed from the axial dataset acquired during the portal venous phase of contrast enhancement.

The increased temporal resolution and decreased scan times of 16- and 64-row detector scanners have resulted in a modification in the time intervals applied between the start of contrast injection and image acquisition. To ensure that all body parts are scanned at the optimum peak of contrast enhancement, it is preferable to scan the chest (30 to 35 seconds) independently from the abdomen and pelvis (65 to 75 seconds), rather than with a continuous scan encompassing all three regions and starting at approximately 60 seconds. The split scan method avoids the potential need for rescanning the chest in order to obtain true CT angiography images of the thoracic aorta, essentially eliminating the need for catheter angiography for suspected thoracic aortic injury. Scan time for each body part is approximately 4 to 8 seconds (for 16- and 64-row detector scanners), and there is a pause of 30 to 35 seconds between scans of the chest and abdomen. The only drawback in separating the thorax from the abdomen and pelvis is in the generation of multiplanar reformations. These acquisitions are, for all intents and purposes, two different studies and necessitate separate multiplanar reformats, which makes image analysis slightly more tedious. However, the benefits of an optimal study of the aortic arch and great vessels outweigh this drawback. With the 4-row detector and helical CT scanners, most CT protocols include a single continuous acquisition of the chest, abdomen, and pelvis 30 to 40 seconds after intravenous injection of 100 to 150 mL of contrast material. With this delay, although optimal for the abdomen and pelvis, the aortic arch and great vessels are not visualized at the peak of the arterial phase. Not uncommonly, when there is a question about the integrity of these vessels, repeat CT angiography or catheter aortography is necessary. This requires injecting a second bolus of contrast and may cause potential delays in diagnosis.

In addition to portal venous phase imaging, the acquisition of delayed images has become an increasingly important part of the trauma CT evaluation. Delayed images can be useful in evaluating vascular injuries as well as injuries to both the solid organs and the bowel and mesentery. Delayed CT acquisitions allow for improved characterization of solid organ injuries by helping to differentiate contained injuries (such as arterial pseudoaneurysms and arteriovenous fistulas) from uncontrolled active extravasation of contrast-enhanced blood. On delayed images, areas of active extravasation persist as hyperattenuating foci (relative to the aorta) and change configuration as blood (with contrast) diffuses into a potential space (Fig. 3-3), whereas pseudoaneurysms show an attenuation coefficient that remains similar to the aorta, with no change in overall size or shape. Delayed images also improve detection and characterization of bladder and renal injuries, as discussed later in this chapter. Finally, delayed scans can help in the characterization of findings seen on portal venous phase images that could potentially represent foci of extravasation and could be related to the acute injury (Fig. 3-4). However, the routine use of delayed images is unnecessary and should be discouraged, since the majority of trauma CT scans performed in emergency rooms today show no evidence of abdominal injury and the additional radiation dose is unnecessary. As an alternative, delayed images can be acquired selectively and used only when solid organ or bowel injry is detected or suspected on the initial CT acquisition. Additionally, since the sole purpose of this delayed scan is to characterize an injury seen or suspected on the initial scan, it is possible to employ a reduced radiation dose technique, typically 100 milliAmpere second (mAs) (or similar dose reduction with automated dose modulation).

In the past, oral contrast was considered a mandatory component of trauma CT protocols. However, reports in the radiological and surgical literature have suggested that imaging by MDCT without oral contrast is similarly accurate for the detection of bowel and mesenteric injuries at the time of initial CT evaluation. Occasionally, the initial scan may be inconclusive as to the presence of a bowel injury. In this case, and if there is a specific question of bowel injury on the initial scan, a follow-up CT (typically 12 hours later) with oral contrast can be performed at the discretion of the interpreting radiologist. If oral contrast is used to opacify

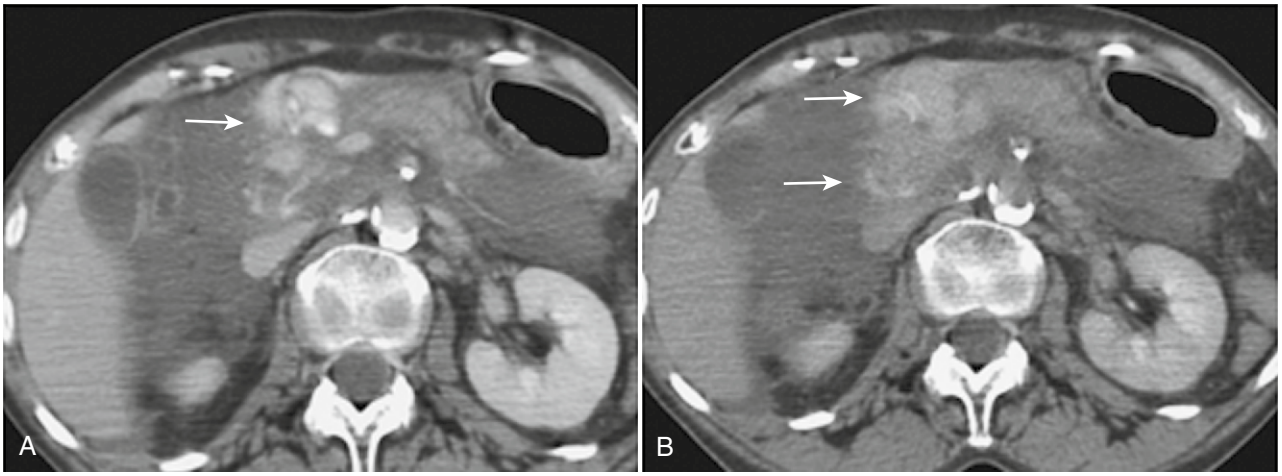


FIGURE 3-3. Active contrast extravasation following blunt abdominal trauma. **A,** CT obtained during the portal venous phase shows contrast extravasation into the peripancreatic region due to an acute vascular injury *(arrow)*. **B,** On the 5-minute delay CT, the contrast continues to diffuse into the soft tissue at the site of injury *(arrows)*.

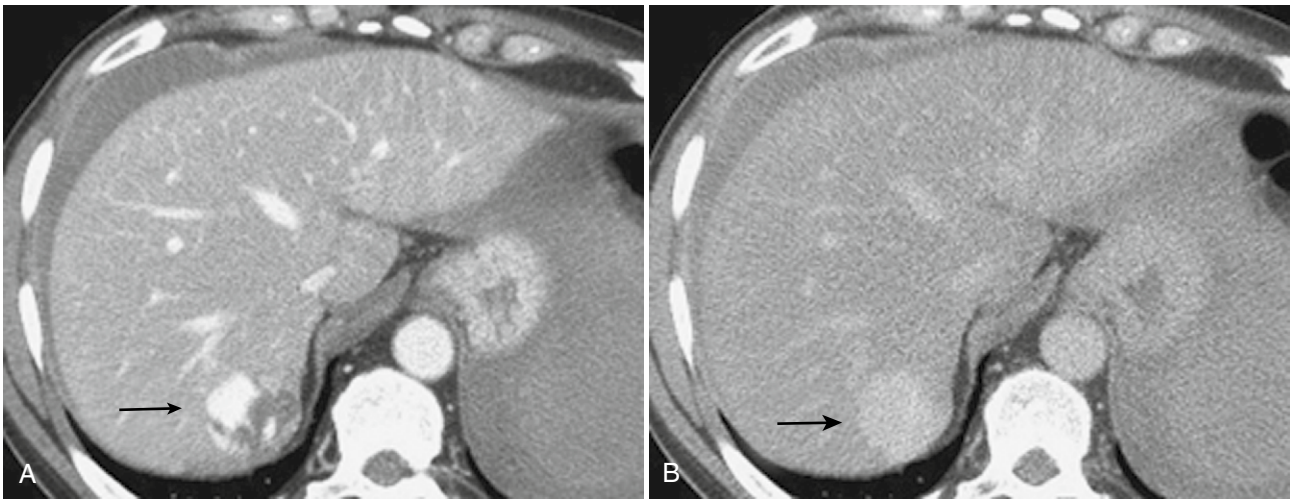


Figure 3-4. Hemangioma in young female patient detected during trauma CT. **A,** Portal venous phase CT shows focal puddling of contrast in the posterior segment of the right lobe of the liver *(arrow)*. Initially, there was some question as to the presence of a focal liver injury with active bleeding. Free fluid is present adjacent to the liver margin. **B,** The 5-minute delay CT shows retention of contrast within a focal liver lesion *(arrow)*, which excludes focal liver injury. Instead, the diagnosis of a benign hemangioma was confirmed.

the bowel in the setting of acute trauma, patients generally receive water-soluble contrast agents due to the potential for contrast extravasation into the peritoneal cavity from an acute bowel injury. Oral contrast can be given by mouth or by insertion into an indwelling nasogastric tube. The method chosen depends on the level of consciousness of the patient and associated injuries. CT imaging should not be delayed while waiting for the contrast to migrate into the distal small bowel.

With isotropic voxel scanning, CT has truly become a multiplanar modality. As described above, sagittal and coronal reformations have become a common component of trauma CT protocols. As the number of images generated for trauma patients increases, review of multiplanar images is one possible solution for improving interpretation efficiency. Coronal and sagittal reformations are also a useful, intuitive tool for communicating with clinical colleagues, as large amounts of information are represented on fewer images. Multiplanar image review is particularly useful for several trauma applications: evaluation of potential spine injuries, a more complete appreciation of often-complex injuries of solid organs, hollow viscera, and diaphragm, and for CT angiography, where longer segments of vessels may be visualized in sagittal and coronal planes.

HEPATIC TRAUMA

The liver is one of the most commonly injured organs in the abdomen, with the prevalence of injury in patients who have sustained multiple blunt trauma on the order of 1% to 8%. Despite the wide array of hepatic injuries, the vast majority of patients are treated conservatively, without the need for direct therapeutic intervention. Patients with extensive and complex lacerations and large parenchymal hematomas are increasingly being managed with observation and supportive measures alone. Endovascular therapy with embolization is reserved for definitive treatment of patients with significant vascular injury and active bleeding. The growing trend toward successful nonsurgical management of liver injuries is in part related to major advances in imaging technology and CT techniques in the past decade. Specifically, the focus is to rapidly demonstrate areas of potentially life-threatening active bleeding that require immediate attention. MDCT and US are the main modalities employed for initial detection and characterization of hepatic injuries. Other modalities, such as MRI with MR cholangiopancreatography (MRCP), hepatobiliary scintigraphy, and endoscopic retrograde cholangiopancreatography (ERCP), are reserved for detecting subacute or delayed complications, such as bile duct leaks, bilomas, and biliary strictures. Since CT with proper technique is sufficient to demonstrate the extent and significance of essentially all liver injuries, catheter angiography is reserved for confirmation of CT findings that suggest major vascular injury and, especially, as a means to treat those lesions that require intervention via embolization.

Ultrasonography

Sonographic evaluation for hepatic injuries is mostly limited to screening the trauma patient for indirect signs of injury, such as free fluid adjacent to the liver (as part of the FAST scan). When fluid is detected along the margin of the liver, it can appear complex and can contain echogenic clot due to its hemorrhagic nature. Although a careful inspection of the liver can demonstrate lacerations and contusions as focal areas of parenchymal distortion, various factors limit the use of US beyond the search for free peritoneal fluid. These include technical limitations such as difficult access to appropriate sonographic windows and the variability in operator experience and availability. However, advances in US technology and the development of sonographic contrast agents has led to increased use of this modality for direct evaluation of the solid parenchymal organs, including the liver, especially in European countries. On noncontrast US examinations, hepatic parenchymal injuries can produce three different morphological patterns. The most common pattern is that of a focal area of increased echogenicity with respect to the background

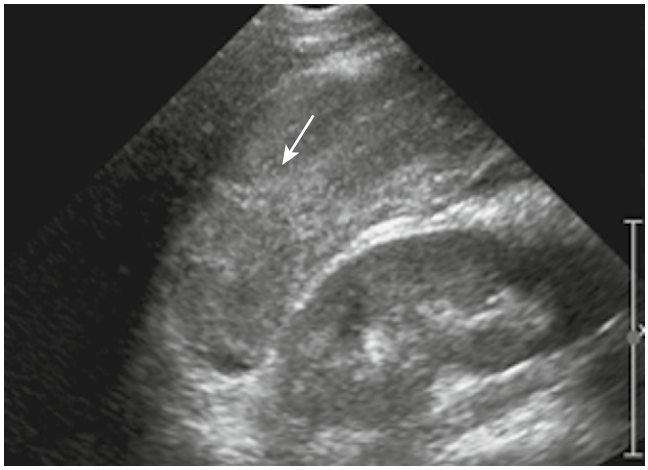


FIGURE 3-5. Liver laceration detected by ultrasound. Sagittal image of the right upper quadrant demonstrates a focal linear echogenic abnormality in the liver, compatible with an acute liver laceration *(arrow)*.

liver, which is thought to correspond to the focal lacerations or hematomas seen on CT. The other two are a more diffuse area of increased echogenicity and focal areas of decreased echogenicity. Liver lacerations can be difficult to detect on initial exams, often appearing more prominent in the days following the initial injury (Fig. 3-5). The advent of sonographic contrast agents has increased the ability of ultrasound to detect acute hepatic injuries. Generally, the contrast agent is given in a bolus and the area of interest is scanned continuously for 4 to 6 minutes. On contrast-enhanced US, liver injuries are best seen during the portal venous phase of imaging. Liver lacerations can also appear as focal linear or branching hypoechoic areas, often oriented perpendicular to the liver surface. Contusions may appear as geographic areas of decreased echogenicity, often with ill-defined borders. Similar to active contrast extravasation on CT, active bleeding can be detected by the presence of microbubbles (contrast material) extending into a hematoma. In general, despite recent advances in technology, US is still considered an adjunctive test.

Computed Tomography

CT is the dominant imaging modality in emergency rooms in the United States and most other Western countries. Improvements in the rate of CT detection of liver injuries, as well as in the proper characterization of most injuries, are some of the reasons that support the trend toward conservative management of such injuries. As previously mentioned, liver injuries are optimally seen on CT performed during the portal venous phase of contrast enhancement. Once identified, it is important to document the type and location of such injury. In addition, it is especially important to note the presence of active extravasation of contrast-enhanced blood and the potential for injury to central hepatic vessels such as the hepatic veins and inferior vena cava. Hepatic injuries are typically characterized as either lacerations or hematomas (subcapsular or parenchymal). While many radiologists rely exclusively on morphological descriptors in their report, it is useful to understand the liver injury scale developed by the American Association for the Surgery of Trauma (AAST) (Table 3-1). This grading scale takes into account features such as the size of subcapsular or parenchymal hematomas and lacerations, as well as evidence of active extravasation and major vascular injuries of the liver; these findings are all readily identified on well-performed CT examinations. The value of this scale lies more in the ability to communicate properly with trauma surgeons about the extent of the injury than in the ability to predict individual patient prognosis or the type of therapy necessary.

TABLE 3-1 AAST Classification of Traumatic Liver Injury

Grade	Description
I	Hematoma: Subcapsular, <10% surface area Laceration: Capsular tear, <1 cm in parenchymal depth
II	Hematoma: Subcapsular, 10%–50% surface area; intraparenchymal, <10 cm in diameter Laceration: 1–3 cm in parenchymal depth, <10 cm in length
III	Hematoma: Subcapsular, >50% surface area or expanding or ruptured subcapsular hematoma with active bleeding; intraparenchymal, >10 cm or expanding or ruptured Laceration: >3 cm in parenchymal depth, <10 cm in length
IV	Hematoma: Ruptured intraparenchymal hematoma with active bleeding Laceration: Parenchymal disruption involving 25%–75% of a hepatic lobe or one to three Couinaud segments within a single lobe
V	Laceration: Parenchymal disruption involving >75% of a hepatic lobe or more than three Couinaud segments within a single lobe Vascular: Juxtahepatic venous injuries (i.e., retrohepatic vena cava or central major hepatic veins)
VI	Vascular: Hepatic avulsion

A subcapsular hematoma is typically hypodense to the enhancing liver parenchyma and appears elliptical, conforming to the confines of the liver capsule (Fig. 3-6). Such collections are usually easily distinguished from perihepatic fluid. Intraparenchymal hematoma appears as an ill-defined hypoattenuating region within the liver. If seen on noncontrast CT, hematomas are typically hyperdense to the background liver parenchyma. Liver lacerations appear as hypoattenuating linear, often branching, and complex regions within the parenchyma of the liver (Fig. 3-7). Extension to the hepatic surface is very common. Even small lacerations can be associated with perihepatic blood. It is important to identify lacerations that extend to the periportal region, since these patients are at an increased risk for the development of delayed bile leaks due to injury of the biliary ductal system.

CT can also readily identify hepatic vascular injuries. Active extravasation of intravenous contrast, when seen during routine portal venous phase images, suggests ongoing hemorrhage from a hepatic arterial or portal venous source. Active extravasation may be confined to the hepatic parenchyma or may be seen as hyperattenuating collections of contrast-enhanced blood accumulating in the perihepatic spaces. On delayed CT images, the focus of active extravasation typically increases in size as the material continues to diffuse throughout the

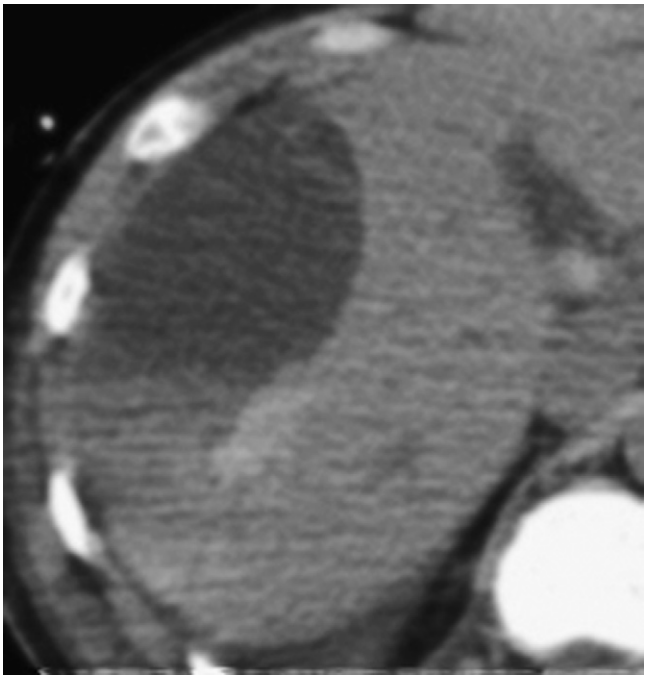


Figure 3-6. Subcapsular hematoma following blunt abdominal injury. Axial CT acquired during the portal venous phase shows a focal subcapsular elliptical hematoma in the right lobe of the liver.

area of expanding hematoma (Fig. 3-8). In the past, active extravasation was considered an indication of the need for prompt surgical management. Currently, the demonstration of a sizable focus of active extravasation is more likely to trigger a response from the vascular interventional team for catheter angiography and coil embolization (see Fig. 3-8). Even patients with high-grade injuries can be managed conservatively using such techniques. Injuries to major hepatic vessels may also be directly depicted with CT. For example, direct evidence of portal venous injury may be seen as abrupt termination of a branch of an intrahepatic portal vein. Parenchymal injuries may extend centrally to involve the hepatic veins and inferior vena cava, seen on CT as abrupt termination of the hepatic veins, which may just begin to enhance during routine portal venous phase images. Such major venous injuries are more likely to require surgical management, since they can cause continued bleeding and hemodynamic instability, and are not readily treated by interventional radiology techniques (Fig. 3-9). Major venous injuries are also commonly associated with hepatic arterial trauma. Complications of hepatic vascular injuries include traumatic fistulas between various hepatic structures, including arterioportal, fistulas between hepatic arteries and biliary ducts, and, rarely, between a hepatic artery and adjacent bowel. Hepatic pseudoaneurysms can also occur as a result of hepatic injury and are extremely important to detect and document since they are at risk for delayed rupture, a potentially lethal complication. Hepatic artery pseudoaneurysms were considered rare, but are now detected more frequently due to improvements in the spatial resolution of CT and the ability to scan at the peak of contrast enhancement throughout the scan routinely (Fig. 3-10). Pseudoaneurysms appear as hyperattenuating foci on the early phase images and demonstrate washout on delayed phase images. If delayed rupture and hemorrhage are suspected based on clinical or laboratory parameters, CT is also the best method to detect subacute hemorrhage. On follow-up CT, delayed hemorrhage presents as an increase in the size of a previous hematoma. The more acute hemorrhage appears as focal hyperattenuating material in a previously documented hematoma or along the margin of the liver, the so-called "sentinel clot" sign. In addition to pseudoaneurysm formation and delayed hemorrhage, other complications of hepatic trauma result from associated bile duct injury and include the development of bilomas and abscess collections, persistent bile leaks with bile peritonitis, and bile duct strictures.

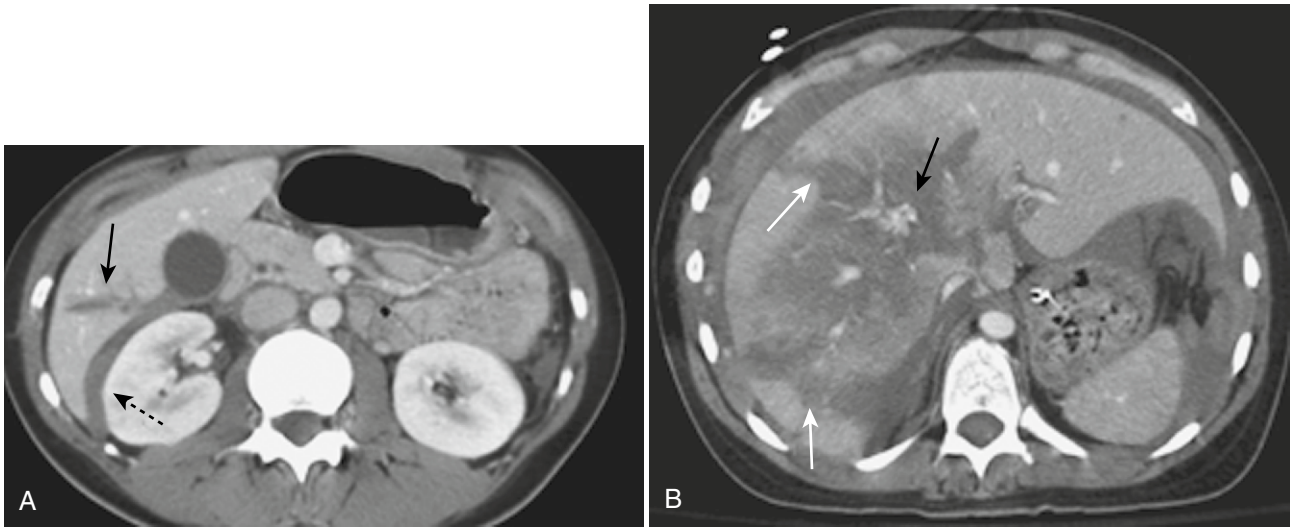


Figure 3-7. CT depiction of liver lacerations following blunt abdominal trauma. **A,** Portal venous phase axial CT image demonstrates a focal liver laceration in the right lobe of the liver *(solid arrow)* with perihepatic blood in Morrison's pouch *(dashed arrow)*. **B,** Portal venous phase CT in a different patient following motor vehicle accident shows a more complex liver laceration *(white arrows)* with a focal area of active contrast extravasation *(black arrow)*.

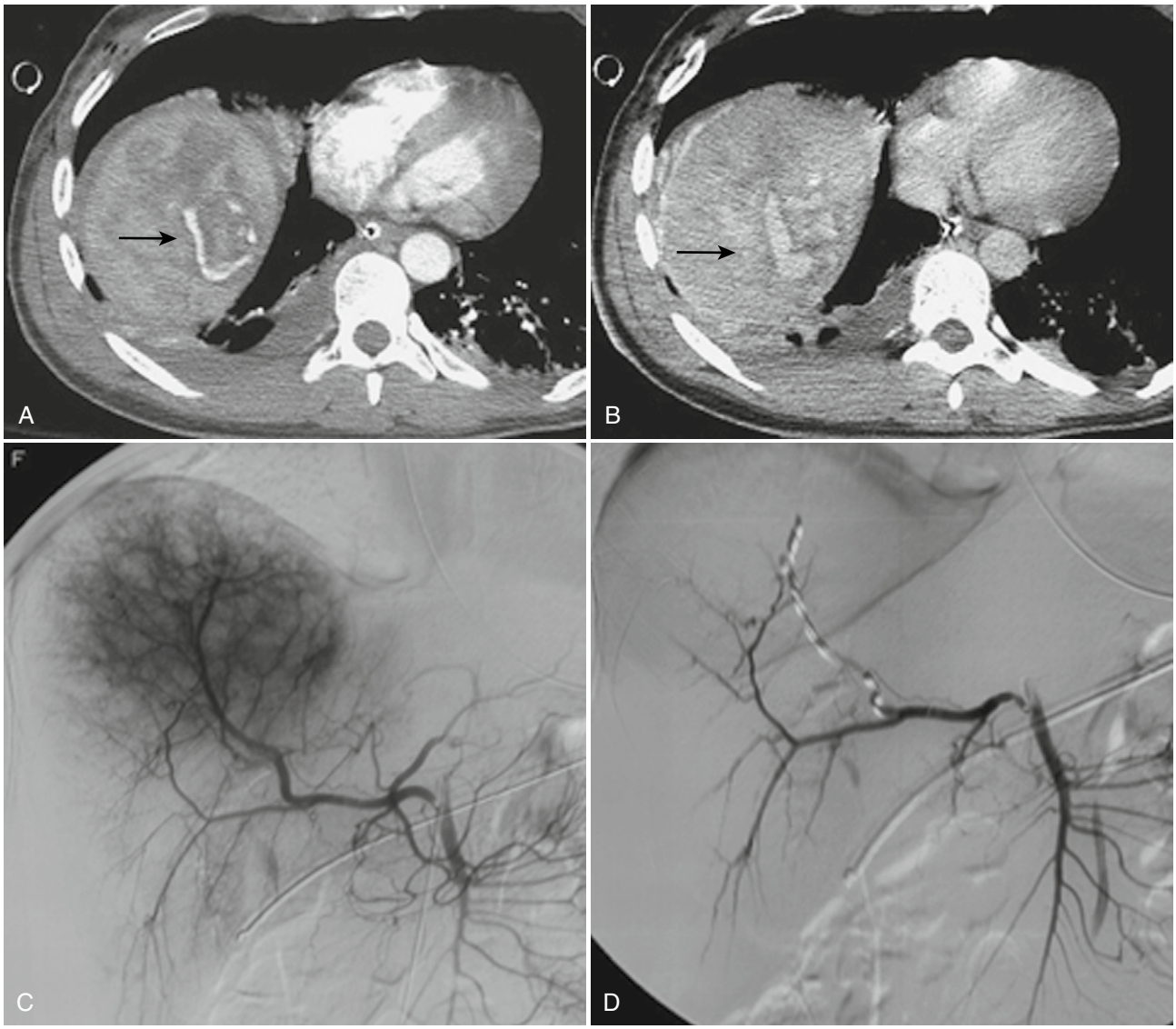


FIGURE 3-8. Active contrast extravasation following acute abdominal trauma. **A,** Axial CT obtained during the portal venous phase shows a complex liver laceration with active contrast extravasation *(arrow)*. **B,** The 5-minute delay CT shows ongoing bleeding with contrast continuing to diffuse into the area of injury *(arrow)*. **C,** Selective catheterization of the superior mesenteric artery (due to a replaced right hepatic artery) shows active bleeding as a large blush of contrast in the right lobe of the liver. **D,** After embolization, the postprocedure angiogram shows resolution of the contrast blush with adequate control of active bleeding.

GALLBLADDER AND BILE DUCT TRAUMA

Blunt trauma may result in injury to the biliary tract, including the gallbladder and intrahepatic or extrahepatic bile ducts. The gallbladder and extrahepatic ducts are protected by the liver, and this may explain the low frequency of injury to these structures with blunt trauma. The most common location of extrahepatic biliary tract injuries is the gallbladder, followed by the common bile duct. Gallbladder injury is almost invariably associated with additional significant injuries. Liver, splenic, and duodenal injuries are most common, occurring in up to 91%, 54%, and 54% of cases, respectively. Extrahepatic bile duct injuries are very rare and are also usually associated with injuries to other organs. Gallbladder and bile duct injury may occur due to torsion, shearing, or compression forces. Certain factors may predispose to gallbladder injury. These include distention of the gallbladder in a preprandial state, which makes the gallbladder more vulnerable to compression injury. Injuries to the gallbladder are classified into three main categories: contusion, laceration/perforation, and complete avulsion. In general, contusions are considered to represent intramural hematomas, are the mildest form of gallbladder injury, and are treated conservatively. Lacerations and perforations are full-thickness wall injuries, requiring cholecystectomy. Avulsion of the gallbladder may involve variable portions of the gallbladder and cystic duct. Any of these lesions can be associated with transection of the cystic artery and major blood loss.

Extrahepatic duct injuries may occur at sites of anatomic fixation, such as the intrapancreatic portion of the common bile duct, and are frequently caused by blunt impact or acute deceleration, possibly with compression against the



Figure 3-9. Portal venous injury following blunt abdominal trauma. Axial CT obtained during the portal venous phase shows a complex injury involving the left lobe of the liver with active contrast extravasation. At surgery, a laceration of the left portal vein was detected that required surgical repair.

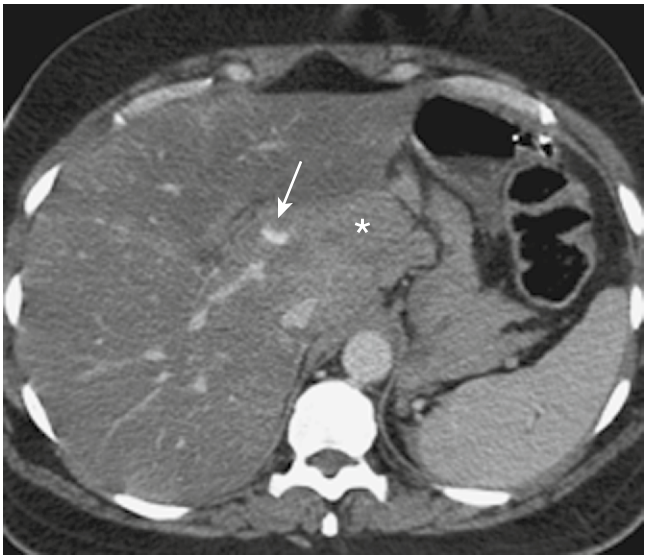


Figure 3-10. Hepatic arterial pseudoaneurysm following a motor vehicle accident. Axial CT obtained during the portal venous phase shows a large hematoma in the porta hepatis *(asterisk)* with a small pseudoaneurysm of the left hepatic artery *(arrow)*. This injury required surgical intervention to repair a laceration of the left hepatic artery.

spine. Elevation of the liver following blunt trauma may cause stretching of the relatively fixed common duct. Injuries to the intrahepatic bile ducts are seen in patients with severe liver lacerations.

Delayed complications of gallbladder or bile duct injury, such as sepsis, may result from leakage of bile into the peritoneal cavity and subsequent infection. Sterile bile within the peritoneum undergoes continuous peritoneal reabsorption and may initially lead to surprisingly few symptoms. Since bile in the peritoneum usually does not cause symptoms until infected, bile leakage may occur for weeks or months before being detected clinically. When signs and symptoms are present, they are nonspecific and include vague abdominal pain, nausea, vomiting, and occasionally jaundice. With extrahepatic bile duct injury, diagnosis may be particularly difficult; up to 20% of such injuries are not detected at surgery. Injury to either extra- or intrahepatic bile ducts may also result in biliary strictures. Patients may present weeks, months, or even years later with signs of biliary obstruction or infection due to the development of foca l strictures at the site of injury.

Ultrasonography

Acute gallbladder trauma is only rarely detected by US. There may be gallbladder wall thickening or complex echogenic fluid within the gallbladder that might suggest the presence of intraluminal blood. However, sonographic examination may be limited by underdistention of the gallbladder in a nonfasting patient. Ultrasound plays little role in the detection of acute injuries of the biliary system.

Computed Tomography

Gallbladder injuries are most often diagnosed at the time of the initial trauma CT scan. Contusions appear as diffuse gallbladder wall thickening. The presence of pericholecystic fluid is not specific, but may be an associated finding. High-attenuation fluid within the gallbladder lumen suggests hemorrhage and is a good indicator of acute injury. However, differentiation between high-attenuation sludge and blood may be difficult. Lacerations of the gallbladder wall are seen as focal disruption of the normal mural enhancement of the gallbladder wall. Dense contrast material in the gallbladder lumen or in the gallbladder fossa suggests active bleeding from injury to the cystic artery. If the gallbladder is avulsed from its pedicle, it may be displaced from the gallbladder fossa (Fig. 3-11). Injury of the extrahepatic bile ducts can be difficult to diagnose on CT, since perihepatic fluid is often caused by injury to other organs in the abdomen. Intrahepatic biliary ductal injury may be suggested on follow-up CT by the development or persistence of low-attenuation perihepatic fluid collections, usually with an obvious associated hepatic injury.

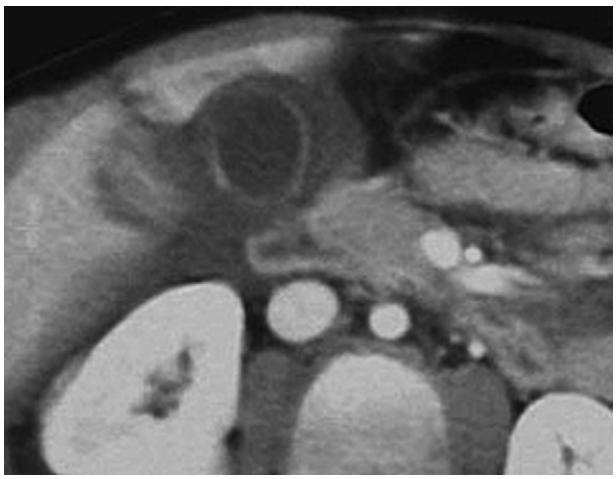


Figure 3-11. Avulsion of the gallbladder due to blunt trauma. CT obtained during the portal venous phase shows incomplete enhancement of the gallbladder wall with blood adjacent to the gallbladder. The gallbladder appeared inferiorly displaced at the time of CT. At surgery, avulsion of the gallbladder was confirmed requiring cholecystectomy. (Reprinted with permission from Gupta A, Stuhlfaut JW, Fleming KW, et al: Blunt trauma of the pancreas and biliary tract: A multimodality imaging approach to diagnosis. RadioGraphics 24:1381–1395, 2004.)

Hepatobiliary Scintigraphy

Once the patient with complex liver trauma has survived the acute phase of hepatic trauma, when bleeding and possible exsanguination are the main concerns, the possibility of developing bile leaks with complicating abscess and sepsis must be considered and treated. Persistent perihepatic fluid collections and increasing low-attenuation intraperitoneal fluid are common indicators of bile leaks that require direct therapy. Biliary scintigraphy is a simple and useful method for detecting and characterizing bile duct injuries. Hepatobiliary radiopharmaceutical agents are taken up by hepatocytes and excreted into the bile ducts. Sequential imaging over 1 to 2 hours identifies extraluminal collections that develop as the radiotracer is excreted into the biliary system and drains into the small bowel lumen. In some cases, images delayed 4 hours are necessary when there is no evidence of injury on the initial image acquisition. On hepatobiliary scintigraphy, accumulation of the radiopharmaceutical agent outside the bile ducts is indicative of a bile leak, which can be either contained (Fig. 3-12) or free if it extends into the peritoneal cavity.

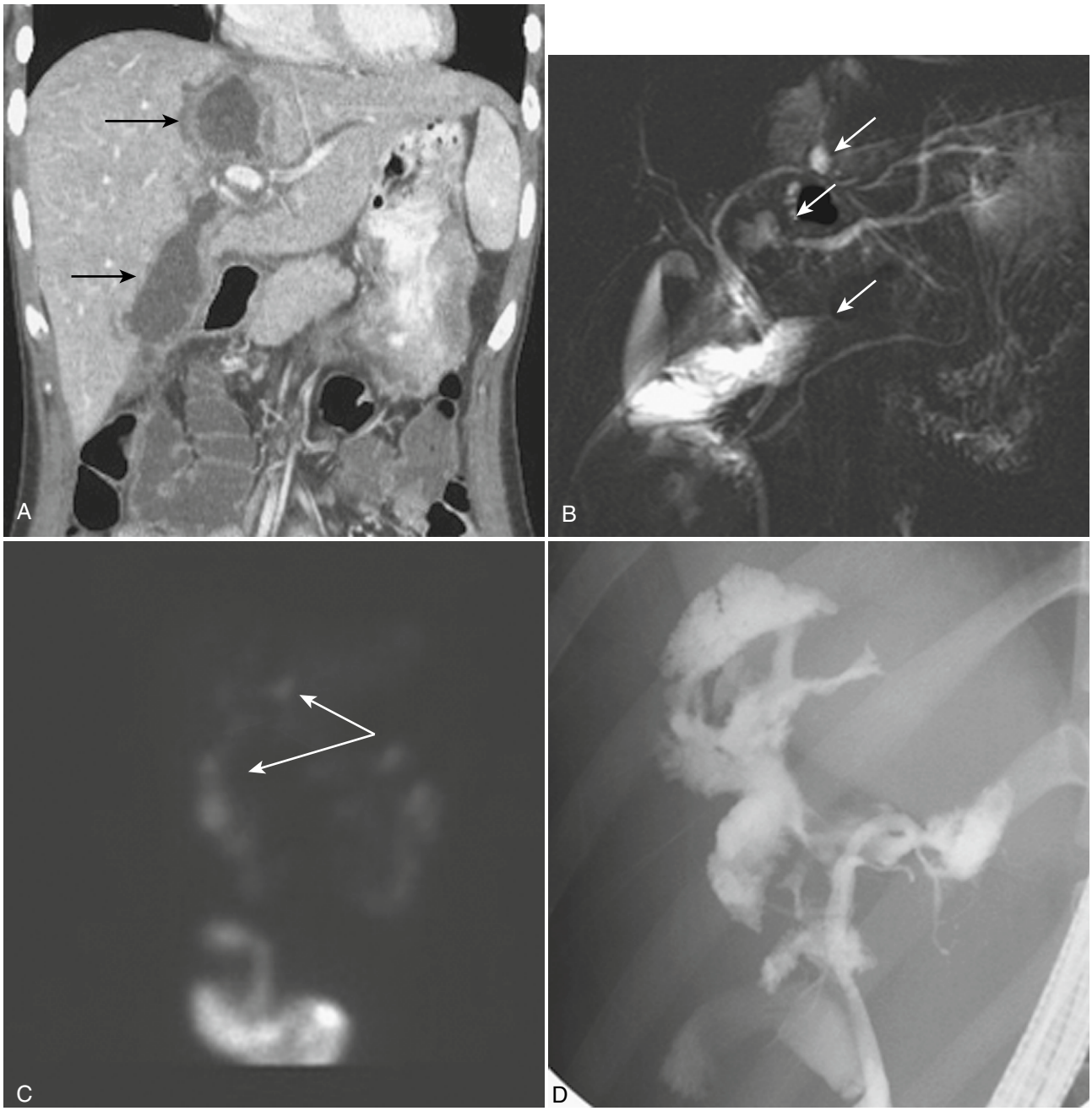


FIGURE 3-12. Biliary leak with biloma following blunt abdominal trauma. **A,** Coronal CT image obtained several days following the initial trauma demonstrates two focal fluid collections in the intrahepatic and perihepatic regions *(arrows)*. **B,** Coronal thick slab MR cholangiopancreatography (MRCP) also demonstrates the presence of several extraluminal fluid collections as focal areas of increased signal on this fluid sensitive sequence *(arrows)*. **C,** Hepatobiliary scan obtained in the anterior projection confirms the presence of bilomas with radiotracer located outside the expected lumen of the biliary tree *(arrows)*. **D,** Endoscopic retrograde cholangiopancreatography (ERCP) was performed to further characterize the injury and for possible stent placement and confirms the presence of bile duct injury.

Small bilomas can be treated conservatively and followed, whereas larger collections may require percutaneous drainage, especially if there is superimposed infection. Early detection of bile leaks allows proper treatment by either percutaneous drainage or by ERCP with sphincterotomy and stent placement (see Fig. 3-12). A possible delayed complication of bile duct injury is the development of a bile duct stricture with obstruction and infection. MRCP is an ideal method for following hepatobiliary injuries for possible development of strictures.

SPLENIC TRAUMA

The spleen is the most commonly injured organ in the abdomen as a result of blunt trauma. In the past, exploratory laparotomy with splenectomy was the dominant treatment for splenic injuries. However, improvements in our understanding of the natural history of splenic injuries as well as in the quality and access to imaging methods have modified treatment algorithms. Nonoperative management is used initially for the vast majority of splenic injuries. Splenectomy is reserved for the most complex injuries in unstable patients who do not respond to resuscitative efforts and for patients in whom conservative therapy fails. Patients who would otherwise be candidates for conservative management, but who require laparotomy for other abdominal injuries, may still undergo a splenectomy.

Splenic trauma is typically difficult to detect clinically. Patients can present with left upper quadrant pain, although associated severe injuries may confound the clinical picture or distract attention from the spleen or abdomen. Instead, most injuries are detected with imaging studies performed in these trauma patients, by either US or CT. The admission portable radiograph may demonstrate left rib fractures and alert trauma surgeons to the possibility of underlying splenic injury. However, plain film radiographs have no role in the direct demonstration of splenic injury. Once an injury is detected, and while the resuscitation process is ongoing, the interventional radiology team should be alerted, as catheter angiography may become necessary for treating vascular injuries, thus avoiding the need for splenectomy. However, splenectomy may still become necessary if the injury is severe and bleeding cannot be controlled by nonoperative means.

Splenic injuries are characterized as either hematomas or lacerations. As it has for the liver, the AAST has developed a scale for grading splenic trauma that is still commonly used for describing specific patterns of injury (Table 3-2). The prognostic implications of this scale are limited, since even complex injuries can heal without specific therapy. It is important to describe the type of injury, the location (parenchymal versus subcapsular), the size of the hematoma or laceration, and all associated complications. Severe injuries can affect the hilar vascular structures, leading to total or subtotal organ devascularization. Injuries to the splenic artery or branch vessels can cause active bleeding, which can be easily demonstrated with current MDCT examinations. Finally, splenic injuries can lead to the development of pseudoaneurysms, which are extremely important to note, since these patients have an increased risk of delayed morbidity and mortality due to pseudoaneurysm rupture.

Table 3-2 AAST Classification of Traumatic Splenic Injury

Grade	Description
I	Hematoma: Subcapsular, <10% of surface area Laceration: Capsular tear, <1 cm of parenchymal depth
II	Hematoma: Subcapsular, 10%–50% of surface area; intraparenchymal hematoma, <5 cm in diameter Laceration: 1–3 cm in parenchymal depth not involving a parenchymal vessel
III	Hematoma: Subcapsular, >50% of surface area or expanding or ruptured subcapsular or parenchymal hematoma; intraparenchymal hematoma, >5 cm in diameter Laceration of >3 cm parenchymal depth or involving trabecular vessels
IV	Laceration of segmental or hilar vessels producing major devascularization (>25% of spleen)
V	Completely shattered spleen Vascular hilar injury with devascularized spleen

Ultrasonography

Splenic injuries can be detected by US evaluation of the abdomen and may be suspected based on the results of the initial FAST scan. However, the parenchymal injury can be difficult to detect. Instead, indirect evidence of injury is often identified, including hemoperitoneum and focal echogenic clot adjacent to the spleen. Splenic hematomas appear as heterogeneous and hypoechoic compared with the background spleen (Fig. 3-13). The borders are ill-defined and there is no associated mass effect or vessel displacement. Lacerations appear as linear or branching areas of decreased echogenicity compared with the normal spleen, often extending to the splenic surface. Although not commonly used in many countries, sonographic contrast agents have been shown to improve the ability to detect splenic injuries. The spleen can be readily imaged by contrast-enhanced US since it retains contrast for up to 5 to 7 minutes following intravenous injection. If the vascular pedicle is injured, there may be total or subtotal loss of enhancement in the spleen. Active contrast extravasation can be identified as a hyperechoic collection that develops in the early phase after contrast injection.

Computed Tomography

MDCT is the main imaging modality used to detect, characterize, and follow splenic trauma. Most splenic injuries are optimally detected on portal venous phase images of the abdomen following intravenous contrast injection. Splenic hematomas appear as focal areas of decreased attenuation compared with the background-enhancing splenic tissue (Fig. 3-14). Hematomas can be intraparenchymal or subcapsular in location. Lacerations appear as linear, irregular, and often branching areas of decreased attenuation (Fig. 3-15). Higher-grade injuries tend to be larger and involve more of the total volume of the spleen (Fig. 3-16). Injuries of the vascular pedicle lead to focal wedge-shaped areas of decreased

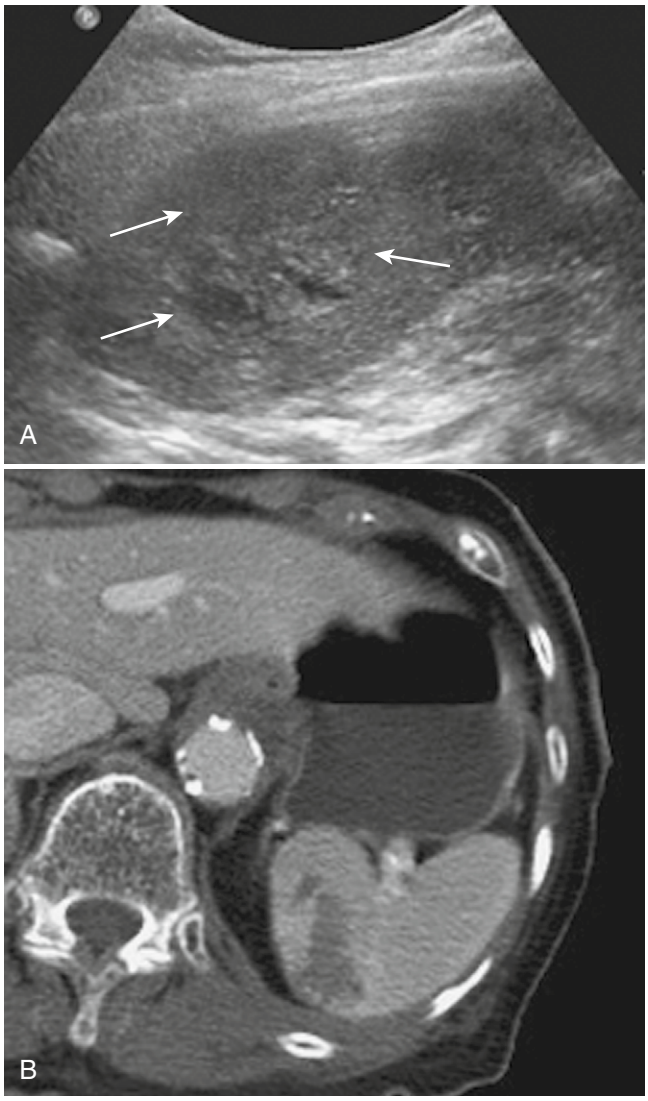


FIGURE 3-13. Splenic hematoma. **A,** Focused ultrasound of the left upper quadrant demonstrates a focal region of heterogeneity in the spleen *(arrows)*, suggestive of an acute splenic injury. **B,** CT performed following the initial ultrasound confirms the presence of an acute splenic hematoma.

enhancement, while severe injuries of the vascular pedicle may produce a markedly decreased or absent enhancement of most or all of the spleen on CT. In addition to describing the type of injury, it is important to note the presence of either active contrast extravasation or pseudoaneurysm formation. Active contrast extravasation in the spleen is characterized on CT by contrast density outside the expected lumen of the vessel, similar or higher in attenuation as compared with the adjacent vessels (Fig. 3-17). The shape is often irregular, with poorly defined margins due to the diffusion of the contrast material into the site of injury. Typically, contrast extravasation is identified within the splenic parenchyma or in a hematoma adjacent to the site of laceration in the perisplenic spaces. In contrast, splenic pseudoaneurysms are contained extraluminal collections that often have a more round or ovoid appearance (Fig. 3-18). These injuries are usually confined to the splenic parenchyma. In some cases, it is difficult to distinguish between active



FIGURE 3-14. Splenic hematoma following motor vehicle collision. Axial CT during the portal venous phase demonstrates a wedge-shaped hypodense region in the spleen *(arrow)*, consistent with a subcapsular hematoma and characterized as a grade II injury according to the AAST trauma scale (see Table 3-2).

extravasation and pseudoaneurysms. If there is any question, delayed images are often useful in making this differentiation. On delayed CT images, active contrast extravasation



FIGURE 3-15. Splenic laceration following motor vehicle accident. Axial CT image obtained during the portal venous phase of contrast enhancement demonstrates a focal linear laceration in the spleen *(arrow)* that extends from the anterior to posterior surface, fracturing the spleen into two fragments. Perisplenic hematoma *(asterisk)* is evident posterior to the area of injury.



Figure 3-16. Shattered spleen. Axial CT image obtained during the portal venous phase of contrast enhancement following motor vehicle injury. There is no definable splenic tissue in the left upper quadrant. Instead, the shattered splenic tissue is surrounded by a large amount of perisplenic hematoma that extends to the midline. Blood is also present along the surface of the right lobe of the liver. The patient required emergent splenectomy to control the severe blood loss from this acute splenic injury.

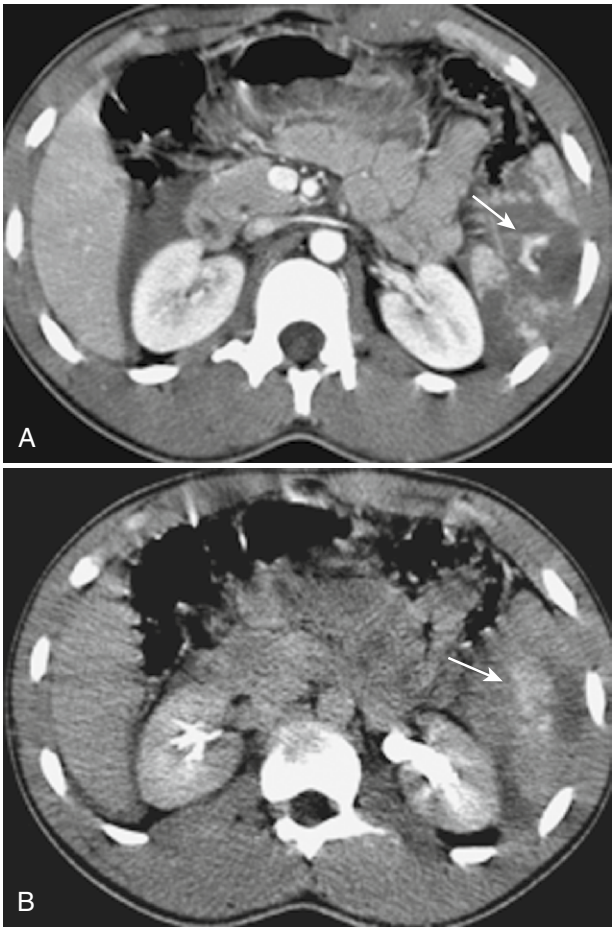


Figure 3-17. Splenic injury following blunt abdominal trauma. **A,** Axial CT image obtained during the portal venous phase of contrast enhancement demonstrates a complex splenic injury containing both complex lacerations and parenchymal hematoma. Active contrast extravasation is present *(arrow)*. **B,** Delayed image obtained 5 minutes later with decreased radiation dose (100 mAs) confirms the presence of active extravasation (as opposed to a focal pseudoaneurysm) by demonstrating continued diffusion of the contrast into the surrounding parenchymal hematoma *(arrow)*.

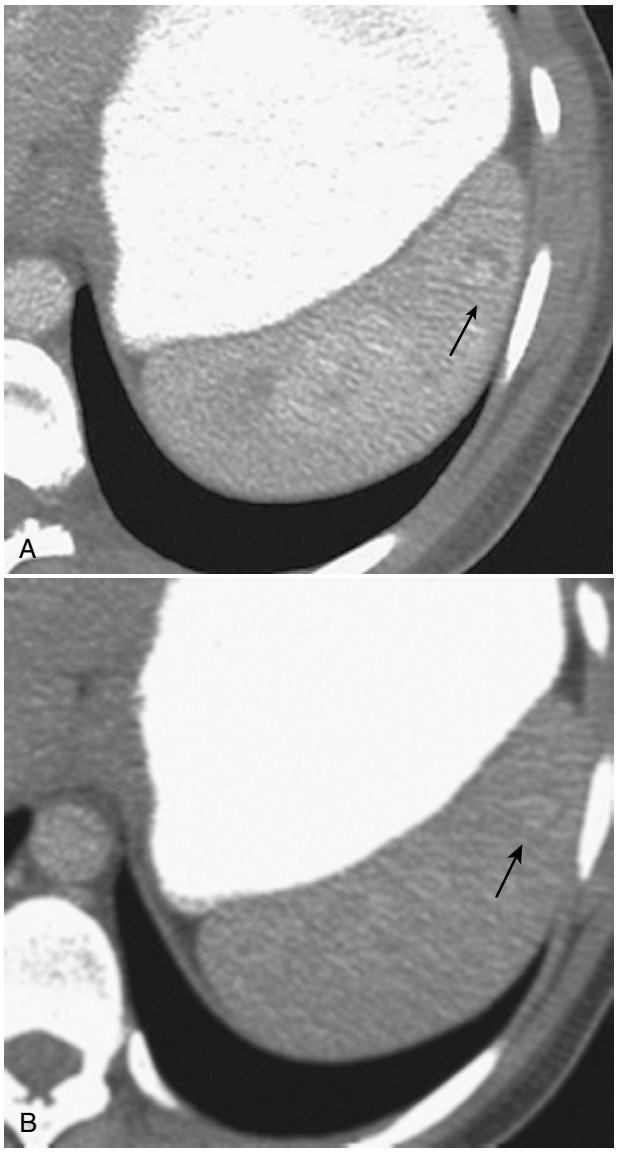


Figure 3-18. Splenic pseudoaneurysm. **A,** Axial CT obtained during the portal venous phase demonstrates a focal collection of contrast in the spleen *(arrow)* with enhancement similar to the aorta. **B,** The contrast collection is contained on the 5-minute delay CT and has decreased in density similar to the aorta *(arrow)*, consistent with the presence of a focal splenic pseudoaneurysm.

shows a change in shape and usually an increase in size as the material continues to diffuse into the site of injury (see Fig. 3-17). On the other hand, pseudoaneurysms do not change in size or shape at different points in time, and the attenuation of the pseudoaneurysm tends to follow that of adjacent arteries such as the splenic artery or aorta (see Fig. 3-18). Other focal vascular injuries include the development of arteriovenous fistulas. Such injuries can be difficult to distinguish by CT alone, and are better characterized with catheter angiography. Once active contrast extravasation or a focal vascular injury such as a pseudoaneurysm is detected, the need for catheter angiography and possible endovascular therapy should be carefully assessed. Although practices vary among institutions, patients with proved active extravasation are more likely to undergo splenectomy, whereas contained

vascular injuries such as pseudoaneurysms are more amenable to endovascular therapy with coil embolization.

PANCREATIC INJURY

Traumatic injuries of the pancreas are much less common than injury of the liver and spleen. In fact, pancreatic injury is reported to occur in less than 1% of all patients suffering blunt abdominal trauma. However, detection of such injuries is critical, since a delay in diagnosis can be a cause of significant morbidity and mortality. Unlike most injuries to the liver and spleen, injuries of the pancreas can be extremely difficult to detect and require a careful evaluation of MDCT images and use of complementary studies, such as MRCP and ERCP.

The pancreas is vulnerable to crushing injury from impact against the adjacent vertebral column. Two thirds of pancreatic injuries occur in the pancreatic neck (junction of body and head) and body, and the remainder are equally distributed between the head and tail. Isolated pancreatic injuries are rare; injuries to other organs, especially the liver, stomach, duodenum, and spleen, occur in more than 90% of cases. Not uncommonly, three or more organs are involved. In adults, more than 75% of blunt injuries to the pancreas are due to motor vehicle collisions. In children, bicycle injury is a common mechanism, and child abuse should be suspected in cases of infants with pancreatic trauma. Clinical findings are not very helpful in detecting such injuries, and more often the injury is suspected when amylase and lipase levels are found to be elevated. However, CT is still the mainstay for diagnosing pancreatic injury in trauma patients.

Injuries to the pancreatic head are almost twice as likely to be fatal (28%) than are injuries to the tail (16%), due to associated involvement of the inferior vena cava, superior mesenteric vein, or portal vein in the latter. In addition, the location of injury influences the surgical approach. Removal of more than 50% of the gland may lead to glucose regulation abnormalities or frank diabetes, and pancreas-sparing procedures are often attempted. Duct injuries occurring in the tail of the pancreas may be treated successfully by partial pancreatectomy with little risk of endocrine or exocrine dysfunction.

The main source of delayed morbidity and mortality from pancreatic trauma is disruption of the main pancreatic duct. The risk of abscess and fistula formation in patients with disruption of the pancreatic duct approaches 25% and 50%, respectively. Conversely, patients without duct injuries develop abscess or fistula in less than 10% of cases. Disruption of the pancreatic duct is treated surgically or by therapeutic endoscopy with stent placement, while injuries without duct involvement are usually treated nonsurgically. As such, it is critical that imaging focus on determining the integrity of the pancreatic duct directly or on indirect findings that suggest damage to the duct.

The imaging appearance of pancreatic trauma usually mimics the type of injury present. The role of ultrasonography is limited, but gland lacerations and transection can be seen as hypoechoic linear defects within the pancreatic parenchyma (Fig. 3-19). CT diagnosis of pancreatic injury is often difficult, with a reported sensitivity of 65% to 75% (although the sensitivity with newer MDCT scanners may be higher). Pancreatic injuries are typically detected on portal venous phase CT images of the abdomen. It is important to closely inspect the pancreas on thin-section images with liberal use of multiplanar reconstruction when available, since the many clefts of the pancreas can mimic or hide subtle injuries.

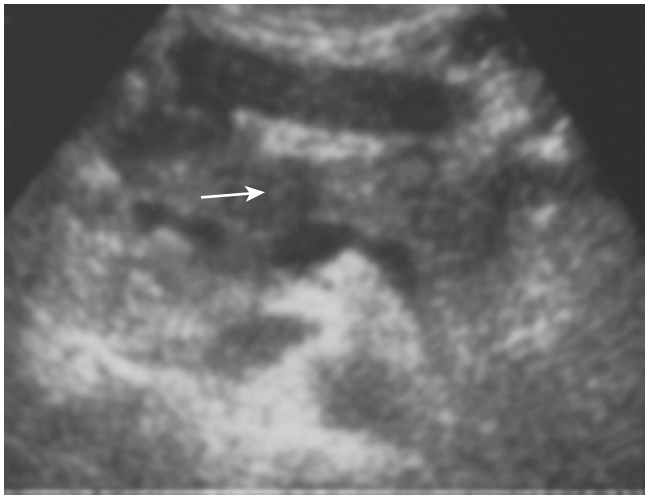


FIGURE 3-19. Pancreatic laceration. Ultrasound of the abdomen in a patient with pain following acute trauma shows a focal hypoechoic line *(arrow)* extending into the parenchyma of the pancreas, consistent with a focal laceration.

On contrast-enhanced CT, crush injuries (contusions) may show focal or diffuse enlargement and edema within the pancreas, characterized by areas of low attenuation extending through the planes of tissue within the gland (Fig. 3-20). Lacerations are detected as focal low-attenuation lines, most often perpendicular to the plane of the gland and duct (Fig. 3-21) and which may extend completely through the pancreas (termed *pancreatic transection*; Fig. 3-22). Additional indirect signs of injury include peripancreatic fluid/stranding as well as retroperitoneal hematoma in the peripancreatic region. A crucial part of the imaging

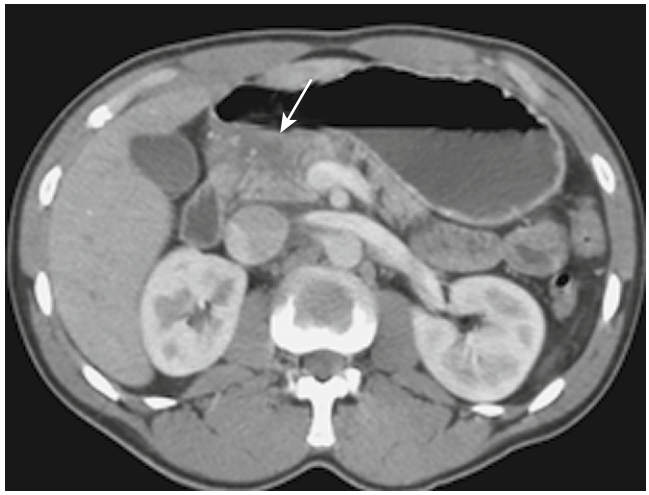


FIGURE 3-20. Pancreatic trauma after blunt rugby injury. Axial CT during the portal venous phase shows a contusion of the pancreatic head *(arrow)*. This patient was managed conservatively without the need for surgical intervention.

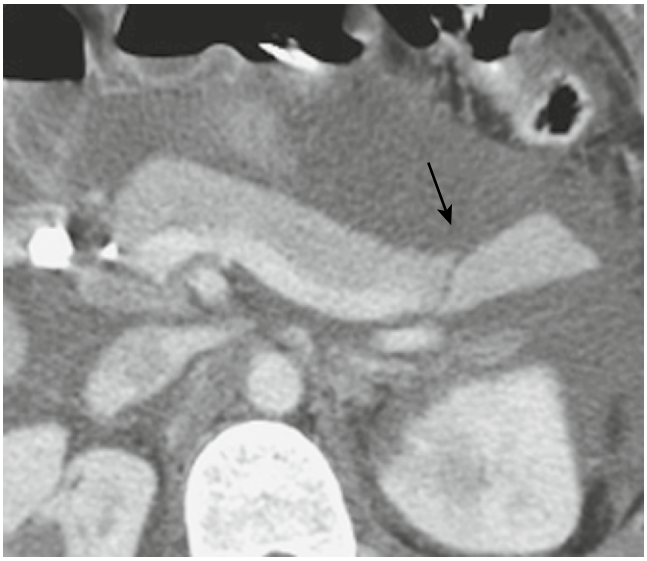


Figure 3-21. Pancreatic laceration. CT obtained in the portal venous phase demonstrates a focal low attenuation line *(arrow)* running through the pancreatic parenchyma in the tail of the pancreas, consistent with a focal pancreatic laceration.

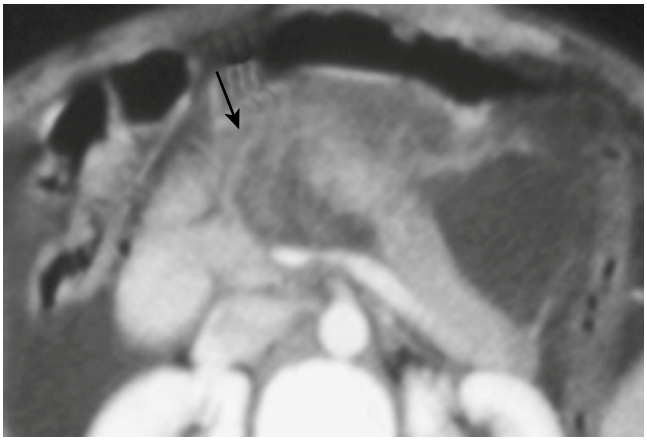


Figure 3-22. Pancreatic transection. Trauma CT demonstrating complete transection of the body of the pancreas *(arrow)* due to blunt traumatic injury.

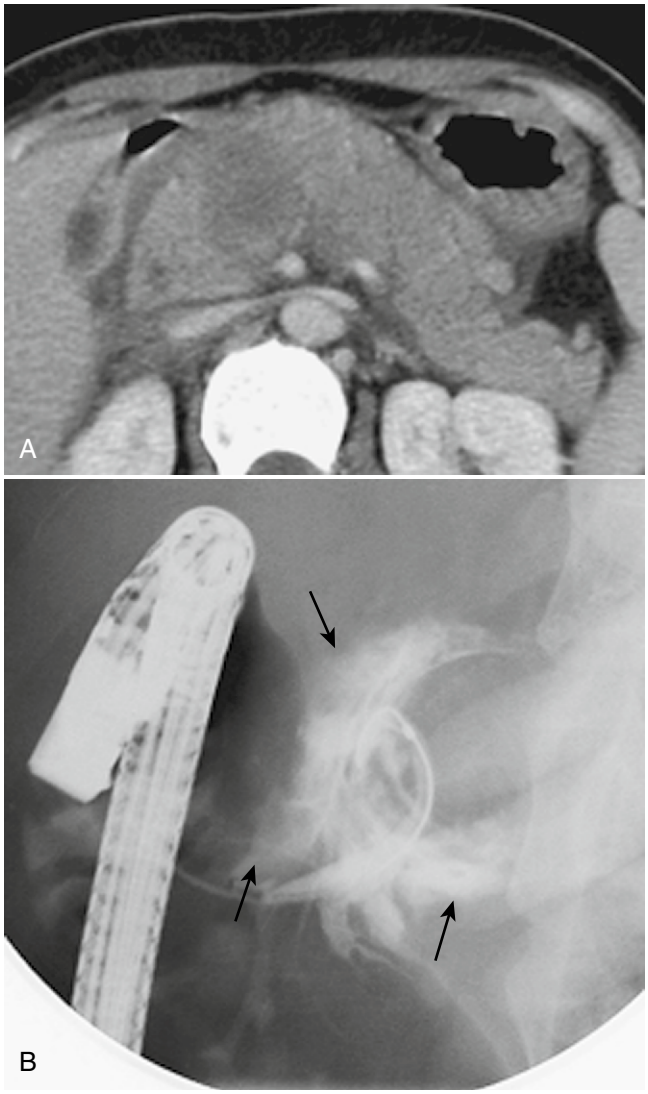


Figure 3-23. Pancreatic laceration with main duct injury. **A,** Axial CT obtained at the time of initial evaluation demonstrates a complex laceration of the pancreatic head–neck junction with near-complete transection. Injury of the main pancreatic duct was suspected. **B,** ERCP obtained to evaluate the extent of injury demonstrates contrast extravasation at the site of injury *(arrows)*, confirming the presence of injury to the main pancreatic duct.

characterization of pancreatic injury is to determine the depth of a laceration and any possible involvement of the main pancreatic duct. With modern MDCT technology, the pancreatic duct can be seen directly in the majority of patients. The depth of a laceration is also a useful predictor of main duct involvement: involvement of more than 50% of the anteroposterior thickness of the gland is often associated with duct transection (Fig. 3-23). While not commonly used, at least one CT grading system that parallels the surgical classification of Moore has been suggested: grade A, pancreatitis or superficial laceration (less than 50% pancreatic thickness); grade B1, deep laceration (greater than 50% pancreatic thickness) of the pancreatic tail; grade B2, transection of the pancreatic tail; grade C1, deep laceration of the pancreatic head; and grade C2, transection of the pancreatic head. Delayed complications, such as arterial pseudoaneurysms, abscesses, and pseudocysts, are all readily imaged by CT. Pseudoaneurysms typically appear as focal collections of contrast that enhance similarly to the aorta on all phases of imaging (Fig. 3-24). Pseudocysts and abscesses appear as focal pancreatic fluid collections of varying size. Percutaneous sampling under imaging guidance is very useful to confirm the diagnosis of superimposed infection.

One potential pitfall to be avoided is the misinterpretation of isolated low-attenuation fluid around the pancreas, without direct evidence of parenchymal trauma, as evidence of pancreatic injury (Fig. 3-25). In the trauma population, this can be the result of accumulation of fluid in the retroperitoneum from rapid or excessive administration of fluids for resuscitation. If there is a question, a repeat CT 24 to 48 hours later is advisable. Fluid

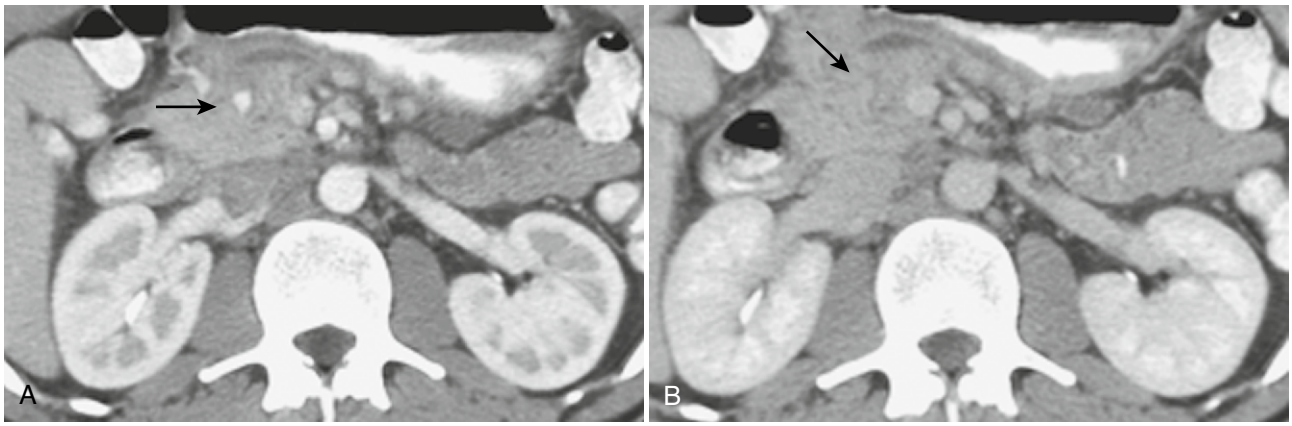


FIGURE 3-24. Pancreatic pseudoaneurysm following blunt trauma. **A,** Axial CT performed during the portal venous phase demonstrates a focal contained collection of contrast in the pancreatic head/neck region *(arrow)* at the site of previous pancreatic laceration with enhancement similar to the aorta. **B,** The delayed CT image obtained 5 minutes following the initial contrast injection confirms the presence of a pseudoaneurysm, with the focal collection *(arrow)* now decreased in attenuation as it mirrors enhancement characteristics of the adjacent vessels (including the aorta). This pseudoaneurysm resolved several days later and did not require further intervention.

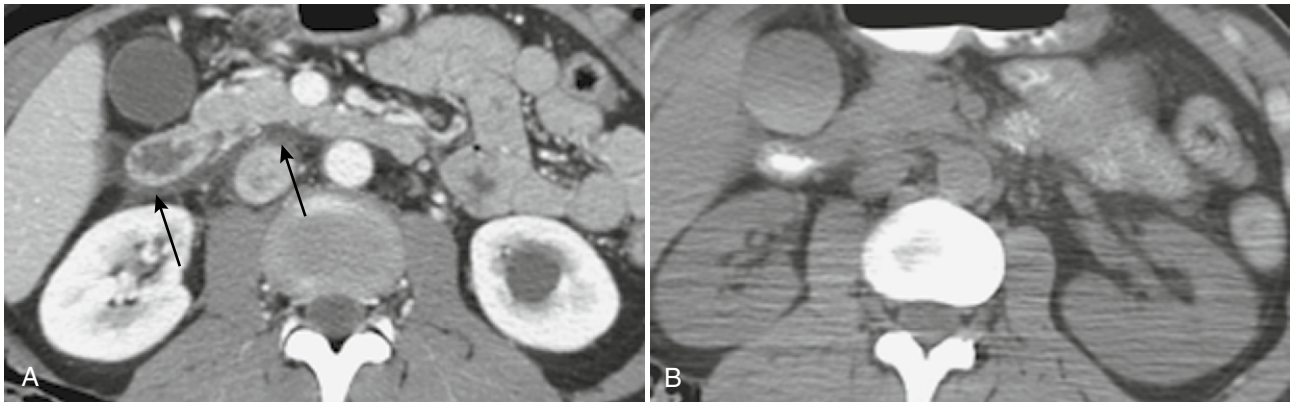


FIGURE 3-25. Retroperitoneal fluid mimicking pancreatic injury. **A,** Axial CT image during the portal venous phase following motor vehicle accident shows low-density fluid *(arrows)* in the retroperitoneum posterior to the pancreas tracking anterior to the inferior vena cava and posterior to the duodenum. The possibility of pancreatic or duodenal injury was initially raised, although the patient did not exhibit clinical signs of either injury. Thus, follow-up CT was requested. **B,** Axial CT image with oral and intravenous contrast obtained 24 hours later shows that the fluid has nearly resolved, suggesting that the initial CT findings were due to fluid resuscitation and not to pancreatic or bowel injury.

related exclusively to exogenously administered replacements will decrease or resolve, whereas true pancreatic injuries lead to growing fluid collections and hematomas. Also, pancreatic lacerations may be very subtle on initial CT scans. Thus, if the patient develops abdominal pain after admission, a repeat CT with special attention to the pancreas is indicated.

Once injury to the pancreas is identified, MR and MRCP can help in further assessing the status of the main pancreatic duct, especially for follow-up of pancreatic injuries in these typically young patients in whom unnecessary radiation should be avoided if possible (Fig. 3-26). Common MR pulse sequences acquired include fat-suppressed T1- and T2-weighted sequences and MRCP, performed by using heavily T2-weighted breath-hold or non-breath-hold sequences. Fast spin-echo (two-dimensional or three-dimensional) and rapid acquisition with relaxation enhancement (RARE) sequences performed in the coronal and axial planes are usually sufficient. In addition to evaluating the pancreatic duct, MR can be used to assess for pancreatic fluid collections that may have developed due to the pancreatic ductal injury (Fig. 3-27). Hemorrhagic components are also easily detected with MR. Although MRCP is useful for evaluating the pancreatic duct, ERCP is important because of its potential to definitively confirm communication of an apparently interrupted duct with surrounding fluid collections (see Fig. 3-23). In addition, ERCP provides a means for possible endoscopic therapy of pancreatic duct leaks and fluid collections.

BOWEL AND MESENTERIC INJURY

Injuries to the bowel and mesentery are uncommon but potentially devastating, since they are difficult to diagnose both clinically and with imaging. Most blunt injuries are secondary to motor vehicle collisions, although other

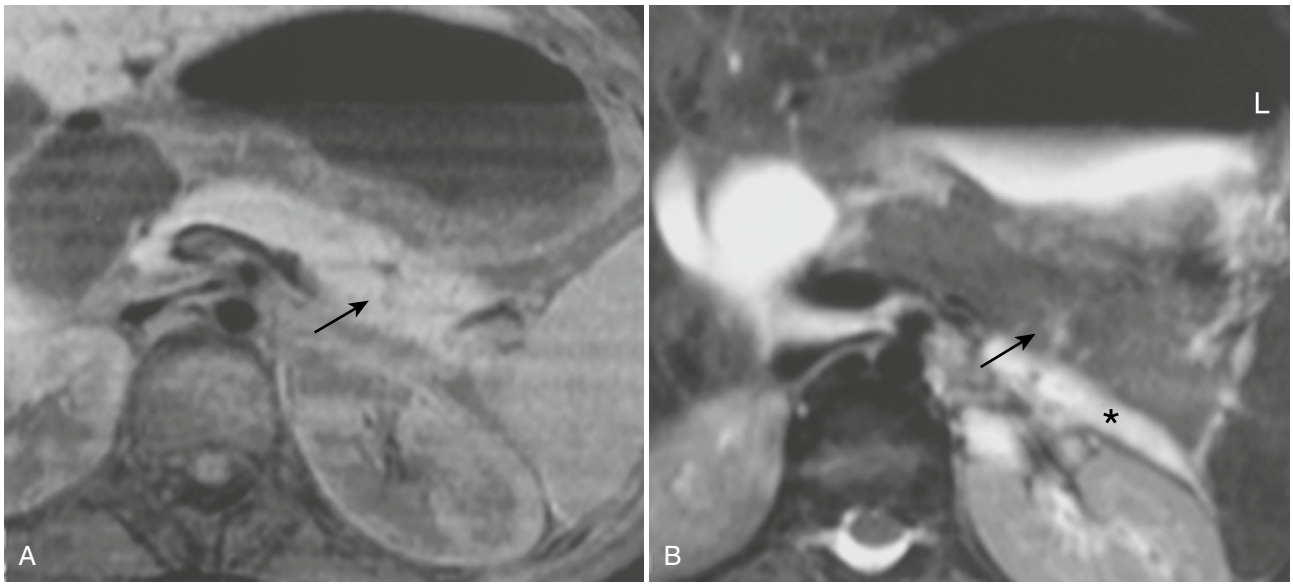


Figure 3-26. MR appearance of pancreatic injury. **A,** Axial T1 with chemical fat saturation demonstrates a focal laceration *(arrow),* which appears as low signal intensity on this pulse sequence. **B,** Axial fat-saturated T2-weighted sequence shows the laceration as focal linear increased signal in the tail of the pancreas *(arrow).* The fluid-sensitive T2 sequence also shows the presence of peripancreatic fluid *(asterisk).*

mechanisms, including assaults and sports-related trauma, produce such injury. Injury of the small bowel is much more common than injury of the colon or stomach in the setting of blunt trauma (Box 3-1).

Although bowel and mesenteric injuries can occur in isolation, most patients present with injuries to other organ systems, typically the liver or spleen. Three different mechanisms have been described. The first type of injury, a crush injury, generally occurs due to impaction of the bowel between the anterior abdominal wall and the spine or other solid organ. This type of injury leads to bowel wall contusions, mural hematomas, and lacerations, and often involves the duodenum and transverse colon. The second type of injury, a shearing injury, occurs at the sites of fixed anatomic structures, such as at acquired adhesions or at normal points of bowel fixation (such as the ligament of Treitz and the ileocecal valve). During brief periods of rapid deceleration, mobile loops of bowel are pulled away from points of fixation, leading to shearing-type injuries, which include bowel or mesenteric lacerations, mesenteric vascular injuries, and degloving injuries where the serosa is stripped away from the rest of the wall. The third type of injury, the burst injury, is due to sudden increases in intraluminal pressure that lead to focal bowel perforation or laceration.

Delayed diagnosis of bowel or mesenteric injuries is a leading cause of morbidity and mortality in victims of

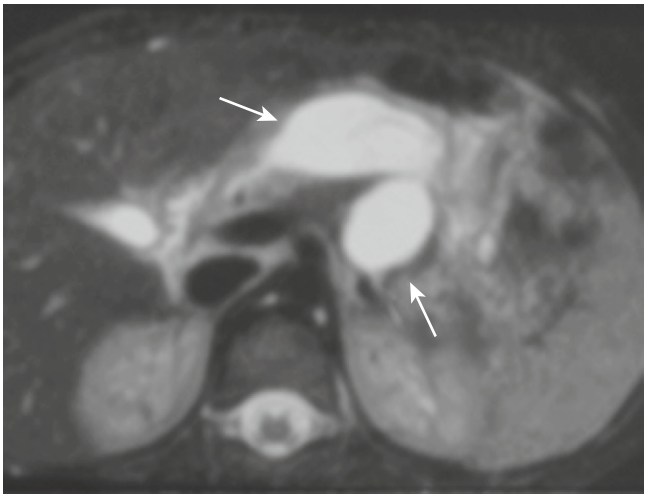


Figure 3-27. Pancreatic fluid collections, MR appearance. Axial fat-saturated T2 pulse sequence demonstrates two distinct fluid collections *(arrows)* as high signal intensity. The collections developed secondary to a pancreatic laceration with ductal injury that occurred at the time of the initial trauma.

Box 3-1. **Typical Locations of Bowel Injuries Due to Blunt or Penetrating Trauma**

STOMACH

Anterior wall > greater curve > lesser curvature > posterior wall

SMALL INTESTINE

Duodenum (second and third segment injury most common)
Jejunum (near ligament of Trietz)
Ileum (distal near ileocecal valve)

COLON

Left colon (more common in blunt trauma)
Right colon and transverse colon (more common in penetrating trauma)
Rectum (more common in penetrating trauma, rare in blunt trauma)

blunt trauma. The clinical diagnosis of a focal injury to the bowel or mesentery can be extremely challenging. Trauma patients are often intoxicated and have distracting injuries, altered levels of consciousness, or closed head injuries that preclude the accurate detection of physical symptoms and may mask the clinical manifestations of bowel injury. In the past, trauma surgeons relied on invasive tests such as diagnostic peritoneal lavage as a means of detecting intestinal contents or blood in the peritoneal cavity. However, this test is invasive and not specific and often led to a large number of nontherapeutic exploratory laparotomies. Peritoneal lavage has been replaced by CT as the main diagnostic modality. Improvements in technology and increased awareness of the many (often subtle) CT signs of bowel and mesenteric injuries have resulted in earlier detection. Ultrasonography is not reliable for direct demonstration of the bowel injury, although the finding of free peritoneal fluid on the initial FAST scan may serve as indirect evidence of injury and heighten clinical suspicion.

CT diagnosis of injuries to the bowel and mesentery is not always straightforward. Unlike most solid organ injuries, which are often obvious, the radiologist needs to carefully inspect the images for direct and indirect signs, each having varying ranges of sensitivity and specificity. Numerous CT signs have been reported to occur in the setting of bowel and mesenteric trauma (Box 3-2).

Since the detection of bowel and mesenteric injuries is challenging, and so many reported CT signs must be carefully sought for, it may be more useful to consider the types of injury and the possible appearance of such injury on trauma CT scans. According to the AAST injury scale for the bowel (including stomach, duodenum, small intestine, and colon), injuries tend to vary from mild grade I injuries such as bowel wall hematomas to severe grade V injuries including devascularization and complete bowel wall transection. Mesenteric vascular injuries vary from grade I distal branch vessel injury to grades III and IV superior mesenteric trunk and celiac axis injuries, with grade V injury reserved for major abdominal vessel (aortic, caval, or extrahepatic portal vein) injury. Thus, the frequency of individual CT signs found in bowel and mesenteric injuries depends on the type and severity of injury that has occurred.

Box 3-2. **CT Signs of Injury**

CT SIGNS OF BOWEL INJURY
Intramural hematoma
Intramural gas
Bowel wall disruption
Bowel wall transection
Abnormal bowel wall enhancement
Free intraperitoneal air
Free retroperitoneal air
Free intraperitoneal fluid
Free retroperitoneal fluid
Extravasated extraluminal oral contrast
Bowel wall thickening

CT SIGNS OF MESENTERIC INJURY
Mesenteric hematoma
Mesenteric vascular beading
Mesenteric active contrast extravasation

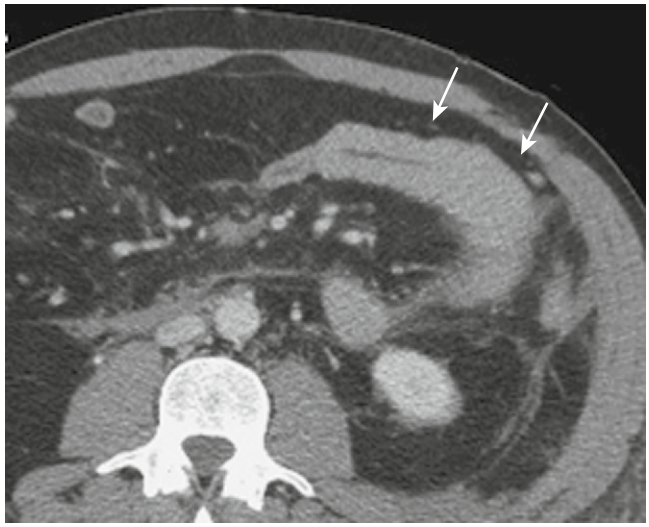


FIGURE 3-28. Bowel wall hematoma. Axial CT without oral contrast demonstrates focal bowel wall thickening *(arrows)* in this patient following motor vehicle collision. The bowel wall is thickened and increased in density compared with the adjacent muscle.

Bowel wall hematomas and contusions, when visible by CT, typically present with focal thickening of the bowel wall. The area of thickening may appear hyperattenuating relative to the normal bowel wall due to the presence of acute blood (Fig. 3-28). Depending on the severity of the injury, the hematoma may be eccentric or concentric in appearance. More severe injuries, which include lacerations of the bowel wall, are only rarely directly seen on CT as focal wall interruptions or frank discontinuity. Instead, other secondary signs of bowel laceration may be present to suggest such an injury. Free intraperitoneal air is one of the more common findings in patients with focal bowel wall lacerations (Fig. 3-29). However, the overall sensitivity of this finding varies between 20% and 75%. Free air may be found locally, adjacent to the site of perforation, or remotely in the upper abdomen near the surface of the liver or along the undersurface of the peritoneum. The presence of free air is not 100% specific for bowel injury, and other benign iatrogenic and traumatic causes (such as bladder rupture and air introduced at the time of Foley catheter placement) must be considered (Box 3-3).

Free intraperitoneal fluid is another sign associated with bowel and mesenteric trauma. In fact, it has been reported as the most common individual finding. This fluid can be seen adjacent to the site of the injury within the leaves of the mesentery, or diffusely throughout the abdomen and pelvis. While often present in combination with other CT findings, the significance of isolated free fluid on trauma CT scans is controversial, but it appears to be less commonly associated with bowel and mesenteric injuries than was once thought (see discussion on free fluid later in this chapter). However, isolated small puddles of free fluid trapped within the mesentery, seen on CT as small triangles outlining the mesenteric leaves (Fig. 3-30), should prompt a very careful review of the bowel loops for direct evidence of injury.

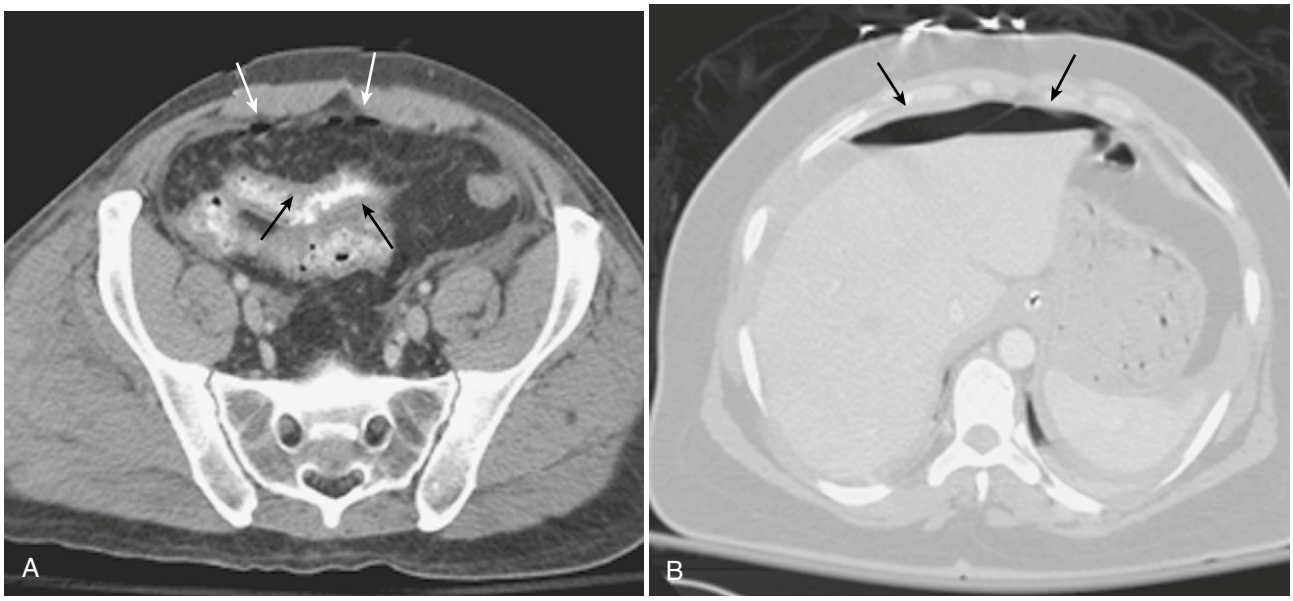


Figure 3-29. Free intraperitoneal air due to bowel injury. **A,** Axial CT performed with oral and intravenous contrast shows focal wall thickening of the distal ileum *(black arrows)* with small bubbles of free air in the lower abdomen *(white arrow)*. A focal 1-cm ileal perforation was confirmed at surgery. **B,** Axial CT performed during the portal venous phase shows a large collection of free air in the upper abdomen *(arrows)*. A sigmoid laceration was detected at surgery.

Box 3-3. **Causes of Free Intraperitoneal Air on Trauma CT Exams**

TRAUMATIC CAUSES
Bowel injury
Bladder injury

NONTRAUMATIC CAUSES
Penetrating injury without organ damage
Iatrogenic
Diagnostic peritoneal lavage
Pneumothorax
Pneumomediastinum
Mechanical ventilation

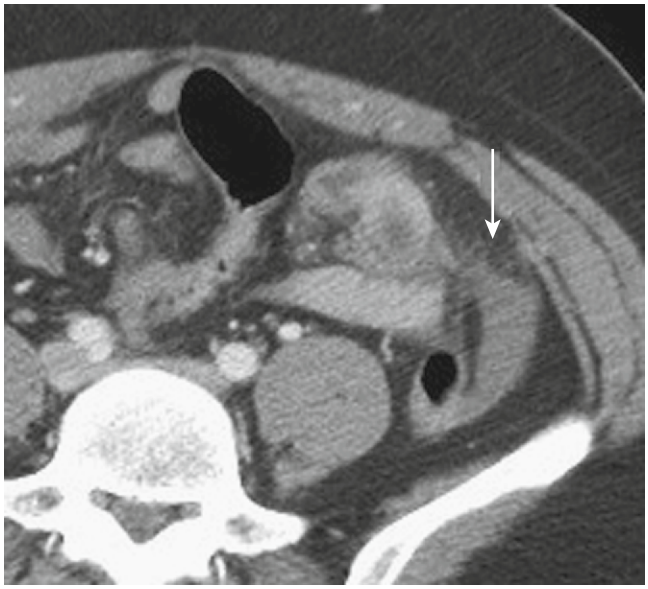


Figure 3-30. Mesenteric hematoma. Axial CT in this patient demonstrates a focal triangular-shaped hematoma in the bowel mesentery *(arrow)*. Mesenteric hematomas are often subtle, so careful inspection of the mesentery is required to exclude the presence of injury. The presence of mesenteric hematoma should raise the index of suspicion for associated bowel injury.

In addition to extraluminal air and fluid, oral contrast may also escape into the peritoneal cavity when a bowel laceration is present (Fig. 3-31). Unfortunately, this is an uncommon finding, with reported sensitivities as low as 6%, and is highly unlikely to be present as an isolated finding. This is the main reason why the mandatory use of oral contrast in blunt trauma has been questioned, and there is now a growing trend toward non-oral contrast CT for this indication. It should be noted that focal lacerations of the duodenum may produce free air and free fluid that is isolated to the retroperitoneum (Fig. 3-32). Close inspection of the duodenal wall should be made when such findings are present.

Bowel injuries may also produce focal changes in the appearance of the bowel wall itself that can be readily detected with MDCT. Partial thickness injuries may allow air to escape into the bowel wall, producing focal pneumatosis. Other findings include focal wall thickening and focal abnormal wall enhancement following intravenous contrast administration (Fig. 3-33). Enhancement may be increased or decreased, as occurs with severe devascularization from degloving injuries. Focal abnormal wall enhancement almost always indicates that an injury requiring surgical intervention has occurred. Colonic injuries may also manifest as focal wall thickening, usually with surrounding mesenteric hematoma (Fig. 3-34).

Blunt trauma can result in significant injuries that are isolated to the mesentery, such as lacerations and vascular injuries. Mesenteric lacerations cannot be directly seen;



FIGURE 3-31. Bowel wall laceration involving the jejunum. Acute bowel wall injury in this patient was confirmed by the presence of oral contrast outside the expected lumen of bowel *(arrow)*.

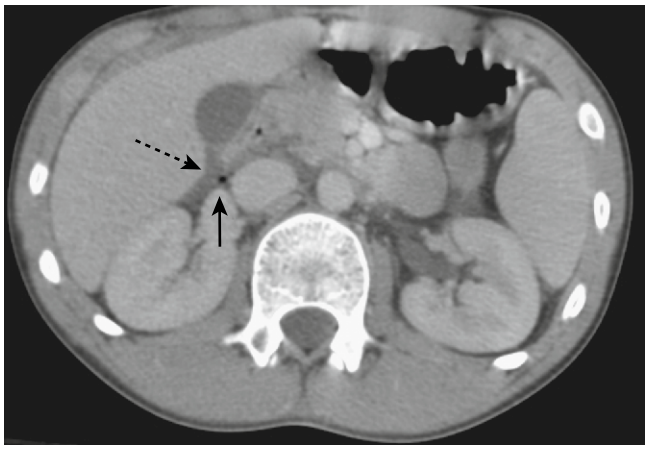


FIGURE 3-32. Duodenal laceration after a motor vehicle accident. Axial CT image during the portal venous phase demonstrates a small bubble of air in the retroperitoneum *(solid arrow)* with associated retroperitoneal fluid *(dashed arrow)*. A duodenal injury was suspected based on the CT findings and a focal laceration was confirmed at the time of surgery.

however, they often produce indirect CT signs, such as mesenteric "stranding" (focal ill-defined increase in attenuation) or the formation of a frank mesenteric hematoma due to small vessel injury (Fig. 3-35). When larger vessels are injured, active contrast extravasation may be present (Fig. 3-36). Additionally, mesenteric lacerations can lead to the development of internal hernias. Close clinical follow-up of mesenteric injury is mandatory, because even small hematomas associated with small vessel injury can produce vascular compromise of the associated segment of bowel. The resulting bowel ischemia may be seen as a focal hypoenhancing segment by CT; however, delayed presentation of such injuries, such as bowel obstruction secondary to an ischemic stricture, is possible.

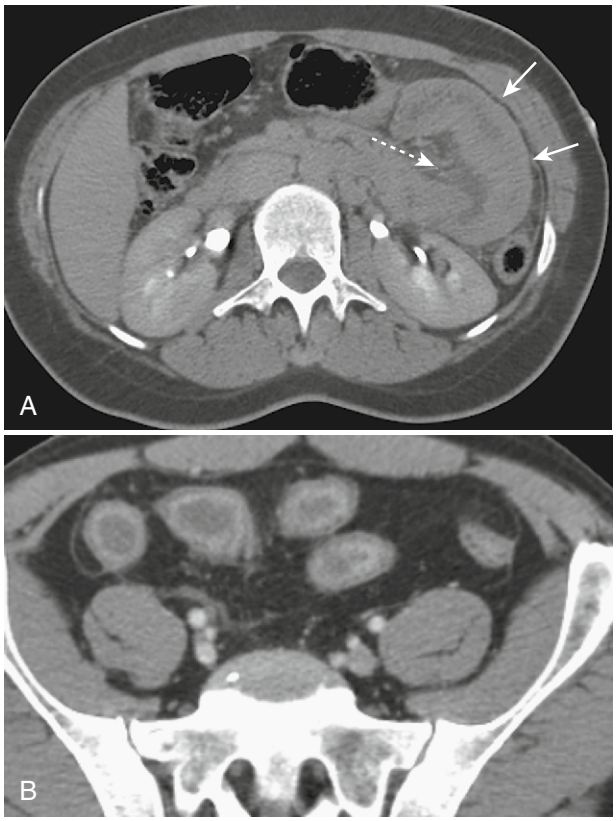


FIGURE 3-33. CT findings suggestive of focal bowel wall injury. **A,** Axial CT obtained at 5-minute delay shows focal thickening of the jejunum *(solid arrows)* with fluid in the mesentery *(dashed arrow)* due to a focal jejunal laceration that required surgical repair. **B,** Axial CT in another patient with a distal ileum laceration shows abnormal enhancement of the bowel wall greater than the adjacent psoas muscle. (**B,** Reprinted with permission from Stuhlfaut JW, Lucey BC, Varghese J, et al: Blunt abdominal trauma: Utility of 5-minute delayed CT with a reduced radiation dose. Radiology 238:473–479, 2006.)

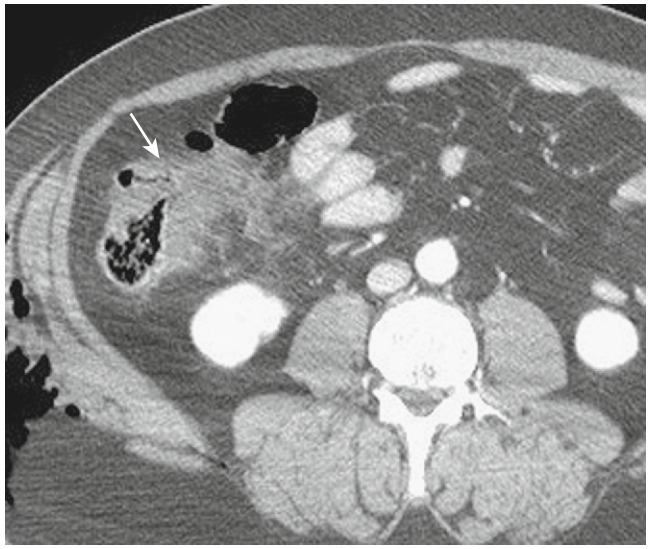


FIGURE 3-34. Focal colon injury after blunt trauma. Axial CT demonstrates focal bowel wall thickening of the ascending colon *(arrow)* with adjacent mesenteric hematoma. This patient required surgery to repair a focal laceration.

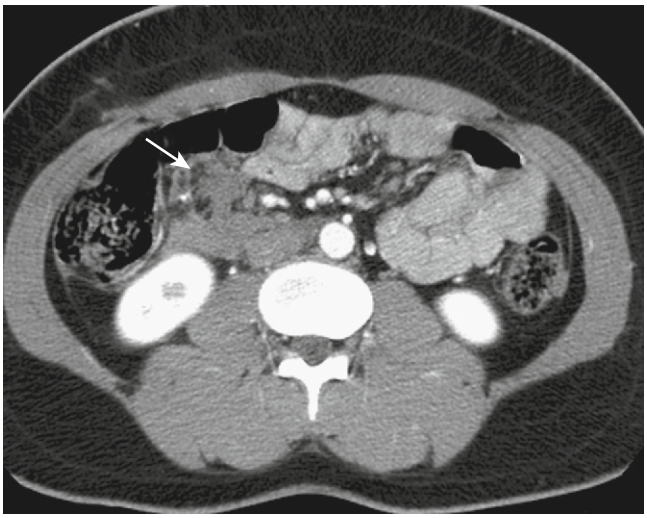


Figure 3-35. Mesenteric hematoma after motor vehicle blunt trauma. Axial CT image following administration of intravenous contrast demonstrates a focal hematoma in the mesentery *(arrow)* without evidence of bowel injury. A mesenteric laceration that required repair was identified at surgery; no bowel injury was detected.

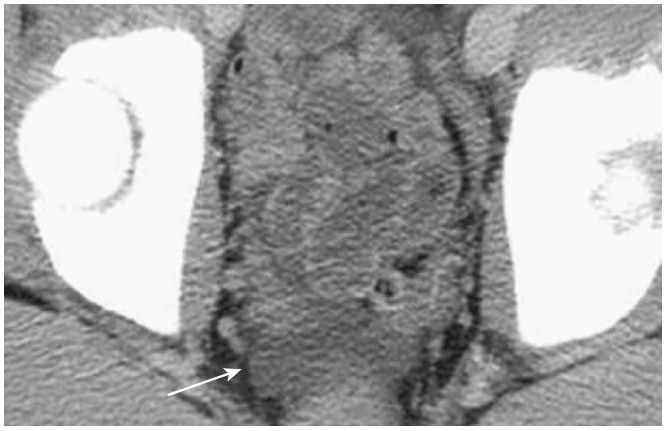


Figure 3-37. Free pelvic fluid in a male patient after blunt trauma. Axial CT demonstrates a small amount of free fluid in the recto-vesicle space (*arrow*) in this male patient following a motor vehicle collision. No solid organ injury or bowel injury was detected, and the patient recovered without the need for further imaging or intervention.

FREE PERITONEAL FLUID

Previous studies have shown that isolated free fluid is present in approximately 3% of all trauma CT scans. In the past, trauma surgeons often elected to surgically explore this subset of patients to fully evaluate the bowel for the presence of injury. However, these patients are now increasingly being managed nonoperatively. One study found that only 27% of patients with isolated free fluid require therapeutic laparotomy. Often, such patients are managed expectantly unless other clinical criteria are present to suggest acute bowel injury. The appearance and location of free fluid are often helpful in selecting patients for nonoperative management. Isolated free pelvic fluid in females is often of no clinical significance; there is also growing evidence to suggest that small amounts of low-attenuation fluid in male patients may be a benign finding, not associated with significant bowel or mesenteric injury (Fig. 3-37).

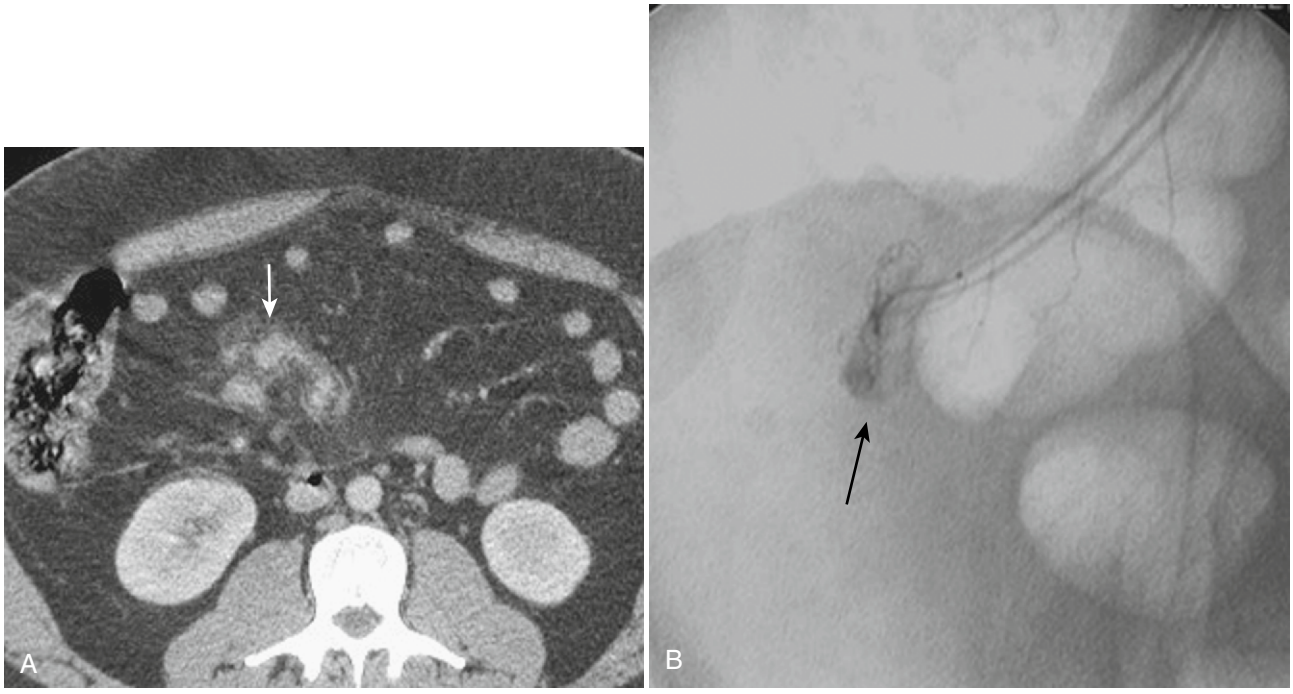


Figure 3-36. Mesenteric injury with active bleeding. **A,** Axial CT obtained during the portal venous phase demonstrates mesenteric stranding with a focal collection of extraluminal contrast *(arrow)* consistent with active extravasation. **B,** Catheter angiography was requested. A single digital subtraction image following selective injection of SMA branch vessels demonstrates a focal blush of contrast *(arrow)* that confirms the presence of active bleeding. This patient was treated with coil embolization.



FIGURE 3-38. Free intraperitoneal fluid. Sagittal reformatted image in this male patient after a motor vehicle collision demonstrates a large amount of dense fluid in the left lower quadrant and in the perisplenic region (*arrows*). While no injury to the bowel, mesentery, or solid organs was identified, the patient was taken to surgery based on the CT findings. A laceration of the middle colic artery was found and repaired at the time of exploration.

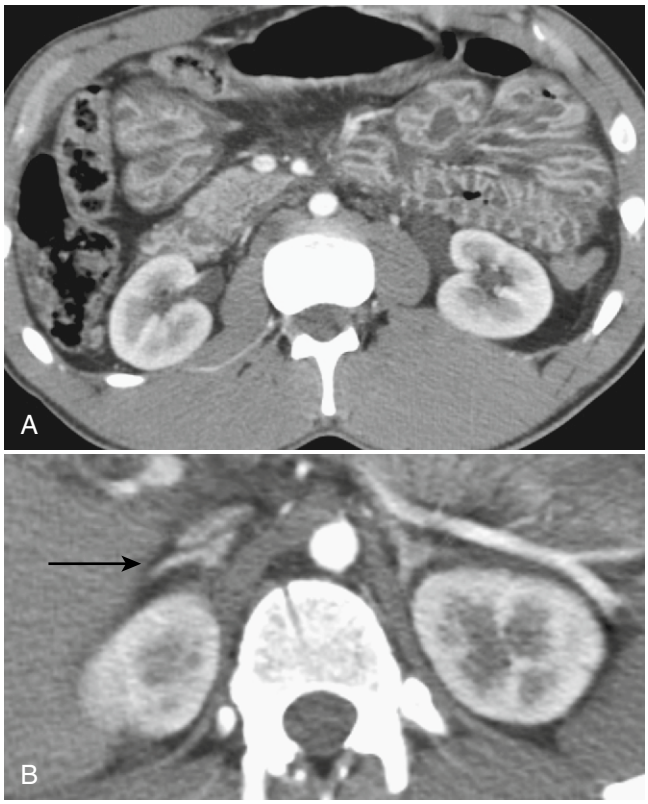


FIGURE 3-39. Hypovolemic shock, CT appearance. **A,** Axial CT obtained in the portal venous phase demonstrates diffuse mural thickening and intense enhancement of the small bowel mucosa in this patient with profound hypovolemic shock following a motor vehicle accident. **B,** In addition to the bowel findings in **A,** this patient has a flat IVC and small-caliber aorta, and there is increased enhancement of the adrenal glands (*arrow* depicts abnormal right adrenal, the left is partially imaged at this level), all signs of hypovolemic shock.

However, large amounts of free fluid in males or females (especially if high in attenuation), focal mesenteric fluid, and free fluid in more than one space or location may be indicative of an underlying injury and may warrant surgery (Fig. 3-38), close clinical observation, or CT follow-up.

Unfortunately, the surgeon and radiologist are often faced with patients whose clinical evaluation and CT examination, although not entirely normal, do not conclusively confirm the presence of a bowel injury that warrants laparotomy. These include findings such as questionable focal wall thickening, small isolated mesenteric hematomas, or isolated free intraperitoneal fluid. These patients should be admitted for close clinical observation. If the patient develops signs or symptoms consistent with peritoneal irritation, surgical intervention is then advised. Otherwise, a repeat CT with water-soluble oral contrast 12 to 24 hours after the admission CT should be considered before discharging the patient. Given the high morbidity associated with a delayed diagnosis of bowel injury, this careful approach is recommendable.

Finally, in addition to focal bowel injury, the initial trauma CT may show a diffuse abnormality of the bowel that can be seen in patients with hypovolemic shock (so-called shock bowel). Typically, the small intestine is diffusely thickened and there is increased enhancement of the small bowel mucosa (Fig. 3-39). The etiology of the intense mucosal enhancement is not completely understood, although it is thought to be due to increased vascular permeability of the bowel mucosa due to hypoperfusion. Occasionally, the bowel may appear dilated. This appearance is fairly classic and is usually reversible once the patient is appropriately resuscitated. In addition to small bowel abnormalities, profound hypovolemia is also associated with flattening of the inferior vena cava, decrease in caliber of the abdominal aorta, pancreatic swelling, and increased enhancement of the adrenal glands (typically greater than adjacent vascular structures), which maintain normal size and shape.

RENAL AND URETERAL TRAUMA

Renal Injury

Injuries of the genitourinary system involve the kidney, adrenal gland, ureter, bladder, and urethra. The most commonly injured organ is the kidney, which accounts for approximately 90% of all injuries to the genitourinary system. Most renal injuries occur as a result of blunt trauma such as motor vehicle collisions or sports-related injuries. The main clinical finding leading to suspected renal trauma is gross or microscopic hematuria, although many patients are asymptomatic or may have associated injuries

Table 3-3 AAST Classification of Traumatic Renal Injury

Grade	Description
I	Contusion Subcapsular hematoma
II	Nonexpanding perinephric hematomas confined to the retroperitoneum Superficial cortical lacerations <1 cm in depth without collecting system injury
III	Renal lacerations >1 cm in depth that do not involve the collecting system
IV	Renal lacerations extending through the kidney into the collecting system Injuries involving the main renal artery or vein with contained hemorrhage Segmental infarctions without associated lacerations Expanding subcapsular hematomas compressing the kidney
V	Shattered or devascularized kidney Ureteropelvic avulsions Complete laceration or thrombus of the main renal artery or vein

that confound the clinical presentation. In addition, up to 14% of patients with trauma to the kidneys may present without hematuria, including some with severe injuries. CT and, less often, US are used to identify renal injuries. If a renal or ureteral injury is suspected prior to imaging, or if the initial images show signs of injury, delayed images should be obtained to better evaluate the integrity of the collecting system and to determine the need for further intervention.

The types of injuries that can affect the kidneys include renal contusions, hematomas, lacerations, fractures, shattered kidney, and renal vascular pedicle injury. Again, the AAST has developed a grading system for renal injury that can serve as a guideline for characterizing injuries at the time of CT interpretation (Table 3-3). Overall, most renal injuries fall into one of two categories: contusion and laceration. These injuries may appear severe at CT, due to the associated lack of enhancement of the traumatized segment, but are often stable and require no further intervention or follow-up. Contusions represent parenchymal injuries that produce interstitial edema and hemorrhage. The contused kidney is often swollen and hypofunctioning, either focally at the site of injury or diffusely with more severe injury. Lacerations represent focal tears in the parenchyma. If a laceration is present, the patient is at risk of developing a perirenal urinoma and hematoma. Only about 5% of traumatic lesions are classified as renal fractures, shattered kidneys, or vascular pedicle injury. These injuries may be unstable and usually require further intervention, either by catheter angiography or by surgical repair.

Ultrasonography

Sonography is particularly limited for evaluation of the kidneys following blunt trauma. Acute hematomas are typically hyperechoic and difficult to differentiate from the echogenic renal sinus or perirenal fat (Fig. 3-40). Although early experience suggests that detection of parenchymal injuries is enhanced with the use of ultrasound contrast agents, their use in practice is limited, as is the case for most trauma applications. When seen, renal lacerations appear as linear hypoechoic defects within the parenchyma and may extend to the renal capsule. Injury to the vascular pedicle may be identified by total lack of enhancement of the kidney following contrast injection.

Computed Tomography

On CT, renal contusions appear hypoattenuating relative to the surrounding enhanced parenchyma and are optimally seen on the nephrographic phase of contrast enhancement, which typically occurs 90 to 120 seconds following initiation of intravenous contrast infusion. However, most injuries are also well seen in the portal venous phase of

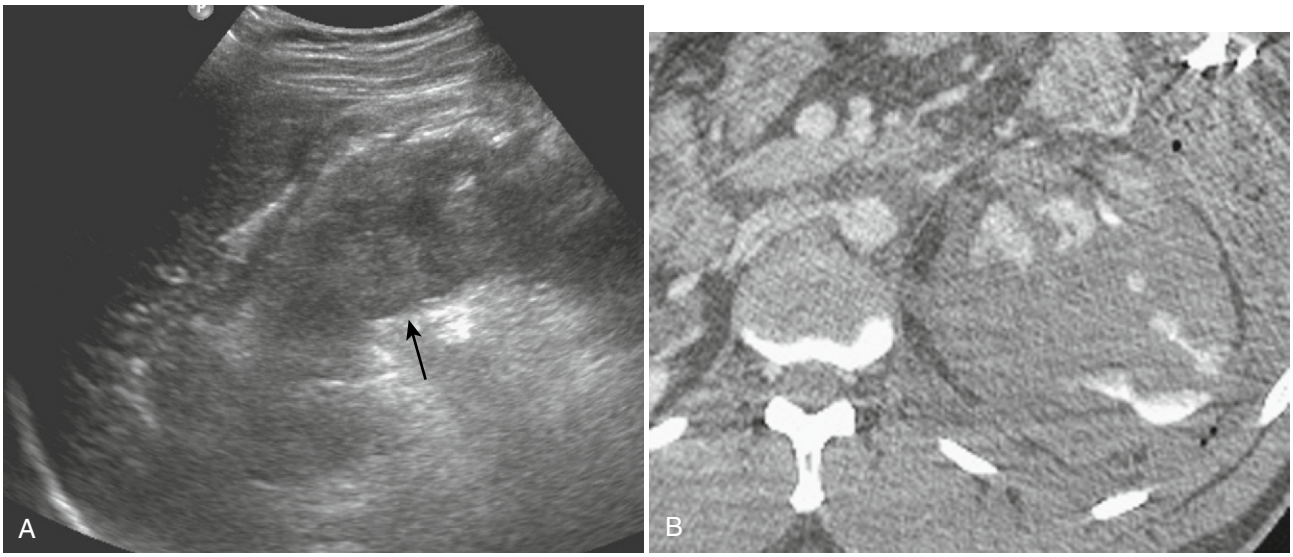


Figure 3-40. Shattered kidney. **A,** Ultrasound of the left flank demonstrates increased echogenicity in the expected location of the left kidney *(arrow)*, without readily identifiable renal parenchyma. **B,** CT performed following the initial ultrasound confirms the presence of a shattered kidney. The increased echotexture on ultrasound corresponds to hematoma, which appears as low density on this CT.



FIGURE 3-41. Renal contusion. Axial CT image obtained following blunt abdominal injury during the portal venous phase of contrast enhancement. There is a focal area of hypodensity *(arrow)* in the upper portion of the right kidney with minimal stranding due to blood in the perirenal fat. This injury is typical of a renal contusion and typically requires no further management.



FIGURE 3-42. Renal laceration. Axial CT in patient after a motor vehicle collision demonstrates a focal low density line *(arrow)* in the renal cortex diagnostic of a focal renal laceration. Perinephric hematoma is present in the fat adjacent to the injury.

hepatic contrast enhancement, the timing used for most abdominal trauma CT scans. A contused kidney is often hypofunctioning, and CT demonstrates a delay in enhancement relative to the normal-functioning contralateral kidney or the ipsilateral noncontused areas (Fig. 3-41). On later phases, the contused kidneys may show a persistent nephrogram with delayed excretion of contrast into the collecting system. Renal laceration represents a tear in the parenchyma and manifests as a focal area of linear low attenuation on CT. The laceration typically extends to the surface and is often associated with a perirenal hematoma or fluid collection (Fig. 3-42). Once a laceration is identified, delayed images are extremely important for demonstrating a potential leak of urine containing dense contrast material into the perinephric space (Fig. 3-43). In addition, some lacerations are associated with active extravasation of contrast-enhanced blood (Fig. 3-44). Unless there is associated major vascular injury, most lacerations will heal without any specific therapy.

A renal fracture represents a severe form of laceration in which the kidney is separated into at least two complete independent fragments. If the kidney is fractured into more than three parts, the injury is typically described as a shattered kidney. This injury is often easier to characterize with the help of multiplanar reformations, which afford the opportunity to identify fracture lines running in different planes. Once detected, any significant perirenal hematoma or focus of active contrast extravasation should be noted since these patients may require further intervention. If the patient is stable and surgery can be avoided, catheter angiography is often helpful to identify isolated arterial injuries that may benefit from embolization. Shattered kidneys more often require surgical intervention and nephrectomy to control bleeding from multiple injured branch vessels.

Finally, injury of the vascular pedicle typically represents either an acute traumatic dissection or transection of

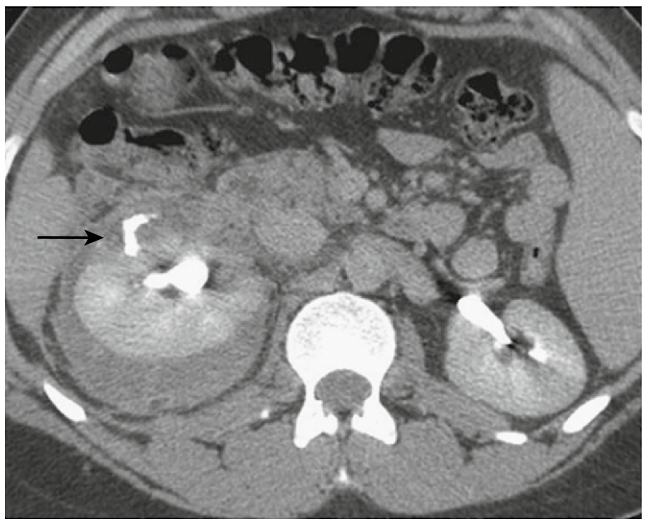


FIGURE 3-43. Renal laceration. Axial CT in this patient was obtained at 5-minute delay to assess the integrity of the collecting system. In addition to a small laceration with perinephric hematoma, a focal collection of contrast *(arrow)* is present in the perinephric space, consistent with a small urine leak.

the renal artery or vein (Fig. 3-45). When such an injury occurs, the kidney will show an absence or near absence of contrast enhancement on the portal venous phase CT exam and there may be associated perirenal hematoma. This injury is severe, and patients may present in hypovolemic shock due to profound blood loss. This injury may be treated by surgical revascularization if detected early (typically within the first 6 hours following the initial trauma); otherwise, nephrectomy is indicated as the kidney is

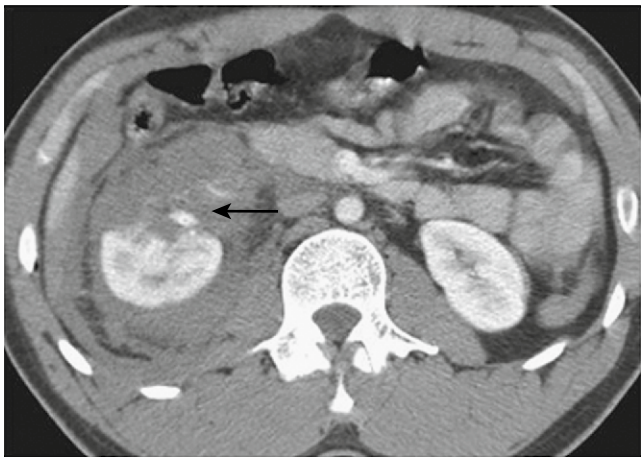


Figure 3-44. Complex renal injury with active contrast extravasation. Axial CT obtained during the portal venous phase demonstrates a complex right renal laceration with pooling of extraluminal contrast *(arrow)* within a large perinephric hematoma. This patient underwent coil embolization to repair this vascular injury.

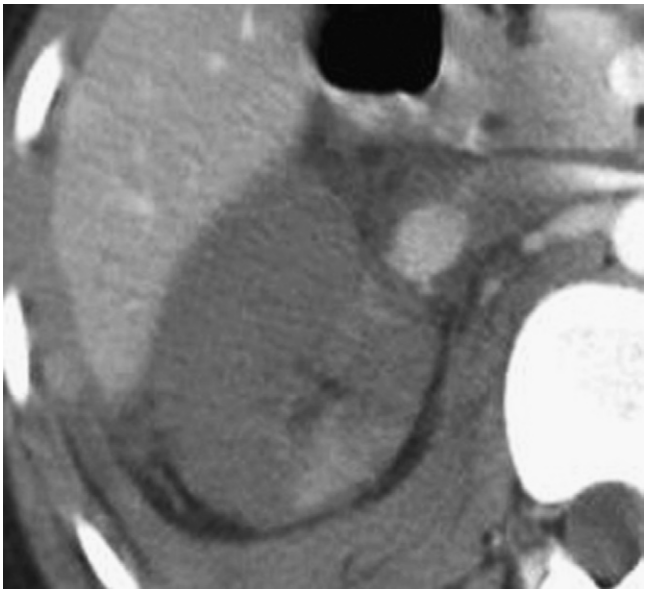


Figure 3-45. Renal vascular pedicle injury. Axial CT image in this patient following a high-speed motor vehicle collision demonstrates diminished enhancement in a large portion of the right kidney due to this vascular pedicle injury.

unsalvageable if the diagnosis is delayed or if the patient presents too long after the time of initial injury.

Ureteral Injury

The ureter is the least commonly injured segment in the genitourinary system, accounting for less than 1% of all injuries. Most ureteral injuries are penetrating injuries such as gunshot wounds. Injury can occur anywhere along the course of the ureter, and most often is confined to one side of the body. Similar to other organs of the genitourinary system, ureteral injuries often present clinically with gross or microscopic hematuria. However, hematuria may not be present in up to 25% of patients with ureteral

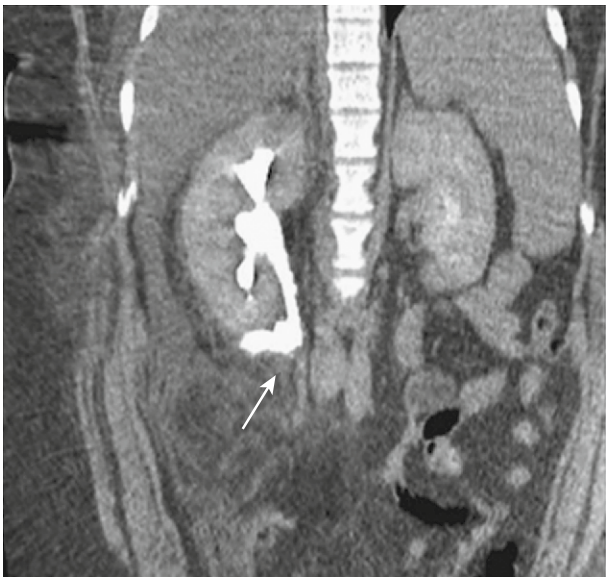


Figure 3-46. Ureteral trauma. Coronal reformatted image obtained at 5-minute delay demonstrates abrupt termination of the proximal right ureter with extraluminal contrast just lateral to the site of injury, adjacent to the lower pole of the right kidney *(arrow)*. This patient required stent placement to treat the injury. (Reprinted with permission from Stuhlfaut JW, Soto JA, Lucey BC, et al: Blunt abdominal trauma: Performance of CT without oral contrast material. Radiology 233:689–694, 2004.)

trauma. Thus, these injuries may not be suspected at the time of abdominal CT or exploratory surgery (especially in the case of penetrating trauma). In the past, intravenous urography (IVU) was the imaging test of choice for detecting ureteral injuries; however, CT has essentially replaced IVU in that setting.

Typically, the trauma IVU consists of a scout radiograph of the abdomen followed by hand injection of a water-soluble intravenous contrast agent. A second image is then taken approximately 10 to 15 minutes later to assess the integrity of the collecting system and ureters. A normal IVU is a good indication that there is no major injury of the genitourinary system. Ureteral injury is identified as contrast-filled urine accumulating in the retroperitoneal space. It is important to evaluate the entire ureter to exclude distal injuries within the pelvis.

More commonly, the ureter is evaluated with the routine trauma CT. When a focal injury of the collecting system or ureter is suspected, delayed CT images are mandatory. These are typically obtained 5 to 7 minutes following contrast injection to avoid unnecessary delay in patient care while the patient is undergoing diagnostic imaging evaluation. Early portal venous phase images may show abnormal fluid or stranding adjacent to the ureter; delayed images show extravasation of urine with contrast at the site of injury (Fig. 3-46). Multiplanar reformations are useful in highlighting the site of injury and may aid the urologist in treatment planning.

ADRENAL TRAUMA

Injury of the adrenal gland is uncommon. It occurs in approximately 1% of all patients sustaining abdominal trauma. Isolated adrenal injury is even rarer, occurring in

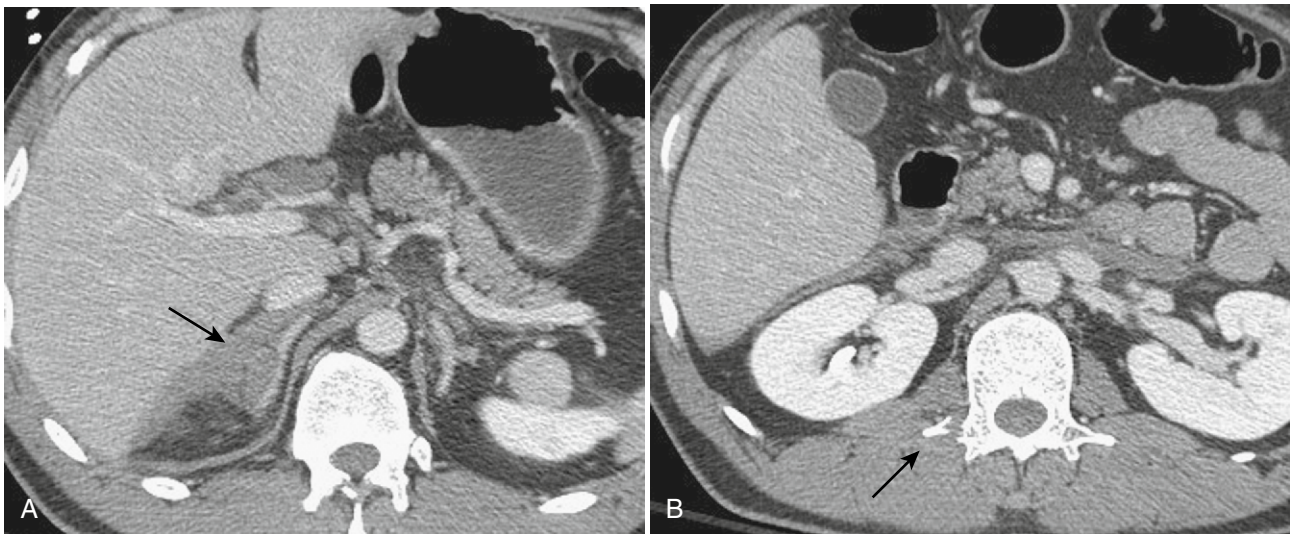


FIGURE 3-47. Adrenal injury. **A,** Transverse CT image in this patient following blunt trauma depicts a right adrenal hematoma *(arrow)* with stranding of soft tissue in the periadrenal region. **B**, Adrenal injuries are often associated with fractures of the transverse process, as was evident in this patient at a level below the site of adrenal injury *(arrow)*.

less than 5% of all patients with adrenal trauma. Instead, most patients with adrenal injuries also have injury to one or more other solid organs in the abdomen, most commonly the liver, spleen, or kidney. Ipsilateral rib fractures are also common. Adrenal injuries typically occur on the right side and are much less commonly seen in isolation in the left adrenal gland. Possible explanations for this discrepancy that have been offered include the position of the right adrenal gland in relatively tight quarters between the spine and the liver and the right adrenal gland being subject to higher venous pressure than the left when increased abdominal pressure occurs at the time of injury. The right adrenal gland might see relatively higher venous pressures transmitted from the vena cava, while venous pressures are filtered by the left renal vein before reaching the left adrenal gland. Regardless, injury to the adrenal gland can be readily identified on routine trauma CT imaging. Typically, adrenal injuries appear as round or ovoid nodules replacing the normal adrenal gland. Not uncommonly, there is a fracture of an ipsilateral transverse process (Fig. 3-47). These hematomas can be associated with surrounding periadrenal fat stranding on CT. It is important to distinguish adrenal hematomas from incidental adrenal nodules, which are commonly seen in the trauma population (and in the general population). It is helpful to measure the attenuation of the lesion. Most adrenal hematomas have attenuation coefficients higher than 50 Hounsfield units (HU). Adrenal injuries typically have a higher HU than other adrenal lesions such as adenomas, which often have attenuation measurements less than 10 HU. If available, delayed images (10 to 15 minutes after contrast injection) can help characterize the lesion by determining the washout characteristics. If there is any question, follow-up imaging can be obtained to assess for interval change in the suspected adrenal injury. On follow-up CT, adrenal hematomas typically regress or calcify. In addition, pseudocysts can develop as sequelae of adrenal injury. Rarely, patients with bilateral adrenal injury can develop clinical manifestations of adrenal insufficiency.

PELVIC TRAUMA

Although the pelvis communicates with the peritoneal and extraperitoneal compartments of the abdominal cavity and is imaged concomitantly with the abdomen at the time of admission CT, the unique anatomic disposition of the pelvic ring and the types of injuries encountered deserve a separate discussion in this chapter. In most settings, a portable radiograph of the pelvis is obtained upon arrival of a multiple-trauma patient to the trauma bay. If a displaced (and possibly unstable) fracture of the pelvic ring is demonstrated, the pelvic cavity should be investigated carefully for associated injuries to the vascular structures, rectum, bladder, or urethra. Strong forces are necessary to disrupt the osseous pelvic ring; the radiographic evaluation of trauma to the bony pelvis is discussed in detail in chapter 4 on trauma of the extremities.

The possibility of vascular injury and major (sometimes life-threatening) bleeding should be considered in every patient with a disruption of the pelvic ring. CT has been shown to be valuable in evaluating for vascular injury in patients with pelvic trauma. Large hematomas and foci of active extravasation are the main findings that may prompt a consult to the interventional radiology service for possible endovascular therapy via embolization. Multiphasic CT imaging provides a temporal assessment of change in the size of the hematoma, and provides an indirect means of estimating the rate of bleeding (Fig. 3-48).

Bladder Trauma

Bladder injuries result from blunt (70% to 80%) or penetrating trauma (20% to 30%). Common causes of bladder rupture include direct impact with the steering wheel or seatbelt in motor vehicle accidents and assaults to the lower abdomen by a kick or blow. The likelihood of bladder trauma is directly related to the degree of distention at the time of the injury, with a full bladder more likely to rupture than an empty one. A high clinical suspicion and

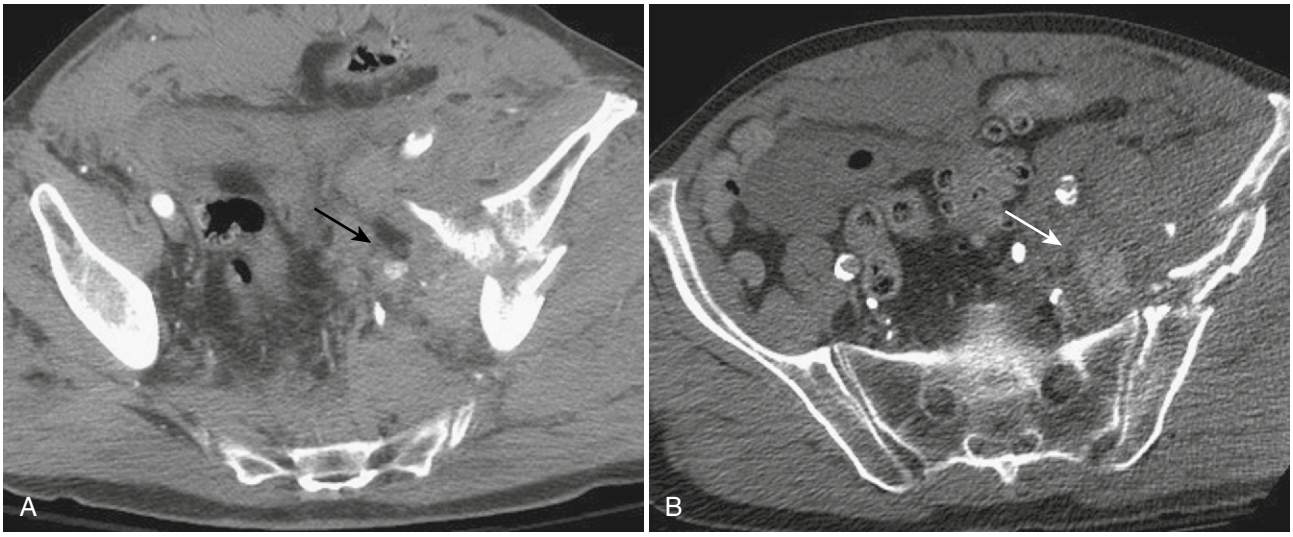


Figure 3-48. Complex pelvic fracture with active bleeding. **A,** Transverse CT obtained as part of a CT angiogram demonstrates a complex fracture of the left ilium with a large pelvic hematoma and active contrast extravasation *(arrow).* **B,** CT obtained at 5-minute delay shows an increase in size of the hematoma with continued diffusion of blood and contrast *(arrow)* into the site of injury.

timely diagnosis are the keys to successful medical or surgical treatment. Approximately 10% of patients with pelvic fractures have bladder injuries, and the likelihood of bladder injury is directly related to the severity of the fracture. There is also a high association between bladder rupture and urethral disruption.

Patients with signs and symptoms suggestive of a bladder injury typically have a history of pelvic trauma, often with a fracture evident on the admission radiograph. Although the clinical signs of bladder injury are nonspecific, a triad of symptoms is often present: suprapubic pain, gross hematuria, and an inability to void or difficulty in doing so. The hallmark of a bladder rupture is hematuria, which is almost invariably present. More than 95% of bladder ruptures are associated with gross hematuria, and 5% are associated with microscopic hematuria. Since some patients can still void, the ability to urinate does not exclude bladder injury or perforation. Whenever a bladder injury is suspected, the patient should be further evaluated with conventional cystography or CT cystography and the threshold for performing these tests should be very low.

Cystography

A well-performed cystogram begins with an abdominal radiograph (scout view). This serves to evaluate the pelvic bones and to determine if there is any displaced fracture that could limit the patient's ability to position properly. Subsequently, a Foley catheter should be placed into the bladder. However, it is mandatory to carefully inspect the urethral meatus for evidence of gross blood before attempting to catheterize the bladder. Blood at the urethral meatus is an absolute indication for retrograde urethrography to assess urethral integrity before attempting to blindly pass a Foley catheter. Approximately 10% to 20% of men with a posterior urethral injury have an associated bladder injury. Blind passage of a urethral catheter may convert a partial disruption of the urethra into a complete tear. If a posterior urethral injury is present, placement of a percutaneous suprapubic catheter may be necessary to evaluate bladder integrity.

Once the lumen of the bladder has been catheterized, diluted water-soluble contrast material (usually 50% contrast and 50% sterile saline) is slowly instilled by gravity (approximately 75 cm above the pelvis). The examination should be performed under continuous fluoroscopic observation. If gross extravasation is noted, no further distention is necessary. If extravasation is absent, the remainder of the contrast is infused (to 300 to 400 mL total) until full distention is achieved. Spot fluoroscopic images should be obtained as necessary. Standard static projections include anteroposterior and oblique views of the bladder filled with contrast, along with another anteroposterior film obtained after drainage. Oblique films are often difficult to obtain in a patient with pelvic fractures and may be omitted in selected cases. The total volume of contrast administered is less important than ensuring that adequate bladder distention is achieved, in order to demonstrate small injuries that may otherwise go undetected. Some superficial lacerations may seal temporarily by wall edema or by an overlying hematoma, omentum, or adjacent segment of large or small bowel. Full distention helps prevent this false negative result. Also, the postdrainage film is a critical part of the study because it may disclose small foci of extravasation that may be hidden by the distended bladder. The accuracy of a well-performed cystogram ranges between 90% and 98%.

CT Cystography

Most patients with bladder injuries have suffered multiple trauma and require abdominal or pelvic CT scans as part of their evaluation. The CT scan of the pelvis provides information on the status of the pelvic organs and osseous pelvis. Occasionally, bladder rupture is shown on the initial pelvic CT images with contrast-filled urine accumulating in the perivesical space or peritoneal cavity (Fig. 3-49). However, bladder integrity is not confirmed until full distention of the bladder with homogeneously opacified fluid is achieved. A CT cystogram is performed after the abdominopelvic CT is completed. With a Foley catheter

secured in the bladder, diluted contrast is instilled to achieve full distention. CT images limited to the pelvis are then obtained. Although CT cystography lacks the temporal, dynamic information provided by fluoroscopy, the superior contrast resolution compensates for this limitation, often showing small accumulations of extravesical contrast. In the majority of major trauma centers, CT cystography has replaced conventional cystography as the most widely used method to assess bladder integrity.

Types of Bladder Rupture

Bladder ruptures are classified as extraperitoneal, intraperitoneal, or combined (intra- and extraperitoneal). This distinction is critical, as management varies considerably: intraperitoneal ruptures require immediate surgical therapy, whereas extraperitoneal ruptures are usually managed with bladder drainage and delayed reconstruction, when necessary. Extraperitoneal injuries account for approximately 70%, intraperitoneal injuries account for approximately 20%, and combined perforations account for approximately 10% of all injuries. The proportion of intraperitoneal ruptures is considerably higher in children due to the predominantly intra-abdominal location of the bladder in this age group, as the bladder descends into the pelvis usually by the age of 20 years.

In blunt trauma, extraperitoneal bladder ruptures are almost invariably associated with pelvic fractures. Rupture may occur either from a direct perforation by a bony fragment (as with fractures of the anterior pubic arch) or from a burst injury or sudden shearing force from the pelvic ring at the time of the impact. The classic finding on cystography or CT cystography is contrast extravasation around the base of the bladder confined to the peri- and prevesical space (of Retzius); flame- or starburst-shape areas of contrast extravasation are characteristic (see Figs. 3-49 and 3-50). An associated pelvic hematoma may give the bladder a teardrop shape. With a more complex injury, the contrast material extends to the thigh, scrotum (or labia), penis, or perineum, or into the anterior abdominal wall (Fig. 3-51). Extravasation will reach the scrotum when the superior fascia of the urogenital diaphragm or the urogenital diaphragm itself has been disrupted. If the inferior fascia of the urogenital diaphragm is violated, the contrast material will reach the thigh and penis (contained by Colles' fascia).

A typical intraperitoneal rupture results from a horizontal tear occurring in the dome of the bladder. The dome is the weakest and least supported area and the only portion of the adult bladder covered by peritoneum. The mechanism of injury is usually a direct blow to a fully distended urinary bladder. Initial CT images often demonstrate low-attenuation fluid within the peritoneal cavity, and gas if a Foley catheter has been introduced (Fig. 3-52). On cystography, contrast accumulates in the peritoneal cavity, outlines loops of bowel, and fills the paracolic gutters, pouch of Douglas, and other peritoneal spaces, including the subphrenic spaces. In combined intraperitoneal and extraperitoneal ruptures, cystography reveals contrast outlining the abdominal viscera and perivesical space. Combined ruptures are common after penetrating injuries from a high-velocity bullet or knife traversing the bladder.

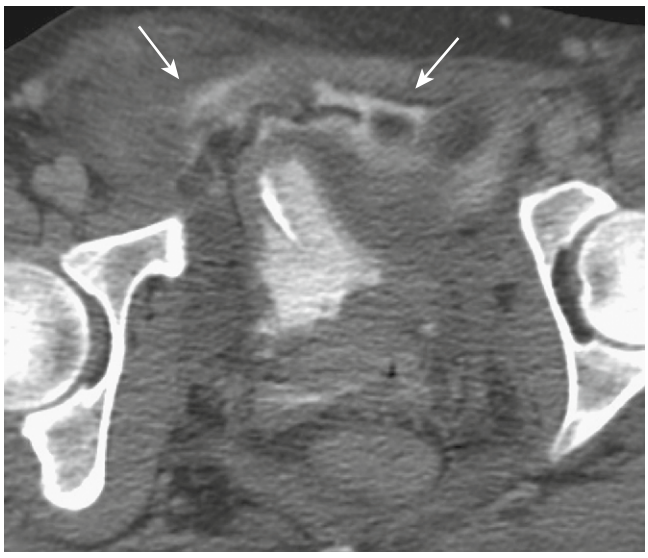


FIGURE 3-49. Extraperitoneal bladder rupture. Axial CT obtained 5 minutes after the injection of intravenous contrast demonstrates extraluminal contrast *(arrows)* in the space of Retzius secondary to a traumatic bladder rupture.

Urethral Injury

Early recognition of urethral injuries is necessary in order to prevent serious long-term sequelae such as strictures that require recurrent interventions to prevent infectious complications. The vast majority of urethral injuries occur in men. Most urethral injuries are associated with major blunt trauma such as that caused by motor vehicle accidents or falls, but penetrating injuries, although rarely, may be the cause as well. Given the severity of the traumatic event that caused the urethral injury, many of these men have associated neurologic and orthopedic injuries that further complicate therapy. Iatrogenic causes, such as traumatic catheter placement or transurethral dilation, can also occur.

Urethral injuries are usually classified as belonging to one of two types, based on the anatomical site of the tear: posterior urethra or anterior urethra. Posterior urethral injuries are more common and usually occur at the junction of the prostatic and membranous segments, where the urethra is fixed by the attachments of the puboprostatic ligaments. Thus, posterior urethral injuries are typically caused by severe blunt trauma with fractures of the anterior pelvis; displacement of the bone fragments overstretches the short membranous segment. Male patients with pelvic fractures have a 5% to 10% incidence of posterior urethral injury.

Anterior urethral injuries affect the bulbar or penile segments and are usually the result of trauma to the perineum, such as straddle injuries. Relatively minor trauma can injure the bulbar urethra, but the diagnosis may be delayed by months or even years, when patients present with urethral strictures. Occasionally, tears of the penile urethra are seen in the setting of a penile fracture.

Diagnosis Retrograde Urethrogram

The possibility of a urethral injury should be considered in every patient with a pelvic fracture before blindly inserting a Foley catheter into the bladder. Other potential antecedent history, such as traumatic catheterization, straddle

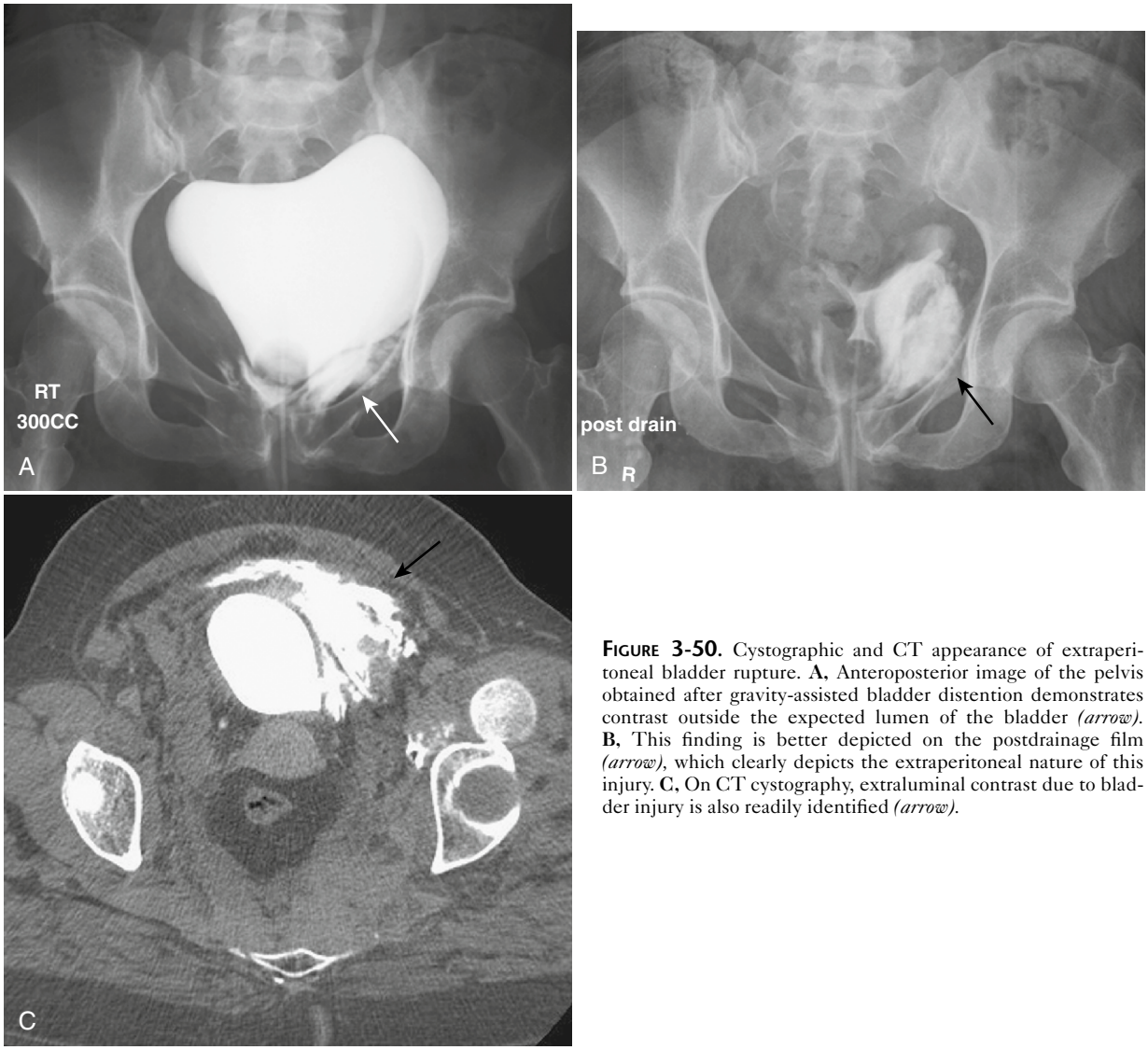


FIGURE 3-50. Cystographic and CT appearance of extraperitoneal bladder rupture. **A,** Anteroposterior image of the pelvis obtained after gravity-assisted bladder distention demonstrates contrast outside the expected lumen of the bladder *(arrow)*. **B,** This finding is better depicted on the postdrainage film *(arrow)*, which clearly depicts the extraperitoneal nature of this injury. **C,** On CT cystography, extraluminal contrast due to bladder injury is also readily identified *(arrow)*.



FIGURE 3-51. Extraperitoneal bladder injury. Axial image from a CT cystogram demonstrates extraluminal contrast within the pre-vesicle space due to an acute extraperitoneal bladder injury. In addition, contrast has tracked inferiorly and laterally in the left inguinal region.

injury, or any penetrating injury near the urethra, should also raise suspicion. Symptoms include hematuria and an inability to void. However, these are rarely useful in the setting of major acute trauma, when patients are intubated and sedated or unconscious. On physical examination, the hallmark finding is presence of blood at the meatus or a high-riding prostate gland on rectal examination.

The diagnosis is confirmed with a retrograde urethrogram, which must be performed prior to insertion of a catheter into the bladder in order to avoid further injury to the urethra. For the retrograde urethrogram, a Foley catheter is generally preferred over the Brodney clamp. A 16-F catheter is placed into the distal urethra, and the balloon (3 mL) inflated within the fossa navicularis. Then 30 to 60 mL of water-soluble contrast material is injected under fluoroscopic guidance using a 60-mL piston syringe. Oblique views (when possible) are usually the most helpful.

Urethrography serves to assess integrity and to localize and characterize tears as complete or incomplete. In posterior urethral injuries, contrast material accumulates outside the urethra in the retropubic extraperitoneal space

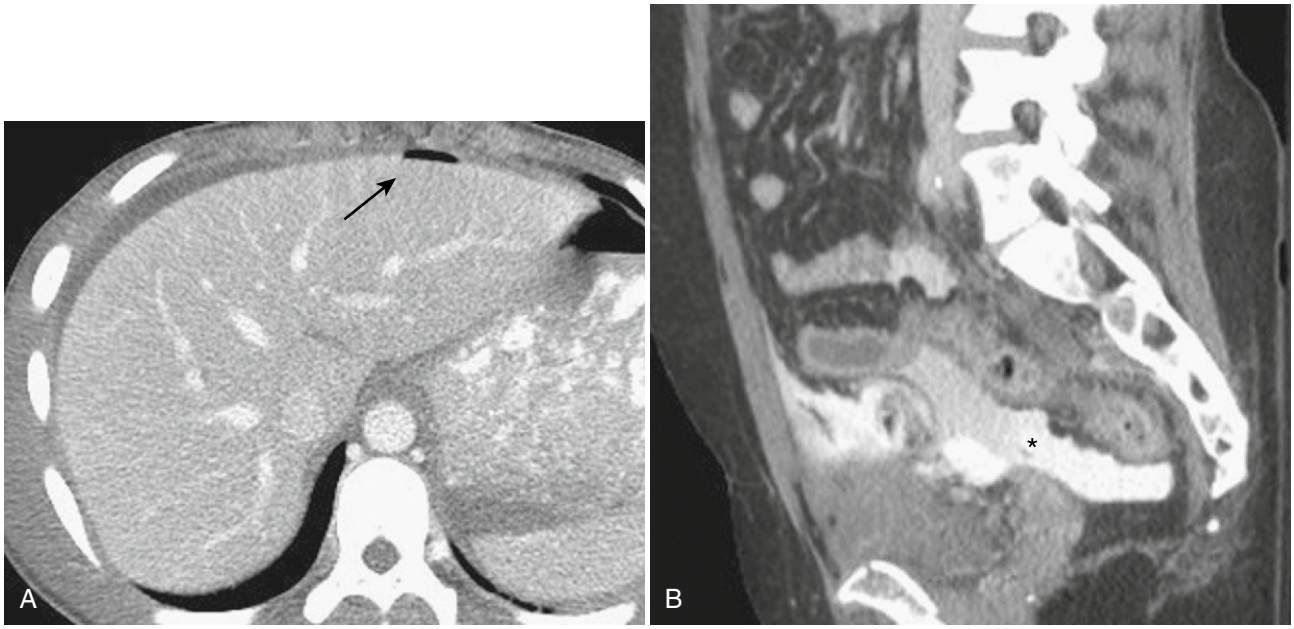


FIGURE 3-52. Intraperitoneal bladder injury. **A,** Axial CT image demonstrates free air in the peritoneal cavity *(arrow)* in addition to free fluid along the liver margin. No bowel injury was detected. Prior to this CT, a Foley catheter had been placed and the free air was thought to be due to an acute bladder injury. **B,** Sagittal reformat from the subsequent CT cystogram depicts contrast in the peritoneal cavity *(asterisk)* due to an intraperitoneal bladder rupture.

(Fig. 3-53). In partial rupture, there is at least some continuity, which allows partial filling of the bladder, in addition to the extravasated contrast. Complete tears are shown as an interruption of the urethra. Involvement of the urogenital diaphragm is assumed when contrast accumulates in the perineum. Partial tears of the posterior urethra usually heal uneventfully, whereas complete tears may heal with formation of a stricture. Other long-term symptoms associated with severe urethral injuries include impotence and, rarely, incontinence. These sequelae are more likely a reflection of the severity of the initial trauma, rather than caused by the urethral injury itself. In anterior urethral injuries, contrast may fill the corpora cavernosa or corpus spongiosum or it may reflux into the draining veins.

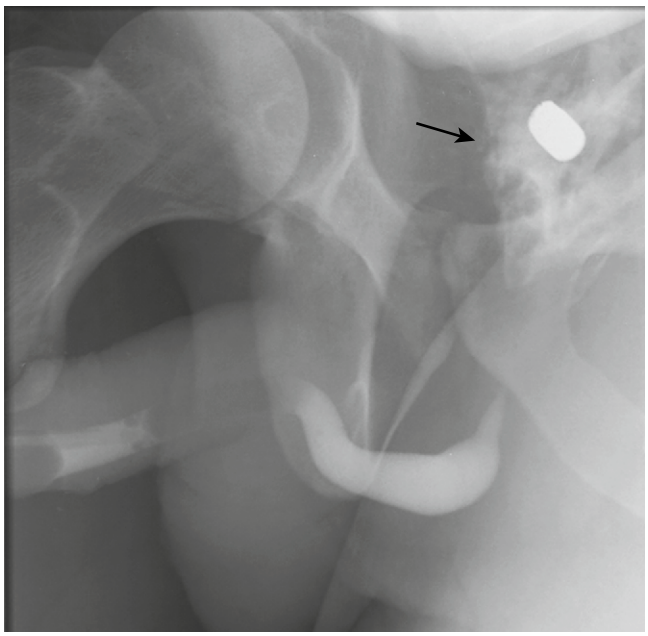


FIGURE 3-53. Posterior urethral injury following acute trauma. Image obtained at the time of retrograde urethrography demonstrates extravasation of contrast into the retropubic space *(arrow)* from a posterior urethral injury.

Rectal Injury

The rectum is rarely injured as a result of blunt trauma. When injured, there is often a history of direct perineal force at the time of the traumatic event, and patients often have associated pelvic fractures. Rectal injury can be difficult to detect clinically, although some patients present with bright red blood per rectum. Physical exam may detect the presence of blood or bone fragments in the rectal vault, indicating a high likelihood of injury. Often, patients with suspected injury are evaluated directly by rigid sigmoidoscope. However, rectal injuries are increasingly diagnosed at the time of diagnostic CT imaging. CT imaging may show focal rectal wall thickening (Fig. 3-54) or localized free air in the perirectal fat. In addition, hematoma may be present in the perirectal fat as a result of such injury. Water-soluble contrast administered as an enema may be necessary to demonstrate the site of perforation in questionable cases (Fig. 3-55).

PENETRATING ABDOMINAL TRAUMA

Penetrating abdominal trauma caused by stab or gunshot wounds is a frequent cause of admission to emergency departments in large urban centers. The pathophysiology involved in penetrating trauma is unpredictable and the pattern of injuries differs from blunt abdominal trauma. Compared with blunt trauma, injuries to the bowel, mesentery,



Figure 3-54. Acute rectal injury. Sagittal reformat obtained after trauma CT shows focal thickening of the posterior rectal wall *(arrow)* with fluid in the presacral space. Rectal laceration was confirmed at surgery.

and diaphragm are more common with penetrating trauma. Bowel injuries may remain clinically occult for several hours after trauma occurs. Thus, early detection of bowel injuries is a major concern in this patient group. In the past, exploratory laparotomy was considered mandatory for diagnosis and treatment of all patients with confirmed penetration of the peritoneum. This surgical approach is based on the following assumptions: laparotomy is necessary to exclude intra-abdominal injuries; diagnostic laparotomy is associated with little morbidity; and increased morbidity and mortality are associated with delayed treatment of injuries to the hollow viscera. Immediate laparotomy is still mandated when the penetrating injury is associated with definite signs of peritoneal irritation, hemodynamic instability, gastrointestinal bleeding, or evisceration. However, if all penetrating abdominal injuries are managed with surgery, even without clinical evidence to suggest visceral involvement, the frequency of negative or nontherapeutic laparotomy varies between 20% and 40%. The rate of complications is also high, in the range of 5% to 20%, for patients with negative or nontherapeutic laparotomy findings.

The high proportion of negative laparotomy findings and the relatively high frequency of complications led some surgeons to question the need for mandatory surgical exploration in this setting. Knowledge gained from conservative or nonsurgical treatment of blunt trauma has resulted in an extension of this alternative treatment to some victims of penetrating stab injuries and, more recently, to select groups of victims of gunshot wounds. With a conservative approach, penetrating trauma patients who do not have an indication for immediate laparotomy at presentation are admitted to the hospital and observed during 24 hours or more. During the period of clinical observation, laparotomy becomes necessary if the abdominal pain (which is almost invariably present at admission) worsens progressively or if the patient develops rebound tenderness, generalized abdominal guarding, hypoperistalsis, unexplained shock, or gastrointestinal bleeding. The downside is that the delay generated by the period of observation may increase the severity of peritoneal involvement and cause a longer postoperative course if laparotomy is eventually required and a hollow viscus injury found. Thus, this conservative approach has resulted in a growing interest in using diagnostic procedures and imaging tests such as peritoneal lavage, laparoscopy, US, and CT to identify patients with occult injuries that require operative management before they become clinically apparent. These include injuries to the hollow viscera, mesentery, large vessels, and diaphragm.

Peritoneal lavage has high sensitivity but low specificity. Use of an elevated cell count as a criterion for need for laparotomy is not uniform and has not been adjusted to the modern concept of nonsurgical treatment of wounds

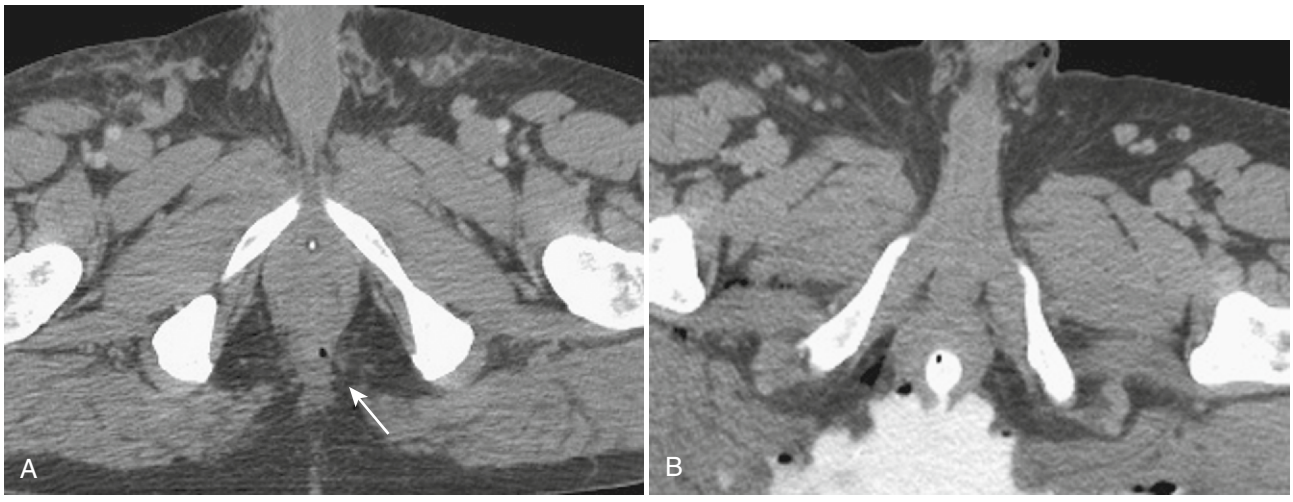


Figure 3-55. Acute rectal injury following blunt injury. **A,** Axial CT obtained during the initial trauma CT demonstrates stranding in the soft tissue posterior to the distal rectum, suspicious for an acute injury. **B,** After administration of water-soluble rectal contrast, a posterior laceration with contrast extravasation is readily identified.

to the solid viscera. In general, patients with occult hollow viscus injury are not well evaluated by means of diagnostic peritoneal lavage. Laparoscopy is useful for diagnosis of peritoneal violation and wounds of the diaphragm, and, in some patients, therapeutic procedures can be performed at the same time. The downside is that this is an invasive procedure that requires general anesthesia and that the evaluation of the retroperitoneum is limited and visualization of all the hollow viscera incomplete.

Ultrasonography

As described previously, the main use of US in blunt trauma is for detecting (and grossly quantifying) free intraperitoneal fluid. US has also been proposed for stable patients who have penetrating torso injuries caused by gunshots or by sharp objects. Unfortunately, the finding of free fluid is not a specific indicator of an occult gastrointestinal tract or major vascular injury. Furthermore, when the results of US are negative, injuries to the hollow viscera or diaphragm are not excluded, and other diagnostic studies must be performed. Thus, US findings are of very little help in the decision-making process and the method is not particularly useful for the evaluation of penetrating abdominal trauma.

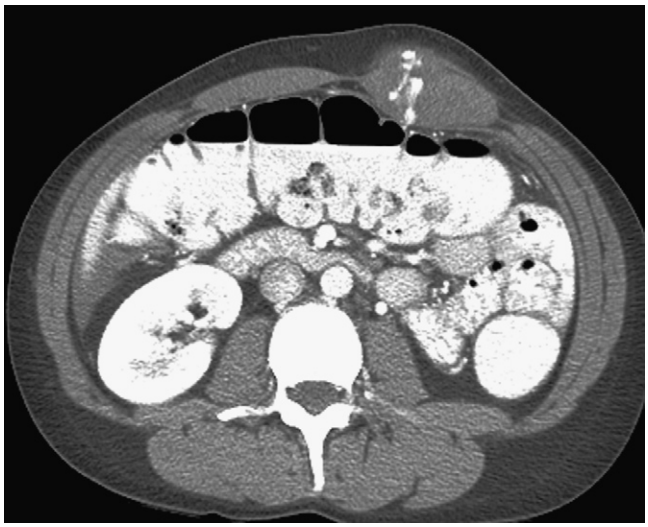


FIGURE 3-56. Penetrating injury with rectus abdominus hematoma. Axial CT obtained to evaluate a stab wound to the anterior abdomen demonstrates thickening of the left rectus muscle with active contrast extravasation. Free fluid is present in the right abdomen, but the bowel appeared completely normal. This patient recovered without need for exploratory surgery.

Computed Tomography

Whereas CT is widely used for blunt trauma, it is not widely used in the evaluation of penetrating injuries. Initial reports on the use of CT for penetrating trauma were limited to asymptomatic patients with injuries in the back and flank, since they infrequently have associated injury to critical retroperitoneal viscera due to the good protection provided by the ribs, spine, and large paraspinal muscles. Given the higher frequency of hollow viscus injuries that occurs in penetrating trauma, it is mandatory that patients receive intravenous, oral, and rectal contrast material ("triple-contrast" CT) in order to maximize the diagnostic potential of CT for penetrating trauma. Typically, patients receive 600 to 800 mL of diluted (2% to 3% concentration) water-soluble (iodinated) contrast material orally and a 1- to 1.5-liter enema of similarly diluted water-soluble contrast material. Oral contrast should be administered within 30 minutes of CT data acquisition. Rectal contrast is typically administered on the CT table, immediately prior to CT scanning. Several studies have found this approach to be highly sensitive and specific for detecting and ruling out hollow viscus injuries. As for blunt trauma patients, delayed images (3 to 5 minutes following initiation of intravenous contrast material injection) should be acquired for a complete evaluation of the renal collecting system and ureters and for characterization of extravascular collections of contrast-enhanced blood.

The diagnostic criteria used for interpretation of blunt trauma CT scans cannot be applied to penetrating trauma patients. Presence of free intraperitoneal air or free peritoneal fluid is a sign of peritoneal violation but is not definitive evidence of bowel injury, since air can be introduced into the peritoneal cavity by a bullet or knife wound and free fluid can be the result of bleeding from the peritoneal lining itself (Fig. 3-56). The only unequivocal sign of hollow viscus injury is the presence of extraluminal collections of oral or rectal contrast material (Fig. 3-57). Other CT findings considered highly indicative of bowel injury include the presence of focal bowel wall thickening or discontinuity and a bowel wall hematoma. Mesenteric injuries are confirmed by finding active extravasation of contrast material, as shown by the portal venous and delayed



FIGURE 3-57. Bowel injury after penetrating trauma. Sagittal reformat CT obtained to evaluate a gunshot wound demonstrates extraluminal contrast *(arrow)* from an acute, full-thickness, small bowel injury.

phase scans, or a focal mesenteric hematoma. Injuries to solid organs resulting from penetrating injuries are similar in appearance to those from blunt trauma (Fig. 3-58). Injury to the diaphragm is suspected when the trajectory of the missile or sharp object appears to extend toward or to the diaphragm. More specific signs, however, include finding herniated abdominal content into the chest through the diaphragmatic rent (Fig. 3-59), the CT "collar" sign (focal constriction of herniated abdominal fat or viscera at the site of diaphragmatic defect), and the finding of injured organs on either side of the diaphragm when only one injury was inflicted (thoracoabdominal injury). CT findings of potential diaphragm injury include a penetrating injury tract that extends to the diaphragm, thickening of the diaphragm, and an isolated focal defect in the normal continuity of the diaphragm without adjacent hemorrhage. If a question concerning the presence of peritoneal penetration persists during the period of clinical observation, laparoscopy should be performed as a definitive test.

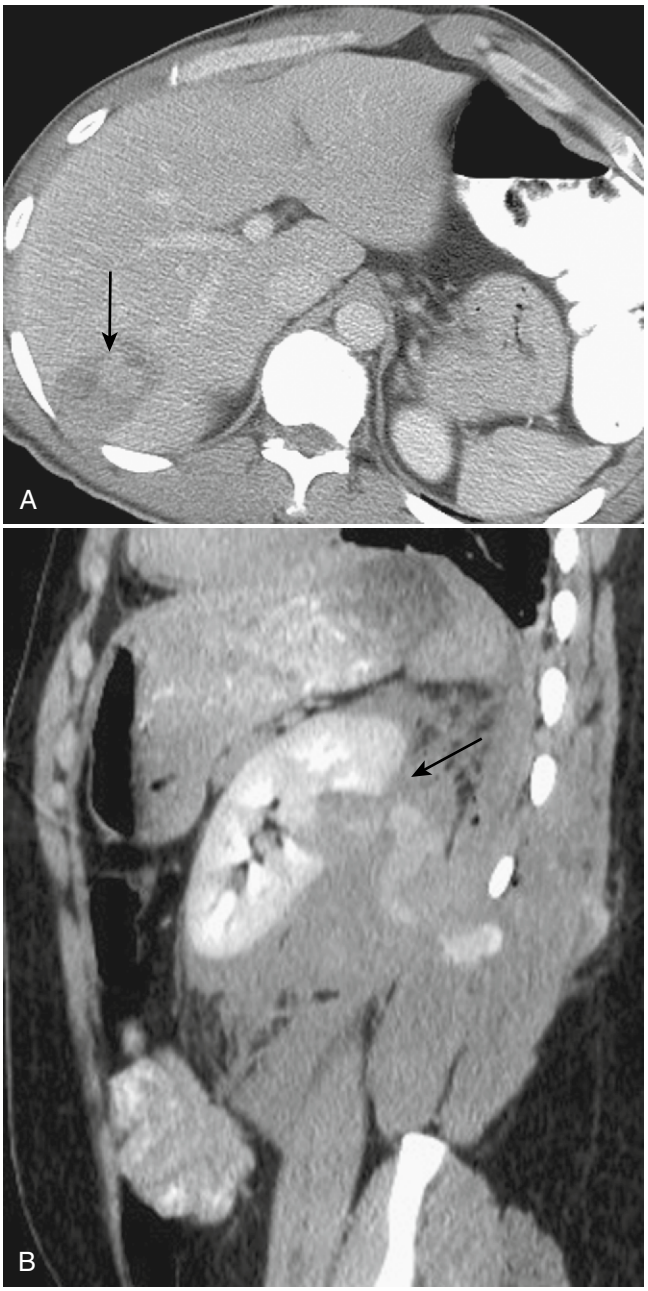


Figure 3-58. Solid organ injury after acute gunshot injury. **A,** Axial CT obtained following the acute injury demonstrates a focal liver laceration in segment 7 *(arrow)*. **B,** Sagittal reformat also demonstrates a focal renal laceration with large perinephric hematoma *(arrow)*.

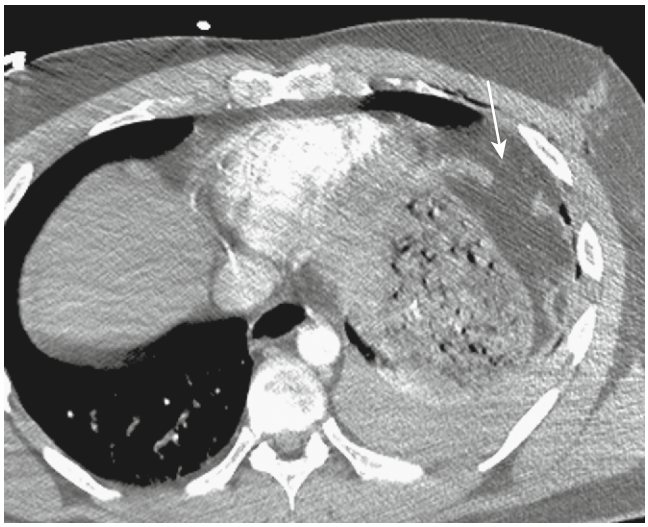


Figure 3-59. Diaphragmatic injury. Axial CT obtained following a gunshot injury demonstrates a focal rent in the diaphragm *(arrow)*. The stomach has herniated into the left chest through the defect.

Suggested Readings

Becker CD, Spring P, Glattli A, et al: Blunt splenic trauma in adults: Can CT findings be used to determine the need for surgery? Radiographics 25:87–104, 2005.

Brasel KJ, Olson CJ, Stafford RE, Johnson TJ: Incidence and significance of free fluid on abdominal computed tomographic scan in blunt trauma. J Trauma 44:889–892, 1998.

Breen DJ, Janzen DL, Zwirewich CV, et al: Blunt bowel and mesenteric injury: Diagnostic performance of CT signs. J Comput Assist Tomogr 21:706–712, 1997.

Brofman N, Atri M, Epid D, et al: Evaluation of bowel and mesenteric blunt trauma with multidetector CT. Radiographics 26:1119–1131, 2006.

Clancy TV, Ragozzino MW, Ranshaw D, et al: Oral contrast is not necessary in the evaluation of blunt abdominal trauma by computed tomography. Am J Surg 166:680–683, 1993.

Farahmand N, Sirlin CB, Brown MA, et al: Hypotensive patients with blunt abdominal trauma: Performance of screening US. Radiology 235:436–443, 2005.

Fleming KW, Lucey BC, Soto JA, et al: Posttraumatic bile leaks: Role of diagnostic imaging and impact on patient outcome. Emerg Radiol 12:103–107, 2006.

Gralla J, Spycher F, Pignolet C, et al: Evaluation of a 16-MDCT scanner in an emergency department: Initial clinical experience and workflow analysis. AJR Am J Roentgenol 185:232–238, 2005.

Gupta A, Stuhlfaut JW, Fleming KW, et al: Blunt trauma of the pancreas and biliary tract: A multimodality imaging approach to diagnosis. Radiographics 24:1381–1395, 2004.

Hanks PW, Brody JM: Blunt injury to the mesentery and small bowel: CT evaluation. Radiol Clin North Am 41:1171–1182, 2003.

Killeen KL, Shanmuganathan K, Poletti PA, et al: Helical computed tomography of bowel and mesenteric injuries. J Trauma 51:26–36, 2001.

Kuan JK, Wright JL, Nathens, AB, et al: American Association for the Surgery of Trauma. American Association for the Surgery of Trauma Organ Injury Scale for kidney injuries predicts nephrectomy, dialysis, and death in patients with blunt injury and nephrectomy for penetrating injuries. J Trauma 60:351–356, 2006.

Levine CD, Gonzales RN, Wachsberg RH: CT findings in bowel and mesenteric injury. J Comput Assist Tomogr 21:974–979, 1997.

Lingawi SS, Buckley AR: Focused abdominal US in patients with trauma. Radiology 217:426–429, 2000.

MacLean AA, Durso A, Cohn SM, et al: A clinically relevant liver injury grading system by CT, preliminary report. Emerg Radiol 12:34–37, 2005.

McGahan JP, Wang L, Richards JR: From the RSNA Refresher Courses: Focused abdominal US for trauma. Radiographics 21(Suppl):S191–S199, 2001.

Moore EE, Cogbill TH, Jurkovich JG, et al: Organ injury scaling III: Chest wall, abdominal vascular, ureter, bladder, and urethra. J Trauma 33:337–339, 1992.
Moore EE, Cogbill TH, Malangoni MA: Organ injury scaling II: Pancreas, duodenum, small bowel, colon, and rectum. J Trauma 30:1427–1429, 1990.
Perry JF Jr: A five-year survey of 152 acute abdominal injuries. J Trauma 5:53–56, 1965.
Pinto A, Scaglione M, Pinto F, et al: Adrenal injuries: Spectrum of CT findings. Emerg Radiol 10:30–33, 2003.
Rana AI, Kenney PJ, Lockhart ME, et al: Adrenal gland hematomas in trauma patients. Radiology 230:669–675, 2004.
Richards JR, McGahan JP, Pali MJ, et al: Sonographic detection of blunt hepatic trauma: Hemoperitoneum and parenchymal patterns of injury. Trauma 47:1092–1097, 1999.
Rizzo MJ, Federle MP, Griffiths BG: Bowel and mesenteric injury following blunt abdominal trauma; Evaluation with CT. Radiology 173:143–148, 1989.
Rodriguez C, Barone JE, Wilbanks TO: Isolated free fluid on computed tomographic scan in blunt abdominal trauma: A systematic review of incidence and management. J Trauma 53:79–85, 2002.
Shanmuganathan K, Mirvis SE, Boyd-Kranis R, et al: Nonsurgical management of blunt splenic injury: Use of CT criteria to select patients for splenic arteriography and potential endovascular therapy. Radiology 217:75–82, 2000.
Sharma OP, Oswanski MF, Singer D: The role of computed tomography in diagnosis of blunt intestinal and mesenteric trauma. J Emerg Med 27:55–67, 2004.
Sinelnikov AO, Abujudeh HH, Chan D, et al: CT manifestations of adrenal trauma: Experience with 73 cases. Emerg Radiol 13:313–318, 2007.
Soto JA, Lucey BC, Stuhlfaut JW, Varghese JC: Use of 3D imaging in CT of the acute trauma patient: Impact of a PACS-based software package. Emerg Radiol 11:173–176, 2005.
Stafford RE, McGonigal MD, Weigelt JA, et al: Oral contrast solution and computerized tomography for blunt abdominal trauma: A randomized study. Arch Surg 34:622–627, 1999.
Stuhlfaut JS, Anderson SW, Soto JA: Blunt abdominal trauma: Current imaging techniques and CT findings in patients with solid organ, bowel, and mesenteric injury. Semin Ultrasound CT MR 28:115–129, 2007.
Stuhlfaut JW, Lucey BC, Varghese JC, et al: Blunt abdominal trauma: Utility of 5-minute delayed CT with a reduced radiation dose. Radiology 238:473–479, 2006.
Stuhlfaut JW, Soto JA, Lucey BC, et al: Blunt abdominal trauma: Performance of CT without oral contrast material. Radiology 233:689–694, 2004.
Tsang BD, Panacek EA, Brant WE, et al: Effect of oral contrast administration for abdominal computed tomography in the evaluation of acute blunt trauma. Ann Emerg Med 30:7–13, 1997.
Vaccaro JP, Brody JM: CT cystography in the evaluation of major bladder trauma. Radiographics 20:1373–1381, 2000.
Valentino M, Serra C, Pavlica P, et al: Contrast enhanced ultrasound for blunt abdominal trauma. Semin Ultrasound CT MR 28:130–140, 2007.
Vasanawala SS, Desser T, Jeffrey RB: Value of delayed imaging in MDCT of the abdomen and pelvis. AJR Am J Roentgenol 187:154–163, 2006.
Wittenberg A, Minotti AJ: CT diagnosis of traumatic gallbladder injury. AJR Am J Roentgenol 185:1573–1574, 2005.
Yoon W, Jeong YY, Kim JK, et al: CT in blunt liver trauma. Radiographics 25:87–104, 2005.

CHAPTER 4

Extremity Trauma

Ajay K. Singh and Rathachai Kaewlai

Medical imaging for evaluation of patients with orthopedic trauma has contributed to accurate diagnosis and subsequent management. In the era of modern medical technology, there is a wide range of imaging modalities for assessment of orthopedic trauma. Availability, invasiveness, cost-effectiveness, and image resolution dictate the use of each modality. *Conventional radiography* is the primary diagnostic modality for assessment of fractures and dislocations. Routine radiography includes two orthogonal views supplemented by additional projections. Most fractures and dislocations are sufficiently identified and managed with conventional radiographs alone. In addition, radiographs are useful for assessment of limb length, overall alignment, and monitoring of fracture healing. *Computed tomography* (CT) is helpful for evaluation of complex extremity fractures and spine injuries. Typical indications for CT of extremity trauma include fractures of the proximal humerus, scapula, pelvis, tibial plateau, tibial plafond, calcaneus, and midfoot. Postoperative evaluation of fracture reduction and monitoring of fracture healing are increasingly assessed by CT scan. *Magnetic resonance (MR) imaging* plays a leading role in the detection of soft tissue injuries, bone contusions, and occult fracture such as femoral neck and scaphoid fractures.

Knowing the important steps in interpretation of skeletal trauma is useful for increasing diagnostic accuracy (Box 4-1). Fracture terminology and a guide to fracture description are summarized in Box 4-2 and Box 4-3.

Besides direct visualization of the fracture line, indirect diagnostic clues to the presence of fractures include soft tissue swelling, obliteration or displacement of fat stripes, periosteal and endosteal reaction, joint effusion, lipohemarthrosis, double cortical line, and buckling of cortex.

Box 4-1. Important Steps for Interpretation of Skeletal Trauma

1. Have a high index of suspicion
2. Know where the patient hurts
3. Obtain optimal radiographs
4. Know the frequent sites of injury and look specifically for them
5. Know what is commonly missed
6. Once a fracture is identified, do not forget to look at the rest of the image(s)

Box 4-2. Fracture Terminology

Fracture—complete disruption in continuity of a bone

Incomplete fracture—disruption of bone trabeculae while others are bent or remain intact

Open fracture—fracture communicates with the outside environment; fractures caused by gunshot wounds or shrapnel and traumatic amputations

Segmental fracture—segment of a shaft isolated by proximal and distal lines of fracture

Butterfly fragment—a triangular fragment of bone detached from two other larger fragments of a long bone

Fatigue fracture—fracture of a normal bone due to abnormal stress

Insufficiency fracture—fracture of an abnormal bone due to a normal stress

Stress fracture—a group of fractures composed of fatigue and insufficiency fractures

Avulsion fracture—fracture where a fragment is pulled away from the bone at the ligamentous or tendinous insertion

Pathologic fracture—fracture secondary to preexisting bone abnormality

Dislocation—complete disruption of a joint where there is no contact of articular surfaces

Subluxation—minor disruption of a joint where some articular contact remains

Box 4-3. Fracture Description

1. Anatomic site and extent—use anatomic landmarks for description; in long bone, divide the shaft into thirds
2. Type—complete or incomplete, simple or slightly/moderately/markedly comminuted, presence of butterfly fragment, segmental fracture
3. Alignment—displacement, angulation, rotation, foreshortening, distraction
4. Direction of fracture line in relation to longitudinal axis of the bone—transverse, oblique, spiral, longitudinal
5. Special features—impaction, depression, compression
6. Status of adjacent joints—normal, subluxation, dislocation, diastasis, intra-articular extension of fracture line
7. Special types of fractures—stress fracture, pathologic fracture, avulsion fracture
8. Open or closed fracture—preferably determined by clinical exam

UPPER EXTREMITY

The following diagram shows sites of common fractures of the upper extremity.

Fractures of the Scapula (Box 4-4)

The scapula provides a strong support to the upper extremity through its articulation with the humerus. At least 18 different muscles attach to this thin, broad bone. Therefore, fractures of the scapula often occur as a result of severe direct blunt trauma. Scapular fractures are associated with other significant injuries in up to 80% to 90% of cases, including trauma to the thoracic cage, glenohumeral joint, and brachial plexus, as well as axillary artery injuries. Attention is commonly diverted to these concomitant injuries, resulting in delayed diagnosis. Scapular fractures are classified according to their location: body, spine,

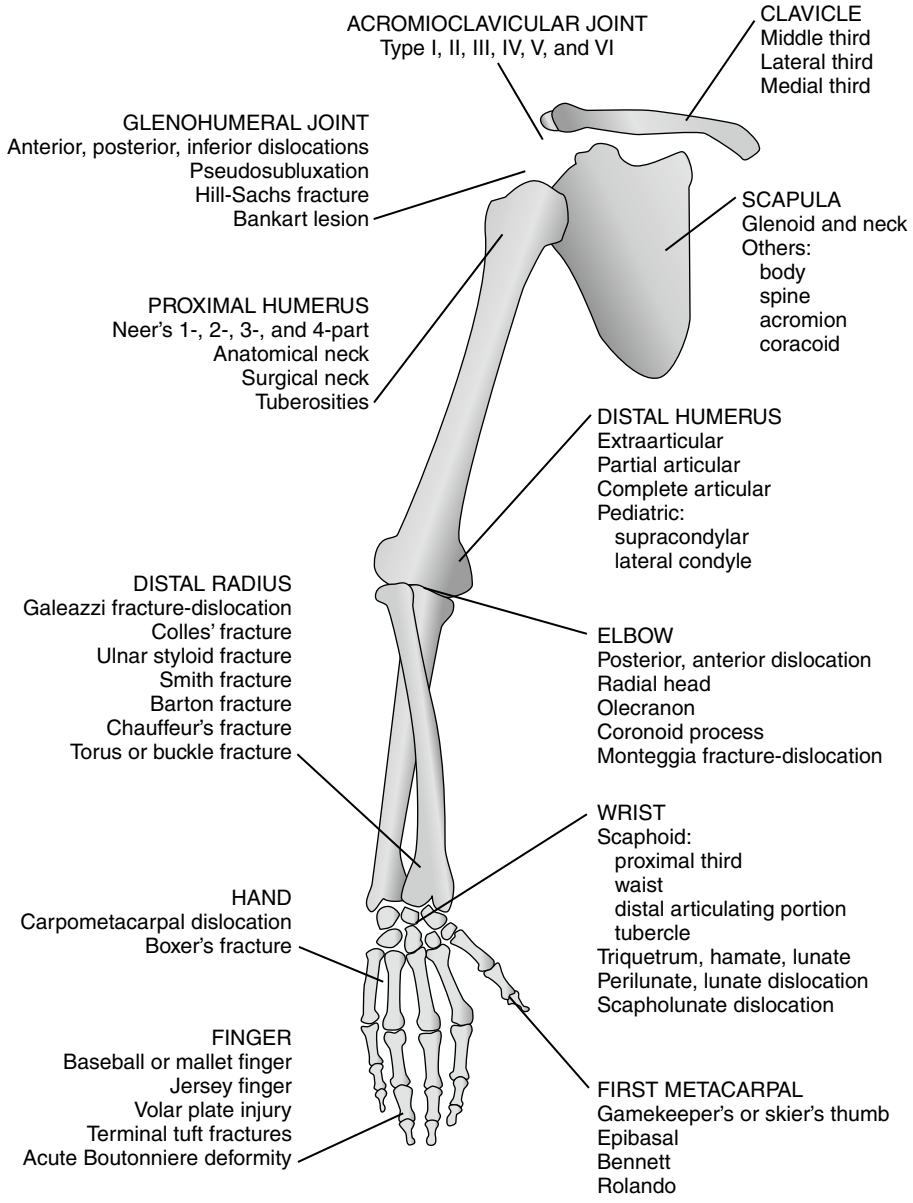
***Box 4-4.* Fractures of the Scapula**

STANDARD VIEWS
AP and lateral views of scapula

FREQUENT SITES OF INJURIES
Body, spine, and neck of the scapula

FREQUENTLY MISSED INJURIES
Fractures of the acromion process, coracoid process

FRACTURE MIMICS
Os acromiale—unfused acromial ossification center with smooth, straight, uniformly sclerotic margins distinguishing it from a true fracture
Scapular foramen—a well-circumscribed hole in the center of the scapular body
Nutrient foramina/canals—in the neck and body of the scapula



Common fractures of the upper extremity.

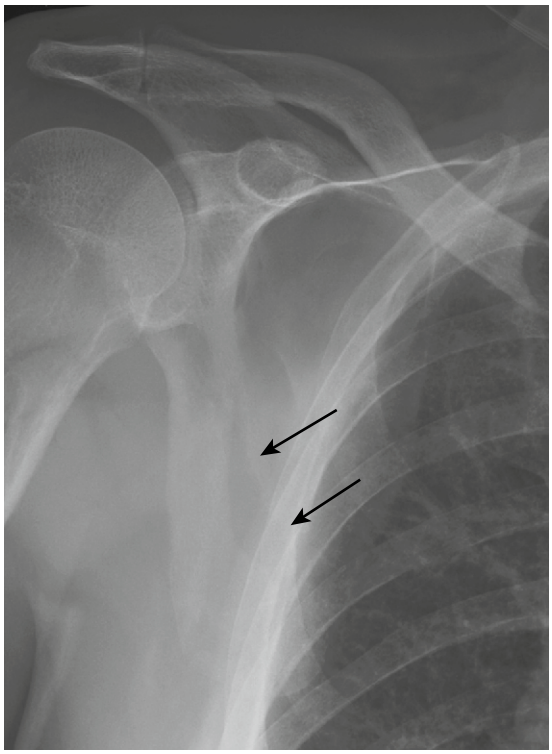


Figure 4-1. Fracture of the scapula. Anteroposterior radiograph of the shoulder demonstrates a fracture *(arrows)* in the body of the scapula.

neck, glenoid, acromion process, and coracoid process. Approximately 80% of fractures of the scapula involve either the body (Fig. 4-1) or the neck. Glenoid and neck fractures have the potential to threaten the function of the shoulder girdle, as malalignment of these fractures can contribute to instability of the glenohumeral joint, arthrosis, and dysfunction of the rotator cuff and girdle musculatures. They may require open reduction and internal fixation. Fractures that pass through the suprascapular notch or spinoglenoid notch are at risk for neurovascular bundle injury. Early recognition may lead to a change in the type of therapy provided to polytrauma patients.

Fractures of the Clavicle

The primary mechanism causing fractures of the clavicle (Box 4-5) is a fall onto the superolateral shoulder. Because of the strength of the sternoclavicular ligament, the force exits the clavicle in the midshaft, resulting in the most common pattern of clavicle fracture: fracture of the middle third. The most widely used classification system (by Allman) divides clavicular fractures into three groups by location: group 1, middle third; group 2, lateral third; and group 3, medial third. Group 2 (or lateral third) fractures are further divided into three distinct types by Neer, depending on whether the coracoclavicular ligament is involved. The middle third of the clavicle (group 1) (Fig. 4-2A) is involved in 65% to 85% of all fractures. Complete fractures typically result in superior displacement of the medial fragment (due to pull of the sternocleidomastoid muscle) and inferior displacement of the lateral fragment (due to gravity pull by the shoulder joint). Overriding of fragments is common, with the lateral fragment underlying the

***Box 4-5.* Fractures of the Clavicle**

STANDARD VIEWS
Straight PA and PA with 15-degree caudad angle; if patient cannot lie prone, straight AP and AP with 15-degree cephalad angle acceptable

FREQUENT SITE OF INJURY
Middle third

FREQUENTLY MISSED INJURIES
Medial third, associated subluxation of AC and sternoclavicular (SC) joints

RELEVANT NORMAL ANATOMY
Sternocleidomastoid muscle distal attachment—inner surface of medial third of the clavicle
Coracoclavicular ligaments consist of trapezoid (lateral) and conoid (medial) ligaments

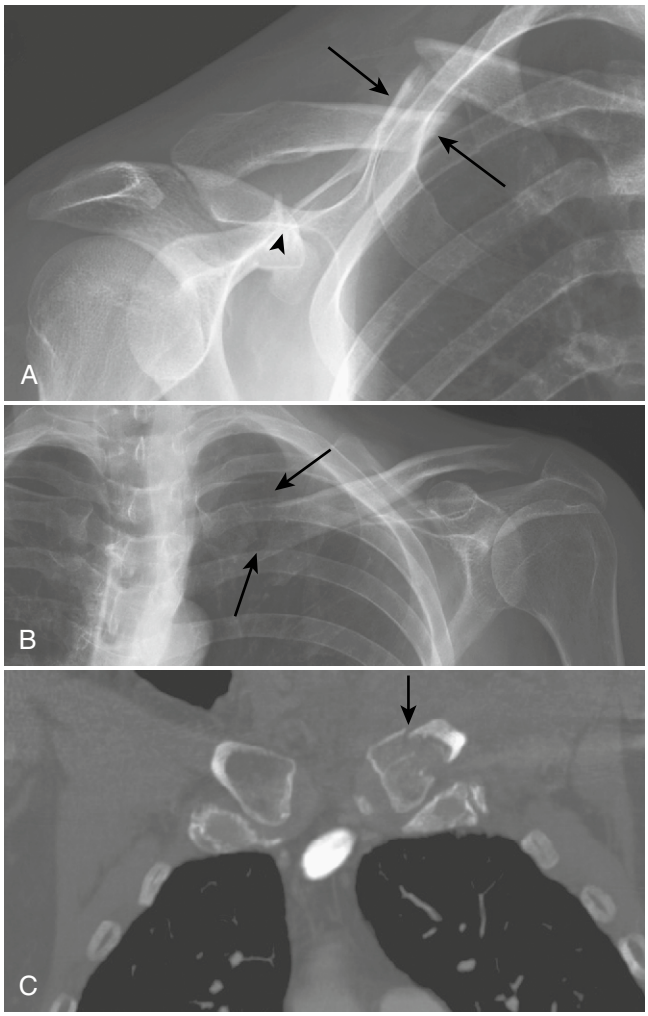


Figure 4-2. Fractures of the clavicle. **A,** Segmental fracture of the middle third *(arrows)* is shown in the anteroposterior radiograph of the clavicle. This is the most common pattern with a classic superior displacement of the medial fracture fragment and inferior displacement of the lateral fragment. There is a coexisting fracture of the superior border of the scapula *(arrowhead)*. **B,** Anteroposterior radiograph of the clavicle demonstrates a fracture of the medial third of clavicle *(arrows)* with displacement. **C,** Coronal reformatted CT image shows a fracture of the medial third of the clavicle *(arrow)* in a different patient.

medial fragment. The lateral third of the clavicle (group 2 fracture) is involved in 15% to 30% of cases. In this group, the integrity of the coracoclavicular ligaments influences the severity of displacement. The fracture may extend between the two portions of the coracoclavicular ligaments (medial conoid and lateral trapezoid ligaments) either without causing ligamentous disruption or involving the conoid ligament. The latter is a type II fracture that is more prone to delayed union and nonunion. A stress radiograph is often useful to make an accurate determination. Rarely, the fracture line involves only the joint margin and extends into the acromioclavicular joint. Fractures of the medial third of the clavicle (group 3) (Fig. 4-2B and C) are rare, accounting for only 5% of all clavicular fractures. These fractures are easily overlooked on conventional radiographs because of their lack of displacement and the overlapping ribs and spine. CT should be obtained when there is a question of injury to the medial third of the clavicle or the sternoclavicular joint. Unusual patterns of clavicular fractures include medial physeal separation and periosteal sleeve fracture that occur in the most medial and most lateral portions of the clavicle, respectively, in children and young adults.

Acromioclavicular Joint Injuries

Acromioclavicular (AC) injuries (Box 4-6) commonly result from a direct injury owing to a fall on the lateral aspect of the shoulder with an adducted arm during athletic activities. The initial trauma is directed at the AC joint capsule, and with greater force there is disruption of the coracoclavicular ligaments and detachment of the trapezius and deltoid muscles surrounding the joint. The name understates the importance of the status of the coracoclavicular ligaments, which are the most important structures maintaining alignment of the clavicle and scapula. Radiographic evaluation of the AC joint injury typically includes a standard anteroposterior view with the x-ray beam directed 15 degrees cephalad in the upright position. Both shoulders should be included in the same image. Stress radiographs may be performed with a patient holding a 10- to 15-pound weight if the initial radiograph without weight is normal. However, the increasing trend toward nonoperative management of even severe injuries has made stress radiographs less clinically relevant. There are six types of AC joint injuries. In type I injury (ligament sprain, intact coracoclavicular ligament), there is a normal AC joint space in radiographs obtained with and without weight bearing. In type II injury (Fig. 4-3A), the AC joint may be normal or slightly widened on nonstress radiographs. On the stress view (Fig. 4-3B), the AC joint is wide, which implies partial or complete ligament tear. In type III injury (Fig. 4-3C), there is a complete disruption of the acromioclavicular and coracoclavicular ligaments, resulting in widened acromioclavicular and coracoclavicular distances on nonstress radiographs. The distal clavicle is displaced superiorly. In type IV injury, the clavicle is displaced posteriorly; this is best visualized on the axillary projection. Type V and type VI injuries have associated separation of the sternoclavicular joint and are the result of severe trauma with other, accompanying fractures.

Box 4-6. **Acromioclavicular Joint Injuries**

STANDARD VIEW

AP with beam directed 15 degrees cephalad in upright position without weight (both shoulders on the same image)

FREQUENTLY MISSED INJURY

Coracoid fracture

RELEVANT NORMAL ANATOMY

Coracoclavicular ligament is the most important ligament in stabilizing the clavicle and scapula

Normal AC joint space less than 8 mm; right and left differing less than 2 to 3 mm

Distal inferior cortical margin of clavicle and acromion are in the same plane

Coracoclavicular distance less than 11 mm; right and left differing less than 5 mm

FRACTURE MIMICS

Unilateral erosions of the distal clavicle—post-traumatic osteolysis, gout, neoplasm such as multiple myeloma

Bilateral erosions of the distal clavicle—rheumatoid arthritis, hyperparathyroidism, scleroderma

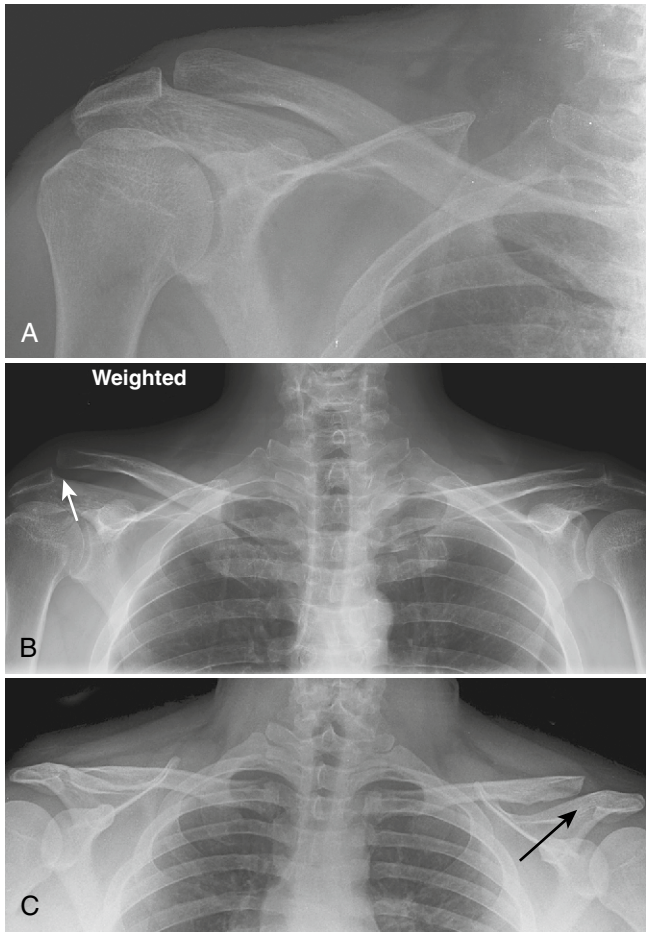


FIGURE 4-3. Acromioclavicular (AC) joint injury. Type II injury. Anteroposterior radiograph of the AC joint, without weight. **A,** A normal AC space. **B,** With weight-bearing, there is widening of the joint space. **C,** Anteroposterior radiograph of both AC joints demonstrates a type III injury. Differentiation between these two types may not be clinically relevant due to a trend toward nonoperative management in both categories.

Box 4-7. Subluxations and Dislocations About the Glenohumeral Joint

STANDARD VIEWS
AP in external rotation and axillary views of the shoulder
Near view or transthoracic view if axillary view cannot be obtained

FREQUENT SITES OF INJURIES
Anterior dislocation
Hill-Sachs fracture

FREQUENTLY MISSED INJURIES
Posterior dislocation
Bankart lesion

RELEVANT NORMAL ANATOMY
On routine AP view of the shoulder, articular surface of humeral head should overlap the glenoid shadow

Subluxations and Dislocations About the Glenohumeral Joint

The glenohumeral joint (Box 4-7) is the most frequent site of dislocation of any joint in the body. Most commonly, these are post-traumatic dislocations. However, non-traumatic etiologies such as seizures and voluntary dislocations do occur. The type of dislocation is determined by the final resting place of the humeral head relative to the glenoid: anterior, posterior, superior, or inferior.

Anterior Dislocation

The vast majority of glenohumeral joint dislocations are anterior dislocations (Fig. 4-4A). This usually occurs as a result of indirect force applied to the arm in abduction, extension, and external rotation. Subcoracoid anterior dislocation is the most common subtype, followed by subglenoid, subclavicular, and intrathoracic. It is readily diagnosed on clinical exam and frontal radiographs as a medially and

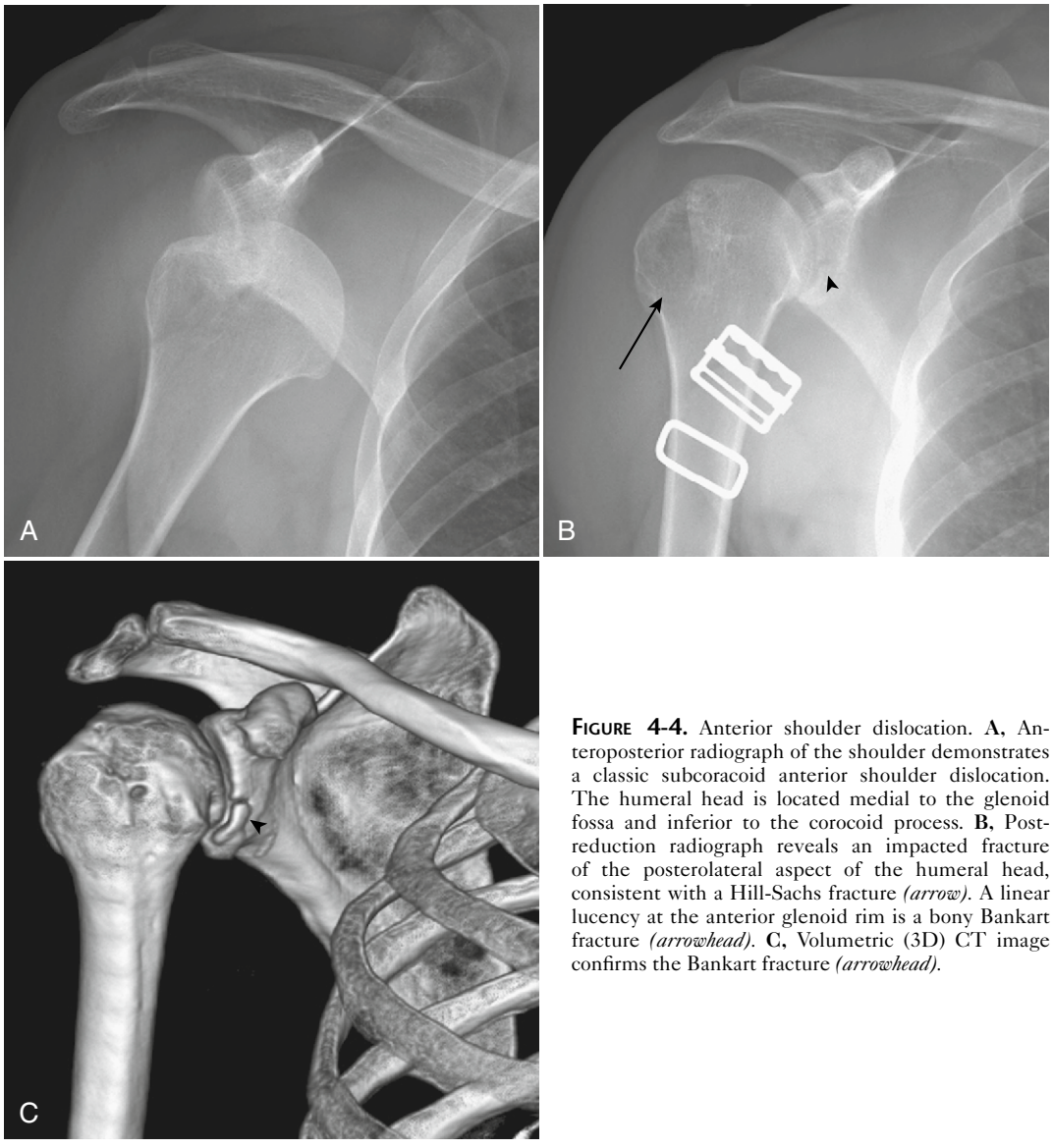


Figure 4-4. Anterior shoulder dislocation. **A,** Anteroposterior radiograph of the shoulder demonstrates a classic subcoracoid anterior shoulder dislocation. The humeral head is located medial to the glenoid fossa and inferior to the corocoid process. **B,** Post-reduction radiograph reveals an impacted fracture of the posterolateral aspect of the humeral head, consistent with a Hill-Sachs fracture *(arrow)*. A linear lucency at the anterior glenoid rim is a bony Bankart fracture *(arrowhead)*. **C,** Volumetric (3D) CT image confirms the Bankart fracture *(arrowhead)*.

inferiorly located humeral head relative to the glenoid. The common associated injuries are Hill-Sachs fracture and Bankart lesion as a result of impaction of the humeral head against the glenoid during the movement of dislocation. The Hill-Sachs fracture (Fig. 4-4B) is a large defect or groove in the posterolateral aspect of the humeral head, best visualized in the internally rotated anteroposterior (AP) projection. Bankart lesions (Fig. 4-4B and C) may be composed of soft tissue (fibro-cartilaginous, cartilaginous labrum) or a piece of bone avulsed from the anteroinferior portion of the glenoid rim. They are less common than Hill-Sachs fractures. Neither one of these lesions is a sign of recurrent or previous dislocations, because they do occur at the initial dislocation.

Posterior Dislocation

Posterior dislocations of the glenohumeral joint (Fig. 4-5) usually occur with violent muscle contractions, as seen with seizures, or electric shocks. The dislocation can be either subacromial, subglenoid, or subspinous. It is an uncommon injury that frequently coexists with an impacted fracture of the anterior humeral head due to trauma to the humeral head on the glenoid fossa during dislocation. It is difficult to detect clinically, especially in obese or muscular individuals. On frontal radiographs, posterior dislocations may go unrecognized in up to 50% of cases. Multiple signs have been described as helpful for detection of this subtle injury on frontal projections. The "positive rim" sign is an increase in the distance between the articular cortex of the humeral head and the anterior glenoid rim to more than 6 mm. The "light bulb" sign is a humeral head fixed in internal rotation, resembling a light bulb. The "trough line" is a curvilinear dense line parallel to the articular margin of the humeral head, representing an impacted fracture of the anterior aspect of the humeral head that coexists with the dislocation.

Inferior Subluxation (Luxatio Erecta)

Luxatio erecta is a rare type of subglenoid inferior dislocation; the arm is severely hyperabducted, and the humerus is directed superiorly so that the long axis of the humeral

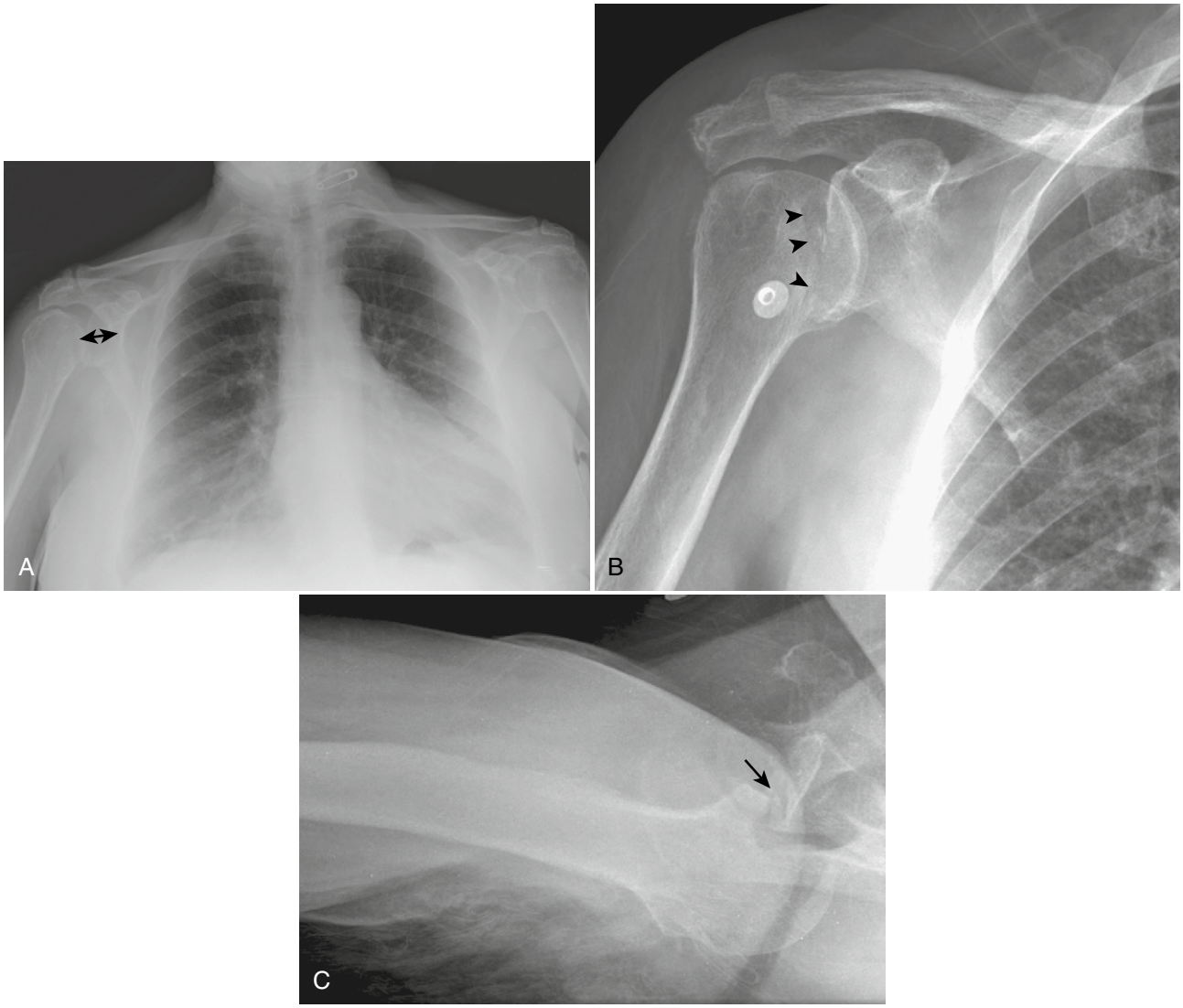


FIGURE 4-5. Posterior shoulder dislocation. **A,** Chest radiograph shows increased distance between the articular cortex of the humeral head and the anterior glenoid rim *(double-headed arrow)*. Anteroposterior shoulder radiograph **(B)** of the same patient shows a "trough line" sign as a curvilinear density *(arrowheads)* consistent with an impacted reverse Hill-Sachs fracture *(arrow)*, confirmed in the axillary projection **(C,** *arrow*).

shaft is perpendicular to the lateral chest wall. This rare entity is associated with Hill-Sachs fractures, other humeral head fractures, and occlusion of the axillary artery.

Pseudosubluxation

Pseudosubluxation describes the drooping of the humeral head with respect to the glenoid, and is usually apparent only in erect examinations. It is secondary to joint distension of traumatic or non-traumatic etiologies, for example, hemarthrosis, lipohemarthrosis, disruption of the joint capsule in chronic or recurrent dislocation, and others.

Fractures of the Proximal Segment and Shaft of the Humerus

Fractures of the Proximal Humerus

The proximal humerus consists of the humeral head, anatomical neck, greater tuberosity, lesser tuberosity, surgical neck, and proximal shaft. Fractures of the proximal humerus (Box 4-8) are associated with osteoporosis. The majority of fractures are the result of indirect forces such as a fall onto an outstretched arm. Patterns of fracture and displacement are dictated by the position of the humerus at the time of injury, by bone quality, and by the direction of muscular pull on humeral fracture fragments. By counting the number of major displaced fragments and defining specific parts of involvement (head, greater tuberosity, lesser tuberosity, and shaft), Neer classified fractures of the proximal humerus into one-, two-, three-, and four-part fractures. Each of the four fracture sites results in a potential fragment, or "part." A fragment is considered a "part" if it is displaced more than 1 cm or rotated more than 45 degrees. Regardless of the number of fracture lines, a lesser degree of displacement is considered to be minimal. One-part fractures (Fig. 4-6A) are nondisplaced or minimally displaced fractures. Muscles inserting on the proximal humerus influence the direction of fragment displacement fragments. The pectoralis major pulls the humeral shaft anteromedially. The supraspinatous and infraspinatous pull the greater tuberosity posterosuperiorly, and the subscapularis pulls the lesser tuberosity medially. When describing fractures of the proximal humerus, it is important to specify the type (one-, two-, three-, or four-part; surgical or anatomical neck) and the involved fragments (shaft, greater, lesser tuberosity). According to Neer's description, 80% of fractures of the proximal humerus are one-part fractures and the majority of them are fractures of the surgical neck. Nondisplaced surgical neck fractures usually have a good prognosis because blood supply to the humeral head is preserved. On the contrary, fractures of the anatomical neck heal poorly because of the completely disrupted vascular supply that results in avascular necrosis and secondary osteoarthritis. Two-part fractures (Fig. 4-6B and C) account for 10% of all fractures of the proximal humerus. Displaced fractures of the surgical neck may injure the brachial plexus or axillary artery because these structures lie immediately anterior to the humeral head and surgical neck. Isolated fractures of the lesser tuberosity are unusual. A four-part fracture (Fig. 4-6D and E) is one in which the articular segment is isolated from both tuberosities and the humeral shaft. A "classic" four-part fracture is a fracture-dislocation, in which the articular segment dislocates anteriorly with no remaining soft tissue attachments. This results in an increased risk of osteonecrosis. Another important variant of a four-part fracture is the "valgus-impacted" fracture, which has a better prognosis due to maintained residual vascularity.

Fractures of the Shaft of the Humerus

A humeral shaft fracture (see Box 4-8) is defined when the main fracture line is distal to the surgical neck of the proximal humerus, and proximal to the supracondylar ridge. Fractures of the humeral shaft are common. They are classified according to their location: above or below the pectoralis major insertion and above or below the deltoid insertion. Location of the fracture line affects the way the fragments are displaced. With fractures occurring above the pectoralis major insertion, the distal fragment is displaced anteromedially by the pull of the pectoralis major. Fractures occurring between the insertions of the pectoralis and deltoid muscles (Fig. 4-7) are associated with lateral displacement of the distal fragment. Fractures occurring distal to the deltoid insertion result in abduction of the proximal fragment by the deltoid and shortening of the arm by the pull of the brachialis and biceps muscles, which remain attached to the distal fragment. Associated injuries of the radial nerve are common, especially with fractures located at the junction of the mid and distal thirds. Pathologic fractures of the humerus are common in adults as a result of metastatic disease. In children, this usually occurs through a simple bone cyst of the proximal humerus.

Box 4-8. Fractures of the Proximal Humerus and Shaft of the Humerus

STANDARD VIEWS
AP, lateral (transthoracic) of the shaft of humerus

FREQUENT SITE OF INJURY
Fractures of the surgical neck

RELEVANT NORMAL ANATOMY
- Anatomical neck is a narrow groove, separating the head from the tuberosities; it is an attachment site for the glenohumeral joint capsule
- Surgical neck is a constriction below the greater and lesser tuberosities
- Pectoralis major insertion—outer bicipital ridge of the humerus (anterior aspect of the upper third)
- Deltoid insertion—outer aspect of the middle third of the humerus

Fractures and Dislocations Around the Elbow (Box 4-9)

The Fat Pad Sign

Normal thin layers of fat lie between the synovium and the joint capsule of the elbow anteriorly and posteriorly. In a normal flexed elbow, the anterior fat pad is visible, while the posterior fat pad is hidden in the intercondylar depression on the posterior surface of the humerus. In the presence of a joint effusion, the posterior fat pad (Fig. 4-8) becomes visible on the lateral radiograph of the flexed

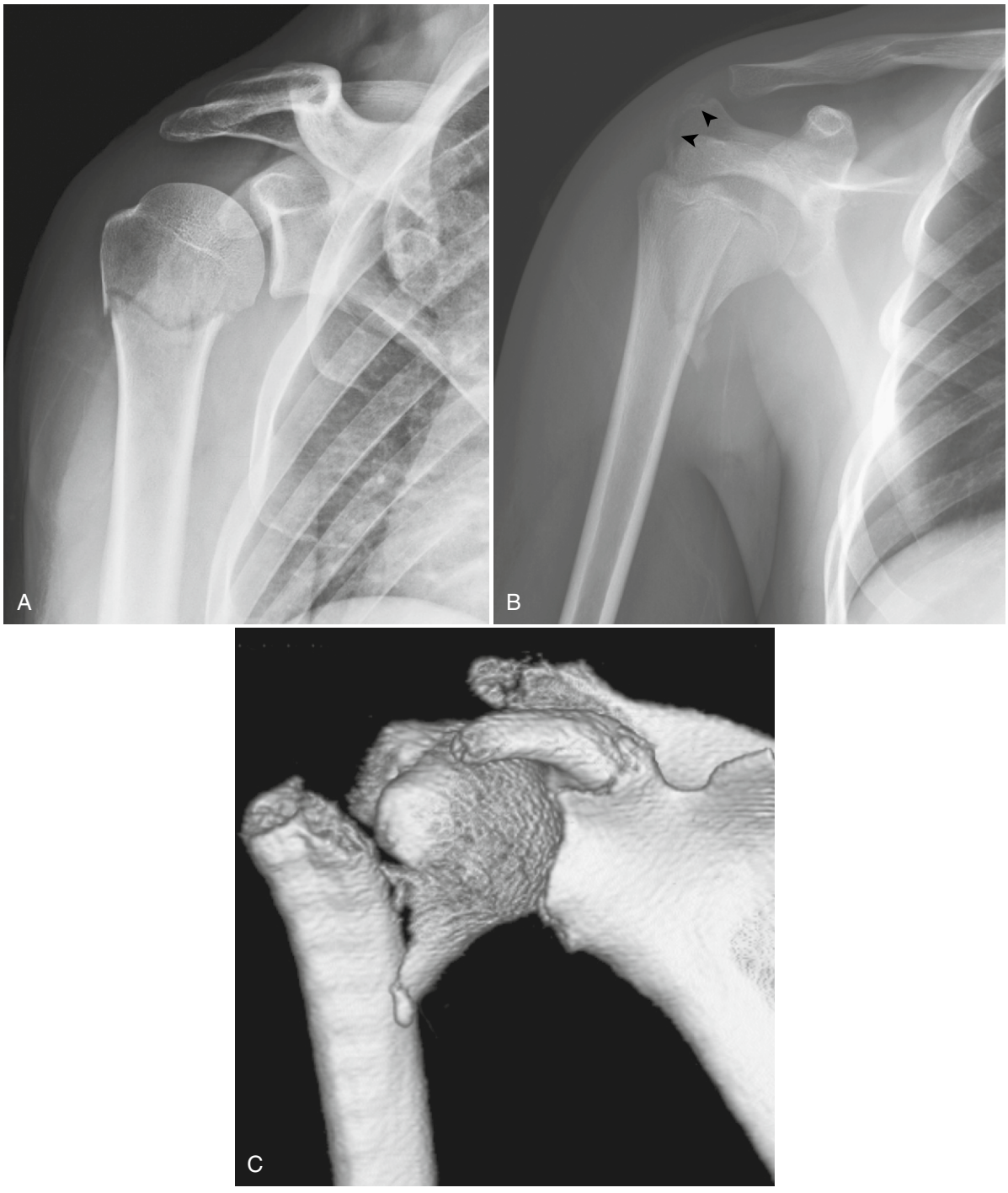


FIGURE 4-6. Fracture of the proximal humerus. **A,** Anteroposterior radiograph of the shoulder demonstrates a nondisplaced ("one-part") fracture of the surgical neck of the humerus. **B** and **C,** Anteroposterior radiograph and volumetric (3D) CT reformation of the shoulder reveal a comminuted fracture of the surgical neck. This is a "two-part" fracture (proximal articulating part, and shaft): only two fragments are considered "parts" because they are displaced more than 1 cm. In addition, there is a nondisplaced fracture of the acromion process (**B,** *arrowheads*).

Continued

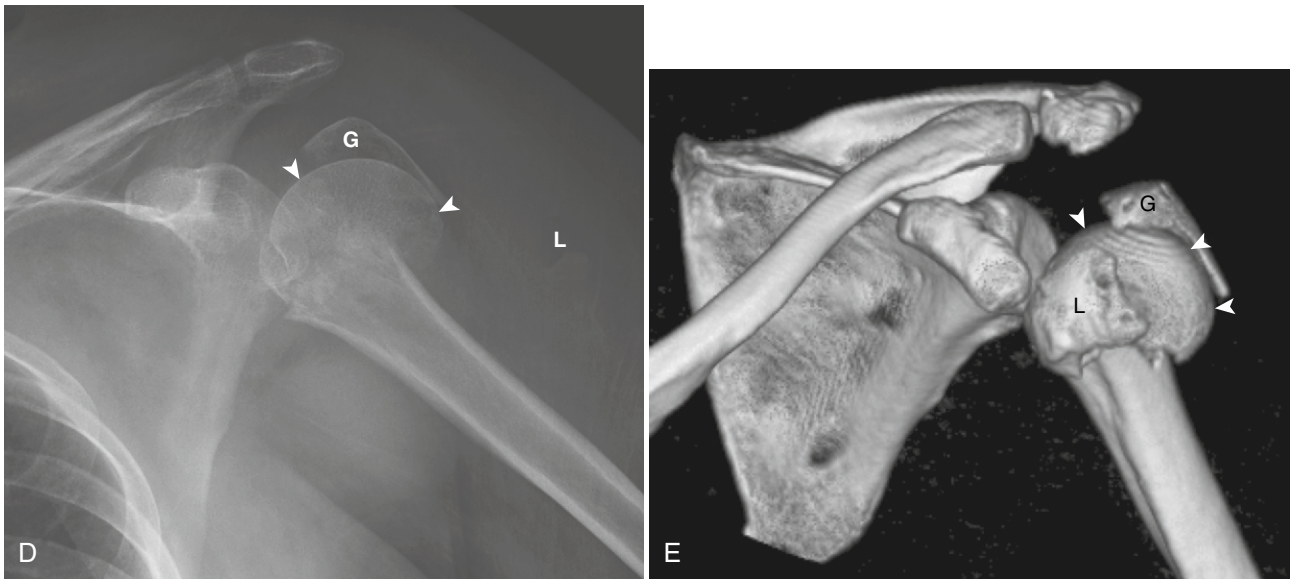


Figure 4-6.—Cont'd D and **E,** Four-part fracture with valgus impaction is shown in an anteroposterior radiograph and a volumetric (3D) CT reformation. The greater tuberosity *(G)* and articulating part of the humeral head *(white arrowheads)* and shaft are separated from each other by more than 1 cm. The "L" indicates that this is the left shoulder.

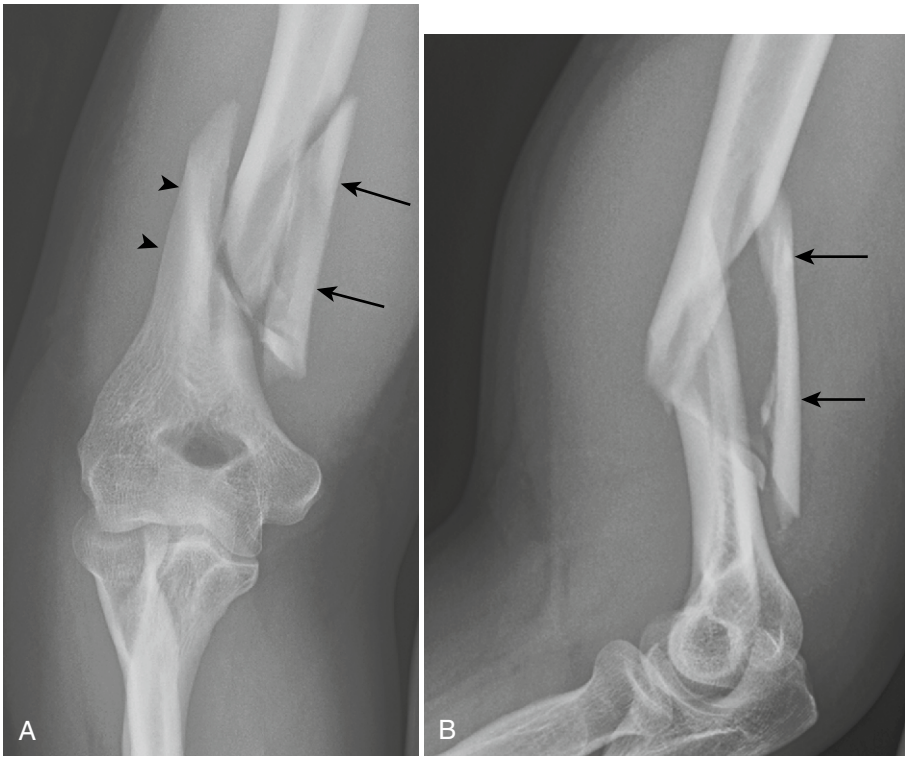


Figure 4-7. Fracture of the shaft of the humerus. **A** and **B,** Anteroposterior and lateral radiographs demonstrate a comminuted fracture of the distal third of the humerus with a large butterfly fragment *(arrows).* The butterfly fragment is pulled medially and posteriorly, while the distal fragment *(arrowheads)* is retracted proximally due to the pull by the deltoid muscle.

Box 4-9. **Fractures and Dislocations Around the Elbow**

STANDARD VIEWS

AP, lateral (90-degree flexed elbow with hand in lateral position), both obliques; in children, only AP and lateral views

Optional—radial head view (must be accompanied by a full elbow series)

FREQUENT SITES OF INJURIES

Children—supracondyle, lateral condyle of distal humerus

Adults—radial head, olecranon

RELEVANT NORMAL ANATOMY

Distal humerus consists of supracondylar region, medial and lateral condyles, medial and lateral epicondyles

Anterior humeral line—downward extension of anterior cortex of the distal humeral shaft; on lateral radiograph, it intersects the capitellum near the junction of its anterior and middle thirds

Radiocapitellar line—a line bisecting the proximal radial shaft that should pass through the capitellum on every radiographic view

Normal carrying angle of the elbow (valgus)—165 degrees

elbow because it is displaced posteriorly and the anterior fat pad becomes more elevated. In the acute trauma setting, elbow joint effusions can be a result of an intra-articular fracture or traumatic synovitis. This sign is usually present in children and adolescents, where 70% to 90% of patients with a posterior fat pad sign prove to have a fracture on initial or subsequent examinations. In adults, the sign is less frequently seen, and its absence cannot be used to exclude a fracture. This sign is not present in elbow dislocations, displaced intra-articular fractures with a torn joint capsule, and fracture-dislocations because it requires an intact synovium to prevent blood from mixing with extrasynovial fat. An optimal-quality lateral radiograph of the elbow is essential for evaluation of the fat pad sign. The image is taken when the elbow is flexed at 90 degrees with the hand in a lateral position. On the radiograph, three concentric arcs of the distal humerus (trochlear groove, capitellum, and medial trochlea) should be visualized.

Fractures Around the Elbow in Children

Supracondylar fractures are the most common type of fracture of the distal humerus. They are frequently seen in children aged 9 to12 years and occur as a hyperextension injury in which the olecranon acts as a fulcrum. When displaced, the fracture is easily recognized and characteristically displaced posteriorly. The brachial artery and median nerve may be stretched or interposed between fragments. Presence of abnormal cubitus valgus or varus should be assessed because either of these findings may alter the choice of therapy. Volkmann's ischemic contracture is the most serious complication of this type of fracture and is caused by diminished blood flow to the rest of the arm. Subtle fractures are difficult to visualize directly; presence of a posterior fat pad sign and an abnormal anterior humeral line are important clues in this circumstance.

Lateral condylar fracture (Fig. 4-9) is the second most common type of fracture occurring around the elbow in children. This fracture is caused by a lateral blow to the

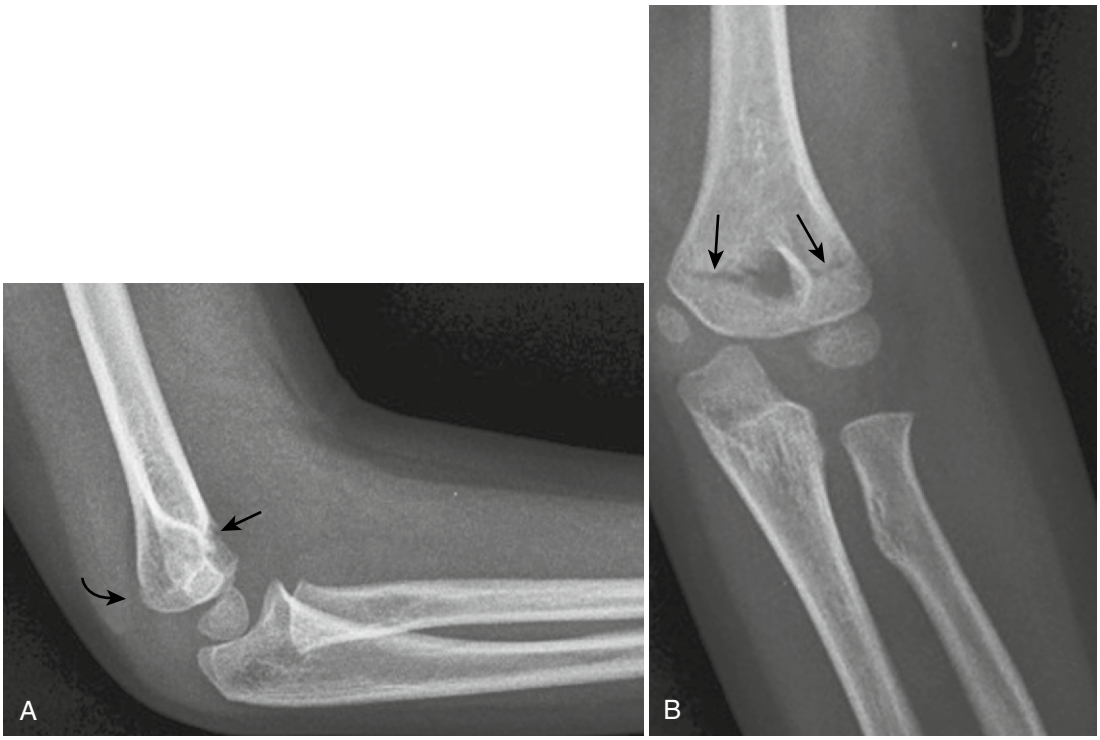


FIGURE 4-8. Supracondylar fracture in children. **A,** Lateral radiograph of the elbow demonstrates a posterior fat pad sign *(curved arrow)*, indicating presence of an intra-articular fracture. A subtle cortical break is seen on this view *(arrow)*. **B,** Anteroposterior view confirms the fracture line *(arrows)*.

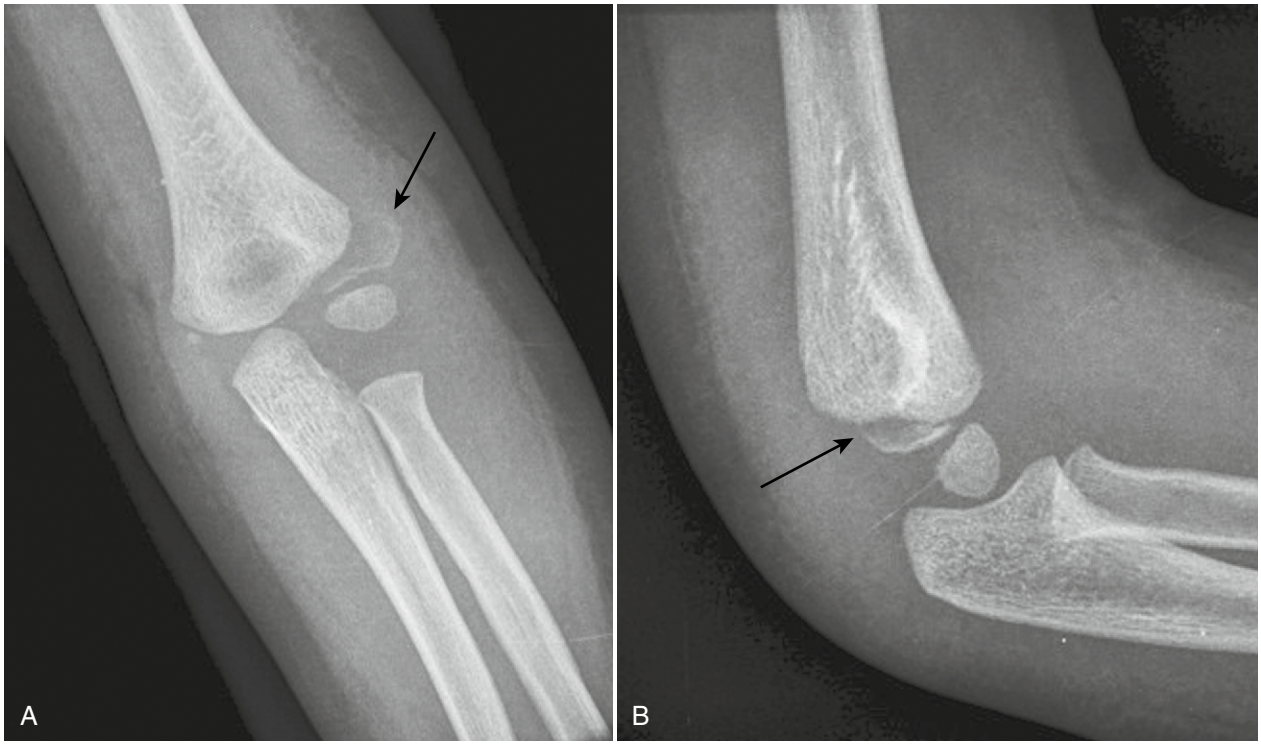


Figure 4-9. Lateral condylar fracture in children. Anteroposterior and lateral radiographs (**A** and **B,** respectively) of the elbow demonstrate a displaced lateral condylar fracture *(arrows),* which is the second most common fracture around the elbow in children.

forearm, resulting in varus stress across the elbow. Typically, the fracture line runs across or along the physis, with or without a small metaphyseal fragment. Fractures may terminate in the physis (incomplete) or extend beyond the physis through the ossified capitellum or unossified cartilage (complete). Differentiation between incomplete and complete fractures can be difficult because most of the fractures extend through the unossified cartilage. Additional imaging with magnetic resonance imaging (MRI) or intraoperative assessment with arthrography is often needed.

Fractures of the Distal Humerus

The distal humerus consists of two columns of medial and lateral epicondylar ridges located at the distal humeral metaphysis and a central articulating axis (trochlea). The most distal part of the lateral column is the capitellum, and that of the medial column is the nonarticular medial epicondyle. Between the two columns lies the trochlea, which serves as a "tie-arch." Although the column anatomy is not important for stability of the elbow, it is essential for determining the type of surgical reconstruction. An increasing trend toward operative treatment of these fractures requires a more comprehensive classification system. The AO/OTA (Orthopedic Trauma Association) classified distal humeral fractures into three types. Type A is an extra-articular fracture, type B is a partial articular fracture, and type C is a complete articular fracture. Ninety-five percent of distal humeral fractures in adults are intra-articular.

Type A extra-articular fractures (Fig. 4-10A and B) include apophyseal avulsion fractures (avulsion of the lateral epicondyle, medial epicondyle) and simple and complex nonarticular metaphyseal transcolumn fractures. Type B partial articular fractures (Fig. 4-10C and D) are intra-articular fractures that involve only one column (either medial or lateral) with one or more sites of intra-articular extension (capitellum, trochlea, or both). They are subtyped into lateral sagittal fractures, medial sagittal fractures, and frontal fractures. Sagittal fractures are either transcapitellar or transtrochlear fractures depending on the fracture line involvement. Frontal fractures are isolated fractures of the capitellum, trochlea, or both, without metaphyseal extension. Fractures of the capitellum account for 10% of all distal humeral fractures in adults. A shearing force transmitted by the radial head or trochlear groove results in this type of injury. The fragment is visualized on the lateral radiograph of the elbow and is characteristically displaced proximally above the radial head and coronoid process.

Type C, complete articular fractures (Fig. 4-10E and F), are fractures that involve both the medial and lateral columns, with articular extension. These fractures are further subclassified according to the nature (simple or complex) of the column fracture and the presence of intra-articular extension.

Fractures of the Proximal Radius

A radial head fracture (Fig. 4-11A and B) is the most common elbow injury in adults. It is intra-articular and usually produces hemarthrosis. It can be very subtle due to minimal cortical disruption and is usually not seen on all projections. Two patterns of fractures are usually seen: a single longitudinal fracture through the proximal articular surface, and impaction of the intact radial head into the radial neck. The former presents as a step-off or abrupt angulation of the joint surface, or depression of the fragment (double line of cortical bone). The latter creates an abrupt step-off between the normally gentle concave curve of the

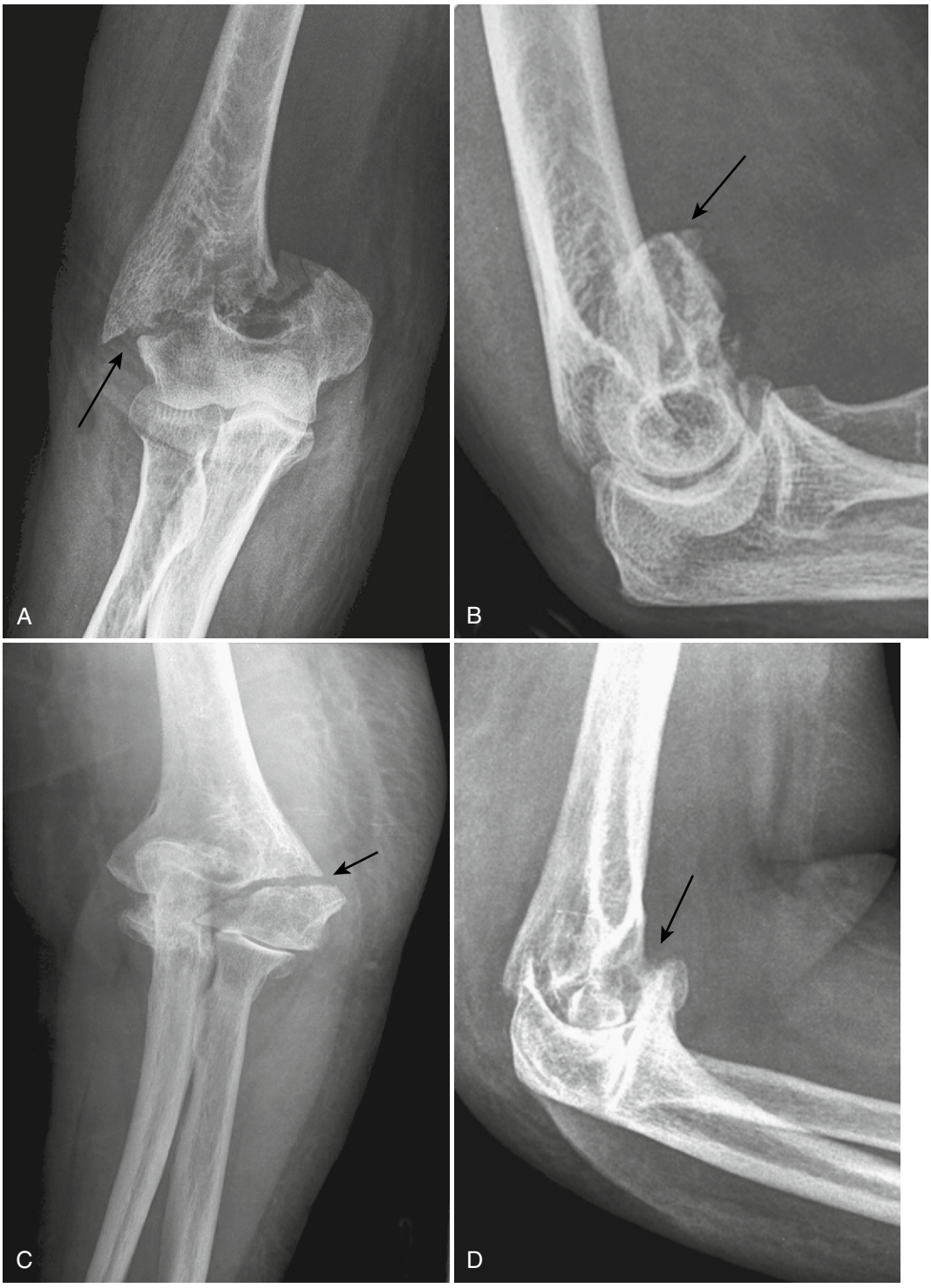


FIGURE 4-10. Fractures of distal humerus. **A** and **B,** Anteroposterior and lateral radiographs of the elbow show a comminuted transverse extra-articular metaphyseal fracture (type A) *(arrows)* with medial and volar displacement of the distal fragment. **C** and **D,** Transtrochlear fracture (partial articular, type B) *(arrows)* with mild displacement. The fracture extends from the trochlea to the lateral column of the distal humerus.

Continued

radial head and neck. Three types of radial head fractures were described by Mason, and later modified by Morrey to include a type IV fracture. Type I is a nondisplaced fracture, which accounts for 50% of cases. Type II is a displaced fracture without comminution, and type III is a comminuted fracture. Type IV is a radial head fracture-dislocation. The fracture is considered displaced if a fragment involves 30% or more of the articular surface and is displaced more than 2 mm. Open reduction with internal fixation is sometimes used to correct this fracture, especially with a large displaced fragment.

Presence of comminuted radial head and neck fractures due to high-energy trauma should raise suspicion for additional elbow and forearm injuries, such as capitellar and

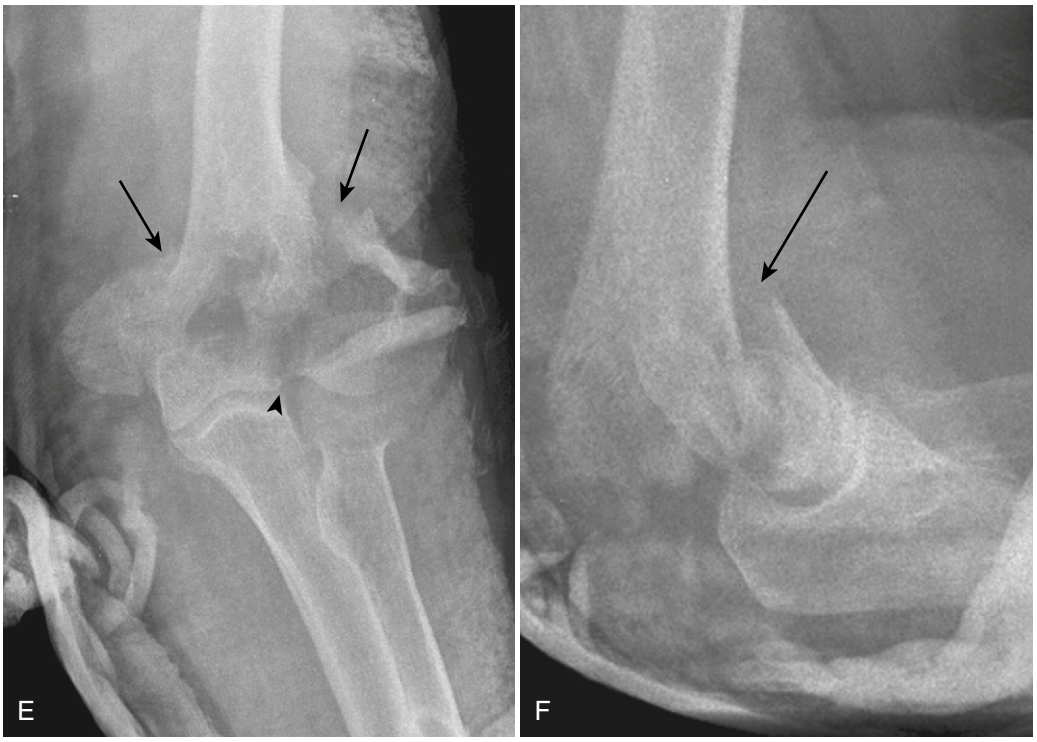


Figure 4-10.—Cont'd E and **F,** Complete articular fracture (type C) with marked displacement. The fracture lines extend to both medial and lateral columns *(arrows)* of the distal humerus, as well as to the articular surface of the elbow *(arrowhead).* Distinction between type B and type C is based on the number of columns involved.

coronoid process fractures, elbow dislocation, and the Essex-Lopresti fracture. The latter consists of an unstable, comminuted fracture of the radial head and neck, and proximal migration or subluxation of the distal radioulnar joint that leads to an acute tear of the interosseous ligament of the forearm. Fractures of the olecranon (Fig. 4-11C) are the second most common type of elbow fractures in adults. They can be caused by a direct injury to the olecranon itself, which usually presents with comminution and distracted fragments, or by an indirect injury (e.g., a fall on the forearm) that results in simple fractures. If the periosteum is completely torn, traction by the triceps will displace the proximal fragment proximally resulting in a wide fracture gap. Although the fractures are usually obvious on lateral radiographs, soft tissue swelling in the olecranon bursa is an important clue to the presence of a subtle fracture.

Fractures of the coronoid process (Fig. 4-12) are usually oriented in the coronal plane and are caused by a shearing mechanism, most commonly from a posterior elbow dislocation. These fractures are pathognomonic of an episode of elbow instability. In every posterior dislocation, the coronoid process should be examined closely to exclude a fracture. A free intra-articular bone fragment within the elbow joint of an adult with posterior dislocation is most likely a displaced coronoid process fracture.

Dislocations of the Elbow

The elbow is one of the most commonly dislocated joints of the body. Elbow dislocations usually occur in young people, with a peak in individuals between 5 and 25 years of age. Dislocations of both the radius and ulna, with respect to the distal end of the humerus, are the most frequently seen type. More than 80% are posterior or posterolateral dislocations (see Fig. 4-12). Less commonly, the radius and ulna dislocate in divergent directions. Common associated injuries include fractures of the coronoid process, radial head, and medial epicondyle of the humerus. "Terrible triad" fracture-dislocations describe the combination of elbow dislocation with radial head and coronoid process fractures. This condition is prone to early recurrent instability and post-traumatic arthritis.

Fractures of the Shafts and Distal Radius and Ulna (Box 4-10)

Abnormal Pronator Quadratus Sign

The pronator quadratus is a thin flat muscle located on the volar aspect of the interosseous membrane at the level of the distal radioulnar joint. It is normally seen on lateral radiographs, outlined by a thin radiolucent fat stripe. When there is hemorrhage beneath the muscle, the contour of the muscle bulges anteriorly. This could present as a volar bulge of the thin fat stripe superficial to the muscle, or as a loss of definition of the lucent fat stripe overlying the muscle itself. It is usually caused by injuries to the distal third of the radius and ulna.

Monteggia Fracture-Dislocation

Monteggia fracture-dislocation is a combination of a fracture of the proximal ulnar shaft and subluxation or dislocation of the radial head. The term "Monteggia lesion" describes a number of traumatic lesions that have in common disruption of the radial head and fracture of the ulna at any level. Four types of Monteggia fracture-dislocation (Bado

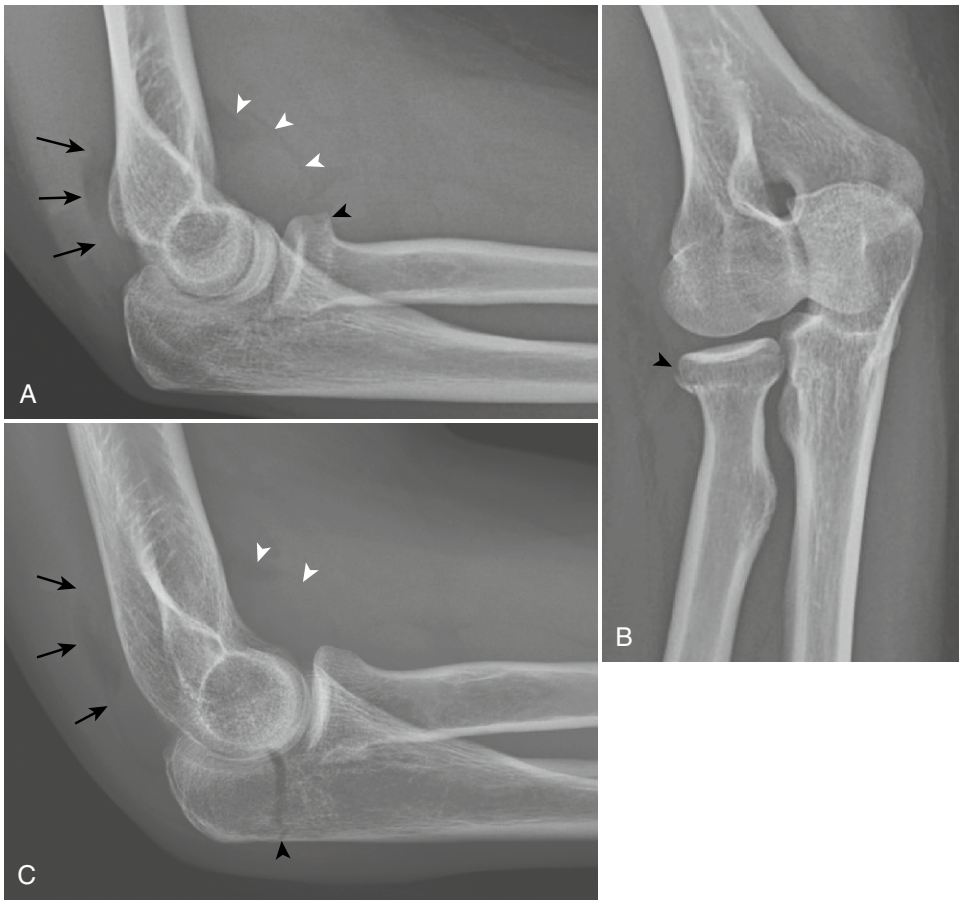


FIGURE 4-11. Fractures of the radial head and olecranon process. **A,** Lateral radiograph of the elbow demonstrates a classic posterior fat pad sign *(arrows)* produced by posterior bulge of the extrasynovial fat. In addition, there is an elevated anterior fat pad *(white arrowheads)*. The cause of the joint effusion is a radial head fracture *(black arrowhead)*. **B,** The black arrowhead demonstrates a nondisplaced fracture of the radial head. **C,** Lateral radiograph of the elbow shows a transverse fracture of the olecranon process *(black arrowhead)*, a posterior fat pad sign *(arrows)*, and elevated anterior fat pad *(white arrowheads)*.



FIGURE 4-12. Elbow dislocation and fracture of the coronoid process. Lateral radiograph of the elbow demonstrates a posterior dislocation of the radius and ulna with respect to the distal humerus. A coronoid process fracture is noted *(arrowheads)*.

Box 4-10. **Fractures of the Shafts and Distal Radius and Ulna**

STANDARD VIEWS

AP (supination) and lateral views (with elbow flexed 90 degrees and hand in lateral position) of the forearm; distal radius is imaged with wrist protocol

FREQUENT SITES OF INJURIES

Distal end of radius
Ulnar styloid process

FREQUENTLY MISSED INJURY

Distal radioulnar joint injury

classification) are described according to the direction of the displaced ulnar fracture and the dislocated radial head. Type I is the most common; it is a fracture-dislocation with volar angulation at the fracture site and volar dislocation of the radial head. Type II, or reverse Monteggia fracture-dislocation (Fig. 4-13), is more likely to be seen in adults. This type has dorsal angulation at the fracture site and dorsal dislocation of the radial head. Type III is the most severe of all Monteggia fracture-dislocations. The fracture fragments are laterally displaced, with lateral or anterolateral dislocation of the radial head. Type IV is a fracture-dislocation that includes fractures of the proximal radius and proximal ulna along with volar dislocation of the radial

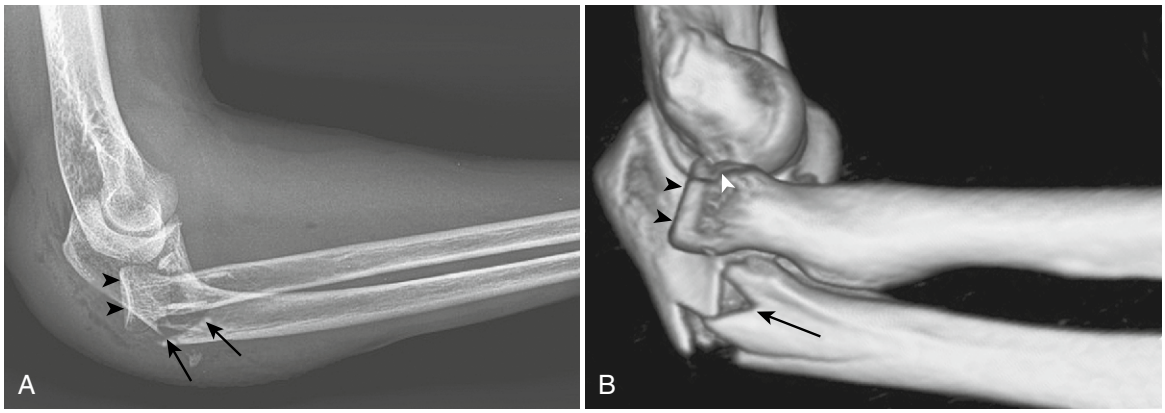


Figure 4-13. Monteggia fracture-dislocation. **A,** Lateral radiograph of the forearm demonstrates dorsal dislocation of the radial head *(black arrowheads)*, along with an angulated comminuted fracture of the proximal third of the ulna *(arrows)*. Soft tissue gas indicates an open injury. This is a type II Monteggia fracture-dislocation. **B,** Volumetric (3D) CT reformation reveals an impacted fracture of the radial head *(white arrowhead)* along with the Monteggia fracture-dislocation.

head. In the presence of an isolated fracture of the shaft of a forearm bone, one must always anticipate the possibility of injuries to other bones.

Galeazzi Fracture-Dislocation

Galeazzi fracture-dislocations (Fig. 4-14) are uncommon, accounting for 3% to 6% of all forearm fractures. They consist of a fracture of the distal third of the radial shaft and dislocation or subluxation of the distal radioulnar joint (DRUJ). When one is faced with an isolated radial shaft fracture, injury of the DRUJ should be sought. The following signs suggest traumatic disruption of the DRUJ: fracture of the ulnar styloid at its base, widened DRUJ space on a frontal radiograph, dislocation of the radius relative to the ulna on a lateral radiograph, and radial foreshortening.

Fractures of the Distal Radius

Fractures of the distal radius are exceedingly common and usually the result of low-energy trauma. They affect women more than men and their incidence increases with advancing age. Although the classification of these fractures as Colles', Smith, or Barton types continues to be used in practice, most distal radial fractures do not fall into one of these categories. The more clinically useful way to describe the fractures of the distal radius is to use the number of fracture "parts" and to define whether the fracture is intra- or extra-articular. Extra-articular fractures do not affect either the radiocarpal joint or the DRUJ. They characteristically occur in the distal 3 to 4 cm of the radius and are composed of two parts. Intra-articular fractures can have two, three, four, or more parts. They extend into the radiocarpal joint

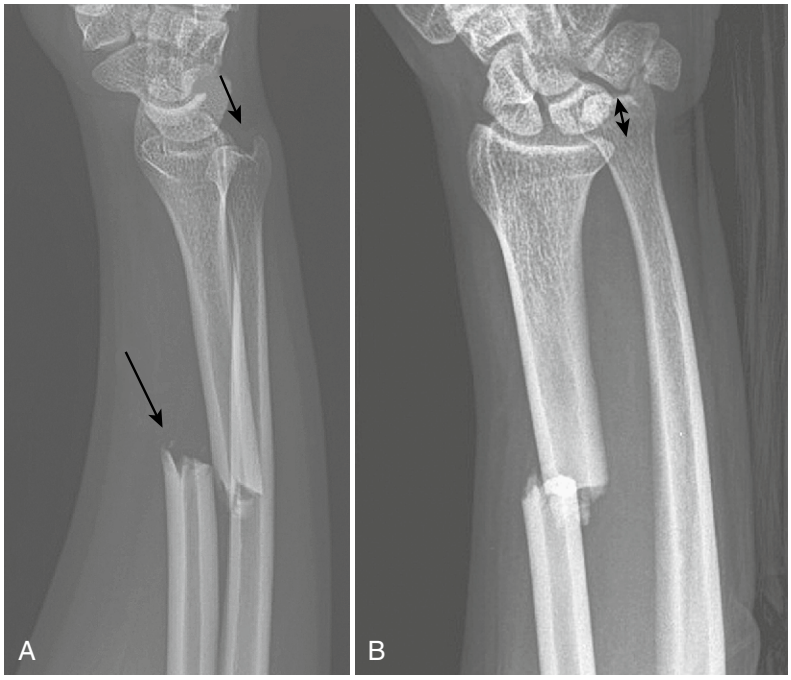


Figure 4-14. Galeazzi fracture-dislocation. **A** and **B,** Lateral and anteroposterior radiographs of the forearm show a displaced transverse fracture of the radial shaft at the junction of the middle and distal thirds, along with dislocation of the distal radioulnar joint (DRUJ). Dislocation of the radius relative to the ulna on the lateral radiograph and radial foreshortening *(double-headed arrow)* are clues suggesting DRUJ disruption.

or DRUJ. Barton and Chauffeur's fractures fall into this category. The degree of intra-articular incongruity is the most clinically significant predictor of functional outcome and future degenerative changes of the radiocarpal joint, especially if there are 2 mm or more incongruity. Stability of these fractures is determined by the degree of angulation, comminution of the dorsal metaphysis, presence of intra-articular extension, and the patient's age.

Colles' fracture (Fig. 4-15A and B) is a transverse extra-articular fracture of the distal radius with dorsal displacement of the distal fragment along with the bones of the wrist and hand. It usually occurs as a result of a fall on the

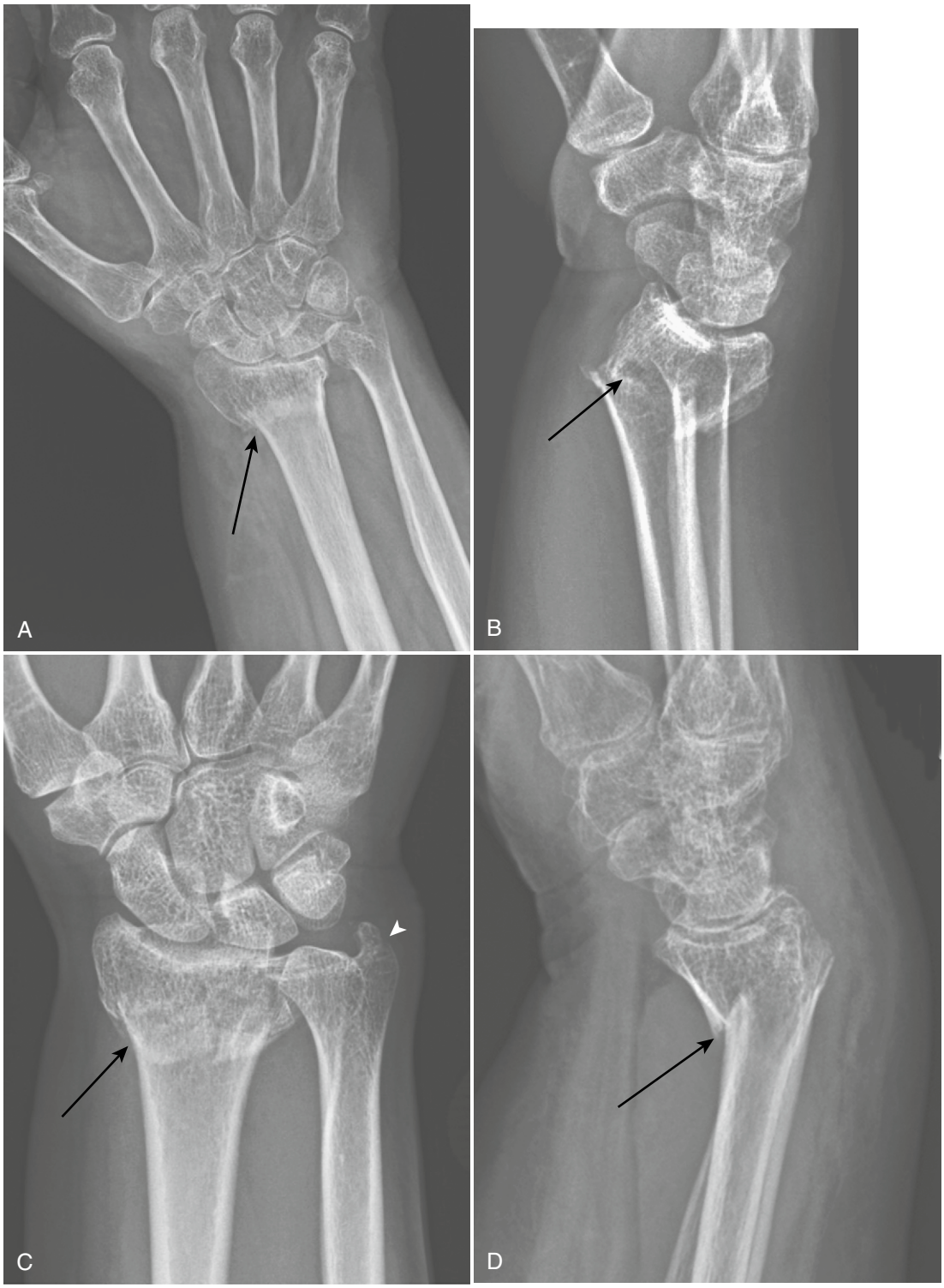


FIGURE 4-15. Fractures of the distal radius. **A** and **B,** Posteroanterior and lateral wrist radiographs demonstrate a transverse extra-articular fracture of the distal end of the radius *(arrows)* with dorsal displacement of the distal fracture fragment, producing a "dinner fork" deformity. This is a classic Colles' fracture. **C** and **D,** Smith, or reverse Colles', fracture is demonstrated and characterized by volar displacement of the distal fracture fragment.



Figure 4-16. Fractures of the distal radius. **A** and **B,** Frontal and lateral radiographs of the wrist demonstrate an oblique coronal fracture of the distal radius with intra-articular extension. The fracture line extends to the volar aspect of the distal radius (volar Barton fracture). **C,** Frontal radiograph of the wrist shows a nondisplaced transverse fracture of the radial styloid process, or a Chauffeur's fracture.

outstretched hand. It is commonly associated with an ulnar styloid process avulsion fracture, scapholunate dissociation, and other carpal dislocations or fractures.

Fractures of the ulnar styloid occur in approximately 60% to 70% of distal radial fractures. The majority of them are small avulsions involving the tip of the ulnar styloid. Choice of treatment remains controversial, although the injury may well produce symptoms owing to the fracture itself or to associated injury to the triangular fibrocartilage complex. Treatment may be indicated if the fracture involves the base of the ulnar styloid with significant displacement and/or gross translation of the radius relative to the ulna.

The Smith fracture (Fig. 4-15C and D) is a transverse fracture of the distal radius with volar displacement of the distal fragment together with the carpus and hand; therefore the term "reverse Colles' fracture" has been used.

The Barton fracture (Fig. 4-16A and B) is an oblique coronal fracture of the dorsal or volar margins of the distal radius with intra-articular extension. If the fracture line extends to the volar aspect of the distal radius, it is called a volar Barton

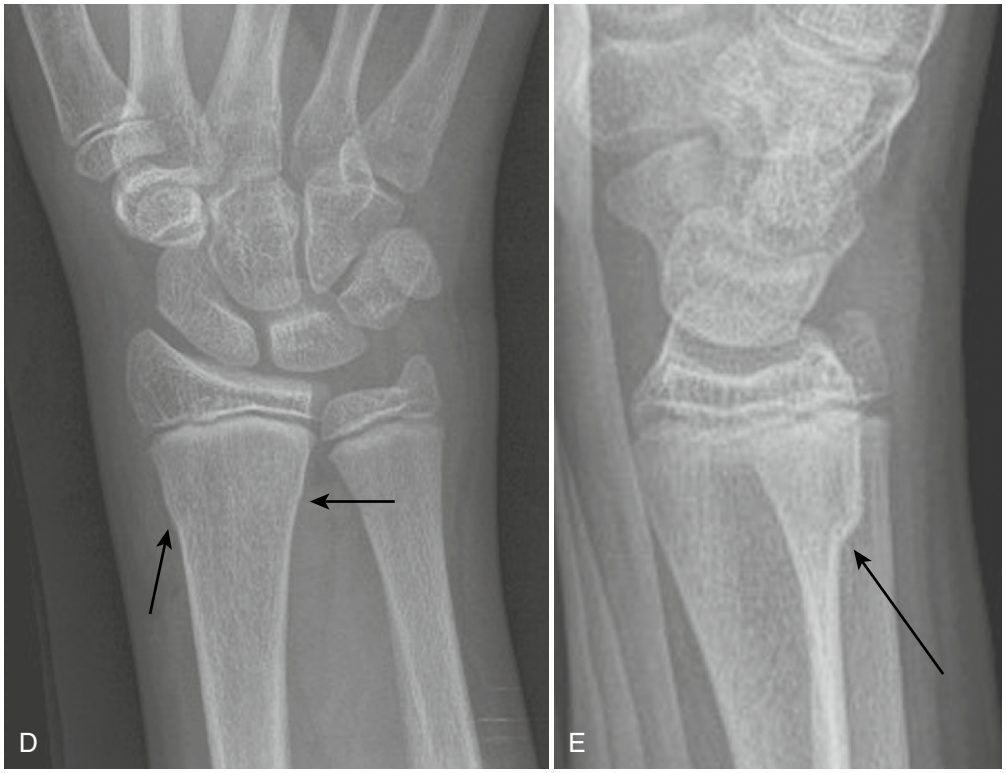


FIGURE 4-16.—CONT'D D and **E,** Torus fracture. Posteroanterior and lateral radiographs of the wrist of a child reveal a subtle undulation in the distal radial metaphysis *(arrows).* This is a classic location for a fracture of the dorsal cortex of the distal radial metaphysis.

fracture. The volar Barton fracture is more common than its counterpart, the dorsal Barton fracture, in which the fracture line extends to the dorsal aspect of the distal radius.

Chauffeur's fracture (Hutchinson fracture) (Fig. 4-16C) is an intra-articular fracture of the base of the radial styloid process. The name comes from the era when hand cranking was needed to start motor vehicles. At present, it is most frequently caused by a fall on an outstretched hand, resulting in an avulsion of the radial collateral ligament, or a direct blow to the radial styloid process.

Torus fracture (buckle fracture) (Fig. 4-16D and E) is the most common fracture of the distal forearm in young children. It is usually caused by a fall on an outstretched hand. Characteristically, the fracture involves only one side of the cortex on the compression side, usually 2 to 3 cm proximal to the physis. The periosteum and cortex are intact on the side opposite to the fracture, hence this fracture has a good prognosis.

Fractures and Dislocations of the Carpus (Box 4-11)

Scaphoid Fracture

Scaphoid fractures (Fig. 4-17) are the most common fractures of the carpal bones. They occur almost exclusively in young adults due to a fall on an outstretched hand, athletic injuries, or motor vehicle accidents. A strong index of suspicion is the key to early diagnosis, because scaphoid fractures may produce only limited motion with little pain or swelling. Although a series of four radiographic views of the wrist is usually sufficient for diagnosis, up to 30% of scaphoid fractures are radiographically occult. Presence of "snuffbox" tenderness and a history of trauma, even with negative radiographs, necessitates immobilization or further imaging with CT or MRI. If immobilization is used, obtaining follow-up radiographs after 10 days usually reveals abnormalities, with either resorption of the fracture line (clearly visible lucent line) or faint sclerosis around the fracture. MRI is the current gold standard for diagnosis of wrist injuries. By excluding a fracture, MRI can eliminate the need for prolonged immobilization. CT is becoming a more common investigation in acute wrist trauma because of its widespread availability and short scan time. Scaphoid fractures are classified based on their anatomic location: proximal third (proximal pole), middle third (waist), distal articulating portion, and tubercle. The most common location is at the waist (80%), followed by the proximal pole (15%), tubercle (4%), and distal articular portion (1%). Location of the fracture determines prognosis because of the characteristic blood supply to the scaphoid. The scaphoid is supplied by two major vascular pedicles. One enters the tubercle, supplies the distal third, and accounts for 20% to 30% of the blood flow. The second one enters a foramen on the spiral groove at the waist and provides 70% to 80% of the blood supply in a retrograde fashion: from the waist to the proximal pole. The more proximal the fracture line, the greater the incidence of avascular necrosis. Stability of the fracture depends on the presence of displacement, degree of comminution, and associated injuries.

Triquetral Fracture

Triquetral fractures (Fig. 4-18A and B) are the second most common fractures of the carpal bones. They commonly

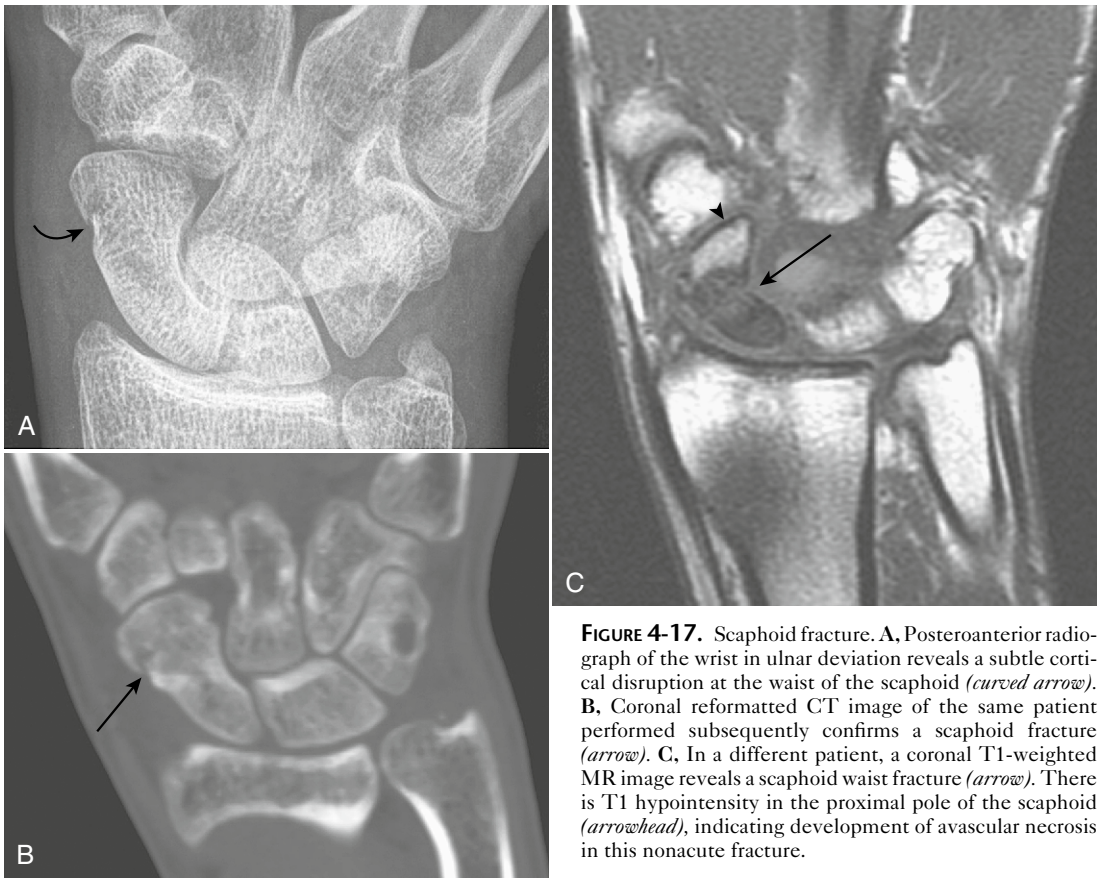


FIGURE 4-17. Scaphoid fracture. **A,** Posteroanterior radiograph of the wrist in ulnar deviation reveals a subtle cortical disruption at the waist of the scaphoid *(curved arrow)*. **B,** Coronal reformatted CT image of the same patient performed subsequently confirms a scaphoid fracture *(arrow)*. **C,** In a different patient, a coronal T1-weighted MR image reveals a scaphoid waist fracture *(arrow)*. There is T1 hypointensity in the proximal pole of the scaphoid *(arrowhead)*, indicating development of avascular necrosis in this nonacute fracture.

involve the dorsal surface, as a result of a shear or chisel injury from impingement of the ulnar styloid on the dorsal aspect of the triquetrum when the wrist is forcibly dorsiflexed and ulnarly deviated. Pain and tenderness are localized to the dorsolateral portion of the wrist. A flake of bone fragment is best visualized in the lateral or pronated oblique projections. A transverse fracture of the triquetral body is easily identified on a standard posteroanterior view.

Box 4-11. **Fractures and Dislocations of the Carpus**

STANDARD VIEWS

PA, lateral, internal, and external oblique views

Scaphoid view, if performed, must be accompanied by a full wrist series

FREQUENT SITES OF INJURIES

Children—torus fractures

Adolescents/young adults – carpal fractures (scaphoid, triquetrum)

Adults—Colles' fractures

FREQUENTLY MISSED INJURIES

Nondisplaced scaphoid fractures

Hook of hamate fractures

Perilunate dislocations

RELEVANT NORMAL ANATOMY

Normal fat stripe anterior to pronator quadratus is thin, smooth, without volar bulge

Normal radiocarpal angle = 15-degree ulnar inclination (frontal projection) and 15-degree volar inclination (lateral projection)

Ulnar variance (radial length)—at the site of articulation with lunate, radius and ulna are normally on the same level; in negative ulnar variance, the articular surface of ulna projects 5 mm proximal to the radiolunate articulation; in positive ulnar variance, the articular surface of ulna projects 8 mm distal to the radiolunate articulation

Normal carpal bone alignment (frontal projection; three smooth arcs of Gilula): arc I joins proximal articular surfaces of the scaphoid, lunate, and triquetrum; arc II is formed by distal convexities of the scaphoid, lunate, and triquetrum; arc III is formed by proximal convexities of the capitate and hamate

Normal carpal bone alignment (lateral projection): long axis of distal radius, lunate, and capitate is linear; long axis of scaphoid is at an angle of 30 to 60 degrees to the axis of distal radius, lunate, and capitate (scapholunate angle)

Three carpal columns—central (radius-lunate-capitate), ulnar (ulna-triquetrum-hamate), and radial (radius-scaphoid-trapezoid-trapezium)

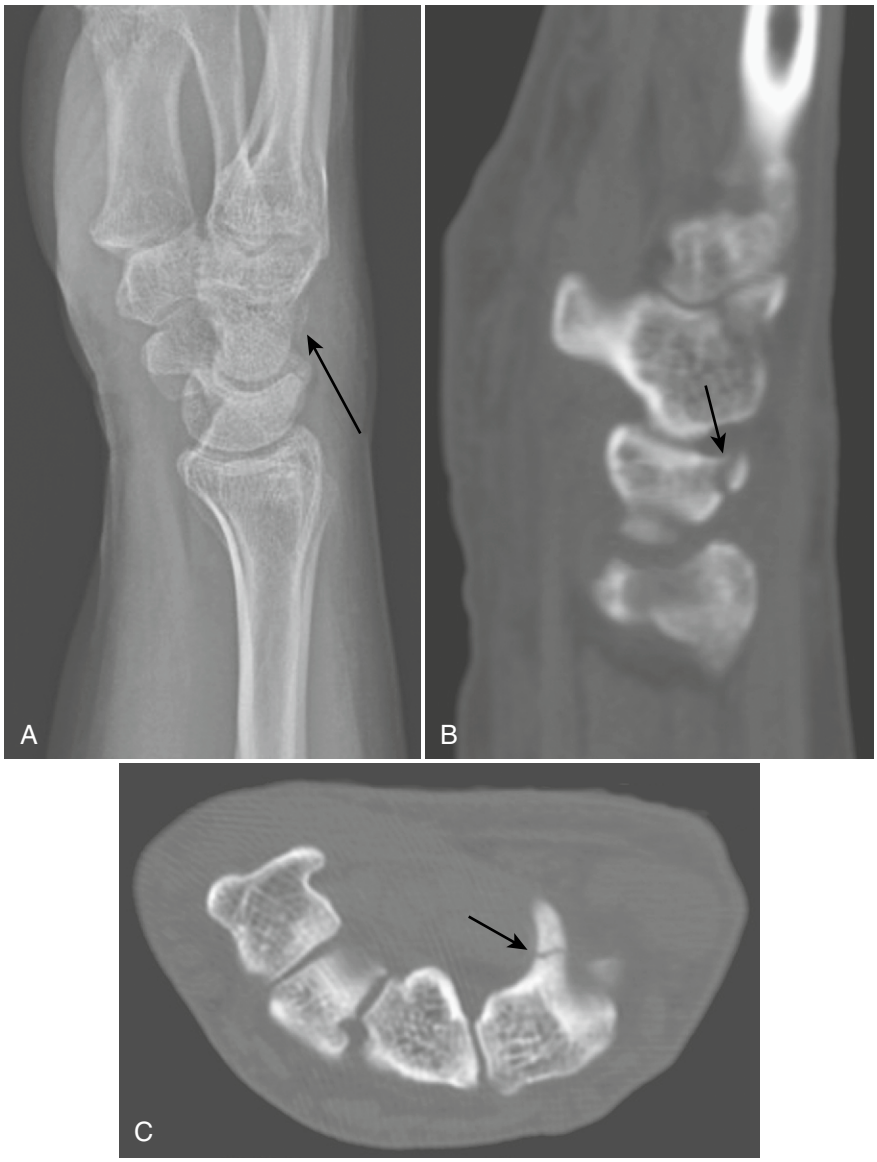


FIGURE 4-18. Other carpal fractures. **A** and **B,** Lateral radiograph of the wrist and sagittal reformatted CT image, respectively, demonstrate a small dorsal triquetral fracture *(arrows)* with overlying soft tissue swelling. **C,** Hook of hamate fracture. Axial CT image shows a nondisplaced fracture of the hook of the hamate.

However, CT may be required to determine the extent of injury.

Hamate Fracture

Fractures of the hamate (Fig. 4-18C) are rare and frequently missed on radiographs. They can involve the body or the hook of the hamate. The latter is more common and can produce significant disability. Either a direct blow to the hook or an avulsion of the transverse carpal ligament and pisohamate ligaments can cause this fracture. It is best visualized on a carpal tunnel view or on CT scan. Absence or indistinctness of the "eye" sign (an oval, dense, cortical ring shadow over the hamate) is a finding that suggests a fracture of the hook of the hamate on frontal radiographs.

Lunate Fracture

The lunate is the fourth most commonly fractured carpal bone, after the scaphoid, triquetrum, and trapezium. Most patients have a hyperextension injury, or repetitive stress of the wrist. Isolated acute lunate fractures are frequently unrecognized on radiographs because of lack of displacement and superimposed structures. CT and MRI provide more precise detail and accurate diagnosis. Fragmentation of the lunate occurs in Kienbock's disease (idiopathic avascular osteonecrosis of the lunate). This condition is sometimes confused with lunate fractures. Multiple causes predispose to Kienbock's disease: primary fracture, repetitive trauma, injury to the ligament carrying blood to the lunate, and presence of ulnar negative variance. In an early stage, the lunate may appear normal on radiographs. Later on, sclerosis, loss of lunate height, fragmentation, and eventually wrist collapse and arthritis ensue.

Carpal Dislocations

The mechanism responsible for most carpal dislocations is an axial compression-hyperextension injury usually from a fall onto the outstretched hand. Failure of the connecting structures bridging the proximal and distal rows of



Figure 4-19. Carpal dislocations and instabilities. **A** and **B,** Perilunate dislocation. Posteroanterior radiograph (**A**) of the wrist shows a wide scapholunate space, loss of congruity of the three carpal arcs, and triangular configuration of the lunate (L). Lateral radiograph (**B**) confirms dislocation of the carpal bones *(curved arrow)* with the lunate (L) remaining in normal position with respect to the distal radius. **C** and **D,** Lunate dislocation. Lateral view (**D**) demonstrates a dislocated lunate (L) with respect to the distal radius and other carpal bones, giving the appearance of a "spilled teacup" *(curved arrow)*. **E,** Scapholunate dissociation is shown as widening of the scapholunate space *(arrow)* to more than 5 mm ("Terry Thomas" sign).

the carpus results in dorsal displacement of the distal row (perilunate dislocation). If the force is more severe, a complete lunate dislocation may occur. These injuries are easily diagnosed on lateral radiographs. Perilunate dislocation (Fig. 4-19A and B) is the most common type of wrist dislocation. There is a dorsal dislocation of the carpal bones (scaphoid, triquetrum, and other carpal bones) about the lunate, while the lunate itself remains in normal position with respect to the distal radius. Loss of congruity of the three carpal arcs and an abnormal triangular configuration of the lunate with the apex pointing distally are signs on frontal radiographs. On the lateral projection, there is a normal relationship of the lunate and distal radius, but all other carpal bones are located posterior to the lunate. When it occurs in association with a scaphoid waist fracture, it is called a transscaphoid perilunate dislocation.

In lunate dislocation (Fig. 4-19C and D), the lunate is dislocated volarly with respect to the distal radius, and all other carpal bones lie dorsal to the lunate. This produces a radiographic "spilled teacup" sign on the lateral radiograph.

The capitate migrates proximally and sits in the lunate fossa. On the frontal projection, the congruity of the three carpal arcs is lost, and there is superimposition of the base of the capitate and lunate. Lunate dislocations commonly occur in association with scaphoid fractures.

Carpal Instabilities

The radiographic signs of carpal instabilities include disruption of one or all of the three carpal arcs (arcs of Gilula), alteration of the symmetrical intercarpal joint spaces, and changes in contour of an individual carpal bone.

Scapholunate dissociation, or rotatory subluxation of the scaphoid (Fig. 4-19E), is a spectrum of injuries caused by interruption of the scapholunate ligament and extrinsic ligaments that stabilize this articulation, resulting in abnormal motion between the scaphoid and lunate. It is the most common pattern of carpal instability. Due to the normal compressive forces across the wrist, which tend to force the scaphoid into further palmar flexion, disruption of the scapholunate ligament seen in scapholunate dissociation will allow an abnormal degree of palmar flexion of the scaphoid. Thus, the key finding on the lateral radiograph is an increased scapholunate angle of more than 60 degrees. On frontal radiographs, there is a widening of the scapholunate space of more than 3 mm measured at or distal to the midpoint of the joint space (5 mm is considered to be pathognomonic); this is called the "Terry Thomas" sign. If in doubt, comparison between the scapholunate space and lunotriquetral space should reveal a significant widening of the former in the case of scapholunate dissociation. The "cortical ring" sign is another radiographic finding of this condition, describing the cortex of the distal pole of the palmar-flexed scaphoid seen end-on on the frontal radiograph. This type of injury can be isolated or associated with distal radial fractures. Without treatment, it may lead to scapholunate advanced collapse.

Dorsal intercalated segmental instability (DISI, or dorsiflexion instability) is usually associated with scapholunate dissociation. It is a derangement of the radial side of the wrist and is often associated with radial-sided symptoms. On a lateral radiograph, the lunate tilts dorsally, resulting in an increased capitolunate angle of greater than 20 or 30 degrees. Lateral fluoroscopy of the wrist in flexion is more definitive, as the static radiographic configuration of DISI can occasionally be seen as a normal variant. DISI is most frequently observed with displaced scaphoid fractures and scapholunate dissociation.

Volar intercalated segmental instability (VISI, or volar flexion instability) is much less common than DISI, although it is the most common pattern of carpal instability seen in patients with rheumatoid arthritis. It is a result of ulnar-sided ligament derangement. The lunate tilts volarly and the capitolunate angle is greater than 20 or 30 degrees.

Fractures and Dislocations of the Hand (Box 4-12)

First Metacarpal (Thumb) Fractures and Dislocations

Fractures of the base of the first metacarpal account for 80% of thumb fractures. They usually result from an axial load to the partially flexed first metacarpal. Four types include epibasal (extra-articular) (Fig. 4-20A), Bennett, Rolando, and comminuted fractures. Bennett fractures (Fig. 4-20B) are intra-articular oblique fractures through the proximal articular surface of the first metacarpal, usually in two separate fragments. Due to traction by the abductor pollicis tendon, which inserts on the dorsal surface of this metacarpal, the large distal fragment together with the rest of the thumb is retracted proximally. Rolando fractures (Fig. 4-20C) are intra-articular comminuted fractures consisting of three major fragments. In Rolando and comminuted fractures (Fig. 4-20D), instead of being retracted, the large distal fragment is impacted into the two smaller fragments.

Gamekeeper's or skier's thumb (Fig. 4-21) signifies the injury to the ulnar collateral ligament of the first metacarpophalangeal joint owing to forceful abduction of the first proximal phalanx. The spectrum of injuries ranges from a pure ligamentous injury to an avulsion of the ulnar aspect of the distal attachment site of the ligament or a transverse fracture of the base of the proximal phalanx.

Dislocations of the Carpometacarpal Joints

A very complex network of dense carpometacarpal and intermetacarpal ligaments holds the carpometacarpal (CMC) joints together. Therefore, it requires a major force to cause injuries to this region. Dislocation at the first CMC joint usually occurs with high-energy trauma, with concomitant neurovascular injuries. Pure thumb CMC dislocation is mostly dorsal and results from axial loading on a partially flexed thumb. Of the other CMC joints, fractures and

***Box 4-12.* Fractures and Dislocations of the Hand**

STANDARD VIEWS
Hand—PA, lateral, internal oblique
Thumb—AP, lateral, oblique
Fingers—PA, lateral, oblique

FREQUENT SITES OF INJURIES
Phalanges
Base of the thumb metacarpal

FREQUENTLY MISSED INJURIES
Fourth and fifth carpometacarpal dislocations
Volar plate fractures
Mallet fingers
Bennett fractures

RELEVANT NORMAL ANATOMY
Volar plate—dense fibrous band forms the volar aspect of the thumb's metacarpophalangeal and fingers' proximal interphalangeal joints
Sesamoid—two constant sesamoids are at the first MCP

FRACTURE MIMICS
Nutrient artery canals: oblique lucent line located near middle third of shafts of the phalanges and metacarpal bones—should not be mistaken for fractures



Figure 4-20. Fractures of the base of the first metacarpal. Four types of fractures *(arrows)* are shown. **A,** Epibasal extra-articular type. **B,** Bennett, or intra-articular oblique fracture, with two separate fragments. **C,** Rolando fracture, a comminuted fracture with three separate fragments. **D,** Comminuted fracture.



FIGURE 4-21. Gamekeeper's or skier's thumb. Avulsion fracture *(curved arrow)* of the ulnar aspect of the base of the proximal phalanx of the thumb.

dislocations frequently occur at the fourth and fifth CMC joints (Fig. 4-22) because of their greater flexibility and mobility.

Metacarpal Fractures

Fractures of the metacarpal bones are classified according to their location; base, shaft, neck, or head. They are commonly oblique or spiral, rather than transverse, in configuration, and are usually obvious. The exception is a nondisplaced fracture at the base of the lateral metacarpal bones, which is frequently occult because of the bony configuration, superimposition in this region, and minimal displacement of fragments. Boxer's fracture (Fig. 4-23) is a metacarpal neck fracture with volar angulation of the distal fragment as a result of a direct impact on the metacarpal head with a clenched fist. It is most commonly seen in the fifth metacarpal. The description of boxer's fracture is somewhat misleading since professional fighters are more likely to sustain a second or third metacarpal neck fracture. Fractures of the base of the metacarpals are divided into four types: epibasal, two-part (reverse Bennett), three-part, and comminuted. In the reverse Bennett type, the flexor and extensor carpi ulnaris muscles usually retract the larger distal fragment proximally.

Dislocations of the Metacarpophalangeal Joints

The most common type of metacarpophalangeal (MCP) joint dislocation is dorsal dislocation. Volar dislocation is rare, but potentially unstable. When a fracture is clinically

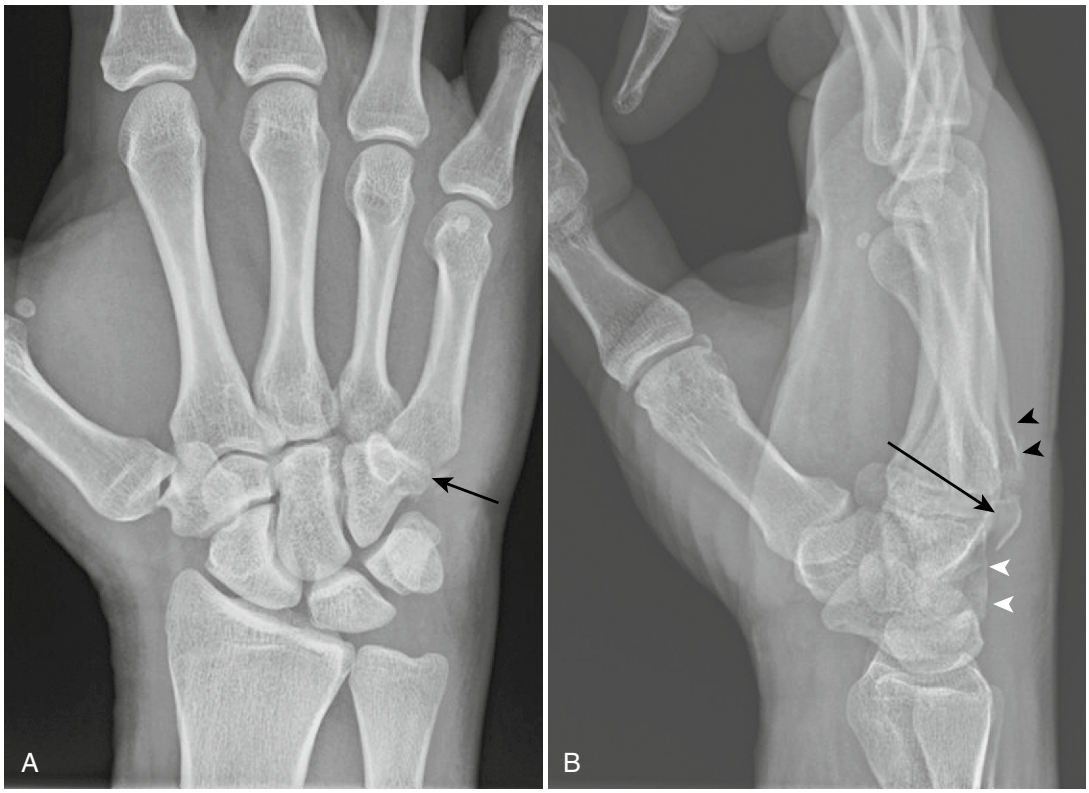


FIGURE 4-22. Carpometacarpal dislocation. **A,** Posteroanterior radiograph of the hand demonstrates a subtle overlap *(arrow)* of the proximal end of the fifth metacarpal and the hamate. **B,** Lateral radiograph reveals dorsal dislocation of the fifth metacarpal *(black arrowheads)* with respect to the carpal bones *(white arrowheads)*. A fracture of the body of the hamate is also visualized *(arrow)*.



Figure 4-23. Boxer's fracture. A posteroanterior radiograph of the hand demonstrates a metacarpal neck fracture *(arrow)* with volar angulation of the distal fragment.



Figure 4-24. Transverse fracture of the distal phalanx. This fracture is commonly associated with nail bed injuries.

irreducible, it is called a complex dislocation that is most often due to volar plate interposition. A radiographic sign of complex dislocation is the appearance of a small piece of bone in the joint space representing an interposed volar plate.

Phalangeal Fractures

Phalangeal fractures are more common than metacarpal bone fractures. They may be classified as either extra-articular (involving the shaft) or intra-articular (involving the proximal or distal margins). The distal phalanx is most commonly involved, accounting for more than half of hand fractures. They vary from a comminuted, longitudinal split to a transverse fracture, and frequently are associated with lacerations of the nail bed. Fractures of the proximal phalanx (P1), middle phalanx (P2), and distal phalanx (P3) (Fig. 4-24) are described according to their location (head, neck, shaft, and base) and appearance. Baseball or mallet finger (Fig. 4-25A) is a flexion deformity at the distal interphalangeal (DIP) joint due to an avulsion of the extensor tendon at its insertion on the dorsal lip at the base of the distal phalanx. The injury occurs when an extended DIP joint is forcibly flexed, as occurs when the finger is jammed by a baseball striking the tip of the finger. A small piece of bone may or may not be avulsed along with the tendon. Radiographs may reveal no fracture but only flexion deformity of the DIP joint.

Jersey finger is an avulsion of the flexor digitorum profundus tendon from its insertion at the volar base of the distal phalanx. It is caused by forced extension while in flexion of the DIP joint, such as when grabbing a jersey of a football player. It is similar to the volar plate injury.



Figure 4-25. Fractures and dislocations involving the interphalangeal joint. **A,** Mallet finger. Lateral radiograph of the finger shows an avulsion fracture *(arrow)* at the dorsal lip of the base of the distal phalanx, resulting in flexion deformity of the distal interphalangeal joint. **B,** Volar plate fracture. Lateral radiograph of the finger demonstrates an avulsion fracture of the volar lip of the base of the middle phalanx.

Volar plate injury (Fig. 4-25B) is an avulsion injury at the insertion of the volar plate on the volar surface of the base of the middle phalanx at the proximal interphalangeal (PIP) joint. It is a hyperextension injury that can occur with or without bony avulsion. In the latter, a small avulsed bone fragment is usually nondisplaced. The fragment is often a thin sliver of bone, minute and easily overlooked. It is best visualized on lateral or oblique projections of the involved finger.

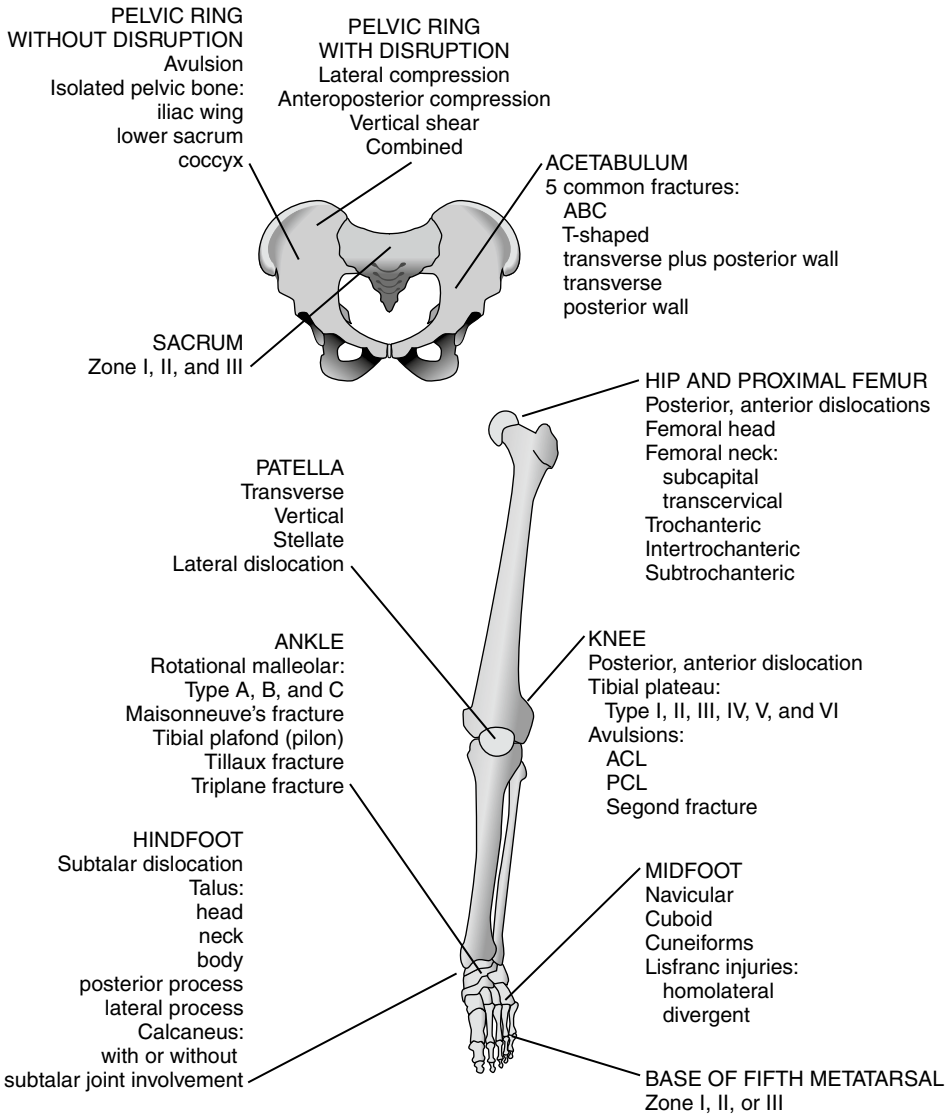
Boutonniere deformity is a flexion deformity of the PIP joint with hyperextension of the DIP joint. It is caused by a tear or avulsion of the middle slip of the extensor mechanism that allows the PIP joint to flex while the DIP is extended. The site of avulsion is on the dorsal surface of the base of the middle phalanx. At the time of the initial injury, the patient may complain only of pain and swelling about the PIP joint. The characteristic deformity develops subsequently.

Dislocations of the Interphalangeal Joints

Dislocations of the interphalangeal joints are a result of hyperextension injury. Most of these are dorsal dislocations in which the affected phalanx is displaced dorsally. They are associated with a volar plate rupture that manifests as an avulsion with or without a small flake of bone from the volar margin of the base of the phalanx. Irreducible dorsal dislocations are most often due to a trapped volar plate, trapped flexor digitorum profundus tendon, or a buttonholed middle phalanx through the volar plate or a rent in the flexor digitorum profundus tendon. On rare occasions, an irreducible dislocation is caused by interposition of a sesamoid bone within the joint.

LOWER EXTREMITY

The diagram below shows sites of common fractures of the lower extremity.



Common fractures of the lower extremity.

Box 4-13. **Fractures of the Pelvic Ring**

STANDARD VIEWS
AP and inlet views of the pelvis

RELEVANT NORMAL ANATOMY
Sacral arcuate line—arcs of superior surface of sacral foramina are those tangent to the x-ray beam; normally sharply defined, smooth, and bilaterally symmetrical

Fractures of the Pelvic Ring (Box 4-13)

The pelvic ring is a round or oval plane that includes the sacral promontory, inferior margin of the sacroiliac joints, iliopectineal line to superior margin of superior pubic rami, and pubic symphysis. The pelvic ring is divided into anterior and posterior portions by an imaginary line connecting the ischial spines. Fractures of the bony pelvis are divided into two main types based on the presence or absence of pelvic ring disruption.

Isolated Injuries Without Disruption of the Pelvic Ring

Avulsion injuries (Fig. 4-26) are secondary to sudden muscular contractions or abrupt changes of speed or direction, as seen during athletic activities. They are frequent in adolescents before closure of the apophyses because the muscles and tendons are stronger than the apophyseal attachments. Typical locations are at the anterior superior iliac spine (Sartorius), anterior inferior iliac spine (rectus femoris), ischial tuberosity (biceps femoris), and inferior margin of the pubic body (adductor group). The fractures are displaced due to the mechanical pull by the muscles and are usually obvious on radiographs at the initial injury. The contour of the displaced fragment mirrors the adjacent (donor) portion of the pelvis. These injuries, if not detected at the initial presentation, may heal with exuberant callus and radiographically mimic bone tumors.

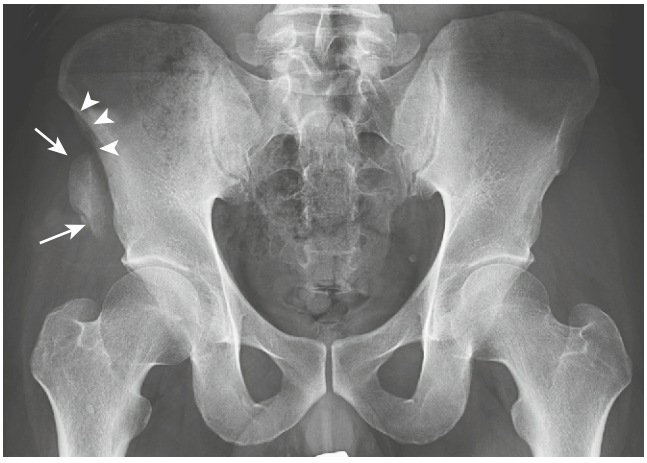


Figure 4-26. Pelvic fracture without pelvic ring disruption. Anteroposterior radiograph of the pelvis demonstrates an avulsed right anterior superior iliac spine *(arrows)* due to a sudden muscular contraction of the sartorius. *Arrowheads* indicate the donor site.

Isolated fractures of the pelvic bones that do not disrupt the pelvic ring include fractures of the iliac wing (Duverney fracture) and transverse fractures of the lower sacral and coccygeal segments. Sacrococcygeal dislocations and coccygeal fractures are in this category.

Pelvic Ring Disruption

The most common mechanism causing a fracture with pelvic ring disruption is a motor vehicle accident. Depending on the Injury Severity Score and age of the patient, it is associated with a high mortality rate of 5% to 50%. Interruption of the pelvic ring at two or more sites on opposite sides, either by fractures or diastasis, indicates a potentially unstable injury. The rule of thumb is that a disruption at one site of the pelvic ring must accompany another on the contralateral side of the ring. Therefore, when one encounters a pelvic ring disruption, a fracture or separation of the contralateral side of the ring must be carefully searched for. The exceptions to this rule are pediatric patients before fusion of the triradiate cartilage and stress or insufficiency fractures. It should be noted that acetabular fractures do not constitute any component of pelvic ring disruption. Classification schemes are helpful in defining the injuries, allowing optimal communication, and assisting in treatment planning. However, their ability to predict associated injuries, morbidity, or mortality has not been rigorously tested.

The most widely accepted classification of pelvic ring disruption is the Young-Burgess system. This system divides pelvic ring disruptions into four types according to the direction of forces to the pelvis: lateral compression (LC), anteroposterior compression (APC), vertical shear (VS), and combined mechanism (CM). In the LC category (Fig. 4-27A) are the transverse fractures of the pubic rami with ipsilateral or contralateral posterior ring injuries. In the APC category (Fig. 4-27B and C), there is a symphyseal diastasis or longitudinal fracture of the pubic rami and a disruption of the sacroiliac joint. In the VS category (Fig. 4-27D), there is vertical displacement anteriorly through a symphyseal diastasis and posteriorly through the sacroiliac joints, or, occasionally, the iliac wing or sacrum. The most common pattern of combined mechanism is a combined LC/VS injury.

Common terms previously used to describe pelvic ring disruption include *Malgaigne injury*, *bucket-handle injury*, and *open book injury*. Malgaigne injury is a vertical shear injury that results in disruption of the ipsilateral anterior and posterior arches. There is superior displacement of the involved hemipelvis with respect to the opposite side, resulting in clinically visible shortening of that extremity. Bucket-handle injury is a disruption of the contralateral anterior and posterior arches. Open book injury describes an anteroposterior compression mechanism that results in a pubic diastasis along with lateral rotation of the hemipelvis due to posterior arch disruption (classically, sacroiliac diastasis).

Determination of the stability of pelvic fractures relies mainly on clinical grounds. In general, a single break in the pelvic ring is a stable injury (e.g., single pubic ramus, unilateral pubic rami, Duverney fracture, transverse sacral fracture), and two or more breaks in the pelvic ring are considered unstable. It should be noted that the initial radiographic exams might not demonstrate instability when the pelvis is indeed unstable.

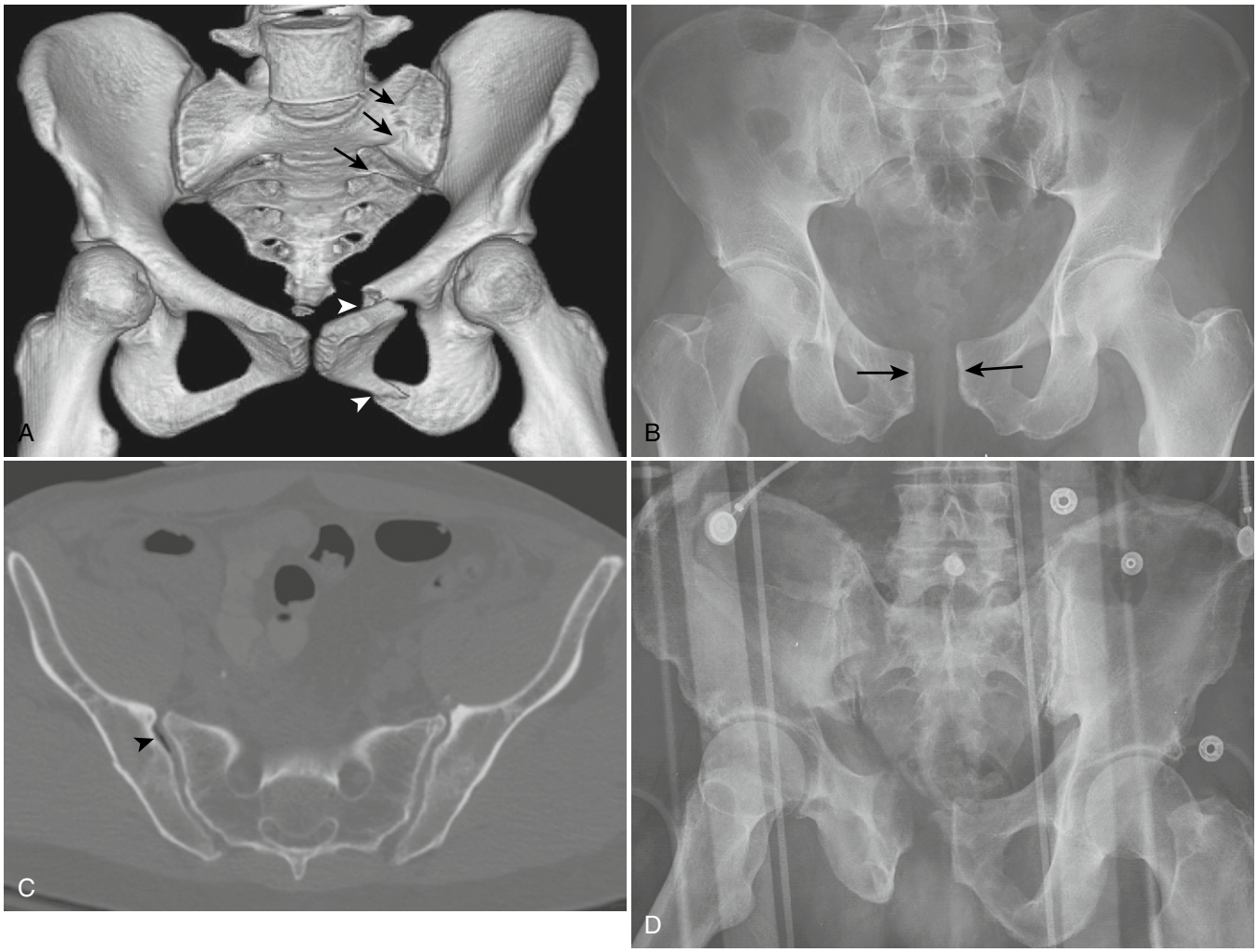


FIGURE 4-27. Pelvic fractures with pelvic ring disruption. **A,** A volumetric (3D) CT reformation demonstrates a lateral compression (LC) type of pelvic ring disruption. Vertical fractures of the left superior and inferior pubic rami (anterior ring disruption, *white arrowheads*) with overlap of medial and lateral fragments are shown. There is a vertical fracture of the left ala of the sacrum through its neural foramina *(black arrows).* **B** and **C,** Anteroposterior compression. Anteroposterior radiograph of the pelvis (**B**) and axial CT image (**C**) at the level of the mid-sacrum demonstrate diastasis of the symphysis pubis (anterior ring disruption, *arrows*). The radiograph fails to provide information about a posterior ring abnormality. Axial CT image reveals mild widening of the right sacroiliac joint, indicating an injury to the posterior ring. **D,** Vertical shear. Anteroposterior radiograph of the pelvis demonstrates diastasis of the pubic symphysis (anterior ring disruption) and vertical fracture of the right iliac wing involving the pelvic inlet (posterior ring disruption). There is vertical displacement, with foreshortening, of the whole right lower extremity, indicating a vertical shear injury.

Sacral Fractures

The majority of sacral fractures are associated with pelvic or lumbar spine fractures. They are frequently oriented in the vertical plane (only 5% to 10% are transverse). The Denis classification divides the sacrum into three zones and describes the risk of neurological deficits associated with fractures in each zone. Zone I (Fig. 4-28A) is located lateral to the sacral foramina, and fractures rarely cause neurological deficit. Zone II fractures (Fig. 4-28B) occur through the sacral foramina (transforaminal); there is an approximately 28% chance of neurological deficit. Zone III fractures involve the central canal and carry a 57% risk of neurological deficit.

Associated Pelvic Injuries

Pelvic hemorrhage is the primary concern in patients with pelvic ring disruption. To reduce the risk of bleeding, patient manipulation and movement should be restricted until conditions are stabilized. Therefore, the initial radiographic exams are restricted to the AP view of the pelvis (and/or outlet view, CT scan). Urinary tract injury is more common with specific types of pelvic fractures, such as symphyseal diastasis and pubic rami fractures. Clinically, gross hematuria is the most obvious sign of urinary tract injury associated with pelvic fractures. The presence of microscopic hematuria is rarely associated with a urinary tract injury requiring surgical intervention. If indicated, complete evaluation of the urinary tract requires CT, cystography (conventional or CT), and urethrography. Direct injury to the gastrointestinal tract is usually caused by fracture fragments lacerating the anus or rectum. The injury often extends to the perineum. For a more complete discussion of associated injuries in pelvic fractures please refer to Chapters 3, 7, and 11.

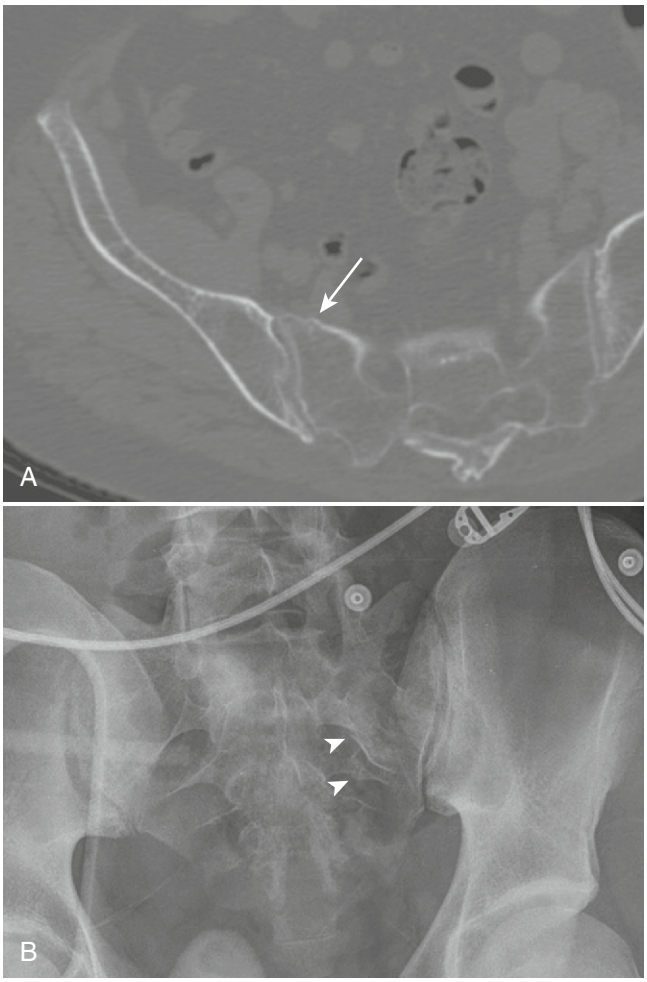


FIGURE 4-28. Sacral fractures. **A,** Zone I injury. Axial CT image at the level of the mid-sacrum demonstrates a subtle irregularity of the anterior cortex of the right sacral wing, indicating a nondisplaced fracture *(white arrow)*. The fracture is located lateral to the sacral neural foramina. **B,** Zone II injury. Anteroposterior radiograph of the pelvis shows abnormal disrupted concavities of multiple left sacral neural foramina, indicating a vertical fracture *(arrowheads)*.

Box 4-14. **Fractures of the Acetabulum**

STANDARD VIEWS
AP view of the pelvis
AP and Judet views of the hip

FREQUENT SITES OF INJURIES
Associated both column (ABC)
T-shaped
Transverse plus posterior wall
Transverse
Posterior wall

RELEVANT NORMAL ANATOMY
Acetabulum—located in the concavity of an arch formed by two columns of bone: anterior and posterior columns in an inverted V-shaped configuration
Iliopectineal line—from sciatic notch to pubic tubercle; break indicates anterior column fracture
Ilioischial line—from sciatic notch, quadrilateral plate, to internal cortex of ischium; break indicates posterior column fracture
Anterior lip—break indicates anterior column or wall fracture
Posterior lip—break indicates posterior column or wall fracture; on AP projection, it is slightly lateral to the anterior lip
Roof—break indicates superior articular surface fracture
Radiographic teardrop—composite U-shaped shadow at anteroinferior portion of the acetabular fossa

FRACTURE MIMICS
Os acetabuli—secondary ossification center on the superior aspect of the posterior acetabular lip (mimics posterior wall fracture)

MAKING THE DISTINCTION
Integrity of the obturator ring—break indicates two common possibilities: ABC and T-shaped fractures
Oblique fracture of the iliac bone—indicates ABC or anterior column fracture
Spur sign—pathognomonic for ABC fracture
Fracture plane on CT—column fracture is shown as a coronally oriented fracture

Fractures of the Acetabulum

Acetabular fractures (Box 4-14) are commonly associated with pelvic fractures. They are usually the result of motor vehicle accidents. Radiographic evaluation aims to answer the following questions: whether the fracture involves the columns, walls, or dome; whether there is any entrapped bone fragment in the joint; and if there is an associated femoral head fracture. CT better defines the degree of rotational displacement, presence of intra-articular fragments, articular impaction, and femoral head injury. The Judet-Letournel system classifies fractures of the acetabulum into 10 different types: 5 elementary and 5 associated types. The elementary type is a simple fracture that runs in one main direction, including fractures of the anterior column, posterior column (Fig. 4-29A and B), anterior wall, posterior wall, and a transverse fracture. Column fractures involve the acetabulum and its corresponding pubic ramus (anterior column fractures have superior pubic ramus involvement and posterior column fractures have inferior pubic ramus involvement). It should be noted that there is no anatomic boundary separating the anterior and posterior columns. Acetabular column fractures are named according to the portion of the acetabulum that is separated from the intact ilium. Wall fractures differ from column fractures in that they separate only a portion of the column's articular surface. Associated-type fractures are complex; the fracture line runs in more than one plane. Because of the complexity of the anatomy and the fracture classification, it is easier to define an acetabular fracture as one of three main types: wall fracture, column fracture, or transverse fracture. Over 90% of acetabular fractures fall into five common types: associated both column (ABC) fracture, T-shaped fracture, transverse fracture plus posterior wall, transverse fracture, and posterior wall fracture.

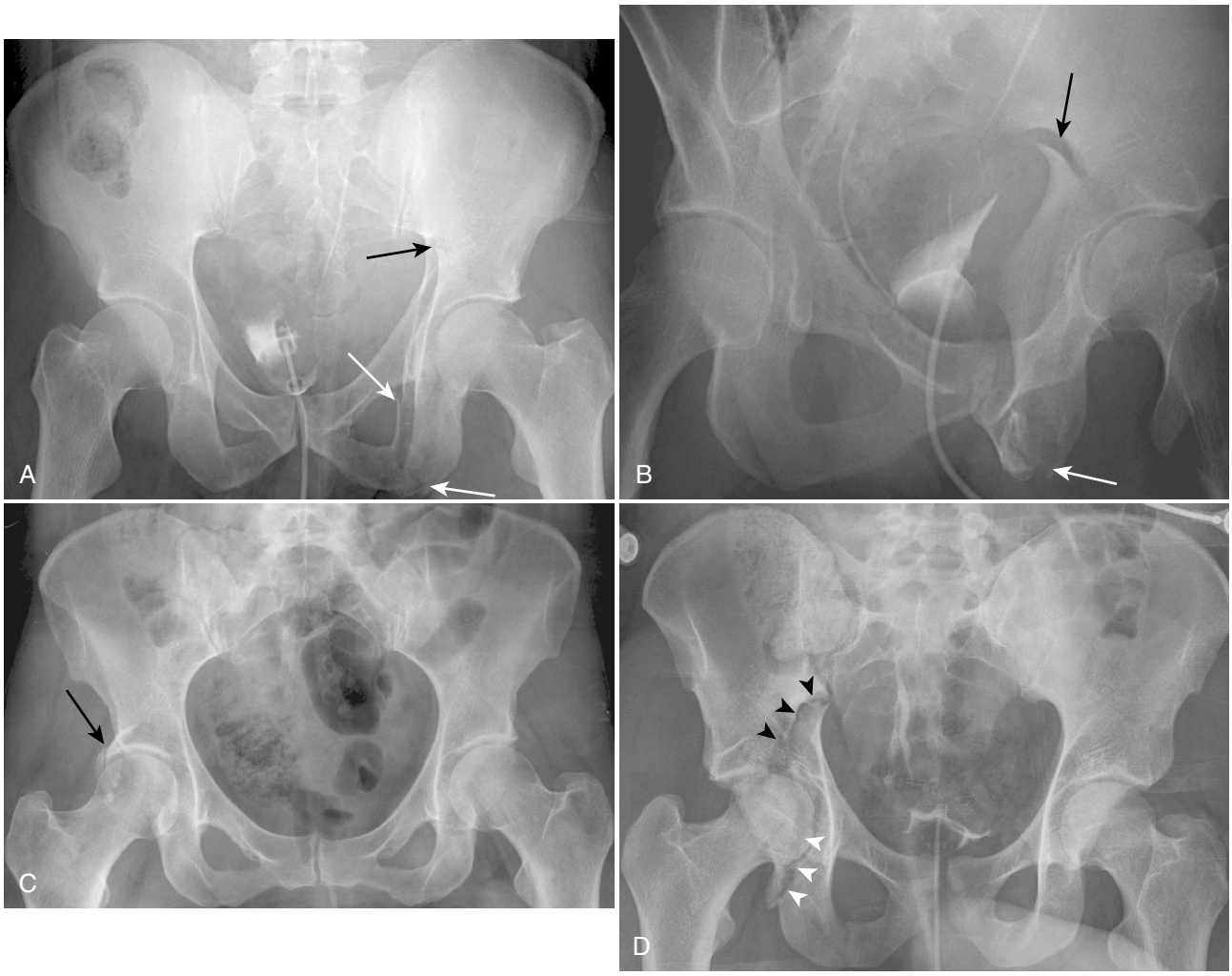


FIGURE 4-29. Acetabular fractures. **A** and **B,** Posterior column fracture. Anteroposterior radiograph of the pelvis shows a break in the obturator ring at the inferior pubic ramus *(white arrows)*. A fracture through the posterior border of the innominate bone *(black arrow)* is better visualized on the oblique view of the left hip. **C,** Posterior wall fracture *(arrow)* is visualized with no associated disruption of the iliopectineal or ilioischial lines or obturator ring. **D,** Transverse wall fracture. Anteroposterior radiograph of the pelvis demonstrates a transverse fracture of the innominate bone *(black arrowheads)* and a posterior wall fracture *(white arrowheads)*.

Posterior Wall Fractures

Posterior wall fractures (Fig. 4-29C) are the most common type of acetabular fractures, accounting for one third of them. There is disruption of a variable amount of the posterior wall of the acetabulum. The fracture may have one single fragment or multiple fragments, the latter being more common.

Transverse Fractures

The transverse fracture line (Fig. 4-29D) separates the innominate bone and acetabulum into two segments: a superior iliac segment and an ischiopubic segment containing both rami. It disrupts both the iliopectineal and ilioischial lines and crosses the acetabulum horizontally or obliquely. Its frequency ranges from 5% to 19% of all acetabular fractures.

Transverse Plus Posterior Wall Fractures

A combination of transverse and posterior wall fractures accounts for 20% of all acetabular fractures. In up to 96% of cases there are associated hip dislocations.

Associated Both Column Fractures

ABC fractures are the most common associated-type fractures of the acetabulum and the second most common (23%) overall. There is no portion of the articular surface of the acetabulum remaining in contact with the innominate bone, and there is a split between the anterior and posterior column components. The "spur" sign represents an external cortex of the most caudal portion of the intact ilium. It is visualized because the femoral head is displaced medially along with all portions of the acetabular surface. This sign is pathognomonic for an ABC fracture and is best demonstrated on the Judet's obturator oblique projection.

T-Shaped Fractures

These fractures represent 7% of all acetabular fractures. There is a transverse fracture with an associated vertical fracture line running across the quadrilateral plate and disrupting the obturator foramen.

Box 4-15. **Hip Dislocations and Fractures of the Proximal Femur**

STANDARD VIEWS
AP and inlet views of the pelvis
True lateral and AP views of the injured hip with foot inverted 15 degrees

FREQUENT SITE OF INJURY
Subcapital femoral neck

FREQUENTLY MISSED INJURY
Isolated greater trochanter fracture

RELEVANT NORMAL ANATOMY
Sweep of cortex extending from the neck to the head of the femur is smooth and symmetrical
Asymmetric femoral head with respect to the neck, even when seen in only one projection, is abnormal
Fovea centralis—an insertion site of ligamentum teres carries 10% of blood supply to the femoral head
Capsule of the hip joint attaches to the intertrochanteric line of the femur anteriorly, above the intertrochanteric crest posteriorly, and above the lesser trochanter medially

Hip Dislocations and Fractures of the Proximal Femur (Box 4-15)

Hip Dislocations

Posterior dislocation of the hip (Fig. 4-30) is the result of an abrupt deceleration injury such as occurs in motor vehicle accidents when the knee strikes the dashboard. It is commonly associated with fractures of the posterior rim or wall of the acetabulum. In adolescents, this injury may cause separation of the capital femoral epiphysis. On frontal radiographs, the femoral head is dislocated from the acetabulum and lies in a superolateral position. The involved femoral head appears smaller than the contralateral one because it is located closer to the radiographic plate (or film), and there is internal rotation of the femur. The injury is obvious on a true lateral projection. Osteonecrosis of the femoral head and secondary osteoarthritis of the hip joint are known complications.

Anterior dislocation of the hip accounts for 10% to 15% of all hip dislocations. It is caused by forced abduction and external rotation of the hip. The femoral head is displaced either anteromedially toward the superior pubic ramus or toward the obturator foramen. Usually, it is a simple dislocation without associated injury. An impacted fracture of the femoral head due to compression of the head on the dense acetabular rim (Hill-Sachs type of fracture) may occur. On frontal radiographs, there is medial displacement of the femoral head with respect to the acetabulum. A lateral view of the hip is diagnostic.

Central hip dislocation (protrusio) is nearly always associated with acetabular fractures. The femoral head protrudes into the pelvic cavity through the fractures of the acetabulum.

Fractures of the Proximal Femur

Fractures of the proximal femur are classified on the basis of their anatomic location into femoral head, neck, trochanteric, intertrochanteric, and subtrochanteric. These fractures can also be categorized by their relationship to the joint capsule into two groups: intracapsular or extracapsular. Fractures of the femoral head and neck (subcapital and transcervical types) are considered intracapsular. Trochanteric, intertrochanteric, and subtrochanteric fractures are extracapsular. Basicervical femoral neck fractures are generally acknowledged as extracapsular fractures. The distinction between the two is important for determination of treatment and prediction of outcome. Intracapsular fractures have a significantly increased incidence of avascular necrosis. Extracapsular fractures usually heal well but are more prone to be unstable. In elderly patients, proximal femoral fractures can be very subtle and may occur in the setting of minor trauma owing to underlying osteoporosis. MRI should be strongly considered for evaluation of the

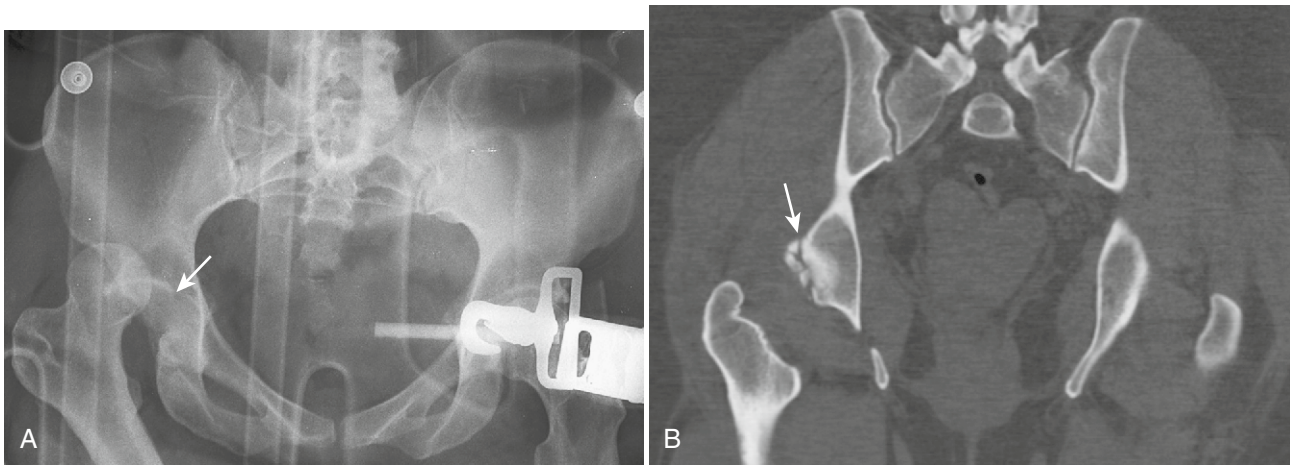


Figure 4-30. Dislocations of the hip. **A,** Anteroposterior radiograph of the pelvis demonstrates a superolaterally dislocated right femoral head relative to the acetabulum *(arrow)*. This is a classic appearance of a posterior dislocation, in contrast to anterior dislocations in which the femoral head lies anteromedial to the acetabulum. **B,** Coronal reformatted CT image at the level of the posterior acetabulum reveals a comminuted fracture of the posterior wall *(arrow)*, an injury commonly associated with posterior hip dislocation.

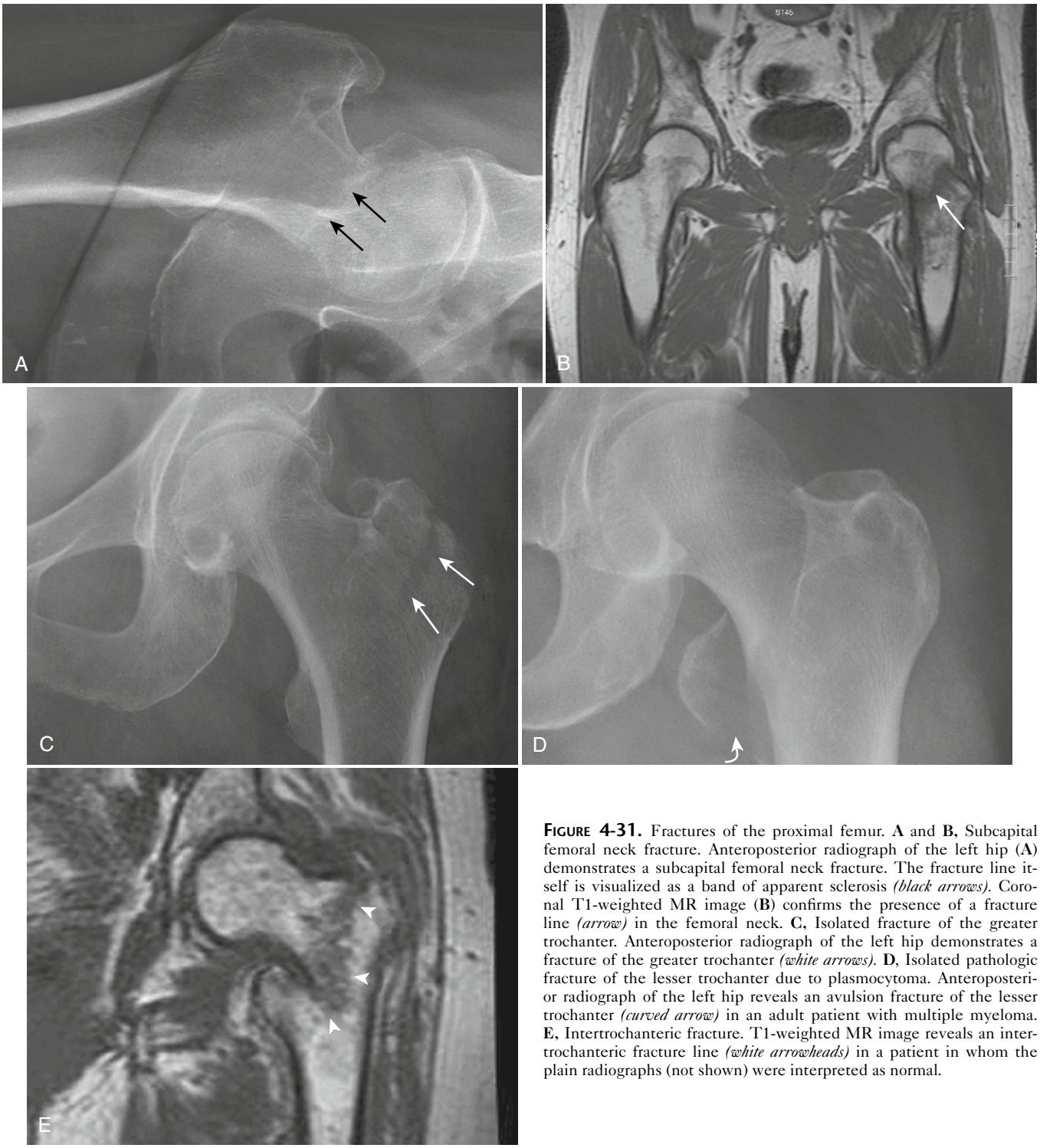


FIGURE 4-31. Fractures of the proximal femur. **A** and **B,** Subcapital femoral neck fracture. Anteroposterior radiograph of the left hip (**A**) demonstrates a subcapital femoral neck fracture. The fracture line itself is visualized as a band of apparent sclerosis *(black arrows).* Coronal T1-weighted MR image (**B**) confirms the presence of a fracture line *(arrow)* in the femoral neck. **C,** Isolated fracture of the greater trochanter. Anteroposterior radiograph of the left hip demonstrates a fracture of the greater trochanter *(white arrows).* **D**, Isolated pathologic fracture of the lesser trochanter due to plasmocytoma. Anteroposterior radiograph of the left hip reveals an avulsion fracture of the lesser trochanter *(curved arrow)* in an adult patient with multiple myeloma. **E,** Intertrochanteric fracture. T1-weighted MR image reveals an intertrochanteric fracture line *(white arrowheads)* in a patient in whom the plain radiographs (not shown) were interpreted as normal.

hip in this context, even after negative plain radiographs. Fractures of the femoral head occur with dislocations and appear as impaction or shear injury.

Fractures of the Femoral Neck

Femoral neck fractures are common in the elderly population, particularly women, due to the high prevalence of osteoporosis, which is strongly associated with this type of fracture. They are divided into subcapital, transcervical, and basicervical types. The more proximal and displaced, the higher is the incidence of avascular necrosis and nonunion.

Subcapital fracture (Fig. 4-31A and B) is the most common type and may be extremely subtle. There is a disruption and angulation at the junction of the superior cortex of the femoral neck with the femoral head. The

Garden classification categorizes subcapital fractures into four stages based on the position of the principal (medial) compressive trabeculae of the femoral head and neck and the acetabular trabeculae on frontal radiographs. Stage I fractures are incomplete fractures that spare the inferior femoral neck trabeculae. There is abduction of the superior portion of the femoral neck due to external rotation of the femoral shaft and valgus of the femoral head. The principal compressive trabeculae of the head and neck are aligned in a mild valgus position. Stage II fractures are complete fractures without displacement. The principal compressive trabeculae of the femoral head and neck are aligned in mild varus or near anatomic position. Stage I and stage II fractures are generally stable and have a good prognosis. However, when this fracture is subtle and impacted in near anatomic position, it may permit ambulation and be relatively painless. Stage III fractures are complete fractures with partial displacement. There is more severe varus alignment of the trabeculae of the femoral head and neck. In addition, the trabeculae of the femoral head are not aligned with the acetabular trabeculae. Stage IV fractures are complete fractures with full displacement. The femoral shaft is not only externally rotated but also telescoped, and the femoral head remains in anatomic alignment with the acetabulum; therefore the trabeculae of the femoral head and the acetabulum are parallel.

Transcervical and basicervical fractures are rare. Transcervical fractures are usually visible on frontal projections and have a varus deformity at the fracture site. Basicervical fractures are located at the base of the femoral neck, just proximal to the intertrochanteric crest. They have a higher incidence of avascular necrosis than the more distal intertrochanteric fractures.

Trochanteric Fractures

Isolated fractures of the greater trochanter (Fig. 4-31C) are common in osteoporotic women with a history of fall on their lateral side. The normal irregularity in this region makes it difficult to detect this type of fracture, especially when it is not displaced.

Isolated fractures of the lesser trochanter in children or adolescents are usually due to avulsion injuries of the apophysis from a forceful pull by the iliopsoas muscle tendon, which inserts on the lesser trochanter. In adults, an isolated lesser trochanter fracture (Fig. 4-31D) is unusual and should raise the suspicion of underlying pathology, especially metastatic disease.

Intertrochanteric Fractures

Intertrochanteric fractures (Fig. 4-31E) are the most common type of extracapsular fracture of the proximal femur. These fractures occur in an older population than do femoral neck fractures; men and women are equally affected. They are classified according to the number of separate fragments into two-, three-, or four-part, depending on the involvement of the lesser or greater trochanter. The main fracture line is usually an oblique line extending along the plane that joins the greater and lesser trochanters. Type 0 fractures are nondisplaced and most subtle. Type I fractures are two-part fractures. Type II fractures are three-part fractures consisting of a proximal fragment, a distal fragment, and either trochanter. Type III fractures are four-part fractures consisting of a proximal fragment, a distal fragment, and both trochanters. The status of the lesser trochanter is a very important component of intertrochanteric fractures because, if fractured, it typically includes a large fragment of cortex of the femoral neck. Comminution of the posteromedial cortex, subtrochanteric extension, or a reverse obliquity pattern (when the main fracture line runs perpendicular to the line joining the greater and lesser trochanters) makes the fracture unstable.

Subtrochanteric Fractures

The subtrochanteric region encompasses the area below the lesser trochanter to 5 cm distally in the shaft of the femur. Fractures in this region are distinguished from intertrochanteric fractures by the location of the fracture line in the proximal femoral shaft. They are frequently comminuted with marked displacement owing to the various muscle attachments.

Fractures of the Femoral Shaft

Femoral shaft fractures are the most common long bone fractures in patients with multiple injuries. A violent, severe, high-energy trauma is required to cause these fractures because the femur is the strongest and the heaviest bone in the body. Radiographic evaluation must include the regions of the hip and tibia to assess for potential associated injuries such as proximal femoral fractures, acetabular fractures, and tibial fractures.

Fractures and Dislocations Around the Knee (Box 4-16)

Hemarthrosis/Lipohemarthrosis

The appearance of knee hemarthrosis is similar to other types of joint effusion in that there is an oval-shaped density obliterating the lucent space anterior to the femoral cortex on the lateral radiograph (suprapatellar recess). If the effusion is large, it will cause anterior displacement of the quadriceps femoris muscle, suprapatellar tendon, and patella.

On the other hand, the presence of blood mixed with liquid fat in the knee joint, or lipohemarthrosis (Fig. 4-32), suggests the presence of an intra-articular fracture of the distal femur or proximal tibia. The fracture permits the flow of blood and liquid fat from the medullary cavity into the joint space. The sign is visualized in a horizontal-beam (cross-table) lateral radiograph taken with the patient in the supine position. The joint capsule is distended with a layering fat–blood interface that resembles an air–fluid level, called the "fat–blood interface" (FBI) sign. The presence of lipohemarthrosis is very useful as it aids in the identification of a minimally displaced intra-articular fracture. Pneumolipohemarthrosis and pneumohemarthrosis have a very similar radiologic characteristic, except that air has greater lucency than fat. It signifies an open, intra-articular fracture of the distal femur or proximal tibia.

Fractures of the Distal Femur

Fractures of the distal femur are caused by a severe axial load with varus, valgus, or rotational force. In younger individuals, these are usually a result of motor vehicle

Box 4-16. **Fractures and Dislocations Around the Knee**

STANDARD VIEWS

Knee—AP, lateral (20 degrees flexion of the knee), both oblique views
Patella—skyline view and full knee series
Femur—AP and lateral views

FREQUENT SITE OF INJURY

Tibial plateau

RELEVANT NORMAL ANATOMY

Medial femoral condyle is larger than lateral condyle—this helps when viewing the knee on lateral or axial patellar projections
Suprapatellar recess—recess between the suprapatellar tendon and the anterior cortex of the femur, normally relatively radiolucent
Anterior cruciate ligament distal attachment—medial spine of the intercondylar eminence of the tibia
Normal patellar length—approximately equal to the length of the patellar tendon (variation not to exceed 20%)
Normal location of patella—on frontal view, the inferior pole of the patella should lie within 2 cm of a plane formed by the distal femoral condyles; on lateral view with 90-degree flexion, the superior pole of the patella should lie inferior to the anterior surface of the femoral shaft

accidents. In elderly populations, a minor slip and fall on a flexed knee can result in these types of fractures. The supracondylar area of the femur is defined as the zone between the femoral condyles and the junction of the distal metaphysis and diaphysis of the femur. There are three types of supracondylar fractures, classified by the AO/OTA: extra-articular supracondylar, intra-articular unicondylar, and intra-articular bicondylar. Extension to the knee joint is frequently the result of a vertical intercondylar component. "Floating knee" (Fig. 4-33) is a term used when these fractures are associated with tibial shaft fractures, creating a free, large, segmental fragment that includes the knee joint. The incidence of arterial injury is low at 2% in supracondylar fractures.

Knee Dislocations

Knee dislocation is a rare injury. It is classified according to the relationship of the tibia with the femur into anterior, posterior, medial, lateral, and rotational dislocations. Anterior dislocation (Fig. 4-34A and B) is the most common type, resulting from severe hyperextension. The incidence of vascular injuries in knee dislocations varies from 7% to 64% in different series. Clinical evidence of vascular injuries should be sought in every knee dislocation. Knee dislocations are commonly associated with avulsion fractures of the tibial articular surface and with tears of the cruciate ligaments, joint capsule, and extracapsular ligaments. Injuries to these stabilizing structures are best evaluated with MR.

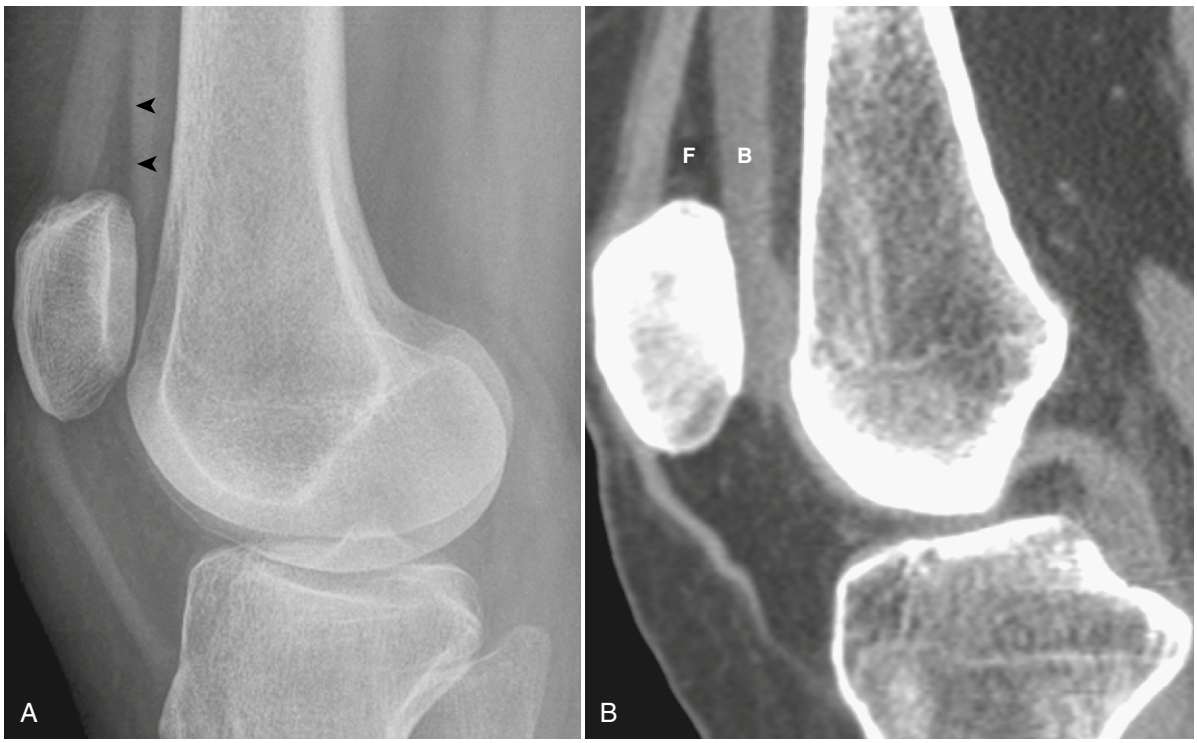


FIGURE 4-32. Lipohemarthrosis and pneumohemarthrosis. **A** and **B,** Lipohemarthrosis. Lateral cross-table radiograph of the knee shows a fat fluid level *(arrowheads)* in the suprapatellar bursa. Sagittal reformatted CT image of the same patient depicts the same finding. The fat blood interface (FBI) sign of lipohemarthrosis is shown.

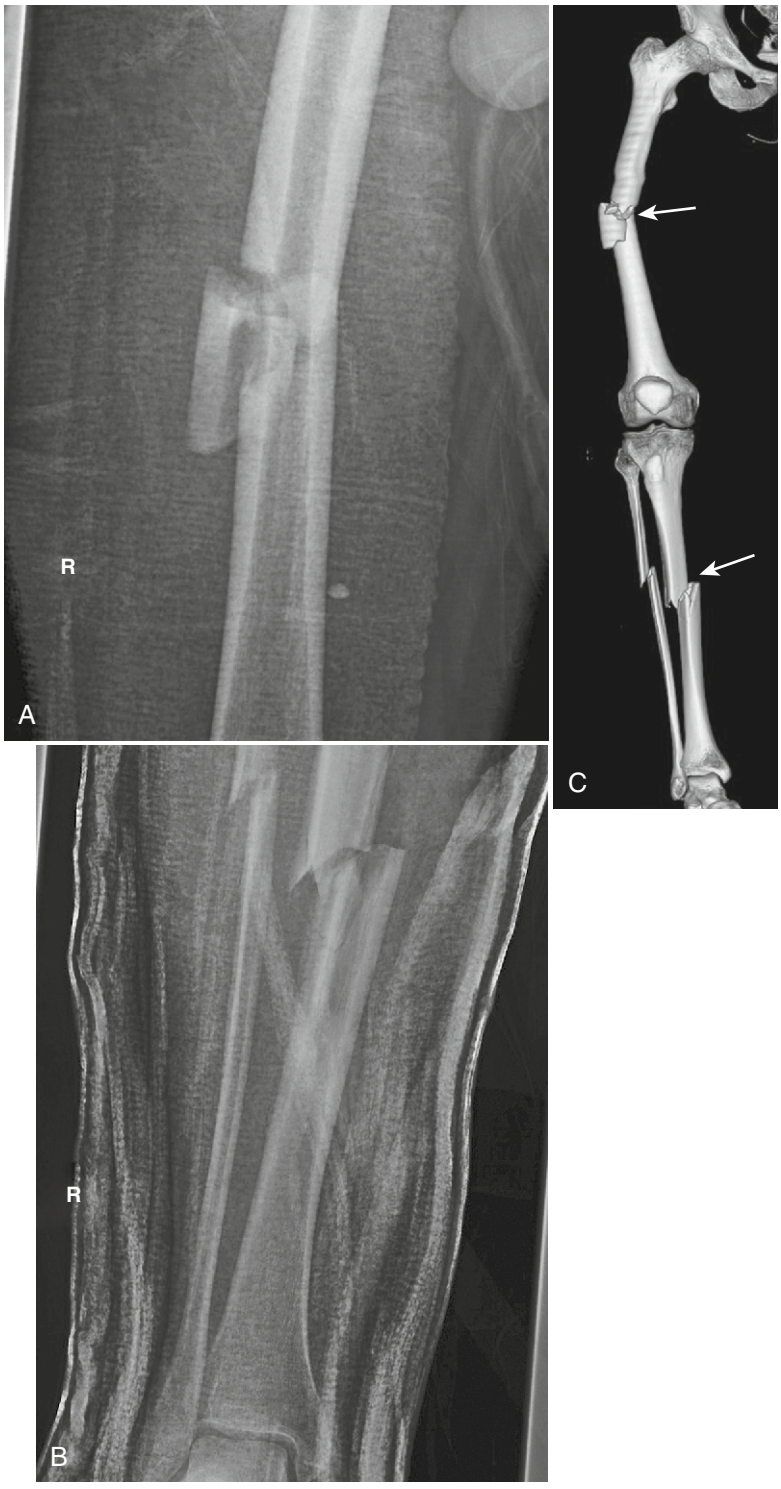


Figure 4-33. Floating knee. **A** and **B,** Frontal radiographs of the femur, tibia, and fibula of the right (R) leg reveal a segmental fracture of the midshaft of the femur, and midshaft fractures of both bones of the leg. This combination of fractures results in a free, large segmental fragment consisting of the knee joint. **C,** Volumetric (3D) CT reformation beautifully displays the long bone fracture sites *(white arrows)*.

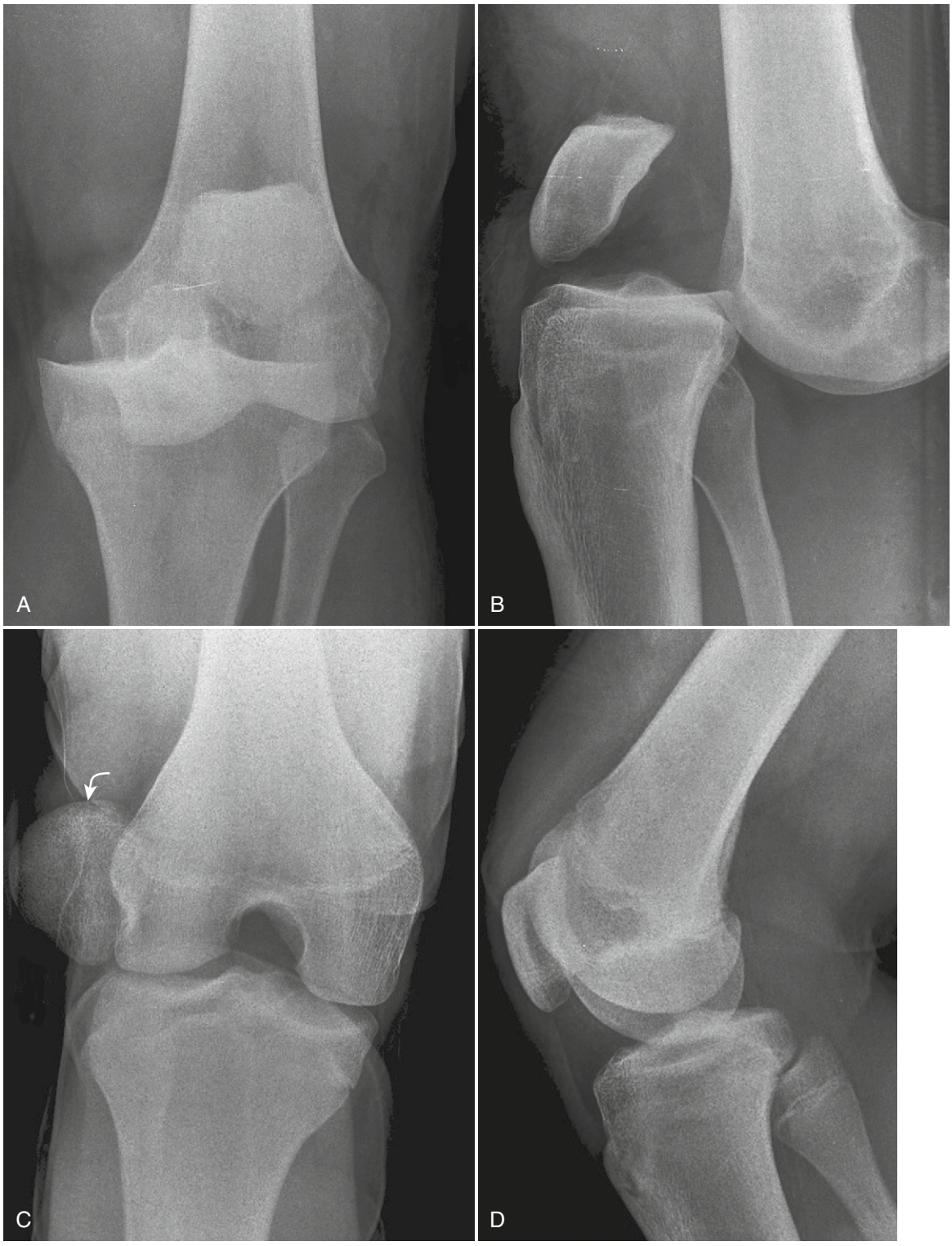


FIGURE 4-34. Dislocations around the knee. **A** and **B,** Frontal and lateral radiographs of the knee demonstrate an anteriorly dislocated tibia relative to the femur. This is a classic anterior knee dislocation with a complete bicruciate ligament tear subsequently confirmed with MRI (not shown). Anterior knee dislocation is frequently associated with traction injury of the popliteal artery. **C** and **D,** Lateral patellar dislocation is depicted on frontal *(curved arrow)* and lateral radiographs of the knee.

Patellar Dislocations

The patella is normally located in the sulcus of the anterior distal femur. Dislocations of the patella (Fig. 4-34C and D) are caused by excessive internal rotation of the femur on a fixed foot, and are usually relocated prior to clinical presentation. These dislocations are invariably lateral, with disruption of the medial retinaculum. The preferential lateral dislocation occurs because the lateral femoral condyle arc is shallower than the medial condyle. Patellar dislocations may be associated with chondral or osteochondral fractures, which typically arise from the lateral margin of the lateral femoral condyle or from the articular surface of the medial patellar facet. Presence of fragments in the joint space may impair joint motion and lead to locking or degenerative changes of the knee. The classic MR imaging findings of recent patellar dislocation include hemarthrosis, disruption of the medial patellar retinaculum, lateral patellar tilt, and bone contusions in the lateral femoral condyle and medial patellar facet.

Fractures of the Patella

The majority of fractures of the patella are caused by a direct blow from a fall or motor vehicle accident. Approximately 60% of patellar fractures involve the mid-body and are transverse (Fig. 4-35A and B), 25% are stellate or comminuted, and 15% are vertical (Fig. 4-35C). Displacement is present when there is separation of the fragments of more than 3 mm, or articular incongruity of 2 mm or greater. Displaced fractures may occur at the proximal or distal pole. The former may cause a low-lying patella due to the unopposed pull from the patellar tendon inferiorly (patella baja) (Fig. 4-35D). Alternatively, patella baja is seen in patients with quadriceps tendon tear. A high-riding patella (patella alta) (Fig. 4-35E and F) may be seen in distal pole fractures or in patients with patellar tendon tears.

Fractures of the Tibial Plateau

Fractures of the tibial plateau are severe injuries caused by high-speed motor vehicle accidents or falls from high altitudes. Axial loading, valgus stress, or both is the usual mechanism. The fractures may involve the medial plateau, the lateral plateau, or both, with extension into the metadiaphysis of the tibia. Fractures of the lateral plateau are the most common type because of the stronger cancellous trabeculae of the medial plateau. As a result, an isolated medial plateau fracture is the least frequent type. Schatzker's widely used classification system categorizes tibial plateau fractures into six types according to fracture appearance, location, and extension. Type I is a split fracture of the lateral plateau. The fracture line causes a wedge-shaped fracture fragment. Type II (Fig. 4-36A and B) is a split-depression fracture of the lateral plateau. In addition to a cleavage fracture of the lateral plateau, the articular surface is depressed into the metaphysis. Type III (Fig. 4-36C) is a pure depression fracture of the lateral plateau with an intact osseous rim. Type IV is a medial plateau fracture, subdivided into IVA (split) and IVB (depressed) subtypes. In type V, the fracture line has the configuration of an inverted "Y." The metaphysis and diaphysis remain intact. Type VI (Fig. 4-36D and E) is a tibial plateau fracture with dissociation between the tibial metaphysis and diaphysis.

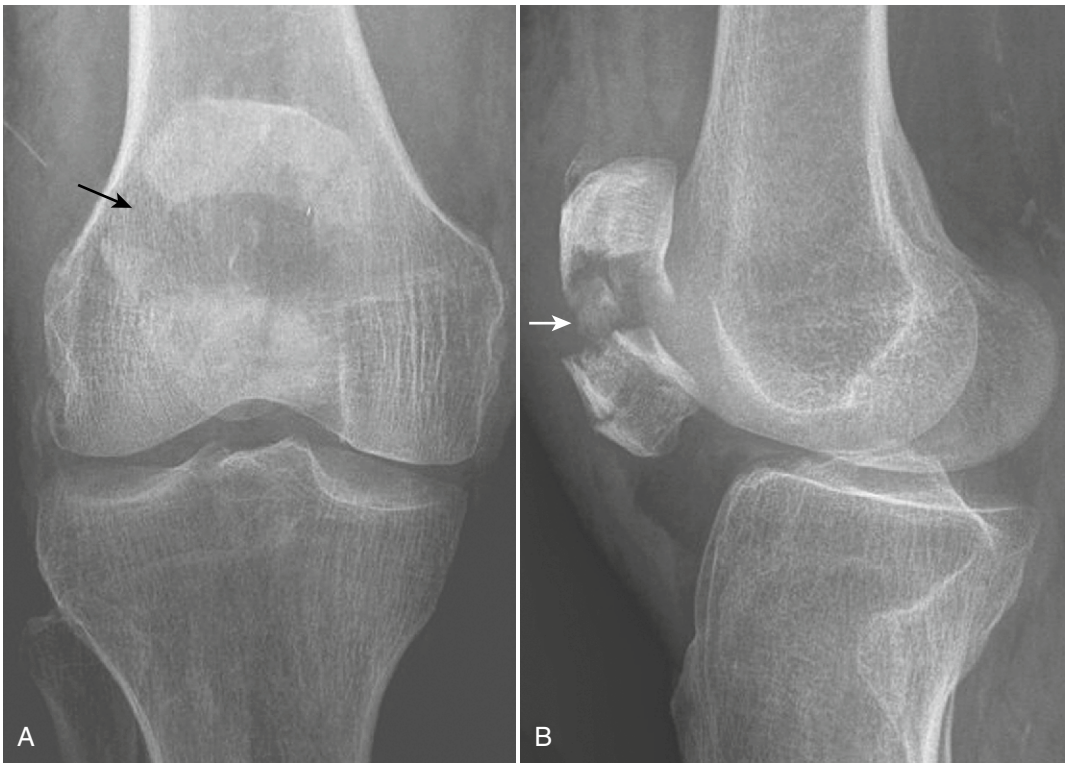


Figure 4-35. Fractures of the patella. **A** and **B,** Frontal and lateral radiographs of the knee demonstrate a comminuted fracture of the patella with the main transverse fracture line *(arrow)* traversing through its mid-body. There is separation of the proximal and distal fragments due to traction from the quadriceps superiorly and patellar tendon inferiorly.

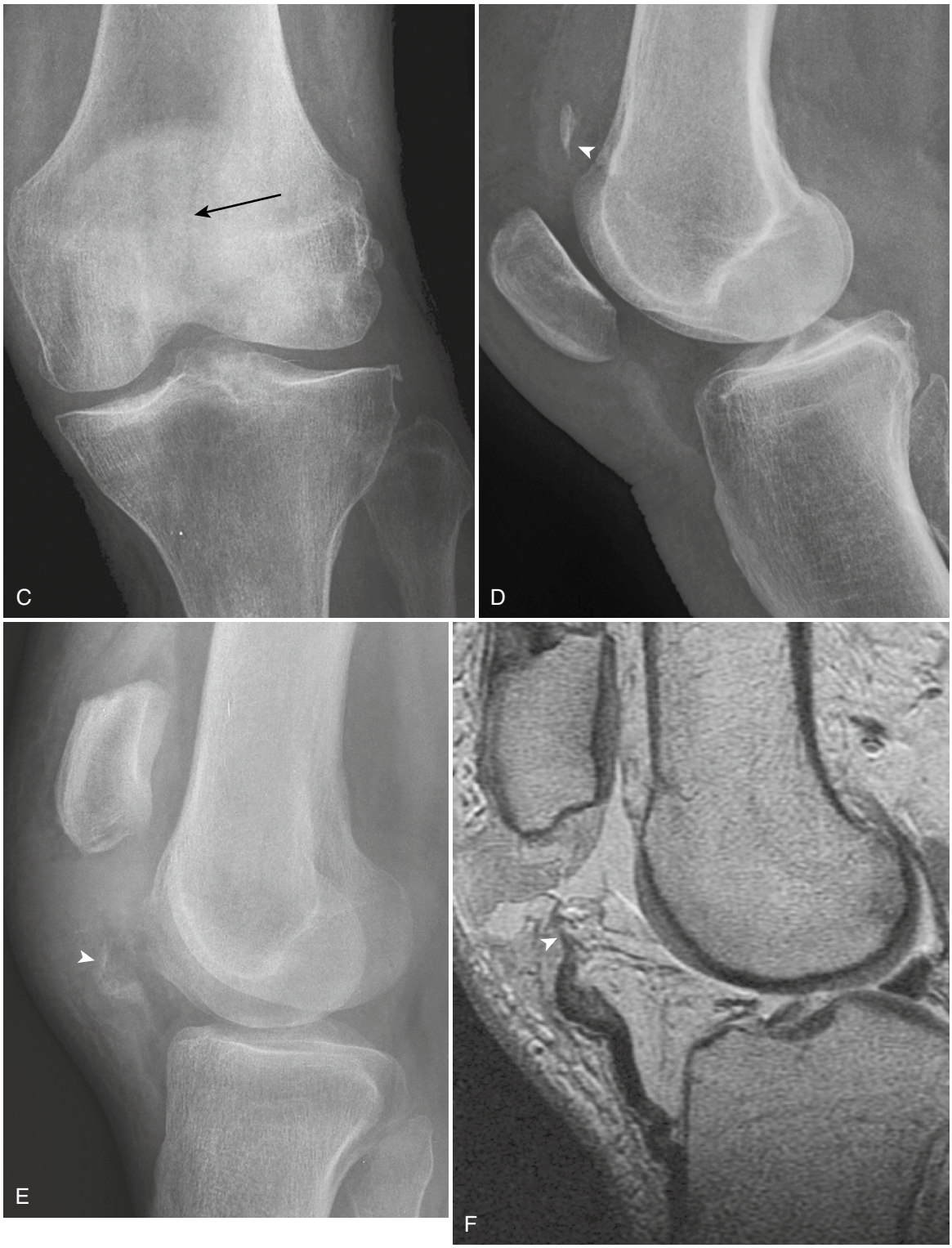


FIGURE 4-35.—CONT'D C, Vertical nondisplaced fracture *(arrow)* of the patella is barely seen on the frontal radiograph. This emphasizes the need for obtaining routine four views of the knee in patients with acute knee injury. **D,** Lateral radiograph of the knee shows an avulsion fracture of the proximal pole of the patella *(arrowhead)*, which causes low-lying patella due to unopposed pull from the patellar tendon (patella baja). **E** and **F**, High-riding patella (patella alta) is due to unopposed action of the quadriceps in this patient with distal pole fracture of the patella *(arrowhead)*. Sagittal MR image **(F)** confirms a complete disruption with retraction of the patellar tendon *(arrowhead)*.

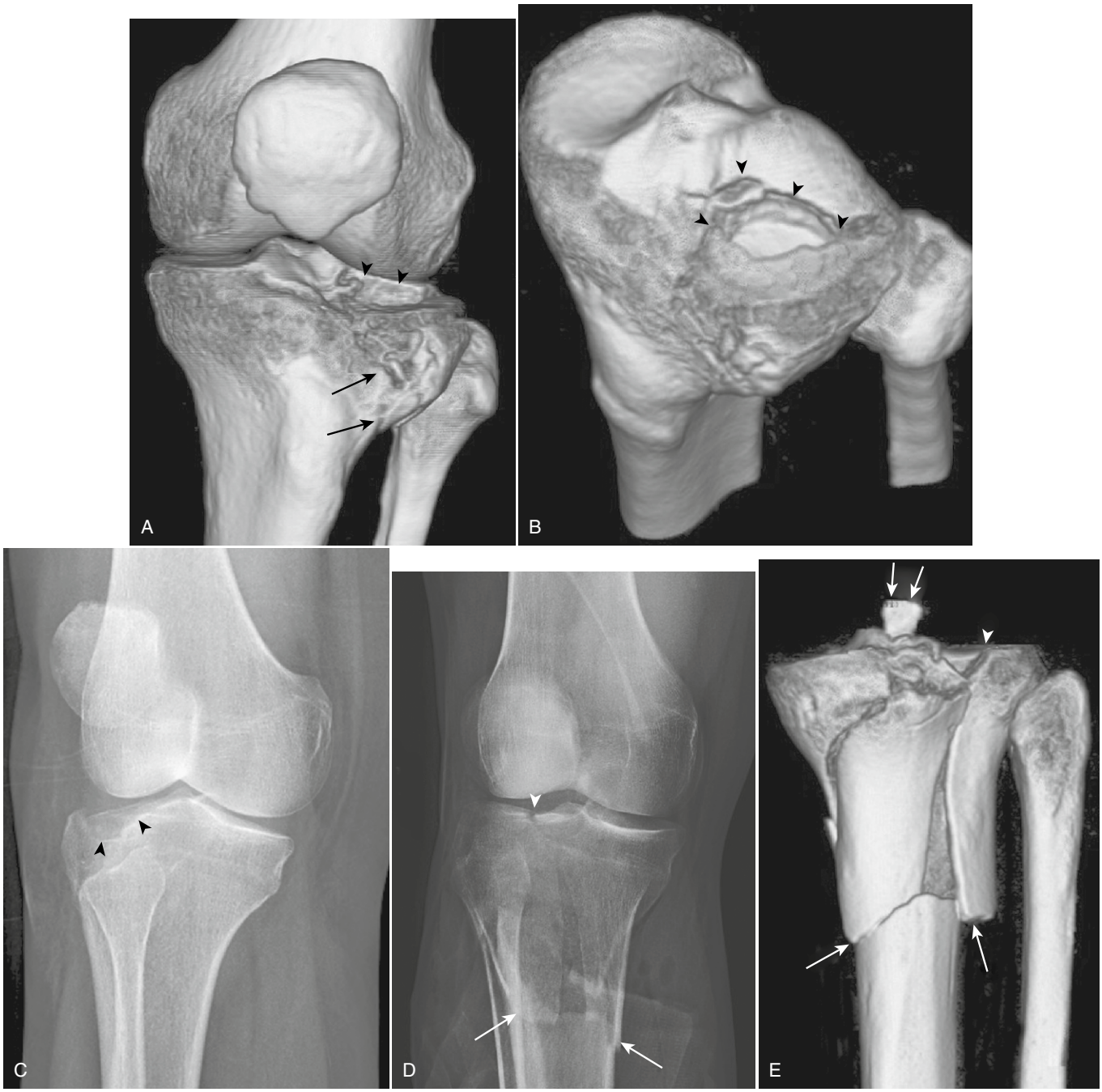


FIGURE 4-36. Fractures of the tibial plateau. **A** and **B**, Volumetric (3D) CT images demonstrate a fracture of the lateral tibial plateau that has two components of a split *(arrows)* and depression *(arrowheads)* (type II) fracture. CT accurately depicts the fragments, degree of depression, amount of joint space involved, and displacement. **C**, Oblique radiograph of the knee shows a pure depression fracture of the lateral tibial plateau *(arrowheads)* (type III). **D** and **E**, Oblique radiograph of the knee and volumetric (3D) CT image demonstrate a comminuted fracture of both medial and lateral tibial plateaus *(arrowhead)* with dissociation between the tibial metaphysis and diaphysis (arrows). An avulsion fracture of the tibial spine is noted *(short arrows)* on the CT reformation **(E)**.

These fractures may involve either one or both plateaus, and have varying degrees of comminution. The goal of imaging is to demonstrate the number of fracture fragments, degree of displacement, degree of depression, location, and type of plateau fractures. Meniscal injuries, especially of the lateral meniscus, are seen in up to 50% of cases of tibial plateau fractures. Injuries to the medial collateral ligament and anterior cruciate ligament are also common.

Avulsions About the Knee

Avulsion of the Anterior Cruciate Ligament Insertion

The distal attachment of the anterior cruciate ligament (ACL) is at the medial spine of the intercondylar eminence of the tibia. Avulsions of the medial tibial spine usually occur in children or adolescents. Radiographic findings include a fracture at the base of the intercondylar eminence, or of the medial tibial spine (Fig. 4-37A), which indicates that the ACL has been detached. It should be noted that isolated fractures of the lateral tibial spine do not involve either cruciate ligament. In some cases, the presence of avulsed bony fragments in the joint may have an appearance similar to a loose body or an osteochondral fracture.

Avulsion of the Posterior Cruciate Ligament Insertion

The posterior cruciate ligament (PCL) inserts distally on the posterior aspect of the tibial plateau. An avulsed bony fragment from this type of fracture is best visualized on the lateral radiograph as a fragment projecting over the posterior aspect of the plateaus (Fig. 4-37B and C).

Segond fracture is an avulsion fracture at the lateral aspect of the lateral proximal tibia just below the level of the tibial plateau (Fig. 4-37D) and is the result of lateral capsular ligament pull. This fracture should be differentiated from an iliotibial band avulsion of Gerdy's tubercle, which is located more anteriorly, and should not be confused with an avulsion of the lateral collateral ligament that inserts on the fibular head. There is widening of the lateral tibiofemoral compartment of the knee joint, a small sliver of bone adjacent to the lateral tibial plateau in the mid-coronal section near the joint line, and joint effusion. It is caused by forceful internal rotation of a flexed knee. ACL and meniscal injuries are frequently associated with Segond fractures.

Fractures and Dislocations Around the Ankle

Fractures of the Ankle

Ankle fractures (Box 4-17) are most commonly classified by their appearance on radiographs. Certain radiographic features can be used to determine the mechanism and to understand these complex injuries. Two major mechanisms responsible for ankle fractures are rotational and axial-loading injuries. Rotational malleolar fractures are less severe injuries than axial-loading tibial plafond or pilon fractures.

Rotational malleolar fractures are caused by combinations of different forces: supination, pronation, external rotation, adduction, and abduction. These forces result in either impaction injury or avulsion injury to the malleoli.

***Box 4-17.* Fractures and Dislocations Around the Ankle**

STANDARD VIEWS

Ankle—AP, lateral, and mortise (10-degree internal rotation) views (include the base of the fifth metatarsal)

Lower leg—AP and lateral views

FREQUENT SITE OF INJURY

Malleoli

RELEVANT NORMAL ANATOMY

Ankle mortise consists of medial malleolus, lateral malleolus, and horizontal plate of the distal articular surface of the tibia (tibial plafond)

Ankle joint—joint between ankle mortise and superior articular surface of the talus

Ligamentous complex of the ankle—medial collateral (deltoid) ligament, lateral collateral ligaments, and distal tibiofibular complex (most important for ankle stability)

Medial clear space—on mortise view, the medial ankle joint space should be equal to the superior joint space, and less than 4 mm wide; widening indicates lateral talar shift

Tibiofibular clear space—distance between medial wall of distal fibula and incisural surface of the tibia should be less than 6 mm on both AP and mortise views; widening indicates syndesmosis disruption

The characteristic of impaction injury is an oblique fracture line, while the characteristic of an avulsion injury is a horizontal fracture line. These fractures are typically described by the location of malleolar fracture lines (medial, lateral, or posterior malleoli, or more). Bimalleolar or trimalleolar fractures are injuries that involve more than one structure. The detailed description should include the level of the fibular fracture, orientation of the fracture line (horizontal or oblique), possibility of syndesmosis disruption, involvement of the tibial plafond, and size of the various fragments. Several classifications are used in the assessment of ankle fractures. The Weber/AO classification is simple and correlates well with treatment and prognosis. The level of the fibular fracture determines the extent of injury to the syndesmotic complex, and is used to categorize fractures in this classification. In general, the higher the fibular fracture, the more extensive the damage to the syndesmosis and the greater the risk of ankle instability. Type A (Fig. 4-38A) is a supination-adduction injury with the fibular fracture located below the syndesmosis. There is a transverse fracture of the lateral malleolus or lateral collateral ligament rupture and an oblique fracture of the medial malleolus. Type B (Fig. 4-38B) is a supination-external rotation or pronation-abduction injury resulting in a fracture of the fibula at the level of the syndesmosis. There is an oblique fracture of the lateral malleolus and a horizontal fracture of the medial malleolus or deltoid ligament rupture. There is partial disruption of the syndesmosis. Type C is a pronation-external rotation injury with a fracture of

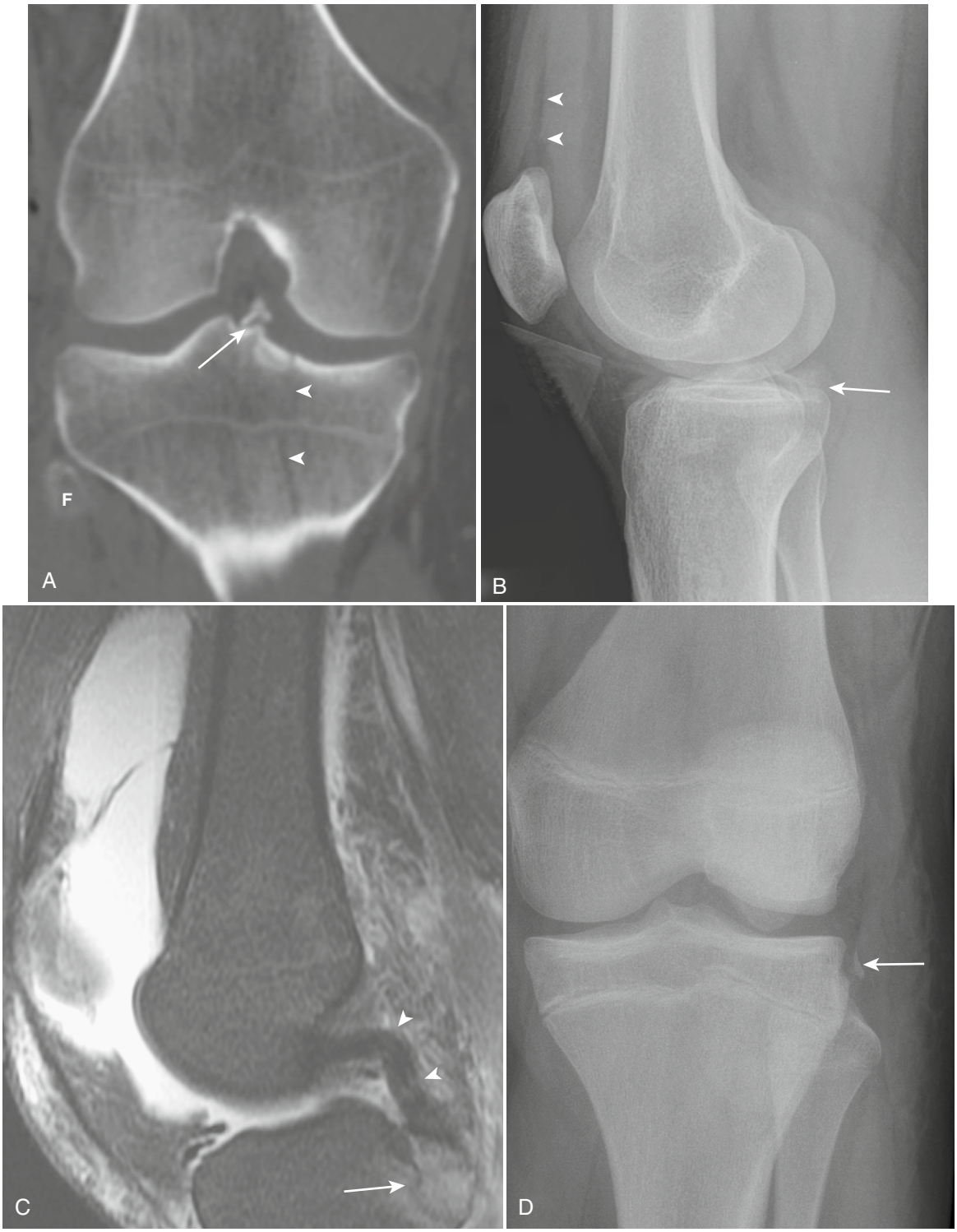


FIGURE 4-37. Avulsions about the knee. **A**, Anterior cruciate ligament (ACL) avulsion. Coronal reformatted CT image of the knee shows an avulsion fracture of the medial tibial spine *(arrow)*, the attachment site of the ACL. In addition, there is a nondisplaced split fracture *(arrowheads)* of the medial tibial plateau. **B** and **C**, Posterior cruciate ligament (PCL) avulsion. Lateral cross-table radiograph **(B)** of the knee demonstrates a lipohemarthrosis *(arrowheads)*. A subtle bone fragment *(arrow)* is visualized at the tibial attachment of the PCL. Sagittal fat-suppressed T2-weighted MR image **(C)** confirms the fracture site *(arrow)* at the distal attachment of the PCL *(arrowheads)*. **D**, Segond fracture. An avulsion fracture *(arrow)* of the lateral tibial plateau is shown in a frontal radiograph of the knee. ACL and meniscal injuries are commonly associated with Segond fracture.



FIGURE 4-38. Fractures of the ankle. Three types of rotational malleolar fracture. **A**, Type A. The fibular fracture line *(arrows)* is located completely below the level of the syndesmosis. **B**, Type B. The fibular fracture *(arrows)* begins at the level of the syndesmosis. There is widening of the medial mortise *(arrowheads)* indicating a deltoid ligament injury. **C**, Type C. Fibular fracture *(arrows)* is above the level of syndesmosis. There is disruption of the syndesmosis (widening of the tibiofibular space, *white arrowheads*) up to the level of the fibular fracture as well as a deltoid ligament injury with a widened mortise *(black arrowheads)*.

Continued

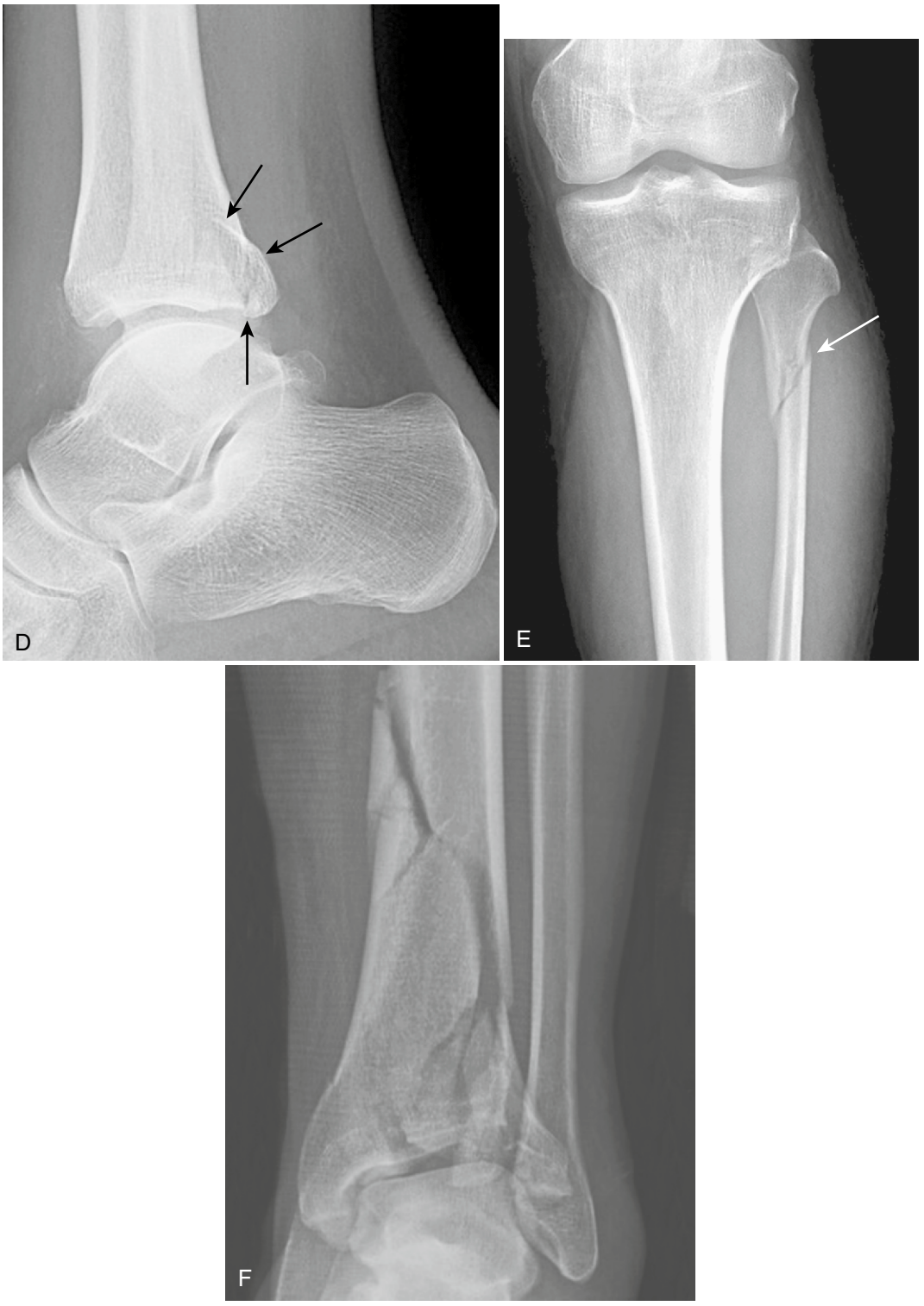


Figure 4-38.—Cont'd D and **E**, Maisonneuve's fracture. Frontal radiograph of the ankle shows an isolated posterior malleolar fracture *(arrows)* that prompted a request for an additional radiograph to include the whole length of the fibula. An oblique fracture *(arrow)* of the proximal fibula is revealed. **F,** Tibial plafond (pilon) fracture. Anteroposterior radiograph of the ankle demonstrates a severely comminuted intra-articular fracture of the distal tibia extending to the tibial plafond. The malleoli are in anatomical alignment.

the fibula above the level of the syndesmosis. There is a transverse fracture of the medial malleolus or deltoid rupture, and rupture of the syndesmosis. Type C (Fig. 4-38C) is usually treated with syndesmotic fixation in addition to stabilization of the lateral malleolus. Maisonneuve's fracture (Fig. 4-38D and E) is part of the spectrum of pronation-external rotation injuries, in which the fibular fracture is more proximal and there is a tear of the full length of the interosseous membrane. Fractures of the proximal fibula are easily overlooked because of the distracting painful injuries at the ankle. The diagnosis of Maisonneuve's fracture should be considered in the following situations: isolated fracture of the posterior lip of the tibia, isolated displaced fracture of the medial malleolus, and widening of the medial or lateral clear spaces without evident fracture of the lateral malleolus or fibula. In these circumstances, full-length views of the tibia and fibula should be obtained to identify associated fractures of the proximal fibula.

Axial loading to the ankle joint drives the talus against the distal tibial articular surface, resulting in tibial plafond fractures (Fig. 4-38F). The malleoli usually maintain an anatomic relationship with the talus. These fractures are more severe than the rotational malleolar fractures. They are comminuted, intra-articular fractures of the distal tibia. Differentiation of these fractures from trimalleolar fractures lies in the profound comminution of the distal tibia, intra-articular extension to involve the dome of the plafond, common association with talar fractures, and preservation of the tibiofibular syndesmosis. Post-traumatic arthritis is a common complication of displaced plafond fractures. Tillaux fracture is an avulsion of the anteroinferior tibiofibular ligament from the lateral distal tibial margin, created by forceful external rotation of the foot. The vertical fracture line extends from the distal articular surface of the tibia superiorly to the lateral tibial cortex. If there is lateral displacement of more than 2 mm, or step-off of the articular surface of the distal tibia, surgical fixation is usually required. In children, this fracture is a Salter Harris type III, since the medial side of the growth plate fuses earlier than the lateral side. In adults, this is usually a ligamentous injury. An avulsion fracture of the medial margin of the fibula at the attachment of the anterior tibiofibular ligament is known as the Wagstaffe-LeFort fracture. Isolated Tillaux fractures and Wagstaffe-LeFort fractures do occur, but are more commonly part of more extensive injuries to the ankle mortise and are associated with malleolar fractures.

Triplane fractures (Fig. 4-39A–C) are distinct fractures of the distal tibial epiphysis, caused by plantar flexion and external rotation. There are fracture lines in three planes: a horizontal plane within the growth plate or physis, a sagittal



FIGURE 4-39. Fractures of the ankle. **A,** Tillaux fracture. Mortise view of the ankle shows a vertical fracture of the distal articular surface of the tibia extending to the lateral tibial cortex (*arrow,* Salter Harris type III in this case). **B** and **C,** Triplane fracture. Coronal reformatted CT image **(B)** demonstrates the typical findings of a Tillaux fracture *(arrows)*. On the sagittal reformation **(C)** there is a coronally oriented vertical metaphyseal component of the fracture *(arrowhead)*, thereby completing the three components of a triplane fracture. Note also a nondisplaced fracture of the calcaneus. Triplane fracture is a combination of a fracture line extending in three planes (sagittal epiphysis, axial physis, and coronal metaphysis). Note a nondisplaced fracture of the calcaneus *(curved arrow)*.

plane through the epiphysis, and an oblique vertical plane in the posterior distal metaphysis. There are two distinct types of triplane fractures: two-fragment and three-fragment fractures. The appearance of the two-fragment fractures is very similar to that of Tillaux fractures, except that there is a metaphyseal component on the lateral view. In the three-fragment fracture, the entire epiphysis is usually displaced posteriorly, whereas in a two-fragment fracture only a portion of the epiphysis is displaced. It is important to distinguish between the two because three-fragment fractures usually require open reduction and internal fixation to preserve the joint.

Fractures and Dislocations of the Foot (Box 4-18)

Injuries to the Hindfoot

Subtalar or peritalar dislocation is a rare injury characterized by concomitant dislocations of the subtalar and talonavicular joints with normal tibiotalar relationship. Findings are obvious on lateral radiographs, with absence of the talar head in the cup of the navicular. Medial subtalar dislocation (Fig. 4-40A and B) is far more common than lateral subtalar dislocation, while the latter is more severe. Total talar dislocation is a combined complete dislocation of both the tibiotalar (ankle) and subtalar joints. It is the most serious of all talar injuries.

Box 4-18. **Fractures and Dislocations of the Foot**

STANDARD VIEWS
Foot—dorsoplantar, lateral, and oblique views
Calcaneus—lateral and Harris (tangential 45-degree) views
Toe—dorsoplantar, lateral, and oblique views

FREQUENT SITE OF INJURY
Phalanges

FREQUENTLY MISSED INJURIES
Fracture of the lateral process of the talus
Lisfranc's injury

RELEVANT NORMAL ANATOMY
Three parts of the foot—hindfoot (calcaneus, talus), midfoot (navicular, cuboid, cuneiforms), and forefoot (metatarsals, phalanges)
Chopart joint—transverse tarsal joint between the hindfoot and midfoot
Lisfranc joint—tarsometatarsal joint between the midfoot and forefoot
Boehler's angle—normal 20 to 40 degrees (angle formed by intersection of lines drawn tangentially to the anterior and posterior elements of the superior calcaneal surface)

FRACTURE MIMICS
Sesamoid bone on the plantar aspect of the first metatarsal
Os trigonum (mimics fracture of the posterior process of talus)
Nutrient artery canal—midshaft of metatarsal
Calcaneal apophysis—fragmented, irregularly dense, and more dense than calcaneus

Fractures of the Talus

Talar fractures are the second most common site of tarsal fracture and are usually caused by forced dorsiflexion. Fractures are classified by anatomic location: head, neck, body, posterior process, and lateral process. Fractures of the talar head are rare; they usually involve the talonavicular joint and are associated with talonavicular subluxation. The talar neck is the most vulnerable site. Fractures of the talar neck (Fig. 4-40C) are defined when the fracture line is anterior to the lateral process of the talus. They are usually oriented in a vertical plane and not displaced. Hawkins's classification divides these fractures into four types. Type I is a nondisplaced fracture. Type II is a fracture with subtalar subluxation or dislocation. Type III is a fracture with subtalar and tibiotalar dislocation. Type IV is a fracture with subtalar subluxation and dislocation of the talonavicular joint. The risk of avascular necrosis is 15%, 40% to 50%, and 100%, respectively, for types I, II, and III/IV. Aviator's astragalus is an eponym for a displaced fracture of the talar neck that results in medial displacement and rotation of the distal fragment together with the bones of the foot. Fractures extending into, or posterior to, the lateral process of the talus are defined as fractures of the talar body. These are intra-articular fractures and have a high rate of avascular necrosis. Fractures of the posterior process of the talus are uncommon and best seen on the lateral view. An os trigonum is the main differential diagnosis, although this usually has a well-corticated edge and smooth surface. Isolated fractures of the lateral process are frequently overlooked and misinterpreted as a severe sprain. This is usually an avulsion fracture and best visualized on the mortise view.

Fractures of the Calcaneus

The calcaneus is the most common site of tarsal bone fracture. Fractures are classified by their location and the presence of subtalar joint involvement. Calcaneal fractures with subtalar joint involvement (Fig. 4-40D and E) are more common (75% of all calcaneal fractures). They result from axial-loading forces to the body of the calcaneus through the talus. Typically, there is loss of height, increased width, and disruption of the subtalar joint facet. Boehler's angle is generally decreased. The axial-loading force produces two separate fracture lines: shear and compression lines. The shear fracture line is a sagittal plane fracture through the posterior facet, dividing it into sustentacular and tuberosity fragments. The tuberosity fragment is usually impacted, rotated, and displaced laterally, resulting in loss of calcaneal height and increased calcaneal width. The compression fracture line is a coronal plane fracture that splits the middle facet. When viewed from the lateral side, this line has the shape of an inverted Y. The Sander classification relies on the number of articular pieces of the posterior facet of the subtalar joint; prognosis worsens as the number of fragments increases. Occasionally, there is ligament entrapment between the fragments, or involvement of the sinus tarsi. Calcaneal fractures are frequently bilateral, and 10% are associated with fractures of the thoracolumbar spine.



FIGURE 4-40. Fractures and dislocation of the hindfoot. **A** and **B**, Subtalar dislocation. Frontal and lateral radiographs of the ankle demonstrate a medial subtalar dislocation. On the lateral projection, the empty navicular cup is obvious *(arrowheads)*. **C**, A fracture of the talar neck *(arrows)* is seen on a lateral radiograph. **D**, Lateral radiograph shows a comminuted fracture of the calcaneus extending vertically *(black arrowheads)* through the body, posterior to the subtalar joint, and longitudinally toward the posterior facet *(white arrowheads)*. Subtalar joint extension is suspected *(star)*. Bohler's angle (formed by the black and white lines) is decreased to less than 20 degrees *(white arrow)*. **E**, Coronal reformatted CT image at the widest point of the lateral process of the talus helps classify the type of fracture. This fracture has a single subtalar joint extension *(arrow)*, therefore producing two articular pieces.

The rest of the fractures, which do not involve the posterior facet, are in this category. This includes fractures of the anterior process, mid-calcaneus (body, sustentaculum tali, peroneal tubercle, lateral calcaneal process), and posterior calcaneus (tuberosity, medial calcaneal tubercle). They account for 25% of all calcaneal fractures. Fractures of the mid-calcaneus are usually the results of axial-loading mechanisms, while avulsion forces or inversion injuries cause the others.

Injuries to the Midfoot

The midfoot is defined as the region distal to Chopart's joint and proximal to Lisfranc's joint. The navicular, cuboid, and medial, middle, and lateral cuneiforms make up the bones of the midfoot. The midfoot is responsible for maintaining the relationship between the forefoot and the hindfoot. Navicular fractures are commonly due to an indirect force that occurs in sports-related injuries, falls, or motor vehicle accidents. Less likely, they may be the result of a direct blow that causes an avulsion of the talonavicular or naviculocuneiform ligaments. These fractures are categorized by their location: tuberosity (medial prominence of the navicular) and body. An accessory navicular (os tibiale externum) bone can be mistaken for a fracture of the tuberosity. This accessory ossicle is present in up to 25% of the population, and is bilateral 90% of the time. Cuboid and cuneiform injuries are commonly seen with other injuries to the midfoot and Lisfranc's joint.

Tarsometatarsal (Lisfranc) Injuries

Injuries to the tarsometatarsal joint range from a stable sprain to a grossly unstable deformity. These injuries can result in a prolonged recovery period and significant long-term disability, and it is therefore important to recognize and treat them early. Up to 20% are missed on initial presentation. They are commonly the result of indirect forces that cause plantar hyperflexion across the long axis of the foot. This can occur with minimal trauma (e.g., foot entrapment on the car brake pedal, or a minor fall), and as a sports-related injury (e.g., opponent falling on the foot in fixed equinus). A key anatomic structure related to this type of injury is Lisfranc's ligament. This is the strongest and largest ligament of this joint complex, originating from the lateral plantar aspect of the medial cuneiform and inserting on the medial plantar aspect of the second metatarsal base. It is an indirect link between the first and second metatarsals, and the only ligamentous support between the medial portion of the forefoot and the rest. The nidus of Lisfranc's injuries is typically at the medial cuneiform and the base of the second metatarsal, where Lisfranc's ligament is located. This ligament may be torn, without fractures of the medial cuneiform or base of the second metatarsal, or may be intact with a fracture of the base of the second metatarsal. Two major types of these injuries are described. The homolateral type (Fig. 4-41) is a lateral dislocation of the four lateral metatarsals or all metatarsals. The divergent type is a less common, but more severe injury. In this type, there is lateral displacement of the second through fifth metatarsals with medial displacement of the first metatarsal. Rarely, an isolated medial dislocation of the first metatarsal and medial cuneiform may occur. The most common fractures associated with these dislocations are fractures of the base of the second metatarsal. Chip fractures of the distal margin of the cuboid, and base of other metatarsals, are frequent.



Figure 4-41. Lisfranc's injury. Anteroposterior radiograph of the foot demonstrates homolateral lateral dislocation of the tarsometatarsal joints. Lisfranc's ligament is completely torn, as indicated by the complete lateral dislocation of the second metatarsal with respect to the medial and middle cuneiforms.

Injuries to the Forefoot

Metatarsal Fractures

The majority of injuries to the fifth metatarsal are related to sporting or athletic activities. These fractures are separated into two groups: proximal base fractures and distal spiral or dancer's fractures. There are three distinct fracture patterns of the proximal fifth metatarsal as defined by the location of the fracture line. Zone 1 injury (Fig. 4-42A) is an avulsion fracture at the base of the fifth metatarsal that usually occurs from an indirect load. Tension is produced along the insertion of the lateral band of the plantar aponeuroses during sudden inversion of the hindfoot, causing disruption of the bony cortex. Zone 2 injuries (Fig. 4-42B) are true Jones fractures and involve the metadiaphyseal junction of this bone. The fracture line propagates from the lateral aspect of the proximal metatarsal toward the articular surface between the fourth and fifth metatarsal bones and may progress into the metatarsocuboid joint. It is the result of tensile stress along the lateral border of the metatarsal. Zone 3 injuries are located in the proximal fifth metatarsal. Relative frequency of these fractures is 93% zone 1, 4% zone 2, and 3% zone 3. An apophysis of the fifth metatarsal should not be mistaken for a fracture as it has an obliquely longitudinal orientation to the axis of the metatarsal. Dancer's fracture is a spiral, oblique fracture of

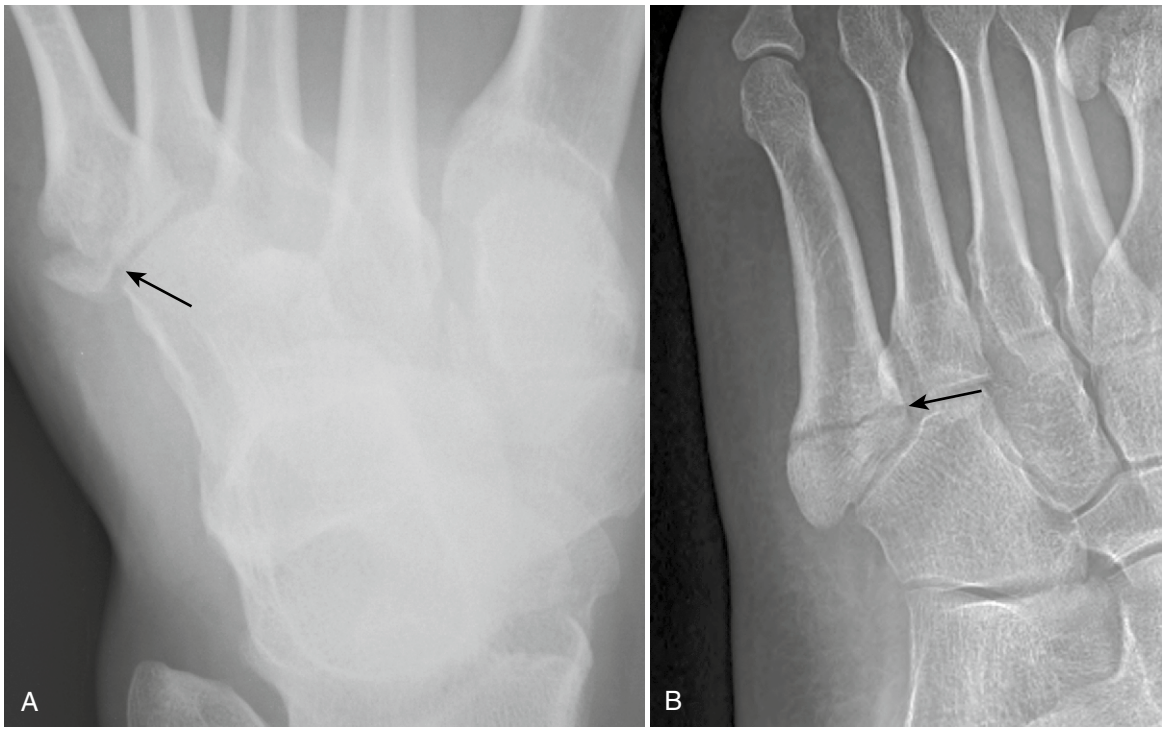


FIGURE 4-42. Fractures of the proximal fifth metatarsal bone. **A,** Zone 1 injury is an avulsion fracture at the base of the fifth metatarsal *(arrow)*. This is the most common type of fracture of the proximal fifth metatarsal. **B,** Zone 2 injury, or "true Jones fracture," involves the metadiaphyseal junction *(arrow)*.

the distal fifth metatarsal caused by rolling over the outer border of the foot.

Metatarsophalangeal Injuries

Injuries to the metatarsophalangeal (MTP) joint complex can occur in isolation or as part of multiple trauma. Most commonly, they involve the first MTP joint, which normally provides stable load sharing between the metatarsal head and the toe. Dislocations of the first MTP joint can be complicated with avulsion injuries of the medial or lateral collateral ligaments, or displacement of the sesamoid structures. The sesamoids function within the first MTP joint complex as shock absorbers and fulcrums to support the weight-bearing function of the first toe. The spectrum of sesamoid injuries is wide, ranging from sesamoiditis to stress fracture and acute fracture. Acute fractures are caused by a direct blow, axial loading, or hyperpronation. Depending on the mechanism of injury, the fractures can be transverse, comminuted, or stellate. The medial sesamoid is more commonly injured than the lateral. A partite sesamoid can be distinguished from a fracture by its smooth, sclerotic edge.

Phalangeal fractures are the most common injury to the forefoot. Fractures occur most commonly in the proximal phalanges. Of these, the proximal phalanx of the fifth toe is involved most often. Two major mechanisms result in fractures: direct blow (e.g., heavy object dropped onto the foot) and axial loading (stubbing injury). The former usually causes a comminuted or transverse fracture. The latter tends to produce more deformity due to secondary valgus or varus forces, and results in spiral or oblique fractures.

Interphalangeal dislocations are a result of axial loading applied to the terminal end of the unprotected digit. Proximal interphalangeal joint dislocations are more common.

SPECIAL CONSIDERATIONS

CT Angiography of the Extremities in Trauma

Traumatic arterial injuries to the extremities may occur with either blunt or penetrating trauma. Clinical signs of arterial injuries are divided into two categories: hard and soft signs. The hard signs include the presence of pulsatile bleeding, expanding hematoma, pulse deficit, bruit/thrill, and distal limb ischemia. The patients in this category usually require immediate surgical intervention. The soft signs are stable hematoma, hypotension, neurological deficit, and proximity to the major artery. Conventional angiography has been the traditional means for evaluation of possible arterial injury in trauma patients. However, its major disadvantages are the cost of the procedure, the delay that occurs before angiography, and the need for a specialized team. With the implementation of multidetector computed tomography (MDCT) in the emergency department, the indications for CT angiography have been expanded to include the assessment of trauma to the peripheral arteries, a result of fast acquisition times that allow rapid assessment, high spatial resolution, increased anatomic coverage, and high-quality multiplanar and volumetric reconstructions. Direct signs of arterial injuries on CT angiography are extravasation of contrast medium, wall irregularity, abrupt change in arterial caliber, enhancement difference, and intimal flap. Other indirect signs include perivascular hematoma, bullet trajectory through the artery, and a fragment adjacent

to the artery. The known pitfalls, which may render the exams uninterpretable or indeterminate, include exams with poor arterial opacification, motion artifacts, and streak artifacts (especially in penetrating missile injuries). Slow blood flow distal to an arterial injury may limit the evaluation of the run-off vessels. Detection of injuries to the distal, small arteries below the ankle or elbow is limited by the spatial resolution of CT angiography. CT angiography should be performed only if immediate surgery is not indicated. Stable patients with diminished pulse, expanding hematoma, bruit/thrill, and anatomically susceptible injury site may benefit from this study.

Volumetric (3D) Reconstruction and Image Post-Processing

A combination of MDCT and volumetric (3D) reconstruction has proved valuable in the diagnosis of complex orthopedic injuries and in their treatment planning. CT scan techniques for this purpose include the helical (spiral) acquisition, narrow collimation, and lower pitch with small reconstruction increments. The raw data of axial images are interpolated to create overlapping sections, and then mapped with the appropriate rendering algorithm into a 3D volume. Shaded surface rendering and volume rendering are major reconstruction algorithms for 3D musculoskeletal imaging. The former technique beautifully displays the gross relationships of the structures. The latter conveys the information of the lesions hidden beneath the bone surface and is less likely to be limited by stair-step artifacts. Routine use of multiplanar (2D) reformations and volumetric (3D) reconstructions is a critical part of the CT exams when they are utilized for musculoskeletal trauma, as they can potentially lead to a change in management decisions.

Suggested Readings

Brandser E: The pelvis. In Rogers LF (ed): Radiology of Skeletal Trauma, 3rd ed. Philadelphia, Churchill Livingstone, 2002, pp 930–1029.

Butters KP: Fractures of the scapula. In Bucholz RW, Heckman JD, Court-Brown C (eds): Rockwood and Green's Fractures in Adults, 6th ed. Philadelphia, Lippincott Williams & Wilkins, 2006, pp 1257–1284.

Daftary A, Haims AH, Baumgaertner MR: Fractures of the calcaneus: A review with emphasis on CT. Radiographics 25:1215–1226, 2005.

Early JS: Fractures and dislocations of the midfoot and forefoot. In Bucholz RW, Heckman JD, Court-Brown C (eds): Rockwood and Green's Fractures in Adults, 6th ed. Philadelphia, Lippincott Williams & Wilkins, 2006, pp 2337–2400.

Egol KA, Koval KJ: Fractures of the proximal tibia. In Bucholz RW, Heckman JD, Court-Brown C (eds): Rockwood and Green's Fractures in Adults, 6th ed. Philadelphia, Lippincott Williams & Wilkins, 2006, pp 2000–2029.

Falchi M, Rollandi GA: CT of pelvic fractures. Eur J Radiol 50:96–105, 2004.

Gaebler C: Fractures and dislocations of the carpus. In Bucholz RW, Heckman JD, Court-Brown C (eds): Rockwood and Green's Fractures in Adults, 6th ed. Philadelphia, Lippincott Williams & Wilkins, 2006, pp 857–908.

Galatz LM, Williams R Jr.: Acromioclavicular joint injuries. In Bucholz RW, Heckman JD, Court-Brown C (eds): Rockwood and Green's Fractures in Adults, 6th ed. Philadelphia, Lippincott Williams & Wilkins, 2006, pp 1331–1364.

Goldfarb CA, Yin Y, Gilula LA, et al: Wrist fractures: What the clinician wants to know. Radiology 219:11–28, 2001.

Greenspan A: Orthopedic Imaging: A Practical Approach. Philadelphia, Lippincott Williams & Wilkins, 2004.

Harris JH, Harris WH: The Radiology of Emergency Medicine. 4th ed. Philadelphia, Lippincott Williams & Wilkins, 2000.

Harris RM: Fractures of the patella and injuries to the extensor mechanism. In Bucholz RW, Heckman JD, Court-Brown C (eds): Rockwood and Green's Fractures in Adults, 6th ed. Philadelphia, Lippincott Williams & Wilkins, 2006, pp 1970–1997.

Helms CA, Major NM: The knee and shafts of the tibia and fibula. In Rogers LF (ed): Radiology of Skeletal Trauma, 3rd ed. Philadelphia, Churchill Livingstone, 2002, pp 1111–1221.

John SD, Wherry K, Swischuk LE, et al: Improving detection of pediatric elbow fractures by understanding their biomechanics. Radiographics 16:1443–1460, 1996.

Jupiter JB, Axelrod TS, Belsky MR: Fractures and dislocations of the hand. In Browner BD, Jupiter JB, Levine AM, et al (eds): Skeletal Trauma: Basic Science, Management, and Reconstruction, 3rd ed. Philadelphia, WB Saunders, 2003, pp 1153–1265.

Jupiter JB, Kellam JF: Diaphyseal fractures of the forearm. In Browner BD, Jupiter JB, Levine AM, et al (eds): Skeletal Trauma: Basic Science, Management, and Reconstruction, 3rd ed. Philadelphia, WB Saunders, 2003, pp 1363–1403.

Kasser JR, Beaty JH: Supracondylar fractures of the distal humerus. In Beaty JH, Kasser JR (eds): Rockwood and Wilkin's Fractures in Children, 6th ed. Philadelphia, Lippincott Williams & Wilkins, 2006, pp 543–589.

Koval KJ, Cantu RV: Intertrochanteric fractures. In Bucholz RW, Heckman JD, Court-Brown C (eds): Rockwood and Green's Fractures in Adults, 6th ed. Philadelphia, Lippincott Williams & Wilkins, 2006, pp 1793–1825.

Kwon YW, Zuckerman JD: Subluxations and dislocations about the glenohumeral joint. In Bucholz RW, Heckman JD, Court-Brown C (eds): Rockwood and Green's Fractures in Adults, 6th ed. Philadelphia, Lippincott Williams & Wilkins, 2006, pp 1285–1330.

Lazarus MD, Seon C: Fractures of the clavicle. In Bucholz RW, Heckman JD, Court-Brown C (eds): Rockwood and Green's Fractures in Adults, 6th ed. Philadelphia, Lippincott Williams & Wilkins, 2006, pp 1211–1255.

Leighton RK: Fractures of the neck of the femur. In Bucholz RW, Heckman JD, Court-Brown C (eds): Rockwood and Green's Fractures in Adults, 6th ed. Philadelphia, Lippincott Williams & Wilkins, 2006, pp 1753–1791.

Leung K: Subtrochanteric fractures. In Bucholz RW, Heckman JD, Court-Brown C (eds): Rockwood and Green's Fractures in Adults, 6th ed. Philadelphia, Lippincott Williams & Wilkins, 2006, pp 1827–1844.

Levine AM: Fractures of the sacrum. In Browner BD, Jupiter JB, Levine AM, et al (eds): Skeletal Trauma: Basic Science, Management, and Reconstruction, 3rd ed. Philadelphia, WB Saunders, 2003, pp 1031–1051.

Marsh JL, Saltzman CL: Ankle fractures. In Bucholz RW, Heckman JD, Court-Brown C (eds): Rockwood and Green's Fractures in Adults, 6th ed. Philadelphia, Lippincott Williams & Wilkins, 2006, pp 2146–2247.

Matta JM: Surgical treatment of acetabular fractures. In Browner BD, Jupiter JB, Levine AM, et al (eds): Skeletal Trauma: Basic Science, Management, and Reconstruction, 3rd ed. Philadelphia, WB Saunders, 2003, pp 1109–1149.

Miller-Thomas MM, West OC, Cohen AM: Diagnosing traumatic arterial injury in the extremities with CT angiography: Pearls and pitfalls. Radiographics 25(Suppl 1):S133–S142, 2005.

O'Brien PJ, Meek RN, Blachut PA, et al: Fractures of the distal femur. In Bucholz RW, Heckman JD, Court-Brown C (eds): Rockwood and Green's Fractures in Adults, 6th ed. Philadelphia, Lippincott Williams & Wilkins, 2006, pp 1915–1967.

Potok PS, Hopper KD, Umlauf MJ: Fractures of the acetabulum: Imaging, classification, and understanding. Radiographics 15:7–23, 1995.

Pretorius ES, Fishman EK: Volume-rendered three-dimensional spiral CT: Musculoskeletal applications. Radiographics 19:1143–1160, 1999.

Reilly MC: Fractures of the acetabulum. In Bucholz RW, Heckman JD, Court-Brown C (eds): Rockwood and Green's Fractures in Adults, 6th ed. Philadelphia, Lippincott Williams & Wilkins, 2006, pp 1665–1714.

Resnick D, Goergen T: Physical injury: Concepts and terminology. In Resnick D, Kransdorf MJ (eds): Bone and Joint Imaging, 3rd ed. Philadelphia, Elsevier Saunders, 2004, pp 789–830.

Ring D: Fractures and dislocations of the elbow. In Bucholz RW, Heckman JD, Court-Brown C (eds): Rockwood and Green's Fractures in Adults, 6th ed. Philadelphia, Lippincott Williams & Wilkins, 2006, pp 989–1049.

Robinson CM: Fractures of the distal humerus. In Bucholz RW, Heckman JD, Court-Brown C (eds): Rockwood and Green's Fractures in Adults, 6th ed. Philadelphia, Lippincott Williams & Wilkins, 2006, pp 1052–1116.

Rogers LF, Ashman CJ, Yu JS: The hip and femoral shaft. In Rogers LF (ed): Radiology of Skeletal Trauma, 3rd ed. Philadelphia, Churchill Livingstone, 2002, pp 1030–1109.

Rogers LF, Chew FS, Hendrix RW: Imaging of fractures: Detection and description. In Rogers LF (ed): Radiology of Skeletal Trauma, 3rd ed. Philadelphia, Churchill Livingstone, 2002, pp 41–110.

Rogers LF, Cox TD, Sonin A: The elbow and forearm. In Rogers LF (ed): Radiology of Skeletal Trauma, 3rd ed. Philadelphia, Churchill Livingstone, 2002, pp 683–778.

Rogers LF, Keogh C, Bergin D, et al: The wrist. In Rogers LF (ed): Radiology of Skeletal Trauma, 3rd ed. Philadelphia, Churchill Livingstone, 2002, pp 779–873.

Rogers LF, Lenchik L: The shoulder and humeral shaft. In Rogers LF (ed): Radiology of Skeletal Trauma, 3rd ed. Philadelphia, Churchill Livingstone, 2002, pp 593–682.

Sanders DW: Fractures of the talus. In Bucholz RW, Heckman JD, Court-Brown C (eds): Rockwood and Green's Fractures in Adults, 6th ed. Philadelphia, Lippincott Williams & Wilkins, 2006, pp 2249–2291.

Sanders RW, Clare MP: Fractures of the calcaneus. In Bucholz RW, Heckman JD, Court-Brown C (eds): Rockwood and Green's Fractures in Adults, 6th ed. Philadelphia, Lippincott Williams & Wilkins, 2006, pp 2293–2336.

Schenck RC Jr, Stannard JP, Wascher DC: Dislocations and fracture-dislocations of the knee. In Bucholz RW, Heckman JD, Court-Brown C (eds): Rockwood and Green's Fractures in Adults, 6th ed. Philadelphia, Lippincott Williams & Wilkins, 2006, pp 2031–2078.

Schweitzer ME, Karasick D: The foot. In Rogers LF (ed): Radiology of Skeletal Trauma, 3rd ed. Philadelphia, Churchill Livingstone, 2002, pp 1319–1406.
Starr AJ, Malekzadeh AS: Fractures of the pelvic ring. In Bucholz RW, Heckman JD, Court-Brown C (eds): Rockwood and Green's Fractures in Adults, 6th ed. Philadelphia, Lippincott Williams & Wilkins, 2006, pp 1583–1664.
Warner JP, Costouros JG, Gerber C: Fractures of the proximal humerus. In Bucholz RW, Heckman JD, Court-Brown C (eds): Rockwood and Green's Fractures in Adults, 6th ed. Philadelphia, Lippincott Williams & Wilkins, 2006, pp 1161–1209.

CHAPTER 5

Extremities: Nontrauma

Luis E. Diaz

Most true emergencies of the musculoskeletal system are traumatic in nature. Musculoskeletal trauma is reviewed in other chapters. Neck and back pain are the most common nontraumatic musculoskeletal conditions leading to emergency room visits (National Hospital Ambulatory Medical Care Survey—Emergency Department 2004. Data obtained from U.S. Department of Health and Human Services, Centers for Disease Control and Prevention, National Center for Health Statistics).

Shoulder pain, the painful hip, and musculoskeletal infection are three common clinical problems in patients presenting to the emergency room with minimal, unrecognized, or no acute trauma. This chapter discusses the clinical presentations and imaging findings that can be expected with these conditions; conventional radiographic and advanced imaging features are described in detail. As cross-sectional imaging studies continue to be acquired with increasing frequency in the emergency setting, a comprehensive knowledge of imaging findings on these modalities is thus necessary.

SHOULDER PAIN

Evaluation of "nontraumatic" shoulder pain in the acute setting is challenging for clinicians and radiologists alike. The imaging features of the most common conditions presenting in clinical practice with shoulder pain are reviewed in an effort to assist radiologists and clinicians who work in the emergency room setting in the radiographic assessment of the shoulder. Some of these entities, however, may be the result of minor, remote, or unrecognized trauma.

Conventional radiographs should be obtained as the initial exam in most patients presenting with shoulder pain. Two standard views of the shoulder are performed in the anteroposterior projection with the humerus in external and internal rotation. The external rotation view is easily recognized as the one in which the greater tuberosity is seen in profile on the lateral aspect of the humerus. With internal rotation, the bicipital groove of the humerus translates medially, leaving the lesser tuberosity partially in profile. The glenohumeral joint is oriented obliquely approximately 30 degrees in the axial plane (anterior glenoid medially situated relative to the posterior glenoid) and, thus, is not seen in profile on the standard anteroposterior view. Additional radiographic views of the shoulder include the axillary view and the scapular "Y" view. The axillary view is preferable if the patient can tolerate this position. When properly performed, the axillary view provides excellent visualization of the acromion, coracoid process, and glenohumeral joint. Although an "impingement radiographic series" may be requested by the orthopedic surgeon, these are only rarely performed in the emergency setting.

Careful evaluation of shoulder radiographs requires a detailed review of the periarticular and intra-articular soft tissues for abnormal mineral deposits, the osseous structures for alignment and bone mineralization (regional and general), and the acromioclavicular joint, glenohumeral joints, and subacromial space.

Calcium Hydroxyapatite Deposition Disease

Hydroxyapatite deposition disease is a common entity characterized by pain and periarticular deposition of calcium phosphate crystals. The soft tissues around the shoulder are the most common locations for deposits occurring in tendons, joint capsule, ligaments, and bursae. Although this disease process has been assigned multiple names, it is mostly known as calcific bursitis/tendinitis. Middle-aged patients are most commonly affected, and it is slightly more common in men than in women. More than 30% of individuals with calcific deposits about the shoulder are asymptomatic. When clinically apparent, patients present with varying degrees of pain and disability, which may last for weeks or months if left untreated. It is important to note that the finding of hydroxyapatite deposits within the rotator cuff tendons ("calcific tendinitis") has no relationship with the subsequent development of rotator cuff tears.

Calcific deposits are more easily identified and characterized with radiographs, computed tomography (CT), and ultrasonography (US) than with magnetic resonance (MR). On radiographs, most calcific deposits appear as homogeneous and amorphous densities, ovoid, linear, or triangular in shape, with and without internal trabeculations (Fig. 5-1A). The precise appearance and location varies with the phase of the disease process and specific anatomical structure involved. The supraspinatus is the most frequently affected tendon. US is highly sensitive for detecting even very small calcific deposits and may be used to guide puncture, aspiration, and lavage as therapeutic options. Hyperechoic foci with minimal or no significant posterior shadowing are identified, sometimes as ill defined and fluffy or as discrete, well-defined calcifications that are linear or rounded (Fig. 5-1B). Calcific deposits may be seen on MR as nodular foci of low signal intensity in all pulse sequences (Fig. 5-1C), and may be easier to identify on gradient-echo sequences, as they may induce blooming artifact. Inflammatory changes in surrounding soft tissues may be present and identified as heterogeneous hyperintensity in fluid-sensitive

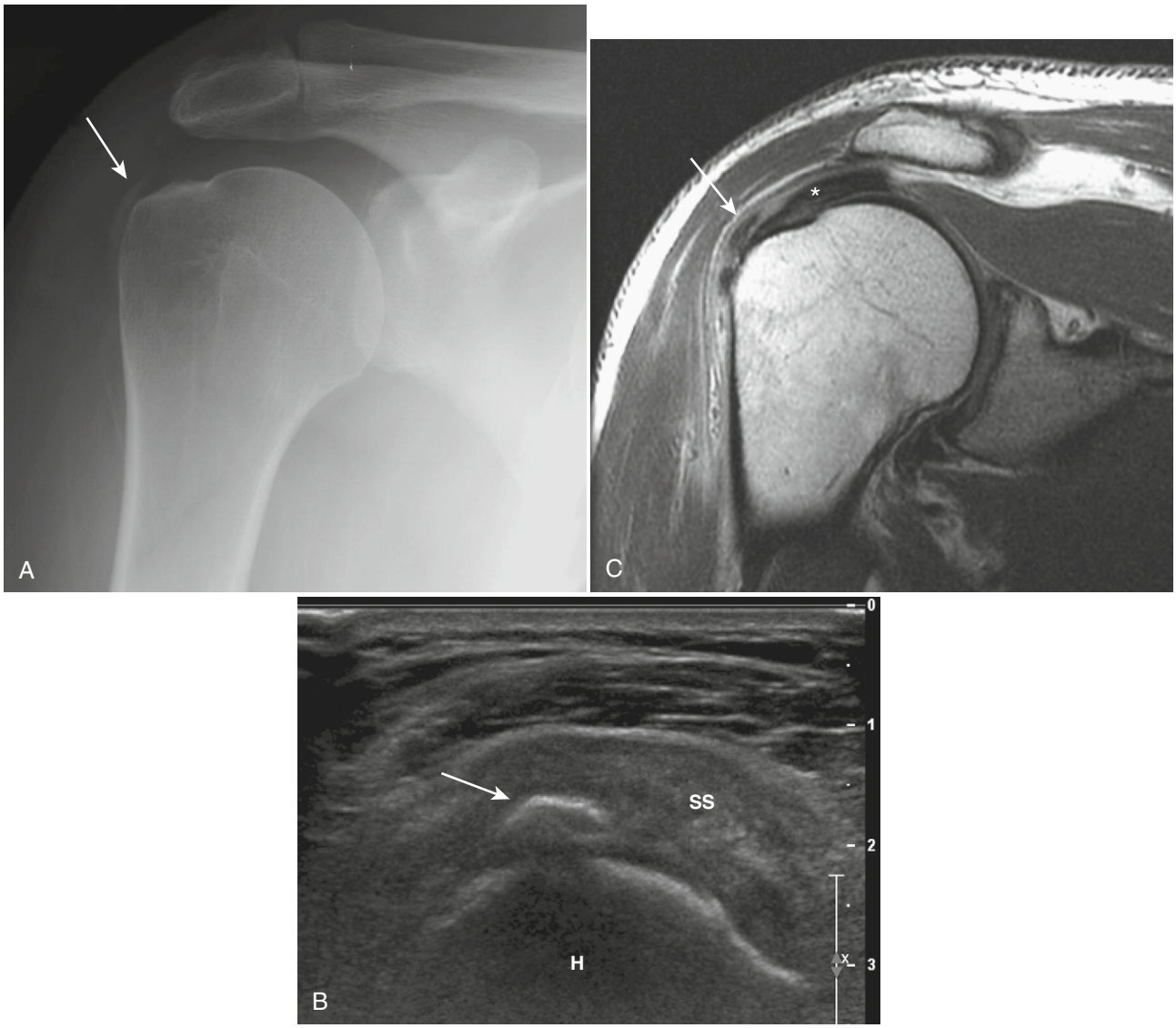


FIGURE 5-1. Calcific bursitis. **A,** External rotation view of the right shoulder in an adult patient presenting to the emergency room with acute exacerbation of right shoulder pain demonstrates periarticular mineralization *(arrow)* adjacent to the greater tuberosity of the humerus. **B,** Oblique longitudinal US image of the shoulder in a different patient also presenting with shoulder pain shows a curvilinear hyperechoic focus *(arrow)* within the supraspinatus (SS) tendon near its humeral (H) insertion. **C,** Oblique coronal proton density MR image in the same patient as **A** shows an amorphous focus of low signal intensity in the subacromial-subdeltoid bursa *(arrow)* superficial to the SS tendon *(asterisk)*.

(T2-weighted and short T1 inversion recovery [STIR]) sequences.

Rotator Cuff Abnormalities and Impingement

The concept of extrinsic subacromial impingement was initially described by Neer in 1972 and continues to be a very controversial topic even today. The notion of impingement is based on the anatomical arrangement of the shoulder joint (fixed component) and on the motion of the humeral head relative to the other components of the shoulder joint (dynamic component). In essence, the rotator cuff tendons (primarily the supraspinatus) and muscles, as well as the subacromial-subdeltoid bursa located between the coracoacromial arch and the humeral head, may be impinged with motion of the arm. It is thought that this repetitive microtrauma from friction will lead to tendon degeneration, bursal inflammation, and, ultimately, a tear of the cuff. The "critical zone" is particularly susceptible to this pathophysiological process; this critical zone has been described as a hypovascular area located on the anterior aspect of the supraspinatus tendon, approximately 1 cm from its insertion. Other factors described as potential contributors to the impingement process are narrowing of the subacromial space by enthesophytes arising from the undersurface of the acromion, advanced acromioclavicular joint osteoarthritis with hypertrophic changes, a type III acromion (anteriorly hooked), and the presence of an os acromiale (secondary ossification center at the tip of the acromion that persists after skeletal maturity as a separate bone). However, impingement can occur without any visible anatomic predisposing factor, and the presence of anatomic variations does not necessarily indicate that there is impingement. Thus, the diagnosis of shoulder

impingement is made mainly on clinical grounds, rather than on the basis of the radiographs alone. The radiologist should focus on describing, characterizing, and grading rotator cuff disease, as well as on identifying potential contributing sources to the impingement process.

The spectrum of rotator cuff pathology includes tendinopathy or tedinosis, partial- and full-thickness tendon tears, and subacromial-subdeltoid bursitis. Most rotator cuff tears are chronic and occur as the result of repetitive microtrauma. Acute rotator cuff tears are rare but do occur, especially in older patients with preexisting chronic impingement and degenerative tendon changes. It is not unusual, however, for patients with acute or chronic rotator cuff tears to seek care at the emergency room on an urgent basis because of severe or acutely worsening shoulder pain.

Radiographs should always be performed initially for evaluation of shoulder pain. However, they are often not contributory. The presence of gas from vacuum phenomenon in the glenohumeral joint strongly suggests the absence of a full-thickness rotator cuff tear. The rotator cuff tendons cannot be directly seen on radiographs; rather, there are a number of radiographic findings that serve as indirect evidence of cuff pathology and impingement (Fig. 5-2). These include superior subluxation of the humerus with a decreased subacromial space (less than 8 mm) and secondary changes in the humeral head, such as sclerosis, flattening, surface irregularity, and cystic changes. Radiographs may also demonstrate potential anatomic causes of impingement (Fig. 5-3).

Direct visualization of the rotator cuff tendons is achieved with MR or US. One of these two methods is usually required to accurately diagnose and characterize rotator cuff tears. Selection of the modality depends on availability, individual expertise, and preference of the interpreting radiologist. Both offer relative advantages and disadvantages, which determine preference, and practice trends vary among different world countries. For example, in the United States, MR is used more commonly than US, perhaps because of its faster learning curve and because the method is easily reproducible and less operator dependent than US. On the other hand, US is a great cost-effective alternative in experienced hands and is the first alternative in many institutions throughout the world.

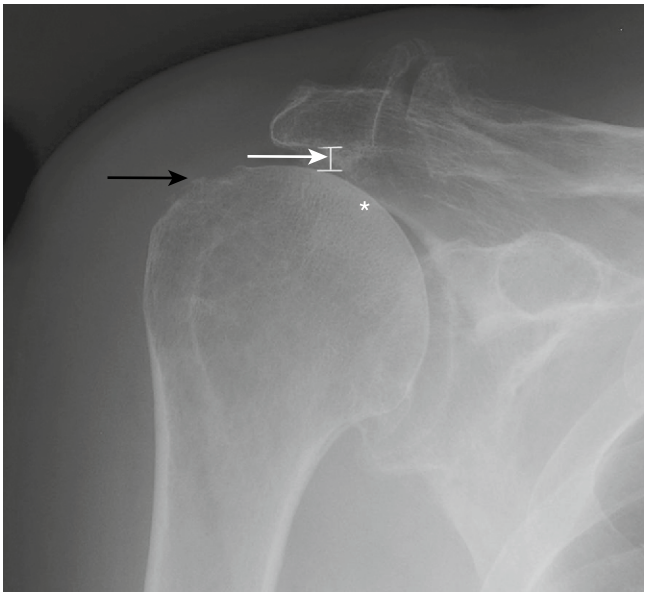


Figure 5-2. Chronic rotator cuff tear indirect signs. External rotation view of the shoulder shows superior subluxation of the humeral head with decreased subacromial space to 4 mm *(white arrow)*, sclerosis of the humeral head *(asterisk)*, and surface irregularity at the greater tuberosity *(black arrow)*.

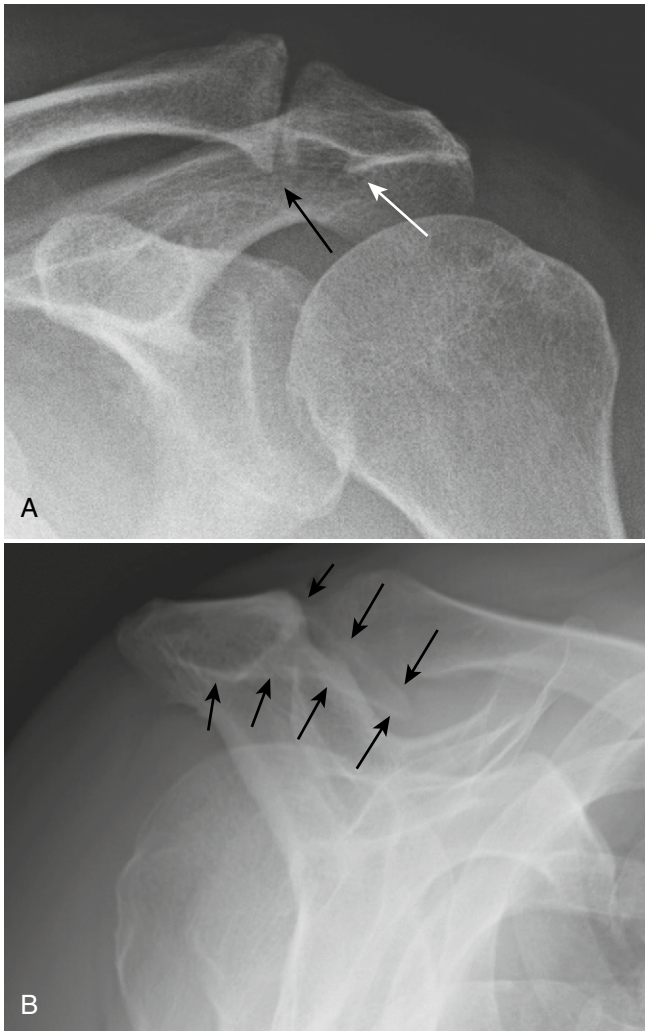


Figure 5-3. Potential anatomic sources of impingement. **A,** Internal rotation view of the shoulder shows an enthesophyte at the undersurface of the acromion *(white arrow)* and hypertrophic changes at the acromioclavicular joint *(black arrow)*. **B,** Y-view of the shoulder reveals a type III (anteriorly hooked) acromion *(arrows)*.

Rotator cuff tendinopathy (tendon degeneration) is characterized on MR by increased signal within the tendon on low TE sequences (T1 and proton density). The tendon may demonstrate associated focal or diffuse thickening, but this is not a constant finding (Fig. 5-4A). Abnormal signal within the rotator cuff tendons in low TE sequences may be seen in a variety of normal situations, and thus there is need for close clinical correlation: most commonly, magic angle artifact as an area of increased signal at 55 degrees from the main magnetic field, which, on oblique coronal planes, coincides with the supraspinatus "critical zone." Cuff tendon tears present as disruption (interruption) of

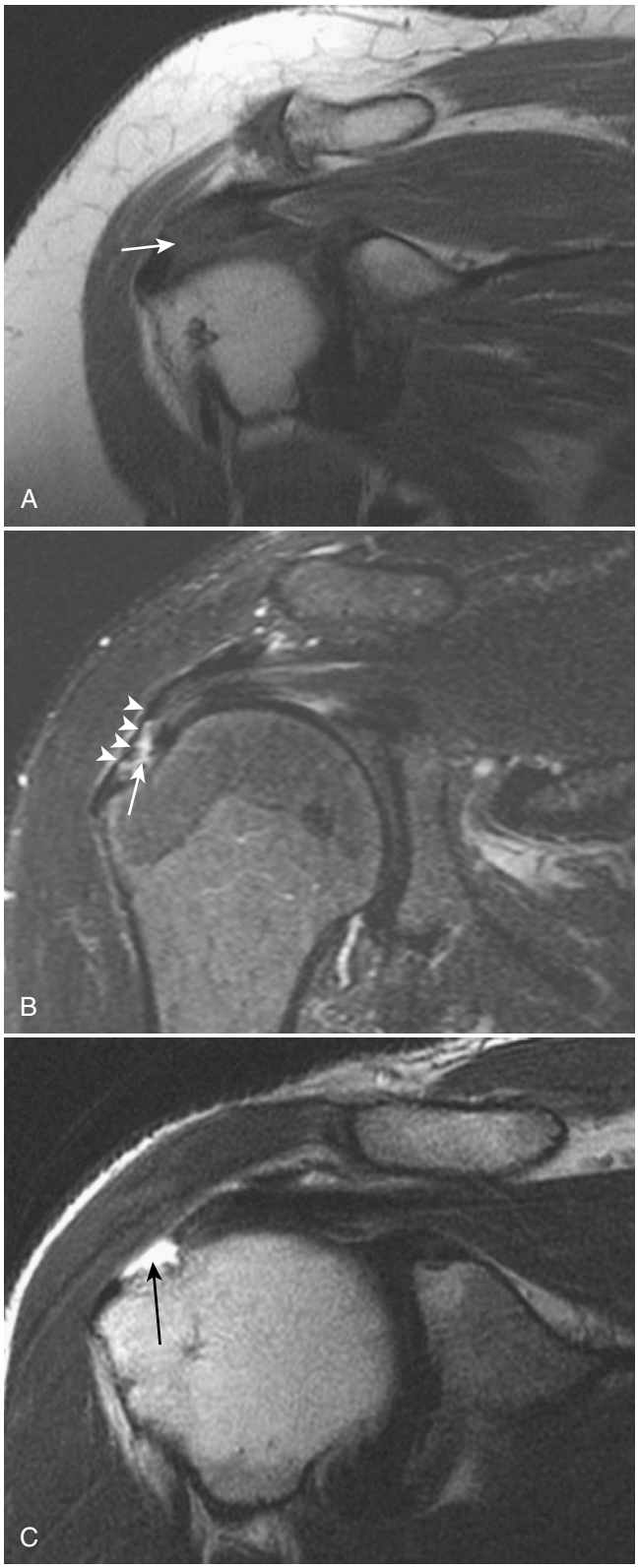


FIGURE 5-4. Spectrum of rotator cuff pathology seen on MR. **A,** Tendinopathy or tendinosis is characterized in this proton-density image as increased signal and thickening *(arrow)* of the supraspinatus (SS) tendon. **B,** Partial thickness, articular surface tear of the SS tendon on an oblique coronal STIR image characterized by fluid signal *(arrow)* between the disrupted articular surface and interstitial fibers and the intact bursal surface fibers *(arrowheads).* **C,** Full-thickness tear of the SS tendon seen on an oblique coronal T2-weighted sequence as fluid signal *(arrow)* extending across the entire thickness of the tendon.

fibers and may be either partial or full-thickness in the craniocaudal plane. High-signal fluid is seen separating the disrupted fibers. This fluid may extend from the articular (inferior) surface superiorly in varying degrees to the bursal (superior) surface (Fig. 5-4B). Partial thickness tears affecting the articular surface are more common than isolated bursal surface tears. In full-thickness tears, fluid invariably extends across the tendon (Fig. 5-4C) into the subacromial-subdeltoid bursa. Subacromial-subdeltoid bursitis may occur in isolation or in conjunction with rotator cuff tears.

Figure 5-5A shows an intact supraspinatus and its relation to the humeral head and deltoid muscle. The primary or direct signs of full-thickness supraspinatus tear in US include nonvisualization of the tendon and a hypoechoic or anechoic full-thickness defect filling the gap of the torn tendon (Fig. 5-5B). Secondary or indirect signs that are helpful to correlate with the primary signs include sagging of the peribursal fat, cortical irregularity at the greater tuberosity, fluid in the subacromial-subdeltoid bursa, and muscle atrophy. Partial-thickness tears manifest sonographically as focal areas of hypoechoic or anechoic tendon defects involving the bursal or articular surface (Fig. 5-5C). An adequate exam requires evaluation of the extension of the defect on two orthogonal planes to confirm the findings. Tendon degeneration is demonstrated as internal heterogeneous echogenicity.

Acromioclavicular Joint Disease (Osteolysis and Osteoarthritis)

The incidence of acromioclavicular joint pathology as a cause of shoulder pain is higher than generally realized. The acromioclavicular joint is often ignored, to the point that it has been termed the "forgotten" or "overlooked" joint. Osteolysis and osteoarthritis are two of the most common causes of shoulder pain arising from the acromioclavicular joint.

Osteolysis

Destruction of bone (osteolysis) may be seen as the result of multiple localized or generalized conditions. Destruction of the distal end of the clavicle is not uncommon and may be idiopathic, post-traumatic, or caused by rheumatoid arthritis, hyperparathyroidism, metastatic disease, multiple myeloma, primary osteolysis syndromes, and infection.

Post-traumatic osteolysis deserves special attention because of its relative frequency as a cause of debilitating pain and painful shoulder motion, and because it very often goes unrecognized. This entity can occur after a single or multiple episodes of minimal or major injury to this region. Most important is the recognition that post-traumatic osteolysis can occur without an obvious acute or known traumatic episode, and in those situations it is thought to be due to repetitive stress, as seen in weightlifters, judo practitioners, and pneumatic tool workers. The pathogenesis is poorly understood, and several theories have been formulated, including a neurologic and/or vascular mechanism, hyperemia, and autonomic phenomenon. More recently, it has been proposed that osteolysis may be the result of a reactive process originating in the synovium or a subchondral fracture.

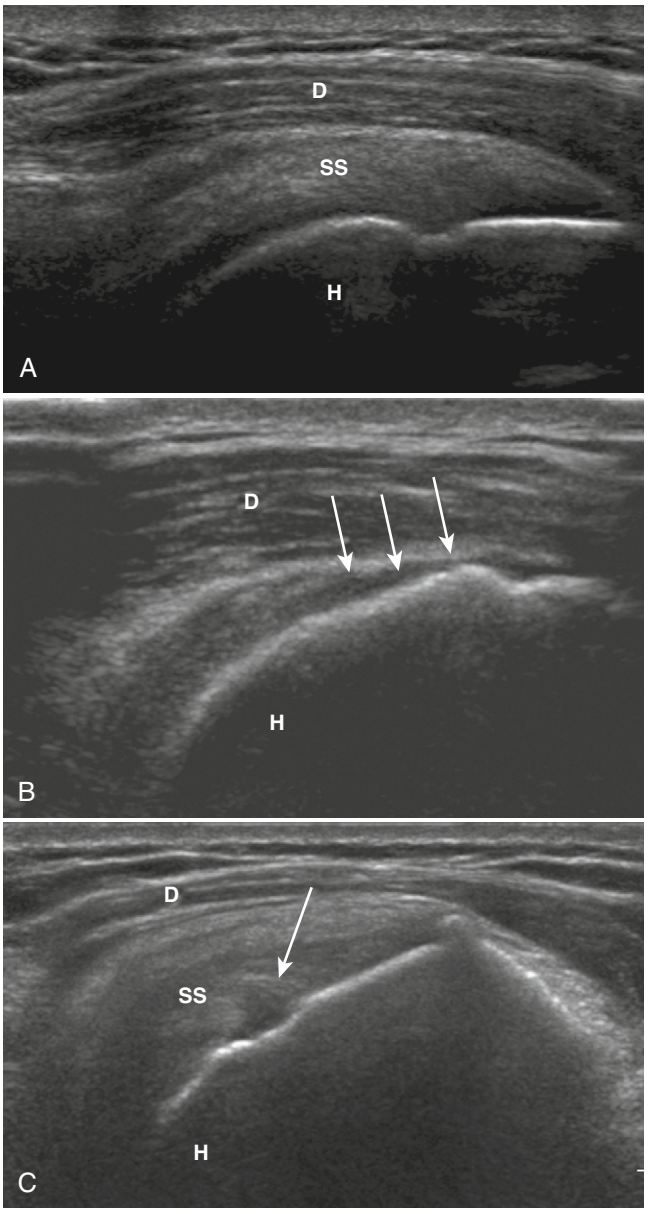


Figure 5-5. Spectrum of rotator cuff pathology on US. **A,** Normal longitudinal image of the left shoulder demonstrating an intact supraspinatus (SS) and its relation to the humeral head (H) and deltoid muscle (D). **B,** Longitudinal US image of the left shoulder with nonvisualization of a fully torn and retracted SS tendon. There is a gap in the expected location of the tendon *(arrows).* **C,** Longitudinal US image of the left shoulder demonstrating a partial-thickness articular surface tear of the SS tendon as a focal hypoechoic area at its insertion *(arrow).* (Courtesy of Alda Cossi, MD.)

When advanced, resorption of the distal clavicle may be easily recognized radiographically (Fig. 5-6), with loss of up to 3 cm of bone and widening of the acromioclavicular joint. The radiologist, however, should focus on identifying early signs, as immobilization seems to diminish the amount of bone loss and shorten the natural course of the lytic phase. Early radiographic signs include soft tissue swelling, demineralization, and loss of the subarticular sclerotic cortex at the distal end of the clavicle. MR findings usually precede radiographic findings. Initially, there is periarticular soft tissue swelling/edema, and a bone

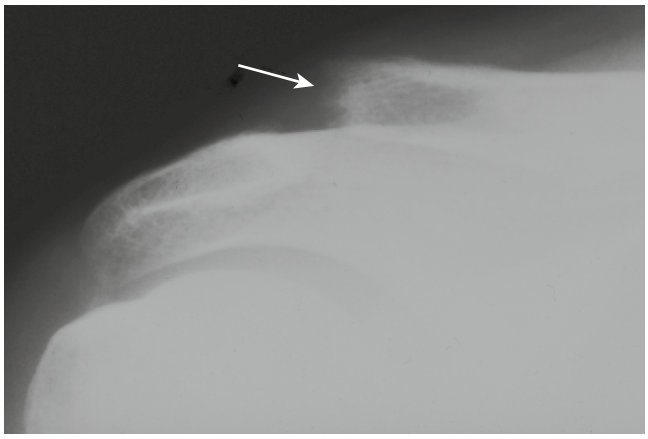


Figure 5-6. Post-traumatic osteolysis. A 28-year-old weightlifter with no recognizable acute trauma presented with acute shoulder pain. Anteroposterior radiograph of the right shoulder revealed a widened acromioclavicular joint and resorption of the distal end of the clavicle *(arrow).*

marrow edema pattern may be evident. The marrow signal abnormality can be limited to the distal end of the clavicle or involve the acromion as well, albeit to a lesser degree. There may be an associated joint effusion, although this finding is variable. The disease process then progresses to bone erosion and frank destruction. Other MR findings include cortical irregularity, subchondral erosion or cystic changes, and a subchondral line suggestive of a subchondral fracture.

Osteoarthritis

Any arthropathy can involve the synovial acromioclavicular joint. Osteoarthritis is, however, the one most commonly found in clinical practice and a very important cause of disability and loss of work hours. The acromioclavicular joint is almost universally affected in the elderly population with osteoarthritis. Shoulder pain caused by osteoarthritis can be severe and incapacitating and can cause affected patients to seek emergency medical attention.

The radiographic hallmarks of osteoarthritis include joint space narrowing, subchondral sclerosis ("eburnation"), subchondral cyst formation, osteophytes, deformity, and malalignment. Although MR is not necessary to detect acromioclavicular osteoarthritis, the acromioclavicular joint should be included in the field of view of all shoulder MR examinations. All imaging findings described on radiographs can be seen on MR. Additionally, MR may depict joint effusions, capsular hypertrophy, and subchondral bone marrow edema pattern. The clinical significance of MR and radiographic findings is poorly understood, as these abnormalities are present in both symptomatic and asymptomatic patients. Some studies suggest that the presence of bone marrow edema pattern and an effusion is associated with pain and that the thickness of the capsule (greater than 3 mm) may be a predictor of a good response to intra-articular injections.

Glenohumeral Joint Disease (Arthropathy and Adhesive Capsulitis)

The glenohumeral joint may be affected by a multitude of conditions. The discussion in this section is limited

to adhesive capsulitis, because of its frequency and complexity, and to rheumatoid arthritis, as this is a very common arthropathy affecting this joint. Only osteoarthritis is more common, and the imaging features of osteoarthritis have already been described for the acromioclavicular joint.

Rheumatoid Arthritis

Rheumatoid arthritis is a symmetric inflammatory arthropathy affecting predominantly the small joints of the hand, wrist, and feet. Involvement of the glenohumeral joint is not infrequent and occurs later in the disease course. Approximately half of patients with rheumatoid arthritis have shoulder symptoms during the first 2 years of their disease.

Conventional radiographs are still important for diagnosis and classification of rheumatoid arthritis. Classically, there is uniform joint space narrowing, periarticular demineralization, subchondral cystic changes, and marginal erosions. Erosions in the shoulder have a predilection for the lateral portion of the humeral head and may resemble a Hill-Sachs deformity (Fig. 5-7). Characteristically, there is lack of productive bone changes. Superior subluxation of the humeral head can also be seen, as chronic rotator cuff tear or cuff atrophy occurs frequently in patients with rheumatoid arthritis. The role of other imaging tests for rheumatoid arthritis is still evolving. US and MR are more sensitive for detection of erosions and soft tissue findings. There may be a role for these modalities in early detection and for evaluation of disease activity or response to therapy. MR can demonstrate erosions earlier than plain radiographs, as well as subchondral cystic changes on both sides of the joint. Erosions are commonly located in the humeral head near the insertion of the rotator cuff tendons. MR can also show common findings not identifiable in radiographs, like joint effusion, signs of synovitis, tears or atrophy of the rotator cuff muscles and tendons, synovial cysts, bursitis, and rice bodies. Routine MR is limited for evaluation of glenohumeral articular cartilage.

Adhesive Capsulitis

Also known as a "frozen shoulder," adhesive capsulitis is a commonly recognized but poorly understood disorder causing severe shoulder pain, stiffness, and disability. Even though the diagnosis of this condition is made clinically, rather than on the basis of imaging findings, radiographs and other tests are often performed to exclude other conditions that can cause shoulder pain and to identify features that may support the diagnosis. Although most imaging is performed on a nonemergent basis, patients with adhesive capsulitis often present in an urgent setting with significant shoulder pain.

Adhesive capsulitis is a synovitis that may be idiopathic or the result of other conditions including multiple arthropathies and trauma. Pathologically, it is shown to be a synovial inflammation with preferential involvement of the rotator interval, axillary pouch, and subscapularis recess. Imaging findings parallel histological findings. Radiographs are not contributory, as might be expected from the description of the underlying pathology. Likewise, MR examinations may show no abnormalities. Findings that support the diagnosis include synovial prominence at the rotator interval with obliteration of the subcoracoid fat, thickening of the coracohumeral and/or superior glenohumeral ligaments, and capsular thickening at the axillary pouch. After intravenous administration of gadolinium chelates, enhancement of the rotator interval and/or axillary recess may be demonstrated. MR arthrography has been advocated because of the added information obtained from estimating the volume of fluid necessary to achieve joint distention (typically decreased in adhesive capsulitis), and the potentially decreased capacity of the axillary pouch and bicipital tendon sheath. However, these findings have

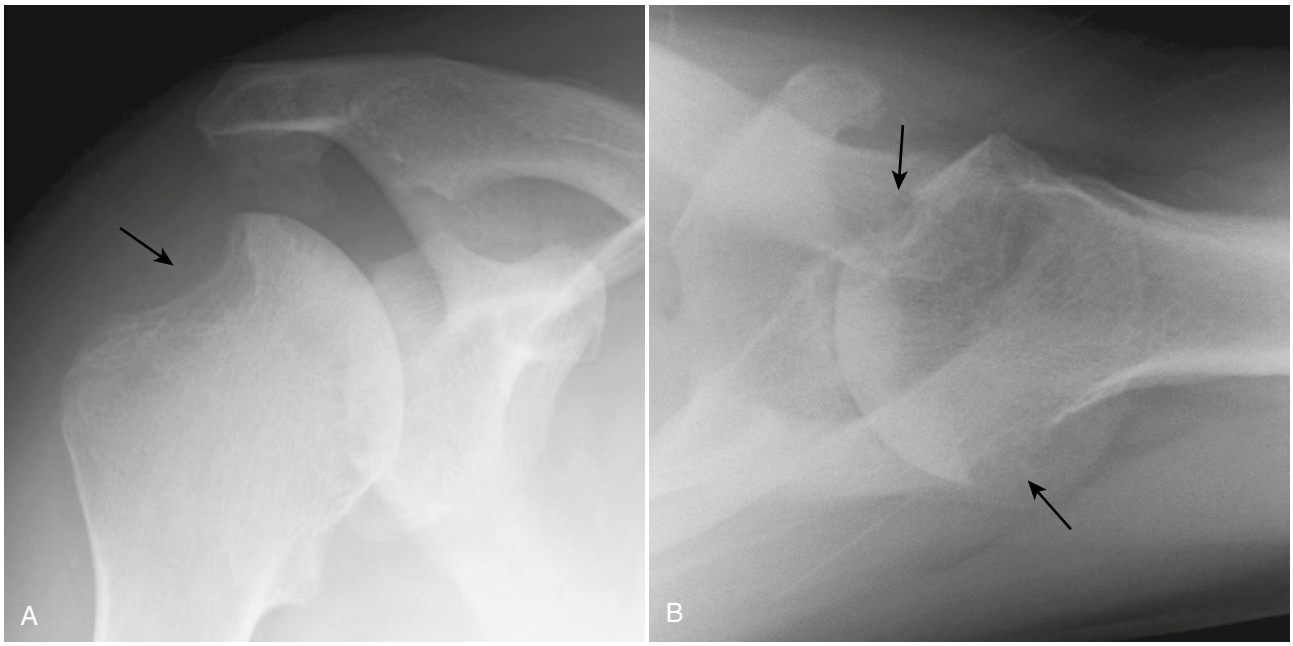


FIGURE 5-7. Rheumatoid arthritis of the glenohumeral joint. Anteroposterior (**A**) and axillary (**B**) views of the right shoulder demonstrate uniform joint space narrowing and large humeral head erosions *(arrows)*.

not been reproduced consistently and there is probably limited added value from MR arthrography as a diagnostic tool for this condition.

THE PAINFUL HIP

Similar to shoulder pain, evaluation of the painful hip in the absence of recognizable acute trauma is challenging and often a diagnostic quandary. Hip pain is also a very common source of emergent and nonemergent medical visits. The causes of hip pain are multiple, and pain may be due to localized abnormalities in the soft tissues, synovium, cartilage, bone, or bone marrow, or may come from distant causes, for example, referred pain from the spine or knee. This section is dedicated to discussing the imaging features of the most common conditions presenting with hip pain, excluding infectious causes, which are described later in this chapter.

As with most other joints, the imaging evaluation of hip pain typically begins with conventional radiographs, even in the absence of history of trauma. The routine examination should include an anteroposterior and a frog leg lateral view of the hip along with an anteroposterior view of the pelvis. The view of the pelvis is essential for comparison with the opposite hip and for detection of subtle abnormalities. The anteroposterior view should be obtained with internal rotation to optimally evaluate the femoral neck. Unfortunately, most patients with hip pain tend to flex and externally rotate the hip for pain relief. This position tends to shorten the femoral neck and makes the evaluation more difficult. The frog leg lateral radiograph is obtained with the hip in abduction and provides a tangential view of the anterior and posterior surfaces of the femoral head.

A systematic evaluation of the radiographs should begin with the soft tissues for swelling, displacement of fat pads, and calcifications. Overall bone alignment, including the acetabular coverage of the femoral head, should be assessed. The width of the symptomatic joint space, as well as symmetry with the contralateral hip, may provide clues about presence of an articular process. The pattern of bone mineralization and trabeculation is also important. Finally, it is mandatory to carefully evaluate for preservation of the pelvic lines and bony contours, particularly of the femoral neck.

Insufficiency Fractures

Insufficiency fractures are a type of stress fracture that occurs when a usual strength or physiologic force is applied to an abnormal or weakened bone. Most insufficiency fractures are caused by osteoporosis. In the pelvis, subcapital neck fractures (Fig. 5-8) are by far the most common. However, these fractures are usually associated with some degree of trauma. Common locations in the pelvis not usually associated with trauma include the sacrum, pubic rami, and supra-acetabular region. Undisplaced insufficiency fractures are very difficult to diagnose on conventional radiographs. Good radiographic technique and a high index of suspicion, especially when evaluating demineralized bones, are essential. If a stress fracture is suspected clinically and radiographs are not diagnostic, an MR examination should be obtained if available. MR is more accurate than scintigraphy. Additionally, MR may

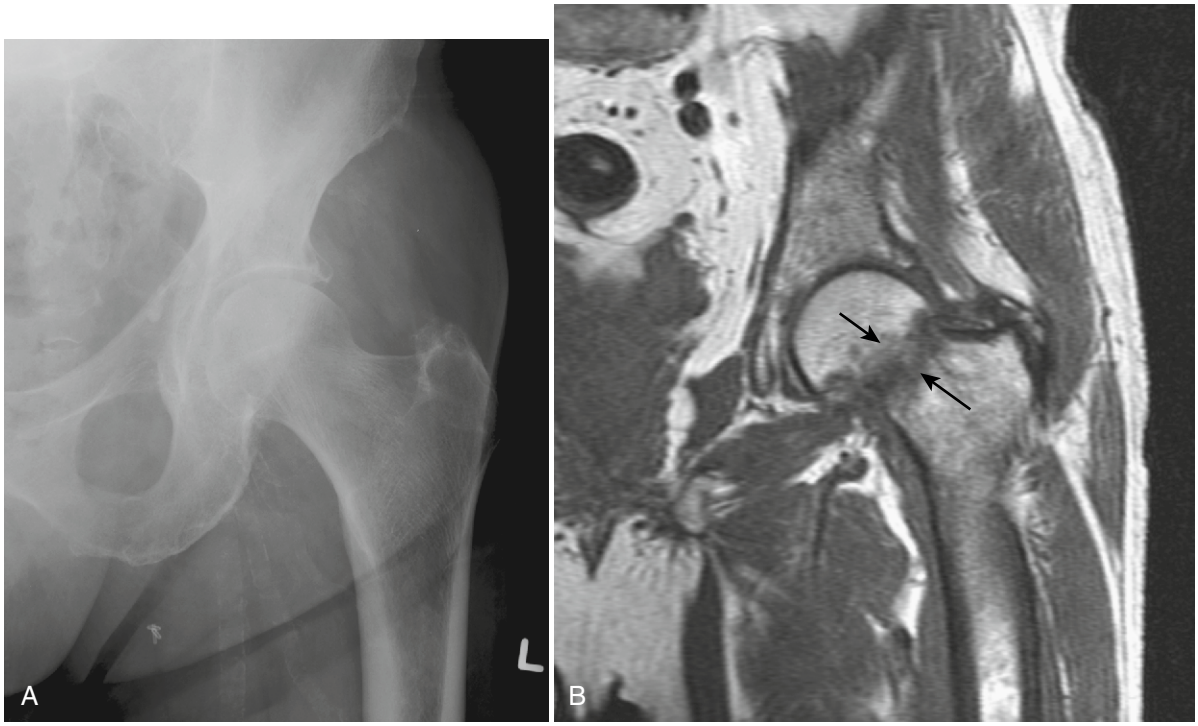


Figure 5-8. Radiographically occult insufficiency subcapital femoral neck fracture. A 74-year-old man presenting to the emergency room with left hip pain and no history of trauma. Anteroposterior view (**A**) of the left hip demonstrates mild demineralization of the bones but no evidence of fracture. Coronal T1 image of the left hip (**B**) revealed an undisplaced subcapital femoral neck fracture characterized by a dark linear band *(arrows)*.

demonstrate coexisting conditions or alternative diagnoses that may influence management.

Radiographic findings may be occult or very difficult to detect and depend on the site of the fracture. Most commonly, a sclerotic band or line is evident. This finding is usually subtle and most often the only indication of a stress fracture. Evaluation for symmetry on the anteroposterior view of the pelvis is essential. Other potential findings include a fracture line, cortical disruption, and periosteal reaction. Supra-acetabular insufficiency fractures should be considered in elderly females with hip pain and no history of trauma. Particular attention should be paid to the distinct trabecular pattern of the acetabulum. Dense trabeculae outline a more lucent triangular area immediately above the sclerotic acetabular roof. A band of sclerosis within this triangular lucent region, parallel to the roof of the acetabulum, is characteristic and should be diagnostic of a stress fracture in most cases (Fig. 5-9).

MR is a highly sensitive and accurate tool for the diagnosis of insufficiency fractures. T1-weighted images may identify the fracture line itself as a serpiginous line of low signal intensity. On T2-weighted images with fat saturation and STIR sequences, the fracture line (high or low signal) may be obscured by the surrounding marrow edema in the acute setting. Linear low-signal intensity on both T1- and T2-weighted sequences located in the supra-acetabular region running parallel to the acetabular roof is the characteristic finding of an insufficiency fracture (see Fig. 5-9).

Bone scintigraphy is also a sensitive modality for the diagnosis of insufficiency fractures. Many times, however, it lacks specificity, demonstrating increased uptake of tracer in the area of fracture.

Transient Bone Marrow Edema and Transient Osteoporosis of the Hip

Transient bone marrow edema describes a painful condition of the hip that eventually resolves without treatment. Transient osteoporosis of the hip is a related condition in which, additionally, there is transient demineralization evident radiographically. Some authors refer to these conditions interchangeably, while others (more purist ones) treat them separately, and reserve the term "osteoporosis" for cases where demineralization is documented. It is unclear whether the high sensitivity of MR for detecting marrow edema pattern enables the diagnosis of the same condition earlier, before demineralization is evident on radiographs. Transient osteoporosis was first described in pregnant women during the third trimester. It is now recognized more commonly in middle-aged men. Complete resolution of symptoms and imaging findings occurs, an average of 6 months after onset. The condition may reappear in the same or other joints after a short interval, and the condition is then called "regional migratory bone marrow edema syndrome" or "regional migratory osteoporosis." The underlying cause of transient bone marrow edema is unknown. Many theories, including aborted osteonecrosis, synovitis, reflex sympathetic dystrophy, and occult trauma, have been proposed.

Transient bone marrow edema or osteoporosis of the hip remains a diagnosis of exclusion. Differential considerations

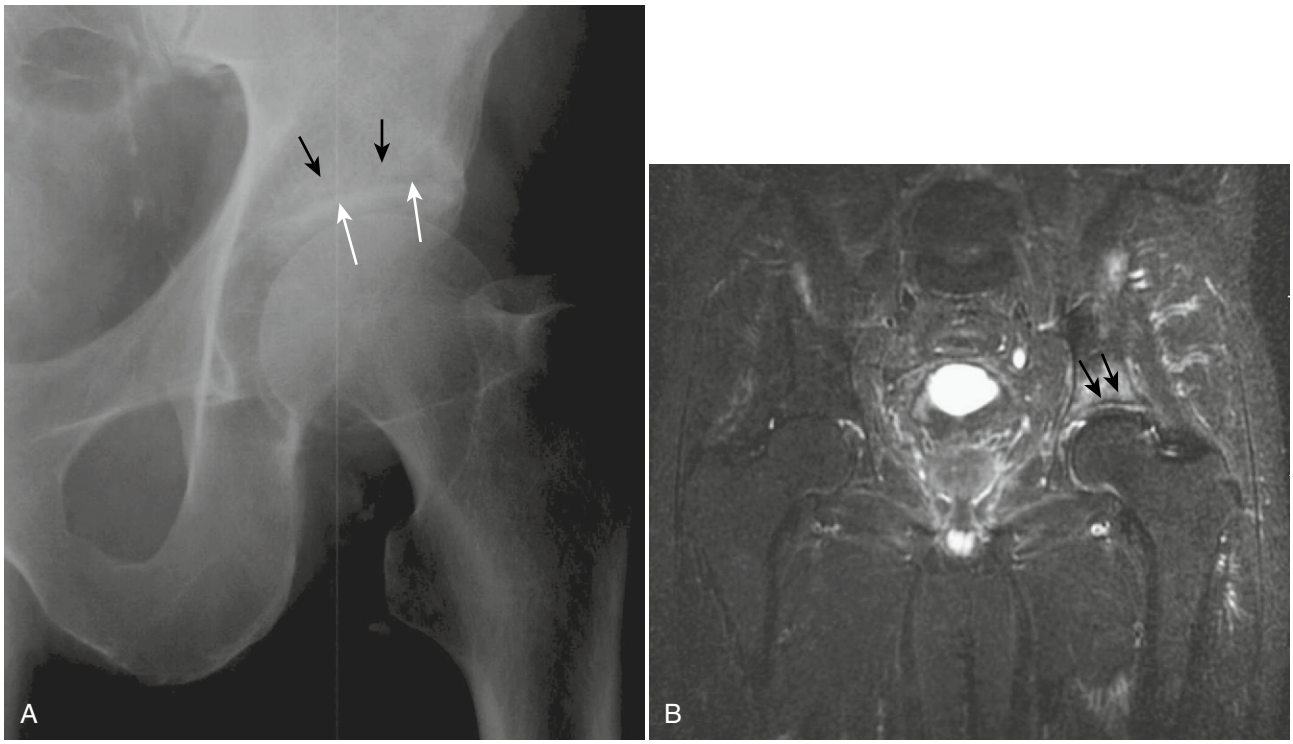


FIGURE 5-9. Insufficiency fracture, left acetabulum. Elderly male with history of prostate cancer, left hip pain, and no history of trauma. Anteroposterior radiograph of the left hip (**A**) demonstrates a band of sclerosis *(black arrows)* parallel and immediately superior to the sclerotic acetabular roof *(white arrows)*. Coronal STIR (**B**) image of the pelvis reveals a bone marrow edema pattern and a low signal line parallel and just superior to the acetabular roof *(arrows)*.

for bone marrow edema affecting only the femoral side of the hip joint include fractures, osteonecrosis, osteomyelitis, and neoplasms.

Conventional radiographs are normal initially and, over time, show variable degrees of demineralization involving the femoral head and neck regions (Fig. 5-10A). The acetabulum may occasionally be involved, but to a lesser degree. The joint space is preserved. Loss of the subchondral cortex of the femoral head is characteristic. Bone scintigraphy is abnormal before radiography. Increased, often extensive and homogeneous, uptake is evident in the femoral head and neck (Fig. 5-10B). MR shows a bone marrow edema pattern in the head and neck of the femur, sometimes extending into the intertrochanteric region (Fig. 5-10C). Mild involvement of the acetabulum is an inconsistent finding. Heterogeneous low-signal intensity on T1 and high-signal intensity on fluid-sensitive sequences are noted. A joint effusion is frequently present. The surrounding soft tissue and the contralateral side are normal.

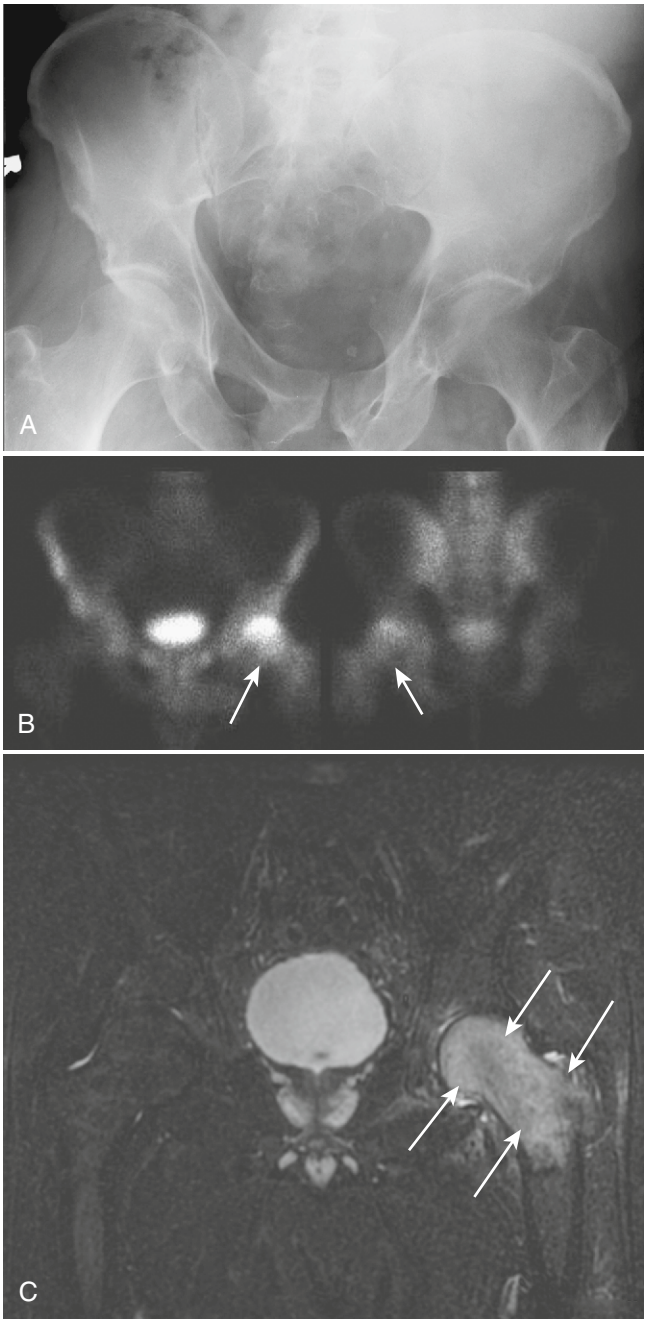


Figure 5-10. Transient osteoporosis of the hip. A 55-year-old male with sudden, severe onset of left hip pain. **A,** Anteroposterior view of the pelvis demonstrates demineralization of the left femoral head and neck. **B,** Anterior and posterior planar bone scintigraphy images of the pelvis demonstrate increased tracer uptake in the left femoral head and neck *(arrows)*. **C,** Coronal STIR image of the pelvis reveals a diffuse bone marrow edema pattern involving the left femoral head and neck extending into the intertrochanteric region *(arrows)*.

Osteonecrosis of the Femoral Head

Avascular necrosis can be defined as ischemic necrosis of bone affecting the epyphyseal or subarticular locations. Histopathological findings are identical to bone infarcts, but by convention the term "bone infarct" is reserved for ischemic necrosis occurring in the metaphyseal or diaphyseal locations. Osteonecrosis, a more descriptive term, can be used for any location. Potential causative factors are multiple, and include trauma, medications (especially steroids), alcoholism, pancreatitis, hemoglobinopathies, radiation therapy, dialysis, hypercoagulable states, barotrauma, and storage diseases (such as Gaucher's disease). Often, however, a specific predisposing factor cannot be identified (idiopathic avascular necrosis). Regardless of the cause, the patterns of bone injury, reactive response, and imaging findings are very similar.

Even though there is no universally satisfactory therapy for early stage disease, diagnosis of this entity before the joint is affected leads to an improved long-term prognosis. The Ficat classification, described in the 1980s, describes five stages based on clinical and radiographic findings (Table 5-1). Additional classification systems incorporating MR findings have also been developed. Imaging plays a pivotal role for the diagnosis, the determination of prognosis, and planning appropriate treatment. The size of the osteonecrosis lesion is an essential parameter for determining prognosis. The presence of bone collapse and joint involvement influences potential treatment options.

Initially, conventional radiographs are normal. In the reparative phase, both lytic and sclerotic areas are identified in the femoral head (Fig. 5-11A). Next, a subchondral fracture may develop. This manifests itself on radiographs as a subchondral crescent lucency ("crescent" sign) and is best seen on the frog leg lateral view (Fig. 5-11B). As

Table 5-1 Osteonecrosis: Ficat Classification

Stage	Pain	Radiography
0	–	Normal
I	+	Normal
II	+	Cysts and/or sclerosis
III	++	Collapse ("crescent" sign, step-off in contour, flattening of articular surface)
IV	+++	Osteoarthrosis (joint space narrowing, acetabular disease)

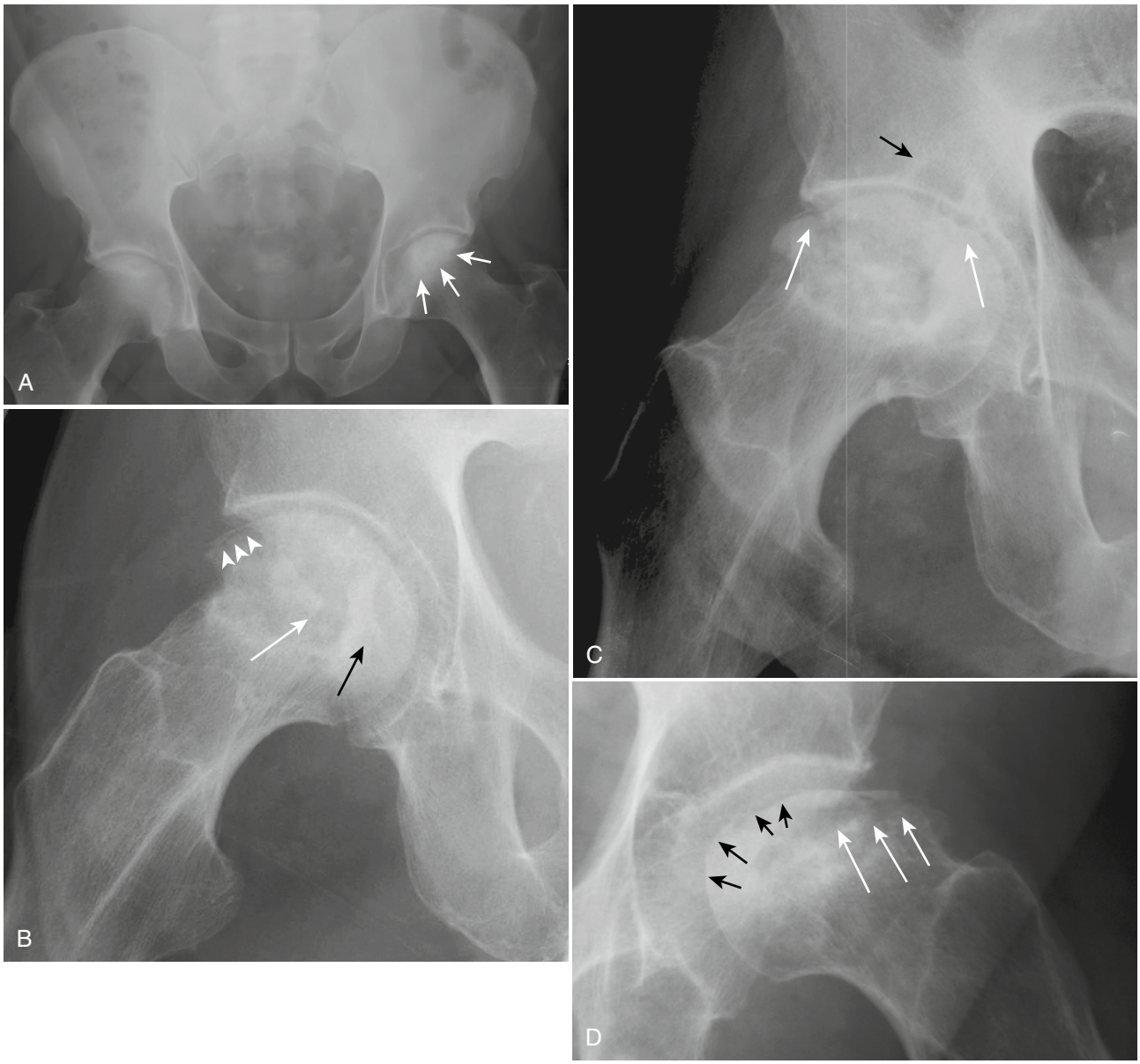


FIGURE 5-11. Osteonecrosis of the femoral head, radiographic spectrum. **A,** Anteroposterior radiograph of the pelvis in a patient with left hip pain demonstrates sclerosis of the left femoral head *(arrows)* and a radiographically normal-appearing right side. MR (not shown) showed findings of osteonecrosis bilaterally (Ficat stage 0 on the right and stage II on the left). **B,** Frog leg lateral view of the right hip in a different patient showing more advanced osteonecrosis with sclerotic *(black arrow)* and lytic areas *(white arrow)* as well as a subchondral crescentic lucency *(arrowheads)* consistent with a subchondral fracture (Ficat stage III). **C,** Frog leg lateral view of the right hip on the same patient as in **B** 6 months later shows more advanced subarticular collapse with new loss of the normal rounded contour of the femoral head *(white arrows)* as well as joint space narrowing and involvement of the acetabulum *(black arrow)* (Ficat stage IV). **D,** Frog leg lateral view of the left hip in a different patient with advanced collapse of the femoral head *(black arrows)* also shows a subchondral fracture *(white arrows)* but preservation of the hip joint (Ficat stage III).

the disease progresses, subarticular collapse may follow; this is seen as a loss of the normal rounded contour and flattening of the femoral head (Fig. 5-11D). Ultimately, severe collapse and destruction of the femoral head will lead to secondary osteoarthritis with joint space narrowing, osteophytes, subchondral cyst formation, and involvement of the acetabulum (Fig. 5-11C).

MR is more sensitive and specific than radiography and scintigraphy (Fig. 5-12). MR provides an accurate estimation of the size of the lesion and demonstrates early subarticular collapse and secondary osteoarthritis. It is essential that the MR examination include both hip joints, as osteonecrosis is bilateral in more than 50% of cases. The superoanteromedial quadrant of the femoral head is most frequently involved. A focal abnormality is seen outlined by a low-signal intensity margin. This margin represents the reactive interface between necrotic and viable bone and extends to the subchondral bone. The characteristic "double line" sign is seen on T2-weighted images and consists of an inner rim or band of high-signal intensity outlined by an outer low-signal margin. A subchondral fracture appears as a high-signal subchondral crescent on fluid-sensitive sequences. Identification of subchondral collapse, when present, is crucial. Flattening of the articular

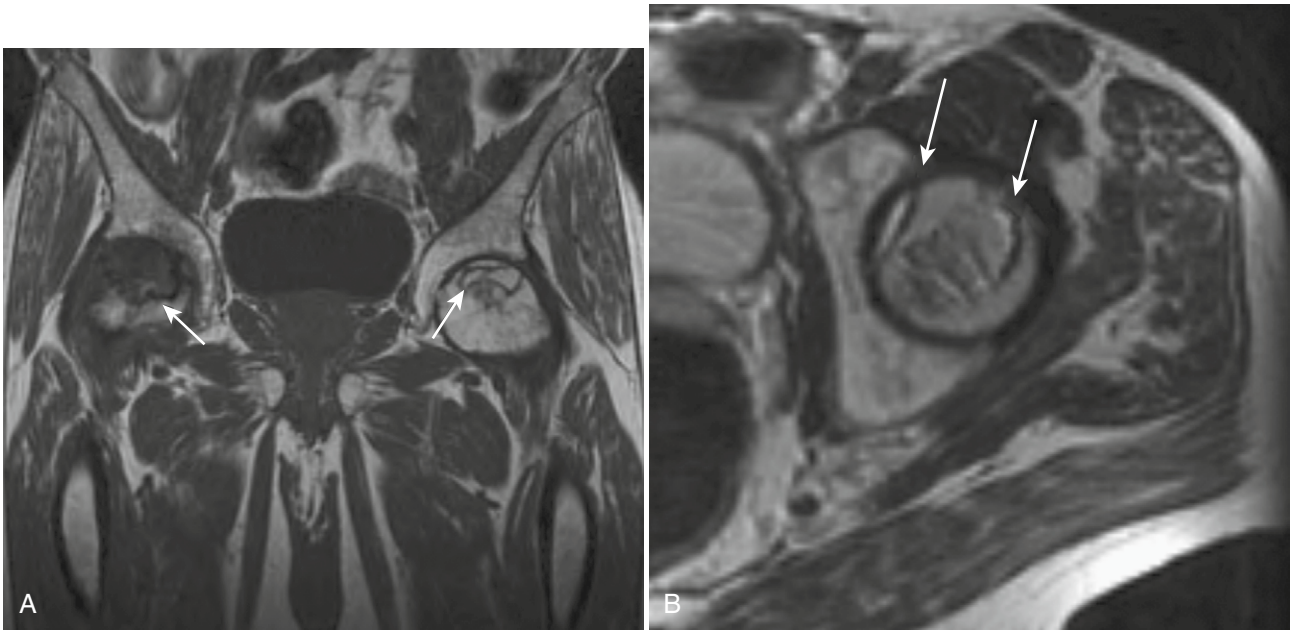


Figure 5-12. Osteonecrosis of the femoral head, MRI spectrum. **A,** T1-weighted coronal image of both hips demonstrates abnormal bone marrow signal in both femoral heads in a distribution pattern consistent with bilateral osteonecrosis. Note focal bone marrow abnormality outlined by a low signal margin *(arrows)*. **B,** Double line sign *(arrows)* on an axial T2-weighted image of the left hip. Linear increased signal outlined by a dark signal characteristic of osteonecrosis.

surface is often seen earlier on the sagittal plane. The MR appearance of late osteonecrosis with severe joint destruction is confusing and may be misinterpreted as neuropathic arthropathy or septic joint. Prior history and prior imaging are of utmost importance for making the differential diagnosis.

Arthropathies

Different types of arthropathies commonly affect the hip joint and can be the source of debilitating and acute pain. Imaging findings may be very subtle. When evaluating the hip joint for a possible arthropathy, the radiologist must carefully evaluate the width of the joint space. The joint space may be widened if there is a sizable joint effusion; this is an important finding of septic arthropathy, discussed later in this chapter. Most arthropathies cause joint space narrowing. The pattern of joint space narrowing provides clues for classifying the arthropathy and limiting the differential diagnosis. Uniform narrowing is typical of inflammatory arthropathies, whereas a nonuniform joint space narrowing is characteristic of degenerative arthropathy. Depositional arthropathies present with preservation of the joint space, but degenerative changes may ensue as the disease progresses, with consequent narrowing of the joint space. Conventional radiographs are usually sufficient to diagnose and categorize hip arthropathies. MR may allow earlier detection of some articular findings and might be useful for evaluating the soft tissue findings that accompany some arthritides.

Osteoarthritis is by far the most common arthropathy affecting the hip. Nonuniform joint space narrowing occurs most commonly superiorly, with the femoral head migrating superomedially or, more commonly, superolaterally. Buttressing (thickening of bone) of the femoral neck is a characteristic but not pathognomonic finding. The classic findings of osteoarthritis, namely, marginal osteophytes, subchondral cyst formation, and eburnation, can also be found in the hip (Fig. 5-13A). Occasionally, acetabular protrusio can be a result of osteoarthritis. In this condition, medial (rather than superior) migration of the femoral head occurs (Fig. 5-13B). Other causes of protrusio include Paget's disease, rheumatoid arthritis, osteomalacia, trauma, ankylosing spondylitis, radiation, and infection. A particularly destructive but rare form of osteoarthritis can be seen with a rapid progression of disease, mainly in the elderly. Awareness of rapidly destructive osteoarthritis is important to avoid misdiagnosis as a more aggressive or infectious arthropathy (Fig. 5-13C). In osteoarthritis, MR directly demonstrates loss of articular cartilage earlier and may also identify synovial cysts. MR is particularly useful in the differential diagnosis of osteoarthritis in cases with a confusing clinical presentation and nonspecific radiographic findings.

Rheumatoid arthritis can affect the hip joint and causes uniform joint space narrowing. Characteristic radiographic findings include bilateral and symmetric periarticular demineralization, erosions, and lack of proliferative changes (Fig. 5-14). Acetabular protrusion if bilateral and symmetric, should favor the diagnosis of rheumatoid arthritis. Additional findings seen on MR examinations include joint effusion, trochanteric or iliopsoas bursitis, tendon ruptures, pannus, and rice bodies.

The seronegative spondyloarthropathies commonly affect the hip joint. These are a group of joint conditions that include ankylosing spondylitis, reactive arthritis (e.g., Reiter's syndrome), psoriatic arthritis, arthritis associated with inflammatory bowel disease, and undifferentiated spondyloarthropathies. The joint space appears uniformly narrowed with productive bone changes. Bone

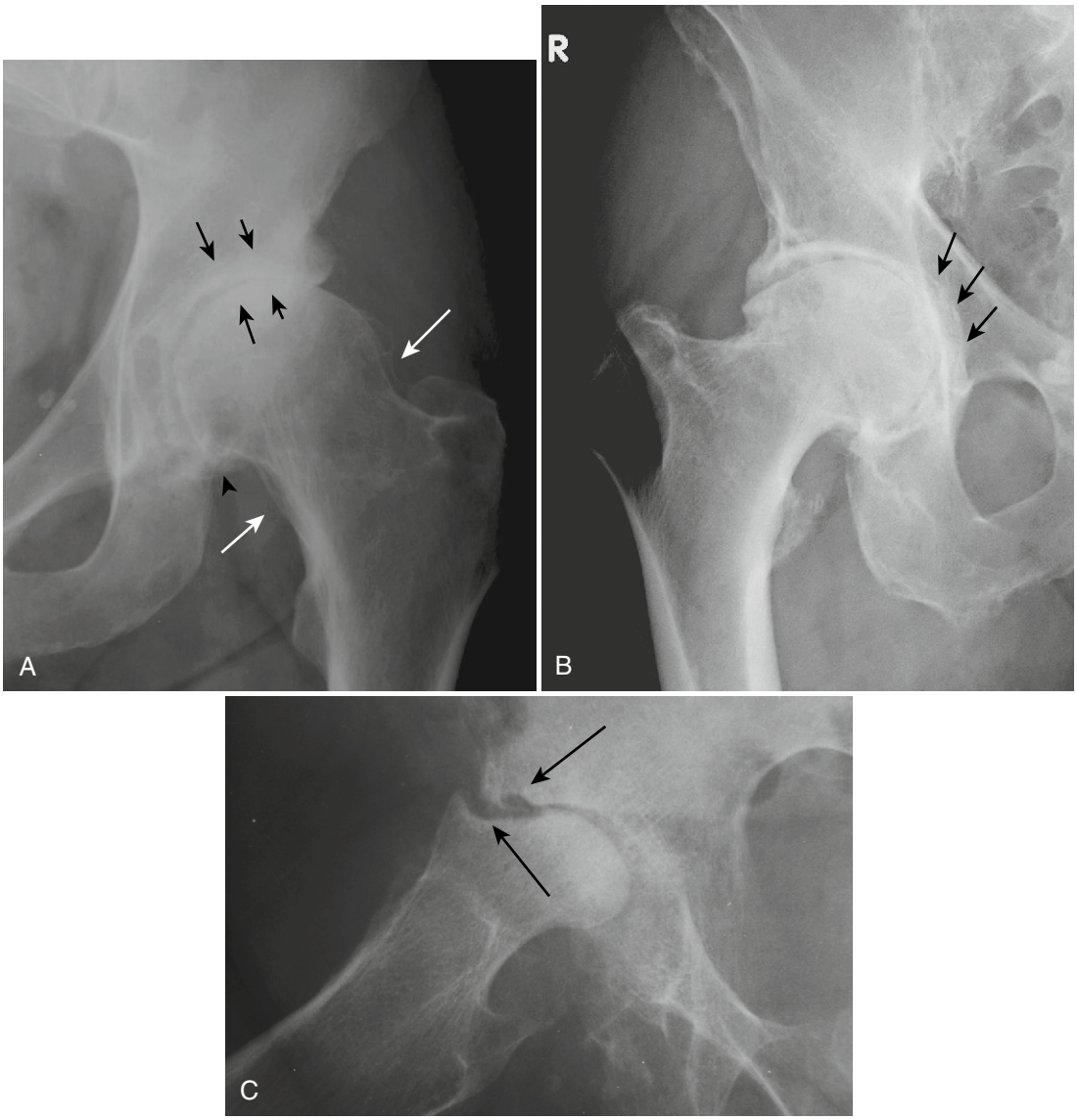


FIGURE 5-13. Osteoarthritis. **A,** Anteroposterior radiograph of the left hip with classic osteoarthritis manifested by nonuniform, superolateral hip joint narrowing, subchondral eburnation *(black arrows)*, marginal osteophytes *(arrowhead)*, and buttressing *(white arrows)*. **B,** Anteroposterior radiograph of the right hip in a patient with protrusio defined as intrapelvic displacement of the medial wall of the acetabulum *(arrows)*. **C,** Rapidly destructive osteoarthritis. Lateral frog-leg view of the right hip in a 72-year-old female with severe right hip joint pain (**C**) demonstrates rapidly progressing destruction as compared to near-normal radiographs 6 months earlier (not shown). Note the destructive changes on both sides of the joint *(arrows)*.

mineralization is relatively preserved. Enthesophytes (proliferative bone changes that occur at the insertions of ligaments and tendons) occur commonly. Late-stage complications include acetabular protrusion and ankylosis. Careful attention must be paid to the sacroiliac joints, which often reveal bilateral symmetric involvement in ankylosing spondylitis (Fig. 5-15) and unilateral or bilateral asymmetric involvement in the other spondyloarthropathies.

Other arthropathies that may involve the hip and may occasionally present with acute pain are synovial chondromatosis and pigmented villonodular synovitis (PVNS). These entities are proliferative diseases of the synovium characterized clinically by joint pain and limited motion. Radiographic appearance is similar for both, with pressure erosion usually along the neck of the femur, periarticular demineralization, and late joint space narrowing. Subchondral cystic changes favor PVNS. The intra-articular deposits of synovial osteochondromatosis often calcify, whereas those of PVNS typically do not. MR typically demonstrates the hemosiderin content on PVNS as focal areas of low signal in all imaging sequences. MR findings on synovial chondromatosis are variable depending on the degree of mineralization of the intra-articular deposits, but most commonly reveal intra-articular areas of low to intermediate signal on T1- and very high signal on T2-weighted images with areas of hypointense calcifications. Similar radiographic and MR findings can be expected with involvement of other joints with PVNS or synovial chondromatosis.

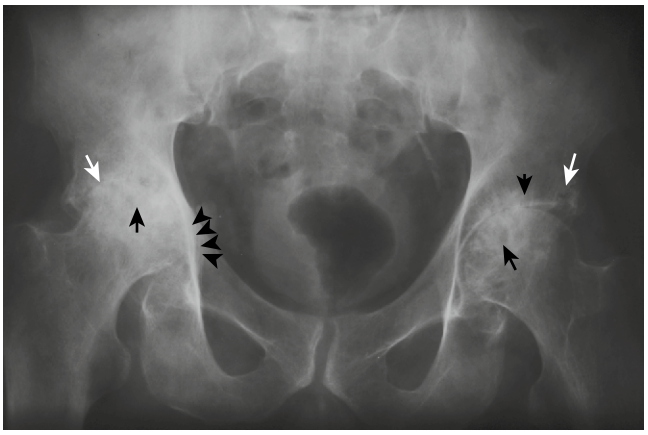


Figure 5-14. Rheumatoid arthritis, hip involvement. Anteroposterior radiograph of the pelvis demonstrates bilateral, symmetric, uniform joint space narrowing. There is mild right protrusio *(arrowheads)*, erosions *(white arrows)*, and subchondral cystic changes *(black arrows)*.

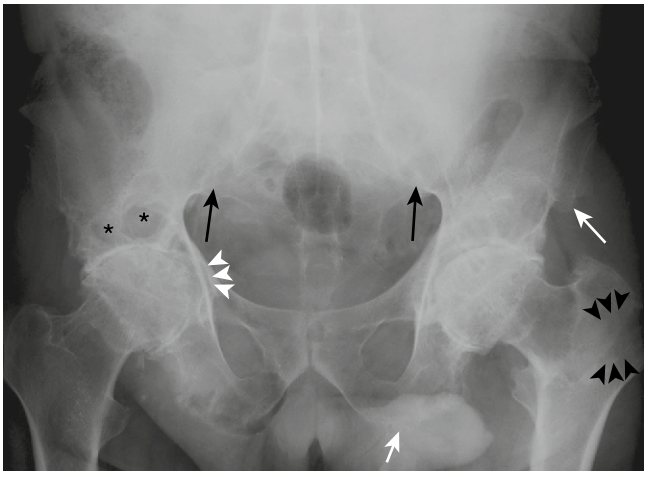


Figure 5-15. Ankylosing spondylitis. A 62-year-old patient presenting to the emergency room with an intertrochanteric fracture after a fall. Anteroposterior view of the pelvis demonstrates a mildly displaced left intertrochanteric fracture *(black arrowheads)*. Also note the symmetric, uniform joint space narrowing of the hips with large subchondral cystic changes *(asterisks)*, enthesophytes *(white arrows)*, ankylosis of the sacroiliac joints *(black arrows)*, and right acetabular protrusio *(white arrowheads)*.

APPENDICULAR MUSCULOSKELETAL INFECTION

Musculoskeletal infection is a common clinical problem. Even though clinical and laboratory findings are of paramount importance, imaging always plays a critical role in the diagnosis and evaluation of the extent of the infectious process. Frequently, imaging identifies involvement of additional sites and other tissues that may not be evident clinically. Early detection and accurate determination of extension are essential to prescribe the appropriate treatment regimen, to decrease morbidity, to avoid complications, and to improve prognosis. This section discusses the imaging features of infections involving the soft tissues, bones, and joints.

Conventional radiographs should always be performed initially despite the lack of sensitivity for soft tissue and early bone infection. The demonstration of bone involvement with radiographs may obviate the need for more expensive imaging tests in some cases. Radiographs may clarify confusing findings of other imaging modalities and may narrow potential differential diagnoses. US is a great tool for appendicular soft tissue infections. Sonography is quick, readily available, and highly sensitive for detecting fluid collections that often accompany focal infections, and may be used to guide interventional procedures such as needle aspirations. The roles of CT and scintigraphy have decreased with the advent and wide use of MR. MR is far more sensitive than both CT and scintigraphy for early detection of soft tissue and bone infection.

Soft Tissue Infection

Cellulitis, an acute suppurative infection of the dermis and subcutaneous tissues, is usually the result of contiguous spread of infection from skin breakdown, and is the initial step in the development of deep soft tissue infections. Findings on radiographs are minimal and nonspecific: increased soft tissue density, soft tissue swelling, and infiltration of the subcutaneous fat. Small radiolucent foci may be seen if gas is present (Fig. 5-16). CT may demonstrate thickening of the skin, subcutaneous tissues, and fascia (Fig. 5-17). US demonstrates increased echogenicity of the involved tissues and anechoic bands traversing the subcutaneous tissues, giving them a cobblestone appearance (Fig. 5-18). Findings on MR are similar, with decreased T1 signal and increased T2 signal in the thickened and infiltrated skin, subcutaneous tissues, and fascia (Fig. 5-19). Enhancement is variable. In clinically confusing cases, the finding of intense enhancement favors the diagnosis of cellulitis over noninfectious causes of subcutaneous edema that otherwise could have the same imaging findings. Three-phase bone scintigraphy demonstrates increased blood flow (initial phase) and blood pool (early phase) activity. Delayed images (third phase) are normal or demonstrate only mild increased uptake of the involved soft tissues.

Necrotizing fasciitis is a rare but very aggressive and often fatal condition characterized by necrosis of subcutaneous and deep fascial tissues. Patients with underlying conditions leading to decreased immunity, such as the elderly, those with HIV infection and leukemia, drug abusers, alcoholics, and those taking immunosuppressive medication,



Figure 5-16. Foot cellulitis. Lateral radiograph of the left foot shows swelling, increased density, and gas *(black arrows)* within the plantar and dorsal soft tissues. Note an ulcer at the plantar aspect of the forefoot *(white arrow)*.

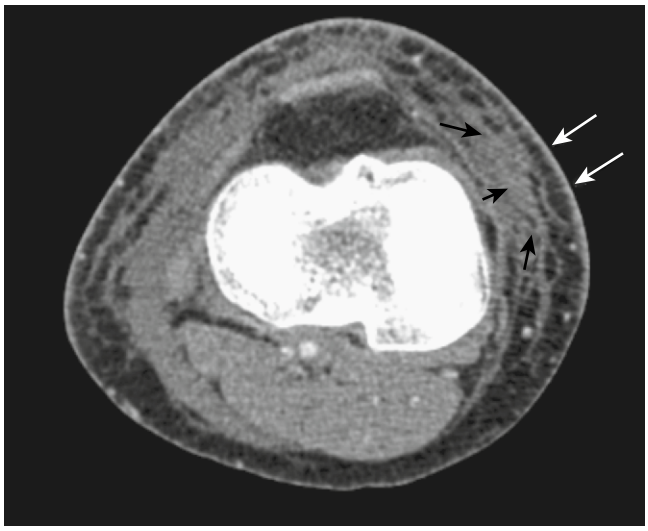


FIGURE 5-17. Leg cellulitis CT. Axial image at the level of the proximal tibia demonstrates skin thickening *(white arrows)*, septations, and inflammatory stranding of the subcutaneous fat *(black arrows)*. These findings, however, are nonspecific and may be seen in multiple conditions that cause subcutaneous edema. CT can demonstrate extension to the deeper tissues and formation of organized fluid collections (abscess).

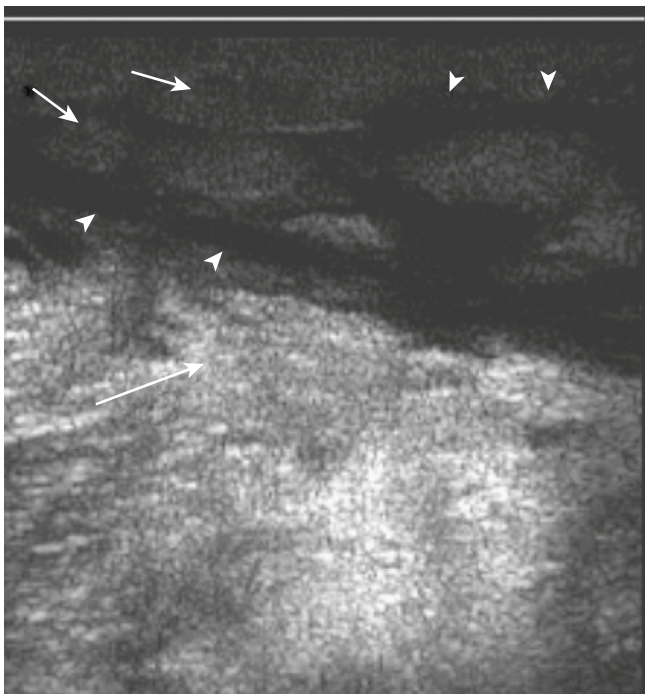


FIGURE 5-18. Leg cellulitis US. Longitudinal image of the leg shows thickening and increased echogenicity of the subcutaneous tissues *(arrows)* with intermixed anechoic bands *(arrowheads)* giving a cobblestone appearance.

are all at increased risk of developing this lethal disease. The infection is most commonly polymicrobial, with both aerobic and anaerobic organisms. The disease is a surgical emergency requiring fasciotomy and extensive débridement of the necrotic tissue. Rapid diagnosis and prompt surgical intervention are essential. Cellulitis has clinical and imaging characteristics similar to those of necrotizing fasciitis, but the treatment is not surgical.

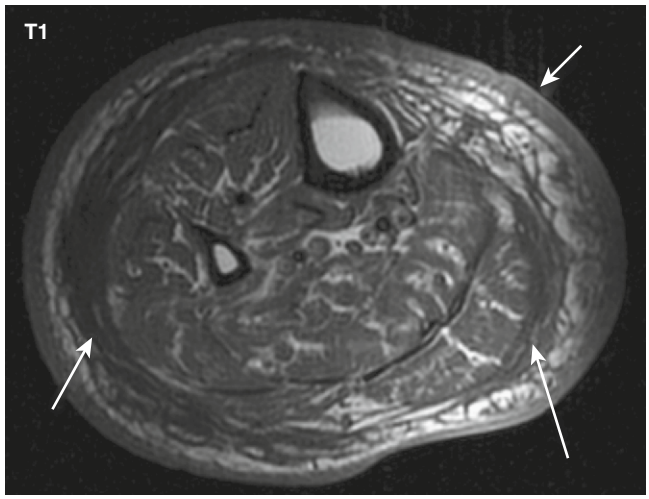


FIGURE 5-19. Leg cellulitis MR. T1, fat-saturated image of the right lower extremity shows decreased signal in the thickened, infiltrated skin and subcutaneous tissues *(arrows)*.

The clinical dilemma always lies between acting rapidly and waiting for imaging test results that may or may not be helpful. If imaging cannot be done expeditiously, delaying surgical intervention is not justified. Radiographic and sonographic findings are similar to those of cellulitis, but with more severe involvement (Fig. 5-20). Presence of soft tissue gas on radiographs is an ominous sign. Severe asymmetric thickening, with air and fluid collections, is the hallmark of necrotizing fasciitis on CT. However, this constellation of findings occurs inconsistently. CT often demonstrates nonspecific thickening and enhancement of the superficial and deep fascial layers. MR images show thickening, high T2 signal, and abnormal enhancement in the subcutaneous tissues and deep fascial planes. However, when necrosis is established, only minimal or peripheral enhancement surrounding the area of necrosis may be present. MR overestimates the extent of deep fascial involvement as compared with findings at the time of surgery. The absence of deep fascial involvement on MR virtually excludes the diagnosis of necrotizing fasciitis.

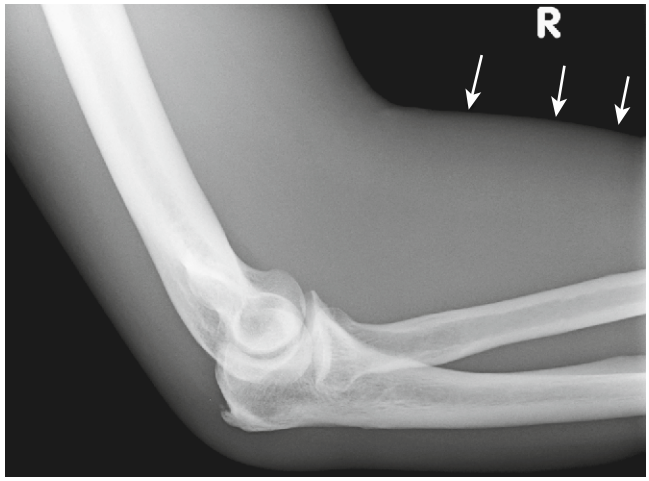


FIGURE 5-20. Forearm necrotizing fasciitis. Lateral radiograph of the elbow demonstrates nonspecific soft tissue swelling and increased soft tissue density *(arrows)*. Necrotizing fasciitis was found at surgery.

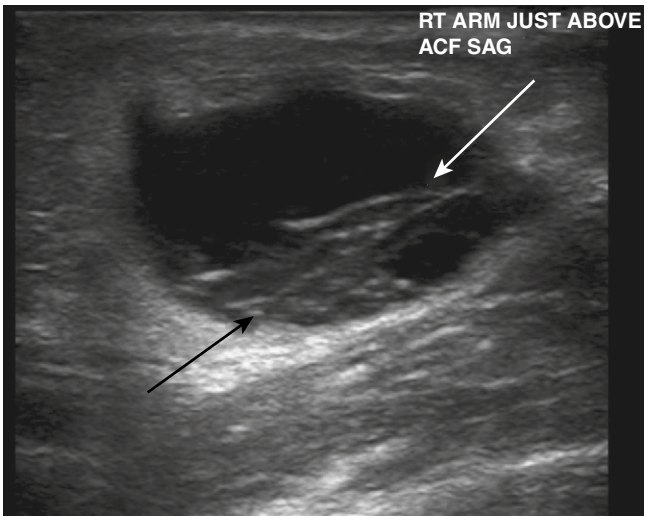


Figure 5-21. Arm abscess US. Single longitudinal US image of the arm just superior to the antecubital fossa in a patient with soft tissue infection demonstrates a complex, hypoechoic, predominantly cystic fluid collection with increased through-transmission internal septations *(white arrow)* and dependent debris *(black arrow)*.

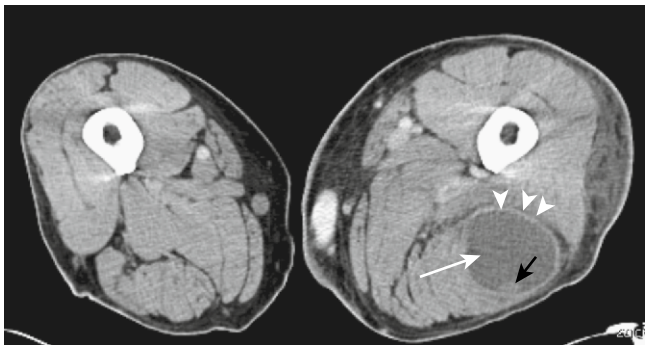


Figure 5-22. CT image of a posterior thigh abscess. Axial image of a contrast-enhanced CT scan of the thigh shows a well-defined low-attenuation fluid collection *(white arrow)* with a thick enhancing wall *(arrowheads)* and an internal focus of high attenuation *(black arrow)*.

An abscess is defined as a localized collection of pus (necrotic tissue, inflammatory debris, and bacteria). An earlier stage in the development of an abscess, before liquefaction and organization ensue, is called a phlegmon. An abscess can occur anywhere in the soft tissues and, when located in a skeletal muscle (which is relatively resistant to infection), the term pyomyositis is used. Radiographs may be noncontributory, showing only diffuse or focal increased soft tissue density, focal prominence of the affected soft tissues, and displacement of fat pads. The sonographic appearance of abscesses is variable. Most commonly, a complex hypoechoic, predominantly fluid-containing mass with increased through-transmission is identified. The margins of the mass may be well or ill defined, depending on the stage of evolution. Internal septations and amorphous internal echoes are additional common findings (Fig. 5-21). Often, dynamic evaluation of the area with gentle compression is necessary to reveal the liquid nature of the contents. Color or power Doppler demonstrates absent internal flow and hyperemia of the wall and adjacent tissues. CT reveals an organized low attenuation fluid collection with an enhancing wall of variable thickness (Fig. 5-22), internal septations, and high-attenuation internal foci. Surrounding edema or findings of cellulitis are common. MR depicts abscesses and adjacent soft tissue changes to greater advantage (Fig. 5-23). Focal fluid collections demonstrating low or intermediate signal on T1- and high signal on T2-weighted sequences surrounded by reticulated, edematous soft tissue are characteristic. Intravenous contrast increases the conspicuity of the lesion with intense peripheral (wall) enhancement.

Infectious Arthritis

Infectious arthritis is a common clinical problem with devastating consequences if not diagnosed and treated early. It is classified as pyogenic (septic) or nonpyogenic. Pyogenic causes are divided into gonococcal and nongonococcal. Staphylococcus and streptococcus species are the most common pathogens causing nongonococcal septic arthritis. Nonpyogenic pathogens include mycobacteria, fungi, and viruses. Synovial involvement occurs first and may be the result of hematogenous spread, spread from a contiguous focus, direct implantation, or postsurgical contamination. Septic arthritis is monoarticular in the majority of cases and can affect any joint. The prevalence of the specific joint affected depends on the mechanism of infection and the patient population studied. Risk factors include advanced age, diabetes, underlying rheumatoid arthritis, recent joint surgery, presence of soft tissue infection, intravenous drug abuse, infection with HIV, and other immunosuppression states. Although the imaging findings of septic arthritis are discussed in this section, it should always be kept in mind that the most rapid and definitive test for making a diagnosis of septic arthritis is arthrocentesis and microbiological evaluation of the aspirated joint fluid.

Early findings on conventional radiographs include periarticular demineralization, joint widening/effusion, and soft tissue swelling. Later, there may be joint space narrowing, periosteal reaction, erosions (both marginal and central), destruction of the subchondral bone, subluxations and dislocations, and, ultimately, ankylosis (Figs. 5-24 and 5-25). Intra-articular gas is a rare finding. The diagnosis of septic joint superimposed on known rheumatoid arthritis or other inflammatory arthropathy is very challenging. Infection should be suspected if there is widening of the joint space along with rapid articular destruction and significant soft tissue asymmetry.

Sonography is very sensitive for demonstrating a joint effusion and an excellent tool for aspiration guidance. Synovial thickening is seen consistently in infectious and inflammatory arthropathies. Bone scintigraphy demonstrates increased blood flow, prominent blood pool, and increased delayed activity in the distribution of the affected joint. The use of gallium citrate as a marker of inflammation has been greatly replaced by imaging with labeled leukocytes, either with indium 111 or technetium 99m hexamethylpropylene-amine-oxime. Increased tracer uptake of these agents in the joint improves specificity for the diagnosis of infectious arthritis (see Fig. 5-24).

CT is rarely used for imaging patients with suspected joint infection, except for patients with orthopedic hardware. All findings described in conventional radiographs may

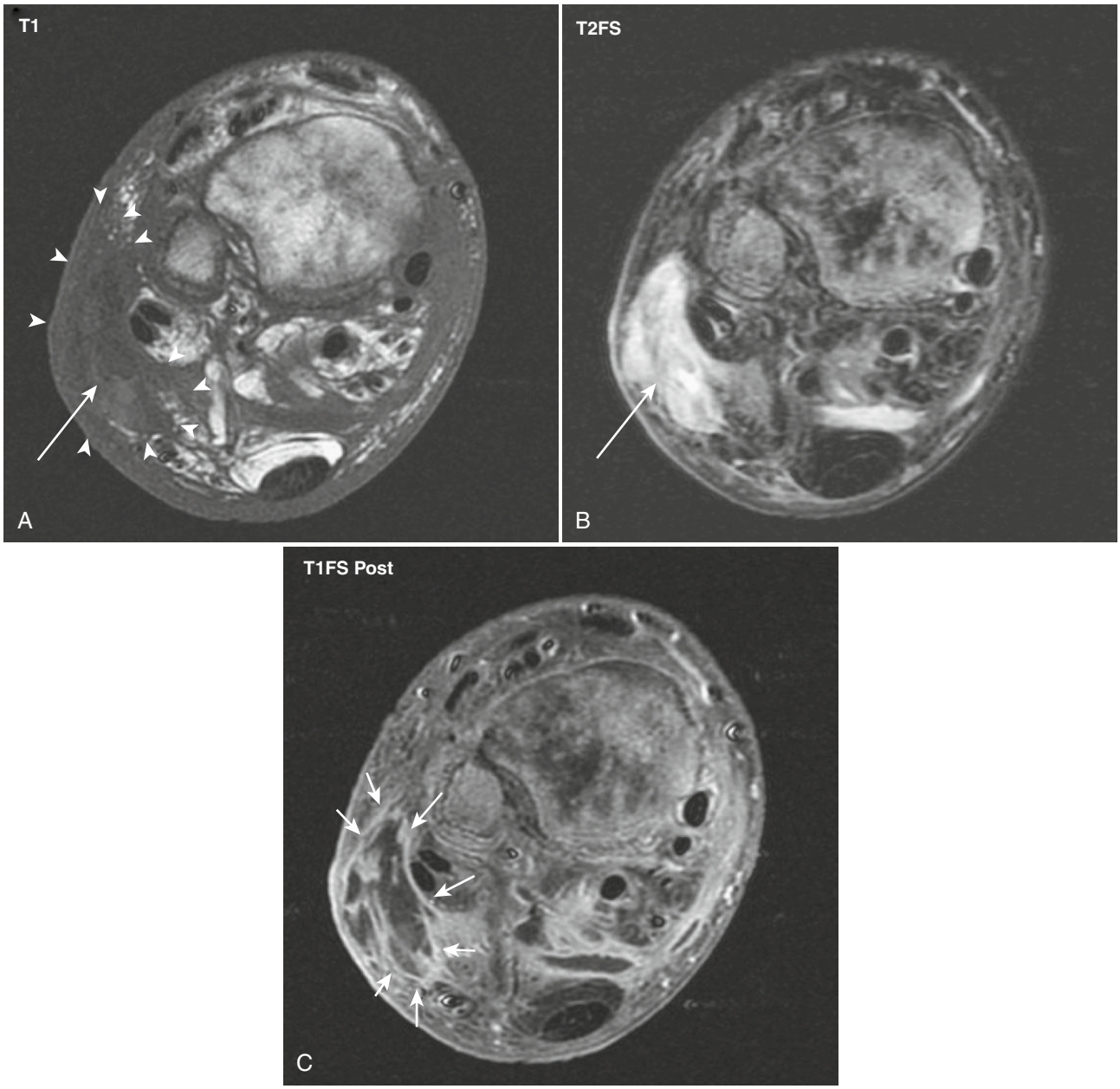


FIGURE 5-23. Subcutaneous abscess at the posterolateral ankle. T1 (**A**), fat-suppessed T2 (**B**), and fat-suppressed, post-contrast T1 (**C**) axial images of the ankle demonstrate a focal complex fluid collection with heterogeneous foci of low T1 and high T2 signal (**A** and **B,** *arrows*). Note the peripheral enhancement (**C,** *arrows*) and adjacent edematous soft tissues (**A,** *arrowheads*).

be seen on CT, easier and earlier (see Fig. 5-24). Additionally, synovial thickening may be identified. Synovial and periartcular soft tissue enhancement is variable.

MR is highly sensitive and more specific than other imaging modalities for the detection of septic arthritis. MR easily demonstrates even a small joint effusion, which is often the first sign of an infected joint. However, an effusion does not necessarily indicate the presence of infection. Other MR findings include synovial thickening and perisynovial edema, seen as periarticular areas of increased signal on fluid-sensitive sequences. Focal abnormal bone marrow signal in the adjacent bone is not diagnostic of superimposed osteomyelitis, as it may be a reactive change. Superimposed osteomyelitis is favored when the bone marrow signal abnormality is diffuse and is seen mostly as decreased signal on T1-weighted images. After intravenous administration of gadolinium chelates, there is synovial and perisynovial soft tissue enhancement. Intense synovial enhancement is not a normal finding in a healthy joint.

Acute Osteomyelitis

A proper use of pertinent terms is important when discussing imaging of osteomyelitis. Osteomyelitis indicates infectious involvement of the bone marrow. Infective osteitis is infection of the bone cortex and infective periostitis infection of the periosteum. These entities are often seen together, as the infectious process may extend outward from the marrow or inward from the soft tissues. As with infectious arthritis, multiple mechanisms can cause the

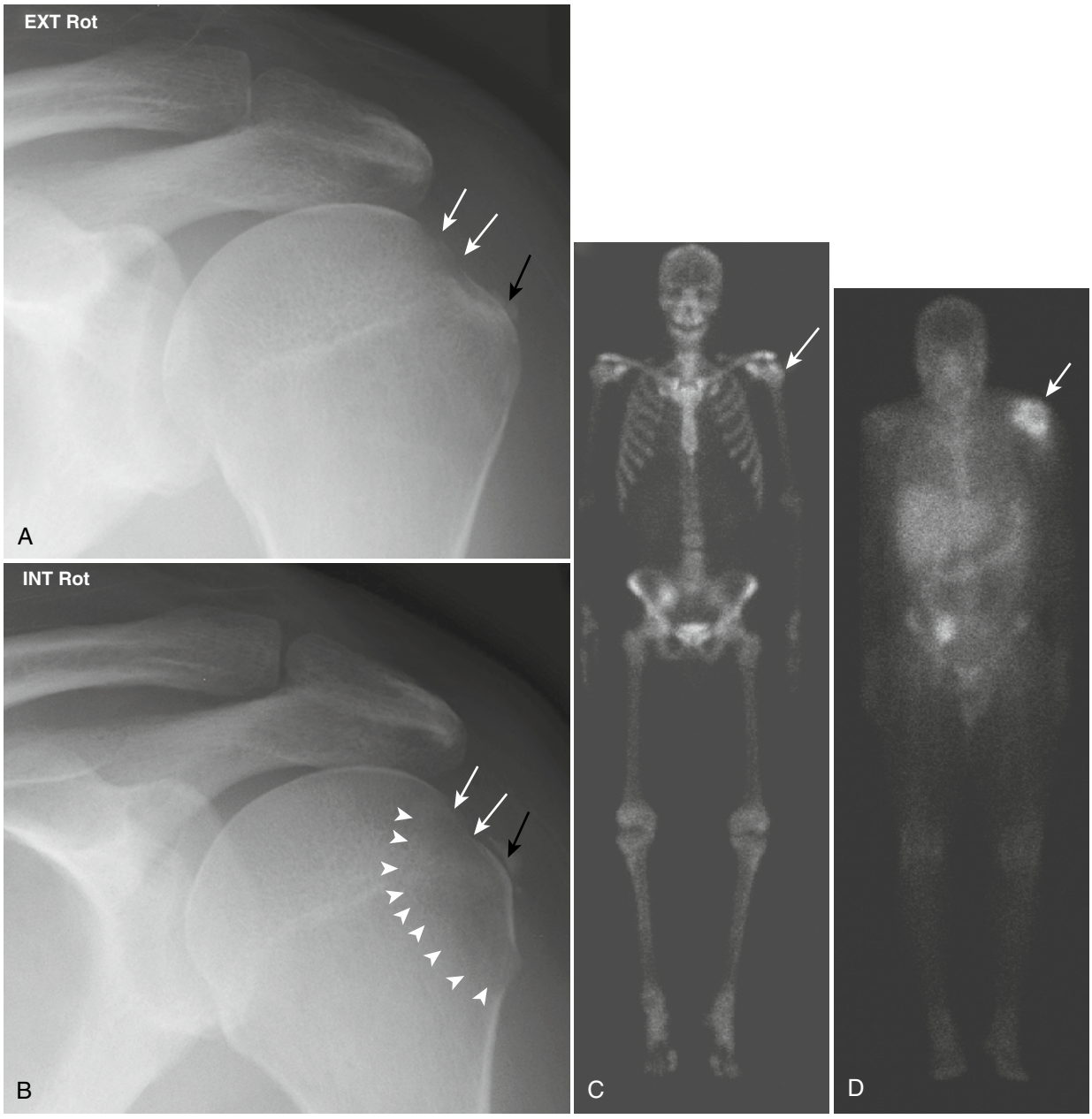


Figure 5-24. Septic arthritis of the left shoulder and humeral head osteomyelitis in a 36-year-old intravenous drug–addicted male patient presenting to the emergency room with left shoulder pain. External rotation (**A**) and internal rotation (**B**) anteroposterior radiographs of the left shoulder show cortical irregularity and destruction of the subchondral bone *(white arrows)* as well as well-demarcated focal osteopenia *(arrowheads)*. Incidental calcific bursitis is also noted *(black arrows)*. Total body anterior bone scintigram (**C**) and anterior total body gallium scan (**D**) demonstrate abnormal increased uptake in the left shoulder region *(arrows)*. Note that the extent of involvement is much greater in the gallium scan, suggesting additional involvement of the soft tissues.

inoculation of an infectious agent into the bone. Hematogenous spread is rarely the source of acute primary osteomyelitis in the adult appendicular skeleton. More commonly, osteomyelitis in the adult occurs from direct spread or surgery. Contiguous spread from ulcerations is most common in patients with foot ulcers (such as the diabetic foot), patients who suffered a spinal cord injury, and bedridden patients.

The overall sensitivity of conventional radiographs for early osteomyelitis is poor. Appearance of radiographic findings may be delayed for weeks after the initial infection. The earliest sign is usually swelling of the deep soft tissues. Early radiographic findings in the bone itself include focal demineralization and periosteal reaction. However, periosteal reaction may be absent in small bones such as those of the feet. Later, cortical lucency and frank bone destruction occur (see Fig. 5-25). Sonography is limited for the diagnosis of acute osteomyelitis. Deep soft tissue swelling, adjacent to the bone, may be seen, but this finding is nonspecific. A fluid collection immediately adjacent to the bone in the proper clinical setting is highly suggestive of osteomyelitis, but is rarely observed. CT is helpful in selected cases of acute osteomyelitis, although osseous findings may be detected to greater advantage and earlier than in radiographs. These include focal demineralization of the affected bone, cortical destruction, periosteal

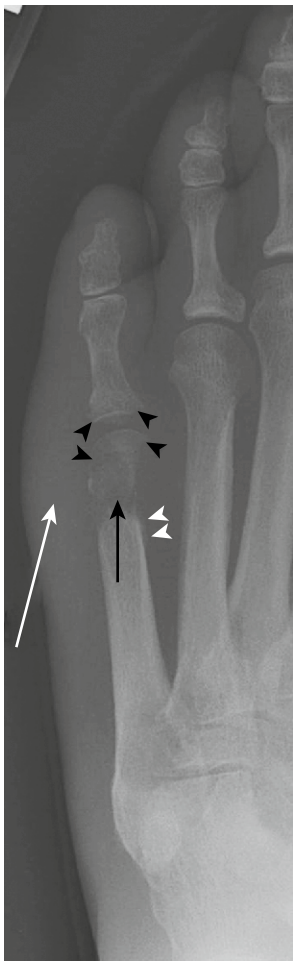


FIGURE 5-25. Osteomyelitis. Anteroposterior radiograph in a diabetic patient with osteomyelitis of the left fifth metatarsal head and septic arthritis of the metatarsophalangeal joint demonstrates focal soft tissue swelling *(white arrow)*, focal demineralization *(black arrow)*, frank bone destruction, and minimal periosteal reaction *(white arrowheads)*. Note widening of the metatarsophalangeal joint and marginal erosions at both sides of the joint *(black arrowheads)*.

reaction, and hyperattenuation of the bone marrow. Soft tissue findings associated with osteomyelitis can also be demonstrated.

Three-phase bone scintigraphy is a highly sensitive test for the diagnosis of osteomyelitis. There is increased focal or regional uptake in the initial blood flow and early blood pool images. Focal increased activity in the affected area of the bone is noted on delayed images. A normal bone scan excludes the diagnosis of osteomyelitis, unless there is severe underlying vascular disease. Unfortunately, the specificity of bone scintigraphy is low, as many other conditions, such as trauma, prior surgery, or underlying arthropathy, can present with similarly abnormal findings. Labeled white blood cell scintigraphy or gallium scan may be performed in conjunction with bone scan to increase specificity. Focal accumulation of radiotracer paralleling bone scan findings is consistent with osteomyelitis.

MR is the imaging test of choice that should be obtained whenever osteomyelitis is suspected and radiographs show normal findings. Furthermore, MR may be indicated even in the presence of abnormal radiographs for evaluation of extent of infection and for planning potential surgical interventions. MR may also be helpful in limiting the differential diagnosis of patients with complex radiographic abnormalities, or whenever the presence of underlying bone pathology limits the specificity of plain radiographs. MR findings of osteomyelitis can be divided into those affecting the osseous structures and those affecting the soft tissues.

Soft tissue findings are almost invariably seen in patients with osteomyelitis. Soft tissue findings include ulcers, sinus tracts, cellulitis, and abscess formation (Fig. 5-26). The MR features of most of these conditions have already been described in this chapter. An ulcer presents on MR as a cutaneous and soft tissue defect with granulation tissue at its base, which usually enhances avidly after administration of gadolinium chelates. Sinus tracts may extend outward from the bone to the superficial soft tissues and skin or inward from an ulcer toward the bone. Sinus tracts

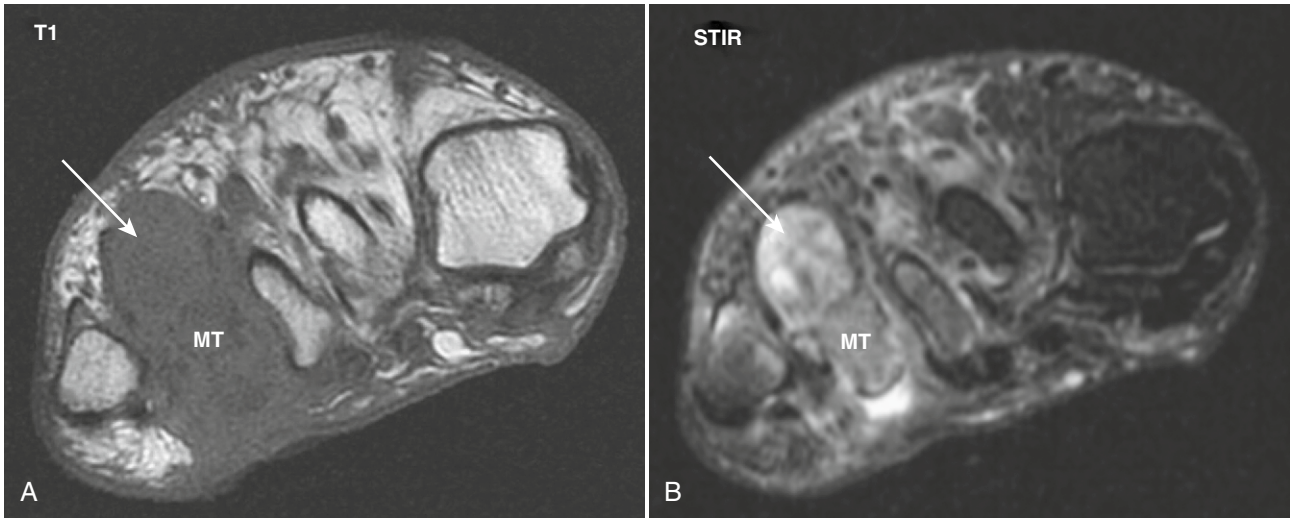


FIGURE 5-26. Osteomyelitis. Short axis T1-weighted (**A**) and STIR (**B**) MR images of the forefoot reveal a periosteal abscess *(arrows)* at the fourth metatarsal head (MT) as a heterogeneous low T1 and high STIR signal fluid collection. Note the replacement of the metatarsal (MT) marrow signal consistent with osteomyelitis.

appear as linear areas of increased signal on fluid-sensitive sequences, but they are much more easily identified after contrast administration as parallel linear areas of enhancement in a "tram–track" pattern.

Osseous findings include abnormal bone marrow signal and enhancement, cortical interruption or destruction, and periosteal reaction. A focus demonstrating low signal intensity on T1-weighted, high signal intensity on T2-weighted or STIR sequences, and enhancement is highly consistent with the diagnosis of osteomyelitis. However, these findings are not completely specific and should be analyzed in the context of the clinical presentation, underlying osseous or articular pathology, and soft tissue involvement. The negative predictive value of a normal STIR sequence is very high, approaching 100%. Periosteal reaction appears as a thin linear edema-like pattern and enhancement paralleling or surrounding the bone cortex.

Foreign Bodies

Puncture wounds and suspected retained foreign bodies (FBs) are a common cause of emergency room visits. Retained FBs are frequently overlooked initially, leading to inflammatory and infectious complications that are often severe. Therefore, prompt detection and removal are imperative. Precise localization of the object is extremely useful as this may minimize the extent of surgical dissection and shorten surgical time. A high clinical suspicion is always necessary, especially in patients with neuropathy who may be unaware of a prior puncture and present with a soft tissue infection (Fig. 5-27A and B). Wood, glass, and metal account for the vast majority of retained FBs encountered. On conventional radiographs, metal is almost always visible. Glass is seen radiographically in more than 90% of cases. On the other hand, wood is identified in only a minority of patients (approximately 15% or less).

Ultrasound is highly sensitive and specific in the detection of retained FBs. US is rapid, inexpensive, accessible, and lacks ionizing radiation. It should be the modality of choice for radiographically occult FBs in the superficial soft tissues. All FBs are hyperechoic with acoustic posterior shadowing (see Fig. 5-27C). The degree of acoustic shadowing is variable and depends on the surface characteristics rather than the composition of the FB. Flat, smooth surfaces often encountered in metal and glass produce reverberation artifact or "dirty" shadowing, whereas irregular surfaces usually produce "clean" shadowing. Sonographic detection may be enhanced by the presence of a hypoechoic rim surrounding the FB. This rim may be seen after at least 24 hours, when an inflammatory reaction has developed. US also allows examination of the surrounding tissues for infectious complications and associated soft tissue injuries.

MR is rarely used in the acute setting for the detection of foreign bodies. More commonly, FBs may be detected incidentally on MR scans performed for the work-up of musculoskeletal infection. Foreign bodies exhibit low signal intensity on all pulse sequences and may show magnetic susceptibility artifact. Conspicuity on MR depends on size, location, and composition. Small FBs are difficult to distinguish from adjacent low-signal structures such as tendons, scars, and calcifications. Foreign objects may incite an inflammatory reaction, seen as surrounding areas of low signal intensity on T1- and high signal intensity on T2-weighted images. MR is highly accurate for identifying infectious musculoskeletal complications (see Fig. 5-27D). Not infrequently, small FBs may become chronically embedded within the soft tissues and form foreign body granulomas. These lesions generate variable degrees of inflammatory response but often present with little or no T2 signal changes. They should be suspected when there is an area of magnetic susceptibility or signal void with peripheral enhancement.

Infected Orthopedic Hardware

There have been important improvements in orthopedic surgical technique and preoperative and postoperative care leading to a considerable decrease in overall postsurgical infections. The frequency of hardware infections has been reduced from nearly 10% in the early years to somewhere between 0.5% and 2% currently. Nonetheless, postoperative infection continues to be an important cause of morbidity and mortality. Prompt detection and localization of hardware infection are essential for appropriate patient management and to avoid even more serious consequences.

Approximately one third of arthroplasty-related infections occur within the first 3 months after the operation. The remainder occur beyond this time period and are considered late infections. Late infections are more indolent and can be difficult to diagnose. Differentiating between late infection and other causes of hardware failure is challenging clinically, radiographically, and histopathologically. In most (but not all) cases, the diagnosis of hardware infection is made by isolating organisms from the fluid or tissues around the hardware. Occasionally, organisms are not found around hardware later proven to be infected. Pain, increased white cell count, elevated C-reactive protein, and increased erythrocyte sedimentation rate are often present, but lack specificity in the postoperative period. Clinicians must utilize a combination of clinical, laboratory, and imaging data to confirm or exclude the diagnosis of hardware infection. Imaging plays an important role and helps guide the clinical management of these patients.

Radiographs should be performed initially for suspected hardware infection. Most often, there are no radiographic findings suggestive of infection especially in the patients with acute presentations. Radiographic findings include periosteal reaction, osteolysis, cortical irregularity, erosions, and frank bone destruction. Chronic infections can produce areas of bone sclerosis. Additionally, radiographs may serve to suggest or exclude other causes of postoperative pain and hardware failure. The temporal evolution is extremely useful when prior radiographs are available. Rapid development of the previously discussed radiographic abnormalities should be viewed as highly suspicious for infection. Cross-sectional imaging studies such as CT and MR can also help when evaluating potentially infected hardware. Unfortunately, image quality with both modalities is degraded by the presence of metallic hardware. With the advent of multidetector CT, the severity of beam hardening artifact from metal has been reduced.



FIGURE 5-27. Foreign body, right hand. Adult diabetic patient presenting to the emergency room with a red and swollen right hand after working in his garden. Anteroposterior radiograph at initial presentation (**A**) shows soft tissue swelling and diffuse increased density in the region of the thenar eminence *(arrow)*. Anteroposterior radiograph of the hand 8 weeks later (**B**), obtained after a second visit to the emergency room for worsening swelling and erythema, demonstrates periosteal reaction *(white arrows)* and sclerosis *(black arrows)* of the second metacarpal bone. No radio-opaque foreign body was identified. Transverse US image (**C**) shows a linear hyperechoic foreign body *(arrows)* adjacent to the second metacarpal (MC) with posterior shadowing and a surrounding hypoechoic rim *(arrowheads)*. Axial STIR image (**D**) of the right hand demonstrates the foreign body *(arrow)* as a low-signal structure surrounded by a rim of high signal, adjacent to the second metacarpal bone. At surgery, a thorn was extracted.

CT exquisitely depicts osseous findings of hardware infection: periosteal reaction, cortical erosion, cortical tracts, osseous fistulae, bony sequestrae, and areas of osteolysis. MR depicts the soft tissue findings to greater advantage.

Radionuclide imaging plays an important role in the evaluation of orthopedic hardware infection and is used in many centers as the second line of imaging after radiographs. Multiple radionuclides have been used for the detection of musculoskeletal infection and all show areas of increased tracer activity in the infected tissue, albeit via different mechanisms of uptake. Nuclear scintigraphy studies currently being used for the detection of musculoskeletal infection include technetium 99m methylene diphosphonate (MDP), radionuclide-labeled white blood cells (WBCs), and gallium-67 citrate imaging. More recently, F18-fluorodeoxyglucose positron emission tomography (FDG PET) has emerged as an alternative for imaging infection and inflammation.

Technetium 99m MDP localizes in areas of increased bone turnover. The sensitivity of bone scintigraphy is very high, and the lack of accumulation virtually excludes bone infection. The overall specificity for bone infection is low, and it is even worse in the postoperative period when bone uptake related to the surgical procedure itself can be seen to variable degrees within the first year, which is also when most infections occur. Additionally, uptake may be abnormally high in multiple noninfectious postoperative complications.

Radionuclide-labeled WBCs can be performed using indium (In)-111 or technetium 99m hexamethylpropyleneamine. These tracers accumulate in areas of neutrophil-mediated inflammation and infection. The sensitivity is similar to and the specificity is better than that of bone scintigraphy. Labeled WBC scans are more useful for acute hardware infections than for chronic, low-grade cases. In the past, gallium-67 citrate was a popular agent used to image infection, although the mechanism of tracer localization in infection is poorly understood. In view of the lower accuracy, unfavorable imaging characteristics, and long wait prior to imaging, gallium has been largely replaced by other agents. Although initial reports suggested that FDG PET could differentiate between infection and other causes of hardware failure (specifically aseptic loosening), more recent data are less convincing. Advantages of FDG PET over other modalities include faster imaging times, higher spatial resolution, and increased sensitivity for low-grade infections. Cost and availability also limit its utilization.

Suggested Readings

Ahmadi ME, Morrison WB, Carrino JA, et al: Neuropathic arthropathy of the foot with and without superimposed osteomyelitis: MR imaging characteristics. Radiology 238:622–631, 2006.

Andrews CL: From the RSNA refresher courses: Evaluation of the marrow space in the adult hip. Radiographics 20(Suppl):S27–S42, 2000.

Bauer TW, Parvizi J, Kobayashi N, Krebs V: Diagnosis of periprosthetic infection. J Bone Joint Surg Am 88:869–882, 2006.

Berquist TH: Imaging of joint replacement procedures. Radiol Clin North Am 44:419–439, 2006.

Bigliani LU, Levine WN: Current concepts review: Subacromial impingement syndrome. J Bone Joint Surg Am 79:1854–1868, 1997.

Bigoni BJ, Chung CB: MR imaging of the rotator cuff interval. Magn Reson Imaging Clin N Am 12:61–73, 2004.

Bock GW, Garcia A, Weisman MH, et al: Rapidly destructive hip disease: Clinical and imaging abnormalities. Radiology 186:461–466, 1993.

Boyse TD, Fessell DP, Jacobson JA, et al: US of soft tissue foreign bodies and associated complications with surgical correlation. Radiographics 21:1251–1256, 2001.

Brower AC, Kransdorf M: Imaging of hip disorders. Radiol Clin North Am 28: 955–974, 1990.

Bureau NJ, Chhem RK, Cardinal E: Musculoskeletal infections: US manifestations. Radiographics 19:1585–1592, 1999.

Cahill BR: Osteolysis of the distal part of the clavicle in male athletes. J Bone Joint Surg Am 64:1053–1058, 1982.

Chen AL, Joseph TN, Zuckerman JD: Rheumatoid arthritis of the shoulder. J Am Acad Orthop Surg 11:12–14, 2003.

Connell D, Padmanabhan R, Buchbinder R: Adhesive capsulitis: Role of MR imaging in differential diagnosis. Eur Radiol:2100–2106, 2002.

Cooper KL, Beabout JW, McLeod RA: Supraacetabular insufficiency fractures. Radiology 157:15–17, 1985.

del Cura JL, Torre I, Zabala R, Legorburu A: Sonographically guided percutaneous needle lavage in calcific tendonitis of the shoulder: Short- and long-term results. AJR Am J Roentgenol 189:W128–W134, 2007.

Erdman WZ, Tamburro F, Jayson HT, et al: Osteomyelitis: Characteristics and pitfalls of diagnosis with MR imaging. Radiology 180:533–539, 1991.

Erickson SJ, Kneeland JB, Komorowski RA, et al: Post-traumatic osteolysis of the clavicle: MR features. J Comput Assist Tomogr 14:835–837, 1990.

Fang C, Teh J: Imaging of the hip. Imaging 15:205–216, 2003.

Fayad LM, Carrino JA, Fishman EK: Musculoskeletal infection: Role of CT in the emergency department. Radiographics 27:1723–1736, 2007.

Fugitt JB, Puckett ML, Quigley MM, Kerr SM: Necrotizing fasciitis. Radiographics 24:1472–1476, 2004.

Hayes CW, Conway WF: Calcium hydroxyapatite deposition disease. Radiographics 10:1031–1048, 1990.

Hayes CW, Conway WF, Daniel WW: MR imaging of bone marrow edema pattern: Transient osteoporosis, transient bone marrow edema syndrome or osteonecrosis. Radiographics 13:1001–1011, 1993.

Jordan LK, Kenter K, Griffiths HL: Relationship between MRI and clinical findings in the acromioclavicular joint. Skeletal Radiol 31:516–521, 2002.

Karachalios T, Karantanas AH, Malizos K: Hip osteoarthritis: What the radiologist wants to know. Eur J Radiol 61:36–48, 2007.

Karantanas AH: Acute bone marrow edema of the hip: Role of MR imaging. Eur Radiol 17:2225–2236, 2007.

Karchevsky M, Schweitzer ME, Morrison WB, Parellada JA: MRI findings of septic arthritis and associated osteomyelitis in adults. AJR Am J Roentgenol 182:119–122, 2004.

Kassarjian A, Bencardino JT, Palmer WE: MR imaging of the rotator cuff. Magn Reson Imaging Clin N Am 12:39–60, 2004.

Kassarjian A, Llopis E, Palmer WE: Distal clavicular osteolysis: MR evidence for subchondral fracture. Skeletal Radiol 36:17–22, 2007. Epub 2006 Oct 5.

Levine AH, Pais MJ, Schwartz EE: Posttraumatic osteolysis of the distal clavicle with emphasis on early radiologic changes. AJR Am J Roentgenol 127:781–784, 1976.

Love C, Thomas MB, Tronco GG, Palestro CJ: FDG PET of infection and inflammation. Radiographics 25:1357–1368, 2005.

Malizos KN, Karantanas AH, Varitimidis SE, et al: Osteonecrosis of the femoral head: Etiology, imaging and treatment. Eur J Radiol 63:16–28, 2007.

Manaster, BJ: From the RSNA refresher courses. Adult chronic hip pain: Radiographic evaluation. Radiographics 20(Suppl):S3–S25, 2000.

Manton GL, Schweitzer ME, Weishaupt D, Karasick D: Utility of MR arthrography in the diagnosis of adhesive capsulitis. Skeletal Radiol 30:326–330, 2001.

Mengiardi B, Pfirrmann CW, Gerber C, et al: Frozen shoulder: MR arthographic findings. Radiology 233:486–492, 2004.

Mitchell M, Howard B, Haller J, et al: Septic arthritis. Radiol Clin North Am 26:1295–1313, 1988.

Moosikasuwan JB, Miller TT, Burke BJ: Rotator cuff tears: Clinical, radiographic and US findings. Radiographics 25:1591–1607, 2005.

Morag Y, Jacobson JA, Miller B, et al: MR imaging of rotator cuff injury: What the clinician needs to know. Radiographics 26:1045–1065, 2006.

Morrison WB: Ledermann HP: Work-up of the diabetic foot. Radiol Clin North Am 40:1171–1192, 2002.

Ohashi K, El-Khoury G, Bennett DL, et al: Orthopedic hardware complications diagnosed with multi-detector row CT. Radiology 237:570–577, 2005.

Otte MT, Helms CA, Fritz RC: MR imaging of supra-acetabular insufficiency fractures. Skeletal Radiol 26:279–283, 1997.

Peh WC, Khong PL, Yin Y, et al: Imaging of pelvic insufficiency fractures. Radiographics 16:335–348, 1996.

Peterson JJ, Bancroft LW, Kransdorf MJ: Wooden foreign bodies: Imaging appearance. AJR Am J Roentgenol 178:557–562, 2002.

Rahmouni A, Chosidow O, Mathieu D, et al: MR imaging in acute infectious cellulitis. Radiology 192:493–496, 1994.

Rogers LF, Hendrix RW: The painful shoulder. Radiol Clin North Am 26: 1359–1371, 1988.

Sadro C: Current concepts in magnetic resonance imaging of the adult hip and pelvis. Semin Roentgenol 35:231–248, 2000.

Steinbach LS: Rotator cuff disease. In Steinbach LS, Tirman PFJ, Peterfy CG, Feller JF (eds): Shoulder Magnetic Resonance Imaging. Philadelphia, Lippincott Williams & Wilkins, 1988, pp 99–133.

Steinberg DR, Steinberg ME, Garino JP, et al: Determining lesion size in osteonecrosis of the femoral head. J Bone Joint Surg Am 88(Suppl 3):S27–S34, 2006.

Stiles RG, Otte MT: Imaging of the shoulder. Radiology 188:603–613, 1993.

Strobel K, Pfirrmann CW, Zanetti M, et al: MRI features of the acromioclavicular joint that predict pain relief from intraarticular injection. AJR Am J Roentgenol 181:755–760, 2003.

Tang JS, Gold RH, Bassett LW, Seeger LL: Musculoskeletal infection of the extremities: Evaluation with MR imaging. Radiology 166:205–209, 1988.

Tehranzadeh J, Wong E, Wang F, Sadighpour M: Imaging of osteomyelitis in the mature skeleton. Radiol Clin North Am 39:223–250, 2001.

Turpin S, Lambert R: Role of scintigraphy in musculoskeletal and spinal infections. Radiol Clin North Am 39:169–189, 2001.

Watson RM, Roach NA, Dalinka MK: Avascular necrosis and bone marrow edema syndrome. Radiol Clin North Am 42:207–219, 2004.

Weishaupt D, Schweitzer ME: MR imaging of septic arthritis and rheumatoid arthritis of the shoulder. Magn Reson Imaging Clin N Am 12:111–124, 2004.

Winalski CS, Aliabadi P, Wright RJ, et al: Enhancement of joint fluid with intravenously administrated gadopentetate dimeglumine: Technique, rationale and implications. Radiology 187:179–185, 1993.

Wysoki MG, Santora TA, Shah RM, Friedman AC: Necrotizing fasciitis: CT characteristics. Radiology 203:859–863, 1997.

Zanca P: Shoulder pain: Involvement of the acromioclavicular joint (Analysis of 1000 cases). Am J Roentgenol Radium Ther Nucl Med 112:493–506, 1971.

CHAPTER 6

Imaging Evaluation of Common Pediatric Emergencies

Sarah D. Bixby and Sarah Sarvis Milla

Limiting radiation exposure to young patients, while at the same time acquiring diagnostic information, is a primary goal of the pediatric radiologist. The imaging evaluation of common pediatric emergencies relies heavily on plain radiographs, fluoroscopy, and ultrasound. While computed tomography (CT) is useful in the evaluation of some children, CT is often reserved for cases where ultrasound and plain films are nondiagnostic. This chapter illustrates the imaging manifestations of some of the most common pediatric emergencies.

NEONATAL EMERGENCIES

Neonates make up a small subset of pediatric patients with their own unique diagnoses. Even seemingly healthy, full-term babies may become distressed and require immediate imaging evaluation. With ongoing advances in prenatal imaging a number of conditions that require urgent treatment are diagnosed before birth, such as posterior urethral valves and esophageal atresia. In many infants the diagnosis may be suggested for the first time on the basis of imaging performed in the first days and weeks of life.

Respiratory Distress

It is important to recognize the radiographic patterns of conditions that may lead to severe respiratory distress in the neonate. Common respiratory illnesses encountered in the Neonatal Intensive Care Unit (NICU) include surfactant deficiency disease (SDD) and/or its complications, transient tachypnea of the newborn (TTN), neonatal pneumonia, and meconium aspiration syndrome (MAS). Neonates with these conditions are commonly evaluated with chest radiographs. The patient's clinical information is critical for the correct interpretation of the radiographs, such as gestational age, method of delivery, and other factors surrounding the birth.

Surfactant Deficiency Disease

SDD, also termed *hyaline membrane disease*, almost exclusively affects premature infants (i.e., less than 36 to 38 weeks gestation). The lack of surfactant in the lungs of premature infants causes collapse of pulmonary alveoli, which leads to poor oxygenation. Infants with SDD demonstrate signs and symptoms of respiratory distress at birth, manifested by grunting, nasal flaring, retracting, and tachypnea. The radiographic findings of SDD may be present at birth, although in some cases the findings evolve after 12 to 24 hours. Classic radiographic findings of SDD are low lung volumes with diffuse, bilateral, granular opacities (Fig. 6-1). These opacities improve after treatment with exogenous surfactant. Infants with SDD are often in severe respiratory distress and require mechanical ventilation.

Air Block Complications

Infants on mechanical ventilators are at risk of developing complications secondary to barotrauma or volutrauma. This is especially true for infants with underlying lung disease such as SDD. Air may rupture outside of the alveoli, entering the perivascular or peribronchiolar spaces and giving rise to interstitial lucencies termed *pulmonary interstitial emphysema* (Fig. 6-2). The air may also dissect into the mediastinum, pleural space, or pericardium. On a supine chest radiograph, a pneumothorax tends to collect anteriorly along the heart border or inferiorly above the diaphragm (Fig. 6-3), and is manifested as a paracardiac lucency (for a medial pneumothorax) or a deep costophrenic sulcus (for an inferior pneumothorax). A cross-table lateral view is often necessary to demonstrate the anterior location of the air (Fig. 6-4). Pneumomediastinum causes anterior displacement of the

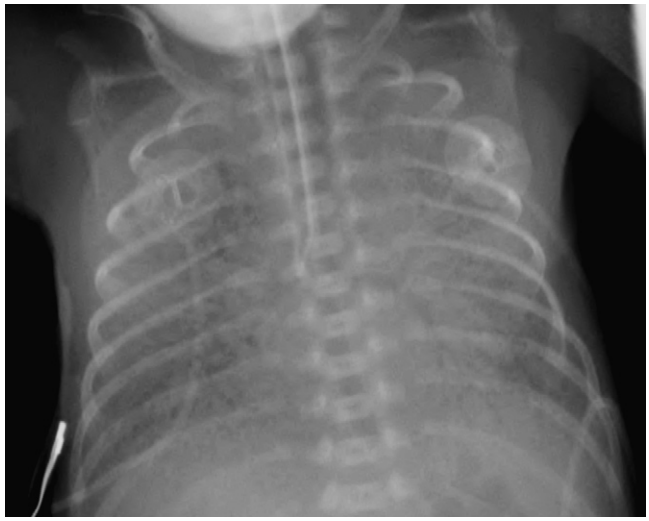


FIGURE 6-1. Chest radiograph in a premature infant with surfactant deficiency demonstrates an endotracheal tube in place. There are bilateral, diffuse granular opacities within the lungs with air bronchograms.

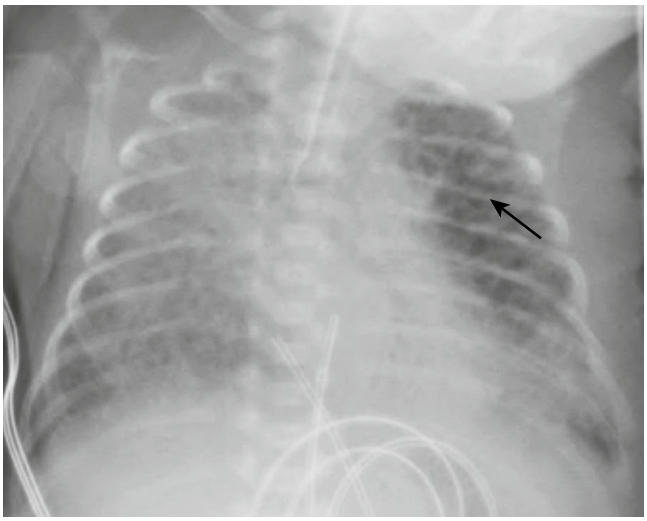


Figure 6-2. Chest radiograph in a premature male infant demonstrates an endotracheal tube in place. Branching cystic lucencies within the left upper lobe *(arrow)* are consistent with "pulmonary interstitial emphysema."

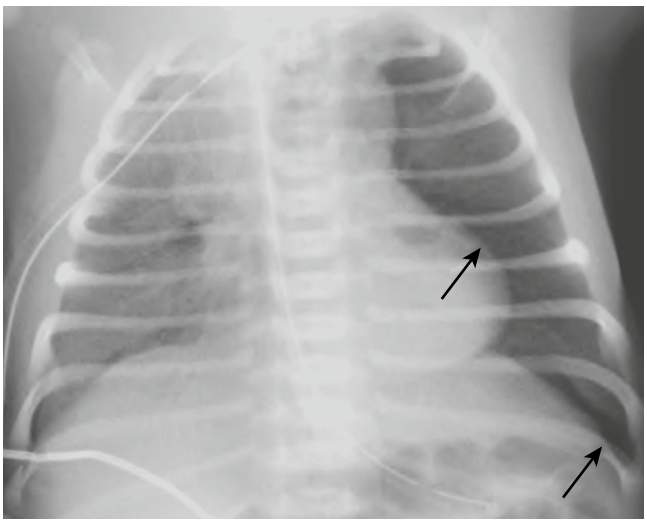


Figure 6-3. In this premature infant lucency adjacent to the left heart border and projecting over the left hemidiaphragm *(arrows)* indicates the presence of a pneumothorax.

thymus in a "spinnaker sail" configuration (Fig. 6-5). Pneumopericardium outlines the heart border without extending superior to the great vessels (Fig. 6-6).

Transient Tachypnea of the Newborn

Infants with TTN are often full-term infants delivered via cesarean section. The course of delivery does not effectively clear the fetal lung fluid, which is why this entity is also referred to as "retained fetal lung fluid." Coarse interstitial opacities on chest radiographs are often present, indicative of underlying pulmonary edema. A pleural effusion, and/or fluid tracking along the fissures, is commonly present. The hallmark of TTN is return of the radiograph to normal in 24 to 48 hours, which coincides with resolution of tachypnea.

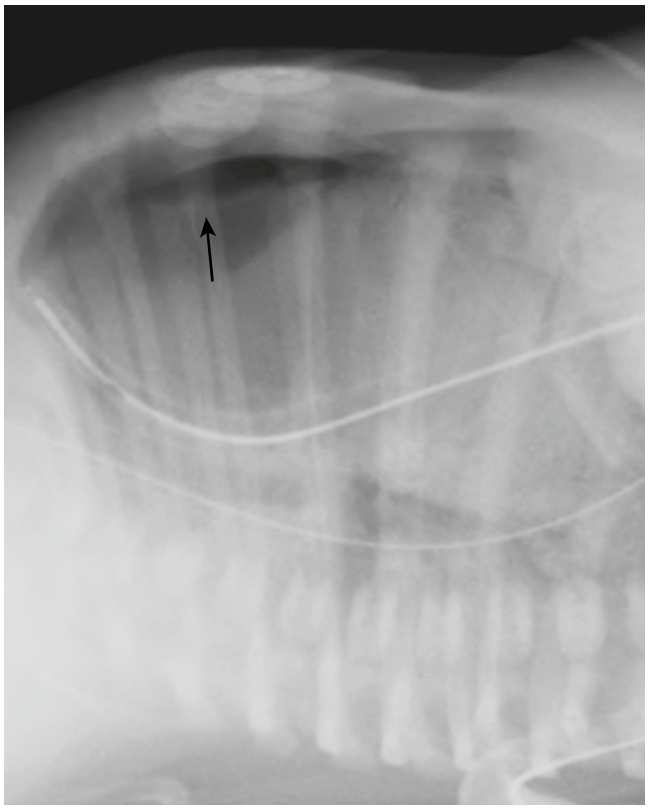


Figure 6-4. A cross-table lateral chest radiograph in the same infant as in Figure 6-3 demonstrates the anterior location of the pneumothorax *(arrow)*.

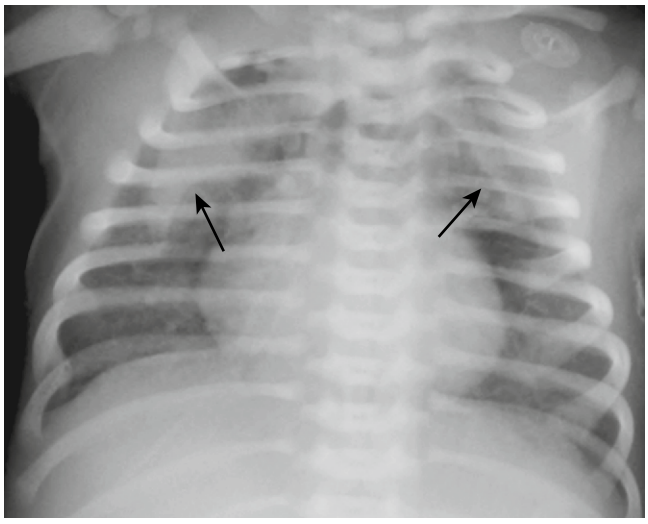


Figure 6-5. Chest radiograph in this premature baby demonstrates the thymus displaced anteriorly by pneumomediastinum *(arrows)*.

Neonatal Pneumonia

Neonatal pneumonia is most commonly secondary to an ascending vaginal infection, the most common infectious agent being Group B streptococcus. A major risk factor for neonatal pneumonia is prolonged rupture of the amniotic membranes. The most common finding on chest radiographs in neonates with pneumonia is bilateral alveolar densities with air bronchograms. The radiographic findings are often difficult to distinguish from other conditions,

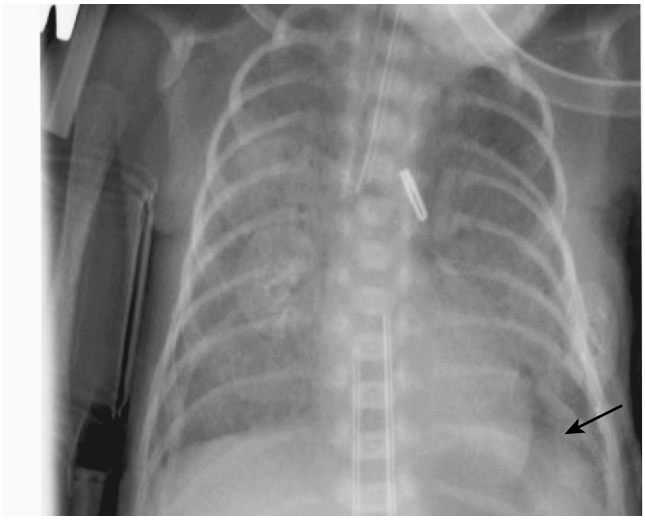


FIGURE 6-6. Chest radiograph in this premature infant status post ligation of a patent ductus arteriosus demonstrates a lucency projecting adjacent to the cardiac apex *(arrow)*, consistent with pneumopericardium.

such as SDD or MAS. Serial films are most helpful in distinguishing between these entities.

Meconium Aspiration Syndrome

MAS is diagnosed by the presence of meconium below the level of the vocal cords at birth. Infants with MAS are usually post-mature, or have experienced intrauterine stress. The thick, tenacious meconium causes obstruction of small- and medium-sized airways, which leads to areas of both atelectasis and overinflation. The meconium can cause a chemical pneumonitis and also inactivates surfactant within lung alveoli. Chest radiographs in infants with MAS reveal coarsened interstitial densities and bilateral parenchymal opacities interspersed with areas of hyperaeration (Fig. 6-7). MAS is the most common respiratory disease to cause a pleural effusion in the first few days of life.

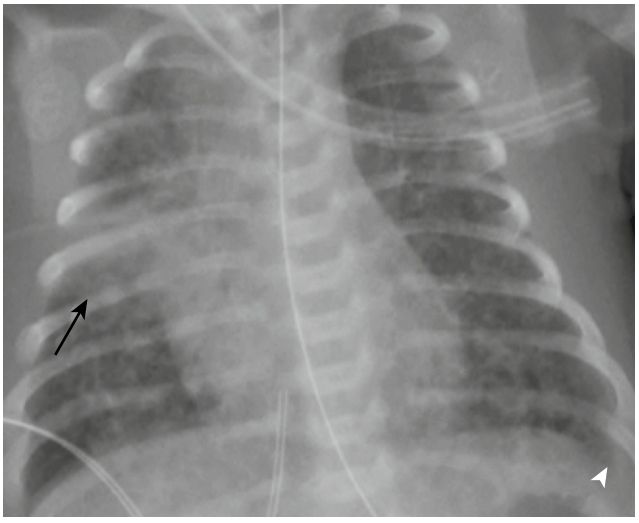


FIGURE 6-7. Chest radiograph in a full-term baby girl with meconium aspiration demonstrates coarse interstitial lung markings, a focal opacity projecting over the right mid-lung *(arrow)*, and a small left pleural effusion *(arrowhead)*.

Posterior Urethral Valves

Posterior urethral valves (PUVs) are the most common congenital cause of *bilateral* renal obstruction. Their embryologic development is complex and has been previously described in the literature. Briefly, PUVs consist of an obstructing membrane, or persistent urogenital membrane, at the level of the verumontanum in the posterior urethra of male infants. This membrane causes varying degrees of bladder outlet obstruction and bilateral hydroureteronephrosis. The diagnosis is often made in utero and should be suspected in any male patient who fails to void within 24 hours of birth.

Ultrasound (US) examination of patients with PUVs reveals dilated renal collecting systems and ureters bilaterally (Fig. 6-8). The bladder is often greatly distended,

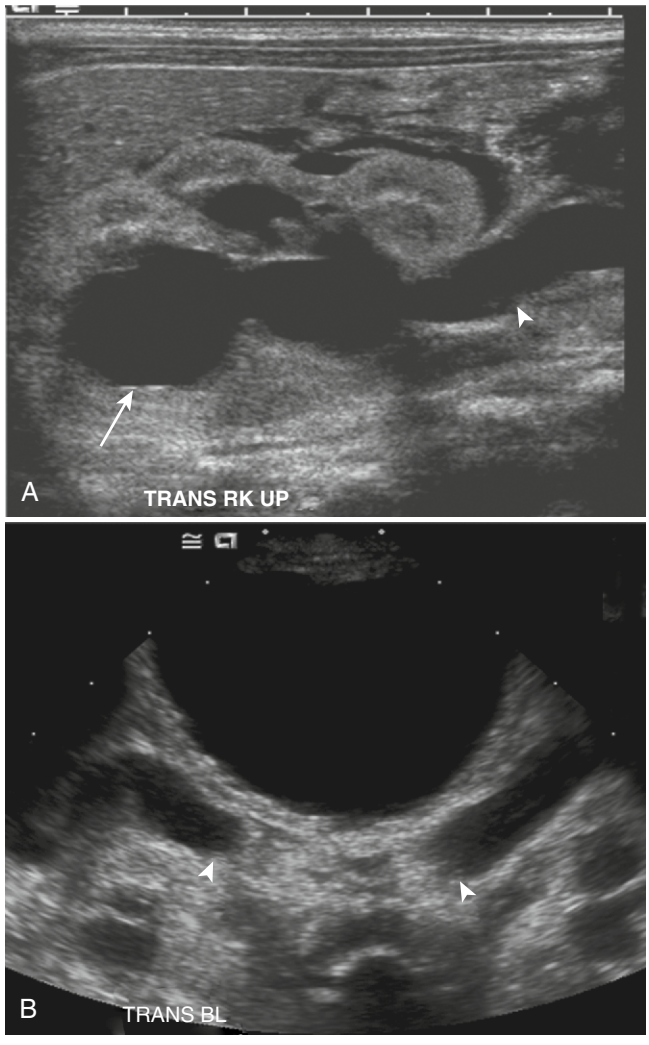


FIGURE 6-8. **A,** Sagittal US image of the right kidney in a male infant with posterior urethral valves demonstrates dilated renal calyces *(arrow)* and a dilated proximal ureter *(arrowhead)*. **B,** Transverse US image of the bladder in the same patient demonstrates a distended urinary bladder. Dilated distal ureters can be appreciated posterior to the bladder *(arrowheads)*.

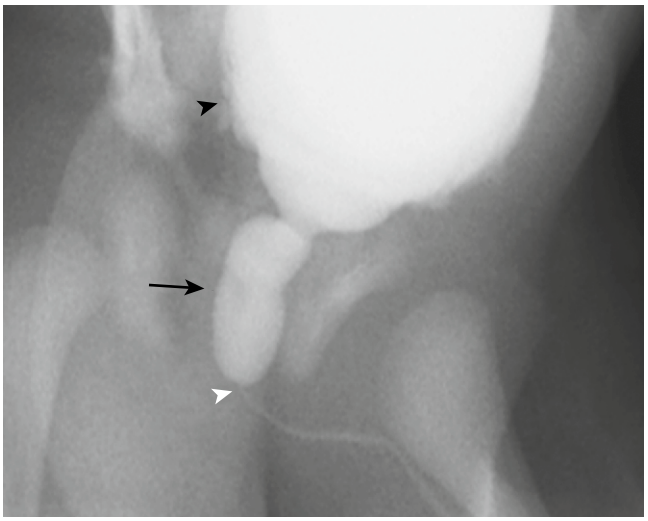


Figure 6-9. Lateral-oblique voiding fluoroscopic image acquired during voiding cystourethrogram (VCUG) on same patient as in Figure 6-8 demonstrates a distended urinary bladder with several small diverticulae *(black arrowhead)*. There is an abrupt change in caliber from the dilated posterior urethra to the anterior urethra *(white arrowhead)*. The enlarged verumontanum can be identified as a filling defect in the posterior urethra *(arrow)*.

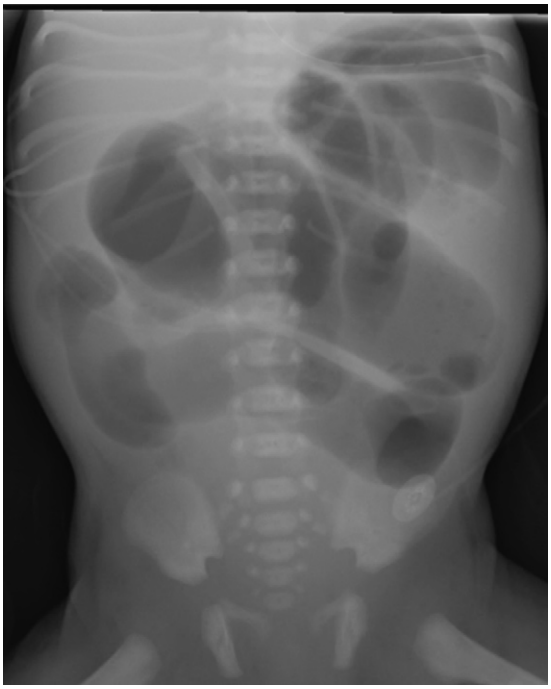


Figure 6-10. Plain radiograph of the abdomen in a full-term newborn infant with bilious vomiting demonstrates multiple dilated loops of bowel.

and the bladder wall may appear sacculated, thickened, or trabeculated. The dilated posterior urethra has a "keyhole" configuration at ultrasound. Voiding cystourethrogram (VCUG) is the standard of care for the diagnosis of PUVs. The bladder is usually of large caliber and may require a larger than expected volume of contrast to reach capacity. Bladder wall trabeculations and diverticula are often present. When reflux is present, the refluxed contrast will be diluted by the preexisting urine within the dilated ureter and renal collecting system. The degree of hydronephrosis is often massive. Images of the urethra acquired during voiding demonstrate an abrupt change in caliber between the dilated posterior urethra and the normal-caliber anterior urethra (Fig. 6-9). In some cases the obstructing membrane is identified at the point of transition. The verumontanum is often enlarged and is identified as an intraluminal filling defect along the posterior wall of the urethra just proximal to the valves.

The treatment for PUVs is ablation. Even after the valves are ablated the long-term sequelae of the bladder outlet obstruction in utero can be catastrophic with renal failure developing by early childhood. Ultimately, the degree of renal function is of primary importance in determining patient outcome, as massive vesicoureteral reflux (VUR) in utero may cause severe renal dysplasia that leads to renal failure. PUVs must be differentiated from other causes of bilateral hydroureteronephrosis in infancy, including prune-belly syndrome, bilateral ureterovesicu lar junction obstruction, transient bilateral VUR, and the rare "megacystis-microcolon-intestinal hypoperistalsis syndrome." The findings at VCUG should readily differentiate PUVs from these other entities.

Intestinal Obstruction

Intestinal obstruction is one of the most common neonatal abdominal emergencies. The obstruction is classified as either a high or low obstruction depending on whether it occurs above or below the level of mid-ileum. Babies typically present with abdominal distention, vomiting, and failure to pass meconium within 24 to 48 hours. The distinction between a high and a low obstruction is often made on the basis of plain abdominal radiographs. If the radiograph demonstrates one or few dilated loops of bowel, the obstruction is likely a high obstruction. If the radiograph reveals multiple dilated loops of bowel, the obstruction is a low obstruction (Fig. 6-10). In a baby with intestinal obstruction the correct interpretation of the plain film is critical in directing the most appropriate next course of action.

A high intestinal obstruction may be secondary to duodenal atresia or stenosis, jejunal atresia or stenosis, or malrotation. An upper gastrointestinal (UGI) examination is often requested in order to identify the level of obstruction. The UGI also assists the surgeon in determining the urgency of surgery. In duodenal atresia or stenosis, the obstruction almost always occurs at the level of the ampulla of Vater. Abdominal radiographs in duodenal atresia often reveal the classic "double bubble" sign in an otherwise gasless abdomen. The dilated gas-filled "bubbles" represent the stomach and duodenal bulb. This is virtually diagnostic of duodenal atresia in the correct clinical setting. In cases of incomplete duodenal obstruction, radiographs will reveal gas in distal bowel loops. At UGI examination, there is often a focal area of narrowing within the duodenum through which a tiny amount of contrast may pass. In some cases, the stenosis may be secondary to a duodenal web, which appears as a curvilinear filling defect extending across the duodenal lumen (Fig. 6-11). Coexistent congenital anomalies are not uncommon, most often in the form of congenital heart disease. Approximately 30% of babies with duodenal atresia or stenosis have Down syndrome.

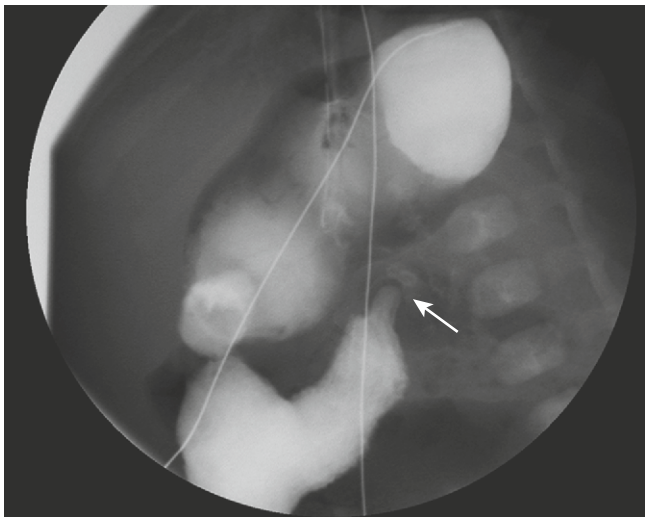


FIGURE 6-11. Fluoroscopic spot image acquired during upper gastrointestinal examination in a newborn infant with bilious vomiting demonstrates a dilated duodenum proximal to a partially obstructing duodenal web *(arrow)*.

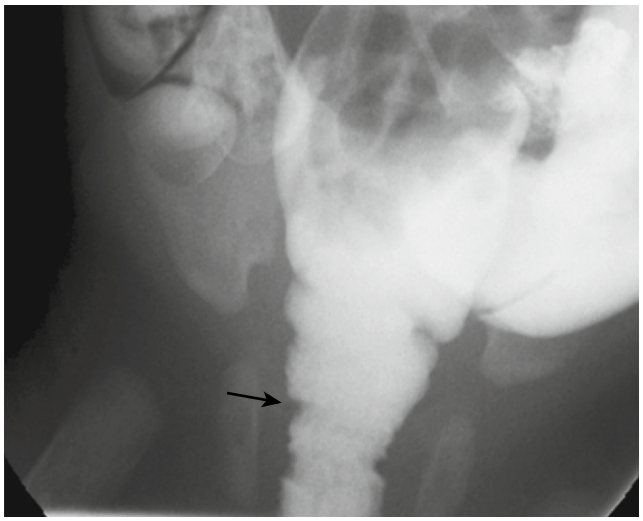


FIGURE 6-12. Anteroposterior fluoroscopic spot image during contrast enema in a newborn baby with bowel obstruction reveals a "sawtooth" mucosal pattern in the rectum *(arrow)*. The recto–sigmoid relationship is reversed. This child had Hirschsprung's disease.

Low intestinal obstruction may be secondary to meconium ileus, ileal atresia, small left colon syndrome (functional immaturity of the colon), colonic atresia, and Hirschsprung's disease. A contrast enema is the study of choice to elucidate the diagnosis. Meconium ileus almost always occurs in infants with cystic fibrosis. On contrast enema, a microcolon is present. A microcolon is a colon of universally small caliber (1 cm or less in diameter). Its presence implies that the colon has never been used. Bowel atresia proximal to the distal ileum does not lead to a microcolon because the succus entericus produced by the distal small bowel allows the colon to achieve a normal caliber. In patients with meconium ileus refluxed contrast in the distal ileum reveals multiple filling defects within the distal small bowel. These filling defects represent inspissated meconium. In ileal atresia, on the other hand, it is not possible to reflux contrast past the atresia into the terminal ileum. In functional immaturity of the colon, the descending colon and sigmoid colon are small in caliber compared with the normal ascending and transverse colon. These patients are often infants of diabetic mothers. In colonic atresia the visualized colon at contrast enema will be a microcolon, and contrast will be unable to pass proximal to the atresia. In Hirschsprung's disease there is a transition from normal bowel that is of normal caliber to aganglionic bowel that is small in caliber (Fig. 6-12). Classically, this transition occurs at the level of the rectosigmoid. In normal infants the rectal diameter should be greater than the sigmoid diameter, although in Hirschsprung's disease this relationship is reversed. Ultimately, a biopsy is required to confirm the diagnosis.

Esophageal Atresia

Congenital atresia of the esophagus is a rare abnormality that may occur as an isolated abnormality or as part of a larger spectrum of abnormalities. In most cases there is an associated fistula to the trachea. The diagnosis is almost always suspected clinically when an infant has trouble feeding, or there is difficulty passing a nasogastric tube into the stomach.

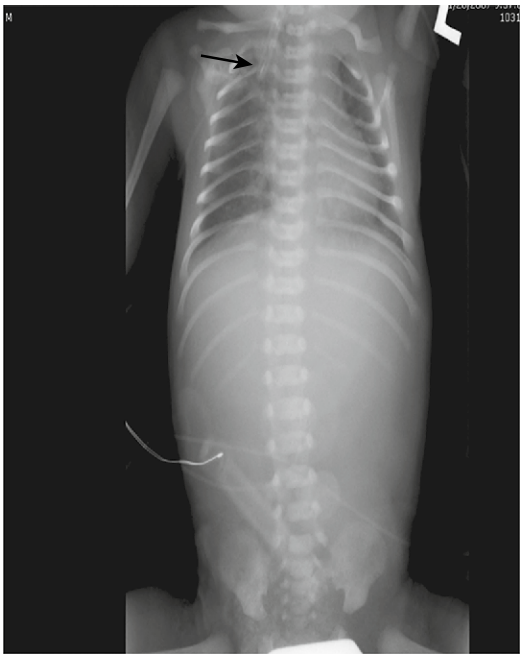


FIGURE 6-13. Babygram performed on this newborn demonstrates a nasogastric tube within a dilated esophageal pouch in this baby with esophageal atresia *(arrow)*. There is no gas within the abdomen to suggest a tracheoesophageal fistula.

Radiographs help to confirm the diagnosis when there is no gas identified within any bowel loops in the abdomen. If placement of a nasogastric tube has been attempted, the tube will be identified above the diaphragm on the radiograph, often in a dilated, gas-filled, esophageal pouch (Fig. 6-13).

Necrotizing Enterocolitis

Necrotizing enterocolitis (NEC) is a gastrointestinal condition that occurs in 2% to 3% of neonates, most commonly premature infants. Mortality rates in infants

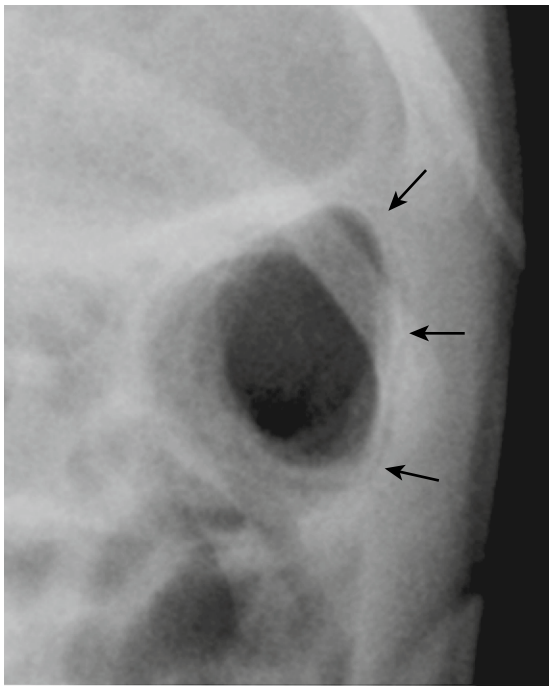


Figure 6-14. Abdominal radiograph in this premature infant with necrotizing enterocolitis demonstrates circumferential lucencies surrounding a bowel loop in the left upper quadrant consistent with pneumatosis intestinalis *(arrows)*.

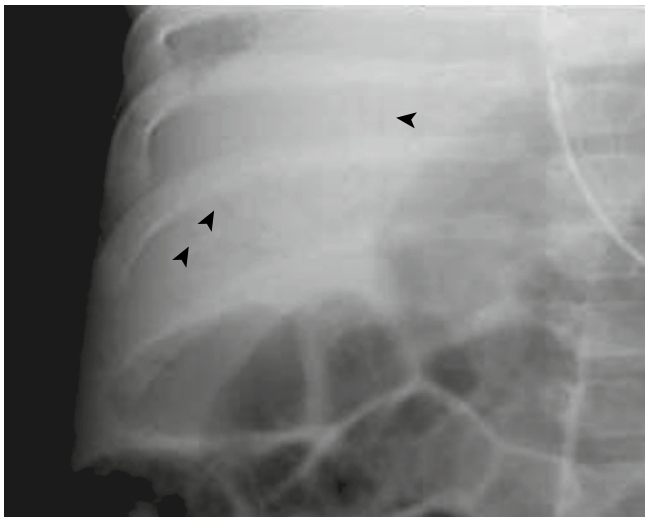


Figure 6-15. Abdominal radiograph in this male infant with severe bowel ischemia secondary to congenital heart disease reveals branching lucencies in the liver consistent with portal venous gas *(arrowheads)*.

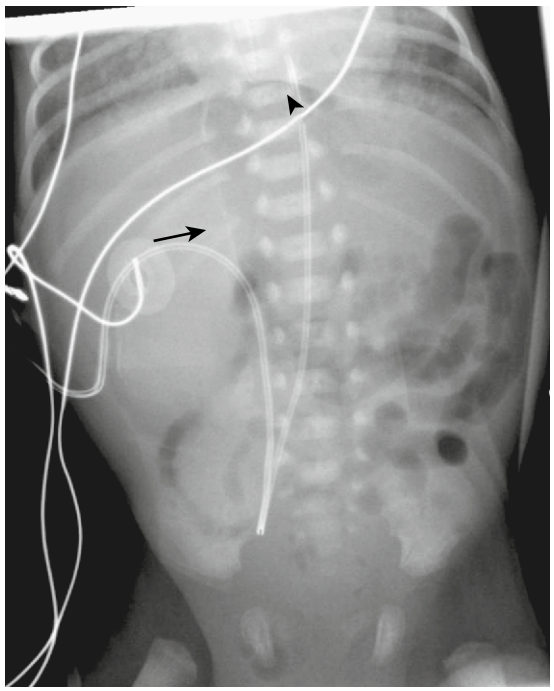


Figure 6-16. Abdominal radiograph in a premature infant with clinical necrotizing enterocolitis demonstrates air outlining the falciform ligament *(arrow)* as well as air outlining the undersurface of the diaphragm *(arrowhead)*. This child had a perforation in his ileum at surgery.

with NEC range from 15% to 40%. The pathogenesis of the disease is thought to be related to relative immaturity of intestinal motility and barrier function, as well as abnormal bacterial colonization. Neonates with NEC often present within the first 2 weeks of life with feeding intolerance, vomiting, abdominal distention, blood in the stool, and/or generalized lethargy. Abdominal radiographs are the modality of choice for the initial evaluation of neonates with suspected NEC and for monitoring its progression. An early sign of NEC is a mildly dilated and fixed loop (or loops) of bowel on serial abdominal radiographs. Pneumatosis intestinalis, or air within the wall of the bowel, is considered a hallmark of NEC (Fig. 6-14). Pneumatosis represents by-products of the metabolism of bacteria within the intestinal wall. While the bubbly lucencies of pneumatosis can often be mistaken for stool on an abdominal radiograph, it is uncommon for an infant younger than 2 weeks of age to have stool within the colon. The presence of portal venous gas and pneumoperitoneum on an abdominal radiograph usually indicates more severe disease and/or perforation of the bowel. Portal venous gas appears on abdominal radiographs as lucent, branching, linear structures within the liver (Fig. 6-15). When pneumoperitoneum is present the falciform ligament is visualized on a radiograph secondary to the presence of outlining air on both sides (Fig. 6-16). Both sides of the bowel wall are also visible (Fig. 6-17). The abdomen may appear abnormally lucent when large amounts of gas collect anteriorly within the abdomen on a supine film (Fig. 6-18). A cross-table lateral view of the abdomen is helpful in confirming the presence of free air under the diaphragm (Fig. 6-19).

Most cases of NEC are treated medically, usually with bowel rest, gastric suction, antibiotics, and hydration. Surgery is usually not performed unless there is evidence of bowel perforation (i.e., free air). Plain radiographs are critical in evaluating the progression of the disease. A changing bowel gas pattern, as opposed to dilated bowel loops that remain fixed on serial abdominal radiographs, is an important radiographic sign, as this often coincides with clinical improvement.

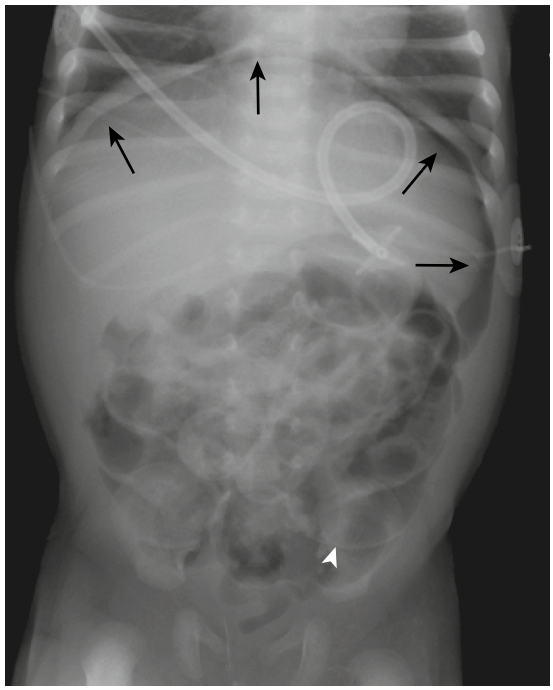


FIGURE 6-17. Abdominal radiograph in this premature infant with perforated necrotizing enterocolitis demonstrates air beneath the diaphragm *(arrows)* and outlining the bowel wall *(arrowhead)*.

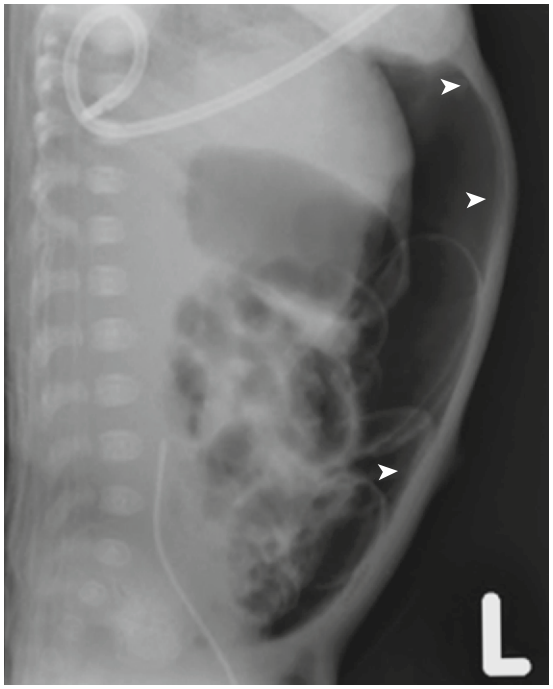


FIGURE 6-19. A cross-table lateral abdominal radiograph in this infant with perforated bowel demonstrates a large amount of free intra-abdominal air *(arrowheads)*.

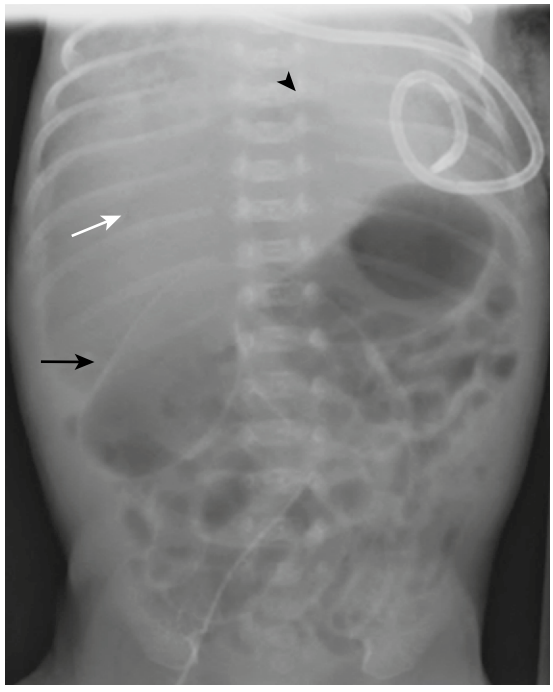


FIGURE 6-18. Abdominal radiograph in the same patient as in Figure 6-16 taken several hours later demonstrates hyperlucency of the liver *(white arrow)* and free air under the diaphragm *(arrowhead)*, as well as air outlining loops of bowel *(black arrow)*.

GASTROINTESTINAL

Abdominal pain and vomiting are common chief complaints in children presenting to the emergency department. Very young patients are unable to verbalize symptoms of pain, and the presence of vomiting may be the first and only sign that there is an underlying gastrointestinal problem. In young infants a history of vomiting invokes a relatively short differential diagnosis that includes hypertrophic pyloric stenosis and intestinal malrotation. In the older child, a history of emesis, especially bilious emesis, invokes a more complicated differential diagnosis, which includes intussusception, appendicitis, bowel obstruction, and gastroenteritis, as well as many other conditions. Further imaging investigation largely depends on other clinical signs and symptoms as well as laboratory markers.

Hypertrophic Pyloric Stenosis

Hypertrophic pyloric stenosis (HPS) is a condition that affects young infants usually between 3 and 6 weeks of age. While normal at birth, these infants develop gradual onset of nonbilious emesis over the first several weeks of life, commonly described as "projectile" in quality. In severe cases dehydration and malnourishment will ensue that may be accompanied by marked electrolyte imbalances. The disease is caused by overgrowth of the muscularis layer of the pylorus. The mucosal layer also becomes hypertrophied and redundant, which causes obstruction of the lumen. The precise etiology for HPS is unclear.

Abdominal radiographs in infants with HPS often demonstrate a dilated, gas-filled stomach (unless the stomach has been decompressed with a nasogastric tube). Peristaltic contractions within the stomach give the appearance of a "caterpillar stomach" (Fig. 6-20). Ultrasound is the imaging study of choice for the diagnosis of HPS. When HPS is present, the pyloric channel is nearly always visualized and appears both thickened and elongated (Fig. 6-21). The

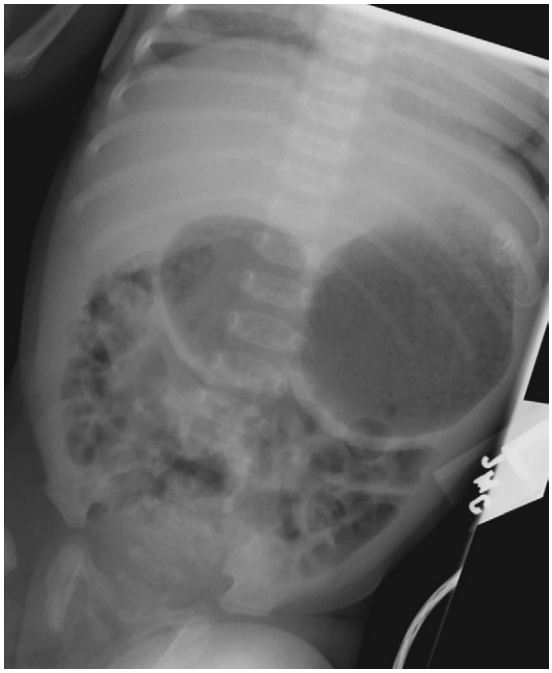


Figure 6-20. Abdominal radiograph in this 1-month-old infant with pyloric stenosis demonstrates a dilated stomach. A wave of peristalsis gives the stomach the appearance of a caterpillar.

hypertrophied pyloric channel fails to relax despite vigorous peristaltic contractions in the stomach. The hyperechoic mucosa is redundant and crowded and often protrudes into the antrum, a finding termed the "nipple" sign. The length of the pyloric channel is variable and can range between 14 and 20+ mm. Measurements of muscle thickness are more reliable for the diagnosis of HPS. A muscle thickness greater than 3 mm is consistent with pyloric stenosis. It is important to document the passage of fluid from the gastric antrum into the duodenal bulb. In normal patients the normal pyloric ring bridges these two structures (Fig. 6-22). Careful observation of this region over the course of

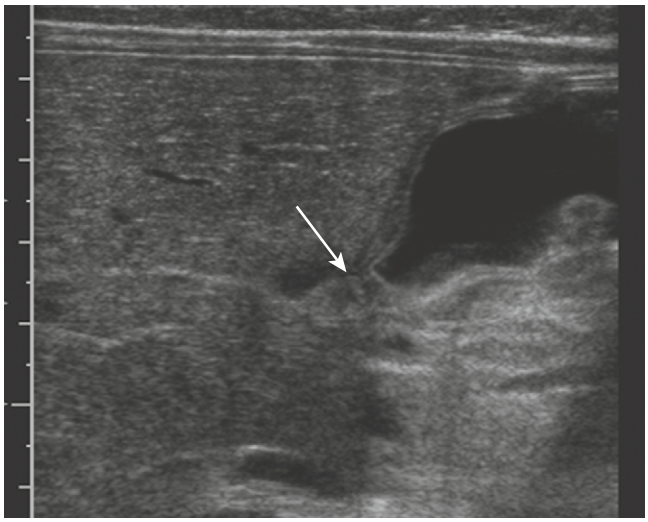


Figure 6-22. Longitudinal US image through a normal pylorus *(arrow)*, which appears as a cleft separating the stomach antrum and the duodenal bulb.

the examination reliably allows differentiation between a normal and an abnormal study.

Prior to the advent of ultrasound, UGI examination was performed to confirm the diagnosis of HPS. While the thickness of the pylorus muscle is not discernible at UGI examination, there are other imaging signs that suggest the diagnosis. The pyloric channel appears elongated at UGI examination as wispy, linear tracts of contrast pass through the canal, a finding called the "string" sign (Fig. 6-23). The "shoulder" sign is the name given to the appearance of the thickened pylorus impression on the dilated stomach antrum. Vigorous peristaltic contractions in the stomach occur without associated relaxation of the pyloric channel. Imaging over time allows reliable diagnosis of pyloric stenosis, as contrast is never able to pass through the channel in more than tiny wisps at a time.

The current treatment for HPS is pyloromyotomy, which can be performed laparoscopically. In this procedure

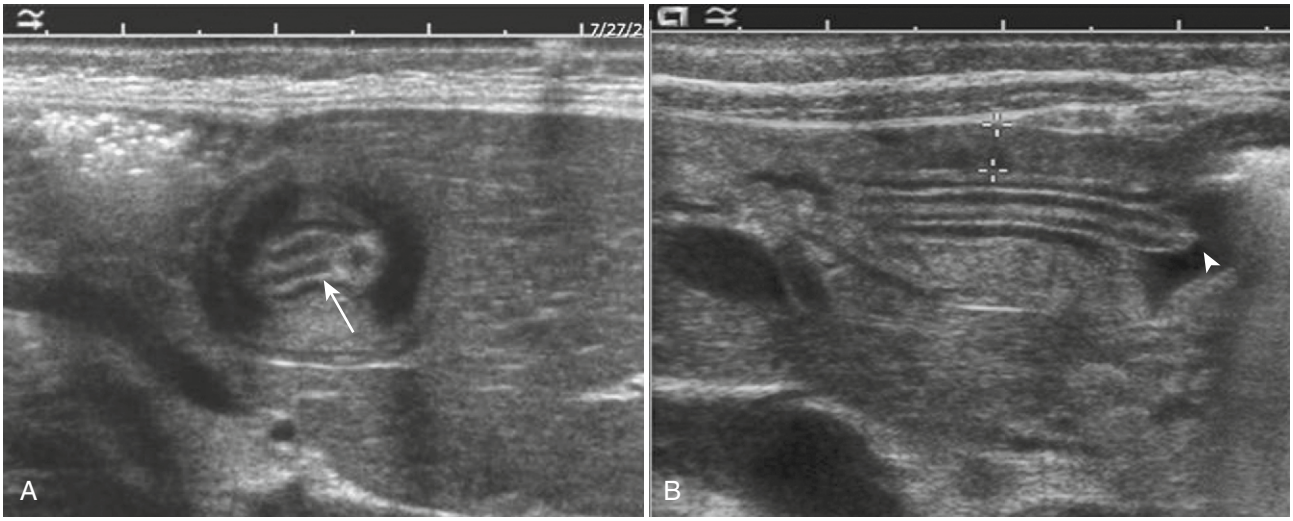


Figure 6-21. A, Transverse US image in a 5-week-old infant demonstrates the thickening of the pylorus and the redundancy of the mucosa in the pyloric channel *(arrow)*. This patient had hypertrophic pyloric stenosis at surgery. **B,** Longitudinal image of the pylorus in the same infant demonstrates the mucosa projecting into the antrum, a finding called the "nipple" sign *(arrowhead)*.

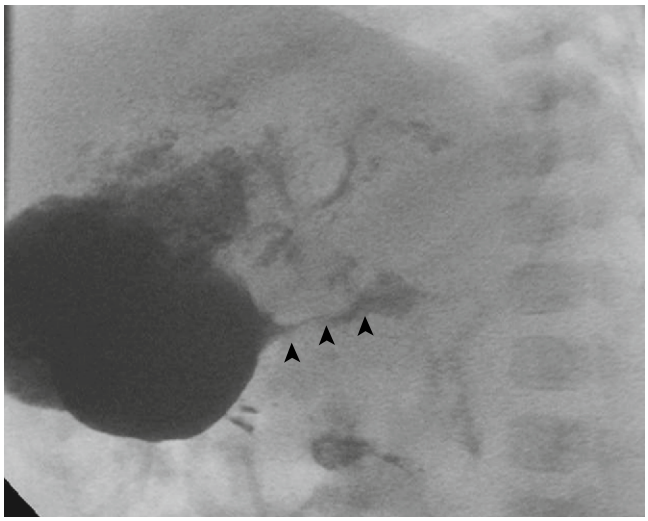


FIGURE 6-23. Fluoroscopic spot image from an upper gastrointestinal examination in a 1-month-old boy with reported bilious emesis. The pyloric channel is elongated, and only a small trickle of contrast is able to pass through *(arrowheads)*. Hypertrophic pyloric stenosis was confirmed at subsequent US.



FIGURE 6-24. Fluoroscopic spot image from a normal upper gastrointestinal examination. The duodenal C-sweep has a characteristic course, and the duodenojejunal junction is located to the left of midline at the level of the pylorus.

the hypertrophied muscularis is divided and the mucosa is allowed to bulge through the incision (i.e., the muscle is not sutured over). This procedure has been extremely effective at reducing the mortality rate in infants with HPS, which is now well below 1%.

Malrotation

"Malrotation" is a term used to describe an arrest in the development of the midgut that may occur at various stages of embryologic growth. This developmental arrest leads to a spectrum of abnormal rotation patterns of the intestinal tract. In patients with malrotation peritoneal or "Ladd's" bands form as a result of disorganized embryologic attempts to fixate the malrotated bowel. These bands may lead to bowel obstruction by crossing over a loop of bowel and compromising the integrity of its lumen. The "malfixated" intestines have a propensity to twist around the mesentery leading to a midgut volvulus. The compromised blood supply to the bowel can lead to bowel infarction, sepsis, and eventually death. In a previously well infant presenting with bilious emesis midgut volvulus is a primary clinical concern. While symptoms related to malrotation may theoretically occur at any age, they are more likely to occur in the first month of life. In most cases malrotation is an isolated defect with no predisposing genetic susceptibility or associated syndromes. Some conditions, however, are nearly universally associated with malrotation, including gastroschisis, congenital diaphragmatic hernia, and omphalocele. The heterotaxy syndromes also are associated with malrotation.

Abdominal radiographs and gastrointestinal contrast studies (UGI) are of paramount importance in making the diagnosis of malrotation. The bowel gas pattern is often normal in the presence of malrotation. A normal abdominal radiograph should not preclude further investigation in a child with clinical concern for malrotation. A UGI examination evaluates the course of the duodenum and the position of the duodeno-jejunal junction (DJJ). In normal patients the duodenum has a characteristic C-sweep that consists of four portions: the duodenal bulb and the descending, transverse, and ascending portions (Fig. 6-24). The descending through ascending portions of the duodenum are fixed in the retroperitoneum. The DJJ is normally located to the left of midline at the level of the duodenal bulb. When the DJJ is inferior or medial to this position, it is considered abnormal (Fig. 6-25). There are a few rare exceptions to this rule, which include previous surgery in the abdomen, abdominal masses that displace bowel, and marked gastric or colonic distention. A "corkscrew" configuration of the duodenum implies that a midgut volvulus is present. Midgut volvulus causes a closed loop bowel obstruction. The bowel may appear tapered or "beaked" at the level of obstruction, with proximally dilated bowel loops. Despite all of these findings, the diagnosis of malrotation remains difficult to make with certainty in up to 30% of cases in light of the subtlety of the findings and the overlap with normal anatomy. If the course of the duodenum is not straightforward, serial abdominal radiographs can be performed to follow the contrast distally to the colon. When malrotation is present, the small bowel is commonly located on the right side of the abdomen, and the cecum may also be abnormally positioned.

The preferred treatment for infants or children with malrotation is a Ladd's procedure. This surgery, often performed laparoscopically, entails reduction of a midgut volvulus, division of obstructing peritoneal bands, placement of the bowel in a state of nonrotation, and appendectomy. The urgency of surgery depends on whether a midgut volvulus is present at the time of diagnosis. Since all patients with malrotation are at risk of volvulus, even those patients without

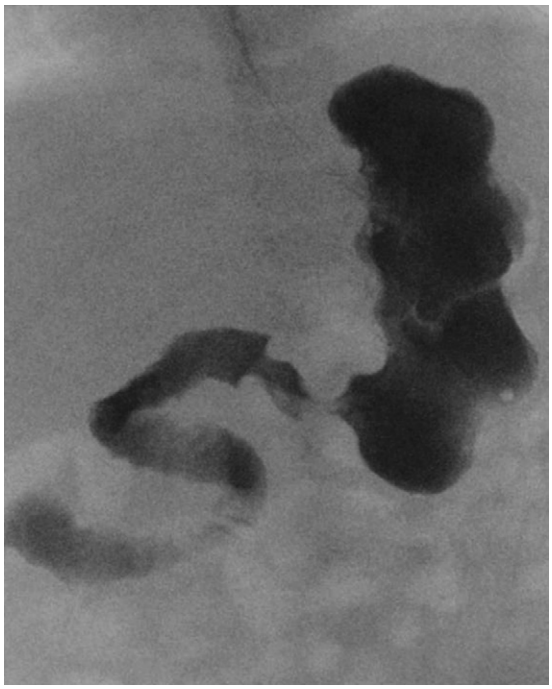


Figure 6-25. Upper gastrointestinal examination in a newborn baby with gastroschisis repair demonstrates malrotation.

a volvulus proceed to surgery semi-urgently. Recurrence of volvulus after Ladd's procedure is rare, but can occur.

Intussusception

Intussusception is one of the most common causes of bowel obstruction in young children. Intussusception occurs when one segment of the bowel (the intussusceptum) telescopes into the bowel immediately distal to it (intussuscipiens). This occurs most often in children between 6 months and 3 years of age. Common presenting symptoms are vomiting, lethargy, and bouts of irritability where the child draws his or her legs to the chest. The more classic symptoms of a palpable abdominal mass and "red currant jelly stool" are present in only the minority of cases and should not be relied on to suggest the diagnosis. Bloody stool is a manifestation of sloughed intestinal mucosa, which is a late finding in the disease and is present in less than half of all cases. The implications of delayed diagnosis may be devastating, as a persistent intussusception leads to bowel ischemia and perforation. Most intussusceptions in children are idiopathic, while the remaining cases are secondary to the presence of a pathologic lead point (PLP). PLPs include Meckel's diverticulum, colonic polyps, lymphoma, duplication cyst, or underlying diseases of the bowel such as Henoch-Schönlein purpura. The most common site for intussusception to occur is at the hepatic flexure, of which ileocolic intussusceptions are the most common type. Small bowel intussusceptions also may occur. Small bowel intussusceptions are usually transient phenomena that may not cause symptoms. They are likely to reduce spontaneously, and air reduction enema is not therapeutic. Imaging evaluation of the child with suspected intussusception begins with abdominal radiographs. Supine and left lateral decubitus views are recommended. The decubitus film, by allowing the cecum and ascending colon to assume a nondependent position in the abdomen, allows air to fill the cecum when an ileocolic intussusception is not present or if the cecum is not filled with stool. The sigmoid colon is often located within the right lower quadrant in young children, and one should be careful when excluding intussusception based on gas-filled bowel loops in this location. The "meniscus" sign and "target" sign are terms used to describe the radiographic appearance of a soft tissue mass in the colon (Fig. 6-26). Small bowel dilatation and air–fluid levels may be present signifying the presence of a small bowel obstruction (Fig. 6-27). Despite these signs, half of all abdominal radiographs are diagnostically unhelpful in the diagnosis of intussusception, and further evaluation is required.

For confirmation of intussusception, ultrasound is the preferred modality. When the sonographer is familiar with its imaging appearance, intussusception is identified in all cases. Intussusception has a characteristic appearance in both transverse and sagittal planes. In the transverse plane, an intussusception appears as a mass usually between 3 and 5 cm in diameter that has a "target" or "doughnut" configuration of alternating hypo- and hyperechoic layers (Fig. 6-28A). In the sagittal plane the mass assumes a "pseudokidney" configuration. Color Doppler is used to evaluate the vascularity of the bowel and is a promising predictor of bowel viability (Fig. 6-28B). Enlarged mesenteric lymph nodes may be present at the site of intussusception, which may function as a lead point. Imaging pitfalls in the diagnosis of intussusception include stool in the cecum, thickened loops of small bowel in the right lower quadrant, and the normal psoas muscle. Each of these structures may be mistaken for an intussusception. It is also important to appreciate the difference between small bowel intussusceptions and ileocolic intussusception. Small bowel intussusceptions

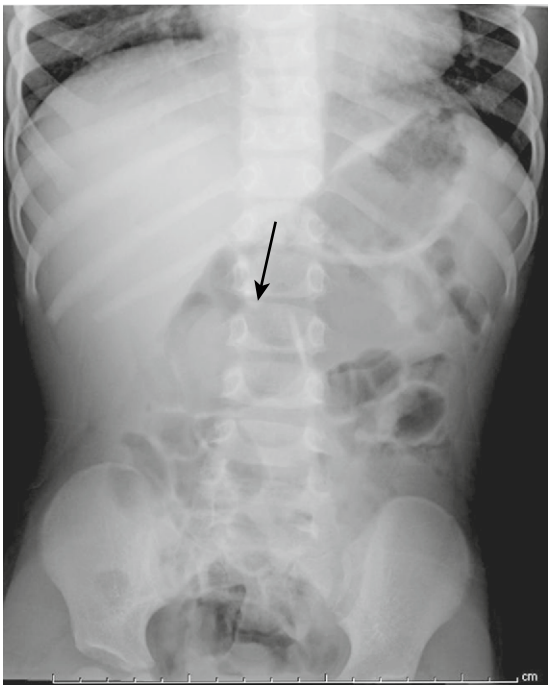


Figure 6-26. Abdominal radiograph in a 2-year-old boy with abdominal pain reveals a soft tissue mass within the right upper quadrant in the region of the hepatic flexure *(arrow)*. This was confirmed with US to represent an ileocolic intussusception.

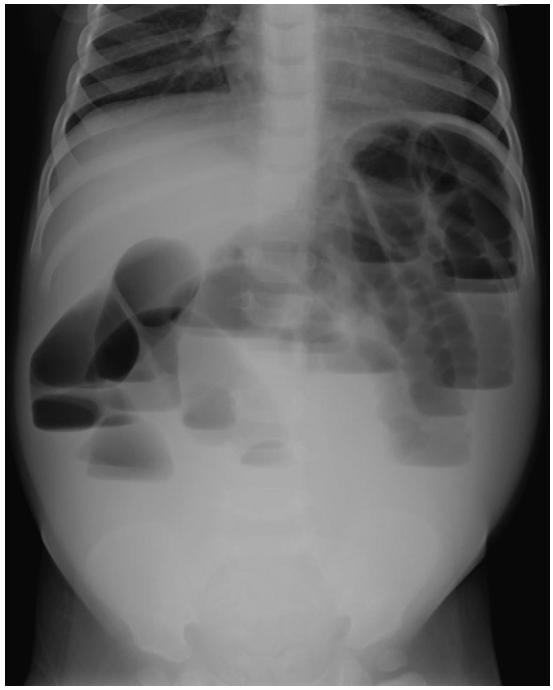


FIGURE 6-27. Abdominal radiograph in a 1-year-old boy demonstrates multiple air–fluid levels and dilated loops of bowel. This child had an ileocolic intussusception confirmed at US.

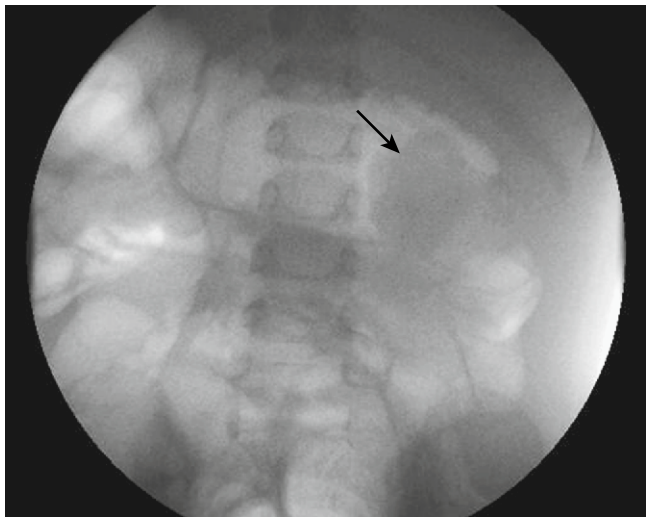


FIGURE 6-29. Fluoroscopic image obtained during air reduction enema in this child (who is prone) demonstrates the soft tissue mass at the hepatic flexure *(arrow)*. Later images demonstrated complete reduction of this ileocolic intussusception.

are usually treated conservatively, whereas ileocolic intussusceptions proceed to enema reduction or surgery. The diagnosis of small bowel intussusception is suggested by the location of the intussusception (outside of the right lower quadrant), small diameter (less than 2 cm), and short-segment involvement (less than 5 cm).

Fluoroscopically guided contrast reduction enema is a widely accepted and utilized method of treatment for ileocolic intussusception. Contraindications to performing an enema include shock, peritonitis, or radiographic evidence of perforation. Although different contrast agents are used, air is preferred at our institution. After inserting a rectal catheter into the buttocks air is insufflated into the colon. The intussusception is visualized fluoroscopically as it is reduced back through the colon (Fig. 6-29). A successful reduction involves the reduction of the intussusception beyond the ileocecal valve (often with a visible "pop") with reflux of air into the small bowel. Air reduction enema is successful in over 80% of cases. When the enema is not successful, surgery is curative. A rare, but serious, complication of the air reduction enema is bowel perforation leading to tension pneumoperitoneum, which necessitates emergent needle decompression. Perforation occurs in approximately 1.5% of cases.

Acute Appendicitis

Acute appendicitis is the most frequent condition in children requiring emergent abdominal surgery. Acute appendicitis is caused by obstruction of the appendiceal lumen

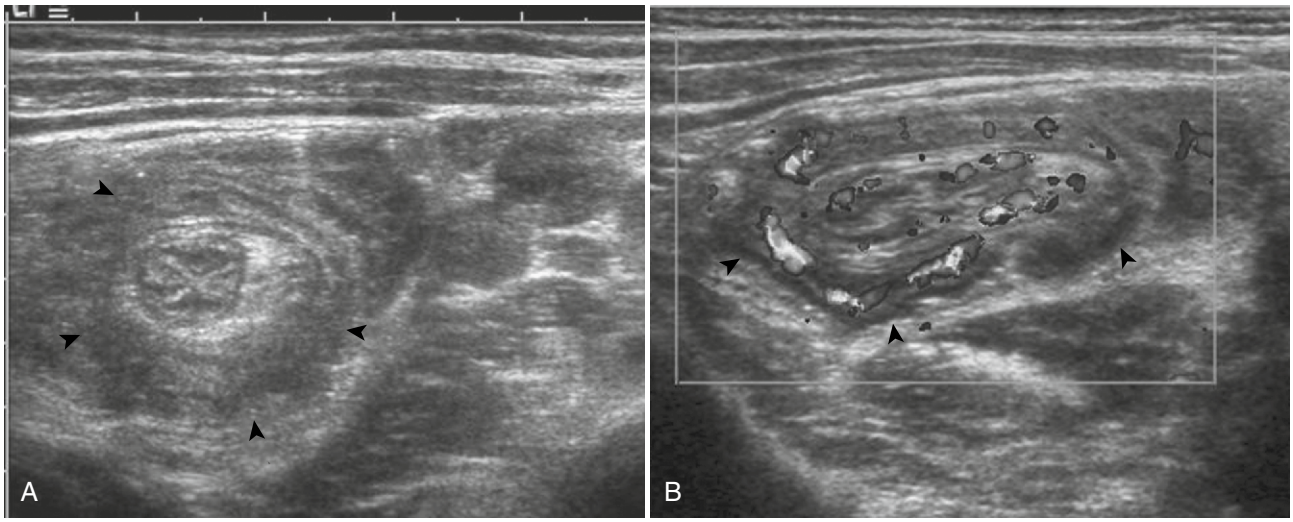


FIGURE 6-28. **A,** Transverse US image in a 1-year-old child with crampy abdominal pain demonstrating the "target" appearance of an ileocolic intussusception. The "intussuscipiens" is delineated by arrowheads. **B,** Sagittal US image in the right lower quadrant in the same patient demonstrates the presence of color Doppler flow to the intussuscipiens *(arrowheads)*.

that leads to accumulation of fluid and secondary inflammation and infection. Luminal obstruction is most often secondary to the presence of a fecalith, but may also be secondary to lymphoid hyperplasia, foreign bodies, or mass lesions (i.e., lymphoma). Perforation is common in pediatric patients. The frequency of perforation increases as the age of the patient decreases. Children who are suspected of having acute appendicitis warrant imaging evaluation that is both expeditious and accurate in order to avoid complications of perforation, such as abscess formation, bowel obstruction, and sepsis.

Graded-compression sonography is an appealing imaging modality for the initial evaluation of children suspected to have acute appendicitis. The advantages of ultrasound include the lack of ionizing radiation, the lack of patient preparation, and the lack of sedation. The patient is often able to precisely localize the site of pain in order to direct the sonographer to the appropriate area. Disadvantages of ultrasound are that US is highly operator dependent, the accuracy of the study is largely impacted by the body habitus of the patient, US is poorly accurate at diagnosing a normal appendix, and US is often not able to determine if the appendix is perforated.

CT examination is highly sensitive for the diagnosis of acute appendicitis. In many cases, CT may also provide an indication that the appendix has perforated. In many institutions, a negative or equivocal ultrasound for appendicitis prompts a CT scan. Depending on the institution, various combinations of oral and intravenous contrast are used. Although CT is more highly accurate at diagnosing appendicitis than US, US is often performed initially in children in an effort to avoid or reduce the inherent risks of radiation exposure. Therefore, it is important to be familiar with the imaging features of acute appendicitis with US as well as CT.

On US, the inflamed appendix appears as a blind-ending, tubular structure with bowel signature. When pressure is applied, the inflamed appendix is noncompressible. On transverse images the appendix will have a "target"-sign configuration that is made up of the alternating layers of the appendiceal wall. While no exact measurement defines an acutely inflamed appendix, in general practice an appendix with a diameter greater than 6 mm is considered abnormal. Secondary signs of appendicitis include free fluid in the abdomen or pelvis, enlarged mesenteric lymph nodes, and fluid collections adjacent to the appendix that represent abscesses.

Many of these same imaging features for US also apply to CT. CT findings of acute appendicitis include a maximal outer luminal diameter greater than 6 mm, lack of oral contrast within the lumen (if oral contrast was administered), an appendicolith, and periappendiceal inflammatory changes. Associated findings include enlarged mesenteric lymph nodes, free fluid, and inflammatory changes in the adjacent bowel. The presence of free air and abscess formation are important signs that the appendix is likely perforated.

Although appendicitis is common, its imaging features are not always straightforward. Given the variability in the location and position of the appendix, the clinical symptoms can be misleading. If the appendix is located within the pelvis in a young woman, appendicitis may simulate an ovarian process such as torsion of the ovary or hemorrhagic ovarian cyst. Likewise, a subhepatic appendix may present with right upper quadrant pain simulating gallstones, or flank pain concerning for pyelonephritis.

Meckel's Diverticulum

Meckel's diverticulum is the most common congenital anomaly of the gastrointestinal tract, found in 2% to 3% of the general population. A Meckel's diverticulum is a true diverticulum along the antimesenteric border of the distal ileum that results from incomplete atrophy of the omphalomesenteric duct in fetal development. Its lining consists of normal small bowel mucosa, though in some cases ectopic gastric or pancreatic mucosa may be present. It is most often located in the right lower quadrant. There is no known association with other congenital malformations. Asymptomatic Meckel's diverticulum occurs with nearly equal frequency in boys as in girls, although symptomatic Meckel's is more common in males. While most Meckel's diverticula are asymptomatic, when symptoms do occur, it is most often a result of a complication of the diverticulum and is more common in children than adults.

Forty percent of children with vitelline duct anomalies such as Meckel's diverticulum are symptomatic. The most common symptoms are abdominal pain, nausea, vomiting, and rectal bleeding. Hemorrhage and obstruction are the most common complications. In patients presenting with hemorrhage related to a Meckel's diverticulum, ectopic gastric mucosa is almost always present. The bleeding is caused by peptic ulceration within the gastric mucosa and/or the adjacent ileal mucosa, and is typically painless. The presence of ectopic gastric mucosa serves as the basis for the "Meckel's scan," or 99m-Tc-pertechnetate scintigraphy. Given the relatively low sensitivity of this examination, however, a negative result often has little impact on clinical management when a Meckel's diverticulum is strongly suspected. Arteriography and contrast studies may be helpful in these instances, although these evaluations may be superseded by colonoscopy or laparoscopy.

Bowel obstruction secondary to Meckel's diverticulum can occur secondary to volvulus, intussusception, inversion of the diverticulum into the bowel lumen, inclusion of the diverticulum into a hernia, or diverticulitis. Persistent attachments of the diverticulum to the umbilicus may be the cause of bowel obstruction. A transition point may be identified on CT where proximal, dilated bowel loops abruptly change caliber to collapsed, distal loops, although the obstructing band itself is not visible. The diverticulum can also serve as a lead point for intussusception and should be suspected in any child presenting with intussusception who is outside the typical age range for idiopathic intussusception. Acute Meckel's diverticulitis may mimic acute appendicitis in a child presenting with abdominal pain, fever, and vomiting. Visualization of a normal appendix is helpful in distinguishing these two entities, as well as identifying the ileum at the base of the diverticulum. This assessment is much more easily made with CT than with US. Identification of an enterolith on abdominal radiographs or CT is useful for suggesting the diagnosis of Meckel's diverticulum in the setting of obstruction, especially when

located in the right lower quadrant. There may be mixed-attenuation fecal material entrapped within the blind-ending diverticulum.

Mesenteric Adenitis

Not all children presenting to the emergency department with abdominal pain have an abnormality requiring emergent diagnosis and treatment. In the absence of other abnormalities, a child's symptoms are often attributed to an entity called "primary mesenteric lymphadenitis." Enlarged mesenteric lymph nodes on CT or US may be the only imaging abnormality present. The etiology for the lymphadenopathy is unclear, although a nonspecific gastrointestinal inflammation may be the underlying cause. While there is no precise size criterion that defines an abnormally enlarged mesenteric lymph node in children, a node with a short axis diameter greater than 8 mm is considered enlarged. Whereas these measurements are based on data acquired with CT, the diagnosis may also be made on the basis of US findings.

Omental Infarction

Omental infarction most often occurs in obese children. This entity is best recognized at CT, although it can also be detected with US. Patients often present with right lower quadrant or diffuse abdominal pain, and fever and elevated white blood cell count are often not present. Imaging studies (CT and US) demonstrate normal-appearing bowel, including the appendix. The presence of hazy, increased attenuation within the anterior abdomen in the region of the omentum is a hallmark of this diagnosis. The diagnosis may also be suggested at US by detection of an echogenic, masslike structure just deep to the anterior abdominal wall in the area of pain. If no other abnormalities are appreciated, this entity can be treated conservatively with prophylactic antibiotics and analgesics.

GENITOURINARY

Urinary Tract Infection

The diagnosis of a urinary tract infection (UTI) in children is based on symptoms, bacterial growth in the urine, and other laboratory markers. Distinguishing between upper tract (i.e., pyelonephritis) and lower tract (i.e., cystitis) infection is based on clinical criteria such as the presence of a fever. Young children with a first-time UTI or any child with a febrile UTI warrants imaging evaluation of the urinary tract. The goal of imaging in children with UTI is to exclude an underlying structural abnormality that predisposes the child to develop infection, to evaluate for an obstructed urinary system or other pathology that would require urgent intervention (e.g., abscess), and to evaluate for evidence of renal damage such as scarring. Pyelonephritis in children is often secondary to vesicoureteral reflux. Although cortical renal scintigraphy is the most sensitive imaging technique for detection of acute pyelonephritis, it is rarely performed emergently. Most young children with a febrile UTI are evaluated for vesicoureteral reflux with a VCUG or radionuclide cystogram (RNC). These evaluations can be performed several days or weeks after the initial infection. Children presenting to the emergency department with a complicated UTI (persistent fevers despite antibiotics, or clinical signs and symptoms concerning for severe illness or sepsis caused by a UTI) warrant evaluation with ultrasound.

In patients with acute pyelonephritis, ultrasound may reveal focal areas of decreased attenuation. These same areas demonstrate decreased vascularity with color Doppler US. Urothelial thickening is often present. A severe infection may evolve into renal abscess or perinephric abscess. At US these collections appear as hypoechoic or anechoic masses with increased through-transmission (Fig. 6-30A). A renal abscess may simulate a solid mass at US. In these instances, contrast-enhanced CT is performed. At CT an abscess will appear as a focal, hypoattenuating mass (Fig. 6-30B). While the wall of the abscess enhances after contrast

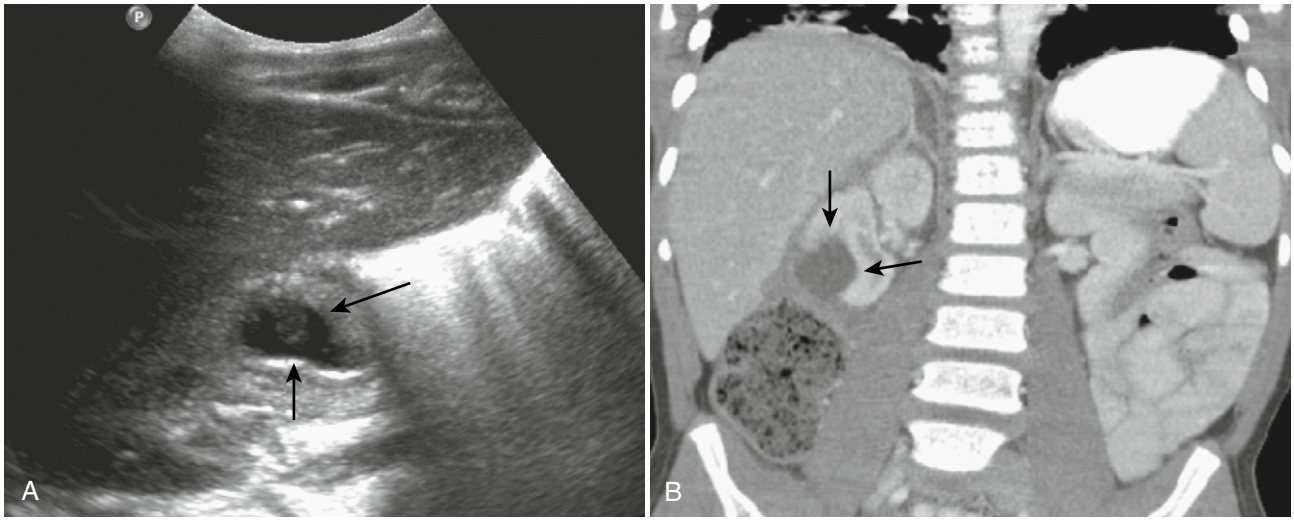


FIGURE 6-30. A, Transverse US image through the kidney in an 8-year-old boy 1 day after a negative appendectomy was performed. A hypoechoic collection is present at the lower pole of the right kidney *(arrows)*. **B,** Coronal reformatted image from a CT scan performed with oral and intravenous contrast demonstrates a hypoattenuating collection at the right lower pole *(arrows)* that does not enhance. This collection was later found to represent a renal abscess, and a drainage catheter was placed. Incidentally, this child had negative urine cultures.

administration, the central portion of the abscess will not enhance. A perinephric abscess is suggested by fluid or soft tissue attenuation within the perinephric space. These collections may penetrate through Gerota's fascia and involve surrounding structures, such as the psoas muscle. Urine cultures in patients with renal abscess are negative in up to 20% of cases.

Hydronephrosis

Hydronephrosis refers to dilatation of the urinary collecting system caused by an obstruction to the normal flow of urine. The obstruction may occur anywhere along the urinary tract from the renal calyces to the urethra. Stasis of urine and increased pressures within the collecting system may have deleterious effects on the kidney over time and lead to progressively worsening renal function. A dilated urinary collecting system is not always obstructed. VUR, for example, causes transient dilatation of the urinary collecting system. An obstructing ureteral calculus or stricture may lead to proximal hydroureteronephrosis (dilatation of both the renal collecting system and the ureter) that is indistinguishable from VUR. Determining the cause for a dilated collecting system is not always straightforward. Often other clinical parameters are necessary to make this determination, as well as additional imaging evaluation.

Ultrasound is the modality of choice for evaluating for hydronephrosis. Communication between multiple cystic-appearing, dilated renal calyces and the renal pelvis is an important finding at US. If these cystic spaces do not communicate with each other or with the renal pelvis it is more likely that the patient has cystic renal disease rather than a dilated collecting system. Color Doppler ultrasound is helpful in demonstrating prominent vessels in the renal hilum so that they are not mistaken for a dilated renal pelvis. The ureters are not typically visualized at US unless they are dilated. A dilated distal ureter can often be visualized posterior to the bladder at the level of the ureterovesicular junction (UVJ). If a single ureter is dilated at this level, the obstruction is likely at the UVJ; if both ureters appear dilated at this level the obstruction is likely within or below the bladder (although bilateral UVJ obstruction can occur). Imaging of the bladder may reveal wall thickening and/or trabeculations in patients with an underlying abnormality, such as a neurogenic bladder. Intraluminal debris or calculi may be present within the bladder of patients with concurrent UTI.

Ureteropelvic Junction Obstruction

A common cause of hydronephrosis in children is ureteropelvic junction obstruction (UPJO). UPJO may be secondary to either intrinsic or extrinsic factors. Prenatal US detects many children with intrinsic UPJO; therefore approximately half of all children presenting later in childhood with intermittent UPJO have an extrinsic abnormality such as a crossing vessel. UPJO is often an intermittent phenomenon. Children with intermittent UPJO present with episodic abdominal pain, nausea, and vomiting. The severity of pain correlates with the rapidity of the onset of symptoms rather than the degree of distention of the collecting system. Hematuria is present in approximately half of patients and aids in elucidating the urinary system, rather than other abdominal organs, as the source of symptoms. UPJO is more common in males, and occurs most often on the left side.

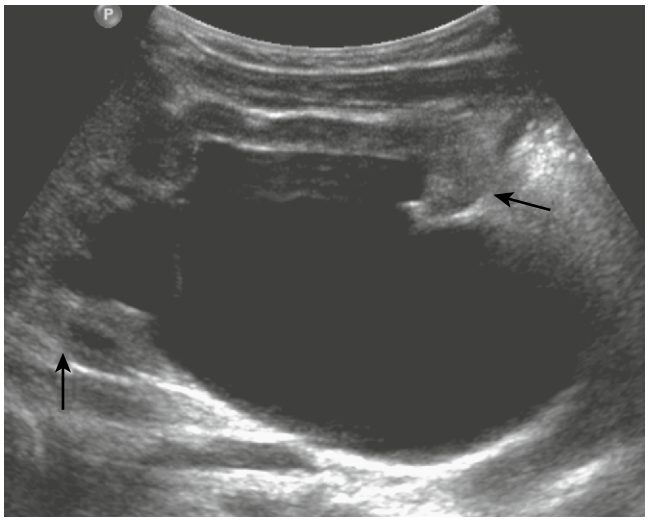


Figure 6-31. Sagittal US image through the kidney in this 6-month-old baby with ureteropelvic junction obstruction. The kidney *(arrows)* is barely visualized secondary to the massive hydronephrosis.

The ultrasound appearance of UPJO is a dilated renal collecting system on the patient's symptomatic side during the acute pain crisis (Fig. 6-31). The proximal ureter will appear dilated with an abrupt tapering at the level of the crossing vessel. US should be performed during the pain crisis since the hydronephrosis is present only when the patient is experiencing symptoms. Unilateral hydronephrosis is not specific for UPJO, nor does US evaluate the functional status of the kidney. While additional investigation is often required before treatment can be initiated, US is critical in the preliminary imaging of patients with suspected urinary tract obstruction.

Urolithiasis

While less common in children than in adults, urinary tract calculi are an important cause of flank pain and urinary tract infection. The majority of urinary tract calculi in children are located in the kidneys or ureters. Boys and girls are affected with nearly equal frequencies. Abdominal or flank pain is the most common presenting complaint, but is present in less than half of children with renal stones. Other signs and symptoms include pyuria, hematuria, nausea, vomiting, fever, and urinary retention. Smaller children who are not able to verbalize their symptoms more commonly present with symptoms of infection rather than specific complaints of pain. The majority of pediatric patients with urolithiasis have an underlying predisposition to forming stones. These predisposing conditions include congenital structural disorders of the urinary system (e.g., UPJO or "horseshoe" kidney), metabolic disorders (e.g., hypercalciuria or cystinuria), prolonged states of immobilization leading to urinary stasis, enteric disease causing intestinal malabsorption, and recurrent urinary tract infections.

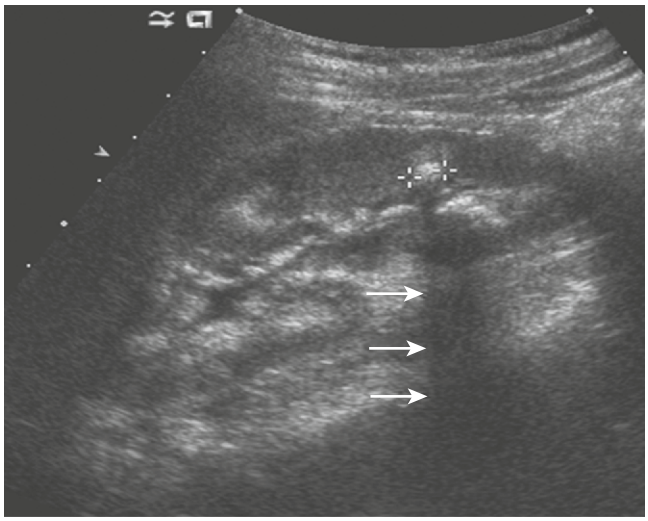


FIGURE 6-32. Sagittal US image through the right kidney in a teenage girl with known renal calculi. An echogenic calculus is present in the lower pole with posterior acoustic shadowing *(arrows)*.



FIGURE 6-33. Axial image from a noncontrast CT performed in a 17-year-old boy with left groin pain and a negative scrotal US. There is a tiny calculus at the left ureterovesicular junction *(white arrowhead)* with periureteral stranding.

The imaging evaluation of a child with suspected urolithiasis is performed with US, CT, or both. US is an appealing first-line imaging modality because it detects complications of urolithiasis such as hydronephrosis or perinephric fluid without the use of ionizing radiation. At US, renal calculi appear as echogenic foci with posterior acoustic shadowing (Fig. 6-32). US also has the advantage of evaluating the renal parenchyma for changes of medical renal disease or evidence of scarring. US is less sensitive than CT for detection of urinary tract calculi and is poorly accurate at diagnosing calculi that are confined to the ureter. CT is often performed in children who have persistent urolithiasis symptoms despite a normal US examination.

Unenhanced CT (without oral or intravenous contrast) is highly sensitive for the detection of urolithiasis in pediatric patients. Lower-dose CT protocols have been developed that minimize radiation risk to patients. Diagnosis of urolithiasis on CT is facilitated because phleboliths, which often mimic ureteral calculi in older patients, are rarely encountered in children. Secondary CT signs of urolithiasis are helpful in confirming the diagnosis, and include proximal ureteral dilatation, renal enlargement, hydronephrosis, decreased renal attenuation, the tissue rim sign, and perinephric stranding. The tissue rim sign refers to the circumferential rim of soft tissue attenuation surrounding a ureteral calculus (Fig. 6-33). These secondary signs of urinary tract calculi are less commonly encountered in pediatric patients versus their adult counterparts. Proximal ureteral dilatation and renal enlargement are the most commonly detected secondary signs, and occur in approximately half of patients. Perinephric or periureteral stranding, rarely encountered in the pediatric patient, may be secondary to the decreased amount of perinephric fat in this population.

Scrotal Hernia

If the testes have not descended into the scrotum by 1 year of age cryptorchidism (failure of the testes to descend into the scrotal sac), inguinal-scrotal hernias, and hydroceles may result. While these conditions are most often detected on physical examination, it is not uncommon to make the diagnosis at ultrasound. Plain films are diagnostic of scrotal hernias in infants when the finding of bowel gas in the scrotum is noted (Fig. 6-34). Since this is not a common finding, US is the imaging modality of choice for evaluation of a scrotal hernia when the physical exam is inconclusive. Herniated omentum appears as an echogenic structure outside of the testis and epididymis. Bowel loops containing both air and fluid may also be visualized within the scrotum. Visualization of bowel peristalsis during imaging is an important finding to note when herniated bowel is identified within

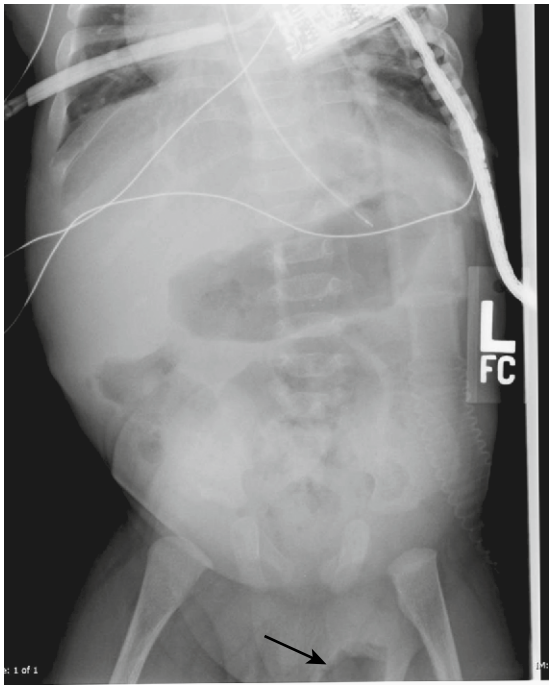


FIGURE 6-34. Abdominal radiograph in a newborn infant with several loops of mildly dilated bowel reveals gas projecting over the scrotum at the inferior aspect of the image *(arrow)*. This infant has a scrotal hernia.

the scrotum. If bowel is identified within the scrotum but no peristalsis is visualized during the entire examination, the bowel may be strangulated. An akinetic, dilated loop of bowel observed at US in a hernia sac is reported as a highly sensitive and specific sign of bowel strangulation. A strangulated scrotal hernia is an indication for urgent surgery.

Epididymitis

Epididymitis, or epididymo-orchitis, is an infection of the epididymis and/or testis and is a common cause of acute-onset scrotal pain in children. Typically, scrotal pain associated with epididymitis or epididymo-orchitis is relieved when the testes are elevated over the symphysis pubis, a maneuver that is called the Prehn sign. In contradistinction, the pain associated with testicular torsion is not relieved by this maneuver. While the causative agent in epididymitis is usually not identified in young children, the infection usually originates in the prostate gland or bladder and spreads to the epididymis and testis via the vas deferens and spermatic cord lymphatics. A congenital anomaly of the urinary tract may be present. In adolescents the cause is most often a sexually transmitted infection.

Ultrasound examination of a child with epididymitis demonstrates enlargement of the epididymis (primarily the head) with heterogeneous echotexture. On color Doppler evaluation there is increased blood flow to the epididymis and/or testis (Fig. 6-35). A reactive hydrocele may be an associated finding. When the entire testis is involved, it is often enlarged and has altered echogenicity. On gray-scale imaging findings alone, the appearance of the testis may mimic a diffusely infiltrative disease such as leukemia or lymphoma, although the clinical presentation should suggest the correct diagnosis.

Torsion of the Testicular Appendages

While there are four testicular appendages, only two are commonly visible at ultrasound: the appendix testis and appendix epididymis. These appendages are remnants of embryonic ducts and serve no real function. Because they are attached by a small pedicle, they are prone to torsion.

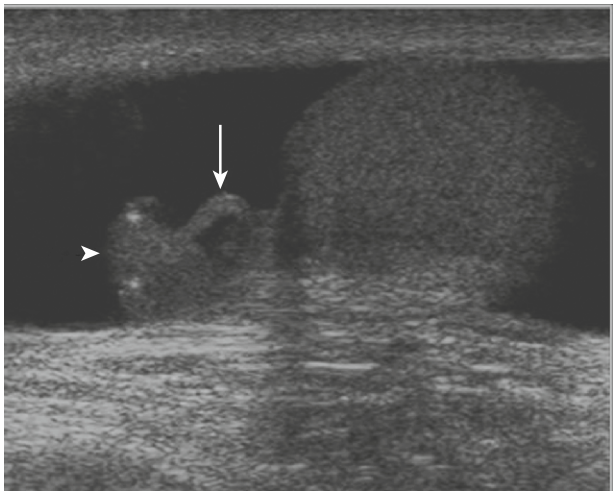


Figure 6-36. Transverse US image through the testis on a teenage boy with scrotal pain. A mixed echogenicity structure *(arrowhead)* is connected to the testis by a thin stalk *(arrow)*. Color Doppler US failed to demonstrate flow within this structure. The child was given a presumed diagnosis of torsed testicular appendage and was treated conservatively.

Torsion of these appendages is one of the most common causes of acute scrotal pain in children. The appendix testis is more commonly affected than the appendix epididymis, although it is often difficult to identify the offending appendage. Patients are usually young, prepubertal males who complain of acute-onset scrotal pain. On clinical examination there may be a bluish discoloration of the skin at the site of pain, which is called the "blue dot" sign and is pathognomonic. At ultrasound the torsed appendix is often identified as a round, extratesticular, extraepididymal mass lacking color Doppler flow (Fig. 6-36). A reactive hydrocele may be present, as well as scrotal wall skin thickening.

Testicular Torsion

The testis and epididymis attach to the inner scrotal wall by a broad attachment. When this attachment is too narrow, it may function as a pedicle around which the testis

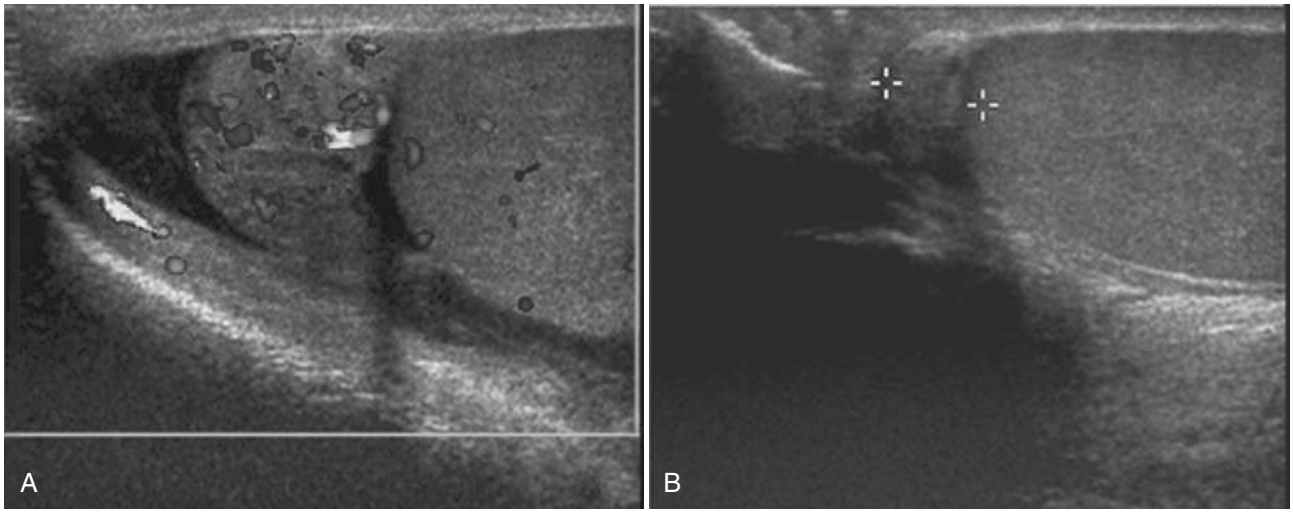


Figure 6-35. A, Sagittal US image through the left testis in this 17-year-old male with left scrotal pain. The left epididymis is enlarged and hyperemic. **B,** Sagittal US image in the same patient demonstrating the normal right testicle for comparison.

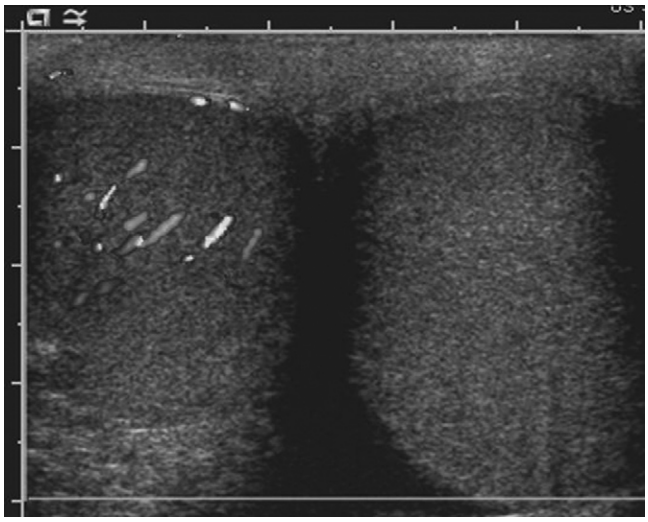


FIGURE 6-37. Transverse US image of bilateral testes in a teenage boy with left testicular pain. There is no color Doppler flow to the left testis. This patient had testicular torsion confirmed at surgery.

may twist. This twisting, or torsion, compromises the blood supply to the testis, which may lead to infarction of the testis. Scrotal pain is often the presenting complaint in boys with testicular torsion, a condition that requires emergent treatment to maintain viability of the affected testis. Testicular salvage rates are greatest when surgery is performed within 6 hours of the onset of symptoms. After 24 hours the testis is usually no longer salvageable. Patients with the "bell clapper" deformity, where the tunica vaginalis joins high on the spermatic cord, are more prone to testicular torsion than the general population.

Ultrasound is the preferred imaging examination for the diagnosis of testicular torsion because of its high sensitivity and specificity. Gray-scale US findings are often completely normal when torsion is present, and the testes may appear symmetric with respect to both size and echogenicity. A small hydrocele may be present on the affected side. Within a few hours of the onset of symptoms, the scrotal wall will appear thickened, and the testis and epididymis appear enlarged and hypoechoic (secondary to inflammation and/or hemorrhage). Color Doppler is crucial for the diagnosis of torsion. The lack of demonstrable blood flow to the affected testis (assuming appropriate US settings are used) is virtually pathognomonic for torsion (Fig. 6-37). In prepubertal patients it is often difficult to demonstrate the presence of blood flow even in normal testes. Testicular scintigraphy is often used as an adjunct to US when a diagnosis of torsion cannot be made with certainty. Given the added delay of scintigraphic examinations, however, some surgeons operate on the basis of an equivocal US. The treatment for testicular torsion is detorsion of the affected testicle, and orchiopexy, where the testis is affixed to the scrotal wall to prevent torsion from recurring in the future.

Ovarian Torsion

Acute onset of adnexal pain in a young or adolescent female is concerning for ovarian torsion. The Fallopian tubes are long in children and the ovaries are hypermobile, which increases their susceptibility to torsion. Although normal ovaries may torse, most often there is an ovarian or paraovarian cyst or mass that predisposes the ovary to torsion by functioning as a fulcrum around which the ovary can twist. The ovary becomes twisted around its pedicle leading to various degrees of hemorrhagic infarction. If surgery is not performed expeditiously, future fertility and hormonal regulation may be compromised. There is a slight predilection for torsion to involve the right ovary. When the right ovary is affected, the diagnosis is more difficult to establish given the number of other conditions that present with right lower quadrant or pelvic pain such as appendicitis, Meckel's diverticulitis, and inflammatory bowel disease. The median age of patients with ovarian torsion is 11 years.

Pelvic US is the study of choice for evaluation of ovarian torsion. Normal ovaries often appear hypoechoic relative to the adjacent pelvic tissue, and have an ovoid or ellipsoid shape. While the size of normal ovaries varies, mean ovarian volumes are approximately 1.2 cm^3 in prepubertal girls and 5.8 cm^3 in pubertal girls. Microcystic follicles are routinely identified in normal ovaries. When the ovaries demonstrate normal gray-scale imaging characteristics and have a normal size and shape, color Doppler evaluation is usually not necessary. If, however, one ovary appears abnormally large relative to the other side, torsion may be present. In nearly all cases of ovarian torsion, the affected ovary is massively enlarged and has a round or globular configuration. In neonates and young girls ovarian torsion is commonly seen as a large cystic mass with fluid–debris levels. In young or adolescent girls the more classic imaging appearance is an enlarged, echogenic ovary with multiple enlarged peripheral follicles. In other cases, the ovary may appear as a complex cystic mass secondary to the presence of an underlying cyst or tumor (Fig. 6-38). Color Doppler evaluation of the ovary will often reveal an absence of blood flow, a finding classically associated with ovarian torsion. However, torsion may be present even if arterial waveforms are demonstrated

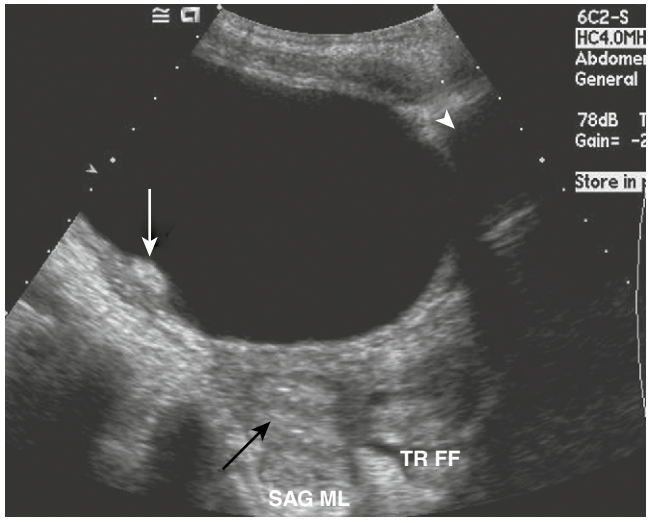


FIGURE 6-38. Sagittal US image of the pelvis in a 15-year-old girl with right lower quadrant pain. The bladder is nearly empty *(arrowhead)*, and there is a large, complex cystic mass within the pelvis that contains a mural nodule *(white arrow)*. The uterus is posterior to this mass *(black arrow)*. Color Doppler revealed no convincing flow to this mass. At surgery the patient was found to have a right ovarian teratoma that had torsed.

because the ovary has a dual blood supply (from both the uterine and ovarian arteries). The presence of arterial waveforms within the ovary should not sway the diagnosis away from ovarian torsion if the gray-scale imaging findings and physical examination are consistent with torsion.

Hemorrhagic Ovarian Cyst

Although hemorrhagic ovarian cysts are common, their imaging appearance is widely variable. Hemorrhagic cysts are almost exclusively encountered in menstruating, adolescent females. Hemorrhagic cysts develop at the time of ovulation when vessels surrounding a corpus luteal cyst rupture, giving rise to hemorrhage within the corpus luteum. As the cyst evolves over time, the sonographic features change with the stage of clot retraction. Patients may present with acute-onset adnexal pain, which may be severe.

Physiologic ovarian follicles measure less than 3.0 cm in diameter. Most hemorrhagic cysts measure 3.0 to 3.5 cm in diameter, have a thin outer wall, and demonstrate posterior acoustic through-transmission. Fine, reticular septations resembling a fishnet pattern are a common finding at US. These septations represent fibrin strands, which contain no blood flow. In some patients the hemorrhagic cyst contains retracting clot. While a large portion of the cyst appears anechoic the retracting clot appears as an adherent, echogenic structure within the cyst that contains no blood flow. In rare cases, when the clot becomes very small it can simulate a mural nodule and raise concern for ovarian neoplasm. Fluid–fluid or fluid–debris levels can also be demonstrated within a hemorrhagic cyst. Hemorrhagic cysts can be complicated by rupture, with free spill of hemorrhagic contents into the pelvis. When this occurs, echogenic fluid is demonstrated within the pelvis surrounding the uterus and adnexa. In some cases, the hemoperitoneum may be massive.

Other causes of adnexal pain include tubo-ovarian abscess, ectopic pregnancy, and pelvic inflammatory disease. In patients who are sexually active, these diagnoses should also be considered within the differential. Human chorionic gonadotropin results are critical for the accurate interpretation of a pelvic US examination in a sexually active female with complaints of pelvic pain.

Hematocolpos/Hematometrocolpos

Patients with imperforate hymen present at the time of adrenarche with cyclic bouts of pelvic pain that correspond to menstruation episodes. The patient may not be aware that she has begun menstruating due to the lack of passage of blood products from the obstructed vagina. The diagnosis of hematocolpos is often made on the basis of physical examination, as the hymen may appear to be bulging outward secondary to accumulated secretions. In some cases US may suggest the diagnosis when a thorough physical examination has not been performed. In rare cases, the patient may have a congenital uterine anomaly with an obstructed hemivagina. In these cases the diagnosis is clinically more confusing since the patient will appear to menstruate normally given the presence of an unobstructed hemivagina.

US examination in these patients reveals a round or oblong-shaped midline or paramidline pelvic mass that compresses the bladder anteriorly and rectum posteriorly.

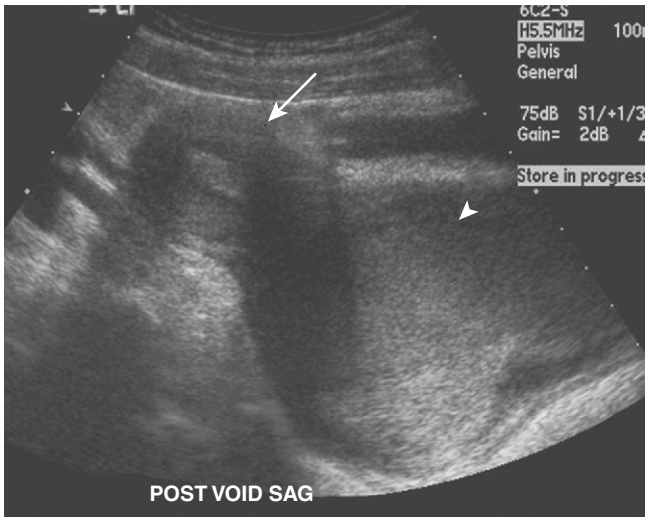


Figure 6-39. Sagittal US image through the pelvis in a 13-year-old female with severe, crampy abdominal pain. Inferior to the uterus *(arrow)* there is an oblong-shaped mass *(arrowhead)* with low-level internal echotexture. The mass is within the vagina. This patient had hematocolpos at surgery.

The mass appears hypoechoic with posterior acoustic transmission. Internal echoes are present within the mass, reflecting the complex nature of its contents (hemorrhage). If only the vagina is involved, the uterus will be visualized separately from this mass (Fig. 6-39). When the uterus is affected, only a thin rind of normal uterine tissue may be visualized. Patients will most often experience relief of symptoms once hymenotomy is performed.

CHEST AND AIRWAY

Stridor

Stridor is a term used to describe a high-pitched sound caused by partial obstruction of the airway. Stridor can have an inspiratory, expiratory, or biphasic pattern (both inspiratory and expiratory). An inspiratory pattern suggests an upper airway cause (e.g., epiglottitis). An expiratory pattern suggests a lower airway etiology (e.g., tracheomalacia). A biphasic pattern suggests a glottic or subglottic obstruction (e.g., subglottic hemangioma). Imaging evaluation of the child with stridor is commonly performed with neck and/or chest radiographs depending on the pattern of stridor and associated clinical findings.

Retropharyngeal Abscess

In addition to stridor, patients with retropharyngeal abscess typically also present with symptoms of neck pain and fever. Radiographs of the neck are often requested to evaluate the retropharyngeal soft tissues. Due to the wide range of ages and sizes within the pediatric population, precise measurements of the retropharyngeal soft tissues are not as reliable as relative measurements for determining the presence of soft tissue swelling. The thickness of the retropharyngeal/prevertebral soft tissues should not be greater than the anteroposterior diameter of the adjacent vertebral body (Figs. 6-40). False thickening of the retropharyngeal/

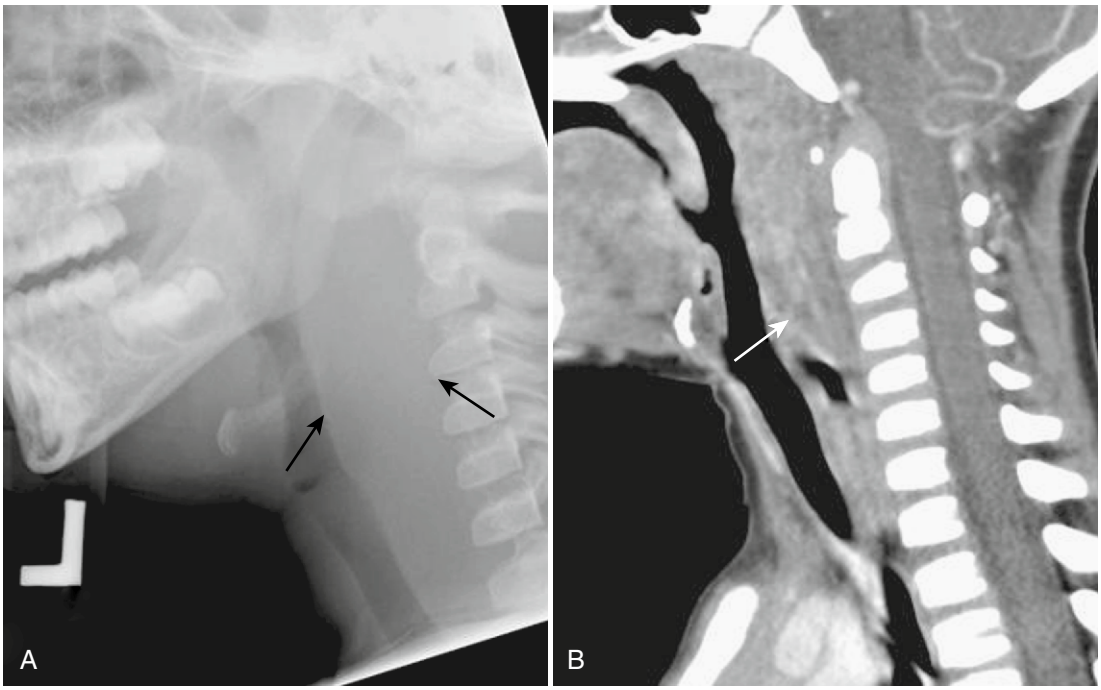


FIGURE 6-40. **A,** Lateral neck radiograph in a 3-year-old child with fever and neck pain reveals thickening of the retropharyngeal soft tissues *(arrows)*. **B,** Sagittal reformatted image obtained from subsequent CT of the neck demonstrates evidence of retropharyngeal cellulitis *(arrow)*.

prevertebral soft tissues can occur if the child's neck is in flexion, or if the film was acquired with the child in end-expiration. Although CT can be used to further evaluate positive findings on neck radiographs, it is often prudent to repeat the lateral radiograph of the neck with the patient in a more exaggerated extension or in full inspiration when the initial radiographs are felt to be falsely positive.

Another common cause of acute stridor within the nasopharynx and oropharynx is enlargement of the tonsils and adenoids. This diagnosis can be readily differentiated from retropharyngeal abscess on the basis of findings made on lateral radiograph of the neck (Fig. 6-41). Enlarged adenoids and tonsils cause encroachment on the nasopharyngeal and oropharyngeal airway, without associated thickening of the retropharyngeal soft tissues.

Epiglottitis

Epiglottitis is inflammation and enlargement of the epiglottis, aryepiglottic folds, and supraglottic tissue. Epiglottitis is a life-threatening condition caused by both viral and bacterial etiologies. Haemophilus influenza B has historically been the most common cause of epiglottitis, although its incidence has decreased since the development of the Haemophilus influenza B vaccine. The epiglottis can be identified at the level of the hyoid bone on lateral radiographs of the neck. On lateral neck radiographs "thumb-like" enlargement of the epiglottis and thickening of the aryepiglottic folds are findings consistent with epiglottitis (Fig. 6-42). Children for whom there is high clinical and radiographic concern for epiglottitis are often examined in the operating room with the presence of an anesthesiologist, as airway compromise may be precipitated by manipulation of the hypopharynx, and urgent intubation or tracheostomy may be necessary.

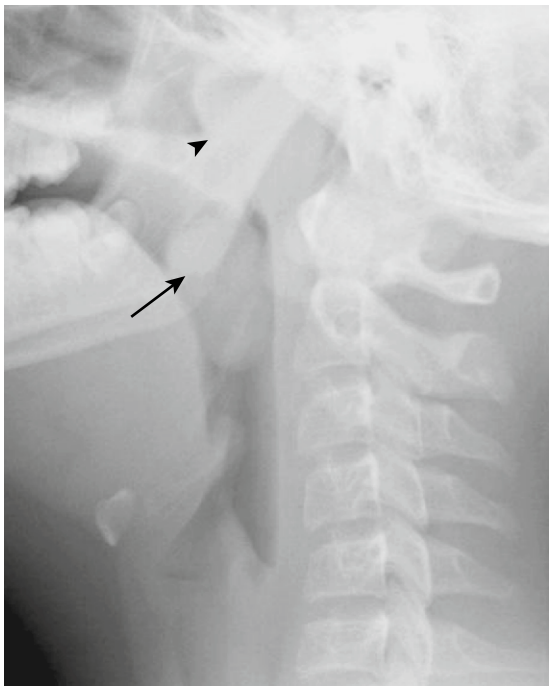


FIGURE 6-41. Lateral radiograph of the neck in an 11-year-old female with difficulty breathing demonstrates enlarged adenoids *(arrowhead)* and palatine tonsils *(arrow)*.

Croup

Viral croup (laryngotracheobronchitis) is the most common cause of acute stridor in children. Findings on chest or neck radiographs include narrowing of the subglottic airway. This is best visualized on the anteroposterior projection as the "steepling" or loss of the normal shouldering in the subglottic region (Fig. 6-43). Bacterial tracheitis, also

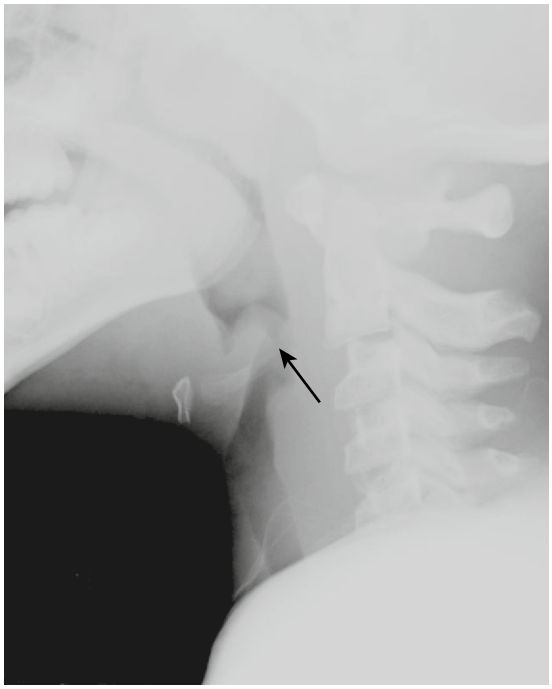


Figure 6-42. Lateral neck radiograph in a 6-year-old boy with fever, sore throat, and drooling. Image demonstrates thumb-like enlargement of the epiglottis *(arrow)*. This child had epiglottitis.

known as membranous croup, is another serious upper airway infection that is seemingly becoming more common as viral croup and epiglottitis have decreased in incidence. The diagnosis of bacterial tracheitis can be suggested on radiographs if subglottic narrowing is seen in conjunction with tracheal irregularity or a soft tissue membrane.

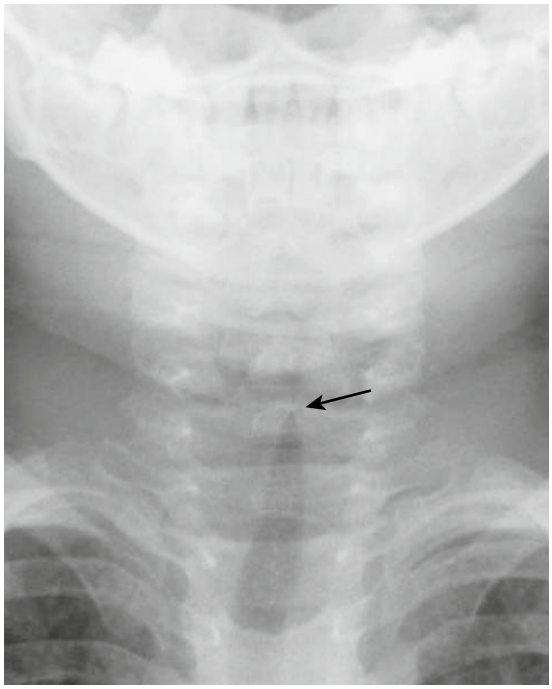


Figure 6-43. Anteroposterior radiograph of the neck in this 2-year-old child with stridor demonstrates "steepling" of the subglottic airway *(arrow)* secondary to viral croup.

Glottic/Subglottic Masses

Subglottic masses may present in an emergent setting when a superimposed viral or bacterial illness causes exacerbation and acuity of symptoms. The most common glottic mass is a papilloma, and the most common subglottic mass is a hemangioma. Extrinsic mass effect from mediastinal or neck masses can cause airway compromise. Bronchogenic cysts, foregut duplication cysts, and vascular rings can cause airway narrowing and acute symptoms when coexistent with an acute respiratory infection. Any abnormal deviation of the trachea (besides the mild contour deformity from the normally positioned left-sided aortic arch) should be investigated (Fig. 6-44). Fluoroscopy and contrast esophagram can be performed to confirm the presence of mass effect on the airway and adjacent esophagus. If these initial studies demonstrate an abnormality, CT or magnetic resonance imaging (MRI) can better visualize the abnormality.

Foreign Body

The majority of patients with an aspirated foreign body (FB) are between the ages of 1 and 3 years. The FB may become embedded anywhere along the airway in children. Symptoms of aspirated FB include choking, wheezing, coughing, and dyspnea. Patients with an aspirated FB require bronchoscopy for removal of the object. Clinical history, radiography, and fluoroscopy can all be used to determine if a FB has been aspirated. If the FB is caught at the level of the vocal cords, the pharynx may appear hyperinflated on neck radiographs. Aspirated FBs are likely to settle into the right mainstem bronchus, given that the

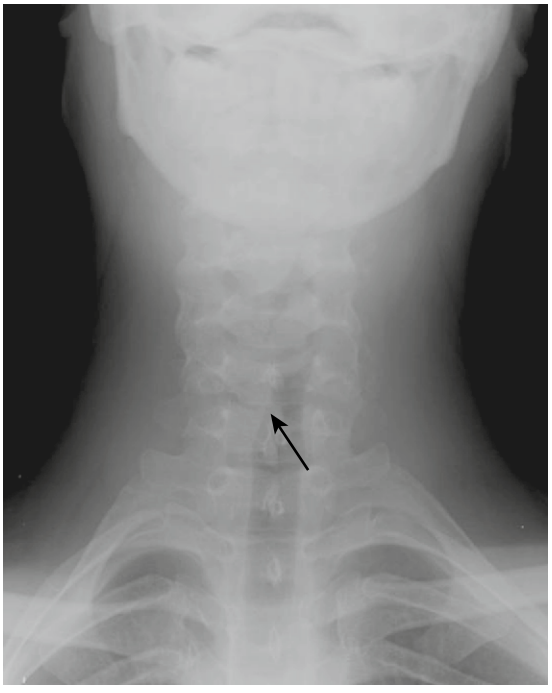


Figure 6-44. Anteroposterior radiograph of the neck in a teenage boy with Down syndrome demonstrates a right lateral impression on the subglottic trachea *(arrow)* secondary to a mass that was later found to represent a spindle cell tumor.

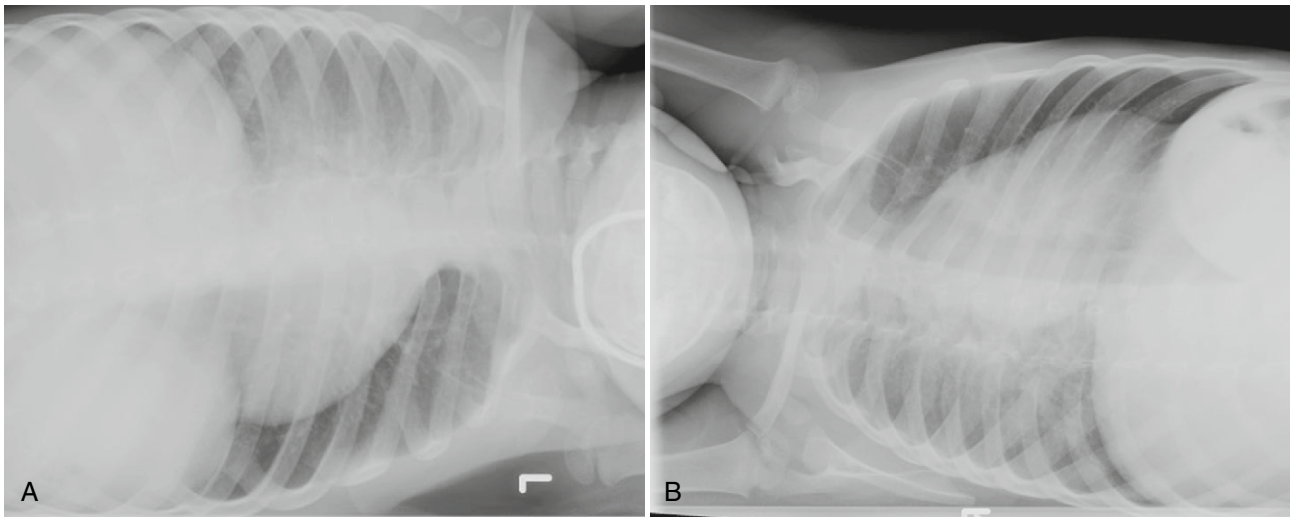


FIGURE 6-45. **A,** Left lateral decubitus chest x-ray in a 22-month-old with cough and suspected foreign body aspiration fails to demonstrate normal collapse of the dependent left lung. **B,** Right lateral decubitus film in the same patient demonstrates normal collapse of the right lung. This patient was found to have a peanut in the left mainstem bronchus at bronchoscopy.

latter typically has a more vertical orientation than the left mainstem bronchus. In children with a history of suspected aspirated foreign body, inspiratory and expiratory chest radiographs evaluating for areas of air trapping are performed. Bilateral decubitus views can be performed in place of expiratory films in younger patients who are not able to cooperate for inspiratory and expiratory imaging. In a normal patient, both lungs should collapse equally on an expiratory film, and the dependent lung should collapse on a lateral decubitus film while the nondependent lung expands. When the dependent lung does not collapse on decubitus films, air trapping is implied, and an aspirated FB must be suspected (Figs. 6-45). Radiographs cannot exclude the presence of an aspirated foreign body, and false-negative radiographs are common. Negative radiographs should not preclude bronchoscopy in a child with a convincing history or physical examination consistent with aspirated FB. Occasionally, when the diagnosis of FB aspiration is delayed, postobstructive pneumonia may develop. In some cases, plain films may reveal that the FB has not been aspirated, but rather is lodged within the esophagus (Fig. 6-46).



FIGURE 6-46. Lateral radiograph of the neck in this child demonstrates an ingested radio-opaque foreign body lodged within the esophagus posterior to the trachea.

Pneumonia

Lower respiratory tract infections are one of the most common indications for imaging the chest in pediatric patients. Bacterial pneumonia is manifested on a chest radiograph as an area of focal air space opacity without associated volume loss (Fig. 6-47). Pneumonia may be complicated by pleural effusion or parenchymal necrosis. Lobar pneumonias are the most common presentation of a bacterial pneumonia in children. Radiographs are often repeated after completion of antibiotic therapy to assess the resolution of the consolidation. If there has been no significant improvement after appropriate treatment, additional imaging with CT is warranted. If a patient has had multiple, appropriately treated, recurrent pneumonias in the same location, a CT scan of the chest may be warranted to assess for an underlying anomaly predisposing the patient to recurrent illnesses, such as pulmonary sequestration. In young children, bacterial pneumonia may also present on chest radiographs as a round mass, aptly called "round pneumonia."

Patients with sickle cell disease are prone to acute infiltrates on radiographs, termed "acute chest syndrome." While these patients are often treated with antibiotics, not all of them truly have an infection. Pulmonary infarctions can have an appearance similar to that of infection, and studies suggest that evaluation of the location and age of the patient may be helpful in predicting whether there is an underlying infection in these "acute chest" patients.

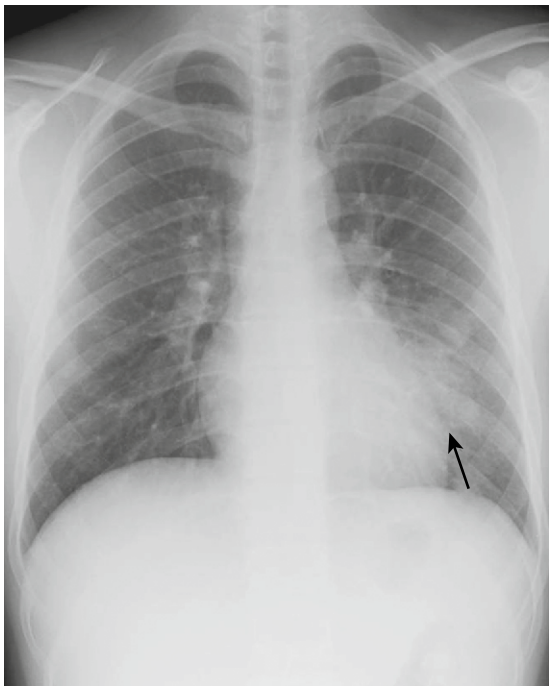


Figure 6-47. Anteroposterior chest radiograph in this teenager with symptoms of pneumonia demonstrates a focal opacity in the lingula *(arrow)*, consistent with pneumonia.

Bronchiolitis

Viral bronchiolitis is one of the most frequent causes of infant hospitalization during the winter. Infants with bronchiolitis present with wheezing, cough, and respiratory distress. Nontoxic-appearing infants with classic symptoms usually require no imaging. Chest radiographs are often obtained when the diagnosis is unclear, or when an underlying bacterial pneumonia is suspected. Chest radiographs often reveal evidence of airway disease, which include areas of atelectasis, air trapping, and bronchiolar wall thickening (Fig. 6-48). Atelectasis and air trapping are findings related to underlying bronchial obstruction caused by edema and secretions. Bronchiolar wall thickening is most prominent in the perihilar regions on chest radiographs.

Pneumothorax

Acute shortness of breath in an older child may be secondary to a spontaneous pneumothorax. Pneumothoraces in this age group are often caused by rupture of a small subpleural bleb, typically located at the lung apex. Chest radiographs reveal variable degrees of collapse of the affected lung, and the visceral pleura will be identified as a discrete line paralleling the chest wall. A shift of the heart and mediastinum to the opposite hemithorax is consistent with tension pneumothorax, which requires immediate decompression (Fig. 6-49). Patients with an underlying parenchymal bleb will often have recurrent pneumothoraces if the bleb is not resected or if pleurodesis is not performed. CT is more sensitive than plain radiographs for visualizing tiny blebs. CT is often performed after reexpansion of the affected lung has occurred to best visualize the peripheral lung parenchyma. Patients with underlying pulmonary disorders such as cystic fibrosis and Langerhans cell histiocytosis are at higher risks for spontaneous pneumothoraces due to the presence of blebs and cysts.



Figure 6-48. Anteroposterior chest radiograph in this infant with wheezing reveals hyperinflated lungs with areas of atelectasis and air trapping, as well as peribronchiolar wall thickening. This child was treated for bronchiolitis.

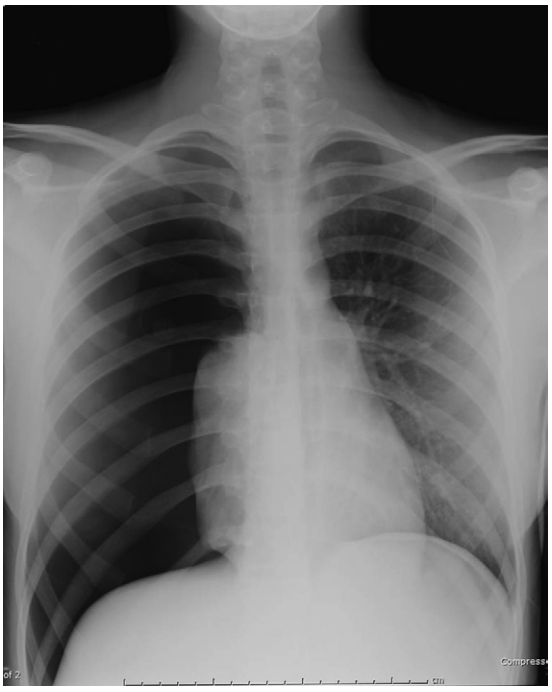


Figure 6-49. An anteroposterior chest radiograph performed on a teenage girl with acute-onset shortness of breath demonstrates complete collapse of the right lung with inferior displacement of the right hemidiaphragm and mild shift of the heart into the left hemithorax, consistent with tension pneumothorax.

CENTRAL NERVOUS SYSTEM

Skull Fractures

The leading cause of death in the pediatric population is traumatic brain injury. Patterns of acute intracranial injury are similar to the adult population and are further discussed

in other chapters. There are, however, certain special considerations to keep in mind when evaluating the pediatric brain. Skull fractures in children are often difficult to detect given the presence of open sutures in these young patients. Plain skull radiographs are useful for evaluating fractures in certain situations, although CT has largely supplanted plain radiographs for this diagnosis. This is largely in part due to the superior capability of CT to evaluate for complications of fracture, such as intracranial hemorrhage. The detection of skull fractures can be subtle even on CT. Skull fractures must be distinguished from the normal sutures (Fig. 6-50). Cranial sutures are usually symmetric and lack overlying soft tissue swelling, in contrast to skull fractures (Fig. 6-51). Accessory and anomalous sutures can also be mistaken for skull fractures. If oriented along the axial plane of the CT scan, skull fractures may not be visible on the axial images. It is critical to evaluate the scout image so that these fractures are detected. The degree of comminution of the fracture, depression or displacement of fragments, and additional intracranial findings such as hemorrhage, mass effect, and edema are all important associated findings. Bilateral fractures, complex fractures, or fractures that cross a suture line, especially in patients without an appropriately significant traumatic history, may be signs of nonaccidental injury (NAI). NAI should be suspected when the history does not support the radiographic findings. Although subdural hematomas may be present in victims of NAI, hemorrhage of different ages does not necessarily equate with abuse, especially in children with underlying enlargement of the extra-axial spaces.

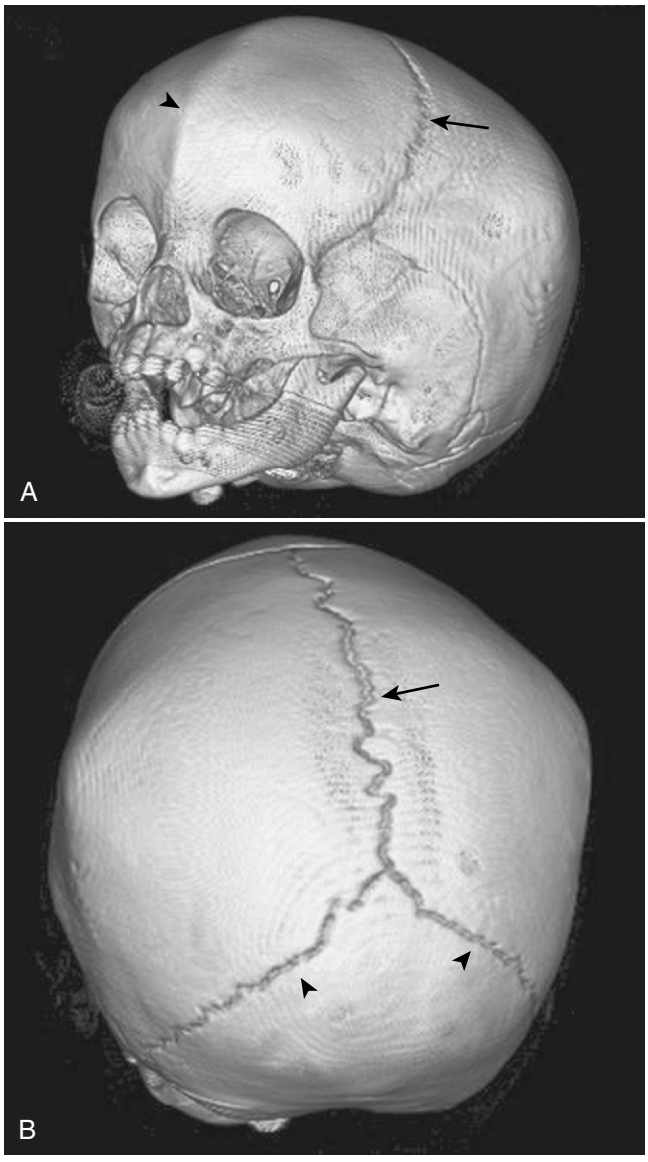


FIGURE 6-50. 3D reconstructed images of the calvarium from a head CT of an infant demonstrate normal sutural anatomy. **A,** The metopic suture has fused *(arrowhead)*. Normal coronal suture *(arrow)*. **B,** Normal sagittal *(arrow)* and lambdoid sutures *(arrowheads)*.

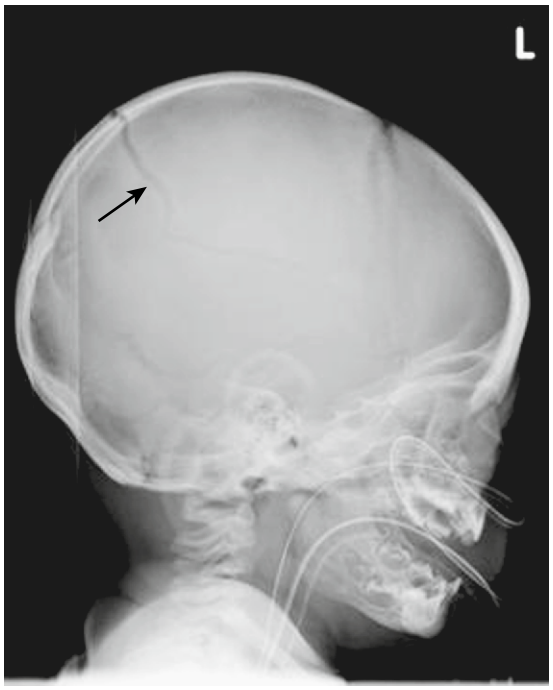


FIGURE 6-51. Lateral skull radiograph in a 6-month-old boy who was a victim of nonaccidental injury demonstrates a right parietal skull fracture *(arrow)*.

Hypoxic Ischemic Injury

Patients who have a history of near-drowning may suffer hypoxic ischemic injury of the brain secondary to profound asphyxiation. The resultant cerebral edema and infarction can be subtle on CT, especially in the early stages after the event. Lack of visualization of normal sulci, an abnormally dense cerebellum, and loss of normal grey/white matter differentiation should suggest underlying cerebral edema. These patients are often followed clinically with imaging repeated over the next several days to further evaluate the extent of hypoxic ischemic injury.

Hydrocephalus

Hydrocephalus refers to the overaccumulation of cerebrospinal fluid within the ventricular system. Children with hydrocephalus often present with headache, vomiting, and lethargy. Hydrocephalus may be secondary to congenital

or acquired factors. Congenital hydrocephalus may be secondary to in utero infection, aqueductal stenosis, or malformations of the brain (Chiari or Dandy-Walker). Acquired causes of hydrocephalus include infection, hemorrhage, and obstructing mass lesions. The ventricles will appear dilated on CT, and hypoattenuating areas adjacent to the ventricles represent sites of transependymal cerebrospinal fluid absorption. Abnormal dilatation of the ventricles may be defined by several criteria, including visualization of the temporal horns of the lateral ventricles (usually not visible), upward bowing of the corpus callosum, and enlargement of the frontal horns of the lateral ventricles as compared with the calvarial diameter measured from the inner tables (greater than 50%). Depending on the cause of the hydrocephalus, all of the ventricles may not be equally dilated. In aquaductal stenosis, for example, the third and lateral ventricles will appear dilated while the fourth ventricle is normal.

Assessing the size of the ventricular system and extra-axial spaces can be challenging in infants. Prominence of the extra-axial spaces in infants is often benign and self-resolving. Infants are often detected at a routine visit to the pediatrician to have an enlarging head circumference. This occurs typically between 3 and 9 months of age with expected resolution by the age of 2 years.

Venous Sinus Thrombosis

Venous sinus thrombosis (VST) can be caused by a variety of different factors, both local and systemic. Local processes include mastoiditis and intracranial neoplasm; systemic processes include genetic predisposition to hypercoagulopathy, underlying malignancies, and medications. In young children, severe dehydration can lead to venous stasis and thrombosis. These patients usually present with lethargy, irritability, and/or seizures.

VST can be detected on the basis of findings made on head ultrasound, CT, and MRI. On US, images obtained through the anterior fontanelle of young infants will demonstrate the lack of Doppler flow within the superior sagittal sinus. On noncontrast CT, thrombus within a venous sinus will appear abnormally dense (Fig. 6-52A). This finding may also be seen in dehydrated patients with an elevated hematocrit level. If this is the case the attenuation of the arteries and veins should appear similar, whereas in VST the sinus will appear denser than the arteries. At contrast-enhanced CT the "empty delta" sign describes the appearance of an intraluminal filling defect (i.e., thrombus) within the dural envelope. MRI is more sensitive for detection of venous thrombosis. Findings on MRI consistent with VST include absence of normal flow voids and abnormal signal intensity within the sinus (Fig. 6-52B). Indirect signs of VST include collateral venous channels, cerebral hemorrhage, and signs of increased intracranial pressure. VST may lead to venous infarction and hemorrhage in the cortex and/or basal ganglia, depending on the sinuses involved.

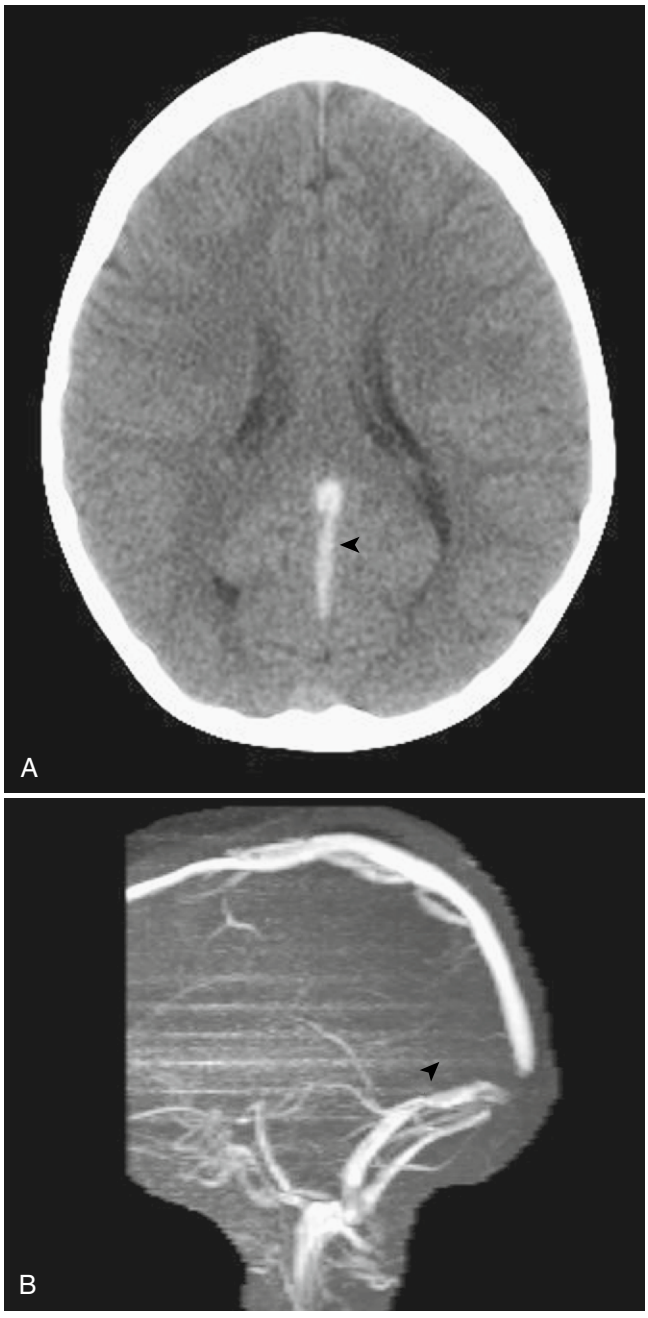


Figure 6-52. **A,** Axial CT image through the brain demonstrates hyperattenuation (*arrowhead)* within the straight sinus. **B,** MR venography confirms the absence of flow within the straight sinus *(arrowhead),* consistent with sinus thrombosis.

Meningitis/Encephalitis

Meningitis is a clinical diagnosis, often made on the basis of history and laboratory markers, including cerebrospinal fluid analysis. Imaging of patients with meningitis is usually not performed unless complications are suspected, such as encephalitis, epidural abscess, or venous sinus thrombosis. In these instances, contrast-enhanced MRI is the most appropriate imaging evaluation, although the diagnosis can also be suggested based on findings made at CT. In a child with clinical and laboratory findings consistent with intracranial infection, the effacement of sulci and subtle differences in attenuation of the cortical gyri on CT scan suggest parenchymal infection such as encephalitis. On MRI, the involved brain parenchyma will appear abnormally increased in signal on fluid-sensitive sequences (Figs. 6-53). Cerebellitis, or inflammation of the cerebellum, may be suggested on noncontrast head CT by areas of

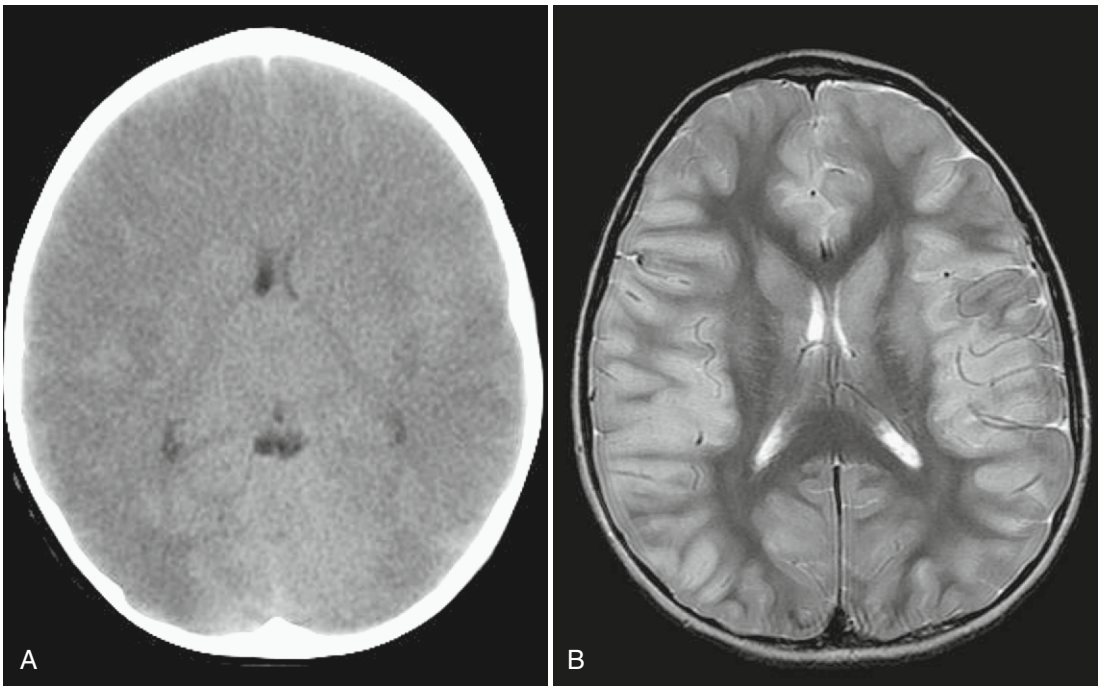


FIGURE 6-53. **A,** Axial CT image through the brain in a 4-year-old boy with a history of otitis media followed by changes in mental status reveals loss of normal gray–white differentiation and effacement of sulci. **B,** T2-weighted MR image reveals diffusely abnormal signal intensity throughout the cerebellar hemispheres. This child had encephalitis.

abnormal hypointense foci within the cerebellum, often in a pattern mimicking the longitudinal pattern of the cerebellar folia (Fig. 6-54). Often a recent history of a viral infection or immunization can be recalled. Cerebellitis may be suggested by CT, but abnormalities may be subtle and MRI is usually the diagnostic study.

Cervical Spine Injury

Pediatric cervical spine injury is relatively uncommon, with an incidence between 1% and 2%. Younger children (less than 8 years) are more apt to injure the upper cervical spine (C1–C2) than older adolescents (greater than 8 years), who are more apt to injure the lower cervical spine (C3–C7). This pattern of injury is thought to be due to the mechanics and structure of the maturing cervical spine. The multiple synchondroses in the upper cervical spine are points of relative instability. The relatively large size of the head in a child in comparison with adults places increased stress on the upper cervical spine. The causes of cervical spine trauma are also different in the two age groups, with motor vehicle accidents being the primary cause of injury in the younger group and sports/recreation injuries the leading cause in the older group.

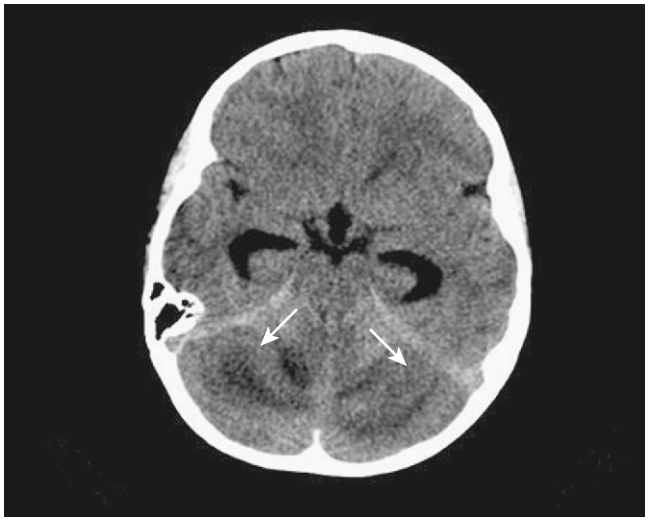


FIGURE 6-54. Axial CT image obtained in a young girl presenting with ataxia reveals abnormal hypoattenuating lesions within the cerebellum *(arrows),* consistent with cerebellitis. This was later confirmed at MRI.

Despite the widespread availability of CT scanners in many emergency departments, plain radiographs of the cervical spine are still the mainstay for evaluating pediatric cervical spine trauma. There are many imaging pitfalls in the evaluation of the cervical spine in children. Knowledge of the multiple synchondroses of C2 is important for the accurate diagnosis of injury. The possibility of fracture at the synchondrosis of the dens should be raised if there is anterior angulation or displacement of the dens in relation to the body of C2. The ring apophyses of the vertebral bodies are normal structures that may be mistaken for avulsion or chip fractures. The normal pseudosubluxation at C2–C3 (due to ligament laxity in young children) may raise concerns in clinicians unfamiliar with this common appearance. Patient cooperation is often limited in the younger age group, and it may be difficult to impossible to obtain odontoid views.

Algorithms to direct the most judicious use of radiology in clearing the cervical spine have been suggested. In an effort to limit the radiation exposure to pediatric patients, limited use of CT for cervical spine evaluation is recommended. Initial evaluation of the pediatric cervical spine should be

performed with plain radiographs. If concern for occult fracture persists after initial radiographs, focused CT can be performed through the levels of concern. If a cervical spine fracture is present CT may then be performed through the entire cervical spine to exclude additional fractures. There is a small subset of patients with injury to the cervical spine without radiographic abnormalities. This more commonly occurs in younger patients (less than 8 years).

Mastoiditis

Fever and ear pain are common symptoms of otitis media (OM) in young children. OM is diagnosed on the basis of physical exam findings, and is commonly treated with antibiotics. Imaging is not indicated for uncomplicated OM. Lack of response or progression of symptoms while on antibiotics may prompt further evaluation for complications of OM or other causes for the patient's symptoms. When mastoiditis or other complications of OM are clinically suspected, a CT through the temporal bones should be performed with intravenous contrast. Fluid within the middle ear on CT scan is consistent with OM. Mastoiditis is often associated with OM and represents extension of infection from the middle ear into the mastoid air cells, as these structures are contiguous. Bony erosion or intracranial extension of infection (such as a subperiosteal abscess) is evidence of coalescent mastoiditis, and surgical intervention may be required (Fig. 6-55). Given the proximity of the dural venous sinuses to the temporal bone, particular attention should be paid in order to exclude secondary venous thrombosis.

Cervical Adenitis

Children presenting to the emergency department with enlarged cervical lymph nodes, fever, and an elevated white count often have a diagnosis of cervical adenitis. Cervical adenitis is a nonspecific inflammation of the lymph nodes that can be secondary to bacterial or viral infection.

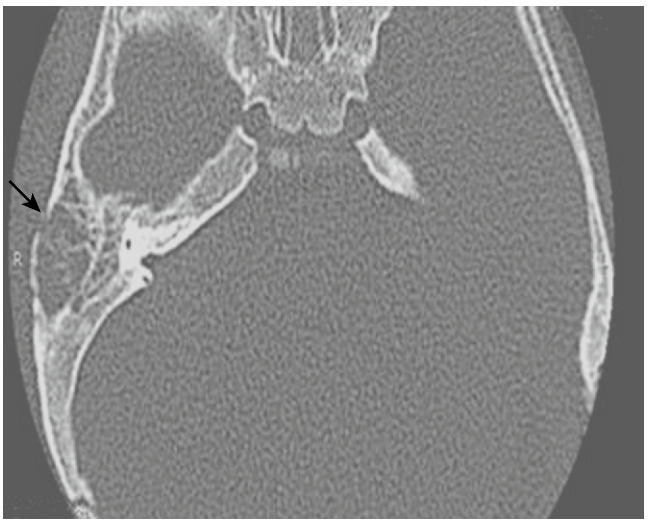


Figure 6-55. Axial CT through the temporal bones in a young child with complicated otitis media demonstrates abnormal fluid attenuation within the mastoid air cells on the right *(arrow)* with osseous destruction consistent with coalescent mastoiditis.

Imaging is performed in cases where there is concern for abscess formation. Ultrasound is often performed initially to evaluate the superficial, or palpable, lymph nodes. US is excellent at differentiating between solid and cystic masses, and can identify abscesses or fluid collections that are amenable to drainage. While US evaluation may be sufficient for evaluating superficial lymph nodes, signs and symptoms of a tonsillar infection such as trismus, drooling, and sore throat may prompt an evaluation with contrast-enhanced CT. CT can identify a potential peritonsillar abscess and assess the mass effect on the airway, as well as assess for displacement, compression, or thrombosis of adjacent vessels. Thrombosis of the internal jugular vein or a tributary vein in association with peritonsillar abscess is termed Lemierre syndrome. Lemierre syndrome is usually caused by the bacterium *fusobacterium*. Nontuberculous mycobacterial infection can be suggested in a child with low-density lymphadenopathy particularly when a draining sinus tract is present. In the absence of a draining sinus tract or signs/symptoms of infection, the differential diagnosis for multiple enlarged lymph nodes in a child includes lymphoproliferative disorders, such as lymphoma.

Anterior midline neck infections should suggest an underlying congenital abnormality such as thyroglossal duct cyst or dermoid cyst. Abscesses along the anterior border of the sternocleidomastoid may represent a sequela from lymphadenitis or superinfection of a second brachial cleft cyst. If CT of an "acute onset" neck mass demonstrates a multicystic collection with internal fluid/fluid levels, the diagnosis may be a lymphatic malformation. This diagnosis becomes even more likely if the multicystic collection crosses compartments within the neck.

MUSCULOSKELETAL

The adage "children are not little adults" is particularly true for the evaluation of the pediatric musculoskeletal system. The pediatric skeleton responds to traumatic forces with different patterns of injury than does that of the adult patient. The classification of pediatric fractures is briefly discussed and illustrated in this text, while the pathology and mechanism of these unique fractures are well discussed in other textbooks.

Salter Harris Fractures

One of the most well known fracture classification systems is the Salter Harris (SH) classification, which describes the different appearance of fractures that occur at the physis of young children. SH1 fractures solely involve the growth plate (physis) (Fig. 6-56). SH2 fractures extend through the metaphysis into the growth plate (Fig. 6-57). SH3 fractures extend through the epiphysis into the growth plate. SH4 fractures extend from the metaphysis, through the growth plate, into the epiphysis. SH5 fractures are crush injuries to the growth plate. The significance of fractures that occur at the physis is that they may cause early fusion of the physis and lead to growth disturbance. Two distinct SH fractures are the triplane and juvenile Tillaux fractures, which typically occur in the older adolescent skeleton and are most common in the distal tibia. The triplane fracture is a complex SH4 injury that has a vertical component



FIGURE 6-56. Anteroposterior radiograph through the wrist demonstrates widening of the distal radial physis *(arrow)*. The patient was focally tender at this site. This finding is consistent with an SH1 fracture.

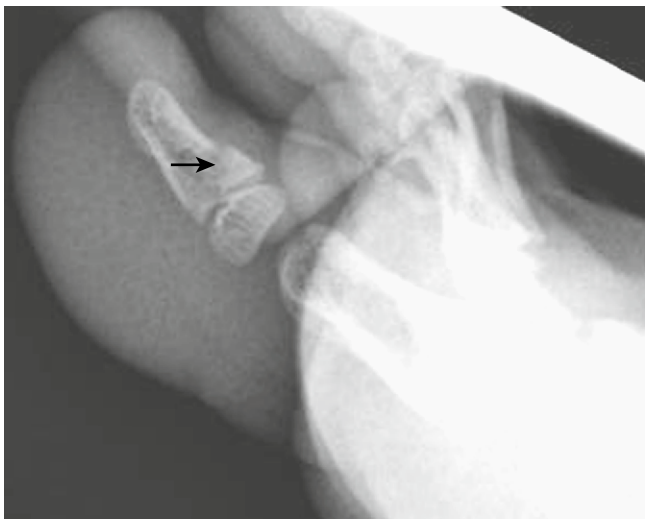


FIGURE 6-57. Lateral radiograph through the distal phalanx of the great toe demonstrates an SH2 fracture *(arrow)*.

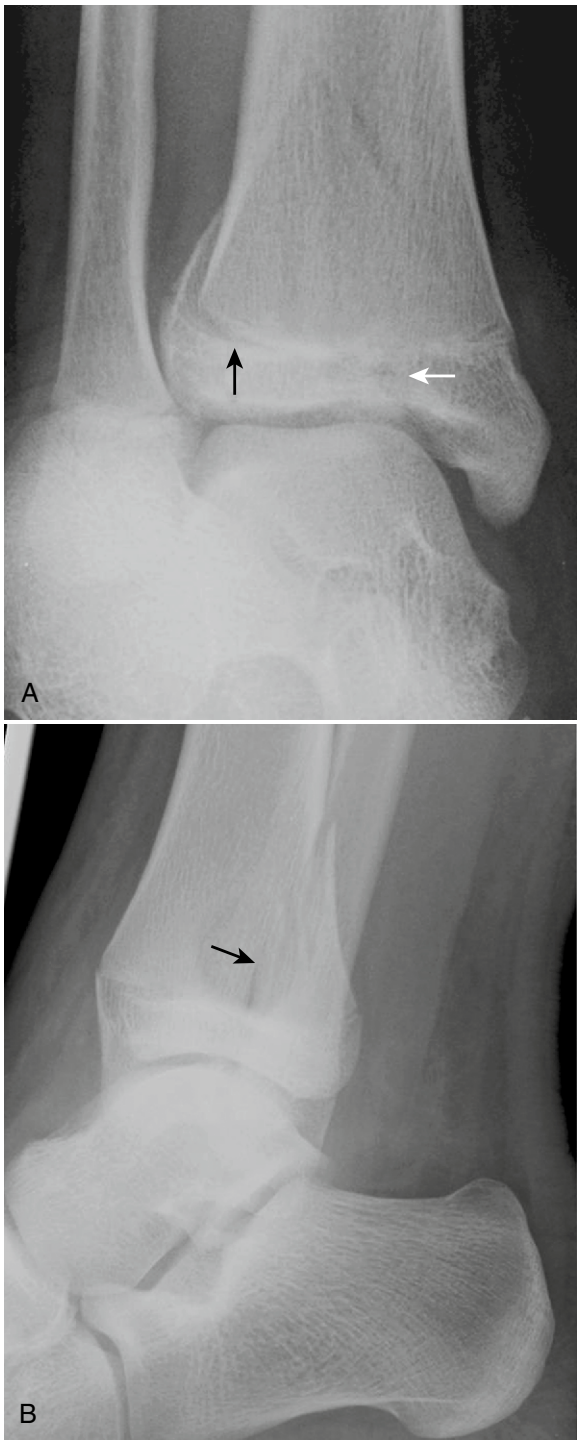


FIGURE 6-58. **A,** Anteroposterior radiograph through the ankle in this teenage boy after a sporting injury reveals a fracture through the tibial epiphysis *(white arrow)* that extends through the lateral portion of the physis *(arrow)*. **B,** Lateral radiograph of the ankle reveals the obliquely oriented metaphyseal component of this triplane SH4 fracture *(arrow)*.

through the epiphysis, a horizontal component through the growth plate, and an oblique component through the metaphysis (Fig. 6-58). The Tillaux fracture is an SH3 injury involving fracture of the anterolateral aspect of the growth plate and epiphysis (Fig. 6-59). Fusion of the tibial growth plate begins centrally, proceeds medially, and completes laterally. The Tillaux pattern is secondary to injury after the medial distal tibial growth plate has fused. When Tillaux or triplane injuries are suspected or diagnosed by radiographs, CT is typically performed, because decisions for orthopedic repair hinge on the appearance of the fractures and measurements of distraction.

Plastic Bending Fractures

Plastic bending fractures are seen in the long bones of children who have suffered axial load injuries. These fractures appear as bowing contour deformities. Buckle or torus fractures are seen as minimal disruptions or irregularities in the cortical contours, particularly common in the long bones of the forearm (Fig. 6-60). Greenstick fractures demonstrate cortical continuity along one aspect of the bone and obvious fracturing or splintering of the opposite cortical margin. Toddler's fractures are hairline cortical tibial fractures seen in walking older infants and young children (Fig. 6-61). These pediatric



Figure 6-59. Coronal reformatted image obtained from a CT examination through the ankle in this teenage boy after his having sustained injury to his ankle reveals a fracture through the distal tibial epiphysis *(arrow)* that extends through the lateral portion of the physis *(arrowhead)*. This is called a Tillaux fracture, a specific type of SH3 injury.

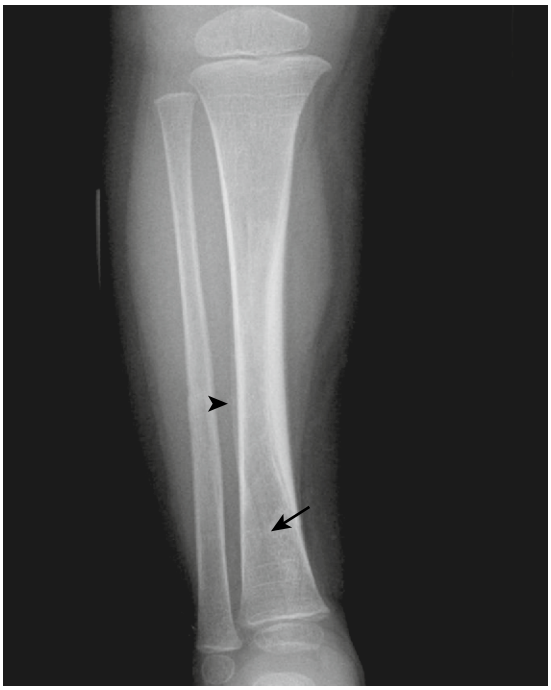


Figure 6-61. Anteroposterior radiograph of the tibia in a toddler demonstrates a subtle lucency within the shaft of the distal tibia *(arrow)* as well as periosteal reaction along the lateral cortical surface of the bone *(arrowhead)*. This child sustained a toddler's fracture of her tibia.

fractures are often initially overlooked, due to the subtle differences in angulation or cortical continuity. Certain buckle fractures, plastic fractures (bowing deformities), hairline fractures, SH1 fractures, and impaction fractures can be subtle and are more evident if a contralateral view is obtained. When clinical suspicion is high but initial radiographs appear normal, follow-up radiographs may demonstrate periosteal reaction, sclerosis, or increased conspicuity of the fracture line as evidence of healing injury.

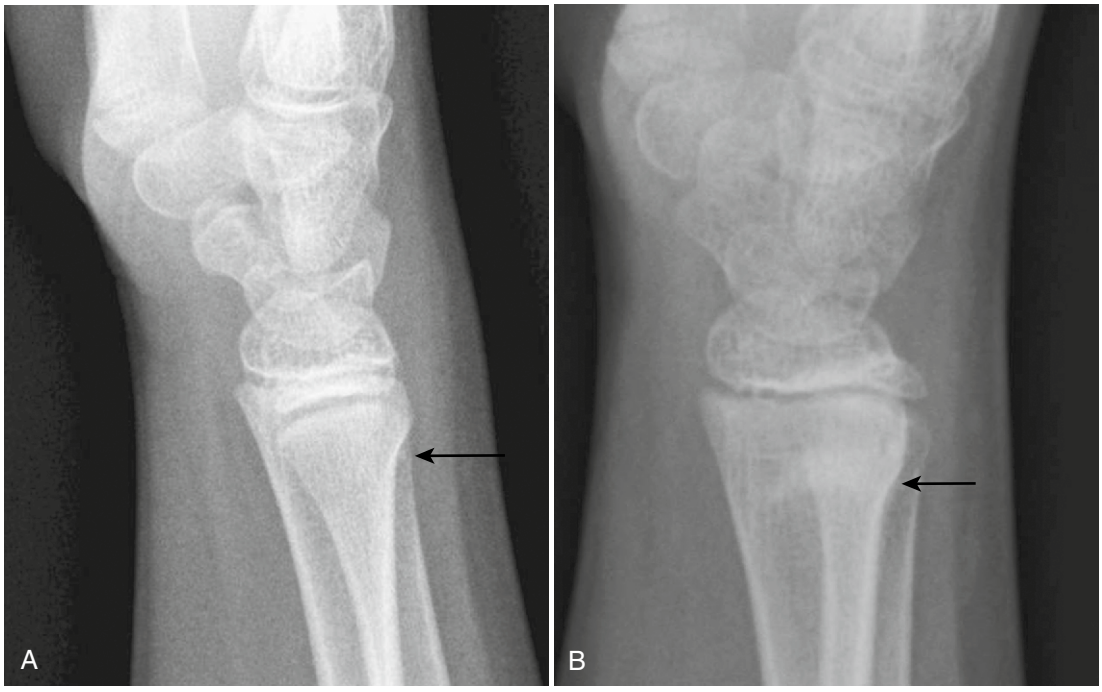


Figure 6-60. A, Initial lateral radiograph of the wrist obtained at the time of injury in this young girl with wrist pain demonstrates a subtle buckle fracture of the distal radius *(arrow)*. **B,** A follow-up radiograph performed 10 days later reveals linear sclerosis at the fracture site *(arrow)* indicative of healing.



FIGURE 6-62. Lateral radiograph of the elbow demonstrates the "sail" sign of an elbow effusion *(arrow)*. The posterior fat pad is also visible *(arrowhead)*. This child was treated for an occult supracondylar fracture.

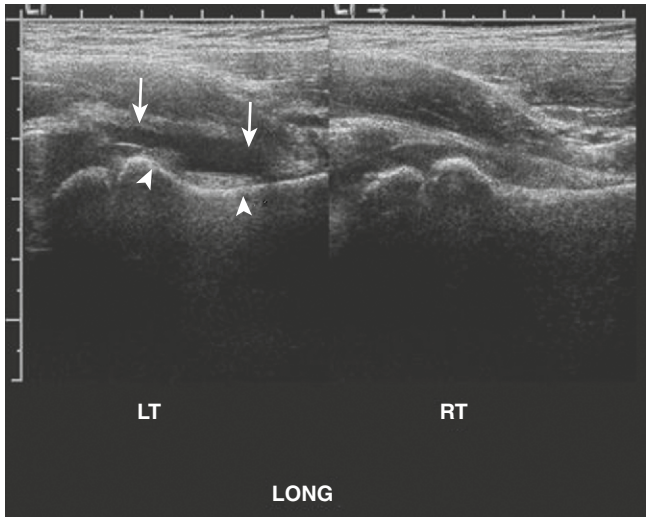


FIGURE 6-63. US images obtained along the long axis of the hips bilaterally demonstrate evidence of a hip effusion on the left *(arrows)*, the patient's symptomatic side. Note cortical surface of the femur *(arrowheads)*.

Elbow Fractures

The elbow is a particularly complex joint to evaluate for injury in the pediatric skeleton. Due to the multiple ossification centers, predominance of radiolucent cartilage, and common site of injury, elbow fractures are particularly prone to false negative plain film interpretations. Knowledge of the normal anatomic alignment of the elbow, as well as of the appearance and timing of the ossification centers, is essential when evaluating the elbow. "CRITOE" is a common mnemonic that describes the typical order in which the ossification centers appear (capitellum, radial head, internal epicondyle, trochlea, olecrenon, external epicondyle). Bowing of the anterior fat pad ("sail" sign) and visualization of the posterior fat pad indicate a joint effusion (Fig. 6-62). The presence of an effusion does not necessarily connote a fracture, although it reflects significant traumatic injury to the joint. The radiocapitellar line drawn through the midshaft of the radius should always intersect the capitellum. Absence of this relationship represents dislocation of the radial head from its normal anatomic articulation with the capitellum. The anterior humeral line drawn along the anterior cortex of the humerus should intersect the middle third of the capitellum. If the line intersects the anterior third of the capitellum or passes anterior to the capitellum, a supracondylar fracture should be suspected. This line can lead to false positive assessments in nonlateral projections. Care should also be used in the extremely young patients with minimal ossification of the capitellum. A mnemonic such as FOOL (*f*at pads, cortical *o*utlines, *o*ssification centers, anterior humeral and radiocapitellar *l*ines) can remind the busy radiologist to look for the presence of effusions, subtle buckle fractures, avulsed or "missing" ossification centers, and radial head dislocations or subtle supracondylar fractures.

Septic Hip

Patients presenting with hip pain may have septic arthritis of the hip joint, which requires emergent diagnosis in order to avoid permanent joint damage. The presence of a hip effusion can be suggested on anteroposterior radiographs of the pelvis by asymmetric widening of the femoral head–acetabular teardrop distance on the affected side, although radiographs are not sensitive for this diagnosis. Ultrasound is an excellent tool for determining the presence of a hip effusion. Using a high frequency linear transducer along the long axis of the femoral metaphysis, an effusion will appear as a hypoechoic collection ballooning outward from the cortex of the femoral head and neck (Fig. 6-63). Imaging the normal asymptomatic side demonstrates the asymmetry in the amount of fluid in the symptomatic joint. Transient synovitis cannot be differentiated from a septic hip sonographically. The diagnosis is determined by the histopathologic evaluation of the aspirated fluid. In a child with hip pain, the presence of fever, elevated white blood count, increased erythrocyte sedimentation rate, and elevated C-reactive protein should help direct the decision to perform hip aspiration.

Other causes of hip pain in children include Legg-Calve-Perthes (LCP) disease and slipped capital femoral epiphysis (SCFE). LCP is idiopathic avascular necrosis of the hip. Most commonly occurring in 4- to 8-year-olds, the early radiographic signs may be subtle. Subcortical lucency along the proximal femoral epiphysis may be the first imaging sign of the disease. Cortical collapse, sclerosis, and deformity of the head and neck are seen in more advanced disease. SCFE is often diagnosed in the slightly older age group (ages 8 to 12), and is more common in overweight children. On anteroposterior radiographs, early SCFE can be seen as subtle asymmetry of the growth plates, while more advanced SCFE will have lateral displacement of the proximal femoral metaphysis with respect to the epiphysis. Often the slip is better seen on the frog leg lateral view, where the offset of the epiphysis and metaphysis is better demonstrated (Fig. 6-64).

Nonaccidental Injury

When interpreting pediatric imaging studies, one must be constantly on the lookout for signs of nonaccidental injury. Certain types of osseous injuries have a high specificity for NAI. Posterior rib fractures, for example, are highly specific

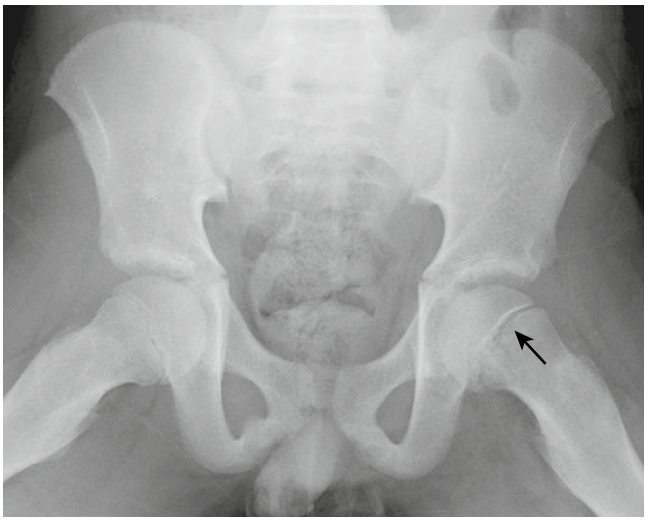


Figure 6-64. Frog leg lateral view of bilateral hips reveals widening of the physis on the left *(arrow)* and posteromedial displacement of the left femoral epiphysis, consistent with slipped capital femoral epiphysis.

for NAI and may be detected on chest or abdominal radiographs obtained for unrelated history, such as cough or vomiting (Fig. 6-65). Other fractures highly suggestive of child abuse are classic metaphyseal lesions, sometimes referred to as corner or bucket-handle fractures (Fig. 6-66). Spiral fractures of the long bones in infants who are not ambulatory are also worrisome for NAI. When clinical concern is raised or when a radiographic finding is suggestive of NAI, a full skeletal survey should be performed with high-quality, small-field-of-view technique. Multiple fractures, particularly if they are of varying ages, should alert radiologists to the possibility of abuse. A follow-up skeletal survey in 2 weeks can be suggested to assess for additional injuries that may not be visible on initial radiographs. There are few metabolic disorders that can mimic the osseous injuries seen in NAI, the most common being

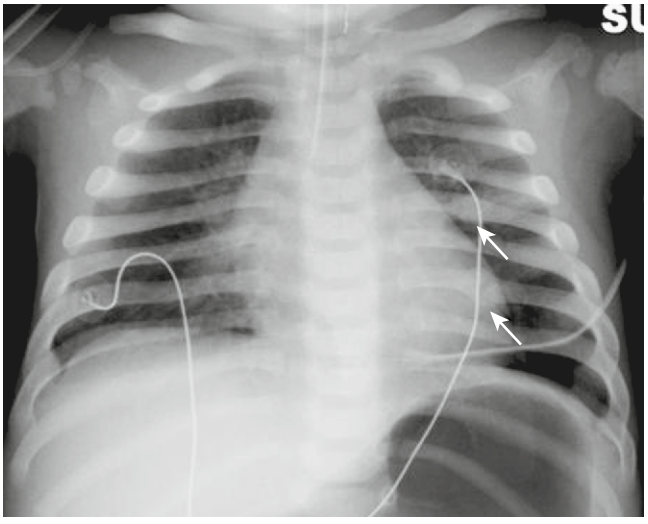


Figure 6-65. Anteroposterior radiograph of the chest in this 6-month-old boy who was a victim of a nonaccidental injury reveals healing left posterior rib fractures *(arrows)*.



Figure 6-66. Anteroposterior radiograph of the femur in the same child as in Figure 6-65 reveals a metaphyseal fracture of the distal tibia *(arrow)*.

osteogenesis imperfecta (OI). These disorders are very rare, and often there are other clinical findings or a family history to suggest the diagnosis.

Suggested Readings

Agrons GA, Harty MP: Lung disease in premature neonates: Impact of new treatments and technologies. Semin Roentgenol 33:101–116, 1998.

Anderson RCE, Scaife ER, Fenton SJ, et al: Cervical spine clearance after trauma in children. J Neurosurg 105(Suppl 5):S361–S364, 2006.

Artz GJ, Reilly JS, Mattei P: Stridor in an infant. Clin Pediatr 45:578–581, 2006.

Atabaki SM: Pediatric head injury. Pediatr Rev 28:215–223, 2007.

Atkinson GO Jr, Patrick LE, Ball TI Jr, et al: The normal and abnormal scrotum in children: Evaluation with color Doppler sonography. AJR Am J Roentgenol 158:613–617, 1992.

Bixby SD, Lucey BC, Soto JA, et al: Perforated versus nonperforated acute appendicitis: Accuracy of multidetector CT detection. Radiology 241:780–786, 2006.

Blanch AJ, Perel SB, Acworth JP: Paediatric intussusception: Epidemiology and outcome. Emerg Med Australas 19:45–50, 2007.

Bruce J, Huh Y, Cooney D, et al: Intussusception; Evolution of current management. J Pediatr Gastroenterol Nutr 6:663–664, 1987.

Buonomo C: Neonatal gastrointestinal emergencies. Radiol Clin North Am 35:845–864, 1997.

Choi H, Snyder HM III, Duckett JW: Urolithiasis in childhood: Current management. J Pediatr Surg 22:158–164, 1987.

Choudhary AK, Sellars MEK, Wallis C, et al: Primary spontaneous pneumothorax in children: The role of CT in guiding management. Clin Radiol 60:508–511, 2005.

Cleveland RH: A radiologic update on medical diseases of the newborn chest. Pediatr Radiol 25:631–637, 1995.

Daneman A, Navarro O: Intussusception part 1: A review of diagnostic approaches. Pediatr Radiol 33:79–85, 2003.

Daneman A, Navarro O: Intussusception part 2: An update on the evolution of management. Pediatr Radiol 34:97–108, 2004.

Dillon PW, Cilley RE: Newborn surgical emergencies. Gastrointestinal anomalies, abdominal wall defects. Pediatr Clin North Am 40:1289–1314, 1994.

Donnelly LF: Traumatic elbow effusions in children are not synonymous with occult fracture—even with evaluation by MR imaging. AJR Am J Roentgenol 179:531–532, 2002.

Donnelly LF, Emery KH, Brody AS, et al: Minimizing radiation dose for pediatric body applications of single-detector helical CT: Strategies at a large children's hospital. AJR Am J Roentgenol 176:303–306, 2001.

Eich GF, Superti-Furga A, Umbricht FS, et al: The painful hip: Evaluation of criteria for clinical decision-making. Eur J Pediatr 158:923–928, 1999.

Ein SH, Alton D, Palder SB: Intussusception in the 1990s: Has 25 years made a difference? Pediatr Surg Int 12:374–376, 1997.
Epelman M, Daneman A, Navarro OM, et al: Necrotizing enterocolitis: Review of state-of-the-art imaging findings with pathologic correlation. Radiographics 27:285–305, 2007.
Evans ED, Kramer SS, Kravitz RM: Pediatric diseases of the lower airways. Semin Roentgenol 33:136–150, 1998.
Fassett DR, McCall R, Brockmeyer DL: Odontoid synchondrosis fractures in children. Neurosurg Focus 20:E7, 2006.
Findlay RD, Taeusch HW, Walther FJ: Surfactant replacement therapy for meconium aspiration syndrome. Pediatrics 97:48–52, 1996.
Fiorella DJ, Donnelly LF: Frequency of right lower quadrant position of the sigmoid colon in infants and young children. Radiology 219:91–94, 2001.
Ford EG, Senac MO, Srikanth MS, et al: Malrotation of the intestines in children. Ann Surg 215:172–178, 1992.
Fragoso AC, Pereira JM, Estevao-Costa J: Nonoperative management of omental infarction—a case report. J Pediatr Surg 41:1777–1779, 2006.
Freed HA, Shields NN: Most frequently overlooked radiographically apparent fractures in a teaching hospital emergency department. Ann Emerg Med 13:900–904, 1984.
Garel L, Dubois J, Grignon A, et al: US of the pediatric female pelvis: A clinical perspective. Radiographics 21:1393–1407, 2001.
Godbole P, Stringer MD: Bilious vomiting in the newborn: How often is it pathologic? J Pediatr Surg 6:909–911, 2002.
Goodman TR, McHugh K: The role of radiology in the evaluation of stridor. Arch Dis Child 81:456–459, 1999.
Graif M, Itzchak Y: Sonographic evaluation of ovarian torsion in childhood and adolescence. Am J Roentgenol 150:647–649, 1988.
Greason KL, Thompson WR, Downey EC, et al: Laparoscopic pyloromyotomy for infantile hypertrophic stenosis: Report of 11 cases. J Pediatr Surg 30:1571–1574, 1995.
Guthrie SO, Gordon PV, Thomas V, et al: Necrotizing enterocolitis among neonates in the United States. J Perinatol 23:279–285, 2003.
Haney PJ, Bohlman M, Sun CC: Radiographic findings in neonatal pneumonia. AJR Am J Roentgenol 143:23–26, 1984.
Hernanz–Schulman M: Infantile hypertrophic pyloric stenosis. Radiology 227:319–331, 2003.
Hernanz–Schulman M, Sells LL, Ambrosino MM, et al: Hypertrophic pyloric stenosis in the infant without a palpable olive: Accuracy of sonographic diagnosis. Radiology 193:771–776, 1994.
Hertzberg BS, Kliewer MA, Paulson EK: Ovarian cyst rupture causing hemoperitoneum: Imaging features and the potential for misdiagnosis. Abdom Imaging 24:304–308, 1999.
Hopkins A, Lahiri T, Salerno R, et al: Changing epidemiology of life-threatening upper airway infections: The reemergence of bacterial tracheitis. Pediatrics 118:1418–1421, 2006.
Jagannathan J, Dumont AS, Prevedello DM, et al: Cervical spine injuries in pediatric athletes: Mechanisms and management. Neurosurg Focus 21:E4(1–5), 2006.
Jain KA: Sonographic spectrum of hemorrhagic ovarian cysts. J Ultrasound Med 21:879–886, 2002.
Karmazyn B, Werner EA, Rejaie B, et al: Mesenteric lymph nodes in children: What is normal? Pediatr Radiol 35:774–777, 2005.
Kawashima A, Sandler CM, Goldman SM: Imaging in acute renal infection. BJU Int 86(Suppl 1):S70–S79, 2000.
Kleinman PK: Differentiation of child abuse and osteogenesis imperfecta: Medical and legal implications. AJR Am J Roentgenol 154:1047–1048, 1990.
Kleinman PK, Nimkin K, Spevak MR, et al: Follow-up skeletal surveys in suspected child abuse. AJR Am J Roentgenol 167:893–896, 1996.
Ko HS, Schenk JP, Troger J, et al: Current radiological management of intussusception in children. Eur Radiol 17:2411–2421, 2007.
Kocher MS, Mandiga R, Zurakowski D, et al: Validation of a clinical prediction rule for the differentiation between septic arthritis and transient synovitis of the hip in children. J Bone Joint Surg Am 86:1629–1635, 2004.
Kornecki A, Daneman A, Navarro O, et al: Spontaneous reduction of intussusception: Clinical spectrum, management, and outcome. Pediatr Radiol 30:58–63, 2000.
Kosloske AM, Musemeche CA, Ball WS, et al: Necrotizing enterocolitis: Value of radiographic findings to predict outcome. AJR Am J Roentgenol 151:771–774, 1988.
Krishnan A, De Souza A, Konijeti R, et al: The anatomy and embryology of posterior urethral valves. J Urol 175:1214–1220, 2006.
Lavocat MP, Granjon D, Allard D, et al: Imaging of pyelonephritis. Pediatr Radiol 27:159–165, 1997.
Lee SE, Kim HY, Jung SE, et al: Situs anomalies and gastrointestinal abnormalities. J Pediatr Surg 41:1237–1242, 2006.
Lim HK, Bae SH, Lee KH, et al: Assessment of reducibility of ileocolic intussusception in children: Usefulness of color Doppler sonography. Radiology 191:781–785, 1994.
Lin PW, Stoll BJ: Necrotizing enterocolitis. The Lancet 368(9543):1271–1283, 2006.
Lonergan GJ, Baker AM, Morey MK, et al: From the archives of the AFIP: Child abuse: Radiologic–pathologic correlation. Radiographics 23:811–845, 2003.
Long FR, Kramer SS, Markowitz RI, et al: Intestinal malrotation in children: Tutorial on radiographic diagnosis in difficult cases. Radiology 198:775–780, 1996.
Long WA, Lawson EE, Harned HS, et al: Pleural effusion in the first days of life: A prospective study. Am J Perinatol 1:190–194, 1984.
Lumerman J, Gershbaum MD, Hines J, et al: Unenhanced helical computed tomography for the evaluation of suspected renal colic in the adolescent population: A pilot study. Urology 57:342–346, 2001.
Macpherson RI, Leithiser RE, Gordon L, et al: Posterior urethral valves: An update and review. Radiographics 6:753–791, 1986.
Martin L, Buonomo C: Acute chest syndrome of sickle cell disease: Radiographic and clinical analysis of 70 cases. Pediatr Radiol 27:637–641, 1997.
Mazeh H, Kaliner E, Udassin R: Three recurrent episodes of malrotation in an infant. J Pediatr Surg 42:E1–3, 2007.
McCall R, Fassett D, Brockmeyer D: Cervical spine trauma in children: A review. Neurosurg Focus 20:E5(1–8), 2006.
McNeely PD, Atkinson JD, Saigal G, et al: Subdural hematomas in infants with benign enlargement of the subarachnoid spaces are not pathognomonic for child abuse. Am J Neuroradiol 27:1725–1728, 2006.
Merten DF, Goetzman BW, Wennberg RP: Persistent fetal circulation: An evolving clinical and radiographic concept of pulmonary hypertension of the newborn. Pediatr Radiol 6:74–80, 1984.
Meservy CJ, Towbin R, McLaurin RL, et al: Radiographic characteristics of skull fractures resulting from child abuse. AJR Am J Roentgenol 149:173–175, 1987.
Milliner DS, Murphy ME: Urolithiasis in pediatric patients. Mayo Clin Proc 68:241–248, 1993.
Montenegro MA, Santos SL, Li LM, et al: Neuroimaging of acute cerebellitis. J Neuroimaging 12:72–74, 2002.
Moore TC: Omphalomesenteric duct malformations. Semin Pediatr Surg 5:116–123, 1996.
Nance ML, Adamson WT, Hedrick HL: Appendicitis in the young child: A continuing diagnostic challenge. Pediatr Emerg Care 16:160–162, 2000.
Navarro O, Daneman A: Intussusception part 3: Diagnosis and management of those with an identifiable or predisposing cause and those that reduce spontaneously. Pediatr Radiol 34:305–312, 2004.
Ogata M, Imai S, Hosotani R, et al: Abdominal ultrasonography for the diagnosis of strangulation in small bowel obstruction. Br J Surg 81:421–424, 1994.
Özokutan BH, Küçükaydin M, Gündüz Z, et al: Urolithiasis in childhood. Pediatr Surg Int 16:60–63, 2000.
Palmer JS, Donaher ER, O'Riordan MA, et al: Diagnosis of pediatric urolithiasis: Role of ultrasound and computerized tomography. J Urol 174(4 Pt 1):1413–1416, 2005.
Patriquin HB, Yazbeck S, Trinh B, et al: Testicular torsion in infants and children: Diagnosis with Doppler sonography. Radiology 188:781–785, 1993.
Platzer P, Jaindl M, Thalhammer G, et al: Cervical spine injuries in pediatric patients. J Trauma 62:389–396, 2007.
Rao PM, Rhea JT, Novelline RA: Helical CT technique for the diagnosis of appendicitis: Prospective evaluation of a focused appendix CT examination. Radiology 202:139–144, 1997.
Romano C, Brown T, Frewen TC: Assessment of pediatric near–drowning victims: Is there a role for cranial CT? Pediatr Radiol 23:261–263, 1993.
Rooks VR, Lebowitz RL: Extrinsic ureteropelvic junction obstruction from a crossing renal vessel: Demography and imaging. Pediatr Radiol 31:120–124, 2001.
Rosado WM, Trambert MA, Gosink BB, et al: Adnexal torsion: Diagnosis by using Doppler sonography. AJR Am J Roentgenol 159:1251–1253, 1992.
Rudman DT, Elmaraghy CA, Shiels WE, et al: The role of airway fluoroscopy in the evaluation of stridor in children. Arch Otolaryngol Head Neck Surg 129:305–309, 2003.
Rushton HG: Urinary tract infections in children. Epidemiology, evaluation, and management. Pediatr Clin North Am 44:1133–1169, 1997.
Sadow KB, Atabaki SM, Johns CMS, et al: Bilious emesis in the pediatric emergency department: Etiology and outcome. Clin Pediatr 41:475–479, 2002.
Sargent MA, Babyn P, Alton DJ: Plain abdominal radiography in suspected intussusception: A reassessment. Pediatr Radiol 24:17–20, 1994.
Schuh S, Lalani A, Allen U, et al: Evaluation of the utility of radiography in acute bronchiolitis. J Pediatrics 150:429–433, 2007.
Servaes S, Zurakowski D, Laufer MR, et al: Sonographic findings of ovarian torsion in children. Pediatr Radiol 37:446–451, 2007.
Shah RK, Roberson DW, Jones DT: Epiglottitis in the Hemophilus influenza type B vaccine era: Changing trends. Laryngoscope 114:557–560, 2004.
Skibo L, Reed MH: A criterion for a true lateral radiograph of the elbow in children. Can Assoc Radiol J 45:287–291, 1994.
Smergel E, Greenberg SB, Crisci KL, et al: CT urograms in pediatric patients with ureteral calculi: Do adult criteria work? Pediatr Radiol 31:720–723, 2001.
Stark KE, Siegel MJ: Ovarian torsion in prepubertal and pubertal girls: Sonographic findings. AJR Am J Roentgenol 163:1479–1482, 1994.
Stoodley N: Controversies in non-accidental head injury in infants. Br J Radiol 79:550–553, 2006.
Strouse PJ: Disorders of intestinal rotation and fixation ("malrotation"). Pediatr Radiol 34:837–851, 2004.
St-Vil D, Brandt ML, Panic S, et al: Meckel's diverticulum in children: A 20-year review. J Pediatr Surg 26:1289–1292, 1991.
Swaniker F, Soldes O, Hirschi RB: The utility of technetium 99m pertechnetate scintigraphy in the evaluation of patients with Meckel's diverticulum. J Pediatr Surg 34:760–764, 1999.
Swischuk LE, Hernandez JA: Frequently missed fractures in children (value of comparative views). Emerg Radiol 11:22–28, 2004.
Thornbury JR: Acute renal infections. Urol Radiol 12:209–213, 1991.

Tsai JD, Huang FY, Lin CC, et al: Intermittent hydronephrosis secondary to ureteropelvic junction obstruction: Clinical and imaging features. Pediatrics 117:139–146, 2006.
Tung GA, Kumar M, Richardson RC, et al: Comparison of accidental and nonaccidental traumatic head injury in children on noncontrast computed tomography. Pediatrics 118:626–633, 2006.
Vane DW, West KW, Grosfeld JL: Vitelline duct anomalies: Experience with 217 childhood cases. Arch Surg 122:542–547, 1987.
Verschelden P, Filiatrault D, Garel L, et al: Intussusception in children: Reliability of US diagnosis—a prospective study. Radiology 8:343–347, 1992.
Vogl TJ, Bergman C, Villriner A, et al: Dural sinus thrombosis: Value of venous MR angiography for diagnosis and follow-up. AJR Am J Roentgenol 162:1191–1198, 1994.
Zerella JT, Dimier M, McGill LC, et al: Foreign body aspiration in children: Value of radiography and complications of bronchoscopy. J Pediatr Surg 33:1651–1654, 1998.

CHAPTER 7

Traumatic and Nontraumatic Spine Emergencies

Glenn D. Barest

TRAUMATIC SPINE INJURY

Background and Imaging Algorithms

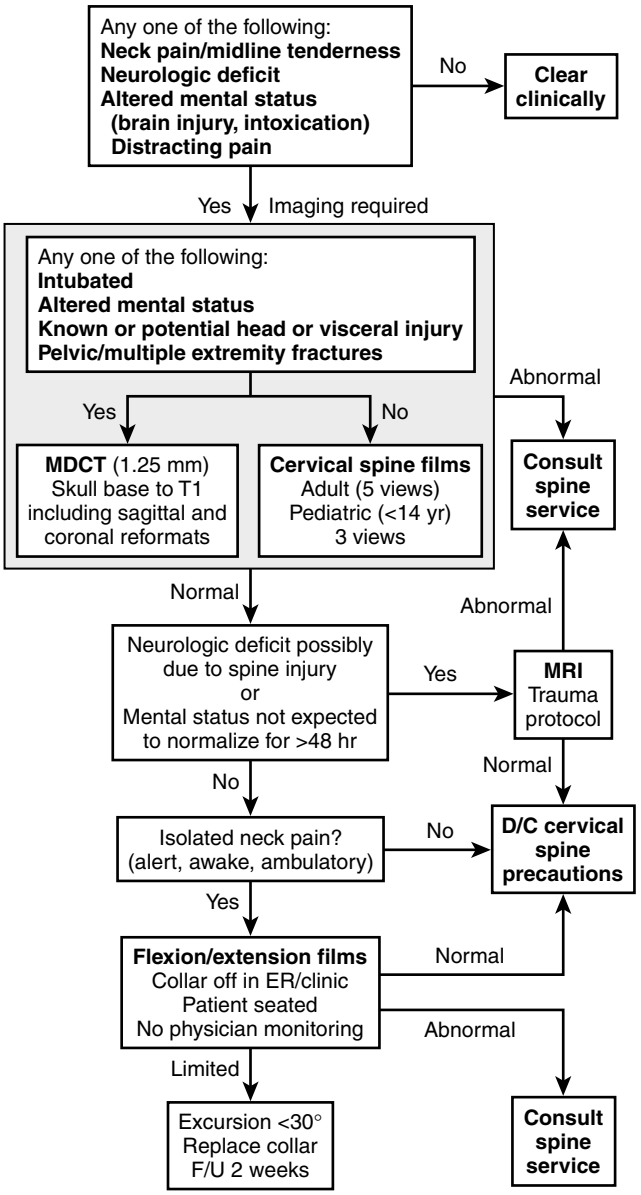
Cervical spine injuries are quite common, causing an estimated 6000 deaths and 5000 new cases of quadriplegia annually in the United States. Imaging is liberally applied with a positive yield of from 1% to 3% of all exams, resulting in an annual cost of approximately $3 billion. Approximately 14,000 cases of spinal cord injury occur each year in the United States, the majority affecting young adults. The cost to individuals and society is enormous due to their long life expectancy. Understandably, this is one area of medicine in which attempts have been made to develop evidence-based diagnostic algorithms. Multivariate analysis of data derived from two major clinical research initiatives, the National Emergency X-Radiography Utilization Study (NEXUS) and the Canadian C-Spine Study, has provided the basis for acute spine trauma imaging pathway development. Decision rules have been created that allow for discrimination of patients in need of imaging and those for whom imaging can be safely avoided, thereby reducing costs when possible. Once the decision to image has been made, the next step is to select the most appropriate modality. Plain film radiography has traditionally been the initial examination to evaluate for possible fracture or malalignment. It is readily available, relatively inexpensive to perform, and highly sensitive. It continues to be a cost-effective option for patients with a low probability of injury. However, it has been supplanted by computed tomography (CT) in the setting of moderate-to-high probability of injury, based on cost-effectiveness analysis that takes into account the high medical and legal costs of the rare missed fracture that leads to severe neurologic deficit. Studies of CT as the initial modality have demonstrated higher sensitivity for the detection of fractures; however, the clinical significance of many of the radiographically occult injuries is uncertain owing to the lack of studies addressing outcomes. Another clinical prediction rule that has been developed, based on data from the Harborview study, may be used to stratify risk based on injury mechanism and other clinical parameters. This type of approach is supported by trauma surgery societies and is commonly applied at trauma centers.

With the increasing availability of multidetector-row CT (MDCT), it seems that this is quickly becoming the new standard of care, even for patients with a low probability of injury. A zero-tolerance (for missed injury) approach to diagnosis using the fastest, most accurate exam is easily adopted by the emergency department or trauma team rather than an evidence-based approach. It used to be that for patients with negative radiographs but persistent pain, tenderness, or limited range of motion, symptomatic treatment with analgesics, soft collar application, and clinical follow-up were the rule. At the follow-up visit, if symptoms had not resolved, flexion-extension radiographs were obtained to evaluate for the possibility of ligamentous injury or instability. Flexion-extension views have been shown to have little utility in the acute setting, primarily due to limited range of motion secondary to muscle spasm. In low-probability settings, this approach may still be followed, but more commonly, CT is requested to exclude occult fracture. The higher direct cost of CT may be offset by the increase in emergency department throughput, albeit at a higher radiation exposure. On some occasions, after a negative CT exam, magnetic resonance (MR) imaging may be pursued to screen for signs of potential ligamentous injury before allowing the patient to be discharged.

The cost-effectiveness of MR for the detection of clinically significant ligamentous injuries has not yet been determined. This is another instance where technology is being applied because of its availability and perhaps for theoretical limitation of liability. Clearly, when a neurologic deficit is present and CT fails to identify a cause, MR may offer additional sensitivity for the detection of soft tissue injuries, including disc extrusion, hematoma within the spinal canal, cord compression or contusion, and unstable ligamentous injury. Other injuries such as unsuspected bone marrow edema (microfractures) and vascular injuries may also be detected. One study that correlated MR imaging and intraoperative findings found that MR had moderate to high sensitivity for injury to specific ligamentous structures but suggested that it may overestimate the extent of disruptive injury. MR, with its increased sensitivity, also brings with it a small false-positive rate that may lead to added costs related to treatment/workup of clinically insignificant or unrelated abnormalities, such as thyroid lesions and lymphadenopathy. Special consideration has been given to the obtunded patient, since some studies have shown a 2% incidence of unstable cervical spine injuries that were not detected by radiography and CT due to the lack of associated fracture or malalignment. Although other authors have suggested that it is not necessary, MR "clearance" of the cervical spine has become a reality. At

our institution, we generally adhere to the algorithm shown below.

Regarding the thoracolumbar spine, clinical prediction rules have been evaluated but provide only a very small decrease in the number of exams performed. In those patients with blunt trauma undergoing CT of the chest, abdomen, and pelvis with thin-section CT (2.5 mm or less), sagittal and coronal reformats have been shown to be more sensitive and specific for detection of fractures, and therefore radiography can be avoided. When the viscera are not in need of examination, the role of CT for screening the spine is not as clear. Mechanism of injury is an important determinant for further workup in this category of patients. Similar to the logic applied to the cervical spine, screening is warranted if a high-energy mechanism of injury is known or suspected, including falls from significant height (greater than 10 feet), motor vehicle or bicycle crash, pedestrians struck, assault, sport or crush accident, and a concomitant cervical spine fracture. Other valid indications are altered mental status, evidence of intoxication with ethanol or drugs, painful distracting injuries, neurologic deficits, and spine pain or palpation tenderness.



For patients with neurologic deficits referable to a thoracolumbar spine injury, current Eastern Association for the Surgery of Trauma guidelines recommend obtaining an MR exam as soon as possible after admission to the emergency department. Early decompression of mass lesions, such as traumatic herniated discs or epidural hematomas, is likely to improve neurologic outcome.

A somewhat unintuitive finding is that the absence of symptoms does not exclude injury to the thoracolumbar spine. In one study, only 60% of trauma patients with a confirmed fracture were symptomatic. In a review from Maryland's Shock Trauma Center of 183 fractures in 110 patients who were neurologically intact with a Glasgow Coma Scale score between 13 and 15 and considered amenable to clinical examination, 31% of these patients were recorded as having no pain or tenderness, yet all had fractures. The evidence would suggest that many of these fractures were not truly asymptomatic but rather occult as a result of intoxication or an unreliable physical exam. It is clear from the literature that no imaging modality is accurate 100% of the time. Most studies have found that radiographs of the thoracolumbar spine are commonly inadequate, especially in obese patients, and provide a sensitivity and specificity of only 60% to 70%.

Separate studies to develop guidelines for the pediatric population have not been performed. The increasing use of MDCT and the long-term effects of radiation exposure are topics of concern and current research.

Patterns of Spine Injury and Imaging Findings

Following is a brief review of the many different types of spine injuries that one must be familiar with when evaluating victims of trauma. There are many texts devoted solely to the imaging of spine trauma, with a few that truly reward the reader with insight into the anatomy, physiology, biomechanics, and pathology of this extensive topic. This section should serve as a valuable aid to the radiologist on call and be used as a starting point for further study. Rather than taking a how-to approach to evaluating spinal imaging, this section relies on a working knowledge of the normal anatomy and basic principles of plain film, CT, and MR analysis. The general classifications of injuries are covered through a review of classic examples, using primarily CT with important plain film and MR correlations where appropriate.

Imaging of the spine can be thought of as a continuum, with radiography providing an overview of alignment and soft tissues, CT adding greater detail regarding fractures, and MR yielding finer detail with respect to soft tissues including the spinal cord. Attention must be paid to the technical factors necessary to achieve a satisfactory (and safe) exam, including patient immobilization and positioning, image acquisition parameters, and multiplanar analysis.

Lateral, anteroposterior, and open-mouth odontoid views are the minimum requirement for plain films. A "swimmer's" view may be necessary to adequately

demonstrate the cervicothoracic junction. Thin-section CT (section thickness of 2 mm or less) with similar-thickness sagittal and coronal reformats generally suffices. However, anecdotal cases have arisen in which hairline fractures were detected on scans performed with submillimeter thickness that were not detected prospectively with the standard technique. Clearly there is a trade-off between level of anatomic detail and number of images that must be reviewed. With isotropic voxel size now possible with modern scanners, some have proposed primary review of sagittal and coronal reformats in order to increase patient throughput. Thankfully, many of the missed fractures will be clinically insignificant due to their small size and inherent stability. In addition to the standard T1- and T2-weighted sequences used to evaluate the cervical spine, fat-suppressed T2-weighted sequences, with either chemical selective or short tau inversion recovery (STIR) technique and gradient-echo sagittal imaging, are useful in the trauma setting. MR angiographic sequences may be indicated in certain circumstances.

Careful analysis of the structures (vertebrae, intervertebral discs, spinal cord, and other soft tissues) and their normal and abnormal attributes (size, shape, alignment, density, and signal intensity) requires an understanding of mechanisms of injury, including magnitude and acuity, and underlying diseases. The mechanisms can generally be grouped into hyperflexion, hyperextension, rotation, axial loading, lateral flexion, and others. Box 7-1 attempts to categorize the injuries of the cervical spine based on these mechanisms. Combined mechanisms, such as flexion and rotation, are common and may lead to multiple injuries at different sites and vertebral levels within the same patient. Rather than relaxing after detecting an injury, the examiner should intensify the search for other lesions.

The determination of instability, which may be associated with or have the potential to progress to neurologic injury, major deformity, or incapacitating pain, is an important part of this process. There are general principles that may apply based on specific imaging findings, but the final determination is probably best made by an expert in the treatment of these injuries. One should note that the classifications of these injuries are constantly being revised based on new treatment techniques and clinical outcomes. Some of the more commonly used classifications will be mentioned. The three-column approach to stability proposed by Denis divides the spine into anterior column (anterior longitudinal ligament, annulus, and anterior two thirds of the vertebral body and disc), middle column (posterior third of vertebral body and disc, annulus, posterior longitudinal ligament), and posterior column (posterior elements, ligamentum flavum, joint capsules, intertransverse, interspinal, and supraspinal ligaments). Instability is generally based on disruption of two of the three columns.

Box 7-1. **Categories of Injuries of the Cervical Spine Based on Mechanism**

HYPERFLEXION
Anterior subluxation (including atlantoaxial dissociation)
Clay shoveler's fracture
Facet fracture-dislocation
Flexion teardrop
Interfacetal dislocation (unilateral or bilateral)
Wedge compression fracture

HYPEREXTENSION
Articular mass fracture
Avulsion of anterior arch of C1
Extension teardrop
Fracture of posterior arch of C1
Hangman fracture (C2 spondylolysis/spondylolisthesis)
Hyperextension dislocation
Hyperextension fracture-dislocation
Laminar fracture
Pedicolaminar fracture-separation

AXIAL LOADING
Burst fracture
Jefferson fracture (C1 burst)

LATERAL FLEXION
C1 lateral mass fracture
Occipital condyle fracture
Transverse process fracture
Uncinate process fracture

OTHER OR UNKNOWN MECHANISMS
Atlantoaxial rotatory subluxation
Atlanto-occipital (craniocervical) dissociation
Odontoid fracture

Injuries of the Cervicocranium

The cervical spine can be subdivided into the cervicocranium (including the basiocciput, craniocervical junction, atlas [C1], and axis [C2]) and the subaxial spine (C3 through C7). Following is a top-down review of the major types of injuries and the mechanisms that cause them. It is not possible to describe all of the features of each injury in this abbreviated format; however, the general principles and commonly used classifications are described.

Occipital Condyle

Occipital condyle fractures are relatively rare and often classified into three types. Type I is a longitudinal fracture from axial loading. Type II is a continuation of a fracture from the flat part of the occipital bone. Type III is the most serious, an avulsion of the condyle at the attachment of the alar ligament, and may be unstable (Fig. 7-1).

Atlanto-occipital Dislocation

Atlanto-occipital dislocation (AOD) refers to disruption of the articulations of the skull and spine. Atlanto-occipital dissociation (synonymous with craniocervical dissociation) is a broader term encompassing partial (subluxation) and complete (dislocation) disruption of the articulations. Following high-speed motor vehicle collisions, this injury is more often diagnosed at autopsy than at the trauma center. Although no method is perfect, measurement of the basion-dental interval (BDI) or the basion-posterior axial line interval (BAI) of more than 12 mm was reported to be 100% sensitive in one published study (Fig. 7-2).

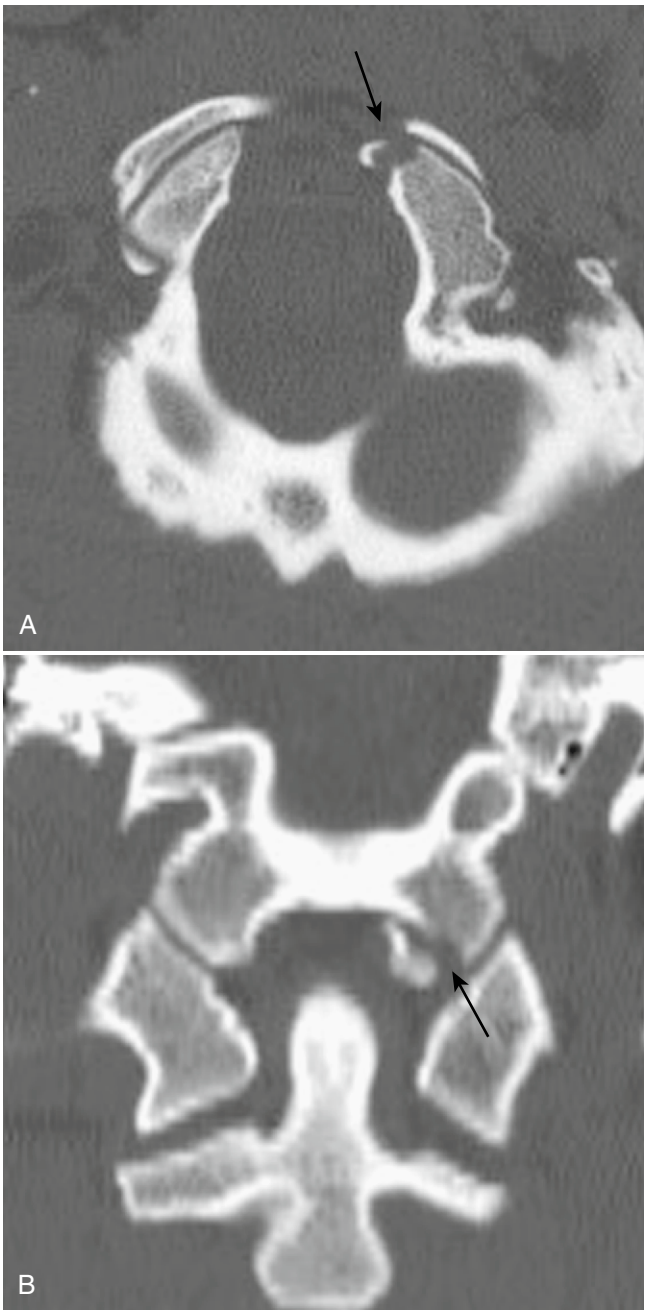


Figure 7-1. Occipital condyle fracture. **A,** Axial CT. **B,** Coronal reformat images show an avulsion fracture of the left occipital condyle at the attachment of the alar ligament (type III).

C1 Fractures

The classic Jefferson burst fracture of the atlas (C1) is due to disruption of the anterior and posterior arches (with several possible variations). Lateral displacement of the lateral masses of C1 with respect to C2 is seen on the open mouth view radiograph or the CT coronal reformatted image (Fig. 7-3). Isolated anterior arch (which goes against the pretzel ring theory) or lateral mass fractures may also occur at this level.

Atlantoaxial Dissociation

Atlantoaxial dissociation includes partial (subluxation) and complete (dislocation) disruptions of the articulations of C1 and C2. Disruption of the transverse atlantal ligament (TAL), the horizontal component of the cruciform ligament complex, allows for widening of the anterior atlantodental interval (AADI) (Fig. 7-4). Greater than 3 mm in adults or greater than 5 mm in children is considered abnormal. Conditions that may predispose

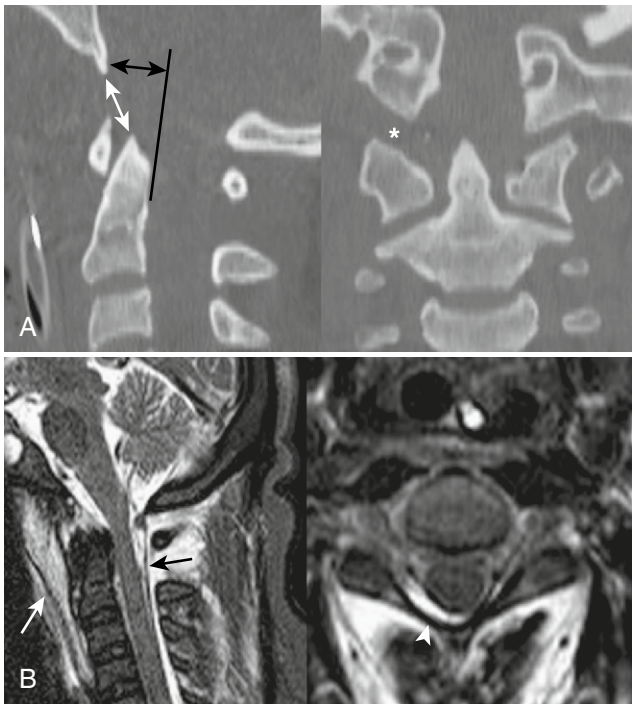


Figure 7-2. Atlanto-occipital dislocation. **A,** CT sagittal reformat shows widened BDI *(white double arrow)* and basion-posterior axial line interval BAI *(black double arrow).* Coronal reformat shows widened right atlanto-occipital joint *(asterisk).* **B,** MR STIR sagittal image shows prevertebral hematoma *(white arrow)* and displacement of the dura *(black arrow)* by a posterior epidural hematoma. Axial T2-weighted image shows the crescentic hyperintense epidural hematoma *(white arrowhead).*

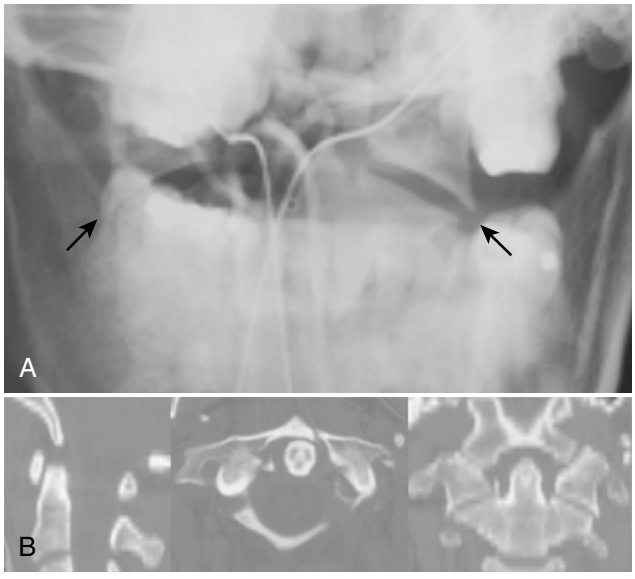


Figure 7-3. C1 Jefferson fracture. **A,** Odontoid view shows overhanging margins of lateral masses of C1 *(arrows).* **B,** CT sagittal reformat shows normal relationships. The axial source image shows fractures of anterior and posterior arches of C1. Coronal reformat shows overhanging margins of C1 as seen on plain radiograph.

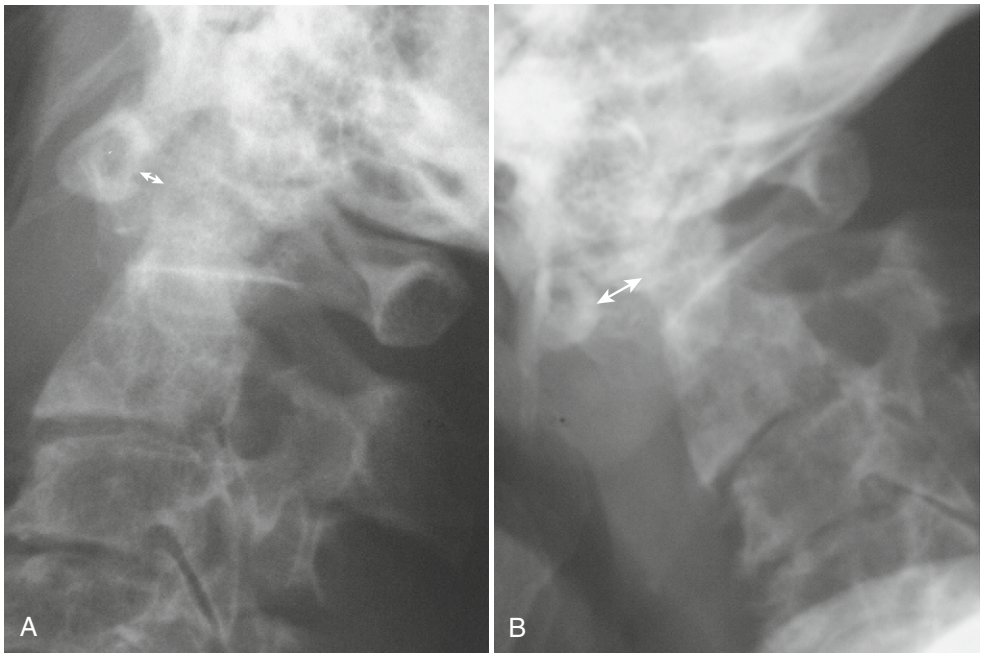


FIGURE 7-4. Atlantoaxial dissociation. **A,** Extension view shows a normal anterior atlanto-dental interval (AADI). **B,** The AADI is abnormally widened on flexion view, confirming disruption of the TAL. The abnormal atlanto-axial relationship was incidentally noted on a routine head CT done after a minor fall at the nursing home. The patient had a history of mild chronic neck pain, without exacerbation reported.

to atlantoaxial dissociation include rheumatoid arthritis, Down syndrome, neurofibromatosis, and other syndromes and congenital anomalies. Rotatory dissociation (fixation) is rare and has been subdivided into four types based on extent and direction of displacement of the atlas. Type I may appear similar to physiologic rotation. Therefore, to confirm the diagnosis, CT may be repeated after voluntary contralateral rotation of the head to assess for a locked position. Torticollis refers to simultaneous lateral tilt and rotation of the head and may be caused by disorders affecting either the atlantoaxial joint or the sternocleidomastoid muscle. Since it may produce the same imaging findings as type I rotatory fixation, diagnosis may rely on clinical judgment and a trial of conservative treatment. Types II, III, and IV are determined based on direction and extent of displacement of the cranium.

C2 Fractures

Approximately 20% of cervical fractures involve the axis (C2). Of these, more than half are traumatic spondylolysis/spondylolisthesis—fracture between the superior and inferior facets (pars interarticularis) of C2—often described as the "hangman" fracture (Fig. 7-5). Due to the unique shape of C2, this fracture involves the pedicles, whereas a pars fracture of the subaxial spine is termed the "pillar" fracture. Aside from the mechanism implied by the name, other forms of hyperextension, such as motor vehicle dashboard impact, are usually to blame. At least three types have been described, based on degree of fragment distraction, angulation at the fracture site, and disruption of the C2-C3 disc.

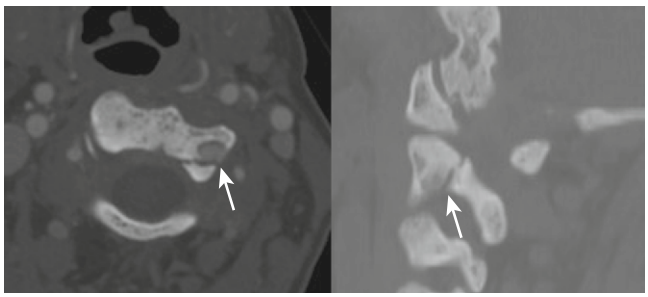


FIGURE 7-5. C2 hangman fracture. Contrast-enhanced axial CT *(left)* shows fracture through the body of C2 involving the left transverse foramen. Sagittal reformat *(right)* shows the oblique course of the fracture that separates the superior and inferior articulating facets of C2.

The dens (odontoid process) may be involved in approximately 25% of C2 fractures. The classification system of Anderson and D'Alonso is commonly applied. Type I is uncommon—an avulsion of the tip by the alar ligament—and may be associated with AOD. Type II is the most common (about 60%) and involves the base of the dens (Fig. 7-6). Operative repair via transoral screw fixation or posterior arthrodesis of C1 and C2 is often necessary. Type III involves the dens and body of C2. Due to the larger surface area, this type of fracture is more likely to heal without the need for instrumentation (Fig. 7-7). As the plane may be nearly horizontal, dens fractures may be quite subtle on axial CT. Sagittal reformats therefore demand careful review. Beware of misregistration artifact of axial CT, due to patient movement between adjacent images, although this has become less of a problem since the advent of helical and MDCT techniques. Since the scanning process is so fast with these techniques, a different type of artifact can result—motion blur. Distorted images should signal the need to repeat the scan. For uncooperative patients, a lateral plain film may provide complementary demonstration of proper alignment.

Injuries of the Subaxial Cervical Spine

Hyperflexion

Injury of the subaxial spine generally follows a set of patterns based on the mechanism and degree to which the subaxial spine has been stressed beyond physiologic limits. Of the injuries caused by hyperflexion, the simple wedge

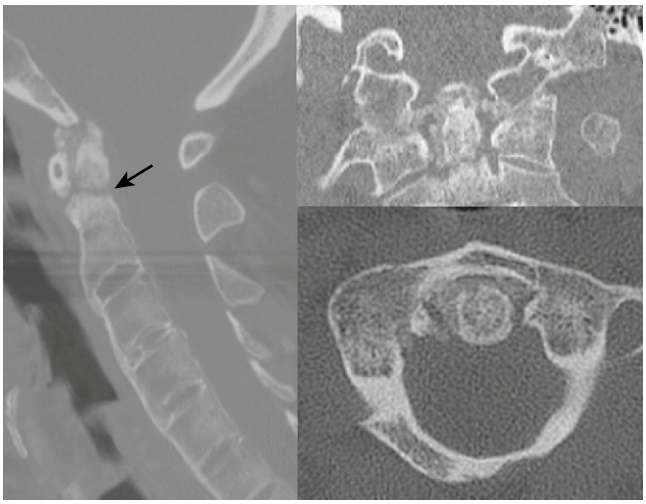


Figure 7-6. Ankylosing spondylitis—C2 fracture. CT sagittal reformat *(left)* shows dens fracture and ankylosis of C2 through C6 vertebral bodies. Coronal reformat *(right upper)* and axial source image *(right lower)* show extensive hypertrophic bone formation resulting in ankylosis of the occiput to C1 and C1 to the tip of the dens. The altered biomechanics are a setup for dens fracture.

compression fracture (involving the anterior column) and the isolated spinous process (clay shoveler) fracture are relatively straightforward in terms of diagnosis. Although generally considered stable injuries, they can occur in association with other, more insidious injuries, and therefore flexion/extension radiographs or MR may be indicated. Anterior subluxation (or hyperflexion sprain) is indicative of injury to the posterior ligamentous structures. It can be quite subtle, presenting with focal kyphotic angulation, very mild malalignment of facets, and widening of the posterior margin of the disc space and interspinous distance. Failure to diagnose and treat this injury may result in delayed instability in up to 50% of cases. As the degree of anterior vertebral body translation, facet joint distraction, and "fanning" of spinous processes increases, the signs of instability become more obvious. Facets may become perched or jumped (complete dislocation). Anterior translation of a vertebral body by more than 50% relative to the subjacent body is a sign of bilateral interfacetal dislocation (BID) (Figs. 7-8 and 7-9). With perched facets, the "naked facet" sign will be seen on axial CT. With BID, the convex surfaces of the articular masses will be apposed rather than the usual concave articular surfaces. Anterior, middle, and the posterior ligamentous structures will be disrupted, and the extent of soft tissue injuries (including cord compression and contusion) will be best assessed by MR. If there is any rotational component to the mechanism of injury, unilateral interfacetal dislocation (UID) or combination of perched and jumped facets may occur. Fractures of the subjacent vertebral body or articular masses will result in a fracture-dislocation. The flexion teardrop fracture is thought to result from a combination of hyperflexion and axial loading. It is feared because of the high incidence of permanent neurologic damage resulting from the more complex variety, which usually includes fractures of the posterior elements. Although it can be difficult to distinguish this from the hyperextension teardrop fracture based on the configuration of the vertebral body fracture alone, the kyphosis and posterior element distraction are important clues.

Hyperextension

The types of injuries to the subaxial spine resulting from hyperextension mechanisms are analogous to those sustained by hyperflexion, but with a few differences. Hyperextension sprain, dislocation, and fracture-dislocation encompass a spectrum that may result from a blow to the

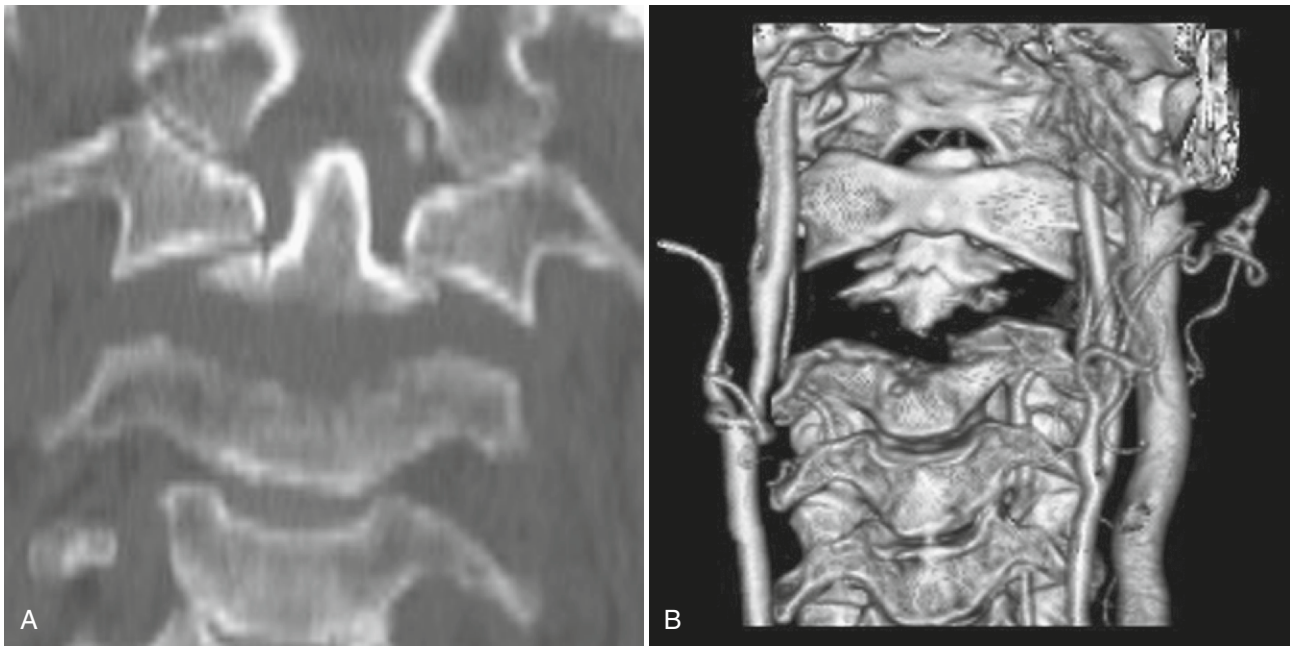


Figure 7-7. Dens fracture—type III. CT coronal reformat **(A)** and volume-rendered image from CT angiogram **(B)** show fracture of the dens involving the body of C2 and distraction of fragments.

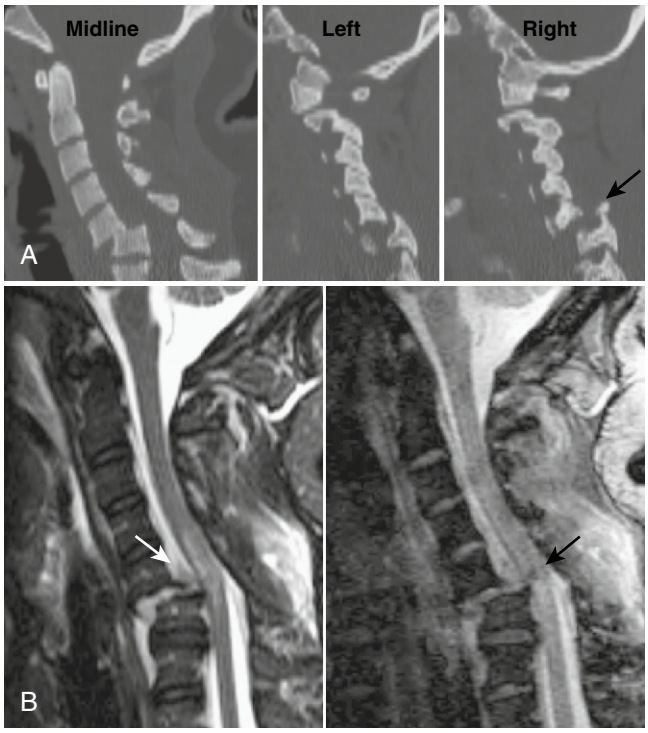


FIGURE 7-8. Hyperflexion—bilateral interfacetal dislocation. **A,** CT sagittal reformats show greater than 50% offset of C5 on C6, jumped left facet, and fracture of right C5 inferior facet *(black arrow)* with dislocation. **B,** Sagittal STIR and gradient-echo images show associated small epidural hematoma versus C5-C6 disc extrusion *(white arrow)*. Also note hemorrhage in the disc space extending inferiorly in the prevertebral region. Hyperintense signal in the spinal cord is consistent with edema. The central isointense region is noted to be hypointense on gradient-echo image *(black arrow)*, indicating hemorrhage (cord contusion).

face, as from impact against the dashboard during a motor vehicle collision, an assault, or a fall. Soft tissue structures are involved in a progressive fashion from anterior to posterior, including prevertebral muscles, anterior longitudinal ligament, anterior portion of annulus, intervertebral disc, posterior longitudinal ligament, and so on. A sprain usually leaves the middle and posterior columns intact. A dislocation also disrupts the middle and possibly posterior ligaments. A fracture-dislocation may result in fractures of the posterior aspect of the vertebral body and any of the posterior elements due to impaction forces. When underlying ankylosis is present, such as in diffuse idiopathic skeletal hyperostosis or ankylosing spondylitis, a relatively mild hyperextension force may result in fracture-dislocation (see Fig. 7-6). This is due to the loss of normal ligamentous laxity, a lever arm up to several spinal segments long, and coexistent osteoporosis. An extension teardrop fracture fragment is the result of avulsion by the anterior longitudinal ligament. The vertical dimension of the fragment is generally greater than the horizontal dimension (Fig. 7-10).

Extension combined with rotation and lateral or tilting forces may result in articular mass (also known as pillar) fractures (Fig. 7-11). A fracture of the pedicle and ipsilateral lamina may result in a freely mobile articular mass (pedicolaminar separation). Occasionally, isolated fracture(s) of the lamina(e) will be occult on anteroposterior and lateral films. This is one advantage of oblique radiographs. Another advantage is confirmation of unilateral facet dislocation, but, alas, MDCT has made these films nearly obsolete. It is the rare technologist who can still obtain perfect trauma oblique views taken without removing the cervical collar or turning the patient's head. It seems that most centers have abandoned oblique views from the routine cervical spine series. The extra clues provided by oblique views may still have value in centers where trainees interpret plain film exams on call.



FIGURE 7-9. Hyperflexion—anterior subluxation. Lateral radiograph shows complete subluxation of C5 on C6 (spondyloptosis). This patient with previous C3 through C5 laminectomies for canal stenosis was the unfortunate victim of an accidental gas main explosion.

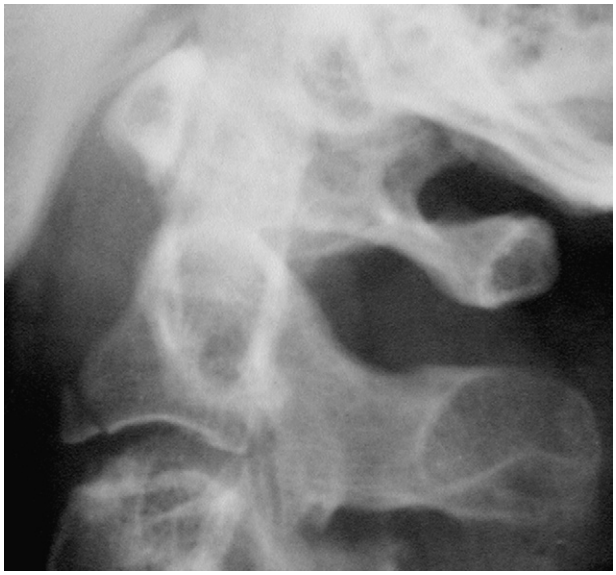


FIGURE 7-10. Extension teardrop fracture. Lateral radiograph shows that the height of the fracture fragment is greater than the width.

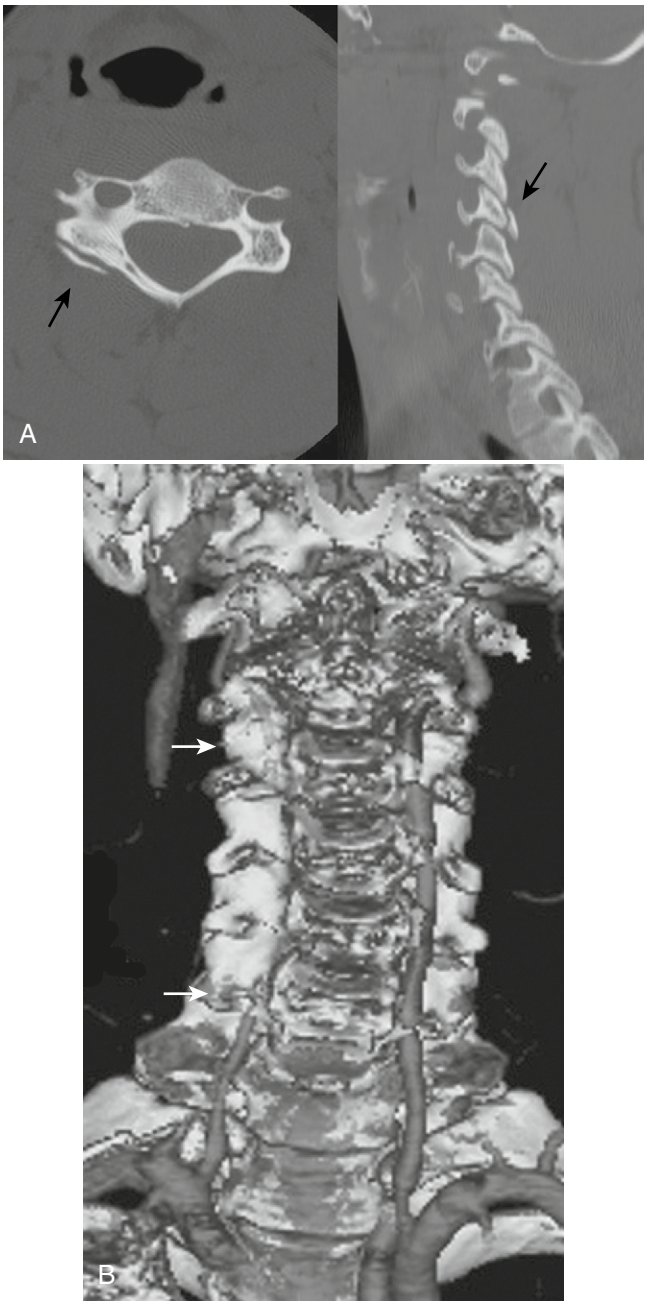


Figure 7-11. Articular facet fracture—vascular injury. **A,** CT axial and sagittal reformats show C4 right pillar fracture. **B,** Volume-rendered image from CT angiogram shows segmental occlusion of the right vertebral artery. Reconstitution via muscular collaterals is a common finding in vertebral artery injuries.

Axial Loading

Axial loading due to diving injuries, falls, or ejections from vehicles may result in a burst fracture, with comminuted fractures of the vertebral body and often displaced fractures of the posterior elements. As pressure is transmitted through the intervertebral disc, the body may be split in a sagittal plane, or the disc may lose vertical height, causing retropulsion of the posterior portion of the body into the spinal canal. The latter form clearly has a higher potential to result in spinal cord injury. Involvement of the anterior and middle columns is generally considered an unstable injury and requires operative fixation.

Many of the injuries described above may present with relatively preserved alignment owing to rebound of structures after traumatic displacement. The snapshot provided by imaging after stabilization and transport to the trauma center may provide clues to the cause of a neurologic deficit. In many cases, the cause will still be evident—cord compression due to severe canal stenosis, malalignment, displaced bone fragment, hematoma within the spinal canal, cord contusion, or edema.

Lateral Bending

Injuries due to lateral bending do not seem to be very common, but an occasional uncinate process or transverse process fracture may be detected by CT. Fracture involving the foramen transversarium brings a risk of dissection or occlusion of the vertebral artery and, with it, the possibility of stroke. A discussion of the workup of vascular injuries of the neck and head is included in Chapter 1 in the section on cerebrovascular disorders.

Pitfalls in Spine Imaging

One must become familiar with the normal pattern of development and congenital anomalies in children, such as os odontoideum, incomplete ossification of the neural arches, and pseudosubluxation in order to avoid false-positive diagnoses (Fig. 7-12).

It is often helpful to realize that abnormalities need to be evaluated in context. For example, not every malalignment is an acute one. Mild subluxations of the cervical spine are quite common due to chronic osteoarthritis. Therefore, analysis of the pattern of facet hypertrophy may provide confidence that the deformity is chronic. Dynamic testing with flexion-extension radiographs may support such a conclusion. On the other hand, sometimes it is necessary to call attention to a clearly chronic finding detected serendipitously. An os odontoideum that is well corticated but chronically unstable provides just one such example (Fig. 7-13).

Injuries of the Thoracolumbar Spine

Although similar mechanisms of injury apply, differences in biomechanics between the cervical and thoracolumbar spine result in different patterns of findings. Compression fractures due to flexion are very common (Fig. 7-14). Osteoporotic compression fractures are common, with more than 700,000 occurring annually in the United States, with costs from treatment approaching $1.5 billion. While the majority may be considered stable, medical therapies required to treat the associated pain may lead to other serious complications. The increase in age-adjusted 5-year mortality approaches 25% for female patients. Use of alcohol and certain medications, including steroids, anticonvulsants, cytotoxic drugs, thyroid hormones, and heparin, may all be associated with osteoporotic compression fractures. Metastatic disease may predispose to the development of pathologic compression fractures. One fracture also increases the risk for development of other fractures due to altered biomechanics of the kyphotic spine. Vertebroplasty

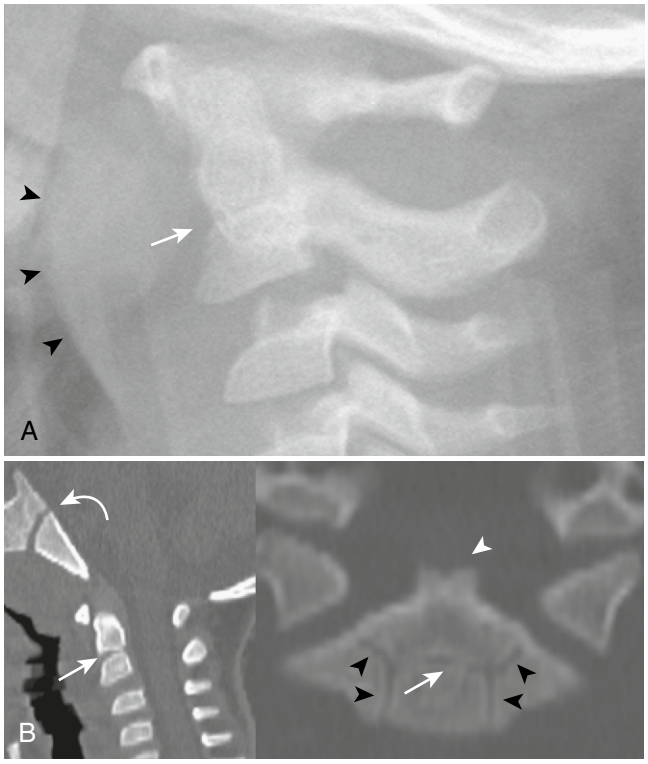


FIGURE 7-12. Normal developmental anatomy—C2. **A,** Lateral radiograph in a small child was interpreted as prevertebral soft tissue swelling *(arrowheads)* and dens fracture *(arrow)*. **B,** CT sagittal and coronal reformats show normal developmental anatomy—subdental synchondrosis *(white arrow)*, neurocentral and neurodental synchondroses *(black arrowheads)*. Tip of dens ossification center (ossiculum terminale) is not yet visible *(white arrowhead)*. The apparent soft tissue swelling was due to normally lax tissues and phase of respiration. Note also the normal spheno-occipital synchondrosis *(curved arrow)*.

and kyphoplasty are minimally invasive spine procedures that are possible treatments for those patients who do not respond to an appropriate trial of conservative therapies. With more than 50% loss of anterior vertebral body height, disruption of the posterior longitudinal ligament may occur, leading to the possibility of instability.

Axial loading mechanism may result in a burst fracture. These fractures occur most commonly near the thoracolumbar junction but may also affect the mid- and lower lumbar levels. The extent of retropulsion of the posterior portion of the vertebral body, the relative size of the spinal canal, and the position of the conus medullaris are factors affecting the risk of neurologic injury. Screening exam of the thoracolumbar spine should be performed when calcaneal fractures result from a jump or fall from a height due to the high association of these injuries (Fig. 7-15).

The combination of flexion and distraction, common in lap belt deceleration injuries, results in a rather unique pattern of findings. A horizontally oriented fracture plane through the intervertebral disc and posterior elements has come to be called the "Chance" fracture. Since there are many variations in terms of bony and ligamentous components, the term "Chance-type fracture" may be applied to these horizontal fractures most commonly affecting the upper lumbar spine (Fig. 7-16). The abdominal viscera should be carefully evaluated in patients with Chance-type fractures, since there is strong association with intestinal and solid organ injuries.

Hyperextension injuries may result in disc and anterior ligamentous injury or impaction fractures of the posterior elements. Patients with ankylosing spondylitis are particularly prone to extension injuries and may also develop horizontally oriented fractures through the vertebral bodies.

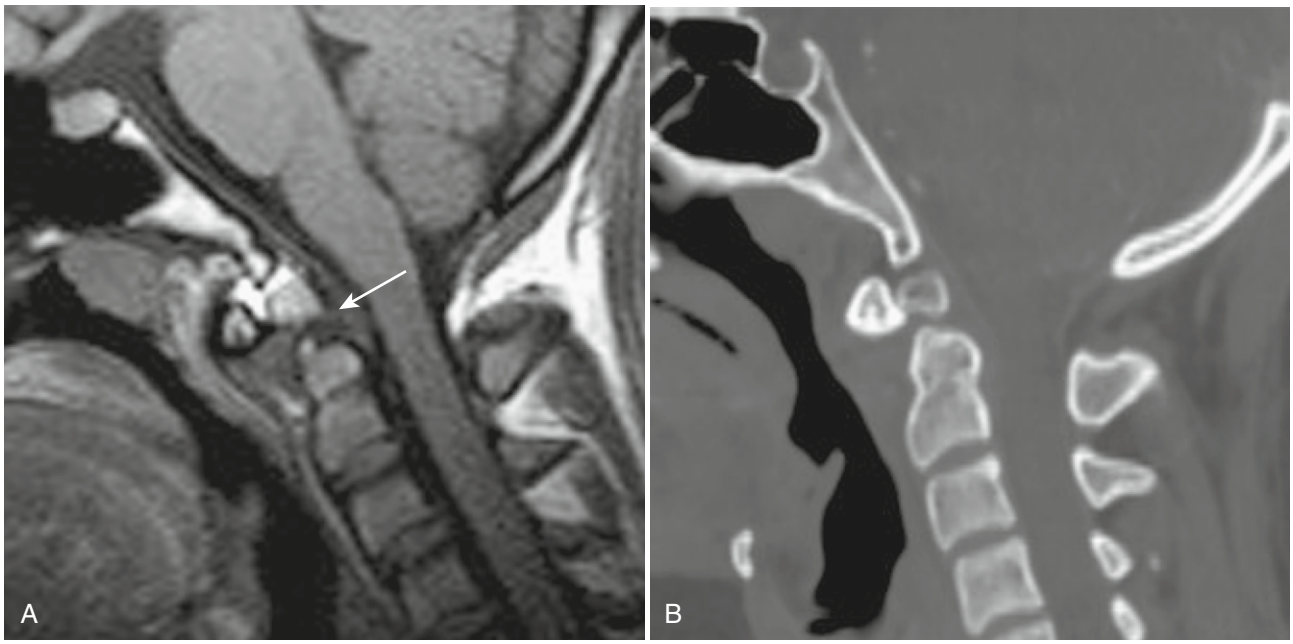


FIGURE 7-13. Os odontoideum—unstable. **A,** Sagittal T1-weighted image of a teenager with headaches and visual scotomata revealed an anomaly of the cervicocranium *(arrow)*. **B,** Sagittal reformat of cervical spine CT confirmed an os odontoideum and incomplete posterior arch of C1 variants. Flexion-extension radiographs demonstrated instability (not shown). Transient compression of the basilar artery related to instability was thought to be responsible for the visual changes. The patient is asymptomatic following C1-C2 fusion.

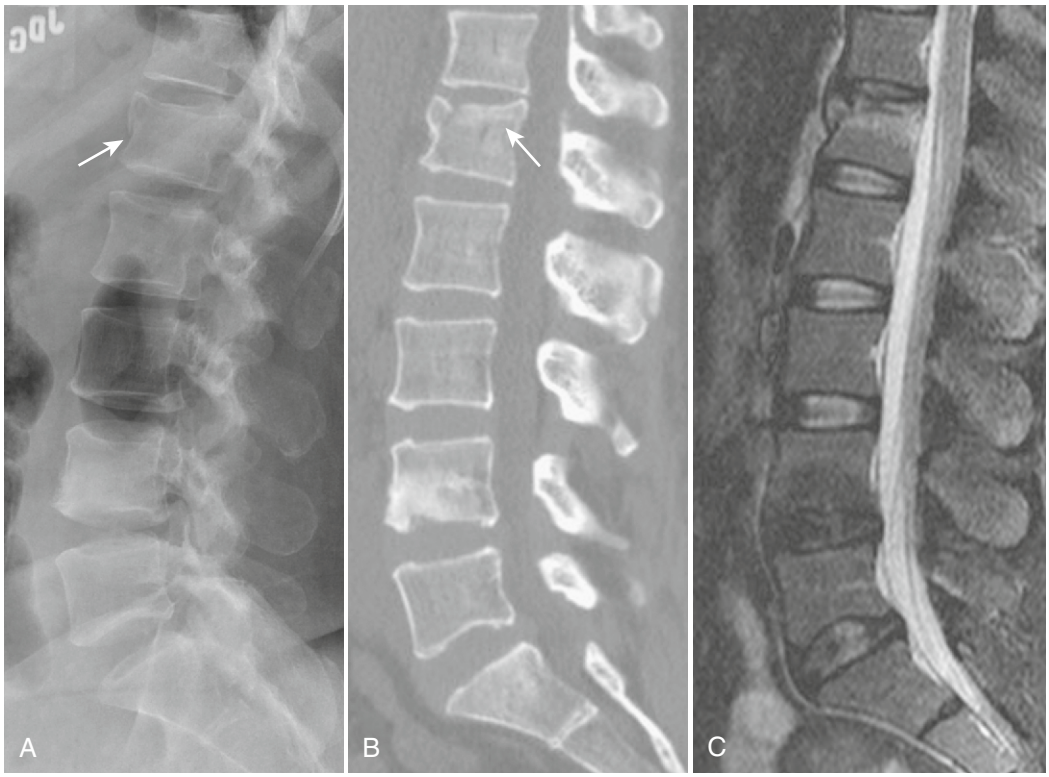


Figure 7-14. Lumbar compression fracture. **A,** Lateral radiograph in a patient with calcaneal fractures after jumping from a roof. Slight anterior wedging of L1 vertebral body with a triangular fragment. **B,** CT sagittal reformat shows increased density of impaction zone. **C,** MR STIR sagittal image shows fracture fragment, marrow edema in impaction zone, and small prevertebral hematoma. Contrast these findings with the endplate irregularity and sclerotic changes at the inferior aspect of L4 vertebral body due to chronic degenerative disease.

A type of injury unique to the thoracic region is rib dislocation. It is usually not found as an isolated injury. Spinal cord transection due to the guillotine effect of a displaced rib has been reported but is exceedingly rare.

Lumbar transverse process fractures due to avulsions by the paraspinal muscles are commonly detected in association with visceral injuries, sacral fractures, and pelvic fractures. When detected on plain films, CT of the abdomen and pelvis may be in order due to this association. Sacral fractures and sacroiliac joint disruptions are easily diagnosed by pelvic CT when displacement is gross. As with any other portion of the spine, subtle displacements may be easily overlooked. Insufficiency fractures of the sacrum are common in the setting of osteoporosis. Attention to the arcuate lines of the sacrum is important when reviewing plain films of the pelvis. Coccygeal fractures may be a source of persistent pain, with patients therefore presenting to the urgent care clinic. Plain film radiography is generally sufficient to assess this site of injury. Anatomic variations are common, many presumably the result of prior trauma.

Evaluation of Spinal Soft Tissue Injuries

Spinal Cord Injury

In some of the cases illustrated so far, findings of spinal cord injury (SCI) have been present. In each of these cases, there were injuries to the spinal column as well. Spinal cord injuries may also occur in the absence of injury to the spinal column. The acronym SCIWORA (spinal cord injury without radiographic abnormality) was coined in 1982. SCIWORA may be due to longitudinal distraction of the cord; in some cases, MR imaging may demonstrate evidence of the cause of spinal cord dysfunction due to hemorrhage or edema within the cord or from extrinsic compression or transection. SCI may be complete (complete loss of motor and sensory function) or incomplete (partial loss of sensory and/or motor function). Different constellations of neurologic dysfunction may result owing to the topographic organization of pathways, including anterior cord, central cord, and Brown-Séquard and conus medullaris syndromes. Cauda equina syndrome results from injury to spinal nerve roots. Spinal cord concussion is analogous to the cerebral transient ischemic attack.

Spinal cord edema appears as a zone of T2 hyperintensity almost immediately upon injury. Gross swelling of the cord may be very subtle. In many cases it may be possible to detect hemorrhage located centrally within the region of edema (a true contusion). This may appear relatively isointense or hypointense to normal cord with greater sensitivity on gradient-echo usually due to the presence of deoxyhemoglobin. Within a few days, T1 hyperintensity, and still later T2 hyperintensity, may develop due to the conversion to methemoglobin. Many authors have attempted to develop classification systems to predict functional outcomes based on MR imaging findings, and these have worked to varying degrees. Detection of a hemorrhage larger than 1 cm in longitudinal dimension and lack of resolution of signal abnormalities on follow-up imaging generally indicate the poorest prognosis for recovery. Normal cord signal or edema alone is more likely



FIGURE 7-15. Thoracic burst fracture. Sagittal T1-weighted image *(left)* and T2-weighted image *(right)* show retropulsion of the posterior portion of the T11 vertebral body resulting in cord compression. Cord T2 hyperintensity is consistent with edema. A contusion should be suspected based on the degree of compression; however, there is no T2 or gradient-echo hypointensity to confirm the presence of hemorrhage.

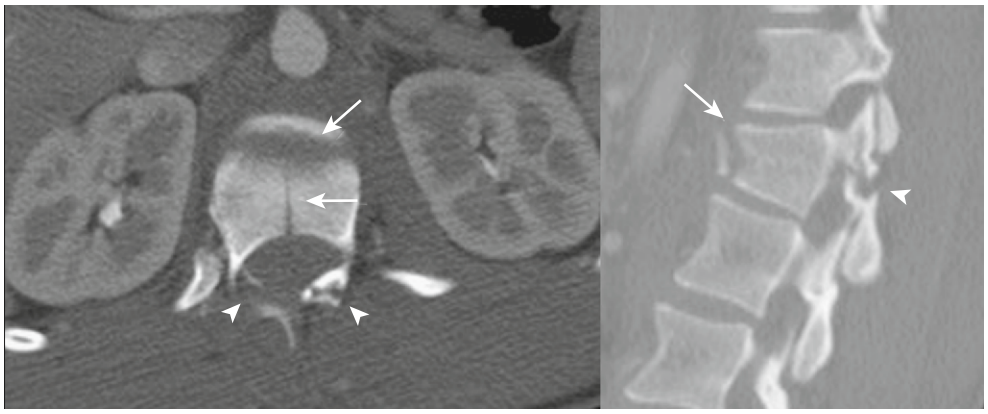


FIGURE 7-16. Chance-type fracture. Axial *(left)* and sagittal reformatted *(right)* images from a contrast-enhanced CT of the abdomen following a motor vehicle collision. Images show anterior wedge deformity of a lower thoracic vertebra. Note longitudinal *(arrows)* and horizontal *(arrowheads)* fracture planes and distraction of the posterior elements.

to be associated with better clinical outcomes. It should be noted that cord compression by bone fragments, disc, or hematoma is predictive of development of hemorrhage and is, therefore, the basis for early decompression by many spine surgeons.

Diagnosis of injury to any of the other soft tissue structures listed below can be based on T2 hyperintensity. In addition, anterior and posterior longitudinal ligaments may be displaced (elevated) or disrupted. Discs may be widened or extruded. Facet capsules may be widened and fluid-filled, or facets may be dislocated. Ligamentum flavum and interspinous ligaments may be disrupted. Cervical root avulsion as a cause of brachial plexopathy may present with abnormal enlargement of nerve root sleeve(s)—pseudomeningocele (Fig. 7-17).

Although MR is indicated primarily for evaluation of soft tissues, STIR sequence is especially well suited for the detection of bone marrow edema. Fractures may be detected as changes in shape of the vertebrae or linear hypointensities but are generally more easily detected using CT.

Spinal Hematomas

Hemorrhage within the spinal cord is most often the result of trauma. Spontaneous hemorrhage within the spinal cord (intramedullary hemorrhage) can result from intrinsic cord

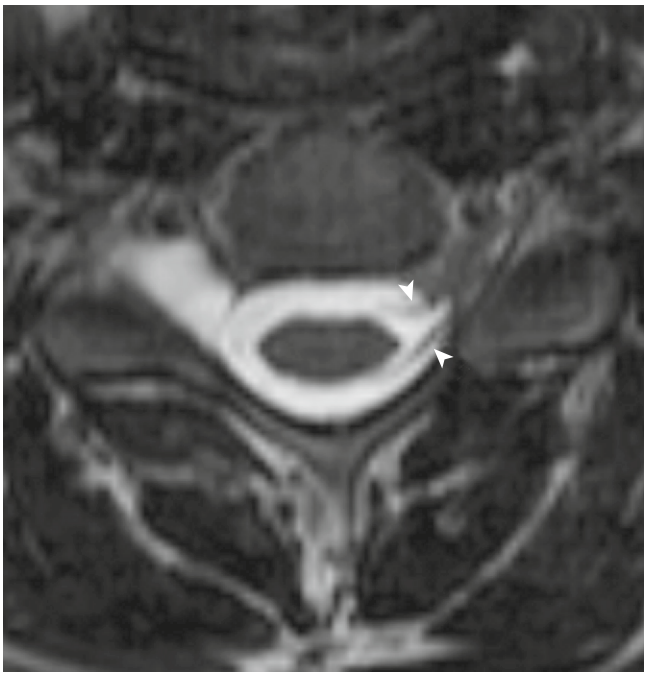


Figure 7-17. Cervical root avulsion. Axial T2-weighted image in a patient with right brachial plexopathy following a motorcycle collision. Note the right-sided pseudomeningocele and nonvisualization of ventral and dorsal roots. Normal roots are indicated on the left side *(white arrowheads)*.

lesions, such as ependymoma or cavernous malformation, and may present with sudden onset of weakness of the extremities.

Hemorrhage can occur within the other compartments of the spinal canal, usually as a result of trauma but, on occasion, without provocation. The spinal epidural, subdural, and subarachnoid spaces are contiguous with their intracranial counterparts. Hematoma/hemorrhage can collect in these areas by extension or occur primarily within the spine. As seen in many of the figures demonstrating spine fractures and subluxations, epidural hematomas arise commonly in the setting of trauma, and, if they are causing cord or conus compression, emergent evacuation may prove beneficial. Emergency surgical evacuation is generally considered the standard treatment for patients with disabling and/or persistent neurologic deficit. A conservative approach under close neurologic observation may be suitable for patients with no, or mild, deficits, for patients who show early and continuous clinical improvement, and for patients with noncompressive epidural hematomas. Reported cases of spontaneous remission are very rare.

MR imaging features of spinal epidural hematoma include variable, often heterogeneous T1 and T2 signal intensity; capping of epidural fat; direct continuity with the adjacent osseous structures; compression of epidural fat, subarachnoid sac, and spinal cord; and usual posterolateral location in the spinal canal. Tapered appearance of the cerebrospinal fluid space due to extrinsic hematoma is usually apparent.

On the other hand, hemorrhage confined by the thecal sac must be within either the subdural or subarachnoid space. Differentiation of the three types of extramedullary spinal hemorrhage can sometimes be quite difficult. Extension into the neural foramen, beyond the expected confines of the thecal sac, is a sure indication that the hemorrhage is in the epidural space. Subarachnoid hemorrhage often collects in a uniform circumferential configuration around the spinal cord, mixes uniformly with cerebrospinal fluid and intermingles with the roots of cauda equina, and seeks a dependent position in the spinal canal. Spinal subdural hematoma is easiest to differentiate when the arachnoid mater and roots are displaced by a hematoma confined to the thecal sac (Figs. 7-18 to 7-20).

Advanced MR techniques are now being applied to spine imaging, with much research in the field of spinal cord injury. Diffusion-weighted and diffusion tensor imaging, MR spectroscopy, and functional imaging have great potential for future clinical applications. These techniques are not yet widely available. There are still many technical limitations to be overcome before they can be routinely applied.

Vascular Injuries of the Neck Associated with Spine Trauma

The spectrum of traumatic vascular injuries of the neck related to spine trauma and the imaging features are reviewed in Chapter 1.

NONTRAUMATIC SPINE EMERGENCIES

The spontaneous development of limb weakness, pain or paresthesia, and progressive inability to ambulate may be causes for presentation to the emergency department. In many cases, the history and physical exam localize the abnormality to the spine and prompt imaging is required to evaluate for the possibility of cord or root compression or an intrinsic process of the spinal cord. MR imaging is generally the modality of choice; the addition of gadolinium-enhanced sequences, especially with fat-suppression, to the routine protocols is often useful. The following brief review illustrates the spectrum of nontraumatic disorders and the common differential diagnoses to be considered.

Congenital Disorders

Although congenital/developmental anomalies and abnormalities are not likely to present emergently, they may be unknown until an unrelated acute event occurs. Occasionally, a Chiari I malformation may be found during a trauma workup. A preexisting syrinx should not be mistaken for an acute spinal cord injury. A tethered cord or lipoma of the filum terminale might be found in the process of workup for an acute episode of sciatica.

Degenerative Disease/Arthropathy

As mentioned in the section on spine trauma, underlying conditions resulting in narrowing of the spinal canal are often found in patients presenting with spinal cord injuries, sometimes resulting from rather minor trauma. There are many causes of canal stenosis, including routine spondylosis, ossification of the posterior longitudinal ligament (OPLL) ossification of ligamentum flavum, synovial cyst, and epidural lipomatosis. Underlying disorders such as these are often discovered in the setting of an acute disc extrusion that results in a new neurologic

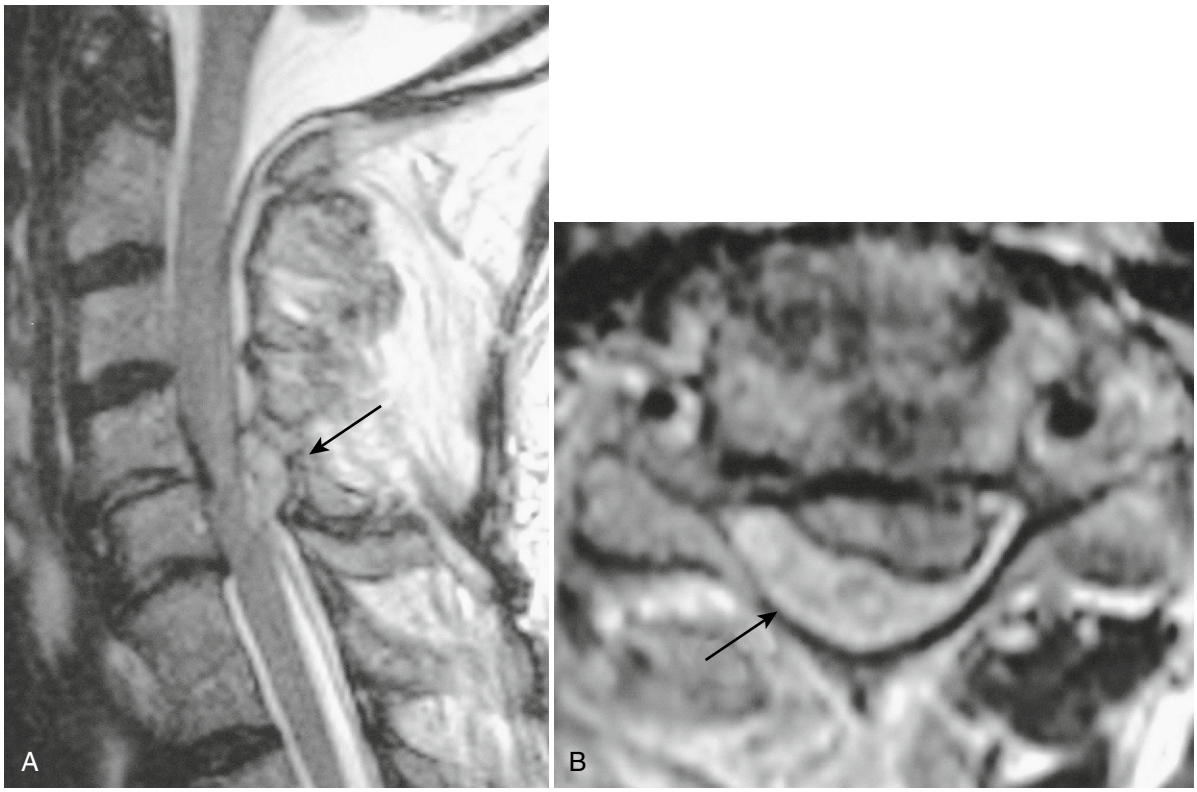


FIGURE 7-18. Spinal epidural hematoma—cord compression. This patient sustained an isolated C4 lamina fracture after a fall from a loading dock and developed right hand weakness following CT. **A,** Sagittal T2-weighted image shows an intermediate-intensity posterior epidural hematoma causing cord compression. **B,** Axial gradient-echo T2-weighted image shows the extent of cord compression.

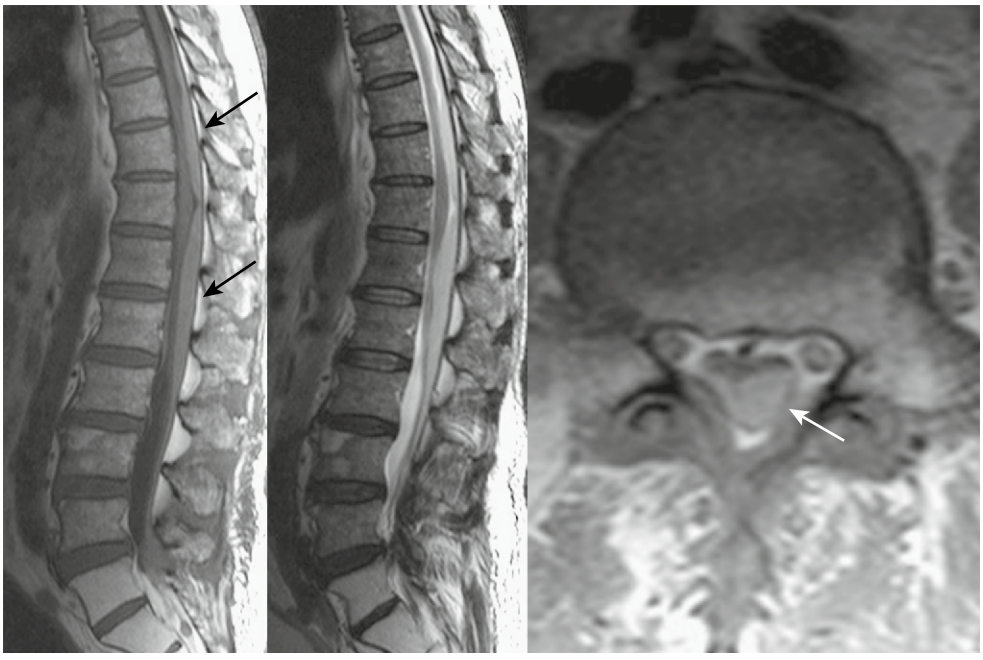


FIGURE 7-19. Spinal subdural hematoma. Sagittal T1-weighted image and T2-weighted image and axial T1-weighted image demonstrate a long, lobulated intradural hematoma that displaces the roots of cauda equina. The hematoma is limited by the displaced arachnoid membrane.

deficit. Degenerative disc disease is ubiquitous, and the imaging findings are generally straightforward. One should not be fooled by the T2 hyperintensity of a disc extrusion that simulates fluid or by a sequestered fragment displaced a considerable distance from the remainder of the disc. Gadolinium-enhanced images may help to identify root inflammation or arachnoiditis and differentiate granulation tissue (scar) from a recurrent disc extrusion in the setting of a postoperative patient presenting with recurrent symptoms. Familiarity with expected routine postoperative findings is important, but one must also be able to analyze features in a systematic

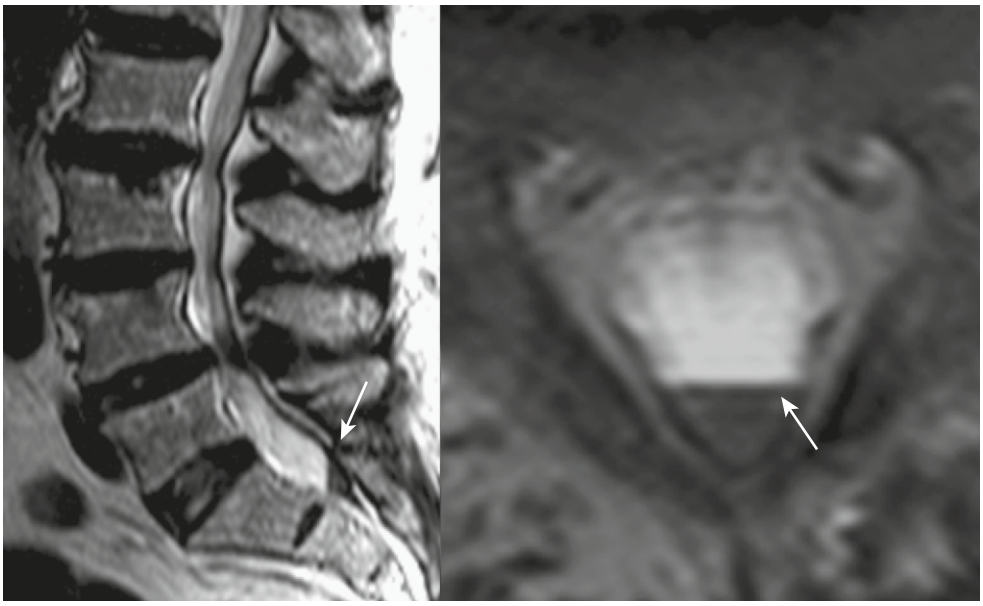


Figure 7-20. Spinal subarachnoid hemorrhage. Sagittal and axial T2-weighted images show a hypointense fluid level within the subarachnoid space.

fashion, for example, to determine if a cerebrospinal fluid leak/pseudomeningocele might be causing root compression (Fig. 7-21).

Patients with rheumatoid arthritis may show a variety of findings, including laxity of the transverse atlantal ligament and atlantoaxial subluxation, vertical subluxation or erosion of the odontoid, or development of granulation tissue around the odontoid (pannus). Spinal cord compression can result from acute trauma or the combination of pannus and chronic instability.

Other arthritides such as amyloidosis or crystal pyrophosphate deposition may present with mass lesions or destructive changes of the spine, mimicking malignancy or infection (Fig. 7-22).

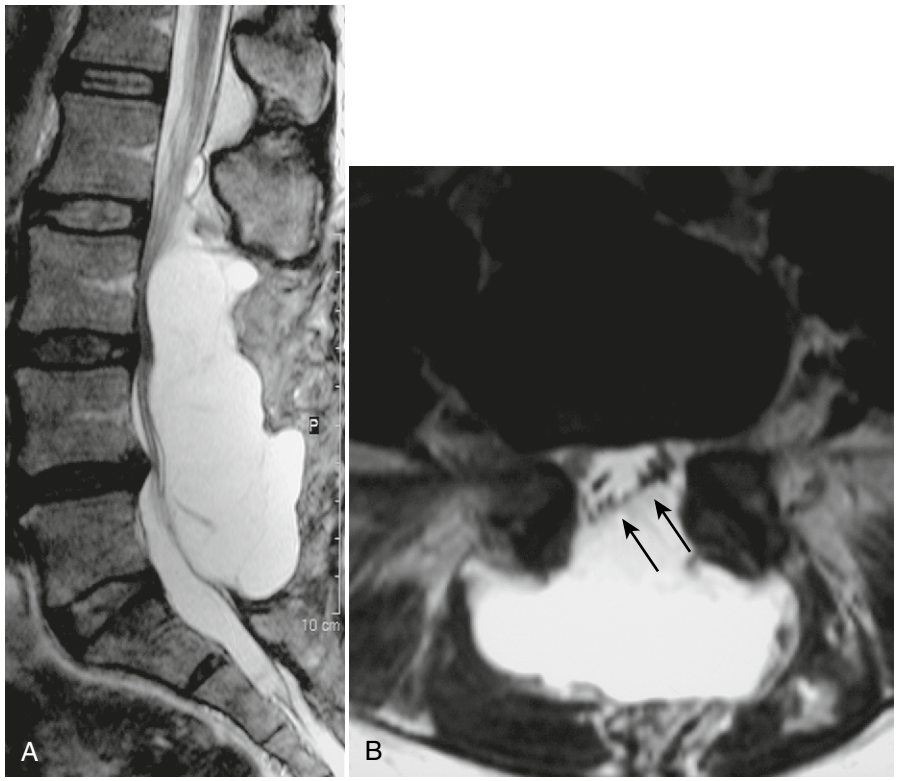


Figure 7-21. Postoperative pseudomeningocele—root compression. This patient developed progressive weakness 1 week after decompressive laminectomies for spinal stenosis. Sagittal (**A**) and axial (**B**) T2-weighted images show large fluid collection with signal isointense to cerebrospinal fluid, which causes root displacement and compression. Neurologic improvement followed repair of the leak.

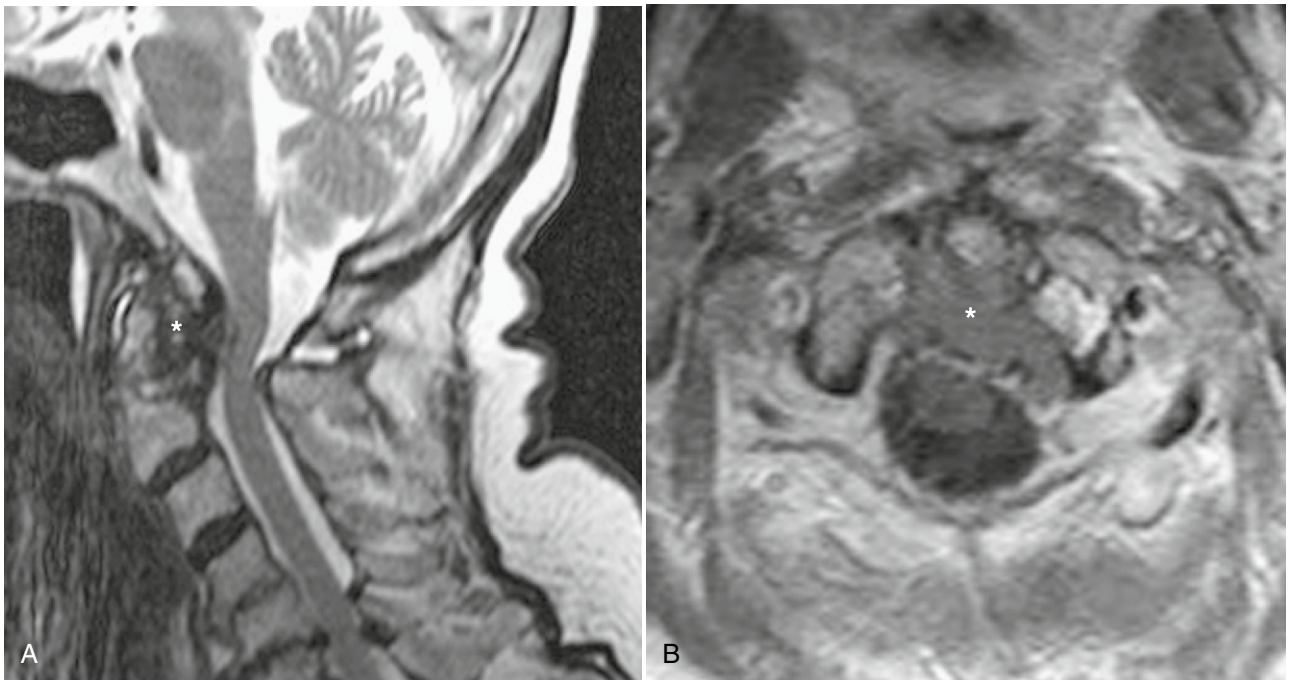


FIGURE 7-22. Calcium pyrophosphate disease—cord compression. Sagittal (**A**) T2-weighted image and axial (**B**) T1-weighted image show a soft tissue pannus related to the dens *(asterisk)* in a patient with "pseudogout" who developed symptoms of myelopathy as a result of chronic cord compression.

Neoplasms and Tumorlike Conditions

Tumors of the spine may be divided into intramedullary, and extramedullary intradural and extradural, categories. Development of symptoms is usually slowly progressive, but acute presentations due to inability to ambulate or incontinence, or related to hemorrhage, are not uncommon.

Extradural lesions are encountered most commonly, and these include the disc herniations and degenerative changes from arthritis and traumatic conditions already discussed. Metastatic disease makes up the majority of the neoplastic extradural masses, usually from carcinomas of the lung, breast, and prostate. Although metastasis to the bone with extradural extension is typical, metastasis to or primary involvement of the extradural soft tissues may also result in neural compromise. Lymphoma may present this way or by extension from the retroperitoneum through the neural foramen (Fig. 7-23). Vertebral involvement by multiple myeloma may present with an extradural mass or pathologic compression fracture (Fig. 7-24). Common osseous lesions such as aneurysmal bone cyst, osteoblastoma, osteochondroma, and Paget disease may occasionally present with symptoms related to cord compression. Chordoma, a destructive bone tumor arising from notochord rests, accounts for approximately 5% of primary bone tumors. Most commonly occurring in the sacrum, it may also arise in the clivus, cervical, or lumbar region. A large soft tissue mass, calcifications, and residual bone fragments are typical features.

Many tumorlike lesions may affect the spine. Hemangiomas are commonly found in the vertebral bodies on routine exams and are generally not cause for concern. Composed of thin-walled blood vessels and a variable amount of adipose tissue within the bony trabeculae, these lesions have signal characteristics determined by the relative amounts of vascular, bone, and fat components. They are usually slow-growing, benign lesions, but, occasionally, expansion of the vertebral body and extension of the lesion into the epidural space may compromise the spinal canal. Thoracic cord compression due to extramedullary hematopoiesis occurs rarely in patients with hematologic disorders, such as thalassemia. Notice of diffuse signal abnormality of the vertebral marrow may be important to making this diagnosis.

Extramedullary intradural masses include meningiomas, tumors of nerve sheath origin, metastases, and others. Meningiomas and nerve sheath tumors (schwannomas and neurofibromas) account for approximately half of all intraspinal neoplasms. These three lesions may be associated with neurofibromatosis (types I and II), but a description of the patterns of occurrence are beyond the scope of this review. Like their intracranial counterparts, spinal meningiomas are more commonly found in women, especially in the thoracic region. Schwannomas are found equally in males and females and occur throughout the spine. Secondary signs of bone remodeling may be seen due to these slow-growing lesions. Combined intradural-extradural or isolated extradural involvement of nerve sheath tumors and meningiomas occurs much less commonly than the usual intradural extramedullary form. Lipomas, dermoids, and epidermoids may occur in this compartment and occasionally have combined intramedullary involvement as well.

Extramedullary intradural metastatic disease more commonly arises from tumors of the central nervous system via cerebrospinal fluid dissemination. These include ependymoma, pineal tumors, and choroid plexus tumors. Seeding generally results in nodular lesions in the lumbosacral subarachnoid space. The majority of metastases

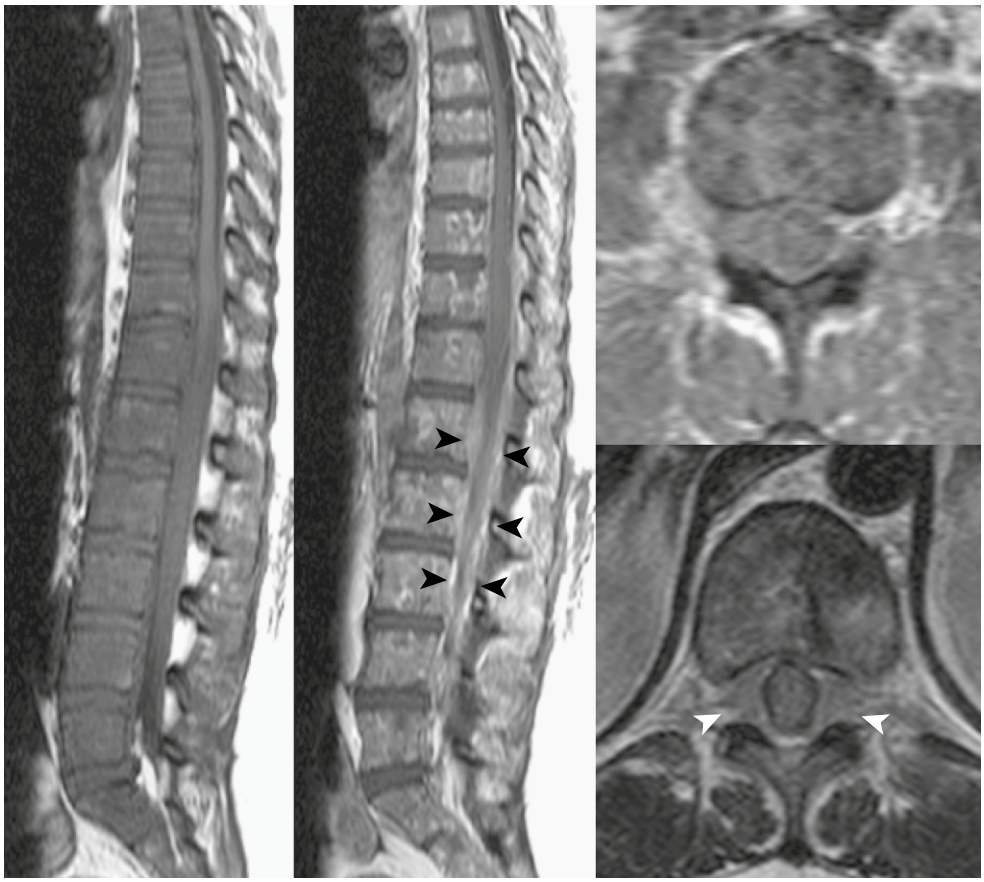


Figure 7-23. Epidural lymphoma—conus compression. Sagittal pre- and postgadolinium T1-weighted images *(left)* show an enhancing extradural mass *(arrowheads)* that surrounds the conus medullaris in a patient with AIDS. Axial post-gadolinium T1-weighted image *(right upper)* and T2-weighted image *(right lower)* show tumor filling the neural foramina *(arrowheads)* and causing mild compression of the conus.

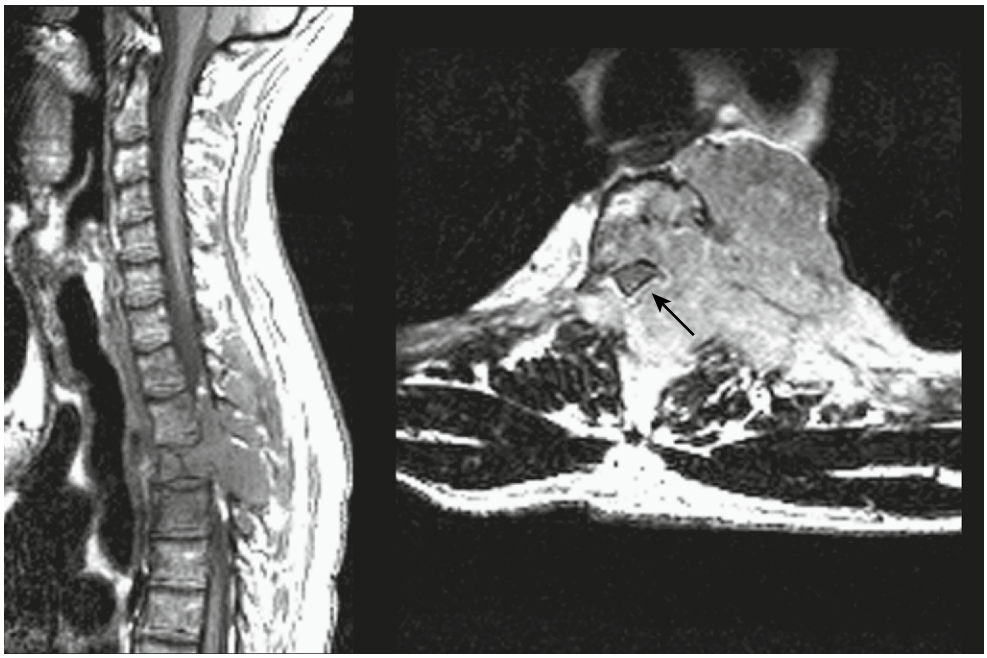


Figure 7-24. Multiple myeloma—cord compression. Sagittal pre- and axial postgadolinium T1-weighted images show a large mass arising within an upper thoracic vertebra with extraosseous extension that results in cord compression. Note the diamond shape of the cord *(arrow)*.

via hematogenous spread are the result of lung and breast carcinoma and melanoma.

Intramedullary tumors account for approximately 10% of primary intraspinal tumors; the majority of these are gliomas (approximately 70% ependymomas and the rest astrocytomas). These may be indistinguishable by imaging; both may show enlargement of the cord and irregular T2 hyperintensity and enhancement, and have associated cystic changes or syrinx formation (Fig. 7-25). Ependymomas have a predilection for the conus medullaris and a tendency to bleed. Slow-growing primary lesions may cause expansion of the spinal canal, scalloping of the posterior margins



FIGURE 7-25. Ependymoma. Sagittal T2-weighted image and post-gadolinium T1-weighted image show a multiseptate fluid collection that expands the thoracic cord with a solid enhancing nodule *(arrow)*. This 45-year-old female presented with progressive difficulty ambulating.

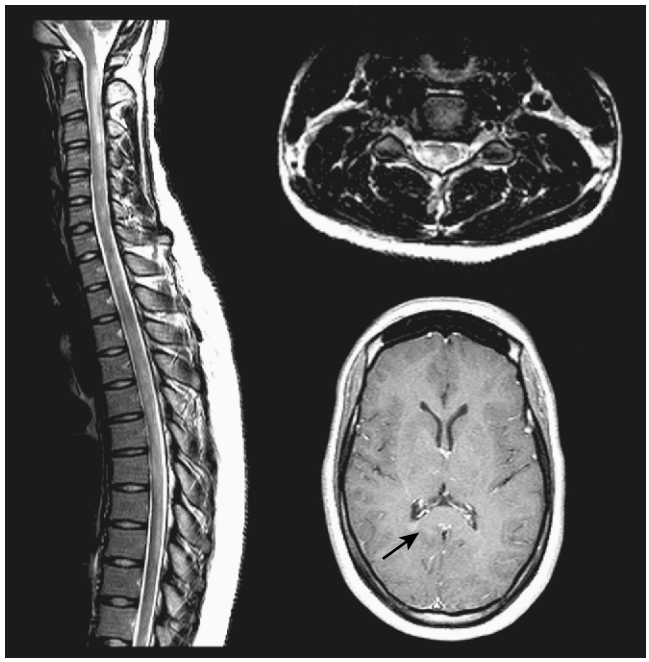


FIGURE 7-26. Multiple sclerosis. Sagittal and axial T2-weighted images show patchy hyperintensities throughout the entire spinal cord. None of the spine lesions showed abnormal enhancement. The post-gadolinium axial T1-weighted image of the brain in the same patient shows an enhancing plaque in the periventricular white matter *(arrow)*.

of the vertebral bodies, and pressure atrophy of pedicles. Other intramedullary tumors include hemangioblastoma, medulloblastoma, and metastatic disease from pineal or other intracranial site.

Inflammation/Demyelination

Multiple sclerosis (MS) may be the first disorder that comes to mind in this category. The cause of this disorder, characterized by breakdown of the myelin sheath and inflammation, is unknown. Spinal cord plaques tend to occur most frequently in the cervical region and show imaging features similar to those found in the brain—T1 iso- to hypointense, T2 hyperintense—and may enhance following contrast administration (Fig. 7-26). The cord may be swollen due to active inflammation. Lesions in different states of activity and the presence of lesions in the brain add to confidence in the diagnosis of MS. Cord atrophy and lack of enhancement may be expected in the chronic phase.

Imaging features of myelitis are nonspecific and include T2 hyperintensity, swelling, and variable enhancement. Idiopathic inflammation of the cord (transverse myelitis) or inflammation due to connective tissue disorders (lupus, rheumatoid arthritis, etc.) may have the same appearance. Postinfectious demyelination is sometimes the cause. Follow-up may be necessary to differentiate these disorders from a spinal cord neoplasm.

Sarcoidosis is a noncaseating, granulomatous disease that may affect the brain and spinal cord. Simultaneous involvement of the cord and meninges may help to distinguish it from other causes of myelitis. Of course, other granulomatous processes such as tuberculosis would have to be considered.

Guillain-Barré syndrome, an acute inflammatory demyelinating neuropathy, and a chronic form (CIDP) may present with ascending progressive muscle weakness, areflexia, and other symptoms including cranial neuropathy. Enhancement of lumbosacral roots, especially isolated involvement of ventral roots, may be detected by MR imaging.

Infection

Abscess formation within the spinal cord (intramedullary) is extremely uncommon, usually occurring secondary to spread from another location. Intravenous drug use and HIV infection are risk factors.

On the other hand, meningitis is extremely common. Of the infectious cases, viral infection is most common, with bacterial, fungal, and parasitic making up the rest. Noninfectious causes include nonsteroidal anti-inflammatory medications and antibiotics. Neoplastic causes are mentioned below. Imaging is generally reserved for complex cases, such as those with localizing neurologic deficits or those that do not respond to therapy, in order to locate a parameningeal focus of infection. Thickened enhancement of meninges and nerve roots may be seen.

Epidural (bacterial) abscess may arise via hematogenous route or from direct extension of discitis/osteomyelitis or other paraspinal source (Fig. 7-27). *Staphylococcus aureus* is the most common organism, and risk factors include spinal instrumentation, intravenous drug use, immunodeficiency, diabetes, renal failure, alcoholism, and malignancy. Because of the loose connection of the dura to the spine, infection may spread along multiple contiguous levels.

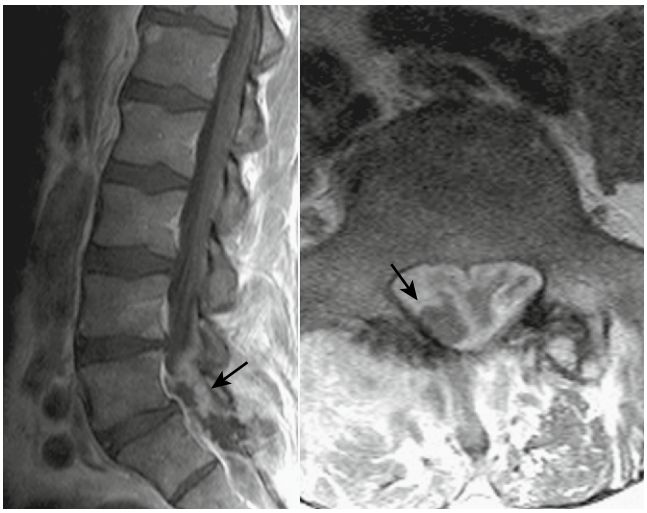


Figure 7-27. Epidural abscess. Sagittal post-gadolinium T1-weighted image *(left)* shows abnormal enhancing soft tissue in the epidural space. The axial postgadolinium T1-weighted image *(right)* more clearly shows a nonenhancing fluid collection in this patient with recent intravenous drug use and sciatica.

Lumbar and cervical regions are most commonly affected. On MR, this appears as a rim-enhancing, tapered fluid collection that displaces the dura. The collection may be located anteriorly, posteriorly, or circumferentially around the thecal sac and may cause compression of the spinal cord or cauda equina. The term "phlegmon" may be applied to an enhancing inflammatory mass without a central fluid collection. Definitive treatment is surgical, although mild cases without a focal neurologic deficit may be treated with antibiotics and careful monitoring. Determination of the cranial and caudal extent of the infection is imperative prior to any planned intervention.

Pyogenic discitis/osteomyelitis may be suspected based on abnormal T2 hyperintensity and contrast-enhancement of the disc and adjacent portions of the vertebral bodies. Since degenerative changes, such as a Schmorl node, may produce identical imaging findings, clinical context is important. Sometimes, percutaneous CT-guided needle aspiration is required to confirm the diagnosis.

Tuberculous spondylitis has a preference for spreading along the anterior longitudinal ligament, affecting multiple vertebral bodies with relative sparing of the intervertebral discs. Posterior vertebral body and posterior element involvement are more common than with pyogenic infections. These features are in concert with an indolent course and may make this process indistinguishable from malignancy. Needle aspiration/biopsy is often required for definitive diagnosis since the treatment is not trivial. Patients from endemic regions may develop other nonbacterial infections such as cysticercosis and schistosomiasis; the features are nonspecific and can be quite complex, eventually resulting in arachnoiditis, myelomalacia, and syrinx formation.

Vascular

Infarction of the spinal cord is rare and may be due to a large variety of causes such as atherosclerotic disease of the aorta, hypotension, dissection of the aorta or vertebral arteries, and compromise of spinal arteries resulting from emboli, sickle cell disease, or vasculitis. Imaging findings may be subtle, including T2 hyperintensity and enlargement of the cord. There are several reports of the value of diffusion-weighted imaging, but technical issues have limited widespread application in this setting. Venous obstruction/infarct as a result of cord compression is one possible mechanism of spinal cord injury. Infarcts can affect any portion of the cord, with extensive infarcts occurring due to involvement of the artery of Adamkiewicz.

Spinal dural arteriovenous fistula is a rare vascular disorder that may lead to the development of venous congestion of the cord and present with slowly progressive myelopathy affecting the lower extremities in older adults. T2 hyperintensity, possible enlargement of the cord, and dilated subarachnoid vessels are the clues to diagnosis. MR angiography may be helpful with conventional angiography for confirmation and possible endovascular treatment. Cavernous malformation (cavernous angioma) less commonly occurs in the spinal cord than the brain, but has the same imaging characteristics. A mulberry-shape, internal mixed T1 and T2 hyperintensity due to blood products of different ages, and a complete hemosiderin rim are classic. Minimal, if any, mass effect, lack of surrounding edema, and variable enhancement are typical and help with diagnosis. However, acute hemorrhage may cause expansion of the cord and associated edema, raising concern for neoplasm.

This concludes the whirlwind review of radiologic findings of traumatic and nontraumatic emergencies involving the brain, head, neck, and spine. Hopefully it has covered more than just the tip of the iceberg and has provided you with a useful framework for future practice.

Suggested Readings

Blackmore CC, Emerson SS, Mann FA, et al: Cervical spine imaging in patients with trauma: Determination of fracture risk to optimize use. Radiology 211: 759–765, 1999.

Blake SP, Connors AM: Sacral insufficiency fracture. Br J Radiol 77:891–896, 2004.

Darouiche RO: Spinal epidural abscess. N Engl J Med 355:2012–2020, 2006.

Denis F: Spinal instability as defined by the three-column spine concept in acute spinal trauma. Clin Orthop 189:65–76, 1984.

Goradia D, Linnau KF, Cohen WA: Correlation of MR imaging findings with intraoperative findings after cervical spine trauma. Am J Neuroradiol 28:209–215, 2007.

Harris JH, Carson GC, Wagner LK, et al: Radiologic diagnosis of traumatic occipitovertebral dissociation: 2. Comparison of three methods of detecting occipitovertebral relationships on lateral radiographs of supine subjects. AJR Am J Roentgenol 162:887–892, 1994.

Harris JH Jr: The cervicocranium: Its radiographic assessment. Radiology 218: 337–351, 2001.

Harris JH Jr, Mirvis SE: The Radiology of Acute Cervical Spine Trauma, 3rd ed. Baltimore, Williams and Wilkins, 1996.

Hogan GJ, Mirvis SE, Shanmuganathan K, et al: Exclusion of unstable cervical spine injury in obtunded patients with blunt trauma: Is MR imaging needed when Multi-detector row CT findings are normal? Radiology 237:106–113, 2005.

Katzberg RW, Benedetti PF, Drake CM, et al: Acute cervical spine injuries: Prospective MR imaging assessment at a level 1 trauma center. Radiology 213:203–212, 1999.

Koeller KK, Rosenblum RS, Morrison AL: Neoplasms of the spinal cord and filum terminale: Radiologic-pathologic correlation. Radiographics 20:1721–1749, 2000.

Kwon BK, Hilibrand AS: Management of cervical fractures in patients with diffuse idiopathic skeletal hyperostosis. Curr Opin Ortho 14:187–192, 2003.

Labler L, Eid K, Platz A, et al: Atlanto-occipital dislocation: Four case reports of survival in adults and review of the literature. Eur Spine J 13:172–180, 2004.

Leone A, Cerase A, Colosimo C, et al: Occipital condylar fractures: A review. Radiology 216:635–644, 2000.

Lustrin ES, Karakas SP, Ortiz AO, et al: Pediatric cervical spine: Normal anatomy, variants, and trauma. Radiographics 23:539–560, 2003.

Munday TL, Johnson MH, Hayes CW, et al: Musculoskeletal causes of spinal axis compromise: Beyond the usual suspects. Radiographics 14:1225–1245, 1994.

Platzer P, Jaindl M, Thalhammer G, et al: Clearing the cervical spine in critically injured patients: A comprehensive C-spine protocol to avoid unnecessary delays in diagnosis. Eur Spine J 15:1801–1810, 2006.

Pollack CV Jr, Hendey GW, Martin DR, et al: Use of flexion-extension radiographs of the cervical spine in blunt trauma. Ann Emerg Med 38:8–11, 2001.
Schuster R, Waxman K, Sanchez B, et al: Magnetic resonance imaging is not needed to clear cervical spines in blunt trauma patients with normal computed tomographic results and no motor deficits. Arch Surg 140:762–766, 2005.
Schwartz ED, Flanders AE (eds): Spinal Trauma. Philadelphia, Lippincott Williams and Wilkins, 2007.
Sklar EM, Post JM, Falcone S: MRI of acute spinal epidural hematomas. J Comput Assist Tomogr 23:238–243, 1999.
Wang YF, Teng MM, Chang CY, et al: Imaging manifestations of spinal fractures in ankylosing spondylitis. Am J Neuroradiol 26:2067–2076, 2005.

CHAPTER 8

Nontraumatic Emergency Radiology of the Thorax

Scott White, Alejandra Duran-Mendicuti, Aaron Sodickson, Salvatore Viscomi, Michael Stella, and M. Stephen Ledbetter

An emergency medicine physician once told a bright-eyed medical student on the first clinical shift:

> All kinds of problems bring people in to see us with chest complaints. But just remember this—your job is to make sure nobody leaves the emergency department with any of only four entities undiagnosed, and those four entities are pneumothorax, aortic dissection, pulmonary embolism, and myocardial infarction. Now repeat that list to me four times (the medical student regurgitates the list four times). Good. Beyond these four entities, anything that's causing their problem won't cause you much of a problem.

While that is a rather spartan synopsis of nontraumatic thoracic pathology encountered in the emergency department (ED), the underlying tenet stands up well in the practical evaluation of ED patients presenting with chest pain and other symptoms. Accordingly, this chapter on nontraumatic emergency thoracic radiology is organized primarily around evaluation of these entities, beginning with a review of chest radiography technique, and followed by sections on the pleura/mediastinum, aortic diseases, pulmonary embolism, and acute coronary syndrome (ACS). Lung parenchymal findings are covered with less emphasis, but are readily available with greater detail in other texts, such as *Thoracic Radiology: The Requisites*.

Multidetector computed tomography (MDCT) technique deserves and receives special emphasis in this chapter because it has overtaken and continues to overtake other imaging modalities for chest evaluation in ED patients. Clinicians have become enamored with the rapid, highly accurate, and thereby efficient diagnostic capability CT provides. The CT industry and the radiology profession continue to further these advantages with faster, higher-resolution scanners allowing for greater clinical applications and increasingly refined diagnoses. Similarly, the pressure for greater diagnostic sensitivity and specificity in the ED is at odds with decreased imaging utilization. The volume of chest CT exams ordered by ED physicians will almost certainly continue to rise. Perhaps the only significant counterbalance to increased utilization is the concern for population radiation exposure and the associated risk of cancers induced by ionizing radiation. Radiologists should be familiar with and sensitive to these concerns, readily able to advise clinicians and protect patients by being good stewards of radiation safety.

CHEST RADIOGRAPHY

In a clinical environment where radiologists and ED physicians frequently have available "high-tech" CT scanners with dozens, even hundreds of detector rows, multiple radiograph sources, and electrocardiographic (EKG) gating, it is tempting to neglect or dismiss the value of the "low-tech" chest x-ray (CXR). However, neglecting the CXR and failing to develop the knowledge and skills needed for expert CXR interpretation is a mistake. Despite the advances in CT technology, the CXR remains the mainstay of first-line imaging for ED patients with chest complaints. The 2004 National Hospital Ambulatory Medical Survey (NHAMES) recorded 110.2 million ED visits, which resulted in 20.19 million CXRs performed. Indeed, a CXR is the most often ordered imaging exam as part of an ED patient visit. This compares to totals of approximately 22 million for all other x-rays combined, and 10.3 million for CT or magnetic resonance imaging (MRI) (the CT and MRI data were combined in the NHAMES report). Therefore, the emergency radiologist needs to have highly developed interpretive skills for chest radiography. Detailed instruction on CXR interpretation is well beyond the scope of this chapter, but many excellent sources are available for this, including the Requisites text on thoracic radiology.

One principle that serves radiologists well is the establishment of a systematic pattern through which the interpreter progresses as he or she reads a CXR. While naturally drawn to look at the lungs, and while evaluation of pulmonary parenchyma is paramount, the interpreter must unerringly include assessment of extrapulmonary anatomy on every CXR. This includes evaluation of anatomy below the diaphragm, of lung parenchyma posterior to the diaphragm, of the bony thorax, spine, shoulders, and chest wall soft tissues, of the heart contours, mediastinum, and pulmonary hila, of pleural surfaces and interfaces, and of complex areas such as the pulmonary apices. Establishing a pattern of evaluation that systematically includes all of the anatomy encountered on a CXR will serve to avoid unfortunate errors of CXR interpretation (Fig. 8-1).

For evaluation of the lung parenchyma, CXR has been in use for nearly a century. Pulmonary pathology is detected primarily by changes in pulmonary parenchymal density, as either decreased parenchymal density (cystic lung diseases and pneumothorax) or increased parenchymal density

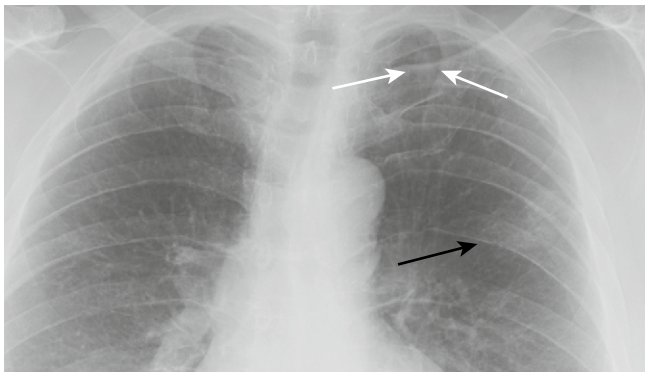


FIGURE 8-1. Chest x-ray (CXR) of a patient presenting with cough and fever. A faint area of opacification within the left midlung proved to be pneumonia *(black arrow)*. Additionally, a small left apical carcinoma was detected *(white arrows)*. Due to multiple overlying structures, including the first ribs and the clavicles, the pulmonary apices are a "danger" area in terms of risk of missed findings on CXR. Close inspection of the apices is warranted on every CXR.

(masses, fluid, infection, fibrosis, or atelectasis). Roughly 10.3% of ED visits fall within the category of respiratory diseases, with 3.1% due to upper respiratory infections, 1.7% due to asthma, and 1.4% due to pneumonia (3.4% in patients over 65 years old).

Pneumonia

CXR and chest imaging are generally of limited value in upper respiratory infections. On CXR, pneumonia manifests as areas of increased density within the pulmonary parenchyma. The increased density is usually focal but may be multifocal or diffuse. Depending on the causative organism and the health and immune status of the patient, the density may manifest as confluent parenchymal consolidation (where vessels are obscured within the density), as hazy ground glass density (where vessel margins can be detected within the density), or as coarse reticular or reticulonodular opacities. These densities may be marginated by pleural or fissural boundaries. If available, the use of both posteroanterior (PA) and lateral projections is often helpful in detecting, confirming, or localizing areas of increased parenchymal density (Figs. 8-2 and 8-3).

Heart Failure

There were 5.2 million ED visits for congestive heart failure (CHF) in 2004. At age 40, the lifetime risk of developing CHF for both men and women is one in five. Progression or exacerbation of CHF can cause dyspnea due to pulmonary vascular congestion or its more

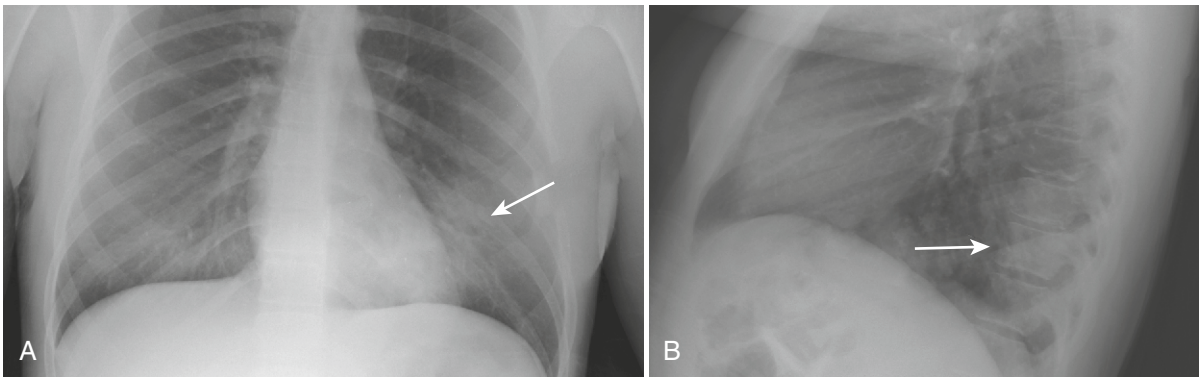


FIGURE 8-2. Chest x-ray of a patient with pneumonia. **A,** Posteroanterior view reveals a patchy opacity overlying the left lung base *(large arrow)*. Note that the left cardiac border is preserved, indicating that the pneumonia is more likely in the left lower lobe. If it were lingular and abutting the left cardiac border, the left cardiac border would be obscured (the "silhouette" sign). **B,** The lateral view confirms left lower lobe location of the pneumonia, as indicated by increased density of the lower thoracic vertebral bodies *(arrow)*. Normally, on a lateral chest x-ray, the thoracic vertebral bodies become increasingly lucent from superior to inferior. Increased density of lower thoracic vertebral bodies indicates the presence of radiodense material (in this case, a left lower lobe pneumonia) attenuating the x-ray beam.

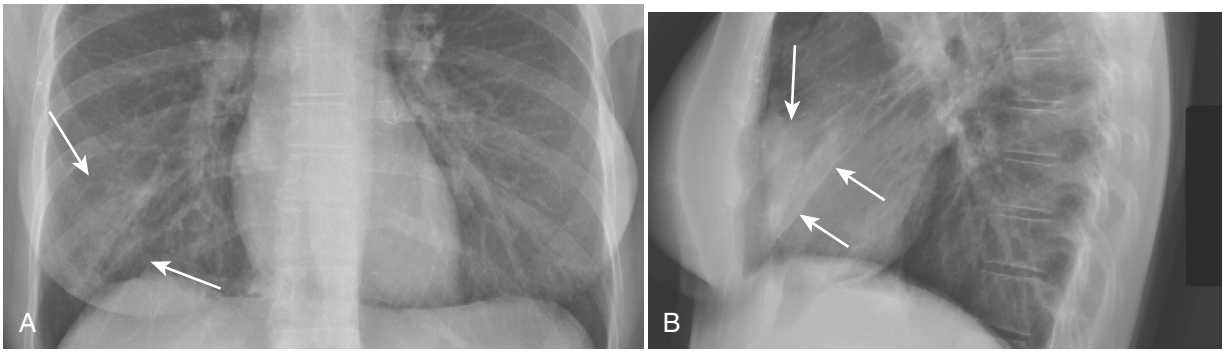


FIGURE 8-3. Chest x-ray of another patient with pneumonia. **A,** Posteroanterior view reveals a faint opacity overlying the right lung base *(arrows)*. The density does not abut the right heart or diaphragm, and thus the "silhouette" sign is of no help in determining middle versus lower lobe location. **B,** The lateral view reveals increased density overlying the heart *(longer arrow)*, confined by the major fissure *(shorter arrows)*, indicating right middle lobe location of the pneumonia. Note the vertebral bodies become more lucent from superior to inferior, indicating the absence of lower lobe processes overlying the vertebrae.

advanced form, pulmonary edema. Pulmonary edema can be classified as of hydrostatic origin (increased intravascular pressure, as in left ventricular failure or volume overload) or of permeability origin (increased permeability of the pulmonary alveolar-capillary membrane, as in acute respiratory distress syndrome [ARDS]). Although there is likely some overlap in the pathophysiology, the etiology of pulmonary edema cannot routinely be distinguished by CXR.

The sequence by which CHF leads to pulmonary edema and may manifest on CXR is familiar. Left ventricular failure results in increased pressure within the pulmonary venous system leading to pulmonary venous distention. The increased size of pulmonary veins on CXR, particularly in the upper lobes, manifests as "cephalization," for which the determination can be relatively subjective at imaging. As pulmonary venous capacitance is exceeded, pulmonary vessels begin to leak transudative fluid into the pulmonary interstitium, including the septal, peribronchial, and perivascular spaces, and into the pleural space. The CXR correlates include septal lines (or "Kerley B" lines), peribronchial cuffing, indistinctness of vessel margins, and pleural effusions, respectively. With further progression, fluid begins to accumulate in alveolar spaces resulting in more confluent density that obscures vessel margins but in contrast accentuates the appearance of bronchial airways resulting in air bronchograms (Fig. 8-4).

COMPUTED TOMOGRAPHY

CT of the Pulmonary Parenchyma

Computed tomography allows for more refined analysis of the pulmonary parenchyma. Similar to CXR, pulmonary parenchymal pathology is detected by changes in parenchymal density and architecture. With section thicknesses of 2 mm or less, axial images allow for evaluation of pulmonary parenchymal architecture at the level of the secondary pulmonary lobule, the smallest unit of lung structure marginated by connective tissue septa. The secondary pulmonary lobule consists of small and terminal bronchioles (accompanied by terminal arterioles) along with their associated acini (usually 12 or fewer in number). This complex of terminal bronchovascular structures and their associated acini is confined by interlobular septae. The interlobular septae contain pulmonary veins and pulmonary lymphatics, the latter also found along the bronchovascular complex. Changes to the architecture of the secondary pulmonary lobule occur in a multitude of disease processes, and characterization of the architectural changes allows for refinement of differential diagnostic considerations. Of course, larger-order anatomy is clearly defined by CT as well.

Changes to the architecture and density of the secondary pulmonary lobule can be organized according to the structures involved, including peripherally located septal structures, centrally located bronchovascular structures, and more generalized abnormalities affecting both. A detailed instruction on CT of pulmonary parenchyma is beyond the scope of this chapter, but several excellent resources are available on this subject, including the Requisites text on thoracic radiology. However, a general overview of the differential considerations associated with architectural derangements described above is useful, and a brief synopsis is provided below.

Septal thickening may be smooth, nodular, or irregular. Differential considerations for smooth septal thickening include pulmonary edema (with septal thickening being the equivalent of "Kerley B" lines seen on CXR) or ARDS, and pneumonia or pulmonary hemorrhage (Fig. 8-5). Septal thickening seen with these entities may be associated with "ground glass" density, the so-called crazy paving pattern. The "crazy paving" pattern has also been described as characteristic of alveolar proteinosis. Nodular septal thickening may be seen in lymphangitic metastases as well as sarcoidosis and silicosis. Nodules seen in sarcoidosis are characterized as perilymphatic, and thus may be centrilobular or septal (lymphatics are associated with both the septae and bronchovascular structures). Pulmonary fibrosis may also result in septal thickening, which may be irregular in nature and may be associated with honeycombing or other common findings of fibrosis, such as traction bronchiectasis.

Centrilobular opacities or nodules generally imply abnormalities of the small airways or vascular diseases, and are usually related to bronchiolitis of varying etiologies. The combination of centrilobular opacities/nodules with dilated/opacified bronchioles has been termed the "tree-in-bud" sign (Fig. 8-6). In the ED, centrilobular opacities/nodules are usually seen in the setting of an infectious bronchiolitis that may be due to bacterial or atypical organisms. Pulmonary aspiration can give a similar appearance. Other differential considerations for centrilobular opacities/nodules include pulmonary edema and hemorrhage, vasculitis, bronchoalveolar cell carcinoma, acute or subacute hypersensitivity pneumonitis, noninfectious bronchiolitis (as can be seen in smoking-related interstitial lung disease/respiratory bronchiolitis), and panbronchiolitis.

More generalized (panlobular) processes may lead to either ground glass or more consolidated opacities. If ground glass opacities are detected, the differential diagnosis is assisted by identification of ancillary findings. Ground glass opacities in the presence of honeycombing or other findings of fibrosis should point toward differential considerations among fibrotic lung diseases. Ground glass opacities in the presence of septal thickening ("crazy paving" pattern) should raise differential considerations including pulmonary edema, pneumonias of varying etiologies, and pulmonary hemorrhage, as well as entities less commonly encountered in the ED, including hypersensitivity pneumonitis, ARDS, and alveolar proteinosis. If ground glass opacities are encountered in the absence of ancillary findings the differential considerations become even broader and include interstitial pneumonia, infection, and drug reaction, in addition to the entities listed above (Fig. 8-7). Differential considerations for more consolidated densities include entities such as pneumonias, pulmonary edema, ARDS, and pulmonary hemorrhage, as well as acute eosinophilic pneumonia, masses, and fibrotic processes. Familiarity with the concept of evaluating pulmonary parenchyma based on analysis of the structures of the secondary pulmonary lobule will serve emergency radiologists well in their approach to formulating differential diagnoses for parenchymal disease.

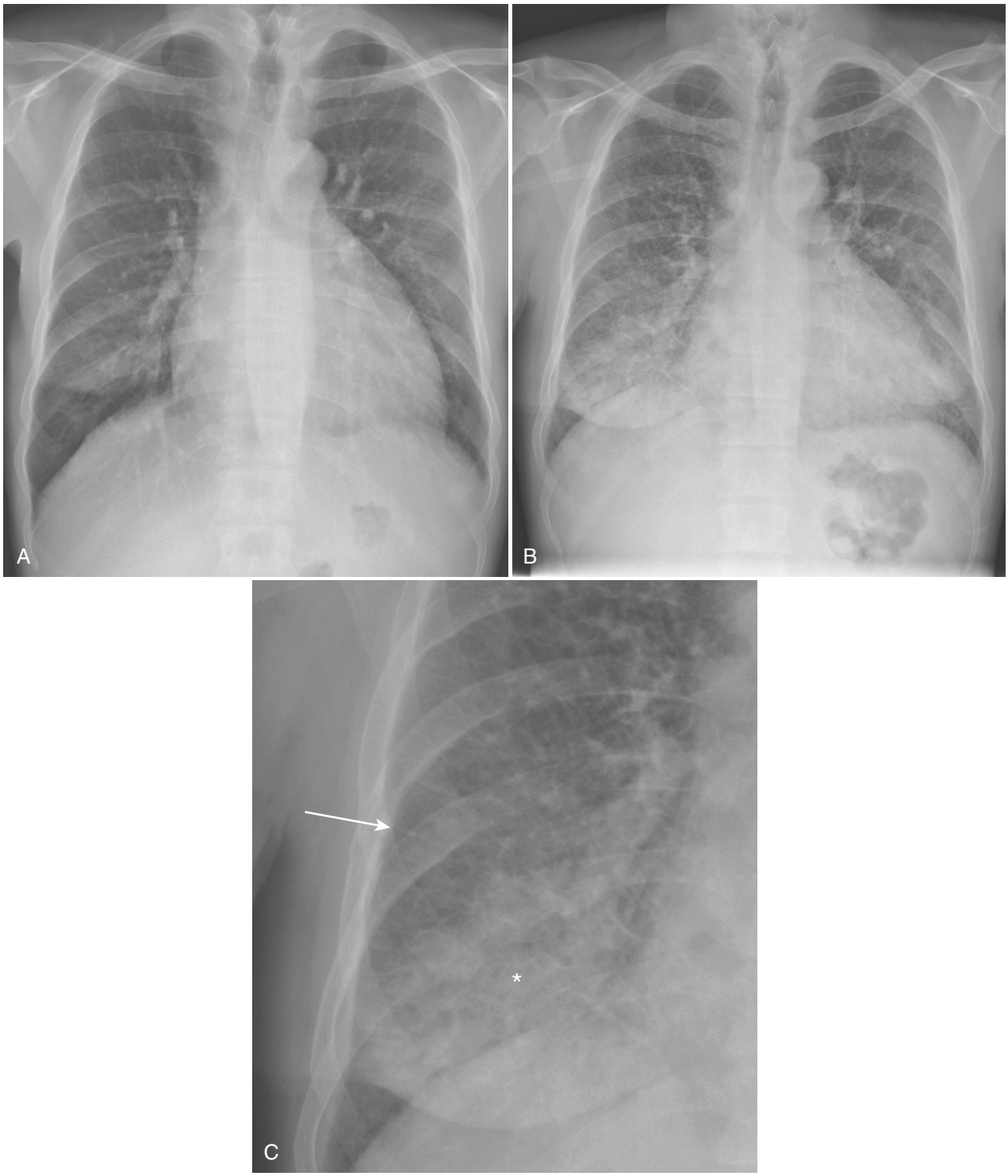


FIGURE 8-4. Patient with cardiomegaly and recurrent episodes of congestive heart failure. **A,** Posteroanterior view obtained when the patient was otherwise healthy reveals grossly clear lungs and cardiomegaly. There is a normal paucity of lung markings at the periphery of the lungs near the pleural margins. **B,** A posteroanterior view obtained when the patient was in congestive heart failure with pulmonary edema reveals diffusely increased lung markings and faint opacification at the bases. **C,** A magnified view of the right lung base reveals prominent septal markings in the subpleural lung periphery, or "Kerley B" lines *(arrow)*, as well as more consolidated density overlying the right lung base *(asterisk)*.

Chest CT Techniques and Protocols

This section outlines general principles guiding the selection of CT techniques and scan parameters. While there can be wide variability between scanner types and manufacturers in technological capabilities, nomenclature, and technical detail, the basic underlying considerations are applicable across these platforms. A working knowledge of these considerations can aid the radiologist in optimizing CT scan performance while remaining good stewards of radiation safety.

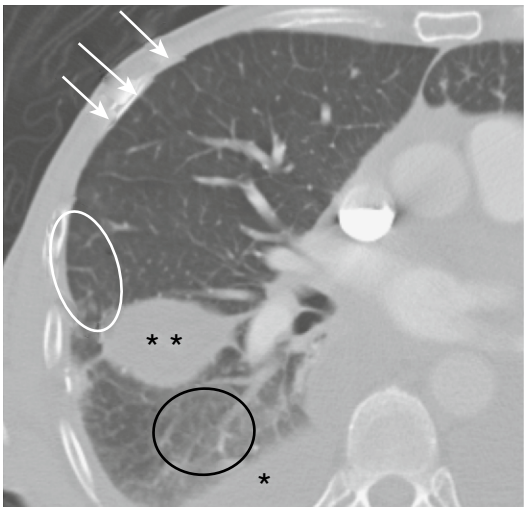


Figure 8-5. Patient with congestive heart failure and pulmonary edema. Thickened interlobular septae *(arrows)* define the borders of the intervening secondary pulmonary lobules. Additional findings that may be seen in congestive heart failure/pulmonary edema are shown, including centrilobular opacities *(white oval)*, ground glass opacity *(black oval)*, and pleural fluid seen posteriorly *(single asterisk)* and within the major fissure *(double asterisks)*.

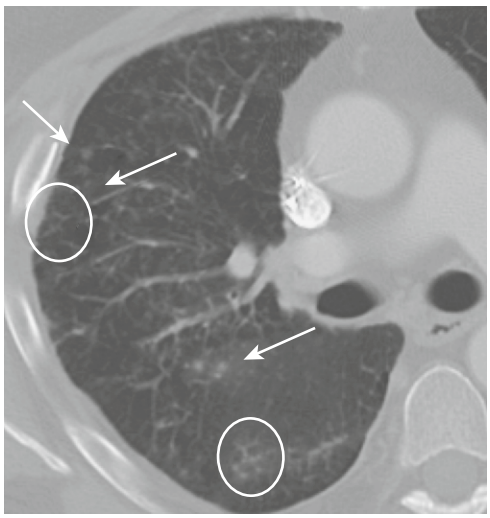


Figure 8-6. Examples of centrilobular opacities *(arrows)* and the "tree-in-bud" sign *(ovals)* in a patient with a history of nonspecific interstitial lung disease who presented with an acute cough. Subsequent CT scan (images not provided) showed resolution of the centrilobular opacities, which were therefore presumed infectious (bronchiolitis or bronchopneumonia) in etiology.

Patient Screening

Intravenous Contrast Material

All patients must be screened for allergy to intravenous contrast material (IVCM). While IVCM is a critical part of evaluation for pulmonary embolus and aortic dissection, it can be omitted if the clinical indication is primarily for abnormalities of the lungs. Although protocols vary by institution, all policies should include screening for a history of contrast allergy and risk factors for contrast-induced nephropathy.

Pregnancy

Women of child-bearing age should be screened, as concerns regarding the use of ionizing radiation during pregnancy must be weighed against medical necessity (e.g., pretest probability, urgency), exam performance characteristics (e.g., sensitivity, specificity), and alternative methods of imaging (e.g., MRI, ultrasound). Medically unnecessary exams should not be performed. Alternative imaging methods with similar exam performance characteristics should be employed when available. If CT or radiography is used, protocol modifications are frequently warranted during pregnancy, such as restricting to a single PA view chest radiograph with shielding of the abdomen, or elimination of pelvis and lower extremity scanning as part of CT evaluation for pulmonary embolus. Multiple-phase CT scanning, or so-called multi-pass CT protocols, should be altered to single-phase scanning unless multiple phases are critical to patient evaluation. The number of nondiagnostic scans should be minimized by taking proactive steps to optimize CT scan quality (e.g., patient coaching for breathing and motion, excellent IV placement), thereby reducing the need for repeat scanning.

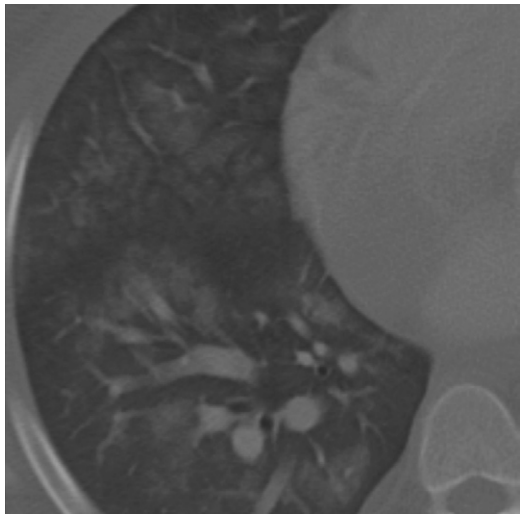


Figure 8-7. Example of ground glass opacities due to pulmonary edema in a postpartum patient with a history of preeclampsia, who presented with leg swelling and shortness of breath. Note the patchy hazy density that does not obscure the underlying vascular structures.

Patient Preparation

Intravenous Line Placement

Whenever possible, contrast-enhanced chest CT studies should be performed through a 20-gauge or larger peripheral IV, preferably located in a right antecubital location. An 18- to 20-gauge size will easily allow for power-injected flow rates of 3 to 6 cc per second. Right-sided IV placement reduces streak artifact over the anterior superior mediastinum as compared with left-sided placement, due to elimination of dense IV contrast passing through the left brachiocephalic vein. Antecubital placement results in more reproducible contrast inflow characteristics and a reduced rate of infiltration as compared with more peripheral placement.

Heart Rate Control

Cardiac gated protocols (coronary CT angiography [CTA] for gated aortic dissection) generally require a regular cardiac rhythm. With current single-source 64-MDCT techniques, coronary CTA is best performed with heart rate

controlled to 65 beats or less per minute. However, further advances such as quicker gantry rotation, greater numbers of detector rows, and/or dual x-ray source scanners are likely to lessen or obviate the current requirement for lower or regular heart rates.

Scan Protocol Considerations

Contrast Timing Principles and Techniques

Care must be taken to optimize the timing of the CT scan relative to the injection rate, injection profile, and duration of IVCM administration. The specific timing details vary greatly depending on the duration of the scan (which depends greatly on the CT technology in use), and on the flow rate and quantity of injected contrast material. As a general rule of thumb, IV contrast should be injected at a minimum rate of 3 mL per second for CT evaluation of pulmonary embolus, aortic dissection, or traumatic aortic injury. Higher flow rates of 4 or more mL per second are preferable, but they shorten the duration of the contrast bolus. As a result, scan timing must be scrutinized to ensure that contrast opacification remains adequate throughout all portions of the scan.

Three techniques are commonly used to determine the initial scan delay after the start of IVCM injection:

- Fixed, or empiric delay. The time delay is selected based on scanner speed, experienced best estimates of time required to reach the vascular bed of interest, and, if applicable, patient factors such as cardiac output and IV location.
- Automated contrast bolus detection, or bolus tracking. A monitoring scan is repeated at a fixed scan position, and the acquisition scan is triggered when the contrast density exceeds a preset threshold in a vessel selected as the region of interest.
- Timing bolus. The transit time from the injection site to the vascular bed of interest is directly observed by repeat scanning at a fixed position following administration of 10 to 20 mL of IVCM (and a saline flush at the same injection rate). Time to peak enhancement is determined based on the timing bolus, and the corresponding timing delay is subsequently used for IVCM during the acquisition scan.

Radiation Exposure and Techniques for Dose Reduction

Emergent (and overall) CT utilization continues to rise rapidly as a result of further technological advances, additional clinical applications, and greater CT availability. The associated radiation risks due to individual exposures, as well as population exposure levels, are gaining attention. The momentum behind these concerns will almost certainly lead to greater scrutiny around CT use. Radiologists are compelled to heed these concerns and to show that they are doing their part to optimize techniques that will reduce radiation exposure while maintaining high-quality imaging. Likewise, medical vendors are eager to advance their imaging technologies with tools that allow for reduced exposure. A variety of techniques exist to control patient exposure during CT. Radiologists should have a working knowledge of these techniques.

Many current CT scanners (and virtually all new scanners) include the capacity for automatic exposure control and dose modulation. In general, these functions should be enabled when available. Automatic exposure control adjusts the overall x-ray tube current to a predetermined quality or noise standard, or reference milliAmpere per second (mAs). Dose modulation rapidly adjusts tube output during the scan, either along the axis of the patient (longitudinal modulation) or during the gantry rotation around the patient (angular modulation) as the patient's thickness and density vary in these directions. Additionally, most scanners intended for cardiac CT offer the capability for ECG-dose modulation, in which x-ray tube output is greatly reduced during systole.

Imaging of structures with a high degree of intrinsic tissue contrast can tolerate a higher level of noise than imaging structures of near uniform CT density. Both routine chest CT and CTA often involve inherently high-contrast structures, allowing for lower-dose techniques to be used. Dose reduction during CTA has been successfully performed without detriment to image quality by reducing kilovoltage (kV) to match the low K-edge of iodine in contrast-enhanced vessels.

Bismuth breast and thyroid shields have been successfully used to reduce doses to these radiation-sensitive organs by preferentially attenuating the lower-energy x-rays that do not contribute significantly to image quality. These are expected to play a more widespread role during CT imaging, particularly of younger patients.

Image Reconstruction

Routine image reconstructions should include the following:

- 5-mm axial lung algorithm images
- Axial soft tissue algorithm images:
  Routine chest: 5 mm
  Dissection CTA: 3 or fewer mm
  Pulmonary embolus CTA: 2.5 or fewer mm, preferably 1 to 1.5 mm

Additional imaging is often helpful, but frequently indication specific. For example, coronal and/or sagittal multiplanar reformations (MPRs) have become routine at many institutions. These are particularly useful in assessment of vascular anatomy and osseous structures, but can also aid localization of parenchymal lesions relative to the fissures, and to confirm motion artifacts on pulmonary embolism (PE) or dissection CTA. Routine sagittal oblique ("candy cane") MPR should be added to any aorta evaluation. Thick maximum intensity projection (MIP) images may be added for PE detection. Minimum intensity projection (MINIP) images are useful in evaluation of the airways.

Indication-specific CT Protocol Techniques

Routine Chest CT

This is often performed without IVCM to further assess a radiographic parenchymal abnormality (e.g., pulmonary nodule). However, IVCM is helpful for assessment of empyema or mediastinal or hilar abnormalities.

Pulmonary Embolus CTA

A typical protocol includes bolus detection on the main pulmonary artery, followed by a breathhold delay and scanning in the caudal to cranial direction. Most other thoracic CT protocols utilize a cranial to caudal scan direction.

This scan direction is often reversed in pulmonary embolus CTA (CTPA) in order to minimize respiratory motion artifact in the lower lobes, where the majority of pulmonary emboli occur.

If a lower extremity venogram is not included, a high-quality CTPA may be performed with approximately 80 mL of IV contrast injected at 4 mL per second. If a lower extremity venogram is performed following CTPA, 100 to 125 mL of IVCM are instead needed, and images are acquired at intervals from the pelvis to the knees after an approximately 3-minute delay.

Upper Extremity Deep Venous Thrombosis or Superior Vena Cava Syndrome

A delayed venous phase scan should be performed if there is high clinical suspicion for upper extremity or central vein thrombosis. The delayed phase produces more uniform venous opacification and eliminates the mixing artifacts typically observed from dense IVCM injected through one arm mixing in the SVC with the unopacified blood arriving from the other arm (Fig. 8-8). Coronal reformations can greatly aid diagnosis.

Aortic Dissection CTA

Currently, full dissection CTA protocols may include:

- A noncontrast scan of the chest only.
- An arterial phase scan through the chest (+/- abdomen and pelvis) performed either with or without cardiac gating.
- A delayed phase scan through the chest, abdomen, and pelvis.

The initial noncontrast scan is used to assess for a thrombosed false lumen or isolated intramural hematoma, both of which will appear denser than the unopacified blood in the aortic lumen. If a noncontrast scan was not initially obtained (such as a pulmonary embolus CTA study), a 20- to 30-minute postcontrast delayed scan can be obtained, as IVCM will have adequately cleared the intravascular space. This permits the radiologist to troubleshoot the rare case in which a contrast-enhanced scan may raise suspicion for isolated intramural hematoma but is not sufficiently diagnostic for the radiologist.

The arterial phase scan is often performed with cardiac gating in order to reduce the pulsation artifact, which can mimic focal aortic dissection at the aortic root. However, this artifact has a characteristic appearance on axial and MPR images, and can typically be readily differentiated from aortic dissection (Fig. 8-9). If the radiologist is readily familiar with this diagnostic pitfall, a nongated arterial phase scan can be used so as to reduce radiation exposure, which is significantly greater on cardiac-gated scans. If cardiac gating is utilized, a regular heart rate is required, preferably 65 or fewer beats per minute. For younger ED patients (generally younger than 50 years old) with a low pretest probability of aortic dissection and a low incidence of significant atherosclerotic disease, we screen with a physician-monitored, nongated, contrast-enhanced chest CT only in order to reduce the radiation exposure from multiple phase protocols. If needed, additional scanning can be readily undertaken if results of this scan show anything other than a normal aorta. Very rarely is this necessary.

The CT scan through the abdomen and pelvis is performed to assess distal extension of the intimomedial flap, involvement of visceral or iliac arteries, and end organ ischemia. Therefore, it should be prescribed as routine in high-risk patients or those with known aortic dissection presenting with acute symptoms. But the abdomen and pelvis can be scanned selectively in patients with low pretest probability. For those in whom dissection was identified by active physician monitoring of the screening chest CT, the scan can readily be continued through the abdomen and pelvis during the arterial phase with delayed imaging acquired as needed. This is a viable option

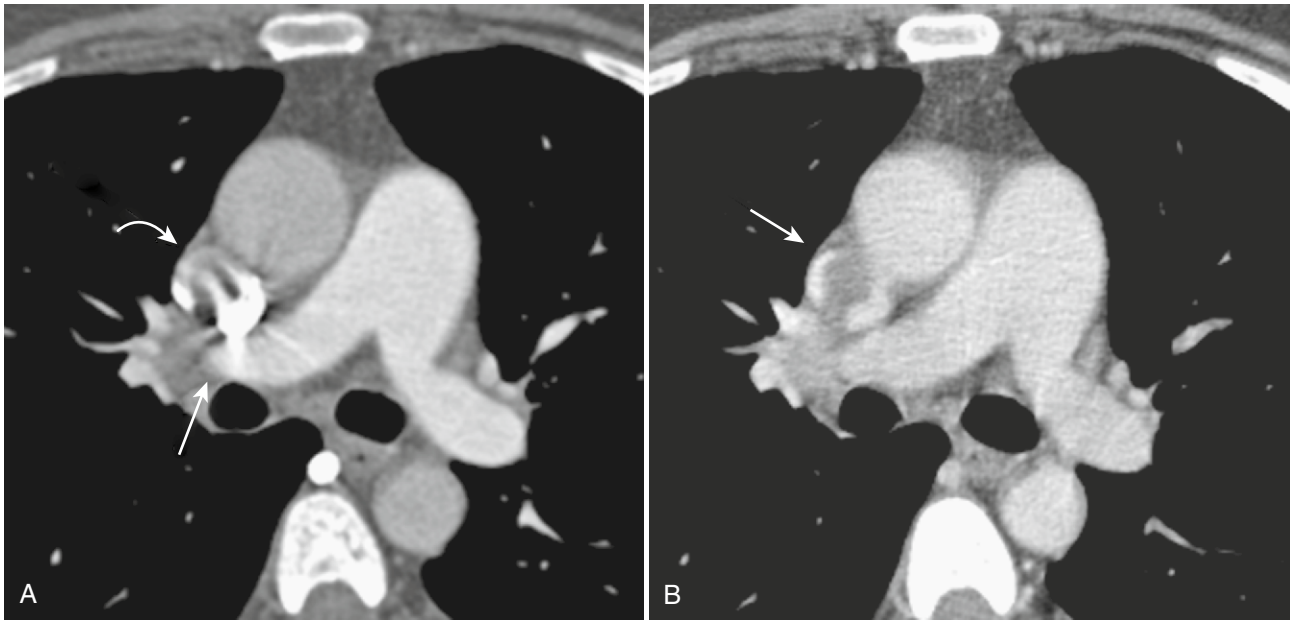


Figure 8-8. Superior vena cava (SVC) thrombus following recent central line removal. **A,** Early phase axial image. Dense contrast in the SVC *(curved arrow)* produces streak artifact that partially obscures the SVC thrombus *(arrow)* and makes it difficult to differentiate streak artifact from mixing artifact with unopacified blood from the left brachiocephalic vein. **B,** Delayed (90 seconds) phase axial image eliminates streak and mixing artifacts.

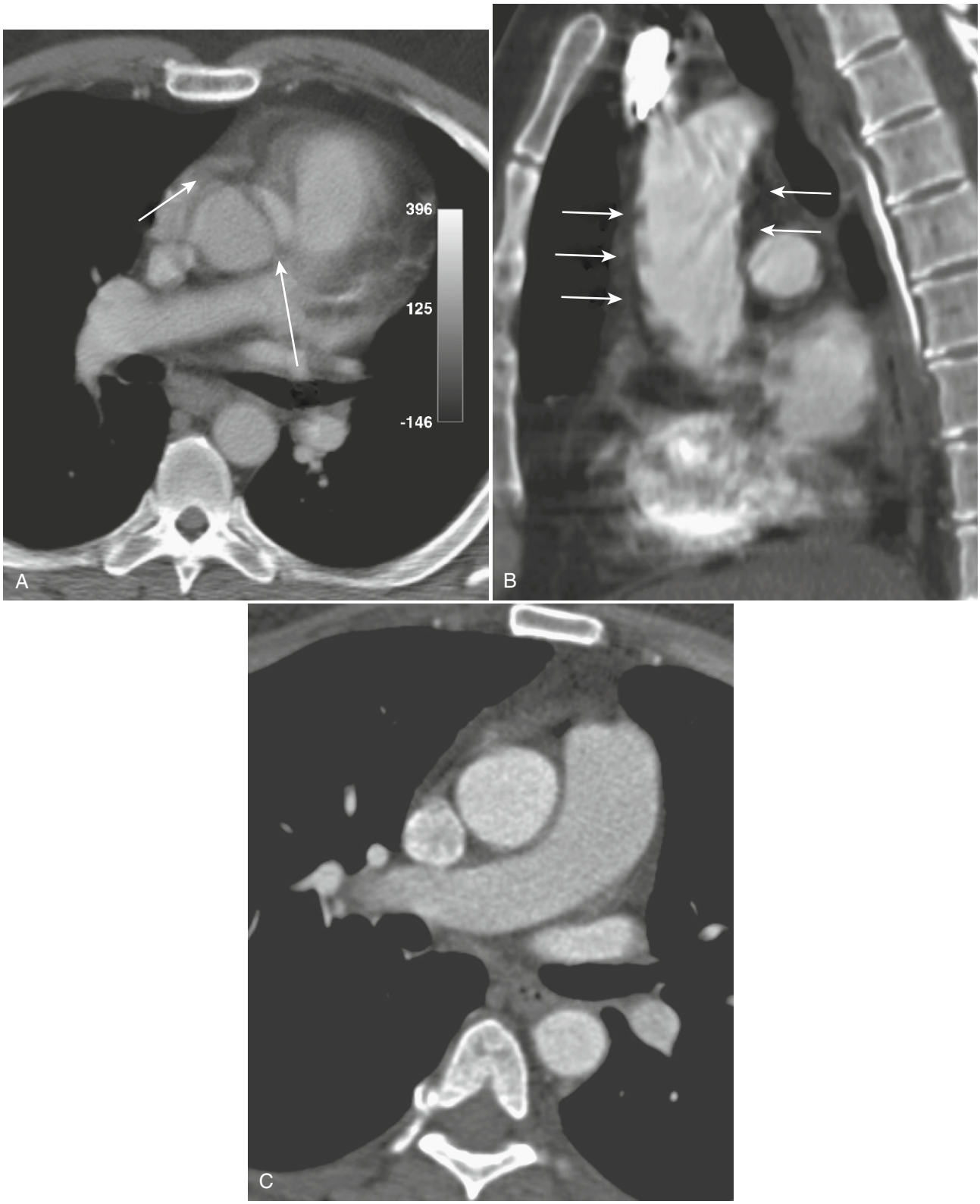


FIGURE 8-9. Pulsation artifact: typical aortic root pulsation artifact from a non-gated study, not to be confused with aortic dissection. **A,** A sharply defined band of low-density artifact *(longer arrow)* extends across the left side of the proximal ascending aorta. The artifact extends beyond the aortic margin to the right atrial appendage *(shorter arrow)*, helping to confirm its artifactual nature. **B,** Sagittal reformation showing motion artifacts *(arrows)* arising in each cardiac cycle. **C,** Repeat study performed the following day with cardiac gating, eliminating the cardiac motion artifact.

for institutions with radiologists who can actively monitor CT acquisitions while the patient is on the gantry table. Although the 24/7 operations of the ED can make this challenging to implement during nonbusiness hours, greater organization around the practice of emergency radiology is likely to make this more feasible in the future.

Pneumomediastinum and/or Evaluation of Esophageal Injury

In the ED, CT is often used rather than fluoroscopy to assess for possible esophageal injury. The scan protocol should include an initial scan with neither oral nor intravenous contrast. Subsequently, the patient should take a few swallows of Gastrografin, and a repeat scan (with or without intravenous contrast, depending on indication) should be performed. The "scout" noncontrast scan is included in order to readily differentiate Gastrografin extravasation from soft tissue calcification or a small foreign body (e.g., a fish bone). Because both gas and contrast material extravasation are intrinsically high-contrast evaluations, low-dose techniques can be used to reduce radiation exposure.

Coronary CTA

There can be significant variability in CT scan technique depending on local CT scanner technology and institutional decisions about whether to perform a focused coronary CTA only or a "triple rule-out" that simultaneously assesses the aorta and pulmonary and coronary arteries. The numerous variables and technical details are beyond the scope of this chapter. Briefly, however, the study may be prescribed from a topogram or a low-dose unenhanced chest CT performed for calcium scoring. The CTA is then either initiated by automated bolus detection or, following a scan delay, derived from a test bolus. Cardiac gating is required, preferably with a heart rate equal to or less than 65 beats per minute. Tube current dose modulation schemes, if available, are recommended to reduce the associated radiation exposure by limiting tube current during the systolic portion of the cardiac cycle. Images are reconstructed at multiple intervals of the cardiac cycle to permit identification of image sets free of cardiac motion artifact. Numerous efforts in CT scanner technology are aimed at optimizing coronary CTA evaluation. As these technological advances are exploited through innovative clinical applications, CT protocols and scanning requirements for coronary CTA are likely to evolve in the short term.

THE PLEURA, PERICARDIUM, AND MEDIASTINUM

The Pleura

The pleura is a specialized tissue layer covering the lungs and the internal surface of the chest cavity. The visceral and parietal components form a continuous layer and create a potential cavity, the pleural space, which is generally visualized radiographically only when local or systemic pathology develops. Normally a small amount of fluid (15 to 20 mL) lies in each pleural cavity and lubricates the sliding lung surface during the respiratory cycle. Pleural fluid originates in the interstitium and is drawn away from the pleural space along a gradient toward the low-pressure pleural capillaries, ultimately draining into the pulmonary venous system. Pleural fluid is continuously secreted and absorbed; disruption of this equilibrium leads to effusion.

The pleural space is maintained below ambient pressure by chest wall recoil, the actions of gravity, and muscular contraction of the diaphragm. Loss of vacuum integrity leads to rapid collapse of the lung airspaces.

Pneumothorax

Pneumothorax is the presence of air within the pleural space. The etiologies of pneumothorax are multifactorial (Table 8-1). The most common imaging test performed to assess for pneumothorax is the chest radiograph, or CXR. Ideally, this is performed with upright patient positioning so that the air–pleural interface can be readily identified toward the apices. Expiratory imaging may accentuate the contrast between lung tissue and intrapleural gas. This method may be particularly helpful for smaller pneumothoraces, but is generally not required. The presence of pneumothorax is often more subtle on supine radiography, and small pneumothoraces can be easily overlooked.

Spontaneous pneumothorax occurs more frequently in smokers, asthmatics, and thin young men. The relative risk for male smokers is up to 20 times higher than for nonsmoking males. Risk increases in a linear relationship to the amount of smoking. Blebs are often found at thoracoscopy of patients presenting with spontaneous pneumothorax, and can be visualized by CT in up to 89% of patients. For this reason, chest CT is often ordered as a follow-on study to a CXR showing an unexpected spontaneous pneumothorax.

Primary spontaneous pneumothorax is differentiated from secondary spontaneous pneumothorax by the absence of underlying lung disease. Secondary spontaneous pneumothorax is due to underlying pleural or parenchymal disease, usually in the form of blebs or cysts. These may result from disease entities such as emphysema, *Pneumocystis carinii* pneumonia infection, or lymphangioleiomyomatosis. Spontaneous pneumothorax is sufficiently common as a component of the differential diagnosis for chest pain and dyspnea that a high index of suspicion should be maintained when evaluating routine chest radiographs for these indications. The frequency of central line placement in the ED is another reason to maintain a high index of suspicion for pneumothorax when evaluating all ED chest radiographs.

A tension pneumothorax occurs when air enters but cannot exit the pleural space. This can occur when the pleural

Table 8-1 Etiologies of Pneumothorax

Etiology	Types
Trauma	Penetrating or blunt; barotrauma
Idiopathic	Primary or secondary
Iatrogenic	Following biopsy, surgery, central line placement, thoracentesis, mechanical ventilation, bronchoscopy
Infection	Pneumocystis carinii, necrotizing pneumonia
Neoplastic	Langerhans' cell histiocytosis, sarcoma, lung cancer, various others
Congenital/Acquired	Emphysema, congenital bullae, lymphangioleiomyomatosis

defect allowing air passage into the pleural cavity mechanically functions like a ball-valve resulting in unidirectional air transit. The increasing intrapleural gas creates mass effect, and eventually can displace the mediastinum and compromise venous blood return to the heart. Progressive accumulation of air in the pleural cavity can lead to cardiovascular impairment and, if left untreated, death. Tension pneumothorax should be suspected when the trachea, heart, and/or mediastinum have been displaced from the midline, when the ipsilateral rib spaces have widened, and/or when the contralateral lung appears relatively compressed.

Several estimation methods for pneumothorax size are based on CXR measurements, but these are subject to wide interobserver variations in practice. A pragmatic rule of thumb is that a large pneumothorax is one that completely dehisces from the chest wall, while a small one does so only partially. This simple criterion identifies the majority of pneumothoraces requiring evacuation. If there is ambiguity as to whether an apical lucency represents intrapleural air or a large bulla, CT is generally definitive. Chest CT also permits volumetric or percent measurements of pneumothorax size that are more precise, although intervention usually occurs prior to CT evaluation.

Small pneumothoraces are usually followed radiographically to resolution. Failure of resolution and interval enlargement are common indications for invasive management. The treatment for a large pneumothorax (generally 15% or more of the hemithorax) is air aspiration or evacuation by intercostal chest tube or catheter. The radiologist should be familiar with the normal locations for appropriately inserted chest tubes. Intraparenchymal, extrathoracic, and interlobar placements should be communicated to the treating physician to allow for repositioning. The multiple sideports of the chest tube should all lie within the thoracic cavity. Increasing subcutaneous emphysema on repeat chest radiographs is a clue to the potential presence of an extrathoracic sideport and the need for repositioning or downsizing of the chest tube.

Additional radiographic signs associated with pneumothorax include the deep costophrenic sulcus sign seen on the supine radiograph. The "double diaphragm" sign is caused by nondependent air outlining the anterior diaphragmatic attachment. Mimics of pneumothorax are multiple and may be due to overlying sheets, clothing, medical equipment, or skin folds. Repeat chest radiography after rearranging or removing the external structures is often adequate to exclude pneumothorax.

Recently, ultrasound (US) has gained attention as a rapid assessment tool to evaluate for pneumothorax in the ED and after chest interventions. The performance of US has been shown to be as good if not better than radiography, although it generally underperforms as a follow-up study. Additionally, greater variation in results should be expected due to differences in sonographer skill and experience. Traumatic pneumothorax is discussed in this text in Chapter 2, so only a brief comment is made here. The seal of the pleural space is easily broken by penetrating injury, and it is vulnerable because it is spread over a large surface area. Significant blunt trauma is estimated to cause pneumothorax in up to 30% to 40% of cases. It can lead to pneumothorax when broken ribs or other sharp structures expose the pleural space to atmospheric pressure, or when a preexisting bleb is ruptured. Fractured ribs on imaging should invoke a secondary search for pneumothorax. With positive pressure ventilation, barotrauma can lead to pneumothorax, particularly in patients with relatively noncompliant lung tissue (e.g., those with ARDS or interstitial lung disease). Barotrauma may also occur during sport diving or from nonpenetrating blast injuries resulting from explosive devices.

Pleural Effusion

Pleural effusion, defined as abnormally increased fluid within the pleural space, may be transudative or exudative in etiology. Transudative fluid is generally low in protein and typically develops in the setting of left heart failure, decreased oncotic pressure, or other systemic abnormality. Exudative fluid is often a consequence of breakdown of the barrier function of the pleura, leading to leakage of macromolecules and proteins. Less commonly encountered complex exudative pleural effusions include hemorrhagic fluid related to tuberculous infection, chylothorax related to thoracic duct injury, and eosinophilic effusions related to hypersensitivity (Table 8-2).

Pleural fluid volume as low as 5 mL can be visualized on decubitus imaging. Approximately 200 mL is required to blunt the costophrenic sulcus on upright radiography. Small fluid collections can routinely be characterized on CT, US, and MRI. The CT appearance of pleural fluid varies depending on the density. Transudative effusions are near water density (i.e., approximately 0 Hounsfield units [HU]); hemorrhage and pus typically demonstrate increased density, often with a hematocrit effect in the case of hemorrhage. Low density on CT does not, however, exclude exudate. Long-standing infections may show complex septations or gas. US may help to characterize effusions by showing areas of loculation and septation, and is also commonly used for drainage guidance.

Pleural effusions may also be seen in the setting of malignancy, and occasionally in the setting of benign lesions, as seen in Meigs syndrome. Classically, Meigs syndrome is the presence of ascites and pleural effusion caused by benign ovarian fibroma, although other ovarian neoplasms are now commonly invoked as well. Meigs syndrome is uncommon and the pathophysiology is unclear. Most sources accept the explanation that the fluid is generated by the tumor itself and is often, but not exclusively, a transudate.

Hemothorax

Traumatic hemothorax can occur following blunt or penetrating trauma. Blunt trauma may cause direct venous or arterial rupture or may disrupt vessels secondary to rib fracture. Penetrating trauma is capable of mediastinal,

TABLE 8-2 Etiologies of Pleural Collections

Etiology	Types
Trauma	Hemothorax, chylothorax
Infectious	Empyema, tuberculous effusion
Gestational/Fertility	Ovarian hyperstimulation
Inflammatory	Postpericardiotomy, eosinophilic
Drug induced	Multiple factors
Reactive	Ascitic, pancreatitis

intercostal, substernal, or diaphragmatic vascular injury with resultant intrapleural hemorrhage.

Intrapleural blood may manifest on the conventional radiograph as a localized collection or as diffuse relative opacification of one or both hemithoraces. Much smaller collections can be detected on CT with the added certainty of density characterization allowed by evaluation of HU in a region of interest. CT, particularly when performed during intravenous contrast administration, may identify active extravasation from arterial injury. Progressive enlargement of hemothorax is likely due to arterial injury, while venous hemorrhage is more likely to stabilize. Unevacuated hemothorax, particularly if large, can develop adhesions and fibrothorax, potentially restricting lung function.

Empyema

Empyema refers to abscess formation in the pleural space. Although usually secondary to adjacent pneumonia, it is also known to develop after hematogenous seeding, trauma, or iatrogenesis. In the setting of suspected empyema, chest CT should be performed with administration of IVCM. The presence of a "split pleura" sign is strongly suggestive of empyema. Several studies have shown improved health outcomes with early evacuation of empyema, often in conjunction with fibrinolytic therapy.

Chylothorax

Chylothorax is the development of effusion containing lymphatic fluid, most often secondary to thoracic duct injury or malignant invasion. The thoracic duct drains into the junction of the left axillary and internal jugular veins, with the majority of the course from the cisterna chyli lying on the right. Consequently, most chylous effusions are right-sided. A minority are bilateral. CT is helpful in diagnosis, as chylous fluid contains fats, which manifest as HU measurements less than zero.

Pericardium

The pericardium is an investing connective tissue layer covering the heart and proximal great vessels, separating the cardiac structures from the remainder of the middle mediastinum.

Pericardial Effusion

The etiologies of pericardial effusion are many and imaging is often nonspecific in this regard. Etiologies may include idiopathic, drug-induced, collagen vascular diseases, radiation-induced, malignancy, hypothyroidism, chylous effusion, infection (pericarditis), cardiac failure, and renal failure.

Hemopericardium

Hemopericardium is most often the result of acute blunt or penetrating trauma, from direct pericardial damage, myocardial contusion, or proximal aortic injury. Hemorrhage into the pericardial sac can rapidly lead to tamponade and circulatory collapse. In the absence of a history of trauma, type A aortic dissection, coronary artery aneurysm rupture, or postinfarct cardiac rupture must be considered. However, a dense pericardial effusion is not a sine qua non of hemopericardium or incipient tamponade. Radiographic and CT findings must be interpreted in conjunction with history and physical exam findings. Echocardiography should be performed if there are features causing concern for hemodynamic compromise (Fig. 8-10).

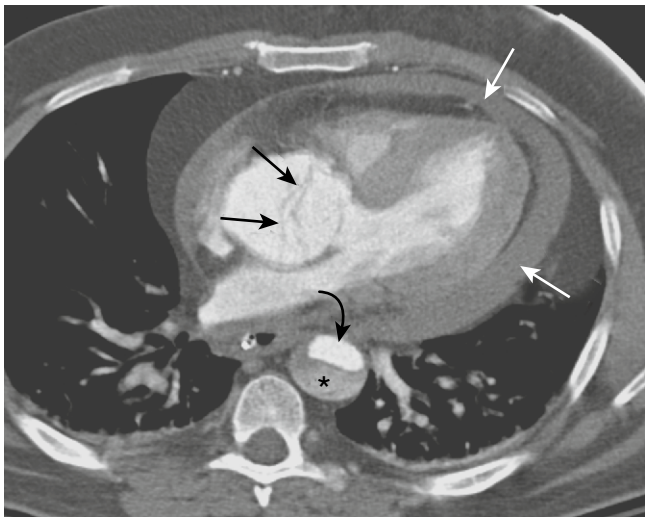


Figure 8-10. Axial CT images showing hemopericardium *(white arrows)* secondary to type A aortic dissection (*black arrows* indicate type A dissection flap within the ascending aorta; apparent duplication of the flap may be due to motion). Dissection extending into the descending thoracic aorta, with a hyperdense true lumen *(curved arrow)* and hypodense false lumen *(asterisk)*, is noted.

Cardiac Tamponade

Cardiac tamponade is a potentially life-threatening restriction of cardiac function due to rapid influx of fluid or gas into the pericardial space, regardless of its source or nature.

Pneumopericardium

Pneumopericardium can result, uncommonly, from blunt trauma or penetrating injury, or may develop after positive pressure ventilation, often in association with pneumothorax. It has also been associated with illicit drug use, particularly crack cocaine inhalation, and is thought to be probably secondary to repeated Valsalva maneuvers. Although pneumopericardium generally resolves with withdrawal of the causative insult, tension pneumopericardium can develop due to a ball-valve mechanism and should be suspected if the cardiac contour is abnormally diminished, known as the "small heart" sign.

Malignancy

Metastatic involvement of the heart and pericardium is not unusual, occurring in 10% to 12% of all cancer patients and 30% of those with lung malignancy. The development of symptoms such as dyspnea, cough, and chest pain are potential clues to cardiac or pericardial spread, although these are quite nonspecific. Contrast-enhanced chest CT to exclude pulmonary embolism is a common initial evaluation for oncology patients presenting to the ED with new chest symptoms. Foreknowledge of a patient history of malignancy, particularly lung cancer, should prompt careful visual review of the heart and pericardium for alternative or additional explanation of symptoms.

Other pericardial diseases include pericarditis and constrictive pericarditis. Pericarditis may cause a pericardial effusion and/or pericardial thickening. The normal pericardial thickness varies from 1 to 3 mm, depending on the location and cardiac phase. Constrictive pericarditis may or may not be associated with pericardial thickening.

Mediastinum

Anatomy

The mediastinum is a space within the central chest cavity bounded laterally by the medial pleural surfaces, anteriorly by the sternum, and posteriorly by the spinal column. The inferior margin is bounded by the diaphragm, while the superior limit is usually arbitrarily defined by a line drawn horizontally from the manubriosternal joint to the T4 vertebra.

There are several ways to segment the mediastinum anatomically. The simplest method trisects the intrathoracic structures into anterior, middle, and posterior mediastinal compartments based on location relative to the heart.

Because the three main mediastinal compartments contain very different structures, localization of a lesion to one of the mediastinal compartments considerably aids the differential diagnosis for most abnormalities. The anterior compartment normally contains thymus (or thymic remnant), lymph nodes, and fat. During embryonic development, pluripotent germ cells migrate inferiorly through this region. The middle mediastinum contains the heart and pericardium, great vessels, tracheal bifurcation, phrenic nerves, and lymph nodes. The posterior mediastinum contains the esophagus, thoracic duct, vagus nerve and sympathetic chain branches, the azygos and hemiazygos veins, and the descending aorta.

Masses

The anatomic compartmentalization of the mediastinum described above assists the radiologist in formulating differential diagnostic considerations for mediastinal masses. Mediastinal masses may be detected as incidental findings in ED patients undergoing chest imaging, or they may be the cause of the patients' presenting symptoms, such as chest pain, dysphagia or dyspnea, cough, hemoptysis, or SVC syndrome.

Pneumomediastinum

Typical causes of pneumomediastinum include trauma, asthma, drug use (Valsalva-induced), infection, and spontaneous pneumomediastinum. Traumatic causes (other than typical blunt or penetrating external trauma) may be the result of scope, tube, or line insertion (i.e., iatrogenic), positive pressure ventilation, or internal barotrauma related to vomiting (Boerhaave syndrome) or coughing against a closed glottis (Fig. 8-11). Pneumomediastinum generally requires no treatment apart from addressing the underlying cause.



FIGURE 8-11. CT showing spontaneous pneumomediastinum *(black and white arrows)* in an asthmatic patient.

Infection

Acute mediastinitis is a relatively rare entity, most commonly (90%) related to esophageal rupture. Other causes include tumor necrosis, spread of infection from adjacent compartments (e.g., descending cervical infection due to spread of oropharyngeal or deep neck infection along fascial planes), and infection secondary to procedures (e.g., sternotomy, mediastinoscopy). Signs and symptoms are nonspecific and include fever, tachycardia, and chest pain. Dysphagia is often noted in cases related to esophageal perforation. Conventional radiography may reveal tracking of air along the mediastinal planes, with variable extension into the soft tissues of the neck. CT lung windows are much more sensitive than radiography.

SVC Syndrome

SVC syndrome refers to the development of facial and upper extremity edema, swelling, and collateral venous engorgement secondary to superior vena cava obstruction. Associated findings include upper body erythema, confusion, chest pain, and hoarseness. In the developed world, most cases are related to malignant invasion of the SVC. Historically, tuberculous infection and syphilitic aneurysm were more common causes. Indwelling central catheters have come to play a larger role in recent years and can lead to SVC syndrome via stricture and thrombosis. Other causes of SVC syndrome include extrinsic compression by aneurysm or lymphadenopathy and fibrosing mediastinitis usually secondary to the inflammatory response elicited by infection with *Histoplasmosis capsulatum*. In younger patients, benign causes predominate. Malignancy is the most common cause over age 40.

Because SVC obstruction impairs venous drainage of the head and neck, cerebral and laryngeal edema may occur. For these reasons, the development of SVC syndrome is considered a medical emergency, although only a minority of patients are at risk of death from cerebral edema.

CXR may reveal a mediastinal abnormality in patients with clinically suspected SVC syndrome, such as a mediastinal mass or lymphadenopathy. Contrast-enhanced CT and MR angiography are the most reliable noninvasive methods of definitive diagnosis. CT is generally preferred as the initial study, owing to the prevalence of lung cancer and lymphoma as causative factors in the adult population and the ease and accuracy with which CT delineates these findings (Fig. 8-12).

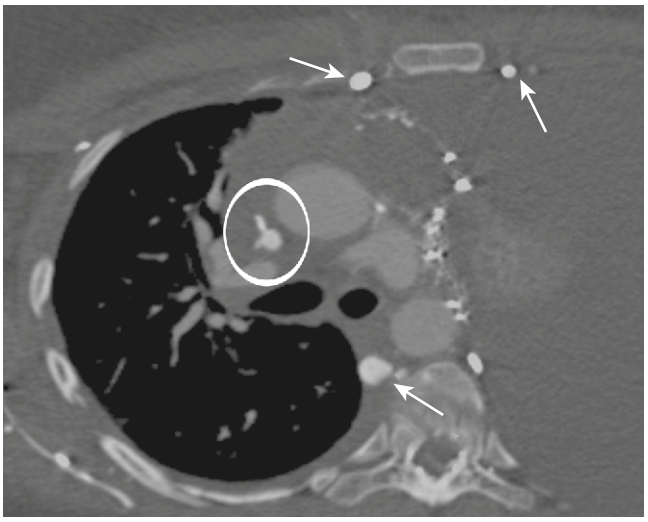


Figure 8-12. SVC syndrome: axial and coronal contrast-enhanced CT. Multiple collaterals and dilatation of azygos and internal mammary veins *(arrows)* in a patient with severe SVC narrowing due to tumor mass encasement *(oval)*.

THE THORACIC AORTA

Relevant CT Anatomy

On axial sections, the aorta is generally round and its diameter should gradually taper more distally as vessels branch from its lumen, although there are some notable exceptions that represent normal variants in its size and shape. It is important to be familiar with the appearance of these variants at imaging so that they are not mistaken for disease.

Normal variants of the aortic contour identified on CTA are best recognized on MPR or three-dimensional (3D) images; these include the aortic spindle, ductus diverticulum, branch vessel diverticula, and pseudocoarctation. The aortic spindle is a smooth circumferential bulge below the region of the isthmus, representing normal mild dilatation of the region of the posterior arch. The ductus diverticulum is a focal convex bulge along the anterior undersurface of the aortic isthmus. The obtuse angles it forms with the aorta can be used to help distinguish it from a post-traumatic pseudoaneurysm, which more characteristically forms acute angles with the aortic wall. Branch vessel diverticula show smooth obtuse margins with a branch vessel emanating from the apex of the infundibulum. These too can be mistaken for a post-traumatic pseudoaneurysm at a branch vessel origin. Recognition of these is aided by their tendency to occur in characteristic locations, such as the left subclavian artery and the third right intercostal artery. Pseudocoarctation results from elongation of the aortic arch, which characteristically results in kinking at the site where the aorta is tethered by the ligamentum arteriosum. Aortic wall thickness is best evaluated on axial CT images. Imaging of healthy adults has shown that the aortic wall thickness is less than 1 mm or imperceptible on axial CTA images.

Aneurysm

Thoracic aortic aneurysm is defined as an aortic size that is 50% greater than the expected aortic diameter. However, in practice, a 5-cm axial dimension is most often used since intervention is otherwise rarely considered in the asymptomatic patient. Distal aortic segments should generally be smaller in diameter than more proximal segments except for the previously noted anatomic variants. If this relationship is reversed, aortic monitoring for aneurysm development should be considered. CT can characterize thoracic aneurysms by their location and shape. Three fourths of aortic aneurysms are atherosclerotic in etiology, fusiform in shape, and located in the descending aorta. However, approximately 20% of atherosclerotic aneurysms are saccular, particularly in the arch and descending portions. Incidence of aortic rupture is related to aneurysm size. An important goal for imaging is to provide accurate measurements. Conventional catheter-based aortography underestimates true aortic diameter, as it reflects only the size of the patent lumen and does not include contributions from intraluminal thrombus or mural thickening. CT accurately evaluates aneurysm dimensions, the extent of intralumenal thrombus and mural thickening, the integrity of the aortic wall, and its relationship with contiguous structures. The chapter in this text on vascular emergencies contains a more detailed section on thoracic and abdominal aortic aneurysms and their complications. Thoracic aortic aneurysms carry a high incidence of concomitant abdominal aortic aneurysms such that screening of the abdomen should generally be undertaken with CT or US when thoracic aneurysm is detected.

Infectious Aortitis

An infected aorta, whether normal caliber or aneurysmal, can represent a diagnostic challenge, as patients may be asymptomatic until late stages or may present with nonspecific clinical symptoms. Nearly 50% of infected aneurysms occur in the thoracic or thoracoabdominal aorta, a significantly higher than expected rate given distribution of atherosclerotic aortic aneurysms. More than 90% show a saccular morphology, often lobulated. Early detection by CT can permit intervention before a rapidly progressive course with sepsis and/or rupture. CT reveals subtle periaortic edema, stranding, and fluid in the initial stages. Rim enhancement of periaortic soft tissues followed by disruption or loss of intimal calcifications often precedes aortic enlargement. Close follow-up CT is advised since development of large aneurysms and marked growth have been reported in short intervals. An infected aorta may also maintain a normal caliber. Periaortic gas and gas within the aortic wall are specific findings but are seen in less than 10% of cases. Lack of mural calcification within an aneurysm suggests a nonatherosclerotic etiology and therefore raises greater concern for infection. Nuclear scintigraphy with labeled leukocytes or gallium-67, when correlated with CT findings, can increase confidence in this diagnosis.

Syphilis, a now infrequent cause of infectious aortitis, has a typical course that can be assessed by CT. CT demonstrates enlargement of the aorta, which progresses to an aneurysm formation that most commonly involves the ascending portion or arch. Most syphilitic aneurysms are saccular, but about 25% are fusiform. The pattern of fine and pencil-line dystrophic calcification is characteristically seen. However, this finding is often obscured by thick, irregular, coarse calcifications of secondary atherosclerosis.

Aortic Dissection

Aortic dissection occurs when intravascular blood breaches the intima and dissects within the media of the aortic wall. Imaging is critical for establishing this diagnosis and for guiding medical or surgical intervention. Chest radiography continues to play a role in the initial assessment of patients with suspected aortic dissection, principally because it provides readily available diagnostic information that helps to exclude other differential considerations (e.g., pneumothorax). Its value is otherwise limited, since a normal CXR cannot exclude, nor can an abnormal CXR confirm, aortic dissection. Findings of aortic and/or mediastinal widening lack specificity and require further evaluation with cross-sectional imaging, while up to 25% of dissection cases will appear normal at radiography. Patients for whom radiography provides insufficient alternate explanation of their symptoms and for whom aortic dissection remains a diagnostic consideration must undergo cross-sectional imaging to exclude dissection.

CT, MRI, and transesophageal echo (TEE) have all been utilized for the diagnosis of acute dissection. CT compares well with MRI and TEE. Although all three modalities were reported to have 100% sensitivity, specificity was highest for CT at 100%. Aortography has a sensitivity of only 88% with false negative diagnoses often related to thrombosed or faint opacification of the false lumen, equal opacification of true and false lumen, unusual intimal tears, and intimal tears proximal to the catheter tip. When CT findings were directly compared with surgical findings, Yoshida found 100% accuracy, sensitivity, and specificity for CT. CT was also effective in identifying the entry site of the intimal tear, as well as determining whether there was pericardial effusion or aortic arch involvement, with 95% sensitivity and 100% specificity as confirmed with surgical results. The advantage of CT in aortic arch involvement has also been confirmed by Sommer, who found a sensitivity/specificity of 93%/97% for CT, compared with 60%/85% for TEE and 67%/88% for MRI.

The principal criterion for CT diagnosis of aortic dissection is the presence of an intimomedial flap separating the true lumen from the false lumen. After intravenous contrast administration, the false lumen may opacify completely, partially, or, if thrombosed, not at all. An intimal flap was identified in 70% of conventional CT studies but has been reported in 100% of volumetric CT studies. Secondary findings, which are less specific but may be helpful in equivocal cases, include displacement of intimal calcifications toward the lumen, aortic widening, and mediastinal and pleural hemorrhage. Calcification of neointimized mural thrombus can occasionally mimic displaced intimal calcifications and lead to false positive diagnosis if not recognized.

CT reliably classifies dissections as either type A or type B (Fig. 8-13; see also Fig. 8-10), the principal criterion for determining surgical (type A) versus medical (type B) intervention. In addition, CTA has been shown to reliably differentiate the true from false lumen. Distinguishing the true from false lumen had been less important with conventional surgical therapy but has since become critical for endovascular management. The false lumen is usually located in the right anterolateral position of the ascending aorta, the superior aspect of the arch, and the left lateral position of the descending aorta. However, the configuration of aortic dissection can be quite variable. The most reliable imaging criteria are identifying the continuity of the true lumen with the undissected portion of the normal aorta either proximally or distally, and identifying the false lumen's termination into a blind sac. Establishing continuity can be more difficult for dissections that involve the aortic root, originate at the aortic arch, or involve the entire aorta. Lepage found that an acute angle between the dissection flap and outer wall on an axial CT image (the "beak" sign) and a larger luminal cross-sectional area were the two most useful indicators of the false lumen for both acute and chronic dissections as they were both sensitive and specific. The false lumen can be filled with either contrast-enhanced blood or thrombus. "Cobwebs," which represent thin radiolucent filling defects attached to the aortic wall, are also highly specific for the false lumen but are seen infrequently. Outer wall calcifications are useful for indicating the true lumen in acute dissection but are unreliable in chronic dissection since neointima within a false lumen may calcify. While the direction of flap curvature is not a useful indicator, direct visualization of intimomedial rupture, seen as intimal discontinuity, evaginating intraluminal flap, and communication of the two lumina, reliably identifies the direction of entrance tear and differentiates true from false lumen. Identification of the tear site is important since both surgical and endovascular treatment aim to occlude the tear and induce thrombosis of the false lumen. In patients with aortic arch involvement, one lumen often spirals around the other, resulting in the appearance of three lumens on an axial CT image. The inner lumen invariably represents the true lumen. Enhanced CT typically shows either isodensity or hyperdensity of the true lumen (see Fig. 8-13).

Periodic imaging of patients with dissection is important regardless of prior surgery. A notable advantage of CT is the detection and characterization of thoracic and abdominal complications. Irregularity of the aortic wall, extravasation of contrast, and hyperattenuating pleural collections may indicate aortic rupture. Retrograde and anterograde extension of the dissection can be readily recognized when compared with prior studies. Chronic dissections should be closely monitored for aneurysmal formation, which occurs in about one third of cases. These aneurysms are prone to rupture and are the most frequent cause of late death.

Type A complications include intrapericardial rupture causing tamponade and great vessel or coronary artery involvement; CT can readily identify these (see Fig. 8-13). With ECG-gated MDCT, coronary and cerebral perfusion can be evaluated using the same contrast bolus. Moreover, ECG-gated MDCT permits dynamic imaging of the left ventricular outflow tract and assessment of aortic valve regurgitation. Further imaging to include an abdominal CTA may also be useful as a predictor of postoperative death in acute aortic dissection. The number of abdominal organs demonstrating decreased parenchymal enhancement was shown to be a strong factor in outcome for patients with acute aortic dissection, whereas the number of dissected branches was not a factor in postoperative death.

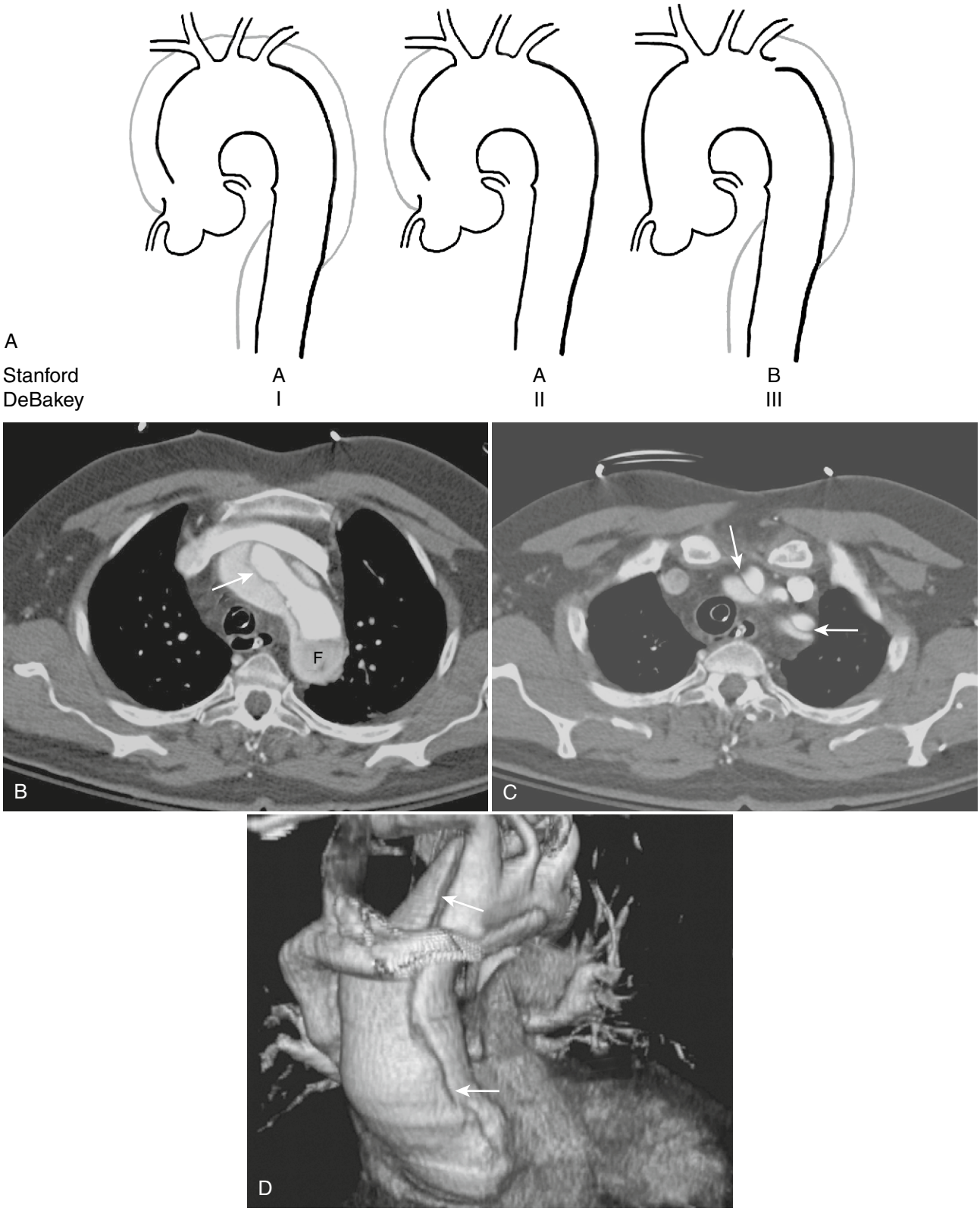


Figure 8-13. Aortic dissection. **A,** Diagram of Stanford aortic dissection classification. Type A dissections involve the ascending aorta, while type B dissections involve the descending aorta only. Although no longer in common clinical use, the older DeBakey classification scheme is included for reference. **B,** Image is of the patient shown in Figure 8-10. Axial image at the level of the aortic arch shows an intimal flap *(arrow)*. The false lumen is hypoattenuating as a result of slow flow (F). **C,** Axial image at a level just above the arch shows involvement of the great vessels *(arrows)*. **D,** 3D image with volume rendering clearly reveals extent of dissection *(arrows)*.

Acute Intramural Hematoma

Intramural hematoma (IMH) constitutes 10% to 20% of acute aortic syndromes. Acute IMH may be the result of rupture of the vasa vasorum with hypertension proposed as the most frequent risk factor. The clinical presentation of patients with acute IMH is quite similar to other acute aortic syndromes. Therefore, CT has a major role in the initial diagnosis of IMH and in the detection of early (e.g., ulceration, saccular aneurysm, dissection) and late complications (e.g., fusiform aneurysm, rupture).

CT is the study of choice for making the initial diagnosis and has a reported accuracy of 100%. In the acute stage, unenhanced axial images reveal a hyperdense, smooth crescentic collection located eccentrically in the aortic wall, often without significant narrowing of the adjacent aortic lumen (Fig. 8-14). CT shows the IMH to have a constant circumferential relationship with the aortic wall rather than the spiraling configuration of aortic dissection. Internal displacement of intimal calcifications toward the lumen is typically seen. The ascending aorta and proximal descending aorta are most frequently involved. CTA images show no enhancement within the area of the IMH, and typically there is no branch occlusion.

It is important to recognize the potential pitfalls in the diagnosis of IMH. If an unenhanced CT is not obtained, contrast in the aortic lumen can diminish conspicuity and even obscure detection of more subtle IMH on enhanced CTA images (see Fig. 8-14). IMH is not to be confused with mural hematoma, which is often associated with atheromatous plaque or aneurysm and is typically irregular and low in attenuation. The distinction is best appreciated on noncontrast axial CT images where calcifications are frequently a marker of the intima. Mural thrombus layers over the calcified intima, whereas IMH is subintimal in location.

While there has been controversy regarding the prognosis and management of IMH, serial CT scans best identify resolution, progression, and/or complications. CT has documented favorable responses with medical treatment with complete resolution of the hematoma and low complication rates. Other studies have found these lesions to be more

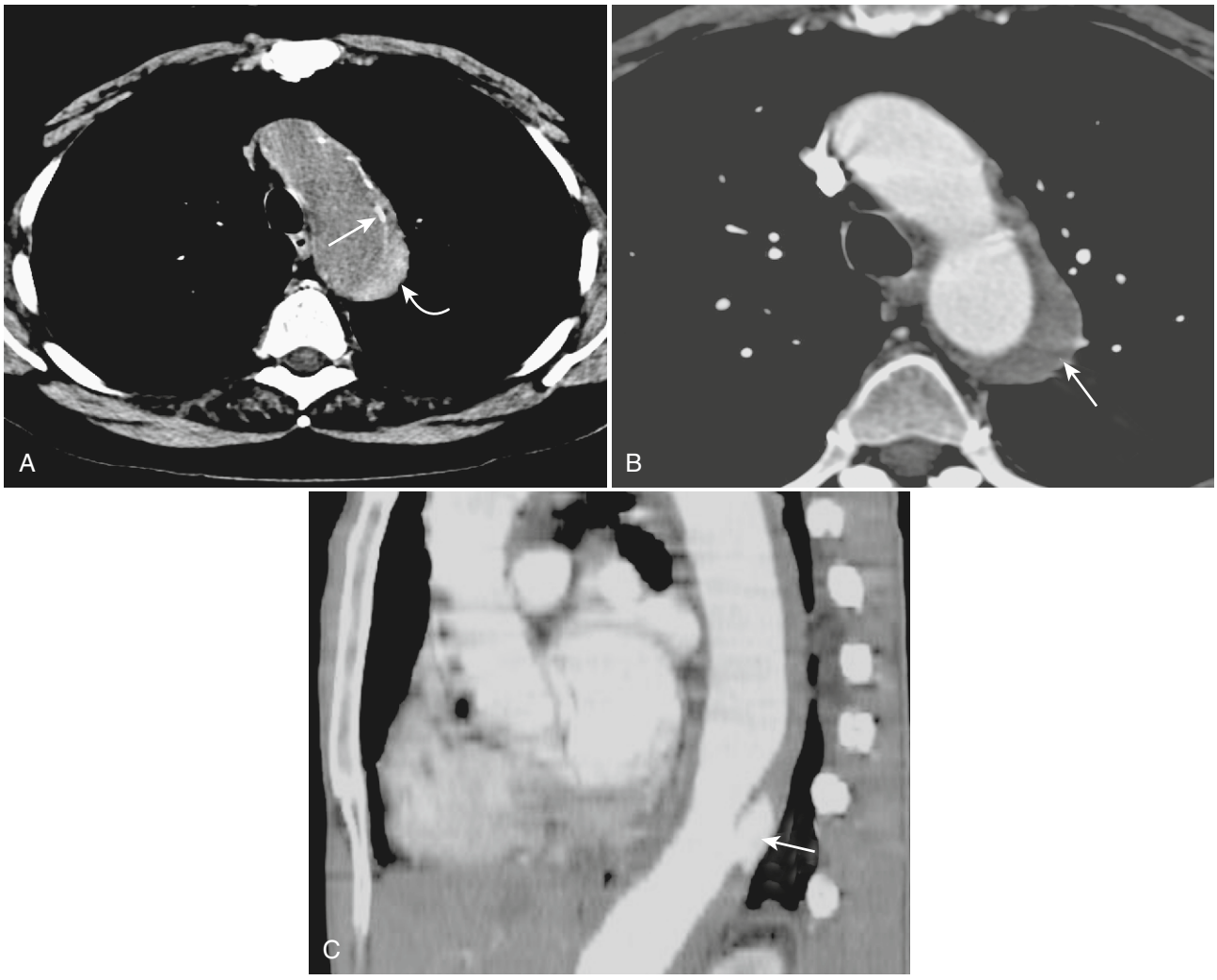


FIGURE 8-14. Intramural hematoma (IMH). **A,** Axial noncontrast image shows an acute IMH as a hyperdense crescentic collection in the distal arch *(curved arrow)* with internal displacement of intimal calcifications *(arrow)*. **B,** Axial CT angiography image shows the decreased conspicuity of the arch hematoma *(arrow)* on contrast-enhanced study. **C,** Sagittal CT angiography image in a patient presenting concomitantly with an IMH and ulcer-like projection *(arrow)* in the distal descending thoracic aorta.

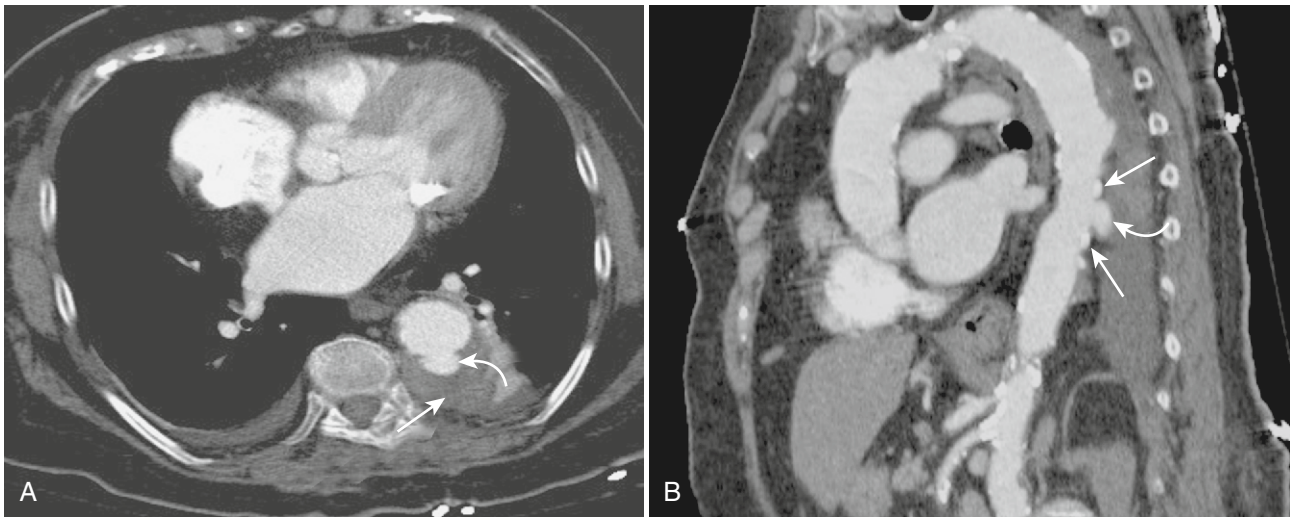


Figure 8-15. Penetrating atherosclerotic ulcer with acute hematoma. **A,** Axial CT angiography image reveals a focal outpouching of an aortic ulcer *(curved arrow)* with adjacent acute hematoma *(arrow)*. **B,** Sagittal reformation shows relationship of ulcer *(curved arrow)* with intimal calcifications *(arrows)* and the typical location and extent of atherosclerosis.

serious than dissection and recommend surgical replacement of the aorta to prevent a high rate of early rupture. For example, a multicenter study demonstrated a 50% complication rate within 30 days of initial presentation consisting of contained rupture, dissection, and aneurysm. The discrepancy seems to be partly related to patient presentation. In patients with acute chest pain, complications are more common, but a benign course is likely in lesions seen incidentally in patients imaged by CT for nonvascular reasons.

IMH is classified as type A or B using the same criteria as the Stanford dissection classification. Location is important in determining prognosis. Type A IMH has been shown more likely to progress to complications such as ulcer, dissection, and aneurysm, whereas IMH localized in the descending thoracic aorta without an associated ulcer demonstrates less frequent complications on CT follow-up. In addition, a maximum aortic diameter greater than 5 cm on the initial CT imaging has been shown to be an independent predictor of progression of type A IMH.

IMH can occur with or without any other aortic abnormality. While most intramural hematomas resolve on follow-up CT, follow-up imaging is still important in the acute stages to assess for the development of ulcers (see Fig. 8-14). Ulcers can lead to saccular aneurysms and, less frequently, to overt dissection. Expansion of the hematoma may be a sign of impending rupture and is readily identified by CT. Although many cases of IMH not associated with ulcer have a stable early radiographic and clinical course, long-term follow-up may be indicated since fusiform aneurysm formation can be a common late complication in these patients.

Ulcerlike Diseases

There is some controversy in the literature regarding nomenclature and clinical significance of aortic ulcers identified radiographically. Stanson first described a penetrating atherosclerotic ulcer (PAU) as a distinct entity from dissection and aneurysm, and defined it as an ulcerating atherosclerotic lesion that penetrates the internal elastic lamina allowing for hematoma formation within the media of the aortic wall. The principal CT characteristics (Fig. 8-15) seen in nearly all patients include advanced atherosclerotic disease of the thoracic aorta and a focal ulcer with adjacent subintimal hematoma beneath a frequently calcified and inwardly displaced intima. Clinical presentation varies from asymptomatic to acute chest pain similar to aortic dissection. Location can be helpful, since most cases of PAU are identified in the middle and distal thirds of the descending thoracic aorta, compared with type B dissection, which involves the proximal descending thoracic aorta.

Ulcerlike lesions that occur in the setting of IMH (see Fig. 8-14) are likely distinct from penetrating atherosclerotic ulcers and tend to have a more aggressive course. CT identifies these ulcerlike projections (ULPs) along with or following the resolution of acute IMH in patients typically presenting with chest pain. As opposed to PAUs, ULPs are located predominantly in the ascending aorta, distal aortic arch, and proximal descending thoracic aorta.

Regardless of ulcer classification, clinical presentation is the most important factor in patient management. Incidentally identified ulcers have shown a generally benign course, while those initially diagnosed in symptomatic patients show an unpredictable course with frequent clinical and radiographic progression. Because neither the presence nor absence of subsequent clinical symptoms in an initially symptomatic patient is a reliable predictor of clinical course, serial CT is recommended to document resolution.

While multiple studies have reported similar initial CT characteristics during the acute stage of the ulcer regardless of clinical outcome, serial CT findings determine progression and help determine whether patients should be managed conservatively or surgically. For example, interval change in ulcer size and morphology can be helpful in prognosis. Ulcers that demonstrate a diameter of greater than 20 mm and depth of greater than 10 mm have a very high risk of progression. In the early follow-up period,

CT identifies frequent progression of ascending aorta and arch ULPs to saccular aneurysm formation, rupture, and dissection. Aneurysms that develop from incorporation of the ulcer into the aortic lumen are further characterized by a faster than average growth rate. Overt aortic dissection generally occurs within the first month of follow-up, and a 38% rupture rate has been reported during the initial hospital admission. Finally, the presence and interval increase of pleural effusions on serial CT have been found to be an independent factor for clinical and radiographic progression.

Postoperative Thoracic Aorta

Grafts, and, more recently, stents, can be used for thoracic aortic surgical repair. Two widely performed techniques utilize prosthetic grafts or homografts for thoracic aortic repair or replacement. In the interposition graft technique, there is total excision of the diseased segment of native aorta with graft anastomoses to the proximal and distal excision sites. The inclusion graft technique implies closure of the remaining diseased aorta around the graft, thus creating a potential space between the graft and the native aortic wall that can contain thrombus, flowing blood, or both.

Normal Graft Postoperative Findings

Quint conducted a study on 235 CT studies on 114 patients to describe the normal postoperative appearance of thoracic aortic interposition grafts on serial CT studies. Low-density material surrounding or adjacent to the aortic graft (including anterior mediastinum for ascending grafts and extrapleural for descending grafts) was noted in a large number of patients for months to several years after surgery. The volume of material decreased over time in many patients, while in others it remained unchanged, possibly representing hematoma that evolved into fibrous tissue. The presence of such material on postoperative CT studies should be confirmed to be of low density and should not be mistaken for evidence of leak or infection.

In aortic graft interposition, felt strips are used to buttress the anastomosis in patients with dissection or other disease of the aortic wall. Felt pledgets are often used to repair the bypass cannulation site in the native aorta and the air evacuation needle site in the graft. Potential pitfalls can occur with felt strips and felt pledgets, as these high-density structures simulate contrast material or contained leak. Knowledge of the operative material used and routine initial noncontrast CT can assist in avoiding these potential pitfalls. Furthermore, the high density of the felt strips helps to readily detect the anastomotic site on CT.

Another potential pitfall lies in the variable appearances of coronary artery anastomoses after aortic arch reconstruction. The coronary artery grafts may be anastomosed with a button of native aortic root, which when conspicuous can simulate a pseudoaneurysm at the proximal graft anastomosis. Total arch replacement with re-implantation of the head and neck vessels into the graft can also result in complex appearances on enhanced CT. In cases of type A dissection repair, small outpouchings at the anastomotic site are identified and develop when there is a perfused false lumen distal to the anastomotic site. Another postoperative appearance that should be recognized occurs when a stage 1 "elephant trunk" technique is performed to replace the ascending aorta and arch in patients with diffuse aneurysmal processes. The presence of a free segment of graft material projecting into the proximal descending aorta identifies patients who may require subsequent repair of the descending aorta.

Rofsky described the normal postoperative CT and MRI appearance in 34 patients after undergoing continuous-suture graft-inclusion technique for repair of aortic aneurysms and dissection involving the ascending aorta. Perigraft thickening was noted in 33% of CT studies, best seen on axial images. The perigraft thickening was symmetric with a concentric distribution around the graft. Thrombi within and outside the wrap were detected in 24% of the cases with CT. Mass effect on the graft was seen in 13% of the CT studies, mostly in cases with coexistent perigraft flow. There was no evidence of clinical compromise on the basis of follow-up examination. In patients with aortic dissection repair, 40% of CT studies demonstrated an intimal flap distal to the graft, and 40% of the studies showed extension of the dissection to the great vessels.

In aneurysm repair, the length of the graft does not always match the extent of the aneurysm, with persistent dilatation of the remaining native aorta. With chronic dissection repair, a double-channel aorta distal to the site of repair is an expected finding and is deliberately preserved to ensure perfusion of those organs dependent on the false lumen for their blood supply.

Graft Complications

CT can identify important early mediastinal complications related to the grafting procedure, such as mediastinal abscess, anastomotic dehiscence, or postoperative bleeding. Delayed complications detected by CT include anastomotic dehiscence and leakage, pseudoaneurysm formation (Fig. 8-16), infection, and new or progressing disease of the native aorta. Paravalvular leaks can also be seen after aortic valve repair.

CT is recognized as the most sensitive method of detecting leak. A leak is confidently diagnosed when contrast extravasation is identified. To avoid pitfalls, an unenhanced scan should be performed in postoperative patients to obtain an unequivocal baseline appearance of postoperative repair for comparison with the contrast-enhanced CTA images. Leak can originate at both the proximal and distal ends of the graft, referred to as perigraft leaks. Leakage at the proximal end of the graft seam predisposes to aortic rupture and underscores the importance of adequate follow-up imaging and early diagnosis.

Pseudoaneurysm formation is a major complication of the graft-interposition techniques resulting from partial dehiscence of one of the suture lines and is not surrounded by any layer of the native aorta. CT is a sensitive method for the diagnosis of anastomotic pseudoaneurysm after aortic reconstruction. A pseudoaneurysm is identified as an outpouching of the graft contour and is usually partially thrombosed. Perigraft flow seen after graft inclusion technique can be considered a "protected" pseudoaneurysm. However, the presence of perigraft flow after interposition techniques is more ominous since there is no jacket of native aorta to confine the flow of blood.

CT should be the first imaging modality performed when there is concern for aortic graft infection due to its

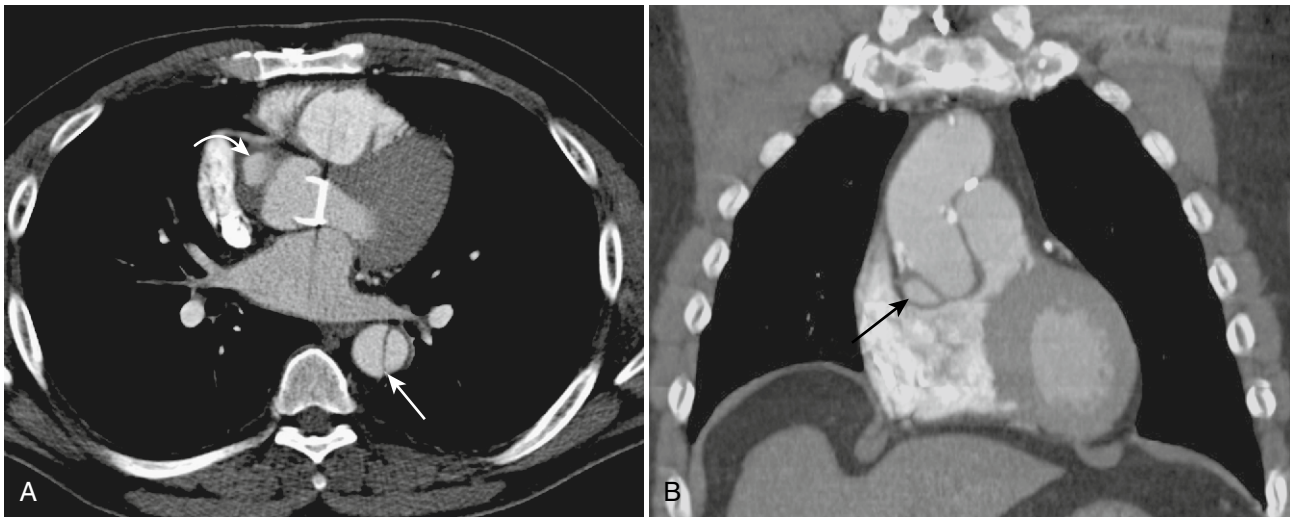


Figure 8-16. Postoperative complications from type A repair. **A,** ECG-gated axial CT angiography image reveals outpouching of contrast *(curved arrow)* consistent with a pseudoaneurysm in the ascending aorta that was not apparent on non-gated images. A dissection flap in the descending aorta is noted *(arrow)*. **B,** Coronal reformatted image better displays the pseudoaneurysm *(arrow)*.

high sensitivity and specificity. However, it can be difficult to distinguish normal postoperative findings from signs of infection in the early postoperative period. It is rare to find perigraft air beyond 1 week after surgery, but many do not consider it pathognomonic of graft infection until 4 to 7 weeks after surgery. Other authors suggest it is definitely abnormal beyond 2 weeks. After the early postoperative period, axial images show a ring of fat density around the graft. Perigraft fluid that persists beyond 6 to 12 weeks after surgery should be considered highly suspicious of infection.

Thoracic Aortic Stent-Grafts

The main goals of endovascular repair, as demonstrated by CT, include absence of flow in the aneurysm sac and cessation of aneurysmal growth. In the immediate post-treatment phase of thoracic aneurysms, slight expansion of the aneurysm diameter, presumably related to inflammatory changes, has been reported in up to 30% of patients. However, aneurysm diameter and volume decrease in 48% to 67%, remain unchanged in *22%*, and mildly increase in 11% to *22%* in the absence of detectable endoleak at 1-year follow-up. After the 1-year follow-up period, diameter and sac volume remain constant in this group. CT volumetric measurements have been shown to be more sensitive and less variable when compared with maximal diameter measurements. Cross-sectional diameter may not accurately reflect all the changes in the shape of thoracic aortic aneurysms, which can have irregular fusiform or bizarre saccular configurations.

In successful endovascular treatment of dissection, CTA immediately demonstrates an obliteration of the entry tear, excluding flow through the intimal tear and redirecting flow exclusively into the true lumen. Follow-up CT demonstrates an interval decrease in the mean diameter of the false lumen and increase in the caliber of the true lumen. The false lumen also demonstrates partial or complete thrombosis.

Stent-Graft Complications

CTA can accurately identify and classify endoleaks. Five types of endoleaks described include type I, flow around the graft attachment sites (proximal or distal); type II, retrograde flow from side branches into the aneurysmal sac; type III, graft disruption or graft malfunction; type IV, graft leaking or porosity; and type V, endotensive enlargement of the aneurysm sac without a visualized leak. An initial unenhanced scan should be performed to avoid mistaking high-density mineralization or postoperative materials for contrast leakage. A late acquisition is recommended, particularly for detecting type II endoleaks, since retrograde filling of the sac may be apparent only on the delayed phase. In addition, very narrow windows are recommended to detect subtle endoleaks. Interval increase in aneurysm diameter or sac volume can be an indirect sign of an endoleak. Axial CTA images can then confirm the presence and indicate the cause of the endoleak based on the configuration and localization of the leakage in relation to the stent-graft. Type I endoleaks are readily detectable (Fig. 8-17) and can cause a substantial increase in aneurysm size and lead to rupture if undetected or untreated. However, in the early postoperative period, CTA can detect very small type I endoleaks that have a tendency to seal spontaneously. Serial CTA can be used to monitor these cases for persistent leak and associated interval increases in aneurysm dimensions.

Type I endoleaks in thoracic aneurysms have been reported to occur when the proximal neck length is less than 2 cm, emphasizing the importance of accurate initial CT dimensional criteria. Fattori reports that late endoleaks nearly always result from dilatation of the aortic neck, which should be measured on each follow-up CT scan to anticipate potential endoleak. There is usually an interval increase in the proximal and distal neck diameter in the first year of follow-up, but no further increases generally occur afterward. Stent migration is a less common cause of type I leak and is best depicted on orthogonal images.

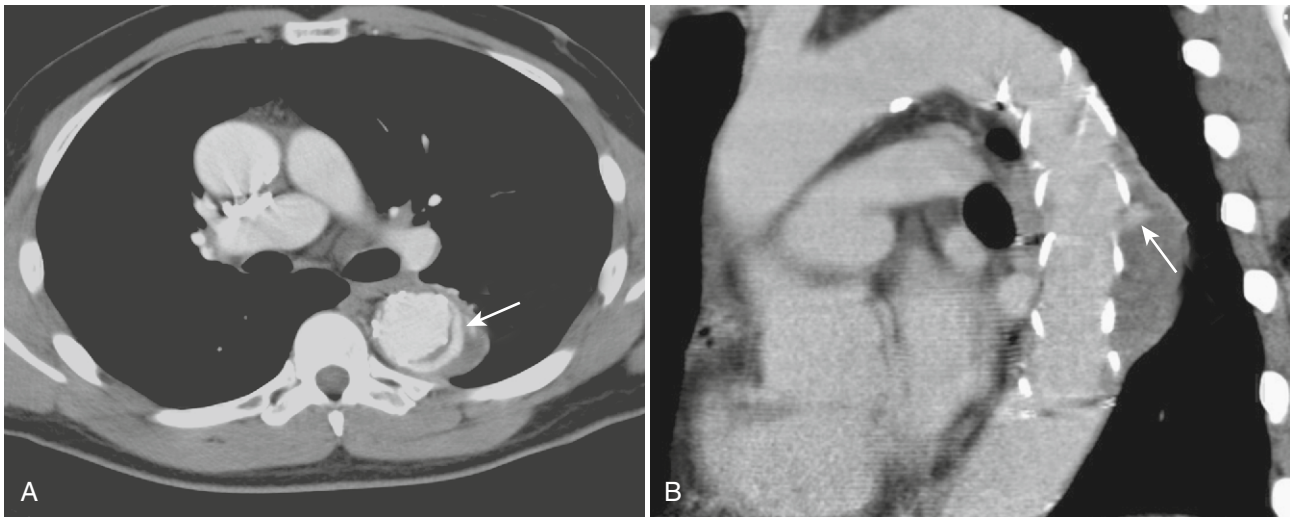


FIGURE 8-17. Type I endoleak after endovascular repair of an enlarging penetrating aortic ulcer. **A,** Axial CT angiography image shows extravasation of contrast adjacent to proximal edge of stent *(arrow)*. **B,** Sagittal reformatted image shows focal area of high density within sac *(arrow)* not present on precontrast images, consistent with leakage.

Type II endoleaks result from an incompletely thrombosed aneurysm sac with retrograde perfusion by a feeding vessel, typically an intercostal artery. Serial CT usually shows spontaneous sealing or no increase in aneurysm dimensions. However, continued CT surveillance is generally recommended because of the potential risk of rapid expansion or rupture.

Thrombosis of the stent-graft can complicate endovascular repair of the aorta. CT identifies partial thrombi within the aortic stent-graft as nonenhancing peripheral circular or semicircular filling defects. Short-interval CT follow-up is warranted, since prognosis varies from interval resolution to complete thrombosis. Shortening in the craniocaudal axis of the treated aneurysm, and, less commonly, stent migration, can result in kinking of the unsupported portion of the graft. MIP and MPR images are superior to axial sections in demonstrating a kink and planning repair.

Additional potential fatal complications identified by CT are dissection and pseudoaneurysm formation. Introduction of the delivery system can cause iatrogenic intimal injury and a resulting false lumen. In endovascular repair of type B dissection, extension of the dissection to the ascending aorta, originating from the proximal uncovered part of the stent-graft, is readily detected by CTA. Pseudoaneurysms at the anastomotic site are rarely seen with endografts but, when present, are often detected far from the free edge of the stent-graft, possibly related to hydraulic stresses or intimal defects associated with deployment.

Assessment of Aortic Coarctation after Surgery

CTA imaging assesses all clinically relevant anatomic features after surgical treatment of aortic coarctation. When directly compared with the imaging findings of catheter angiography and correlated with pressure measurements, CTA was found to be reliable enough to replace catheter angiography in the postoperative care of patients with coarctation. CTA detects subtle findings of stenosis, aneurysms, pouches, and intimal flaps before any clinical complications are manifested (Fig. 8-18). Intramural calcification at the former coarctation site marks the site at risk for potential future dissection and atherosclerotic disease. Detection of such calcification is an advantage of CT over MRI, given the susceptibility artifact usually encountered with the latter. CTA also provides the necessary information for those patients requiring further invasive procedures. Narrowing on 3D images should be further evaluated by systolic pressure gradients directed in the region of morphologic abnormality, thereby decreasing contrast dose and number of projections needed.

IMAGING EVALUATION OF PULMONARY EMBOLISM

Clinical Considerations

Pulmonary embolism (PE) is the third most common acute cardiovascular disease after myocardial infarction and stroke, and is associated with a high mortality rate. The risk of death is particularly high during the acute phase but then decreases over time. Two-week mortality or in-hospital clinical worsening in patients with undiagnosed pulmonary embolism ranges between 25% and 38% versus less than 1% to 20% in the diagnosed and treated patients. Therefore, mortality due to PE can be reduced by prompt diagnosis and treatment in the ED as well as early prognostic stratification and identification of patients at high risk for hemodynamic deterioration.

The difficulty of diagnosing acute PE based on clinical and laboratory findings alone is why imaging studies play such a key role in the diagnostic algorithm for PE evaluation. After a brief review of the epidemiology and pathophysiology of this disease and discussion of relevant clinical findings, the different imaging modalities commonly employed for evaluation are described. Emphasis is given to CT pulmonary angiography, given its clear advantages in the ED setting. The rapid examination time afforded

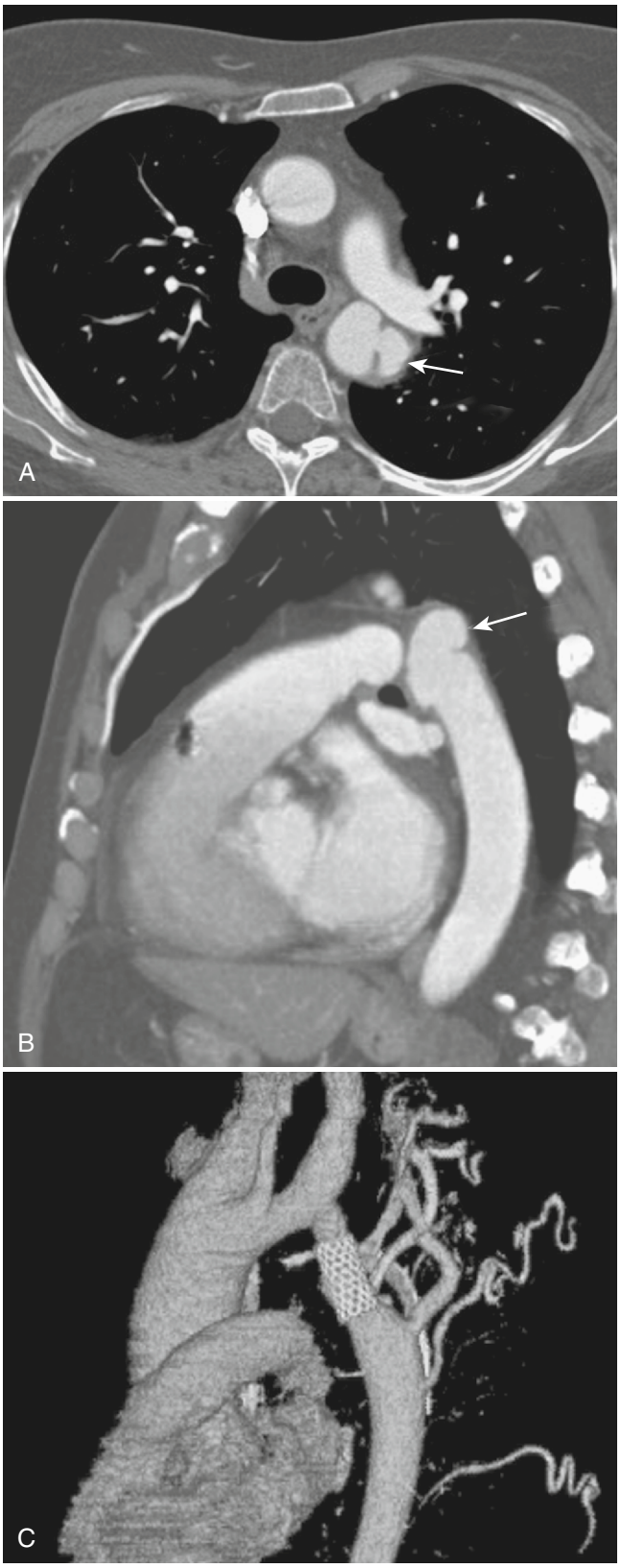


Figure 8-18. Post-coarctation repair. **A,** Axial CT angiography image in a patient presenting with blood pressure discrepancy between the upper and lower extremities after surgical repair revealed a focal bulge in the descending thoracic aorta *(arrow)*. **B,** Parasagittal reformatted image more clearly reveals a postoperative pseudoaneurysm *(arrow)*. **C,** Example of 3D volume rendering after endovascular stent placement in another patient shows no complication.

by CT, its widespread availability, and, perhaps most importantly, its accuracy in evaluation of PE and a host of additional thoracic abnormalities all make it the imaging exam of choice.

Epidemiology

The incidence of venous thromboembolism (both deep venous thrombosis and pulmonary embolism) increases exponentially with age for both men and women. Incidence rates are somewhat higher in women of childbearing age, whereas, after the age of 45 years, incidence rates are generally higher for men. Venous thromboembolism (VTE) recurs frequently; about 30% of patients develop recurrence within the next 10 years. The hazard of recurrence is highest within the first 6 to 12 months.

Independent risk factors include patient age, surgery, trauma, hospital or nursing home confinement, active malignancy with or without concurrent chemotherapy, central vein catheterization or transvenous pacemaker, prior superficial vein thrombosis, varicose veins, and neurological disease with extremity paresis. Among women, additional risk factors include oral contraceptive use, hormone therapy, pregnancy, and the postpartum period.

Pathophysiology

Thrombi present in the deep veins of the upper and, more commonly, lower extremities may dislodge and embolize to the pulmonary arteries. The resultant pulmonary arterial obstruction increases the pulmonary vascular resistance and induce, the release of vasoactive agents such as serotonin by platelets. The alveolar dead space is increased and impairs gas exchange. As right ventricular afterload and pressure increase, right ventricle failure may result. Paradoxical embolism can occur in the presence of a patent foramen ovale or atrial septal defect. Pulmonary emboli are often multiple and have a predilection for the lower lobes, likely related to increased pulmonary blood flow to the lung bases. Only a minority of pulmonary emboli result in lung infarction because of the bronchial arterial collateral circulation.

Clinical Findings

Objective assessment of the clinical probability of PE should be made prior to imaging. Examples of indices used include the Wells and Geneva scores. The PIOPED II investigators have published recommendations regarding the diagnostic pathways for PE. A normal D-dimer in a patient with a low or moderate probability of PE by clinical assessment requires no further testing. If there is high probability by clinical assessment, further testing is needed regardless of the D-dimer results. If the pulmonary CT angiography is negative and CT venography was not performed or was technically inadequa te, venous US or MR venography is recommended. If the pulmonary CT angiography and CT venography are negative, other options include serial venous US, pulmonary digital subtraction angiography, and pulmonary scintigraphy. If the D-dimer is abnormal, the majority of the PIOPED investigators preferred the combination of

CT pulmonary angiography and CT venography. However, patient radiation dose is always a concern; thus, in younger and female patients, venous US should be considered as an alternative to CT venography. In patients with severe allergy to iodinated contrast material, pulmonary scintigraphy may be a useful alternative. Other options include serial venous US examinations, CT pulmonary angiography with gadolinium, or MR pulmonary angiography with gadolinium. In patients with impaired renal function, venous US is recommended. If negative, then pulmonary scintigraphy should be performed. In pregnant patients, although often positive, D dimer testing should still be performed. If the D dimer is positive, venous US is recommended. If the US is negative, most of the PIOPED II investigators recommend pulmonary scintigraphy over CT pulmonary angiography, although some studies indicate that the absorbed dose to the fetus is less with CT pulmonary angiography than with a perfusion scan.

Imaging Techniques

The following paragraphs discuss the imaging techniques for pulmonary embolism (Box 8-1).

Chest Radiograph

Although the chest radiograph is a poor predictor of PE, it remains one of the initial steps in the work-up of ED patients presenting with chest pain and for whom there is clinical suspicion for PE. It can be diagnostic of other causes for patients' presenting symptoms mimicking PE such as pneumothorax, pneumonia, and pulmonary edema. Chest radiography plays an essential role if a ventilation-perfusion scan is chosen as the imaging modality to confirm or exclude PE.

In the observations from the PIOPED study, the most common radiographic findings in patients with PE were atelectasis and/or parenchymal areas of increased opacity in the lower lung zones and pleural effusions. A negative chest radiograph had a negative predictive value of only 74%. Although infrequently observed, some CXR findings have been described as more suggestive of PE. The Hampton sign refers to a well-defined pleural-based area of increased opacity with a convex medial border, and relates to pulmonary infarction. It can help to differentiate pulmonary infarct from pleural thickening or effusion (Fig. 8-19). The Westermark sign refers to an area of oligemia distal to a large vessel that is occluded by PE. In the PIOPED study, oligemia was relatively uncommon but a highly specific radiographic finding for prediction of PE at angiography. The Fleischner sign refers to a prominent central artery, caused either by pulmonary hypertension secondary to peripheral emboli or by distention of the vessel by a large clot (Fig. 8-20). However, the PIOPED study concluded that there were no differences between patients with PE and those without PE in regard to most chest radiographic findings. Thus, the chest radiograph cannot exclude or confirm the presence of PE. It is most useful for detecting alternate chest pathologies and as a correlate exam for a ventilation-perfusion exam.

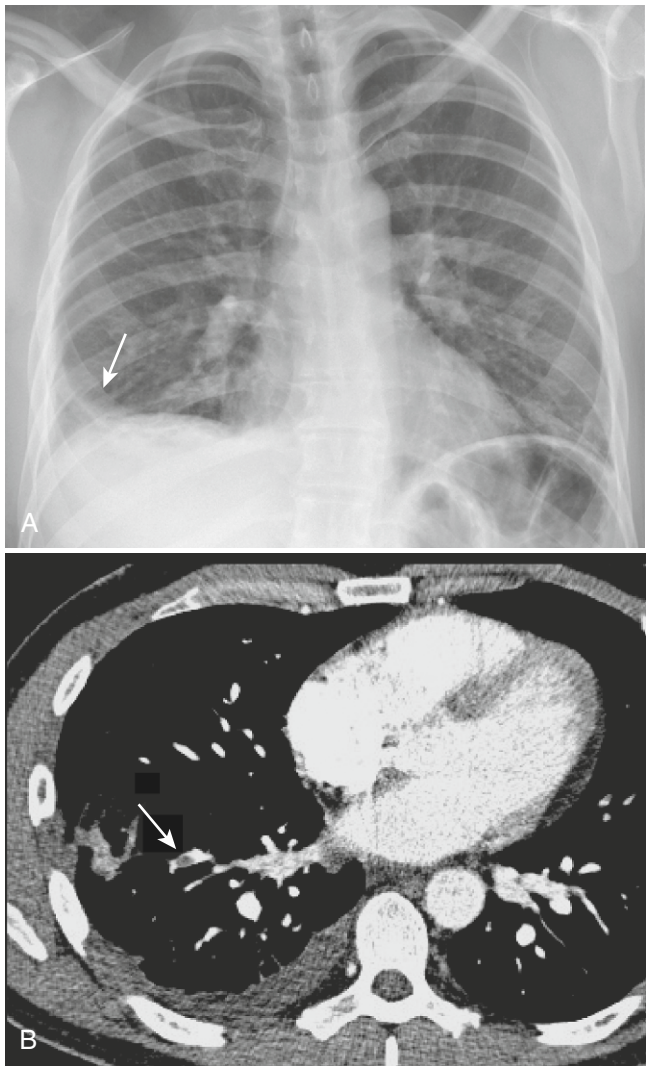


FIGURE 8-19. Atelectasis versus infarcts (Hampton sign). **A,** Posteroanterior view of the chest shows right base peripheral opacities *(arrow)* and a small right pleural effusion. **B,** Contrast-enhanced CT reveals segmental and subsegmental filling defects *(arrow)* in the right lower lobe.

BOX 8-1 Pulmonary Imaging Techniques

1. Chest radiograph (CXR)
2. Ventilation-perfusion scan (VQ)
3. CT pulmonary angiography (CTPA) and CT venography (CTV)
4. MR pulmonary angiography (MRPA) and MR venography (MRV)
5. Conventional pulmonary angiography (PAgram)

Ventilation-Perfusion Scan

Ventilation-perfusion (VQ) scan is often the second modality of choice when pulmonary embolism is suspected. Data from the PIOPED study showed that although it has a very high sensitivity (98%), the specificity is very low (10%). Technetium 99m macroaggregate albumin (MAA) is the radiopharmaceutical agent used for pulmonary

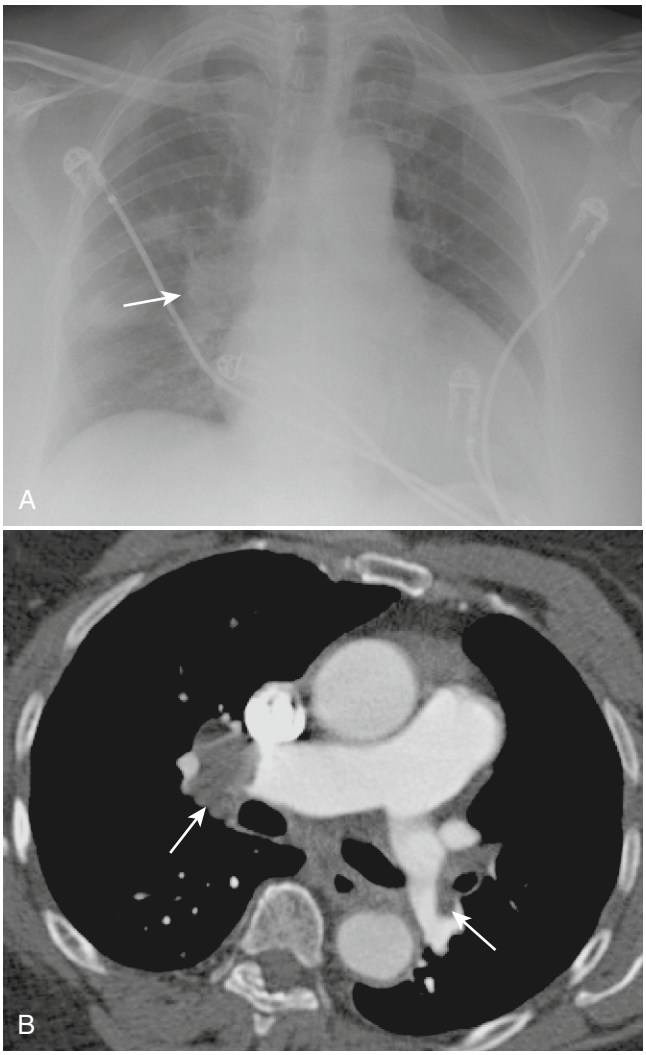


FIGURE 8-20. Fleischner sign. **A,** Portable film showing an asymmetrically enlarged right pulmonary artery *(arrow)*. **B,** Contrast-enhanced CT shows bilateral pulmonary emboli with large clot in the right pulmonary artery *(arrow)*.

BOX 8-2 **Revised PIOPED Ventilation-Perfusion Scan Criteria**

HIGH PROBABILITY (≥80%)
≥2 large mismatched segmental perfusion defects or the arithmetic equivalent in moderate or large plus moderate defects*

INTERMEDIATE PROBABILITY (20%–70%)
One moderate to two large mismatched segmental perfusion defects or the arithmetic equivalent in moderate or large plus moderate defects*
Single matched ventilation-perfusion defect with clear chest radiograph†
Difficult to categorize as low or high, or not described as low or high

LOW PROBABILITY (≤19%)
Nonsegmental perfusion defects (e.g., cardiomegaly, enlarged aorta, enlarged hila, elevated diaphragm)
Any perfusion defect with a substantially larger chest radiographic abnormality
Perfusion defects matched by ventilation abnormality† provided that there is (1) a clear chest radiograph and (2) some areas of normal perfusion in the lungs
Any number of small perfusion defects with a normal radiograph

NORMAL
No perfusion defects or perfusion outlines exactly the shape of the lungs seen on the chest radiograph (note that hilar and aortic impressions may be seen and the chest radiograph and/or ventilation study may be abnormal)

*Two large mismatched perfusion defects are borderline for "high probability." Individual readers may correctly interpret individual scans with this pattern as "high probability." In general, it is recommended that more than this degree of mismatch be present for the "high probability" category.
†Very extensive matched defects can be categorized as "low probability." Single VQ matches are borderline for "low probability" and thus should be categorized as "intermediate" in most circumstances by most readers, although individual readers may correctly interpret individual scans with this pattern as "low probability."
From Gottschalk A, Sostman HD, Coleman RE, et al: Ventilation-perfusion scintigraphy in the PIOPED study. Part II: Evaluation of the scintigraphic criteria and interpretations. J Nucl Med 34:1119–1126, 1993. Reprinted with permission.

perfusion, and it is injected intravenously with the patient in a supine position. If the perfusion images and the chest film are normal, the study is of low probability and the exam may be concluded. Otherwise, ventilation imaging is performed with xenon 133. The scintigraphic hallmark of pulmonary embolism is a perfusion defect corresponding to a bronchopulmonary segment that displays normal ventilation and with no correlating abnormality in the chest film. The modified PIOPED criteria are used for interpretation, determining if the study is normal, and determining if it is of low, intermediate, or high probability (Box 8-2). This subject is discussed in depth in *Nuclear Medicine: The Requisites* and in Chapter 12.

CT Pulmonary Angiography and CT Venography

CT Pulmonary Angiography

In routine practice, CTPA performed on MDCT scanners has become the imaging modality of choice when the diagnosis of PE is suspected. Sensitivities ranging from 53% to 100% and specificities ranging from 83% to 100% have been reported, although these wide ranges are explained mostly by technological improvements over time, most notably the advent of multidetector-row technology for image acquisition, but also the use of picture archival communication system (PACS) for image interpretation. Today, CTPA is considered the "gold standard" for evaluation of PE. The negative predictive value of a normal CTPA study is high, close to 98%, regardless of whether multidetector-row technology was used or underlying lung disease was present. It is therefore a very valuable tool for the evaluation of patients presenting to the ED in whom clinical suspicion for PE warrants imaging.

The benefits of CTPA include evaluation of the lung parenchyma, mediastinal structures, and chest wall, along with direct visualization of pulmonary emboli. Thus, in addition to high accuracy for pulmonary emboli diagnosis, CTPA

can accurately detect numerous alternative or concurrent pathologies such as aortic dissection, pneumothorax, pneumonia, or malignancy. For ED patients who often present with nonspecific chest complaints, this is one of the most compelling benefits of CT, the ability to broadly assess and exclude not just one, but most diagnoses under clinical consideration.

Technical Factors in CTPA. When interpreting a CTPA examination, the quality of the study should be assessed and reported, as it reflects diagnostic confidence. Adequate contrast opacification is essential at all levels of the pulmonary arterial tree (Fig. 8-21). If the entirety of the pulmonary arterial tree is not well opacified, one cannot state to which level of the pulmonary arterial branches one can confidently evaluate for the presence of pulmonary embolism.

A careful and systematic evaluation at the main, segmental, and subsegmental pulmonary arterial branches is required. Volumetric acquisition and multidetector-row technology allow a relatively facile review of hundreds of images by scrolling or cine mode. Appropriate windowing is necessary to optimize emboli detection. With a window width too narrow, small nonocclusive emboli can be obscured. Brink and colleagues suggest a window width equal to the measured mean attenuation of the enhanced main pulmonary artery plus two standard deviations and a window level equal to one half of this value. Varying the window width and level until the pulmonary valve is visualized within the contrast-opacified pulmonary artery is another means of appropriate window/level selection. These modified window settings can increase the conspicuity of artifacts caused by image noise and flow. Evaluation of the pulmonary vessels and bronchi in lung window settings is useful for confirming motion artifact.

Diagnostic Criteria for CTPA. The following CTPA findings are used as diagnostic criteria for acute pulmonary embolism:

1. Complete arterial occlusion by thrombus with lack of enhancement of the lumen, plus or minus enlargement of the vessel (Fig. 8-22**).**
2. Partial filling defect of the vessel surrounded by contrast, the "polo mint" sign if the image is acquired perpendicular to the long axis of the vessel and the "railway track" sign if the image is acquired parallel to the long axis of the vessel (Fig. 8-23).
3. Peripheral intraluminal filling defect that forms acute angles with the arterial wall (Figs. 8-24 and 8-25).

Ancillary findings of acute PE, although not specific, include peripheral wedge-shaped areas suggestive of lung infarct and linear bands.

The CTPA findings used as diagnostic criteria for chronic PE include:

1. Complete occlusion of the vessel (by thrombus) with vessel diameter smaller than adjacent patent vessels.
2. Peripheral, crescent-shaped intralumenal defect that forms obtuse angles with the vessel wall.
3. Contrast-opacified thick-walled vessels (due to recanalization), with affected vessels that may be smaller than adjacent nondiseased vessels.

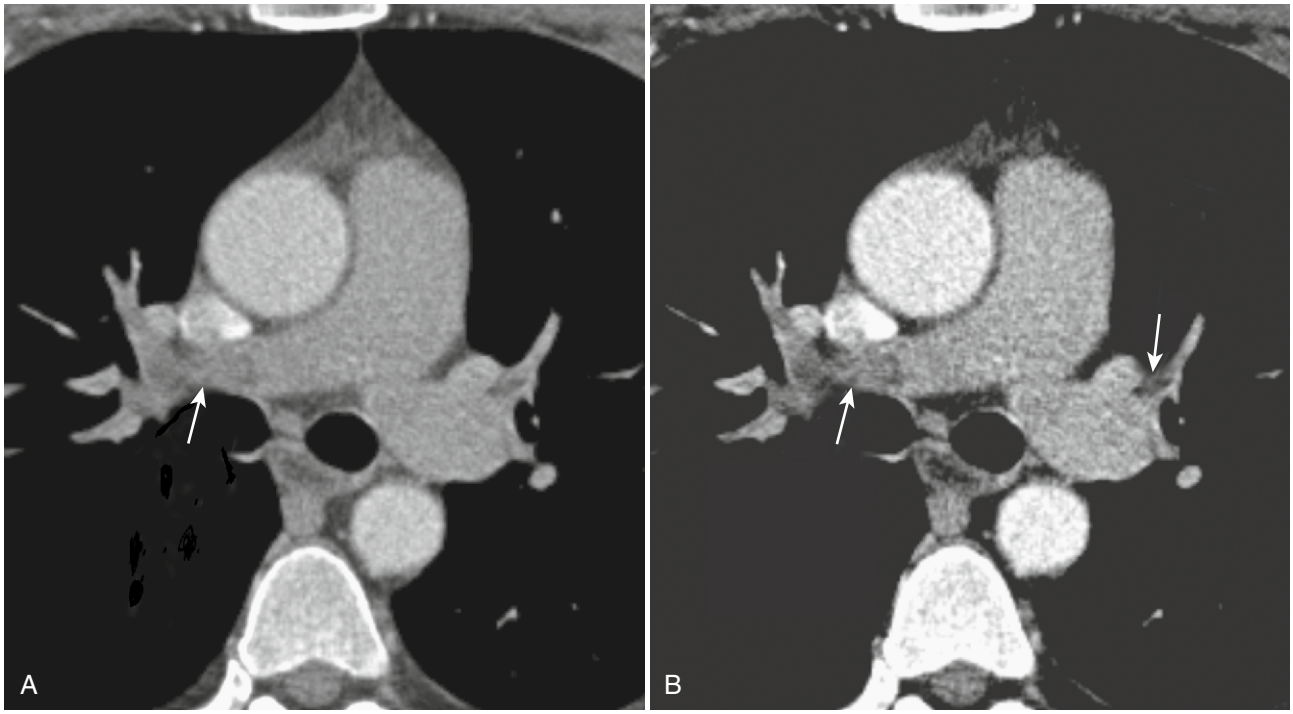


FIGURE 8-21. Poor opacification of the pulmonary arteries due to delayed imaging relative to the contrast bolus enhancement peak. **A,** The aorta is much more densely opacified than the pulmonary artery. Thrombus in the right main pulmonary artery *(arrow)* is difficult to discern. **B,** Using a narrower window improves visualization of the right main pulmonary thrombus *(arrow at left)* as well as a thrombus within the anterior left upper lobe segmental artery *(arrow at right).*

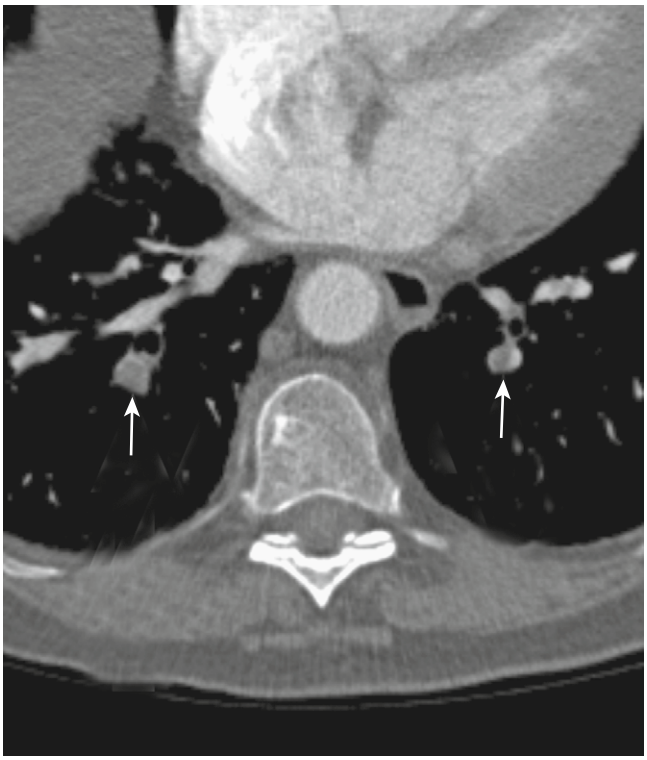


Figure 8-22. Acute pulmonary embolism. A right lower lobe segmental artery reveals complete occlusion by thrombus *(arrow at left)*. This vessel is enlarged compared with the contralateral left lower lobe segmental artery *(arrow at right)*, which also contains a large but nonoccluding thrombus.

4. Web or flap within a contrast-opacified vessel (Fig. 8-26).
5. Extensive bronchial or other systemic collateral vessels.
6. Accompanying mosaic pattern of perfusion of the lung.
7. Calcification within eccentric vessel thickening.

CTPA Interpretation Errors. The interpreting radiologist has to be aware of several artifacts that can occur with CTPA. These potential pitfalls have been divided into three categories: technical, anatomic, and physiological. Knowledge of these pitfalls will improve the radiologist's performance and confidence in the interpretation of CTPA.

Technically related pitfalls include breathing artifacts and suboptimal arterial opacification resulting from an inappropriate scan delay, poor contrast delivery, or contrast extravasation. Knowledge of the bronchovascular segmental anatomy is mandatory to avoid anatomically related pitfalls, such as mistaking a poorly enhanced pulmonary vein for an occluded artery. Segmental arteries are always seen near the accompanying branches of the bronchial tree. Knowledge of the size and location of hilar lymph nodes is of great importance as they can mimic the appearance of pulmonary emboli. Coronal reformations are helpful in avoiding this anatomic pitfall.

The quality of arterial enhancement in CTPA depends highly on the physiologic conditions under which the study is performed. Abnormalities of venous inflow, extrapulmonary shunts, and intrapulmonary shunts can

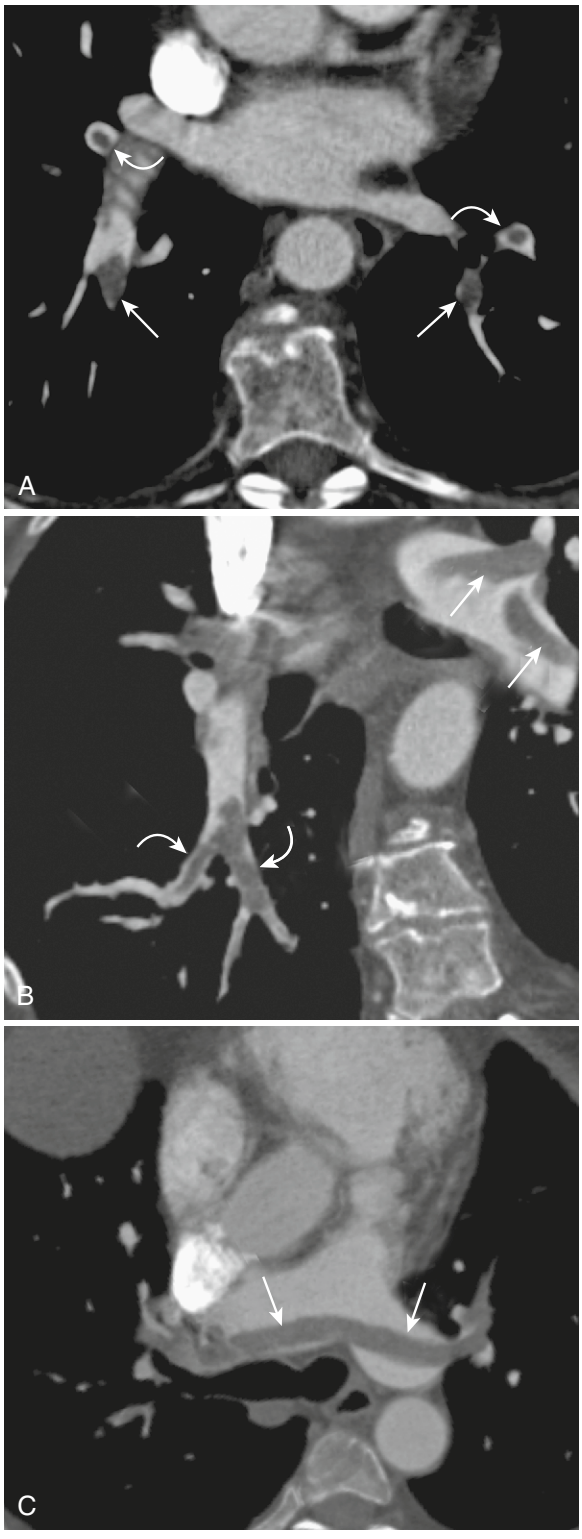


Figure 8-23. Acute pulmonary embolism. **A,** Bilateral lower lobe emboli exhibit the "polo mint" sign *(curved arrows)*. Partial filling defects within the vessels are surrounded by contrast. More occlusive thrombi are seen in nearby arteries *(arrows)*. **B,** Oblique coronal reformatted image of right lower lobe pulmonary embolism showing the "railway track" sign *(curved arrows)*, the longitudinal axis equivalent of the "polo mint" sign. Left-sided emboli are also seen *(arrows)*. **C,** Oblique axial reformatted image showing a "saddle" embolus, right and left main pulmonary emboli straddling the bifurcation *(arrows)*.

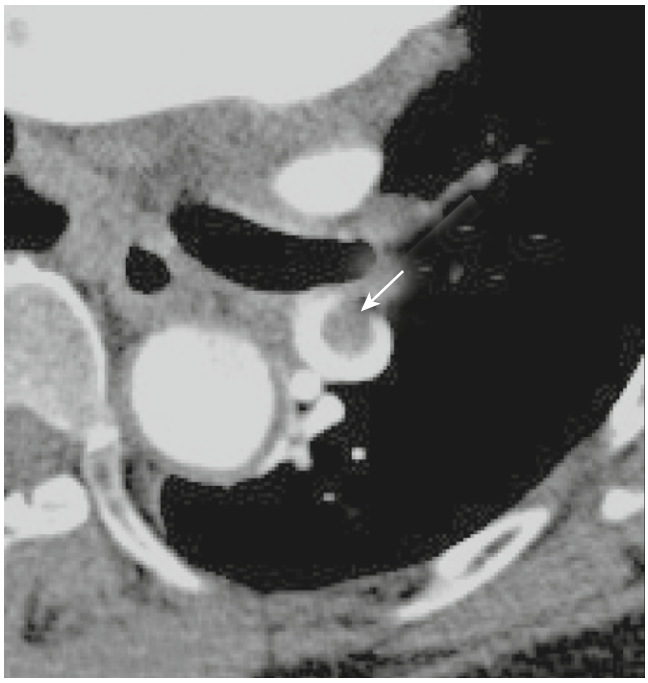


FIGURE 8-24. Acute pulmonary embolism. Axial contrast-enhanced CT image showing an eccentrically positioned partial filling defect in the left interlobar artery *(arrow)*, forming acute angles with the arterial wall.

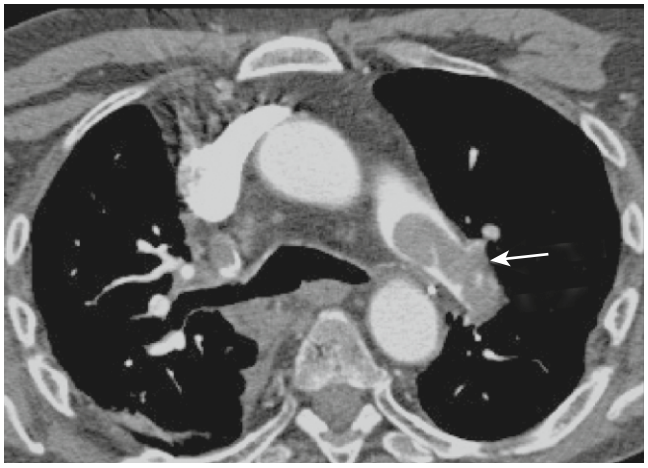


FIGURE 8-25. Acute pulmonary embolism. Axial CT image shows massive clot in the left main pulmonary artery *(arrow)*.

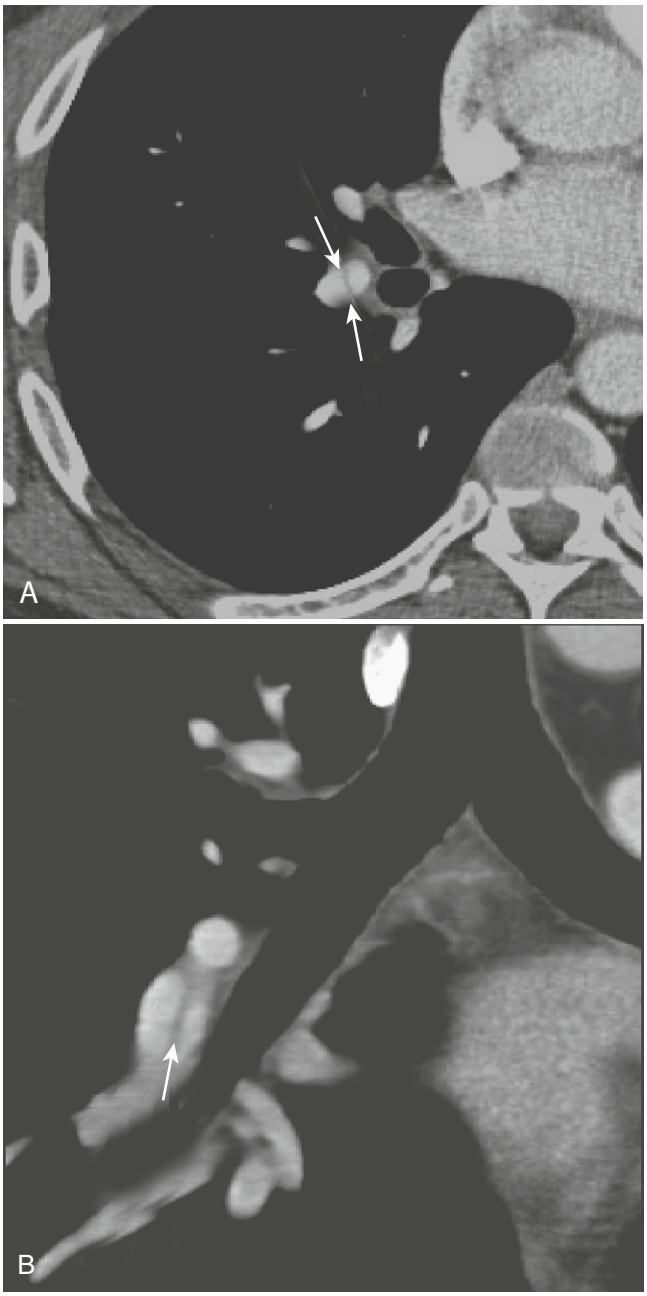


FIGURE 8-26. Chronic puolmonary embolism. **A,** Axial contrast-enhanced CT image shows a linear filling defect in the right interlobar artery *(arrows)* consistent with a web in a patient with prior pulmonary embolism. **B,** Coronal reformation displays the extension of the web *(arrow)*.

adversely influence pulmonary arterial enhancement. Another physiological artifact that may occur is the transient interruption of the contrast column in the pulmonary arteries, a result of increased venous return of unopacified blood from the inferior vena cava. This occurs when negative intrathoracic pressure is generated by inspiratory effort immediately prior to imaging. A variable amount of unopacified blood enters the right atrium, diluting and potentially even disrupting the contrast column. The column of unopacified blood that flows through the pulmonary arteries can simulate pulmonary emboli. Clues to help identify this artifact include lack of opacification in multiple vessels at the same level bilaterally without vascular expansion, and the presence of unopacified blood in the right heart chambers on the preceding images followed by the presence of unopacified blood in the left atrium, ventricle, and aorta on later images. The most common causes for a nondiagnostic CTPA are poor contrast bolus, respiratory motion, and graininess of the images owing to patients' body habitus.

Prognostic Factors for CTPA. Most late deaths in patients diagnosed with PE are due to underlying diseases. However, the main cause of death within 30 days is right ventricular failure. It is therefore important to identify patients at high risk of right ventricular failure in order to establish the appropriate treatment. Thrombolysis,

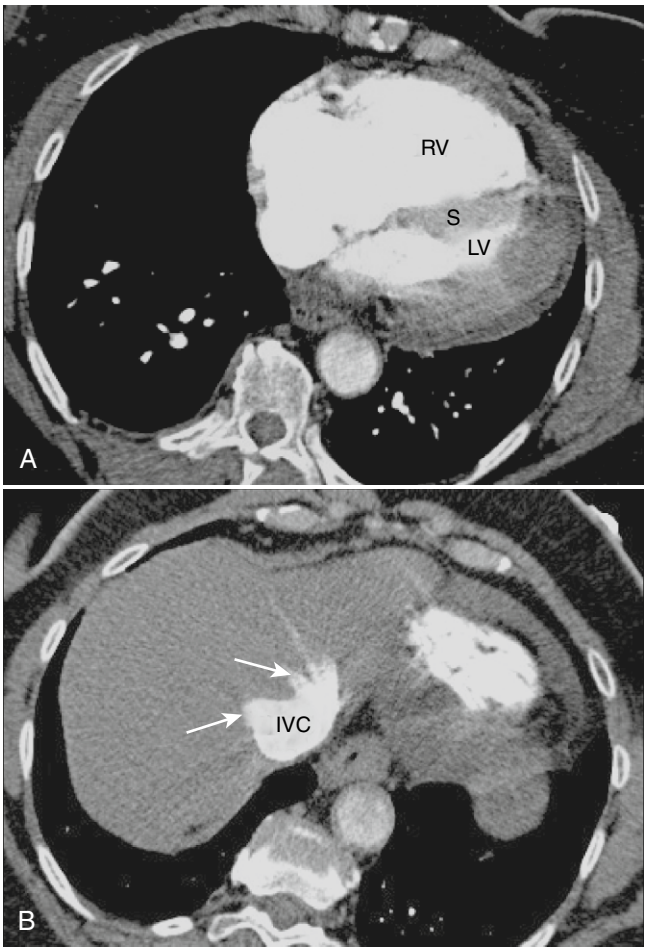


Figure 8-27. Right heart strain in patient with bilateral pulmonary emboli. **A,** Axial CT image showing right ventricle enlargement (RV). Note also straightening or leftward bowing of the interventricular septum (S), with resultant diminutive-appearing left ventricular cavity (LV). **B,** Axial image reveals reflux of contrast into the inferior vena cava (IVC) and hepatic veins *(arrows)*.

catheter intervention, and surgical embolectomy may be performed as adjuncts to anticoagulation and may reverse right ventricular failure and reduce the risk of recurrence and death. With newer-generation scanners, standardized cardiac views can be obtained when performing CTPA. Right ventricle enlargement on a four-chamber view in the setting of acute PE correlates with right ventricle dysfunction by echocardiography (Fig. 8-27). Right ventricle enlargement is present when the ratio of the diameter of the right ventricle to the diameter of the left ventricle is greater than 0.9. Other cardiovascular parameters seen on CTPA have been evaluated as predictors of mortality in patients with severe PE. These include findings such as reflux of contrast into the inferior vena cava, convex leftward bowing of the interventricular septum, and increased diameter of the azygos vein, superior vena cava, and aorta.

CT Venography

Limited lower extremity CT venography (CTV) provides direct imaging of the inferior vena cava, pelvic veins, and lower extremity veins immediately after CTPA with the same contrast bolus. Technical limitations are not uncommon and include poor venous enhancement and streak artifacts from orthopedic hardware. The reported sensitivity and specificity using MDCT are 100% and 97%, respectively.

The drawbacks of combining CTV with CTPA include the higher volume of contrast required to produce adequate vein opacification and the additional radiation exposure to ovaries and testes. Radiation exposure to the gonads can be reduced by starting to scan at the acetabulum. Because of these issues, the value of combining CTV with CTPA is still debated.

MR Pulmonary Angiography and MR Venography

MR pulmonary angiography (MRPA) and MR venography (MRV) are considered second-line diagnostic tools (particularly in the ED) in the evaluation of PE. Practical considerations include their higher cost, limited availability, longer examination times, and reduced performance as compared with MDCT. As technology improves, MR imaging may play a greater role in the evaluation of patients with venous thromboembolic disease, particularly those patients with allergies to iodinated contrast material.

MR Pulmonary Angiography

The routine use of MRPA in the evaluation of pulmonary embolism has been limited by technical and practical factors. Image degradation from respiratory and cardiac motion is common. High spatial resolution is necessary because of the small diameter of the branch vessels of the pulmonary arterial tree. High temporal resolution is required to produce arterial-phase-only images, thus avoiding the pulmonary venous enhancement that can obscure the evaluation of the arteries. MRPA studies are performed during suspended respiration. The timing of the acquisition with respect to the gadolinium-based contrast injection can be crucial if one is to capture the pulmonary arterial phase.

Conventional 3D-gadolinium-enhanced MR angiography (MRA) can be performed by acquiring a single coronal 3D MRA with a large field of view (FOV), encompassing both lungs, using a single dose of gadolinium chelate. To avoid wraparound artifact, the FOV must be large enough to cover the two lungs, along with the arms and shoulders. Another approach is to perform two separate sagittal acquisitions, one for each lung, with smaller FOV and higher spatial resolution during two separate breath-holds and contrast injections. This method has the disadvantage of requiring two separate acquisitions rather than one, and, furthermore, sagittal volumes may not optimally cover the central pulmonary circulation.

Another option for data acquisition is time-resolved MR angiography, an approach that eliminates the need for bolus timing. Using very fast acquisition methods, a time series of 3D images is acquired. One of these 3D datasets is expected to capture the arterial enhancement, while a later dataset captures venous enhancement. This method has higher temporal resolution and lower spatial resolution as compared with conventional 3D-gadolinium-enhanced MRA. Although the spatial resolution of time-resolved 3D MR angiography is less than that of CT pulmonary angiography, confident diagnoses can be made at the main, lobar, and segmental levels.

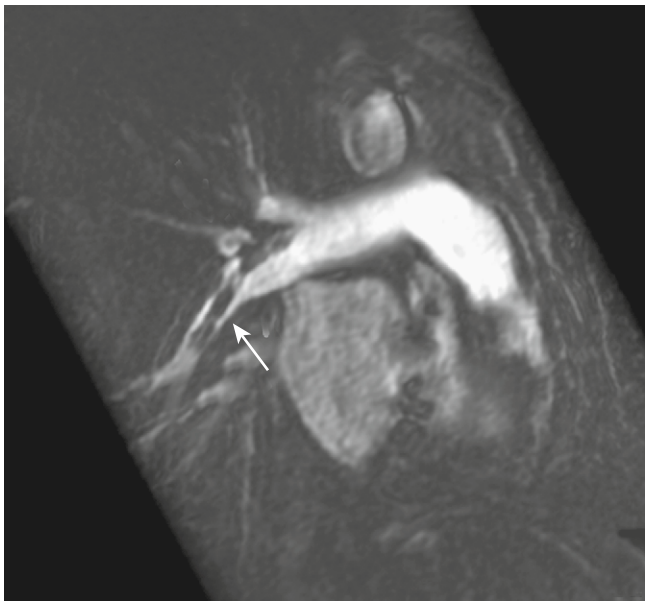


FIGURE 8-28. Acute pulmonary embolism *(arrow)*. A 56-year-old man presented with chest pain and shortness of breath. Axial oblique maximum intensity projection image of 3D dynamic contrast-enhanced MR acquisition.

Emboli are detected as intraluminal filling defects or vascular cutoffs, just as in CTPA (Fig. 8-28). Gupta and colleagues emphasized the need to perform and review overlapping, small, subvolume targeted MIP images, as pulmonary emboli often lodge where abrupt changes in vessel diameter are found; this typically occurs where vessels branch. It may be difficult on single thin coronal sections to tell the difference between a normal bifurcation and a small embolus, and the review of targeted MIP images may help with this distinction. Because there is often some degree of unwanted pulmonary venous opacification, it is useful to obtain larger subvolume MIP images so that vessels can be followed to the hilum, thus allowing the differentiation of arteries and veins. Major drawbacks for pulmonary MRA include cardiac and respiratory motion artifacts, losses of signal in the presence of complex blood flow patterns, and magnetic susceptibility effects from the air-containing lungs.

MR Venography

MRV, like CTV, is clearly superior to venous US in the task of delineating the inferior vena cava and pelvic veins. MRV is significantly more sensitive and accurate than US in the detection of lower extremity thrombosis.

MRV can be performed without intravenous contrast agents, using time-of-flight (TOF) MRA techniques, although gadolinium-enhanced techniques tend to provide faster acquisitions, better signal-to-noise ratio, and greater accuracy in states of slow flow or tortuous venous anatomy. Gadolinium-enhanced MRV is performed as two large FOV coronal two-dimensional (2D) or 3D gradient-echo volumes encompassing deep veins of the abdomen and pelvis, and then the thighs. The reported sensitivity and specificity of the MR venogram in the pelvis and thighs are 100% and 95%, respectively. In the calf, the sensitivity and specificity reported are lower, noted to be 87% and 97%, respectively. The combination of MRA and MRV in a single exam stands up as a strong diagnostic modality in the evaluation of thromboembolic disease.

Conventional Pulmonary Angiography (PAgram)

At most institutions, percutaneous, catheter-based pulmonary angiography has been replaced by CTPA as the standard method of reference for the evaluation of PE. A PAgram is associated with minimal but definite morbidity and mortality, and, thus, many clinicians are reluctant to refer patients for this procedure even when there is diagnostic uncertainty. In the emergency setting, the greater accessibility of MDCT at all times of day, coupled with the added value of a complete assessment of the entire thorax, which includes most relevant differential considerations other than PE, has firmly positioned it as the modality of choice. The criteria for the diagnosis of PE at PAgram are similar to those at CTPA and include the findings of an intravascular filling defect or an abrupt vessel cutoff.

CORONARY CT ANGIOGRAPHY IN THE ED

Evaluation of Chest Pain for Exclusion of Acute Coronary Syndrome

For patients presenting to the ED with chest pain, medical imaging has been established as a primary means of delineating life-threatening entities such as acute aortic syndromes, pulmonary embolism, and pneumothorax. This section defines the emerging role of coronary CT angiography (CCTA) in evaluating ED patients suffering with chest pain potentially due to acute coronary syndrome (ACS), and provides a review of CT-based coronary artery anatomy, anomalies, and findings in coronary disease.

Acute Coronary Syndrome

The American Heart Association defines coronary heart disease (CHD) as a category that includes acute myocardial infarction, other acute ischemic (coronary) heart disease, angina pectoris, atherosclerotic cardiovascular disease, and all other forms of chronic ischemic heart disease. The term *acute coronary syndrome* describes patients who present with either acute myocardial infarction (MI) or unstable angina (UA). Our understanding of coronary artery disease (CAD) continues to evolve.

Conventional, catheter-based coronary angiography allows identification of significantly narrowed coronary arteries, or stenotic "culprit lesions," to which targeted revascularization therapy can be directed. The need for revascularization therapy of a particular culprit lesion should be supported by evidence of myocardial ischemia (using ECG, cardiac biomarkers, perfusion imaging, stress testing, etc.). Treating culprit lesions without supporting evidence of ischemia or symptoms has been coined the "occulostenotic reflex."

More recently, the concept of the "vulnerable plaque" has gained favor; this refers to a soft, inflammatory atherosclerotic plaque with a thin or discontinuous fibrous cap. These are at risk for rupture or thrombosis, which often leads to coronary luminal compromise or occlusion. Due

to positive (outward) remodeling, vulnerable plaques may not be stenotic and may therefore be occult when evaluated by conventional angiography since this visualizes only the patent vessel lumen. This concept, too, is in evolution in that vulnerable plaques are likely numerous rather than solitary, and in that disrupted, unstable, and/or ulcerated plaques extend beyond the culprit lesion. Thus, the concept of a vulnerable plaque may in fact extend further to the concept of a "vulnerable artery" or even a "vulnerable patient."

With the advent of ECG-gated multidetector (and now multisource) CCTA, noninvasive visualization and analysis of the coronary arterial tree/system have become feasible. CCTA has already shown high accuracy in defining significant (greater than 50%) coronary stenoses, as well as the ability to detect soft and calcific plaques. It shows great promise as an ED triage tool that can help identify and discriminate patients with ACS from those with chest pain of other etiologies.

Epidemiology

It is estimated that 15.8 million Americans aged 20 or older suffer from CHD. In 2007 an estimated 700,000 Americans had new coronary attack and about 500,000 will have a recurrent attack. It is estimated that an additional 175,000 silent first heart attacks occur each year, and the subsequent lifetime risk of developing CHD after age 40 is 49% for men and 32% for women.

From 2002 to 2004, the Centers for Disease Control recorded more than 110 million ED visits in the United States, of which approximately 30 million had a primary diagnosis of "injury." Of the remaining 80 million, roughly 7.3 million (approximately 10%) had a primary diagnosis of chest pain (nonspecific), heart disease, or heart attack or other ischemic heart disease. Acute chest pain prompts 6 million patients annually to undergo an ED evaluation in order to exclude ACS.

Clinical Considerations

Triage of patients presenting with acute chest pain is a common task performed in the ED. Clinical findings, EKG changes, and cardiac biomarkers (troponin or CK-MB) are the current standard of care tools used to exclude ACS in these patients. Unfortunately, triage decisions based on these indices are often ineffective. Normal cardiac biomarkers on ED presentation do not exclude ACS, and serial testing at intervals requiring up to 6 to 10 hours of hospital time is necessary to exclude MI. Furthermore, reported rates of missed ACS have ranged from 2% to 8%. Missed ACS carries a twofold increase in mortality and accounts for 20% of ED malpractice dollar losses.

Concern for missing ACS in ED patients with chest pain often prompts admission, or at least prolonged observation and testing (delayed cardiac biomarkers, stress testing, or perfusion imaging) in the ED or an observation unit, of approximately 2.8 million such patients per year in the United States, at a cost of $6 to $12 billion annually. Up to 60% of these patients do not have an ACS and would have been eligible for early discharge, thus highlighting the need for a rapid and more accurate triage tool for this patient population.

A recent report of ED trends and projections shows the importance of achieving this goal. The decade between 1994 and 2004 saw an increase of 18% in ED visits and a 12% decline in hospitals offering ED services. EDs in the United States are overcrowded, with 40% to 50% reportedly pushed beyond capacity between 2003 and 2004, and nearly 60% of patients waiting 30 minutes or more to be seen by an ED physician. Changes in process, technology, and staffing are being considered to improve ED throughput, but diagnostic imaging will surely continue to play a key role toward achieving this goal.

CCTA is showing promise as a tool that could rapidly exclude ACS in low- or intermediate-risk ED patients presenting with chest pain. CCTA has proven effective in visualizing calcific and soft atherosclerotic plaques as well as in identifying significant (greater than 50%) coronary stenoses. Moreover, CCTA has shown a very high negative predictive value in excluding significant CAD and stenoses in normal or insignificantly diseased coronary arteries.

Because of its high negative predictive value, CCTA is well suited to rapidly and safely exclude CAD in low or intermediate/indeterminate-risk patients presenting to the ED with nonspecific chest pain. Several pilot studies on relatively small numbers of patients have shown good performance of CCTA for this application, with a negative CCTA accurately indicating the absence of ACS as well as an extremely low risk of near-term cardiac events following ED discharge. While CCTA is not currently in widespread clinical practice in the management of ED patients with chest pain, innovator sites have begun to implement this technique, and the impending significance of CCTA in this emerging application warrants review in this chapter.

Coronary Artery Anatomy

The coronary arteries are the first branches off the ascending aorta, located immediately above the aortic valve. Between the aortic valve and the sinotubular ridge are three focal outpouchings called the sinuses of Valsalva. Normally, the right coronary artery (RCA) ostium arises from the right sinus of Valsalva, and the left main coronary artery (LMA) ostium arises from the left sinus of Valsalva. The posterior or non-coronary sinus normally has no coronary ostium.

The word *coronary* is derived from the Latin *coronalis*, which means "of, relating to, or resembling a crown." The coronary arteries can be envisioned as a set of two crossing rings which encircle (or "crown") the heart, with the rings defined by the intersecting atrioventricular sulcus and interventricular septum (Fig. 8-29). Respectively, the RCA and left circumflex (LCX) arteries mirror one another and course within the right and left hemi-rings of the atrioventricular sulcus, while the left anterior descending (LAD) and posterior descending (PDA) arteries course within the anterior and posterior hemi-rings formed over the interventricular septum (Figs. 8-30 and 8-31).

"Coronary dominance" describes which artery supplies the PDA as well as the posterolateral left ventricular branch (PLA) and the artery to the atrioventricular (AV) node. In right coronary dominance (approximately 85% of the population), the RCA supplies the PDA, along with the left posterolateral branches and AV nodal artery. In left

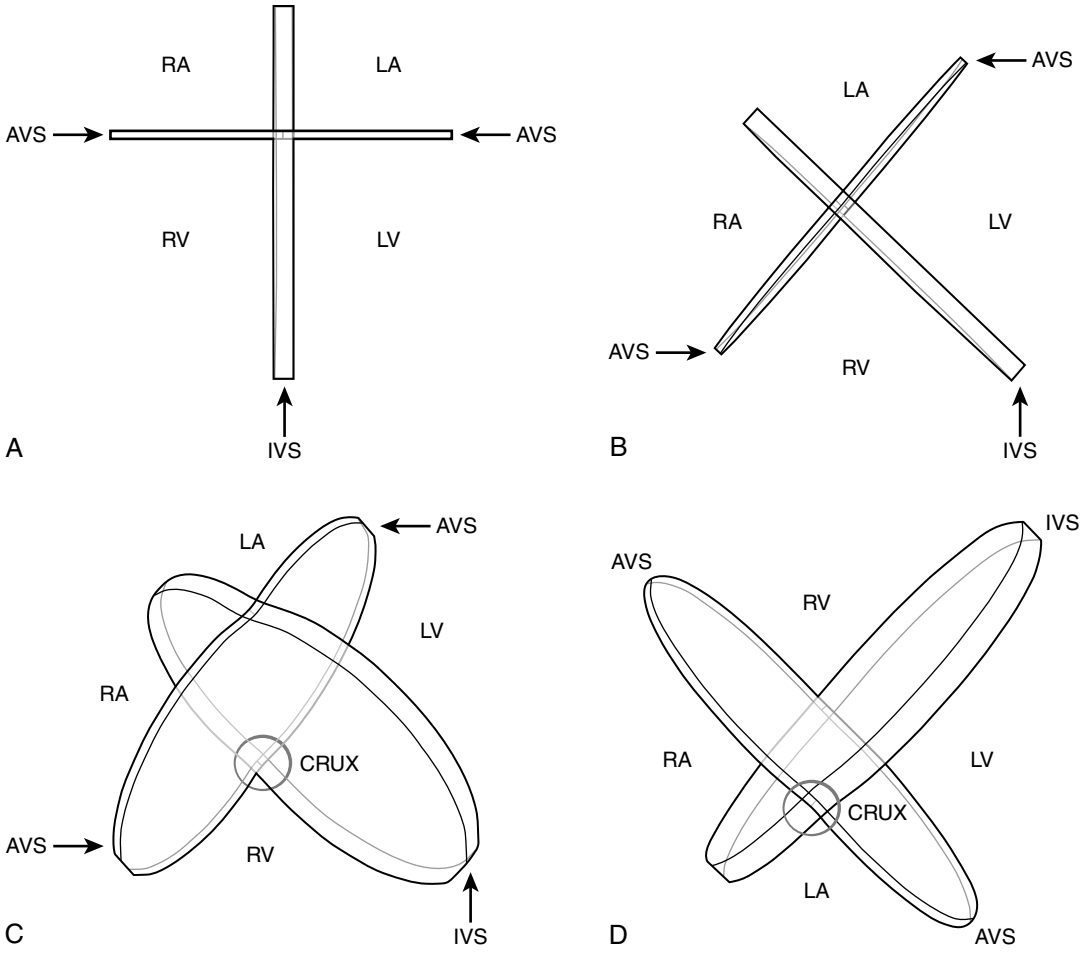
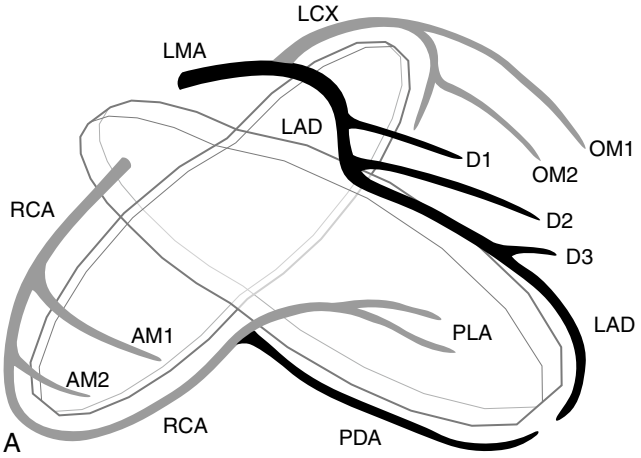


FIGURE 8-29. Crossing ring diagrams of the coronary arteries. **A,** The architectural skeleton of the heart and coronary arteries can be envisioned as a set of "crossing rings," with the atrioventricular sulci (AVS) and interventricular septum (IVS) defining the planes within which the crossing rings (and coronary arteries) lie. **B,** As viewed from the front, the heart is "tilted" within the thorax, or oriented such that the IVS points inferolaterally toward the left. **C,** When viewed from the front, the heart is rotated about the IVS long axis such that the right atrium and right ventricle (RA and RV) are positioned more anteriorly relative to the left atrium and ventricle (LA and LV). **D,** Finally, viewed inferiorly, as in a standard axial CT image, the RV is positioned relatively anterior, the LA relatively posterior, and the LV and RA toward the patient's left and right, respectively. The right coronary artery (RCA) and left circumflex arteries (LCX) course within the right and left atrioventricular sulci, respectively. The left anterior descending (LAD) and the posterior descending arteries (PDA) course over the anterior and posterior aspects of the interventricular septum, respectively. The posterior junction of the AVS and IVS is termed the "crux," and is the point where the RCA (in a right dominant circulation) takes a downward turn to supply the PDA.

coronary dominance (approximately 8%), these vessels are supplied by the LCX. In co-dominant coronary circulation (approximately 7%), both the LCX and RCA contribute to these vessels.

RCA

After arising from the right (or anterior) sinus of Valsalva, the RCA courses deep to the right atrial appendage within the right AV groove, following the AV groove until it intersects with the posterior interventricular septum, at the "crux" of the heart (see Fig. 8-29). For the purposes of clinical description of lesion location, the RCA is often divided into proximal (ostium to first main right ventricular branch), mid (first main branch to the acute margin), and distal (acute margin to the crux). Usually, the first branch off the RCA is the conus branch; however, the conus branch often (23% to 51%) has a separate ostium off the right sinus of Valsalva. The conus branch courses anteriorly in an arc over the conus or infundibulum and may form a collateral bridge to LAD branches (the "arc of Vieussens"), thus offering protection in cases of proximal RCA or LMA/LAD disease. The sinoatrial (SA) nodal branch/artery most commonly arises from the proximal RCA (60%) but often originates from the LCX (40%). This branch extends posteriorly along the interatrial groove and supplies branches to both atria as well as the SA node. The right ventricular, or acute marginal, branches emerge at right or acute angles from the RCA and vary in size and number as they supply the right ventricular myocardium. In right dominant circulations, the RCA continues in the atrioventricular sulcus until it intersects with the posterior interventricular septum at the crux, where the RCA gives off the PDA branch that courses along the posterior interventricular septum, supplying the lower third of the interventricular septum, as well as PLA branches (which supply the inferior wall of the left ventricle and the interventricular septum) and the AV nodal branch (which extends cephalad from the crux to the AV node).



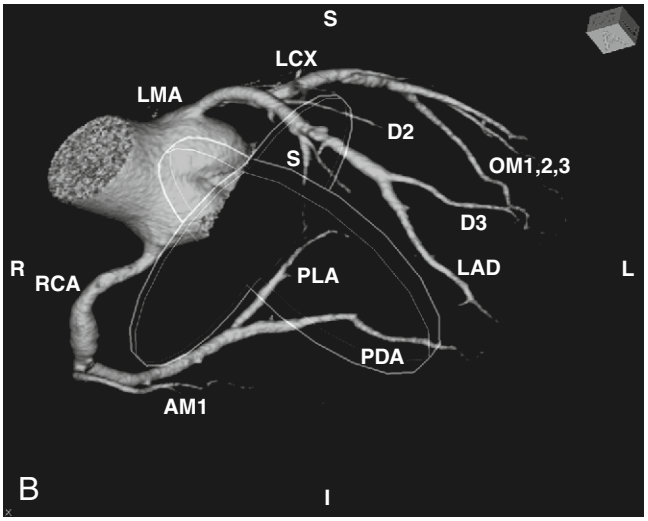


Figure 8-30. Coronary arteries applied to the crossing ring diagram. **A,** Diagram of the coronary arterial tree (right dominant circulation) superimposed on a frontal view of the "crossing ring" AVS and IVS architectural skeleton. The RCA arises from the aortic right sinus of Valsalva and courses within the right AVS to the crux, where it gives off the PDA branch (which travels under the inferior margin of the IVS) as well as posterolateral branches (PLA, which supply the inferior and inferolateral left ventricle walls). The acute marginal (AM1, AM2, etc.) branches off the RCA supply the right ventricle walls. The LCX arises from the left main coronary artery (LMA) and mirrors the RCA as it courses within the left AVS. It supplies obtuse marginal (OM1, OM2, etc.) branches, which perfuse the lateral wall of the left ventricle. The LMA arises from the left sinus of Valsalva. The LAD (essentially a continuation of the LMA) turns to course over the anterior aspect of the IVS and usually continues over the cardiac apex. The LAD supplies diagonal branches (D1, D2, D3, etc.), which perfuse the anterior, and anterolateral, walls of the left ventricle. **B,** 3D reformatted image of CCTA superimposed on a frontal view of the "crossing ring" architectural skeleton. Vessels are labeled as in Figure 30A. Diagonal 1 is very small and not labeled, seen just above D2. Vessel labeled "S" is a large septal perforator arising from the LAD. The three OM branches are prominent, and the LCX is not seen beyond the OM3 origin. In a left dominant circulation, the LCX would continue to the crux to supply the PLA and PDA branches.

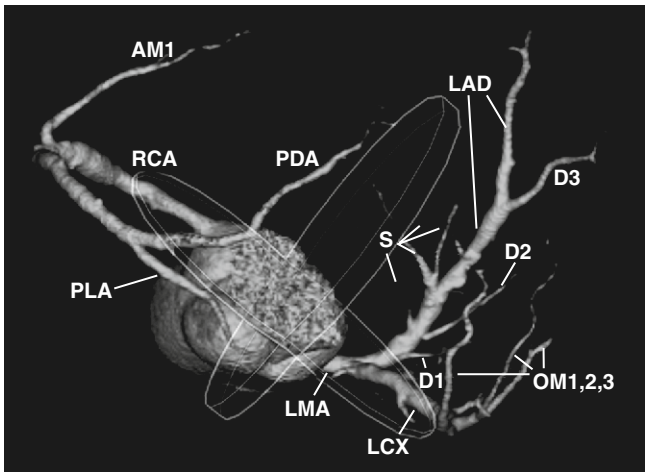


Figure 8-31. Axial view of the coronary arteries. 3D reformatted image of CCTA as viewed from the inferior aspect of a patient, as in a standard axial CT, superimposed on a diagram of the architectural skeleton of the AVS and IVS. The RCA arises from the right sinus of Valsalva at approximately the 10–12 o'clock position, and the left main coronary artery (LMA) arises from the left sinus of Valsalva generally at the 2–5 o'clock position. The RCA and LCX course within the right and left AVS, respectively, and the LAD and PDA course over the anterior and inferior borders of the IVS, respectively. On an axial image, the diagonal branches (D1, D2, etc.) extend toward the patient's left from the LAD, and the septal perforators (S) extend toward the patient's right from the LAD.

LMA

The LMA arises from the left sinus of Valsalva and follows a short (usually 1 to 2 cm) course between the pulmonary trunk anteriorly and left atrial appendage posteriorly (Fig. 8-32). It normally bifurcates into the LAD and LCX arteries but may trifurcate with a third intermediate artery arising between the LAD and LCX. This intermediate artery has various names, including "ramus intermediate" or "ramus medians," "median artery," "left diagonal artery," and "straight left ventricular artery," and supplies different portions of the anterolateral left ventricular wall.

LAD

The LAD arises from the LMA and courses around the left side of the pulmonary trunk toward the proximal interventricular septum where it takes a roughly 90-degree downward turn and courses over the interventricular septum toward the apex (see Fig. 8-32). This downward turn over the proximal interventricular septum has clinical significance, as this is the point where the LAD becomes amenable to surgical bypass. The second diagonal branch often originates near this downward turn. By convention, the LAD is divided into three segments: proximal (LAD origin to first septal perforator), middle (first septal perforator to downward turn along interventricular sulcus/origin of second diagonal), and distal (second diagonal origin to vessel end). The LAD provides two major types of branches: the septal perforators, which generally arise at 90-degree angles from the LAD and penetrate into the interventricular septum to supply the upper two thirds of the septum, and the diagonal (D) branches, which arise at acute angles from the LAD to course over and supply the anterior/anterolateral wall of the left ventricle. The number of diagonal arteries varies, and they are named in order of their origin from the LAD (D1, D2, etc.). The LAD usually extends over the apex to supply the distal inferior wall and interventricular septum, but the PDA may supply these regions as well, and this distal LAD-PDA confluence is a source of potential collateralization in cases of RCA or LAD disease.

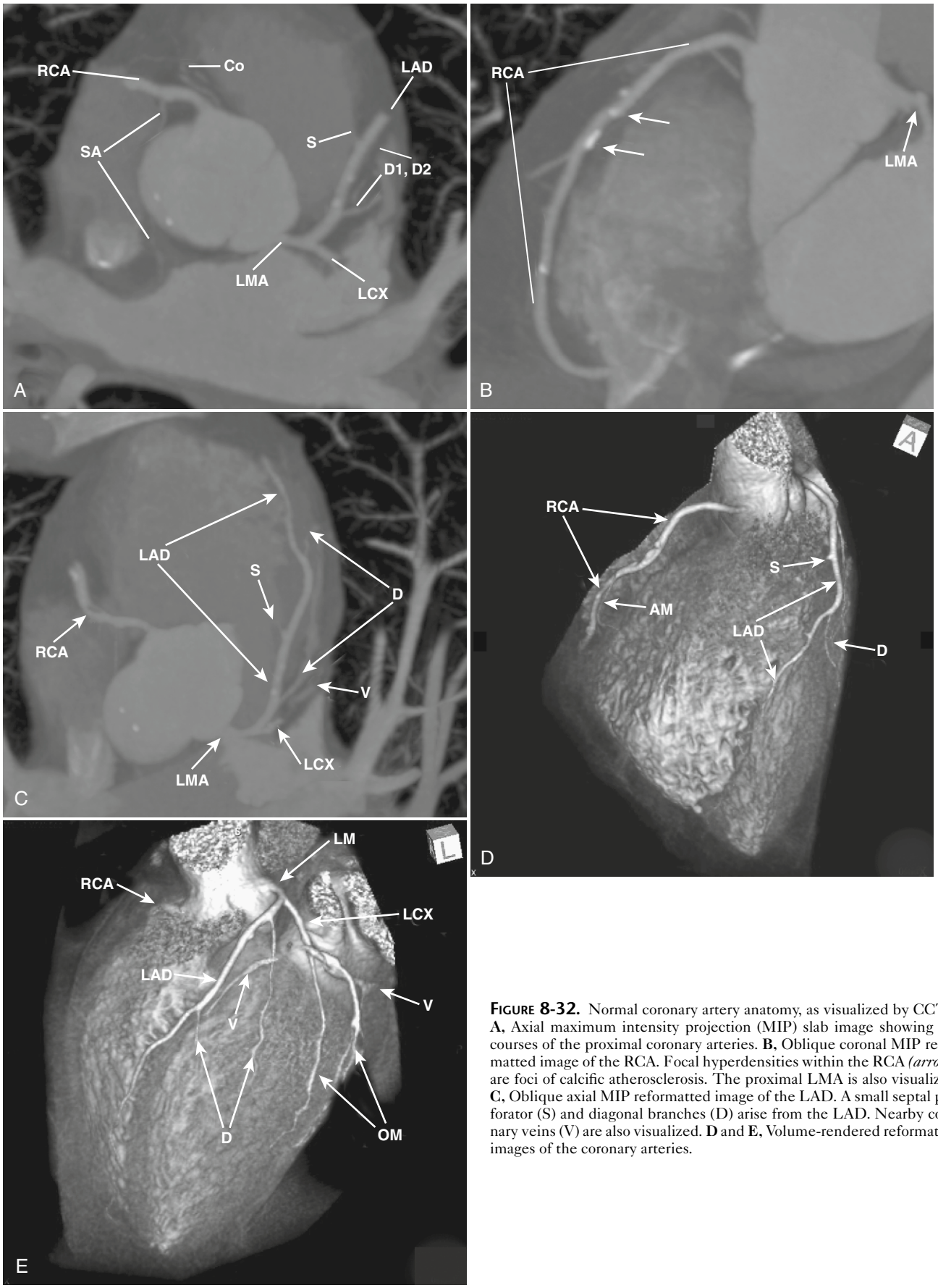


FIGURE 8-32. Normal coronary artery anatomy, as visualized by CCTA. **A,** Axial maximum intensity projection (MIP) slab image showing the courses of the proximal coronary arteries. **B,** Oblique coronal MIP reformatted image of the RCA. Focal hyperdensities within the RCA *(arrows)* are foci of calcific atherosclerosis. The proximal LMA is also visualized. **C,** Oblique axial MIP reformatted image of the LAD. A small septal perforator (S) and diagonal branches (D) arise from the LAD. Nearby coronary veins (V) are also visualized. **D** and **E,** Volume-rendered reformatted images of the coronary arteries.

LCX

The LCX arises from the LMA, and its course mirrors that of the RCA as it courses under the left atrial appendage to follow the left atrioventricular sulcus toward the crux. The major branches off the LCX are the marginal (or obtuse marginal) branches which vary in size and number. The obtuse marginal (OM) branches overlie and supply the lateral wall of the left ventricle and are labeled according to the order of their origin off the LCX (OM1, OM2, etc.). For clinical description, the LCX is divided into three segments: proximal (from LCX ostium to first major obtuse marginal branch [OM1]), mid (between OM1 and OM2), and distal (vessel distal to OM2). In a right dominant circulation the LCX will terminate short of the crux, whereas in co-dominant and left dominant circulations the LCX will make respectively greater contributions to the PDA, PLA, and AV nodal circulations.

Coronary Artery Anomalies

Coronary artery anomalies are a heterogeneous constellation of anatomic variants (Fig. 8-33). While relatively uncommon (0.46% to 5.6% of normal population), certain forms carry elevated risk, making it important for the radiologist to detect and accurately define these variants. In particular, coronary anomalies cause up to 19% to 30% of sudden deaths in athletes. CCTA is superior to conventional angiography in delineating the ostial origin and proximal path of anomalous coronary arteries. Anomalies may be classified by the presence or absence of a shunt, or they may be classified as "malignant" or "nonmalignant" depending on their course and propensity to cause clinical symptoms or sudden death.

Anomalies not resulting in a shunt include anomalous coronary artery origins (origin from another coronary artery, another sinus of Valsalva or above the sinotubular ridge, and independent branch origins from the sinus of Valsalva), myocardial bridges, congenital aneurysms, and hypoplasia/atresia. Anomalies resulting in a shunt include artery origin from the pulmonary artery (called Bland-White-Garland syndrome for the LMA) and fistulas.

Malignant variants (associated with an increased risk of MI and sudden death) primarily consist of anomalous artery origins that result in an interarterial course, with the anomalous artery coursing between the aorta and pulmonary artery (see Fig. 8-33). Several factors contribute to jeopardizing the anomalous vessel in this position, including compression of the vessel between the aorta and pulmonary artery, especially during exercise, and acute-angle take-off and narrow ostial area of the proximal vessel resulting in diminished flow or occlusion. The most common interarterial variant is the RCA arising from the left sinus of Valsalva and coursing between the aorta and pulmonary artery to reach the right AV sulcus, although an LMA or LAD arising from the right sinus of Valsalva with an interarterial course may pose a higher risk to the patient. Anomalous coronary artery origin from the pulmonary artery is also considered malignant and is associated with myocardial ischemia and sudden death in early childhood.

Myocardial bridging occurs when a coronary artery (usually the middle third of the LAD) deviates from a normal epicardial course to reside under superficial myocardial fibers for a short distance before reemerging to a normal epicardial position (Fig. 8-34). The prevalence and clinical significance of myocardial bridging are nebulous. While angiographic series report prevalence between 0.5% and 2.5%, pathologic series have reported prevalence between 15% and 85%. Generally thought to be benign, any specific case of myocardial bridging may have clinical significance, and cases have been associated with angina, myocardial ischemia and infarction, and sudden death. CCTA is effective at diagnosing myocardial bridging, due to its ability to visualize the myocardium as well as coronary arteries. The ability to image in diastolic and systolic phases may help gauge the clinical significance by defining the severity of lumenal compromise during systole. Interestingly, the bridged segment is often free of atherosclerotic disease. Because of this potential for clinical significance, myocardial bridging warrants reporting when encountered.

Coronary artery fistulas are abnormal communications between a coronary artery and another vascular structure such as the right ventricle (45%), the right atrium (25%), a pulmonary artery (15%), or the superior vena cava, left atrium, or left ventricle (less than 10%) (see Fig. 8-33). The involved coronary is often dilated and tortuous, and the anomalous connection may result in a left-to-right shunt, a hemodynamic steal phenomenon, and hypoperfusion or ischemia of the myocardium normally perfused by the involved vessel.

Image Evaluation

A potentially very important triage tool in the ED, the function of CCTA is to detect or exclude the presence of CAD in a patient with chest pain. Therefore, familiarity with the CCTA findings in CAD is required. CCTA detects CAD primarily by defining two findings: coronary artery stenoses and mural atherosclerotic plaque. These two findings permit the radiologist to exclude or confirm CAD in ED patients. Ancillary evaluation depends on scanning technique and software availability, and includes evaluation of left ventricular wall motion and function (which bestows important physiologic/functional correlation with coronary artery findings) and possibly evaluation of myocardial perfusion defects (scar/ischemia imaging) or delayed enhancement (scar/viability imaging). This section focuses on coronary stenosis and mural atherosclerotic plaque.

Coronary Artery Stenosis

As neither CCTA nor conventional angiography can measure the hemodynamic effect of a particular lesion, the degree of stenosis is used as a surrogate to determine lesion significance. The CCTA threshold most often used to define a significant stenosis is 50% or greater luminal narrowing, using a nearby "normal" segment of the vessel as a reference. A 50% stenosis by CCTA corresponds to approximately 70% stenosis on conventional planimetric angiography.

While acquiring an ECG-gated CCTA exam, images are obtained in each of (generally) 10 to 20 phases throughout the cardiac cycle. Images from the (usually diastolic) phase in which the least coronary motion artifact is present are then utilized for image analysis. To evaluate CCTA images, review of the axial images as well as MPR and MIP images is performed (Figs. 8-35 and 8-36). Although reformatted images are valuable in defining and delineating

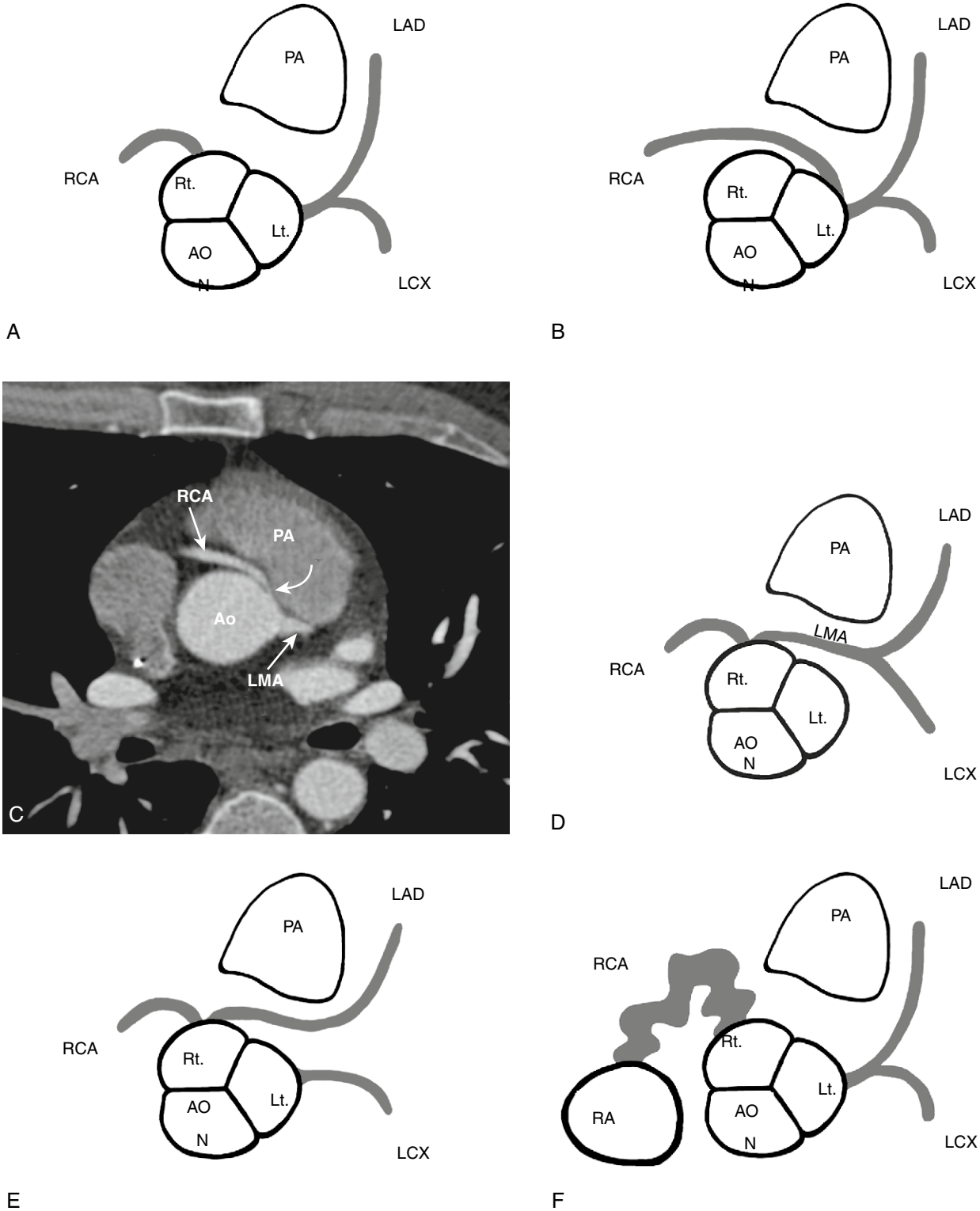


FIGURE 8-33. Diagrams of coronary artery variants, as they would be visualized on axial CT images. **A,** Diagram of normal proximal coronary artery anatomy. Normally, the RCA arises from the right coronary sinus (Rt), and the LMA (which supplies the LCX and LAD) arises from the left coronary sinus (Lt) of the aorta (Ao). **B–F,** Examples of *malignant* "interarterial" anatomic variants. These variants portend increased risk for clinical symptoms or sudden cardiac death. The RCA may arise from the left sinus of Valsalva and course between the aorta and pulmonary artery (PA) **(B)** to achieve its normal right AVS position. **C** is an axial source image from a patient with this variant. Note the acute angle take-off and narrow ostial area of the anomalous RCA *(curved arrow)* as compared with the normal LMA. Position of the anomalous interarterial RCA between the aorta and pulmonary artery also results in increased risk of RCA compression, especially during exercise. Conversely, either the LMA **(D)** or the LAD **(E)** may arise from the right sinus of Valsalva and follow an interarterial course. Coronary anomalies resulting in a shunt **(F)** include coronary atrioventricular (AV) fistulas and coronary artery origins from the PA. These variants predispose to ischemia or symptoms/sudden death and are thus considered *malignant*. **F** is a diagram of an AV fistula, with dilated RCA draining to the right atrium (RA), rather than draining normally into the coronary sinus and left atrium.

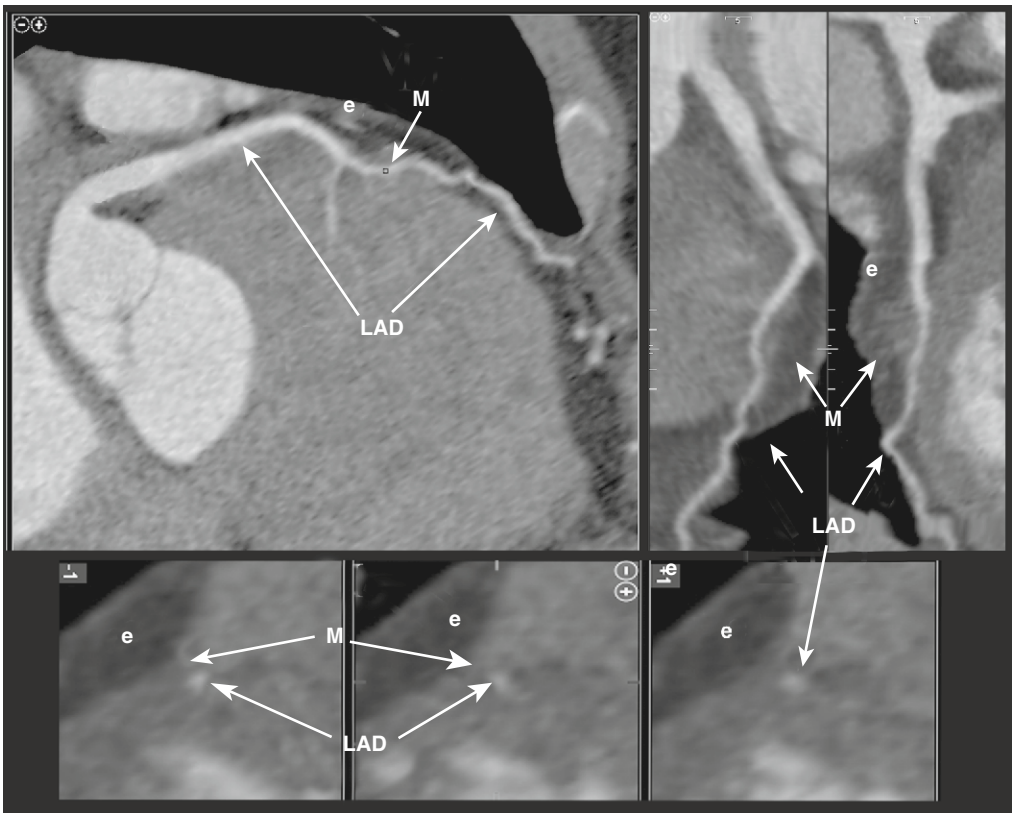


Figure 8-34. Example of myocardial bridging of the LAD. Long axis maximum intensity projection *(top left)*, long axis curved multiplanar reformatted images *(two top right images)*, and cross-section reformatted images *(bottom row of three images)* of the LAD. The proximal LAD is in its normal position within the epicardial fat (e) overlying the interventricular septum. However, the LAD deviates from its normal epicardial course to course under superficial myocardial fibers (M) for a short distance before reemerging to assume its normal epicardial course. Bottom row of cross-section reformatted images shows a "bridge" of myocardial fibers (M) overlying the LAD at the level of the myocardial bridging. The myocardial fibers separate the LAD from the epicardial fat (e).

stenoses, the axial images remain the cornerstone of the evaluation, as virtually all pathologies can be identified on the axial images. Once a stenosis is detected on the axial images, further evaluation of the lesion is best performed with two long-axis reformats through the vessel. Generally, 3- to 5-mm thin-slab MIP images are also useful for evaluating lesions in the long axis, and interactive evaluation is facilitated with sliding or rotating thin-slab MIP images. The interpreter should be aware that when using MIP images, stenoses may be masked or obscured by volume averaging.

Once detected, a stenosis can be visually measured, or estimated, using a nearby "normal" segment of the vessel as a reference, or software-assisted quantitative assessment of the stenosis may be employed (see Fig. 8-35). Comparison of the visual estimate/measurement method versus

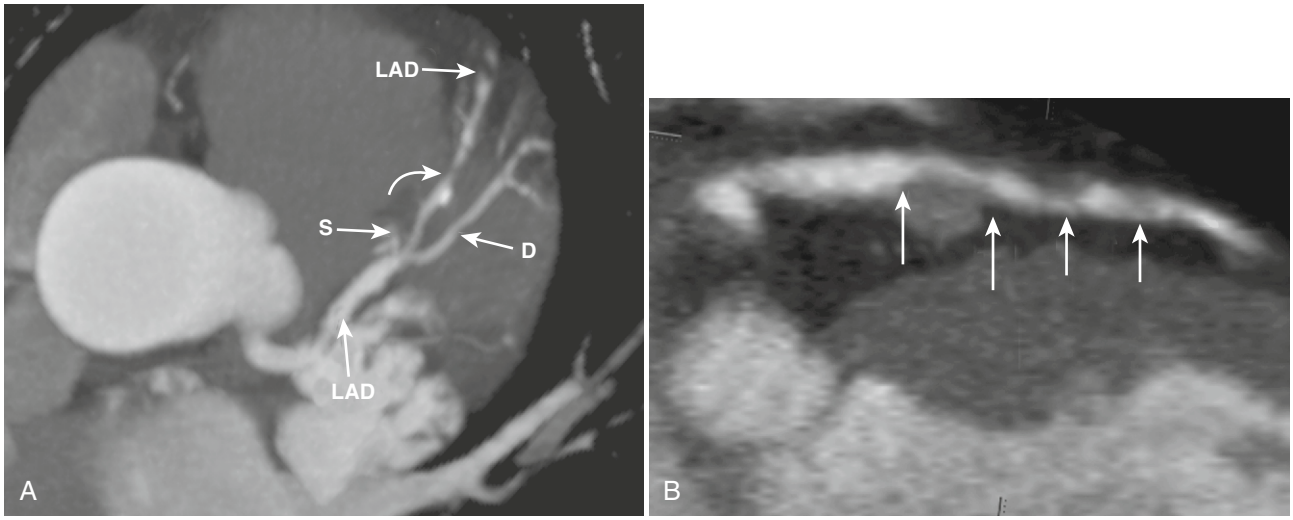


Figure 8-35. Examples of coronary artery stenosis. **A,** An oblique axial maximum intensity projection reformatted image of the LAD reveals disease beyond the origins of septal (S) and diagonal (D) branches. A significant appearing stenosis is noted *(curved arrow)*. **B,** An oblique long axis reformatted image through a diagonal artery in another patient shows a severe stenosis *(between the two long arrows)*. Areas of apparent stenosis or occlusion are artifactual, related to volume averaging with adjacent epicardial fat *(small arrows)*.

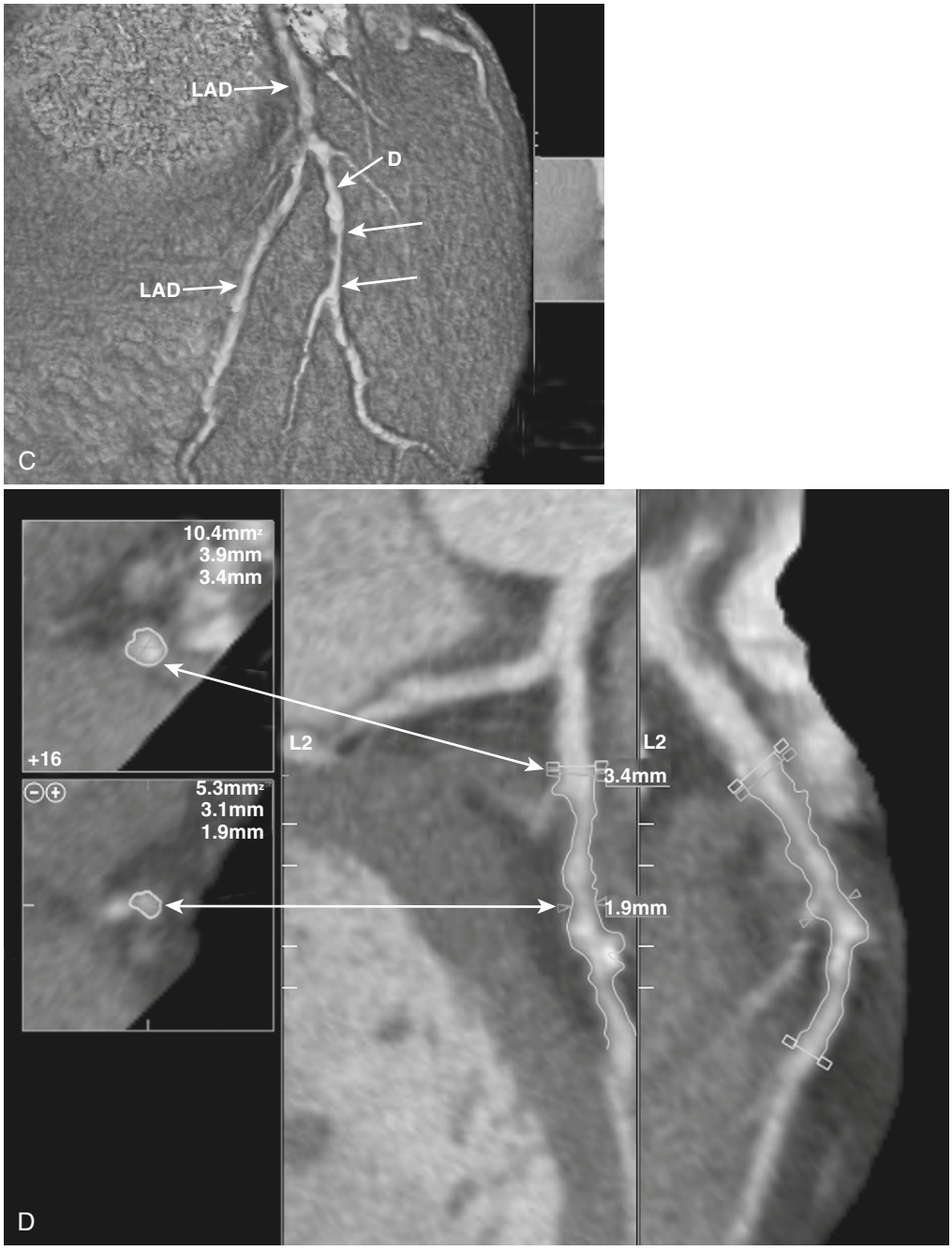


FIGURE 8-35—CONT'D. **C,** Volume-rendered reconstruction of the diagonal artery stenosis *(between long arrows)* seen in **B. D,** An example of software-assisted quantitative assessment of coronary stenosis. Middle and right images are orthogonal long-axis curved multiplanar reformatted images through the vessel (LAD in this case), and the two left images are short-axis cross-sectional reformatted images through the vessel. Double-headed arrows indicate the levels of the cross-section reformatted images relative to the long-axis images. The software can automatically detect the "edge" of the coronary artery (based on a threshold of attenuation or attenuation difference) and draw a line at the detected borders. With the vessel borders defined, the diameters and cross-sectional areas at any particular point can be calculated, and with these values the severity of stenosis can be quantified.

quantitative software-assisted assessment of stenoses has revealed that software-assisted assessment provides higher accuracy for about the same user time required for visual estimation. However, while 64-slice CCTA has shown high accuracy in detecting 50% or greater stenoses, the ability to provide exact, quantitative measures of stenosis severity is hampered by current limits in spatial resolution. Because of this, the severity of stenoses is often classified in quartiles (0% to 25%, 26% to 50%, 51% to 75%, 76% or greater) or tertiles (0% to 30%, 31% to 70%, 71% to 99%), or some other variant, depending on local radiologist/cardiologist preferences.

Despite this relative lack of quantitative accuracy, CCTA has proven highly accurate in detecting 50% or greater stenoses, and has shown high negative predictive values (generally 95% to 100%) in excluding significant coronary disease. Since the ED chest pain patient population evaluated by CCTA should have a low prevalence of disease (low or intermediate ACS risk patient with normal cardiac

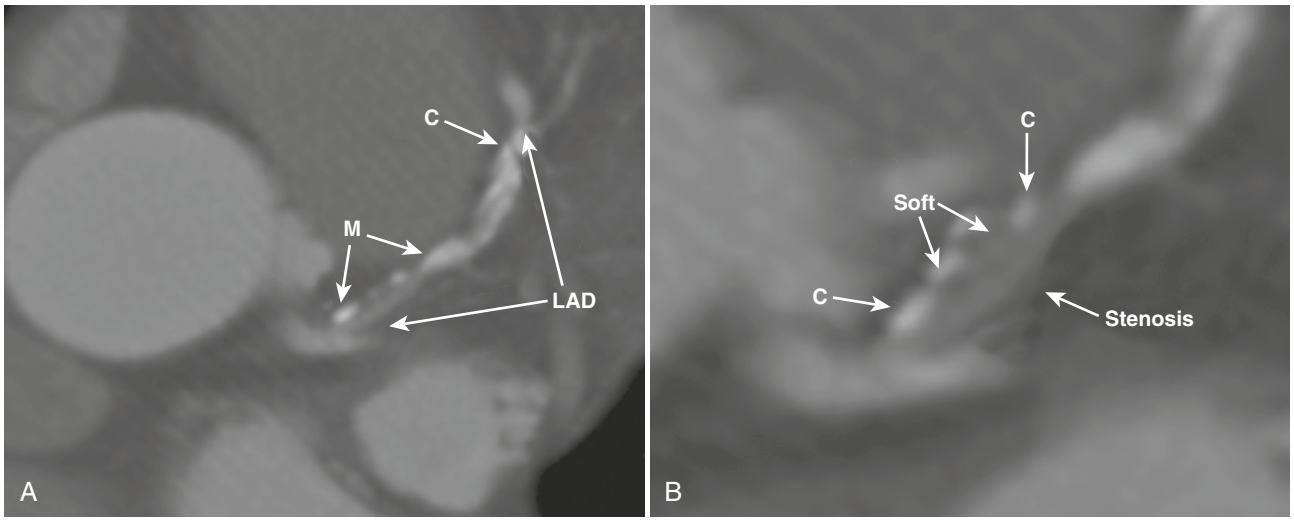


Figure 8-36. Coronary artery atherosclerotic plaque, as visualized by CCTA. **A,** A diffusely diseased LAD reveals hyperdense calcific (C) atherosclerotic plaque as well as mixed (M) "soft" and calcific atherosclerotic plaque. The mixed plaque appears to be causing stenosis. **B,** Magnified image of **A,** showing components of the mixed plaque. Calcific components (C) appear as hyperdense relative to the opacified vessel, while the "soft" components (Soft) are hypodense. The mixed plaque is causing stenosis of the vessel.

biomarkers and EKGs), the majority of CCTA scans done for ED patients should be essentially normal, which should facilitate more rapid image evaluation/interpretation and thus more rapid discharge or appropriate treatment for non-ACS ED patients with chest pain.

Atherosclerotic Plaque Imaging

The presence of coronary artery plaque increases ACS risk even in the absence of coronary artery stenoses. While higher total volume or burden of atherosclerotic plaque carries higher ACS risk, different types of plaque also impart different levels of ACS risk, as plaque vulnerability varies depending on plaque composition. Histologically, atherosclerotic plaque consists of numerous components including calcification (generally calcium hydroxyapatite), fibrous tissue, inflammatory cells (predominantly macrophages and monocytes), smooth muscle, lipid components (lipid-laden macrophages, necrotic lipid cores, etc.), and hemorrhagic foci.

Both major and minor histologic criteria for defining plaque vulnerability have been described. Major histologic criteria include active inflammation, a thin cap with a large lipid-necrotic core, endothelial denudation with platelet aggregation, fissured plaques, and stenosis larger than 90%. Minor histologic criteria include superficial calcified nodules, glistening yellow plaque (seen at angioscopy), intraplaque hemorrhage, endothelial dysfunction, and positive (outward) remodeling.

For coronary plaque analysis, CCTA has inherent limits in spatial and contrast resolution that prevent discernment of many of the components of plaque. However, calcium is well defined by CCTA and can be distinguished from "soft" plaque components (see Fig. 8-36). Coronary calcium scoring, or quantification of calcific coronary atherosclerotic plaque utilizing electron beam and MDCT, has been in use for over a decade. Generally, a threshold of 130 Hounsfield units is used to define calcified atherosclerotic plaque. "Soft," or noncalcified, plaque can be discerned from calcified plaque on CCTA in this manner. Noncalcified soft plaque is heterogeneous in composition, consisting of various quantities of components as described above. On CCTA, soft coronary artery plaque is visualized as a structure that can be clearly assignable to the vessel wall (in at least two views) with densities less than the intraluminal contrast (see Fig. 8-36). On CCTA, plaque is generally classified as calcified, noncalcified, or mixed.

Whereas CCTA has only limited ability to define the specific composition of noncalcified plaque, lower CT density generally indicates a greater lipid concentration, and, in fact, larger lipid pools or lipid cores (larger than 2 mm) may be visualized within the plaque of larger coronary arteries as hypodense spots demonstrating a density of at least 20 Hounsfield units less than the average surrounding noncalcified plaque tissue. Thus, despite inherent limitations, CCTA may be able to identify some of the major and minor plaque vulnerability criteria, including larger lipid-necrotic cores, stenoses greater than 90%, superficial calcified nodules, and positive (outward) remodeling.

As regards calcium scoring, both electronic beam CT and gated MDCT have been shown to be reliable methods of quantifying coronary calcified plaque. However, with CCTA (using intravascular ultrasound as a gold standard), plaque volume per vessel tends to be underestimated for mixed and noncalcified plaque, and overestimated for calcified plaque. Despite these limits, it remains true that an individual's ACS risk will increase with both increasing total plaque volume/burden and increasing plaque vulnerability, as defined by the characteristics described above. While the relevance and clinical significance of CCTA-detected nonstenotic coronary plaque in ED chest pain patients is not currently well defined, knowledge of the presence, type, and general burden of coronary plaque might in the future aid in further refining treatment pathways by better stratifying patient risk for ED physicians treating chest pain (and potential ACS) patients.

Combined Evaluation of the Aorta and Pulmonary and Coronary Arteries

The combined evaluation for aortic dissection, PE, and ACS has been seductively coined the "triple rule-out." While the potential that MDCT holds for rapid evaluation and triage of ED chest pain patients is appealing, limitations still exist. One such current limitation is the limited thoracic coverage of the imaging dataset volume during peak contrast enhancement. Further CT advances will likely help to overcome this limitation in the short term, but for now, imaging evaluation cannot be routinely optimized for all three of these diagnoses at once; triple rule-out evaluation involves some compromises and trade-offs as compared with traditional dedicated evaluations for each of these diseases.

Optimized CCTA images are restricted in the X and Y (transverse and anteroposterior) planes to the cardiac and near paracardiac structures in order to allow for higher resolution imaging of the coronary arteries. This limitation might be overcome by reconstruction of the dataset to produce images that include the entire thorax (in the axial plane), thus allowing evaluation of anatomy out to the chest wall and beyond. However, CCTA scans are also restricted in the Z (craniocaudal) axis (to just above and below the heart), and there is no way to evaluate thoracic anatomy outside this zone without additional imaging, and therefore additional radiation dose.

To address this, several investigators have proposed incorporating a CCTA exam within an acquisition of an entire thoracic MDCT image dataset. This would allow evaluation of the coronary arteries as well as the pulmonary arteries and thoracic aorta. Although termed a "triple rule-out" exam (rule out ACS, PE, and aortic dissection), it would probably be more aptly called a *comprehensive* or *global assessment* exam, as the entire thorax (and thus all potential thoracic pathologic entities) could be interrogated in a single exam.

Several small investigations have provided generally encouraging results, indicating that a comprehensive assessment protocol chest CT/CCTA is feasible and can reproduce the accuracy and negative predictive value for excluding coronary disease shown by a dedicated or focused CCTA exam. However, larger and prospective/multicenter studies would be required to confirm these early impressions. It is important to realize that the radiation dose for a comprehensive assessment exam could be as much as 50% greater than that for a dedicated CCTA exam, owing to the extended field of view. A dedicated CCTA exam alone is already considered to be a relatively high radiation dose exam (8 to 22 milliSieverts), and these low- to intermediate-risk patients are likely to be younger than higher-risk patients. Furthermore, the incidence of PE and aortic dissection in chest pain patients without suggestive signs and symptoms is low. Therefore, some authors suggest avoiding a comprehensive assessment type of CT exam protocol unless clinical symptomatology does not permit greater pretest probability to be readily assigned to one entity over another. Concern regarding CT-related ionizing radiation exposure to patients also mandates that greater scrutiny be directed at the use of exam protocols that include multiple scans for the purpose of excluding diagnoses with very low pretest probability.

One must remember that the place CCTA (and global assessment CT) holds within the chest pain evaluation algorithm is at present unclear. Despite these uncertainties, the rapid evolution of CT technology and the clear advantages it holds over current management strategies strongly suggest that MDCT (using either dedicated CCTA or comprehensive assessment-type protocols) will likely become an integrated part of the clinical algorithm for evaluating ED patients presenting with acute chest pain.

Suggested Readings

Aberle D, Wierner-Kronish J, Webb R, et al: Hydrostatic versus increased permeability pulmonary edema: Diagnosis based on radiographic criteria in critically ill patients. Radiology 168:73–79, 1988.

Achenbach S: Computed tomography coronary angiography. J Am Coll Cardiol 48:1919–1928, 2006.

Alpert JS, Smith R, Carlson J, et al: Mortality in patients treated for pulmonary embolism. JAMA 236:1477–1480, 1976.

Anderson FA Jr, Wheeler HB, Goldberg RJ, et al: A population-based perspective of the hospital incidence and case-fatality rates of deep vein thrombosis and pulmonary embolism. The Worcester DVT Study. Arch Intern Med 151: 933–938, 1991.

Bae KT: Peak contrast enhancement in CTA and MRA: When does it occur and why? Radiology 216:872–880, 2000.

Becattini C, Agnelli G: Acute pulmonary embolism: Risk stratification in the emergency department. Intern Emerg Med 2:119–129, 2007.

Begemann PG, Bonacker M, Kemper J, et al: Evaluation of the deep venous system in patients with suspected pulmonary embolism with multi-detector CT: A prospective study in comparison to Doppler sonography. J Comput Assist Tomogr 27:399–409, 2003.

Bejvan SM, Godwin JD: Pneumomediastinum: Old signs and new signs. AJR Am J Roentgenol 166:1041–1048, 1996.

Brink JA, Woodard PK, Horesh L, et al: Depiction of pulmonary emboli with spiral CT: Optimization of display window settings in a porcine model. Radiology 204:703–708, 1997.

Busch S, Johnson TR, Nikolaou K, et al: Visual and automatic grading of coronary artery stenoses with 64-slice CT angiography in reference to invasive angiography. Eur Radiol 17:1445–1451, 2007.

Chan SS: Emergency bedside ultrasound to detect pneumothorax. Acad Emerg Med 10:91–94, 2003.

Chiles C, Woodard PK, Gutierrez FR, et al: Metastatic involvement of the heart and pericardium: CT and MR imaging. Radiographics 21:439–449, 2001.

Coche EE, Muller NL, Kim KI, et al: Acute pulmonary embolism: Ancillary findings at spiral CT. Radiology 207:753–758, 1998.

Cook JV, Kyriou J: Radiation from CT and perfusion scanning in pregnancy. BMJ 331:350, 2005.

Dake MD, Miller DC, Semba CP, et al: Descending thoracic aortic aneurysm: CT findings after endovascular stent-graft placement. Radiology 212:169–174, 1999.

Dalen JE: Pulmonary embolism: What have we learned since Virchow? Treatment and prevention. Chest 122:1801–1817, 2002.

de Hoyos A, Sundaresan S: Thoracic empyema. Surg Clin North Am 82:643–671, viii, 2002.

DeBakey ME, McCollum CH, Crawford ES, et al: Dissection and dissecting aneurysms of the aorta: Twenty-year follow-up of five hundred twenty-seven patients treated surgically. Surgery 92:1118–1134, 1982.

Demos TC, Posniak HV, Marsan RE: CT of aortic dissection. Semin Roentgenol 22:22–37, 1989.

Earnest F 4th, Muhm JR, Sheedy PF: Roentgenographic findings in thoracic aortic dissection. Mayo Clin Proc 54:43–50, 1979.

Elefteriades JA: Natural history of thoracic aortic aneurysms: Indications for surgery, and surgical versus nonsurgical risks. Ann Thorac Surg 74:1877–1880, 2002.

Erasmus JJ, Goodman PC, Patz EF: Management of malignant pleural effusions and pneumothorax. Radiol Clin North Am 38:375–383, 2000.

Erbel R, Engberding R, Daniel W, et al: Echocardiography in diagnosis of aortic dissection. Lancet 1:**457–461, 1989.**

Ersoy H, Goldhaber SZ, Cai T, et al: Time-resolved MR angiography: A primary screening examination of patients with suspected pulmonary embolism and contraindications to administration of iodinated contrast material. AJR Am J Roentgenol 188:1246–1254, 2007.

Evans AJ, Sostman HD, Knelson MH, et al: 1992 ARRS Executive Council Award. Detection of deep venous thrombosis: Prospective comparison of MR imaging with contrast venography. AJR Am J Roentgenol 161:131–139, 1993.

Evans AJ, Sostman HD, Witty LA, et al: Detection of deep venous thrombosis: Prospective comparison of MR imaging and sonography. J Magn Reson Imaging 6:44–51, 1996.

Farkouh ME, Smars PA, Reeder GS, et al: A clinical trial of a chest pain observation unit for patients with unstable angina. New Engl J Med 339: 1882–1888, 1998.

Fisher ER, Stern EJ, Godwin JD, et al: Acute aortic dissection. Radiographics 14:1263–1271, 1994.
Fisher RG, Sanchez-Torres M, Whigham CJ, Thomas JW, et al: "Lumps" and "bumps" that mimic acute aortic and brachiocephalic vessel injury. Radiographics 17:825–834, 1997.
Fiss DM: Normal coronary anatomy and anatomic variations: Applications in cardiac imaging. Appl Radiol 36(Suppl):14–26, 2007.
Fricke BL, Donnelly LF, Frush DP, et al: In-plane bismuth breast shields for pediatric CT: Effects on radiation dose and image quality using experimental and clinical data. AJR Am J Roentgenol 180:407–411, 2003.
Froehner SC, Wagner M, Brunn J, et al: CT angiography for assessment of coronary artery anomalies. In Schoepf UJ, (ed): CT of the Heart: Principles and Applications, Totowa, NJ, Humana Press, 2004.
Gallagher MJ, Raff GL: Use of multislice CT for the evaluation of emergency room patients with chest pain. Catheter Cardiovasc Interv 71:92–99, 2007.
Ganaha F, Miller DC, Sugimoto K, et al: Prognosis of intramural hematoma with and without penetrating ulcer: A clinical and radiological analysis. Circulation 106:342–348, 2002.
Ghaye B, Ghuysen A, Willems V, et al: Severe pulmonary embolism: Pulmonary artery clot load scores and cardiovascular parameters as predictors of mortality. Radiology 239:884–891, 2006.
Ghaye B, Remy J, Remy-Jardin M: Non-traumatic thoracic emergencies. CT diagnosis of acute pulmonary embolism: The first 10 years. Eur Radiol 12:1886–1905, 2002.
Gibler WB, Cannon CP, Blomkalns AL, et al: American Heart Association Scientific Statement: Practical Implementation of the Guidelines for Unstable Angina/Non–ST-Segment Elevation Myocardial Infarction in the Emergency Department. A scientific statement from the American Heart Association Council on Clinical Cardiology (Subcommittee on Acute Cardiac Care), Council of Cardiovascular Nursing, and Quality of Care and Outcomes Research Interdisciplinary Working Group, in collaboration with the Society of Chest Pain Centers. Circulation 111:2699–2710, 2005.
Giuntini C, Di Ricco G, Marini C, et al: Pulmonary embolism: Epidemiology. Chest 107(Suppl 1):3S–9S, 1995.
Goldstein JA: Cardiac tamponade, constrictive pericarditis, and restrictive cardiomyopathy. Curr Probl Cardiol 29:503–567, 2004.
Goldstein JA, Gallagher MJ, O'Neill WW, et al: A randomized controlled trial of multi-slice coronary computed tomography for evaluation of acute chest pain. J Am Coll Cardiol 49:863–871, 2007.
Golzarian J, Dussaussois L, Abada HT, et al: Helical CT of aorta after endolumenal stent-graft therapy: Value of biphasic acquisition. AJR Am J Roentgenol 171:329–331, 1998.
Gomes MN, Choyke PL: Infected aortic aneurysms: CT diagnosis. J Cardiovasc Surg 33:684–689, 1992.
Gordon R: The deep sulcus sign. Radiology 136:25–27, 1980.
Gorich J, Rilinger N, Sokiranski R, et al: Leakages after endovascular repair of aortic aneurysms. Radiology 213:767–772, 1999.
Gosselin MV, Rassner UA, Thieszen SL, et al: Contrast dynamics during CT pulmonary angiogram: Analysis of an inspiration associated artifact. J Thorac Imaging 19:1–7, 2004.
Gottschalk A, Sostman HD, Coleman RE, et al: Ventilation-perfusion scintigraphy in the PIOPED study. Part II: Evaluation of the scintigraphic criteria and interpretations. J Nucl Med 34:1119–1126, 1993.
Gottschalk A, Stein PD, Goodman LR, Sostman HD: Overview of prospective investigation of pulmonary embolism diagnosis II. Semin Nucl Med 32:173–182, 2002.
Gotway MB, Dawn SK: Thoracic aorta imaging with multisclice CT. Radiol Clin North Am 41:521–543, 2003.
Gotway MB, Marder SR, Hanks DK, et al: Thoracic complications of illicit drug use: An organ system approach. Radiographics 22(Special issue):S119–S135, 2002.
Guinet C, Buy JN, Ghossain MA, et al: Aortic anastomotic pseudoaneurysms: US, CT, MR, and angiography. J Comput Assist Tomogr 16:182–188, 1992.
Gupta A, Frazer CK, Ferguson JM, et al: Acute pulmonary embolism: Diagnosis with MR angiography. Radiology 210:353–359, 1999.
Gurney JW: No fooling around: Direct visualization of pulmonary embolism. Radiology 188:618–619, 1993.
Hager A, Kaemmerer H, Leppert A, et al: Follow-up of adults with coarctation of the aorta: Comparison of helical CT and MRI, and impact on assessing diameter changes. Chest 126:1169–1176, 2004.
Halliday KE, Al-Kutoubi A: Draped aorta: CT sign of contained leak in aortic aneurysms. Radiology 199:41–43, 1996.
Hansell DM, Armstrong P, Lynch DA, McAdams H: Imaging of Diseases of the Chest. Philadelphia, Elsevier Mosby, 2005.
Harris JA, Bis KG, Glover JL, et al: Penetrating atherosclerotic ulcers of the aorta. J Vasc Surg 19:90–98, 1994.
Hayashi H, Matsuoka Y, Sakamoto I, et al: Penetrating atherosclerotic ulcer of the aorta: Imaging features and disease concept. Radiographics 20:995–1005, 2000.
Hazirolan T, Canyigit M, Karcaaltincaba M, et al: Myocardial bridging on MDCT. AJR Am J Roentgenol 188:1074–1080, 2007.
Heart Disease and Stroke Statistics – 2007 Update, American Heart Association.
Heit JA: Venous thromboembolism epidemiology: Implications for prevention and management. Semin Thromb Hemost 28(Suppl 2):S3–S13, 2002.
Hoffmann U, Ferencik M, Cury RC, et al: Coronary CT angiography. J Nucl Med 47:797–806, 2006.
Hoffmann U, Nagurney JT, Moselewski F, et al: Coronary multidetector computed tomography in the assessment of patients with acute chest pain. Circulation 114:2251–2260, 2006.
Hoffmann U, Pena AJ, Cury RC, et al: Cardiac CT in emergency department patients with acute chest pain. Radiographics 26:963–980, 2006.
Hoffmann U, Pena AJ, Moselewski F, et al: MDCT in the early triage of patients with acute chest pain. AJR Am J Radiol 187:1240–1247, 2006.
Hutschala D, Fleck T, Czerny M, et al: Endolumenal stent-graft placement in patients with acute aortic dissection type B. Eur J Cardiothorac Surg 21:964–969, 2002.
Jeudy J, White CS: Evaluation of acute chest pain in the emergency department: Utility of multidetector computed tomography. Semin Ultrasound CT MR 28:109–114, 2007.
Johnson KW, Rutherford RB, Tilson MD, et al: Suggested standards for reporting on arterial aneurysms. J Vasc Surg 13:452–458, 1991.
Jones G, Sharma A, Bennett B, et al: Innovations in Operations. Tomorrow's ED: An Emergency Diagnostic Center Proprietary Analysis by Sg2 Health Care Intelligence, Skokie, Ill, 2007. Available at www.sg2.com.
Kaji S, Akasaka T, Horibata Y, et al: Long-term prognosis of patients with type A aortic intramural hematoma. Circulation 106(Suppl 1):S248–S252, 2002.
Kaji S, Nishigami K, Akasawa T, et al: Prediction of progression or regression of type A aortic intramural hematoma by computed tomography. Circulation 100:II281–286, 1999.
Kalra MK, Maher MM, Toth TL, et al: Strategies for CT radiation dose optimization. Radiology:619–628, 2004.
Kanne JP, Lalani TA: Role of computed tomography and magnetic resonance imaging for deep venous thrombosis and pulmonary embolism. Circulation 109(12, Suppl 1):I15–21, 2004.
Kapoor V, Ferris JV, Fuhrman CR: Intimomedial rupture: A new CT finding to distinguish true from false lumen in aortic dissection. AJR Am J Roentgenol 183:109–112, 2004.
Kasper W, Konstantinides S, Geibel A, et al: Management strategies and determinants of outcome in acute major pulmonary embolism: Results of a multicenter registry. J Am Coll Cardiol 30:1165–1171, 1997.
Kazerooni EA, Bree RL, Williams DM: Penetrating atherosclerotic ulcers of the descending thoracic aorta: Evaluation with CT and distinction from aortic dissection. Radiology 183:759–765, 1992.
Kim SY, Leo JB, Do KH, et al: Coronary artery anomalies: Classification and ECG-gated multi-detector row CT findings with angiographic correlation. Radiographics 26:317–334, 2006.
Ko SM, Kwon JH: Multidetector-row CT coronary angiographic finding of myocardial bridging. Int J Card Imaging 23:71, 2007.
Kuhlman JE, Pozniak MA, Collins J, et al: Radiographic and CT findings of blunt chest trauma: Aortic injuries and looking beyond them. Radiographics 18:1085–1106, discussion 1107–1108; quiz 1, 1998.
Lande A, Berkmen YM: Aortitis: Pathologic, clinical and arteriographic review. Radiol Clin North Am 14:219–240, 1976.
Langwieler TE, Steffani KD, Bogoevski DP, et al: Spontaneous pneumomediastinum. Ann Thorac Surg 78:711–713, 2004.
Leber AW, Becker A, Knez A, et al: Accuracy of 64–slice computed tomography to classify and quantify plaque volumes in the proximal coronary system: A comparative study using intravascular ultrasound. J Am Coll Cardiol 47:672–677, 2006.
Leber AW, Knez A, von Ziegler F, et al: Quantification of obstructive and nonobstructive coronary lesions by 64-slice computed tomography: A comparative study with quantitative coronary angiography and intravascular ultrasound. J Am Coll Cardiol 46:147–154, 2005.
Ledbetter S, Stuk JL, Kaufman JA: Helical (spiral) CT in the evaluation of emergent thoracic aortic syndromes. Radiol Clin North Am 37:575–589, 1999.
LePage MA, Quint LE, Sonnad SS, et al: Aortic dissection: CT features that distinguish true lumen from false lumen. AJR Am J Roentgenol 177:207–211, 2001.
Libby P: Atherosclerosis: Disease biology affecting the coronary vasculature. Am J Cardiol 98(Suppl 12A):3Q–9Q, 2006.
Light RW: Parapneumonic effusions and empyema. Proc Am Thorac Soc 3:75–80, 2006.
Macedo TA, Stanson AW, Oderich GS, et al: Infected aortic aneurysms: Imaging findings. Radiology 231:250–257, 2004.
Mark AS, McCarthy SM, Moss AV, et al: Detection of abdominal aortic graft infection: Comparison of CT and In-labelled white blood cell scans. AJR Am J Roentgenol 144:315–318, 1985.
McCaig LF, Nawar EN: National Hospital Ambulatory Medical Care Survey: 2004 Emergency Department Summary. Advance Data from Vital and Health Statistics, no 372. Hyattsville, MD, National Center for Health Statistics, 2006.
McCollough CH, Bruesewitz MR, Kofler JM: CT dose reduction and dose management tools: Overview of available options. Radiographics 26:503–512, 2006.
McLoud C: Thoracic Radiology: The Requisites. Philadelphia, Mosby, 1998.
Meaney JF, Weg JG, Chenevert TL, et al: Diagnosis of pulmonary embolism with magnetic resonance angiography. N Engl J Med 336:1422–1427, 1997.
Miller LA: Chest wall, lung, and pleural space trauma. Radiol Clin North Am 44:213–224, viii, 2006.
Mirvis SE: Diagnostic imaging of acute thoracic injury. Semin Ultrasound CT MR 25:156–179, 2004.

Mirvis SE, Shanmuganathan K: Imaging in Trauma and Critical Care. Philadelphia, WB Saunders, 2003.
Mita T, Arita T, Matsunaga N, et al: Complications of endovascular repair for thoracic and abdominal aortic aneurysm: An imaging spectrum. Radiographics 20:1263–1278, 2000.
Naghavi M, Libby P, Falk E, et al: From vulnerable plaque to vulnerable patient: A call for new definitions and risk assessment strategies—part I. Circulation 108:1664–1672, 2003.
Naghavi M, Libby P, Falk E, et al: From vulnerable plaque to vulnerable patient: A call for new definitions and risk assessment strategies—part II. Circulation 108:1772–1778, 2003.
Noppen M, Alexander P, Driesen P, et al: Werkgroep voor Medische Thoracoscopie en Interventionele Bronchoscopie. Quantification of the size of primary spontaneous pneumothorax: Accuracy of the Light index. Respiration 68:396–399, 2001.
O'Connor AR, Morgan WE: Radiological review of pneumothorax. BMJ 330:1493–1497, 2005.
O'Hara PJ, Borkowski GP, Hertzer NR, et al: Natural history of periprosthetic air on computerized axial tomographic examination of the abdomen following abdominal aortic aneurysm repair. J Vasc Surg 1:429–433, 1984.
Orton DF, LeVeen RF, Saigh JA, et al: Aortic prosthetic graft infections: Radiologic manifestations and implications for management. Radiographics 20:977–993, 2000.
Oudkerk M, van Beek EJ, Wielopolski P, et al: Comparison of contrast-enhanced magnetic resonance angiography and conventional pulmonary angiography for the diagnosis of pulmonary embolism: A prospective study. The Lancet 359:1643–1647, 2002.
Park JH, Chung JW, Im J, et al: Takayasu arteritis: Evaluation of mural changes in the aorta and pulmonary artery with CT angiography. Radiology 196:89–93, 1995.
Patel K, Makeryus A, Meraj P, et al: 64-detector coronary angiography for the quantification of acute angle take-off and narrow ostial areas in patients with anomalous coronary arteries. Int. J Cardiovasc Imaging 23:103, 2007.
Porcel JM, Light RW: Diagnostic approach to pleural effusion in adults. Am Fam Physician 73:1211–1220, 2006.
Posniak HV, Olson MC, Demos TC, et al: CT of thoracic aortic aneurysms. Radiographics 10:839–855, 1990.
Prasad SR, Wittram C, Shepard A, et al: Standard-dose and 50%-reduced-dose chest CT: Comparing the effect on image quality. AJR Am J Roentgenol 179:461–465, 2002.
Quint LE, Francis IR, Williams DM, et al: Synthetic interposition grafts of the thoracic aorta: Postoperative appearance on serial CT studies. Radiology 211:317–324, 1999.
Quint LE, Williams DE, Francis IR, et al: Ulcerlike lesions of the aorta: Imaging features and natural history. Radiology 218:719–723, 2001.
Quiroz R, Kucher N, Schoepf UJ, et al: Right ventricular enlargement on chest computed tomography: Prognostic role in acute pulmonary embolism. Circulation 109:2401–2404, 2004.
Qureshi NR, Gleeson FV: Imaging of pleural disease. Clin Chest Med 27:193–213, 2006.
Qvarfordt PG, Reilly LM, Mark AS, et al: Computerized tomographic assessment of graft incorporation after aortic reconstruction. Am J Surg 150:227–231, 1985.
Remy-Jardin M, Bahepar J, Lafitte JJ, et al: Multi-detector row CT angiography of pulmonary circulation with gadolinium-based contrast agents: Prospective evaluation in 60 patients. Radiology 238:1022–1035, 2006.
Remy-Jardin M, Remy J, Artaud D, et al: Spiral CT of pulmonary embolism: Technical considerations and interpretive pitfalls. J Thorac Imaging 12:103–117, 1997.
Remy-Jardin M, Tillie-Leblond I, Szapiro D, et al: CT angiography of pulmonary embolism in patients with underlying respiratory disease: Impact of multislice CT on image quality and negative predictive value. Eur Radiol 12:1971–1978, 2002.
Riley P, Rooney S, Bonser R, Guest P: Imaging the post-operative thoracic aorta: Normal anatomy and pitfalls. BJR 74:1150–1158, 2001.
Rofsky NM, Weinreb JC, Grossi EA, et al: Aortic aneurysm and dissection: Normal MR imaging and CT findings after surgical repair with the continuous-suture graft-inclusion technique. Radiology 186:195–201, 1993.
Roos JE, Willmann JK, Weishaupt D, et al: Thoracic aorta: Motion artifact reduction with retrospective and prospective electrocardiography-assisted multi-detector row CT. Radiology 272:271–277, 2002.
Rozenblit A, Marin ML, Veith FJ, et al: Endovascular repair of abdominal aortic aneurysm: Value of postoperative follow-up with helical CT. AJR Am J Roentgenol 16:1473–1479, 1995.
Rozmus G, Daubert JP, Huang DT, et al: Venous thrombosis and stenosis after implantation of pacemakers and defibrillators. J Interv Card Electrophysiol 13:9–19, 2005.
Sahn SA, Heffner JE: Spontaneous pneumothorax. N Engl J Med 342:868–874, 2000.
Sakai T, Dake MD, Semba CP, et al: Descending thoracic aortic aneurysm: Thoracic CT findings after endovascular stent-graft placement. Radiology 212:169–174, 1999.
Sartori S, Tombesi P, Trevisani L, et al: Accuracy of transthoracic sonography in detection of pneumothorax after sonographically guided lung biopsy: Prospective comparison with chest radiography. AJR Am J Roentgenol 188:37–41, 2007.
Savino G, Herzog C, Costello P, et al: 64 slice cardiovascular CT in the ED: Concepts and first experiences. La Radiologica Medica (Italy) 111:481–496, 2006.
Schaffler GJ, Sorantin E, Groell R, et al: Helical CT angiography with maximum intensity projection in the assessment of aortic coarctation after surgery. AJR Am J Roentgenol 175:1041–1045, 2000.
Schoder M, Cartes-Zumelzu F, Grabenwoger M, et al: Elective endovascular stent-graft repair of thoracic aortic aneurysms: Clinical results and midterm follow-up. AJR Am J Roentgenol 180:709–715, 2003.
Schoepf UJ, Costello P: CT angiography for diagnosis of pulmonary embolism: State of the art. Radiology 230:329–337, 2004.
Schoepf UJ, Goldhaber SZ, Costello P: Spiral computed tomography for acute pulmonary embolism. Circulation 109:2160–2167, 2004.
Schoepf UJ, Kucher N, Kipfmueller F, et al: Right ventricular enlargement on chest computed tomography: A predictor of early death in acute pulmonary embolism. Circulation 110:3276–3280, 2004.
Schoepf UJ, Zwerner PL, Savino G, et al: How I do it: Coronary CT angiography. Radiology 244:48–63, 2007.
Schueller-Weidekamm C, Schaefer-Prokop CM, Weber M, et al: CT angiography of pulmonary arteries to detect pulmonary embolism: Improvement of vascular enhancement with low kilovoltage settings. Radiology 241:899–907, 2006.
Siegel CL, Cohan RH, Korobkin M, et al: Abdominal aortic aneurysm morphology: CT features in patients with ruptured and unruptured aneurysms. AJR Am J Roentgenol 163:1123–1129, 1994.
Small JH, Dixon AK, Coulden RA, et al: Fast CT for aortic dissection. BJR 69:900–905, 1996.
Sommer T, Fehske W, Holzknecht N, et al: Aortic dissection: A comparative study of diagnosis with spiral CT, multiplanar transesophageal echocardiography, and MR imaging. Radiology 199:347–352, 1996.
Song JK, Kim HS, Song JM, et al: Outcomes of medically treated patients with aortic intramural hematoma. Am J Med 113:181–187, 2002.
Spodick DH: Acute cardiac tamponade. N Engl J Med 349:684–690, 2003.
Stanson AW, Kazmier FJ, Hollier LH, et al: Penetrating atherosclerotic ulcers of the thoracic aorta: Natural history and clinicopathologic correlations. Ann Vasc Surg 1:15–23, 1986.
Stein PD, Athanasoulis C, Alavi A, et al: Complications and validity of pulmonary angiography in acute pulmonary embolism. Circulation 85:462–468, 1992.
Stein PD, Hull RD, Pineo G: Strategy that includes serial noninvasive leg tests for diagnosis of thromboembolic disease in patients with suspected acute pulmonary embolism based on data from PIOPED: Prospective Investigation of Pulmonary Embolism Diagnosis. Arch Intern Med 155:2101–2104, 1995.
Stein PD, Woodard PK, Hull RD, et al: Gadolinium-enhanced magnetic resonance angiography for detection of acute pulmonary embolism: An in-depth review. Chest 124:2324–2328, 2003.
Stein PD, Woodard PK, Weg JG, et al: Diagnostic pathways in acute pulmonary embolism: Recommendations of the PIOPED II investigators. Radiology 242:15–21, 2007.
Stern EJ, Frank MS: Acute traumatic hemopericardium. AJR Am J Roentgenol 162:1305–1306, 1994.
Sudwarts G, Foler D: Best evidence topic report: Does plain radiography predict pneumothorax size? Emerg Med J 24:49, 2007.
Sueyoshi E, Matsuoka Y, Imada T, et al: New development of an ulcerlike projection in aortic intramural hematoma: CT evaluation. Radiology 224: 536–541, 2002.
Sueyoshi E, Matsuoka Y, Sakamoto I: Fate of intramural hematoma of the aorta: CT evaluation. J Comput Assist Tomogr 21:931–938, 1997.
Tatli S, Yucel EK, Lipton MJ: CT and MR imaging of the thoracic aorta: Current techniques and clinical applications. Radiol Clin North Am 42:565–585, 2004.
Thilo C, Costello P, Schoepf UJ: Coronary artery anomalies at 64 slice coronary CT angiography. Scientific exhibit at the annual meeting of the European Congress of Radiology, 2007.
Tillie-Leblond I, Mastora I, Radenne F, et al: Risk of pulmonary embolism after a negative spiral CT angiogram in patients with pulmonary disease: 1-year clinical follow-up study. Radiology 223:461–467, 2002.
Tittle SL, Lynch RJ, Cole PE, et al: Midterm follow-up of penetrating ulcer and intramural hematoma of the aorta. J Thorac Cardiovasc Surg 123:1051–1059, 2002.
Tokuda Y, Matsushima D, Stein GH, et al: Intrapleural fibrinolytic agents for empyema and complicated parapneumonic effusions: A meta-analysis. Chest 129:783–790, 2006.
Value of the ventilation/perfusion scan in acute pulmonary embolism: Results of the prospective investigation of pulmonary embolism diagnosis (PIOPED). The PIOPED Investigators. JAMA 263:2753–2759, 1990 .
Van Dyke CW, Flamm SD, White RD: Disease of the thoracic aorta. In Freundlich IM, Bragg DG (eds): A Radiologic Approach to Disease, 2nd ed, Baltimore, MD, Williams and Wilkins, 1997.
Van Guens RJM, Cademartiri F: Anatomy of the coronary arteries and veins in CT imaging. In Schoepf UJ (ed): CT of the Heart Principles and Applications: Totowa, NJ, Humana Press, 2004.
Van Marrewijk C, Buth J, Harris PL, et al: Significance of endoleaks after endovascular repair of abdominal aortic aneurysms. J Vasc Surg 35:461–473, 2002.
Vernhet H, Serfaty JM, Serhal M, et al: Abdominal CT angiography before surgery as a predictor of postoperative death in acute aortic dissection. AJR Am J Roentgenol 182:875–879, 2004.

Von Kodolitsch Y, Csosz SK, Koschyk DH, et al: Intramural hematoma of the aorta: Predictors of progression to dissection and rupture. Circulation 107:1158–1163, 2003.
Vrachliotis TG, Bis KG, Haidary A, et al: Atypical chest pain: Coronary, aortic, and pulmonary vasculature enhancement at biphasic single-injection 64-section CT angiography. Radiology 243:368–376, 2007.
Wang ZJ, Reddy GP, Gotway MB, et al: CT and MR imaging of pericardial disease. Radiographics 23(Special issue):S167–S180, 2003.
Washington L, Goodman LR, Gonyo MB: CT for thromboembolic disease. Radiol Clin North Am 40:751–771, 2002.
Webb RW, Muller NL, Naidich DP: High-Resolution CT of the Lung. 3rd ed. Philadelphia, Lippincott Williams & Wilkins, 2001, pp 49–192.
Wells PS, Ginsberg JS, Anderson DR, et al: Use of a clinical model for safe management of patients with suspected pulmonary embolism. Ann Intern Med 129:997–1005, 1998.
Wever JJ, Blankensteijn JD, van Rijn JC, et al: Inter- and intraobserver variability of CT measurements obtained after endovascular repair of abdominal aortic aneurysms. AJR Am J Roentgenol 175:1279–1282, 2000.
White CS, Kuo D: Chest pain in the emergency department: Role of multidetector CT. Radiology 245:672–681, 2007.
Wilson LD, Detterbeck FC, Yahalom J: Clinical practice: Superior vena cava syndrome with malignant causes. N Engl J Med 356:1862–1869, 2007.
Wittram C: How I do it: CT pulmonary angiography. AJR Am J Roentgenol 188:1255–1261, 2007.
Wittram C, Maher MM, Yoo AJ, et al: CT angiography of pulmonary embolism: Diagnostic criteria and causes of misdiagnosis. Radiographics 24:1219–1238, 2004.
Wolfe MW, Lee RT, Feldstein ML, et al: Prognostic significance of right ventricular hypokinesis and perfusion lung scan defects in pulmonary embolism. Am Heart J 127:1371–1375, 1994.
Woodard PK: Pulmonary arteries must be seen before they can be assessed. Radiology 204:1112, 1997.
Worsley DF, Alavi A, Aronchick JM, et al: Chest radiographic findings in patients with acute pulmonary embolism: Observations from the PIOPED study. Radiology 189:133–136, 1993.
Yamada I, Nakagawa T, Himeno Y, et al: Takayasu arteritis: Evaluation of the thoracic aorta with CT angiography. Radiology 209:103–109, 1998.
Yoshida S, Akiba H, Yama N, et al: Thoracic involvement of type A aortic dissection and intramural hematoma. Radiology 228:430–435, 2003.

CHAPTER 9

Nontrauma Abdomen

Stephan W. Anderson, Brian C. Lucey, and Jorge A. Soto

Nontraumatic causes of acute abdominal pain may be secondary to a wide variety of etiologies. When diagnostic imaging is clinically indicated in evaluating these patients, it is critical to localize signs and symptoms to properly triage the patient to the correct imaging modality. For example, in women with pelvic pain, ultrasonography is the imaging modality of choice for initial evaluation. For the abdomen, ultrasonography or computed tomography (CT) is typically used, possibly preceded by plain radiography, depending on the patient's presentation.

In patients with acute abdominal pain, one may consider broad categories of disease including inflammatory, infectious, obstructive, and vascular conditions. In the following sections, these broad categories should be remembered as the various causes of acute abdominal pain are discussed, including bowel, pancreaticobiliary, liver, genitourinary, and splenic. Finally, nonspecific emergent imaging findings with a host of underlying etiologies, often requiring urgent clinical intervention, are discussed.

BOWEL DISEASE

Pathology related to the bowel, including small bowel and colon, represents a significant percentage of acute abdominal pain. Again, one may consider the underlying etiologies of bowel disease in the categories of obstructive, infectious, inflammatory, and vascular. Often, plain radiographs of the abdomen are acquired in patients with suspected underlying bowel disease, commonly followed by CT for more definitive characterization.

Diseases Causing Bowel Obstruction

Diseases causing bowel obstruction include gastric outlet obstruction and volvulus, peptic ulcer disease, mechanical small bowel obstruction, small bowel volvulus, colonic obstruction and volvulus, and adynamic ileus. These are covered in the following sections.

Gastric Outlet Obstruction

Gastric outlet obstruction refers to any entity causing a mechanical obstruction to gastric emptying. Differential considerations are broad and include malignant etiologies such as pancreatic cancer, gastric cancer, and ampullary and duodenal cancer, as well as cholangiocarcinoma. Benign causes of gastric outlet obstruction in adults include peptic ulcer disease, gastric polyps, bezoars, caustic ingestion, gallstones (Bouveret syndrome), and pancreatic pseudocysts. Secondary inflammation or spasm resulting from pancreatitis or acute cholecystitis can cause gastric outlet obstruction. Infectious etiologies of gastric outlet obstruction include abdominal tuberculosis. Gastroduodenal intussusception is a rare cause of mechanical obstruction, typically related to an underlying lead point, which includes benign and malignant neoplasms.

Patients with gastric outlet obstruction present with nausea and vomiting, the hallmark symptoms. Normally these symptoms are temporally related to recent ingestion of a meal, and the vomiting often consists of undigested food. In more chronic cases, weight loss may be described, and in severe cases, patients may present with dehydration and electrolyte imbalances.

Imaging Findings

Plain radiographs may demonstrate a markedly dilated stomach, which may be either air or fluid filled. Infrequently, plain radiography may suggest an underlying diagnosis, for example, an irregular mass lesion identified as a filling defect in cases of malignancy such as gastric cancer. Filling defects may also be identified on plain radiographs in cases of bezoar obstruction. In Bouveret syndrome, a calcified gallstone may be identified in the duodenal bulb.

In patients presenting with acute symptoms of nausea and vomiting, a CT scan may be acquired for further evaluation. Similar to radiography, CT clearly demonstrates the often marked distention of the stomach. CT is also helpful in characterizing the underlying etiologies of obstruction. Malignant causes are seen as enhancing soft tissue mass lesions arising in the stomach in cases of gastric cancer, or slightly more distally around the pancreatic head or ampulla in cases of pancreatic cancer, cholangiocarcinoma, and ampullary and duodenal cancers. Distinction among the latter can be difficult because the area of origin contains quite a bit of overlap.

In cases of peptic ulcer disease (PUD) obstructing the stomach, the ulcer may, rarely, be identified, but the secondary CT findings of gastritis are typically seen as focal thickening of the gastric wall with hyperenhancement of the mucosa related to the inflammation. In these cases, the focal area of inflammation should be scrutinized for a central ulcer seen in PUD. Often, the distinction between PUD and underlying carcinoma is difficult in these cases based on CT. Similar to PUD, in cases of obstruction secondary to inflammatory etiologies such as pancreatitis or cholecystitis, the epicenter of inflammation will be seen around the respective organs, but the secondary inflammation of the stomach may be identified on CT as mural thickening, possibly with hyperenhancement of the mucosa.

Gastric outlet obstruction secondary to various benign etiologies is often apparent, as in cases of pancreatic pseudocyst obstruction. Hyperplastic polyps, the most common form of gastric polyp, may, rarely, cause gastric obstruction and may be seen in the region of the prepyloric antrum as they cause obstruction by prolapse into the pyloric channel. On CT, the appearance is that of a pedunculated, soft-tissue attenuation filling defect. In cases of Bouveret

syndrome, the obstructing gallstone may be identified as a calcified filling defect in the duodenal bulb. Bezoars are seen at CT as mottled-appearing filling defects within the stomach, although these may be seen more distally within the gastrointestinal tract and have been reported to cause small bowel obstructions.

Gastric Volvulus

Gastric volvulus, an abnormal rotation of the stomach around its axis, in its acute form represents a surgical emergency. Gastric volvulus may be classified as one of two forms or a combination of the two: mesenteroaxial or organoaxial. In the mesenteroaxial form, the less common form, the stomach rotates around the axis bisecting both the lesser and greater curvatures of the stomach. In the organoaxial form, the stomach rotates around the axis connecting the gastroesophageal junction (GEJ) and the pylorus.

In cases of gastric volvulus, the Borchardt triad of upper abdominal pain, retching without vomiting, and inability to pass a nasogastric tube may be present. This triad is reported in up to 70% of acute cases of gastric volvulus.

Imaging Findings

The most common causative factor of gastric volvulus in the adult population is diaphragmatic defects, so plain radiographs may demonstrate an intrathoracic, gas-filled viscus. In cases of mesenteroaxial volvulus, supine radiographs may demonstrate typical findings of a spherical lucency with a characteristic "beak" in the region of the distal stomach. Upright radiographs show differential air–fluid levels at different heights in cases of mesenteroaxial volvulus. Organoaxial volvulus, on the other hand, characteristically reveals a single air–fluid level in an abnormally transversely oriented stomach.

In patients presenting with a clinical suspicion of a gastric volvulus, an urgent upper gastrointestinal series can secure a prompt diagnosis. In cases of gastric volvulus, an obstruction may be identified at the site of volvulus. Mesenteroaxial volvulus demonstrates a barium-filled stomach with the GEJ below the antrum and with the typical "beak" seen in the region of the distal stomach, as on radiography. If barium gets past the GEJ, an "upside-down" stomach is seen. Transverse position of the stomach as well as an abnormal inferior location of the GEJ suggest organoaxial volvulus.

With the multiplanar capabilities of multidetector CT (MDCT) scanners, patients with suspected gastric volvulus may undergo a CT scan in the initial diagnostic evaluation. As on radiography, CT typically demonstrates the presence of a hiatal hernia, commonly the paraesophageal type, or diaphragmatic eventration, which increases the likelihood of organoaxial gastric volvulus. Multiplanar reformations are particularly useful in defining precisely the anatomy of the volvulus. Like fluoroscopy, CT demonstrates the abnormally positioned gastric antrum located superior to the GEJ; an "upside-down" stomach when the rotation is complete. Organoaxial volvulus demonstrates an abnormally transverse lie of the stomach and an inferiorly positioned GEJ given its axis of rotation. As organoaxial volvulus is more often associated with diaphragmatic defects, the stomach is often identified in the thorax at the time of volvulus.

In cases of gastric volvulus on CT, especially the organoaxial type, complications of ischemia may be identified, including pneumatosis and portomesenteric vein gas. Mesenteroaxial, unlike organoaxial, volvulus is more frequently incomplete and less likely to cause acute complications such as necrosis.

Peptic Ulcer Disease

Peptic ulcer disease, most commonly secondary to *Helicobacter pylori,* rarely presents acutely. However, complications relating to PUD, such as acute hemorrhage or gastroduodenal perforation, may present acutely. Additionally, the somewhat more subacute presentation of gastric outlet obstruction may require imaging evaluation, as detailed above. Causes of peptic ulcers other than *H. pylori* include nonsteroidal antiinflammatory drug use, Zollinger-Ellison syndrome, various infections such as cytomegalovirus, chemotherapy, and radiation. Bleeding complications related to PUD usually do not require imaging evaluation.

Epigastric to left upper quadrant burning pain and bloating, temporally related to meals and possibly radiating to the back, are the common description of PUD-related pain. Nausea and vomiting as well as anorexia may be described. A sudden onset of pain suggests perforation. Patients with acute hemorrhage often present with hematemesis.

Imaging Findings

In patients with acute perforation related to PUD, pneumoperitoneum may be identified on initial plain radiographs. Like plain radiography, CT scan may identify findings of pneumoperitoneum in cases of ulcer perforation. Often, the underlying ulcer or mural rent is not clearly identified. Small foci of air may be seen around the area of perforation in the stomach or duodenum and suggest the underlying etiology. There may be focal wall thickening in the region of the ulcer in the stomach or duodenum. When oral contrast is administered in cases of unsuspected hollow viscus perforation, extravasation of contrast into the peritoneal cavity is often identified. CT scan may characterize underlying PUD in cases of gastric outlet obstruction, as detailed above.

Mechanical Small Bowel Obstruction

Mechanical small bowel obstruction represents a relatively common cause of abdominal pain and is a frequent indication for abdominal imaging. The most common cause of mechanical small bowel obstruction is adhesions from prior surgical intervention. Other common causes include malignancy, acute inflammatory processes, and hernias. Less common causes include gallstone ileus and small bowel intussusception.

Patients with mechanical small bowel obstruction typically present with abdominal pain, nausea, vomiting, abdominal distention, and constipation. Commonly, the abdominal pain is colicky or intermittently cramping. Initially it may be mild, with progression of symptoms as the duration increases. Vomiting initially consists of gastric contents, followed by more distal bowel contents including bile and finally feculent material. The temporal relationship between the onset of bowel obstruction and symptoms of vomiting is related to position of the obstruction, with more proximal causes presenting with vomiting earlier in

the episode of obstruction. The vomiting may result in dehydration and electrolyte imbalances. In comparison with colonic obstruction, vomiting occurs earlier and commonly precedes constipation.

Imaging Findings

The initial imaging evaluation of patients with suspected mechanical small bowel obstruction often includes plain radiographs. The diagnosis of small bowel obstruction on plain radiography involves the visualization of distended loops of small bowel filled with air or fluid. The differentiation of small bowel loops from the colon is achieved by identifying the valvulae conniventes, also known as plicae circulares, of the small bowel, which are thin, mucosal folds extending across the entire small bowel loops. The haustral folds of the colon, on the other hand, are thicker bands alternating with the thick folds termed plicae semilunares, which do not cross the entire lumen of the colon. The small bowel loops are more central in the abdomen, with the colon seen along the periphery. Typically, 3 cm is accepted as the upper limit of normal for the diameter of the small bowel. The presence of a hernia as the cause of a small bowel obstruction may be suggested by plain radiographs based on the presence of small bowel loops in unusual locations, such as the inguinal canal, distal to dilated loops of small bowel. Alternatively, radiographs demonstrating protrusion of a segment of small bowel, as evidenced by a short segment of bowel clearly outlined by air outside the abdominal wall, again distal to dilated loops of small bowel, may indicate a hernia as the underlying etiology.

CT is often used for further characterization in patients with suspected mechanical small bowel obstruction. Similar to radiography, the diagnosis on CT involves identifying distended air- and fluid-filled loops of small bowel, typically greater than 3 cm in diameter. The small bowel "feces" sign, which is the presence of air and particulate matter within loops of small bowel resembling feces, is a finding commonly seen in small bowel obstruction and is helpful in its diagnosis by suggesting increased bowel transit time. Often, CT allows for the diagnosis of the exact point of transition between distended loops of small bowel and the more normal collapsed loops of small bowel and possibly for identifying the underlying cause of the small bowel obstruction (Fig. 9-1).

Closed loop obstructions are a subset of mechanical small bowel obstructions demanding acute clinical intervention. The term *closed loop obstruction* signifies the presence of two transition points, one of which is found at the proximal extent of the closed loop and one at its distal extent. The vascular supply of these segments of small bowel is often compromised in this setting, and ischemia and necrosis may quickly ensue. Although the diagnosis of a closed loop obstruction might be suggested on plain radiographs by the presence of a short segment of distended small bowel, as well as transition points that may or may not be visualized, this diagnosis is typically confirmed by CT. The CT imaging findings include a sharp transition point, or "beak," at the proximal and distal extent of the closed loop. CT findings suggesting ischemia, including vascular engorgement, and ascites, as well as abnormally decreased enhancement following intravenous contrast administration, often require emergent intervention. More ominous CT imaging findings, including pneumatosis intestinalis, may also be seen and are discussed below.

As noted, adhesions from prior surgical intervention are the most common cause of small bowel obstruction and are notoriously difficult to directly visualize with imaging, and often diagnosis remains one of exclusion. However,

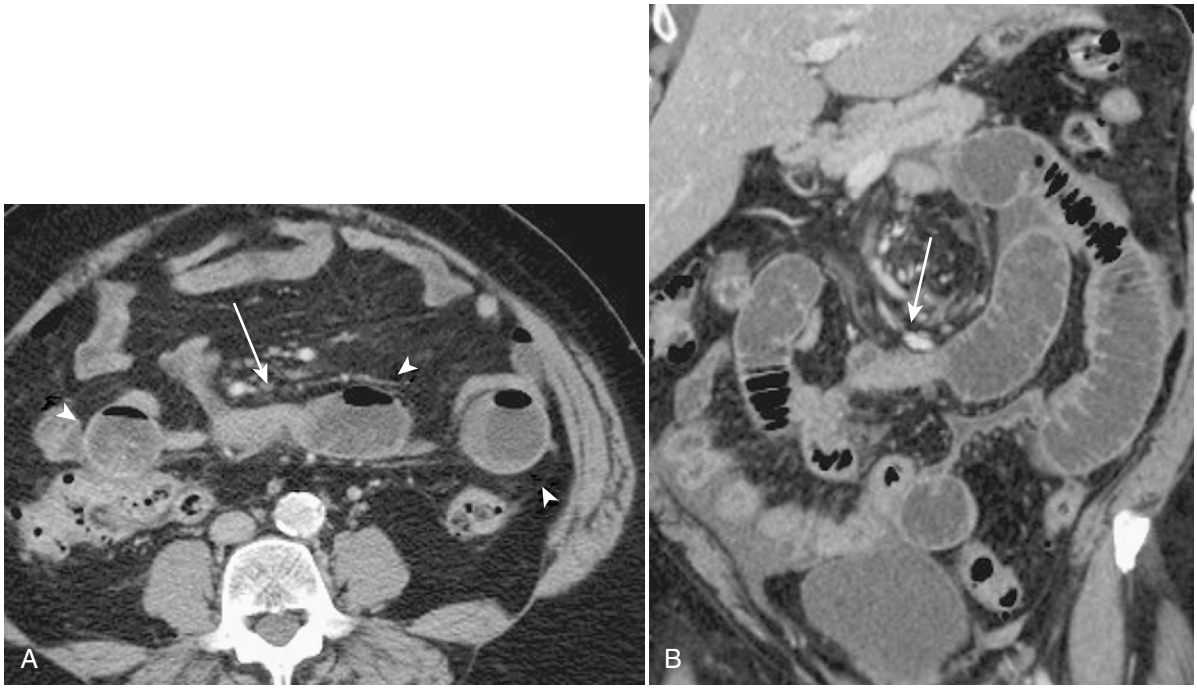


FIGURE 9-1. A 76-year-old female with mechanical small bowel obstruction. Axial **(A)** and coronal **(B)** portal venous phase CT images demonstrate multiple dilated loops of small bowel (*arrowheads*, **A**) with rapid transition from dilated loops to more normal appearing, collapsed loops identified *(arrows)* secondary to postsurgical adhesions on operative repair.

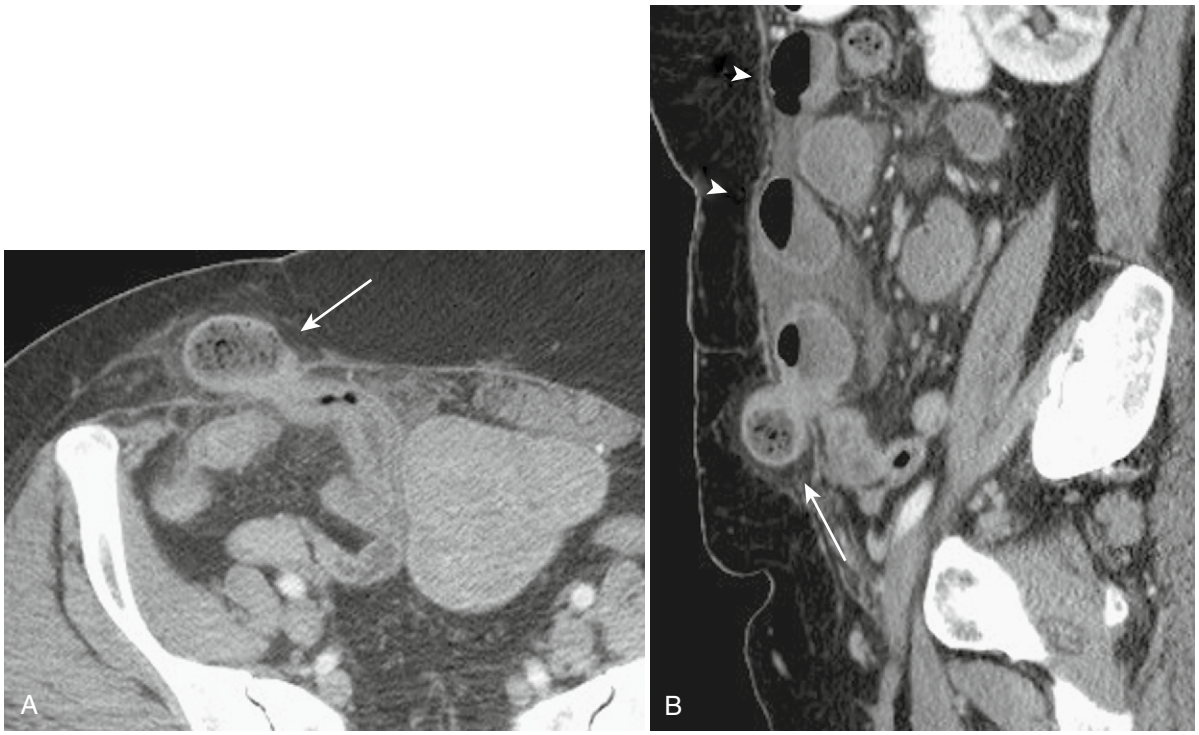


Figure 9-2. A 32-year-old female with incarcerated incisional hernia. Axial **(A)** and sagittal **(B)** portal venous phase images demonstrate incarcerated loop of small bowel *(arrows)* demonstrating fecalization with proximally obstructed loops of small bowel identified (*arrowheads*, **B**).

secondary signs such as abrupt angulation of small bowel loops, and adherence of small bowel loops to nondependent surfaces such as the anterior parietal peritoneum, lend credence to a diagnosis of adhesions as the underlying cause, especially when found at the transition between distended and normal small bowel loops.

Hernias are a second common cause of small bowel obstruction. CT is used to further characterize these hernias, which may be complex in some cases. Common types of hernias include inguinal hernias, umbilical hernias, incisional hernias, and Spigelian hernias in the location of the linea semilunaris (Fig. 9-2). Among less common causes of mechanical small bowel obstruction are internal hernias, including congenital or surgically acquired rents within the mesentery as well as a myriad of other named internal hernias that have been described. CT images including multiplanar reformations are often employed to further characterize these complex hernias.

Gallstone ileus is a rare but interesting form of mechanical small bowel obstruction. In this case, a gallstone erodes into the adjacent duodenum and goes on to obstruct the small bowel, most commonly at the ileocecal valve. Typical imaging findings include the presence of air within the gallbladder or bile ducts as well as dilated loops of small bowel, often with a calcified gallstone at the distal extent. These findings may be seen on plain radiographs as well as on CT. If the gallstone erodes more proximally and obstructs the duodenal bulb, similar imaging appearances of biliary gas, obstruction, and often visualization of the calcified gallstone are seen and are termed *Bouveret syndrome*.

Although more common in the pediatric population, small bowel intussusception may also be seen in adults and can cause obstruction of small bowel loops proximally. In adults, one must always consider the possibility of a lead point such as a neoplasm. Other causes of small bowel intussusception in adults include Meckel's diverticulum and postoperative states especially after gastric bypass. With the increasingly widespread use of CT, transient small bowel intussusceptions are more commonly seen. One may suggest the diagnosis of a transient intussusception based on location and length, as well as the absence of proximal small bowel dilatation (Fig. 9-3).

Small Bowel Volvulus

Although it is often considered a pediatric diagnosis, adults may also present acutely with a small bowel volvulus. Small bowel volvulus can be categorized as either primary or secondary; those with secondary volvulus have an underlying abnormality predisposing to volvulus, such as pregnancy, gastrointestinal tumor, small bowel diverticulum, or intraperitoneal adhesions. A form of small bowel volvulus that often presents within the first month of life is *midgut volvulus*. It is secondary to malrotation and may also affect adult patients. In these cases, a lack of rotation or incomplete rotation of the gut around the axis of the superior mesenteric artery during embryogenesis, termed *midgut malrotation*, may lead to acute volvulus of the entire midgut.

Clinical findings are often nonspecific and include abdominal pain, nausea, and vomiting. More specific clinical histories include those in which the patient describes intermittent epigastric pain, possibly related to meals.

Imaging Findings

Plain radiographs are also nonspecific in patients with small bowel volvulus but may demonstrate proximal small bowel obstruction. In cases of midgut volvulus related to

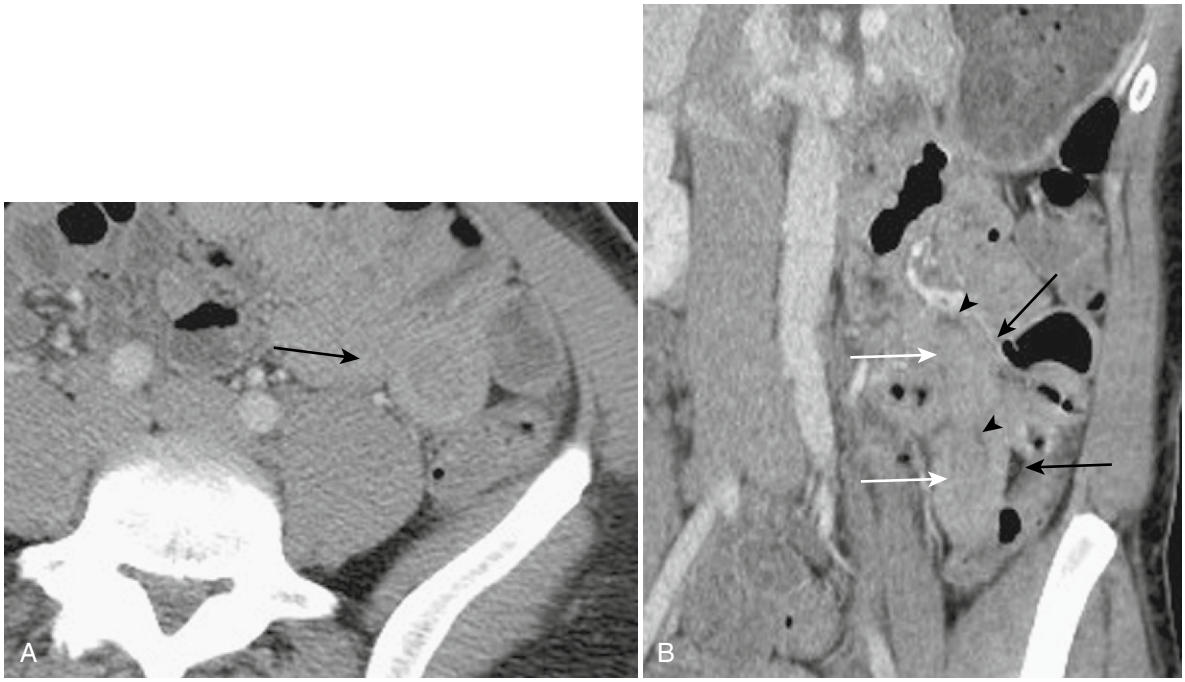


FIGURE 9-3. A 30-year-old female with transient intussusception. Axial **(A)** portal venous phase image reveals the presence of a small bowel intussusception *(arrow)*. Coronal image **(B)** clearly shows the intussusceptum *(white arrows)* within the receiving loop of small bowel and the intussuscipiens *(black arrows)*, surrounded by small amounts of mesenteric fat *(arrowheads)*.

underlying malrotation, plain radiographs may demonstrate partial duodenal obstruction with a dilated, air-filled stomach and proximal duodenum.

Currently, CT is the imaging modality of choice in diagnosing small bowel volvulus. As on plain radiographs, secondary small bowel obstruction may be identified proximal to the volvulus. The CT "whirl" sign is often associated with volvulus of the bowel and is seen as a swirling of mesenteric vessels, strands of soft tissue, and loops of bowel. Although sensitive in the diagnosis of small bowel volvulus, the finding lacks specificity, in that most patients demonstrating this finding have been shown not to have a diagnosis of small bowel volvulus. Nevertheless, the "whirl" sign of twisting mesenteric structures, including loops of small bowel, should raise suspicion of a volvulus, and other CT findings such as infiltration of the mesentery and proximal small bowel dilatation may increase specificity. Small bowel volvulus can rapidly lead to vascular compromise, and the CT images should be scrutinized for findings of ischemia, such as abnormal hypoenhancement of the small bowel. As in cases of small bowel volvulus, the "whirl" sign, in which the superior mesenteric vein and loops of bowel are seen to rotate around the superior mesenteric artery, may be demonstrated on CT in cases of midgut volvulus.

Colonic Obstruction

In the adult population, the most common consideration in colonic obstruction is malignancy, specifically adenocarcinoma. Other causes include diverticulitis, volvulus, intussusception, ischemia, adhesions, fecal impaction, and strictures from a number of prior insults, including radiation. Another possible cause of dilated loops of colon is acute or chronic megacolon. When there is underlying severe inflammation of the colon, acute megacolon is referred to as "toxic" megacolon. When no underlying colonic abnormality is present, this condition is referred to as Ogilvie syndrome. Ogilvie syndrome typically presents in hospitalized patients with significant underlying medical illnesses. The acute forms of megacolon are medical emergencies, given the risks of complication, which include sepsis, ischemia, and perforation. The risks of perforation increase significantly when the diameter of the cecum exceeds 12 cm. The cecum is the most likely portion of the colon to perforate, based on Laplace's law.

Patients with colonic obstruction typically present with abdominal distention and pain as well as nausea and vomiting. Constipation commonly precedes vomiting in colonic obstruction. Depending on the underlying cause, presentation may be acute or more chronic, possibly with changes in the caliber of stool in the case of colonic malignancy. Peritoneal signs are an ominous finding and suggest the possibility of perforation.

Imaging Findings

Typically, plain radiographs demonstrate evidence of air- and fluid-filled loops of dilated colon. A diameter of 8 cm is considered the upper limit of normal for the cecum, whereas 5 cm is considered the upper limit of normal for the remainder of the colon. When acute, colonic obstruction is a medical emergency, given the potential for rapidly developing ischemia, sepsis, or perforation.

CT demonstrates dilated loops of air- or fluid-filled colon proximal to the site of obstruction and is accurate in determining the cause of the obstruction. The CT scans should be scrutinized for signs of perforation, such as free intraperitoneal fluid or air, as well as for signs of ischemia such as abnormal hypoenhancement of the colon. Unlike in

the pediatric population, colonic obstruction secondary to intussusception is generally managed surgically, as opposed to radiologically, with reduction via air enema, for example, given the high likelihood of an underlying malignancy. On CT, toxic megacolon demonstrates dilation of air- or fluid-filled colon with wall thickening and a distorted colonic contour or a lack of the expected haustral pattern. Because Ogilvie syndrome lacks the colonic inflammation, CT is unlikely to demonstrate a similar degree of wall thickening and submucosal edema as toxic megacolon. The chronic form of megacolon represents a functional failure of the colon secondary to various underlying etiologies, including chronic constipation. In these patients, it is often helpful, when prior radiographs are available for comparison, to exclude acute colonic obstruction or megacolon.

Colonic Volvulus

Sigmoid volvulus is the most common form of gastrointestinal volvulus. Cecal volvulus is also a relatively common form of colonic volvulus. Sigmoid volvulus represents twisting of the sigmoid colon around its mesenteric axis. Three forms of cecal volvulus are described: axial torsion type, loop type, and cecal bascule. The axial torsion and loop types represent the most common forms. In the axial torsion type, the cecum rotates around its long axis, appearing in the right lower quadrant. In the loop type, the cecum twists and then inverts, ending in the left upper quadrant. In the cecal bascule, the cecum simply folds medially to the descending colon, producing an occlusion at the site of flexion.

Colonic volvulus typically presents with an acute abdomen with sudden onset of colicky pain. Abdominal distention with a tympanitic abdomen may be appreciated. Constipation with inability to pass flatus or stool accompanies cases of colonic volvulus. Borborygmus is frequently seen in cases of colonic volvulus.

Imaging Findings

Plain radiographs demonstrate the beaked tapering of the efferent and afferent limbs of the dilated loop of sigmoid colon. The classic plain radiograph description of the sigmoid volvulus is that of a coffee-bean-shaped collection of air-filled bowel occupying the left upper quadrant. In cases of axial torsion type cecal volvulus, a markedly distended loop of large bowel may be identified extending from the right lower quadrant to the epigastrium or left upper quadrant. The distended cecum may be identified anywhere in the abdomen, depending on the mobility of the right colon. The cecal bascule is generally identified as an air-filled structure occupying the mid-abdomen on plain radiography.

CT demonstrates similar beaking as well as the "whirl" sign of bowel around mesenteric vasculature common to all types of volvulus. CT has been shown to be accurate in diagnosing cecal volvulus and in differentiating between the various subtypes based on the location of the cecum. Less common forms of colonic volvulus are also encountered, including volvulus of the splenic flexure as well as various segments of the transverse colon.

Adynamic Ileus

Another etiology for bowel dilatation, including small bowel and colon, is adynamic ileus. There are numerous causes of adynamic ileus, also termed paralytic ileus, including recent surgery, drugs including opiates, sepsis, intra-abdominal infection or inflammation, trauma, and central nervous system injuries, among others. The typical symptoms of ileus are mild abdominal pain, nausea, vomiting, and constipation. In contradistinction to mechanical causes of obstruction, adynamic ileus demonstrates diffuse mild dilatation of bowel loops. Focal ileus, the so-called "sentinel loop" sign, may be identified around areas of inflammation within the abdomen and may be helpful in localizing pathology on radiography.

Patients with adynamic ileus typically present with mild abdominal pain, constipation, and bloating. Nausea and vomiting may be associated.

Imaging Findings

Plain radiographs demonstrate dilated bowel loops, often diffusely when the etiology is systemic. When secondary to focal inflammation such as pancreatitis, a more localized ileus may be identified and may be useful in localizing intra-abdominal pathology.

CT has been shown to have a high diagnostic accuracy in distinguishing paralytic ileus from mechanical causes. The CT findings typical of a mechanical cause of obstruction such as a distinct transition point will not be identified in cases of adynamic ileus, which demonstrate mildly dilated loops of bowel diffusely.

Infectious and Inflammatory Diseases

Infectious and inflammatory diseases of the bowel are discussed in the following sections. They include infectious small bowel enteritis, Crohn's disease and diverticulitis of the small bowel, appendicitis, epiploic appendagitis, omental infarction, diverticulitis, inflammatory bowel disease of the colon, infectious colitis, and foreign bodies.

Infectious Small Bowel Enteritis

A multitude of infectious etiologies may cause small bowel enteritis, including viral etiologies such as rotovirus, norovirus, and adenovirus, bacterial causes such as *Campylobacter jejuni*, and parasites including *Giardia lamblia*, all of which may affect the immunocompetent host. Common infectious agents of small bowel enteritis in the immunocompromised host include cytomegalovirus, cryptosporidiosis, and *Mycobacterium avium intracellulare*.

Nonspecific signs and symptoms of infectious enteritis include abdominal cramping, vomiting, and diarrhea. Although the abdomen may be distended with gas, borborygmi are present, distinguishing this from ileus. Patients may be febrile, and leukocytosis may be present. Especially in immunocompetent hosts, the disease is often self-limited, lasting up to several days. When infectious enteritis is severe, dehydration is a relatively common complication of infectious small bowel enteritis. Currently, fecal testing and, increasingly, immunoassays are used in the clinical diagnosis.

Imaging Findings

Plain radiographs are often nonspecific but may demonstrate mildly dilated loops of small bowel similar to adynamic ileus. In more severe cases, the degree of small bowel dilatation may approach the appearance of a small bowel obstruction.

CT imaging, when acquired, is also often nonspecific and may demonstrate mild to moderate small bowel dilatation and mural thickening (Fig. 9-4). Often, the small bowel is diffusely affected; however, certain infections may present in more specific locations such as the proximal small bowel in cases of giardiasis. In the immunocompromised host, a myriad of other infectious etiologies should be considered, as noted above. Typically, nonspecific small bowel wall thickening and mucosal irregularity are identified in cases of cytomegalovirus and cryptosporidium. In patients affected by *Mycobacterium avium intracellulare*, hepatic and splenic enlargement, jejunal wall thickening, and enlarged soft tissue attenuation or, less commonly but more characteristically, low-attenuation lymphadenopathy are described.

Crohn's Disease, Small Bowel

Although Crohn's disease can affect any portion of the gastrointestinal tract, the terminal ileum portion of the small bowel is the most commonly involved. Crohn's disease may affect isolated segments of small bowel proximal to the terminal ileum. Usually, however, in cases of small bowel involvement, the colon is also affected.

Common gastrointestinal symptoms include abdominal pain, diarrhea, and weight loss. The crampy abdominal pain associated with Crohn's disease may be temporarily relieved following defecation. The area of bowel involved may determine the nature of the diarrhea, with those affected by ileitis presenting with watery, large-volume stools.

Imaging Findings

In patients presenting with acute abdominal symptoms related to Crohn's disease of the small bowel, plain radiographs may demonstrate dilatation of proximal bowel loops due to a functional mechanical obstruction secondary to enteritis. Mural thickening of the affected small bowel loops may also be visualized on plain radiographs.

The manifestations of Crohn's disease of the small bowel typically demonstrate nonspecific CT signs of inflammation such as mural thickening. However, findings more specific are often identified. These include isolation to the terminal ileum, hypervascularity and prominence of the vasa recta, the "comb" sign, increased mesenteric fat surrounding loops of small bowel, and "creeping" fat, as well as intra-abdominal fistulae and abscesses (Fig. 9-5).

Small Bowel Diverticulitis

Meckel's diverticulum, the most common congenital anomaly of the gastrointestinal tract, remains asymptomatic in the majority of patients. However, various complications can ensue, including inflammation, termed Meckel's diverticulitis. Although less commonly seen than in the colon, diverticula formation may affect any portion of the small bowel from the duodenum to the ileum. Potential complications include bacterial overgrowth and malabsorptive states. Diverticulitis may also affect the small bowel.

Patients with small bowel diverticulitis may present with localized tenderness in the region affected; however, no specific signs and symptoms are pathognomonic for this diagnosis. Often, these patients are febrile and may present with a leukocytosis. Moreover, malabsorptive states may develop and patients may present with diarrhea and weight loss. Although this is a secondary finding unrelated to diverticulitis, it may add credence to a consideration of small bowel diverticulitis. Plain radiographs, not usually used in the diagnosis of small bowel diverticulitis, may show a focal ileus or "sentinel loop" sign in the area of inflammation.

Imaging Findings

Meckel's diverticulitis may be diagnosed by CT. A Meckel's diverticulum is evident as a blind-ending pouch of variable length containing fluid, air, or particulate debris, often located near the midline but seen anywhere from the right lower quadrant to the mid-abdomen. When the diverticulum is inflamed, mural thickening and surrounding inflammatory stranding may be identified (Fig. 9-6). This might be complicated by frank perforation, possibly yielding an intra-abdominal abscess. In cases of diverticulitis unrelated to Meckel's diverticulum, CT demonstrates focal luminal outpouchings with surrounding inflammatory changes.

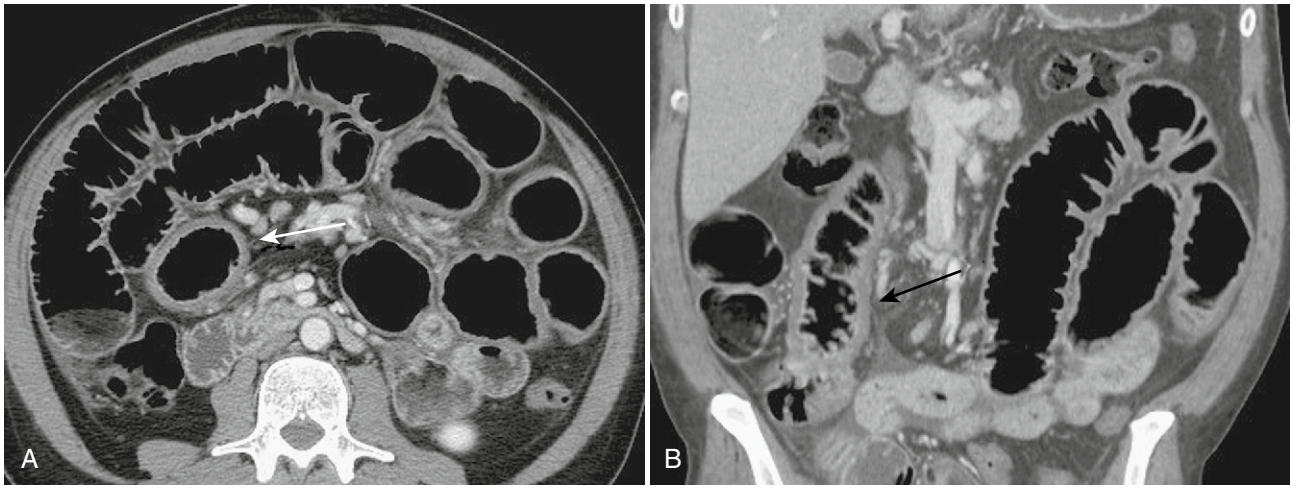


FIGURE 9-4. A 40-year-old male with viral gastroenteritis. Axial **(A)** and coronal **(B)** portal venous phase CT images reveal diffuse small bowel dilatation as well as mural thickening *(arrows)*.

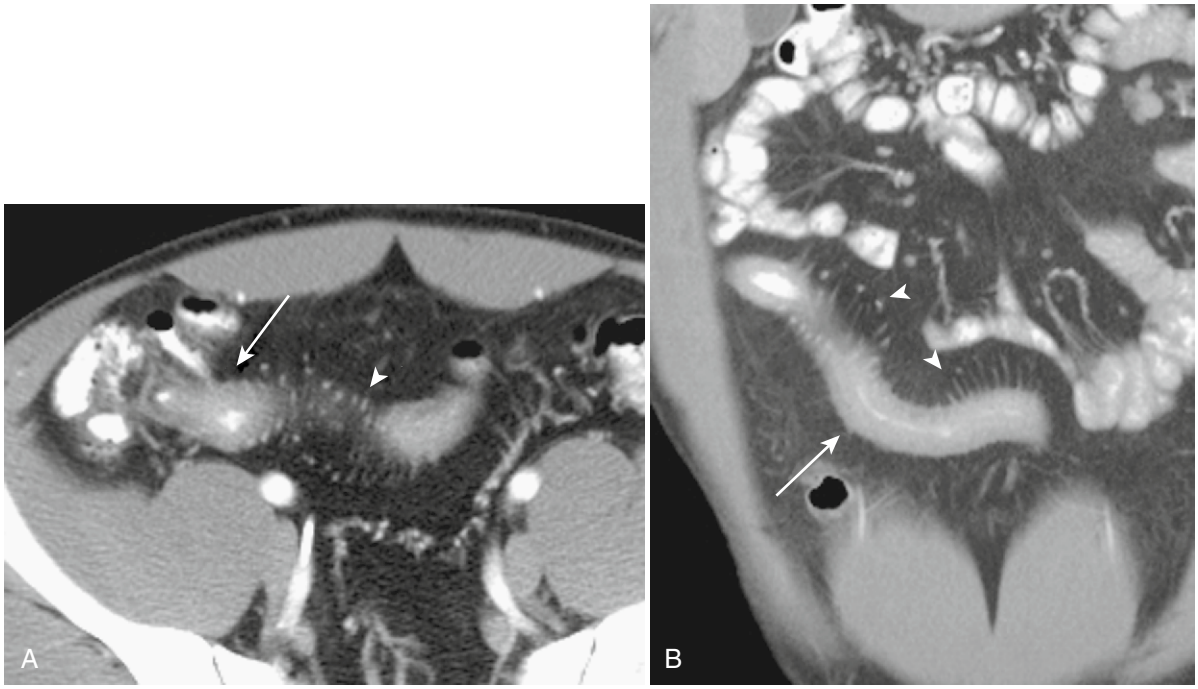


Figure 9-5. A 24-year-old male with Crohn's disease. Axial **(A)** and coronal **(B)** portal venous phase CT images demonstrate thickening of the terminal ileum *(arrows)* with prominence of the vasa recta along the mesenteric border *(arrowheads)*, the so-called "comb" sign.

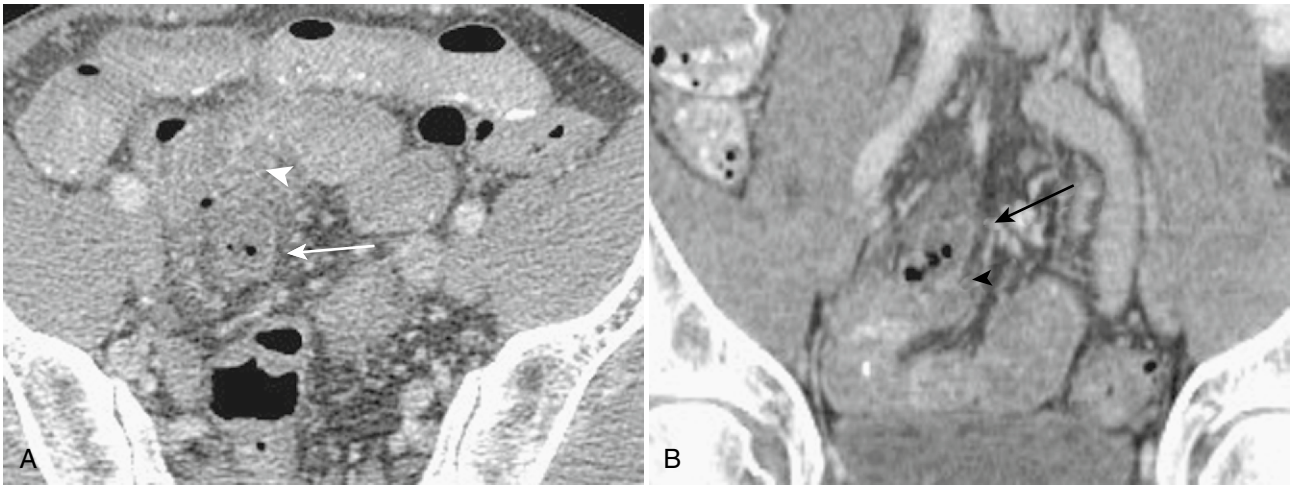


Figure 9-6. A 38-year-old male with Meckel's diverticulitis. Axial **(A)** and coronal **(B)** portal venous phase images reveal a tubular, blind-ending pouch *(arrows)* emanating from adjacent small bowel *(arrowheads)* with surrounding inflammatory changes, findings consistent with Meckel's diverticulitis.

Again, gross perforation with abscess formation may also be seen.

Appendicitis

Appendicitis is a common clinical concern in patients presenting to the emergency department with abdominal pain. In those patients presenting with the classic signs and symptoms, including right lower quadrant pain, leukocytosis, and fever, imaging may not be necessary in making the diagnosis of appendicitis. However, in those patients with atypical presentations or those requiring further characterization of the suspected diagnosis, imaging is often employed. Initially, the appendiceal lumen occludes secondary to a number of causes including fecaliths and lymphoid hyperplasia. Once occluded, intraluminal fluid continues to accumulate, distending the appendix and eventually increasing the intraluminal and intramural pressures to the point of vascular and lymphatic obstruction. Ineffective venous and lymphatic drainage allows bacterial invasion of the appendiceal wall and lumen. If untreated, perforation of the appendix may be a complication.

As noted, the classic description of patients presenting with appendicitis includes right lower quadrant pain, leukocytosis, and fever. Classically, these findings are preceded by anorexia and periumbilical pain. The migration of pain from the periumbilical region to the right lower quadrant is both sensitive and specific in the diagnosis of

appendicitis. However, given the normal range of locations of the appendix as well as varying degrees of appendiceal inflammation, patients often present with atypical signs and symptoms.

Imaging Findings

Abdominal radiographs have been shown to have little clinical utility in patients with suspected appendicitis; therefore, cross-sectional imaging may be the initial diagnostic examination of choice. In the minority of cases, a calcified fecalith may be identified in the right lower quadrant. Also, the "sentinel loop" sign may be identified secondary to appendiceal inflammation.

In the younger population, and especially in females, ultrasonography may be used as an initial imaging evaluation given radiation concerns involved with CT. Ultrasound has been shown to have a high diagnostic accuracy in evaluating for suspected appendicitis. Typical findings include the visualization of a blind-ending tubular structure measuring greater than 6 mm in diameter during graded compression. When present, an appendicolith may also be identified as an echogenic, shadowing focus within the lumen of the appendix. Secondary signs of active inflammation, including free intraperitoneal fluid, may be seen. The complications of appendicitis, which include rupture and abscess formation, may also be detected using ultrasound. Technical limitations of ultrasound include patients with an obese body habitus; moreover, given the wide variety of locations of the normal appendix, those located more posteriorly within the peritoneal cavity pose increased difficulty for evaluation.

Pregnant women often pose a diagnostic challenge when presenting with suspected appendicitis. Typically, ultrasound examination is completed to rule out other causes of abdominal pain in this patient population, such as ectopic pregnancy or ovarian torsion. However, as the gravid uterus enlarges, the appendix becomes displaced from its expected location in the right lower quadrant, and it may be difficult to visualize. Unfortunately, the normal appendix is highly unlikely to be visualized by ultrasonography in pregnancy, and further imaging is often requested to definitively exclude appendicitis. However, when the appendix is visualized on ultrasound, the findings of acute appendicitis are similar to those in nonpregnant patients and include the visualization of a blind-ending tubular structure measuring greater than 6 mm in diameter using a graded compression technique.

When the ultrasound results are equivocal or the appendix is not visualized, CT is often employed in patients with suspected appendicitis. In older or significantly obese patients, CT may be the initial imaging examination. CT has been shown to have a very high diagnostic accuracy in the diagnosis of appendicitis. In those patients with appendicitis, the appendix appears enlarged, often with surrounding inflammatory changes, including the free intraperitoneal fluid. When present, appendicoliths are readily identified on CT (Fig. 9-7). There is a large variety in the diameter of the appendix in normal patients, with sizes ranging up to 1 cm. However, mean values range between 5 and 7 mm depending on whether or not the appendix is distended with air. Therefore, in a patient with an appendix measuring slightly greater than the standard cutoff value of 6 mm, secondary signs of inflammation should be sought, such as hyperenhancement, periappendiceal fat stranding or fluid, fascial thickening, or edema at the origin of the appendix as evidenced by thickening of the adjacent cecum, the so-called "arrowhead" sign (Fig. 9-8). Filling of the appendix by orally or rectally introduced positive contrast material is

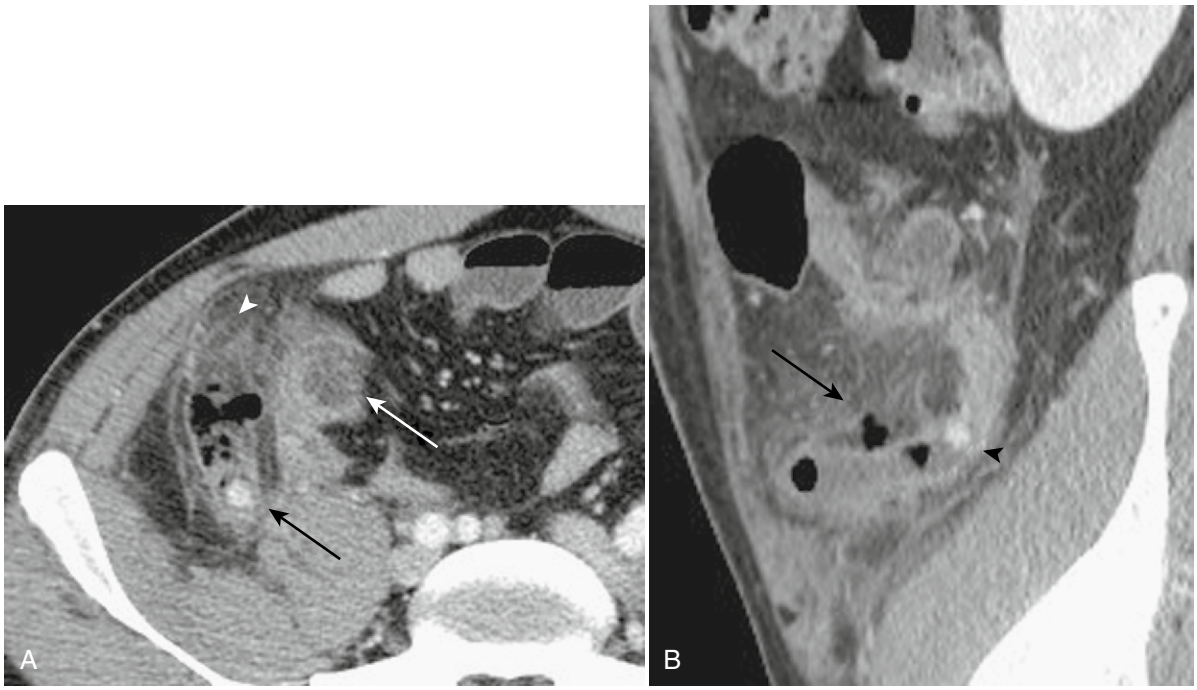


FIGURE 9-7. A 46-year-old male with perforated appendicitis. Axial portal venous phase CT image **(A)** demonstrates an inflamed appendix with periappendiceal fat stranding *(arrowhead)* and phlegmon *(white arrow)*, as well as an appendicolith at the appendiceal base *(black arrow)*. Sagittal portal venous phase CT image **(B)** demonstrates extraluminal air *(black arrow)* consistent with perforation as well as the appendicolith *(arrowhead)*.

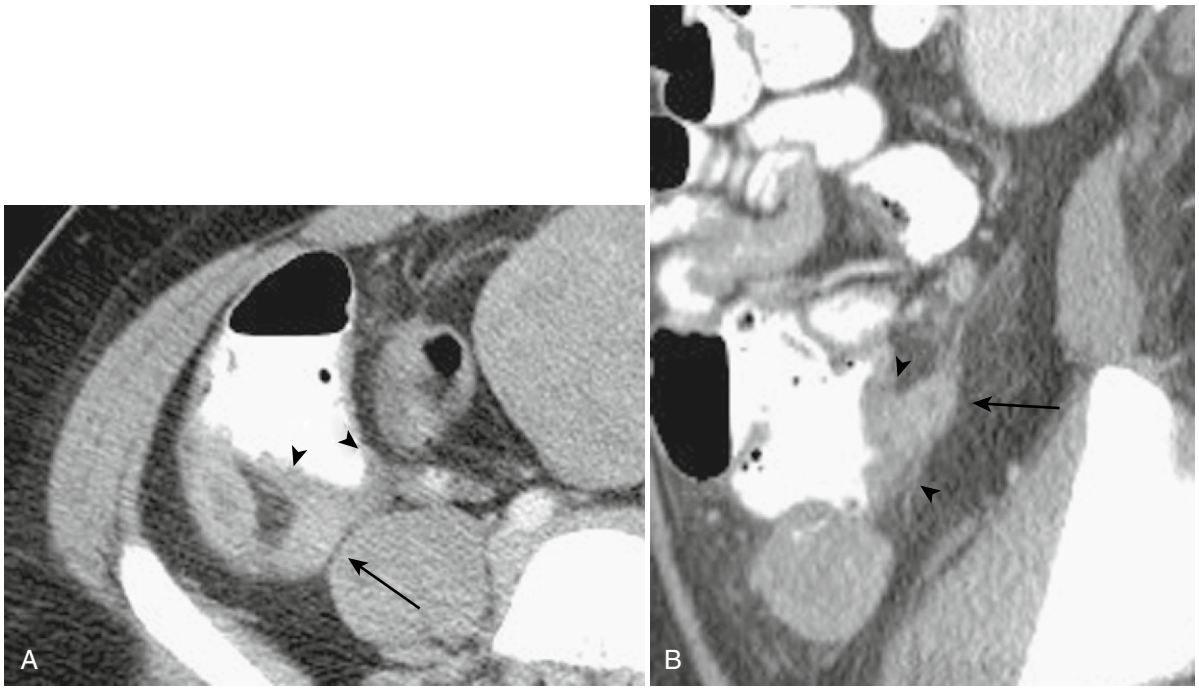


Figure 9-8. A 20-year-old female with appendicitis. Axial **(A)** and sagittal **(B)** portal venous phase CT images demonstrate dilated appendix consistent with appendicitis *(arrows)*. Though not necessary in this case given significant appendiceal dilatation, secondary signs of adjacent cecal wall thickening (*arrowheads*, **B**), the so-called "arrowhead" sign, may be useful in equivocal cases.

a useful means of excluding obstruction of the appendix and, therefore, acute appendicitis. When the appendix is not visualized, this finding, in the absence of right lower quadrant inflammation, carries a high negative predictive value of appendicitis.

In pregnant patients, ultrasonography is typically employed initially, given risks of ionizing radiation. However, in those patients with an inconclusive ultrasound examination, both CT and, with increasing frequency, magnetic resonance imaging (MRI) are often used. The findings of acute appendicitis on CT in pregnant patients are similar to those in the nonpregnant population.

Given concerns regarding radiation dose to the fetus, MRI is frequently employed to evaluate for suspected appendicitis in pregnant patients. MRI offers high diagnostic accuracy and is an excellent modality for excluding appendicitis. The appendix is considered normal when it is less than or equal to 6 mm in diameter, or is filled with air or contrast material. As on CT, secondary findings such as periappendiceal inflammation are used to increase specificity when the appendix is at the upper limits of normal size. As the gravid uterus enlarges, the cecum and therefore the appendix may be in atypical locations, displaced superiorly by the uterus. Therefore, it is helpful to identify the landmarks of the terminal ileum and cecum in attempting to localize the appendix on MRI in pregnant patients.

Epiploic Appendagitis

Epiploic appendages are small fat-containing, serosal-covered outpouchings of the colon that project into the peritoneal cavity. Appendagitis represents torsion of these outpouchings with subsequent inflammation and thrombosis of the venous supply located centrally. Alternatively, spontaneous venous thrombosis has been described to increase the predilection of subsequent torsion.

Prior to the increasing utilization of CT, epiploic appendagitis was often misdiagnosed as acute appendicitis or diverticulitis given similar clinical presentations. Typically, symptoms include rapid onset of localized pain in the right or left flank, although more chronic torsion of the appendages may result in minimal or no symptoms. The pain is usually constant, and rebound tenderness is often elicited. Patients may present with low-grade fever and leukocytosis.

Imaging Findings

Given the increasingly routine use of CT imaging in patients with abdominal pain, the imaging manifestations of epiploic appendagitis have been well described. The characteristic imaging findings include an ovoid lesion containing fat, abutting the colon, with surrounding inflammatory stranding (Fig. 9-9). A central high-attenuation focus has been described and is thought to be related to a thrombosed vein. Although helpful when seen, the absence of this finding does not exclude the diagnosis.

Although epiploic appendagitis is typically a CT diagnosis, findings have been well described using both ultrasonography and MRI. The diagnosis using these modalities also includes the demonstration of the ovoid fatty lesion with surrounding inflammatory changes.

Omental Infarction

Omental infarction is often idiopathic in its etiology. It has been hypothesized that there may be a congenital anomalous, atypically tenuous blood supply to the omentum in some patients. However, a significant portion of cases are related to recent intra-abdominal surgery. Other

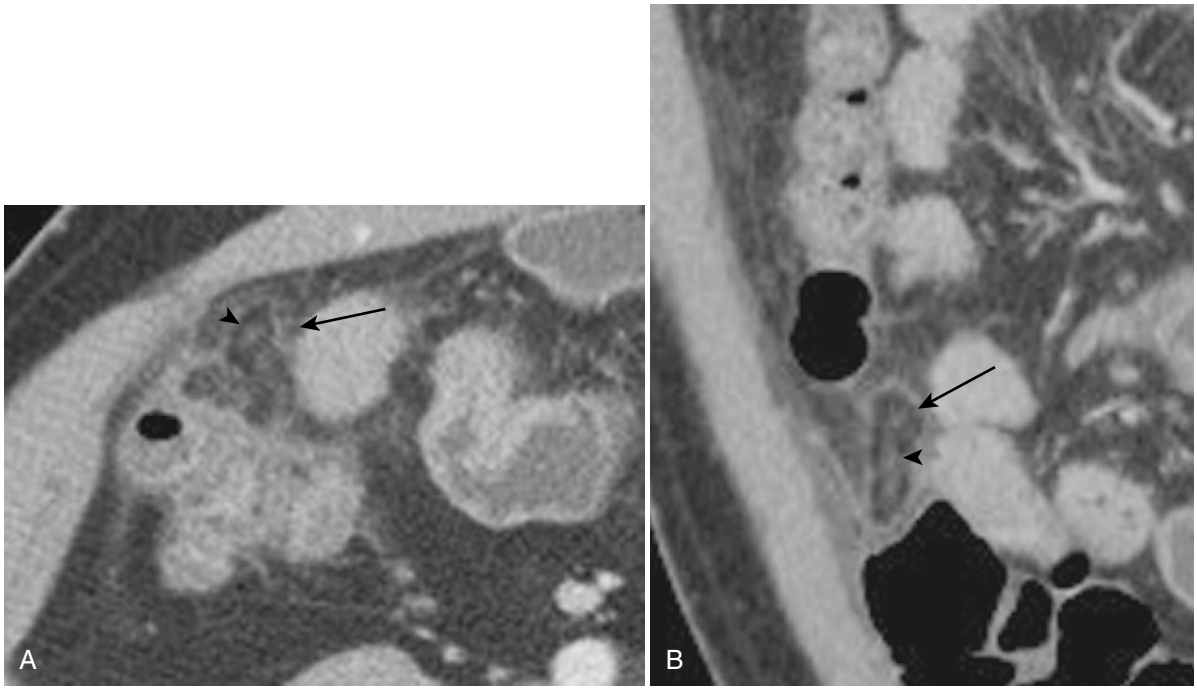


FIGURE 9-9. A 42-year-old male with epiploic appendagitis. Axial **(A)** and coronal **(B)** portal venous phase CT images demonstrate a pericolonic, ovoid, fat-containing lesion *(arrows)* with a central high-attenuation focus *(arrowheads)* consistent with epiploic appendagitis.

associations include strangulation of the omentum such as in inguinal hernias that include portions of the omentum.

Omental infarction may present with acute abdominal pain, but, as in epiploic appendagitis, it typically represents a benign, self-limited disease process. Patients present with acute or subacute focal abdominal pain that may mimic the acute pain of appendicitis and diverticulitis. Again, patients may present with low-grade fever and leukocytosis. Occasionally, the area of infarction may be palpated as an intra-abdominal mass lesion. In some cases, especially those with more severe and prolonged symptoms, operative management is successfully employed.

Imaging Findings

Omental infarction is an alternative diagnosis that often presents with imaging features somewhat similar to epiploic appendagitis. CT reveals an ill-defined focal area of fat with evidence of inflammation and heterogeneous attenuation that may appear somewhat masslike. Follow-up CT imaging often demonstrates a more well-defined area of fat attenuation with heterogeneous attenuation throughout.

Like epiploic appendagitis, omental infarction can be readily diagnosed with ultrasound. Ultrasonography may identify the findings of a fat-containing lesion, as evidenced by a hyperechoic, noncompressible lesion in the region of the omentum.

Diverticulitis

Diverticulitis is a relatively common cause of abdominal pain and is predominantly seen to affect the colon. Diverticulitis represents the inflammation of small outpouchings, known as pulsion diverticula or pseudodiverticula of mucosa and submucosa through the regions of the underlying muscularis propria penetrated by the vasa recta. This is commonly secondary to raised intraluminal pressures common in Western, low-fiber diets and constipation; the sigmoid colon is postulated to be most commonly affected, as it has the smallest diameter leading to the greatest intraluminal pressures. Diverticulitis typically presents as localized, usually left-sided, abdominal pain. More severe disease, especially with the presence of complicating abscesses, may present with systemic symptoms such as fever and may develop a leukocytosis. These patients may also present with anorexia, nausea, and vomiting. The signs of peritonitis may develop with cases of more gross perforation.

Imaging Findings

Although ultrasound has been shown to be accurate in the diagnosis of acute diverticulitis, this disease is more commonly diagnosed using CT. CT scans typically involve the use of oral and intravenous contrast. Left-sided diverticulitis predominates with the typical CT imaging findings, including colonic wall thickening and pericolonic fat stranding seen in close proximity to a diverticulum. Typically, diverticulosis is noted throughout a longer segment of adjacent colon, although only a single diverticulum is necessary to cause acute diverticulitis. Often, several small foci of extraluminal gas may be identified in the region of inflammation.

Multiple complications are associated with acute diverticulitis including intramural sinus tracts or abscess, as well as extracolonic phlegmon or abscess formation (Fig. 9-10). Frank perforation with gross free intraperitoneal air may also be encountered in patients with diverticulitis. Other complications include the formation of fistulae, most commonly colovesicular, as well as colovaginal, coloenteric, and colouterine. In those patients with a CT diagnosis of diverticulitis, follow-up colonoscopy is normally advised to rule out underlying malignancy masquerading as diverticulitis.

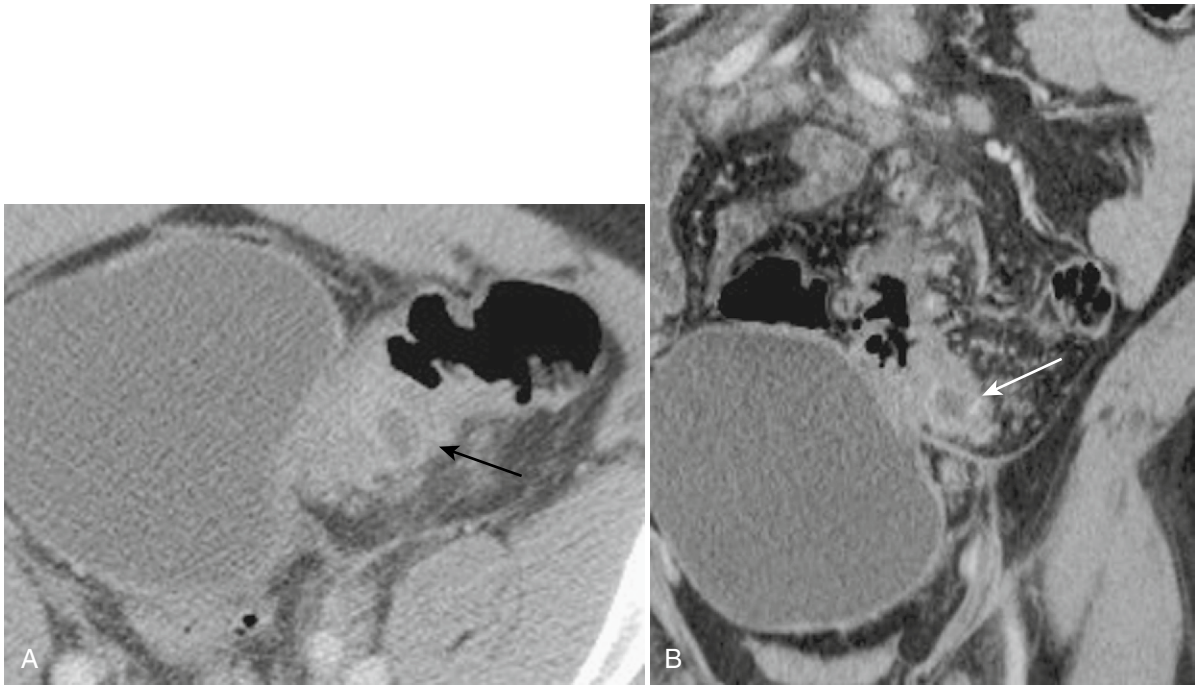


Figure 9-10. A 50-year-old male with diverticulitis. Axial **(A)** and coronal **(B)** portal venous phase CT images reveal thickening of the sigmoid colon with a central low-attenuation focus consistent with an intramural abscess *(arrows)*.

Inflammatory Bowel Disease, Colon

Inflammatory causes of colitis include Crohn's disease and ulcerative colitis, both of which may present with acute signs and symptoms. Crohn's disease represents granulomatous, transmural inflammation of the bowel with skip lesions in which noncontiguous segments of bowel are affected. Skip lesions are not present in ulcerative colitis. Crohn's disease most commonly demonstrates an ileocolic distribution, affecting both the colon and ileum, followed by disease isolated to the ileum, typically in its distal portion, or disease limited to the colon. Ulcerative colitis, on the other hand, involves the rectum with continuous involvement of more proximal bowel, and, unlike the transmural involvement of Crohn's disease, is limited to the mucosa and submucosa with formation of crypt abscesses and mucosal ulceration.

Typical clinical presentations in Crohn's disease and ulcerative colitis include abdominal pain, tenesmus, and diarrhea. A distinguishing feature may be the presentation of bloody diarrhea in patients with ulcerative colitis, a finding rarely seen in Crohn's disease. Especially with more severe disease, systemic symptoms such as nausea and vomiting along with malaise and low-grade fever may develop. Typically, Crohn's disease presents somewhat more insidiously and symptoms may have persisted for several years prior to diagnosis. Also, patients with Crohn's disease often have perianal disease in the form of fistulae and sinus tracts. Whereas ulcerative colitis rarely involves the small bowel, Crohn's disease more commonly causes weight loss secondary to malabsorption related to small bowel involvement.

Imaging Findings

In patients with inflammatory bowel disease and acute abdominal pain, intramural edema may be identified as thumb printing of the colonic wall. In patients with ulcerative colitis, the colon should be evaluated for signs of toxic megacolon as evidenced by a long segment of air-filled, significantly distended colon, often greater than 6 cm in diameter. Also, dilatation of the bowel proximal to areas of active inflammation or stricture may be identified. Secondary findings in patients with inflammatory bowel disease include extraintestinal manifestations, such as sacroiliitis, cholelithiasis, and renal stones, that may be identified on plain radiography.

Typically, in patients presenting acutely, a CT scan is acquired in the emergency department setting. Crohn's disease demonstrates bowel wall thickening in the affected segments, which are most commonly right-sided; diffuse colitis may also be seen, although isolated left-sided involvement with Crohn's disease is atypical (Fig. 9-11). Ulcerative colitis, unlike Crohn's disease, demonstrates contiguous involvement of the bowel from the rectum proximally. Therefore, the CT findings are usually isolated to the left side. The bowel wall may demonstrate stratification, also known as the "water halo" sign, in which the bowel wall consists of two or three symmetrically thickened layers. In the case of three symmetrically thickened layers, also known as the "target" sign, the inner hypoattenuating layer is thought to represent edema within the submucosa. In patients with chronic inflammation, as in Crohn's disease or ulcerative colitis, a pattern known as the "fat halo" sign may be seen in which there is three-layer stratification with the middle layer demonstrating fat attenuation (Fig. 9-12). The finding of a "fat halo" sign is more commonly associated with ulcerative colitis. Although these are nonspecific signs, taken in context with the remainder of the imaging findings as well as the clinical presentation, they may suggest a potential diagnosis of inflammatory bowel disease. Also, hyperenhancement of the bowel after contrast administration is

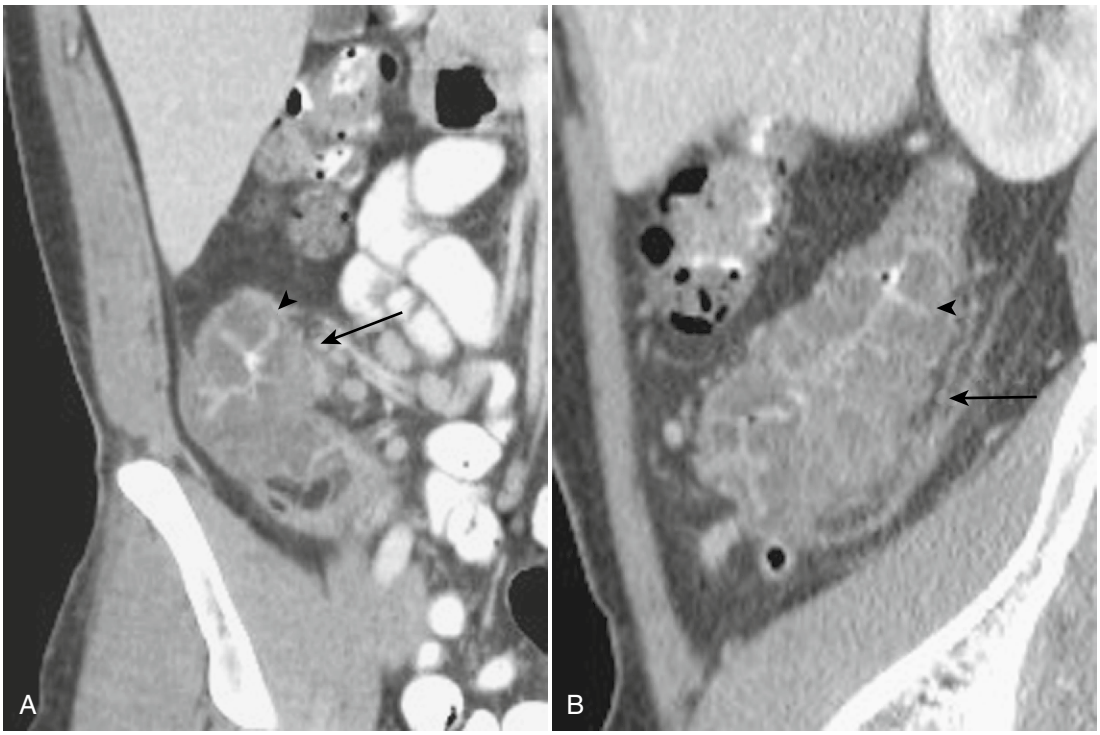


FIGURE 9-11. A 38-year-old male with Crohn's disease. Coronal **(A)** and sagittal **(B)** portal venous phase images demonstrate significant cecal wall thickening *(arrows)* with oral contrast identified between the thickened haustra *(arrowheads)*, the so-called "accordion" sign.

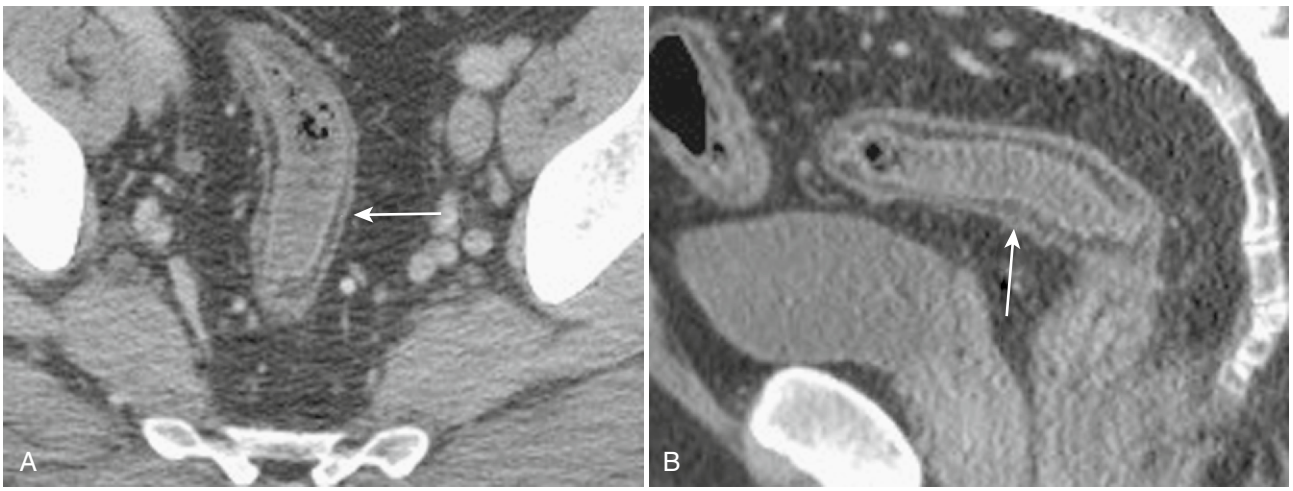


FIGURE 9-12. A 44-year-old male with chronic ulcerative colitis. Axial **(A)** and sagittal **(B)** portal venous phase CT images reveal fat attenuation within the wall of the sigmoid *(arrows)*, the so-called "fat halo" sign.

useful in differentiating between chronically thickened loops of bowel secondary to fibrosis and those with active inflammation.

Another classic finding in patients with Crohn's disease is the so-called "creeping" fat, which represents fibrofatty proliferation of the mesenteric fat. Also, the vasa recta may be engorged in cases of acute inflammation, the so-called "comb" sign. Again, taken in isolation, this is not a specific finding for Crohn's disease, as it can be seen in any hypervascular inflammation of the colon. As the rectum is typically involved in patients with ulcerative colitis, the chronic inflammation causes proliferation of the perirectal fat resulting in an increase in the presacral space.

Abscess and phlegmon formation are commonly encountered complications in patients with Crohn's disease given its transmural nature. Abscesses can be successfully managed percutaneously to avoid unnecessary surgery. Another complication given the transmural extent of Crohn's disease is the formation of sinus tracts and fistulae. Common fistulae include enteroenteric and enterocolonic as well as fistulae within the urinary system (Fig. 9-13). Other commonly encountered fistulae are perianal and enterocutaneous fistulae. Although less common, fistulas may also be encountered in patients with ulcerative colitis.

Unlike ulcerative colitis, Crohn's disease affects the colon somewhat asymmetrically, as the mesenteric side

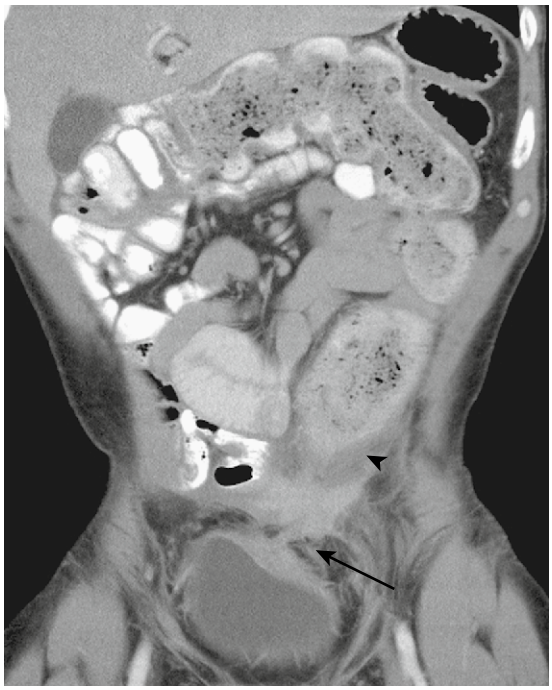


Figure 9-13. A 47-year-old male with Crohn's disease. Coronal portal venous phase CT image reveals a colovesical fistula *(arrow)* with obstruction of the colon proximally *(arrowhead)* secondary to the inflammation related to the patient's Crohn's disease.

may be more severely affected than the antimesenteric portion of the colon. This may result in the formation of sacculations, also known as pseudodiverticula.

Extracolonic manifestations of inflammatory bowel disease may be identified on abdominal CT and add specificity to a presumed diagnosis. These include sacroiliitis, which may be seen in up to 30% of patients with Crohn's disease. These changes may result in eventual fusion around the sacroiliac joints in this patient population. Another manifestation of inflammatory bowel disease, which may be seen on abdominal CT, is primary sclerosing cholangitis. Although more commonly associated with ulcerative colitis, this may also be seen in association with Crohn's disease. When primary sclerosing cholangitis is present, the typical CT findings include pruning, beading, or skip dilatations of the bile ducts. Additionally, the bile duct walls may be thickened on CT; expected normal bile duct wall thickness is approximately 1 to 2 mm. When incidentally identified, these extraintestinal manifestations of inflammatory bowel disease may increase confidence in the diagnosis in patients presenting with acute abdominal pain.

In patients with known inflammatory bowel disease presenting acutely with pain, MRI is being used more frequently given concerns of ionizing radiation associated with CT. Like CT, MRI may demonstrate focal bowel wall thickening associated with hyperenhancement after contrast administration as well as surrounding inflammatory changes. Associated findings described above, such as engorgement of the vasa recta, may also be identified on MRI, as may complications of inflammatory bowel disease including abscess or fistula formation. Perianal disease in patients with Crohn's disease, in particular, is elegantly delineated with the soft tissue contrast afforded by MRI.

Infectious Colitis

Commonly encountered infectious etiologies of colitis include pseudomembranous colitis secondary to proliferation of *Clostridium difficile* related to antibiotic use, salmonella, shigella, yersinia, tuberculosis, amebiasis, schistosomiasis, *E. coli*, and cytomegalovirus, among others. The diagnosis of pseudomembranous colitis is often suspected as it is temporally related to antibiotic use. Another infectious cause of colitis is tuberculosis. Although the diagnostic dilemma may be somewhat simplified when patients display concurrent pulmonary tuberculosis, the abdominal manifestations may be seen in the absence of pulmonary infection. Neutropenic colitis or typhlitis typically affects the cecum and ascending colon, although the terminal ileum and appendix may also be affected.

The clinical presentation of infectious colitis is somewhat dependent on the underlying etiology, although patients generally present with diffuse, crampy abdominal pain and diarrhea, which may be profuse and bloody. Also, fever and leukocytosis may be associated. In some cases, the diarrhea may be persistent, prompting the presentation.

Imaging Findings

Plain radiographs are nonspecific, but mural edema may be identified within the colon. Again, as in cases of inflammatory bowel disease, one should consider and evaluate for the complication of toxic megacolon.

The CT imaging appearances of the infectious colitides are nonspecific, and there is considerable overlap among the various etiologies. The CT findings typically demonstrate pancolitis with marked colonic wall thickening, approaching the severity of Crohn's disease (Fig. 9-14). The "accordion" sign may be seen as edematous haustral folds, separating the oral-contrast-filled lumen into narrow ridges, similar in appearance to an accordion. Although originally described as specific for patients with pseudomembranous colitis, this finding may be seen in any cause of severe colonic wall edema.

Tuberculous infection of the colon may have a somewhat more specific CT imaging appearance. In these patients, severe colonic wall thickening may be seen, commonly along with thickening of the terminal ileum, as the ileocecal area is the most frequently affected. Lymphadenopathy is classically described as low attenuation secondary to necrosis; calcification may also be seen. Like Crohn's disease, tuberculosis is a well-known cause of intra-abdominal fistulae, as well as sinus tracts. Tuberculosis is also one of the causes of the cone-shaped cecum. Peritoneal thickening and ascites are common manifestations of intra-abdominal tuberculosis. Shallow mucosal ulcers may lead to significant gastrointestinal hemorrhage in patients with colonic involvement by tuberculosis.

The imaging characteristics of neutropenic colitis on CT are fairly nonspecific, demonstrating segmental bowel wall thickening, adjacent fat stranding, and fluid. The diagnosis of typhlitis should be entertained given these nonspecific imaging findings involving the cecum and/or descending colon in the immunocompromised patient population.

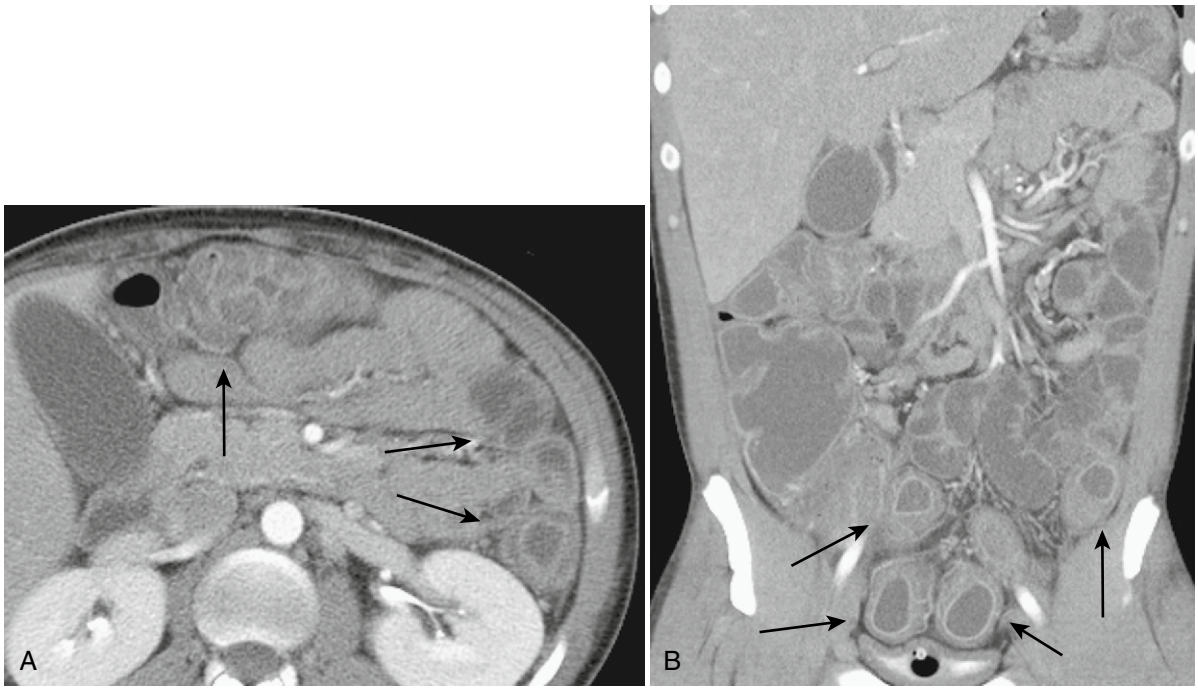


FIGURE 9-14. A 34-year-old male with fever and diarrhea secondary to *Clostridium difficile* colitis from recent antibiotic use. Axial **(A)** and coronal **(B)** portal venous phase CT images demonstrate multiple thickened loops of colon *(arrows)*. Note the relative hypoattenuation of the thickened colon, well seen on the axial image, consistent with submucosal edema.

Rapid diagnosis is critical in avoiding complications of frank bowel necrosis and perforation.

Foreign Bodies

Foreign bodies within the gastrointestinal tract are an uncommon cause of complications. However, in cases of bowel perforation without apparent alternative causes, foreign bodies should be a consideration. In more proximal portions of bowel, the foreign bodies are typically ingested. However, more distally in the rectum, the foreign bodies are also often inserted anally. Patients ingesting foreign bodies orally often have a mental disorder; patients in penitentiaries are also a frequent subset of this population. The ingested foreign bodies may include various household items, including metallic objects. The intentional ingestion of illicit narcotics may be seen in attempts to transport narcotics. Also, foodstuffs, including bones or the pits from fruits, may cause bowel injury. Various anally inserted foreign objects have been described including glass and metallic objects.

Patients with complications related to orally ingested foreign bodies may present with acute abdominal pain. If there is secondary bowel perforation, the signs and symptoms of peritonitis may ensue. Other complications include mechanical bowel obstruction with patients presenting with abdominal pain and distention, possibly with nausea and vomiting. Patients with anally inserted foreign bodies may present with pain, or may present to the emergency department unable to extract the intentionally placed foreign body.

Imaging Findings

Foreign bodies, depending on their composition, may be radio-opaque and readily identified on plain radiographs. However, smaller foreign bodies, as well as those of radiolucent composition, are not identified, although secondary findings of the related complications may be seen. These include evidence of free intraperitoneal air or possibly bowel obstruction. Patients with anally inserted foreign bodies may receive plain radiographs in order to localize the foreign body prior to definitive management. The intentionally ingested illicit narcotics, often wrapped in various protective covers such as balloons or condoms, may be radiographically apparent.

In patients with known foreign body ingestion, CT is infrequently employed for localization and evaluation of potential complications. Also, in patients with bowel perforation, and even in cases of obstruction, one may consider the possibility of a foreign body as the underlying etiology. The foreign bodies, depending on the composition, may also be subtle on CT (Fig. 9-15). However, when complications ensue, these may be helpful in localizing the foreign body. In cases of anally introduced foreign bodies, CT is particularly useful in identifying rectal injuries as evidenced by rectal wall thickening, surrounding fat stranding, and possibly free extra- or intraperitoneal air. CT is also, rarely, employed in the evaluation of illicit narcotic ingestion.

Vascular Diseases

Vascular diseases of the bowel include acute gastrointestinal bleeding and mesenteric ischemia.

Acute Gastrointestinal Bleeding

Acute gastrointestinal bleeding is often classified into upper and lower gastrointestinal categories based on the site of hemorrhage. Noninvasive imaging is uncommonly indicated in upper gastrointestinal hemorrhage, so only

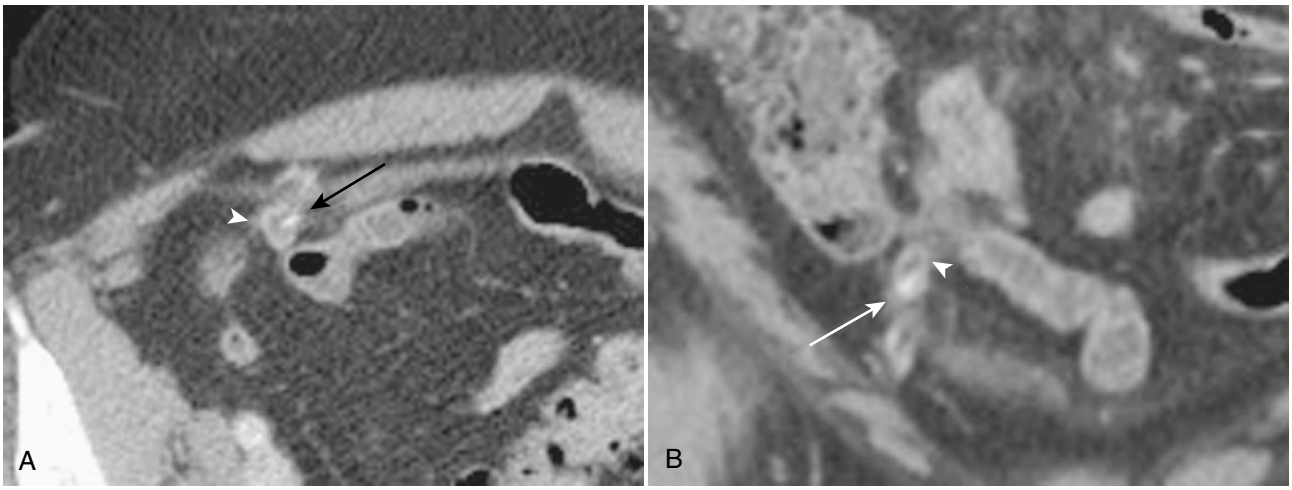


FIGURE 9-15. A 52-year-old female with perforated Meckel's diverticulum secondary to fish bone ingestion. Axial **(A)** and coronal **(B)** portal venous phase CT images reveal a linear, hyperattenuating structure *(arrows)* consistent with a foreign body, which, in this case, happens to be located within a blind-ending tubular pouch *(arrowheads)*. Operative repair revealed a fish bone perforating the patient's Meckel's diverticulum.

a discussion of lower tract bleeding follows. Acute lower gastrointestinal hemorrhage is a common cause of hospital admission with significant associated morbidity and mortality. The most common colonic etiologies include diverticulosis, ischemic and infectious colitis, colonic neoplasm, benign anorectal disease, and arteriovenous malformations (AVMs). Small bowel causes are a much less frequent etiology and are most commonly secondary to diverticulosis, AVM, and neoplasm.

There is no consensus regarding the initial imaging evaluation of patients presenting with acute lower gastrointestinal bleeding. Colonoscopy, technetium 99m (^{99m}Tc)–red blood cell scintigraphy, CT, and conventional mesenteric angiography are all successfully applied, depending on the given scenario. As colonoscopy may be limited in cases of severe, massive hemorrhage secondary to obscured visualization, alternate imaging for localization of the bleeding site is often required prior to possible operative intervention.

Patients with acute lower gastrointestinal hemorrhage report maroon stools or possibly bright red blood in the rectum, depending on the location of the hemorrhage. The signs and symptoms somewhat depend on the underlying etiology. Abdominal pain and diarrhea may be associated with infectious and inflammatory colitis. When severe, gastrointestinal hemorrhage may result in hemodynamic instability and shock.

Imaging Findings

Both ^{99m}Tc-labeled erythrocytes and ^{99m}Tc sulfur colloid are applied in the evaluation of acute gastrointestinal hemorrhage. However, ^{99m}Tc-labeled erythrocytes offer the possibility for delayed imaging in cases of intermittent bleeding. Nuclear scintigraphy has been demonstrated as sensitive in the detection and accurate in the localization of the source of acute gastrointestinal hemorrhage. The diagnosis of gastrointestinal bleeding on nuclear scintigraphy depends on the visualization of an area of tracer localization that persists and is identified to move through the lumen of the bowel secondary to peristalsis. The transit within the bowel may be observed to be antegrade or retrograde; however, localization depends on the initial area of visualization.

Recently, CT has been shown to have a high diagnostic accuracy in both the detection and localization of massive gastrointestinal bleeding. Optimal results necessitate the distention of the bowel with a low-attenuation contrast agent, including water. Both unenhanced and arterial-phase intravenous contrast-enhanced images should be acquired. CT diagnosis relies on the visualization of an area of active arterial contrast extravasation. In some cases, CT may diagnose the underlying etiology of acute hemorrhage, such as in the case of colonic neoplasms.

Currently, given the noninvasive alternatives, the use of conventional mesenteric angiography as the initial imaging examination has decreased. However, catheter-directed therapy such as vasopressin and, more currently, super selective embolization techniques have been shown to be effective methods of treatment.

Mesenteric Ischemia

Mesenteric ischemia most commonly occurs secondary to long-standing atherosclerotic disease, with secondary acute or chronic thrombosis or embolization, as well as any cause of hypotension causing hypoperfusion on a background of narrowed mesenteric arteries. Other common etiologies occur in patients with embolization from proximal sources such as the heart secondary to mechanical heart valves or atrial fibrillation. Various other causes of mesenteric ischemia include vasculitides, bowel obstruction, radiation, corrosive ingestion, and drugs, including immunosuppressives and those agents involved in treating leukemia, lymphoma, and severe inflammation within the peritoneal cavity. Typically, depending on the etiology, segmental portions of the bowel are affected, although more diffuse involvement may also be seen.

The classic description of acute mesenteric ischemia is that of severe abdominal pain out of proportion to findings on physical examination. Typically, the pain is visceral and poorly localized. Nausea, vomiting, and diarrhea are associated. In severe cases, abdominal distention and

peritonitis may ensue. In the minority of patients, gastrointestinal hemorrhage may occur.

Imaging Findings

The diagnosis of mesenteric ischemia may be suggested on plain radiographs by the presence of dilated loops of bowel demonstrating wall thickening, which may be seen as thumb printing, as well as more specific signs such as pneumatosis intestinalis, or air within the bowel wall, and portomesenteric venous gas. Alternatively, the area of bowel ischemia may cause a functional obstruction and the more proximal loops of bowel may become dilated.

On CT, similar findings of dilatation and mural thickening are seen. Other findings, including abnormal decreased enhancement and ascites, as well as later findings of pneumatosis, are also clearly seen on CT. CT also offers the possibility of evaluating both the arterial and venous supply of the small bowel and may directly visualize vascular thrombosis. Therefore, in cases of suspected bowel ischemia, the administration of intravenous contrast is of significant potential benefit. Currently, postprocessing options such as multiplanar reformations afforded by MDCT technology offer a great benefit in evaluation of the mesenteric vasculature in cases of mesenteric ischemia.

PANCREATICOBILIARY DISEASE

Pancreaticobiliary disease is commonly related to inflammatory etiologies including acute and chronic pancreatitis and obstruction, often related to biliary stone disease. Usually the clinical diagnosis and management of uncomplicated pancreatitis do not rely on imaging diagnosis; however, the various complications of pancreatitis are typically identified and characterized on imaging. Also, biliary obstruction and the various complications of stone disease are a frequent cause of abdominal pain, and imaging is often employed in its diagnostic evaluation.

Acute Pancreatitis

Inflammation of the pancreas secondary to injury to the pancreatic parenchyma from release of pancreatic enzymes is a common cause of abdominal pain and may be associated with significant morbidity and mortality. In developed countries, the most common etiology for pancreatitis is alcohol abuse. Another frequent cause is biliary stone disease, which is obstruction of the pancreas by a stone lodging in the pancreatic duct, distal common bile duct, or ampulla of Vater. Other etiologies have been reported, including various medications such as steroids and NSAIDs, infectious etiologies including bacterial and viral pathogens, iatrogenic causes such as endoscopic retrograde cholangiopancreatography (ERCP) direct trauma, obstructing malignancies, hypertriglyceridemia, and ischemia, usually related to surgery. Congenital anomalies such as pancreas divisum have also been implicated in an increased incidence of pancreatitis. CT or MRI imaging of pancreas divisum includes the visualization of a dominant dorsal duct without evidence of communication between the dorsal and ventral ducts.

Patients with acute pancreatitis present with epigastric pain that is typically constant but may improve when the patient is supine. Patients commonly report anorexia, possibly with accompanying nausea and vomiting. Also, patients with acute pancreatitis may be febrile. Bowel sounds are often hypoactive secondary to ileus related to the local inflammation.

Imaging Findings

Plain radiographs may demonstrate a focal ileus secondary to the local inflammation related to the pancreas. Also, in patients with acute or chronic pancreatitis, the secondary signs of chronic pancreatitis as evidenced by parenchymal calcification may be identified.

Although imaging is not typically acquired in uncomplicated cases of acute pancreatitis, it does play a significant role in this disease process. Initial plain radiographs in patients with acute pancreatitis may demonstrate local ileus secondary to inflammation, the so-called "sentinel loop" sign. Other findings may include the visualization of calcifications within the pancreatic parenchyma in those patients presenting with acute on chronic pancreatitis (Fig. 9-16). The main role of ultrasonography in acute pancreatitis is in those patients with suspected gallstone pancreatitis; ultrasound may be used for confirmation of the presence of gallstones. Ultrasound may also be able to identify evidence of choledocholithiasis, although the examination of the distal aspect of the common duct is often limited on ultrasonography. Ultrasound may demonstrate the findings of acute pancreatitis as it affects the pancreatic parenchyma and surrounding peripancreatic tissues. Often, diffuse or focal enlargement of the pancreas is identified along with evidence of edema seen as abnormally hypoechoic parenchyma. Peripancreatic fluid may also be identified on ultrasonography. Although not required for

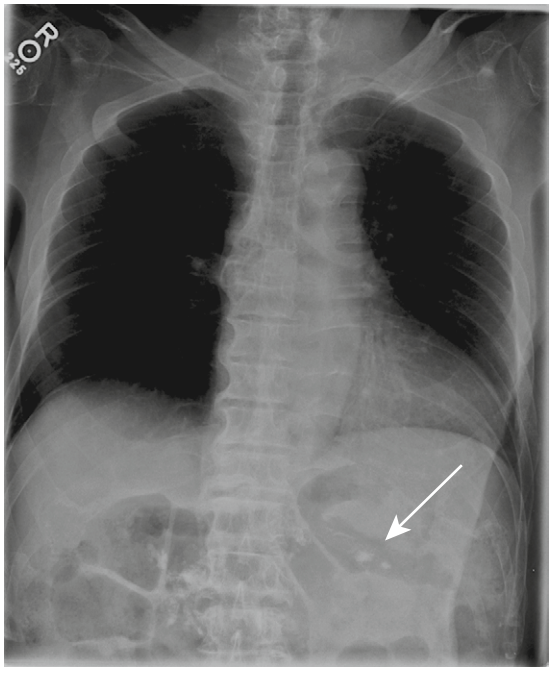


FIGURE 9-16. A 51-year-old male with chronic pancreatitis. Plain radiograph demonstrates multiple punctate foci of calcification overlying the expected location of the pancreas *(arrow)*, a finding consistent with chronic pancreatitis.

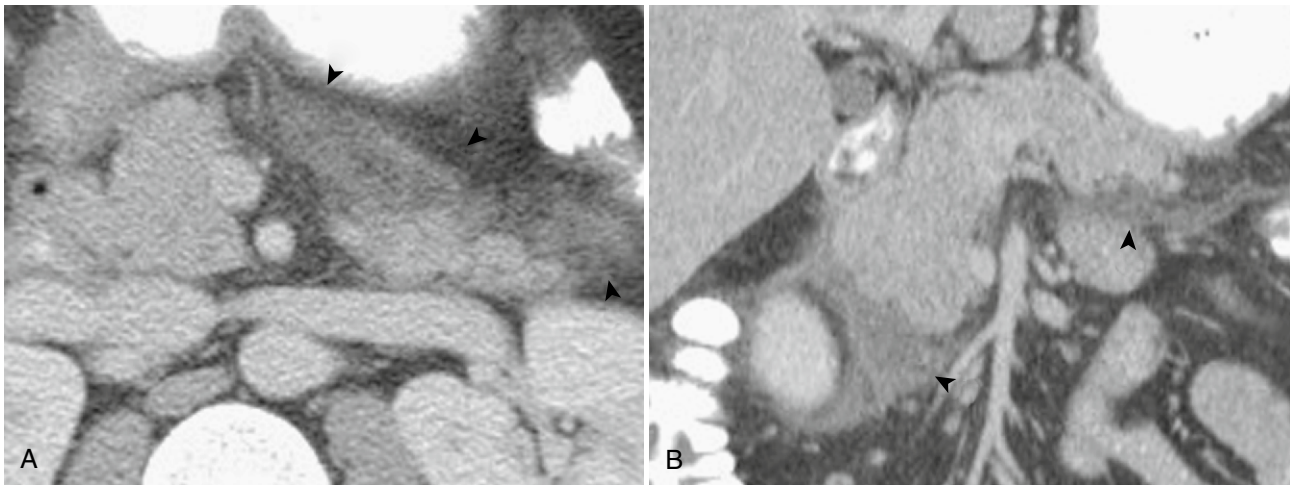


Figure 9-17. A 34-year-old male with acute pancreatitis. Axial **(A)** and coronal **(B)** portal venous phase CT images reveal diffuse enlargement of the pancreas with peripancreatic fluid and stranding *(arrowheads)* consistent with uncomplicated pancreatitis.

the diagnosis of uncomplicated acute pancreatitis, when seen, typical CT findings include focal or diffuse enlargement of the gland as well as edema, identified as abnormal hypoattenuation of the parenchyma and stranding along with free fluid in the peripancreatic tissues (Fig. 9-17).

In those patients suspected of having complicated acute pancreatitis, CT is usually the modality of choice. The use of CT, including the Balthazar CT severity index, has been shown to be valid in prognosticating acute pancreatitis based on the degree of CT findings of peripancreatic inflammation, phlegmon, and necrosis. Necrosis is evidenced by the absence of enhancement of the affected parenchyma when compared with adjacent areas of more normally enhancing pancreatic parenchyma. Therefore, when complicated pancreatitis is of clinical concern, CT scans are typically acquired, both with and without intravenous contrast, to evaluate for degrees of enhancement within the pancreatic parenchyma. The pancreatic necrosis may be seen to affect anywhere from small areas of the pancreatic parenchyma to virtually the entirety of the gland. If these patients receive follow-up CT examinations, the areas of necrosis typically do not regain enhancement and, when treated nonoperatively, may resorb, forming a focal cleft within the gland. If, on follow-up examinations, the initial area of pancreatic necrosis is noted to have increased in size, then these patients are more likely to undergo necrosectomy. A smaller subset of patients will go on to develop pancreatic necrosis after an initially unremarkable CT examination. Recent evidence suggests that these patients may be subject to a particularly high morbidity and mortality. Recently, novel techniques including perfusion CT have been described in the application to acute pancreatitis and may be clinically useful in assessing the status of pancreatic perfusion and possibly in predicting more severe ischemia and necrosis. Areas of pancreatic necrosis may become infected; these patients incur significant increases in morbidity and mortality. Although CT findings, such as gas bubbles within necrotic parenchyma, may be highly suggestive of infected pancreatic necrosis, patients typically undergo ultrasound or CT-guided fine needle aspiration for confirmation.

In severe cases of acute pancreatitis, there is often increased peripancreatic fluid secondary to inflammation. These findings have recently been shown to prognosticate both disease severity and 24-hour mortality, based on the findings of pleural effusions, ascites, or retroperitoneal fluid collections. Typically, pancreatic fluid collections are identified along the anterior or anterolateral aspect of the gland. Other common locations include the anterior pararenal space either bilaterally or asymmetrically depending on the precise location of pancreatic inflammation, as well as within the lesser sac. Less commonly, fluid collections are identified in the posterior pararenal space as well as within the peritoneum around the liver and spleen. These fluid collections also may dissect into the thorax, including the mediastinum.

Other complications that may be identified by CT in patients with acute pancreatitis include sequelae of injury to the splenic vasculature. These include splenic vein thrombosis, splenic infarction or subcapsular hemorrhage, and splenic artery pseudoaneurysm formation (Fig. 9-18). Pseudoaneurysms may communicate, rarely, with the pancreatic duct in a condition known as hemosuccus pancreaticus, in which bleeding occurs into the pancreatic duct and out of the ampulla of Vater to exit into the duodenum (Fig. 9-19). Treatment of splenic artery pseudoaneurysms may be successfully accomplished via transcatheter embolization, as well as by percutaneous techniques.

In the minority of patients with acute pancreatitis who develop pancreatic fluid collections, the fluid collections may go on to form pseudocysts. Typically, the acute fluid collections are resorbed; however, when encapsulated and well defined in shape, they are termed pseudocysts. Acute pancreatitis usually causes small ductal disruption secondary to necrosis of the parenchyma, which allows the fluid collections, and eventually pseudocysts, to form. Pseudocysts typically require at least 3 to 4 weeks to form after an episode of acute pancreatitis, usually up to 6 weeks. As they are formed from pancreatic secretions, these collections are normally amylase and lipase rich. Even when the prototypical encapsulated pseudocyst is formed, the smaller collections are highly likely to undergo complete involution with conservative management. Specifically, pseudocysts greater than 6 cm in diameter have been shown to have a significantly higher rate of operative management than

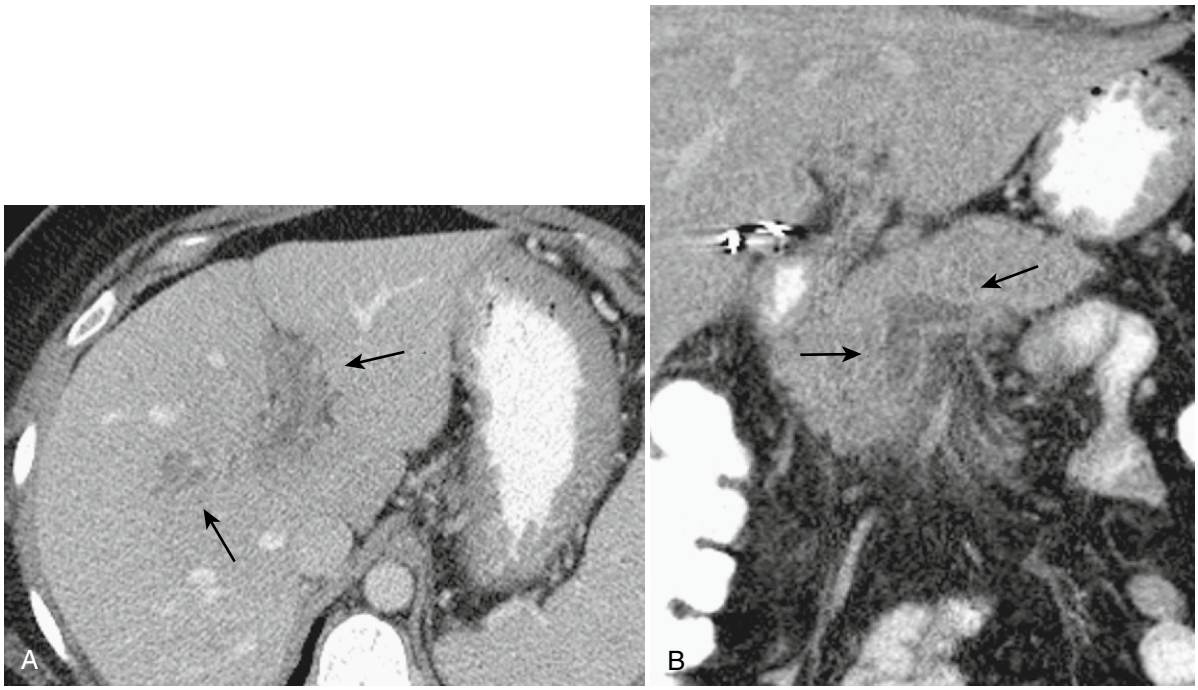


FIGURE 9-18. A 45-year-old female with acute pancreatitis. Axial **(A)** and coronal **(B)** portal venous phase CT images demonstrate complete thrombosis of the splenic, superior mesenteric, and portal veins *(arrows)*.

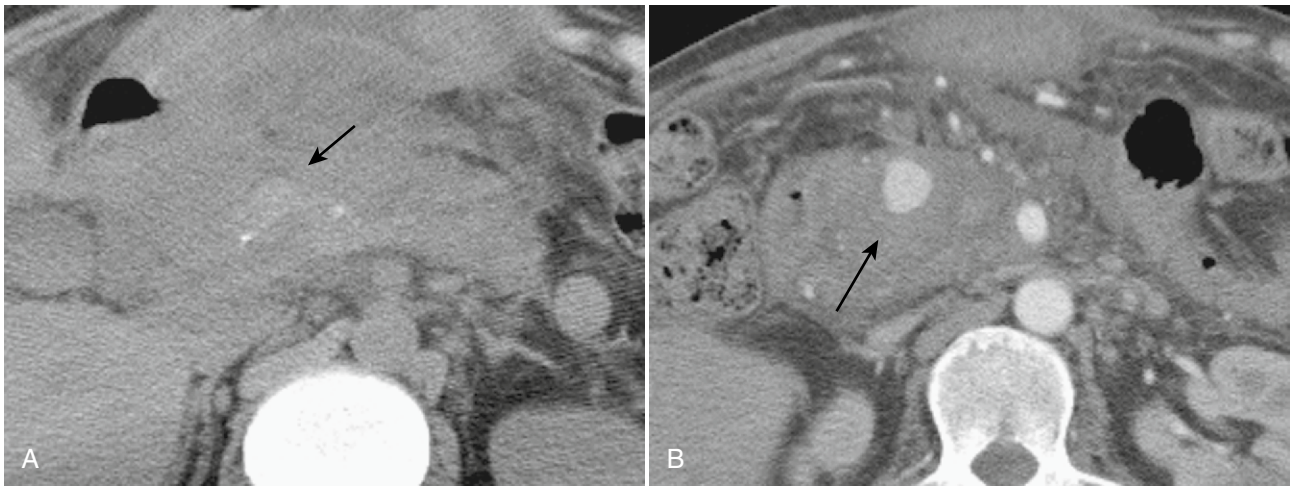


FIGURE 9-19. A 27-year-old male with a history of pancreatitis and known gastroduodenal pseudoaneurysm status post attempted coil embolization with hemosuccus pancreaticus. Axial unenhanced **(A)** CT image demonstrates hyperattenuation within the main pancreatic duct *(arrow)* consistent with hemosuccus pancreaticus, confirmed on subsequent ERCP. Axial arterial phase CT image **(B)** demonstrates round, hyperattenuating focus *(arrow)* consistent with a gastroduodenal artery pseudoaneurysm secondary to the patient's history of pancreatitis.

smaller lesions. For the most part, pseudocysts are treated when they are symptomatic, are causing abdominal pain, are noted to enlarge on serial imaging, are noted to have become infected, or are causing hemorrhage or obstruction of adjacent bowel or bile ducts.

Chronic Pancreatitis

Chronic pancreatitis represents continued, irreversible inflammation leading to fibrosis and calcification. Eventually, patients may develop endocrine as well as exocrine insufficiency. The patient typically presents with chronic abdominal pain, and, unlike with acute pancreatitis, the pancreatic enzyme levels may be either normal or mildly elevated. The most common cause of chronic pancreatitis, like acute pancreatitis, is alcohol abuse. Other causes include hyperlipidemia, hypercalcemia, medications, cystic fibrosis, hereditary metabolic disorders, obstruction from congenital (pancreas divisum) or acquired (e.g., post-traumatic) causes, autoimmune pancreatitis, and idiopathic pancreatitis in up to 30% of cases. The role of gallstones in chronic pancreatitis remains controversial.

Patients with chronic pancreatitis describe intermittent bouts of epigastric abdominal pain that may radiate to the back. The pain may be induced by meals or occur independently of food. With ongoing chronic pancreatitis, exocrine

insufficiency may result in diarrhea and weight loss. Also, endocrine insufficiency may develop.

Imaging Findings

As noted, plain radiographs may demonstrate the pancreatic parenchymal calcifications associated with chronic pancreatitis.

On CT, the findings of chronic pancreatitis include atrophy of the parenchyma, parenchymal calcifications, and dilatation of the pancreatic duct. Pseudocysts may also be visualized in patients with chronic pancreatitis.

The findings of pancreatic parenchymal calcification as echogenic, shadowing foci, as well as the secondary ductal dilatation seen in chronic pancreatitis, are well visualized by ultrasonography. Secretin-enhanced MR cholangiopancreatography provides a functional assessment of pancreatic exocrine function and has been shown to be useful in diagnosing early stages of chronic pancreatitis prior to the morphologic changes noted above.

Cholelithiasis/Choledocholithiasis

Gallstone disease is one of the most common gastrointestinal disorders and is estimated to have a prevalence of between 10% and 15% in the United States. Although the majority of patients with gallstone disease remain asymptomatic, approximately 20% will develop symptoms; this represents a significant disease burden in the adult population. The prevalence increases with increasing age and is more common in females. Additionally, increased rates of obesity in Western countries will likely further increase rates of gallstone disease. Most commonly in developed countries, gallstones are composed primarily of cholesterol, with calcium and pigments, including bilirubin and bilirubinate, composing the remaining minority of stones.

Patients with gallstone disease frequently describe symptoms of biliary colic. Generally, patients describe intermittent bouts of pain localized to the epigastrium or right upper quadrant, gradual in onset, and lasting up to several hours. Fatty meals may inconsistently be associated with bouts of biliary colic. Complications of gallstone disease including cholecystitis may infrequently be the initial presentations.

Imaging Findings

In the minority of patients, gallstones are identified on plain radiographs as calcified foci overlying the expected location of the gallbladder in the right upper quadrant.

Ultrasound is the method of choice for the noninvasive diagnosis of gallstones. Typically, gallstones are identified as freely mobile, echogenic foci demonstrating posterior acoustic shadowing. A small portion of gallstones may be affixed to the gallbladder wall and do not demonstrate mobility during the examination. The absence of posterior acoustic shadowing decreases the specificity of the ultrasound examination; however, discrete echogenic foci without shadowing most commonly represent gallstones. When the gallstones are seen within a contracted gallbladder, the wall echo shadow triad may be identified; the gallbladder mucosa is seen as a thin echogenic line anterior to a second echogenic line corresponding to the anterior wall of the gallstones with complete posterior acoustic shadowing of the more posterior aspect of the gallstones and gallbladder wall. This triad is helpful in differentiating the findings of gallstones from adjacent loops of air-filled bowel.

Although CT is not indicated in the primary detection of patients with suspected gallstone disease, gallstones may be incidentally identified on CT. Gallstones have various appearances on CT based on their composition; cholesterol stones have a range of attenuation values from 0 to several hundred Hounsfield units (HU), although the majority have attenuation values less than 100 HU. Pigmented stones have slightly higher attenuation values, although they also demonstrate a wide range of values. Recently, changing peak voltage settings during CT examination has been shown to significantly increase the detection rates of gallstones.

Cholecystitis

Cholecystitis represents the sequela of obstruction of the cystic duct, most commonly by a gallstone, followed by biliary stasis and secondary infection. In the minority of patients, acute cholecystitis occurs in the absence of gallstones, termed acalculous cholecystitis. These patients, who compose approximately 5% to 10% of all cases of acute cholecystitis, are generally critically ill with significant, prolonged bile stasis.

Patients with cholecystitis present with right upper quadrant pain secondary to peritoneal irritation from the inflamed gallbladder. Pain is typically described as severe and constant. Nausea and vomiting are associated, and the minority of patients present with fever. The Murphy's sign, which is an inspiratory pause with palpation of the right upper quadrant, may be elicited.

Imaging Findings

In patients with suspected acute cholecystitis, ultrasonography is typically employed in the initial diagnostic evaluation. The ultrasound criteria for diagnosing acute cholecystitis include evidence of gallstones, gallbladder wall thickening, and distention, as well as elicitation of a sonographic Murphy's sign. To elicit a sonographic Murphy's sign, the patient is asked to breathe out with the ultrasound probe placed over the right upper quadrant. Upon the subsequent inspiration, if the patient halts the inhalation as the gallbladder passes beneath the ultrasound probe and is visualized, it is considered to be a positive sonographic Murphy's sign (Fig. 9-20). The normal gallbladder wall is typically 2 to 3 mm in diameter; gallbladder wall thickness greater than 3 mm is considered abnormal in patients with suspected acute cholecystitis. A caveat in evaluating gallbladder wall thickness is that there are numerous causes of a thickened gallbladder wall. Gallbladder wall thickening can be seen in common systemic diseases such as cirrhosis, acute hepatitis, hypoproteinemia, renal failure, and congestive heart failure. Often, in patients with gallbladder wall thickening secondary to acute cholecystitis, areas of lucency corresponding to subserosal edema may be seen within the wall. Finally, in patients with acute cholecystitis, the gallbladder is typically significantly distended secondary to obstruction. A measurement of greater than 10 cm in the long axis of the gallbladder or 5 cm in the transverse or anterior-posterior axis is normally used to signify abnormal

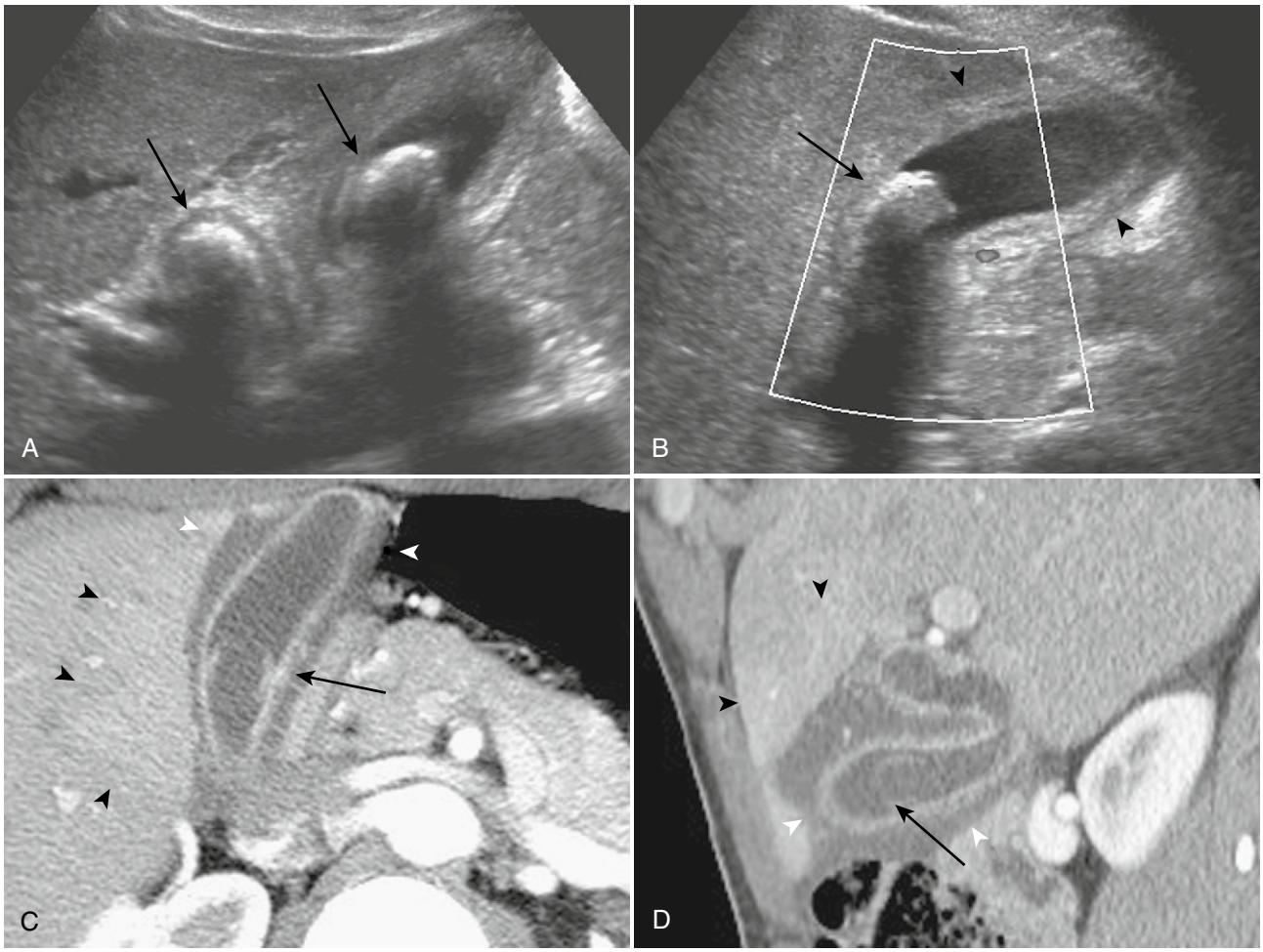


FIGURE 9-20. A 43-year-old male with acute cholecystitis. Ultrasound images **(A** and **B)** demonstrate echogenic, shadowing gallstones *(arrows)* with gallbladder wall thickening *(arrowheads)* in patient in whom a sonographic Murphy's sign was elicited. Axial **(C)** and sagittal **(D)** portal venous phase CT images reveal a gallstone *(arrows)* as well as a thickened gallbladder wall *(white arrowheads)*. Although not acquired in the arterial phase of contrast, hepatic hyperenhancement consistent with secondary inflammation is nevertheless seen *(black arrowheads)*.

distention. Complications include gangrenous cholecystitis, which may demonstrate a striated pattern of gallbladder wall thickening with alternating hyperechoic and hypoechoic layers. Increasingly specific signs in more severe cases include the presence of sloughed mucosa seen within the gallbladder lumen as demonstrated by thin hyperechoic bands. In some cases of severe cholecystitis, hemorrhage may be present within the lumen, termed hemorrhagic cholecystitis. In these cases, ultrasound commonly demonstrates the findings of gangrene, in addition to nonshadowing intraluminal echoes, which may entirely fill the lumen of the gallbladder. Finally, emphysematous cholecystitis represents a rare but life-threatening complication, often associated with diabetes, in which foci of air are identified within the wall and/or lumen of the gallbladder. On ultrasound, echogenic foci or bands are seen with posterior ring-down artifact, or "dirty shadowing." Often, the presence of the gas obscures actual visualization of the gallbladder wall. These findings are specific for this life-threatening complication and should be recognized and treated urgently.

CT is often used for patients with nonspecific clinical presentations of abdominal pain or equivocal findings on the initial ultrasound examination. The findings of acute cholecystitis, including its complications, should be recognized on CT. As on ultrasound, CT demonstrates gallbladder wall thickening, pericholecystic fluid, and possibly pericholecystic fat stranding. In most cases, the obstructing gallstone may be identified, although this is less likely on CT than on ultrasound, as discussed above. In those patients who receive intravenous contrast, especially when imaged during an arterial phase of enhancement, there may be evidence of secondary inflammation of the liver around the gallbladder fossa (see Fig. 9-20). This is seen as relative hyperenhancement of this portion of the liver parenchyma. CT may also demonstrate the complications of acute cholecystitis. In those patients with a gangrenous cholecystitis, the most specific CT imaging findings are shown to be direct evidence of the sloughed membranes within the lumen, irregularity of the gallbladder wall, and perforation including pericholecystic abscess. Hemorrhage is also clearly identified on CT, as evidenced by increased attenuation of the intraluminal bile. Finally, emphysematous cholecystitis is also demonstrated on CT by direct evidence of air within the gallbladder wall and/or lumen.

Hepatobiliary scintigraphy is also a common modality in assessing patients with acute cholecystitis. The examination

depends on a nuclear medicine technologist, who may not be available at all hours, as well as on the length of the examination itself, so it is not typically employed as a first-line modality. The technologist administers a radionuclide in the form of a ^{99m}Tc-labeled iminodiacetic acid derivative, which is taken up by hepatocytes and excreted into the bile ducts. This technique offers a functional assessment of the patency of the cystic duct. Normally, the radionuclide is seen within the bile ducts and gallbladder lumen before being excreted into the duodenum and proximal small bowel. Obstruction of the cystic duct eliminates visualization of the gallbladder lumen. This technique offers very high diagnostic accuracy in the assessment of acute cholecystitis. Increased specificity and the diagnosis of more severe or gangrenous cases of acute cholecystitis are achieved by the visualization of a "rim" sign of relatively increased tracer localization to the hepatic parenchyma surrounding the gallbladder fossa.

Choledocholithiasis

Common bile duct stones typically occur secondary to passage from the gallbladder and represent a cause of increased morbidity and mortality in gallstone disease. Less commonly, the stones may form within the common duct itself. The classic presentation includes colicky right upper quadrant pain, which may be associated with jaundice secondary to biliary obstruction. Alternatively, obstructing common bile duct stones may be complicated by infection, and the classic Charcot triad of fever, right upper quadrant pain, and jaundice may be the initial presentation. Common bile duct stones are also a significant cause of pancreatitis.

As in patients with cholelithiasis, biliary colic is a common presenting symptom in patients with choledocholithiasis. Less frequently, complications of choledocholithiasis, including biliary obstruction with possible cholangitis, may be the initial presenting clinical scenario.

Imaging Findings

In patients with a clinical presentation suggestive of choledocholithiasis, ultrasound may be initially employed to confirm the presence of gallstones as well as to evaluate for the secondary signs of common duct stones such as the presence of biliary dilatation. The common duct stone itself may be directly visualized by ultrasound as an echogenic, shadowing, intraluminal filling defect: however, in the majority of cases, the stones are not directly visualized.

In the acute setting, especially patients presenting with nonspecific signs and symptoms, CT may be one of the initial imaging modalities used. Similar to gallstones, common duct stones display a wide range of attenuation values from isoattenuating to bile to heavily calcified. Therefore, there is a limit to the diagnostic accuracy of routine CT techniques in detecting choledocholithiasis. Optimal protocols for the detection of common bile duct stones are usually considered to include imaging in the absence of oral or intravenous contrast so as to limit interference with the visualization of the hyperattenuating common duct stones. Recently, MDCT has demonstrated moderate sensitivity and specificity in this diagnosis, using routine CT protocols that include intravenous and oral contrast in patients with nonspecific abdominal pain. CT findings of choledocholithiasis include the direct visualization of the common duct stone, often surrounded by lower attenuating bile, the so-called "target" sign. Other common imaging findings include the presence of a hyperattenuating stone seen eccentrically located within the bile duct surrounded by a crescent of lower attenuating bile, termed the "crescent" sign.

In patients with moderate or high clinical suspicion of common duct stones, MR cholangiopancreatography (MRCP) and/or ERCP may be used initially, depending on the degree of clinical confidence. On MRCP, choledocholithiasis is diagnosed by the direct visualization of the common duct stones as low-signal, intraluminal filling defects. Biliary calculi are readily identified as low-signal filling defects surrounded by hyperintense bile using MRCP techniques. Differential considerations for intraluminal filling defects on MRCP include pneumobilia, blood clots, vascular pulsation artifact, and susceptibility artifact from adjacent cholecystectomy clips, among others. Pneumobilia is differentiated by its nondependent location within the bile ducts.

Hepatolithiasis

The presence of intrahepatic bile duct stones proximal to the confluence of the left and right intrahepatic bile ducts is termed hepatolithiasis. This entity is particularly prevalent in East Asia and is thought to be related to bile stasis and recurrent bacterial infections. Typically, the stones are pigment stones with a significant cholesterol component as well. Parasite infection by *Ascaris lumbricoides*, *Clonorchis sinensis*, or *Opisthorchis viverrini* has been implicated as the initial insult followed by recurrent pyogenic seeding of the susceptible bile ducts. Other initial insults include malnutrition. The cycle of recurrent bacterial infections is termed recurrent pyogenic cholangitis.

Patients with recurrent pyogenic cholangitis may present with the signs and symptoms of acute cholangitis: right upper quadrant pain, fever, and jaundice. Also, patients may present with complications related to recurrent infection of the bile ducts, including bacteremia or sepsis, focal hepatic abscess, or, eventually, cholangiocarcinoma.

Imaging Findings

Interestingly, ultrasound has demonstrated difficulty in detecting the biliary stones associated with recurrent pyogenic cholangitis secondary to the soft, "mudlike" consistency of the stones. In some cases, ultrasound may directly visualize parasites within the biliary ducts.

The typical CT findings of hepatolithiasis include direct visualization of the intrahepatic stones, as well as intra- and extrahepatic biliary dilatation and stricture formation (Fig. 9-21). Hepatic parenchymal atrophy may also be identified. During the acute stages, recurrent pyogenic infections demonstrate the typical findings of inflammation on CT, including bile duct wall enhancement and adjacent hepatic parenchymal hyperenhancement. Complications of the acute disease include intrahepatic abscess and biloma formation. The dreaded long-term complication of recurrent pyogenic cholangitis is the development of cholangiocarcinoma. This typically develops in atrophic,

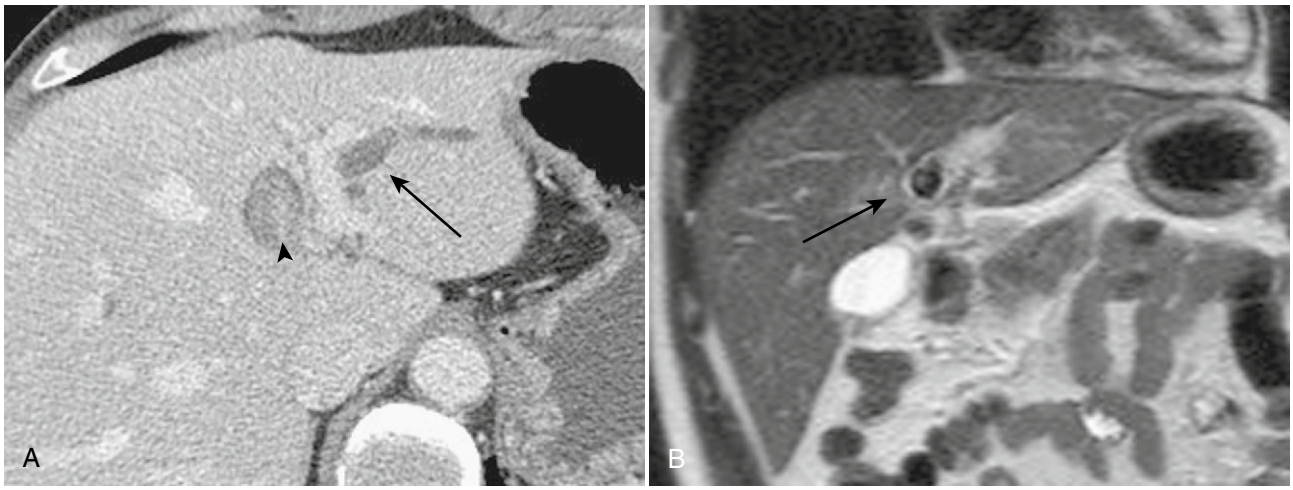


FIGURE 9-21. A 42-year-old male with a history of chronic recurrent cholangitis. Axial portal venous phase CT image **(A)** demonstrates the presence of hepatolithiasis *(arrowhead)* as well as intraductal biliary dilatation *(arrow)* secondary to stricture related to recurrent infection. Coronal T2 MRI image **(B)** confirms the presence of an intrahepatic bile duct stone *(arrow)*.

stone-containing segments of the hepatic parenchyma and is usually associated with narrowing of the adjacent portal vein. As on ultrasound, the presence of intrabiliary parasites may be directly identified on CT.

DISEASES OF THE LIVER

Hepatitis is a relatively common clinical presentation, the diagnosis and management of which typically does not require imaging. However, unsuspected cases may undergo imaging and the radiologist should be aware of the typical imaging characteristics and associated findings of the various hepatitides. Focal hepatic infections, on the other hand, often require imaging both in the diagnosis as well as in the characterization of the underlying etiology. In addition, image-guided therapies are often used in the management of focal hepatic infections.

Focal Hepatic Infections

Pyogenic hepatic abscesses account for the majority of hepatic abscess cases in the United States. Pyogenic hepatic abscess formation is most commonly associated with cryptogenic, post-traumatic, and biliary etiologies. Portal venous seeding secondary to infections drained by the portal venous vasculature, such as appendicitis or diverticulitis, accounts for approximately 10% of cases.

Although bacterial infections are the most common cause of hepatic abscess in the United States, worldwide, *Entamoeba histolytica* is a cause of significant morbidity and mortality. Amebic liver abscess is a common extraintestinal manifestation of *E. histolytica*, an infection with prevalence of approximately 10% worldwide. This infection is rare in the United States; the affected patients are typically from countries where the infection is more common, including Africa, Central and South America, and India, as well as East Asian countries, or they have recently traveled to these areas. Classically, on gross pathology, these collections are filled with blood products, forming a brown, thick consistency described as "anchovy paste."

Finally, *Echinococcus granulosus* is a common parasitic infection that may result in focal hepatic infection. Like amebiasis, infection of the liver occurs through the invasion of the mucosa of the bowel followed by the portal venous system. Rare in the United States, echinococcal disease is common in the Mediterranean region, as well as in areas where sheep raising is more common. The composition of the hydatid cyst results in its characteristic imaging features. At histopathology, it is composed of three layers: the outer pericyst and the inner endocyst separated by a thin membrane termed the ectocyst. The outer pericyst is actually composed of compressed liver parenchyma and fibrosis.

Patients with pyogenic hepatic abscesses typically present with right upper quadrant pain, fever, and malaise. Depending on the size and number of abscesses, the presentation may be acute or more chronic and indolent with weight loss or fever of unknown origin. When irritation of the right hemidiaphragm is associated with the hepatic abscess, patients may complain of referred pain to the right shoulder. Patients with amebic liver abscesses also typically complain of right upper quadrant pain, and the majority of patients present with fever. The presentation of patients with a hydatid cyst involving the liver is variable and may be due to complaints of a mass in the right upper quadrant or upper abdominal discomfort. Cyst rupture may result in a more acute presentation of pain with peritonitis.

Imaging Findings

Ultrasonography may be employed in the diagnosis of pyogenic liver abscess. The typical imaging findings are of a relatively hypoechoic, heterogeneous collection surrounded by normal-appearing liver parenchyma. Often, internal echoes are identified secondary to debris and pus. However, early in the development of these infections, they may be of a more phlegmonous nature and appear ill-defined and hyperechoic relative to the hepatic parenchyma. As they mature, they take on the more classic cystic-appearing features. These collections may also contain air secondary to the presence of gas-forming organisms, and the typical hyperechoic foci demonstrating ring-down artifact are seen

on ultrasound. Amebic liver abscesses demonstrate findings similar to findings of pyogenic infections on ultrasonography; hypoechoic, intraparenchymal collections often demonstrate homogeneous, low-level echoes internally. As it is on CT, the typical imaging appearance of echinococcal disease of the liver may be identified on ultrasonography; uni- or multilocular collections with possible identification of smaller, daughter cysts are common.

On CT, the abscesses are relatively hypoattenuating with the surrounding liver parenchyma (Fig. 9-22). Often, surrounding, smaller collections are identified in the vicinity of the largest abscess cavity. Hyperenhancement of the surrounding liver parenchyma may be identified, possibly related to local portal venous obstruction secondary to the acute inflammation. As on ultrasound, there may be direct evidence of air within the collection. Complications of liver abscesses, including venous thrombosis, are seen in up to half of patients. The hepatic venous system is affected nearly as often as the portal veins. Contrast-enhanced CT demonstrates the nonenhancing hypoattenuating tubular structures of the thrombosed veins.

CT findings of amebic liver abscesses are similar to pyogenic liver abscesses in that a well-defined, hypoattenuating, peripherally enhancing collection is typically identified. Serologic testing, in the appropriate patient population with typical CT findings, often solidifies the diagnosis. Extrahepatic extension of the infection is relatively common, a possible discriminating imaging finding when considering this diagnosis. Extension into the pleural space, chest wall, pericardium, bile ducts, bowel, and surrounding viscera has been described.

Both ultrasound and CT may diagnose the findings of echinococcal disease within the liver. Typically, these cystic lesions are identified as uni- or multilobular collections. Often, small daughter cysts are seen within the larger lobules, a finding highly specific for echinococcal disease. Another fairly specific sign for echinococcal disease is the so-called "water lily" sign, in which the endocyst ruptures and is seen floating dependently within the outer layers of the cyst. Complications, when affecting the liver, include rupture into the peritoneal cavity or into the biliary tracts.

In all three of the aforementioned focal hepatic infections, radiology may play a role in management. In those patients presenting with pyogenic abscesses, ultrasound or CT-guided percutaneous needle aspiration or catheter placement combined with antibiotic therapy results in a definitive treatment for most patients. In patients with amebic liver abscess, medical management with metronidazole is successful in the majority of patients. However, those with more severe disease burden may benefit from percutaneous drainage using ultrasound or CT guidance. Finally, in patients with echinococcal liver disease, surgery remains the cornerstone of treatment. However, percutaneous therapy has been shown to be successful, often in conjunction with scolicidal agents. Typically, patients are treated with albendazole prior to intervention to avoid the risk of anaphylaxis by causing the cyst material to become nonantigenic.

Hepatitis

There are a myriad of underlying etiologies for acute hepatitis, including toxic causes such as alcohol and various medications, infectious causes, and autoimmune causes, among others. Typically, imaging is not utilized in the evaluation and diagnosis of hepatitis, although the findings of hepatitis should be recognized if imaging is acquired for another indication or if the diagnosis of hepatitis is unsuspected.

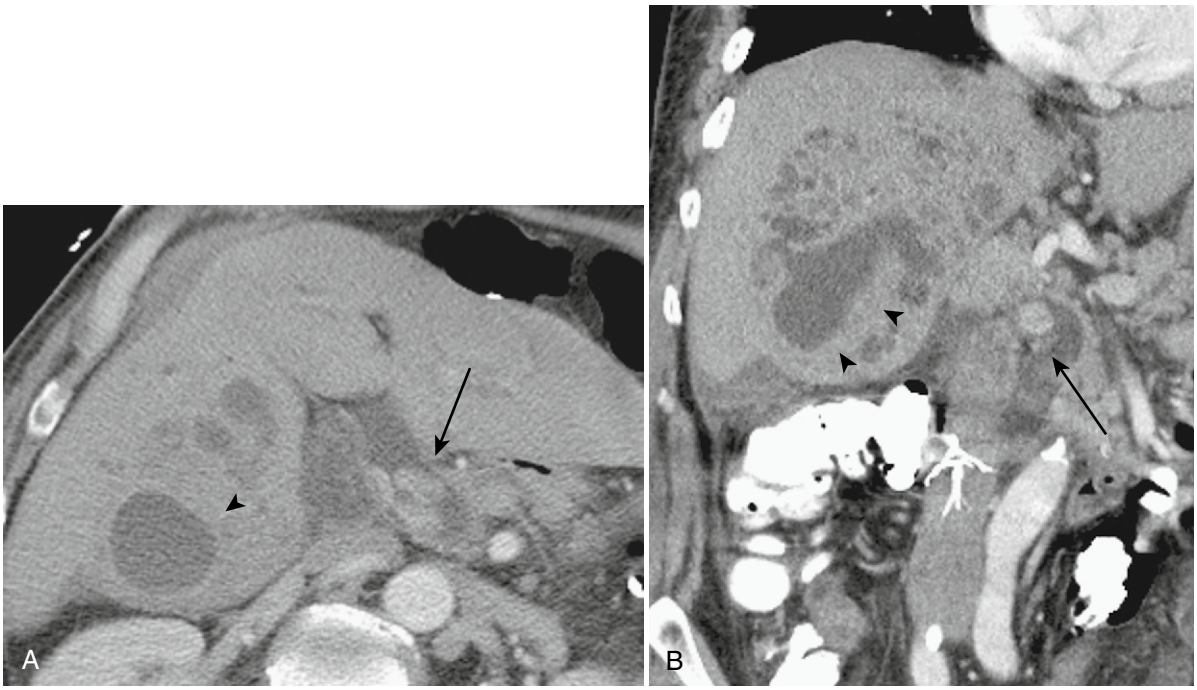


Figure 9-22. A 70-year-old male with choledocholithiasis and hepatic abscess. Axial **(A)** and coronal **(B)** portal venous phase CT images demonstrate large bile duct stones *(arrows)* with a focal intrahepatic fluid collection *(arrowheads)* consistent with the patient's known pyogenic abscess.

Patients with diffuse inflammation of the liver or acute hepatitis may present with a wide range of clinical signs and symptoms from mild forms to fulminant hepatic failure. Often, abdominal discomfort, anorexia, nausea, and vomiting as well as jaundice may be associated.

Imaging Findings

Two distinct ultrasound patterns have been described in patients with acute hepatitis: the bright liver and the "starry sky" appearance. The bright liver refers to increased parenchymal echogenicity and attenuation of sound as it passes through the abnormal liver parenchyma. This pattern is nonspecific and can be seen in patients with acute alcoholic hepatitis, cirrhosis, chronic hepatitis, and diffuse fatty infiltration of the liver. The second pattern, called "starry sky," refers to diffuse decrease in echogenicity of the liver secondary to edema of the hepatocytes, causing the walls of the portal venules to be seen as echogenic areas on the dark background of the edematous hepatic parenchyma. This is also a nonspecific finding and has been described in other pathologies involving the liver including Burkitt's lymphoma and in fasting patients. Another finding that may be identified on ultrasound in patients with acute hepatitis is diffuse gallbladder wall thickening. Viral hepatitides are associated with gallbladder wall thickening, and fairly significant periportal lymphadenopathy may be seen.

Typical CT findings of acute hepatitis are nonspecific and may include findings of periportal edema, also known as a periportal "collar," hepatomegaly, and ascites. As on ultrasound, gallbladder wall thickening and lymphadenopathy may be identified in patients with viral hepatitides.

DISEASES OF THE GENITOURINARY TRACT

Genitourinary disease, especially nephrolithiasis and its complications, represents a significant cause of abdominal pain and commonly requires imaging in its diagnosis. Infectious genitourinary diseases, such as pyelonephritis, less commonly require imaging diagnosis; however, the complications of the various genitourinary infections may necessitate an imaging evaluation. Finally, acute vascular insults of the kidney, including infarcts and renal vein thrombosis, are commonly diagnosed using cross-sectional imaging.

Nephrolithiasis

Renal calculi are usually caused by crystallization of the supersaturated stone-forming materials from urine. Calcium is the most common stone-forming material with uric acid constituting the second largest component. Numerous other less common components are described, including xanthine, cystine, struvite, and precipitation of medications such as protease inhibitors in the HIV population, among others. Alternatively, renal pathology may initiate the formation of crystals within the renal tubules that are extruded into the renal collecting system to undergo further growth. Ureteral calculi are most commonly secondary to renal calculi passing distally into the ureters.

Nephrolithiasis and ureterolithiasis present with pain in the region of the flanks, which may radiate into the groin, especially with distal progression of the stones into the ureter. Costovertebral tenderness is commonly elicited in patients with nephrolithiasis. Also, hematuria is often associated.

Imaging Findings

Nephrolithiasis may be identified as focal calcific densities projecting over the renal shadows. The expected course of the ureters should be analyzed for evidence of ureteral calculi. Also, bladder calculi may be identified on plain radiographs. In patients with a known history of renal calculi who have undergone lithotripsy, plain radiographs may be used to evaluate for residual renal or ureteral calculi. When multiple ureteral calculi are identified following lithotripsy, it is termed *Steinstrasse*. The translation of this German term is "stone street."

Ultrasound is often employed in patients presenting with acute renal failure and may demonstrate findings of nephrolithiasis, possibly with signs of obstruction. Renal calculi are seen as echogenic foci, typically demonstrating posterior acoustic shadowing. Also, signs of hydronephrosis and hydroureter may be identified on ultrasound in patients with acute obstruction. Proximal and distal ureteral stones may be clearly identified on ultrasonography; however, ultrasound is limited in the evaluation of the entirety of the ureter, and, therefore, sensitivity is significantly less than with CT in detecting ureteral calculi.

Renal stone CT protocols are usually acquired without the use of oral or intravenous contrast, which may obscure the underlying stones. CT has a high diagnostic accuracy in the detection of renal and ureteral calculi and may be used to differentiate among stones of various chemical compositions. Recently, ultra-low-dose CT with radiation dose equivalent to a KUB has been shown to be diagnostically sufficient in evaluating renal and ureteral calculi. Renal stones are most commonly composed of calcium in the form of calcium oxalate, calcium phosphate, and calcium urate. Other common stones are struvite, uric acid, and cystine stones. These most common forms of renal stones are all readily identified by routine CT techniques (Fig. 9-23). However, in patients with HIV with a clinical suspicion of nephrolithiasis, protease-inhibitor induced stones, because they are not routinely identified on CT, should be a consideration.

Secondary signs of acute ureteral obstruction include enlargement of the kidney, which often demonstrates diffusely decreased attenuation secondary to edema, perinephric stranding, and dilatation of the ureter and collecting system. Three areas of narrowing in the course of the ureter are common areas for the identification of obstructing ureteral stones. These include the ureteropelvic junction (UPJ), the pelvic brim as the ureter crosses into the pelvis, and the ureterovesical junction. Ureteral stones, when identified in the pelvis, may demonstrate a soft tissue "rim" sign surrounding the calculus, distinguishing a ureteral calculus from adjacent pelvic vein phleboliths.

Pyelonephritis

Pyelonephritis is typically caused by *E. coli* or *Enterococcus faecalis* in the outpatient community population. In patients who fail therapy, or in whom symptoms progress,

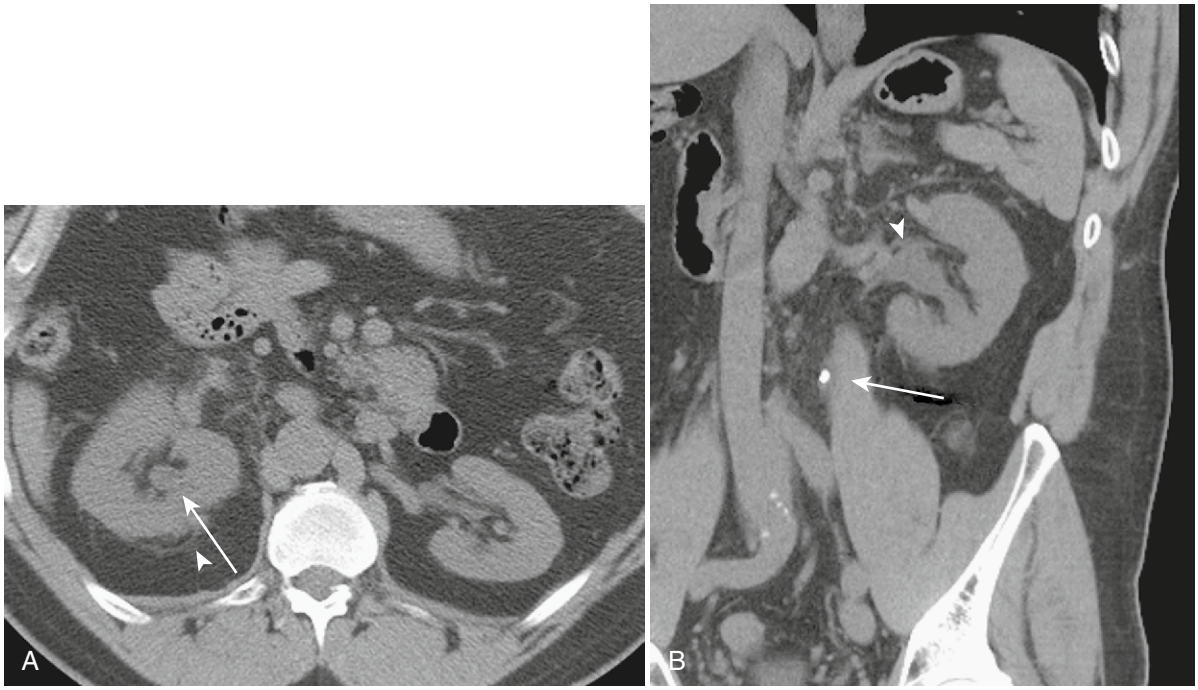


Figure 9-23. A 59-year-old female with obstructing ureteral calculus. Axial unenhanced CT image **(A)** demonstrates mild diffuse enlargement of the right kidney with hydronephrosis *(arrow)* and mild perinephric stranding *(arrowhead)*. Coronal unenhanced CT image **(B)** demonstrates hydronephrosis *(arrowhead)* and the ureteral stone *(arrow)*.

ultrasound or CT may be used to evaluate the various complications of pyelonephritis.

Patients with pyelonephritis may describe a preceding lower urinary tract infection including dysuria, frequency, and lower abdominal pain. Subsequently, patients often develop complaints of flank pain, which may be either uni- or bilateral. Fever and leukocytosis may be associated.

Imaging Findings

Uncomplicated pyelonephritis may demonstrate an enlarged, swollen kidney with areas of increased or decreased renal parenchymal echogenicity. More so in children, power and color Doppler techniques have been used to diagnose pyelonephritis based on focal areas of hypovascularity.

On CT, simple pyelonephritis may demonstrate a striated nephrogram as well as ill-defined hypoattenuating areas within the parenchyma. This is caused by the decreased excretory function of the renal tubules secondary to obstruction by inflammatory debris, vasospasm, and surrounding parenchymal edema. Delayed enhancement secondary to vasospasm may be identified on the affected side. Other findings associated with pyelonephritis on CT may be thickening and hyperenhancement of the urothelium. Also, perinephric stranding may be identified.

Renal Abscess

Renal abscess formation is a potential complication of pyelonephritis, the suspicion of which typically entails the use of imaging for characterization. The imaging characteristics of the abscess, when identified, are used for planning management.

Patients with a renal abscess commonly present with fever, chills, and abdominal pain. Associated urinary tract symptoms may also be reported. Leukocytosis is typically associated.

Imaging Findings

The distinction between a focal renal abscess and acute focal bacterial nephritis has important implications for subsequent management. Renal abscesses usually demonstrate ultrasound findings of a complex, focal, hypoechoic region within the parenchyma, often with internal echotexture but with evidence of increased through-transmission (Fig. 9-24). Focal bacterial nephritis, it has been reported, lacks the increased through-transmission of a renal abscess.

CT demonstrates focal, low-attenuation areas that may extend into the perirenal soft tissues. These areas are more readily identified with intravenous contrast, thereby increasing the attenuation differences between normally enhancing renal parenchyma and the nonenhancing abscess collection. Often, secondary CT signs of inflammation accompany a renal abscess, including perinephric fat stranding.

In patients with a renal abscess, percutaneous drainage via ultrasound or CT guidance may be used to successfully manage the patients, an approach that has been shown to have outcomes similar to those of surgical management. However, smaller abscess collections may be treated successfully using intravenous antibiotics.

Emphysematous Pyelonephritis

Emphysematous pyelonephritis represents a severe renal parenchymal infection, almost exclusively encountered in diabetic patients. The most commonly cultured organism in patients with emphysematous renal tract disease (ERTD) is *E. coli*. As this entity results in significant increases in

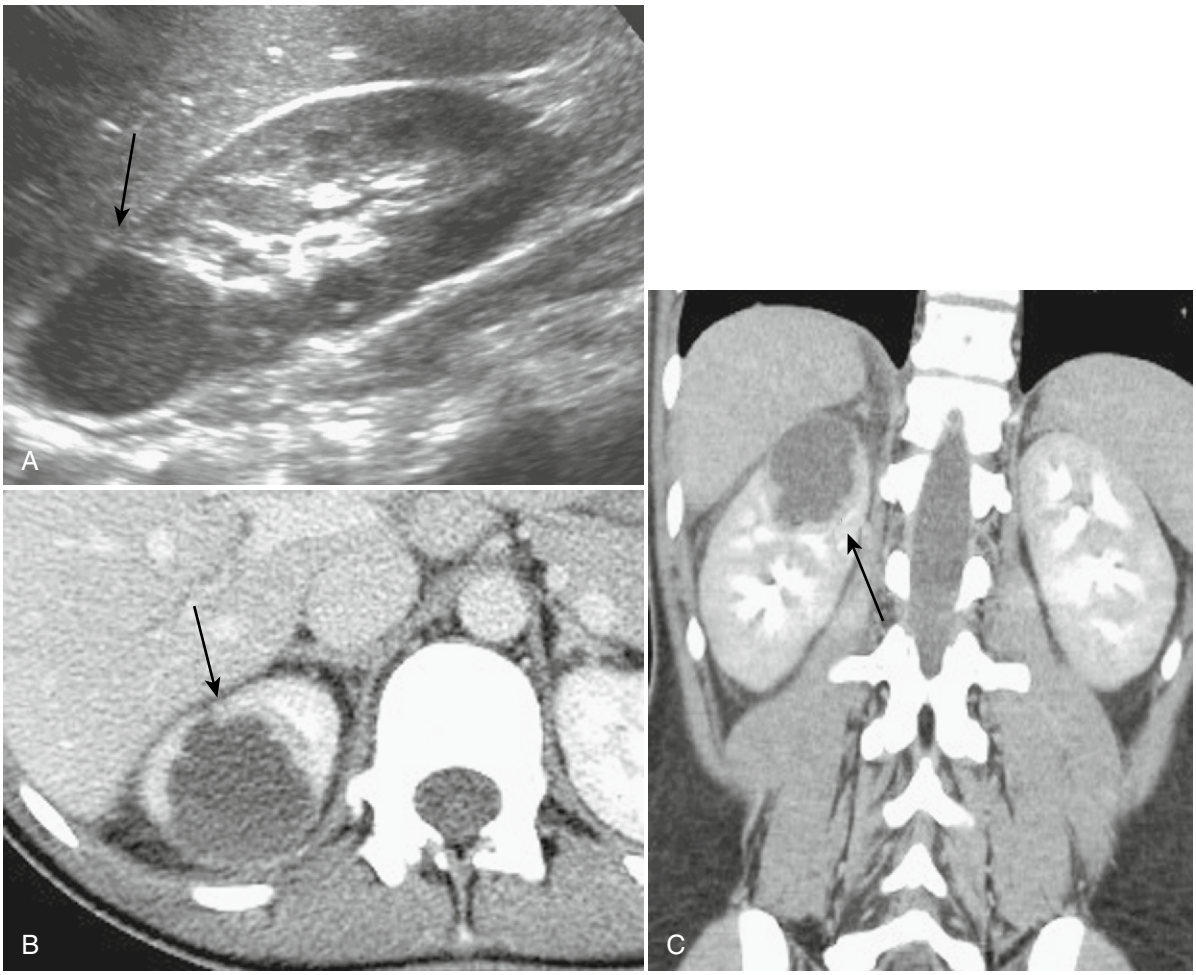


FIGURE 9-24. A 37-year-old female with renal abscess. Ultrasound image **(A)** reveals a focal hypoechoic area within the renal parenchyma with scattered internal echoes *(arrow)*. Axial **(B)** and coronal **(C)** portal venous phase CT images reveal a corresponding focal hypoattenuating area within the parenchyma of the right kidney, findings consistent with a renal abscess.

morbidity and mortality, emphysematous pyelonephritis should be considered in all diabetic patients with signs and symptoms of pyelonephritis.

Patients with emphysematous pyelonephritis often present with fever and flank pain. In severe cases, crepitus may be appreciated. Also, given the severity of the infection, a significant portion of patients may present with frank septic shock.

Imaging Findings

CT is primarily used as the initial imaging modality for evaluating complicated pyelonephritis, including emphysematous infections. CT clearly demonstrates gas within the renal parenchyma that may extend into the perirenal soft tissues. A classification system based on imaging has been shown to have prognostic implications. Two types of emphysematous pyelonephritis are described: type I without, and type II with associated renal or perirenal fluid collections. Those with associated fluid collections have a more favorable prognosis, hypothesized to be secondary to a more favorable immune response as evidenced by the presence of fluid collections. The diagnosis of emphysematous pyelonephritis is a medical emergency and typically requires emergent nephrectomy, although successful management has been described using percutaneous drainage or medical therapy.

Xanthogranulomatous Pyelonephritis

Xanthogranulomatous pyelonephritis (XGP) represents a chronic inflammatory condition of the renal parenchyma. XGP has been associated with urinary tract infections secondary to *E. coli* and *Proteus mirabilis* and is nearly exclusively seen in patients with underlying urinary tract obstruction, commonly secondary to stone disease. Histopathologically, lipid-laden "foamy" macrophages accompany both acute and chronic inflammatory cells. Most commonly, the kidney is affected diffusely, although focal involvement of a portion of the parenchyma may also be identified. CT and ultrasound demonstrate the findings of XGP, although, usually, definitive preoperative diagnosis is difficult as renal malignancy remains on the differential in most cases.

Patients with XGP present with signs and symptoms of a chronic illness: anorexia, weight loss, fevers, and flank pain. As XGP may create a fistula with adjacent soft tissues, patients may initially present with cutaneous fistulas.

Imaging Findings

Few ultrasound imaging characteristics are available to distinguish XGP from a renal tumor. This is because the most common ultrasound finding is that of a circumscribed, solid renal mass, which may be hyper-, iso-, or hypoechoic with respect to the renal cortex. Hydronephrosis and renal calculi are commonly identified on ultrasound.

CT demonstrates renal enlargement with fluid-filled cavities replacing the renal parenchyma, often with extension into the perinephric tissues, findings suggestive of XGP. Again, hydronephrosis and renal calculi may be identified in patients with XGP (Fig. 9-25). CT evidence of fistula formation with surrounding tissues including bowel or skin lends credence to a suspected diagnosis of XGP.

Pyonephrosis

In patients with fever, chills, and flank pain, as well as obstruction of the urinary tract established on imaging, pyonephrosis should be highly suspected. Pyonephrosis represents infection of an obstructed urinary tract and is a medical emergency. Because this scenario of infection within the obstructed collecting system represents "pus under pressure," these patients can rapidly deteriorate and develop septic shock and possible irreversible deterioration of renal function.

Imaging Findings

Typically, ultrasound is indicated to demonstrate obstruction of the affected urinary system as evidenced by hydronephrosis and possibly hydroureter. Also, fluid–fluid levels and coarse or possibly low-level echoes are described in pyonephrosis.

On CT, the findings of renal obstruction as evidenced by hydronephrosis are identified. The obstructing lesion may also be characterized on CT. CT findings of inflammation may be identified, including inflammatory fat stranding around the collecting system and ureter as well as hyperenhancement of the urothelium. Thickening of the urothelium of the renal pelvis may also be identified.

Prompt placement of a percutaneous nephrostomy tube is indicated in these patients with pyonephrosis, who often eventually require subsequent definitive management to treat the underlying obstruction.

Emphysematous Cystitis/Pyelitis

Emphysematous cystitis represents a rare, fulminant infection of the bladder, again associated with underlying diabetes. Repeated urinary tract infections, neurogenic bladder, and bladder outlet obstruction have also been described in association with emphysematous cystitis. Commonly isolated organisms include *E. coli* and *Enterobacter aerogens*. Common causes of air within the bladder should be considered and excluded, such as recent instrumentation like Foley catheter placement or cystoscopy. Less common alternative causes of air within the bladder include fistulas with adjacent loops of bowel. Clinical history is often helpful in excluding these considerations. Unlike emphysematous pyelonephritis, emphysematous cystitis is usually successfully treated conservatively with antibiotics.

Emphysematous pyelitis refers to gas within the renal collecting system. Typically, the gas is secondary to emphysematous infections of the bladder and kidney, although primary infection of the urothelium is a less common cause. Again, other causes of air within the bladder and collecting

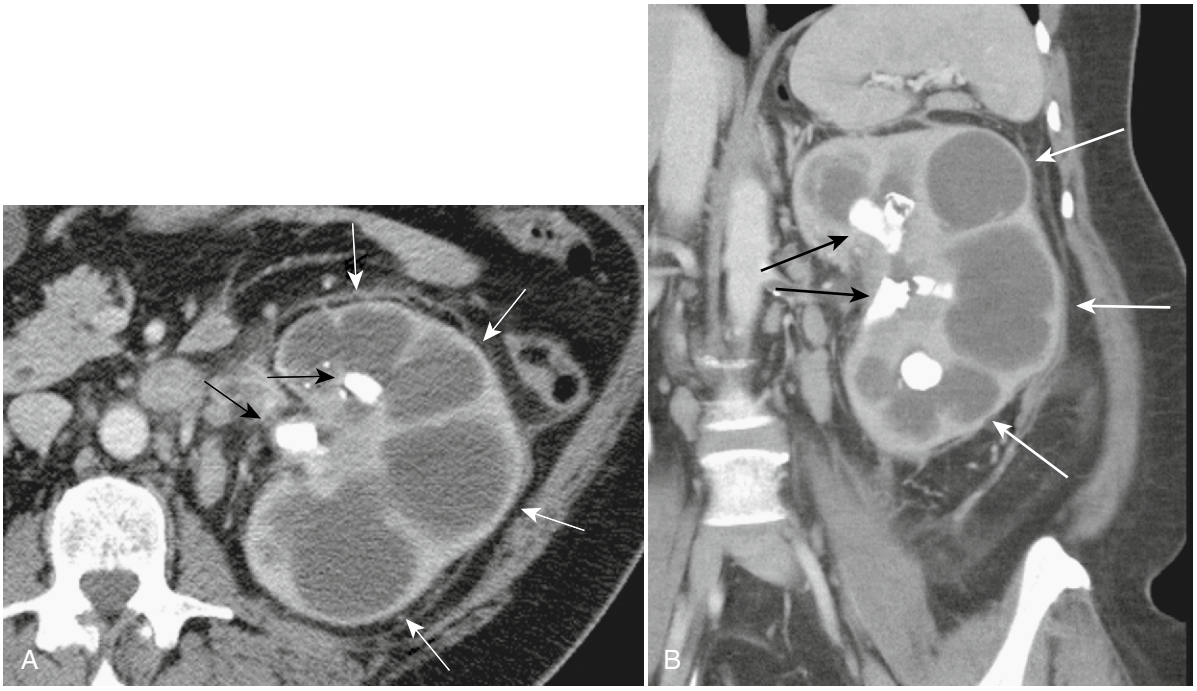


Figure 9-25. A 50-year-old female with xanthogranulomatous pyelonephritis (XGP). Axial **(A)** and coronal **(B)** portal venous phase CT images demonstrate significant enlargement of the left kidney with large renal calculi *(black arrows)* and large, low attenuation infiltration of the renal parenchyma *(white arrows)* characteristic of XGP.

system should be excluded as detailed above. Emphysematous pyelitis, as it is most commonly secondary to infection of the bladder or kidney, is normally managed by treating the underlying abnormality.

Patients with emphysematous cystitis often have fairly subtle clinical presentations, and therefore a high clinical suspicion is necessary in the appropriate patient population. Complaints include dysuria, fever, and hematuria. Although not sensitive, a report of pneumaturia is highly specific to this diagnosis.

Imaging Findings

Plain radiographs may demonstrate mottled or curvilinear lucencies overlying the expected location of the bladder wall. Also, an air–fluid level may be identified in patients with intraluminal air; this level is noted to change position with the patient. The intraluminal air may also outline the irregular mucosal surface, distorted by submucosal blebs, termed the *beaded necklace* appearance.

In patients with emphysematous cystitis, CT is highly sensitive for the finding of air localized within the bladder lumen or wall. It is important to exclude air within the renal parenchyma in these cases.

Renal Infarct

Nontraumatic renal infarcts are typically secondary to embolic phenomena, which may be secondary to atrial fibrillation, left ventricular thrombus in patients with prior myocardial infarction, and atherosclerotic disease in the aorta. Other considerations in cases of renal infarction include infective endocarditis and vasculitides, overwhelming shock and hypoperfusion, sickle cell disease, and iatrogenic injury.

Patients with renal infarction usually present with nonspecific signs and symptoms. Acute onset of low back pain in patients with risk factors of thromboembolic disease has been described as suggestive of renal infarction. Patients may present with fever and leukocytosis as well as hematuria and proteinuria.

Imaging Findings

The majority of patients with renal infarction demonstrate peripheral, wedge-shaped areas of decreased attenuation on contrast-enhanced CT. Smaller subsets of patients have multifocal areas of low attenuation or global infarction. Sickle cell disease may demonstrate multiple "slitlike" areas of infarction, possibly secondary to thrombosis of small venous channels. In cases of global renal infarction, the cortical "rim" sign is seen as a hyperattenuating rim around the cortex as the cortical tissue remains perfused by proximal branches of the renal artery and collateral vessels. As the majority of renal infarcts are secondary to embolic sources, the remainder of the abdomen, including the spleen and bowel, should be scrutinized for further complications of embolic phenomena.

Renal Vein Thrombosis

The most common etiology of renal vein thrombosis is nephrotic syndrome, which leads to a hypercoagulable state with systemic effects and with a predilection for renal vein thrombosis. Another relatively frequent cause of renal vein thrombosis is secondary to extension of renal cell carcinoma. Less likely causes are in patients with renal transplants or hypercoagulability secondary to causes other than nephrotic syndrome. Although usually asymptomatic, renal vein thrombosis may present with acute flank pain and hematuria, similar to nephrolithiasis.

Imaging Findings

Ultrasound can demonstrate enlargement of the affected kidney and potentially may demonstrate direct evidence of the thrombus within the renal vein, as evidenced by an echogenic intraluminal filling defect. Unlike in the renal transplant population, intrarenal arterial Doppler studies in native kidneys have shown inadequate sensitivity and specificity for diagnosing renal vein thrombosis.

CT clearly demonstrates thrombus within the renal vein and may aid in characterizing the underlying etiology, especially in cases of renal cell carcinoma. Other CT findings in renal vein thrombosis include an enlarged kidney with prolonged corticomedullary phase and delayed nephrogenic and excretory phases. Also, significant prolongation of parenchymal enhancement may be seen on follow-up examinations up to many hours later. Because complications include the potential for pulmonary embolism, extension of the thrombus into the inferior vena cava should be evaluated using ultrasound or CT.

DISEASES OF THE SPLEEN

The overwhelming majority of splenic abnormality identified on imaging is benign and represents an incidental finding. However, several splenic abnormalities may present with acute abdominal symptoms, including focal infections of the spleen. Also, vascular insults such as splenic infarcts and torsion, related to "wandering" spleen, may present acutely and require imaging in their diagnosis.

Splenic Abscess

Patients with splenic abscesses commonly have an underlying predisposition to infection, such as diabetes mellitus, leukemia, intravenous drug abuse, or HIV positivity. Other associations include endocarditis and recent splenic infarction from various causes. A variety of bacteria are commonly isolated in these cases, including *E. coli*, *Pseudomonas aeruginosa*, *Staphylococcus aureus*, *Streptococcus*, *Mycobacterium* organisms such as tuberculosis, and fungal organisms. Unilocular abscesses are typically secondary to pyogenic abscesses.

Patients with splenic abscesses typically present with fever and abdominal pain, often localized to the left upper quadrant. Diaphragmatic irritation can cause referred pain in the shoulder, called the Kehr sign. Patients also report pleuritic chest pain.

Imaging Findings

When seen on ultrasound, splenic abscesses appear as focal, hypoechoic areas, often with internal echoes or debris. Rarely, gas may be identified as focal echogenic areas with posterior "dirty shadowing."

Splenic abscesses are for the most part low attenuation on CT. They may demonstrate peripheral rim enhancement and possibly contain gas. Mycobacterial and fungal abscesses typically demonstrate several or many small, hypoattenuating ovoid lesions throughout the splenic parenchyma. *Echinococcus* is another relatively common cause of splenic abscess. As in other areas of involvement, echinococcal disease of the spleen demonstrates the typical multiloculated cystic appearance, possibly with more specific visualization of daughter cysts.

In cases of pyogenic abscess, management may include splenectomy; however, percutaneous ultrasound or CT-guided drainage has been demonstrated as a viable alternative in selected patients.

Splenic Infarction

Splenic infarction is a cause of acute abdominal pain and fever in patients who commonly have underlying hematologic or thromboembolic disorders. However, a small subset of patients remains asymptomatic, and splenic infarction is often incidentally identified on imaging studies obtained for other reasons. Hematologic disorders include both benign diseases such as sickle cell disease and malignant lymphoproliferative disorders including lymphoma and leukemia. Thromboembolic etiologies typically include atherosclerotic disease or emboli originating from the heart, as in endocarditis or atrial fibrillation, or are secondary to prosthetic mitral valves. Splenic vein thrombosis secondary to a variety of causes, including pancreatitis, may result in splenic infarction. As detailed below, a dramatic cause of splenic infarction is torsion of a "wandering" spleen.

Splenic infarction is often incidentally identified on imaging for unrelated clinical indications. However, especially when larger, splenic infarction can cause abdominal pain, typically in the left upper quadrant. As well, these patients may be febrile.

Imaging Findings

The findings of splenic infarction can be seen on both ultrasound and CT as peripheral, hypoechoic in the case of ultrasound, and hypoattenuating wedge-shaped defects in the case of CT.

Less classic appearances of splenic infarction include multiple focal, heterogeneous areas of infarction as well as massive areas involving significant portions of the splenic parenchyma. In contrast to unenhanced CT, intravenous-enhanced CT has been shown to improve detection of splenic infarcts significantly. Complications in cases of splenic infarction are secondary infection and abscess formation, as well as pseudocyst formation, hemorrhage, and even rupture. In cases of chronic splenic infarcts, as seen in patients with sickle cell disease, the spleen appears atrophic and diffusely calcified, a finding that may be apparent on plain radiographs as focal calcification in the left upper quadrant.

One consideration in patients with sickle cell disease is the possibility of splenic sequestration, which might have a somewhat similar imaging appearance to splenic infarction in some cases. Although this is typically a clinical diagnosis based on hematocrit decrease and splenic enlargement, imaging may provide a diagnosis in unsuspected cases. In splenic sequestration, CT findings of multiple, peripheral, nonenhancing areas or diffuse low attenuation involving the majority of the splenic parenchyma are identified.

Splenic Torsion

Splenic torsion results secondary to twisting of the spleen around its vascular pedicle and is associated with the rare condition of "wandering" spleen. The term is used when the spleen is not identified in its expected location but seen elsewhere in the abdomen or pelvis. The underlying cause for the ectopic location is hyperlaxity or abnormal development of the supportive ligaments of the spleen. More commonly seen in children, wandering spleen has been identified in adults, most commonly women. Patient presentation in cases of splenic torsion varies from acute to chronic, intermittent pain. An even less common cause of acute abdominal pain that demonstrates similar imaging appearances, although on a somewhat smaller scale, is the acute torsion of an accessory spleen, or splenule.

Patients with splenic torsion typically present with acute abdominal pain. As these cases are associated with wandering spleen, patients may report a more prolonged history of intermittent abdominal pain. Less commonly, splenic torsion may be asymptomatic with clinical presentation prompted by a palpable abdominal mass caused by the torsed spleen.

Imaging Findings

In cases of torsion related to wandering spleen, a hypo- or avascular mass is identified in the peritoneal cavity on ultrasound. In cases of torsion of a splenule, a smaller hypovascular mass is identified adjacent to the normal-appearing spleen.

CT also demonstrates a hypo- or nonenhancing mass in cases of complete infarction, usually surrounded by inflammatory changes. CT may be used to directly identify the twisted vascular pedicle, described as having a whorled appearance. In cases of torsion of a splenule, a hypovascular soft tissue mass is identified on CT in the left upper quadrant adjacent to a normal spleen.

EMERGENT IMAGING FINDINGS

Several imaging findings are considered emergent findings because they suggest underlying pathology requiring urgent intervention. These include pneumoperitoneum, which, although possibly suggested clinically, is typically an imaging diagnosis. The findings of pneumoperitoneum demand urgent attention, even though there are various underlying causes, some of which are benign, as discussed below. Additionally, intra-abdominal hemorrhage also warrants urgent attention both in acute clinical management and in imaging evaluation to diagnose the underlying cause. Acute urinary and biliary obstruction both have various underlying causes, and although the uncomplicated obstruction does not usually represent an emergent, life-threatening situation, various complications of the obstructions may indeed represent true emergencies as detailed below.

Pneumoperitoneum

Pneumoperitoneum refers to free air within the peritoneal cavity. Common etiologies include perforation of a hollow viscus and iatrogenic causes such as recent surgery and orogenital insufflations, which are the most common cause overall, and extension from other compartments of the body, including pneumomediastinum. In cases of pneumoperitoneum secondary to surgery, one should expect appropriate resolution during the postoperative period. The majority of cases are noted to resolve within 2 days based on radiography; however, many patients have minute areas of free air for several days and even up to several weeks on CT scans postoperatively.

Because the signs and symptoms of pneumoperitoneum are usually related to the underlying etiology, there are a myriad of clinical presentations. When there is perforation of a hollow viscus, peritonitis may ensue; this might be preceded by focal abdominal pain, based on the underlying etiology. Benign causes of pneumoperitoneum, such as those secondary to orogenital insufflations, may be asymptomatic and only incidentally identified on imaging.

Imaging Findings

Plain radiographs are often initially employed to detect free intraperitoneal air. Typically, a supine radiograph, in addition to an upright view of the chest, is acquired to evaluate for free intraperitoneal air (Fig. 9-26). Left lateral decubitus views of the abdomen and lateral chest radiographs are further options. In cases of upright radiographs or left lateral decubitus views, acquisition with the central ray of the x-ray beam at the highest level of the peritoneal cavity has been shown to increase sensitivity. Various signs of pneumoperitoneum on abdominal radiographs have been described: they include the Rigler's sign, in which air is seen on both sides of the bowel wall; the falciform ligament sign, in which air outlines the falciform ligament; the "football" sign, in which air outlines the confines of the peritoneal cavity; the "inverted V" sign, in which air outlines the medial umbilical folds; and the right upper quadrant air sign, in which a focal, typically triangular, collection of gas is seen in the right upper quadrant. At least one of these signs has been reported in slightly more than half of patients with pneumoperitoneum on supine abdominal radiographs. The "cupola" sign of air outlining the median subphrenic space has also been described in the minority of patients with pneumoperitoneum on supine radiographs.

CT is the most sensitive modality for detecting small volumes of pneumoperitoneum. In cases of hollow viscus perforation, it has been shown to be highly accurate in the localization of the site of perforation, especially when thin collimation images and multiplanar reformations are viewed. The findings of focal bowel wall thickening, localized air bubbles, and direct visualization of a rent within the wall of the bowel have been shown to be accurate predictors of the site of perforation.

Spontaneous Hemoperitoneum

Spontaneous hemoperitoneum, in the absence of trauma, may be seen secondary to a variety of causes including splenic, hepatic, vascular, coagulopathic, and gynecologic. Typically a patient presents with acute symptoms including abdominal pain possibly associated with hypotension. Spontaneous splenic hemorrhage may be secondary to underlying lymphoproliferative disease, infection, or rupture

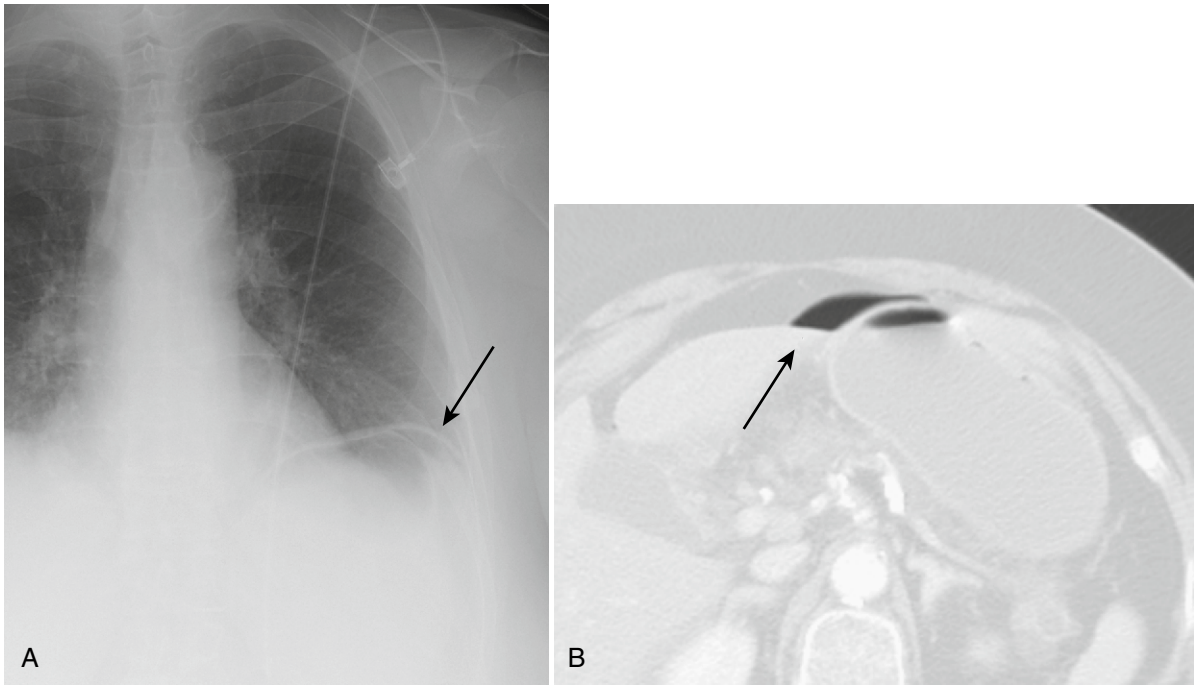


FIGURE 9-26. A 76-year-old female with perforated duodenal ulcer and free intraperitoneal air. Plain upright chest radiograph **(A)** demonstrates lucency *(arrow)* beneath the diaphragm on the left, adjacent to the air-filled stomach, consistent with free intraperitoneal air. Axial CT **(B)** using lung windows clearly demonstrates free intraperitoneal air *(arrow)* adjacent to the stomach, as on the radiograph.

of a splenic artery pseudoaneurysm commonly caused by pancreatitis, among a myriad of other underlying etiologies. Ruptured splenic artery aneurysm, which represents the most common splanchnic vessel aneurysm territory, is also a potential cause of spontaneous splenic hemorrhage.

Spontaneous hemorrhage originating from the liver is usually associated with hepatic tumors, both benign and malignant. As in any splanchnic vascular territory, rupture of hepatic arterial aneurysms or pseudoaneurysms may cause spontaneous hemorrhage. Benign hepatic tumors predisposing to spontaneous hemorrhage include adenomas, while hepatocellular carcinoma and, less likely, metastases account for the malignant etiologies (Fig. 9-27). Spontaneous hemorrhage secondary to other benign hepatic lesions, including focal nodular hyperplasia and cavernous hemangioma, has been described but is much less frequently observed.

Another significant cause of spontaneous intra-abdominal hemorrhage, affecting both intraperitoneal and retroperitoneal compartments, is coagulopathy, including medical anticoagulation. Hemorrhage secondary to coagulopathy most commonly involves the rectus sheath, iliopsoas, and retroperitoneal compartments. Less commonly, the hemorrhage is within the peritoneum, and, rarely, it involves a solid visceral organ such as the spleen or liver. Patients often present with acute abdominal pain and, as the majority of cases involve anticoagulant or antiplatelet administration, are generally known to be coagulopathic.

Patients with spontaneous retroperitoneal hemorrhage often present with acute abdominal pain. When the hemorrhage is extensive, patients may present with hypotension and even frank shock.

Imaging Findings

In these cases, ultrasound can identify hemoperitoneum as free fluid with homogeneous internal echoes. Additionally, a clot may appear as a focal heterogeneous collection, which might seem to be masslike but demonstrates no internal vascularity.

CT is often used as the initial imaging modality in cases of suspected hemoperitoneum or to evaluate for the underlying etiology when hemoperitoneum is identified on ultrasound. On CT, a focal region of high-attenuation clotted blood, known as the "sentinel clot" sign, is useful in localizing the underlying etiology of hemorrhage.

On CT, in cases of spontaneous splenic hemorrhage, the underlying etiology may be clearly visualized as a focal or

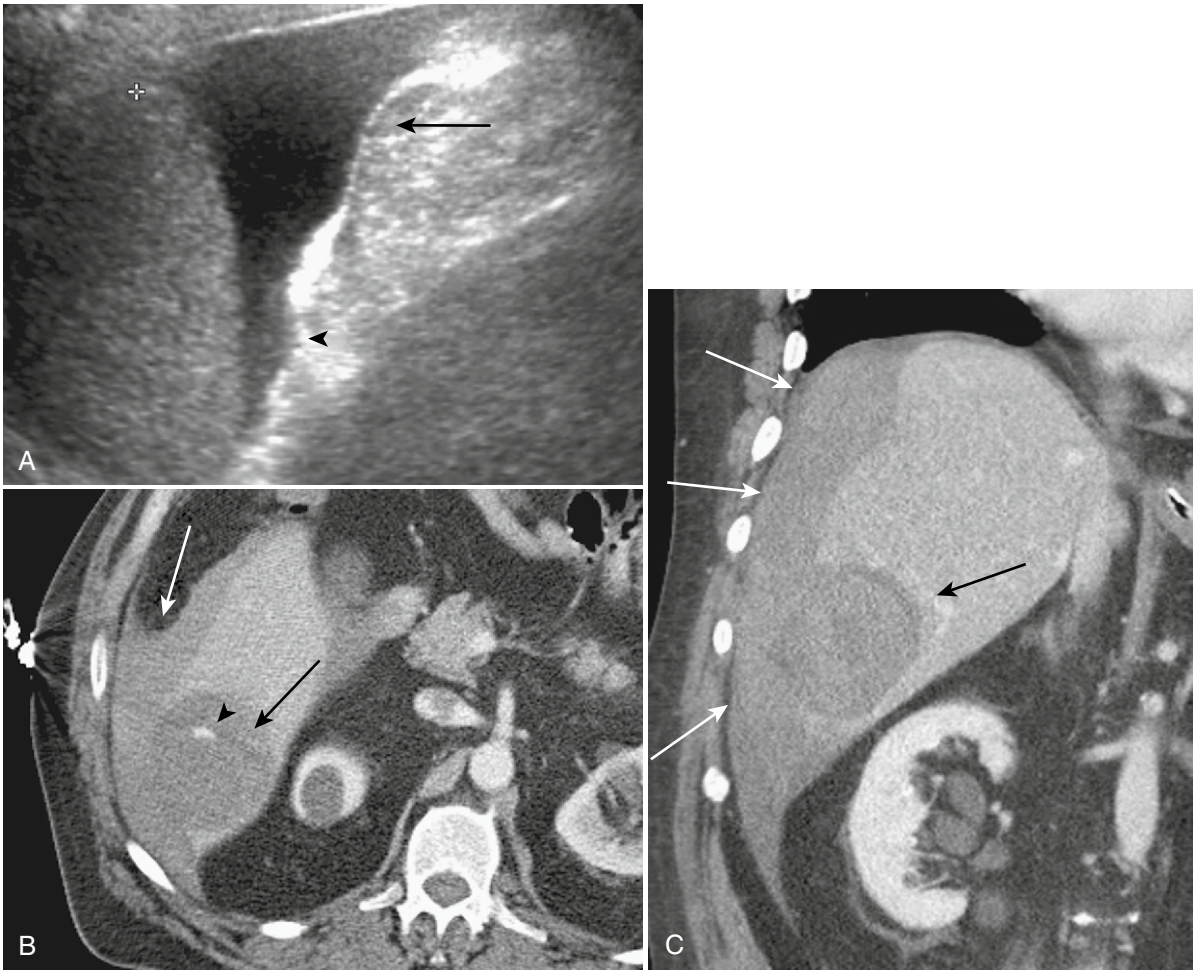


Figure 9-27. A 57-year-old female with ruptured hepatocellular carcinoma. Ultrasound image **(A)** demonstrates free intraperitoneal fluid *(arrow)* with evidence of dependently layering debris *(arrowhead)* consistent with hemoperitoneum. Axial **(B)** and coronal **(C)** portal venous phase images demonstrate the patient's hepatoma *(black arrows)* with a central hyperattenuating focus *(arrowhead)* seen on the axial image consistent with active hemorrhage. Perihepatic hemorrhage is also seen on the CT images *(white arrows)*.

infiltrative mass lesion in cases of malignancy, as diffuse enlargement with or without focal hypoattenuating areas in the case of infection, or as a pseudoaneurysm. In these cases, the CT protocol should include intravenous contrast to allow characterization of intraparenchymal abnormalities and clear visualization of the splenic artery. CT affords potential characterization of the etiology of spontaneous hepatic hemorrhage; however, the hemorrhage may obscure the underlying cause in some cases. In this subset of patients, short-term follow-up CT or MRI is typically utilized to evaluate the etiology once the hemorrhage has organized or resolved.

In coagulopathic patients, CT demonstrates the hematoma in the various intra-abdominal compartments, and, in the majority of cases, a hematocrit effect, or the separation of the cellular components from the plasma, is visualized. This is a sensitive and specific finding suggesting underlying coagulopathy.

Spontaneous Retroperitoneal Hemorrhage

In addition to rupture of the various visceral organ related aneurysms and pseudoaneurysms, a significant cause of spontaneous retroperitoneal hemorrhage is rupture of an abdominal aortic aneurysm (AAA). Although less commonly encountered than spontaneous hemorrhage from underlying hepatic and splenic pathology, spontaneous renal and pancreatic hemorrhage can be severe and life-threatening. The most common causes of spontaneous renal hemorrhage include benign and malignant lesions, commonly renal angiomyolipoma and renal cell carcinoma, respectively. Other causes of renal hemorrhage include vasculitides such as polyarteritis nodosa (PAN) and Wegener's granulomatosis.

Similar to those with intraperitoneal hemorrhage, patients with spontaneous retroperitoneal hemorrhage often present with acute abdominal pain. When the hemorrhage is severe and massive, patients may present with hypotension and possibly even shock. In cases related to underlying renal pathology, hematuria may be associated.

Imaging Findings

Ultrasound may identify the retroperitoneal hemorrhage and possibly characterize the underlying etiology, as in the case of the renal tumors mentioned above; however, CT is often employed.

In cases of ruptured AAA, CT is often the first-line imaging modality (Fig. 9-28). CT protocols may include the

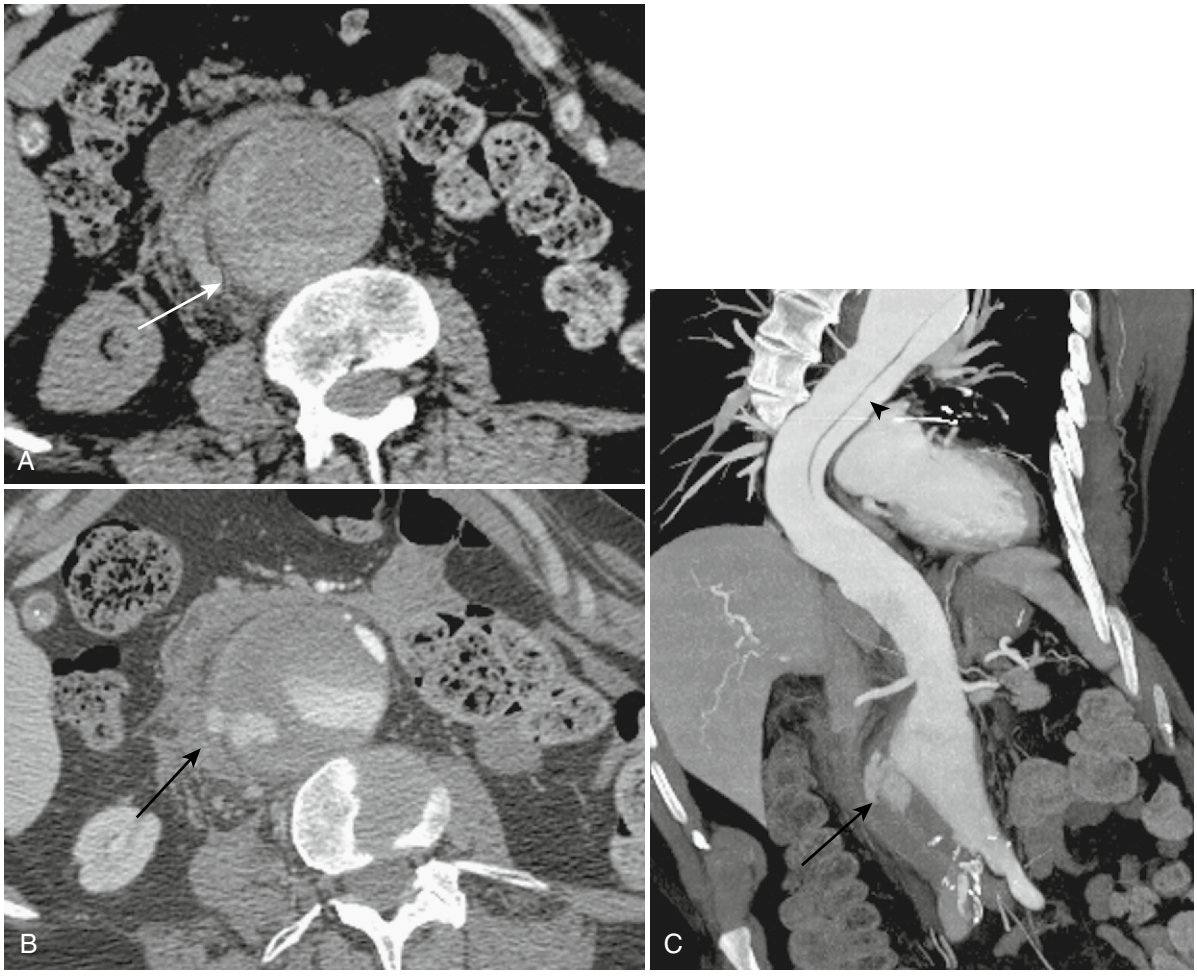


FIGURE 9-28. A 68-year-old male with ruptured abdominal aortic aneurysm. Axial unenhanced CT image **(A)** reveals hyperattenuation within the wall of the aorta *(arrow)*, the so-called "crescent" sign. Axial arterial phase CT image **(B)** reveals extravasation of contrast beyond the confines of the aortic wall *(arrow)*. Coronal maximum intensity projection image **(C)** reveals extraluminal extravasation of contrast *(arrow)*, as well as an incidentally noted thoracic aortic dissection *(arrowhead)*.

use of intravenous contrast to evaluate for active extravasation, although unenhanced CT may readily identify cases of AAA rupture. In cases of rupture, CT demonstrates hematoma within the retroperitoneum, contiguous with the aorta. Often, when large, the hemorrhage is identified within multiple retroperitoneal compartments. CT findings that increase the specificity of the diagnosis of ruptured AAA include the "crescent" sign, which refers to hyperattenuating clefts within mural thrombus or the aneurysmal wall itself; a "draped" aorta, which refers to displacement of the aorta onto the spine with lateral "draping" over a vertebral body; discontinuity of the aortic wall; and frank active contrast extravasation. Ruptured AAA represents a surgical emergency that warrants rapid intervention. In cases of renal tumors, specific findings of angiomyolipoma may be identified, such as areas of macroscopic focal fat. However, these can become somewhat obscured by hemorrhage. Also, in cases of renal malignancy, the underlying mass may become obscured and follow-up imaging by CT and MRI may be necessary for identification and characterization of the mass lesion. The spatial resolution and multiplanar capabilities of the current generation of CT scanners offer the ability to accurately diagnose vascular abnormalities secondary to vasculitis, such as the multiple small aneurysms characteristic of PAN. The common causes of spontaneous hemorrhage specific to the pancreas include hemorrhage related to pseudocysts that cause pseudoaneurysm formation in the surrounding arteries secondary to exposure to the various pancreatic enzymes. Other causes include pancreatic malignancies, a rare etiology.

In cases of spontaneous hemorrhage within the abdomen, conventional angiography may demonstrate ongoing active arterial hemorrhage, and percutaneous transcatheter embolization can be used as definitive treatment of the hemorrhage. However, given the myriad of causes of hemorrhage, its underlying etiology often remains to be definitively managed.

Biliary Obstruction

Patients with acute biliary obstruction may present acutely with abdominal pain, possibly with associated jaundice, depending on the chronicity of the underlying etiology. Etiologies of biliary obstruction include both intrahepatic and extrahepatic causes; common intrahepatic causes of cholestasis include hepatitis (discussed above) and cirrhosis. Typically, these represent chronic processes and are usually diagnosed clinically without the use of imaging. Intrahepatic mass lesions, both primary and secondary to the hepatic parenchyma, may cause focal intrahepatic biliary obstruction. Extrahepatic causes of biliary obstruction include both those extrinsic and those intrinsic to the bile duct. The most common cause is intrinsic obstruction related to choledocholithiasis. However, other intrinsic causes are neoplasia including cholangiocarcinoma, infectious etiologies, and inflammatory causes such as primary sclerosing cholangitis and HIV cholangiopathy. Extrinsic causes of extrahepatic biliary obstruction include neoplasm, commonly pancreatic adenocarcinoma, and inflammation secondary to pancreatitis. Additionally, metastatic lymphadenopathy in the porta hepatis may result in an extrinsic compression and secondary obstruction of the extrahepatic bile ducts.

Mirizzi syndrome is an uncommon cause of extrahepatic biliary obstruction. In this case a gallstone becomes lodged in the cystic duct and the inflammation surrounding this process creates a functional stricture of the common hepatic duct.

In patients with uncomplicated biliary obstruction, typical presentations include signs and symptoms of jaundice, dark urine, and pale stools. Icterus may also be seen, as well as pruritis. Depending on the underlying etiology, as well as the acuity of the obstruction, abdominal pain may be associated.

Imaging Findings

In cases of biliary obstruction, ultrasonography may identify evidence of biliary dilatation, although it may not be present in early obstruction. In some cases, the underlying etiology can be identified as an intraluminal filling defect or extrinsic mass such as in pancreatic neoplasia or pseudocysts secondary to pancreatitis.

In patients with nonspecific clinical presentation, CT may be initially acquired in cases of biliary obstruction. In cases of intrinsic causes of biliary obstruction, the intraductal filling defect may be identified, such as in the case of choledocholithiasis or neoplasm. In cases of Ascaris lumbricoides infection, the organisms themselves can be visualized as tubular intrahepatic filling defects causing the biliary obstruction. Inflammatory etiologies such as HIV cholangiopathy demonstrate concentric biliary ductal wall thickening resulting in a functional stricture. Similar findings are seen in primary sclerosing cholangitis with areas of beading affecting both intra- and extrahepatic bile ducts. Extrinsic causes of extrahepatic biliary obstruction, while they may be identified on ultrasonography, are typically readily identified on CT and MRI (Fig. 9-29).

In cases of Mirizzi syndrome, both ultrasound and CT may demonstrate the typical findings of an impacted stone within the cystic duct, which often demonstrates an abnormally low insertion into the common hepatic duct. Classification of Mirizzi syndrome is based on the absence (type I) or presence (types II–IV, depending on size) of a cholecystocholedochal fistula.

In patients with high clinical suspicion of biliary obstruction, MR cholangiopancreatography, or MRCP, is typically the initial noninvasive imaging examination. MRCP demonstrates intraluminal filling defects of choledocholithiasis as low-signal foci within surrounding hyperintense bile, as described above. As on CT, obstructing neoplasms, including cholangiocarcinoma or pancreatic, may be identified. Infectious and inflammatory causes of biliary obstruction are also well characterized, demonstrating findings similar to those on CT, including biliary ductal wall thickening and hyperenhancement during stages of active inflammation.

Urinary Obstruction

Nephrolithiasis is the most common cause of acute urinary tract obstruction. Other common causes of obstruction include prostatic enlargement in men by compression of the urethra and compression by gynecologic malignancies or the gravid uterus in women. Also, malignancies of the

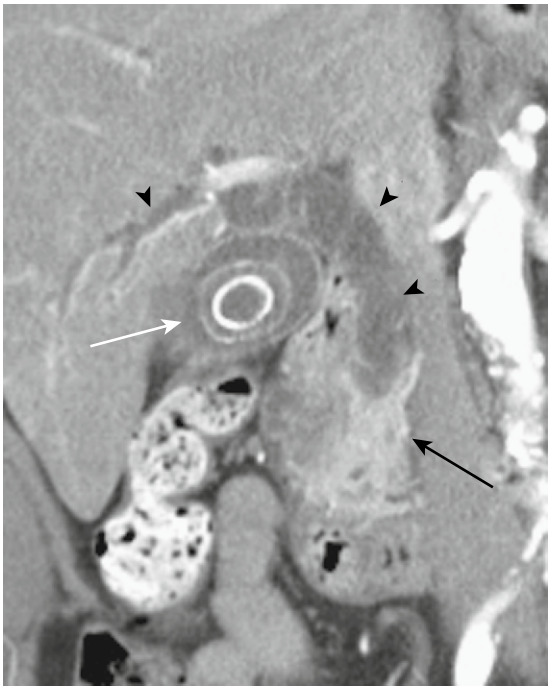


FIGURE 9-29. A 76-year-old female with biliary obstruction secondary to a cholangiocarcinoma. Coronal portal venous phase CT image demonstrates significant intra- and extrahepatic biliary dilatation *(arrowheads)* with abrupt narrowing secondary to a malignant stricture demonstrating enhancing thickened bile duct walls *(black arrow)*. Incidental note is made of a lamellated gallstone *(white arrow)*.

urothelium, most commonly transitional cell carcinoma, may obstruct the ureters when they occur within the bladder, obstructing the ureterovesical junction, or within the ureter itself. Retroperitoneal fibrosis may cause obstruction of the ureters, which are also typically displaced medially in this condition.

Patients with acute urinary obstruction often present with acute, often excruciating, abdominal pain referred to as renal colic. However, more chronic causes of urinary obstruction may be relatively pain free with presentations secondary to changes in urine output, possibly even anuria. Hematuria may be associated, depending on the underlying etiology. Also, patients with urinary obstruction may present with multiple urinary tract infections.

Imaging Findings

Ultrasound is typically employed as the initial imaging modality to diagnose acute urinary tract obstruction. In these cases, hydronephrosis, as evidenced by prominence of the collecting system and displacement of the renal sinus fat, may be identified on ultrasound. In some cases, ultrasound can directly demonstrate the cause of obstruction, especially when the cause is proximal, around the ureteropelvic junction or proximal ureter or within the pelvis, such as in the case of obstruction by benign prostatic hyperplasia or gynecologic malignancies. Also, given the acoustic window of the bladder, intraluminal bladder lesions causing obstruction are readily identified on ultrasound, as in the case of transitional cell carcinoma.

CT is often employed for further characterization in cases of urinary obstruction or in cases in which the cause of obstruction is not identified on the ultrasound examination. As noted, CT clearly identifies renal and ureteral calculi, the most common causes of acute urinary obstruction. Pelvic abnormalities including an enlarged prostate in males or gynecologic malignancies in females may be identified on CT. Retroperitoneal fibrosis, characterized by irregular soft tissue attenuation within the retroperitoneum, often surrounding or abutting the aorta and inferior vena cava, is readily seen on CT. The ureters, when involved, are typically medially displaced and demonstrate abnormal surrounding soft tissue attenuation. The bladder should be scrutinized for filling defects, including neoplasms, which may be identified on unenhanced CT images but are more readily seen if the bladder is distended with iodinated contrast.

CONCLUSION

Patients presenting with nontraumatic abdominal pain present a challenging diagnostic dilemma given the breadth of possible underlying diagnoses. However, the imaging workup may be tailored to the individual patient based on the signs and symptoms of the clinical presentation. There is often significant overlap in the clinical presentations of the various intra-abdominal pathologies, so imaging is crucial in clinical management decisions. With a thorough understanding of intra-abdominal pathology and the ability to triage among the various imaging modalities based on specific clinical concerns, the radiologist plays an integral role in the efficient, successful care of patients with acute abdominal pain.

SUGGESTED READINGS

Balthazar EJ: Acute pancreatitis: Assessment of severity with clinical and CT evaluation. Radiology 223:603–613, 2002.

Birnbaum BA, Balthazar EJ: CT of appendicitis and diverticulitis. Radiol Clin North Am 32:885–898, 1994.

Cho KC, Baker SR: Extraluminal air: Diagnosis and significance. Radiol Clin North Am 32:829–844, 1994.

Colistro R, Torreggiani WC, Lyburn ID, et al: Unenhanced helical CT in the investigation of acute flank pain. Clin Radiol 57:435–441, Review, 2002.

Craig WD, Wagner BJ, Travis MD: Pyelonephritis: Radiologic-pathologic review. Radiographics 28:255–277, 2008.

Espinoza R, Rodríguez A: Traumatic and nontraumatic perforation of hollow viscera. Surg Clin North Am 77:1291–1304, 1997.

Fidler J: MR imaging of the small bowel. Radiol Clin North Am 45:317–331, 2007.

Frager DH, Baer JW: Role of CT in evaluating patients with small-bowel obstruction. Semin Ultrasound CT MR 16:127–140, 1995.

Hoeffel C, Crema MD, Belkacem A, et al: Multi-detector row CT: Spectrum of diseases involving the ileocecal area. Radiographics 26:1373–1390, 2006.

Howarth DM: The role of nuclear medicine in the detection of acute gastrointestinal bleeding. Semin Nucl Med 36:133–146, 2006.

Laing CJ, Tobias T, Rosenblum DI, et al: Acute gastrointestinal bleeding: Emerging role of multidetector CT angiography and review of current imaging techniques. Radiographics 27:1055–1070, 2007.

Lucey BC, Varghese JC, Anderson SW, Soto JA: Spontaneous hemoperitoneum: A bloody mess. Emerg Radiol 14:65–75, 2007. Epub 2007 Mar 7.

Marincek B: Nontraumatic abdominal emergencies: Acute abdominal pain. Diagnostic strategies. Eur Radiol 12:2136–2150, 2002.

Mortelé KJ, Segatto E, Ros PR: The infected liver: Radiologic-pathologic correlation. Radiographics 24:937–955, 2004.

Watanabe Y, Nagayama M, Okumura A, et al: MR imaging of acute biliary disorders. Radiographics 27:477–495, 2007.

CHAPTER 10

Pelvic Emergencies

Brian C. Lucey

Many diseases that affect the abdomen may also extend to involve the pelvis. These are described in Chapter 9. In addition, trauma does not respect anatomic boundaries, and pelvic injuries following trauma are described in Chapter 3. This chapter covers conditions that are for the most part confined to the pelvis, and a great number of them are related to the genitourinary tract. Although there is some overlap, many of these disease entities are gender specific. In the male, these primarily consist of diseases of the testes and prostate and include testicular torsion, orchitis, epididymitis, maldescended testis, and prostatitis. In the female the entities primarily affect the ovaries and uterus and include ovarian cysts, endometriosis, ovarian torsion, tubo-ovarian abscess, and ectopic pregnancy. The most frequent presentation in the male is testicular pain and in the female either pelvic pain or dysfunctional uterine bleeding. The imaging modalities used to investigate these entities include sonography, computed tomography (CT), and magnetic resonance imaging (MRI); however, in the emergency room setting, sonography is the first-line modality of choice for many of these pelvic pathologies.

MALE DISORDERS

Testicular Torsion

The testis and epididymis attach to the inner scrotal wall by a broad attachment. When this attachment is too narrow, it may function as a pedicle around which the testis may twist. This twisting, or torsion, compromises the blood supply to the testis, which may lead to infarction of the testis. Acute scrotal pain is often the presenting complaint in males with testicular torsion, a condition that requires emergent treatment to maintain viability of the affected testis. Testicular salvage rates are greatest when surgery is performed within 6 hours of the onset of symptoms. After 24 hours the testis is usually no longer salvageable. Patients with the "bell clapper" deformity, where the tunica vaginalis joins high on the spermatic cord, are more prone to testicular torsion than the general population.

Sonography is the preferred imaging examination for the diagnosis of testicular torsion because of its high sensitivity and specificity. Gray-scale ultrasound findings are often completely normal when torsion is present, and the testes may appear symmetric with respect to both size and echogenicity. A small hydrocele may be present on the affected side. Within a few hours of the onset of symptoms, the scrotal wall will appear thickened, and the testis and epididymis will appear enlarged and hypoechoic secondary to inflammation and/or hemorrhage. Color Doppler is crucial for the diagnosis of torsion. The lack of demonstrable blood flow to the affected testis, assuming appropriate ultrasound settings are used, is virtually pathognomonic for torsion (Fig. 10-1). In prepubertal patients it is often difficult to demonstrate the presence of blood flow even in normal testes. Two potential false negative scenarios need to be considered when evaluating for torsion. First, a torsed testis may untwist spontaneously with resultant hyperemia on color Doppler, thus mistaking testicular torsion for epididymo-orchitis; and second, incomplete torsion may result in venous occlusion without arterial occlusion, which may result in arterial flow being detected in the testis despite torsion being present.

Testicular scintigraphy is often used as an adjunct to ultrasound when a diagnosis of torsion cannot be made with certainty. Given the added delay of scintigraphic examinations, however, some surgeons operate on the basis of an equivocal ultrasound. The treatment for testicular torsion is de-torsion of the affected testicle, and orchiopexy, where the testis is affixed to the scrotal wall to prevent torsion from recurring in the future.

Torsion of the Testicular Appendages

While there are four testicular appendages, only two are commonly visible at ultrasound: the appendix testis and appendix epididymis. These appendages are remnants of embryonic ducts and serve no real function. Because they are attached by a small pedicle, they are prone to torsion. Torsion of these appendages is one of the most common causes of acute scrotal pain in children. The appendix testis is more commonly affected than the appendix epididymis, although it is often difficult to identify the

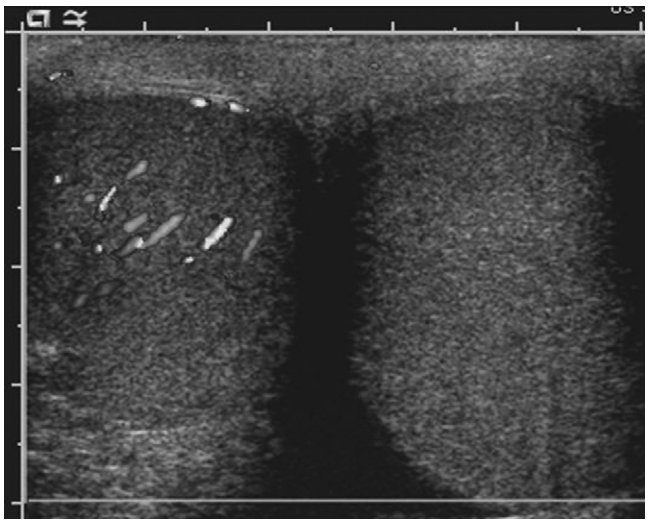


FIGURE 10-1. Sonographic image of a 19-year-old patient with testicular torsion. No flow is identified in the left testis.

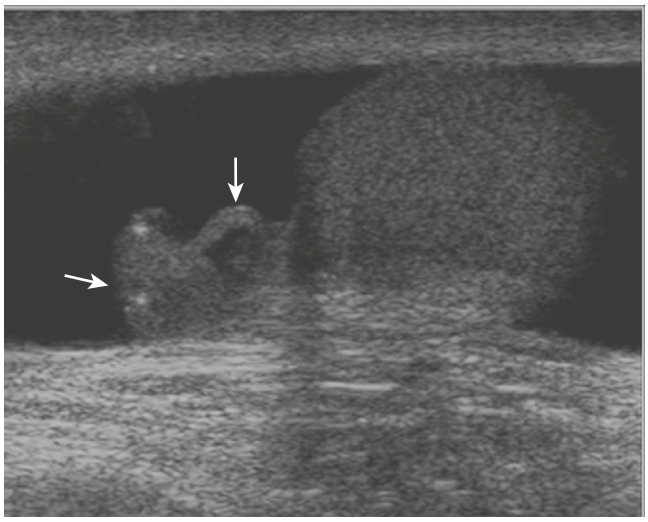


FIGURE 10-2. Sonographic image of the testis of a 9-year-old patient showing torsion of the testicular appendix. The *arrows* show an enlarged swollen appendix testis.

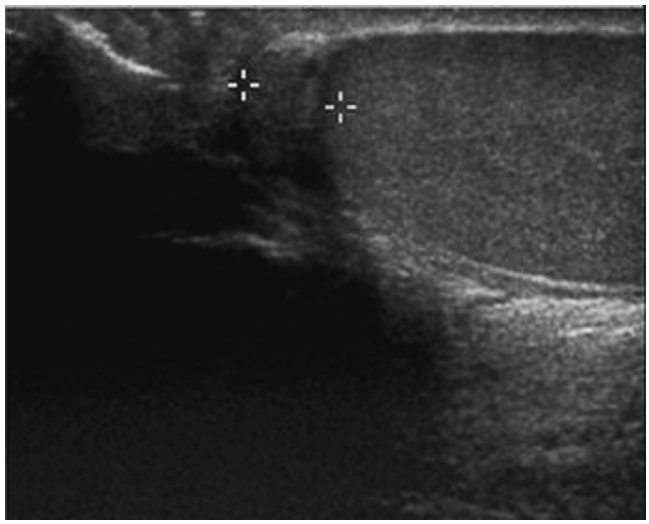


FIGURE 10-3. Sonographic image of a 32-year-old patient with acute epididymitis of the contralateral epididymis. The epididymis is swollen and shows increased vascularity with color Doppler.

offending appendage. Patients are usually young, prepubertal males who complain of acute onset scrotal pain. On clinical examination there may be a bluish discoloration of the skin at the site of pain, which is called the "blue dot" sign and is pathognomonic. At ultrasound the torsed appendix is often identified as a round, extratesticular, extraepididymal mass lacking color Doppler flow (Fig. 10-2). A reactive hydrocele may be present, as well as scrotal wall skin thickening.

Epididymitis and Orchitis

Epididymitis or epididymo-orchitis is an infection of the epididymis and/or testis and is a common cause of acute onset scrotal pain. Typically, scrotal pain associated with epididymitis or epididymo-orchitis is relieved when the testes are elevated over the symphysis pubis, a maneuver called the Prehn sign. In contradistinction, the pain associated with testicular torsion is not relieved by this maneuver. While the causative agent in epididymitis is usually not identified in young children, the infection usually originates in the prostate gland or bladder and spreads to the epididymis and testis via the vas deferens and spermatic cord lymphatics. A congenital anomaly of the urinary tract may be present. In adolescents the cause is most often a sexually transmitted infection.

Ultrasound examination of a patient with epididymitis demonstrates enlargement of the epididymis, primarily the head, with heterogeneous echotexture. On color Doppler evaluation there is increased blood flow to the epididymis and/or testis (Fig. 10-3). A reactive hydrocele may be an associated finding. When the entire testis is involved, it is often enlarged and has altered echogenicity. On gray-scale imaging findings alone, the appearance of the testis may mimic a diffusely infiltrative disease such as leukemia or lymphoma, although the clinical presentation should suggest the correct diagnosis. Untreated epididymo-orchitis may progress to scrotal abscess formation or may result in testicular infarction, which may lead to testicular atrophy. In patients with epididymo-orchitis, a follow-up sonogram performed 4 to 6 weeks following the initial event is advised in all cases to ensure complete resolution of the imaging findings following appropriate interval therapy. This is important in order to exclude an underlying tumor as the cause for the patient's symptoms. It is uncommon for a testicular tumor to present with acute scrotal pain; the accepted figure is less than 10% of tumors. It may occur and is usually due to acute hemorrhage or infarction of the testis that contains the tumor. Orchitis secondary to infection with mumps occurs in approximately 25% of patients that contract the disease. The sonographic findings include an enlarged hypoechoic testis, a small hydrocele, and sometimes thickening of the scrotal wall. Infertility may occasionally result following mumps orchitis. Severe scrotal infection may result in the rare condition called Fournier gangrene. This is a fulminant infectious process involving the scrotal wall and skin of the perineum that is in essence a fasciitis. The severe infection may result in gas formation along the fascial planes of the scrotal wall. Sonographic findings include the findings of epididymo-orchitis along with small echogenic ill-defined foci within the scrotal wall. These foci represent gas, and this finding requires urgent communication to the referring physician as surgical débridement may be required. In questionable cases, CT may be performed, which will clearly show the presence of any gas as hypoattenuating foci within the scrotal wall (Fig. 10-4).

Inguinal Scrotal Hernia

An uncommon cause of acute scrotal pain is incarceration of an inguinal hernia that extends into the scrotum. Indirect inguinal hernias are not uncommon; however, extension into the scrotal sac is rare. The clinical findings are usually obvious with a large swelling in the scrotum, although the mass may not be easily reduced. Sonographically, the appearance may be nonspecific with a heterogeneous mass identified in the scrotum. It is usually easy to identify the mass as separate from the testis, although following the mass along the inguinal canal may not be

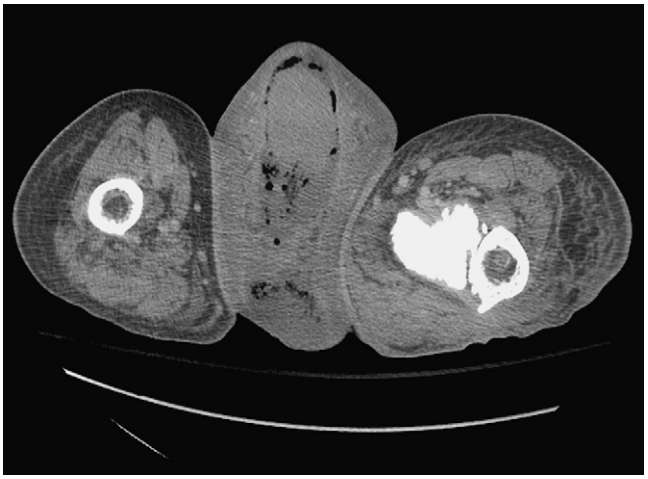


Figure 10-4. CT image of a 65-year-old male patient with Fournier gangrene. The image shows gas within the scrotum with a hydrocele and extensive subcutaneous edema.

easy. The presence of bowel may be detected if the two walls and lumen are clearly visible; however, it is not always clear that the mass represents bowel, and often the mass may merely be omental fat that has herniated into the scrotum. The presence of peristalsis may confirm the diagnosis. In cases where doubt exists, a CT scan could be performed, and this would show the hernia and its contents extending into the scrotum. Signs of incarceration on sonography include the absence of color flow on color Doppler evaluation. Although this may be easy to elicit in identifiable bowel wall, if the hernia consists of omental fat alone, it may be an unreliable sign. On CT, signs of incarceration include edema of the adjacent fat around the hernia, and possibly decreased enhancement of the bowel wall of any bowel loops that may be present in the hernia.

Testicular Trauma

Trauma to the testis may be either penetrating or blunt. Penetrating trauma to the testis, like many other locations, usually requires immediate surgical exploration. Blunt trauma to the testis in a hemodynamically stable patient should be evaluated with sonography. The key diagnosis to make following testicular trauma is the presence or absence of testicular rupture. A ruptured testicle requires immediate surgical repair, and early diagnosis is required to maximize the chances of testicular salvage. A ruptured testicle that is operated on within 72 hours of the trauma has a salvage rate approaching 80%, but this drops to 30% with subsequent delay. The sonographic findings suggesting testicular rupture include loss of clarity of the margins of the testis and abnormal morphology of the testis; on occasion, testicular parenchyma may be identified protruding beyond the testicular capsule. Sonographic findings seen following trauma to the testes that does not result in testicular rupture include altered echogenicity with loss of the normal homogeneity and alternating foci of either increased or decreased echogenicity. Depending on the degree of trauma, the heterogeneity may be focal or more generalized. A focal area of heterogeneity may be mistaken for epididymo-orchitis or even tumor, so an accurate history of testicular trauma is required to help differentiate from these conditions. Despite an accurate history, when focal heterogeneity is seen resulting from trauma, a follow-up scan is advised in 4 to 6 weeks to ensure complete resolution. As with many testicular conditions, a secondary hydrocele is commonly seen following trauma to the scrotum. This appears as a hypoechoic fluid collection within the scrotum. There may be an associated scrotal hematoma, which may also appear as a hypoechoic fluid collection when hyperacute. As this resolves, more complex elements may develop within the scrotum, and the presence of complex fluid in the scrotum following trauma represents resolving hematoma. The long-term sequelae of testicular trauma include complete or incomplete infarction with a resultant smaller testicle, chronic fibrosis, and even calcification.

Cryptorchidism

The arrest in the descent of the testis along its normal path is one of the most common disorders of the genitourinary tract. It occurs in up to 3% of term infants, although the majority of these will descend naturally over the first few months of life. Nearly four out of five maldescended testes in adults are located at or below the level of the inguinal canal. Although maldescended testes are associated with a host of congenital syndromes, this is not always the case and the condition may occur in isolation. The most damaging consequence of maldescended testes is infertility; infertility rates in unilateral maldescent are reported to be close to 20%, but this rises to 75% in cases where the maldescent is bilateral. There is a high rate of germ cell tumors in maldescended testes, and this risk extends to the contralateral descended testis as well. Maldescended testes are also at increased risk of both torsion and trauma and hence should be considered in any patient presenting with pelvic or scrotal pain in which both testes are not clearly palpable. Since the majority of maldescended testes are found in the inguinal canal, the testis may usually be identified by sonography. Maldescended testes appear as small, usually hypoechoic, rounded or oval structures along the line of the inguinal canal (Fig. 10-5). Care should be taken not



Figure 10-5. CT image of a 22-year-old patient with bilateral maldescended testes. These are seen as bilateral oval soft tissue masses in the inguinal canals.

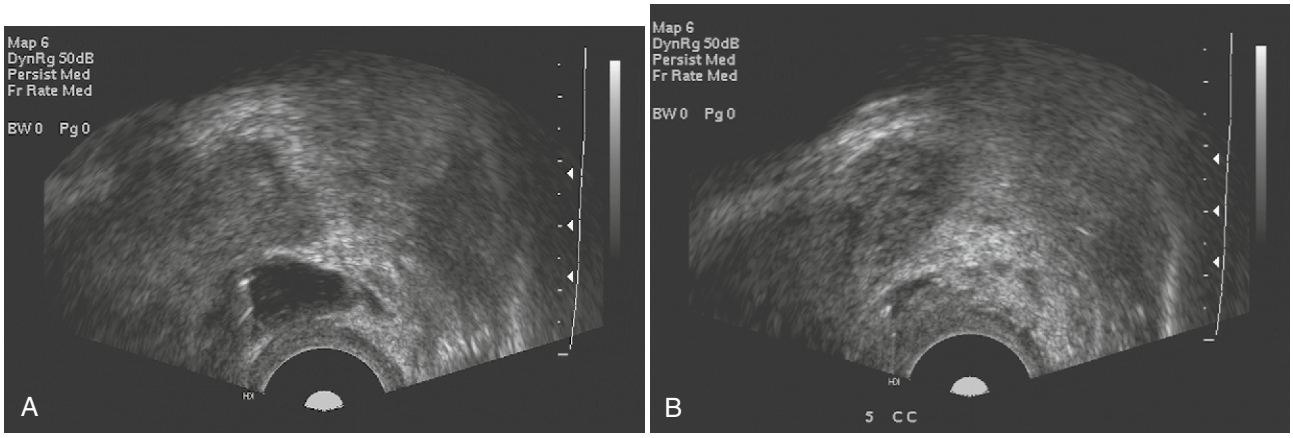


FIGURE 10-6. **A,** Transrectal sonographic image of a 68-year-old patient with a prostatic abscess. This is seen as an irregular hypoechoic collection. **B,** Transrectal sonographic image of the prostate following transrectal drainage of the abscess. The echogenic needle may be seen.

to confuse the small testis with a lymph node. Any focal areas of heterogeneity within the testis could represent malignant degeneration. The sensitivity of sonography for detecting maldescended testis varies between 75% and 97% and depends on whether the testis is palpable or not. Once the maldescended testis lies higher than the inguinal canal, it becomes difficult for sonography to locate it. Other imaging modalities that may be used to locate the testis include CT and MR. With multidetector CT, the small soft tissue mass of the maldescended testis is usually identifiable, a situation that was not always the case in the era of large slice thickness CT. T2-weighted MR imaging may be useful to locate the high signal testis, which may be best identified using coronal plane imaging along the plane of the gonadal vessels.

Prostatitis

Acute prostatitis is, in essence, a clinical diagnosis, and imaging is rarely required to make the diagnosis. It is most commonly caused by recent instrumentation or surgery; however, infection may also spread from the urinary tract. Untreated or inadequately treated prostatitis may lead to prostate abscess formation. Performing transrectal sonography in patients with acute prostatitis may help to make the diagnosis even before imaging, as the passage of the probe may be exquisitely painful. The sonographic appearance of acute prostatitis is primarily of a heterogeneous prostate gland that may show focal areas of hypoechogenicity with demonstrable increased vascularity usually within the peripheral zone. In severe cases, the hypoechogenicity may be more diffuse and the increased vascularity may be seen throughout the gland. Chronic prostatitis usually appears as bands of increased echogenicity representing areas of fibrosis. There is usually little evidence of increased vascularity. Prostatic abscess appears as a well-defined walled collection that contains hypoechoic fluid (Fig. 10-6). The fluid is usually somewhat complex with foci of increased echogenicity within it as well. Gas present in the abscess is seen as irregular foci of increased echogenicity with so-called "dirty" shadowing behind it.

FEMALE DISORDERS

Pelvic conditions that affect women who present to the emergency room may be divided into those causing pelvic pain and those causing dysfunctional uterine bleeding. Conditions causing pelvic pain include ovarian cyst with rupture, endometriosis, tubo-ovarian abscess, and ovarian torsion. Causes of dysfunctional uterine bleeding include spontaneous abortion, endometrial polyp, endometrial hyperplasia, and endometrial cancer. Ectopic pregnancy may present with a combination of these symptoms. Congenital uterine anomalies and cystic lesions of the lower genitourinary tract may be symptomatic but are more commonly incidental findings. The imaging appearance of these are described in the Requisites Series book on ultrasound.

Human chorionic gonadotropin (HCG) results are critical for the accurate interpretation of a pelvic ultrasound examination in a sexually active female with complaints of pelvic pain. Pregnancy status alters the potential diagnosis in many cases, and patients presenting with pelvic pain with or without bleeding with a positive pregnancy test and an empty uterus should be considered to have an ectopic pregnancy until otherwise proven. Sonography is the imaging modality of choice in the evaluation of pelvic pain and dysfunctional bleeding. MR is a favored complementary modality, although with the proliferation of CT imaging in the emergency room setting, particularly in patients presenting with abdominal pain, radiologists are seeing conditions on CT imaging with increasing frequency that once were the preserve of sonography. It is important to recognize these entities for what they are using CT.

Hemorrhagic Ovarian Cyst

Although hemorrhagic ovarian cysts are common, their imaging appearance is widely variable. Hemorrhagic cysts develop at the time of ovulation when vessels surrounding a corpus luteal cyst rupture, giving rise to hemorrhage within the corpus luteum. As the cyst evolves over time, the sonographic features change with the stage of clot retraction. Patients may present with acute onset adnexal pain, which can be severe.

Physiologic ovarian follicles measure less than 3.0 cm in diameter. Most hemorrhagic cysts measure 3.0 to 3.5 cm in diameter, have a thin outer wall, and demonstrate posterior acoustic through-transmission. Fine, reticular septations resembling a fishnet pattern are a common finding at ultrasound. These septations represent fibrin strands, which contain no blood flow. In some patients the hemorrhagic cyst contains retracting clot. While a large portion of the cyst appears anechoic, the retracting clot appears as an adherent, echogenic structure within the cyst that contains no blood flow. In rare cases, when the clot becomes very small it can simulate a mural nodule and raise concern for ovarian neoplasm. Fluid–fluid or fluid–debris levels can also be demonstrated within a hemorrhagic cyst. Hemorrhagic cysts can be complicated by rupture, with free spill of hemorrhagic contents into the pelvis. When this occurs, echogenic fluid will be demonstrated within the pelvis surrounding the uterus and adnexa. In some cases, the hemoperitoneum may be massive. Although the sonographic features are well described, given that many patients with a ruptured hemorrhagic cyst present with pelvic pain, in the emergency room setting this is often interpreted as abdominal pain, and CT imaging may be the first modality used. We are seeing CT imaging of ovarian cysts, hemorrhagic cysts (Fig. 10-7), and ruptured cysts (Fig. 10-8) with increasing frequency. The normal ovaries may be difficult to identify on CT imaging, and identification often depends on hormonal status. When the ovaries are larger, as in younger women of childbearing age, they are more likely to be identified. Similarly, in patients with little pelvic fat, the ovaries may be difficult to distinguish from loops of unopacified bowel in the pelvis. Often the position of the ovaries is assumed and the usual location is either side of the uterus along the margin of the round ligament. In young patients with malignancy that requires pelvic radiation therapy, the ovaries are frequently surgically sutured to the superolateral aspect of the pelvic wall. This is done to move the ovaries out of the path of the treating radiotherapy beam. In these cases, the ovaries appear as solid masses with cystic components located superiorly and laterally to their usual position. These masses should not be mistaken for pathology, particularly tumor, and knowledge of the prior pexy procedure is useful to avoid confusion. The findings of a simple ovarian cyst are similar to those of a cyst elsewhere, namely, a well-defined round or oval mass in the location of the ovary with an imperceptible wall and containing simple fluid with Hounsfield unit (HU) values of 10 or less. A hemorrhagic cyst might be identified as a mass similar to a simple cyst, but there may be an irregular enhancing ring seen within the cyst, which represents the enhancing involuting wall of the cyst. The CT findings of a ruptured cyst are more variable. Often the cyst itself can no longer be identified because the contents have spilled into the peritoneal cavity. What may be seen is free fluid in the cul-de-sac or even in the location of one of the adnexa. This fluid is frequently of slightly higher attenuation than simple fluid and may have an HU value of 60 to 80. This represents the blood from the ruptured cyst. Active extravasation may occasionally be seen as a line of high density representing administered intravenous contrast being lost into the peritoneal cavity.



Figure 10-8. CT image of a 27-year-old patient with a ruptured hemorrhagic cyst. The active bleeding into the peritoneum is seen as an irregular focus of high attenuation in the left adnexa.



Figure 10-7. CT image of a 32-year-old patient with a hemorrhagic ovarian cyst. The linear high-attenuation foci in the right adnexa represents the blood.

Ovarian Torsion

Acute onset of adnexal pain in a female is concerning for ovarian torsion. The Fallopian tubes are relatively long in children and the ovaries are hypermobile, which increases their susceptibility to torsion. Although normal ovaries may torse, most often there is an ovarian or paraovarian cyst or mass that predisposes the ovary to torsion by functioning as a fulcrum around which the ovary can twist. The ovary becomes twisted around its pedicle, leading to various degrees of hemorrhagic infarction. If surgery is not performed expeditiously, future fertility and hormonal regulation may be compromised. There is a slight predilection for torsion to involve the right ovary. When the right ovary is affected, the diagnosis is more difficult to establish given the number of other conditions that present with right lower quadrant or pelvic pain such as appendicitis, Meckel's diverticulitis, and inflammatory bowel disease. The median age of patients with ovarian torsion is 11 years old.

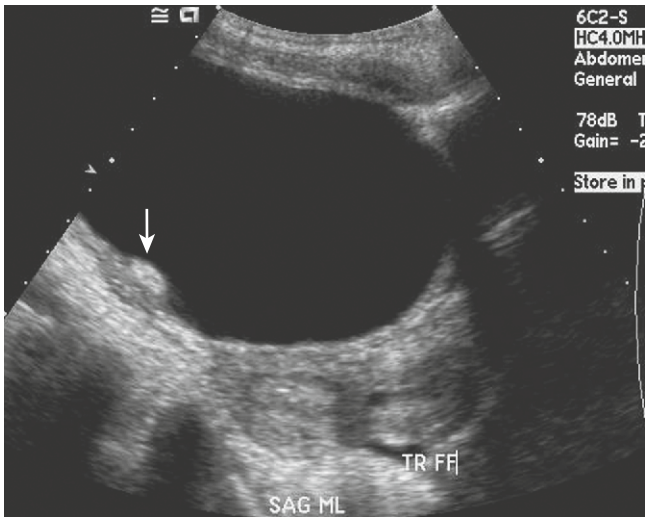


FIGURE 10-9. Sonographic image of a 48-year-old patient with a cystic ovarian mass that underwent torsion. The solid mural nodule is identified by the white arrow.

Pelvic ultrasound is the study of choice for evaluation of ovarian torsion. Normal ovaries often appear hypoechoic relative to the adjacent pelvic tissue and have an ovoid or ellipsoid shape. Microcystic follicles are routinely identified in normal ovaries. When the ovaries demonstrate normal gray-scale imaging characteristics and have a normal size and shape, color Doppler evaluation is usually not necessary. If, however, one ovary appears abnormally large relative to the other side, torsion may be present. In nearly all cases of ovarian torsion, the affected ovary is massively enlarged and has a round or globular configuration. In neonates and young girls ovarian torsion is commonly seen as a large cystic mass with fluid–debris levels. In young or adolescent girls the more classic imaging appearance is an enlarged, echogenic ovary with multiple enlarged peripheral follicles. In other cases, the ovary may appear as a complex cystic mass secondary to the presence of an underlying cyst or tumor (Fig. 10-9). Color Doppler evaluation of the ovary often reveals an absence of blood flow, a finding classically associated with ovarian torsion. However, torsion may be present even if arterial waveforms are demonstrated because the ovary has a dual blood supply (from both the uterine and ovarian arteries). The presence of arterial waveforms within the ovary should not sway the diagnosis away from ovarian torsion if the gray-scale imaging findings and physical examination are consistent with torsion.

Endometriosis

Endometriosis is a condition defined as the presence of endometrial tissue outside of the uterus. The condition may be localized or widespread. Widespread endometriosis may result in extensive endometrial implants throughout the abdomen and pelvis and the diagnosis may be extremely difficult to make. Sonography is of limited value in making this diagnosis, and CT and MR too have both poor sensitivity and poor specificity for making the diagnosis. All three imaging modalities, however, are useful in identifying localized disease. The most frequently encountered presentation of endometriosis is a single or multiple small adnexal masses called endometriomas. These have been referred to as "chocolate cysts" in the past. Patients may present with acute pelvic pain. Sonography is the normal first-line imaging modality, and the sonographic findings are usually diagnostic. On sonography, an endometrioma appears as a complex cystic mass in the adnexa that lies outside of the ovary. The mass is well defined and contains homogeneous low-level echoes throughout the mass. Endometriomas range in size from 1 cm to more than 15 cm, although the vast majority lie in the 3 to 6 cm range. Rarely, a thin septation may be identified within the endometrioma. The sonographic features are classic, although the potential differential diagnosis includes a hemorrhagic cyst and, rarely, an ovarian neoplasm in cases in which the classic features are not easily identified. On CT imaging, an endometrioma appears as a well-defined cystic mass that has a uniform HU value greater than that of a simple cyst, usually lying in the range of 30 to 60 HU. On MR imaging, endometriomas show high signal on T1-weighted imaging with classic "shading" appearance on T2-weighted imaging. The "shading" appearance is a progressive change from high signal at one side of the mass to low signal on the opposite side with varying levels of intermediate signal between them. This pattern of signal intensity is caused by the high level of iron within the endometrioma. Both CT and MR may show evidence of the complications of long-standing endometriosis, which include obstruction to either the ureter or bowel. Endometriosis should be considered in unusual cases of ureteric or bowel obstruction of unknown etiology in females of childbearing age presenting through the emergency room.

Disorders of the Fallopian Tubes

Disorders of the Fallopian tubes include hydrosalpinx, pyosalpinx, and tubo-ovarian abscess. Hydrosalpinx is seldom an acute condition and is most frequently an incidental finding. It results from occlusion of the Fallopian tube and is often bilateral. The most common etiology, infection, often follows instrumentation. The obstruction leads to dilatation of the Fallopian tube, which becomes filled with serous fluid. Although hydrosalpinx can present with acute pelvic pain, the condition may remain asymptomatic; however, long-term consequences include infertility. Sonographic findings are usually characteristic, and a dilated tubular cystic structure with anechoic fluid within is usually found. When a hydrosalpinx becomes secondarily infected the condition is known as pyosalpinx. This presents as acute pelvic pain with the signs and symptoms of acute infection including elevated fever and white cell count. The fluid within the Fallopian tube will no longer be anechoic on sonography, indicating the presence of pus within the tube (Fig. 10-10). Aggressive antibiotic therapy is indicated, but when the tube is extremely distended, percutaneous or transvaginal drainage may be required. A condition that overlaps pyosalpinx and one that occurs more frequently is tubo-ovarian abscess formation. This in essence has a similar etiology to pyosalpinx in that the most common cause is a sexually transmitted disease. The infection travels along the Fallopian tube and results in an

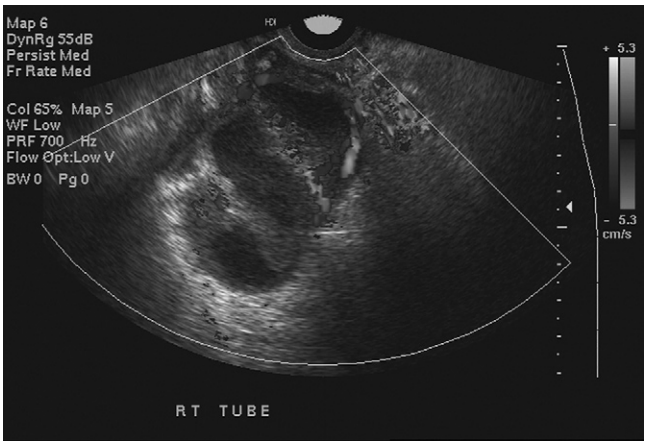


Figure 10-10. Sonographic image of a 38-year-old patient with pyosalpynx. The tubular nature of the hypoechoic lesion may be appreciated. The hypoechoic fluid contains multiple low-level echoes indicating that this is not a hydrosalpynx.

abscess forming in the adnexa. The clinical presentation usually leads to the diagnosis being suspected. Sonography is again the imaging modality of choice. A complex mass may be identified in the adnexa, and the mass may be shown to lie outside of the ovary. On transvaginal sonography, gentle pressure placed directly over this mass will be exquisitely painful. This may help to confirm the diagnosis, as other causes of complex adnexal masses tend not to cause such discomfort. As with other pelvic pathologies, the presentation may be interpreted as abdominal pain, rather than pelvic pain, and CT may be the first-line imaging modality used. In this case, a tubo-ovarian abscess may be seen as a pelvic abscess with thick walls and may contain fluid and/or solid components (Fig. 10-11). The presence of a dilated tubular structure on the ipsilateral side representing a hydro- or pyosalpinx may help to distinguish this abscess as a TOA rather than an appendiceal or diverticular abscess.

Endometritis

Endometritis is defined as inflammation of the endometrium and may be acute or chronic. Endometritis may extend to involve the myometrium or even the parametrium. The most common cause is infection. Most causative agents are *Staphylococcus* or *Streptococcus*, and it usually occurs following instrumentation such as delivery or abortion. The clinical presentation is typically with fever and purulent vaginal discharge and may be associated with vague lower abdominal pain. Chronic endometritis is usually the result of *Chlamydia*, tuberculosis, or chronic pelvic inflammatory disease, and this usually presents as a bloody discharge. The presence of pus within the endometrial canal is called pyometra.

From an imaging perspective, given that lower abdominal pain or pelvic pain is a frequent cause for presenting to the emergency room, sonography is usually the imaging modality first used. The sonographic appearance of acute endometritis may be normal in the early stages. The endometrium may also appear as thickened and heterogeneous, and hypoechoic fluid may be identified in the endometrial canal. Gas is occasionally present and can be identified on sonography as hyperechoic foci with "dirty" posterior shadowing. Given that endometritis is frequently seen in the presence of retained products of conception, signs of this may also be present. These include the presence of a hematoma seen as a heterogeneous intrauterine mass with debris and fluid. Increased vascularity may occasionally be seen with endometritis, although this is an inconsistent finding.

CT may also be the first-line imaging modality used depending on what symptoms the patient presents with. If the gynecologic symptoms of discharge and pelvic pain predominate, sonography will likely be initially requested. If the pain predominates as a symptom and there is a suggestion of abdominal pain rather than pelvic pain, then CT may be requested first. The findings of endometritis on CT are somewhat nonspecific. These include the presence of fluid within the endometrial canal. The canal may

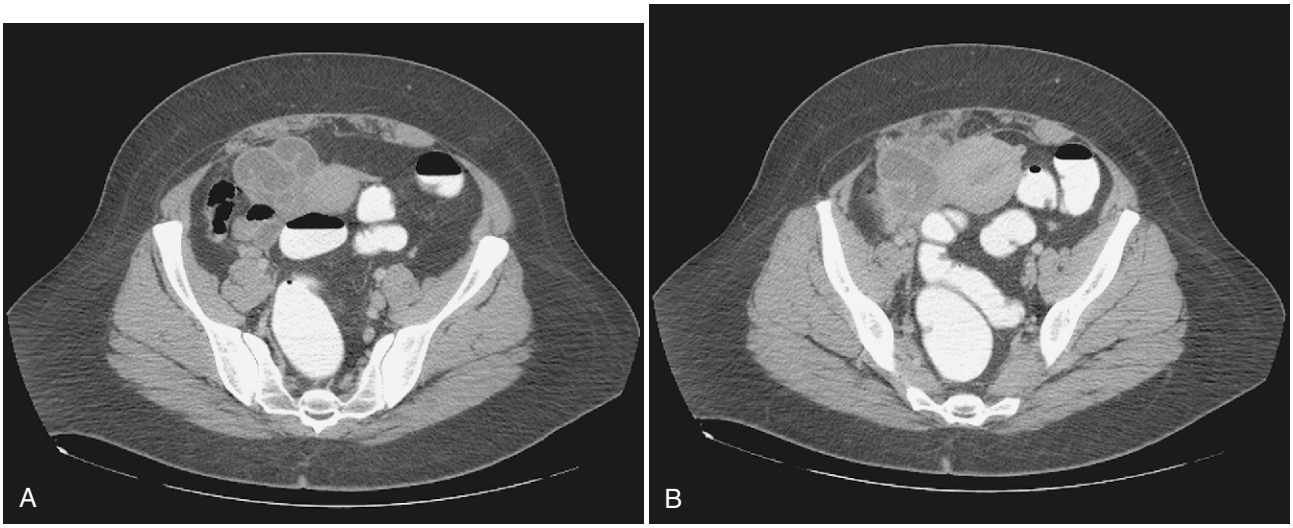


Figure 10-11. A, CT image of a 27-year-old patient with a pyosalpynx. The tubular nature of the lesion in the right adnexa may be appreciated. **B,** Another CT image of the same patient. There are some inflammatory changes in the fat adjacent to the Fallopian tube. This pyosalpynx has progressed to form a tubo-ovarian abscess.

be widened due to the presence of fluid, hematoma, and debris. This might be less easy to appreciate on conventional axial imaging but easier when reviewing the images in the sagittal plane. Gas is also identified on occasion, seen on the CT as tiny black bubbles within the endometrial canal. When endometritis is diagnosed on imaging, care should be taken to exclude further foci of inflammation or infection such as salpingitis or oophritis, as these are common associations of endometritis.

Ectopic Pregnancy

Ectopic pregnancy is a common condition that may result in death if not adequately diagnosed and treated; as such, missing the diagnosis is a far greater sin than making a false positive diagnosis. Ectopic pregnancy is responsible for up to 15% of maternal deaths. By definition, any female patient with a positive pregnancy test and an empty uterus should be regarded as having an ectopic pregnancy until otherwise proven. It is not always possible to identify the ectopic pregnancy directly, and not identifying this should never be taken as evidence that the patient does not have an ectopic pregnancy. Ectopic pregnancy usually presents with pelvic pain and may well be associated with bleeding. On imaging, the best way to determine that an ectopic pregnancy is not present is to identify an appropriately positioned gestational sac. In cases with ectopic pregnancy, the sloughing of the decidua may result in the appearance of a pseudogestational sac. This can be differentiated from a gestational sac as a fluid collection within the endometrial canal surrounded by a single decidual layer, unlike the gestational sac, which appears as a fluid collection within the decidua that abuts the endometrium or as concentric rings, the so-called "double decidual" sign. The most specific sonographic sign confirming ectopic pregnancy is the identification of a live embryo that lies outside the uterus, usually in the adnexa (Fig. 10-12). This sign is positively identified in only approximately 20% to 25% of cases of ectopic pregnancy and therefore cannot be relied on to make the diagnosis. A nonspecific complex adnexal mass in a patient with a positive pregnancy test is strong evidence to support the presence of an ectopic pregnancy. Complex free fluid in the pelvis is also a good indicator in the correct clinical setting (Fig. 10-13). The presence of an adnexal mass in association with complex free fluid has a sensitivity of close to 40% but a specificity of 99% for the detection of an ectopic pregnancy. It is important to remember that up to one third of patients with an ectopic pregnancy may have a completely normal sonogram. Hence the importance of the mantra "positive pregnancy test with an empty uterus equals ectopic pregnancy until proven otherwise."

Another condition that may present with pelvic pain associated with bleeding is early pregnancy failure. This may be characterized by a positive pregnancy test with no demonstrable intrauterine pregnancy and hence may have an appearance similar to ectopic pregnancy. There will usually be fluid within the endometrial canal with perhaps a gestational sac present. The gestational sac will be abnormal and may be enlarged, with no evidence of a developing fetus within it. In cases in which it is not easy to distinguish between early loss of pregnancy and ectopic pregnancy, the key is to monitor the level of HCG. This will continue to rise in patients with an ectopic pregnancy but will start to fall if the pregnancy fails.

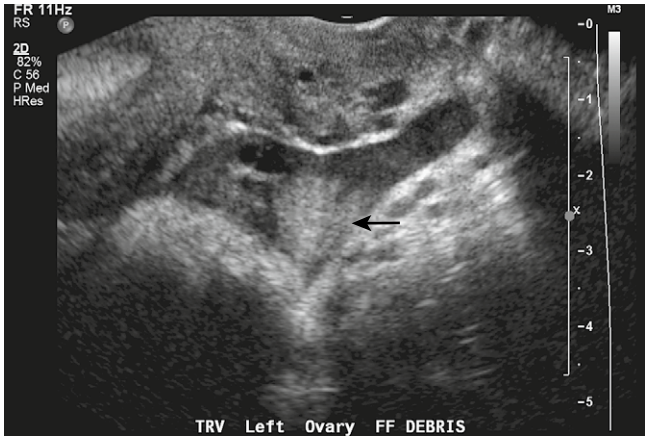


FIGURE 10-12. Sonographic image of a 23-year-old patient with a ruptured ectopic pregnancy. The free fluid containing echogenic debris representing blood is seen in the cul-de-sac *(arrow)*.

Postpartum Bleeding

Patients with postpartum bleeding often first present to the emergency room. The most common cause of postpartum bleeding is retained products of conception (RPOC). It is important to differentiate RPOC from the presence of a simple hematoma within the endometrial canal. Both conditions have similar sonographic appearances, characterized by the presence of a heterogeneous, predominantly echogenic mass located within the endometrial cavity. The most specific sonographic sign that may distinguish these two entities is the presence of vascularity in the RPOC with demonstrable blood flow when using color Doppler. Simple hematoma will not have any blood flow within it. It may not be possible to separate these entities using CT imaging alone, as the hematoma will be of high attenuation in the acute setting just as RPOC will appear as a high-density focus within the uterus. CT is unlikely to be sensitive enough to detect the attenuation difference with the small degree of vascular enhancement that is present with RPOC. It is important to attempt to differentiate these entities when the patient presents to the emergency room, as the management is considerably different. The presence of a hematoma within the endometrial cavity may often be treated conservatively and will frequently resolve spontaneously. RPOC, on the other hand, usually requires evacuation of the endometrial cavity to arrest the bleeding and permit normal uterine contraction.

Ovarian Vein Thrombosis

Ovarian vein thrombosis is a relatively uncommon condition being diagnosed in up to 0.2% of deliveries. It is unilateral in approximately 85% of cases with a right to left predominance of 12:1. It may also result from pelvic inflammatory disease, malignancy, or pelvic surgery. There is morbidity associated not only with the thrombosis but also with any superimposed infection resulting in septic

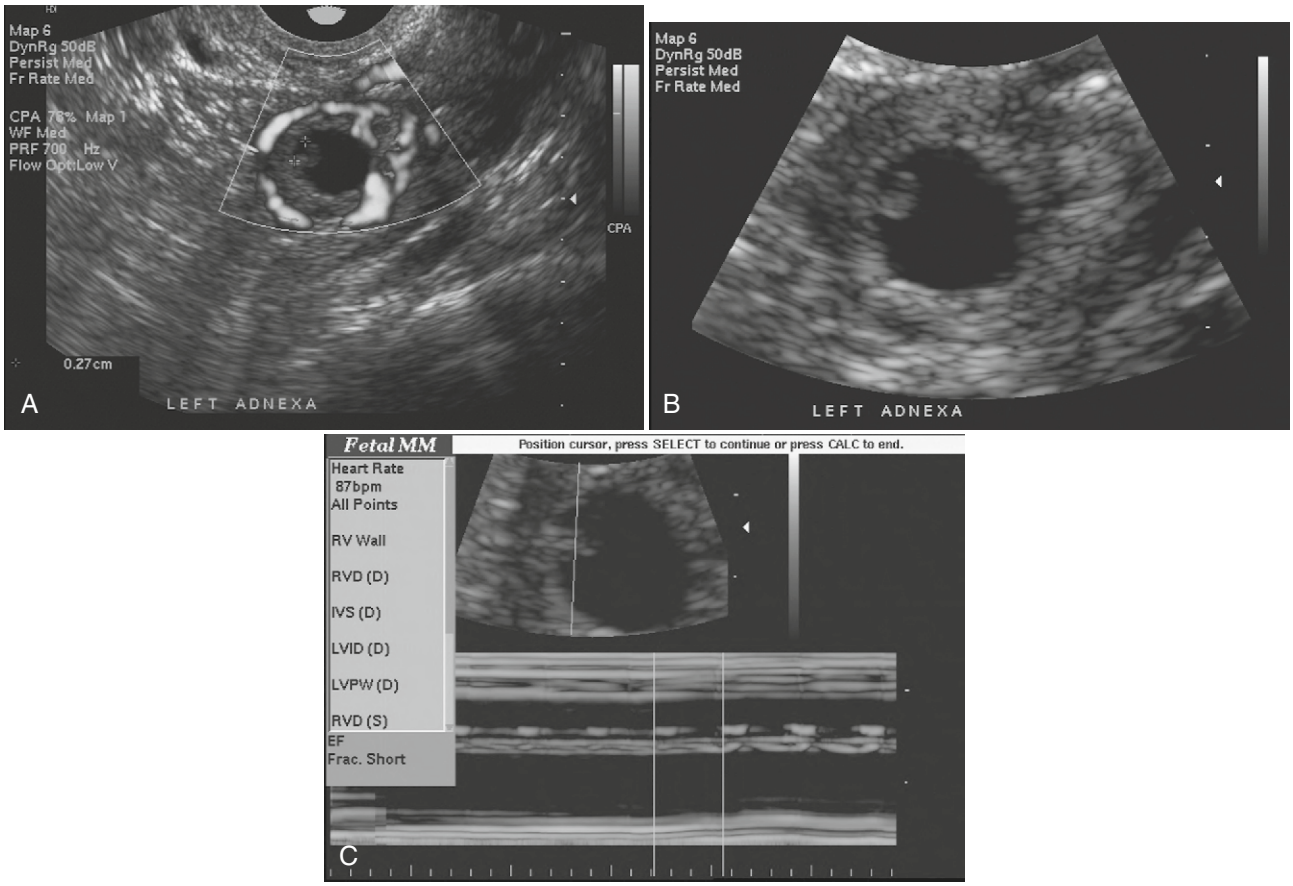


Figure 10-13. **A,** Sonographic image of a 27-year-old patient showing an ectopic pregnancy located in the left adnexa. The classic "ring of fire" is well shown. **B,** Further image of the same patient shows an ectopic pregnancy with a clearly identifiable yolk sac. **C,** Another image from the same patient showing a documented fetal heartbeat with the ectopic pregnancy.

thrombophlebitis. The thrombus may propagate to involve the inferior vena cava or renal veins and may result in pulmonary embolus. The clinical presentation is of pelvic pain and fever. The imaging modalities that may be used to make the diagnosis are sonography, CT, and MRI. The modality that is first used very much depends on how the patient presents and the degree of suspicion for the diagnosis. Ovarian vein thrombosis is often unsuspected at the time of diagnosis, so the onus is very much on the radiologist to suspect and make the diagnosis, particularly when imaging a postpartum patient with either fever or pain.

The diagnosis of ovarian vein thrombosis by sonography is often limited by the presence of overlying bowel gas. The characteristic finding is that of a tubular hypoechoic structure extending from the adnexa cranially. No blood flow may be identified within this structure when interrogated with color Doppler. There may be associated enlargement of the ovary on the affected side, although frequently it is difficult to be certain of this. It may be difficult to definitively discern ovarian vein thrombosis from hydronephrosis or thrombosis of the inferior mesenteric vein. CT is the most likely imaging modality to be used in the emergency room, particularly if the patient presents with fever and abdominal pain. Appendicitis is frequently the suspected diagnosis. The CT findings that make the diagnosis are the identification of an enlarged ovarian vein that contains either occlusive or nonocclusive thrombus (Fig. 10-14). This may be identified as a focus of hypoattenuation within the enhancing vein or as an abruptly occluded vessel that is dilated distally. There is usually some nonspecific stranding of the fat adjacent to the vessel resulting from the thrombosis. This may be exuberant if there is superimposed infection resulting in septic thrombophlebitis (Fig. 10-15).

Dysfunctional Uterine Bleeding

There are a number of conditions that result in dysfunctional uterine bleeding (DUB). The most common entities include submucosal fibroid, endometrial polyp, endometrial hyperplasia, and endometrial carcinoma. Fibroids are a ubiquitous finding on sonographic imaging of the uterus. A small number of fibroids may be located in the submucosa with greater than 50% of their circumference projecting into the endometrial canal. These submucosal fibroids are usually asymptomatic but may cause pelvic pain or DUB. Defining a fibroid as submucosal on sonography alone is not always easy, and hysterosonography may be required. Similarly, endometrial polyps may be difficult to identify on sonography alone, and hysterosonography may also be required. On sonography, the presence of a polyp is often suspected by the presence of an abnormal-appearing endometrial stripe. The heterogeneous polyp

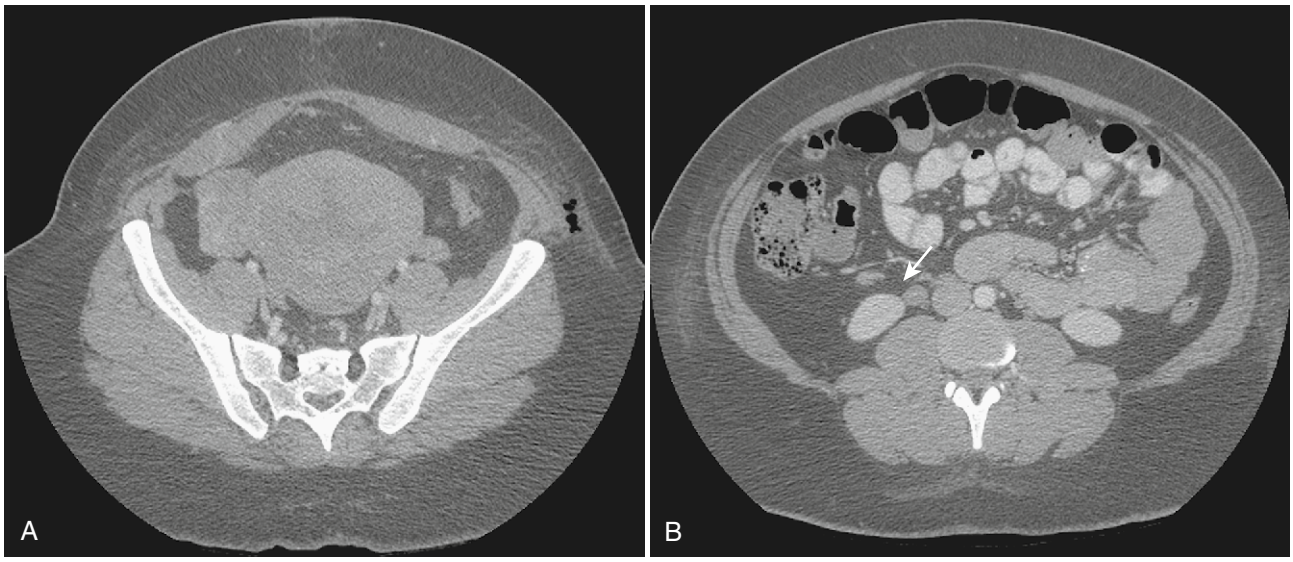


FIGURE 10-14. **A,** CT image of a 34-year-old postpartum patient, showing a large mass in the right adnexa representing a dilated ovary secondary to gonadal vein thrombosis. **B,** CT image shows a dilated thrombosed right gonadal vein *(arrow)*.

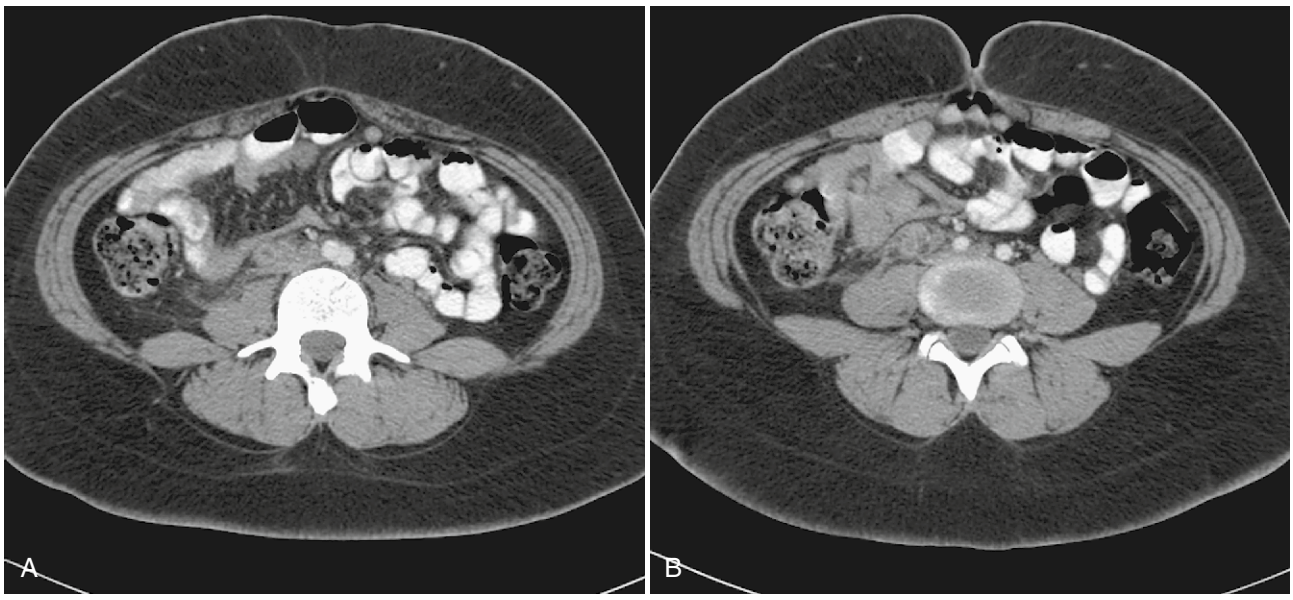


FIGURE 10-15. **A** and **B,** CT images of a 29-year-old patient showing a distended right ovarian vein. The vessel has an enhancing wall and contains thrombus. Inflammatory changes are identified around the vessel, better seen in B. This represents septic thrombophlebitis.

may be indistinguishable from the endometrial stripe, and the appearances may suggest abnormal enlargement of the stripe. Instilling saline into the endometrial canal for the hysterosonogram clearly distinguishes the polyp from the endometrium. Endometrial hyperplasia and more rarely endometrial carcinoma may also present with DUB. Both of these entities will appear as irregular thickening of the endometrial stripe with carcinoma having a more aggressive and extensive appearance. Again, with hysterosonography, these entities are usually clearly distinguished and may certainly be distinguished from submucosal fibroid or polyp.

CONCLUSION

Sonography is the mainstay imaging modality for much pelvic pathology in both male and female patients and is often used to make a definitive diagnosis. In the male, sonography should be used for imaging the testes, scrotum, and prostate. In the female patient, sonography is the preferred imaging modality for gynecologic pathology. Given that many such pathologies present with abdominal pain, however, in today's climate, CT imaging may be the modality first used. It is becoming increasingly important to be able to recognize the CT findings of many of the

conditions traditionally imaged using sonography. MR has a large role to play, particularly in the imaging of gynecologic pathology; however, in the emergency room setting, this is seldom the imaging modality first used. MR is more frequently used as a further tool for more complete evaluation of the patient, either following admission or on an outpatient basis, rather than from the emergency room. The role of MR from the emergency room may well increase over time as more emergency rooms acquire magnets for the exclusive use of the emergency room.

Suggested Readings

Bennett GL, Slywotzky CM, Giovanniello G: Gynecologic causes of acute pelvic pain: Spectrum of CT findings. Radiographics 22:785–801, 2002.

Bignardi T, Alhamdan D, Condous G: Is ultrasound the new gold standard for the diagnosis of ectopic pregnancy? Semin Ultrasound CT MR 29:114–120, 2008.

Gjelsteen AC, Ching BH, Meyermann MW, et al: CT, MRI, PET, PET/CT, and ultrasound in the evaluation of obstetric and gynecologic patients. Surg Clin North Am 88:361–390, vii, 2008.

Guichard G, El Ammari J, Del Coro C, et al: Accuracy of ultrasonography in diagnosis of testicular rupture after blunt scrotal trauma. Urology 71:52–56, 2008.

Kalish GM, Patel MD, Gunn ML, Dubinsky TJ: Computed tomographic and magnetic resonance features of gynecologic abnormalities in women presenting with acute or chronic abdominal pain. Ultrasound Q 23:167–175, 2007.

Lambert MJ, Villa M: Gynecologic ultrasound in emergency medicine. Emerg Med Clin North Am 22:683–696, 2004.

Lee JC, Bhatt S, Dogra VS: Imaging of the epididymis. Ultrasound Q 24:3–16, 2008.

Lin EP, Bhatt S, Rubens DJ, Dogra VS: Testicular torsion: Twists and turns. Semin Ultrasound CT MR 28:317–328, 2007.

Pearl MS, Hill MC: Ultrasound of the scrotum. Semin Ultrasound CT MR 28: 225–248, 2007.

Umeoka S, Koyama T, Togashi K, et al: Vascular dilatation in the pelvis: Identification with CT and MR imaging. Radiographics 24:193–208, 2004.

Van Dyck P, Vanhoenacker P, Goris H, D'Haenens P: Puerperal ovarian vein thrombophlebitis. JBR-BTR 85:168–169, 2002.

CHAPTER 11

Vascular Emergencies

Felipe Munera, Carlos A. Anaya, and Ana Maria Gomez

The term *vascular emergency* carries a critical sense of urgency when you consider that the integrity of the vascular system is crucial to maintain the vital blood supply to the various organ systems. Consequently, certain clinical scenarios demand immediate action to determine whether a blood vessel is intact or damaged and if it is able to maintain adequate blood supply. A broad spectrum of conditions can fit the criteria considered as vascular emergencies, including the various degrees of vascular trauma, spontaneous aneurysm rupture, acute dissection, acute thromboembolic disease, and surgical or interventional procedural complications. A prompt and accurate identification is indispensable to allow the treating physician to determine the best therapeutic approach.

ARTERIAL EMERGENCIES

Improved diagnostic methods and increasing specialization have enhanced our ability to treat vascular emergencies. The treatment of these patients has changed radically in recent years, becoming increasingly complex and involving a team approach, of which diagnostic and interventional radiologists are essential elements. In the evaluation of vascular emergencies the role of catheter angiography as a diagnostic tool is being progressively replaced by computed tomographic angiography (CTA) and sometimes magnetic resonance angiography (MRA). With technological advances these modalities, and particularly multidetector CTA (MD-CTA), have become an integral part in the initial assessment of acute vascular insults, as they are minimally invasive techniques, currently available in most emergency departments and trauma centers, and permit a prompt and accurate diagnosis within a short period of time. These are the methods of choice for the diagnosis of patients who do not have an indication for immediate surgical exploration. In addition, patients with direct signs (Box 11-1) of vascular injury on CTA can be taken to surgery without diagnostic angiography given its high sensitivity for the detection of vascular injuries. Furthermore, CT/CTA can be safely performed in patients with metallic fragments from bullets or other foreign objects, as opposed to MRI/MRA. MD-CTA has been increasingly used to diagnose arterial injuries from blunt and penetrating trauma not only to the chest and abdomen but also to the neck and extremities.

Box 11-1. **Direct Signs of Vascular Trauma on CTA**

Irregular arterial margins
Filling defects
Contrast extravasation
Lack of vascular enhancement
Sudden or abrupt vascular caliber changes

Arterial Emergencies of the Neck

Trauma of the Extracranial Carotid and Vertebral Arteries

Vascular injuries to the neck are frequently the result of penetrating trauma and are seen in 25% of the cases. They can also result from blunt trauma, hyperextension, and blast injuries. CTA has proven to be extremely valuable in the evaluation of these lesions because it provides simultaneous information about cervical spine and aerodigestive tract injuries. The full spectrum of vascular injuries can be identified, ranging from spasm to vessel transection. The majority of arterial injuries involve the carotid arteries, although vertebral arteries can be injured in up to 4% of cases.

Classically, the neck is divided into three zones for injury classification and management purposes. Zone 1 is from the clavicles to the cricoid cartilage, zone 2 is from the cricoid to the angle of the mandible, and zone 3 is from the angle of the mandible to the skull base. Zones 1 and 3 are extremely difficult to approach surgically. Injuries to zone 2 are the most common (60% to 70%), and this represents a clinical advantage since they are readily accessible for physical examination and surgery. The management of unstable patients who have suffered a penetrating neck injury is emergency surgical exploration. For the hemodynamically stable patients who present with a wound that penetrates the platysma there is still some controversy, as the local standards of care and resources may vary (Fig. 11-1). In general, surgeons opt for a conservative approach starting with CT/CTA and use additional diagnostic studies or take the patient to surgery if medically indicated. CTA has high sensitivity and specificity with reported values for the diagnosis of cervical vascular injuries ranging between 90% and 100%, respectively. The routine use of conventional angiography has been discouraged because of the high number of examinations with negative findings and the potential risk for complications due to its invasive nature. Nevertheless, the presence of any indirect sign (Box 11-2) around the carotid artery should warrant a correlation with angiography given the potential catastrophic consequences of missing a lesion in this location.

Blunt traumatic injuries of the extracranial carotid and vertebral arteries may have potential devastating consequences with an incidence that oscillates between 0.33% and 2.7% according to reports from centers performing aggressive angiographic screening. Although CTA and MRA have a great potential as screening tools in patients with blunt cerebrovascular injury, catheter angiography is still considered the gold standard. Intimal dissection and occlusion are more common with blunt trauma than with penetrating injuries (Fig. 11-2). Approximately 10% of patients have focal neurologic findings on initial presentation, and two thirds of the patients develop

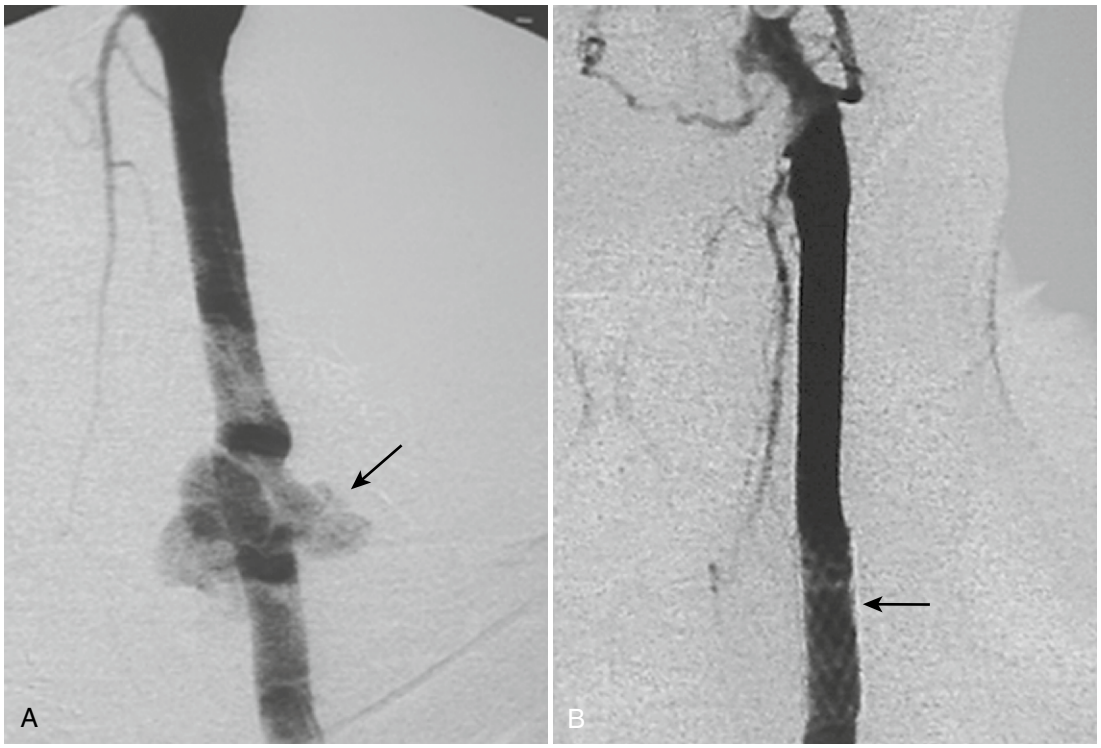


Figure 11-1. **A,** Common carotid artery pseudoaneurysm after penetrating neck trauma. Conventional angiogram demonstrates a large multilobulated pseudoaneurysm. **B,** After treatment with a covered stent the carotid was preserved and the aneurysm occluded. (Courtesy of Dr. F. Gomez, Cali, Colombia.)

symptoms within 24 hours. The remainder may present with neurological findings weeks to months later.

The type of intervention performed for carotid and vertebral injuries is determined by the nature of the lesion, the symptoms and clinical condition of the patient, and the feasibility of accessing the injured segment either with open surgery or with an endovascular approach. In general, intimal flaps and nonocclusive dissections are managed with anticoagulation provided there are no contraindications. Stent placement is reserved for flow-limiting dissections, while covered stents (stent grafts) have been successfully used to treat pseudoaneurysms and arteriovenous arteriovenous (AV) fistulas with good immediate results and patency rates (see Fig. 11-1). Embolization is another alternative for cases of vascular transection where surgical or endovascular vessel wall reconstruction cannot be achieved and adequate collateral pathway is demonstrated.

Nontraumatic Emergencies of the Carotid and Vertebral Arteries

Carotid and Vertebral Artery Dissection

Spontaneous dissection of the carotid or vertebral arteries in the absence of trauma is rare. It usually occurs in patients with underlying history of hypertension, fibromuscular dysplasia, or an underlying collagen disorder such as Marfan or Ehlers-Danlos syndrome. It can occur at any age, and clinical manifestations are variable, including neck pain or ipsilateral headache, Horner syndrome (ptosis, myosis, and unilateral anhydrosis), and acute or chronic focal

Box 11-2. **Indirect Signs of Vascular Trauma on CTA**

Indistinctness of perivascular fat planes
Perivascular hematoma
Bone or bullet fragment less than 5 mm away from major vessel

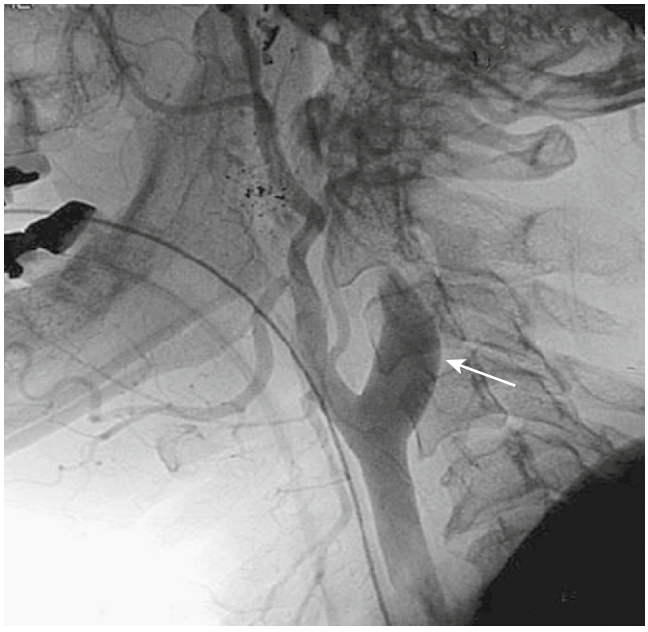


Figure 11-2. Conventional angiogram obtained after gunshot wound to the neck shows complete occlusion of the internal carotid artery secondary to occlusive dissection with the characteristic flame-shaped appearance *(arrow)*. (Courtesy of Dr. F. Gomez, Cali, Colombia.)

neurologic events either in the form of transient ischemic attack or as a permanent neurological deficit. All imaging modalities including ultrasound, CT, and MRI can be used to demonstrate the intimal flap, a compressed true lumen, slow flow in the false lumen, or even thrombus formation. Catheter angiography is generally indicated to better assess flow patterns or the absence of flow (see Fig. 11-2). The majority of patients are successfully treated with anticoagulation, but stent placement in the true lumen may be necessary to maintain or restore cerebral perfusion.

Aortic Emergencies

Acute aortic syndromes encompass a spectrum of aortic emergencies that include traumatic aortic injury (TAI), aortic dissection, penetrating atherosclerotic ulcer of the aorta, intramural hematoma, and aortic aneurysm rupture. Chapter 2 covers the topics of aortic dissection, intramural hematoma, and penetrating ulcer. This section focuses on traumatic aortic injuries.

TAI is a novel term that encompasses a spectrum of injuries characterized by a variable degree of aortic wall laceration and that include intimal tear, intramural hematoma, traumatic dissection, traumatic pseudoaneurysm, and, in the most severe form, aortic transection. TAI may result from rapid decelerations, crush injuries, penetrating wounds, and surgical or angiographic instrumentation. Blunt trauma is the most frequent cause of TAI, usually as the result of shearing, hydrostatic forces, and/or torsion forces applied along the aortic arch during a motor vehicle accident and falls from heights. Less common causes include displaced clavicular and thoracic vertebral fractures with entrapment of the aorta between the anterior chest wall and the spine. The overall mortality at the scene of the accident has been reported to be as high as 80% in autopsy series, with only 10% to 20% of the victims surviving the initial trauma. Bleeding from a laceration or rupture can be controlled by the aortic adventia or the periaortic tissues, which can help the patient survive the initial injury; however, the end result is pseudoaneurysm formation, which, due to its instability, requires prompt diagnosis and treatment (Fig. 11-3). The region of the aorta most susceptible to blunt injury is the isthmus, where the relatively mobile proximal thoracic aorta and arch join the fixed distal arch at the insertion of the ligamentum arteriosum, just distal to the left subclavian artery origin (Fig. 11-4). This area is involved in as many as 90% to 95% of the cases. Other common areas of injury

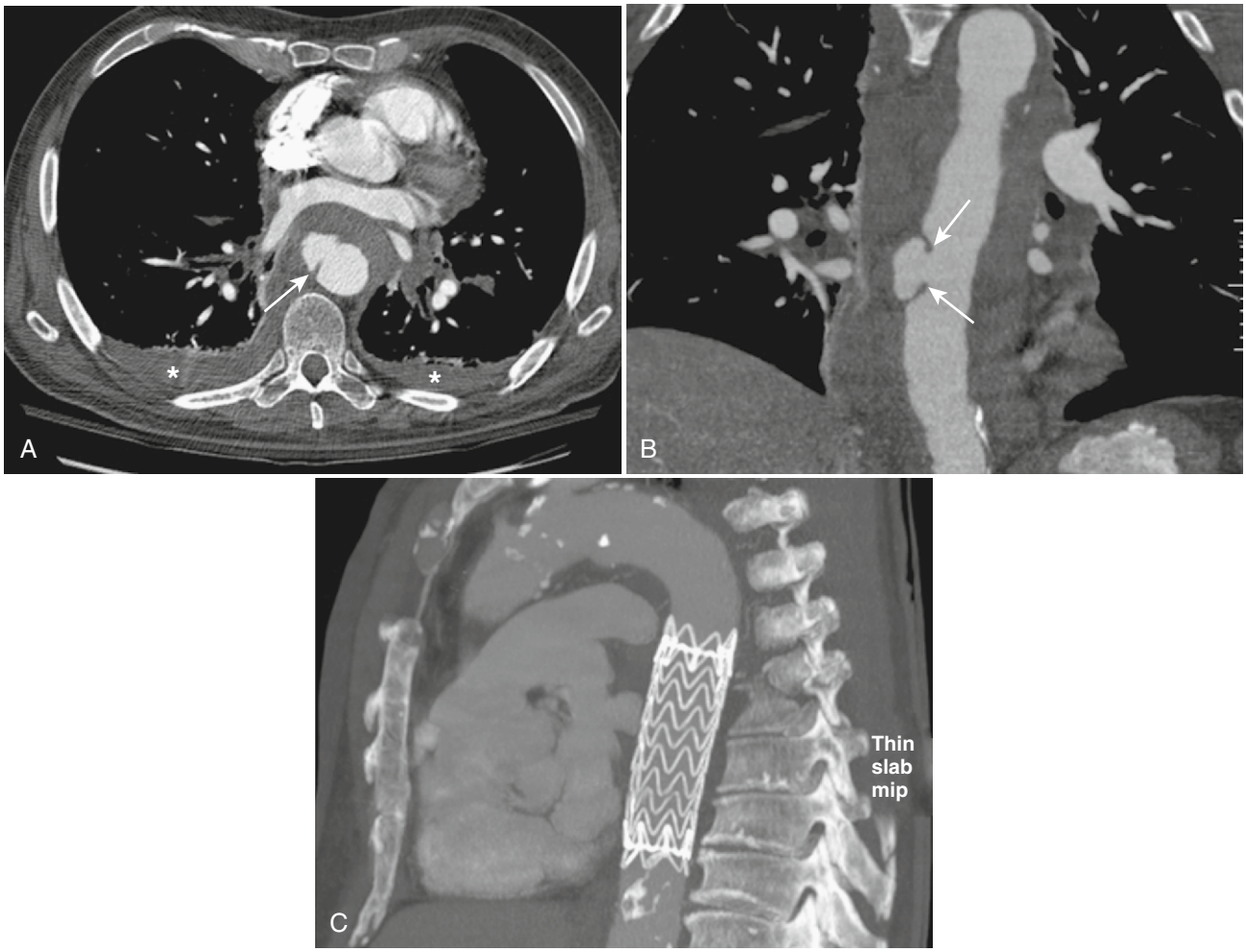


FIGURE 11-3. TAI in the mid-descending aorta following blunt trauma. Axial (**A**) and coronal reformat (**B**) images demonstrate a localized complete rupture of the aortic wall that led to mediastinal periaortic hematoma leaking into both pleural spaces *(asterisks)*. A pseudoaneurysm *(arrows)* has developed at the rupture site. **C,** Thin maximal intensity projection showing complete pseudoaneurysm occlusion after repair with stent graft. (Courtesy of Dr. Daniel J.A. Margolis, UCLA, David Geffen School of Medicine.)

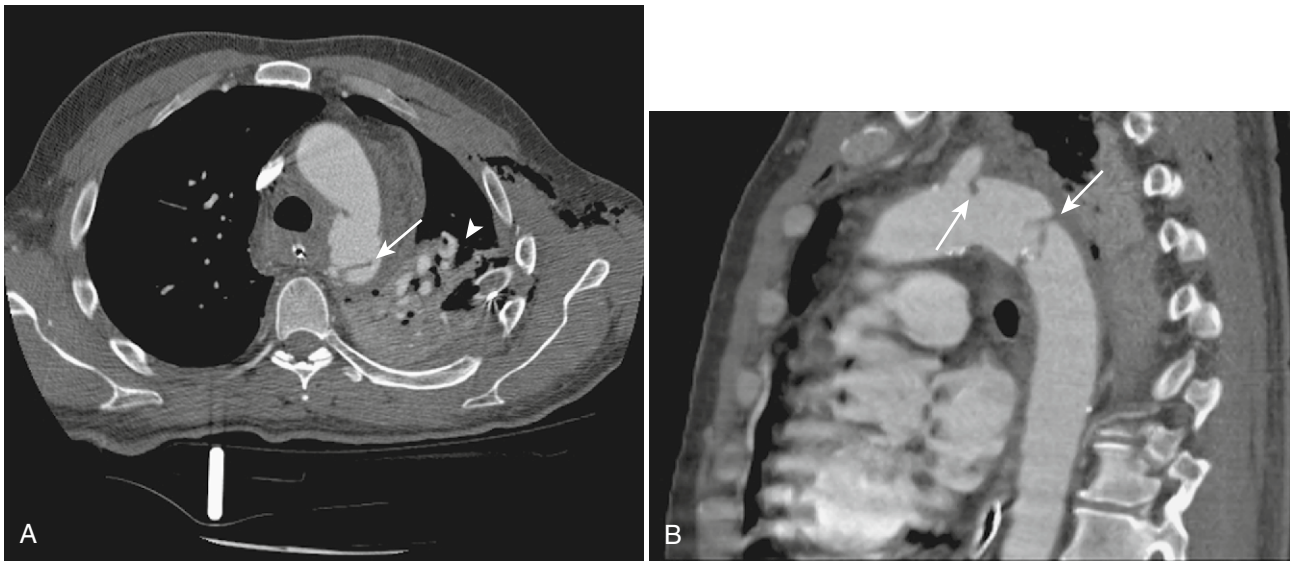


Figure 11-4. Axial CTA (**A**) and sagittal reformat (**B**) demonstrating a TAI with intimal tear *(arrows)* distal to the left subclavian artery origin and surrounding hematoma consistent with a contained aortic rupture. There are also partially visualized left rib fractures, subcutaneous emphysema, and atelectatic left lung *(arrowhead)*. (Courtesy of Dr. Daniel J.A. Margolis, UCLA, David Geffen School of Medicine.)

are the aortic root and the diaphragmatic hiatus. Injuries to the ascending aorta are uncommon (5% to 9%) and usually lethal due to the lack of surrounding connective tissue, resulting in rapid death due to exsanguination or cardiac tamponade. Clinical suspicion as well as a prompt diagnosis and treatment remain of crucial importance in TAI, given that 30% of the victims will die within 6 hours and 40% to 50% will die within 24 hours.

The initial imaging screening of trauma patients is obtained with plain radiographs due to the availability and capacity to quickly assess injuries such as pneumothorax, hemothorax, mediastinal hematoma (Fig. 11-5), and fractures. Clinical signs and symptoms found in patients with TAI include chest pain, back pain, dyspnea, cough, hoarseness, hypotension, pulse discrepancy, shock, and coma; as many as 30% to 50% of these patients may not show external signs of trauma.

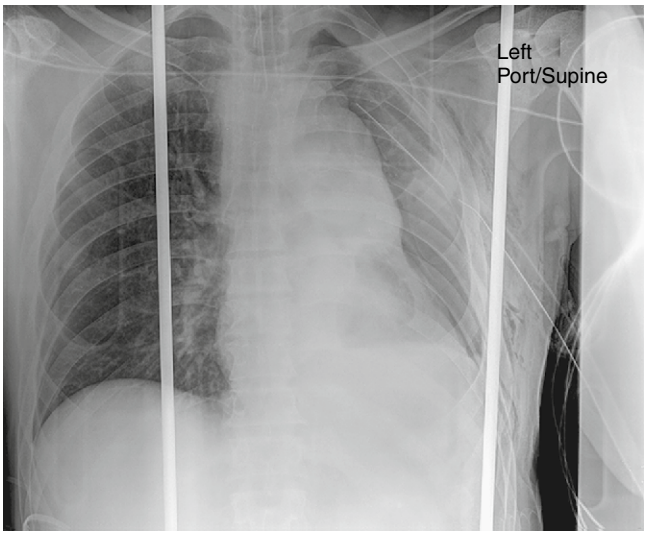


Figure 11-5. Portable radiograph demonstrating multiple signs of TAI including a widened mediastinum, slight tracheal shift, widening of the right paratracheal stripe, left apical cap, obliteration of the aortopulmonary window with poorly defined aortic arch, and a left hemothorax with chest tube in place and rib fractures.

A normal upright chest x-ray (CXR) has a negative predictive value of 98% when evaluating patients for aortic injury; however, these can rarely be obtained in the setting of severe multitrauma patients, who tend to get a frontal poorly inspired film in which mediastinal abnormalities frequently cannot be adequately assessed. Indirect signs for possible TAI in CXR include widening of the mediastinum, tracheal shift, deviation of the nasogastric tube or endotracheal tube to the right of the T3-T4 spinous processes, widening of the left or right paraspinal lines, apical cap, opacification of the aortopulmonary window, hemothorax, depression of the left main stem bronchus, and an ill-defined aortic arch. Mediastinal widening has reported sensitivities ranging between 81% and 100% with specificity of 60%; however, there is significant inter-reader variability when using this sign to predict aortic injury.

Catheter aortogram has long been considered the gold standard for the diagnosis of TAI with reported sensitivities and specificities approaching 100%. However, MD-CTA has become the preferred method for screening major traumatic and nontraumatic aortic emergencies, thanks to its improved spatial and contrast resolution and supplemental postprocessing techniques (thin sections, multiplanar reconstructions [MPRs], three-dimensional volume-rendered images), with a performance that rivals that of catheter angiography. MD-CTA has helped to better characterize the location and extent of TAI and other vascular injuries, allowing for faster diagnosis and treatment planning. In addition, MD-CTA can also recognize a greater number of normal variants of the vascular anatomy and subtle vascular injuries, which were less likely to be seen with conventional CT scans (Fig. 11-6). Furthermore, the need to perform an aortography to confirm the diagnosis of TAI is eliminated when direct signs of injury are present on CTA. Direct signs of TAI in CT include active extravasation of contrast, pseudoaneurysm formation, irregularity of the aortic wall, abrupt change in caliber of the aorta, aortic dissection, intimal flaps, and filling defects. Indirect signs of possible aortic injury include periaortic hematoma and mediastinal hematoma (Fig. 11-7).

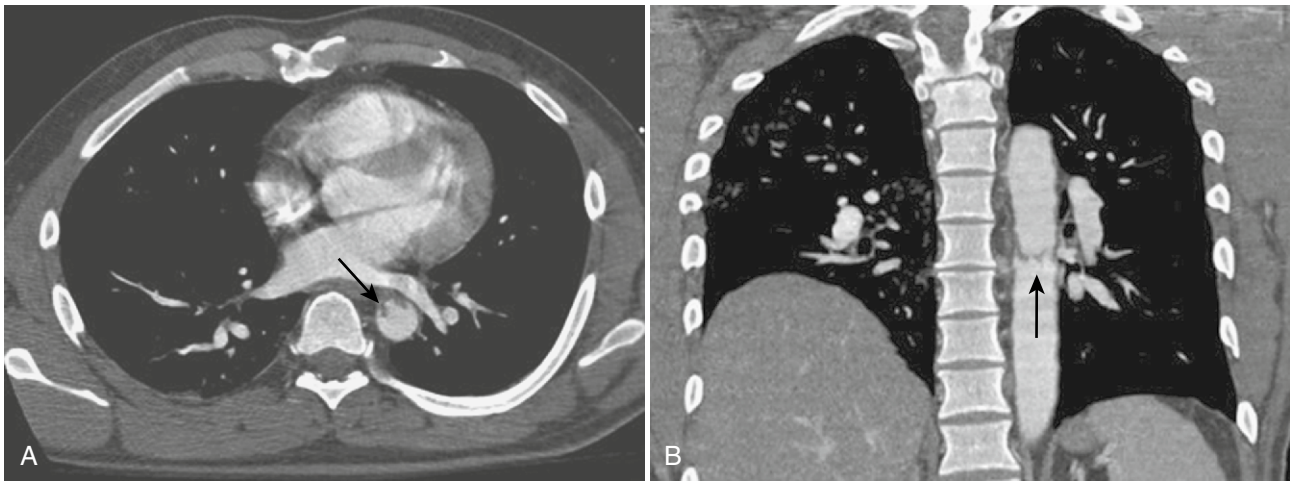


FIGURE 11-6. **A** and **B**, CTA images in the axial and coronal plane obtained after blunt chest trauma demonstrate an intimal tear *(arrows)* in the mid-descending aorta without extravasation or surrounding hematoma. (Courtesy of Dr. Daniel J.A. Margolis, UCLA, David Geffen School of Medicine.)

Catheter angiography can accurately demonstrate abnormalities affecting the aortic lumen; however, it is an invasive procedure that may require higher doses of contrast material, it is time-consuming, and it is limited to diagnosing concurrent injuries in multitrauma patients, risking a delay in management of other potentially lethal injuries. A minority of patients may still require catheter angiography when MD-CTA examinations are nondiagnostic or have equivocal or indirect signs of TAI. The decision to perform a catheter angiogram on patients with indirect findings depends on the experience of the interpreter, the quality of the scan, and the clinical condition of the patient. Angiographic diagnosis of intimal injury is demonstrated by the presence of intimal irregularity, linear defects, or filling defects caused by an intimal flap. The presence of contrast material outside the lumen is consistent with active extravasation. It can be contained or free; both are consistent with a transmural laceration and require immediate attention. The current complication rate for angiography is less than 1%, and complications include aortic rupture, acute renal failure, anaphylaxis, and entry site hematoma.

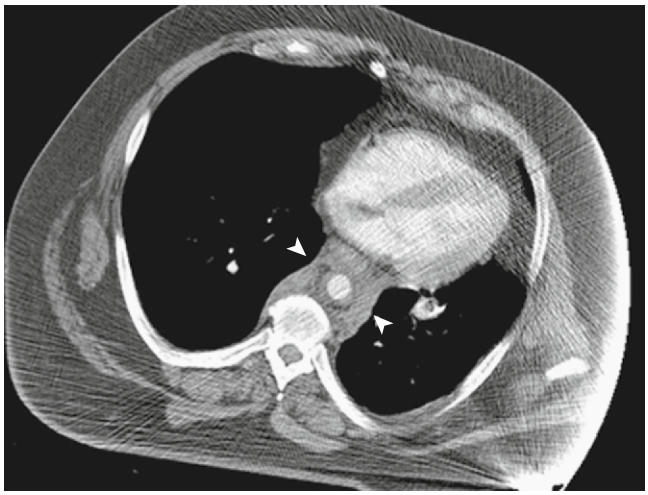


FIGURE 11-7. Contrast CT image obtained in a patient who sustained a motor vehicle accident demonstrating a concentric para-aortic hematoma without active extravasation or obvious wall defects that was managed medically and followed until resolution. (Courtesy of Dr. Daniel J.A. Margolis, UCLA, David Geffen School of Medicine.)

Transesophageal echocardiography (TEE) is another imaging modality that can provide detailed real-time images of the aorta, heart, and pericardium and can be done at the patient's bedside. Studies have shown sensitivity between 63% and 100% and specificity between 84% and 100% for detecting aortic rupture. The wide range of these results is explained by the fact that TEE is operator dependent. Direct signs of aortic injury include the detection of an intimal flap, evidence of intraluminal thick stripes, detection of pseudoaneurysm, aortic occlusion, and aortic wall hematoma. The main TEE limitation is its "blind spot," which represents the lack of visualization of a 3- to 5-cm segment in the distal ascending aorta and proximal arch that can be the site for TAI in 10% to 20% of patients. TEE is an alternative in the evaluation of unstable patients. However, a negative TEE in the setting of suspicious clinical or radiological findings warrants further investigation.

MRA is not currently considered the imaging technique of choice for the evaluation of TAI due to the relatively long acquisition times, the limited access to manage and control hemodynamically unstable patients, and the difficulties in scanning patients with metallic fragments or devices that may preclude the exam.

Treatment. Immediate surgical intervention is the treatment of choice in patients with TAI who are hemodynamically unstable, have persistent bleeding, or have evidence of expanding hematoma. Surgical repair is usually a major intervention requiring thoracotomy, aortic cross-clamping, partial cardiopulmonary bypass, suturing or prosthetic grafting of the aorta, and treatment of concomitant injuries such as the evacuation of pericardial tamponade or large hemothorax. The operative mortality of open thoracotomy ranges between 9% and 28%, with a high rate of major morbidities including paraplegia (up to 20%) due to spinal cord ischemia and stroke. Patient triage and selection are essential to perform a successful thoracotomy since open thoracotomy can worsen the clinical condition of severely injured patients who may not be able to tolerate this procedure.

Alternative management of TAI consists of delayed operative intervention or no operation while the patient is kept under close monitoring and blood pressure (BP)

control to reduce the risk of free rupture. The mainstay of treatment is to maintain systolic BP below 120 mm Hg (mean BP below 80 mm Hg) and allow patients who have suffered associated severe trauma to stabilize before surgical repair. This approach is indicated in hemodynamically stable patients with small aortic tears or those with associated injuries such as significant head, cardiac, or pulmonary trauma, large body surface burns, contaminated wounds, large retroperitoneal hematomas, or other high-risk medical comorbidities. Some of these aortic injuries might develop into a chronic pseudoaneurysm (Fig. 11-8), and others might even resolve during the period of observation. Close clinical and imaging follow-up is imperative to detect injury progression or aortic rupture.

More recently, endovascular treatment of TAI using stent grafts has been introduced as an alternative in the management of hemodynamically stable patients and patients with contraindications to cardiopulmonary bypass, such as severe coagulopathy, extensive additional injuries, and severe underlying cardiac or pulmonary disease. Mortality and morbidity appear to be lower than those of surgery, most likely because of the less invasive nature of the procedure, shorter operation time, and lack of the surgery-related comorbidities. The stent grafts are delivered via a common femoral artery cut-down access and positioned under angiographic and fluoroscopic guidance. The left subclavian artery origin often has to be covered with the endograft to provide adequate proximal support without significant clinical consequence in many patients. A significant number of patients with TAI are young, and therefore their aortic size is small; most stent grafts available today are made for the treatment of larger aortas with degenerative aortic aneurysms. Even though it is usually recommended to oversize the stent graft by 10% to 20% to ensure an adequate seal, excessive oversizing has been associated with type I endoleaks (Table 11-1) and stent graft collapse. Complications related to the endovascular repair include groin hematoma, iliofemoral dissection, endoleak, graft migration, and arterial rupture. Overall morbidity rates have been found to be around 12% with mortality rates of 4%. Clinical and imaging follow-up in both surgical and endovascular treatment modalities is required for early identification of post-treatment complications.

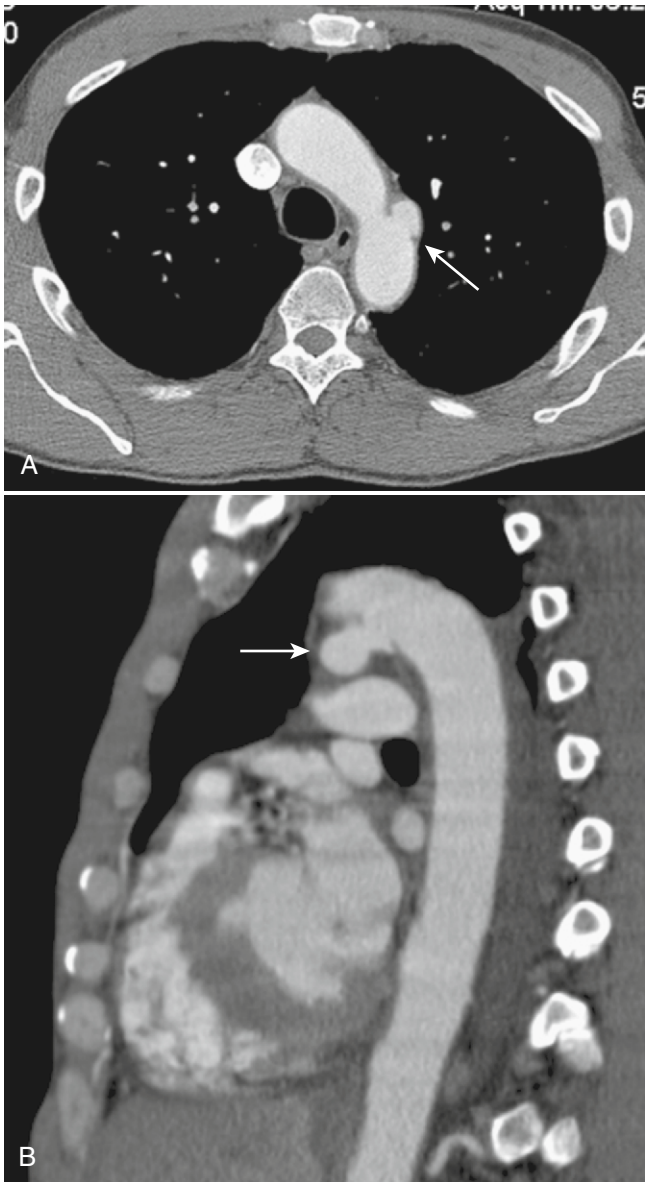


Figure 11-8. **A** and **B,** 68-year-old patient who sustained blunt trauma during motor vehicle accident 1 year before presentation. Axial and sagittal CTA images demonstrate a pseudoaneurysm *(arrows)* in the characteristic proximal descending aorta. The patient refused invasive repair at the time of injury; 1 year follow-up showed stable appearance without interval rupture or growth.

Penetrating Aortic Injury

Penetrating injuries to the intrathoracic great vessels are uncommon, with an incidence of 1%, and a high mortality rate that ranges between 50% and 85% despite advances in trauma care and prehospital resuscitation. These types of injuries can be caused by gunshot wounds (GSWs) or stab wounds (SWs) that traverse the chest or the base of the neck (Fig. 11-9). Overall, GSWs are more common and more lethal than SWs. Penetrating injuries to the thoracic aorta are more common along the ascending aorta and the arch branches, with a documented low incidence of descending thoracic injuries. These types of lesions are commonly associated with coexisting lethal intrathoracic injuries, which worsen the patient's prognosis. Although the aorta is protected by osseous structures, a laceration in this large-caliber vessel with high intraluminal pressure can cause rapid exsanguination. Thoracic aortic injuries have a worse prognosis than injuries to the abdominal aorta, probably due to the retroperitoneal location of the abdominal aorta, which can slow down exsanguination. They usually manifest as hemorrhage into the mediastinum or pleural cavity presenting as a hemothorax, cardiac tamponade, or mediastinal hematoma.

A portable supine chest radiograph continues to be the best initial imaging modality to screen for chest trauma. Radiopaque markers should be placed in the entry and exit sites of the wounds in order to give a guide toward the possible wound trajectory and the organs that might have been injured. Penetrating vascular lesions are suggested by a large hemothorax, widened mediastinum, foreign bodies in the proximity of the great vessels, or a bullet in a position different from its predicted course, suggesting bullet embolism, also known as "missing missile."

TABLE 11-1 Endoleak Classification

Endoleak type I	Inadequate seal around the proximal or distal end of the stent graft
Endoleak type II	Retrograde flow from branch vessels (intercostal, lumbar, inferior mesenteric, gonadal arteries) resulting in persistent filling of aneurysm
Endoleak type III	Stent graft laceration or fabric tears, dislodgment of modular graft devices
Endoleak type IV	Porosity of the graft fabric, diffuse leakage through interstices
Endotension	Excluded sac continues to enlarge without apparent endoleak formation

MDCT/CTA has become an integral part of the assessment of aortic injury due to blunt trauma, and its role in penetrating injuries to the aorta is currently growing due to its availability, short acquisition time, and ability to identify vascular lesions. It is also able to locate bullets and fragments, document the wound tract and bullet path, visualize associated fractures, and evaluate internal organ injuries. Its major role continues to be in hemodynamically stable patients with GSWs suspected to transverse the mediastinum, since it can define the wound tract and its relationship with vascular and aerodigestive structures, helping to plan further treatment.

Aortic angiography remains the gold standard for the diagnosis of vascular lesions due to its ability to show pseudoaneurysm formation, active extravasation, and arteriovenous fistulas. However, fewer catheter aortograms are being performed as a consequence of the already mentioned benefits of noninvasive imaging with MD-CTA. In the case of a penetrating injury to the major vessels, lesions in the major venous structures such as the innominate veins can be present in up to one fourth of the patients, and they account for nearly 22% of fatalities in penetrating chest trauma. When performing catheter angiography, a venous phase should be carried out in all arteriograms, and, if venous injury is suspected, conventional venograms should be considered.

Penetrating injuries to the thoracic aorta are usually treated with urgent surgical repair via an anterolateral thoracotomy. Endovascular repair with stent grafts may be possible for penetrating injuries in selected patients (see TAI section).

Nontraumatic Aneurysms of the Thoracic and Abdominal Aorta

Thoracic Aortic Aneurysms

Thoracic aortic aneurysms (TAAs) are often the result of atherosclerotic disease or cystic medial degeneration with subsequent weakening and dilatation of the aortic wall. It is usually a silent process, less commonly seen than abdominal aortic aneurysm, and generally occurs in older men in their sixth and seventh decades. Based on their morphology, aneurysms are classified as either fusiform aneurysms, which involve the full circumference of the vessel wall, or saccular aneurysms involving only a focal portion. Thoracic aneurysms occur in the ascending aorta in 40% to 60% of the cases, descending aorta in 30% to 40% of the cases, and aortic arch and thoracoabdominal aorta in 10% of the cases. The incidence and prevalence of thoracic aortic disease including TAA are steadily increasing due to the aging population and improved diagnostic techniques. The reported incidence of TAA ranges from 6 to 10 cases per 100,000 patients per year. The natural history of untreated TAA is progressive expansion of the aneurysm and ultimately rupture (Fig. 11-10).

Given that most patients are asymptomatic, TAAs are commonly diagnosed as an incidental finding on imaging studies. However, they can also present with signs and symptoms related to compression of adjacent structures. Ascending aortic aneurysms can compress the coronary arteries

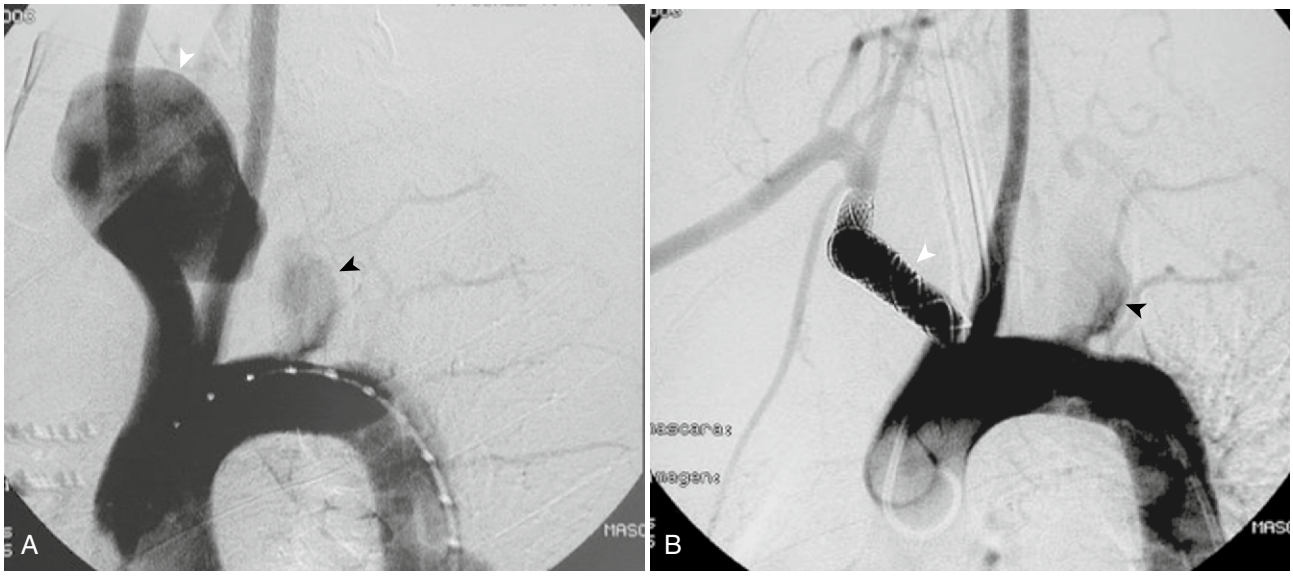


FIGURE 11-9. **A,** Arch angiogram obtained after a stab wound to the neck. There is a large pseudoaneurysm at the level of the distal brachiocephalic trunk *(white arrowhead)* and a second pseudoaneurysm involving the arch and possibly the left subclavian artery origin *(black arrowhead)*. Neither one of the subclavian arteries is visualized. **B,** After treatment with a covered stent *(white arrowhead)* the large brachiocephalic aneurysm has been occluded preserving the right carotid and reestablishing flow in the right subclavian. The aortic pseudoaneurysm was surgically repaired. (Courtesy of Dr. W. Escobar, Cali, Colombia.)

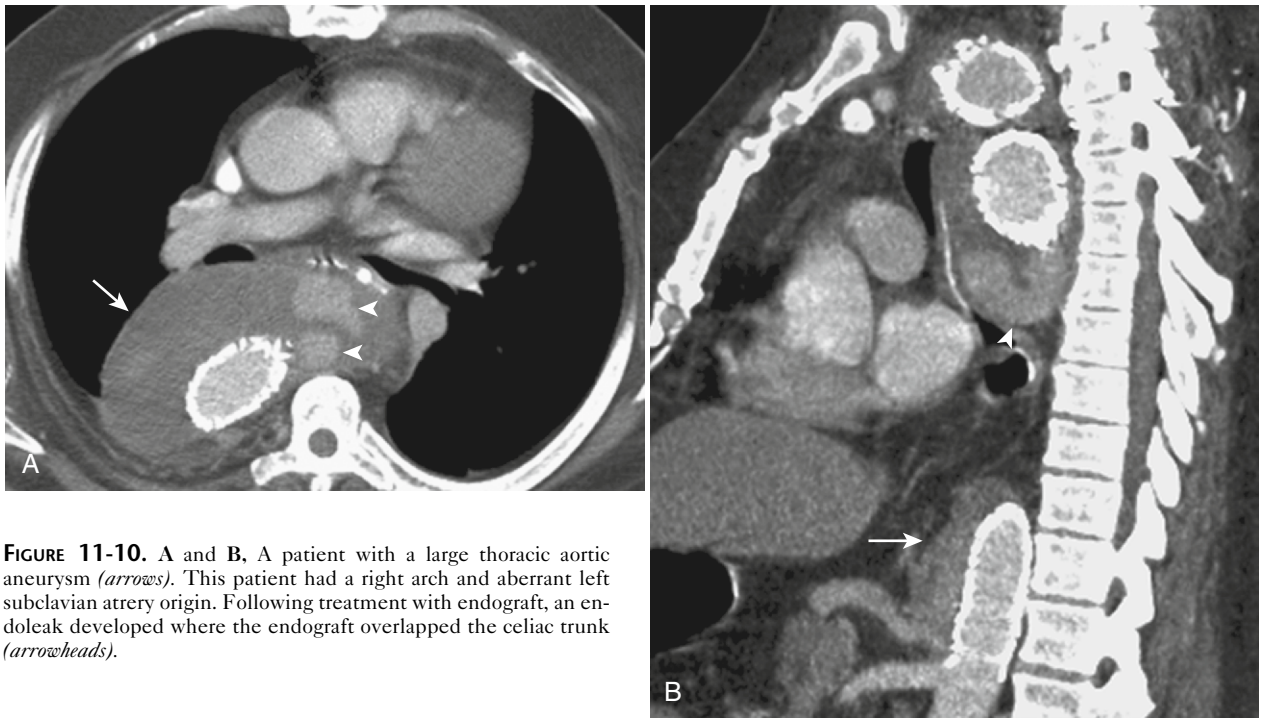


Figure 11-10. A and **B,** A patient with a large thoracic aortic aneurysm *(arrows).* This patient had a right arch and aberrant left subclavian atrery origin. Following treatment with endograft, an endoleak developed where the endograft overlapped the celiac trunk *(arrowheads).*

or the origin of the great vessels causing myocardial or cerebral ischemia; together with arch aneurysms, they can erode into the mediastinum and compress the left recurrent laryngeal nerve causing hoarseness, or the phrenic nerve and lead to hemidiaphragmatic paralysis. They can also press on the tracheobronchial tree causing wheezing, dyspnea, cough, hemoptysis, and pneumonitis; on the esophagus and cause dysphagia; and on the superior vena cava (SVC) causing SVC syndrome. Mural thrombus from the aneurysms can be the source of emboli and cause strokes, as well as renal, mesenteric, or limb ischemia. Heart failure can result from aortic root aneurysms leading to aortic regurgitation, or from the rupture of a sinus of Valsalva aneurysm into the right side of the heart. Chest and back pain are rare symptoms associated with compression of intrathoracic structures or erosion into adjacent bones (Fig. 11-11).

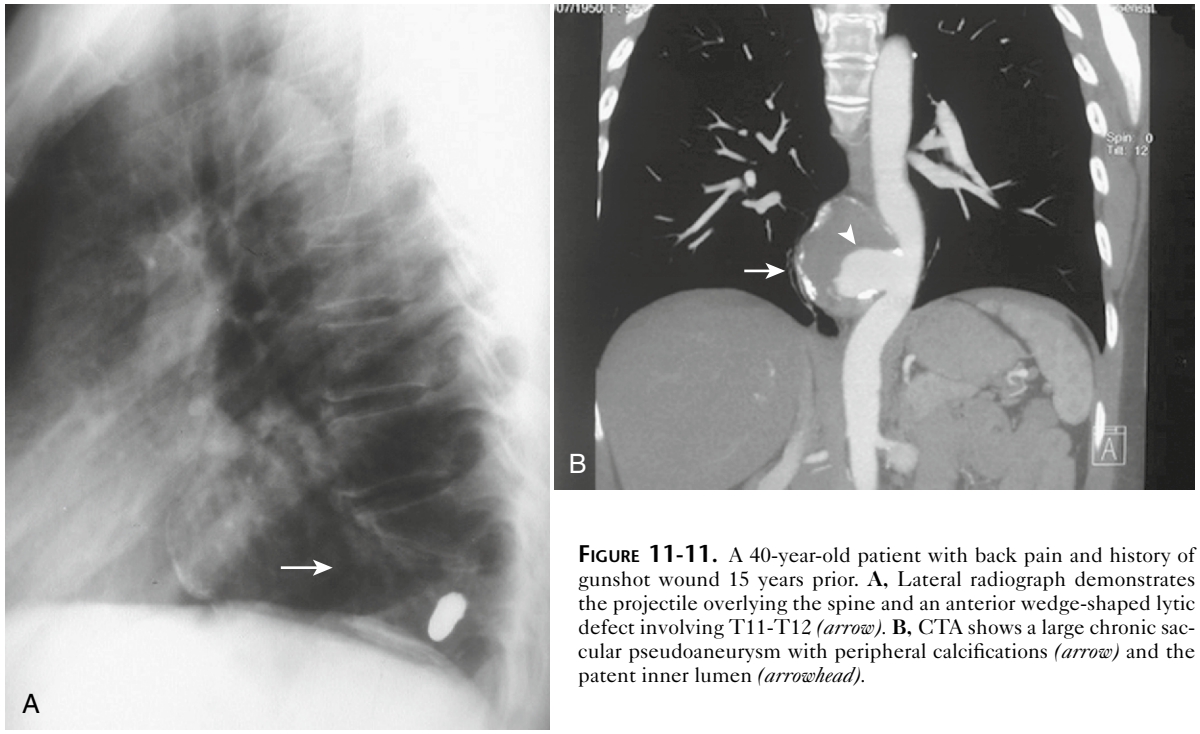


Figure 11-11. A 40-year-old patient with back pain and history of gunshot wound 15 years prior. **A,** Lateral radiograph demonstrates the projectile overlying the spine and an anterior wedge-shaped lytic defect involving T11-T12 *(arrow).* **B,** CTA shows a large chronic saccular pseudoaneurysm with peripheral calcifications *(arrow)* and the patent inner lumen *(arrowhead).*

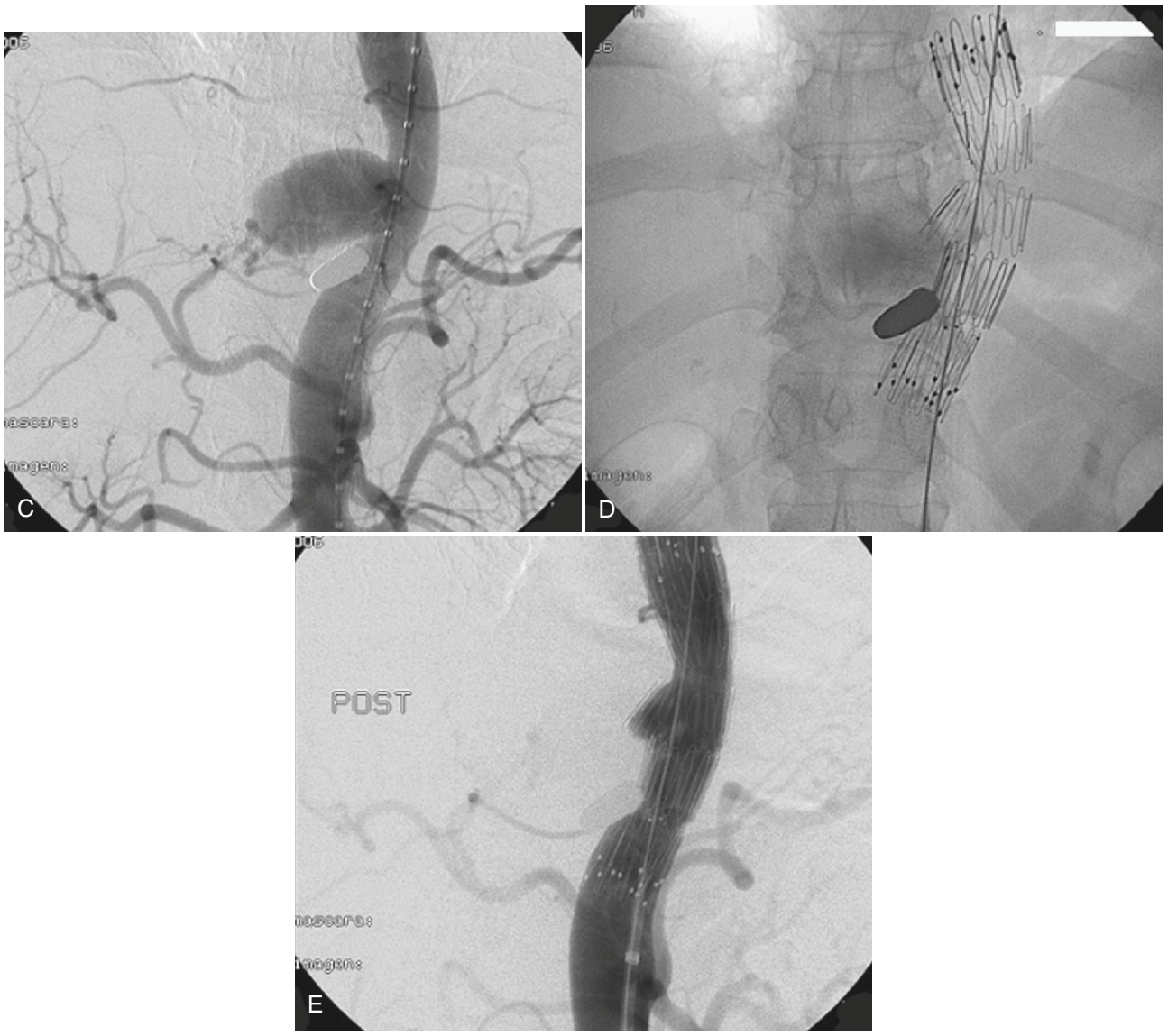


FIGURE 11-11.—CONT'D C, Catheter angiography showing the thoracoabdominal aneurysm with preserved upper abdominal branches. **D** and **E,** Following repair with endograft there is complete exclusion of the aneurysm. (Courtesy of Dr. W. Escobar, Cali, Colombia.)

The most feared complications of TAA are aneurysm dissection and rupture. Dissection can lead to arterial occlusion and end-organ ischemia, while rupture can cause massive hemorrhage that usually cannot be contained by adjacent structures and therefore is considered a surgical emergency. Patients present with hypotension and acute onset of chest pain, abdominal pain, back pain, or neck pain. Rupture occurs more commonly into the left pleural space, but it can also occur into the pericardium causing pericardial tamponade (Fig. 11-12), and into the esophagus resulting in aortoesophageal fistula and dramatic upper gastrointestinal bleeding.

The risk of rupture and dissection of TAA increases with aneurysm size. The mean rate of rupture or dissection for small aneurysms is around 2%; it increases to 3% for aneurysms measuring 5.0 to 5.9 cm, and to 7% in patients with aneurysms 6 cm in diameter or larger. The mean aortic growth rate has been estimated to be 0.1 cm per year. Greater growth rates are seen in patients with Marfan syndrome, aneurysms of the descending aorta, and dissecting aneurysms. Although men are more prone to develop thoracic aneurysms, women have a higher likelihood of rupture and dissection.

Multiple etiologies have been associated with thoracic aortic aneurysms, and they differ depending on their location within the thoracic aorta. Aneurysms of the ascending aorta and aortic arch are more commonly seen in elderly patients secondary to atherosclerosis or aortic valve stenosis leading to poststenotic dilatation. The younger patient population presenting with thoracic aneurysms in the ascending aorta and aortic arch (Tables 11-2 and 11-3) usually have a connective tissue disorder such as Marfan syndrome (mutation of fibrillin-1 gene), Ehlers-Danlos syndrome (defect in type III collagen), Loeys-Dietz syndrome, or Turner syndrome (associated to bicuspid aortic valves). Other infrequent etiologies include mycotic and syphilitic aneurysms. Aneurysms of the sinus of Valsalva can be congenital, infectious, or postsurgical in origin, and they are seen as dilatations in connection with the aortic root. Vasculitis can affect all portions of the

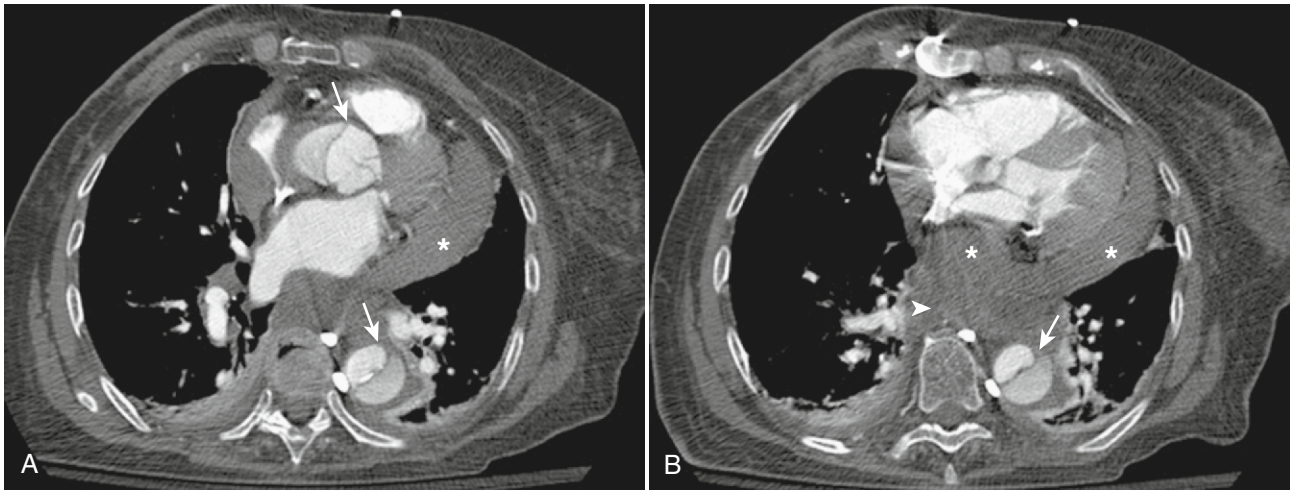


Figure 11-12. **A,** Aortic dissection type A with hemopericardium. Dissection flap is identified along the descending and ascending aorta all the way to the aortic root *(top arrow)* and rupture into the pericardium *(asterisk)* and the mediastinum *(arrowhead)*. **B,** There is compression of the left atrium by the hemopericardium consistent with impending tamponade. (Courtesy of Dr. Daniel J.A. Margolis, UCLA, David Geffen School of Medicine.)

thoracic aorta. Takayasu arteritis is one of the most striking entities, characterized by a chronic inflammatory process of unknown etiology that affects the aorta, its major branches, and the pulmonary arteries. It affects the vessel wall causing obliterative luminal changes, occlusion, or dilatation. Aneurysm formation can be a fatal complication of this disease since it may lead to heart failure secondary to aortic valve regurgitation or aortic rupture.

Thoracic aneurysms of the descending aorta are also most commonly degenerative in origin caused by atherosclerosis and usually associated with hypertension, hypercholesterolemia, and smoking. These aneurysms are generally fusiform with significant intimal calcifications and demonstrate associated tortuous aorta and mural thrombus. Other causes include chronic aortic dissection (Stanford type A or B), which can dilate over time as the wall of the false lumen weakens, creating a dissecting aneurysm with a high risk of rupture. Injuries to the descending thoracic aorta associated with blunt trauma can result in pseudoaneurysm formation, characteristically located near the aortic isthmus distal to the subclavian artery, and with a high risk of rupture (these are discussed in the TAI section). As with ascending thoracic aneurysms, younger patients with descending thoracic aortic aneurysms usually have an underlying connective tissue disorder (Table 11-4) or vasculitis. Mycotic aneurysms can also affect this segment.

Table 11-2 Ascending Thoracic Aortic Aneurysms

Degenerative	Associated with atherosclerosis
Inheritable/connective tissue	Marfan syndrome
	Ehlers-Danlos syndrome
	Loeys-Dietz syndrome
	Turner syndrome
	Osteogenesis imperfecta
	Rheumatoid arthritis
	Bicuspid aortic valve
	Aneurysm of sinus of Valsalva
Arteritis	Giant cell arteritis
	Takayasu arteritis
	Behcet's disease
	Relapsing polychondritis
Infectious	Syphilis
	Mycotic aneurysms

Table 11-3 Aortic Arch Aneurysms

Degenerative	Secondary to atherosclerosis
Arteritis	Giant cell
	Takayasu
	Behcet's disease
Infectious	Syphilis

Table 11-4 Descending Thoracic Aortic Aneurysm

Degenerative	Secondary to atherosclerosis
	Focal pseudoaneurysm secondary to penetrating aortic ulcer
Arteritis	Giant cell
	Takayasu
	Behcet's disease
Inherited/connective tissue	Marfan syndrome
	Ductus aneurysm
	Loeys-Dietz syndrome
Infectious	Mycotic aneurysms
Traumatic	Post-traumatic pseudoaneurysms
	Chronic aortic transection

TABLE 11-5 Crawford Classification of Thoracoabdominal Aneurysms

I	Descending thoracic aorta to suprarenal aorta
II	Proximal descending thoracic aorta to infrarenal aorta (below the diaphragm)
III	Mid-descending thoracic aorta to infrarenal aorta
IV	Supravisceral aorta to infrarenal aorta

Aneurysms located in the thoracoabdominal aorta are less frequent than abdominal or thoracic aneurysms, which is fortunate because these are difficult-to-treat lesions due to the numerous visceral branches that arise along this segment. They are divided into four types according to the Crawford classification (Table 11-5). Types II and III are the more complex ones, with type II having the highest risk of treatment-induced spinal cord infarction and renal failure.

Diagnosis. Thoracic aortic aneurysms are usually seen on a routine chest radiograph as an incidental finding. Common findings include a widened mediastinum, enlarged aortic knob, tracheal deviation, aortic kinking, and blunted aortopulmonary window. However, CXR is limited in the diagnosis of thoracic aneurysms as it cannot accurately differentiate a tortuous aorta from an aortic aneurysm and can easily miss small aortic aneurysms.

CTA provides sufficient information to diagnose and follow up progression of TAA; angiographic sequences allow for precise delineation of the extension of the aneurysm, involvement of the great vessels, and other associated thoracic pathology (see Fig. 11-11). Unenhanced CT is used to identify areas of aortic calcification, mural thrombus, acute wall hematoma (circumferential or crescentic), and recent hemorrhage. Contrast administration helps to differentiate the patent lumen from mural thrombus and to demonstrate an intimal flap and a false lumen in areas of aortic dissection. CT also shows the relationship of the aneurysm to the adjacent structures and helps correlate associated patient symptomatology with imaging findings. Mycotic aneurysms can affect any portion of the aorta and are seen as saccular dilatations with multilobulated contour (Fig. 11-13). Cross-sectional CT imaging features include a perianeurysmal soft tissue mass, fluid collection, and occasionally gas-forming inflammation. Syphilitic aortic aneurysms are rarely seen nowadays, but if encountered they usually demonstrate extensive aortic calcification or linear calcifications with longitudinal wrinkling of the wall causing a "shaggy tree-bark" pattern; approximately 75% of the cases exhibit a saccular morphology.

Both CTA and MRA can be used successfully as preprocedural imaging techniques in order to plan surgical or endovascular repair, as they are both able to measure the dimensions of the aneurysm and detect the involved vessels. Accurate measurements are crucial when selecting the appropriate stent graft diameter for endovascular procedures in order to minimize stent-related complications such as endoleak, stent migration, and branch occlusion. CTA with multiplanar reconstruction and digital subtraction angiography (DSA) are considered to be the most useful techniques to depict morphologic characteristics of the aneurysm, as well as to detect graft complications.

Contrast-enhanced MRA (CE-MRA) can provide exquisite detail of the aneurysm and associated dissection or branch involvement; sometimes it can also visualize small vascular structures in greater detail, such as the Adamkiewicz artery, providing valuable information in the planning of surgical repair and helping avoid postoperative neurologic deficits. CE-MRA, however, cannot visualize aortic calcification, which can be important during treatment planning. These two modalities continue to complement each other as one may show certain characteristics that the other cannot.

In either case, serial imaging studies are usually required in this patient population in order to monitor aneurysm size. A repeat study can be obtained 6 months after the initial diagnosis, and if the aneurysm is stable, imaging follow-up can be obtained annually.

Treatment. TAA repair depends on its location. Aneurysms located in the ascending aorta are usually treated surgically via a median sternotomy with aneurysm resection and

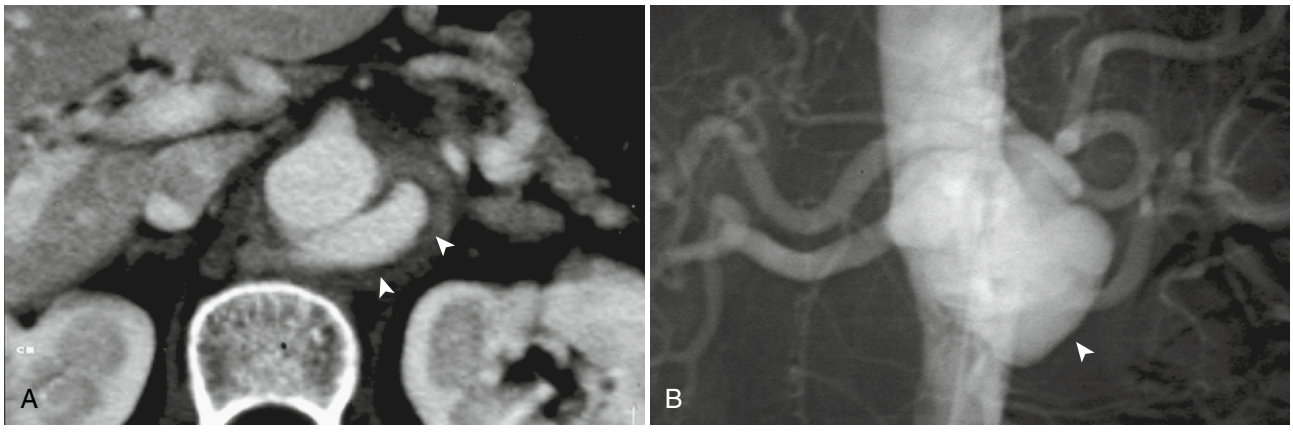


FIGURE 11-13. **A,** Contrast-enhanced CT showing an avidly enhancing posterior aortic wall saccular aneurysm at the level of the celiac trunk; note the absence of atherosclerotic plaque. **B,** Conventional angiogram shows the size of the aneurysm and the proximity to the celiac trunk and renal arteries. These findings are typical for mycotic aneurysms. Salmonella was found on the specimen. (Courtesy of Dr. Javier Casillas, University of Miami.)

***Box 11-3.* Signs of Impending Aneurysm Rupture on CT/CTA**

Enlarging aneurysm
Low thrombus/lumen ratio
Hemorrhage into mural thrombus (seen as hyperdense crescents on unenhanced CT)

prosthetic tube graft placement. Surgical treatment is recommended for patients who are symptomatic, present with large aneurysms, have a high aneurysmal growth rate, or have associated complications. The best time to treat patients with TAA is still uncertain given the limited understanding of its natural history. Nonetheless, for most ascending thoracic aneurysms, repair is considered in patients with aneurysms that are 5.5 cm in diameter or larger. The decision to intervene is made depending on the patient's operative risks versus the risk of developing an aneurysm-related complication such as dissection or rupture (e.g., patients with Marfan syndrome have their aneurysms repaired earlier due to the high risk of dissection and valvular insufficiency). Mortality of elective surgical repair in ascending aortic aneurysms ranges from 3% to 5%, and it carries a high risk of postsurgical morbidity including paraplegia, stroke, and bleeding; however, successful repair practically eliminates the risk of rupture. Lesions that are not treated by a surgical approach can have a mortality rate as high as 74%. Repair of arch aneurysms is even more challenging due to the high risk of stroke during replacement of the abnormal arch and reimplantation of the brachiocephalic vessels. Elective surgical repair for descending thoracic and thoracoabdominal aortic aneurysms has an associated mortality rate of 5% to 14% and a significant risk of paraplegia due to occlusion of the spinal cord blood supply; the risk has decreased with the implementation of protective techniques such as regional epidural hypothermic protection and cerebrospinal fluid drainage. Indications for surgical repair of descending aortic aneurysms include diameter equal to or larger than 6.5 cm, a patent primary entry site, expanding false lumen of either a dissection or aneurysm, symptomatic patients, or signs of impending rupture (Box 11-3).

Endovascular treatment of aortic arch aneurysms requires surgical transposition of supra-aortic vessels and is currently used in selected cases to help reduce the risk inherent in surgical repair. Patients with descending thoracic aortic aneurysms can also be offered endograft repair as an alternative to surgical treatment, in particular those patients with high operative risk. Endografts successfully exclude the aneurysm sac in most patients, with an apparent lower rate of persistent neurologic deficits in the range of 2% to 3% (versus 5% to 6% for surgically treated patients). Nevertheless, stent grafts are also associated with complications such as stroke, paraplegia, and device-related complications such as endoleaks and graft migration. Long-term studies are on their way to assess the durability of endograft aneurysm repair (see Fig. 11-10).

Abdominal Aortic Aneurysms

Abdominal aortic aneurysms (AAAs) are fusiform or saccular dilatations of the abdominal aorta, which form more frequently as a consequence of degeneration of the media from atherosclerotic disease, which causes weakening of the wall and widening of the luminal diameter. In the elderly population, degenerative aneurysms are more frequent, while in younger patients abdominal aneurysms are usually secondary to inheritable diseases such as Marfan syndrome and Ehlers-Danlos syndrome. Predisposing factors that have been associated with AAA include advanced age, family history, male gender, tobacco use, and white race with a lower incidence found in patients of Asian descent. Patients with AAA have a higher incidence of hypertension, atherosclerosis, myocardial infarction, heart failure, and peripheral vascular disease than matched controls for age and gender. Other types of AAA include inflammatory and infectious aneurysms. Inflammatory aneurysms, as their name indicates, show an increased inflammatory reaction in the aneurysm wall and surrounding tissues, and present with a triad of chronic abdominal pain, weight loss, and elevated erythrocyte sedimentation rate. Infectious or mycotic aneurysms are more frequently associated with transient bacteremia with *Staphylococcus* or *Salmonella*, which leads to infection of the vessel wall or an atherosclerotic, plaque by hematogenous spread. There are also rare reports of aneurysms caused by tuberculosis infection.

Patients with AAA are usually asymptomatic, and aneurysms are often detected as an incidental find, on radiologic studies. Sometimes clinical exam can detect AAA if a pulsatile abdominal mass or an abdominal bruit is present; unfortunately, physical exam sensitivity among studies varies widely and confirmatory imaging is usually required. Symptomatic patients usually complain of lower back pain or abdominal pain that can be nonspecific and easily confused with other disease processes. Patients with acute rupture present with abrupt onset pain in the lower back or abdomen, that can be associated with a pulsatile abdominal mass and hypotension. The natural history of abdominal aortic aneurysms is usually characterized by gradual expansion of the aneurysm sac with mural thrombus formation lining the inner surface. The aneurysm may then cause compression of adjacent structures, thromboembolic events, erosion into neighboring structures (e.g., duodenum or iliac vein), and, ultimately, rupture.

AAA rupture is a catastrophic complication with a reported mortality of up to 90%. It usually occurs in the posterolateral aspect of the aorta causing retroperitoneal hemorrhage. Less commonly, it ruptures in the anterolateral aspect causing intraperitoneal bleeding and quick exsanguination. Contained ruptures in the form of retroperitoneal hematomas might be associated with ecchymosis of the flanks, otherwise known as Grey-Turner syndrome. In general, the larger the aneurysm, the higher the risk for spontaneous rupture and the faster it tends to expand. The average expansion rate for aortic aneurysms 4.0 cm in diameter is 1 to 4 mm per year, followed by 4 to 5 mm per year for aneurysms measuring 4.0 to 6.0 cm, and 7 to 8 mm per year in larger aneurysms. The lifetime risk of rupture of abdominal aneurysms larger than 5.0 cm in diameter is 20%; it then increases to 40% for aneurysms that measure more than 6.0 cm, and to more than 50% for aneurysms that exceed 7.0 cm. The corresponding estimated annual rupture rates are 4%, 7%, and 20%, respectively.

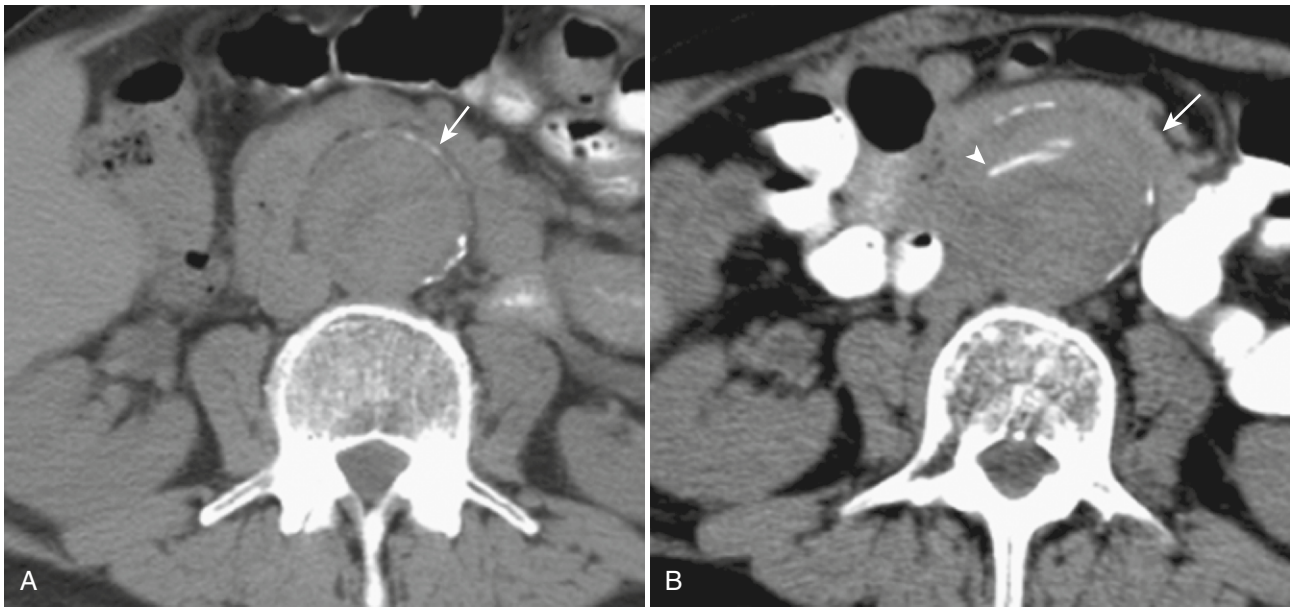


FIGURE 11-14. **A** and **B,** Noncontrast CT images obtained 1 year apart. The first image **(A)** shows an AAA with peripheral plaque and mural thrombus *(arrow)*; 1 year later **(B)** the aneurysm *(arrow)* has increased in size and intramural crescents have developed *(arrowhead)*, raising concern for impending aneurysm rupture.

Other AAA complications that may require immediate treatment are those related to compression or erosion of adjacent structures, as seen in large degenerative AAA, or inflammatory or mycotic aneurysms. Some examples include gastric outlet syndrome secondary to compression of the duodenum, aortoenteric fistula formation causing massive upper gastrointestinal bleed, and venous fistula formation into the inferior vena cava, the left renal vein, or the common iliac vein. These fistulae can have high flow rates and result in acute congestive heart failure or in hematuria and flank pain.

Diagnosis. Early AAA detection is imperative in order to reduce patient morbidity and mortality of this silent disease. The most common site of arterial aneurysms is the abdominal aorta, especially along its infrarenal segment. Abdominal aneurysms are diagnosed when the aorta is 1.5 times greater that the diameter of the normal aorta or when the minimum anteroposterior diameter is greater than 3.0 cm irrespective of age and gender.

Imaging techniques are currently relied on for the diagnosis and follow-up of aortic aneurysms. Real-time ultrasonography is a noninvasive and cost-effective modality useful to screen for AAA, with an accuracy that approaches 100% in the diagnosis of infrarenal aortic aneurysms. Its accuracy in measuring the aortic diameter below the level of the renal arteries has been shown to correlate well with direct intraoperative measurements. The size of the aneurysms is calculated by measuring the maximum anteroposterior aortic diameter or the largest transverse diameter measured in a plane perpendicular to the luminal arterial axis to avoid overestimation of the aneurysm size. AAAs are seen as dilated vessels with irregular lumen and eccentric echogenic thrombus material. Although convenient, ultrasound is limited by the patient's body habitus and the interposition of bowel gas that obscures visualization of the deeper structures. Likewise it is not as reliable as CTA for detecting complications such as rupture, aneurysm extension into the suprarenal aorta, and detection of post-therapeutic complications such as endoleaks.

MD-CTA has emerged as the new gold standard for the diagnosis of aortic abdominal aneurysms, replacing catheter arteriography. MD-CTA offers high-resolution imaging and shorter scan times, allowing the detection and characterization of aneurysms and related complications including impending rupture and contained or complete rupture. Several signs of impending rupture have been identified (see Box 11-3) on CT including increased aneurysm size, a low thrombus-to-lumen ratio, and mural thrombus hemorrhage that is usually identified as high-attenuation crescents in the wall of the aortic aneurysm in unenhanced CT images (Fig. 11-14). There are various signs that suggest a contained AAA rupture, including loss of definition of the posterior aortic wall; presence of an organized hematoma with contour abnormalities of the vessel wall; interruption of a continuous ring of aortic wall calcification; and a posterior wall of the aorta following the contour of the vertebra with or without associated vertebral erosion (sign known as a "draped" aorta). A ruptured AAA is determined by the presence of hemorrhage contiguous to the aorta, almost always involving the retroperitoneal space and rarely the iliopsoas compartment. Periaortic blood might be seen in the pararenal space, perirenal space, or both; a hematocrit sign (cellular-fluid level) and rectus sheath bleeds are more rare but helpful if present, and tend to be associated with coagulopathic hemorrhage (Fig. 11-15).

CT is also useful in differentiating between different types of aortic aneurysms. Mycotic aneurysms are usually seen as saccular-shaped collections with a lobulated contour; other features may include a periaortic soft tissue mass with stranding, retroperitoneal para-aortic fluid collection, vertebral erosion, gas-forming inflammation around the aneurysm, intra-aortic air pockets, and thrombus formation within a false lumen after aneurysmal rupture (see Fig. 11-13). In inflammatory aneurysms, CT and

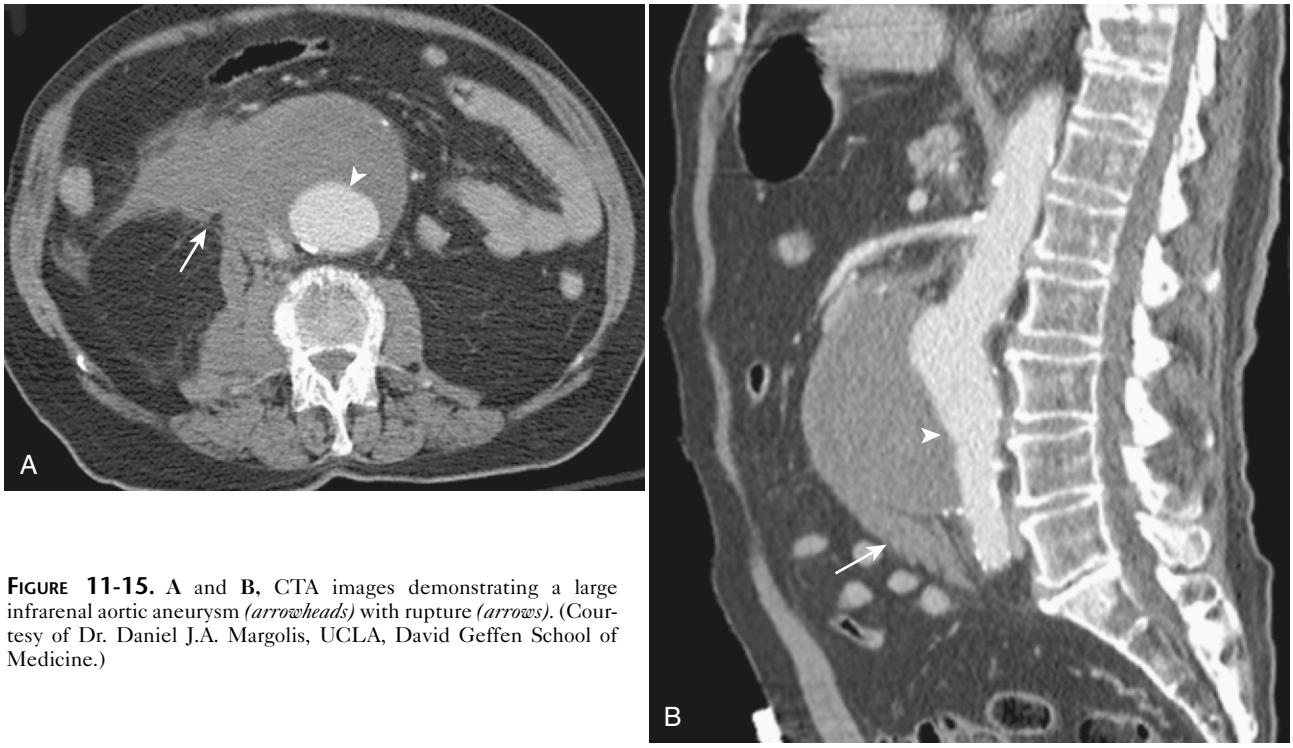


Figure 11-15. **A** and **B**, CTA images demonstrating a large infrarenal aortic aneurysm *(arrowheads)* with rupture *(arrows)*. (Courtesy of Dr. Daniel J.A. Margolis, UCLA, David Geffen School of Medicine.)

MRI can detect the cuff of soft tissue inflammation surrounding the aneurysm, thickening of the aneurysm wall, perianeurysmal and retroperitoneal fibrosis, and adherence of the anterior aneurysm wall to adjacent structures (Fig. 11-16). On precontrast CT images the thickened aortic wall has soft tissue attenuation that enhances after intravenous contrast administration. The arterial wall may become undistinguishable from periaortic fibrosis. Periaortic fibrotic tissue can adhere to the ureters, small bowel, duodenum, and inferior vena cava causing entrapment of these structures and further complicating surgical repair. Preoperative imaging is of great importance in the planning of surgical and endovascular treatment of patients with AAA. Important preoperative features and measurements done on CTA include the maximum transverse aneurysm diameter, relation of the aneurysm to the renal arteries, presence of a proximal neck (renals to aneurysm distance), presence of a distal neck (aneurysm to aortic bifurcation distance), extension of the aneurysm into the iliac arteries, identification of concomitant aneurysms, and appearance of the access pathway including femoral and iliac arteries. Some conditions that limit the delivery of an endograft include very large AAA, markedly tortuous aorta, pelvic arteries with abrupt angles, and extensive calcification causing luminal narrowing. Any of those factors can represent an exclusion criterion depending on the specific anatomy, and the degrees of angulation and stenosis. They determine the suitability or unsuitability for endovascular treatment, and cautious analysis of the images in conjunction with the surgical/interventional team is crucial to decrease the risk of endoleaks, attachment failures, graft migration, and conversion to open repairs. MRA has shown similar properties as CTA for the diagnosis of and for preoperative planning for AAA, providing precise information about the location and extent of the aneurysm. Conventional arteriography is currently used as an adjunct imaging modality for evaluating patients with complex vascular anatomy, for aneurysms that could not be fully characterized with CTA and MRA, and for intraprocedural graft positioning.

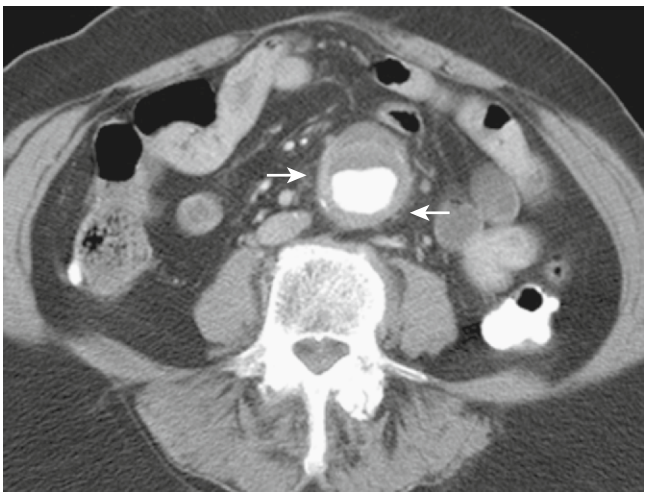


Figure 11-16. CTA demonstrating an aortic aneurysm with enhancing aortic wall, ill-defined margins, and mild stranding of the adjacent fat compatible with inflammatory aortic aneurysm. (Courtesy of Dr. Daniel J.A. Margolis, UCLA, David Geffen School of Medicine.)

Treatment. Treatment is usually recommended for AAAs measuring 5.5 cm or larger to eliminate the risk of rupture, and for symptomatic AAAs regardless of their diameter size. Ruptured aneurysms with hemodynamic compromise require immediate surgical repair. In selected cases, endovascular intervention might be indicated for the management

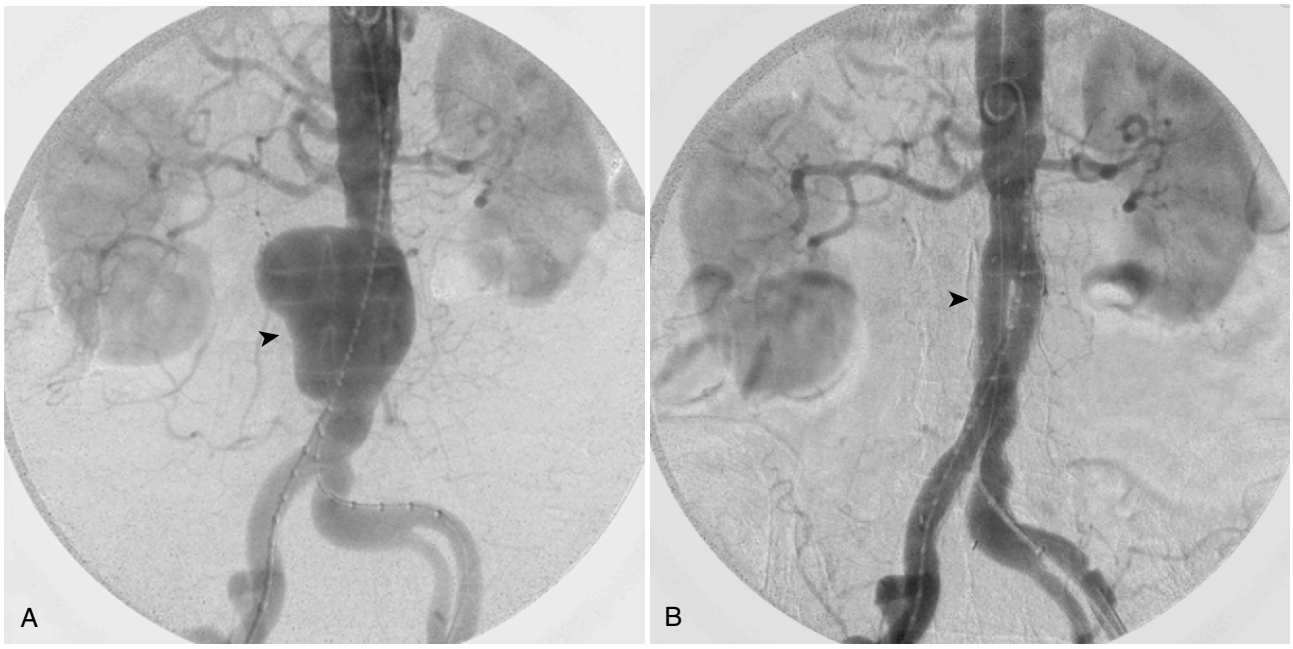


FIGURE 11-17. **A,** Conventional catheter angiography with bilateral marked catheters in place demonstrating a large lobulated infrarenal aortic aneurysm with 4-cm proximal neck suitable for endovascular repair. **B,** Post endovascular repair image demonstrates complete exclusion of the aneurysm with no endoleak and preservation of the renal and hypogastric arteries.

of ruptured aneurysms that remain hemodynamically stable. Patients with aneurysms 4.0 to 5.4 cm in diameter should have imaging follow-up every 6 to 12 months for early detection of expansion. Currently, it is not recommended that patients with asymptomatic aneurysms less than 5.0 cm in men, or less than 4.5 cm in women, undergo elective repair. Higher mortality rates are seen in patients who have emergent repair rather than elective surgery, and it is for this reason that early detection and surveillance of high-risk populations remain crucial in the treatment of abdominal aortic aneurysms.

Open surgical treatment is usually offered to hemodynamically unstable patients and to patients who want an elective surgical repair. It involves a midline transabdominal incision or a left retroperitoneal flank access with subsequent clamping of the aorta, excision of the aneurysm, and placement of a synthetic graft. Aortic clamping can be linked to the development of significant morbidities such as ischemia of the lower extremities or bowel, or paraplegia.

Postoperative complications related to an elective open surgical approach vary between 0.4% and 10% and include pseudoaneurysm formation, graft infection, enteric fistulas, and graft limb occlusion.

Treatment of pararenal and suprarenal aortic aneurysms is more complex, since it requires cross-clamping of the aorta above the visceral arteries and sometimes branch vessel reimplantation, increasing operative morbidity and mortality, with up to 15% of the patients requiring temporary dialysis and 5% going into permanent renal failure. The overall 5-year survival rate among these patients is 40% to 50%.

Endovascular aortic aneurysm repair (EVR) offers a less invasive approach to reduce the operative morbidity and mortality. Blood losses are significantly reduced since the graft is placed intravascularly via femoral access, and, likewise, the risk for lower limb and visceral ischemia is lower since aortic clamping is not performed. EVR is offered to patients who are undergoing repair for asymptomatic AAA or symptomatic nonruptured AAA or those who are at high risk surgically and have significant comorbidities. The role of the endograft is to exclude the aneurysmal sac from the arterial circulation and decrease the mechanical stress over the vessel wall (Fig. 11-17). Studies have shown benefits in the perioperative mortality and a 30-day morbidity and mortality rate of less than 3% with EVR. Despite its short-term advantages, long-term survival and quality-adjusted life expectancy do not seem to vary significantly when compared with open surgery repair.

A common complication related to stent graft placement is the development of endoleaks (Fig. 11-18). An endoleak is defined as an incomplete exclusion of the aneurysmal sac. The estimated incidence oscillates in the 10% to 45% range, and currently lifelong imaging follow-up is recommended in order to detect endoleaks and other graft-related complications. Delayed rupture is rare (0.1% to 1% per year) and has been associated with type I and type III endoleaks, graft migration, and endograft kinking. When type I or type III endoleaks are recognized, immediate treatment is indicated through graft extension, reintervention, or conversion to open repair. Other serious complications include graft infection and occlusion (Fig. 11-19). Occlusion is usually due to distortion of one of the graft limbs and can cause lower extremity ischemia if not promptly treated. Continuous aortic expansion at the "neck" can cause endograft migration and delayed type I endoleak, but this is rare since endografts are oversized at the time of placement by up to 20% to ensure adequate seal.

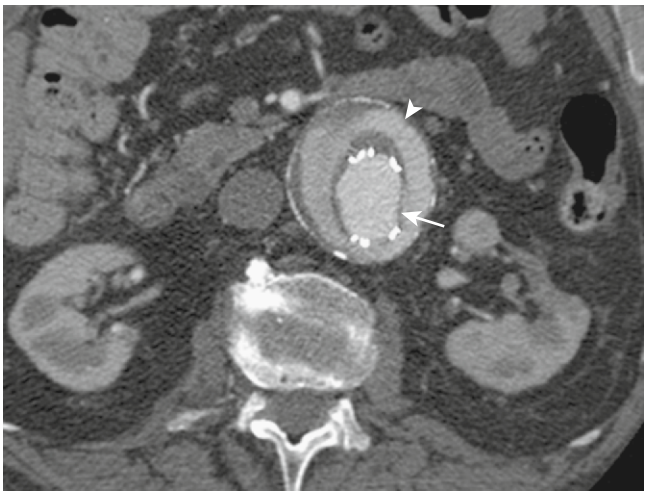


Figure 11-18. CTA demonstrating the proximal end of the stent graft *(arrow)* and prompt enhancement of the surrounding aneurysm sac *(arrowhead)* consistent with type I endoleak. (Courtesy of Dr. Daniel J.A. Margolis, UCLA, David Geffen School of Medicine.)



Figure 11-19. CTA obtained after AAA repair with endografts. The patient presented with fever and elevated white blood cell count. Images demonstrate aortic wall enhancement and a small amount of periaortic fluid *(arrowheads)* consistent with infected aortic stent graft. (Courtesy of Dr. Daniel J.A. Margolis, UCLA, David Geffen School of Medicine.)

Traumatic Abdominal Aortic Injury

Traumatic abdominal aortic injuries are relatively rare, accounting for only 4% to 6% of all aortic injuries. Despite medical advances, it remains one of the most lethal causes of early death in trauma with a mortality rate that ranges between 50% and 80%. Penetrating injuries to the abdominal aorta that cause complete transection are uncommonly seen in the hospital setting due to rapid exsanguination. The most common causes of traumatic penetrating injuries to the aorta include gunshot wounds and stab wounds. Besides the obvious risk that a direct aortic injury implies, the high mortality is also linked to the high incidence of associated injuries to other organs. Abdominal aortic injuries due to penetrating trauma have lower mortality rates when compared with thoracic aortic injuries due to the compartmental retroperitoneal location of the abdominal aorta. However, when the aortic rupture extends beyond the retroperitoneum into the suprarenal segment or intraperitoneally, the protective effect of retroperitoneal tamponade is lost and the risk of death increases. Common complications seen in patients who survive penetrating injuries include arteriovenous fistula and pseudoaneurysm formation (see Fig. 11-11).

Blunt abdominal aortic injuries are due to direct forceful compression of the aorta against the spine, as seen with fast deceleration seat belt injuries. These more frequently result in intimal tears or traumatic dissection, but pseudoaneurysms, thrombosis of the aorta, and aortic rupture may occur. Traumatic abdominal injuries account for 17% of abdominal aortic dissections, which can lead to other serious comorbidities in up to 60% of the cases, such as branch vessel occlusion with visceral or limb ischemia and paraplegia. Due to its high mortality, a high clinical suspicion index is required to make a timely diagnosis. Acute manifestations include acute abdomen, neurologic deficits, and acute arterial insufficiencies. MD-CTA is currently the imaging technique of choice. CTA can detect multiple organ and vascular injuries, and can characterize aortic dissections and recognize associated complications such as aortic thrombosis, false aneurysm formation, and aortic rupture. Indirect findings of aortic rupture and dissection are retroperitoneal hematoma and abnormal opacification of the aortic lumen. A small amount of peritoneal fluid and hemoperitoneum can be easily detected with MDCT in cases of trauma, and therefore close attention has to be paid to the dependent portions of the peritoneal cavity such as Morrison's pouch, paracolic gutters, areas adjacent to the bladder, and pelvis and perihepatic and perisplenic spaces. Attenuation measurements can be obtained for all areas of fluid accumulation in order to help differentiate between simple fluid, blood (hematoma), and active bleeding. CT attenuation values for free blood measures between 20 and 40 Hounsfield units (HU), while clotted blood measures between 40 and 70 HU and active bleeding in contrast-enhanced images shows density measurements within 10 HU of the density of vascular contrast material seen within an adjacent major vessel. Thrombosis of the false lumen as well as aortic aneurysm formation may mask aortic dissection in CT imaging. Catheter angiography of the abdominal aorta is indicated if questions persist after MD-CTA has been performed. The thoracic aorta must always be examined as well to rule out serious injuries at this level.

The management of traumatic aortic injuries varies depending on the specific lesion, the clinical condition of the patient, and the available resources. Traumatic aortic injury is frequently associated with other significant injuries, and a delay in treatment can be detrimental.

Emergency surgery is recommended in medically uncontrolled hemodynamic shock and lower limb or other end-organ acute ischemia.

Endovascular treatment using stent grafts and noncovered stents has been widely reported as a treatment option in acute traumatic abdominal aortic injuries and dissections. Stent graft placement is usually performed in hemodynamically stable patients with viable extremities. This therapeutic method is less invasive, offers a shorter time of surgical intervention, and avoids aortic cross-clamping. Because there is no need for open surgical exposure, blood loss is reduced to a minimum, and the risk of infection and contamination

of the graft due to peritoneal soiling from intestinal injury decreases dramatically. If endograft repair is being considered, precise measurements of the aorta are obtained from the MD-CTA images in order to ensure that the proper stent graft size is selected. Grafts must be placed in order to cover the entire extent of the injury, whether dealing with pseudoaneurysm or a dissection. Sparing of the ostia is preferred to avoid inducing visceral ischemia. Associated arteriovenous fistulas or pseudoaneurysms of branch vessels can be treated at the same time with coil embolization if the patient's hemodynamic condition permits. In cases of extensive flow-limiting aortic dissection causing infradiaphragmatic ischemia, percutaneous balloon fenestration of the dissection flap to reestablish flow is a therapeutic alternative.

Nontraumatic Aortic Dissection

Spontaneous isolated dissection of the abdominal aorta is a rare event with an estimated incidence of 2% to 4% and is more frequently the extension of a thoracic aortic dissection. It is caused by a tear in the intima, usually associated with degeneration of the media or cystic medial necrosis. Blood separates the intima from its surrounding media creating a false lumen filled with blood, which can propagate distally or proximally to the initial tear. Isolated abdominal aorta dissections more frequently originate below the renal arteries with some originating even lower, near the inferior mesenteric artery. Propagation of the dissection can involve branch vessels including the renals and the celiac and mesenteric arteries or can extend into the iliac arteries (Fig. 11-20). The renal arteries are involved most frequently. The most common predisposing factors to abdominal aortic dissection are hypertension and atherosclerosis. Other etiologies include penetrating atherosclerotic ulcer, aortic aneurysms, trauma, Marfan syndrome, fibromuscular dysplasia, and iatrogenic causes secondary to surgical or angiographic procedures. Clinical presentation is usually characterized by sudden onset abdominal or back pain, but it may vary from completely asymptomatic to frank visceral or limb

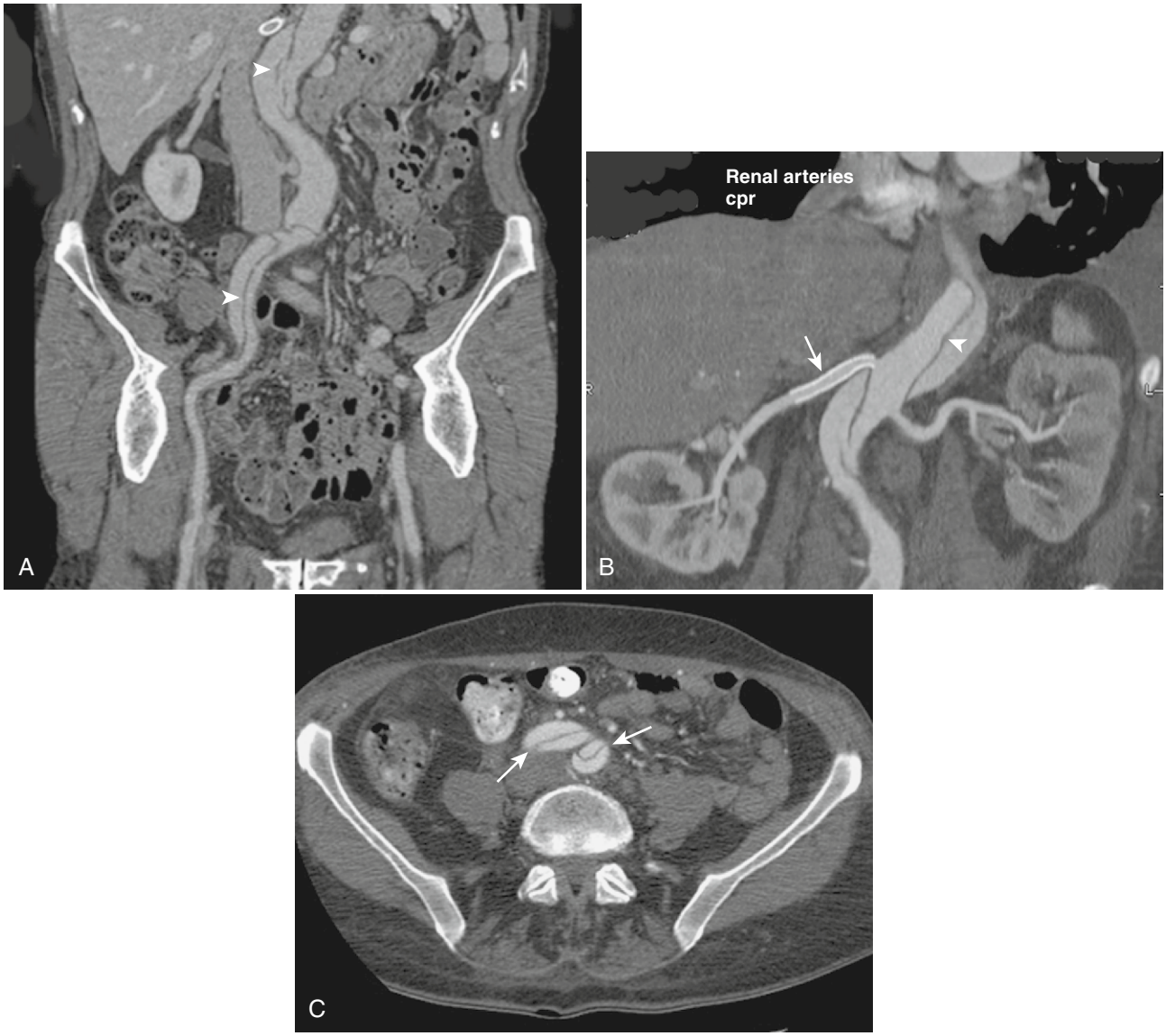


FIGURE 11-20. **A** to **C,** CTA demonstrating a complex dissection flap extending from the thoracic aorta along the abdominal aorta *(arrowheads)* and into the iliac arteries *(arrows).* The right renal artery had previously undergone stenting, and the renal flow is preserved.

ischemia. MD-CTA allows a fast, accurate, and precise diagnosis. CTA findings of aortic dissection include visualization of an intimal flap separating the true and false lumen, inhomogeneous enhancement of the aortic lumen, presence of a double channel in the aorta, and asymmetric vessel wall thickening. Unenhanced images can help identify internal displacement of the intimal calcifications. The imaging findings that help distinguish the false lumen from the true lumen include the "beak" sign, which represents a wedge-shaped area of the false lumen at the edge of the dissection; the "cobweb" sign, manifested as low-attenuation linear densities that represent residual strands of medial tissue that did not separate completely from the intima during the dissection and are floating in the false lumen; and a relatively larger cross-sectional area of the false lumen with respect to the true lumen. CT can also assess the extent of the dissection and possible involvement of visceral and iliac vessels (see Fig. 11-20). MRA is also a highly accurate diagnostic tool that has the advantage of showing different sequences and can even demonstrate flow dynamics with the implementation of flow-enhanced sequences and cine images. In addition, some of the non-contrast MRA sequences offer an alternative to those patients in whom the use of contrast is limited because of severe impairment of the renal function or iodine allergy. Unfortunately, MRI/MRA has restricted availability in the emergency setting, is usually more time-consuming, and has limited applicability in emergency patients who may have noncompatible implants, metallic fragments, and numerous monitoring devices attached. MRI is then usually reserved for stable patients to confirm the diagnosis after equivocal imaging findings in previous exams.

Conservative treatment of spontaneous abdominal dissection is usually administered in cases of asymptomatic chronic dissection and includes antihypertensive medication as well as close clinical and imaging follow-up. Treatment of spontaneous abdominal dissection is necessary in the presence of associated rupture, lower extremity ischemia, unremitting pain, and associated aneurysms with high risk of rupture. Surgical treatment in patients with ruptured abdominal aorta consists of emergent aortic repair with tube grafts or aortobifemoral bypass grafts. The objective of surgical treatment is to create a reentry point that decompresses the false lumen and allows perfusion of the major branches.

Endovascular treatment of aortic abdominal dissection has been successfully reported in multiple cases. In short-segment dissection, the rationale is to bring the intimal flap back to the aortic wall and compress it in order to close the false lumen. An uncovered stent can be used to maintain the false lumen compressed and excluded.

Acute Abdominal Aortic Occlusion

Acute aortic occlusion (AAO) usually results from thrombosis or embolism into a previously diseased aorta. The differentiation between embolus and thrombus can be difficult. Acute thrombosis is the most common cause of acute aortic occlusion and usually results from end-stage atherosclerotic aortoiliac disease in association with low flow states secondary to cardiac dysfunction or dehydration.

Emboli can also be the source of acute occlusion, more frequently originating from the heart in patients with a history of arrhythmia, myocardial infarction, endocarditis, or cardiac tumors. Other sources that have been described include emboli from thoracic aortic aneurysms and ulcerated plaques, and, rarely, from paradoxical embolization from a deep venous thrombus in patients with aortic septal defects or other causes of right to left shunt.

Acute thrombosis of an AAA causing AAO is rare. Aortic dissection can also cause AAO by propagation of the dissection to the aortic bifurcation and compression of the true lumen by the false lumen. This is also a rare event and is considered an emergency requiring urgent surgical repair or fenestration of the dissection. Less common causes of acute aortic thrombosis include trauma, iatrogenic injuries, and hypercoagulable states (antithrombin III, protein C/protein S deficiencies, lupus, among others). AAO is usually preceded by a progressive stenosis with associated signs and symptoms of chronic ischemia, such as lower extremity claudication and rest pain. A partial occlusion allows for collateral circulation to build over time and maintain supply even in the setting of a superimposed acute event; these patients present with worsening claudication or pain at rest. However, presentation may be more severe, as symptoms typically get aggravated with development of cyanosis below the level of the umbilicus, pallor and coldness of the lower extremities, absent femoral pulses, and neurologic symptoms ranging from numbness and weakness to complete anesthesia and paralysis. The diagnosis of AAO can be made with ultrasound, CTA, and catheter angiography. The use of MRA is limited for the various reasons cited previously but can also be used if readily available. All cross-sectional modalities can also detect branch vessel involvement and determine the extension of the thrombus; however, ultrasound is operator dependent and can be limited by the patient's habitus and bowel gas interposition. MD/CTA scanning can evaluate the complete thoracoabdominal aorta and the cardiac chambers when looking for a cardiac source of emboli (Fig. 11-21). The treatment of AAO requires immediate systemic anticoagulation to prevent thrombus propagation, hydration, and optimization of cardiac and renal function. As mentioned above, surgery is the first treatment option and should be performed promptly. A delay in treatment can predispose to the development of limb ischemia, compartment syndrome, thrombus propagation to renal and mesenteric arteries, reperfusion syndrome, limb loss, and even death. Surgery usually involves aortic repair attempt, aortobifemoral bypass, or, in high surgical risk patients, an axillobifemoral bypass. Despite surgical intervention, acute abdominal aortic occlusion has a high mortality rate of approximately 50%. In select patients, catheter angiography may provide a therapeutic alternative if there is realistic probability of reestablishing patency and signs of irreversible ischemia are not yet present (Fig. 11-22).

Abdominal Compartment Syndrome

Compartment syndrome (CS) is defined as an increased pressure in a body compartment that causes deficient tissue perfusion and risks tissue and organ viability. Abdominal CS (ACS) is a critical condition characterized by a continuous elevation of the intra-abdominal pressure (IAP, normal 0 to 5 mm Hg) associated with abdominal distention and leading to respiratory insufficiency with decreased lung capacity, increased airway pressure, hypoxia, hypercarbia, reduced cardiac

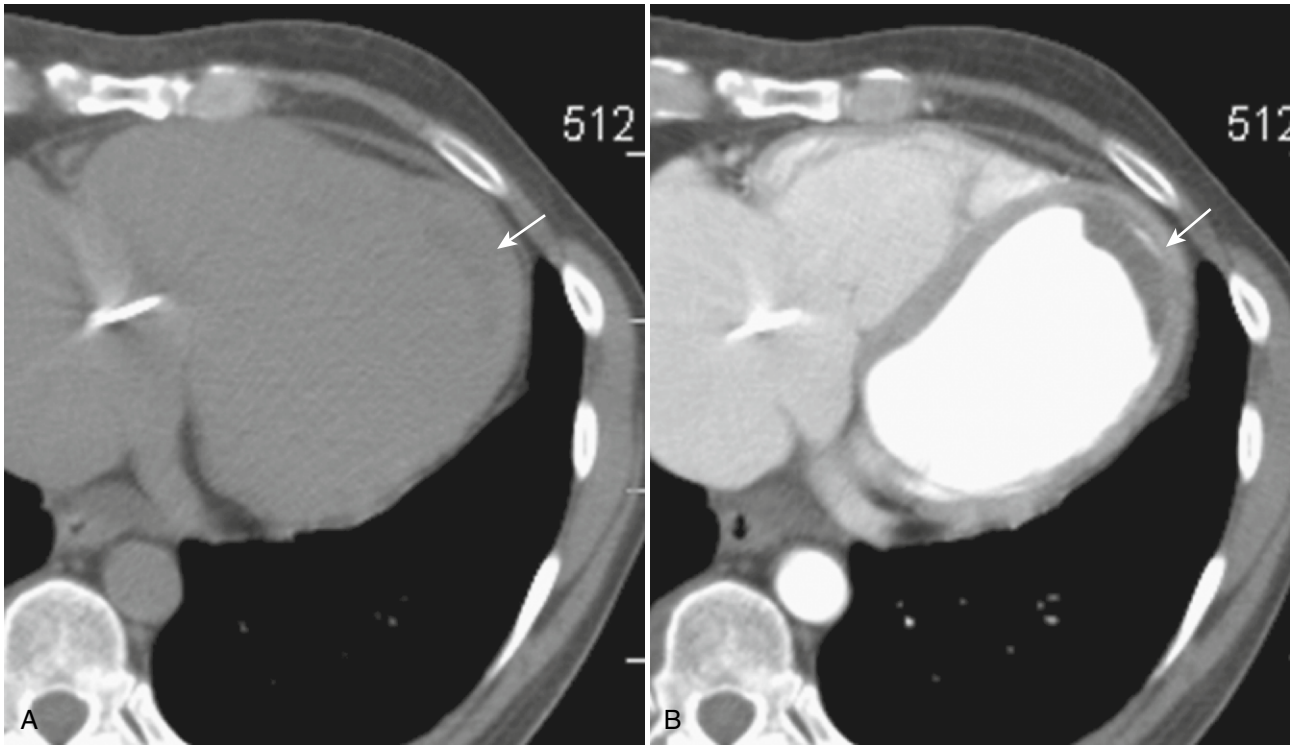


FIGURE 11-21. **A** and **B**, Pre- and postcontrast CT images showing an intraventricular apical hypodensity *(arrows)* surrounded by contrast in the contrast-enhanced CT, consistent with an intraventricular apical thrombus.

output, oliguria, and eventually multiorgan failure. Increased intracranial pressure and impairment of the portosystemic circulation can also result from the rise in central venous pressure. Abdominal trauma with hepatic, vascular, and/or splenic injury is the most common cause of acute ACS. Other causes are massive fluid resuscitation and packing for uncontrolled hemorrhage. Ruptured aortic aneurysms can cause ACS by increasing abdominal fluid volume (Box 11-4).

CT findings of ACS include compression of the inferior vena cava, hemoperitoneum or acute ascites, bowel wall thickening with increased wall enhancement, and massive abdominal distention with an increased anteroposterior/transverse abdominal diameter ratio (greater than 1:0.80), also known as the "round belly" sign. The most accurate way to diagnose ACS is to measure IAP. This can be done directly through insertion of a catheter into the peritoneal cavity, or indirectly through the bladder. When IAP measurements are consistently above 20 to 25 mm Hg, abdominal compartment syndrome is diagnosed and immediate decompression is mandatory. Abdominal decompression can also be done prophylactically after laparotomy when there is evidence of massive edema, tight closure, packing, and hemodynamic instability. In the case of ACS abdominal decompression should bring immediate clinical improvement. The mortality rate is high, approximating 70%.

Vascular Emergencies of the Mesenteric-Visceral Arteries

Splanchnic Vascular Trauma

When penetrating or blunt abdominal trauma occurs, there can be isolated vascular injuries, isolated visceral injuries, or a combination of both. Unstable patients with extensive visceral organ and vascular involvement are taken directly to surgery. When arterial and vascular injury are suspected and the patient's hemodynamic status permits, they can be taken to CT and then to angiography for embolization. Patients who have a history of previous liver trauma, biopsy, or other interventional procedure and present with delayed hemobilia constitute a separate group that will also require angiography to evaluate for the presence of an arterial to biliary fistula that can be treated with embolization.

The spleen is a commonly affected solid visceral organ in abdominal trauma. It is well vascularized and in cases of severe trauma splenic injury can lead to hemodynamic instability due to continuing hemorrhage. In the case of severe trauma, immediate surgery for splenic repair or resection may be required. When clinically feasible, CT evaluation is the ideal modality to characterize the degree of splenic injury. Embolization is a management alternative in patients with injured but viable spleen. Both selective embolization of focal areas of extravasation and embolization of the main splenic artery have been described. Selective embolization carries a risk of focal infarcts and abscess formation. Embolization of the main splenic artery decreases the overall flow to the spleen allowing the clotting mechanisms to stop the bleeding but without creating an infarction, as collateral flow via short gastric arteries is maintained.

Nontraumatic Emergencies of the Mesenteric and Visceral Vasculature

Acute Mesenteric Ischemia

This is a critical condition, poorly tolerated, with high mortality rates even in the setting of early intervention. A delayed diagnosis further complicates the overall prognosis of the patient and is almost always lethal. More than

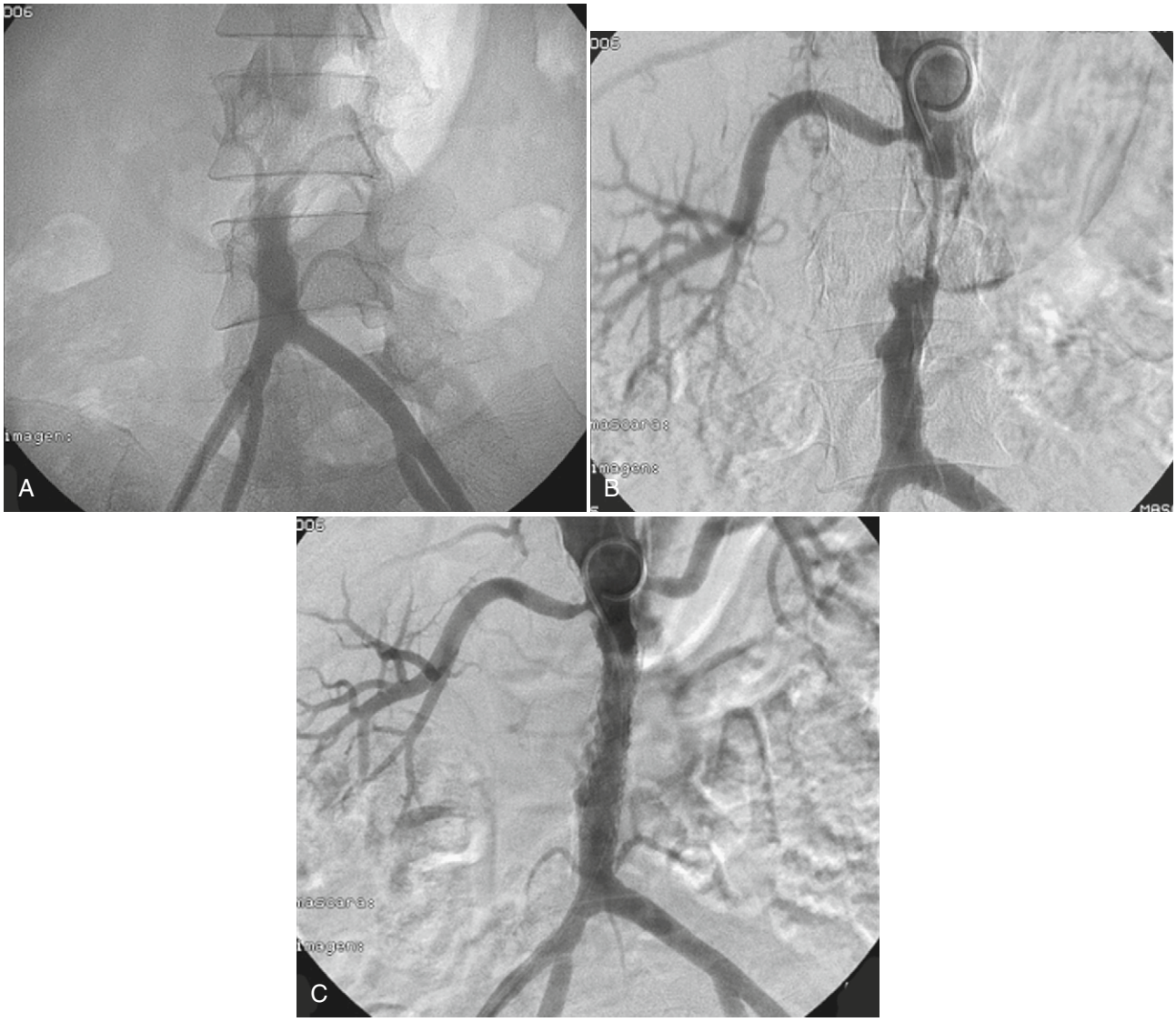


Figure 11-22. **A** to **C,** A 52-year-old diabetic female patient who presented with unstable angina. Conventional angiogram demonstrates abdominal aortic occlusion. After crossing the occlusion, simultaneous injection via "pigtail" catheter and access sheath better shows the length of the occluded segment. Following stent placement, patency was reestablished.

Box 11-4. **Risk Factors for the Development of Acute ACS**

Penetrating or blunt trauma
Retroperitoneal hemorrhage
Ruptured abdominal aortic aneurysm
Pancreatitis
Massive ascites
Neoplasm
Pneumoperitoneum
Burns of the abdominal wall—extrinsic compression
Massive fluid resuscitation
Postoperative forced closure of abdominal wall
Bowel edema
Postoperative ileus
Liver transplantation
Intra-abdominal packing

50% of the cases are embolic in origin; 20% are due to thrombosis of preexistent stenotic lesions, 20% are related to low flow states (nonocclusive mesenteric ischemia), and 10% are due to portomesenteric venous thrombosis. The classic presentation is generalized abdominal pain out of proportion to the physical findings. However, since this is a disease process identified predominantly in the elderly, the presentation can be more subtle, with minimal findings on physical exam and vague pain.

The classic plain film findings of gas in the wall of the affected bowel loops (pneumatosis intestinalis) and in the portal vein occur late in the process, once bowel infarction has already occurred. Early signs are nonspecific and include bowel thickening and dilatation. CT/CTA is the preferred initial imaging modality to evaluate for suspected bowel ischemia, as it allows visualization of the mesenteric arteries, veins, bowel luminal diameter, and wall thickness.

Catheter angiography remains an important diagnostic modality. Mesenteric embolic occlusion characteristically appears as convex filling defects outlined by contrast. Most of the emboli are identified in the proximal segment of the superior mesenteric artery (SMA), resulting in profound ischemia in the absence of collateral flow. The standard management is surgical embolectomy or bypass with resection of the nonviable bowel segment. If there are no signs of irreversible bowel ischemia, endovascular intervention may be indicated. Catheter embolectomy with or without thrombolysis can be attempted.

In the absence of an embolic source, arterial thrombosis secondary to an underlying stenotic lesion is the most frequent etiology. Usually patients have associated history of peripheral vascular disease. Catheter thrombolysis followed by treatment of the underlying stenosis with angioplasty and stenting is the preferred approach, provided that there are no signs of irreversible bowel ischemia.

Nonocclusive mesenteric ischemia is a syndrome characterized by low flow in the superior mesenteric artery without evidence of embolus, thrombus, or any other fixed lesion. It is more frequently encountered in hypotensive patients undergoing infusion of vasopressor agents.

Acute Gastrointestinal Bleeding

Acute gastrointestinal bleeding is classified into upper and lower causes based on its origin proximal or distal to the ligament of Trietz. Upper gastrointestinal (GI) bleeds are approximately five times more common than lower gastrointestinal causes, and lower gastrointestinal bleeding originates in the colon in approximately 80% of the cases. Localization of the bleed is critical to determine management. Upper bleeds occur secondary to gastritis and gastric or duodenal ulcers, while the most common cause of lower GI bleed is colonic diverticulosis followed by angiodysplasia. Depending on the site of origin (proximal or distal) and the severity of the hemorrhage, a GI bleed will manifest as hematemesis, melena, and/or hematochezia (Fig. 11-23). A positive nasogastric aspirate and lavage is an effective way to determine if there is an upper GI bleed. In these patients, the initial evaluation is performed with endoscopy, which not only confirms the diagnosis and identifies the source in more than 95% of the cases, but also can offer therapy with sclerotherapy, clipping, cauterization, or banding. With lower GI bleeds, identification of the bleeding site with colonoscopy is more difficult, with an overall reported success rate of 70%. More than 85% of lower GI bleeds resolve spontaneously with supportive therapy alone (Fig. 11-24). It is crucial that all GI-bleeding patients be stabilized, with large bore venous accesses placed for fluid resuscitation and transfusion as needed. If the source of bleeding is still unknown despite endoscopy and colonoscopy, there are various diagnostic imaging alternatives available. One option is to perform a tagged red-blood cell nuclear scan, which can detect bleeding rates as low as 0.1 mL/min; however, its ability to localize the bleeding to a particular segment of bowel is limited. Catheter angiography is another option, which detects a bleeding rate of approximately 0.5 to 1 mL/min. Given the often intermittent nature of GI bleed, and the time required to stabilize and transfer the patient, angiograms are positive in only about 50% of the cases. However, if performed immediately after a positive tagged red-blood cell scan, or when obtained during an episode of active bleed, the likelihood of finding the source increases. MD-CTA is a promising noninvasive first-line diagnostic modality that offers fast scanning times that vary between 6 and 20 seconds and allows for accurate diagnosis or exclusion of active gastrointestinal hemorrhage by comparing pre– and post–intravenous contrast images and identifying abnormal hyperattenuating areas of extravasated contrast material within the bowel lumen.

During catheter angiography, it is important to first study the vessel that has the highest likelihood of being the source of bleeding with selective angiograms. Visualization of both the arterial and venous phases is required, as some bleeds may be caused by varices related to portal hypertension or

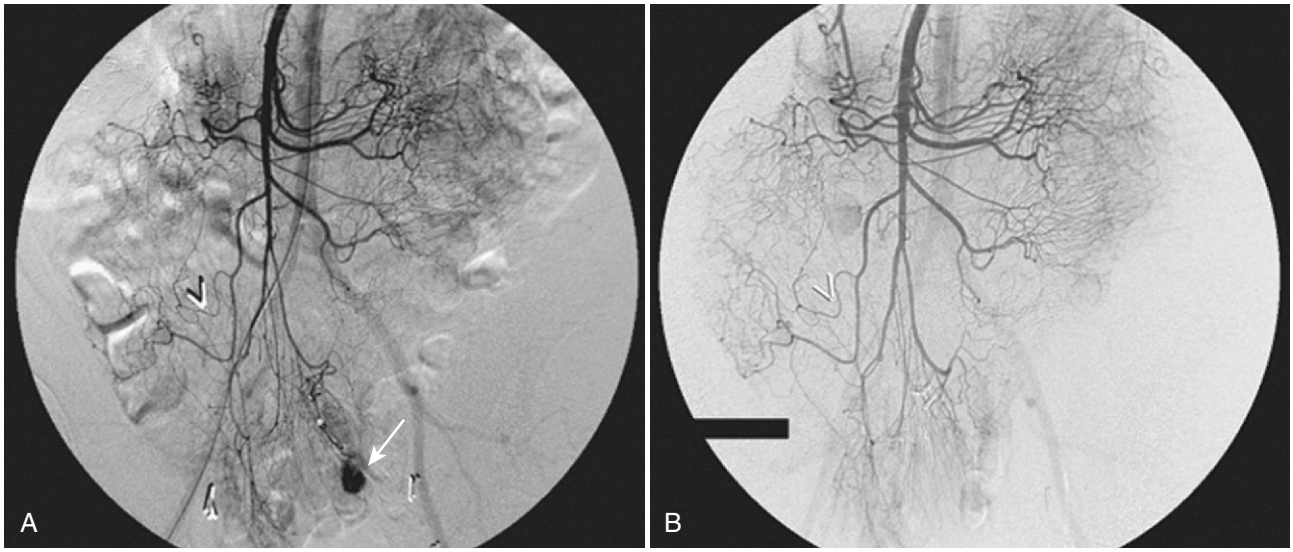


FIGURE 11-23. **A** and **B,** A 75-year-old patient with recurrent lower gastrointestinal hemorrhage. SMA catheter angiography shows a focal area of abnormal contrast pooling fed by one of the distal ileal branches most consistent with a small bowel hemangioma that caused recurrent bleeding episodes. Following coil embolization, the abnormal enhancement was no longer identified and the symptoms resolved.

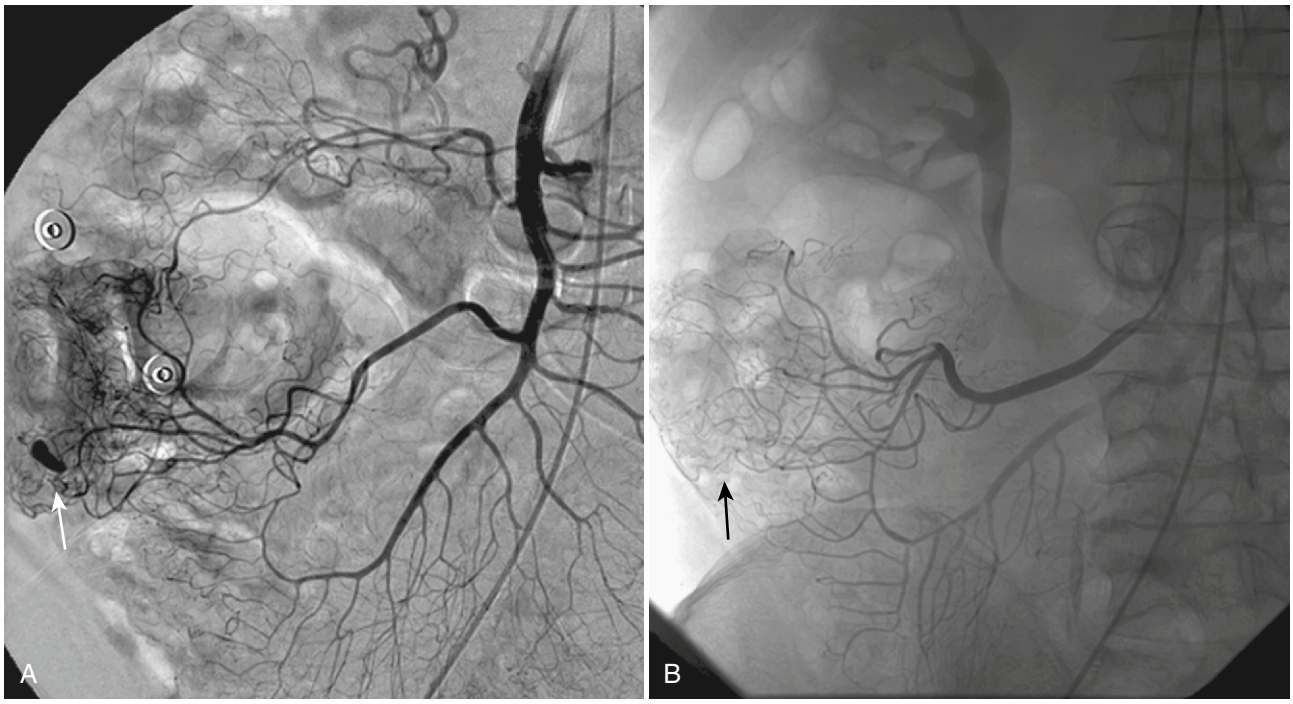


Figure 11-24. **A** and **B,** A patient with hematochezia. Selective SMA angiography demonstrates contrast extravasation at the level of the cecum arising from a branch of the ileocecal artery compatible with a diverticular bleed *(white arrow)*. Subselective embolization could not be performed, but the sheath was kept in place. Repeat angiography the next morning demonstrated spontaneous resolution of the bleed with supportive medical treatment *(black arrow)*.

thrombosis. The presence of contrast extravasation into the bowel is diagnostic. Extravasation is usually seen during the arterial phase and persists after venous washout before slowly dissipating. Catheter-directed therapy options include embolization and vasopressin infusion. When superselective catheterization of the bleeding branch is possible, it can be followed by embolization with Gelfoam, large particles (polyvinyl alcohol or spheres), and microcoils to stop the bleeding. When the bleeding is diverticular, postpolypectomy, or mucosal in origin, then intra-arterial vasopressin infusion is an effective alternative. Vasopressin is not effective for bleeding secondary to pseudoaneurysms or arteriovenous malformations, and is contraindicated in cases of bleeding secondary to ischemic bowel. After embolization, patients should be monitored closely, as approximately 20% of them may have recurrent bleed and some may develop bowel ischemia.

Aneurysms of the Visceral Arteries

Aneurysms of the visceral arteries are rare in comparison to aortoiliac and femoropopliteal aneurysms. The most commonly affected vessels are the splenic, hepatic, and superior mesenteric arteries. The most frequent etiologies for true aneurysms are atherosclerosis and vasculitis, and for pseudoaneurysms pancreatitis, trauma, and infection. The majority of these aneurysms are asymptomatic and discovered as an incidental finding, but some may present with rupture.

Splenic artery aneurysms are the third most common intra-abdominal aneurysm, after aortic and iliac aneurysms, and account for 60% of the cases of visceral aneurysms (Fig. 11-25). Most are saccular, single, and less than 3 cm in diameter. As with other intra-abdominal aneurysms, common causes include pancreatitis, atherosclerosis, trauma, and fibrodysplastic disease. Interestingly, these aneurysms are four times more prevalent in females than males, with higher incidence among pregnant and multiparous women. The catastrophic complication of rupture in pregnancy results in high mortality rates in the order of 70% to 90% for both the mother and fetus. Treatment options include surgical resection and embolization. Endovascular stent graft placement can be another option in select cases.

Hepatic artery aneurysms represent approximately 20% to 40% of all splanchnic artery aneurysms. They can be extrahepatic or intrahepatic, with the former representing about two thirds of cases. The etiologies of hepatic aneurysms include atherosclerosis and trauma. Less common causes include pancreatitis, vasculitis, hereditary telangiectasias, cystic medial necrosis, liver abscess, and tuberculosis.

The SMA is the third most common location for visceral artery aneurysms. The frequency of these aneurysms is estimated at 5.5% of all splanchnic aneurysms and less than 0.5% of all intra-abdominal aneurysms. In the past, it was believed that most of these were of infectious etiology; however, more recent reports have suggested that most cases are due to atherosclerosis. Collagen vascular disorders and polyarteritis nodosa have also been implicated. These aneurysms usually manifest with severe mid-epigastric pain.

Involvement of the celiac, ileocolic, and gastroduodenal arteries has also been described. Aneurysms of the gastroduodenal artery are often associated with pancreatic pathology and can cause bleeding in the peritoneal or retroperitoneal

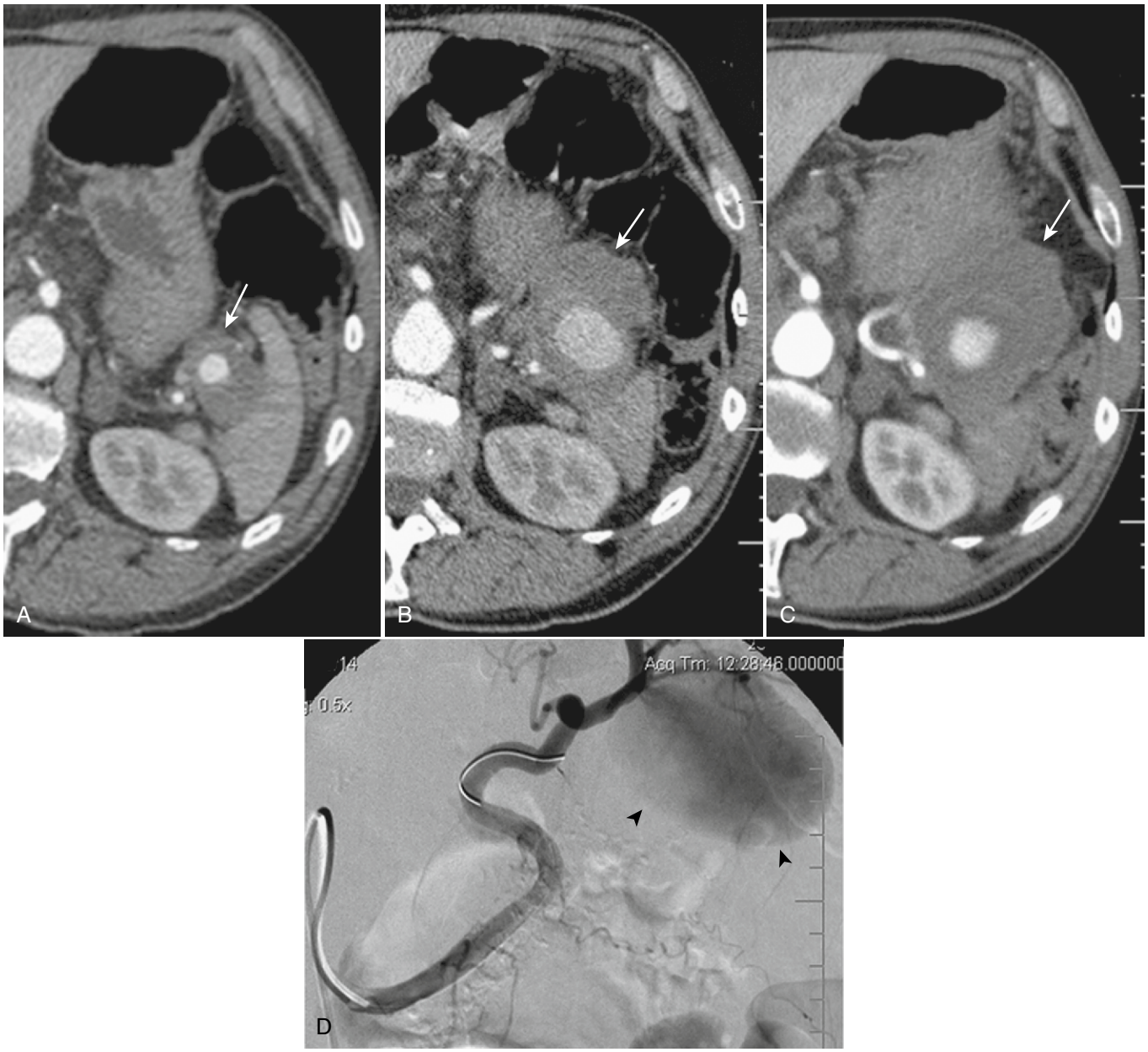


FIGURE 11-25. **A** to **D,** A patient with chronic pancreatitis and enlarging splenic artery pseudoaneurysm. The patient did not want to undergo any invasive procedures, so he was followed with serial CTA every 6 months, where progressive enlargement of the aneurysm was demonstrated *(arrows);* in the last follow-up dense crescents worrisome for impending rupture were identified. Catheter angiography **(D)** showed the aneurysm (*arrowheads*) had increased further in size; the patient was then taken to surgery for aneurysm resection.

space and more rarely into the portal vein or into a pancreatic pseudocyst (Fig. 11-26). In general, elective repair is recommended for splachnic aneurysms when they reach a size greater than 2 to 2.5 cm. Pseudoaneurysms are always considered to carry a high risk of rupture, and so repair is recommended on detection regardless of their size.

Traumatic Injury of the Renal Arteries

The renal arteries are the most frequently injured branch vessels of the abdominal aorta during blunt trauma. More than 80% of renal injuries are mild, and patients present with stable hematomas or hematuria without visible injury and can be managed conservatively. On the other end of the spectrum are the completely shattered kidney and the avulsion of the vascular pedicle with complete devascularization, which requires emergent surgery. Patients with intermediate-grade injuries can usually be managed with angiographic interventions, although surgical repair may be necessary if there is hemodynamic compromise that requires rapid control of hemorrhage.

At CT/CTA, a nonenhancing kidney, a large perirenal hematoma, and active contrast extravasation are all signs of severe renal trauma with vascular involvement; a nonenhancing renal artery or vein is a critical finding that indicates thrombosis, and dissection or transection has to be considered in the diagnosis. Extravasation and pseudoaneurysm formation are usually seen in patients with penetrating trauma. Angiography is indicated when

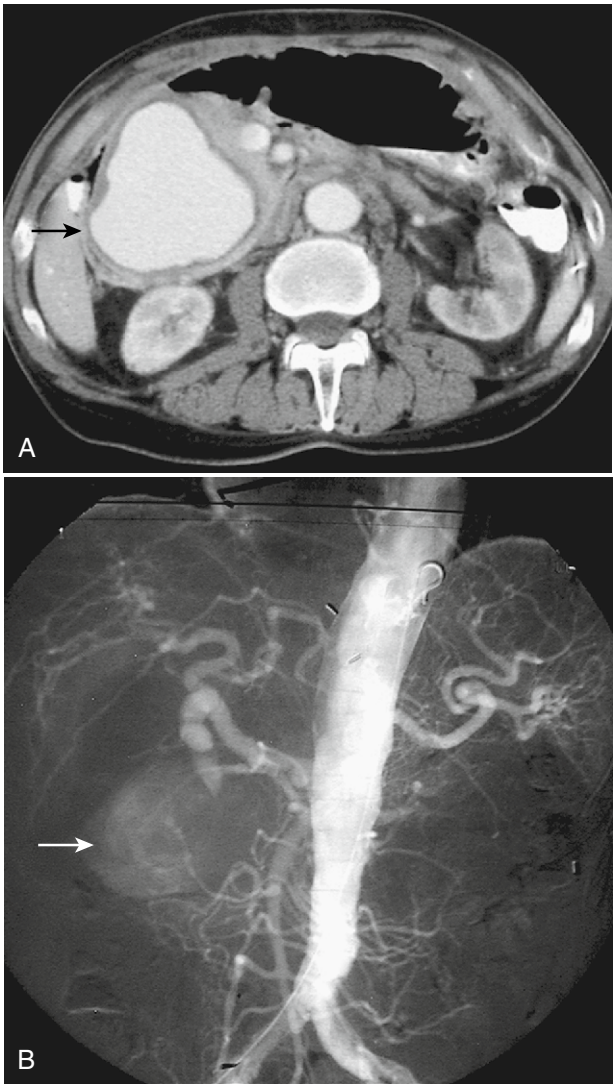


Figure 11-26. **A** and **B,** Contrast-enhanced CT images through the level of the pancreas demonstrate a large heterogeneous mass with enhancement pattern similar to the aorta and located lateral to the head of the pancreas *(arrows)*. The duodenum is not visualized. Findings correspond to a large pseudoaneurysm secondary to pancreatitis. Conventional angiography demonstrates an enlarged gastroduodenal artery feeding a very large aneurysm *(arrow)*. (Courtesy of Dr. Javier Casillas, University of Miami.)

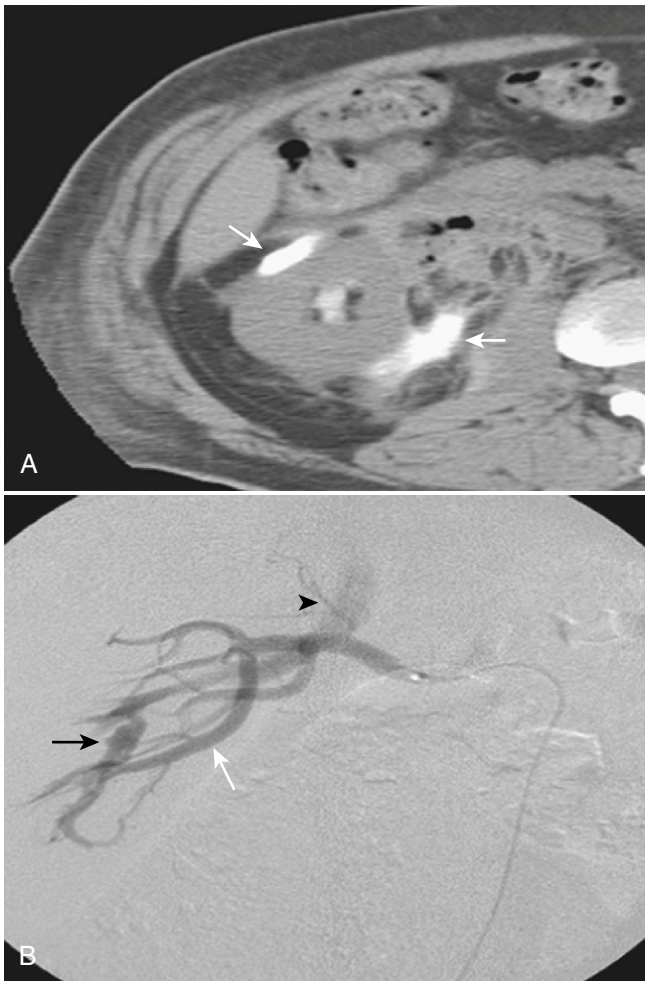


Figure 11-27. **A,** Following transjugular kidney biopsy, the patient developed gross hematuria. CT was obtained, which demonstrates contrast extravasation into the perirenal space (urinoma). The patient was initially managed conservatively but heavy hematuria recurred. **B,** Preembolization angiogram shows an arteriovenous fistula *(black arrow)* fed by the lower polar renal artery *(white arrow)* and early venous drainage with prompt visualization of the IVC *(arrowhead)*.

the diagnosis of a vascular injury is uncertain (a rarity with current CT technology) or when a vascular injury can be treated by endovascular means.

Iatrogenic renal vascular injuries can also be included in this category, as biopsies, ablations, and partial nephrectomies can lead to bleeding or pseudoaneurysms and AV fistula formation. These might result in active extravasation into the perirenal space or the renal collecting system (Fig. 11-27).

Nontraumatic Renal Arterial Emergencies

Acute Renal Ischemia

Normal kidneys have no significant collateral blood supply, and acute occlusion will lead to rapid loss of kidney function if not effectively revascularized within 1 to 2 hours. The most common cause of acute occlusion in middle-aged and elderly patients is embolic disease of a cardiac source, while in the young patient population it is trauma. Other etiologies include aortic or renal artery dissection, thrombosis of a focal stenosis, thromboembolism from renal artery aneurysm, and procedural complications (Fig. 11-28). Patients with acute renal artery ischemia classically present with flank pain and hematuria. Occlusion in the setting of progressive renal artery stenosis is less likely to end in acute ischemia as collateral flow usually via capsular, adrenal, or gonadal arteries will have developed. Both CT and MRI are useful to demonstrate the areas of asymmetric renal perfusion with generalized lack of enhancement seen with complete arterial occlusion or areas of segmental infarction due to smaller emboli. CTA and MRA can demonstrate renal artery stenosis, arterial dissection, and other renal artery anomalies as well as accessory arteries or collateral flow. Revascularization of acute renal artery occlusion is difficult due to the narrow time window before irreversible changes develop. If an occlusive dissection develops during renal artery angioplasty, stenting is indicated; if the occlusion is secondary to thrombosis, then treatment is done with thrombolysis, and thrombectomy or surgical revascularization is indicated.

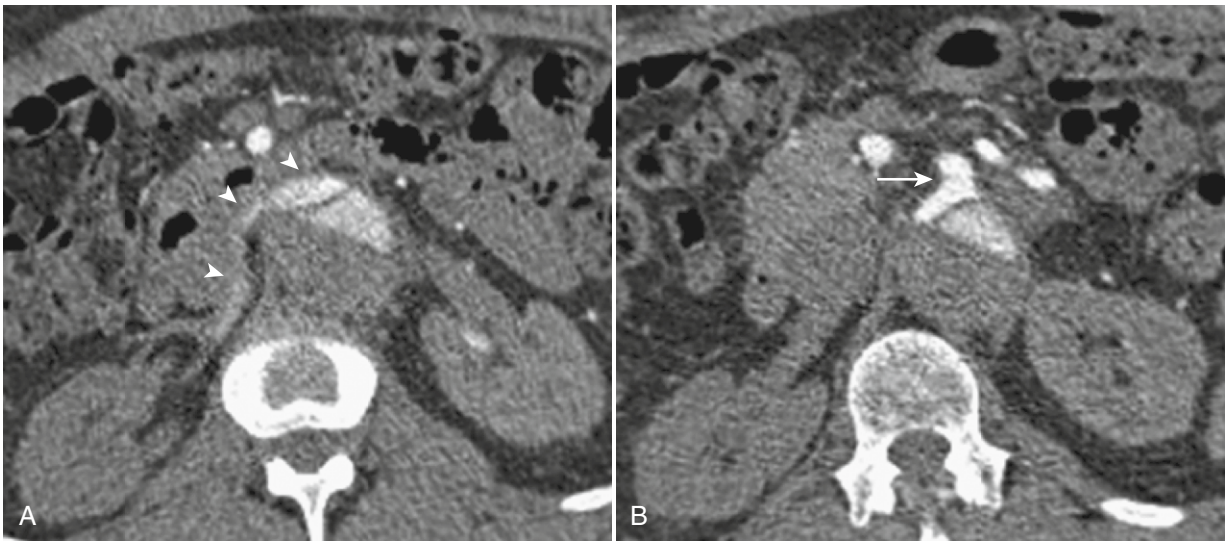


FIGURE 11-28. **A** and **B,** CTA of a complex aortic dissection. Part of the aortic false lumen in the posterior aspect of the aorta has thrombosed. The dissection flap is partially involving the origin of the right renal artery causing flow impairment (**A,** *white arrowheads*); compare to the preserved celiac trunk origin (**B,** *white arrow*).

Aneurysms of the Renal Artery

Aneurysms of the renal arteries are rare. Etiologies include degenerative aneurysms, which are usually asymptomatic, fibromuscular dysplasia, infection, trauma, idiopathic, and iatrogenic. Other etiologies such as polyarteritis nodosa tend to involve small peripheral intraparenchymal branches. The risk of rupture increases when the aneurysm diameter exceeds 2 cm, and this risk has been found to be higher in pregnant patients. These aneurysms may also be complicated with renal infarction, hypertension, and spontaneous fistula formation. The decision to treat depends on aneurysm size and clinical presentation. Minimally invasive angiographic alternatives such as coil embolization and stent graft placement are effective techniques; however, these cannot always be implemented, and surgical reconstruction or bypass may be required.

Renal Neoplasm–Related Vascular Emergencies

Some benign and malignant renal neoplasms can be the source of acute clinical symptoms including pain, hemorrhage, and gross hematuria. Angiomyolipomas are benign renal neoplasms that contain fat, smooth muscle, and blood vessels. They are well known for their association with tuberous sclerosis and their tendency to bleed, particularly when larger than 4 cm. Ultrasound or CT evaluation is usually performed in the emergency setting due to acute flank pain that may be associated with hemodynamic changes. Images will demonstrate the acute renal and perirenal hemorrhage with or without contrast extravasation. The mass itself as well as the characteristic intralesional fat can usually be identified, although it can be difficult in the setting of acute hemorrhage (Fig. 11-29). The presence of other angiomyolipomas can help the diagnosis. These lesions are usually treated with percutaneous embolization using a combination of particles, coils, and sometimes alcohol. Follow-up scans are performed to document resolution of the hematoma and shrinkage of the lesion.

Renal cell carcinomas are the most common malignant renal neoplasm in the adult. The so-called classic triad of flank pain, hematuria, and mass is present in only one third of the patients. Percutaneous embolization for tumor control is generally not indicated except in selected cases where the tumor size is too large for resection and embolization may help control operative bleed. Other indications for percutaneous embolization include severe gross or recurrent hematuria or perirenal hemorrhage.

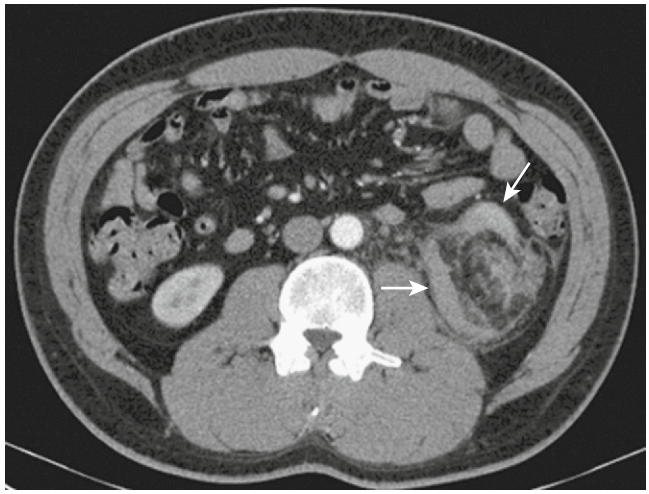


FIGURE 11-29. A 35-year-old patient presented with sudden left flank pain. Contrast CT shows a fatty mass lesion in the lower pole of the left kidney in addition to perirenal fluid *(arrows);* findings are consistent with left renal angiomyolipoma complicated with acute hemorrhage.

Vascular Emergencies of the Pelvis

Trauma of the Pelvic Arteries

Traumatic injury to the vascular structures of the pelvis is more frequently the result of pelvic fractures in combination with violent shear and traction forces. Pelvic vascular injuries can lead to rapid hypovolemic shock and death from exanguination if not treated promptly. Most pelvic fractures are the consequence of lateral compression, and

the majority of those are successfully stabilized with pelvic fixation. There are also unstable pelvic fractures secondary to more complex forces that do not respond well to pelvic fixation and can be aggravated by associated coagulopathy and cancellous bone bleeding. If the patients are hemodynamically stable, an expedited MD-CTA can be quite helpful in characterizing the fracture and assessing the location and degree of vascular involvement. When both intra-abdominal hemorrhage and pelvic fractures are present, the patients are taken directly to the operating room for repair of their abdominal injuries and pelvic fixation. Endovascular intervention is usually postponed until the more emergent conditions are treated, unless CT/CTA determines that the more ominous finding can be best approached with endovascular techniques (Fig. 11-30). Angiography in hemodynamically unstable patients should be directed first to a rapid evaluation of the source of bleeding and then expeditiously to embolization. A previous CT/CTA helps to direct the angiogram and possibly obviate the need for an initial nonselective pelvic angiogram, since the absence of abnormal findings in nonselective angiography does not exclude an active bleed and selective internal and external iliac angiograms are still mandated. It is important to note, however, that an initial pelvic angiogram can be useful to identify massive extravasation and depict the patient's specific anatomy. Also, one should not confuse the normal cavernosal blush at the penoscrotal junction with an area of extravasation. The primary goal of embolization in patients with pelvic fractures is to promptly stop the hemorrhage and decrease the arterial flow to the injured vessel. Gelfoam pieces are mixed with contrast, and vessel embolization is performed until no further extravasation is identified (Fig. 11-31). In stable patients, subselective embolization can be performed, and other embolic agents such as coils and glue can be used. The use of covered stents has also been described with great success, but it is recommended that a specialist familiarized in their use be the one performing the procedure. Both coil embolization and stent graft placement have been used successfully to treat traumatic pseudoaneurysms (Fig. 11-32). After embolization, completion of the angiography is important to exclude other sources of bleeding.

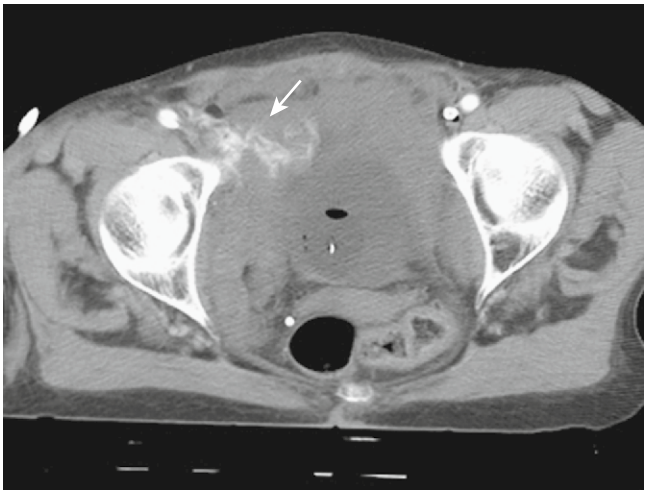


Figure 11-30. The patient experienced a motor vehicle accident with pelvic fracture. After initial stabilization CTA demonstrates active contrast extravasation adjacent to the right superior pubic ramus; the patient was taken to angiography for embolization.

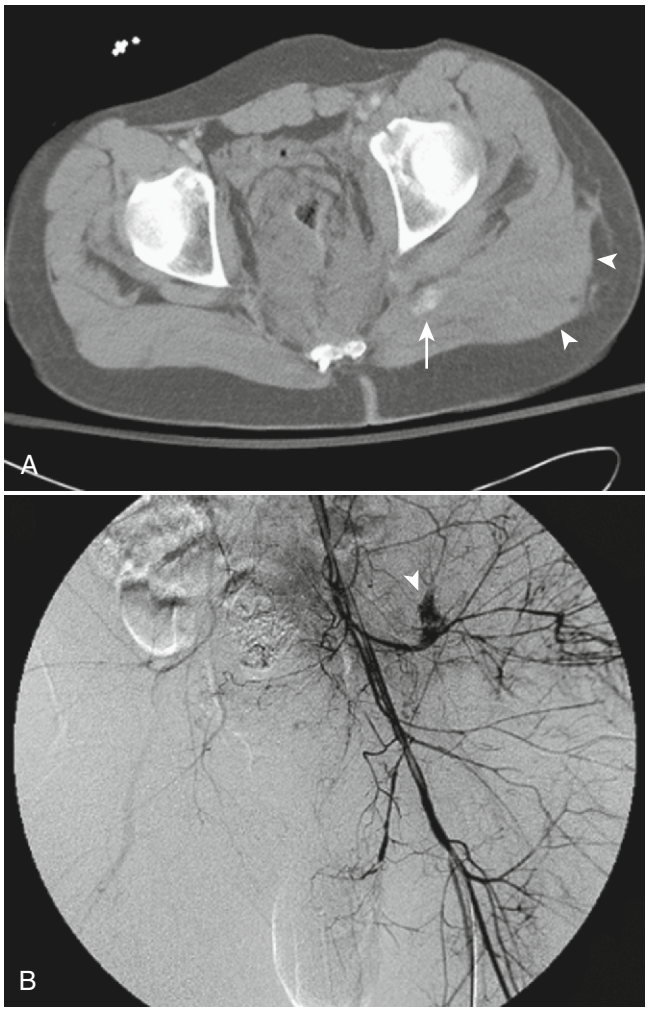


Figure 11-31. A, The patient sustained blunt trauma with fracture of the pelvis. There is a large left gluteal hematoma *(arrowheads)*, and active extravasation is identified in the same area *(arrow)*. **B,** Catheter angiography shows the extravasation arising from the superior gluteal artery *(arrowhead)*. This was embolized using Gelfoam pledgets.

Nontraumatic Emergencies of the Iliac Arteries

Iliac Occlusive Disease

Atherosclerosis is the most common cause of iliac occlusive disease, and it frequently involves the distal aorta. Patients tend to present with unilateral or bilateral leg claudication or ischemia depending on the level of obstruction and the presence of collateral circulation; bilateral symptoms suggest aortic involvement. Aortoiliac occlusive disease is part of the lower extremity peripheral vascular disease spectrum (see section covering the lower extremities), and as such it can lead to loss of the extremity or even the loss of life when it becomes acute. Causes for acute presentation include embolism, thrombosis, dissection, trauma, low cardiac output states, and hypotension. Emboli are the most common cause of sudden lower extremity ischemia, with 80% originating in the heart due to atrial fibrillation, valvular disease, or recent myocardial infarction. Emboli can also originate in the peripheral circulation proximal to the occlusion as

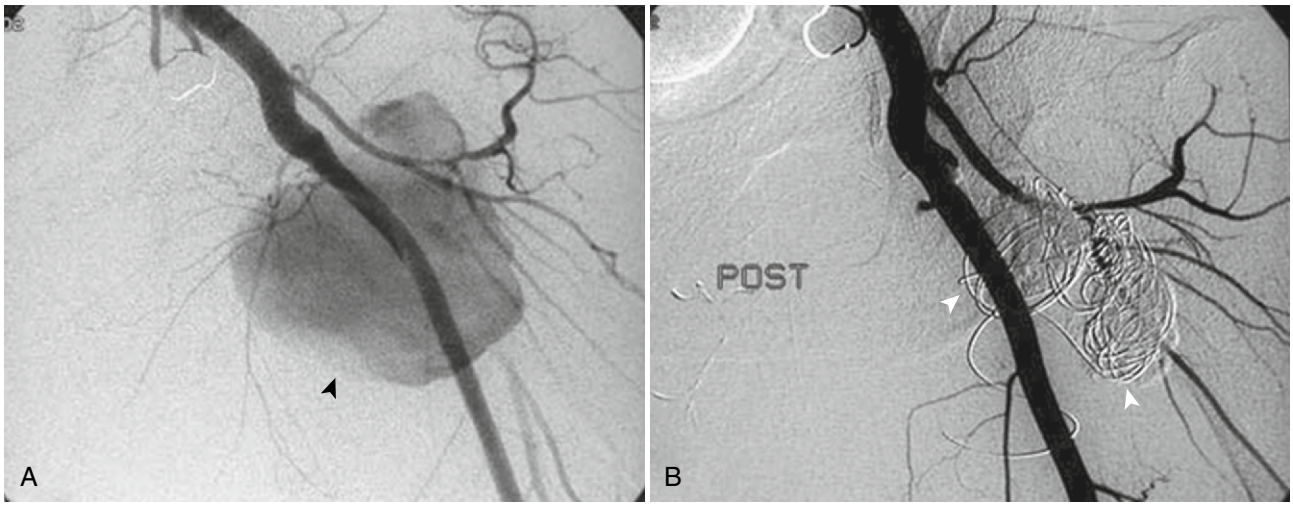


FIGURE 11-32. The patient sustained gunshot wound to the pelvis. **A**, Catheter angiography shows a large pseudoaneurysm arising from a hypogastric artery branch. **B,** After subselective coil embolization the aneurysm has been completely occluded. (Courtesy of Dr. W. Escobar, Cali, Colombia.)

a consequence of irregular or ulcerated plaque, aneurysms, and previous interventions such as stent grafts. Emboli tend to get wedged at bifurcation points or in areas where vessels narrow abruptly. The iliac arteries are involved in 18% of the cases of acute ischemia of the lower extremity, the aorta in 15%. Emboli tend to have a more acute and severe presentation owing to the lack of collateral circulation. Occlusive thrombosis is caused by the disruption of an atheromatous plaque that leads to exposure of its core products with subsequent activation of the coagulation cascade (Fig. 11-33). In patients who present with acute ischemic symptoms, a history of thigh or buttock claudication is suggestive of underlying iliac atherosclerotic disease. Leriche syndrome is described as the combination of intermittent claudication, impotence, and significantly decreased or absent femoral pulses. This syndrome can be identified in approximately one third of male patients with aortoiliac occlusive disease and indicates chronic peripheral arterial insufficiency due to narrowing of the distal aorta. Iliac occlusive disease can also present as "blue toe" syndrome when it causes distal emboli.

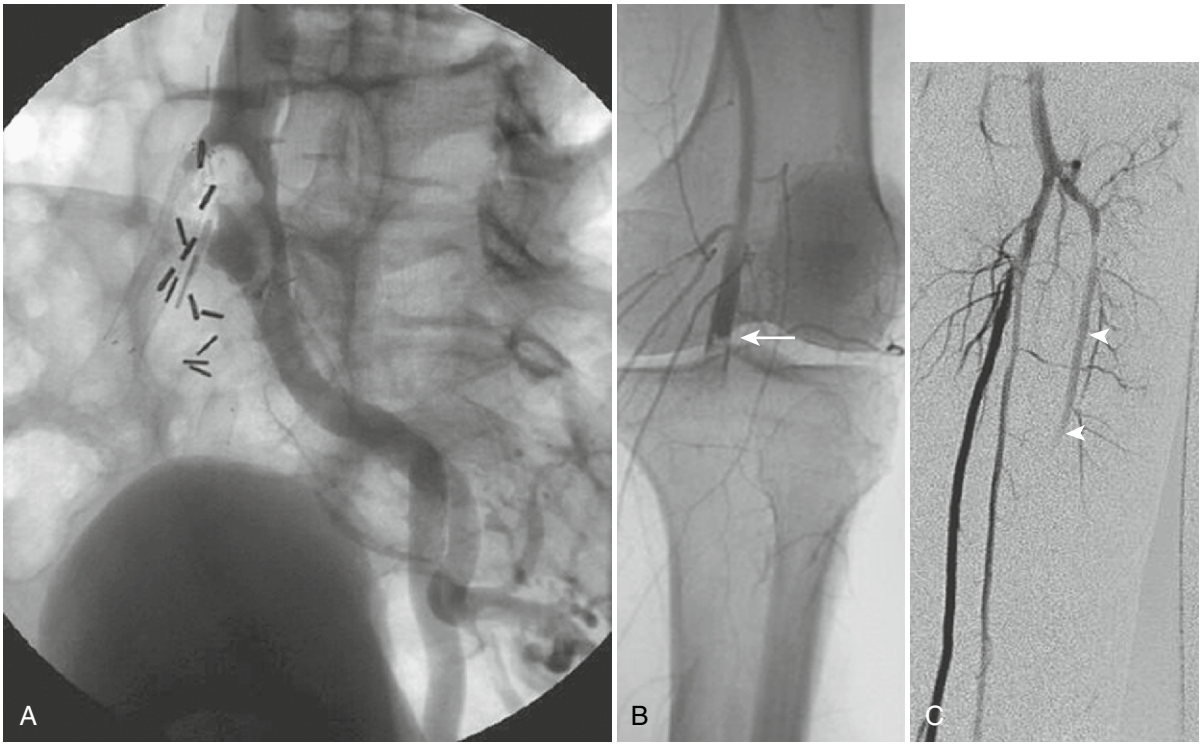


FIGURE 11-33. The patient presented with sudden painful cold left foot. **A,** Catheter angiography shows a large thrombus developing from an occluded right iliac artery stent and extending into the left common iliac artery. **B,** Left lower extremity angiogram shows complete occlusion at the level of the popliteal artery due to an embolus *(arrow)*. **C,** Following catheter-directed thrombolysis, patency of the popliteal, posterior tibial, and peroneal arteries was reestablished, and there is partial restoration of the anterior tibial artery flow.

Examination will reveal the absence of femoral pulses and a decreased ankle brachial index (ABI). Ultrasound evaluation with Doppler of the iliac arteries is difficult; however, the analysis of the duplex spectral waveforms demonstrating spectral broadening and the absence of a normal triphasic pattern can provide valuable information about proximal disease.

CE-MRA and CTA can both detect aortoiliac disease with great sensitivity and specificity and allow for adequate therapeutic planning. CT tends to overestimate the degree of stenosis, particularly in the presence of calcification. MRA offers limited evaluation of segments containing stents, due to the metal-induced susceptibility artifact.

In general, both CTA and MRA provide excellent characterization of the aortoiliac vasculature for diagnosis, follow-up, and therapeutic planning. Occasionally, both are used in cases of conflicting results or when assessment of the calcified wall is important for therapeutic planning.

Catheter angiography is usually reserved for cases where intervention is anticipated or to answer specific inquiries regarding pressure gradient measurements and information on flow dynamics. Definitive treatment of hemodynamically significant aortoiliac disease is usually done by aortobifemoral bypass, with a 5-year patency rate of approximately 90%. Patients in whom aortoiliac disease becomes symptomatic but who have comorbidities that increase the operative risk may benefit from a less invasive approach such as endovascular repair with angioplasty and stenting, axillary-femoral bypass, or femoro-femoral bypass. Focal concentric iliac artery stenosis usually responds well to angioplasty with more than 60% primary patency rate at 4 years; however, since stents are approved for iliac use, most iliac lesions are treated nowadays with primary stenting, with a 4-year patency rate of almost 80% for stenotic lesions and 60% for recanalized occlusions. Minimally invasive treatment of bilateral common iliac artery occlusive disease will require placement of bilateral stents, also known as "kissing" stents when they touch each other at the aortoiliac confluence. When dealing with patients complaining of acute or recent onset of symptoms and a fresh thrombus is suspected, thrombolysis is an excellent recanalization alternative (see Fig. 11-33).

Iliac Aneurysms

Degenerative aneurysms of the iliac arteries tend to involve the common iliac artery (CIA) and are frequently seen in association with abdominal aortic aneurysms or dissection (Fig. 11-34). External and internal iliac artery aneurysms are rare. As with AAA, the most feared complication is aneurysm rupture, which can be free, contained, or into a venous structure. Findings of rupture can be subtle with only mild perivascular stranding noticed, or dramatically florid with retroperitoneal and/or intraperitoneal hemorrhage. Rupture into venous structures causes high output congestive heart failure. Chronic ruptures usually contain thrombus associated with saccular dilatation and disruption of intimal calcification. Isolated CIA aneurysms warrant repair when they reach 2.5 to 3.0 cm in diameter, and they can be managed with stent graft placement provided there is an adequate access pathway and sufficient landing zones to allow appropriate attachment of the graft.

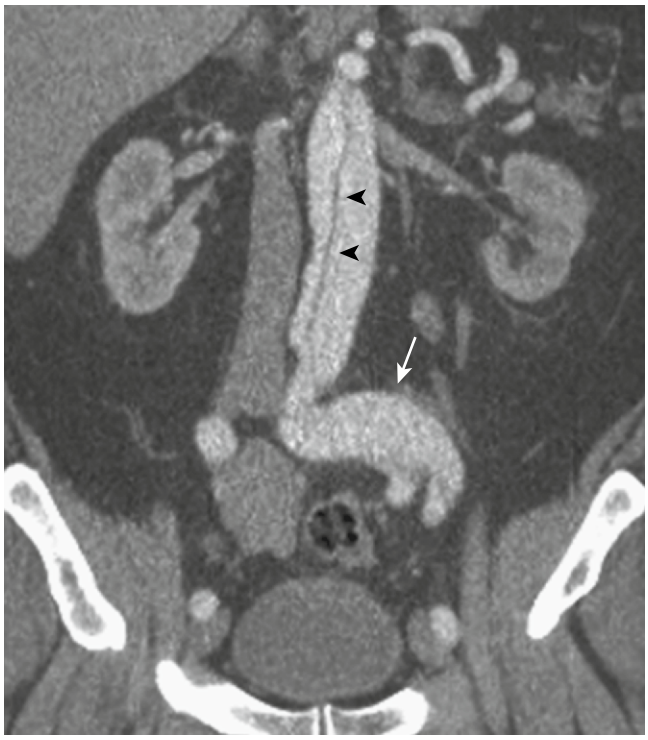


Figure 11-34. Coronal CTA reconstruction demonstrating a 3.5-cm aneurysmal dilatation of the left common iliac artery *(arrow)*. There is also an abdominal aorta dissection flap *(arrowheads)* that extends into the iliac (not shown).

Iliac Artery Dissection

Dissection of the iliac arteries is usually an extension of thoracoabdominal aortic dissection. Primary iliac artery dissection is relatively rare and has been described in association with fibromuscular dysplasia and vigorous training in professional athletes. Both CTA and MRA are excellent for the evaluation of thoracoabdominal and iliac dissection (see Fig. 11-20).

Vascular Emergencies of the Extremities

Arterial Injury of the Upper Extremities

Traumatic vascular lesions to the upper extremities can occur in as many as 40% to 50% of penetrating trauma patients when "hard" (or direct) clinical signs are present. Hard clinical signs include pulsating hemorrhage, expanding hematoma, presence of a thrill or bruit, pulse deficit, and extremity ischemia (Box 11-5). Indirect (or "soft") signs include stable hematoma, extensive soft tissue injury, adjacent fracture or adjacent nerve injury, nonpulsatile bleeding, and delayed capillary refill (Box 11-6). In the

***Box 11-5.* Hard Clinical Signs of Arterial Trauma**

Pulsating hemorrhage
Expanding hematoma
Presence of a thrill or bruit
Pulse deficit
Extremity ischemia

BOX 11-6. Soft Clinical Signs of Arterial Trauma

Stable hematoma
Extensive soft tissue injury
Adjacent fracture
Adjacent nerve injury
Nonpulsatile bleeding
Delayed capillary refill

absence of hard clinical signs the patients can be treated conservatively, and noninvasive imaging modalities play a major role in their evaluation and follow-up. Besides the conventional penetrating and blunt traumatic injuries that any vessel is subject to, the arteries of the upper extremity are also at risk for unique injuries due to the major functional role they play in our lives. Among them are stretch injuries that occur during extreme traction when attempting to stop a fall. The subclavian-axillary segment is particularly at risk, and associated brachial plexus injuries are common. Intimal tears and disruption of the media can then lead to thrombosis and distal embolization (Fig. 11-35). Other injuries include blunt trauma from incorrect use of crutches, affecting the axillary-brachial segment, iatrogenic injuries during central venous access procedures, and injuries related to self-administered drugs.

CTA is the preferred imaging modality to emergently assess the arteries of the proximal upper extremities, reserving catheter angiography for patients with equivocal diagnosis or when therapeutic intervention is required. CTA offers the advantage of simultaneously assessing for additional nonvascular injuries, while conventional angiography offers the advantage of diagnosing and treating at the same time. Both modalities can identify any of the vascular injuries including intimal tear, occlusion, pseudoaneurysm, active extravasation, complete transection, and arteriovenous fistulas. Branch vessel extravasation and pseudoaneurysms can be treated with coil embolization. Main arterial pseudoaneurysms and fistulas can also be treated with embolization or covered stents (Fig. 11-36).

Nontraumatic Arterial Emergencies of the Upper Extremities

Acute upper extremity ischemia most frequently presents with hand and digit symptoms, and can vary from mild coldness to complete necrosis. On occasion, digital ischemia can occur in the presence of normal palpable pulses. The location of symptoms depends on the level of occlusion. The most common cause of acute nontraumatic upper extremity ischemia is embolization of cardiac origin and is suggested by recurrent ischemic events that may affect the extremity or the central nervous system. Other possible etiologies include trauma, aortic dissection, and steal phenomenon in patients with a recent history of surgical AV shunting for dialysis access. Malignancy and hypercoagulable states can also present with acute digit ischemia. Recurrent events limited to one arm are compatible with a source localized proximally within that extremity, like an aneurysm or stenosis in the subclavian artery, in which case thoracic outlet syndrome with arterial involvement has to be considered. Thoracic outlet syndrome is defined as the symptomatic extrinsic compression of the neurovascular structures of the upper extremities as they exit the upper thorax. Neural and venous compressions represent the majority of the cases, while arterial compressions are rare; however, embolic events can occur in as many as 40% of patients. Arterial compression usually occurs at the scalene triangle secondary to anomalous osseous or ligamentous structures or muscle hypertrophy. The arterial pulsation causes repetitive focal trauma that results in development of focal narrowing and poststenotic dilatation, where thrombus may form and cause distal embolization. Imaging should evaluate not only the arterial lumen but also the surrounding structures to detect anatomic anomalies causing the compression. CTA and MRA are both useful for depiction of the vessel lumen and surrounding tissues.

One of the most expeditious ways to obtain an objective imaging evaluation of the upper extremity circulation is through ultrasound imaging. However, the subclavian artery cannot always be visualized in its entirety, and in the emergency setting obtaining a full arterial duplex examination may prove to be too time consuming if the operator is not

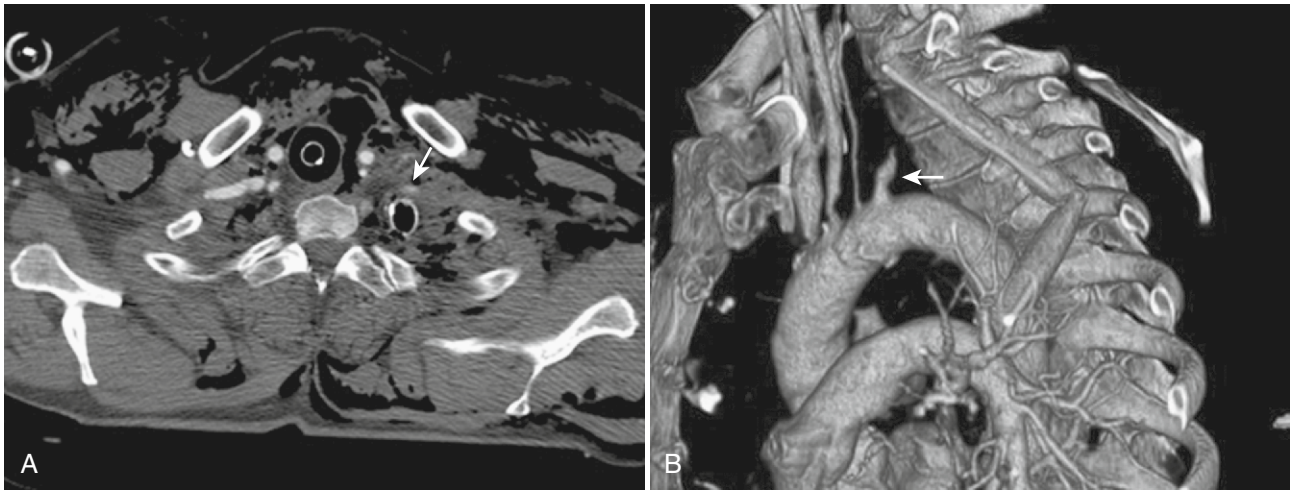


FIGURE 11-35. This patient sustained blunt chest trauma during motor vehicle accident. **A,** CTA shows a thinned left subclavian artery origin *(arrow)*. **B,** Volume-rendered reconstruction better shows the left subclavian artery occlusive dissection *(arrow)*.

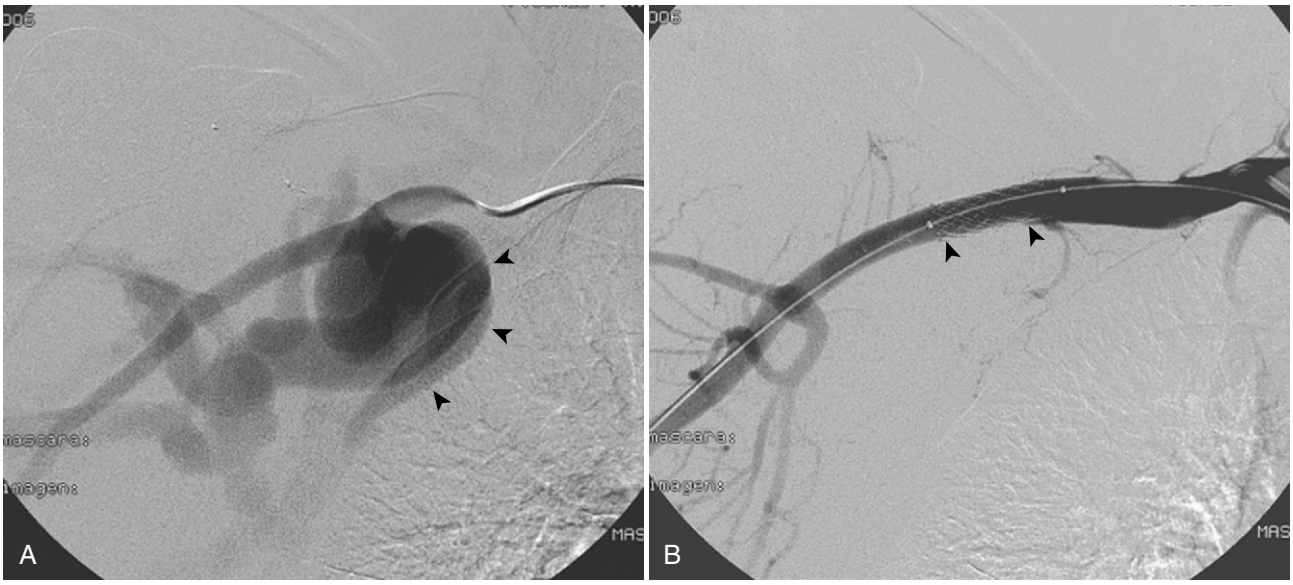


Figure 11-36. This 25-year-old male patient sustained a gunshot wound to the right shoulder area 5 years prior and now presented with congenital heart failure. **A,** Selective angiogram of the right subclavian artery shows a high flow arteriovenous subclavian fistula with large aneurysmal dilatation of the vein *(arrowheads).* **B,** After endovascular treatment with covered stent the fistula is completely occluded and the subclavian artery preserved. (Courtesy of Dr. W. Escobar, Cali, Colombia.)

well familiarized with the exam. In the setting of nontraumatic upper extremity ischemia, the most accurate imaging modality remains conventional catheter angiography since location of the disease can be as distal as the digit level and noninvasive imaging modalities may not yet provide sufficient resolution or detail to accurately evaluate all cases. Angiographic evaluation of critical hand ischemia secondary to embolic disease usually demonstrates the embolus within the brachial artery; however, magnification views of hand and digits may be required to distinguish between distal emboli and other causes, such as vasculitis.

Any of the systemic vasculidities can affect the upper extremities and present as an acute event. By characterizing the distribution pattern one may contribute to narrowing the differential diagnosis. Takayasu arteritis usually causes stenosis and occlusion of the proximal subclavian arteries; giant cell arteritis tends to involve the subclavian and brachial arteries, while Buerger disease (thromboangitis obliterans) causes occlusion of the main arteries and induces hypertrophy of small perineural collaterals that give the characteristic "corkscrew" angiographic appearance. Finally, systemic lupus erythematosus, rheumatoid arthritis, scleroderma, and mixed connective tissue disorder (MCTD) are likely to cause multiple occlusions of the small arteries, particularly at the digit level.

Critical hand ischemia secondary to embolic disease is usually treated with surgical embolectomy. Thrombolysis should be considered when there is extensive distal thrombus. After recanalization, if the source of embolization is a focal atherosclerotic lesion or an aneurysm, treatment with balloon dilatation or stenting can be attempted accordingly.

Upper Extremity Aneurysms

Upper extremity artery aneurysms are rare; etiologies include atherosclerosis, acute or repetitive trauma, chronic dissection, connective tissue disorders, and, in cases of distal ulnar aneurysms, hypothenar hammer syndrome. Aneurysms of the intrathoracic subclavian artery are usually atherosclerotic in nature, while the ones in the extrathoracic segment are usually secondary to thoracic outlet syndrome. Atherosclerotic aneurysms can present with pain, hoarseness, distal embolization, stroke, and rupture. Occasionally, the dilated origin of an aberrant subclavian artery known as the diverticulum of Kommerell can evolve into a true aneurysm that can be associated with pain, dysphagia, and dissection. CTA and MRA can provide a complete aneurysm characterization that allows for a safer therapeutic planning.

Arterial Trauma of the Lower Extremities

Vascular injuries of the lower extremities are a serious complication of both penetrating and blunt trauma. The rate of limb loss with major injuries is approximately 15%, and 25% of the patients eventually develop some degree of limb dysfunction due to related osseous or nerve injury. As mentioned previously, clinical signs of arterial injury are divided into "hard" and "soft" signs (see Boxes 11-5 and 11-6). Patients with a profoundly ischemic limb or active hemorrhage from the wound are taken directly to surgery, while stable patients with viable limbs should undergo a complete limb and pulse examination. A fast determination of the ABI can be helpful, as the incidence of vascular injury in patients with a normal ABI and normal examination is less than 10%. This number can increase to 20% when there are "soft" signs present and the ABI is less than 1, and increases to 40% when the ABI is less than 1 and the mechanism is a gunshot wound or there is associated pulse deficit or neurologic deficit.

In the setting of a normal physical exam, a penetrating wound in proximity to vascular structures is considered an indication for angiography only in cases in which the bullet tract follows the course of a major artery over a long segment. In the past, some practices called for angiography to be performed on every patient with a penetrating injury in proximity to a runoff vessel and when the overall identification of clinically

relevant vascular injuries was less than 10%. CTA has become a useful minimally invasive tool in this scenario, with the ability to accurately diagnose the type of injury as well as its extent and location. CTA can depict injuries that do not routinely require surgical intervention, such as intimal flaps, branch vessel occlusions, and partial luminal narrowing with preservation of distal flow. Catheter angiography remains as a useful examination for patients with nonconclusive CTA findings and whenever endovascular transcatheter therapy is indicated. In general, partial injuries (such as intimal flaps) are managed conservatively, branch vessel extravasation may require embolization with coils (Fig. 11-37), and pseudoaneurysms are treated with embolization or stent grafts. Major injuries demand open surgical repair when extensive reconstruction or bypass is required.

Knee Dislocation

Knee dislocation can cause arterial injuries in approximately 40% of cases. Most patients are young and have limited collateral flow, which makes them highly vulnerable to popliteal occlusion, and a delay in diagnosis and treatment can lead to amputation due to irreversible ischemic changes. Physical exam with emphasis on the distal pulses and associated signs of vascular injury is crucial for a prompt diagnosis; however, an abnormal pedal pulse as an isolated finding on the initial examination of patients with knee dislocations is not sensitive enough to detect an injury that invariably requires vascular intervention. Patients with signs of ischemic limb should proceed directly to surgery, and, if required, intraoperative angiography can be performed for confirmation. Catheter angiography should include multiple projections in order to exclude intimal tears, spasm, and partial thrombosis. Small and nonocclusive lesions are managed conservatively. Patients who have been treated with prompt reduction and those with normal vascular exams can be further evaluated with CTA to determine the integrity of the popliteal artery.

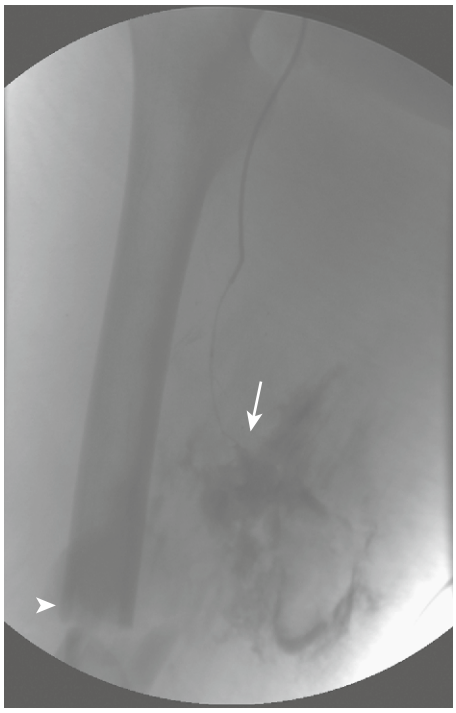


FIGURE 11-37. After a motorcycle accident the patient was noticed to have an enlarging right thigh. Selective angiogram shows a large area of contrast extravasation arising from one of the femoral profunda branches *(arrow)*. Notice the femoral fracture *(arrowhead)*. The extravasation was treated with a combination of Gelfoam and coils.

Femoral Artery Pseudoaneurysm

Pseudoaneurysm of the femoral artery is more frequently the result of an arterial puncture to perform cardiac or peripheral angiography, occurring in 1% to 5% of the cases. Patients may present with a large inguinal hematoma or a pulsatile mass. Most pseudoaneurysms thrombose spontaneously, but up to 3% to 5% may persist, increase in size, or rupture. Because of their location these aneurysms are generally diagnosed with duplex ultrasound. Occasionally MRA or CTA is required when they cannot be adequately characterized with ultrasound due to their large size or multilobulated characteristics, ultrasound's inability to visualize the pedicle, or when they persist despite an initial attempt to treat them. Most femoral pseudoaneurysms can be treated with ultrasound-guided compression of the pedicle (or neck) to interrupt the flow and induce thrombosis; when this fails, thrombin injection can be performed under direct ultrasound visualization to control the aneurysm flow as the thrombin is being administered (Fig. 11-38).

Nontraumatic Acute Lower Extremity Limb Ischemia

Acute lower limb ischemia is most frequently the result of atherosclerosis that gradually progresses to the point of complete occlusion; it manifests with insufficient limb perfusion and worsening pain that may acutely exacerbate. The level of arterial compromise correlates closely with the location of ischemic symptoms; aortoiliac disease manifests as pain in the thigh and buttock, whereas femoropopliteal disease manifests as pain in the calf. Symptoms of chronic peripheral vascular disease are precipitated by walking a predictable distance and are relieved by rest (claudication). Ischemic rest pain is more worrisome; it can be partially relieved by placing the extremity in a dependent position, so that perfusion is facilitated by the effect of gravity. An acute, profoundly ischemic leg is a surgical emergency. Among the causes for acute limb ischemia are emboli, plaque disruption and thrombosis, dissection, trauma, and low cardiac output states. Among the various causes of acute limb ischemia, the major diagnostic goal is to differentiate embolic from thrombotic occlusion. Emboli are the most common cause of sudden lower extremity ischemia, and approximately 80% originate in the heart due to atrial fibrillation, valvular disease, or recent myocardial infarction. Emboli can also originate in the peripheral circulation (proximal to the level of occlusion) as a consequence of irregular or ulcerated plaques, aneurysms, dissection flaps, previous interventions, or stent grafts (Fig. 11-39). Emboli tend to get wedged at bifurcation points or stenotic areas; the femoral artery bifurcation is the most common site (40%), followed by the iliac arteries (20%), the aorta (15%), and the popliteal arteries (15%). Acute thrombosis occurs more often in the setting of established atherosclerotic disease, where the disruption of an existing atheromatous plaque leads to exposure of its core products and subsequent activation of the coagulation cascade.

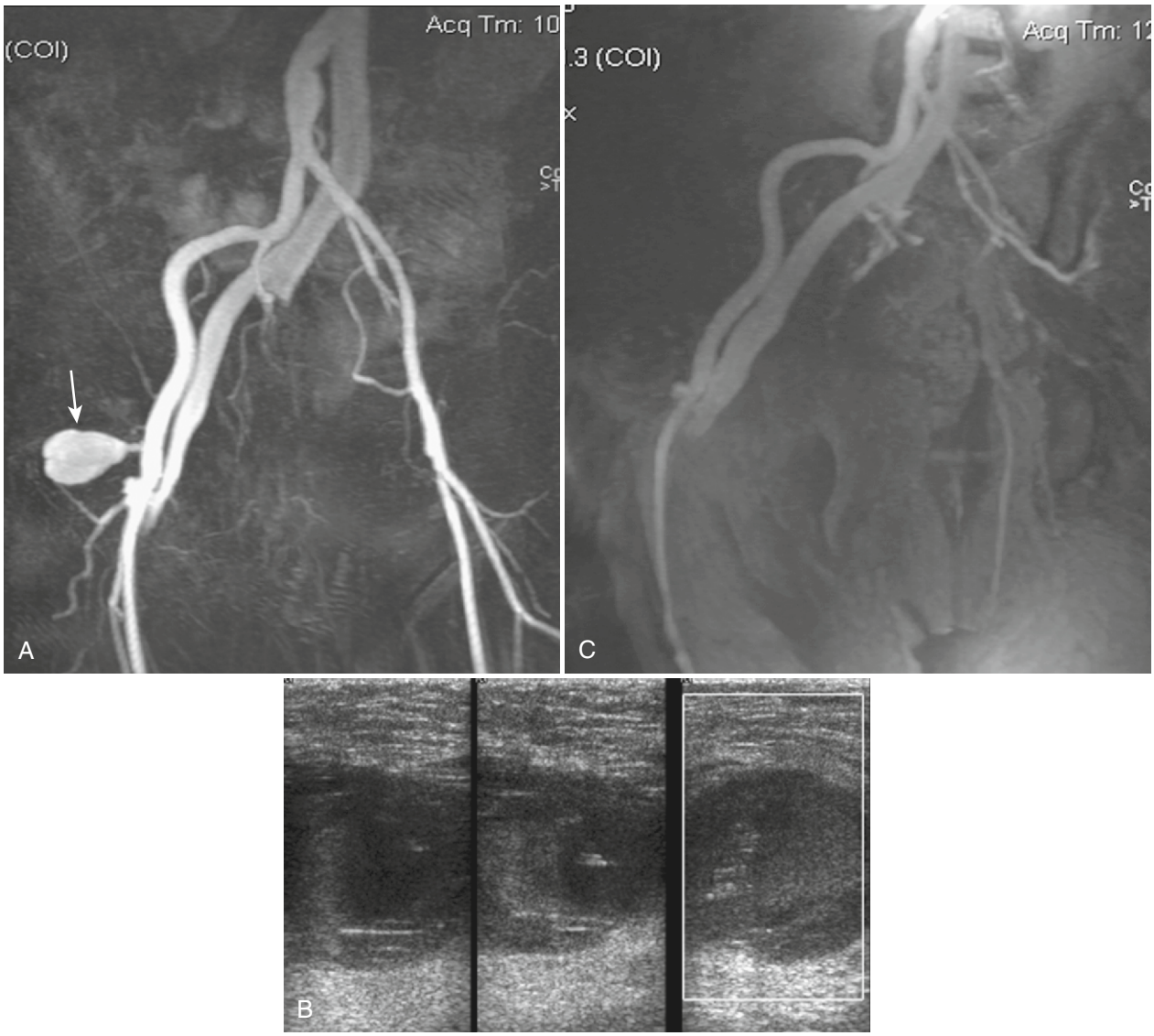


Figure 11-38. **A,** Contrast-enhanced MRA demonstrates a large pseudoaneurysm of the right common femoral artery that occurred as a complication of catheterization for coronary angiography. In addition. there is prompt enhancement of the common femoral vein, iliac vein, and IVC consistent with arteriovenous fistula. **B,** Under ultrasound guidance a 22G needle is advanced into the aneurysm lumen, and thrombin is slowly injected under constant monitoring until complete thrombosis of the sac is achieved. **C,** Post-thrombin therapy MRA demonstrates complete thrombosis of the pseudoaneurysm and persistent AV fistula.

The classic signs of acute limb ischemia are the "5 Ps": pulselessness, pallor, pain, paresthesias, and paralysis. Although not included, coldness of the extremity is an additional valuable sign. Muscle weakness and paresthesia are signs of limb-threatening ischemia, while paralysis and anesthesia are signs of irreversible ischemia, and thrombolysis is contraindicated. Patients with acute limb ischemia should have emergent evaluation by vascular surgery.

In addition to the routine physical exam, the ABI is an easy and prompt way to assess the degree of ischemia. It is obtained by measuring blood pressure at the ankle and the arm using a conventional blood pressure cuff and Doppler ultrasound (since the pulse is frequently not palpable in this setting); the ankle pressure is then divided by the brachial pressure. A normal ABI value is 1 or slightly above 1, and, in general, an ABI less than 0.5 is an indication of severe disease. However, results should be interpreted with caution, as these values may not reflect the acuity of the condition and in the setting of small vessel disease (e.g., diabetes) the ABI may be elevated giving a false impression of normality.

Patients with critical ischemia due to embolus of graft thrombosis should go directly to surgical exploration for embolectomy or bypass. If there is an angiography team that works in close conjunction with the vascular surgeons, the patient can be promptly taken to angiography to determine the site and cause of the occlusion as well as the presence of a distal runoff; the absence of patent distal vasculature decreases the likelihood of successful thrombectomy and thrombolysis might be favored, provided there are no signs of irreversible ischemia. Alternatively, if a patient presents with acute ischemia but without limb-threatening signs, the vascular team may opt to start the patient on heparin and perform a more complete, but still expeditious, diagnostic workup to better plan the therapeutic strategy.

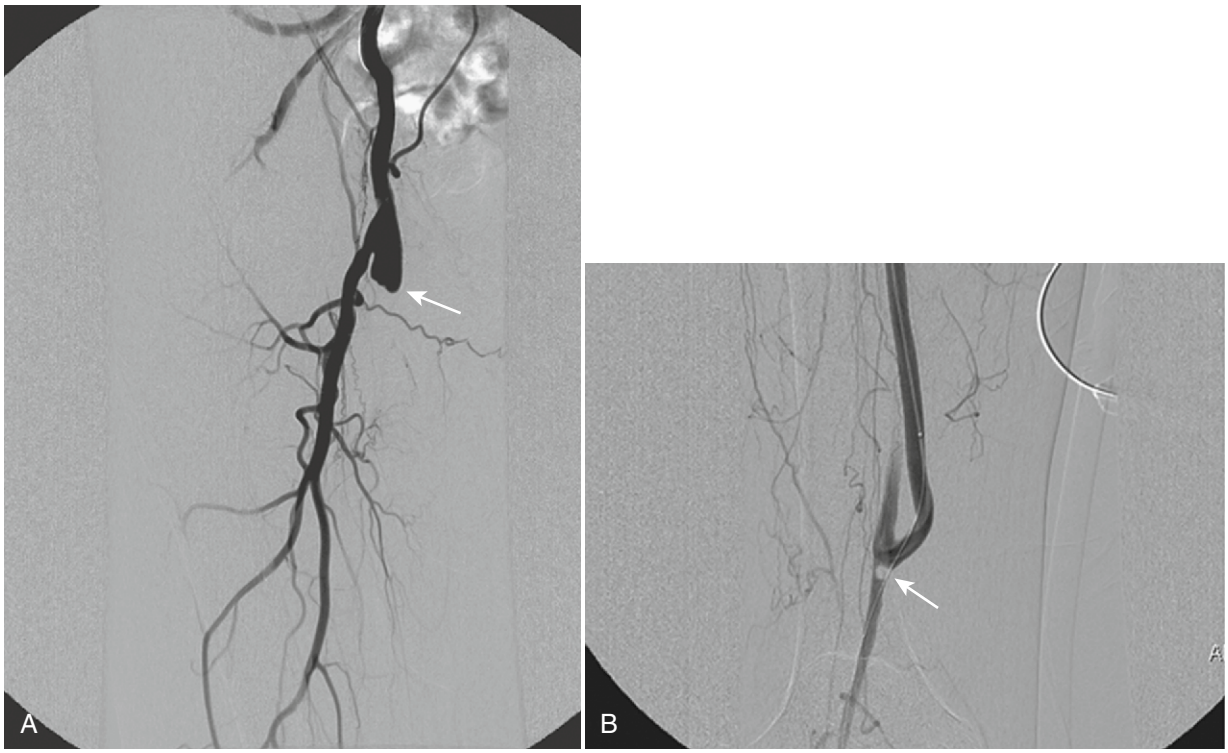


FIGURE 11-39. Patient with known femoropopliteal bypass who presents with acute limb ischemia. **A,** Selective angiogram confirms bypass occlusion *(arrow)*. The bypass was selectively catheterized and thrombolysis performed using tissue plasminogen activator via infusion catheter. **B,** After 24 hours bypass patency has been reestablished; there is a focal round filling defect in the popliteal artery just distal to the anastomosis *(arrow)*, consistent with the embolus that triggered the graft occlusion and for which further lysis was performed.

Duplex ultrasound is useful as a primary noninvasive study to determine flow status. The lower extremities are evaluated over the distal external iliac, femoral, popliteal, posterior tibial, and dorsalis pedis arteries. Duplex ultrasound can provide an accurate evaluation of the vasculature and flow pattern using gray scale and color images, as well as analysis of flow velocities and spectral waveforms. MRA and CTA can be used in this situation, but they have drawbacks that need to be kept in mind: routine MRI/MRA cannot identify vascular calcifications, and vessel lumen evaluation can be difficult with CTA as well, due to artifact in heavily calcified arteries.

Catheter angiography is indicated when emergent surgical revascularization is not required to salvage a viable extremity and is generally reserved for cases where endovascular intervention is anticipated. The evaluation should include the aortic bifurcation and runoff vessels if CTA or MRA has not been performed. If indicated, thrombolysis can be performed (see Fig. 11-39). Thrombolytic therapy is contraindicated in the presence of intracranial tumor, recent surgery, intracranial bleed, severe hypertension, bleeding at a noncompressible site, and gastrointestinal hemorrhage. Contraindications for thrombolysis have been further subdivided into absolute and relative, understanding that clinical judgment for each patient and careful evaluation of the risks and benefits are crucial in the decision-making process (Boxes 11-7 and 11-8). Follow-up angiograms are obtained in patients treated with thrombolytic infusion to reassess patency and determine the underlying cause for the occlusion.

***Box 11-7.* Major Contraindications for Thrombolysis**

Major surgery within the past 2 weeks
Hemorrhagic cerebrovascular accident within the past 2 months
Suspected aortic dissection
Intracranial tumor or arteriovenous malformation
Active internal or GI bleeding

***Box 11-8.* Relative Contraindications for Thrombolysis**

GI bleeding within last 6 months
Heavy vaginal bleeding
Head injury (e.g., subdural hematoma) within previous 4 weeks
Ischemic cerebrovascular accident within past 2 months
Active ulcer
Severe hypertension
Traumatic CPR
Pregnancy
Diabetic retinopathy with hemorrhage, retinal neoplasm, recent laser procedure
Therapeutic INR greater than 3

Aneurysms of the Lower Extremities

True aneurysms of the lower extremities are less frequent than AAA. They can be found at the popliteal and common femoral levels and are bilateral in 60% to 70% of patients. Most are degenerative or atherosclerotic in origin

and occur in association with AAA in more than 50% of the cases. These aneurysms are more frequently asymptomatic and rarely rupture. The most frequent and feared complications are thrombosis and distal embolization. Imaging evaluation should always include the opposite lower extremity and abdominal aorta. Ultrasound is a useful initial modality, but full characterization with MRA or CTA is often required. Popliteal artery aneurysms usually warrant treatment once diagnosed owing to the high incidence of distal embolization. Common femoral aneurysms are usually treated once they reach a diameter of 2.5 cm. Standard treatment is surgical excision and bypass.

VENOUS EMERGENCIES

Traumatic Injury of the Internal Jugular Vein

As previously mentioned, the traditional approach to surgical exploration of all penetrating neck injuries has much evolved in the past few years owing to, among other reasons, the advent of MDCT. However, it has also remained clear that if these patients are hemodynamically unstable or demonstrate direct signs of vascular trauma such as pulsatile bleeding, pulsatile or expanding hematoma, hematemesis, hemoptysis, stridor, or air leak, they should undergo immediate surgical exploration without imaging workup. When these signs are not present, patients can undergo imaging evaluation. Although both ultrasound duplex and conventional angiography have been used to assess penetrating neck injuries, it is MD-CTA that appears to be the more suitable initial evaluation tool due to its availability, speed, and capability of providing information regarding associated injuries. Internal jugular (IJ) vein injuries occur in 15% to 20% of the penetrating neck trauma cases. They can be identified as hematoma surrounding the jugular vein or compressing it; an occasional contrast extravasation can also be identified if images are obtained in a delayed phase. This is also an important consideration during angiography, where acquisition has to be carried into the venous phase if venous injuries are to be identified. In patients who require surgery, ligation and repair of the IJ vein has proven to be of no clinical consequence. In patients with no other indication for emergent surgical exploration, IJ vein injuries identified with MD-CTA have been successfully managed nonoperatively. Endovascular treatment for the management of actively bleeding IJ vein injuries has also been described, but is rarely required and remains experimental.

Venous Emergencies of the Chest

Superior vena cava syndrome (SVCS) represents a constellation of signs and symptoms occurring as a consequence of the occlusion of the SVC and constitutes a medical emergency. Clinical manifestations are dramatic and include severe edema and venous distention of the face and upper extremities with facial swelling, headache, impaired vision, nausea, mental status changes, chest pain, orthopnea, cough, hoarseness, and stridor, and the syndrome can lead to respiratory failure, brain edema, and death. The SVC is a thin-walled, low-pressure, venous structure that can be obstructed by neoplastic invasion associated with intravascular thrombosis or by extrinsic compression alone. More than 80% of cases of SVC syndrome are caused by mediastinal tumors, with bronchogenic carcinomas accounting for 75% to 80% of cases and non-Hodgkin lymphoma for 10% to 15% of cases. Nonmalignant conditions can also cause SVCS, including mediastinal fibrosis (e.g., tuberculosis, histoplasmosis), thrombosis related to central venous catheters, aortic aneurysms, vasculitis, and benign mediastinal tumors such as teratoma, cystic hygroma, and thymoma. Malignant causes of SVCS are predominantly observed in individuals aged 40 to 60 years, while benign causes account for most of the cases in younger individuals. The clinical diagnosis is generally quite apparent. A chest radiograph is the initial modality of choice and generally reveals a widened mediastinum due to the presence of an underlying mass. Clues of previous granulomatous infection include parenchymal changes and calcified mediastinal nodes.

Contrast-enhanced CT has the advantage of providing more accurate information on the location and type of obstruction. It also provides information about other critical structures such as the heart, pericardium, and bronchi. MRI and MR venography can delineate the venous system and the areas of obstruction. Direct contrast venography is performed if percutaneous intervention is being considered. In general, patients with SVCS demonstrate significant clinical improvement with treatment with conservative measures such as elevation of the head of the bed and supplemental oxygen. Aggressive emergency treatment is indicated when brain edema or a threatened upper airway is present. Treatment alternatives include radiotherapy, chemotherapy, or both. Radiation therapy successfully palliates SVC obstruction in 70% of patients with lung carcinoma and in more than 95% with lymphoma, even before tumor shrinkage is identified on plain films. Chemotherapy has also proven to be quite effective and may be preferable for patients with chemosensitive tumors.

Venous Emergencies of the Abdomen

Inferior Vena Cava Obstruction

Causes of inferior vena cava (IVC) obstruction can be intrinsic or extrinsic. It most commonly occurs as a result of extension of iliac vein thrombosis and involves predominantly the infrarenal segment. Some conditions that predispose to IVC thrombosis include a central line extending to the IVC, previous surgery, trauma, and the presence of a caval filter. Direct involvement of the IVC lumen can occur as direct invasion of a renal cell carcinoma or hepatocellular carcinoma. Extrinsic obstruction of the IVC causing luminal compression can be caused by hepatomegaly, tumors, massive lymphadenopathy, retroperitoneal fibrosis, or a large AAA.

The clinical presentation of IVC obstruction varies. A slow, progressive occlusion allows for the development of collateral flow, while a more acute occlusion causes edema of the lower extremities and even hypotension from decreased blood return. Ultrasonography, CT, and MRI can be useful in identifying IVC occlusion, thrombosis, and extrinsic compression by surrounding structures or tumor (Fig. 11-40). Acute thrombus may appear hyperdense on CT. Direct IVC venography is rarely required for diagnosis and is usually obtained only if a filter is being considered or if thrombolysis is to be performed.

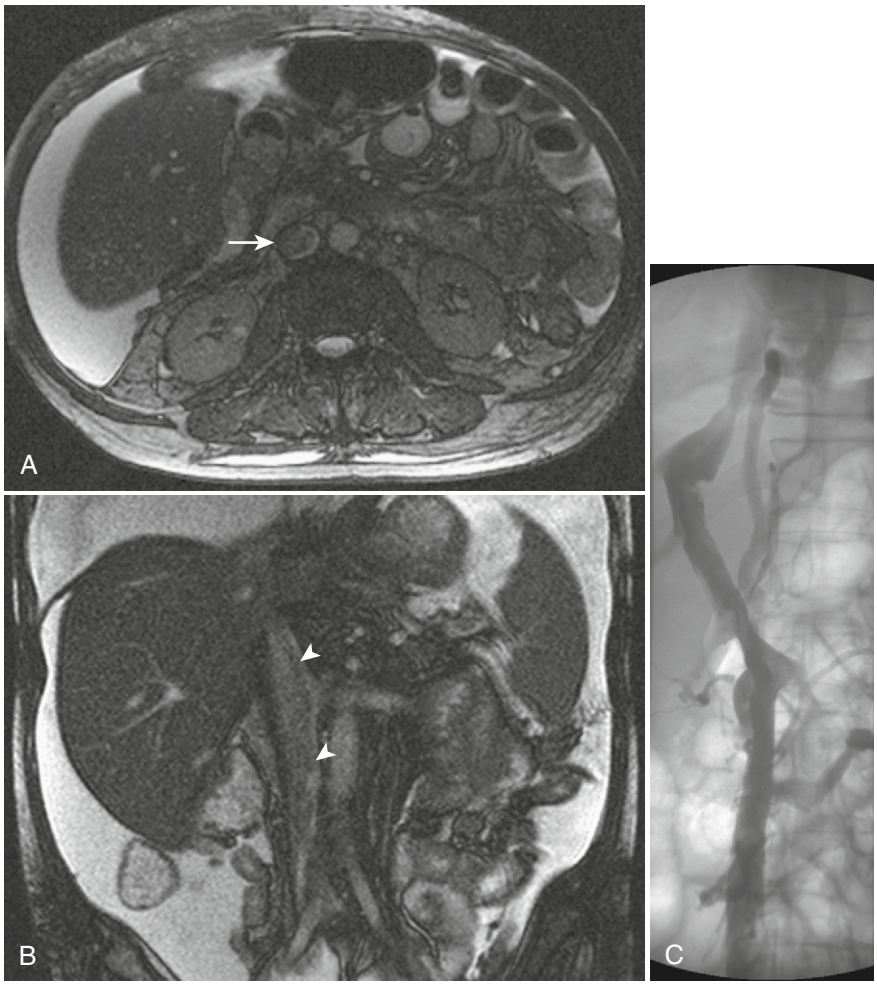


FIGURE 11-40. This patient had worsening ascites and pleural effusion after recent liver transplantation. Axial **(A)** and coronal **(B)** True FISP MR images show a filling defect along the IVC consistent with caval thrombosis. A large amount of ascites is identified. **C,** After catheter-directed thrombolysis, conventional venography shows a patent IVC with a focal stenosis at the suprahepatic IVC anastomosis site. This stenosis was treated with balloon angioplasty.

The standard treatment of IVC thrombosis is anticoagulation. If there is concern for pulmonary emboli, and there usually is, a filter can be placed above the thrombus, usually in the suprarenal segment of the IVC. Catheter-directed thrombolysis can also be performed for rapid relief of symptoms, for prevention of thrombus extension into side branches such as the renal veins, or for prevention of chronic occlusion-related complications. Also, a stent can be placed if an area of stenosis is identified during thrombolysis.

Inferior Vena Cava Trauma

Although the IVC is a low-pressure system, injuries can cause significant blood loss. This leads to hemodynamic compromise, and more than 50% of patients with vena caval injury die before arrival at the hospital. Surgical treatment of vena caval injuries is difficult, with a high intraoperative mortality. Whenever possible, supportive management is preferred to promote tamponade of the bleed through constriction by the hematoma and surrounding structures.

Renal Vein Thrombosis

Acute renal vein thrombosis (RVT) is a relatively common complication of nephrotic syndrome (especially when caused by membranous glomerulonephritis), occurring in as many as 10% of the cases. RVT can also develop as a consequence of thrombus extension from the inferior vena cava and the iliofemoral veins. Common signs and symptoms include flank pain, hematuria, and impaired renal function, or patients can be asymptomatic. Ultrasound can detect renal vein thrombosis, but visualization can be limited. Confirmation with CT or MRI is useful to further characterize the thrombosis and its extent, but the underlying impairment of the renal function may limit the use of intravenous contrast with both modalities.

Acute bland thrombus usually causes renal vein expansion, lack of enhancement of the renal vein, and asymmetric renal enhancement in the postcontrast images. When renal vein thrombosis is identified, tumor thrombus should be kept in mind as a possible differential, but tumor thrombus tends to enhance with contrast.

As with other deep vein thromboses, the standard treatment for RVT is anticoagulation. Systemic thrombolysis has also been described; however, hemorrhagic complications are seen in 15% to 40% of the cases and therefore anticoagulation is not routinely used. Recent studies in patients who presented with symptomatic

RVT and renal dysfunction have shown good outcomes with marked improvement of the renal function following treatment with catheter-directed thrombolysis and thrombectomy.

Portal Vein Thrombosis

Portal vein thrombosis is more frequently chronic in nature, and results from a focal occlusion that leads to the development of collateral pathways, known as cavernous transformation of the portal vein. Eventually, portal hypertension and portosystemic collaterals develop, which may cause variceal gastrointestinal bleed. Acute thrombosis of the portal vein is rare and usually occurs in patients with underlying hypercoagulable states or severe trauma. It may induce thrombosis of the superior mesenteric vein and cause intestinal ischemia. Endovascular recanalization with thrombolysis and thrombectomy can be attempted from a transjugular or transhepatic approach in selected cases (Fig. 11-41).

Mesenteric Venous Thrombosis

Acute superior mesenteric vein (SMV) thrombosis is an uncommon and insidious disease that is potentially lethal. Acute mesenteric thrombosis will cause congestion of the bowel wall and may result in intestinal ischemia. Signs and symptoms may overlap with those of many other diseases, and, thus, diagnosis and treatment can be delayed. Mesenteric venous thrombosis accounts for 5% to 15% of all mesenteric ischemic events. The main predisposing factor is underlying hypercoagulability. Other clinical conditions associated with SMV thrombosis include abdominal trauma, abdominal surgery, pancreatitis, sepsis, portal hypertension, underlying malignancies, and use of estrogens.

Contrast-enhanced MDCT establishes the diagnosis with a sensitivity of 90%. Findings include lack of venous enhancement, expansion of the mesenteric vein, mesenteric stranding, and bowel edema.

In general, anticoagulation is the first line of therapy for SMV thrombosis if no peritoneal signs are present. On the other hand, if signs of peritonitis are present, the management should be surgical. The 30-day mortality for SMV thrombosis varies from 15% to 50% with traditional anticoagulation and resection of the infarcted bowel. Catheter-directed thrombolysis has also been proposed as an alternative therapeutic modality.

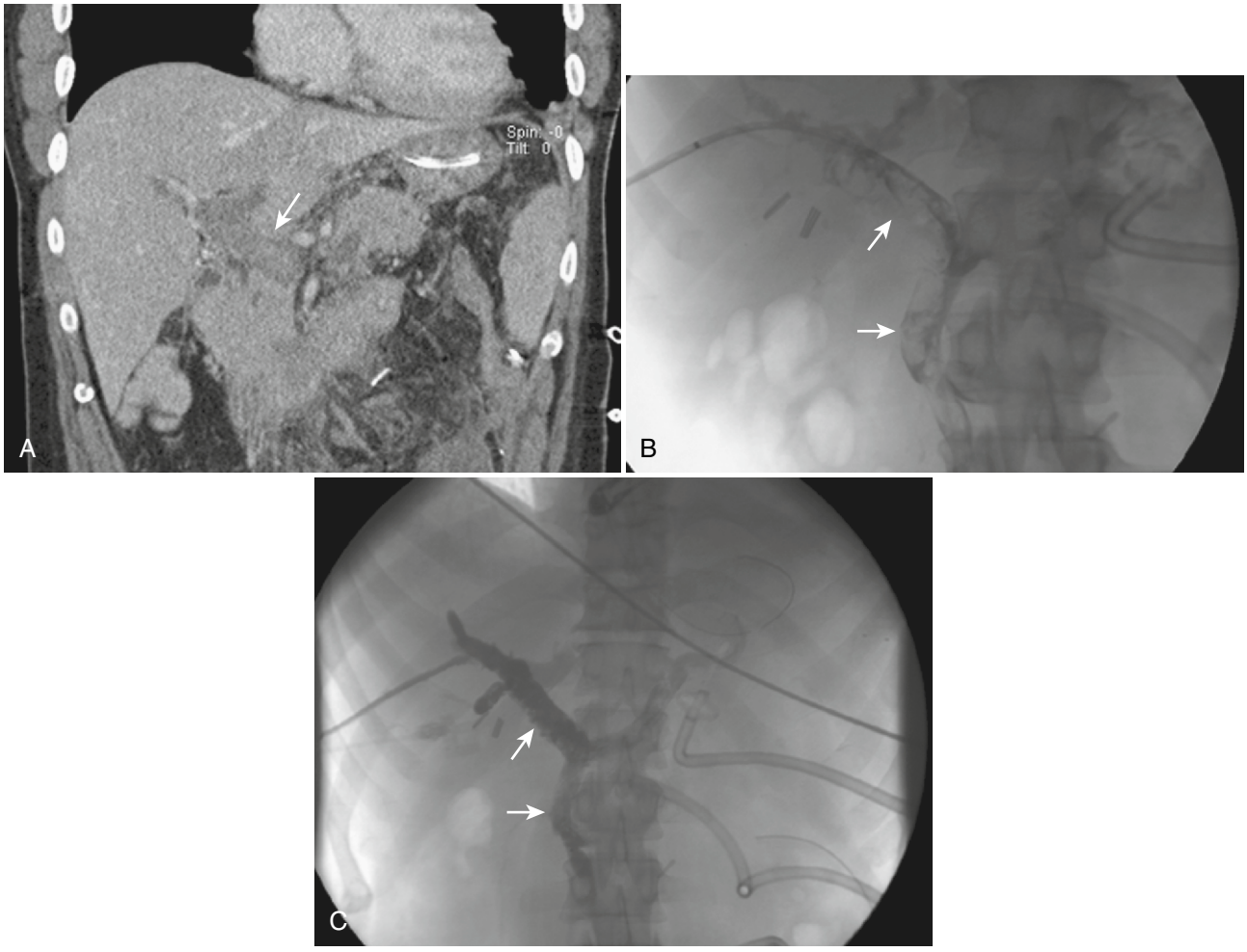


Figure 11-41. **A,** Patient with blunt abdominal trauma who subsequently developed bowel ischemia and required extensive bowel resection. Portal vein thrombosis was found on contrast-enhanced CT *(arrow).* **B,** Using a transhepatic approach, the portal vein was accessed; portal venogram confirms large thrombus burden involving the portal vein and SMV *(arrows).* **C,** After 48 hours of catheter-directed thrombolysis, flow has been reestablished and much of the thrombus has decreased *(arrows);* the patient was then started on anticoagulation therapy.

Hepatic Vein Obstruction

Acute thrombotic occlusion of the main hepatic veins (Budd-Chiari syndrome) can occur secondary to hypercoagulable states, underlying blood dyscrasias, malignancy, oral contraceptive use, or suprahepatic IVC webs. Acute Budd-Chiari syndrome typically causes hepatosplenomegaly, abdominal pain, massive ascites, and signs of liver dysfunction. Ultrasound demonstrates absent flow in the hepatic veins and heterogeneous liver echotexture. CT and MR can identify the lack of enhancement of the hepatic veins and heterogeneous, patchy enhancement of the liver parenchyma ("nutmeg" liver) with sparing of the caudate lobe, which maintains a normal enhancement pattern as a result of its separate, direct, drainage to the IVC. Acute occlusion can be treated with catheter-directed or systemic thrombolysis. If a weblike stenosis is identified, angioplasty or stenting can be attempted as well. Chronic anticoagulation is usually required when no underlying anatomical abnormality is identified. Transjugular intrahepatic portosystemic shunt creation is a therapeutic alternative to treat massive ascites secondary to hepatic venous outflow obstruction.

Venous Emergencies of the Upper Extremities

Venous Thrombosis

Acute thrombosis of superficial veins of the upper extremities is a common complication in patients with multiple intravenous accesses and in IV drug abusers. Central venous catheters are the most common cause of central upper extremity and jugular vein thrombosis, with approximately 50% of the patients developing some thrombus around the catheter, although less than 5% become symptomatic. Upper extremity edema is generally associated with thrombosis of the central veins at the axillary, subclavian, or brachiocephalic levels. Venous expansion can cause dull pain that may extend to the neck if the jugular vein is also involved. The overall rate of pulmonary embolism originating from upper extremity thrombosis is less than 10%; however, in 15% to 30% of central upper extremity thromboses, venous thrombosis may be complicated with pulmonary embolism. Acute thrombosis is characterized by the presence of an intraluminal filling defect that expands the vein and reduces or completely occludes its flow. Ultrasound, CT, and MRI can all demonstrate these changes. Ultrasound is the preferred modality for initial evaluation, but it has limited capability to directly interrogate the central veins, and further evaluation with MR venography or contrast CT is usually necessary. As with other types of venous thrombosis, treatment usually requires anticoagulation and, in specific cases, thrombolysis.

Thoracic Outlet Syndrome

Venous thoracic outlet syndrome frequently presents first as acute thrombosis of the upper extremity. There is frequently an underlying anatomical variant that causes central venous obstruction, such an anomalous muscle or ligament or a cervical rib. The term "effort thrombosis" or Paget-Schroetter syndrome is essentially the same phenomenon of subclavian vein thrombosis occurring in athletic patients probably due to repetitive venous compression secondary to muscle training and hypertrophy. The stenosis induced by progressive intimal hyperplasia leads to the development of collateral flow. Pulmonary embolus is infrequent because the underlying condition is a fixed venous stenosis. Evaluation with ultrasound is helpful in demonstrating the thrombus, but further assessment with CT or MRI can demonstrate the underlying anomaly, the extent of the occlusion, and the amount of collateral flow. Venograms are generally reserved for patients undergoing evaluation for thrombolysis, which is frequently effective in controlling the symptoms and revealing the underlying venous lesion. Patients can then undergo surgical decompression, and further catheter interventions such as balloon venoplasty and stenting are reserved for significant residual or recurrent postsurgical stenosis.

Venous Emergencies of the Pelvis and Lower Extremities

Deep venous thrombosis (DVT) of the lower extremities is a common disorder. Predisposing factors include immobilization, previous DVT, previous surgery (orthopedic surgery of the pelvis and knee and neurosurgical procedures), hypercoagulability syndromes, central venous catheters, oral contraceptives, iliac vein compression (May-Thurner syndrome or pelvic tumors), and IVC filters. Thrombosis originates more frequently in the calf veins, which are involved in more than 90% of the cases. Approximately 25% to 50% progress centrally toward the thigh and pelvis. Thrombosis of the iliac veins is identified and is usually secondary to extension of a more distal thrombus. Acute DVT presents with lower extremity edema, congestion, and pain. Pulmonary embolism can occur in up to 50% of the patients. The risk of embolism is much higher when the DVT extends above the popliteal vein. Clinically, acute DVT can be difficult to differentiate from entities such as cellulitis, ruptured Baker's cyst, superficial thrombophlebitis, chronic thrombosis, venous insufficiency, and other entities causing lower extremity edema. Serum D-dimer has become a popular screening test with a high negative predictive value when results are within normal limits. However, the specificity of this test is limited, and imaging is usually required to confirm the diagnosis. Ultrasound is by far the more frequently used imaging technique to identify lower extremity DVT, with sensitivity and specificity for detection of thrombus at the popliteal level and above higher than 95%. These numbers drop to 80% for veins in the calf region. Noncompressibility of the affected vein remains the single most reliable diagnostic criterion. Additional criteria include intraluminal thrombus visualization, vein enlargement, absent color flow signal, absent Doppler signal, absent respiratory variation and augmentation, and absent response to Valsalva maneuver.

The widespread use of CT to identify pulmonary emboli has led researchers to look for DVT during the same exam. Results demonstrate that thrombus can be identified in up to 10% of the lower extremity and pelvis scans obtained during the venous phase of enhancement of pulmonary CTA. MR venography has a sensitivity and specificity greater than 95% for the detection of DVT; however, its current use in the acute setting remains limited (Fig. 11-42). Conventional catheter venography has been practically abandoned for diagnosis of DVT. Today, catheter venography is **used only in patients who represent**

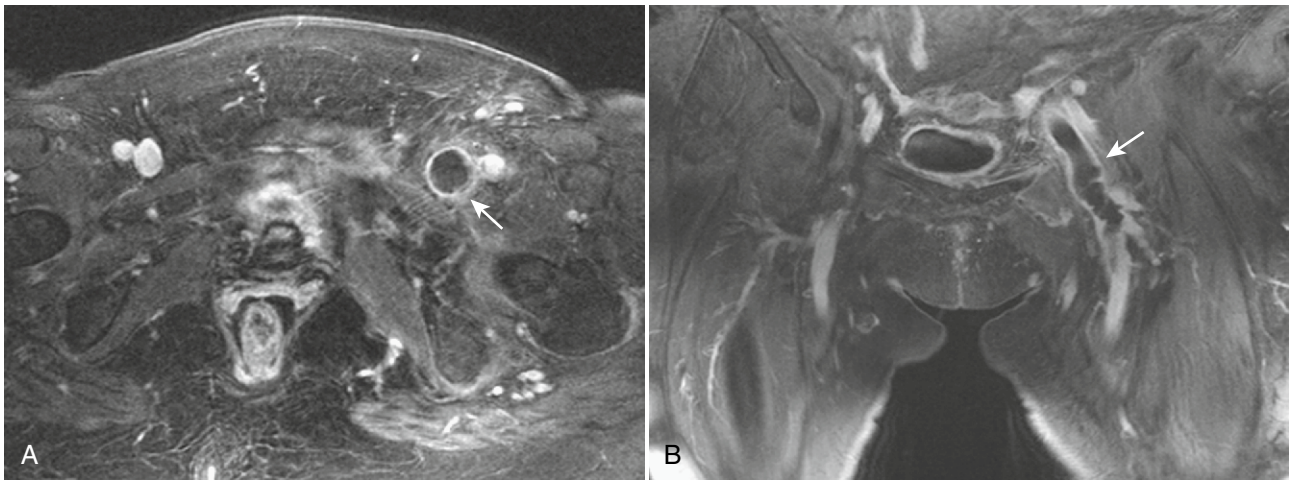


Figure 11-42. **A** and **B**, Axial and coronal fat-suppressed, contrast-enhanced, MR venography images show a large filling defect in the left common femoral and external iliac veins *(arrows)* with contrast surrounding the thrombus and venous enlargement consistent with acute deep vein thrombosis. Due to severe lower extremity edema and functional impairment, the patient subsequently underwent treatment with catheter-directed thrombolysis.

a diagnostic dilemma or in those who require a therapeutic intervention. Thrombi are seen as filling defects outlined by contrast material. Differentiation of acute and chronic DVT can be sometimes challenging but the presence of collateral veins is a helpful sign of chronicity. The traditional treatment of acute DVT is anticoagulation to prevent extension of the thrombus while the endogenous mechanisms progressively lyse the clot and reestablish patency. With this approach, complete resolution of the thrombosis is achieved in up to 50% of the cases. Thrombolysis and mechanical thrombectomy can be performed as well. The principle is to macerate the thrombus to expose greater portions of the thrombus to the lytic agent and at the same time facilitate its removal or breakdown by endogenous mechanisms. The great majority of patients have prompt relief of their symptoms, and venous patency at 1 year is maintained in more than 70% of the patients. There are many contraindications to thrombolytic therapy, mostly involving factors that increase the risk of serious bleeding, such as recent surgery, upper gastrointestinal bleeding, recent CVA, and central nervous system tumor or trauma. Bleeding requiring transfusion was reported in 11% of patients in the National Venous Thrombolysis Registry, and the rate of intracranial bleeding was only 0.2%. Venous stent placement after venous thrombolysis is usually reserved for patients with underlying stenosis of a large vein.

Suggested Readings

AbuRahma AF: Fate of endoleaks detected by CT angiography and missed by color duplex ultrasound in endovascular grafts for abdominal aortic aneurysms. J Endovasc Ther 13:90–95, 2006.

Ahrar K, Smith DC, Bansal RC, et al: Angiography in blunt thoracic aortic injury. J Trauma 42:665–669, 1997.

Al-Bahrani AZ, Abid GH, Sahgal E, et al: A prospective evaluation of CT features predictive of intra-abdominal hypertension and abdominal compartment syndrome in critically ill surgical patients. Clin Radiol 26:676–682, 2007.

Asensio JA, Chahwan S, Hanpeter D, et al: Operative management and outcome of 302 abdominal vascular injuries. Am J Surg 180:528–534, 2000.

Atar E, Belenky A, Hadad M, et al: MR Angiography for abdominal and thoracic aortic aneurysms: Assessment before endovascular repair in patients with impaired renal function. AJR Am J Roentgenol 186:386–393, 2006.

Attia C, Villard J, Boussel L, et al: Endovascular repair of localized pathological lesions of the descending thoracic aorta: Midterm results. Cardiovasc Intervent Radiol 30:628–637, 2007.

Berthet JP, Marty-Ane CH, Veerapen R, et al: Dissection of the abdominal aorta in blunt trauma: Endovascular or conventional surgical management? J Vasc Surg 38:997–1004, 2003.

Bhalla S, Menias CO, Heiken JP: CT of acute abdominal aortic disorders. Radiol Clin North Am 41:153–169, 2003.

Biffi WL, Ray CE Jr, Moore EE, et al: Noninvasive diagnosis of blunt cerebrovascular injuries: A preliminary report. J Trauma 53:850–856, 2002.

Bolognesi R, Manca C, Tsialtas D, et al: Aortic intramural hematoma: An increasingly recognized aortic disease. Cardiology 89:178–183, 1998.

Branchereau A, Jacobs M (eds): Vascular Emergencies. Elmsford, NY: Wiley-Blackwell, 2003.

Brandt M, Wallusheck KP, Jahnke T, et al: Endovascular repair of ruptured abdominal aortic aneurysm: Feasibility and impact on early outcome. Vasc Interv Radiol 16:1309–1312, 2005.

Castaner E, Andreu M, Gallardo X, et al. CT in nontraumatic acute thoracic aortic disease: Typical and atypical features and complications. RadioGraphics 23(Suppl):S93–S110, 2003.

Chan FY, Crawford ES, Coselli JS, et al: In situ prosthetic graft replacement of mycotic aneurysm of the aorta. Ann Thorac Surg 47:193–203, 1989.

Demers P, Miller DG, Mitchell RS, et al: Stent-graft repair of penetrating atherosclerotic ulcers in the descending thoracic aorta: Mid-term results. Ann Thorac Surg 77:81–86, 2004.

Deree J, Shenvi E, Fortlage D, et al: Patient factors and operating room resuscitation predict mortality in traumatic abdominal aortic injury: A 20-year analysis. J Vasc Surg 3:493–497, 2007.

Dogra VS, Bhatt S (eds): Emergency Cross-Sectional Imaging. Radiol Clin of North Am 45, 2007.

Dyer S, Moore EE, Ilke DN, et al: Thoracic aortic injury: How predictive is mechanism and is chest computed tomography a reliable screening tool? A prospective study of 1,561 patients. J Trauma 48:673–683, 2000.

Evangelista A, Mukherjee D, Mehta RH, et al: Acute intramural hematoma of the aorta: A mystery in evolution. Circulation 111:1063–1070, 2005.

Faggioli G, Stella A, Freyrie A, et al: Early and long-term results in the surgical treatment of juxtarenal and pararenal aortic aneurysms. Eur J Vasc Endovasc Surg 15:205–211, 1998.

Fang JF, Wong YC, Lin BC, et al: Usefulness of multidetector computed tomography for the initial assessment of blunt abdominal trauma patients. World J Surg 30:176–182, 2006.

Farber A, Wagner WH, Cossman DV, et al: Isolated dissection of the abdominal aorta: Clinical presentation and therapeutic options. J Vasc Surg 36:205–210, 2002.

Fattori R, Napoli G, Lovato L, et al: Descending thoracic aortic disease: Stent-graft repair. Radiology 229:176–183, 2003.

Federle MP, Pan KT, Pealer KM: CT criteria for differentiating abdominal hemorrhage: Anticoagulation or aortic aneurysm rupture? AJR Am J Roentgenol 188:1324–1330, 2007.

Fishman JE: Imaging of blunt aortic and great vessel trauma. J Thorac Imaging 15:97–103, 2000.

Fishman JE, Nunez D Jr, Kane A, et al: Direct versus indirect signs of traumatic aortic injury revealed by helical CT: Performed characteristics and interobserver agreement. AJR Am J Roentgenol 172:1027–1031, 1999.

Garzon G, Fernandez-Velilla M, Marti M, et al: Endovascular stent-graft treatment of thoracic aortic disease. Radiographics 25(Suppl):S229–S244, 2005.

Gavant ML: Helical CT grading of traumatic aortic injuries: Impact on clinical guidelines for medical and surgical management. Radiol Clin North Am 37:553–573, 1999.

Görich J, Asquan Y, Seifarth H, et al: Initial experience with intentional stent-graft coverage of the subclavian artery during endovascular thoracic aortic repairs. J Endovasc Ther 9(Suppl 2):II-39–II-43, 2002.
Gunn M, Campbell M, Hoffer EK: Traumatic abdominal aortic injury treated by endovascular stent placement. Emerg Radiol 13:329–331, 2007.
Hallet JW: Splenic artery aneurysms. Semin Vasc Surg 8:321–326, 1995.
Halliday KE, al-Kutoubi A: Draped aorta: CT sign of contained leak of aortic aneurysms. Radiology 199:1-3, 1996.
Hellmann DB, Grand DJ, Freischlag JA: Inflammatory abdominal aortic aneurysm. JAMA 297:395–400, 2007.
Hermsen K, Chong WK: Ultrasound evaluation of abdominal aortic and iliac aneurysms and mesenteric ischemia. Radiol Clin North Am 42:365–381, 2004.
Hillemanns P, Knitza R, Muller-Hocker J: Rupture of splenic artery aneurysm in a pregnant patient with portal hypertension. Am J Obstet Gynecol 174:1665–1666, 1996.
Hirsch AT, Haskal ZJ, Hertzer NR, et al: ACC/AHA 2005 Practice Guidelines for the management of patients with peripheral arterial disease (lower extremity, renal, mesenteric, and abdominal aortic): A collaborative report. Circulation 113:e463–e654, 2006.
Hollerman JJ, Fackler ML, Coldwell DM, Ben-Menachem Y: Gunshot wounds: 2. Radiology. AJR Am J Roentgenol 155:691–702, 1990.
Hovsepian DM, Hein AN, Pilgram TK, et al: Endovascular abdominal aortic aneurysm repair in 144 patients: Correlation of aneurysm size, proximal aortic neck length, and procedure-related complications. J Vasc Interv Radiol 12: 1373–1382, 2001.
Inaba K, Munera F, McKenney MG, et al: The nonoperative management of penetrating internal jugular vein injury. J Vasc Surg 43:77–80, 2006.
Ishida M, Kato N, Hirano T, et al: Endovascular stent-graft treatment for thoracic aortic aneurysms: Short- to midterm results. J Vasc Interv Radiol 15:361–367, 2004.
Isselbacher EM: Thoracic and abdominal aortic aneurysms. Circulation 15(111): 16–28, 2005.
Iyer VS, MacKenzie KS, Tse LW, et al: Early outcomes after elective and emergent endovascular repair of the thoracic aorta. J Vasc Surg 43:677–683, 2006.
Kaji S, Nishigami K, Akasaka T, et al: Prediction of progression or regression of type A aortic intramural hematoma by computed tomography. Circulation 100(Suppl 2):II-281–II-286, 1999.
Kasirajan K, Heffernan D, Langsfeld M: Acute thoracic aortic trauma: A comparison of endoluminal stent grafts with open repair and nonoperative management. Ann Vasc Surg 17:589–595, 2003.
Kaufman JA, Lee MJ: Vascular and Interventional Radiology: The Requisites. Philadelphia, Elsevier, 2004.
Kerwin AJ, Bynoe RP, Murray J, et al: Liberalized screening for blunt carotid and vertebral artery injuries is justified. J Trauma 51:308–314, 2001.
Kieffer E, Bahnini A, Koskas F, et al: In situ allograft replacement of infected infrarenal aortic prosthetic graft: Results in forty-five patients. J Vasc Surg 17:349–356, 1993.
Kim HS, Fine DM, Atta MG: Catheter-directed thrombectomy and thrombolysis for acute renal vein thrombosis. J Vasc Interv Radiol 17:815–822, 2006.
Kim HS, Patra A, Khan J, et al: Transhepatic catheter-directed thrombectomy and thrombolysis of acute superior mesenteric venous thrombosis. J Vasc Interv Radiol 16:1685–1691, 2005.
Laffargue G, Taourel P, Saguintaah M, et al: CT diagnosis of abdominal compartment syndrome. AJR Am J Roentgenol 178:771–772, 2002.
Laing CJ, Tobias T, Rosenblum DI, et al: Acute gastrointestinal bleeding: Emerging role of multidetector CT angiography and review of current imaging techniques. Radiographics 27:1055–1070, 2007.
Lamah M, Darke S: Value of routine computed tomography in the preoperative assessment of abdominal aneurysm replacement. World J Surg 23:1076–1080, 1999; discussion 1080–1081.
LaRoy LL, Cormier PJ, Matalon TA, et al: Imaging of abdominal aortic aneurysms. AJR Am J Roentgenol 152:85–92, 1989.
LeBlang SD, Dolich MO: Imaging of penetrating thoracic trauma. J Thorac Imaging 15:28–35, 2000.
Lettinga-van de Poll T, Schurink GW, De Hann MW, et al: Endovascular treatment of traumatic rupture of the thoracic aorta. Br J Surg 94:525–533, 2007.
Levy JR, Heiken JP, Gutierrez FR: Imaging of penetrating atherosclerotic ulcers of the aorta. AJR Am J Roentgenol 173:151–154, 1999.
Lohan DG, Saleh R, Nael K, et al: Contrast-enhanced MRA versus nonenhanced MRA: Pros and cons. Applied Radiol(Suppl):S3–S15, 2007.
Makaroun MS, Dillavou ED, Kee ST, et al: Endovascular treatment of thoracic aortic aneurysms: Results of the phase II multicenter trial of the GORE TAG thoracic endoprosthesis. J Vasc Surg 41:1–9, 2005.
Manghat NE, Morgan-Hughes GJ, Roobottom CA: Multi-detector row computed tomography: Imaging in acute aortic syndrome. Clin Radiol 60:256–267, 2005.
Mark A, LePage MA, Quint LE, Sonnad SS: Aortic dissection: CT features that distinguish true lumen from false lumen. AJR Am J Roentgenol 177:207–211, 2001.
Mattox KL: Injury to the thoracic great vessels. In Moore EE, Mattox KL, Feliciano DV (eds): Trauma, (2nd ed). Norwalk, CT: Appleton & Lange, 1991, p 393.
May J, White GH, Waugh R, et al: Improved survival after endoluminal repair with second-generation prostheses compared with open repair in the treatment of abdominal aortic aneurysms: A 5-year concurrent comparison using life table method. J Vasc Surg 33(Suppl 2):S21–S26, 2001.
McKenney KL, McKenney MG, Cohn SM, et al: Hemoperitoneum score helps determine need for therapeutic laparotomy. J Trauma 50:650–654, 2001.
Miller LA, Shanmuganathan K: Multidetector CT evaluation of abdominal trauma. Radiol Clin North Am 43:1079–1095, 2005.
Mirvis SE, Shanmuganathan K, Miller BH, et al: Traumatic aortic injury: Diagnosis with contrast-enhanced thoracic CT—five-year experience at a major trauma center. Radiology 200:13–22, 1996.
Moizumi Y, Komatsu T, Motoyoshi N, Tabayashi K: Clinical features and long-term outcome of type A and type B intramural hematoma of the aorta. J Thorac Cardiovasc Surg 127:421–427, 2004.
Munera F, Soto JA, Palacio D, et al: Diagnosis of arterial injuries caused by penetrating trauma to the neck: Comparison of helical CT angiography and conventional angiography. Radiology 216:356–362, 2000.
Munera F, Soto JA, Palacio D, et al: Penetrating neck injuries: Helical CT angiography for initial evaluation. Radiology 224:366–372, 2002.
Nienaber CA, Kische S, Ince H: Thoracic aortic stent-graft devices: Problems, failure modes, and applicability. Semin Vasc Surg 20:1–9, 2007.
Noel AA, Gloviczki P, Cherry KJ Jr, et al: Ruptured abdominal aortic aneurysms: The excessive mortality rate of conventional repair. J Vasc Surg 34:41–46, 2001.
O'Sullivan GJ, Lohan DG, Gough N, et al: Pharmacomechanical thrombectomy of acute deep vein thrombosis with the trellis-8 isolated thrombolysis catheter. J Vasc Interv Radiol 18:715–724, 2007.
Pamela T, Johnson PT, Chen JK, Loey BL: Loeys-Dietz syndrome: MDCT angiography findings. AJR Am J Roentgenol 189:29–35, 2007.
Parellada JA, Palmer J, Monill JM, et al: Mycotic aneurysm of the abdominal aorta: CT findings in three patients. Abdom Imaging 22:321–324, 1997.
Patel NH, Stephens KE, Mirvis SE, et al: Imaging of acute thoracic aortic injury due to blunt trauma: A review. Radiology 209:335–348, 1998.
Pauls S, Orend KH, Sunder-Plassmann L, et al: Endovascular repair of symptomatic penetrating atherosclerotic ulcer of the thoracic aorta. Eur J Vasc Endovasc Surg 34:66–73, 2007.
Peterson AH, Williams DM, Rodrigues JL, Francis IR: Percutaneous treatment of a traumatic aortic dissection by balloon fenestration and stent placement. AJR Am J Roentgenol 164:1274–1276, 1995.
Picard E, Marty-Ane CH, Vernhet H, et al: Endovascular management of traumatic infrarenal abdominal aortic dissection. Ann Vas Surg 12:515–521, 1998.
Pickhard PJ, Shimony JS, Heiken JP, et al: The abdominal compartment syndrome: CT findings. AJR Am J Roentgenol 173:575–579, 1999.
Quint LE, Williams DM, Francis IR, et al: Ulcerlike lesions of the aorta: Imaging features and natural history. Radiology 218:719–723, 2001.
Rakita D, Newatia A, Hines JJ, et al: Spectrum of CT findings in rupture and impending rupture of abdominal aortic aneurysms. Radiographics 27:497–507, 2007.
Rivas LA, Munera F, Fishman JE: Multidetector-row computerized tomography of aortic injury. Semin Roentgenol 41:26–36, 2006.
Saletta S, Lederman E, Fein S, et al: Transesophageal echocardiography for the initial evaluation of the widened mediastinum in trauma patients. J Trauma 39:137–142, 1995; discussion 141–142.
Sanchez-Ross M, Anis A, Walia J, et al: Aortic rupture: Comparison of three imaging modalities. Emerg Radiol 13:31–33, 2006.
Schoder M, Grabenwoger M, Holzenbein T, et al: Endovascular stent-graft repair of complicated penetrating atherosclerotic ulcers of the descending thoracic aorta. J Vasc Surg 36:720–726, 2002.
Schwartz SA, Taljanovic MS, Smyth S, et al: CT findings of rupture, impending rupture, and contained rupture of abdominal aortic aneurysms. AJR Am J Roentgenol 188:W57–W62, 2007.
Sebastià C, Pallisa E, Quiroga S, et al: Aortic dissection: Diagnosis and follow-up with helical CT. Radiographics 19:45–60, 1999.
Shanmuganathan K: Multi-detector row CT imaging of blunt abdominal trauma. Semin Ultrasound CT MR 25:180–204, 2004.
Shanmuganathan K, Mirvis SE, Sover ER: Value of contrast-enhanced CT in detecting active hemorrhage in patients with blunt abdominal and pelvic trauma. AJR Am J Roentgenol 161:5–9, 1993.
Shiga T, Wajima Z, Apfel CC, et al: Diagnostic accuracy of transesophageal echocardiography, helical computed tomography, and magnetic resonance imaging for suspected thoracic aortic dissection. Arch Intern Med 166: 1350–1356, 2006.
Sicard GA, Zwolak RM, Sidawy AN, et al: Endovascular abdominal aortic aneurysm repair: Long-term outcome measures in patients at high risk for open surgery. J Vasc Surg 44:229–236, 2006.
Sommer T, Fehske W, Holzknecht N, et al: Aortic dissection: A comparative study of diagnosis with spiral CT, multiplanar transesophageal echocardiography, and MR imaging. Radiology 199:347–452, 1996.
Soto JA, Munera F, Cardoso N, et al: Diagnostic performance of helical CT angiography in trauma to large arteries of the extremities. J Comput Assist Tomogr 23:188–196, 1999.
Soto JA, Munera F, Morales C, et al: Focal arterial injuries of the proximal extremities: Helical CT arteriography as the initial method of diagnosis. Radiology 218:188–194, 2001.
Stone DH, Brewster DC, Kwolek CJ: Stent-graft versus open-surgical repair of the thoracic aorta: Mid-term results. J Vasc Surg 44:188–197, 2006.
Suzuki T, Mehta RH, Ince H, et al: Clinical profiles and outcomes of acute type B aortic dissection in the current era: Lessons from the International Registry of Aortic Dissection (IRAD). Circulation 108(Suppl 2): II-312–II-317, 2003.
Symbas PN, Sherman AJ, Silver JM, et al: Traumatic rupture of the aorta: Immediate or delayed repair? Ann Surg 235:796–802, 2002.

Tespili M, Banfi C, Valsecchi O, et al: Endovascular treatment of thoracic aortic disease: Mid-term follow-up. Catheter Cardiovasc Interv 70:595–601, 2007.
Teufelsbauer H, Polterauer P, Lammer J, et al: Repair of abdominal aortic aneurysms: The benefits of offering both endovascular and open surgical techniques. Perspect Vasc Surg Endovasc Ther 18:238–246, 2006.
Thanila A, Macedo TA, Stantson AW, Oderich GS: Infected aortic aneurysms: Imaging findings. Radiology 231:250–257, 2004.
Thomas TT, Evangelist A, Nienaber CA, et al: Long-term survival in patients presenting with type A acute aortic dissection: Insights from the International Registry of Acute Aortic Dissection (IRAD). Circulation 114:350–356, 2006.
Tsai TT, Nienaber CA, Eagle KA: Acute aortic syndromes. Circulation 112: 3802–3813, 2005.
Veith FJ, Baum RA, Ohki T, et al: Nature and significance of endoleaks and endotension: Summary of opinions expressed at an international conference. J Vasc Surg 35:1029–1035, 2002.
Vernhet H, Marty-Ane CH, Lesnik A, et al: Dissection of the abdominal aorta in blunt trauma: Management by percutaneous stent placement. Cardiovasc Intervent Radiol 20:473–476, 1997.
von Kodolitsch Y, Nienaber CA, Dieckmann C, et al: Chest radiography for the diagnosis of acute aortic syndrome. Am J Med 116:73–77, A-40, 2004.
Weigel S, Tombach B, Waintz D, et al: Thoracic aortic stent graft: Comparison of contrast-enhanced MR angiography and CT angiography in the follow-up: Initial results. Eur Radiol 13:1628–1634, 2003.
White GH, Yu W, May J, et al: Endoleak as a complication of endoluminal grafting of abdominal aortic aneurysms: Classification, incidence, diagnosis, and management. J Endovasc Surg 4:152–168, 1997.
Willens HJ, Kessler KM: Transesophageal echocardiography in the diagnosis of diseases of the thoracic aorta: Part 1. Aortic dissection, aortic intramural hematoma, and penetrating atherosclerotic ulcer of the aorta. Chest 116: 772–779, 1999.
Won JY, Lee DY, Shim WH, et al: Elective endovascular treatment of descending thoracic aortic aneurysms and chronic dissections with stent-grafts. J Vasc Interv Radiol 12:575–582, 2001.
Yang CY, Liu KL, Lee CW, et al: Mycotic aortic aneurysm presenting initially as an aortic intramural air pocket. AJR Am J Roentgenol 185:463-465, 2005.
Yeh TS, Jan YY, Jeng LB, et al: Massive extra-enteric gastrointestinal hemorrhage secondary to splanchnic artery aneurysms. Hepatogastroenterology 44: 1152–1156, 1997.

CHAPTER 12

Emergency Nuclear Radiology

Anna K. Chacko, Rashmikant B. Shah, and J. Andrew Chacko

The fast pace of modern life, the increasing mobility of a rapidly growing population, the increasing communicability of disease, and complications from complex medical surgical interventions have all combined to increase the incidence of emergency medical situations. Furthermore, increasing awareness that timely intervention could halt or forestall dangerous disease conditions, along with the ability to treat such conditions, has resulted in emergency medicine becoming a rapidly developing and expanding medical specialty. This, consequently, has required the increasing support of imaging services.

The staple of imaging support has always been conventional radiography. However, newer modalities have made inroads into the use of plain film. These modalities are interventional radiology, computed tomography (CT), magnetic resonance imaging (MR), ultrasound, and nuclear medicine.

Since the development and refinement of CT, MR, and ultrasound, the use of nuclear medicine in the emergency setting has undergone significant changes. However, with development of fusion imaging—combining the strengths of different modalities while minimizing their weaknesses—we can anticipate a resurgence in the use of nuclear medicine techniques.

To fully exploit the use of radionuclides in the emergent or urgent situation, it is essential to understand the basic premise and promise of the modality. Scintigraphic techniques are inherently exquisitely sensitive while limited in providing spatial resolution. Metabolic changes invariably precede the appearance of anatomic changes. This feature is fundamental to nuclear medicine and consequently provides the information sought.

It is vital to understand, even superficially, the physics of the modality and the kinetics and chemistry of the tracers used.

RADIONUCLIDES

Radionuclides used in nuclear medicine are produced by artificial means in either a nuclear reactor or a particle accelerator. Both production methods involve the bombardment of a target nucleus with high-energy particles, which results in the transformation of stable nuclides into radionuclides.

In a reactor, the target is bombarded with neutrons, producing radioactive products with an excess of neutrons. By contrast, in a cyclotron, the target is bombarded with charged particles such as protons, producing radioactive species whose nuclei contain a deficit of neutrons or an excess of protons. While reactor-produced radionuclides emit β– particles and cyclotron-produced radionuclides emit β+ particles, some of these products emit gamma rays, which makes them useful in nuclear medicine imaging. For an elegant and concise explanation of how reactors and cyclotrons work, the reader is referred to the third edition of *Nuclear Medicine in Clinical Diagnosis and Treatment*, by P.J. Ell and S.S. Gambhir.

Radionuclides used for imaging have to possess certain characteristics that make them suitable for imaging. These properties include the following: gamma emission, short half-life (minutes to hours), high tissue penetration, and high specific activity. When used in tagged (as a radiopharmaceutical) or untagged form, these radionuclides have to provide useful clinical information while exposing the patient to minimal radiation. The chemical properties of the radionuclide should allow for its incorporation into the tracer of choice. The physical half-life of the radionuclide and biologic and effective half-life of the tracer have to effectively allow the study of the organ/metabolic/pathologic process under consideration. Ideally, the emission should be a single gamma ray in the range of 100 to 250 keV allowing good detection efficiency with the thallium-doped sodium iodide (NaI) crystal used in conventional nuclear medicine cameras.

Several of the radionuclides that are made in accelerators or nuclear reactors have half-lives long enough to allow shipment to distant (health care) facilities. When a long-lived radionuclide decays to a shorter-lived radionuclide, the parent nuclide can potentially become a transportable source for the production of the daughter nuclide. Since the parent and daughter radionuclides are chemically different, the daughter can be extracted either for direct use or for tagging. The device for transporting and extracting the daughter radionuclide is called a generator.

The most widely used radionuclide in nuclear medicine is technetium-99m (Tc-99m). Some of the other radionuclides used for clinical emergency situations include xenon-133 and indium-111.

Technetium-99m

Technetium exists only in the form of radioactive isotopes. The first Tc-99m generator was developed in 1958. This allowed convenient transport of the radionuclide and an explosion in the development of medical applications of Tc-99m.

Tc-99m is the most widely used tracer in nuclear medicine, accounting for over 85% of routine diagnostic procedures in a nuclear medicine department. The following radiation characteristics of technetium-99m make it an ideal agent (Fig. 12-1).

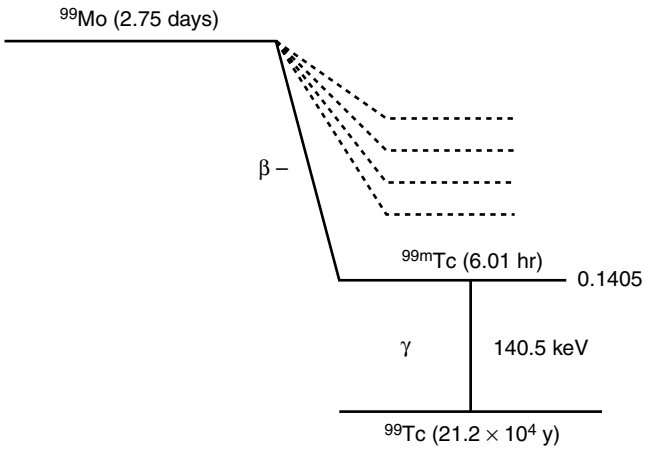


Figure 12-1. Decay scheme showing the isometric transition of Tc-99m.

- Short half-life of 6 hours
- 140.5 keV gamma emission, which gives ideal tissue penetration allowing easy collimation and excellent absorption in the thallium-doped NaI crystal
- Tc-99m decays to technetium-99, which has a half-life of 21,000 years! However, Tc-99 is a low-energy beta emitter.
- Gamma emission allows the use of higher doses while absorbed radiation dose is maintained at acceptable levels.

Gamma rays are attenuated both in tissue and in detector material (thallium-doped NaI). Compton scatter is the predominant interaction in tissue while the photoelectric effect is the interaction occurring in the detector. Radionuclides emitting low-energy gamma rays are likely to be absorbed by photoelectric effect within the tissue and will not reach the detector. This leads to poor resolution images, often requiring larger doses than those with higher-energy gamma rays, which will make it through to the detector.

Tc-99m is obtained from "milking" a molybdenum-99 (Mo-99) generator (Fig. 12-2). Mo-99 is obtained as a by-product from the fission of uranium. Mo-99 is chemically separated from the other radionuclides in the reactor product. Purified Mo-99 as anionic molybdate solution is loaded on to the generator column, which contains alumina. The alumina, which is positively charged, is able to adsorb Mo-99 ions. The assembly is then autoclaved. Several normal saline washings of the column yield eluate containing Tc-99m. These washings are subjected to several quality control tests to determine eluate volume, radionuclide purity ("moly" breakthrough), radiochemical purity (proper chemical form of technetium as pertechnetate), pyrogenicity, sterility, and/or alumina breakthrough. The half-life of Mo-99 is 66 hours allowing for weekly delivery of the generator to elute Tc-99m.

The eluted technetium can now be tagged to the appropriate pharmaceutical for use. When radionuclides such as technetium are tagged to specific pharmaceuticals, they are called radiopharmaceuticals. The pharmaceutical portion of the diagnostic radiopharmaceutical is present in very small amounts and will not elicit any pharmacologic response in the patient. The radioactive component is present in even smaller amounts. The technetium-99m radiopharmaceuticals for use in the emergency situation are listed in Box 12-1.

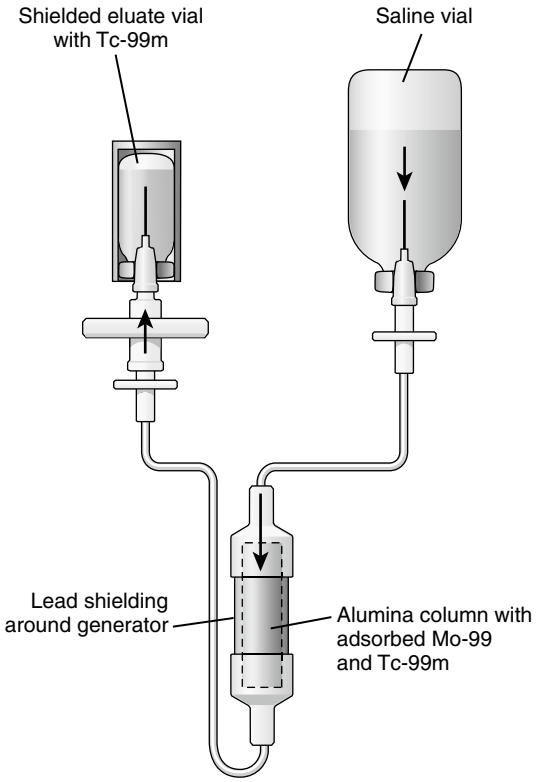


Figure 12-2. Molybdenum-technetium generator.

The radiopharmaceuticals are made up from "cold kits" supplied by manufacturers. With the exception of HMPAO (hexamethylpropyleneamine oxime), the kits are generally stable for up to 12 months. These kits provide a very convenient method of preparing radiopharmaceuticals in facilities that may not be close to laboratories. Technetium-99m can assume oxidation states ranging from I to VII based on the number of electrons available for reaction with ligands. The lower the oxidation state the less stable it is and the most likely to react with ligands. The most stable electronic configuration for technetium is the state with the value of VII where it is present as the pertechnetate ion and unlikely to tag to a ligand. Consequently, in order to produce a Tc-99m–labeled radiopharmaceutical, the technetium

***Box 12-1.* Tc-99m Radiopharmaceuticals**

Tc-99m pertechnetate for scrotal scanning
Tc-99m MAA for perfusion lung scans
Tc-99m sulfur colloid for GI bleeding
Tc-99m DTPA
Tc-99m methylene diphosphonate for bone scanning
Tc-99m pertechnetate
Tc-99m HMPAO (exametazime) or Tc-99m ethyl cysteinate dimer
Tc-99m MAG3 for renal scanning
Tc-99m–labeled RBCs for GI bleeding

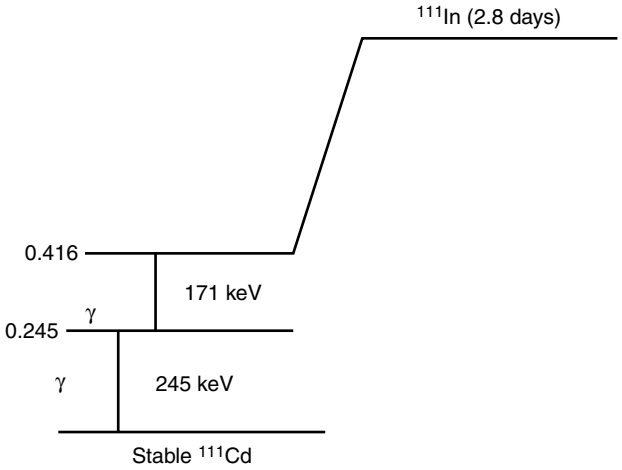


FIGURE 12-3. Decay scheme for In-111—electron capture.

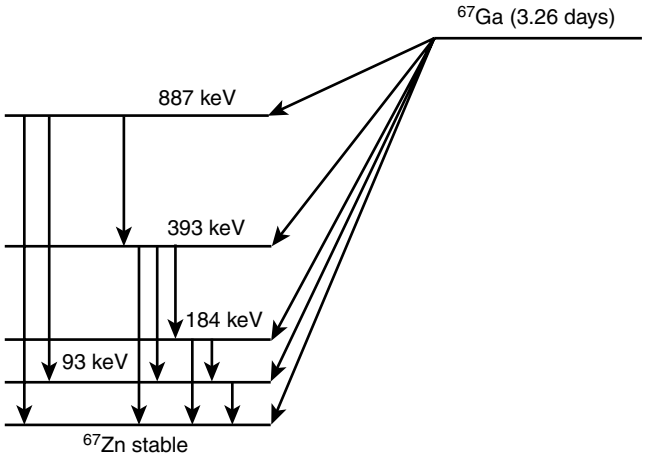


FIGURE 12-4. Decay scheme for gallium-67.

has to be first reduced to a lower oxidation state. This is most commonly accomplished by the addition of tin. As well, some cold kits contain antioxidants such as ascorbic acid or gentisic acid, which not only retard oxidation of the radiolabeled product, but also improve the stability of the kit. Tin II (stannous) supplies electrons and in the process becomes oxidized to tin V (stannic) ion. The various oxidation states of technetium allow the formation of a variety of different radiopharmaceuticals, which adds to the value of technetium as a nuclear medicine staple.

Reagents in the "kit" vial are generally freeze-dried and packed under vacuum. Alternatively, they may be combined with an inert gas such as nitrogen. This ensures that the tin in stannous form will not get oxidized to stannic form by exposure to the atmosphere. The amount of tin in the reagent vial is critical to the preparation of the radiopharmaceutical. Inadequate amounts of tin allow the oxidation of free pertechnetate, which ultimately degrades the image obtained and could potentially render a study nondiagnostic.

Indium-111

In-111 is produced in a cyclotron from the radioactive parent Cd-112. It has a half-life of 67 hours (2.8 days). The principal photons are 178 keV and 247 keV. The relatively long half-life of In-111 allows sequential imaging (Fig. 12-3).

Xenon-133

Xe is an inert and relatively insoluble gas produced by the fission of uranium-235. It is used in its radioactive form most commonly for ventilation studies. Xe-133 has a physical half-life of 5.3 days and, in the face of normal pulmonary function, a biological half-life of approximately 30 seconds.

The main disadvantages of Xe-133 are the low photon abundance (36%) and low tissue penetration of the 81 keV gamma ray. The low photon energy generally mandates the initial use of the xenon, that is, before the administration of the technetium lung perfusion agent. Overlying soft tissue, such as breast, can produce artifacts on the xenon images.

Gallium-67 Citrate

While Ga-67 citrate cannot be used for an emergent situation requiring a diagnostic test within a few hours of requisition, it is an important radionuclide for the workup of infection, which constitutes an emergency of sorts.

Gallium-67 is produced in a cyclotron from the parent zinc-68. Gallium-67 decays by electron capture to stable zinc-67 in 3.26 days (Fig. 12-4). The transition energy, which is 0.997 MeV, is dissipated by several electron capture transitions. Several gamma photons are emitted that are used for imaging. The principal ones are 93 keV with 37% abundance, 185 keV with 20% abundance, 300 keV with 17% abundance, and 394 keV with 5% abundance.

The exact mechanism of uptake of Ga-67 citrate is not precisely known. After intravenous administration of Ga-67, the complex dissociates to become bound to transferrin.

The principal organs that localize gallium are the liver, spleen, and bone marrow. The excretion of gallium is bimodal, initially through the kidneys and later through the GI tract. Persistence of gallium activity in the kidneys beyond 24 hours should be cause for further workup. There is some uptake in the lachrymal and salivary glands and the lactating breast. This is attributed to the high concentration of lactoferrin in these tissues. Both transferrin and lactoferrin are metabolized in the liver, which accounts for the uptake in the liver. Gallium is believed to behave like iron and utilizes the transferrin mechanism and responds to procedures like total body irradiation in a manner similar to iron saturation of transferrin.

IMAGING EQUIPMENT

The components of the detection system/gamma camera (Fig. 12-5) include the following:

Collimator
Scintillation crystal and optical coupling
Array of photomultiplier tubes

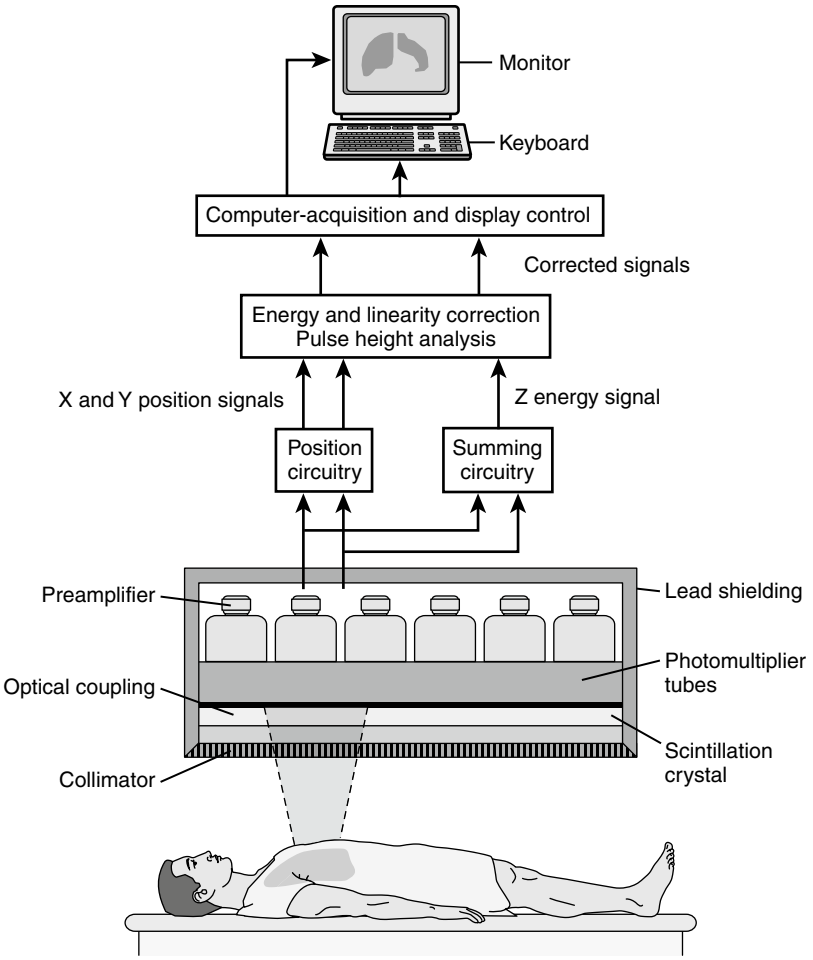


Figure 12-5. Components of a gamma camera.

Signal processor, which analyzes the X-Y position of the signal
Pulse height analyzer
Computer integrated into the camera

Gamma rays emitted from the patient enter the NaI crystal after passing through the collimator. The collimator used varies with the situation. Gamma rays are converted into light within the crystal. An array of photomultiplier tubes is coupled to the scintillation crystal. The light from the crystal is converted into an electric signal, which is proportional to the amount of light generated in the crystal. The electric signals from the photomultiplier tubes are processed by the circuitry to generate position signals and the energy signal. The latter is proportional to the energy of the gamma ray emitted by the radionuclide. The pulse height analyzer analyzes and selects only the signals, which fall in the energy range preset for the radionuclide under consideration. The correction of the X and Y position of the signal, as well as the energy discrimination/pulse height analysis, is performed in the memory of the computer, which is integrated into the gamma camera. The information is recorded as an image in the memory of the computer and displayed on a color or black and white monitor. Each study (which could be composed of several images) is stored to be retrieved for review and reporting.

LUNG SCINTIGRAPHY

The most common indication for lung scintigraphy is to determine the likelihood of pulmonary embolism. Less common indications include lung transplantation, preoperative evaluation, and right-to-left shunt evaluation. We devote this section to the discussion of ventilation and perfusion scanning for pulmonary embolism.

Pulmonary Embolism

The incidence of pulmonary embolism (PE) and its detection have increased with the increasing frequency of long-distance travel and consequent loss of mobility. This has been further complicated by the aging of the population and the increasing incidence of underlying illness such as heart disease and peripheral vascular (including venous) disease.

PE is the third most common cause of death in the United States with 650,000 occurring each year. PE seems to present with greater preponderance in hospitalized

patients. Given the high prevalence of the condition, its lethality, and the fact that a large number of patients with PE have atypical presentations, it is recommended that every patient with chest pain be worked up for PE.

Venous thrombosis, in contrast to arterial thrombosis, is caused by problems with the plasma clotting system. There is minimal platelet participation in the venous versus the arterial process. Furthermore, thrombus formation in the cardiac chambers is seen most commonly with slow flow conditions similar to venous thrombosis.

There is increasing evidence that an underlying coagulopathy may be responsible for spontaneous deep venous thrombosis (DVT) and PE. Hypercoagulability may be congenital or acquired. Primary or acquired deficiencies in protein C, protein S, or antithrombin III are known to be common causes of DVT and PE.

There are many risk factors for DVT and PE. It is well known that, among these, prolonged immobility, recent surgery, pregnancy, and underlying malignancy initiate DVT.

Radiopharmaceuticals and Techniques

The major function of the lungs is to effect the exchange of CO_2 for O_2 from the blood. This is accomplished by perfusion of the capillaries in the walls of the alveoli where inspired air brings in O_2 and is exchanged for CO_2 in the deoxygenated blood. The CO_2 in the alveoli is then discharged to the outside via expiration. These two aspects of the respiratory anatomy and physiology are assessed in nuclear medicine. Pulmonary perfusion is assessed by the administration intravenously of technetium-99m macroaggregated albumin, whereas the various phases of ventilation are studied using gases or aerosols.

In pregnant women, a perfusion-only lung scan should be considered if the chest x-ray is normal and the patient has no history of smoking or lung disease. Since Tc-99m is excreted in the breast milk, the patient should be encouraged to express and store milk for 2 days until the radionuclide has decayed sufficiently.

Perfusion

Technetium-99m macroaggregated albumin (MAA) is the agent of choice for assessing pulmonary perfusion. The mechanism of accumulation with this agent is the blockade of capillaries in the pulmonary arterial circulation.

A minimum of 100,000 particles is necessary to obtain readable images. To obtain optimal images, approximately 200,000 to 600,000 particles are required. The size of the particles ranges from 5μ to 100μ with the majority measuring around 30μ. The desired particle concentration can be obtained by diluting the kit with normal saline. It is important to check the particle size using a microscope or a hemocytometer. Smaller fragments enter into the general circulation and are phagocytized by the liver and spleen.

Approximately 0.1% of capillaries are blocked with one injection. Ordinarily this degree of blockade is of little or no consequence. However, in patients whose pulmonary arterial circulation is tenuous, such as patients with pulmonary hypertension, blockade of the reduced capillary bed can precipitate cardiac complications or exacerbate the underlying condition. In patients with right-to-left shunts, transfer of particles into the systemic arterial circulation could potentially cause adverse coronary or cerebral events. For these patients as well as pediatric patients, we recommend the administration of a lower dose of particles (100,000 to 200,000).

Technetium-99m MAA is produced by the addition of Tc-99m pertechnetate to a sterile "cold kit" containing stannous albumin aggregates as lyophilized powder. Tc-99m pertechnetate is added to the cold kit. The tagged kit is allowed to stand at room temperature for 15 minutes to ensure maximum tagging. The usual administered activity in adults is 3 to 5 mCi (111–185 MBq). The pediatric dose is 25 to 50 mCi/kg of body weight. The lung is the critical organ in this procedure, receiving an absorbed radiation dose of 0.22 rad/mCi.

Tc-99m MAA is administered intravenously in a peripheral vein. Withdrawal of blood back into the syringe could produce clots, which could appear as "hot spots" on the lung scans. Injection into central venous access such as Swan-Ganz catheters is to be avoided. The syringe should be gently agitated to avoid the settling out of the MAA particles. Injecting the dose slowly over three to five deep breaths, as well as having the patient supine, will ensure the even distribution of particles.

The patient is imaged in a sitting position, although images could be obtained with the patient supine. Ideally, the patient is imaged on a large field-of-view (FOV) gamma camera using a parallel-hole collimator. A diverging collimator may be necessary in larger patients to encompass both lungs on the anterior and posterior views. The standard views are the anterior, posterior, right and left laterals, both right and left posterior oblique, and both right and left anterior oblique (Fig. 12-6). Generally, a minimum of 500,000 counts is accumulated per image.

In our institution, we have found single photon emission CT (SPECT) to be of use in determining whether the perfusion defect is segmental or nonsegmental.

Ventilation

Inert gases can be used to perform ventilation studies of the lung in tandem with technetium perfusion studies. Their short biologic half-life allows relatively complete clearance of the lung providing a clean slate, so to speak, for lung imaging with a longer-lived perfusion agent.

Xenon-133

Xenon-133 is relatively inexpensive and is the most commonly used agent for ventilation. Overlying soft tissue easily attenuates the principal gamma emission of 81 keV. Consequently, images of the lungs are generally obtained in the posterior projection. Additional images may be obtained in the posterior oblique projections. Images are rarely obtained in the anterior, anterior oblique, and lateral projections because of the degradation caused by overlying soft tissues such as breast. Consequently, any abnormalities that are seen only in the anterior areas of the lungs will be missed. Exhausting the xenon is a cumbersome and complex process requiring a charcoal trap or a venting system. To avoid contamination with xenon, which is heavier than air, a negative pressure room

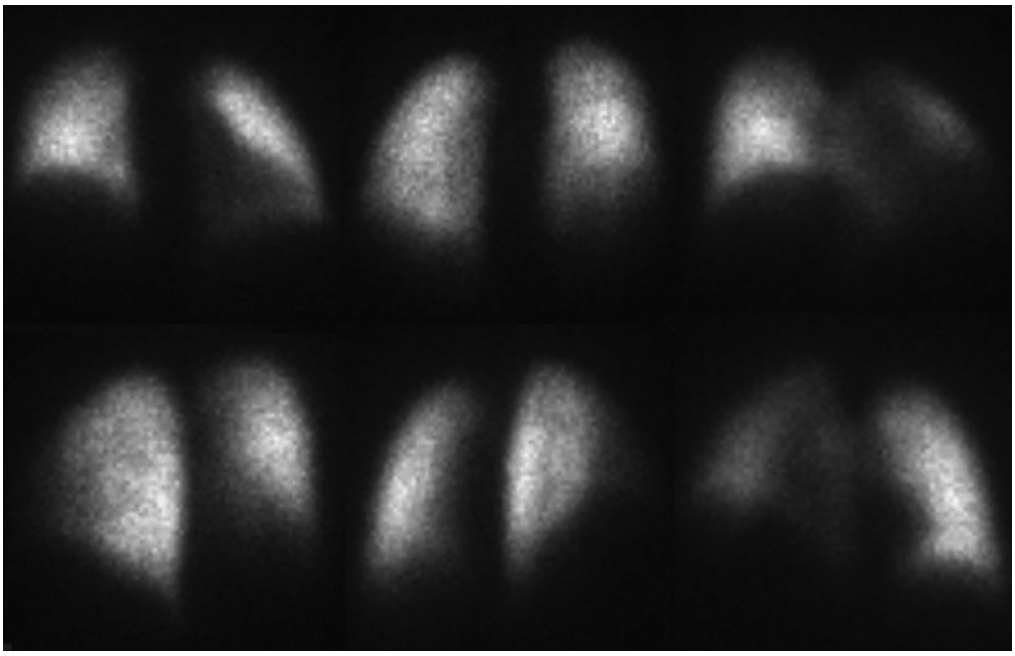


Figure 12-6. Normal Tc-99m perfusion lung scan. Images show a standard six-view study: anterior, posterior, and left anterior oblique views *(top row, left to right);* left posterior oblique, right posterior oblique, and right anterior oblique views *(bottom row, left to right).*

is required. Furthermore, xenon is fat soluble and will adhere to plastic drapes, floor wax, and instrument grease. Consequently, the background level will gradually rise during the workweek.

Xenon can be used to assess all phases of ventilation. The most commonly used technique involves having the patient breathe xenon through a spirometer. The patient exhales as deeply as possible and then inhales 10 to 20 mCi of Xe-133. The respiration is suspended at the end of the inhalation for 15 seconds, while the first image is obtained. The patient breathes xenon out into a spirometer, which constitutes a closed system. Approximately 2 L of oxygen are used to dilute the expired xenon (Fig. 12-7). The patient rebreathes this mixture for 2 to 3 minutes, at which time another static image is obtained. This constitutes the equilibrium image. After equilibrium has been reached,

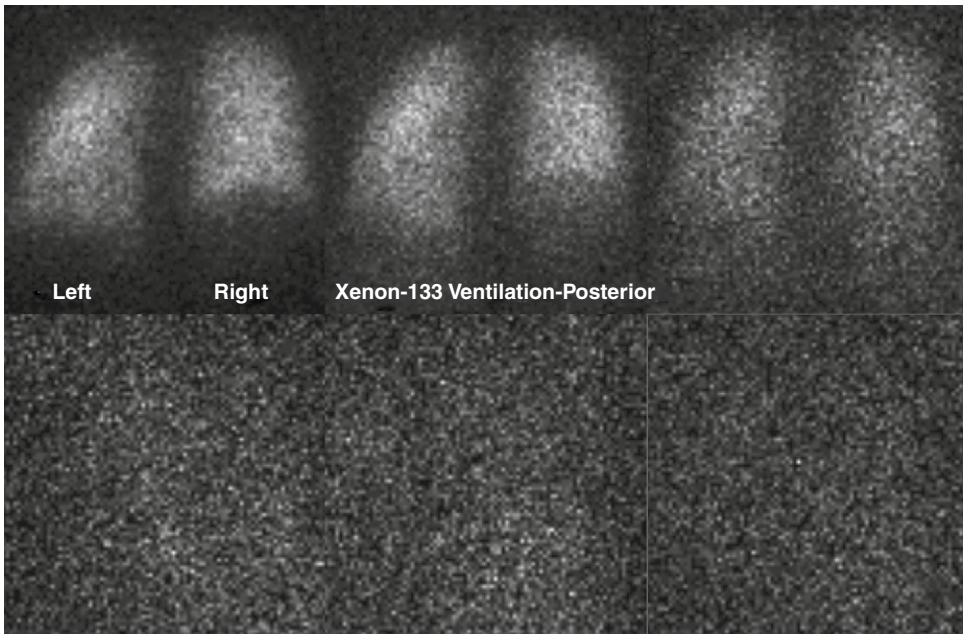


Figure 12-7. Normal xenon-133 ventilation lung scan. The ventilation is usually performed before the perfusion study. Due to rapid clearance of lung activity of xenon-133, a posterior view study is performed to maximize area of the lung seen. Comparison to perfusion is less than optimal.

fresh air is breathed in until the xenon is completely washed out. Images are obtained every 15 seconds for 2 to 3 minutes. For patients with chronic obstructive pulmonary disease (COPD), the washout phase may be delayed up to 5 minutes to image areas of regional airway trapping. This entire process presupposes that the patient is able to cooperate with breathing into a spirometer or a closed system. The initial/single breath reflects the regional ventilatory rate. The equilibrium phase depicts the aerated volume of the lungs, while the washout phase delineates trapping. Xenon is fat soluble and partially soluble in blood, which will cause deposition in the liver, particularly in patients with fatty replacement in the liver.

Krypton-81m

Kr-81m has also been used for ventilation imaging. The photon emissions of 176 and 192 keV and the short half-life of 13 seconds allow equilibrium imaging of the lungs in multiple projections. However, the short half-life precludes obtaining single-breath and washout images. Kr-81m is obtained from rubidium-81, which has a half-life of 4.6 hours. While krypton generators are available, the cost of the generator can be quite high, due to the short half-life of rubidium-81. The activity administered is 1 to 10 mCi.

Radiolabeled Aerosols

Radiolabeled aerosols are used for studying lung ventilation. Aerosol studies do not allow dynamic imaging. Dynamic imaging, while excellent for assessment of respiratory function, is not required for PE studies.

The most commonly used aerosol is Tc-99m diethylene triamine penta-acetic acid (DTPA) in a volume of 2 mL put into the nebulizer of an aerosol delivery system. The aerosol is prepared by injecting 30 mCi of Tc-99m DTPA into the nebulizer of the delivery system. Side tubing in the system allows oxygen to flow through a flow meter at the rate of 8 to 10 L/min. Generally, only a small amount of activity (1 to 2 mCi) is delivered. The trachea is the critical organ in the aerosol ventilation study. One of the major advantages of this system is that it can be attached to an endotracheal or tracheostomy tube. In patients without airway tubing, the aerosol is inhaled through the mouth while a nose clip is applied. In either circumstance, little or no patient effort or cooperation is required to deliver the aerosol into the airway. The aerosol is usually delivered with the patient in a supine position so that it is distributed evenly. No special venting is required with Tc-99m DTPA as it is with xenon. The second major advantage of using Tc-99m DTPA is that the imaging characteristics are ideal. Therefore, the Tc-99m DTPA study can be performed either before or after the Tc-99m MAA study. If the ventilation study is performed before the perfusion, the amount of activity required is between 1 and 2 mCi. However, if the perfusion study is obtained first, the number of counts accumulated for the ventilation study has to be 3 to 4 times greater than for the perfusion.

In the workup for PE, Tc-99m DTPA aerosol is ideal, since images can be obtained in projections to match the ventilation images. After inhalation, aerosol particles are deposited in the distal airways and not the alveoli. Following inhalation, the Tc DTPA particles dissolve in the fluids within the alveoli and ultimately diffuse across the epithelial barrier into the circulation. As long as the epithelial barrier is intact, the aerosol diffuses relatively slowly into the circulation. The half-time disappearance of the aerosol from the alveoli is about 80 minutes. This is much faster in patients whose epithelial barrier may be deficient, as in COPD or in smokers. The Tc DTPA that has entered into the circulation is cleared via the kidneys. Larger particles are deposited in the central airways, the mouth, and the alimentary tract (from swallowed particles) (Fig. 12-8).

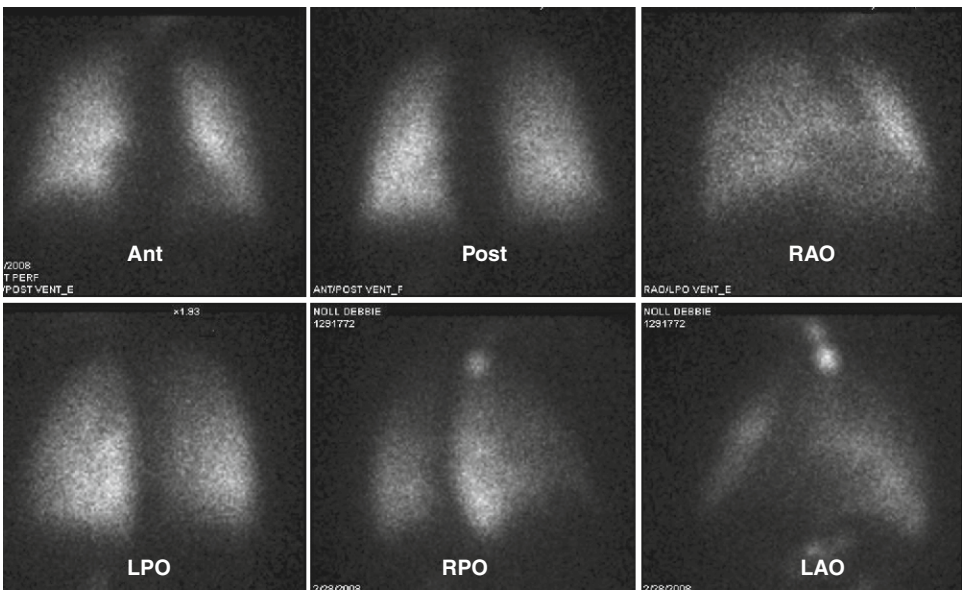


FIGURE 12-8. Tc-99m DTPA aerosol images. Normal study shows six views, and corresponding six views are obtained for perfusion. Comparable images make interpretation of lung scan much easier than with single posterior view xenon-133 study.

Technegas
Technegas is composed of ultrafine particles of Tc-99m-labeled carbon particles produced by combustion of pertechnetate at 2500° C in a graphite crucible. A technegas generator is portable and produces fine images. The smaller particle size makes this a better agent than Tc DTPA aerosol, particularly in patients with COPD.

Chest X-Ray
It is important to have a chest x-ray for evaluation before performing the ventilation-perfusion (VQ) scan (Fig. 12-9). It is good practice to have one that has been obtained within 24 hours of performing the VQ scan. It would be ideal to have a full-inspiration posteroanterior (PA) and lateral chest x-ray available for interpretation. However, a large percentage of the patients who are at risk for PE in the hospital or the intensive care unit setting may have several other cardiopulmonary pathologic processes that could interfere with the reading of the VQ scan. In these patients, one has to be satisfied with the portable radiograph, which is rarely of the quality of the standard PA and lateral radiographic study.

Symptomatology and chest x-ray findings in patients with PE are frequently nonspecific. Hampton's hump and the Westermark sign are findings on chest x-rays that are seen in PE. However, these signs are not often visualized on the chest radiograph. With the introduction of multidetector CT scanners, the majority of patients for PE workup are directly imaged using CT pulmonary angiography. In patients with impending renal compromise, CT angiography with contrast may be fraught with danger. Increasingly, the CTPE has become the gold standard for diagnosis of pulmonary embolism. As well, VQ lung scanning is important for establishing the diagnosis of PE. These studies can indicate whether or not the patient is likely to have PE.

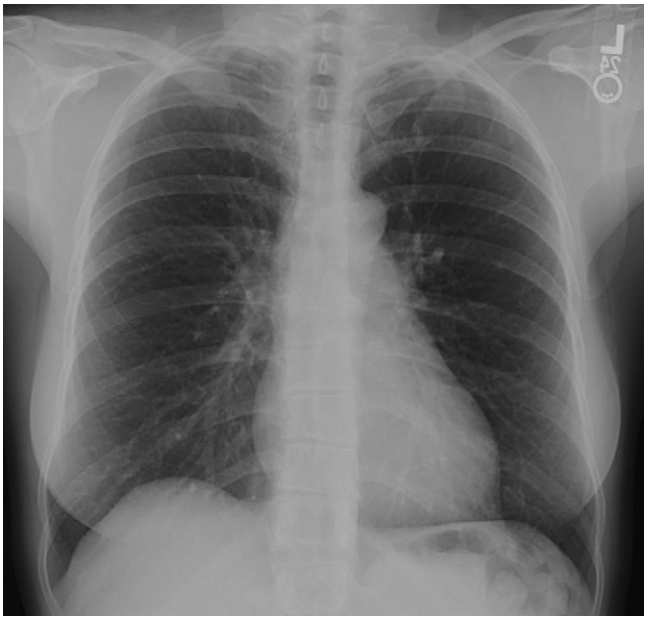


Figure 12-9. Normal chest x-ray. Interpretation of the VQ study for pulmonary embolism.

The Prospective Investigation Of Pulmonary Embolism Diagnosis (PIOPED) study, completed in the 1990s, provided a comprehensive look at the value of ventilation and perfusion scans in acute PE. The PIOPED criteria were based on the use of Xe ventilation scans. With the development of CT pulmonary angiography, the algorithms proposed by the PIOPED study have had to be modified.

A pragmatic approach to the interpretation of VQ scans has been proposed, and the following facts have to be taken into consideration:

- The most important diagnostic feature of PE on VQ scans is the mismatched defect—where there is a perfusion defect with no abnormality on the ventilation scan.
- The basis of the mismatch is that with an uncomplicated PE, the ventilatory architecture remains intact.
- Complete matching of the VQ abnormalities is seen in obstructive lung disease.
- In pulmonary infarction, there is incomplete matching of the VQ defects and a corresponding abnormality on the radiograph.

The *first step* is to obtain a chest x-ray for comparison with the VQ scans.

The *second step* is to scrutinize the perfusion scan for perfusion defects. These should be characterized based on whether they are segmental/subsegmental or nonsegmental. Nonsegmental defects are those that do not correspond anatomically to a segment and are therefore unlikely to be secondary to a pulmonary embolus.

The *third step* is to determine the size of the segmental perfusion defect. A classic segmental perfusion defect corresponds anatomically to a bronchopulmonary segment. These are pleural based and wedge shaped. The defect is categorized as large when it occupies 75% or more of the segment, moderate when occupying 25% to 75% of the segment, and small when it is less than 25%.

The *fourth step* is to ascertain whether the segmental or subsegmental defects are matched on the ventilation study.

Unmatched perfusion defects are not likely due to acute or chronic pulmonary emboli. Pulmonary emboli are multiple in 90% of cases and bilateral in 85%. In the first few days, the defects may disappear or become smaller. New defects may occur because of fragmentation. Changes in regional perfusion pressure could transform a partially obstructing clot into a fully obstructing one.

The *fifth step* is to discuss the likelihood of PE based on the scans in light of the pretest likelihood of PE. If no abnormalities are noted on the perfusion study, the study is considered normal. The likelihood of PE is less than 5%.

Abnormal exams are classified by the size and the number of perfusion abnormalities and concomitant abnormalities (or absence of abnormalities) on the ventilation scan, as follows:

A *high-probability scan* has two or more large, mismatched segmental defects (or equivalents in moderate/large defects) with no abnormality on the ventilation study (Fig. 12-10). In the clinical setting where PE is highly likely,

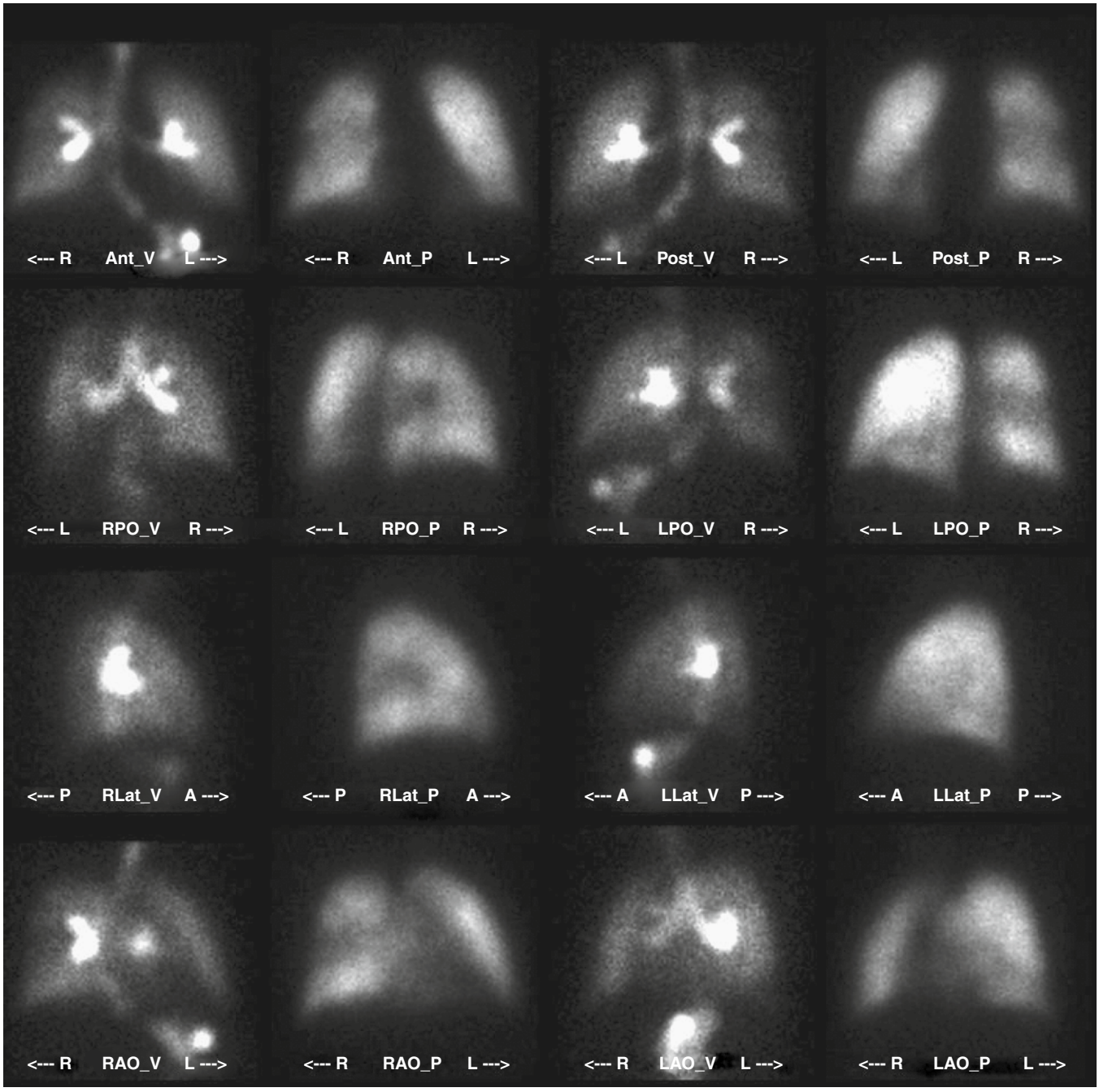


FIGURE 12-10. High-probability lung scan with Tc-99m DTPA aerosol and MAA. Superior segment of the right lower lobe and a major portion of the left lower lobe show perfusion deficit with good ventilation, a VQ mismatch.

a high-probability VQ scan indicates a probability of PE greater than 90%. If the mismatched perfusion defects should resolve within days or weeks, the probability of recent embolism is higher.

A *low-probability scan* is one in which the perfusion scans are smaller than 25% of a segment regardless of the ventilation scan or chest x-ray appearance, matched on ventilation scan, and accompanied by larger radiographic abnormalities (Fig. 12-11).

An *intermediate-probability scan* is one that does not fit into the high or low categories.

Repeat Scans

Because the perfusion picture can evolve over the ensuing weeks or months, it is advisable to repeat the study after 3 weeks. Defects persisting at 3 months are unlikely to resolve. The larger the defect and the older the patient, the less likely is the perfusion scan to revert to normal. In patients with diffuse lung disease, emboli are less likely to resolve completely. Patients with high-probability or intermediate-probability scans who have been treated for PE should be followed up with a 3-month scan.

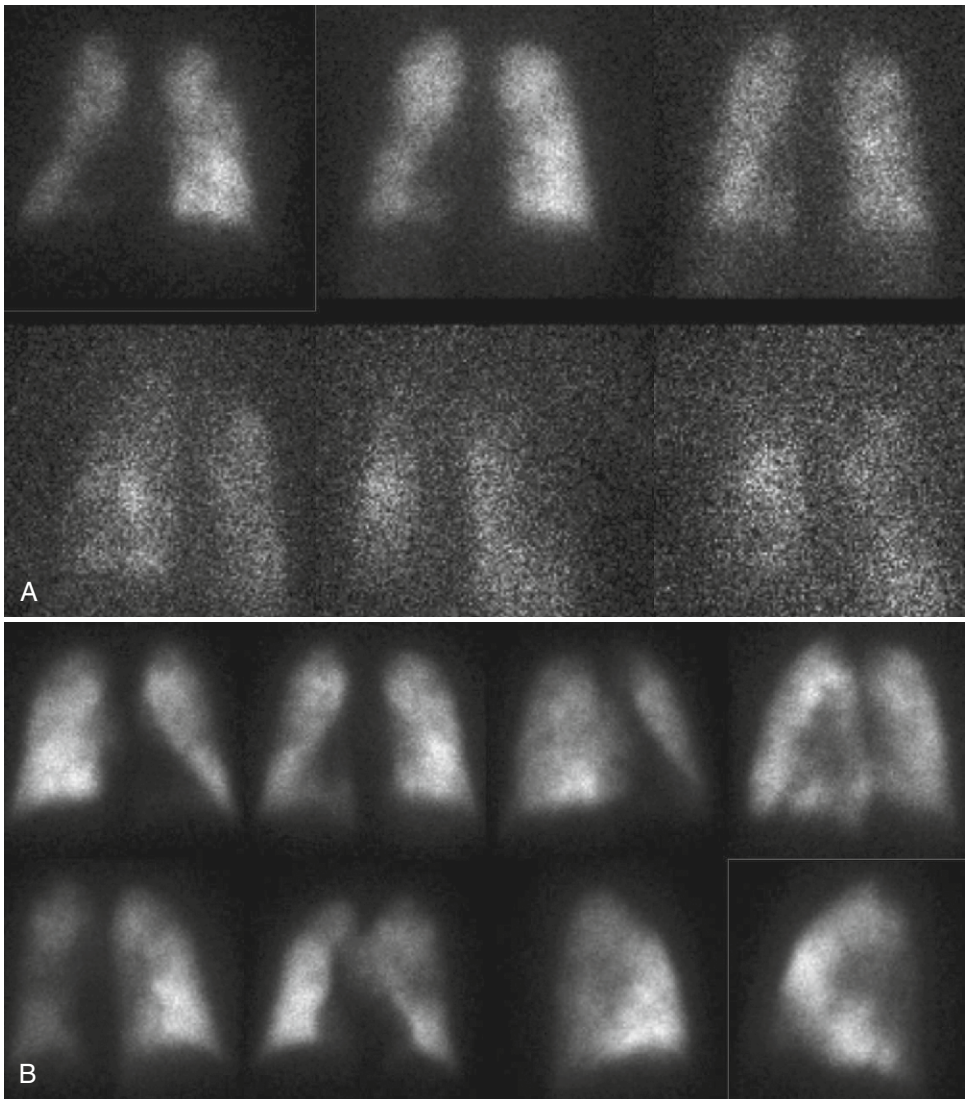


Figure 12-11. Xenon-133 ventilation study **(A)** and Tc-99m MAA study **(B)** show nonsegmental matching abnormalities suggesting a low probability for pulmonary embolism.

BRAIN DEATH

The harvesting of organs for transplantations requires that the diagnosis of irreversible cessation of brain function be made accurately and quickly. The requirement for alacrity of diagnosis is to prevent the organ degradation that occurs with death.

The diagnosis of brain death is primarily a clinical one—clinicians frequently relying on the patient being in a coma with a total absence of brainstem reflexes and spontaneous respiration, and electrocerebral silence. The findings of death have to be present for a finite period of observation (6 to 24 hours). States that mimic brain death include alcohol and barbiturate intoxication, sedative overdose, hypothermia, and hypoglycemic coma. In these instances, electrocerebral activity may drop to a level as to be undetectable. Additionally, the Lazarus sign (spinal reflexes and spontaneous movement of arms and shoulders that may be present after cessation of ventilation) may cause some confusion.

Confirmation of absent intracranial perfusion offers confirmation of brain death. This can be obtained by demonstrating absence of intracranial perfusion and absence of sagittal sinus activity following intravenous administration of tracer. Occasionally the sagittal sinus may be perfused from the external carotid circulation (Fig. 12-12).

Brain death is diagnosed primarily clinically. However, complicating situations such as hypothermia and drug overdose may make a clinical or electroencephalogram (EEG) diagnosis difficult or impossible. Scintigraphic exams are not affected by these conditions. Lack of perfusion on a radionuclide study is specific for brain death, more so than an isoelectric EEG.

Radiopharmaceuticals

The radiopharmaceuticals used for the diagnosis of brain death are Tc-99m DTPA and Tc-99m HMPAO or ECD. Tc-99m DTPA is used on the premise that it provides a

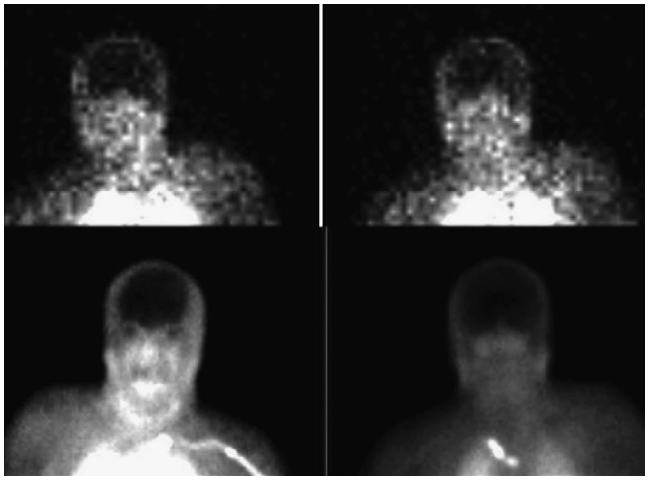


FIGURE 12-12. Tc-99m ECD planar imaging study shows no perfusion and no delayed activity in the skull: the "empty skull" appearance. These findings are better seen with tomographic SPECT imaging of the brain if clinically feasible.

radionuclide angiogram. We prefer Tc-99m HMPAO or ECD since they are brain perfusion agents and will not be picked up in a nonperfused brain. Furthermore, a nuclide angiogram can be performed dynamically while injecting the Tc-99m HMPAO or ECD and additionally followed up with planar static or SPECT images.

Tc-99m DTPA is used in this indication as a nondiffusible blood pool agent. Therefore, it is best used for the radionuclide angiographic portion of the study. The Tc-99m DTPA does not cross the blood–brain barrier.

Tc-99m HMPAO (hexamethyl-propylene oxime or exametazime) can be prepared with or without stabilizer for brain imaging. The Tc-99m HMPAO is lipophilic and is preferentially retained by the brain because it is converted in vivo by glutathione to the hydrophilic complex. This could also occur in vitro with high stannous ion concentration, heat, and free radicals. Hence, only small amounts of stannous chloride must be used. The Tc-99m pertechnetate should be fresh and not more than 30 minutes from eluting. The stabilizer used is methylene blue, which acts as a free-radical scavenger.

Technique

In some nuclear medicine laboratories, a scalp tourniquet is applied to minimize the external carotid perfusion. This measure also reduces scalp perfusion, which could be mistaken for cerebral perfusion. The most commonly used tourniquet is an elastic band placed above the level of the orbits. This is not recommended in children since the application of the tourniquet may increase the intracranial pressure.

In most instances the use of Tc-99m DTPA will suffice. It is injected intravenously as a bolus, and dynamic images may be obtained with the camera centered over the face. Occasionally, it may be difficult to administer a good intravenous bolus. In this case, using Tc-99m DTPA is convenient, in that a repeat injection can be performed.

The use of Tc-99m HMPAO or ECD is recommended in difficult cases. Since the uptake of these agents relies on both perfusion and active uptake by a viable brain, a dynamic flow study may not be necessary and delayed static images will suffice, particularly if the intravenous injection of bolus was unsatisfactory and subsequent dynamic images could not be obtained for a variety of reasons including malfunctioning of the computer.

Since both dynamic flow and static images are used in this study, we prefer to use the low-energy all-purpose (LEAP) collimator, which can be used in both the dynamic and static studies. With Tc-99m DTPA 10 mCi are given intravenously, whereas with Tc-99m HMPAO, 15 to 20 mCi of activity are administered. Because both sets of compounds are tagged with Tc-99m, the window setting is at 15% at a 140 keV peak. The flow study involves obtaining 1- to 2-second images for 30 seconds. Immediate or early planar static images are acquired for 500k to 750k counts in the standard anterior, posterior, and both lateral projections. It is vital to image over the injection site to verify that the dose has not been infiltrated. With Tc-99m HMPAO delayed static images are obtained 2 hours post injection in the standard projections.

Interpretation

On the radionuclide angiogram, flow will be seen in the common carotid arteries. The flow will not be seen beyond the base of the skull. If there is no cerebral blood flow, no uptake will be seen in the brain.

Tc-99m DTPA is used strictly as a blood pool agent in the documentation of brain death. It does not cross the blood–brain barrier, remaining in the blood pool even on delayed static images. Consequently, the delayed static images, which are obtained 5 to 10 minutes after completion of the "flow" study, will not reveal any activity in the territory of the cerebral arteries.

On HMPA and ECD studies, in a normal, viable brain there will be uptake of radionuclide in the brain—preferentially in the cortex. With brain death, no activity will be seen in the brain. Occasionally, there is increased uptake of the radionuclide on the immediate static images in the nasopharyngeal region. This was originally described by Mishkin. However, it has been documented in other instances such as internal carotid occlusion without brain death. This is attributed to the shunting of blood flow into the external carotid circulation. In the presence of clinical signs of brain death, the "hot nose" sign could be used as a secondary or corroborative finding. The sagittal sinus may be visualized faintly due to filling from the external carotid circulation.

With brain death, there is no uptake of HMPAO or ECD radiopharmaceuticals in nonviable brain tissue. This can be further verified by obtaining, if necessary, SPECT images, which will show an "empty skull."

Tomographic SPECT images allow better visualization of activity distribution within the skull, and allow one to see brainstem and cerebellar activity that is hard to see with planar imaging shown above. Figure 12-13 shows the same patient as in Figure 12-12 with SPECT imaging clearly demonstrating activity in the brainstem and cerebellum. The cerebellar and brainstem activity usually clears in 24 to 36 hours and confirms diagnosis of brainstem death

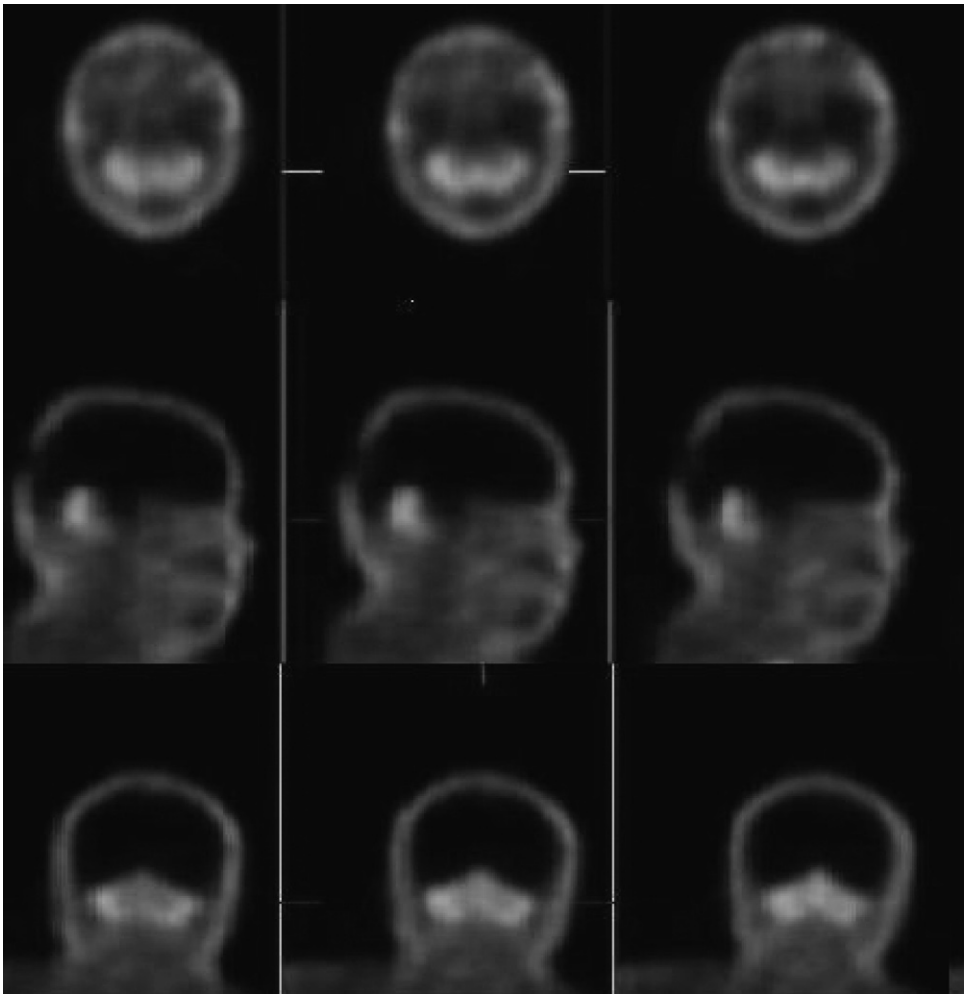


Figure 12-13. Tc-99m ECD brain perfusion SPECT imaging shows complete absence of perfusion in the cerebral hemispheres and minimal uptake in the brainstem and cerebellum. The brainstem and cerebellar activity usually disappears within 24 hours and a second study is required to confirm complete absence of perfusion.

as well. The patient shown in Figures 12-12 and 12-13 showed no activity in the cerebellum or brainstem when study was repeated after 20 hours.

INFECTION

While nuclear medicine plays a very important role in the detection of infection, there are several barriers to the implementation and incorporation into the algorithm for workup, not the least of which is the time it takes to arrive at an answer. Radionuclide imaging is often complementary to CT, which is leading to fusion or simultaneous imaging. Predictably, this will become the direction of the future in equipment production. There are several different agents that are available for the workup of infection, the choice of which varies widely with the situation involved.

Radiopharmaceuticals

The radiopharmaceuticals used include Tc-99m methylene diphosphonate for part of the workup of musculoskeletal infection, gallium-67 citrate, and indium-111 oxime and Tc-99m HMPAO for autologous leukocytes.

Leukocyte Labeling

Leukocytes can be labeled with indium-111 oxime or with technetium-99m HMPAO. Infections that mount a neutrophilic response are best visualized with the leukocyte label. Opportunistic infections, however, are not associated with neutrophilic response; hence these are not ideal for imaging with radionuclide-labeled leukocytes.

The labeling process is performed in vitro, is cumbersome, and requires meticulous attention to detail. Furthermore, the in vitro process carries with it the risk to personnel of handling blood products. The process itself takes 2 to 3 hours. Forty milliliters of blood is withdrawn into a syringe containing anticoagulant. The syringe is kept upright for 1 to 2 hours to allow the red blood cells (RBCs) to sediment. This is further accelerated by the addition of hydroxyethyl starch and the hypotonic lysis of the RBCs. The next step is to separate the leukocytes from platelets by centrifugation. The leukocyte pellet that forms after the separation of the RBCs and platelets is incubated with the radiopharmaceutical, washed, and injected into the patient. The doses of Tc-99m HMPAO-labeled and

In-111–labeled leukocytes are 5 to 10 microCi and 300 to 500 μCi, respectively.

A total white blood cell (WBC) count of at least 2000/mL is essential for obtaining satisfactory images. Neutrophils are the majority of WBCs labeled; hence the images obtained reflect neutrophil-mediated response. Mature granulocytes are highly specialized, short-lived nondividing cells. They generally measure around 12 to 15 microns, and possess a multilobulated nucleus and multiple cytoplasmic granules. These mature in the bone marrow for about 15 days and then reside in the circulation for 10 hours. If they migrate into tissues, they survive about 4 days.

Images obtained with leukocytes labeled with indium or technetium immediately following injection show intense pulmonary activity that clears rapidly. This is believed to be due to leukocyte activation during labeling, which slows their movement through the pulmonary vasculature. Tc-99m HMPAO–labeled WBC studies, on the other hand, can be performed within a few hours of imaging, making this a more desirable study for "emergency" purposes. The advantages and disadvantages of each of these techniques are discussed in a later section.

There are some conditions presenting as emergencies in the workup of infection, particularly osteomyelitis, where the labeling of autologous leukocytes could present a problem. The first of these is sickle cell crises. Here the sickling RBCs cannot be effectively separated from WBCs. The second is leukemia, where the WBCs encountered are abnormal and functionally not responsive to infection.

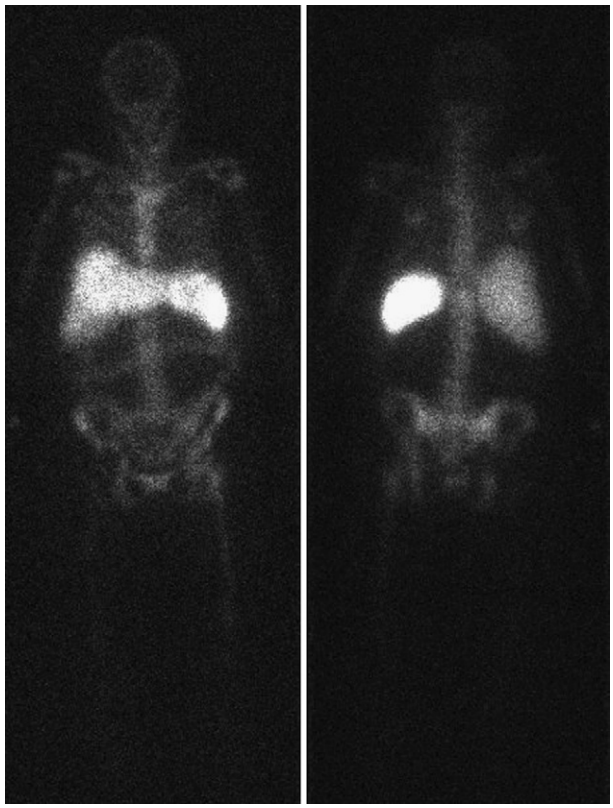


FIGURE 12-14. Normal distribution of In-111 oxine-labeled leukocytes. A large portion of the activity is sequestered in the liver and spleen.

Indium-Labeled Leukocytes

A large FOV gamma camera is used with a medium-energy parallel-hole collimator. A 15% window is centered on the 174-keV photopeak and a 20% window is centered on the 245-keV photopeak.

With indium-111–labeled WBC studies, images are obtained 24 hours after injection, by which time the pulmonary activity would have already cleared. It is important to note that the 24-hour time lag required for indium-labeled infection imaging would remove it from consideration as a "true emergency." At 24 hours following injection, there is normal distribution through the spleen, liver, and bone marrow (Fig. 12-14).

One disadvantage of indium-111 imaging is that the amount of radioactivity administered—0.3 to 0.5 mCi of indium—results in low photon flux and makes it more difficult to accumulate the necessary number of counts to achieve a satisfactory image. Furthermore, the photopeaks are not optimal in comparison with technetium-99m.

The advantages of using the indium label are its long half-life and the fact that the label is stable. Another advantage is that indium can be used in conjunction with other radionuclides such as Tc-99m sulfur colloid bone marrow imaging, particularly with musculoskeletal infection. Here simultaneous dual isotope scans can be acquired, or, alternatively, they can be acquired in tandem. Since some infections can be indolent, such as those involving joint prostheses, the longer half-life of indium makes it a much more useful compound.

Technetium-Labeled Leukocytes

A low-energy, all-purpose, high-resolution collimator is used with a 15% window centered on the 140-keV photopeak of Tc-99m. Granulocyte labeling is selective with the Tc-99m HMPAO complex. Urinary activity and renal parenchymal activity appear soon after injection. Biliary activity is seen in a variable number of patients as early as 3 hours following injection. This accounts for bowel activity appearing at 4 hours. Bone marrow uptake is also seen with Tc-99m–labeled leukocytes, although none is seen in normal bone. Images are routinely obtained at 2 and 4 hours post injection, although 45-minute and 24-hour images may also be obtained if needed (Fig. 12-15).

Technetium Methylene Diphosphonate

Tc-99m methylene diphosphonate (MDP) is one of the agents of choice for evaluation of osteomyelitis. This is the agent used for the triple-phase bone scan. It is injected intravenously, and flow/perfusion studies of the affected part are obtained at one image per second for a total of 30 seconds. For a perfusion study, ideally a high-sensitivity collimator is used. This is followed by the acquisition of "blood pool" images or immediate static images of the area in question. Two to four hours after intravenous administration of the Tc-99m MDP, delayed static images are acquired for 500 K counts per projection utilizing a high-resolution collimator (Fig. 12-16). In smaller nuclear medicine departments it is not uncommon to use a LEAP collimator for both the perfusion and the static images.

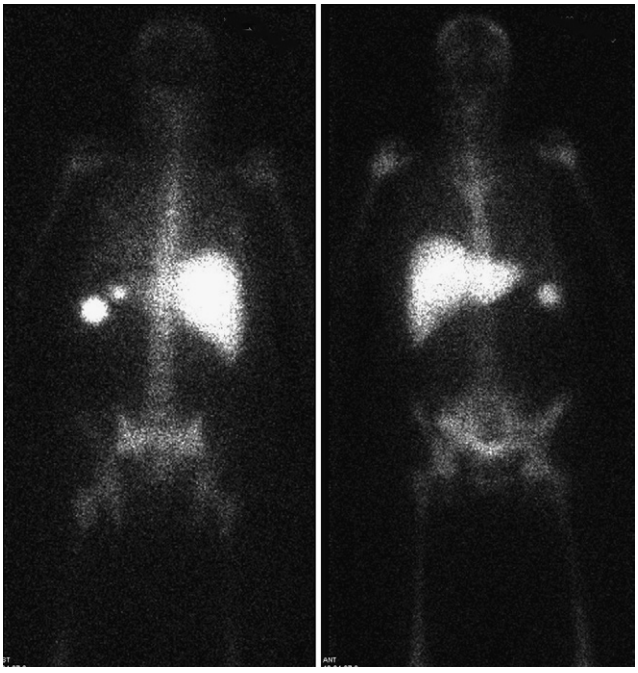


Figure 12-15. Tc-99m HMPAO WBC imaging shows two foci of collection in the left upper quadrant of the abdomen corresponding to suspected abscess on CT scan of the abdomen.

Technetium Sulfur Colloid

Tc-99m sulfur colloid has been traditionally used as a liver–spleen scan agent. Since it is picked up by the reticuloendothelial system, it also serves as a bone marrow agent. Approximately 3 to 10 mCi of Tc-99m sulfur colloid are used intravenously for imaging the bone marrow. The critical organ is the liver with a radiation absorbed dose of 0.34 rad (cGy)/mCi.

When Tc-99m– or In-111–labeled WBC scans are used to evaluate for osteomyelitis, abnormal uptake in infection foci has to be differentiated from normal WBC uptake in the reticuloendothelial elements in bone marrow. When technetium agents are used, they have to be injected in tandem one after the other. However, when indium and technetium are used they can be used simultaneously and a dual isotope study can be performed.

Gallium-67 Citrate

The uptake of gallium in infection is multifactorial. Approximately 90% of the circulating gallium is bound to transferrin. The increased vascularity and increased membrane permeability in inflammatory foci results in the increased deposition of gallium in inflammation. Some of the gallium is delivered through the leukocytes, which bind the radionuclide. A third mechanism is the formation of siderophores by certain bacteria and fungi. These are

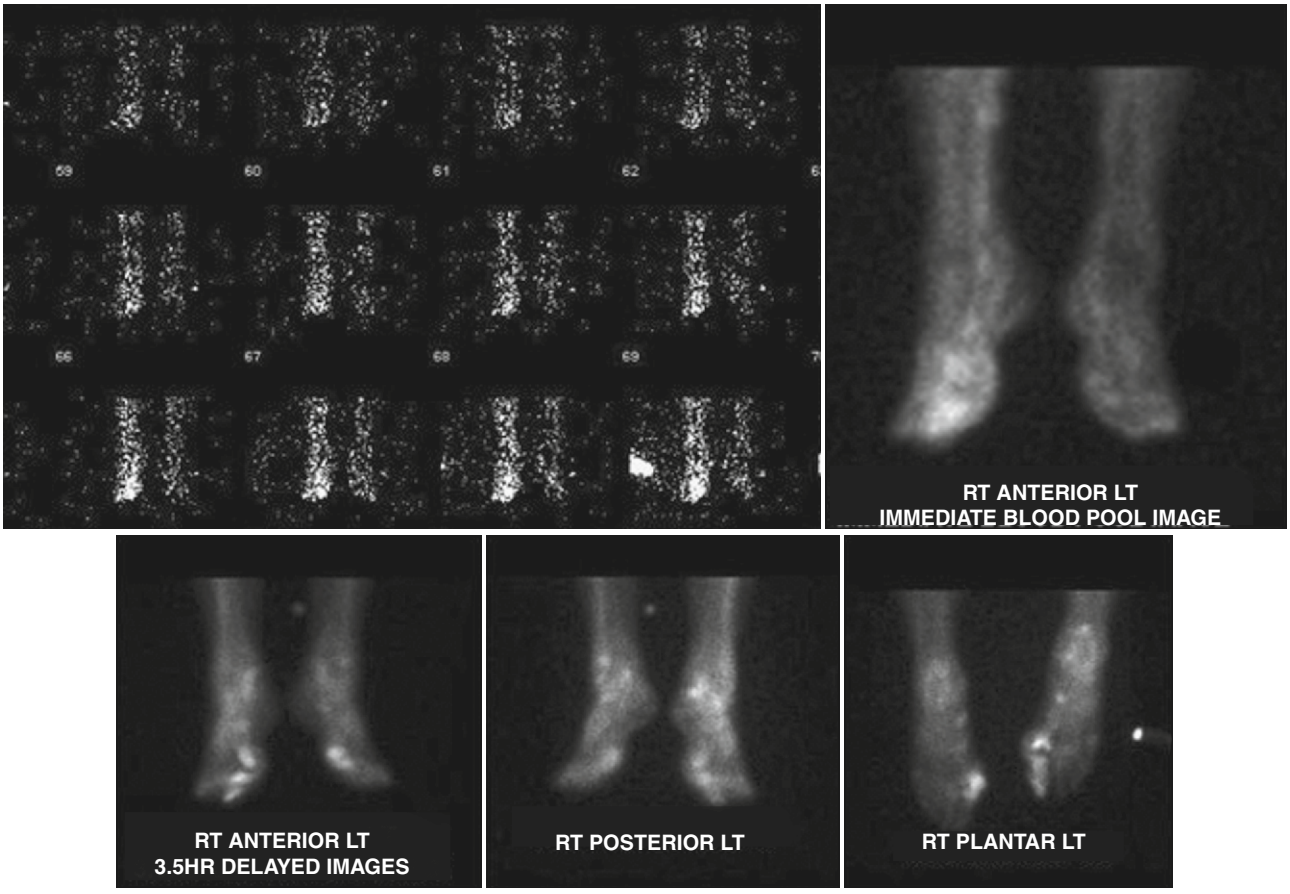


Figure 12-16. Tc-99m MDP scan shows increased flow, blood pool, and delayed activity in the right first MTP joint and great toe region suggesting an osteomyelitis. Increased delayed activity in the left MTP region is due to osteoarthritis and does not show increased flow or blood pool counts.

iron-chelating compounds secreted by microorganisms, which dissolve $Fe\text{-}3^{+}$ ions by chelation and take up the iron by active transport. Since gallium is handled similarly to iron, siderophore–Ga-67 complex is transported into the bacterium, where it stays until the bacterium is phagocytosed by macrophages.

At 24 to 72 hours following the intravenous injection of Ga-67 citrate, images are obtained. Multichannel analyzers on modern gamma cameras allow the inclusion of many of the photopeaks of gallium—93, 184, 296, and 388 keV. A medium-energy collimator is recommended in order to improve the resolution.

Gallium is best utilized in the workup of chronic osteomyelitis and infected joint prostheses. As the infection becomes more chronic, neutrophils are no longer recruited into the process and WBC-labeled imaging agents become decreasingly useful. Gallium then becomes the agent of choice. In acute osteomyelitis, increased gallium uptake frequently precedes the Tc-99m MDP accumulation because osteomyelitis is initially an involvement of the bone marrow. Gallium is also useful in infants under 6 months of age where Tc-99m MDP scans are likely to be negative.

Newer Agents

Since it is cumbersome to label leukocytes in vitro, significant effort has been expended in developing in vivo methods for labeling WBCs. These include the labeling of leukocytes in vivo, peptides, and antigranulocyte antibodies/antibody fragments. Until recently, Tc-99m–labeled monoclonal murine M class immunoglobulins that bind to cluster designation 15 receptors on the surfaces of leukocytes had been the subject of clinical trials. This (fanolesomab) is labeled with Tc-99m pertechnetate. After approximately 10 to 20 mCi are injected intravenously, the agent is distributed in the vasculature, and it is retained in the spleen and liver. The ease of in vivo labeling, the lack of risk of handling blood products by technologists, and the rapid and intense accumulation in regions of infection make quite a compelling case for pursuing these avenues further.

Indications

Infections generally tend to be indolent and rarely present as emergencies. However, when the postsurgical patient presents with symptoms suggestive of infection, there is an excellent case for the workup utilizing nuclear medicine. The accuracy of WBC-labeled studies in abdominal abscesses is greater than 85%, which is comparable with CT.

With the advent of fusion imaging or SPECT CT, the work of the diagnostician is easier and the results far more valuable. The complementary use of the anatomic strengths of CT with the metabolic sensitivity of nuclear medicine will serve to vastly and incrementally increase the usefulness of each of these modalities by overcoming the limitations of each modality.

Abdominal Abscesses

Abdominal abscesses are a common and difficult problem in the postsurgical patient. Although ultrasound is probably the easiest and the most expedient method of diagnosis, surgical dressings, wounds, edema, and the patient's body habitus often provide deterrents to diagnosis using this modality. While CT provides exquisite resolution, it carries with it the inconvenience of administration of oral contrast and risk of precipitating or worsening renal compromise with the administration of intravenous contrast. Furthermore, the radiation exposure with multidetector CT is not trivial, particularly in patients who might need repeated studies. Here nuclear medicine with the use of radiolabeled WBCs can prove invaluable in pinpointing the pathology. The additional advantage of using nuclear medicine procedures is that the entire body can be imaged without additional radiation exposure.

The most common causes of intra-abdominal abscesses include the following:

1. Perforation of a diseased viscus—peptic ulcer, inflamed appendix, or diverticulum
2. Gangrenous cholecystitis
3. Mesenteric ischemia with bowel infarction
4. Pancreatic necrosis or pancreatic abscess progressing to abscess formation
5. Penetrating abdominal trauma
6. Postoperative complications such as anastomotic leaks

The most commonly encountered organism is *Escherichia coli*. Skin flora may cause abscesses following penetrating wounds to the abdomen. *Neisseria gonorrhoeae* and chlamydia are commonly involved in pelvic abscesses in females who might have pelvic inflammatory disease. Microbial flora of the GI tract varies from the proximal to the distal with small numbers of aerobic streptococci in the stomach and proximal small bowel, and large numbers of these organisms as well as large numbers of anaerobic gram-negative bacilli and anaerobic gram-positive flora in the terminal ileum and colon. The differences in the types and concentrations of these microorganisms partially account for differences in septic complications based on the location of the injury or disease. Septic complications from upper GI perforations are far less ominous than those from colonic insults.

With indium-labeled WBC scans, whole body imaging is recommended 4 and 24 hours after intravenous administration of the agent; and with Tc-99m–labeled WBC studies, imaging is done at 1 and 4 hours. Abscesses demonstrate progressively increasing activity, often greater than the liver and outside areas of normal accumulation.

In the case of hepatic abscesses, In-labeled WBCs are preferred because the biliary excretion seen with Tc-99m–labeled WBCs could complicate the interpretation of the image. It is important to note that activity in an abscess will increase on delayed images, while normal uptake regresses. Hence, when searching for hepatic abscesses, we recommend that In-111–labeled WBCs be used. Analysis of the images should definitely not be made on the basis of the early images alone.

Pancreatic abscesses are best studied with Indium-111–labeled studies because of the increased likelihood of spontaneous communication of the abscess with the gut. As a note of caution, unfortunately, WBC scans are positive with pancreatic abscesses and fat necrosis as well as pancreatic pseudocysts.

In patients on peritoneal dialysis with catheter tunnel infection, nuclear medicine provides the ability to

distinguish between early peritonitis and exit site infection. This is of special importance where the clinical management is different based on the site of the infection.

There are six functional compartments within the peritoneal cavity:

1. Pelvis
2. Right paracolic gutter
3. Left paracolic gutter
4. Infradiaphragmatic spaces
5. Lesser sac
6. Interloop potential spaces of the small intestine

Inflammatory Bowel Disease

Tc-99m–labeled WBC studies are believed to be useful in the diagnosis of inflammatory bowel disease (IBD). Early views of the abdomen supply the diagnosis with uptake in the diseased bowel greater than noted in the spleen. Delayed images are less reliable, because with Tc-99m–labeled WBC studies, there may be excretion of Tc-99m–labeled secondary complexes into the bowel. The configuration of the uptake in the bowel is usually sufficient to distinguish IBD from abdominal abscesses.

Musculoskeletal Infections

The major problems of imaging for osteomyelitis with WBC-labeled studies are that (1) osteomyelitis is frequently more chronic and (2) WBCs normally accumulate in the bone marrow where they are destroyed by the reticuloendothelial system. In the imaging of a prosthesis, nuclear medicine imaging is not affected by the prosthesis, whereas the prosthesis is a deterrent to imaging with any of the other imaging modalities. Bone scintigraphy is useful, in that a negative scan essentially excludes a prosthetic complication. Adding Ga-67 citrate increases the accuracy of bone scintigraphy. The combination of leukocyte labeling combined with marrow imaging is believed to have the highest accuracy of all the imaging studies available (Fig. 12-17).

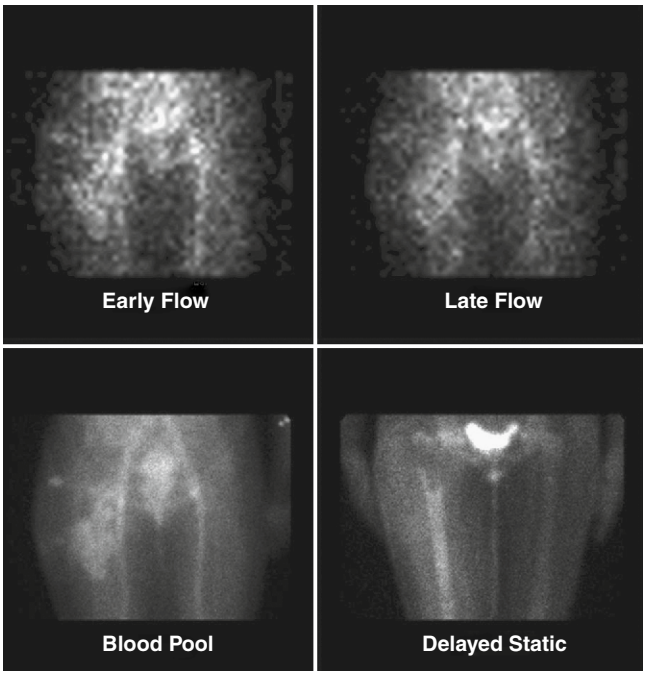


Figure 12-17. Tc-99m MDP bone scan shows soft tissue infection but no evidence of osteomyelitis. Patient is status post removal of right hip prosthesis.

Joint Prostheses

Infection and loosening are the most frequent complications of joint replacement. It is vital to be able to differentiate between these, especially since the management strategy is totally different in each case. With aseptic loosening, the patient requires a single hospital admission for the single-stage revision joint replacement. With an infected prosthesis multiple hospital admissions are required: initially to perform an excisional arthroplasty, then for a prolonged course of antibiotic therapy, and eventually for a revision arthroplasty.

When there is no Tc-99m MDP uptake in and around the prosthesis, the possibility of any actual abnormality is remote. Diffuse periprosthetic uptake is seen in infection as well as aseptic loosening. With the new porous-coated prostheses, periprosthetic bony ingrowth is stimulated; therefore, diffuse periprosthetic uptake is seen because of programmed bony ingrowth and is not necessarily indicative of pathology. This type of uptake when seen in nonporous prosthetics is associated with increased blood flow and osteolysis seen with infection. Tc-99m MDP imaging is of tremendous value because of high negative predictive value.

The most important differentiator between the two clinical entities—loosening and infection—is the level of neutrophils, which are always present in large numbers in infection and absent in loosening. Therefore, Tc-99m–labeled leukocytes would seem to be intuitively the agent of choice. However, since leukocytes are also present in the bone marrow, one has to search for concordance and discordance with accompanying Tc-99m sulfur colloid images. For instance, when the WBC-labeled images show more activity than the Tc-99m sulfur colloid, the discordance is due to infection. The combined technique has an accuracy of greater than 90%.

Ga-67 citrate imaging is also useful because of the high negative predictive value. Gallium uptake is related to inflammation and not necessarily infection alone. This makes this a less specific test. However, Ga-67 may prove to be more useful if the infection is believed to be more chronic and therefore less likely to be mediated by granulocytes.

Osteomyelitis

Osteomyelitis can present following trauma, as a consequence of bacteremia, or as a result of vascular insufficiency such as in a diabetic foot. The common organisms vary with the age of the patient: *Staphylococcus aureus* and *Streptococcus* in neonates and infants, *S. aureus* in adults, and gram-negative bacteria in the elderly. With the changing face of disease, immune status of patients, and exposure to "exotic" microorganisms from previously inaccessible geographic locations, the list of organisms producing osteomyelitis has become much more extensive.

In children osteomyelitis is often hematogenous. Since the epiphyses and metaphyses have separate blood supplies in children, it is common to have only metaphyseal involvement with sparing of the epiphysis. In most instances there is increased accumulation of the radionuclide (Tc-99m MDP) on all three phases, increasing and becoming more focal on the delayed images. Ewing's sarcoma can mimic osteomyelitis on scans. Consequently, clinical correlation is important to differentiate one entity from the other.

In diabetic patients, infection is often complicated by neuropathy. Tc-99m MDP scans are used for anatomic localization. The diagnosis of infection is effected by using WBC-labeled agents. Since there is uptake of WBC label in the bone marrow, one looks for discordant versus concordant uptake to make the diagnosis. Tc-99m sulfur colloid is used to locate the position of the bone marrow. With the use of SPECT-CT, we can anticipate that the use of a single radiopharmaceutical and anatomic correlation with CT will make the diagnosis and follow-up of osteomyelitis easier.

Septic Arthritis

Septic arthritis tends to be monoarticular and shows increased uptake with Tc-99m MDP, WBC-labeled scanning, and Ga-67. This uptake, however, is nonspecific and can be seen in instances of gout, which can manifest as a monoarticular, sterile inflammatory arthropathy. Uptake is seen on both sides of the joint. With associated cellulitis, radionuclide uptake may be detected in areas around the joint or adjacent soft tissues.

Septic arthritis in pediatrics is a true emergency and often affects the hip. The most common mode of presentation with imaging is as a photopenic defect with normal radiograph. The diagnosis is made following hip aspiration.

Transient synovitis can affect the hip in children with a fair degree of frequency. Bone scans are often negative or only mildly positive in this entity.

Infection in Immunocompromised Patients

Infection imaging in immunocompromised patients is best effected using gallium-67 citrate rather than labeled WBCs. A normal chest x-ray (CXR) with a normal gallium scan excludes the presence of infective pathology in the chest. A normal gallium scan in the face of an abnormal CXR is indicative of the inability of the patient to mount a response and carries a poor prognosis. *Pneumocystis carini* and/or bacterial pneumonia show diffuse intense uptake of gallium. Faint uptake in the chest may be seen in mycobacterial or cytomegalovirus (CMV) infections. Lymph node uptake is seen most often with mycobacterial infection or lymphoma. Kaposi's sarcoma will not take up gallium; hence, in the absence of Ga-67 uptake, an abnormal CXR should raise the suspicion of Kaposi's sarcoma.

Infections in the Lung and Other Pulmonary Pathology

Tc-99m HMPAO–labeled WBC scans are ideal for lung abscesses. Surprisingly, lobar pneumonia is usually negative on white cell scanning except early in the course of the pneumonia. This is believed to be due to early termination of WBC migration in the disease. In acute respiratory distress syndrome (ARDS), there is persistent increasing WBC uptake in the lungs, such that delayed images will present with increasing uptake as opposed to the normal transient early uptake described previously in this section.

Infection associated with obstruction in bronchogenic carcinoma and with bronchiectasis shows abnormal uptake with labeled WBCs.

TRAUMA AND BONE INFARCTION

Avascular necrosis of the femoral head is quite common and is seen in several disease states such as trauma, chronic steroid use, and sickle cell crises. There is initial photopenia due to decreased vascularity followed by increased activity reflecting new remodeling. Although bone scanning with Tc-99m MDP is far more sensitive than conventional radiography, magnetic resonance is by far the best imaging modality for workup of infarction.

Accessory ossicles are very easily differentiated from new bone fragments on conventional radiographs. However, in the rare instance where the patient complains of pain citing a possible injury, bone scanning may be of some use in the investigation of the pain. For instance, an inexpert golfer may complain of pain in the region of the hook of the hamate. Radiographs may occasionally be of dubious value in differentiating an os hamuli proprium from an old fracture versus reinjury of the hook of the hamate. Bone scans performed using high-resolution or converging collimators will show increased activity with bony injury.

The pediatric skeleton responds to bony injury much differently than does the mature one because in early childhood the skeleton is more porous and elastic. The thicker periosteum limits fractures from extending through the entire thickness of the bone. Ligaments and tendons are stronger than physes and will resist stress and torque forces; this results in fractures of the growth plate in the setting of trauma. As the child matures and reaches puberty, the increased growth and muscle strength results in avulsion fractures. Although the pediatric skeleton has a higher likelihood for repair and healing, there is a potential for interruption of the vascular supply. This can be catastrophic for achieving complete and normal growth. Fifteen percent of growth plate injuries result in shortening. Avulsion-type injuries occur where there is attachment of large muscle groups. This type of injury is seen with sports activity. While CT and MRI provide exquisite images and the ability to evaluate chondral injury and disruption, bone scans allow the evaluation of the entire skeleton. This can be used to direct focused utilization of any of the other modalities mentioned.

Nonaccidental injury (NAI) in children constitutes part of the spectrum of abuse, including physical abuse, sexual abuse, psychological abuse, and neglect. Four million children each year are abused in the United States, and 200 children die as a result. Radiologic evaluation of NAI is of tremendous importance in the diagnosis of child abuse. It is important to remember that not all children

present with a high clinical suspicion of abuse. The child may present with some other reason for evaluation, which reveals lesions suspicious of NAI. Although opinion is divided among radiologists about the use of conventional radiography and survey of the entire skeleton versus bone, these authors believe that bone scans when positive can provide enough information to preclude exposing the child to a complete skeletal survey. The skeletal lesions can be classified as high-, moderate-, and low-specificity fractures and should lead to a high degree of suspicion for NAI:

1. Corner or bucket handle fractures are considered the most highly specific.
2. Moderate-specificity lesions include multiple fractures, fractures of different ages, epiphyseal separations, vertebral body fractures, and subluxations.
3. Low-specificity lesions include clavicular fractures, long bone shaft fractures, linear skull fractures, and subperiosteal new bone formation.

Our recommendation is that skeletal survey and bone scintigraphy are complementary and should both be performed in suspected NAI.

GASTROINTESTINAL BLEEDING

The causes of gastrointestinal (GI) bleeding are classified into upper and lower GI bleeding. Upper GI bleeding comes from the esophagus, stomach, or duodenum. The most common causes of upper GI bleeding include ingestion of caustic substances, gastric malignancy, peptic ulcers, gastritis, esophageal varices, and Mallory-Weiss tears.

Lower GI bleeding originates from the jejunum, ileum, and the large bowel. Some of the common causes include diverticular disease, angiodysplasia, polyps, hemorrhoids, cancers, IBD, infectious colitis, and anal fissure.

Endoscopy is the first line of diagnostic evaluation when a patient presents with melena. Nuclear medicine studies are fairly innocuous and noninvasive.

The false positives include intramural hematomas and hemangiomas, which concentrate the radiopharmaceutical in the wall of the bowel. This can be distinguished from bleeding into the lumen of the GI tract by the fact that repeated images would not show any progression through the bowel.

Bleeding from ectopic gastric mucosa into a reduplication enteric cyst can also produce a false positive. In this instance as well the tagged RBCs will not progress.

Radiopharmaceuticals

An ideal agent for GI bleeding would be one that quickly accumulates extravascularly at the bleeding site. The ideal agent would also be rapidly cleared from the blood pool providing good target-to-background ratios (TBRs). Since GI bleeding in most instances is slow and intermittent, the ideal agent would detect slow bleeding and allow for reimaging without reinjection.

The two agents that are used for detection of the source of GI bleeding are Tc-99m–labeled RBCs (Fig. 12-18) and Tc-99m sulfur colloid. Neither of these agents is ideal, and each agent has advantages and disadvantages that the other may not possess.

Tc-99m–labeled RBCs remain in the vascular compartment, which allows repeated imaging of the GI tract. However, it is the very persistence in the blood pool of the agent that precludes obtaining an optimal TBR. With the more popular but technically more challenging in vitro technique, the appearance of free pertechnetate can be avoided with meticulous attention to washing. The presence of free pertechnetate can present a problem since it is picked up by the gastric mucosa and can obscure bleeding in the gastric cavity as well as the overlying transverse colon. Since the Tc-99m RBCs stay in the blood pool, images are generally difficult to read because of the presence of the tagged RBCs in the large and capacitance vessels.

Tc-99m sulfur colloid is picked up by the reticuloendothelial system and shows uptake in the liver, spleen, and bone marrow. The advantage of the Tc sulfur colloid is that the high TBR allows the detection of active bleeding at low bleeding rates of 0.5 to 0.1 mL per minute. If the patient is not bleeding at the time of the injection and for the next 15 minutes, and bleeds later, no Tc sulfur colloid will be remaining in the blood pool to allow reimaging. Furthermore, the normal uptake in the liver and spleen can also obscure the flexures should they be the sites of bleeding.

Technique

The patient is positioned supine with the camera placed to include the entire abdomen. If Tc-99m sulfur colloid is being used, a dynamic study is performed immediately after the intravenous injection of the Tc-99m sulfur colloid. Static images are obtained every 10 minutes up to 30 minutes. If Tc-99m–labeled RBC scanning is performed, dynamic images are obtained immediately following intravenous injection of the radiolabeled RBCs. Five-minute images are acquired for a total of 1 hour. If no bleeding is detected, then images are obtained every hour for 4 hours and again at 6 and 24 hours. This should help in detecting intermittent bleeding.

Meckel's Scan

Meckel's diverticulum is the commonest GI anomaly occurring in approximately 2% of the population. This is more common in men than in women. Five to seven percent of these diverticula contain ectopic gastric mucosa, which can present with bleeding. Most of these patients present with rectal bleeding. The diverticula vary in position, frequently located approximately 2 feet from the ileocecal junction. They are most frequently visualized in the suprapubic region as a small focus of intense Tc-99m uptake.

Technique

Ectopic gastric mucosa, whether in a Meckel's diverticulum or in a reduplication cyst, can be detected with ease following the administration of up to 10 mCi of technetium-99m injected intravenously as pertechnetate. "Dynamics" are obtained every 5 minutes for 30 minutes following intravenous injection. Static images can be acquired after the dynamic phase is completed, with images taken at 40, 50, and 60 minutes. Oblique views are helpful in localizing the site of the diverticulum. It is important to note that ectopic

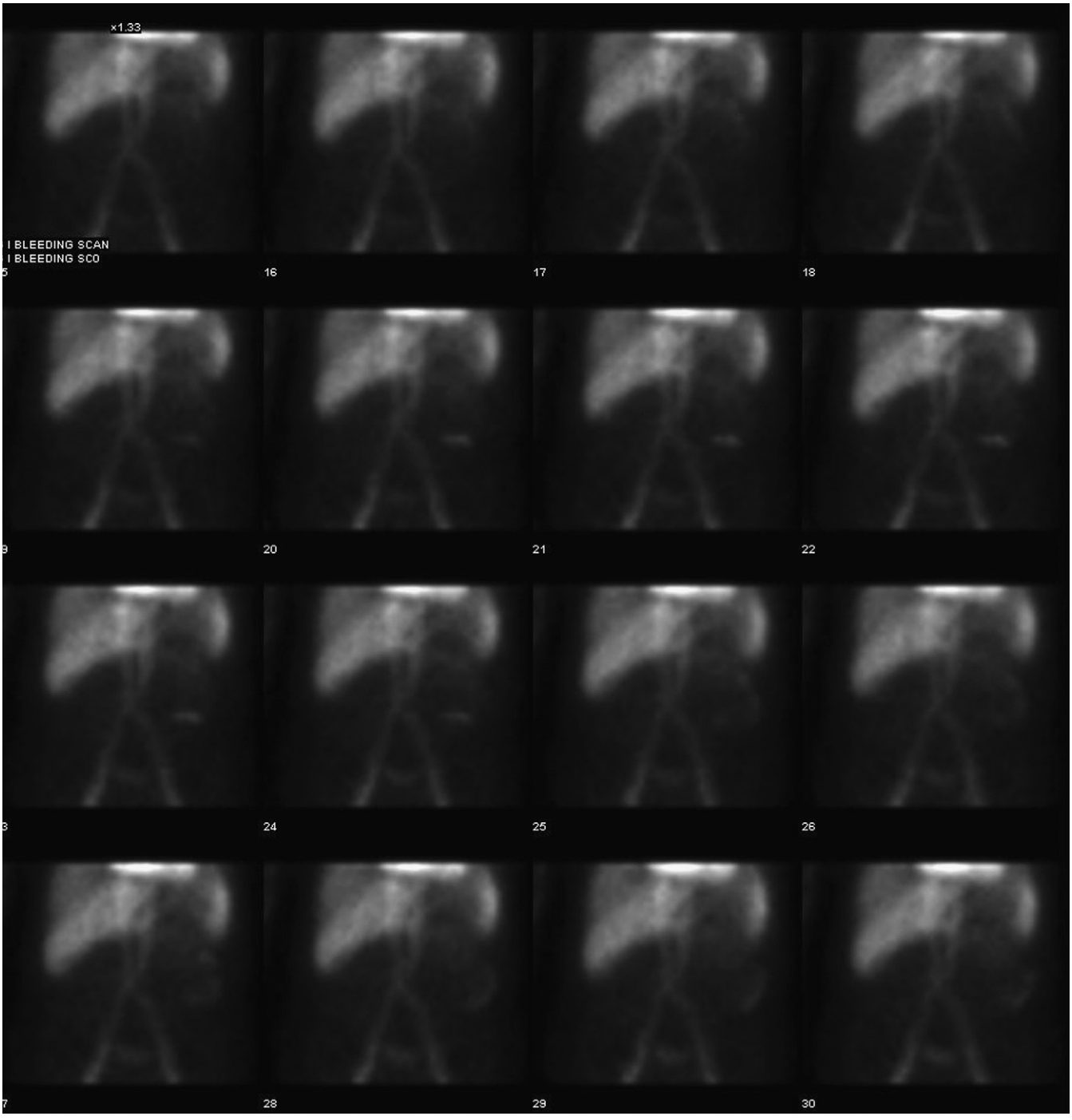


FIGURE 12-18. Tc-99m RBC study shows significant progressive accumulation of activity in the descending colon due to bleeding.

gastric mucosa will behave similarly to regular gastric mucosa, becoming equally intense.

HEPATOBILIARY SCINTIGRAPHY

Hepatobiliary scintigraphy is one of the most important studies performed in the nuclear medicine department on an emergency basis. The most common indications for emergency hepatobiliary scintigraphy are acute cholecystitis and bile leaks.

Patients presenting with right upper quadrant pain are generally worked up for acute cholecystitis. Ultrasound in this instance is generally not useful. However, with chronic cholecystitis, ultrasound would be the preferred method of investigation. A significant percentage of the patients who are liable to be candidates for chronic cholecystitis are also relatively obese, which presents a challenge for ultrasound evaluation. Since chronic cholecystitis is associated with flatulence, bowel gas can also prove to render an ultrasound examination difficult if not impossible to perform.

Hepatobiliary Agents—Mechanism

Bile is produced by the hepatocytes; approximately two thirds of this is excreted into the duodenum via the common bile duct. The remaining one third flows via the cystic duct into the gallbladder where it is stored. When a cholecystagogue (CCK) is administered or is produced in response to a fatty meal, the gallbladder contracts and bile is emptied into the duodenum. If the patient has recently had a meal, the endogenous CCK will prevent the gallbladder from filling. Therefore, the patient is encouraged to not eat for 4 hours before the test. If the patient has been fasting for more than 24 hours, the gallbladder is generally full of viscous bile, which prevents accumulation of tracer. In contrast to bilirubin, the hepatobiliary agents are not conjugated; therefore, abnormalities of the conjugation mechanism are not a contraindication to the use of the hepatobiliary iminodiacetic acid (HIDA) scan or the diisopropyl iminodiacetic acid (DISIDA) scan.

The hepatobiliary agents used most commonly are Tc-99m mebrofenin (HIDA) or Tc-99m disofenin (DISIDA). These radiopharmaceuticals are taken up by the hepatocytes and excreted into the biliary tract. Elevated levels of bilirubin associated with hepatocyte dysfunction may preclude the use of DISIDA since there may be prolonged retention of the tracer in the liver. Following intravenous administration of 3 to 5 mCi of the tracer (HIDA), initial visualization of the cardiac blood pool is noted. Within 5 minutes, the agent appears in the liver. During the next 5 to 7 minutes images of the liver can be obtained in multiple projections. The agent then enters into the biliary tract with "opacification" of the major bile ducts and the common bile duct. At this time, there is appearance of the tracer in the duodenum. The cystic duct and gallbladder are the next to fill. Similar to the bile mentioned above, some of the tracer enters into the gallbladder as long as the cystic duct is patent.

Acute Cholecystitis

The vast majority of patients with acute cholecystitis have cystic obstruction. It is based on this fact that hepatobiliary scintigraphy is used for the diagnosis of acute cholecystitis. Absence of visualization of the gallbladder for up to 4 hours after injection of the radiotracer is considered diagnostic for acute cholecystitis (Fig. 12-19). The appearance of the tracer in the gallbladder effectively excludes the presence of acute cholecystitis. However, in some cases of acalculous cholecystitis, there may be filling of the gallbladder. Additionally, the presence of an accessory cystic duct can cause a filling of the gallbladder through an "alternate" route. Structures that simulate a gallbladder can produce false negatives; these include duodenal diverticula and biliary duplication cysts.

Not infrequently in chronic cholecystitis a gallbladder may not accumulate tracer. Some pharmaceutical interventions may actually prompt the filling of the gallbladder.

If the patient has fasted for a prolonged period of time, the gallbladder may be full of viscous bile. In this case, the administration of CCK prior to or early in the study (while tracer is still available in the liver) will make the gallbladder contract and empty its contents. If the cystic duct is not obstructed, then tracer will enter the gallbladder, effectively excluding the diagnosis of acute cholecystitis.

Intravenous administration of morphine (0.04 mg/kg diluted in 10 mL of normal saline administered over 5 minutes) causes constriction of the sphincter of Oddi, raising intraductal pressure and forcing the filling of the gallbladder (Fig. 12-20). Occasionally there may not be enough tracer in the liver or the biliary tree to fill the gallbladder. This might necessitate a second injection of the tracer. Administration of morphine is a measure that should be used with caution where there is obstruction to the proximal portion of the cystic duct, as evidenced by the "cystic duct" sign. Enough pressure may be generated in the system to force the tracer into the gallbladder, producing a false negative study.

An important note of caution is to not use CCK after administration of morphine. The CCK causes the gallbladder to contract while the morphine raises the intraductal pressure. This can result in severe pain.

There are certain ancillary signs that are of use in the diagnosis of cholecystitis:

1. The "rim" sign: This is a crescentic accumulation of radiopharmaceutical within the parenchyma of the liver, along the inferior margin of the liver above the "empty" gallbladder fossa. Pericholecystic hyperemia associated with acute cholecystitis is believed to be the mechanism producing this finding. The "rim" sign is often but not invariably associated with acute cholecystitis. At least half of these patients may have a perforated or gangrenous gallbladder.
2. The "cystic duct" sign: This is defined as a small nubbin of activity in the cystic duct proximal to the site of obstruction. This sign is believed to be diagnostic of acute cholecystitis.
3. Postsurgical biliary scans.

Tc-99m HIDA/DISIDA scans are of paramount importance in the detection of biliary leaks, postsurgical or posttraumatic (Fig. 12-21). These agents are highly sensitive in detecting biliary leaks, which are not seen with other modalities. Additional views of the paracolic gutter and the pelvis must be obtained. A thorough knowledge of the anatomy of the peritoneal spaces is useful in helping the surgeon with the postoperative care of the patient.

Biliary Atresia Versus Neonatal Hepatitis

Hepatobiliary scintigraphy is useful in the differential diagnosis of biliary atresia versus neonatal hepatitis. Preparation of the patient for a week of phenobarbital (2.5 mg/kg orally twice a day) will stimulate the uptake of the tracer, allowing visualization of a patent biliary tree. This will help rule out atresia.

Biliary atresia occurs after birth in very young infants or neonates. This is characterized by the development of progressive inflammation in the biliary tract causing irreversible damage and disappearance of the bile ducts. The neonate appears normal at birth and then starts to develop obstructive jaundice 2 to 3 weeks after birth. Distinguishing between biliary atresia and neonatal hepatitis is critical since early surgical intervention is mandatory in effecting a good outcome. The procedure known as the Kasai procedure is a roux-en-Y or hepatoportojejunostomy. The chances of success are seriously diminished after the infant is over 3 months old. Hence, every infant with jaundice in

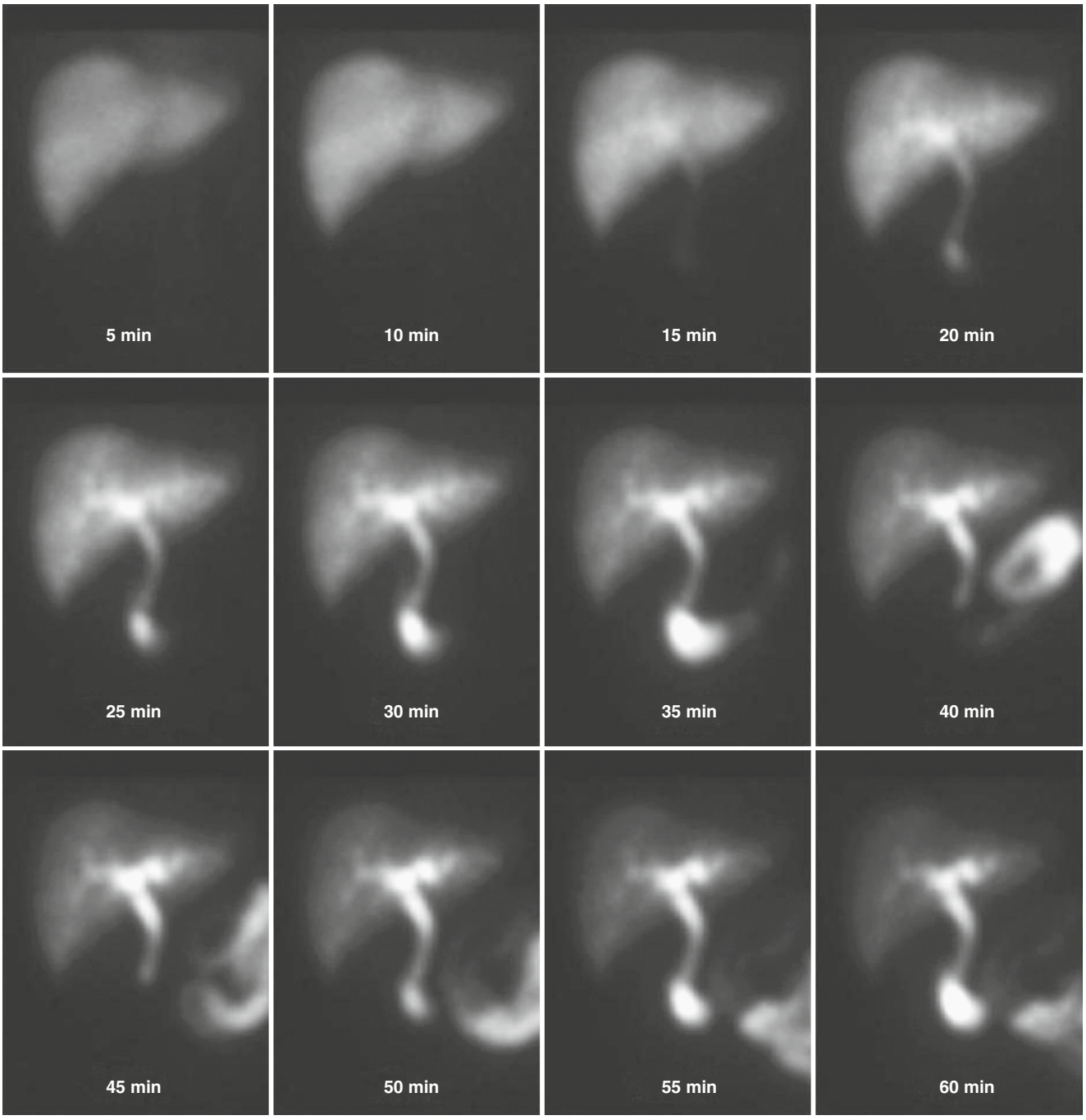


FIGURE 12-19. Acute cholecystitis. Nonvisualization of the gallbladder for 60 minutes with Tc-99m Choletech. The gallbladder fossa is empty, without any activity. Normal appearance of common bile duct and duodenum.

the neonatal period should be studied with Tc-99m hepatobiliary agents (HIDA/DISIDA) to ensure that the surgical treatment is instituted before it is too late.

SCROTAL SCANNING

In the setting of testicular pain, the working diagnosis is either testicular torsion or epididymo-orchitis. Testicular scan and Doppler ultrasound have a high degree of sensitivity in detecting testicular torsion. Since testicular torsion is a surgical emergency a rapid and accurate diagnosis is of paramount importance.

Radiopharmaceuticals and Technique

The patient is placed in a frog-leg position with the scrotum supported on a sling made by using a towel straddled across the front of the patient's thighs. A conventional flow study with dynamic images is obtained after the intravenous administration of 5 to 10 mCi of Tc-99m pertechnetate or Tc-99m DTPA. These are essentially "blood pool" agents. After the dynamic study is completed, blood pool static images are obtained in the anterior projection. Delayed static images are obtained, which will provide additional confirmation of the lack of vascularity to the affected testis in torsion.

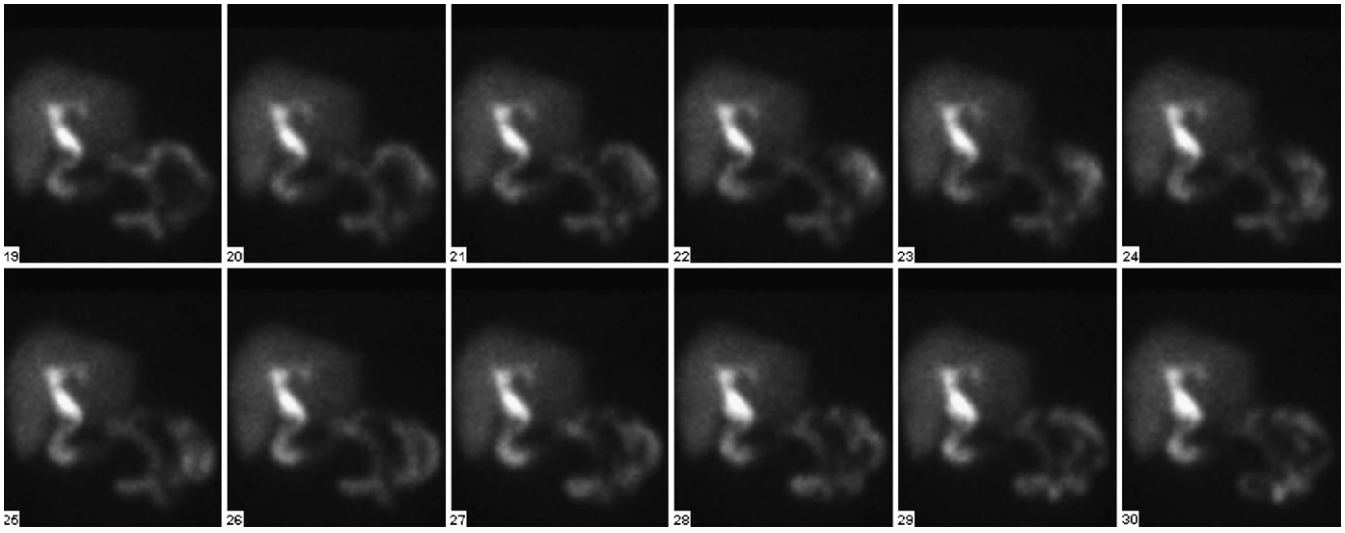


Figure 12-20. Post morphine scan shows that gallbladder is not filled, indicating complete cystic duct obstruction. Retention of activity in the common bile duct is due to contraction of the sphincter of Oddi.

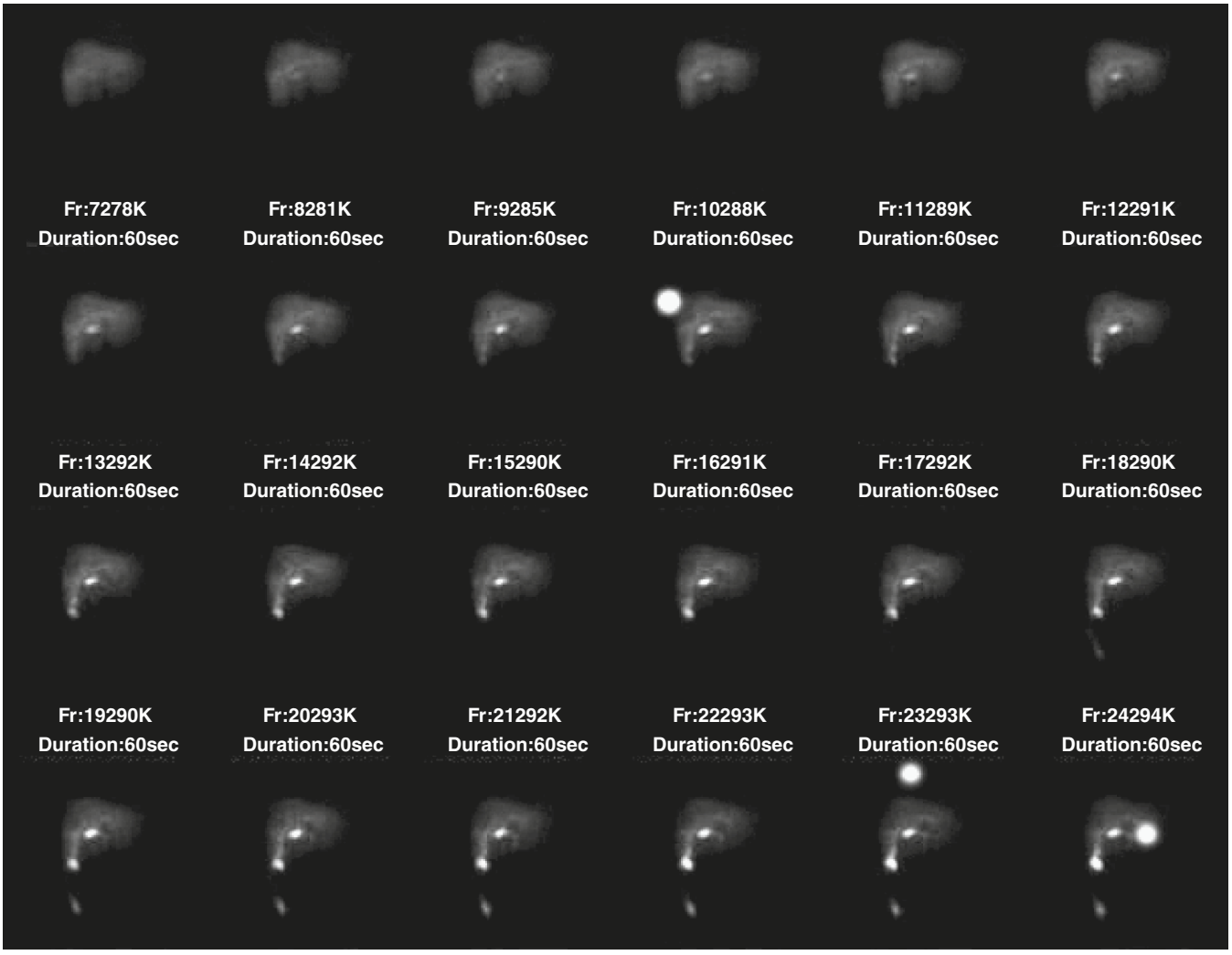


Figure 12-21. Tc-99m DISIDA study shows biliary leak with tracer along the right paracolic gutter.

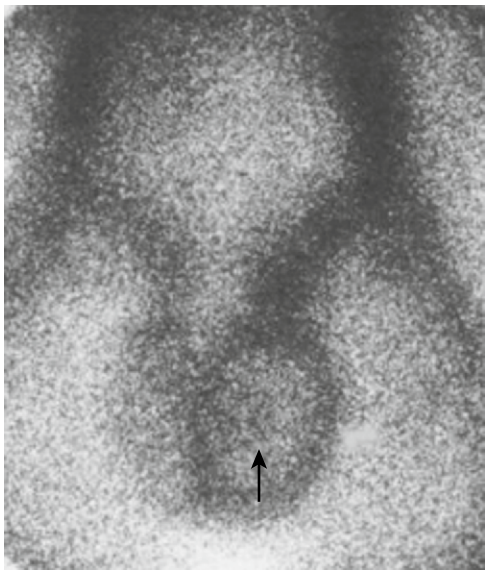


FIGURE 12-22. Left testicular torsion shows increased peripheral flow and absence of central activity ("Hello" sign) consistent with testicular torsion. Minimal activity is noted in the right testicle, which was normal.

It is extremely important to have the technologist mark the side of symptomatology distinctly on the images submitted to the picture archiving and communication system (PACS). Personally, we prefer to use a converging collimator to obtain the images.

Interpretation

Testicular Torsion

In the early stage of torsion, the perfusion to the affected side may be normal. A "nubbin" sign is believed to be pathognomonic for torsion and represents the site of the actual torsion of the testicular vessels. This is believed to be due to visualization of the spermatic artery, which is being filled by the iliac artery (Fig. 12-22). In the later stages of the torsion, that is, 24 hours later, the relative avascular testis is thrown into high relief by the increased flow through the pudendal vessels to the scrotal sac. The now perfused scrotal sac with the absent vascularity in the testis provides a "Hello" sign.

Epididymo-orchitis

This is usually a viral or bacterial condition. Associated with increased vascularity to the affected testis, it typically shows up as increased blood flow to the testicle. In some instances where there may be edema of the testicle, Doppler ultrasound is invaluable in showing preservation of blood flow even though the testis may appear relatively photopenic on the scan.

CONCLUSION

The use of nuclear medicine as an emergency imaging modality had seen a downtrend in the past decade, particularly with the development of the exquisite anatomic resolution provided by CT, the additional physiologic imaging provided by MR, and the convenience of ultrasound. However, with the increasing development of newer agents and better understanding of metabolic processes, combined with fusion of more than one modality, nuclear medicine is back into its own, providing primary as well as complementary workup in the diagnosis of disease and evaluation of treatment efficacy.

Nuclear medicine places an additional onus on the diagnostician to learn not just the appearance of the disease process but also the fundamental physics of the subspecialty, as well as to gain a better understanding of the pathophysiology and the molecular basis of disease.

SUGGESTED READINGS

Bar-shalom R, Yefremov N, Guralnik L, et al: SPECT/CT using Ga 67 and 111 in labeled leukocyte scintigraphy for diagnosis of infection. J Nucl Med 47:587–594, 2006.

Burke J: Advances in 99mTc radiopharmaceutical chemistry. Paper presented at the 148th annual meeting of the APA, San Francisco, March 2001.

Carvalho PA, Anthony PJ: Evaluation of GI bleeding with Tc 99m RBC. http://www.jpnm.org.

Curtin K, Fitzgerald SW, Nemcek AA Jr, et al: CT diagnosis of acute appendicitis: Imaging findings. AJR Am J Roentgenol 164:905, 1995.

Ell PJ, Gambhir SS: Nuclear Medicine in Clinical Diagnosis and Treatment, 3rd ed. Philadelphia, Churchill Livingstone, 1980.

Fayad LM, Johnson P, Fishman EK: Multidetector CT of musculoskeletal disease in the pediatric patient: Principles, techniques, and clinical applications. Radiographics 25:603–618, 2005.

Feied CF: Pulmonary embolism. In Rosen P, Barkin RM, editors: Emergency Medicine Principles and Practice, vol 3, 4th ed. St. Louis, Mosby Year-Book, 1998, p 3.

Heytens l, Verlooy J, Gheuens J, Bossaert L: Lazarus sign and extensor posturing in a brain-dead patient. J Neurosurg 71:449–451, 1989.

Hoffer PB: Gallium 67 Imaging. New York, Wiley, 1978, p 3.

Huang AH: The hot nose sign. Radiology 235:216–217, 2005.

Hussain HM, Barnes CE: Pediatric skeletal trauma: Plain film to MRI. Appl Radiol 36:8, 2007.

Hwang I: Imaging osteomyelitis. www.wramc.amedd.army.mil/departments/nuclear.

Kao SC, Smith WL: Skeletal injuries in the pediatric patient. Radiol Clin North Am 35:727–746, 1997.

Kowalsky RJ, Falen SW: Radiopharmaceuticals in Nuclear Pharmacy and Nuclear Medicine. Washington, DC, APhA, 2004.

Lew DP, Waldvogel FA: Current concepts: Osteomyelitis. New Engl J Med 336:999–1007, 1997.

Love C, Palestro CJ: Radionuclide imaging of infection. J Nucl Med Technol 32:47-57, 2004.

Love C, Tomas MB, Marwin SE, et al: Role of nuclear medicine in diagnosis of the infected joint replacement. Radiographics 21:1229–1238, 2001.

Mandelstam SA, Cook D, Fitzgerald M, et al: Complementary use of radiological skeletal survey and bone scintigraphy in detection of bony injury in suspected child abuse. Arch Dis Childhood 888:387–390, 2003.

McGlone BS, Balan KK: The use of nuclear medicine techniques in the emergency department. Emerg Med J 18:424–429, 2001.

Mettler FA, Guiberteau MJ: Essentials of Nuclear Medicine Imaging, 5th ed. Philadelphia, WB Saunders, 2005.

Mishkin FS, Dyken ML: Increased early radionuclide activity in the nasopharyngeal area in patients with internal carotid artery obstruction: Hot nose. Radiology 96:77–80, 1970.

Oyen WJ, Boerman OC, Corstens FH: Imaging acute appendicitis: Invited commentary. J Nucl Med 41:456, 2000.

PIOPED Investigators: Technescan MAA kit (package insert). St. Louis, MO, Mallinckrodt, 2001.

PIOPED investigators: Value of the ventilation/perfusion scan in acute pulmonary embolism: Results of the prospective investigation of pulmonary embolism diagnosis. JAMA 263:2753–2759, 1990.

Runge MS, Patterson C: Principles of Molecular Medicine, 2nd ed. Washington DC/Berlin, Humana Press, 2006.

Saber AA, LaRaja RD: Abdominal abscesses. Available online: http://emedicine.medscape.com/article/189468-diagnosis.

Schweiger B: Non-accidental injury in children—diagnostic imaging. Pediatric Trauma III. http://nordictraumarad.com/Syllabus04/pedtrauma3.pdf.

Sharp PF, Gemmell HG, Murray AD: Practical Nuclear Medicine, 3rd ed. Washington DC/Berlin, Springer, 2005.

SNM Procedure Guideline for Hepatobiliary Scintigraphy, version 3.0, approved June 23, 2001.

Tofe AJ, Francis MD: In vitro stabilization of low-tin bone imaging agent (^{99m}Tc-Sn-HEDP) by ascorbic acid. J Nucl Med 17:820-825, 1976.

Tucker WD, Greene MW, Weiss AJ, Murrenhoff AP: Methods of preparation of some carrier-free radioisotopes involving sorption on alumina. USAEC Report BNL-3746, Brookhaven National Laboratory, May 29, 1958.

Zeissmann HA: Clinical scintigraphy: cenitourinary system. In O'Malley JP, Thrall JH (eds): The Requisites: Nuclear Medicine, 3rd ed. Philadelphia, Mosby, 2005.

Index

Page numbers followed by b indicate boxes; f, figures; t, tables.

A
AAST trauma classification
  in bowel and mesenteric injuries, 95
  in liver injuries, 83, 83t
  in renal injuries, 100, 100t
  in splenic injuries, 88, 88t
Abdominal abscess, radionuclide scans in, 375–376
Abdominal pain, 275–309
  in gastrointestinal disorders, 275–291
  in genitourinary disease, 299–303
  in liver disease, 297–299
  in pancreaticobiliary disease, 291–297
  in spleen disease, 303–304
Abdominal trauma, 79–111
  of adrenal gland, 102–103
  of bladder, 103–105
  blunt, 79–82
    computed tomography in, 80–82, 80–82f
    ultrasonography in, 79, 79f
  of bowel and mesentery, 93–98
  computed tomography in. *See* Computed tomography, in abdominal trauma
  of gallbladder and bile duct, 85–88
  of kidneys, 99–102
  of liver, 82–85
  of pancreas, 91–93
  penetrating, 107–110
    computed tomography in, 109–110, 109–110f
    ultrasonography in, 109–110
  peritoneal fluid in, 98–99
  of spleen, 88–90
  ultrasonography in. *See* Ultrasonography, in abdominal injuries
  of ureters, 102
  of urethra, 105–107
  vascular injuries in, 339, 356f
Abdominal venous emergencies, 354–357
Abscess
  abdominal, radionuclide scans in, 375–376
  of brain, 27–29, 28f–30f
    pyogenic, 28f
  in dental disease, 54–57, 57f
  of liver, 297–298, 298f
    radionuclide scans in, 375
  of neck, superficial, 48, 49f
  peritonsillar, 44–45
  of prostate, 313, 313f
  renal, 300, 301f
    in children, 195–196, 195f
  retropharyngeal, 45, 46f
    in children, 200–201, 201f
  in sinusitis, 50–52, 51f–52f
  of soft tissues, 175f–177f, 176
  spinal, 231–232, 232f
  of spleen, 303–304
  tubo-ovarian, 315–316, 316f
Acetabular fractures, 140–142, 140b, 141f
  insufficiency, 169, 169f
  Judet-Letournel classification of, 140
  posterior wall, 141, 141f
  transverse, 141, 141f
Acromioclavicular joint, 165–166
  osteoarthritis of, 166
  trauma of, 115, 115f, 115b
    osteolysis in, 165–166, 166f
Acute coronary syndrome, 261–270
  anatomy in, 262–263
  clinical considerations in, 262
  coronary computed tomography angiography in, 261–263
  epidemiology of, 262
Adenitis in children
  cervical, 208
  mesenteric, 195
Adenoids, enlarged, in children, 201, 201f
Adhesive capsulitis of glenohumeral joint, 167–168
Adrenal gland trauma, 102–103, 103f
  computed tomography in, 102–103, 103f
Airway injuries, 43–44, 45f
Allergic sinusitis, 50, 51f
American Association for the Surgery of Trauma (AAST) trauma classification. *See* AAST trauma classification
Amyloid angiopathy, cerebral, intracranial hemorrhage in, 12
Aneurysm
  of abdominal aorta, 332–339
    diagnosis of, 333–334, 333f–334f
    endovascular repair of, 334–335, 335f–336f
    retroperitoneal hemorrhage in, 307–308, 307f
    treatment of, 334–335, 335f–336f
  of aortic arch, 329–332, 330t
  of femoral artery, 353–354
  of gastroduodenal arteries, 342–343, 344f
  of iliac arteries, 348, 348f
  intracranial, subarachnoid hemorrhage in, 5–6, 7f, 20–21, 20f
  of lower extremity arteries, 353–354
  mycotic, of aorta, 331, 331f
  of renal artery, 345
  of thoracic aorta, 246, 327–332, 328f, 330t
    computed tomography angiography in, 328f–329f, 331
    diagnosis of, 331
    dissection and rupture in, 329, 332b
    endovascular repair of, 252–253, 328f, 332
    etiologies of, 329–330, 330t–331t
    graft repair in, 251
  of thoracoabdominal aorta, 328f–329f, 331, 331t
  of upper extremity arteries, 350
  of visceral arteries, 342–343
Angina
  in acute coronary syndrome, 261
  Ludwig's, 54–57, 57f
Angioedema, 50–54
Angiography
  in acute coronary syndrome, 261
  in carotid artery injuries, 321, 322f
  in cerebrovascular disorders, 20–21, 23f
  computed tomography. *See* Computed tomography angiography
  magnetic resonance. *See* Magnetic resonance angiography
  in pulmonary embolism, 261
Angioma, cavernous, 232
Angiomyolipoma, renal, 345, 345f
Ankle-brachial index, 350, 352
Ankle injuries, 151–156, 151b
  fractures in, 151–156, 153f–155f
    rotational malleolar, 151–155
    tibial plafond (pilon), 153f–154f, 155
    triplane, 155–156, 155f
Ankylosing spondylitis
  of cervical spine, 220–221, 220f
  of hip, 172–173, 174f
Antibiotic-associated colitis, 288, 289f
Aorta
  abdominal
    acute occlusion of, 322f, 338, 340f
    aneurysm of. *See* Aneurysm, of abdominal aorta
    dissection of, nontraumatic, 337–338, 337f
    traumatic injury of, 321–339
  arch of, aneurysm in, 329–332, 330t
  coarctation of, 253, 254f
  computed tomography angiography of. *See* Computed tomography angiography, of aorta
  dissection of
    abdominal nontraumatic, 337–338, 337f
    computed tomography angiography in, 240–242, 247, 271
    differentiated from pulsation artifact, 240, 241f
    endovascular repair of, 252–253, 338
    graft repair of, 251
    thoracic, 247, 248f
    types of, 247, 248f
  mycotic aneurysm of, 331, 331f, 333–334
  stent placement in, 252–253, 253f
    in aneurysm, 332, 335, 336f
    in traumatic injury, 326–327, 327f, 336–337
  thoracic, 246–253
    anatomy of, 246
    aneurysm of. *See* Aneurysm, of thoracic aorta
    dissection of, 247, 248f
    hematoma of, intramural, 249–250, 249f
    infections of, 246
    interposition graft procedures, 251–252
    postoperative, 251–253, 252f
    ulcerlike diseases of, 249f–250f, 250–252, 253f
  thoracoabdominal aneurysm of, 328f, 331, 331t
  traumatic injury of, 62–64, 63f, 323–326
    abdominal, 321–339
    blunt, 323–324, 323f, 326f, 336
    common locations of, 323–324, 324f
    computed tomography angiography in, 324f–326f, 325, 330f, 327
    hematoma in, 324, 324f, 331f
    intimal flap in, 64, 65–66f
    intimal tear in, 324f–325f
    penetrating, 326–327, 327f, 336
    pseudoaneurysm in, 64, 64f, 66f, 323–326, 323f, 326f–327f
    signs of, 324, 324f
    transesophageal echocardiography in, 325
    treatment of, 325–326, 327, 327t, 336–337

Aortitis, infectious, 246
Aortoiliac disease, 346–348
Appendicitis, 283f–284f, 285
  arrowhead sign in, 283–284, 284f
  in children, 193–194
  in pregnancy, 283, 284
Appendix epididymis torsion, 198
Appendix testis torsion, 198
Arterial emergencies, 321–354
  of aorta, 323–326
  computed tomography angiography in, 321
    signs of vascular trauma in, 321, 321b, 322b
  of lower extremity, 350–351
  of mesenteric-visceral arteries, 339–345
  of neck, 321–339
  of pelvis, 345–348
  of upper extremity, 348–349
Arteriovenous fistula, spinal dural, 232
Arteriovenous malformations
  intracranial, 20f, 20–21
  spinal, 232
Arthritis
  degenerative
    of acromioclavicular joint, 166
    of hip, 172, 173f
  infectious, 176–177, 178f
    septic, 176, 377. *See also* Septic arthritis
  rheumatoid
    of glenohumeral joint, 167, 167f
    of hip, 172, 174f
    of spine, 228
Arthropathy, 172–173
  of glenohumeral joint, 166–168
  of hip, 172–173
  of spine, 226–228
Arthroplasty, orthopedic hardware infections in, 180
Aspiration
  of foreign bodies, 202–203, 203f
  of meconium, 185, 185f
Astrocytoma, 32f
Atherosclerosis
  aortic ulcer in, 250, 250f
  coronary. *See* Coronary arteries, atherosclerosis of
  of iliac arteries, 346–347
  lower extremity ischemia in, 351
Atlantoaxial dissociation, 218–219, 219f
Atlanto-occipital dislocation, 217, 218f
Atlas (C1)
  in atlantoaxial dissociation, 218–219, 219f
  in atlanto-occipital dislocation, 217, 218f
  Jefferson fracture of, 218, 218f
Atresia in neonates
  biliary, differentiated from hepatitis, 380–381
  colonic, 187
  duodenal, 186
  esophageal, 187, 187f
  ileal, 187
Avulsion injuries
  of cervical spinal nerve root, 225, 226f
  of gallbladder, 86f
  of knee, 151, 152f
  pelvic, 138, 138f
Axial loading mechanisms
  cervical spine injuries in, 222
  thoracolumbar spine injuries in, 223
Axis (C2)
  in atlantoaxial dissociation, 218–219, 219f
  fractures of, 219
    in dens (odontoid process), 219, 220f
    hangman, 219, 219f
Axonal injury, diffuse, 8–9, 10f

B
Bankart lesion in glenohumeral joint injuries, 116–117, 116f
Barton fracture, 126–129, 128f
Bennett fracture, 133, 134f
  reverse, 135
Bile duct stones
  common, 296
  intrahepatic, 296–297
Biliary tract disorders
  atresia, 380–381
  in cholangitis, recurrent, 296–297, 297f
  in cholecystitis, 294–296, 295f
    Murphy's sign in, 294–295, 295f
    radionuclide scans in, 295–296, 379–380, 381f–382f
  in choledocholithiasis, 296, 298f
    obstruction in, 308
  in cholelithiasis, 294
    ileus in, 278
    pancreatitis in, 291–293
  in hepatolithiasis, 296–297, 297f
  obstruction, 309f
    abdominal pain in, 308
    in choledocholithiasis, 308
  radionuclide scans in, 379–381
    in cholecystitis, 295–296, 381f–382f, 379–380
    in trauma, 87–88, 87f
  in trauma, 85–88, 86f
    biloma in, 87–88, 87f
    scintigraphy in, 87–88, 87f
Biloma in abdominal trauma, 87–88, 87f
Bladder
  infections of
    in children, 195
    emphysematous, 302–303
  trauma of, 103–105
  cystography in, 104
    computed tomography technique, 104–105, 105–107f
  rupture of bladder in, 104–105, 105f
    extraperitoneal, 105, 105–106f
    intraperitoneal, 105, 107f
Blunt trauma of abdomen, 79–82
  computed tomography in, 80–82, 80f–82f
  ultrasonography in, 79, 79f
Bone marrow edema of hip, transient, 169–170
Boutonniere deformity, 137
Bowel disorders. *See* Gastrointestinal disorders
Boxer's fracture, 135, 136f
Brain
  abscess of, 27–29, 28f–30f
    pyogenic, 28f
  herniation of, 10–12
    extracranial, 11
    subfalcine, 10
    tonsillar, 11, 11f
    transalar, 12
    transtentorial, 4f, 11
  in hydrocephalus, 25, 205–206
  hypoxic-ischemic injury in children, 205
    neonatal, 15
  infections of, 25–29
  trauma of
    in children, 204–205
    contusion in, 6–7, 9f
    diffuse axonal injury in, 8–9, 10f
  tumors of, 29–31
  vascular disorders of. *See* Cerebrovascular disorders
  white matter disorders of, 31–35
Brain death diagnosis, radionuclide scans in, 370–372, 371f–372f
Branchial cleft cysts, 48, 48f
Bronchiolitis in children, 204, 204f
Buckle fractures, 209–210
  of radius, 128f, 129, 210f
Budd-Chiari syndrome, 357
Bursitis of shoulder, calcific, 162–163, 163f

C
Calcaneal fractures, 156–158, 157f, 223, 225f
Calcific bursitis/tendinitis of shoulder, 162–163, 163f
Calcification
  in pancreatitis, 291–292, 291f
  in subdural hematoma, 4–5, 6f
Calcium pyrophosphate deposition disease
  of shoulder, 162–163, 163f
  of spine, 228, 229f
Calculi
  choledocholithiasis, 296, 298f
    biliary obstruction in, 308
  cholelithiasis, 294
    ileus in, 278
    pancreatitis in, 291–292, 293
  hepatolithiasis, 296–297, 297f
  urinary tract, 299, 300f
    in children, 196–197, 197f
Capsulitis, adhesive, of glenohumeral joint, 167–168
Carcinoma
  endometrial, 318–319
  of lung, metastatic to brain, 33f
  renal cell, 345
Cardiovascular disorders, 321–360
  of aorta. *See* Aorta
  arterial emergencies in, 321–354. *See also* Arterial emergencies
  in atherosclerosis. *See* Atherosclerosis
  venous emergencies in, 354–358. *See also* Venous emergencies
Carotid arteries
  dissection of, 21–23, 22–24f
    intracranial, 23–24
    magnetic resonance imaging in, 23, 24f
    spontaneous, 322–323
  endarterectomy of, neck abscess in, 49f
  pseudoaneurysm of, 322, 322f
  trauma of
    extracranial, 321–322, 322f
    in mandibular fracture, 22f
    in temporal fracture, 42–43, 44f
Carpal bones, 129–133, 130b
  dislocations of, 130b, 131–133, 132f
    lunate, 131–133, 132f
    perilunate, 131–132, 132f
  hamate fracture of, 131, 131f
  instability of, 132f, 133
    dorsal intercalated segmental, 133
    scapholunate dissociation in, 132f, 133
    volar intercalated segmental, 133
  lunate fracture of, 131
  scaphoid fracture of, 129, 130f
  triquetral fracture of, 129–131, 131f
Carpometacarpal joint dislocation, 133–135, 135f
Cavernous sinus thrombosis, 17–20, 53–54
Cellulitis, 174
  cobblestone appearance in, 174, 175f
  of foot, 174f
  of leg, 175f
Central nervous system disorders in children, 204–208
Cerebellitis in children, 206–207, 207f
Cerebral blood flow
  computed tomography perfusion imaging of, 17, 18f
  magnetic resonance perfusion imaging of, 15–17

Cerebral cortex laminar necrosis in ischemic infarction, 17, 19f
Cerebral venous sinus thrombosis, 17–20, 19f
  in children, 206, 206f
  in ear infections, 54–57, 56f
  in paranasal sinus infections, 53–54
Cerebrovascular disorders
  acute, 12–20
  in amyloid angiopathy, 12
  in aneurysms, 20–21, 20f
  in arteriovenous malformations, 20–21, 20f
  of cervicocerebral arteries, 21–24
    in spontaneous dissection, 21, 23–24
    in traumatic injuries, 21–23
  hemorrhagic, 1–2. *See also* Intracranial hemorrhage
  infarction in. *See* Infarction, cerebral
  ischemic, 12–17. *See also* Ischemia, cerebral
Cervical lymphadenitis in children, 208
Cervical spinal nerve root avulsion, 225, 226f
Cervical spine
  ankylosing spondylitis of, 220–221, 220f
  discitis and osteomyelitis of, 45–47, 46f
  rheumatoid arthritis of, 228
  trauma of, 215, 217–222
    atlantoaxial dissociation in, 218–219, 219f
    atlanto-occipital dislocation in, 217, 218f
    atlas (C1) fractures in, 218, 218f
    in axial loading, 222
    axis (C2) fractures in, 219f–220f, 219
    in children, 207–208
    differentiated from normal developmental anatomy, 222, 223f
    in hyperextension, 220–221, 221f–222f
    in hyperflexion, 219–220, 221f
    in lateral bending, 222
    mechanisms of injury in, 217b
Cervicocerebral arterial disorders, 21–24
  computed tomography in, 21–23, 22f
  in spontaneous dissection, 21, 23–24
  in traumatic injuries, 21–23, 42–43, 44f
Chance fracture in thoracolumbar injuries, 223, 225f
Chauffeur's fracture, 126–127, 128f, 129
Chest pain, 234. *See also* Thoracic disorders
Chest trauma, 60
  aortic injuries in, 62–64. *See also* Aorta, traumatic injury of
  cardiac injuries in, 62, 62f
  diaphragmatic injuries in, 70–74
  esophageal injuries in, 60–62
  fractures in, 74–77
  lung contusion in, 65
  lung laceration in, 65–66
  multidetector computed tomography protocol in, 60
  pleural space injuries in, 60
  tracheobronchial injuries in, 66–69
Chiari malformations, 205–206, 226
Children, 183–214
  appendicitis in, 193–194
  bronchiolitis in, 204, 204f
  central nervous system disorders in, 204–208
  cerebellitis in, 206–207, 207f
  croup in, 44–58, 201–202, 202f
  cryptorchidism in, 312–313
  elbow injuries in, 211, 211f
    fat pad sign in, 118–121, 121f, 211, 211f
    fractures in, 121–122, 121f–122f, 211, 211f
  encephalitis in, 206–207, 207f
  epididymitis in, 198, 198f
  epiglottitis in, 48–50, 50f, 201, 202f
  femoral fractures in, trochanteric, 144
  foreign body aspiration in, 202–203, 203f
  glottic/subglottic masses in, 202, 202f
Children *(Continued)*
  hematocolpos/hematometrocolpos in, 200, 200f
  hip pain in, 211, 211f–212f
  hydrocephalus in, 205–206
  hydronephrosis in, 196
  hypoxic-ischemic brain injury in, 205
    in neonates, 15
  intussusception in. *See* Intussusception, in children
  lymphadenitis in
    cervical, 208
    mesenteric, 195
  malrotation of intestines in, 191–192, 192f
  mastoiditis in, 208, 211
  Meckel's diverticulum in, 194–195
  meningitis in, 206–207
  neonatal. *See* Neonates
  nonaccidental injuries in, 211–212
    metaphyseal fractures in, 211–212, 212f
    radionuclide scans in, 377–378
    rib fractures in, 211–212, 212f
    skull fractures in, 204–205, 205f
  omental infarction in, 195
  ovarian cyst in, hemorrhagic, 200
  ovarian torsion in, 199–200, 199f, 314
  plastic bending fractures in, 209–210, 210f
  pneumonia in, 203, 204f
    in neonates, 184–185
  pneumothorax in, 204, 204f
    in neonates, 183–184, 184f
  pyloric stenosis in, hypertrophic, 189–191, 190f–191f
  retropharyngeal abscess in, 200–201, 201f
  Salter Harris fractures in, 208–209, 209–210f
  scrotal hernia in, 197–198, 197f
  skull fractures in, 204–205, 205f
    differentiated from normal cranial sutures, 204–205, 205f
    in nonaccidental injury, 204–205, 205f
  spine injuries in, 216
    cervical, 207–208
  stridor in, 200–204
  testicular appendage torsion in, 198, 198f, 310–311, 311f
  testicular torsion in, 198–199, 199f
  ureteropelvic junction obstruction in, 196, 196f
  urinary tract infections in, 195–196, 195f
  venous sinus thrombosis in, 206, 206f
Cholangiocarcinoma, biliary obstruction in, 308, 309f
Cholangiopancreatography
  endoscopic retrograde
    in biliary injury, 87–88, 87f
    in pancreatic injury, 92f, 93
  magnetic resonance, in pancreatic injury, 93
Cholangitis, recurrent, 296–297, 297f
Cholecystitis, acute, 294–296, 295f
  Murphy's sign in, 294–295, 295f
  radionuclide scans in, 295–296, 379–380, 381f–382f
Cholecystokinin in hepatobiliary scintigraphy, 380
Choledocholithiasis, 296, 298f
  biliary obstruction in, 308
Cholelithiasis, 294
  ileus in, 278
  pancreatitis in, 291–293
Chondromatosis, synovial, of hip, 173
Chylothorax, 244
Clavicle fractures, 114–115, 114b, 114f
Clay shoveler fracture, 219–220
Clostridium difficile colitis, 288, 289f
Coccygeal fractures, 224
Colic artery laceration, 99f
Colitis
  infectious, 288–289, 289f
  ulcerative, 286, 287f
    fat halo sign in, 286–287, 287f
Colles' fracture, 126–128, 127f
Colon
  atresia in neonate, 187
  diverticulitis of, 285, 286f
  functional immaturity in neonate, 187
  inflammatory bowel disease of, 286, 287f–288f, 376
  obstruction of, 279–280
  small left colon syndrome in neonate, 187
  trauma of, 93–94, 94b, 96, 97f
  volvulus of, 280
Colpocephaly, 25
Common bile duct stones, 296
Compartment syndrome, abdominal, 338–339, 340b
Compression fractures in thoracolumbar injuries, 222–223, 224f
Computed tomography
  in abdominal trauma
    blunt, 80–82, 80f–82f
    delayed images in, 81, 81f–82f
    of gallbladder, 86, 86f
    of kidney, 100–102
    of liver, 83–84, 84f–86f
    multidetector scanning in, 80
    of pancreas, 91–92, 92f
    penetrating, 109–110, 109f–110f
    portal venous phase imaging in, 80f–82f, 81
    of spleen, 88–90, 89f–90f
  angiography in. *See* Computed tomography angiography
  contrast agents in. *See* Contrast agents in computed tomography
  in extremity trauma, 112
    angiography technique, 159–160
    volumetric reconstruction and image post-processing in, 160
  in intracranial hemorrhage, 2
    contrast agents in, 2
    in contusion, 6–7, 9f
    in diffuse axonal injury, 8–9, 10f
    epidural, 2, 3f–4f
    subarachnoid, 6, 7f–8f, 20–21, 20f
    subdural, 4–5
  in ischemic stroke, 12–15, 14f
    perfusion imaging in, 17, 18f
  in spine injuries, 215–217
  in thoracic disorders, 236–242
    coronary angiography in, 239
    heart rate control in, 238–239
    image reconstruction in, 239
    multidetector technique, 60, 234
    patient preparation for, 238
    radiation exposure in, 239
    techniques and protocols in, 237
    in trauma, 60
Computed tomography angiography
  in abdominal trauma, 80, 80f
  of aorta
    anatomy in, 246
    in coarctation, 253, 254f
    in dissection, 240–242, 247, 271
    in stent-grafts, 252–253, 253f
    in thoracic aneurysm, 328f–329f, 331
    in traumatic injuries, 324f–326f, 325, 327, 330f
    in triple rule-out, 242, 271
  in arterial emergencies, 321
    signs of vascular trauma in, 321, 321b–322b
  in cervicocerebral arterial injuries, 21–23, 22f

Computed tomography angiography *(Continued)*
coronary, 242, 261–271
anatomy in, 262–263, 263f–265f
anomalies in, 266, 267f–268f
image evaluation in, 266–270
plaque imaging in, 270, 270f
predictive value of, 262
stenosis in, 266–270, 268f–269f, 270f
in triple rule-out, 242, 271
in extremity trauma, 159–160
heart rate control in, 238–239
in pulmonary embolism, 239–240, 254–260, 271
chronic, 257–258, 259f
diagnostic criteria in, 257–258, 258f–259f
interpretation errors in, 258–259
technical factors in, 257, 257f
in triple rule-out examination, 271
venography in, 254–255, 260
pulsation artifact in, 240, 241f
in subarachnoid hemorrhage, 20–21, 20f
triple rule-out, 242, 271
Congenital disorders of the spine, 226
Contrast agents in computed tomography
in abdominal trauma, 81–82, 80f–82f
penetrating, 109
in intracranial hemorrhage, 2
in pulmonary embolism, 257, 257f
in renal trauma, extravasation of, 82f, 100–101
in thoracic disorders, 238–239
Contusion
of bowel wall, 95
of brain, intra-axial hemorrhage in, 6–7, 9f
of gallbladder, 86
of heart, 62
of kidney, 100, 100t
computed tomography in, 100–101, 101f
of liver, 82–83
of lung, 65, 67f
of pancreas, 91–92, 91f
Coronary arteries
anatomy of, 262–266, 263f–265f
anomalies of, 266, 267f–268f
atherosclerosis of
acute coronary syndrome in, 261–262
epidemiology of, 262
image evaluation in, 266–270
plaque imaging in, 270, 270f
stenosis in, 268–269, 266–270, 270f
vulnerable plaque in, 261–262
computed tomography angiography of. *See* Computed tomography angiography, coronary
fistulas of, 266, 267f
left anterior descending
anatomy of, 262, 263f–265f
anomalies of, 266, 267f–268f
myocardial bridging of, 266, 268f
left circumflex, 262, 263f–264f, 266
left main
anatomy of, 262, 264, 264f–265f
anomalies of, 267f, 266
right
anatomy of, 262–266, 263f–265f
anomalies of, 266, 267f
Coronoid process fractures, 124, 125f
Costochondral fractures, lung herniation in, 74–75, 75f
Cranial sutures differentiated from skull fractures, 204–205, 205f
Craniopharyngioma, 32f
Crohn's disease
abscess and fistula in, 287, 288f
accordion sign in, 287f
Crohn's disease *(Continued)*
of colon, 286–288, 287f–288f
comb sign in, 281, 282f, 287
of small bowel, 281, 282f
Croup, 44–58, 50f
in children, 44–58, 201–202, 202f
Cruciate ligament avulsion injuries
anterior, 151, 152f
posterior, 151, 152f
Cryptorchidism, 197–198, 312–313, 312f
Cyst
branchial cleft, 48, 48f
ovarian, hemorrhagic, 200, 313–314, 314f
thyroglossal duct, 47–48
Cysticercosis, brain abscess in, 28–29, 30f
Cystitis
in children, 195
emphysematous, 302–303
Cystography in bladder trauma, 104
computed tomography technique, 104–105, 105f–107f
Cystourethrogram, voiding, in posterior urethral valves of neonate, 185–186, 186f

D
Dancer's fractures, 158–159
Dandy-Walker malformations, 205–206
Degenerative disorders
arthritis in
of acromioclavicular joint, 166
of hip, 172, 173f
of spine, 226–228
Dens fracture, 219, 220f
Dental disease, 54–57
abscess formation in, 54–57, 57f
Ludwig's angina in, 54–57, 57f
Dependent viscera sign in diaphragmatic injuries, 72–74, 72f–74f
Diaphragmatic injuries, 70–74
collar sign in, 72, 73f–74f, 109–110
dependent viscera sign in, 72–74, 72f–74f
mediastinal shift in, 73f
in penetrating trauma, 107–110, 110f
Digital subtraction angiography in cerebrovascular disorders, 20–21, 23f
Discitis, 231–232
of cervical spine, 45–47, 46f
Dislocations
of ankle, 151–156, 151b
atlanto-occipital, 217, 218f
of carpal bones, 130b, 131–133, 132f
lunate, 131–133, 132f
perilunate, 131–132, 132f
of carpometacarpal joints, 133–135, 135f
of elbow, 121b, 124, 125f
in foot, 156–158
of metatarsophalangeal joint, 159
of glenohumeral joint
anterior, 116–117, 116f
posterior, 117, 117f
in hand, 133–137, 133b
of interphalangeal joints, 136f, 137
of metacarpophalangeal joint, 135–136
of hip, 142, 142f
of knee, 145, 145b, 147f
arterial injuries in, 351
of patella, 147f, 148
of radius, 124, 125f
in children, 211
of sternoclavicular joint, 75, 76f
subtalar, 156, 157f
Diverticulitis
of colon, 285, 286f
of small bowel, 281–282, 282f
Diverticulum, Meckel's
in children, 194–195
radionuclide scans in, 378–379
of small bowel, 281–282, 282f
Duodenum
atresia or stenosis in neonates, 186, 187f
double bubble sign in, 186
peptic ulcer disease of, 276
trauma of, 94b
laceration in, 97f

E
Ear infections, 54
Gradenigo syndrome in, 54, 54f
mastoiditis in, 54, 54f–56f
in children, 208, 211
otitis externa in, malignant, 54
otitis media in, 208, 208f
Echocardiography, transesophageal, in aortic traumatic injury, 325
Ectopic pregnancy, 317, 317f–318f
Edema
of hip bone marrow, transient, 169–170
pulmonary, 238f
ground glass opacities in, 238f
of spinal cord, 224–225
Effusions
pericardial, 244
pleural, 243
etiologies of, 243, 243t
Elbow injuries, 121b, 118–124
in children, 211, 211f
fat pad sign in, 118–121, 121f, 211, 211f
fractures in, 121–122, 121f–122f, 211, 211f
coronoid process fractures in, 124, 125f
dislocations in, 121b, 124, 125f
fat pad sign in, 121f, 118–121
in children, 121f, 118–121, 211, 211f
femoral fractures in, 144–145
humerus fractures in, 121f–124f, 121–122
olecranon process fractures in, 123–124, 125f
radius fractures in, 122–124, 125f
Elderly
acetabular fractures in, 169, 169f
aortic aneurysm in, 332
femoral fractures in, proximal, 142–143
Embolectomy in acute ischemic stroke, 17, 18f
Embolism
in aorta, 338
cerebral, embolectomy in, 17, 18f
in iliac arteries, 346–347
lower extremity ischemia in, 351, 353f
pulmonary, 253–261
chest radiography in, 255, 255f–256f, 368–369, 368f
chronic, 257, 259f
clinical considerations in, 253–254, 254–255
computed tomography angiography in. *See* Computed tomography angiography, in pulmonary embolism
computed tomography venography in, 254–255, 260
conventional angiography in, 261
diagnostic criteria in, 257–258, 258f–259f
epidemiology of, 254
Fleischner sign in, 255, 256f
Hampton sign in, 255, 255f
imaging techniques in, 254–255, 255–261, 255b

Embolism *(Continued)*
in lower extremity venous thrombosis, 357–358
magnetic resonance angiography in, 254–255, 260, 261f
magnetic resonance venography in, 254–255, 261, 261f
pathophysiology of, 254
PIOPED study of, 254–256, 256b, 368
railway track sign in, 257, 258f
right ventricular enlargement in, 259–260, 260f
ventilation-perfusion scan in, 255–256, 256b, 364–369
renal infarction in, 303
septic, brain abscess in, 27–28, 30f
upper extremity ischemia in, 349–350
Embolization
in hepatic vascular injuries, 83–84, 85f
in pelvic artery trauma, 345–346, 346f–347f
Emphysema
pulmonary interstitial, in neonates, 183–184, 184f
subcutaneous, in tracheobronchial injuries, 66–68, 70f–71f
Empyema, 244
Encephalitis, 27
in children, 206–207, 207f
herpes simplex, 27, 27f
Encephalomyelitis, acute disseminated, 33, 35f
Encephalopathy
neonatal hypoxic-ischemic, 15
posterior reversible syndrome, 33–35, 36f
toxic, 35–36, 36f
Endarterectomy, carotid, neck abscess in, 49f
Endometrial carcinoma, 318–319
Endometrial polyps, 318–319
Endometriosis, 315
Endometritis, 316–317
Endovascular repair
in aortic aneurysm, 252–253
abdominal, 334–335, 335f–336f
thoracic, 332, 328f
in aortic dissection, 252–253, 338
in aortic traumatic injuries, 326, 327
abdominal, 336–337
endoleaks in, 326, 327t
Enteritis, infectious, 280–281, 281f
Enterocolitis, necrotizing, in neonate, 187–188
falciform ligament appearance in, 187–188, 188f
perforation in, 187–188, 189f
pneumatosis intestinalis in, 187–188, 188f
portal venous gas in, 187–188, 188f
Ependymoma, 230–231, 231f
Epididymitis, 311, 311f
in children, 198, 198f
radionuclide scans in, 383
Epidural hemorrhage, 2, 3f–4f
Epiglottitis, 48–50, 50f
in children, 48–50, 50f, 201, 202f
Epiploic appendagitis, 284, 285f
ERCP (endoscopic retrograde cholangiopancreatography)
in biliary injury, 87–88, 87f
in pancreatic injury, 92f, 93
Erythrocytes, technetium-99m labeled, in gastrointestinal bleeding, 290, 378, 379f
Esophagus
atresia in neonates, 187, 187f
foreign body in, 202–203, 203f
trauma of, 60–62, 242
Essex-Lopresti fracture, 123–124
Ethmoid sinusitis, 52, 53f
Extra-axial hemorrhage, 1, 2–6
Extracranial brain herniation, 11
Extremity trauma, 112
computed tomography in, 112
angiography technique, 159–160
with volumetric reconstruction and image post-processing, 160
of lower extremity, 137–159
arterial injuries in, 350–351, 351f
common locations of fractures in, 137f
magnetic resonance imaging in, 112
steps in interpretation of, 112, 112b
of upper extremity, 113–137
arterial injuries in, 348–349, 348b, 349b, 349f–350f
common locations of fractures in, 113f

F

Facial nerve injury in temporal bone fractures, 43
Falciform ligament appearance in necrotizing enterocolitis of neonate, 187–188, 188f
Fallopian tube disorders, 315–316, 316f
tubo-ovarian abscess in, 315–316, 316f
Fasciitis, necrotizing, 174–175, 175f
FAST (focused abdominal sonography for trauma), 79, 79f
Fat blood interface (FBI) sign in knee injuries, 144, 145f
Fat pad sign in elbow injuries, 118–121, 121f
in children, 118–121, 121f, 211, 211f
Female genitourinary disorders. *See* Genitourinary disorders, in female
Femoral artery aneurysm and pseudoaneurysm, 351, 353–354, 352f
Femur
dislocation of head, 142
fractures of
arterial injuries in, 351f
distal, 144–145, 146f
floating knee in, 144–145, 146f
Garden classification of, 143–144
intertrochanteric, 143f, 144
in neck, 143–144, 143f, 168–169, 168f
proximal, 142–143, 143f
in shaft, 144
subcapital, 143–144, 143f
subtrochanteric, 144
supracondylar, 144–145
trochanteric, 143f, 144
osteonecrosis of head, 170–172, 171f–172f, 170t
double line sign in, 171–172, 172f
Ficat classification of, 170, 170t, 171f
radionuclide scans in, 377
slipped capital epiphysis, 211, 212f
transient bone marrow edema and osteoporosis of, 170, 170f
Fibroids, uterine, 318–319
Ficat classification of femoral head osteonecrosis, 170, 171f, 170t
Fistula
arteriovenous spinal dural, 232
of coronary artery, 266, 267f
in Crohn's disease, 287, 288f
Flail chest, 74, 75f
Fleischner sign in pulmonary embolism, 255, 256f
Flexor digitorum profundus tendon injuries, 136–137
Floating knee, 144–145, 146f
Fluoroscopy in intussusception, 193, 193f
Foot
cellulitis of, 174f
trauma of, 156–158, 156b
Foot *(Continued)*
calcaneal fractures in, 156–158, 157f
in forefoot, 158–159
in hindfoot, 156, 157f
metatarsal fractures in, 158–159, 159f
metatarsophalangeal, 159
in midfoot, 158
phalangeal fractures in, 159
subtalar dislocation in, 156, 157f
talus fractures in, 156, 157f
tarsometatarsal, 158, 158f
Foreign bodies, 180, 181f
aspiration of, 202–203, 203f
gastrointestinal, 289, 290f
Fournier gangrene, 311, 312f
Fractures, 112
acetabular. *See* Acetabular fractures
of ankle, 151–156, 153–155
rotational malleolar, 151, 151–155
tibial plafond (pilon), 153f–154f, 155
triplane, 155–156, 155f
of calcaneus, 156–158, 157f
in chest trauma, 74–77
in children, 208–212
in elbow injuries, 121–122, 121–122f, 211, 211f
femoral trochanteric, 144
metaphyseal, 211–212, 212f
plastic bending, 209–210, 210f
radionuclide scans in, 377–378
of ribs, 211–212, 212f
Salter Harris, 208–209, 209f–210f
of skull, 204–205, 205f
of clavicle, 114–115, 114b, 114f
description of, 112, 112b
in elbow injuries, 118–124, 121b
in children, 121–122, 121f–122f, 211
facial smash, 40, 41f
of femur. *See* Femur, fractures of
in foot, 156–159
of hamate, 131, 131f
of hand, 133–137, 133b
of humerus. *See* Humerus fractures
in knee area, 144–151, 145b
Le Fort, 39, 40f
in lower extremity, 137–159
of lunate, 131
mandibular, 40–41, 42f
arterial dissection in, 22f
maxillofacial, 37–38
metacarpal, 135, 136f
of thumb, 133, 134f
metatarsal, 158–159, 159f
nasal, 39
naso-orbitoethmoid, 39
of occipital condyle, 217, 218f
orbital
blow-out, 38–39, 38f
of roof, 39
of patella, 148, 148f
pelvic. *See* Pelvic fractures
phalangeal. *See* Phalangeal fractures
plastic bending, 209–210, 210f
of radius. *See* Radius, fractures of
of ribs. *See* Ribs, fractures of
of sacrum, 139, 139f–140f
of scaphoid, 129, 130f
of scapula, 113–114, 113b, 114f
of skull. *See* Skull fractures
of sternum, 75, 76f–77f
of talus, 156, 157f
of temporal bone. *See* Temporal bone fractures
terminology related to, 112, 112b
of thoracic spine, 76, 77

Fractures *(Continued)*
of tibia. *See* Tibia fractures
Tillaux, 155, 155f, 208–209, 210f
in toddlers, 209–210, 210f
triquetral, 129–131, 131f
of ulna
distal and shaft, 124–129, 125b
pronator quadratus sign in, 124
in upper extremity, 113–137
zygomaticomaxillary complex, 39, 40f
Frontal sinusitis, 50–52, 51f
Frozen shoulder, 167–168
Fungal sinusitis, 50, 51f

G
Galeazzi fracture-dislocation, 126, 126f
Gallbladder
cholecystitis of, 294–296, 295f
Murphy's sign in, 294–295, 295f
radionuclide scans in, 295–296, 379, 380, 381f–382f
trauma of, 85–88
avulsion injury in, 86f
computed tomography in, 86, 86f
ultrasonography in, 86
Gallium-67 citrate imaging, 363, 363f
in infections, 374–375
in orthopedic hardware, 181, 375–376
Gallstones, 294, 294
ileus in, 278
pancreatitis in, 291–293
Gamekeeper's thumb, 133, 135f
Gangrene, Fournier, 311, 312f
Garden classification of femoral fractures, 143–144
Gastric outlet obstruction, 275–276
Gastroduodenal artery aneurysm and pseudoaneurysm, 342–343, 344f
in pancreatitis, 293f, 344f
Gastroenteritis, viral, 281f
Gastrointestinal disorders, 275–291
appendicitis, 282–284, 283f–284f
in children, 193–194
in children, 189–195
neonatal, 186–187, 186f–187f
colitis
infectious, 288–289, 289f
ulcerative, 286–288, 287f
diverticulitis
of colon, 285, 286f
of small bowel, 281–282, 282f
enteritis, 280–281
enterocolitis, necrotizing, 187–188
of epiploic appendages, 284
in foreign bodies, 289, 290f
hemorrhage, 341–342, 341f–342f
acute, 289–291
radionuclide scans in, 290, 378–379
ileus
adynamic, 280
gallstone, 278
meconium, 187
inflammatory bowel disease. *See* Inflammatory bowel disease
intussusception. *See* Intussusception
Meckel's diverticulum, 194–195, 281–282, 282f, 378–379
obstruction
in children, 186–187
of colon, 279–280
of gastric outlet, 275–276
of small bowel, 276–278, 277f–279f
Gastrointestinal disorders *(Continued)*
omental infarction, 195, 284–285
peptic ulcer disease, 276
pyloric stenosis, hypertrophic, 189–191, 190f
in trauma, 93–97
common locations of injuries in, 93–94, 94b
hematoma in, 95, 95f
hypovolemic shock in, 99, 99f
intraperitoneal air, 95b, 96f
intraperitoneal fluid in, 95b, 98–99
laceration in, 95–96, 96f–97f
penetrating injuries in, 107–110, 109f
volvulus. *See* Volvulus
Genitourinary disorders, 299–303
abdominal pain in, 299–303
in children, 195–200
neonatal, 185–186, 185f–186f
in female, 313–320
in ectopic pregnancy, 317, 317f–318f
in endometriosis, 315
in endometritis, 316–317
in fallopian tube disorders, 315–316, 316f
in hemorrhagic ovarian cyst, 200, 313–314, 314f
in ovarian torsion, 199–200, 199f, 314–315, 315f
in ovarian vein thrombosis, 317–318, 319f
pelvic pain in, 313
uterine bleeding in, 313, 317, 318–319
in male, 310–313
in cryptorchidism, 197–198, 312–313, 312f
in epididymitis, 198, 198f, 311, 311f
in prostatitis, 313, 313f
radionuclide scans in, 381–383, 383f
in testicular appendage torsion, 198, 198f, 310–311, 311f
in testicular torsion, 198–199, 199f, 310, 310f
in testicular trauma, 312
in nephrolithiasis, 299, 300f
in children, 196–197, 197f
obstruction in, 308–309
obstruction, 308–309
in nephrolithiasis, 308–309
in pyelonephritis. *See* Pyelonephritis
in pyonephrosis, 302
in renal abscess, 300, 301f
in children, 195–196, 195f
in renal infarction, 303
traumatic, 103–107
Glenohumeral joint, 166–168
adhesive capsulitis of, 167–168
rheumatoid arthritis of, 167, 167f
trauma of, 116–118, 116b
anterior dislocation in, 116–117, 116f
inferior subluxation in, 117–118
posterior dislocation in, 117, 117f
pseudosubluxation in, 118
trough line sign in, 117f, 121f
Glioblastoma multiforme, 32f
Glottic masses in children, 202
Gradenigo syndrome, 54, 55f
Grafts, aortic interposition, 251–252
Greenstick fractures, 209–210
Guillain-Barré syndrome, 231
Gunshot wounds
abdominal injuries in, 107–110
aortic injury in, 326–327

H
Hamate fracture, 131, 131f
Hampton sign in pulmonary embolism, 255, 255f
Hand injuries, 133–137, 133b
carpometacarpal dislocations in, 133–135, 135f
foreign bodies in, 181f
of interphalangeal joints, 136–137, 136f
metacarpal fractures in, 135, 136f
of thumb, 133, 134f
metacarpophalangeal dislocations in, 135–136
phalangeal fractures in, 136–137, 136f
in thumb, 133, 135f
of thumb, 133, 134f–135f
carpometacarpal dislocation in, 133–135
metacarpal fracture in, 133, 134f
phalangeal fracture in, 133, 135f
Hawkins' classification of talus fractures, 156
Head and neck region
glottic/subglottic masses in, in children, 202, 202f
in hydrocephalus, 25, 205–206
infections of, 44–58
trauma of, 36–44
airway and pharyngeal injuries in, 43–44, 45f
atlanto-occipital dislocation in, 217, 218f
cervical spine injuries in. *See* Cervical spine, trauma of
in children, 204–205, 207–208, 205f
contusion in, 6–7, 9f
diffuse axonal injury in, 8–9, 10f
occipital condyle fractures in, 217, 218f
skull fractures in. *See* Skull fractures
vascular injuries in, 21–23, 22f, 42–43, 44f, 321–322, 322f, 354
zones of injury in, 321
vascular disorders in. *See also* Cerebrovascular disorders
of carotid and vertebral arteries, 321–322, 322f
in spontaneous arterial dissection, 21, 23–24
in traumatic injuries, 21–23, 22f, 42–43, 44f, 321–322, 322f, 354
Heart
injuries in chest trauma, 62, 62f
metastasis to, 244
Heart failure
chest radiography in, 235–236, 237f
computed tomography in, 238f
Heart rate in computed tomography angiography, 238–239
Hello sign in testicular torsion, 383, 383f
Hemangioblastoma, 31f
Hemangioma
in abdominal trauma, 82f
of small bowel, 341f
spinal, 229
Hemarthrosis in knee injuries, 144
Hematocele in lung laceration, 65, 68f
Hematochezia, 341, 342f
Hematocolpos, 200, 200f
Hematoma
in adrenal trauma, 102–103, 103f
aortic intramural, 249–250, 249f
ulcers in, 249f, 250
in bowel injuries, 95, 95b, 95f
epidural, 2, 3f–4f, 227f
in hepatic trauma, 82–83, 84f
classification of injury in, 83t
in mesenteric trauma, 96–97, 96f–98f
in renal trauma, 100, 100f
spinal, 225–226, 227f
in splenic trauma
computed tomography in, 89–90, 88f–90f
ultrasonography in, 88, 89f
subdural, 2–5, 5f, 227f
calcification of, 4–5, 6f
and subarachnoid hemorrhage, 2–6

Hematometrocolpos, 200
Hematuria in bladder trauma, 104
Hemopericardium, 62, 62f, 244, 244f
Hemoperitoneum, spontaneous, 305–307, 306f
Hemorrhage
  in aortic traumatic injury, 323–324
  gastrointestinal, 341–342, 341f–342f
    acute, 289–291
    radionuclide scans in, 290, 378–379
  hemoperitoneum in, 305–307, 306f
  in hepatic trauma, 83–84, 85f
  intracranial, 1–2. *See also* Intracranial hemorrhage
  in mesenteric injury, 96–97, 98f
  in ovarian cyst, 200, 313–314, 314f
  in pelvic trauma, 103, 104f, 139, 345–346, 346f
  peritoneal, in abdominal trauma, 79, 79f
  postpartum, 317
  retroperitoneal, 306–308, 307f
  in spinal cord trauma, 225–226, 227f–228f
  uterine, 313, 318–319
    postpartum, 317
Hemothorax, 243–244
  in chest trauma, 61, 60f
Hepatic artery
  aneurysm of, 342
  trauma of, 83–84, 86f
Hepatic vein obstruction, 357
Hepatitis, 298–299
  neonatal, differentiated from biliary atresia, 380–381
Hepatobiliary scintigraphy, 379–381
  agents used in, 380
  in cholecystitis, 295–296, 379–380, 381f–382f
  in differentiation of neonatal biliary atresia and hepatitis, 380–381
  in liver trauma, 87–88, 87f
Hepatolithiasis, 296–297, 297f
Herniation
  of brain. *See* Brain, herniation of
  of lung, in rib or costochondral fractures, 74–75, 75f
  scrotal, 311–312
    in children, 197–198, 197f
  small bowel obstruction in, 278, 278f
Heroin use, toxic encephalopathy in, 35–36, 36f
Herpes simplex virus encephalitis, 27, 27f
Hill-Sachs fracture, 116–117, 116f
Hip
  acetabular fractures of, 140–141, 140b, 141f
    insufficiency, 169, 169f
  ankylosing spondylitis of, 172–173, 174f
  arthropathy of, 172–173
  bone marrow edema of, transient, 169–170
  dislocation of, 142, 142b, 142f
  insufficiency fractures of, 168–169, 168f–169f
  osteoarthritis of, 172, 173f
  osteonecrosis of femoral head, 170–172, 170t, 171f
  osteoporosis of
    fractures in, 168–169
    transient, 169–170, 170f
  pain in, 168–173
    in children, 211, 211f–212f
  rheumatoid arthritis of, 172, 174f
  septic arthritis of, in children, 211, 211f, 377
Hirschsprung's disease in neonate, 187, 187f
HIV infection and AIDS
  brain abscess in, 27
  leukoencephalopathy in, progressive multifocal, 33, 35f
  meningitis in, 11f, 26–27
Humerus fractures, 118, 118b
  distal, 121–122, 121f–123f
  lateral condylar, 121–122, 122f
Humerus fractures *(Continued)*
  Neer classification of, 118
  pathologic, 118
  proximal, 118, 119f
  in shaft, 118, 120f
  supracondylar, 121, 121f
    in children, 211, 211f
Hutchinson fracture of radius, 128f, 129
Hydrocele, 197–198, 311, 312f
Hydrocephalus, 25, 25f
  in children, 205–206
  normal pressure, 25
  shunt malfunction in, 25, 25f
Hydronephrosis in children, 196
  in ureteropelvic junction obstruction, 196, 196f
Hydrosalpinx, 315–316
Hygroma, subdural, 5
Hymen, imperforate, 200
Hyperextension injuries
  of cervical spine, 220–221, 221f–222f
  of thoracolumbar spine, 223
Hyperflexion injuries of cervical spine, 219–220, 221f
Hypovolemic shock in bowel injuries, 99, 99f
Hypoxic-ischemic brain injury in children, 205
  neonatal, 15

I

Ileocolic intussusception, 192–193, 192f–193f
Ileum
  atresia of, 187
  trauma of, 94b, 96f
Ileus
  adynamic, 280
  gallstone, 278
  meconium, 187
Iliac artery disorders, 346–348, 347f–348f
  aneurysm, 348, 348f
  dissection, 337f, 348
  occlusion, 346–348, 347f
Iliac fractures, 104f, 138, 138f
Immunocompromised patients, infections in, 377
  enteritis in, 280–281
Impingement of rotator cuff, 163–164, 164f
Incisional hernia, small bowel obstruction in, 278, 278f
Indium-111, 363, 363f
  leukocytes labeled with
    in infections, 372–373
    normal distribution of, 373, 373f
Infarction
  cerebral
    computed tomography in, 12–15, 14f
    cortical laminar necrosis in, 17, 19f
    hemorrhagic transformation in, 17, 19f
    magnetic resonance diffusion-weighted imaging in, 14f, 15, 16f
    magnetic resonance perfusion imaging in, 15–17
    in venous sinus thrombosis, 17–20, 19f
  myocardial, coronary computed tomography angiography in, 261–270
  omental, 284–285
    in children, 195
  renal, 303
  of spinal cord, 232
  splenic, 304
Infections
  aortitis in, 246
  arthritis in, 176–177, 178f
    septic. *See* Septic arthritis
Infections *(Continued)*
  of brain, 25–29
  cellulitis in, 174, 175f
  colitis in, 288–289, 289f
  cystitis in
    in children, 195
    emphysematous, 302–303
  of ear. *See* Ear infections
  endometritis in, 316–317
  enteritis in, 280–281, 281f
  epididymitis in, 311, 311f
    in children, 198, 198f
  fasciitis in, necrotizing, 174–175, 175f
  in head and neck region, 44–58
  in immunocompromised patients, 377
    enteritis in, 280–281
  liver abscess in, 297–298, 298f
  mediastinal, 245
  musculoskeletal, 174–182
    radionuclide scans in, 376–377
  nuclear radiology in. *See* Nuclear radiology, in infections
  in orthopedic hardware, 180–182, 375–376
    radionuclide scans in, 181–182, 376
  osteomyelitis in. *See* Osteomyelitis
  pyelonephritis in. *See* Pyelonephritis
  retropharyngeal, 45, 46f
    in children, 200–201, 201f
  sinusitis in. *See* Sinusitis
  of soft tissues, 174–176
  spinal, 231–232, 232f
  of urinary tract in children, 195–196, 195f
Inflammatory bowel disease, 376
  abscess and fistula in, 287, 288f
  accordion sign in, 287f
  of colon, 286–288, 287f–288f, 376
  comb sign in, 281, 282f, 287
  fat halo sign in, 286–287, 287f
  radionuclide scans in, 376
  of small bowel, 281, 282f
Inguinal scrotal hernia, 311–312
  in children, 197–198, 197f
Instability
  carpal, 132f, 133
    dorsal intercalated segmental, 133
    scapholunate dissociation in, 132f, 133
    volar intercalated segmental, 133
  in spinal trauma, 217
Insufficiency fractures of hip, 168–169, 168f–169f
Interphalangeal joint injuries of hand, 136–137, 136f
Intertrochanteric fractures of femur, 143f, 144
Intestinal disorders. *See* Gastrointestinal disorders
Intra-axial hemorrhage, 1, 6–9
Intracranial hemorrhage, 1–2
  contrast-enhanced computed tomography in, 2
  in contusion, 6–7, 9f
    computed tomography in, 6–7, 9f
    magnetic resonance imaging in, 6–7
  in diffuse axonal injury, 8–9, 10f
    computed tomography in, 8–9, 10f
    magnetic resonance imaging in, 8–9, 10f
  epidural, 2, 3f, 4f
    computed tomography in, 2, 3f, 4f
  extra-axial, 1, 2–6
  general imaging characteristics in, 2t
  in hemorrhagic transformation of ischemic infarction, 17, 19f
  intra-axial (parenchymal), 1, 6–9
    spontaneous (acute), 12, 12–13f
  intraventricular, 6, 9f
    magnetic resonance imaging in, 6, 9f
  subarachnoid. *See* Subarachnoid hemorrhage

Intracranial hemorrhage *(Continued)*
subdural, 2–5, 5f
computed tomography in, 4–5
magnetic resonance imaging in, 2–5
Intraperitoneal air in bowel injury, 95, 95b, 96f
Intraperitoneal fluid in abdominal trauma, 95, 95b, 98–99, 99f
Intraventricular hemorrhage, 6, 9f
Intussusception, 192–193
in children, 192–193, 192f–193f
abdominal radiography in, 192, 192f–193f
fluoroscopy and reduction enema in, 193, 193f
target appearance in, 192–193, 193f
ultrasonography in, 192–193, 193f
ileocolic, 192f–193f
small bowel obstruction in, 278, 279f
Ischemia
cerebral, 12–20
in asphyxia of children, 205
computed tomography in, 12–15, 14f
computed tomography perfusion imaging in, 17, 18f
cortical laminar necrosis in, 17, 19f
hemorrhagic transformation in, 17, 19f
and hypoxic-ischemic brain injury, 15, 205
infarction in. *See* Infarction, cerebral
magnetic resonance angiography in, 14f, 15
magnetic resonance diffusion-weighted imaging in, 14f, 15, 16f
magnetic resonance perfusion imaging in, 15–17
in transient attack, 12
in venous sinus thrombosis, 17–20, 19f
lower extremity, 351–353, 353f
mesenteric, 290–291, 339–341
myocardial, coronary computed tomography angiography in, 261–270
renal, 344, 345f
upper extremity, 349–350
Ischial fracture, 138

J
Jefferson fracture of atlas, 218, 218f
Jejunum, trauma of, 94b
laceration in, 97f
Jersey finger, 136
Joint prosthesis disorders, radionuclide scans in, 376
Jones' metatarsal fracture, 158–159, 159f
Judet-Letournel classification of acetabular fractures, 140
Jugular vein
thrombosis of, 357
traumatic injury of, 354

K
Kidneys
abscess of, 300, 301f,
in children, 195–196, 195f
calculi in, 299, 300f
in children, 196–197, 197f
infarction of, 303
pyelitis of, emphysematous, 302–303
pyelonephritis of. *See* Pyelonephritis
pyonephrosis of, 302
renal artery disorders of. *See* Renal artery disorders
renal vein thrombosis of, 303, 355–356
trauma of, 99–102
computed tomography in, 100–102
contrast extravasation in, 100–101, 102f
Kidneys *(Continued)*
fracture of kidney in, 101
renal artery injuries in, 343–344
ultrasonography in, 100, 100f
urine leak in, 100–101, 101f
vascular pedicle injury in, 101–102, 102f
tumors of, 345, 345f
Kienbock's disease in lunate fracture, 131
Knee injuries, 144–151, 145b
avulsion, 151, 152f
dislocation in, 145, 145b, 147f, 148
arterial injuries in, 351
fat blood interface (FBI) sign in, 144, 145f
femoral fractures in, 144–145, 146f
floating knee in, 144–145, 146f
hemarthrosis and lipohemarthrosis in, 144, 145f
patellar fractures in, 148, 148f–149f
tibial plateau fractures in, 148–151, 150f
Krypton-81m ventilation scans, 367

L
Laceration
of bowel, 95–96, 96f–97f
of gallbladder, 86
of kidney, 100, 100t
computed tomography in, 100–101, 101f, 110f
ultrasonography in, 100
of liver, 82, 110f
classification of injury in, 83t
computed tomography in, 83, 84f
ultrasonography in, 82–83, 83f
of lung. *See* Lungs, laceration of
of mesentery, 96–97, 98f
of pancreas
computed tomography in, 91–92, 92f
magnetic resonance imaging in, 94f
ultrasonography in, 91, 91f
of rectum, 108f
of spleen, 88–90, 89f–90f
of trachea, 68
Lacunar infarction, 15, 16f
Ladd's bands, 191
Ladd's procedure, 191–192
Laparotomy in penetrating abdominal trauma, 107–108
Laryngeal injuries, 44, 45f
Laryngotracheobronchitis, 44–58, 50f
in children, 44–58, 201–202, 202f
Lavage, peritoneal, in penetrating abdominal trauma, 108–109
Le Fort fractures, 39, 40f
Leukocytes, radionuclide-labeled, in infection imaging, 372–375
in orthopedic hardware, 181–182
Leukoencephalopathy, progressive multifocal, 33, 35f
Lipohemarthrosis in knee injuries, 144, 145f
Lisfranc injuries, 158, 158f
Lithiasis. *See* Calculi
Liver, 297–299
abscess of, 297–298, 298f, 375
hepatitis of, 298–299
hepatolithiasis of, 296–297, 297f
radionuclide scans of, 379–381
in abscess, 375
in trauma, 87–88, 87f
trauma of, 82–84
AAST classification of, 83, 83t
computed tomography in, 83–84, 84f–86f
contusion in, 82–83
hematoma in, 82–83, 83t, 84f
Liver *(Continued)*
laceration in. *See* Laceration, of liver
in penetrating injuries, 110f
scintigraphy in, 87–88, 87f
ultrasonography in, 82–84, 83f
vascular injuries in, 83–84, 83t, 85–86f
tumors of, hemoperitoneum in, 306, 306f
Lower extremity
trauma of, 137–159
arterial injuries in, 350–351, 351f
common locations of fractures in, 137f
vascular emergencies of
nontraumatic, 351–353
traumatic, 350–351, 351f
Ludwig's angina, 54–57, 57f
Lumbar spine fractures, 224, 224f
Lunate
avascular osteonecrosis of, 131
dislocation of, 131–133, 132f
spilled teacup sign in, 132–133, 132f
in dorsal intercalated segmental instability, 133
fracture of, 131
Kienbock's disease in, 131
in scapholunate dissociation, 132f, 133
in volar intercalated segmental instability, 133
Lungs
carcinoma of, metastatic to brain, 33f
chest radiography of, 234–235
in pneumonia, 235f
computed tomography of, 236
centrilobular opacities in, 236, 238f
tree-in-bud sign in, 236, 238f
contusion of, 65, 67f, 69f,
foreign body in, 202–203, 203f
herniation of, in rib or costochondral fractures, 74–75, 75f
laceration of, 65–66
compression rupture in, 65–66, 69f
nodular appearance in, 65–66, 69f
pneumatocele and hematocele in, 65, 68f
types of, 65–66, 69f
radionuclide scans of, 377
ventilation-perfusion. *See* Ventilation-perfusion scans
Luxatio erecta, 117–118
Lymphadenitis in children
cervical, 208
mesenteric, 195
Lymphadenopathy, cervical, 48
Lymphoma, 229, 230f

M
Magnetic resonance angiography
in aortic aneurysm, 331
in arterial emergencies, 321
in carotid artery dissection, 23, 24f
in ischemic stroke, 15, 14f
in pulmonary embolism, 254–255, 260–261, 261f
venography in, 254–255, 261
Magnetic resonance imaging
angiography technique. *See* Magnetic resonance angiography
in extremity trauma, 112
in intracranial hemorrhage, 2
in contusion, 6–7
in diffuse axonal injury, 8–9, 10f
intraventricular, 6, 9f
signal characteristics in, 2t

Magnetic resonance imaging *(Continued)*
subarachnoid, 6
subdural, 2–5
in ischemic stroke
diffusion-weighted imaging in, 15, 14f, 16f
perfusion imaging in, 15–17
in pancreatic trauma, 94f
in rotator cuff disorders, 164–165, 165f
in spine injuries, 215–217
Maisonneuve's fracture, 151–155, 153f
Male genitourinary disorders. *See* Genitourinary disorders, in male
Malgaigne injury, 138
Malleolus fractures, 151–155
Mallet finger, 136, 136f
Malrotation, intestinal, 191–192, 192f, 278
compared to normal appearance, 191, 191f
Mandibular fracture, 40–41, 42f
carotid artery injury in, 22f
Mastoiditis, 54, 54f–56f
in children, 208, 211
Maxillofacial fractures, 37–38
Meckel's diverticulum
in children, 194–195
radionuclide scans in, 378–379
of small bowel, 281–282, 282f
Meconium aspiration syndrome, 185, 185f
Meconium ileus, 187
Mediastinal disorders, 245
anatomy in, 245
infections, 245
masses, 245
pneumomediastinum, 245, 245f
in superior vena cava syndrome, 245, 246f
Mediastinitis, 245
Megacolon, 279
Meigs syndrome, 243
Meningiomas, spinal, 229
Meningitis, 25–27, 26f–27f, 231
in children, 206–207
Meningoencephalitis, 25–26
cryptococcal, 11f
Mesenteric arteries
aneurysm of, 342
vascular emergencies of, 339–345
Mesenteric injury, 93–97
hematoma in, 96–97, 96f–98f
hemorrhage in, 96–97, 98f
intraperitoneal fluid in, 95b
lacerations in, 96–97, 98f
in penetrating trauma, 107–110
stranding in, 96–97, 98f
Mesenteric ischemia, 290–291, 339–341
Mesenteric lymphadenitis in children, 195
Mesenteric venous thrombosis, 356
Metacarpal fractures, 135, 136f
of thumb, 133, 134f
Metacarpophalangeal joint dislocations, 135–136
Metastasis
to heart and pericardium, 244
of lung carcinoma to brain, 33f
Metatarsal fractures, 158–159, 159f
Metatarsophalangeal joint injuries, 159
Microcolon in neonates, 187
Mirizzi syndrome, 308
Monteggia fracture-dislocation, 124–126, 126f
Morphine in hepatobiliary scintigraphy, 380, 382f
Multiple sclerosis, 33, 34f
spinal cord disorders in, 231, 231f
Mumps orchitis, 311
Murphy's sign in cholecystitis, 294–295, 295f
Musculoskeletal disorders
in fractures. *See* Fractures
in infections, 174–182
Musculoskeletal disorders *(Continued)*
in orthopedic hardware, 180–182, 375
osteomyelitis in. *See* Osteomyelitis
radionuclide scans in, 376–377
in joint prosthesis, 376
in pediatric trauma, 208–212
Myeloma, multiple, 229, 230f

N
Nasal fractures, 39
Navicular fractures, 158
Neck. *See* Head and neck region
Necrosis
cortical laminar, in ischemic infarction, 17, 19f
in pancreatitis, 292
Neer classification of humerus fractures, 118
Neonates, 183–188
biliary atresia in, 380–381
emphysema in, pulmonary interstitial, 183–184, 184f
enterocolitis in, necrotizing. *See* Enterocolitis, necrotizing, in neonate
esophageal atresia in, 187, 187f
hepatitis in, 380–381
hypoxic-ischemic encephalopathy in, 15
intestinal obstruction in, 186–187, 186f–187f
meconium aspiration syndrome in, 185, 185f
meningitis in, 25–26
pneumomediastinum in, 183–184, 184f
pneumonia in, 184–185
pneumopericardium in, 183–184, 185f
pneumothorax in, 183–184, 184f
respiratory distress in, 183
surfactant deficiency disease in, 183, 183f
tachypnea in, transient, 184
urethral valves in, posterior, 185–186, 185f–186f
Nephrolithiasis, 299, 300f
in children, 196–197, 197f
urinary obstruction in, 308–309
Neuritis, optic, in multiple sclerosis, 34f
Neurocysticercosis, brain abscess in, 28–29, 30f
Neurocytoma, central, 32f
Neutropenic colitis, 288–289
Nonaccidental injuries in children, 211–212
metaphyseal fractures in, 211–212, 212f
radionuclide scans in, 377–378
rib fractures in, 211–212, 212f
skull fractures in, 204–205, 205f
Nuclear radiology, 361–383
in brain death diagnosis, 370–372, 371f–372f
equipment used in, 363–364, 364f
in gastrointestinal disorders
in hemorrhage, 378–379
in inflammatory bowel disease, 376
hepatobiliary. *See* Hepatobiliary scintigraphy
in infections, 372–377
in abdominal abscess, 375–376
indications for, 375
musculoskeletal, 376–377
in orthopedic hardware, 181–182, 375–376
in osteomyelitis, 373–377, 374f
radiopharmaceuticals in, 372–375
respiratory, 377
in inflammatory bowel disease, 376
in pulmonary embolism, 255–256, 256b, 364–369
high probability scan in, 368–369, 369f
low probability scan in, 369, 370f
repeated scans in, 369
radionuclides used in, 361–363
scrotal scans in, 381–383, 383f
in trauma, 377–378
of liver, 87–88, 87f

O
Occipital bone
in atlanto-occipital dislocation, 217, 218f
condyle fractures of, 217, 218f
Occipitomastoid suture, normal appearance of, 43, 45f
Odontoid process fracture, 219, 220f
Ogilvie syndrome, 279
Olecranon process fractures, 123–124, 125f
Omental infarction, 284–285
in children, 195
Optic neuritis in multiple sclerosis, 34f
Orbital fractures
blow-out, 38–39, 38f
of roof, 39
Orbital infections, 50–54
Orchitis, 311
radionuclide scans in, 383
Orthopedic hardware infections, 180–182, 375
radionuclide scans in, 181–182, 376
Os odontoideum, 222, 223f
Osteoarthritis
of acromioclavicular joint, 166
of hip, 172, 173f
Osteolysis of acromioclavicular joint, 165–166, 166f
Osteomyelitis, 177–180, 179f
radionuclide scans in, 373–377, 374f
of spine, 231–232
cervical, 45–47, 46f
Osteonecrosis, avascular
of femoral head, 170–172, 170t, 171–172f
double line sign in, 171–172, 172f
Ficat classification of, 170, 170t, 171f
radionuclide scans in, 377
of lunate, 131
Osteoporosis
of hip
fractures in, 168–169
transient, 169–170, 170f
thoracolumbar fractures in, 222–223
Otitis
externa, malignant, 54
media, in children, 208, 208f
Ovarian vein thrombosis, 317–318, 319f
Ovary
cyst of, hemorrhagic, 200, 313–314, 314f
torsion of, 314–315, 315f
in children, 199–200, 199f, 314
in tubo-ovarian abscess, 315–316, 316f

P
Pachymeningitis, 27, 27f
Pain
abdominal, 275–309. *See also* Abdominal pain
in chest, 234. *See also* Thoracic disorders
in hip, 168–173
in children, 211, 211f–212f
pelvic, 313
in pregnancy, 313, 317
scrotal. *See* Scrotal pain
in shoulder, 162–168
Pancreas
abscess of, 375
inflammation of, 291–294
trauma of, 91–93
computed tomography in, 91–92, 92f
contusion in, 91–92, 91f
differentiated from retroperitoneal fluid, 92–93, 93f
fluid collections in, 93, 94f
laceration in. *See* Laceration, of pancreas
magnetic resonance imaging in, 94f

Pancreas *(Continued)*
pseudoaneurysm in, 91–92, 93f
transection in, 91–92, 92f
ultrasonography in, 91, 91f
Pancreatitis
acute, 291–293, 292f–293f
necrosis in, 292
calcification in, 291–292, 291f
chronic, 291f, 293–294
gastroduodenal artery aneurysm and pseudoaneurysm in, 293f, 344f
splenic artery pseudoaneurysm in, 343f
Paranasal sinus infections, 50–54. *See also* Sinusitis
Parenchymal hemorrhage, 6–9
spontaneous (acute), 12, 12f, 13f
Parotid gland disorders, 47
Patella
alta, 148, 148f
baja, 148, 148f
dislocation of, 147f, 148
fractures of, 148, 148f
Pediatric emergencies, 183. *See also* Children
Pelvic disorders, 310–320
in female, 313–319
in male, 310–313
traumatic, 103–107
bladder injuries in, 103–105
fractures in. *See* Pelvic fractures
free fluid in, 98–99, 98f
hemorrhage in, 103, 104f, 139, 345–346, 346f
pseudoaneurysm in, 345–346, 347f
rectal injuries in, 107
urethral injuries in, 105–107
vascular emergencies in, 345–348
Pelvic fractures, 103, 138–139, 138b, 138f
in avulsion injuries, 138, 138f
classification of, 138, 139f
with hemorrhage, 103, 104f, 139, 345–346, 346f
with pelvic ring disruption, 138, 139f
Peptic ulcer disease, 276
gastric outlet obstruction in, 275
Pericardial disorders, 244–245
in chest trauma, 62
effusions, 244
hemopericardium, 62, 62f, 244, 244f
in malignancies, 244–245
pneumopericardium, 244
in neonates, 183–184, 185f
Pericarditis, 245
Perilunate dislocation, 131–132, 132f
Peritoneal fluid in abdominal trauma, 95, 98–99, 99f
Peritoneal hemorrhage in abdominal trauma, 79, 79f
Peritoneal lavage in abdominal trauma, 108–109
Peritonsillar abscess, 44–45
Phalangeal fractures
of foot, 159
Salter Harris, 209f
of hand, 136–137, 136f
in thumb, 133, 135f
Pharyngeal injuries, 43–44
Phenobarbital in hepatobiliary scintigraphy, 380
Phlegmon, 176
Pillar fracture of cervical spine in hyperextension injury, 221, 222f
PIOPED study, 254–256, 256b, 368
Pituitary hemorrhage, 6
Plasminogen activator, tissue, in ischemic stroke, acute, 12–15
Pleural disorders, 242–244
in chest trauma, 60
chylothorax, 244
Pleural disorders *(Continued)*
effusions, 243
etiologies of, 243, 243t
empyema, 244
hemothorax, 60, 61f, 243–244
pneumothorax. *See* Pneumothorax
Pneumatocele in lung laceration, 65, 68f
Pneumatosis intestinalis in necrotizing enterocolitis of neonate, 187–188, 188f
Pneumohemarthrosis in knee injuries, 144, 145f
Pneumomediastinum, 245
computed tomography in, 242, 245f
in neonates, 183–184, 184f
in tracheobronchial injuries, 66–68, 70–71f
Pneumonia
chest radiography in, 235f
in children, 203, 204f
neonatal, 184–185
Pneumopericardium, 244
in neonates, 183–184, 185f
Pneumoperitoneum, 305, 305f
in necrotizing enterocolitis of neonate, 187–188
Pneumothorax, 242–243
in chest trauma, 60, 61f
in children, 204, 204f
neonatal, 183–184, 184f
etiologies of, 242, 242t
spontaneous, 242
tension, 242–243
Polyps, endometrial, 318–319
Popliteal artery aneurysm, 353–354
Portal vein
thrombosis of, 356, 356f
trauma of, 83–84, 86f
Postpartum period
hemorrhage in, 317
retained products of conception in, 317
Pott's puffy tumor, 50–52, 52f
Pregnancy
appendicitis in, 283, 284
computed tomography in, 238, 313
ectopic, 317, 317f–318f
pelvic pain in, 313, 317
pulmonary embolism in, 365
Pronator quadratus sign in radius and ulna injuries, 124
Prostate abscess, 313, 313f
Prostatitis, 313, 313f
Pseudoaneurysm
in aortic injuries, 64f–66f, 323–326, 323f, 326f–327f
in aortic reconstruction, 251, 253
of carotid artery, 322, 322f
of femoral artery, 351, 352f
of gastroduodenal artery, 293f
in hepatic arterial injuries, 83–84, 86f
in pancreatic trauma, 91–92, 93f
in pancreatitis, 292, 293f
in pelvic trauma, 345–346, 347f
of splenic artery, 343f
in splenic trauma, 88–90, 90f
Pseudocyst, pancreatic, 292–293
Pseudogout
of shoulder, 162–163, 163f
of spine, 228, 229f
Pseudomeningocele, 226–228, 228f
in cervical root avulsion, 225, 226f
Pseudosubluxation of glenohumeral joint, 118
Pseudotumor cerebri, 25
Pubic fractures, 138, 139f
Pulmonary artery computed tomography angiography, in triple rule-out, 242, 271
Pulsation artifact in computed tomography angiography, 240, 241f
Pyelitis, emphysematous, 302–303
Pyelonephritis, 299–300
in children, 195–196
emphysematous, 300–301
renal abscess in, 300
xanthogranulomatous, 301–302, 302f
Pyloric stenosis, hypertrophic, 189–191
caterpillar stomach in, 189–190, 190f
compared to normal pylorus, 189–190, 190f
nipple sign in, 189–190, 190f
string sign in, 190, 191f
Pyonephrosis, 302
Pyosalpinx, 315–316, 316f

R
Radiation exposure in computed tomography, 239
Radiography, conventional
in aortic traumatic injury, 324
in extremity trauma, 112
in intussusception, 192, 192f–193f
in pulmonary embolism, 255, 255f–256f, 368–369, 368f
in shoulder pain, 162
in thoracic disorders, 234–236, 235f
in heart failure, 235–236, 237f
interpretation of, 234, 235f
in pneumonia, 235f
Radionuclide scans, 361–383. *See also* Nuclear radiology
Radioulnar joint, distal, in Galeazzi fracture-dislocation, 126, 126f
Radius
dislocation of, 124, 125f
in children, 211
fractures of
buckle, 128f, 129, 210f
distal and shaft, 124–129, 125b
pronator quadratus sign in, 124
proximal, 122–124, 125f
Salter Harris, 209f
in ulnar styloid process, 128
in Galeazzi fracture-dislocation, 126, 126f
in Monteggia fracture-dislocation, 124–126, 126f
Rectal injury, 94b, 107, 108f
Red blood cells, technetium-99m labeled, in gastrointestinal bleeding, 290, 378, 379f
Reflux, vesicoureteral, 186, 196
Renal artery disorders
aneurysm, 345
ischemic, 344, 345f
traumatic, 343–344, 344f
iatrogenic, 344, 344f
Renal vein thrombosis, 303, 355–356
Respiratory disorders
chest radiography in, 235f,
in children, 200–204
neonatal, 183
computed tomography in, 236
in foreign body aspiration, 202–203, 203f
in pneumonia. *See* Pneumonia
in pulmonary embolism. *See* Embolism, pulmonary
radionuclide scans in, 377
Respiratory distress in neonates, 183
Retained products of conception, 317
Retroperitoneal fluid differentiated from pancreatic injury, 92–93, 93f
Retroperitoneal hemorrhage, 306–308, 307f
Retropharyngeal infections, 45, 46f
in children, 200–201, 201f

Rheumatoid arthritis
of glenohumeral joint, 167, 167f
of hip, 172, 174f
of spine, 228
Ribs
dislocation of, 224
fractures of, 74
in children, in nonaccidental injury, 211–212, 212f
flail chest in, 74, 75f
lung herniation in, 74–75, 75f
Rolando fracture of thumb, 133, 134f
Rotator cuff disorders, 163–165, 164f–165f
calcific tendinitis, 162
chronic tear, 164, 164f
critical zone in, 163–165
impingement, 163–164, 164f
magnetic resonance imaging in, 164–165, 165f
ultrasonography in, 164, 165, 166f

S
Sacral fractures, 139, 139f–140f, 224
Sail sign in elbow injuries of children, 211, 211f
Salivary gland disorders, 47, 47f
Salter Harris fractures, 208–209, 209f–210f
Sarcoidosis, 231
Scaphoid
fracture of, 129, 130f
rotatory subluxation of, 132f, 133
Scapholunate dissociation, 132f, 133
Terry Thomas sign in, 132f, 133
Scapula fractures, 113–114, 113b, 114f
Schatzker classification of tibial plateau fractures, 148–151
Scintigraphy. *See* Nuclear radiology
Scrotal pain
in epididymitis, 311, 311f
in children, 198, 198f
radionuclide scans in, 383
in inguinal scrotal hernias, 311–312
in children, 197–198, 197f
in orchitis, 311, 383
radionuclide scans in, 381–383, 383f
in testicular appendage torsion, 310–311, 311f
in children, 198, 198f, 310–311, 311f
in testicular torsion, 310, 310f, 383, 383f
in children, 198–199, 199f
in trauma, 312
Segond fracture, 151, 152f
Septic arthritis, 176
of hip, in children, 211, 211f, 377
radionuclide scans in, 176, 377
of shoulder, 178f
Septic thrombophlebitis
cavernous sinus, 53–54
in mastoiditis, 56f
of ovarian vein, 318, 319f
Shock, hypovolemic, in bowel injuries, 99, 99f
Shoulder
acromioclavicular joint disorders of, 165–166
in trauma, 115, 115b, 115f
calcific bursitis/tendinitis of, 162–163, 163f
calcium hydroxyapatite deposition disease of, 162–163, 163f
frozen, 167–168
glenohumeral joint disorders of, 166–168. *See also* Glenohumeral joint
impingement in, 163–164, 164f
osteoarthritis of, 166
pain in, 162–168
rheumatoid arthritis of, 167, 167f
rotator cuff disorders of. *See* Rotator cuff disorders
Shunts, ventriculoperitoneal, in hydrocephalus, 25, 25f
Sialolithiasis, 47
Sickle cell disease
acute chest syndrome in, 203
spleen in, 304
Sinus infections, paranasal, 50–54. *See also* Sinusitis
Sinus thrombosis, cerebral venous, 17–20, 19f
in children, 206, 206f
in ear infections, 54–57, 56f
in paranasal sinus infections, 53–54
Sinusitis, 50–54
abscess formation in, 50–52, 51f–52f
allergic fungal, 50, 51f
ethmoid, 52, 53f
frontal, 50–52, 51f
Pott's puffy tumor in, 50–52, 52f
venous sinus thrombosis in, 53–54
Skier's thumb, 133, 135f
Skull fractures, 37, 37f
in children, 204–205, 205f
differentiated from normal cranial sutures, 204–205, 205f
in nonaccidental injury, 204–205, 205f
Slipped capital femoral epiphysis, 211, 212f
Small intestine
Crohn's disease of, 281, 282f
diverticulitis of, 281–282, 282f
enteritis of, 280–281, 281f
intussusception of, 278, 279f
obstruction of, 276–278, 277f–279f
closed loop, 277
peptic ulcer disease of, 276
trauma of, 93–94, 94b
hypovolemic shock in, 99, 99f
volvulus of, 278–279
Smash fracture of face, 40, 41f
Smith fracture, 126–128, 127f
Soft tissue infections, 174–176
abscess in, 175–177f, 176
cellulitis in, 174. *See also* Cellulitis
necrotizing fasciitis in, 174–175, 175f
Sonography. *See* Ultrasonography
Spinal cord
infections of, 231–232, 232f
inflammatory/demyelinating disorders of, 231
in multiple sclerosis, 231, 231f
trauma of, 224–226
cervical root avulsion in, 225, 226f
edema in, 224–225
hemorrhage and hematoma in, 225–226, 227f–228f
pseudomeningocele in, 225, 226f
without radiographic abnormality, 224
vascular disorders of, 232
Spine
ankylosing spondylitis of, 220–221, 220f
calcium pyrophosphate deposition disease of, 228, 229f
congenital disorders of, 226
degenerative disorders of, 226–228
discitis and osteomyelitis of, 231–232, 232
cervical, 45–47, 46f
rheumatoid arthritis of, 228
trauma of, 215–226
cervical. *See* Cervical spine, trauma of
in children, 207–208, 216
computed tomography in, 215–217
decision rules and imaging algorithms on, 215–216
instability in, 217
magnetic resonance imaging in, 215–217
mechanisms of injury in, 217, 217b
patterns of injury in, 216–217
Spine *(Continued)*
thoracic fractures in, 76, 77
thoracolumbar. *See* Thoracolumbar spine trauma
tuberculous spondylitis of, 232
tumors of, 229–231, 230f–231f
types of, 216
Splanchnic vascular trauma, 339–345
Spleen, 303–304
abscess of, 303–304
infarction of, 304
in sickle cell disease, 304
torsion of, 304
trauma of, 88–90, 339
AAST classification of, 88, 88t
computed tomography in, 88–90, 89f–90f
hematoma in, 88–90, 89f–90f
laceration in, 88–90, 89f–90f
pseudoaneurysm in, 88–90, 90f
shattered tissue in, 90f
ultrasonography in, 88, 89f
Splenic artery aneurysm, 342, 343f
Spondylitis
ankylosing
of cervical spine, 220–221, 220f
of hip, 172–173, 174f
tuberculous, 232
Spondyloarthropathy, seronegative, of hip, 172–173
Stab wounds
abdominal injuries in, 107–110
aortic injury in, 326, 327f, 336
Stent placement
in aorta, 252–253, 253f
in aneurysm, 332, 335, 336f
in traumatic injury, 326, 327, 327f, 336–337
in carotid artery pseudoaneurysm, 322, 322f
in hepatobiliary injuries, 87–88, 87f
in ureteral trauma, 102f
Sternal fractures, 75, 76f, 77f
Sternoclavicular joint dislocation, 75, 76f
Stomach
outlet obstruction, 275–276
peptic ulcer disease of, 276–277
pyloric stenosis of, hypertrophic, 189–191, 190f
trauma of, 93–94, 94b
volvulus of, 276
Straight sinus thrombosis, 206f
Stress fractures of hip, 168–169
Stridor in children, 200–204
Stroke, 12. *See also* Cerebrovascular disorders
Subarachnoid hemorrhage, 5–6, 7f, 8f
in aneurysm rupture, 5–6, 7f, 20–21, 20f
computed tomography in, 6, 7f–8f, 20–21, 20f
in intracranial arterial dissection, 23–24
magnetic resonance imaging in, 6
in spinal cord trauma, 226, 228f
and subdural hematoma, 2–4, 5–6
Subclavian artery disorders, 349f–350f
Subdural abscess in sinusitis, 51f
Subdural hemorrhage, 2–5, 5f
calcification in, 4–5, 6f
Subfalcine herniation, 10
Subglottic masses in children, 202, 202f
Subluxation
of glenohumeral joint
inferior, 117–118
and pseudosubluxation, 118
of scaphoid, rotatory, 132f, 133
Submandibular gland disorders, 47
Substance abuse
intracranial parenchymal hemorrhage in, 12, 13f
neck abscess in, superficial, 48
toxic encephalopathy in, 35–36, 36f

Subtalar dislocation, 156, 157f
Supracondylar fractures of humerus, 121, 121f
  in children, 211, 211f
Supraspinatus tendon
  critical zone of, 163–165
  tear of, 165, 166f
Surfactant deficiency disease in neonates, 183, 183f
Synovitis, pigmented villonodular, of hip, 173
Syphilis
  aortic aneurysm in, 331
  aortitis in, 246

T
Tachypnea in neonates, transient, 184
Talus
  dislocation of, 156
  fracture of, 156, 157f
    Hawkins' classification of, 156
Tamponade, cardiac, 244
Tarsometatarsal joint injuries, 158, 158f
Teardrop fracture of cervical spine, 215, 221f
Technegas, 368
Technetium 99m, 361–363, 362f
  in brain death diagnosis, 370–371, 371f–372f
    interpretation of, 371–372
    technique in, 371
  diethylene triamine penta-acetic acid (DTPA)
    in brain death diagnosis, 370–372
    in lung scans, 367, 367f, 369f
  ethyl cysteinate dimer (ECD), in brain death diagnosis, 370–371, 371f, 372f
  in hepatobiliary scans, 380, 381f–382f
  hexamethyl-propylene oxime (HMPAO)
    in brain death diagnosis, 370–372
    leukocytes labeled with, in infections, 372–373, 374f
  in infections, 372–374, 374f
  in lung scans, 365, 366f, 370f
    in aerosol studies, 367, 367f
    in pulmonary embolism, 255–256, 365, 369f
  macroaggregated albumin, 365, 369f
  methylene diphosphonate (MDP)
    in joint prosthesis disorders, 376
    in osteomyelitis, 373, 374f, 377
    in soft tissue infections, 376f
  in orthopedic hardware infections, 181–182, 376
  pharmaceuticals tagged with, 362b
  red blood cells labeled with, in gastrointestinal bleeding, 290, 378, 379f
  in scrotal scans, 381–383
  sulfur colloid, 374
    in gastrointestinal bleeding, 290, 378
Temporal bone fractures, 41–43
  carotid artery injury in, 42–43, 44f
  complex, 41, 42f
  longitudinal, 42–43, 43f
  transverse, 43
Temporomandibular joint dislocation, 41
Tendinitis of rotator cuff, calcific, 162
Teratoma, ovarian, 199f
Testicular appendage torsion, 310–311, 311f
  in children, 198, 198f, 310–311, 311f
Testis
  in cryptorchidism, 197–198, 312–313, 312f
  radionuclide scans of, 381–383, 383f
  torsion of, 310, 310f
    in children, 198–199, 199f
    hello sign in, 383, 383f
    radionuclide scans in, 383, 383f
  trauma of, 312
Thoracic disorders, 234–274
  of aorta, 246–253. *See also* Aorta, thoracic
  computed tomography in. *See* Computed tomography, in thoracic disorders
  of coronary artery, 261–271
  differential diagnosis in, 234
  in esophageal injury, 242
  in heart failure, 235–236
    chest radiography in, 235–236, 237f
  mediastinal, 245
  pericardial, 244–245
  pleural, 242–244
  in pneumomediastinum, 242
  in pneumonia, 235
    chest radiography in, 235f
  in pulmonary embolism, 239–240, 253–261
    imaging techniques in, 255–261
  radiography in, 234–236, 235f
    in heart failure, 235–236, 237f
    interpretation of, 234, 235f
    in pneumonia, 235f
  in trauma, 60–78. *See also* Chest trauma
  in vena cava syndrome, superior, 354
Thoracic outlet syndrome, 357
Thoracic spine fractures, 76, 77
Thoracolumbar spine trauma, 222–224
  calcaneal fracture in, 223, 224f
  Chance fracture in, 223, 225f
  compression fractures in, 222–223, 224f
  decision rules and imaging algorithms on, 215–216
Thrombectomy in acute ischemic stroke, 17, 18f
Thrombolytic therapy
  in deep vein thrombosis, 357–358, 358f
  in iliac artery thrombosis, 347f, 348
  in ischemic stroke, acute, 12–15
  in lower extremity ischemia, 353, 353f
    contraindications to, 353, 353b
Thrombophlebitis, septic
  cavernous sinus, 53–54
  in mastoiditis, 56f
  of ovarian vein, 318, 319f
Thrombosis
  aortic, 338, 339f
  cerebral arterial
    thrombectomy in, 17, 18f
    thrombolytic therapy in, 12–15
  cerebral venous sinus, 17–20, 19f
    in children, 206, 206f
    in ear infections, 54–57, 56f
    in paranasal sinus infections, 53–54
  deep venous, 357–358, 358f
    pulmonary embolism in, 254, 357–358. *See also* Embolism, pulmonary
  hepatic vein, 357
  iliac artery, 346–347, 347f, 348
  lower extremity
    arterial, 351
    venous, 357–358, 358f
  mesenteric venous, 356
  ovarian vein, 317–318, 319f
  portal vein, 356, 356f
  renal vein, 303, 355–356
  upper extremity
    arterial, 240
    venous, 253–254
  vena cava obstruction in, inferior, 354–355, 355f
Thumb injuries, 133, 134f–135f
  carpometacarpal dislocation in, 133–135
  metacarpal fracture in, 133, 134f
  phalangeal fracture in, 133, 135f
Thyroglossal duct cyst, 47–48
Thyroid gland disorders, 47–48
  cervical lymphadenopathy in, 48
Thyroiditis, 47
Tibia fractures
  plafond (pilon), 153f–154f, 155
  in plateau, 148–151, 150f
  Salter Harris classification of, 208–209, 209f–210f
  Schatzker classification of, 148–151
  Segond, 151, 152f
  in toddlers, 209–210, 210f
  triplane, 155–156, 155f, 208–209, 209f
Tillaux fracture, 155, 155f, 208–209, 210f
Tissue plasminogen activator in ischemic stroke, 12–15
Toddler's fractures, 209–210, 210f
Tonsillar herniation of brain, 11, 11f
Tonsils, enlarged, in children, 201, 201f
Torsion
  ovarian, 199–200, 199f, 314–315, 315f
  splenic, 304
  testicular, 310, 310f
    in children, 198–199, 199f
    hello sign in, 383, 383f
    radionuclide scans in, 383, 383f
  testicular appendage, 310–311, 311f
    in children, 198, 198f, 310–311, 311f
Torus fractures, 209–210
  of radius, 128f, 129, 210f
Toxic encephalopathy, 35–36, 36f
Toxoplasmosis, brain abscess in, 29f
Trachea laceration, 68
Tracheobronchial injuries, 66–69, 70f, 71f
Transalar brain herniation, 12
Transient ischemic attack, 12
Transtentorial herniation, 4f, 11
Trauma
  abdominal, 79–111. *See also* Abdominal trauma
  of acromioclavicular joint, 115, 115b, 115f
    osteolysis in, 165–166, 166f
  of aorta. *See* Aorta, traumatic injury of
  of carotid arteries
    extracranial, 321–322, 322f
    in mandibular fracture, 22f
    in temporal fracture, 42–43, 44f
  of chest, 60–78. *See also* Chest trauma
  in children, 208–212
    nonaccidental injuries in. *See* Nonaccidental injuries in children
  of esophagus, 60–62, 242
  of foot. *See* Foot, trauma of
  fractures in. *See* Fractures
  of glenohumeral joint. *See* Glenohumeral joint, trauma of
  of hand. *See* Hand injuries
  of head and neck. *See* Head and neck region, trauma of
  of kidneys. *See* Kidneys, trauma of
  of knee. *See* Knee injuries
  of liver. *See* Liver, trauma of
  of lower extremity, 137–159
    arterial injuries in, 350–351, 351f
    common locations of fractures in, 137f
  mesenteric. *See* Mesenteric injury
  of pancreas. *See* Pancreas, trauma of
  radionuclide scans in, 377–378
    hepatobiliary, 87–88, 87f
  of renal arteries, 343–344, 344f
  of spinal cord, 224–226
  of spine, 215–226
  of spleen. *See* Spleen, trauma of
  testicular, 312
  of upper extremity, 113–137
    arterial injuries in, 348–349, 348b–349b, 349f–350f
    common locations of fractures in, 113f

Trauma *(Continued)*
of urethra. *See* Urethral injury
of vena cava, inferior, 355
Triplane fractures of tibia, 155–156, 155f, 208–209, 209f
Triquetral fracture, 129–131, 131f
Trochanteric fractures of femur, 143f, 144
Tuberculosis
cervical lymphadenopathy in, 48
colitis in, 288
spondylitis of, 232
Tubo-ovarian abscess, 315–316, 316f
Tumors
biliary obstruction in, 308, 309f
of brain, 29–31
cervical lymphadenopathy in, 48
endometrial, 318–319
of heart and pericardium, 244–245
of kidney, vascular emergencies in, 345, 345f
of liver, hemoperitoneum in, 306, 306f
of lung, metastatic to brain, 33f
of spine, 216, 229–231, 230f–231f
Tympanosquamous suture, normal appearance of, 43, 45f
Typhlitis, 288–289

U
Ulcerative colitis, 286–288, 287f
fat halo sign in, 286–287, 287f
Ulcers
aortic, 249f, 250–252, 250f
endovascular repair of, 253f
of stomach and duodenum, in peptic ulcer disease, 276
Ulna
dislocation of, 124, 125f
fractures of
distal and shaft, 124–129, 125b
pronator quadratus sign in, 124
in Galeazzi fracture-dislocation, 126, 126f
in Monteggia fracture-dislocation, 124–126, 126f
Ulnar styloid process fractures of radius, 128
Ultrasonography
in abdominal injuries
blunt, 79, 79f
FAST scan in, 79, 79f
of gallbladder, 86
of kidney, 100, 100f
of liver, 82–83, 83f
of pancreas, 91, 91f
penetrating, 109
of spleen, 88, 89f
in intussusception in children, 192–193, 193f
in rotator cuff disorders, 164, 165, 166f
Uncal herniation, 4f, 11
Upper extremity
thrombosis in, 240
trauma of, 113–137
Upper extremity *(Continued)*
arterial injuries in, 348–349, 348b–349b, 349f–350f
common locations of fractures in, 113f
vascular emergencies of
aneurysms, 350–351
nontraumatic, 349–350
traumatic, 348–349, 348b–349b, 349f–350f
venous, 357
Ureterolithiasis, 299, 300f
in children, 196–197, 197f
Ureteropelvic junction obstruction, 196, 196f
Ureters
calculi in, 299, 300f
in children, 196–197, 197f
trauma of, 102, 102f
computed tomography in, 102, 102f
Urethral injury, 105–107, 107f
anterior, 105
posterior, 105
retrograde urethrography in, 105–107, 107f
Urethral valves, posterior, in neonates, 185–186, 185f–186f
Urethrography, retrograde, in urethral injury, 105–107, 107f
Urography, intravenous, in ureteral injury, 102
Urolithiasis in children, 196–197, 197f
Uterus
bleeding from, 313, 318–319
postpartum, 317
endometrial carcinoma of, 318–319
endometrial polyps of, 318–319
endometriosis of, 315
endometritis of, 316–317
fibroids of, 318–319

V
Vascular emergencies, 321–359
arterial, 321–354. *See also* Arterial emergencies
venous, 354–358. *See also* Venous emergencies
Vena cava
inferior
obstruction of, 354–355, 355f
trauma of, 355
superior, syndrome of, 245, 246f, 354
computed tomography in, 240, 240f, 245, 246f
Venography
computed tomography, in pulmonary embolism, 254–255, 260
magnetic resonance, in pulmonary embolism, 254–255, 261
Venous emergencies, 354–358
of abdomen, 354–357
of chest, 354
in jugular vein trauma, 354
of lower extremity and pelvis, 357–358
of upper extremity, 357
Ventilation-perfusion scans, 364–369
aerosol studies in, 367, 367f
in pulmonary embolism, 255–256, 256b, 364–369
high probability scan in, 368–369, 369f
low probability scan in, 369, 370f
repeated scans in, 369
radiopharmaceuticals and techniques in, 365–369
Ventricles, cardiac, right, enlargement in pulmonary embolism, 259–260, 260f
Ventriculoperitoneal shunt in hydrocephalus, 25, 25f
Vertebral arteries
dissection of, 21–23
intracranial, 23–24
spontaneous, 322–323
trauma of, extracranial, 321–322
Visceral arteries
aneurysms of, 342–343
vascular emergencies of, 339–345
Vocal cord injuries, 44
Volar plate injury of hand, 136f, 137
Volvulus
of colon, 280
midgut, 191–192, 278–279
of small intestine, 278–279
of stomach, 276

W
White blood cells, radionuclide-labeled, in infections, 372–375
in orthopedic hardware, 181, 182
White matter disorders, 31–35
Wrist injuries
carpal fractures and dislocations in, 129–133, 130b
radius fractures in, 126–129

X
Xenon-133 scans, 363
of lungs, 365–367, 366f, 370f
in pulmonary embolism, 255–256, 365–367

Y
Young-Burgess classification of pelvic fractures, 138

Z
Zygomaticomaxillary complex fractures, 39, 40f